ICAME 2005

Proceedings of the 28th International Conference
on the Applications of the Mössbauer Effect (ICAME 2005)
held in Montpellier, France, 4-9 September 2005

Volume II (Part III-V/V)

Edited by
P.-E. Lippens
J.-C. Jumas and
J.-M. R. Génin

Springer

ICAME 2005

Proceedings of the 28th International Conference on the Applications of the Mössbauer Effect (ICAME 2005) held in Montpellier, France, 4–9 September 2005

Volume II *(Part III–V/V)*

Edited by

P.-E. LIPPENS

Université Montpellier II - CNRS, Montpellier, France

J.-C. JUMAS

Université Montpellier II - CNRS, Montpellier, France

and

J.-M. R. GÉNIN

Université Henri Poincaré-Nancy I, Villers-lès-Nancy, France

Reprinted from *Hyperfine Interactions*
Volume 167, Nos. 1–3 (2006)
Volume 168, Nos. 1–3 (2006)
Volume 169, Nos. 1–3 (2006)

Springer

A C.I.P. Catalogue record for this book is available from the Library of Congress.

ISBN 3-540-49852-0

Published by Springer
P.O. Box 990, 3300 AZ Dordrecht, The Netherlands

Sold and distributed in North, Central and South America
by Springer
101 Philip Drive, Norwell, MA 02061, U.S.A.

In all other countries, sold and distributed
by Springer
P.O. Box 990, 3300 AZ Dordrecht, The Netherlands

Printed on acid-free paper

Table of Contents

Hyperfine Interact (2006) 167:709–715
DOI 10.1007/s10751-006-9479-y

Synchrotron Mössbauer reflectometry using stroboscopic detection

L. Deák · L. Bottyán · R. Callens · R. Coussement · M. Major · I. Serdons · Y. Yoda

Published online: 7 December 2006

Abstract The concept of the heterodyne/stroboscopic detection of nuclear resonance scattering of synchrotron radiation is extended to the grazing incidence geometry. Model calculations for an antiferromagnetic $[^{57}Fe/Cr]_{20}$ multilayer are shown and discussed. Principles and methodological aspects of stroboscopic synchrotron Mössbauer reflectometry are briefly reviewed.

Key words magnetic multilayers · Mössbauer reflectometry · nuclear resonant scattering of synchrotron radiation

1 Introduction

Synchrotron Mössbauer Reflectometry (SMR), the grazing incidence nuclear resonant scattering of synchrotron radiation, can be applied to perform depth-selective phase analysis and to determine the isotopic and magnetic structure of thin films and multilayers [1–5]. SMR is established in the time and angular regime and combines the sensitivity of Mössbauer spectroscopy to hyperfine interactions with the depth information yielded by reflectometry. The specular SMR measurement is performed in the θ–2θ geometry, in either the time integral (TISMR) or the time differential regime (TDSMR). TISMR means recording the total number of delayed photons within a time interval lasting from t_1 to t_2 as a function of the incident grazing angle θ.t_1 is typically a few nanoseconds, depending on the bunch quality of the radiation source and on the dead time of the detector and the electronics. t_2 is a value somewhat below the bunch repetition time of the storage ring. As a

L. Deák (✉) · L. Bottyán · M. Major
KFKI Research Institute for Particle and Nuclear Physics, P.O.B. 49, 1525 Budapest, Hungary
e-mail: deak@rmki.kfki.hu

R. Callens · R. Coussement · I. Serdons
K.U. Leuven Instituut voor Kern – en Stralingsfysica, Celestijnenlaan 200 D, 3001 Leuven, Belgium

Y. Yoda
SPring-8 JASRI, 1-1-1 Kouto Mikazuki-cho Sayo-gun, Hyogo 679-5198, Japan

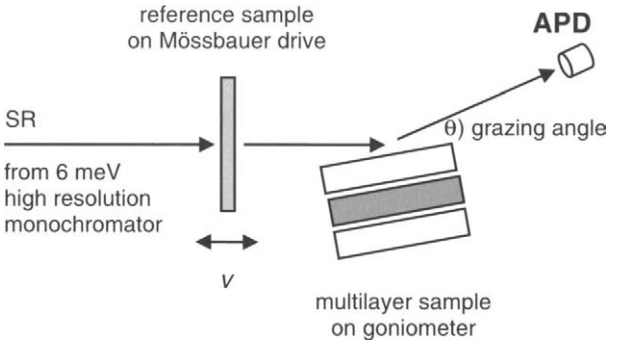

Figure 1 Experimental setup for stroboscopic synchrotron Mössbauer reflectometry.

rule, a θ–2θ scan of the *prompt* photons (conventionally called X-ray reflectometry) is recorded along with a delayed time integral SMR scan. TDSMR consists of a time response measurement at a fixed θ–2θ geometry, performed at different values of θ. Like in the forward scattering case, the presence of hyperfine interactions gives rise to quantum beats in the time response.

2 The stroboscopic synchrotron Mössbauer reflectometry

The heterodyne detection of nuclear resonant *forward* scattering of SR has been suggested by Coussement et al. [6, 7]. In the heterodyne setup, two scatterers are present, the investigated one and an additional single-line Mössbauer absorber, the latter acting as reference sample. The reference sample is mounted on a Mössbauer drive, as shown in Figure 1. The radiation *coherently* scatters on both the sample and reference, as if the two scatterers were a single absorber. The total number of the delayed scattered photons is recorded as a function of the velocity v of the reference absorber. This experimental scheme has the advantage that it is not sensitive to the time structure of the SR. Moreover, it provides energy resolved spectra, similar to those in the usual energy-domain Mössbauer spectroscopy.

Since the heterodyne spectrum is the total number of the delayed scattered photons, it can only be recorded if the prompt radiation is sufficiently reduced, e.g., by a polarizer/analyzer [7] Another approach is detecting the number of delayed counts, integrated over a well-defined time window, as a function of Doppler velocity v of the reference sample. This is called stroboscopic detection (SD) [8, 9]. For stroboscopic experiments, the period length t_p of the observation time window is specially chosen so that

$$\varepsilon = h/t_p, \tag{1}$$

i.e., the Planck constant h times the observation frequency $1/t_p$, has the same order of magnitude as the hyperfine splitting of the investigated sample. The periodic time gating results in a new type of resonances. They appear at Doppler velocities shifted from the Mössbauer resonances of the sample by any integer number m times h/t_p, and are called mth-order stroboscopic resonances [8, 9].

In forward scattering geometry, the prompt electronic scattering *homogeneously* contributes to the stroboscopic spectrum. Therefore, it does not affect the spectral shape. However, in grazing incidence, the stroboscopically detected SMR line shape is

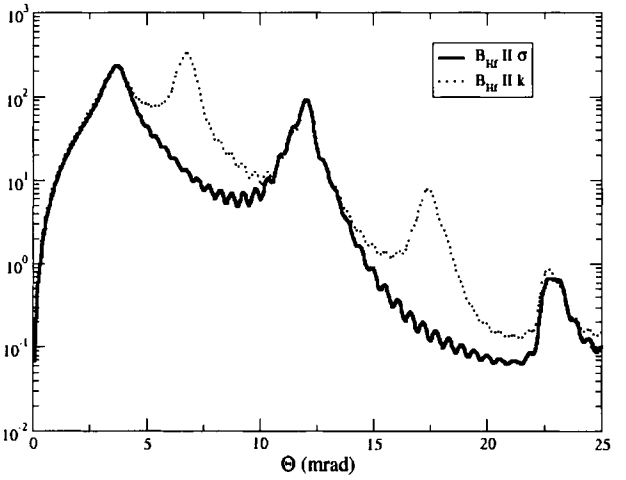

Figure 2 Simulations for TISMR spectra of ^{57}Fe/Cr AF multilayer for different orientations of the hyperfine field.

considerably influenced by the interference between the nuclear and the electronic scattering [10].

The intensity expression of heterodyne/stroboscopic SMR [10] reads

$$I(v,\theta) \propto \sum_{m=-\infty}^{\infty} s_m \int_{-\infty}^{\infty} \mathrm{d}E \mathrm{Tr}\left\{\left[T^{+}(E+m\varepsilon, E_v) - T_{\infty}^{+}\right]\cdot\left[T(E,E_v) - T_{\infty}\right]\rho\right\}, \qquad (2)$$

where m is the integer number indicating the stroboscopic order, s_m is the mth discrete Fourier coefficient of the applied time window function [8, 9] and ρ is the polarization density matrix [11] of the synchrotron source. T is the *total scattering matrix* [12] of the sample-reference system [10]. This matrix depends on the energy E and also on the Doppler energy shift E_v caused by the movement of the reference. Note that the γ-photons coherently scatter on both the atomic electrons and the resonant Mössbauer nuclei. Therefore, scattering matrices have a resonant nuclear and nearly energy-independent electronic contribution. Consequently, for energies being far from the Mössbauer resonances, $E \rightarrow \pm\infty$ on a hyperfine scale, the individual scattering matrices approach their non resonant electronic contribution, T_{∞}. The mth term in the sum of Eq. 2 is called the mth order stroboscopic spectrum component [9]. Indeed, according to Eq. 2, one finds additional resonance lines at energies $E_v = E_i \pm m\varepsilon$ [8–10]. For the interpretation of the stroboscopic spectra, it is useful to express ε in units of mm/s:

$$\varepsilon[\mathrm{mm/s}] = 1000\frac{\lambda[\mathrm{nm}]}{t_{\mathrm{p}}[\mathrm{ns}]}, \qquad (3)$$

where λ is the wavelength of the radiation in units of nm. For the Mössbauer transition of ^{57}Fe in α-iron at room temperature, $\lambda \approx 0.086$nm, the outer line separation of the Mössbauer lines is 10.62 mm/s. It follows from Eq. 3, that choosing t_{p}=8 ns, ε approximately overlaps with the separation between the outer Mössbauer lines. Therefore, choosing this time window period gives rise to an adequate separation of the stroboscopic

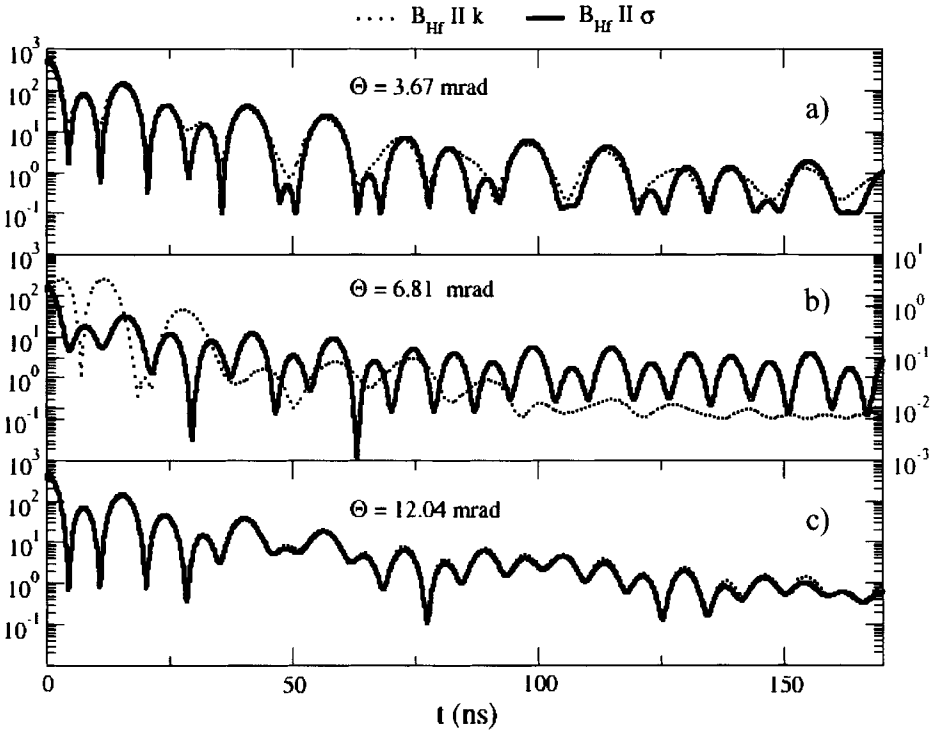

Figure 3 Simulations for TDSMR spectra of ^{57}Fe/Cr AF multilayer for B_{Hf} parallel to the wave vector $\boldsymbol{k}$ (*dotted line*) and B_{Hf} parallel to the σ-polarization (*solid line*) at three different grazing angles. The *right side axis* corresponds to the B_{Hf} parallel to direction of the σ-polarization case at the AF-Bragg position, where having no AF-Bragg peak, the intensity is by two orders of magnitude lower.

resonances. Using Eq. 2 and applying the optical theory of SMR [1, 13], the theoretical expression of stroboscopic SMR is straightforward [10].

3 Results and discussion

The code was merged into the EFFI program [14] and was used for some model simulations of stroboscopic SMR spectra of a MgO/[^{57}Fe(2.6 nm)/Cr(1.3 nm)]$_{20}$ anti-ferromagnetic (AF) multilayer. First the corresponding TISMR curves are considered. Those yield information on the alignment of the individual sublayer magnetization. If there is AF coupling between the Fe layers, TISMR spectra may reveal magnetic multilayer period doubling. This results in additional Bragg peaks, called AF-Bragg peaks.

Figure 2 shows the corresponding TISMR spectra for two different orientations of the hyperfine filed, B_{Hf} being parallel/anti-parallel to the propagation of the SR (direction $\boldsymbol{k}$) and B_{Hf} parallel/anti-parallel to the direction of the σ-polarization (perpendicular to $\boldsymbol{k}$), respectively. Both TISMR spectra have the peak at the critical angle (θ=3.67 mrad) [15] and at the structural Bragg position (at θ=12.04 mrad), the latter being the result of the nuclear/electronic contrast between the Fe and Cr layers. In the case of B_{Hf} being parallel/anti-parallel to the direction of the σ-polarization, or in general, for any orientation being

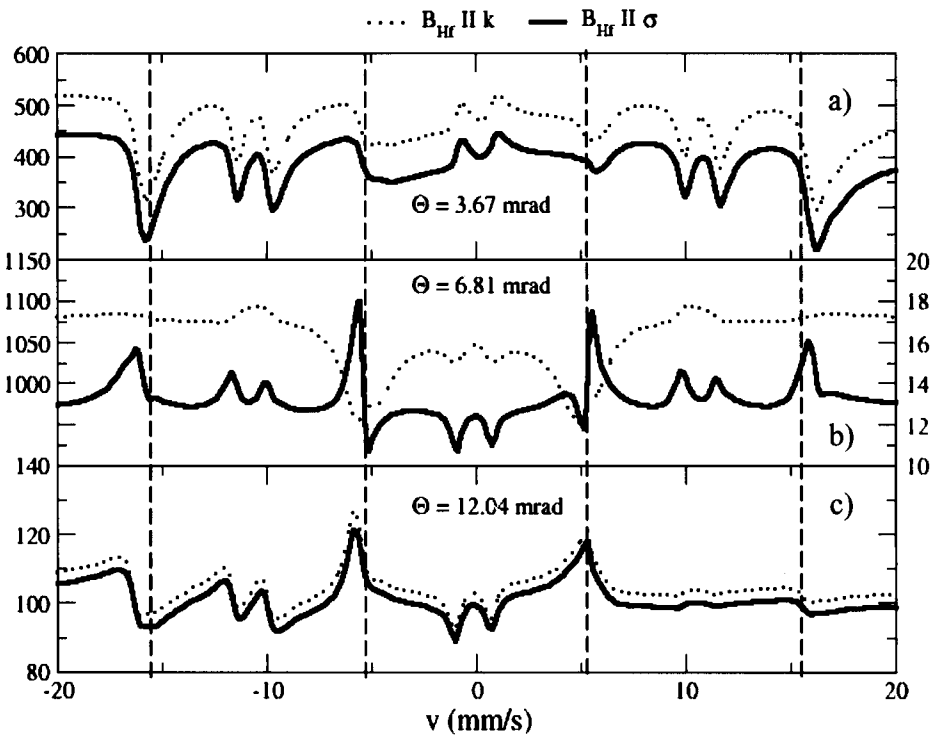

Figure 4 Simulations for stroboscopic SMR spectra of ^{57}Fe/Cr AF multilayer for B_{Hf} parallel to the wave vector $\boldsymbol{k}$ (*dotted line*) and B_{Hf} parallel to the σ-polarization (*solid line*) at three different grazing angles. The *right side axis* corresponds to the B_{Hf} parallel to direction of the σ-polarization case at the AF-Bragg position, where having no AF-Bragg peak, the intensity is by two orders of magnitude lower. The *equidistant vertical dashed lines* (with distance ε) indicates the different stroboscopic orders.

perpendicular to $\boldsymbol{k}$, there is no AF-Bragg peak at θ=6.81 mrad. The reason of this is the special angular dependence of the coherent forward scattering amplitude $\overline{f}$. An AF-Bragg peak exists only, if there is a contrast in the susceptibilities according to the AF symmetry. The only contribution in $\overline{f}$ may result AF contrast is its dependence on the angle of $\boldsymbol{k}$ and B_{Hf} [16], that is the same 90 degree for any direction perpendicular to $\boldsymbol{k}$. However, in the case of B_{Hf} being parallel/anti-parallel to the propagation of the SR those angles are 0 and 180°, respectively, and a strong AF contrast is present.

Figure 3a–c show the TDSMR spectra for the same orientations, at the critical angle (θ= 3.67 mrad), at the AF-Bragg position (θ=6.81 mrad) and at the structural Bragg position (θ= 12.04 mrad), respectively. At the AF-Bragg position, there is a difference of two orders of magnitude in the intensities of both orientations. Also the quantum beat behavior considerably differs. However, making the difference between the two orientations of the hyperfine fields in Figure 3b is hardly possible, there is a small difference in the intensities only.

The stroboscopic SMR spectra in Figure 4 show similar properties we have found in case of TDSMR spectra in Figure 3. Indeed, the simulations related to the two different orientations of the hyperfine fields, the solid and dotted lines, are very similar at the electronic critical angle (Figure 4a) and at the structural Bragg peak (Figure 4c). However, there is a very significant difference between the solid and dotted lines at the AF-Bragg

peak in Figure 4b. The count rate at the base-line of a stroboscopic SMR spectrum, calculated at a certain grazing angle θ, is closely related to the TISMR spectrum at this angle. Therefore, the intensities of the respective stroboscopic SMR spectrum at the AF Bragg peak position (panel b) differ by almost two orders of magnitude. The second huge difference between the solid and dotted lines in panels b of Figure 4 is the shape of the lines, which correspond to the different quantum beat behavior we observed in Figure 3b. Summarizing, the simulated stroboscopic SMR spectra show the same sensitivity to the orientation of the hyperfine fields, therefore like TDSMR, stroboscopic SMR is also capable for studying AF multilayers and thin films.

The advantage of the stroboscopic detection scheme is the possibility of the direct visualization of the Mössbauer resonance lines. In Figure 4 the equidistant vertical dashed lines with distance ε (see Eq. 3) indicate the different stroboscopic orders. For the simulations, an observation period of t_p=8 ns was used, which corresponds to ε= 10.62 mm/s, according to Eq. 3. The zone being symmetric to the zero velocity channel v= 0 mm/s, extending from v=−5.31 mm/s to v=5.31 mm/s, is the 0th order resonance (also called heterodyne spectrum). The −1st and 1st orders are shifted by ε and $-\varepsilon$, respectively. In panels (a) to (c) the four resonance lines of the +1 and −1 stroboscopic orders (right and left side, respectively) can be easily identified.

Note that in Figure 4b the stroboscopic resonances are hardly observable in case of presence of AF contrast (dotted curve). This can be understood by taking into account that the AF Bragg peak is electronically not allowed, however the intensity of the stroboscopic peaks are proportional to the electronic reflectivity [17]. The stroboscopic spectra also show a left/right asymmetry due to the variation of the phase of the total scattering amplitude with energy. This latter allows for phase determination of the scattering amplitude from a set of stroboscopic SMR spectra [17].

4 Conclusion

In conclusion, we discussed a new method, stroboscopic SMR for the determination of hyperfine fields in magnetic multilayers. Like TDSMR, stroboscopic SMR is sensitive to the orientation of the hyperfine magnetic field. The stroboscopic SMR spectra directly show the resonance lines making possible considerable easier identification of the hyperfine fields.

Acknowledgements The authors gratefully acknowledge the support by the Flemish-Hungarian intergovernmental project BIL14/2002, the DYNASYNC Framework Six project of the European Commission (contract number: NMP4-CT-2003-001516) the Fund for Scientific research-Flanders (G.0224.02), the Inter-University Attraction Pole (IUAP P5/1) and the Concerted Action of the KULeuven (GOA/2004/02). L. Deák and R. Callens thank the Deutscher Akademischer Austauschdienst (DAAD) and the FWO-Flanders, respectively, for financial support [18].

Reference

1. Röhlsberger, R.: In: Nuclear condensed matter physics with synchrotron radiation, basic principles, methodology and applications. Springer, Berlin Heidelberg New York (2004) ISBN: 3-540-23244-3
2. Chumakov, A.I., Nagy, D.L., Niesen, L., Alp, E.E.: Hyperfine Interact. **123/124**, 427 (1999)

3. Deák, L., Bayreuther, G., Bottyán, L., Gerdau, E., Korecki, J., Kornilov, E.I., Lauter, H.J., Leupold, O., Nagy, D.L., Petrenko, A.V., Pasyuk-Lauter, V.V., Reuther, H., Richter, E., Röhlsberger, R., Szilágyi, E.: J. Appl. Phys. **85**, 1 (1999)
4. Röhlsberger, R., Bansmann, J., Senz, V., Jonas, K.L., Bettac, A., Meiwes-Broer, K.H.: Phys. Rev. B **67**, 245412 (2003)
5. Deák, L., Bottyán, L., Major, M., Nagy, D.L., Spiering, H., Szilágyi, E., Tanczikó, F.: Hyperfine Interact. **144/145**, 45 (2002)
6. Coussement, R., Cottenier, S., L'abbé, C.: Phys. Rev. B **54**, 16003 (1996)
7. L'abbé, C. et al.: Phys. Rev. B **61**, 4181 (2000)
8. Callens, R., Coussement, R., L'abbe, C., Nasu, S., Vyvey, K., Yamada, T. Yoda, Y., Odeurs, J.: Phys. Rev. B **65**, 160404(R) (2002)
9. Callens, R., Coussement, R., Kawakami, T., Ladriere, J., Nasu, S., Ono, T., Serdons, I., Vyvey, K., Yamada, T., Yoda, Y., Odeurs, J.: Phys. Rev. B **67**, 104423 (2003)
10. Deák, L., Bottyán, L., Callens, R., Coussement, R., Major, M., Nasu, S., Yoda, Y. (submitted to PRB)
11. Blume, M., Kistner, O.C.: Phys. Rev. **171**, 417 (1968)
12. Sturhahn, W., Gerdau, E.: Phys. Rev. B **49**, 9285 (1994)
13. Deák, L., Bottyán, L., Nagy, D.L., Spiering, H.: Physica B **297**, 113 (2001)
14. Spiering, H., Deák, L., Bottyán, L.: Hyperfine Interact. **125**, 197 (2000)
15. Deák, L., Bottyán, L., Nagy, D.L.: Hyperfine Interact. **92**, 1083 (1994)
16. Coussement, R., Odeurs, J., L'abbé, C., Neyens, G.: Hyperfine Interact. **125**, 113 (2000)
17. Deák, L., Bottyan, L., Callens, R., Coussement, R., Nasu, S., Yoda, Y. (to be published in PRB)
18. Bottyán,L., Deák, L., Coussement, C.: SPring8 Fronteries, 59 (2002)

Hyperfine Interact (2006) 167:717–722
DOI 10.1007/s10751-006-9367-5

Synthesis and characterisation of the Fe(II–III) hydroxy-formate green rust

P. Refait · M. Abdelmoula · J.-M. R. Génin · M. Jeannin

Published online: 8 November 2006

Abstract A new methodology was envisioned in order to prepare green rust compounds build on organic anions that could intervene in microbiologically influenced corrosion processes of iron and steel. The formate ion was chosen as an example. The formation of rust was simulated by the oxidation of aqueous suspensions of $Fe(OH)_2$ precipitated from Fe(II) lactate and sodium hydroxide, in the presence of sodium formate to promote the formation of the corresponding green rust. The evolution of the precipitate with time was followed by transmission Mössbauer spectroscopy at 15 K. It was observed that the initial hydroxide was transformed into a new GR compound. Its spectrum is composed of three quadrupole doublets, D_1 (δ=1.28 mm s^{-1}, Δ=2.75 mm s^{-1}) and D_2 (δ=1.28 mm s^{-1}, Δ=2.48 mm s^{-1}) that correspond to Fe(II) and D_3 (δ=0.49 mm s^{-1}, Δ=0.37 mm s^{-1}) that corresponds to Fe(III). The relative area of D_3, close to the proportion of Fe(III) in the GR, was found at 28.5±1.5% (~2/7). Raman spectroscopy confirmed that the intermediate compound was a Fe(II–III) hydroxy-formate, GR($HCOO^-$).

Key words green rust · corrosion · formate · organic matter · steel

1 Introduction

Microbially influenced corrosion of materials results from the combination of chemical, electrochemical, and biological factors. Organic matter is thus present and may by itself modify the corrosion process through various ions and molecules. Moreover, electron donors such as lactate or formate are necessary for providing energy sources. The formation of rust can be simulated by oxidation of aqueous suspensions of $Fe(OH)_2$ obtained by mixing solutions of

P. Refait (✉) · M. Jeannin
Laboratoire d'Etude des Matériaux en Milieux Agressifs, EA3167, Université de La Rochelle, Pôle Sciences et Technologie, Bât. Marie Curie, Av. Michel Crépeau, 17042 La Rochelle cedex 01, France
e-mail: prefait@univ-lr.fr

M. Abdelmoula · J.-M. R. Génin
Laboratoire de Chimie Physique et Microbiologie pour l'Environnement, UMR 7564 CNRS–Université Henri Poincaré–Nancy I, 405, rue de Vandoeuvre, 54600 Villers-Lès-Nancy, France

NaOH and a Fe(II) salt. When the initial ratio of reactants $[Fe^{2+}]/[OH^-]$ is larger than 0.5, an intermediate green rust (GR) compound is obtained between the initial $Fe(OH)_2$ and the end products. GRs are Fe(II–III) hydroxysalts characterised by a crystal structure that consists of the stacking of $Fe(OH)_2$-like layers carrying a positive charge as due to the presence of Fe(III), and of interlayers constituted of anions and water molecules. The anion associated with Fe(II) in the salt induces the formation of the corresponding GR, e.g., using $FeCl_2{\cdot}4H_2O$ leads to GR (Cl^-) [1]. The aim of this study was to study intermediate corrosion products induced by organic species, for instance formate anion $HCOO^-$.

2 Materials and methods

The formation of rust was simulated by the oxidation of aqueous suspensions of $Fe(OH)_2$. Since Fe(II) formate was not available another Fe(II) salt had to be used. Fe(II) lactate was chosen as lactate is a large monovalent anion unfavourable for the stability of a green rust structure. Sodium formate was then added to provide $HCOO^-$ ions. Various formate concentrations, from 0.3 to 1.2 M, were considered, whereas the $Fe(C_3H_5O_3)_2$ and NaOH concentrations were set at 0.18 and 0.3 M, respectively, for all experiments. Chemicals, provided by Aldrich®, ensured a 98% min purity. Magnetic stirring (~500 rpm) in the open air ensured a progressive oxidation of the precipitate and a thermostat maintained the temperature at 25±0.5°C. Reactions were monitored by recording the potential E_h of a platinum electrode immersed in solution, using the saturated calomel electrode as a reference. However, the measured potentials will be given with respect to the standard hydrogen electrode. The pH of the suspension was measured via a glass electrode.

Precipitates were analysed at various reaction times by transmission Mössbauer spectroscopy (TMS) using a constant-acceleration Mössbauer spectrometer calibrated with a 25 μm foil of α-Fe at room temperature, a 512 multichannel analyser (Halder, Elektronic GMBH), and a 50 mCi source of ^{57}Co in Rh. Spectra were computer-fitted with Lorentzian shape lines and errors on the Mössbauer parameters determination were estimated by analysing three samples. Measurements were performed at 15 K, a temperature allowing us to discriminate GRs from $Fe(OH)_2$ and Fe(III) oxyhydroxides [1, 2]. The GR obtained was also analysed by Raman spectroscopy by using a Jobin Yvon spectrometer (LabRAM HR), with a resolution of about 2 cm^{-1}. Excitation was provided by a He–Ne laser (632.33 nm) through an Olympus microscope with a 50× objective. Laser power was varied between 1.94 and 0.07 mW by a set of three density filters to prevent the transformation of the product due to laser heating.

3 Results and discussion

3.1 E_h and pH vs time curves

The shape of E_h and pH vs time curves proved to be independent of NaHCOO concentration. As an example, the curves obtained with [NaHCOO]=0.3 M are displayed in Figure 1. Until reaching point 1, pH decreases from 12 to 8.5 whereas E_h increases from −0.54 to −0.33 V. This corresponds to a progressive precipitation of $Fe(OH)_2$. Since Fe(II) lactate is only slightly soluble in water (~20 g/L at 10°C and 85 g/L at 100°C [3]), it is not completely dissolved when adding the NaOH solution. $Fe(OH)_2$ is much less soluble (pK_s=12.94 at 25°C [4]) and it precipitates from the initial dissolved Fe(II). The solution becomes undersaturated with respect

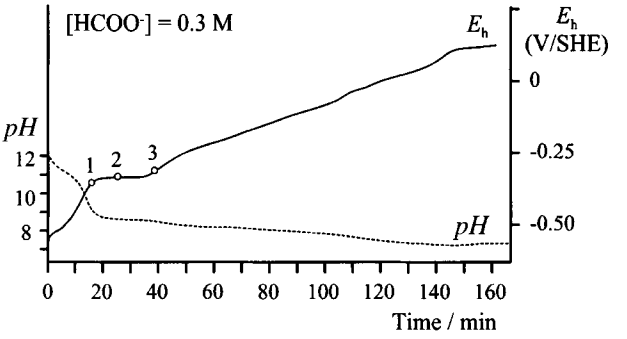

Figure 1 E_h and pH vs time curves recorded during oxidation at 25°C of a $Fe(OH)_2$ precipitate obtained by mixing $Fe(C_3H_5O_3)_2$ (0.18 M), NaOH (0.3 M) and NaHCOO (0.3 M) solutions.

to Fe(II) lactate that dissolves progressively while $Fe(OH)_2$ forms. This process is evidenced by the colour turning from pale green-blue to dark green.

Then, a plateau is observed around point 2 and both E_h and pH stay constant. Potential E_h measured on this plateau depends on the [$HCOO^-$] concentration and is equal to -0.325 ± 0.025, -0.345 ± 0.025 and -0.400 ± 0.025 V for [$HCOO^-$]=0.3, 0.6, 1.2 M, respectively. On such a plateau, the potential value is linked to the equilibrium conditions between the various present phases [2]. Since it depends on the $HCOO^-$ concentration, one of the phases involved in the equilibrium must contain formate. After point 3, both E_h and pH vary continuously and stabilise after about 15 min when the oxidation of Fe(II)-containing phases into Fe(III) oxyhydroxides is accomplished.

3.2 Analyses of the precipitate at various oxidation times

The characterisation of the precipitate during oxidation was achieved by TMS at 15 K. Analyses were performed at intermediate times, denoted as points 1, 2 and 3 on the E_h vs time curve of Figure 1. Spectra are displayed in Figure 2a–c and hyperfine parameters listed in Table I. The spectrum of the precipitate sampled at point 1 is composed of three components. The first one, FH, is an octet characteristic of $Fe(OH)_2$ at such a temperature [1, 5]. The presence of eight lines is due to the fact that the quadrupole-interaction energy and the magnetic-interaction energy are similar, and the levels of the excited state are no longer pure ones. The other spectral components are the quadrupole doublets characteristic of a green rust. Doublet D_{1+2}, with large isomer shift δ and quadrupole splitting Δ, is due to Fe(II) whereas D_3, with smaller δ and Δ values, is due to Fe(III). This compound results from the oxidation of $Fe(OH)_2$. At point 1, Fe(II) lactate is not detected by TMS, confirming that the precipitation of $Fe(OH)_2$ is achieved and that the excess Fe(II) is present as dissolved species according to:

$$6\,Fe(C_3H_5O_3)_2 + 10\,NaOH \Rightarrow 5\,Fe(OH)_2 + 10\,Na^+ + Fe^{2+} + 12\,C_3H_5O_3^- \qquad (1)$$

Since the precipitation rate of $Fe(OH)_2$ that is linked to the dissolution rate of Fe(II) lactate is slow, the oxidation of $Fe(OH)_2$ has already produced some GR before the end of precipitation.

The precipitate obtained at point 2 on the E_h or pH plateau is still composed of a mixture of $Fe(OH)_2$ with GR. The spectrum is fitted with the same components, FH, D_{1+2} and D_3. The only difference with the previous spectrum is that the relative areas have changed, since $Fe(OH)_2$ is transforming progressively into the GR compound.

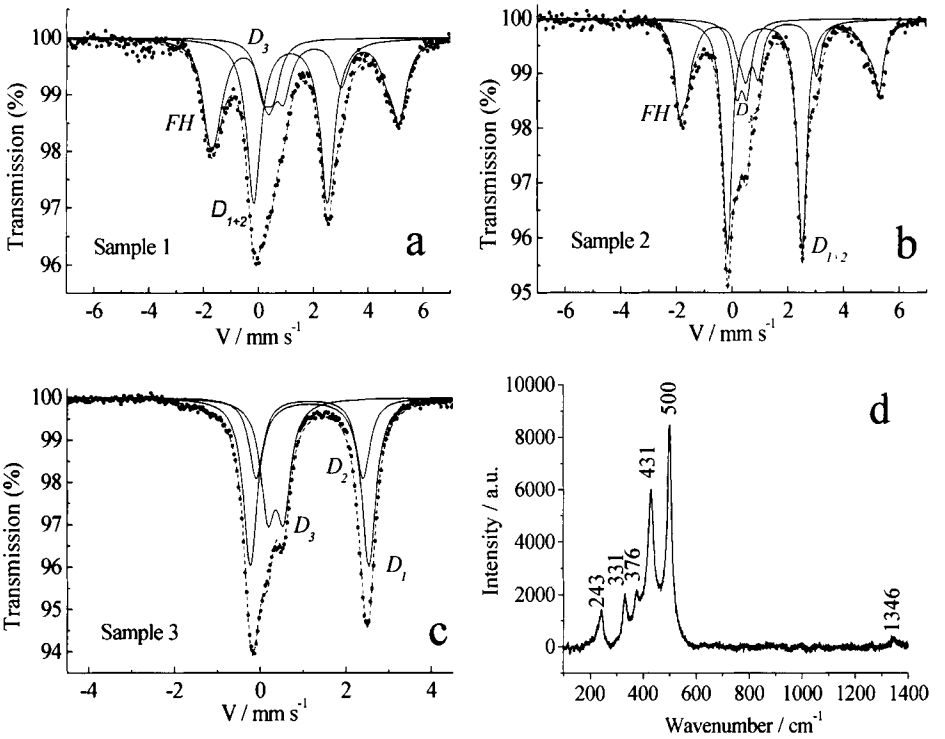

Figure 2 (a-c) Transmission Mössbauer spectra at 15 K of the precipitates sampled at points 1–3 indicated on the E_h vs time curve (Figure 1). Experimental curves *(filled circles)*, elementary components *(solid line)*, global computed curve *(broken line)*. (d) Raman spectrum of the precipitate sampled at point 3. [NaHCOO]= 0.6 M.

Then at point 3, right after the plateau, the spectrum reveals that $Fe(OH)_2$ is totally consumed. Its oxidation has produced a GR compound. The spectrum was acquired on a narrower velocity range in order to precise the hyperfine parameters and two quadrupole doublets, D_1 and D_2, can be fitted. Such doublets are also found in GR(Cl^-) [1] and GR(CO_3^{2-}) [6], whereas only one (D_1) is found in GR(SO_4^{2-}) [2]. The D_1/D_2 area ratio is about two. It was found larger (~3) in GR(CO_3^{2-}) and smaller (~1) in GR(Cl^-). The relative area of D_3, that corresponds approximately to the proportion of Fe(III) in the green rust, is found at 28.5± 1.5%, taking into account the analyses of the GRs obtained with [$HCOO^-$]=0.3 and 1.2 M (not represented).

Since this new GR has a TMS spectrum that differs from those of known GRs and since its equilibrium conditions with $Fe(OH)_2$ depends on the $HCOO^-$ concentration, it must be a Fe(II–III) hydroxy-formate. From the proportion of Fe(III) close to two of seven (~28.5%), the chemical formula $Fe^{II}_5Fe^{III}_2(OH)_{14}(HCOO)_2 \cdot nH_2O$ can be proposed for GR($HCOO^-$). Its formation by oxidation of $Fe(OH)_2$ should then be written as follows:

$$6\,Fe(OH)_2 + Fe^{2+} + 2\,HCOO^- + {}^1/_2O_2 + (n+1)H_2O \Rightarrow Fe^{II}_5Fe^{III}_2(OH)_{14}(HCOO)_2 \cdot nH_2O \quad (2)$$

Equilibrium conditions between $Fe(OH)_2$ and GR($HCOO^-$) would thus correspond to:

$$7\,Fe(OH)_2 + 2\,HCOO^- + n\,H_2O \Rightarrow Fe^{II}_5Fe^{III}_2(OH)_{14}(HCOO)_2 \cdot nH_2O + 2\,e^- \quad (3)$$

Table I TMS analyses at 15 K of samples 1–3, at various stages of the oxidation of $Fe(OH)_2$, as described in Figure 1

	Sample 1				Sample 2				Sample 3			
	δ	Δ	H	RA	δ	Δ	H	RA		δ	Δ	RA
FH	1.4	3.0	190	48	1.4	3.0	190	42	D_1	1.28	2.75	47
D_{1+2}	1.32	2.67	–	41	1.31	2.67	–	45	D_2	1.28	2.48	23
D_3	0.53	0.39	–	11	0.52	0.39	–	13	D_3	0.49	0.37	30

The accuracy is ±0.02 mm s^{-1} for the isomer shift δ and the quadrupole splitting Δ and ±5 kOe for the hyperfine field H.

H hyperfine field in kOe and RA relative abundance in percent.

δ=Isomer shift with respect to metallic α-Fe in mm s^{-1}; Δ=quadrupole splitting in mm $s.^{-1}$

and are given by Nernst's law:

$$E_{eq} = E^o - 0.0591 \log [HCOO^-] \quad (4)$$

As observed experimentally, the equilibrium potential E_{eq} decreases as $[HCOO^-]$ increases.

The Raman spectrum of the GR formed at point 3 is presented in Figure 2d. It displays the two characteristic vibration bands found in all GR compounds at about 430 and 500 cm^{-1} [7–9]. The small band at 1,346 cm^{-1} corresponds to the symmetric stretching mode of the COO group of the formate ion. The three other bands, at 243, 331 and 376 cm^{-1} may be characteristic of GR($HCOO^-$). For instance, GR(CO_3^{2-}) gives rise to vibration bands at 220 and 260 cm^{-1} [9].

4 Conclusion

Using Fe(II) lactate as the source of Fe(II), it proved possible to prepare a Fe(II–III) hydroxy-formate green rust by oxidation of aqueous suspensions of $Fe(OH)_2$. Sodium formate was added to provide the $HCOO^-$ ions to be intercalated in the GR structure. This method should permit to prepare any GR variety, provided that the anion added is more favourable for GR formation than the lactate anion. Mössbauer spectral parameters, as well as the vibration bands displayed on the Raman spectrum, are typical of a GR compound, but slightly different from those of any other known GR compound. The interpretation of the slight modifications induced by the intercalated anion should allow us a more detailed knowledge of the structural properties of GRs [10].

References

1. Refait, P., Abdelmoula, M., Génin, J.-M.R.: Corros. Sci. **40**, 1547 (1998)
2. Refait, P., Bon, C., Simon, L., Bourrié, G., Trolard, F., Bessière, J., Génin, J.-M.R.: Clay Miner. **34**, 499 (1999)
3. Lide, D.R. (ed.): Handbook of Chemistry and Physics, 75th edn. CRC, Boca Raton (1995)
4. Kelsall, G.H., Williams, R.A.: J. Electrochem. Soc. **138**, 931 (1991)
5. Refait, P., Charton, A., Génin, J.-M.R.: Eur. J. Solid State Inorg. Chem. **35**, 655 (1998)
6. Drissi, S.H., Refait, P., Abdelmoula, M., Génin, J.M.: Corros. Sci. **37**, 2025 (1995)
7. Boucherit, N., Hugo Le Goff, A., Joiret, S.: Corros. Sci. **32**, 497 (1991)

8. Simard, S., Odziemkowski, M., Irish, D.E., Brossard, L., Ménard, H.: J. Appl. Electrochem. **31**, 913 (2001)
9. Legrand, L., Sagon, G., Lecomte, S., Chaussé, A., Messina, R.: Corros. Sci. **43**, 1739 (2001)
10. Génin, J.-M.R., Aïssa, R., Abdelmoula, M., Benali, O., Ernstsen, V., Ona-Nguema, G., Upadhyay, C., Ruby, C.: Solid State Sci. **7**, 545 (2005)

Hyperfine Interact (2006) 167:723–727
DOI 10.1007/s10751-006-9349-7

Monitoring structural transformation of hydroxy-sulphate green rust in the presence of sulphate reducing bacteria

M. Abdelmoula · A. Zegeye · F. Jorand · C. Carteret

Published online: 14 November 2006

Abstract The activities of bacterial consortia enable organisms to maximize their metabolic capabilities. This article assesses the synergetic relationship between iron reducing bacteria (IRB), *Shewanella putrefaciens* and sulphate reducing bacteria (SRB) *Desulfovibrio alaskensis*. Thus, the aim of this study was first to form a biogenic hydroxy-sulpahte green rust GR2(SO_4^{2-}) through the bioreduction of lepidocrocite by *S. putrefaciens* and secondly to investigate if sulfate anions intercalated in the biogenic GR2(SO_4^{2-}) could serve as final electron acceptor for a sulfate reducing bacterium, *D. alaskensis*. The results indicate that the IRB lead to the formation of GR2(SO_4^{2-}) and this mineral serve as an electron acceptor for SRB. GR2(SO_4^{2-}) precipitation and its transformation was demonstrated by using X-ray diffraction (DRX), Mössbauer spectroscopy (TMS) and transmission electron spectroscopy (TEM). These observations point out the possible acceleration of steel corrosion in marine environment in presence of IRB/SRB consortia.

Key words green rust · biocorrosion · SRB · iron sulphide · TMS

1 Introduction

It was recently shown that the GR2(SO_4^{2-}) was present among the corrosion product of steel sheet piles immersed for 25 years in seawater and was associated with SRB. If the formation of GR2(SO_4^{2-}) is the consequence of iron chemistry in seawater, then its presence could promote a microbial activity. Indeed, GR2(SO_4^{2-}) could form through a biotic pathway [2] and could serve afterwards as a sulphate reservoir for SRB activity [3].

Therefore, the aim of this article is to clarify the main features of the mechanism of biocorrosion. The starting material in the event, GR2(SO_4^{2-}), was formed through the microbial reduction of lepidocrocite by *S. putrefaciens* under H_2 atmosphere serving as the sole electron source. The GR2(SO_4^{2-}) alteration experiments by *D. alaskensis* were conducted with the biogenic GR2(SO_4^{2-}) as the sole electron acceptor and lactate as the

M. Abdelmoula (✉) · A. Zegeye · F. Jorand · C. Carteret
LCPME, UMR 7564, CNRS-UHP Nancy I, 405 rue de Vandoeuvre, 54600 Villers-lès-Nancy, France
e-mail: Abdelmoula@lcpme.cnrs-nancy.fr

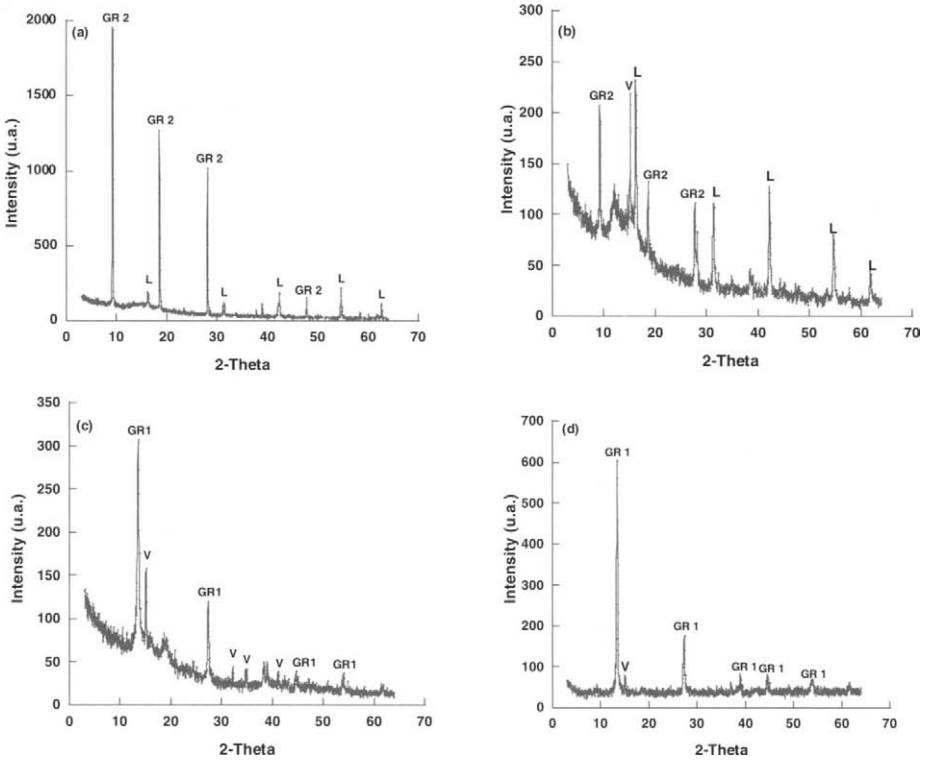

Figure 1 XRD diffractogram of the product during the incubation period. **a**, **b**, **c**, and **d** correspond to t=0, t=3 days, t=20 days and t=300 days, respectively.

electron donor in non-buffered medium. The monitoring versus time of the products, resulting from the biotic transformation of GR2(SO_4^{2-}), was carried out by XRD, TMS and TEM.

2 Experimental methods

The iron reduction experiments were conducted with *S. putrefaciens* as described in [2]. The resulted mineral, GR2(SO_4^{2-}), was used as an electron acceptor for SRB metabolism. These bacteria (*D. alaskensis*) were incubated in a defined mineral medium containing K_2HPO_4 (0.5 g L^{-1}). Sodium lactate served as the electron source (3.5 g L^{-1}).

Three methods were used to characterize the products: DRX, TMS and TEM. Mössbauer spectra were measured by means of a constant-acceleration spectrometer with a 50 mCi ^{57}Co source. Computer fittings were performed with the Recoil Software of Lagarec and Rancourt, using Lorentzian model or pseudo-voigt method based on the least-squares method. The XRD data were collected with a D8 Bruker diffractometer, equipped with a monochromator and position-sensitive detector. The X-ray source was a Co anode (λ= 0.17902 nm). Transmission electron microscopy (TEM) was conducted using a CM20/ STEM Philips TEM, with a voltage of 200 kV.

Table I Mössbauer hyperfine parameters

Incubation time (days) and temperature	δ (mm/s) with respect to α-Fe at RT	Δ or 2ε (mm/s)	H (kOe)	RA (%)
t=0	GR D1 : 1.27	2.92		36
	D2 : 0.48	0.44		21
77 K	Lepido : 0.47	0.62		43
t=3	GR D1 : 1.24	2.87		16
	D2 : 0.53	0.39		10
	Lepido : 0.46	0.73		46
100 K	Vivianite : 1.33	3.2		7
	1.24	2.54		6
	Greigite : 0.47	−0.14	475	9
	0.84	0.02	277	6
t=20	GR D1 : 1.18	2.6		34
	D2 : 0.4	0.5		32
	Lepido : 0.47	0.5		5
215 K	Vivianite : 1.2	2.96		13
	Greigite : 0.41	−0.09	419	11
	0.85	−0.5	387	4
t=300	GR D1 : 1.24	2.67		29
	D2 : 0.45	0.43		17
13 K	Vivianite: 1.27	3.1		14
	Greigite : 0.49	0	280	20
	0.88	−0.5	355	8
	Iron oxide : 0.48	−0.15	504	12

3 Results and discussion

3.1 Bioreduction of lepidocrocite

The green colored product formed from γ-FeOOH bioreduction was characterised by XRD and TMS. The XRD patterns of products obtained after 90 days of incubation exhibit peaks of GR2(SO_4^{2-}) and lepidocrocite (Figure 1a). Experimental GR2 d-spacings are similar to those previously obtained in biotic and abiotic conditions for GR2(SO_4^{2-}) [2]. The Mössbauer spectrum of the greenish phase at 77 K can reasonably be fitted (Table I) with three paramagnetic quadrupole doublets D_1, D_2, and $D_{\text{Lepidocrocite}}$ (Figure 2a). The doublets D_1 (ferrous state) and D_2 (ferric state) correspond to GR2 (57%) and the doublet D_L is assigned to paramagnetic Fe^{3+} in lepidocrocite (43%), with small isomer shifts δ (0.47 mm/s) and quadrupole splitting Δ (0.62 mm/s) values at 77 K [2].

3.2 Reactivity of GR2 with SRB

Two types of XRD patterns exist for GR depending upon the shape of intercalated anions, which induce various stacking sequences. GR1 incorporate planar or spherical anions (Cl^-, CO_3^{2-}) whereas GR2 inserts three-dimensional anions ($SO4^{2-}$) [4]. GR1 compounds have a trigonal structure with sequence A*c*B*i*B*a*C*j*C*b*A*k*A..., where A–C designate OH^- planes, *a*– *c* metal cations layers and i–k intercalated layers. In contrast, GR2 compounds conserve the original hexagonal stacking of the ferrous hydroxide with sequence A*c*B*i*A and crystallize also in the trigonal system, but with a much smaller periodicity (only one single layer repeat

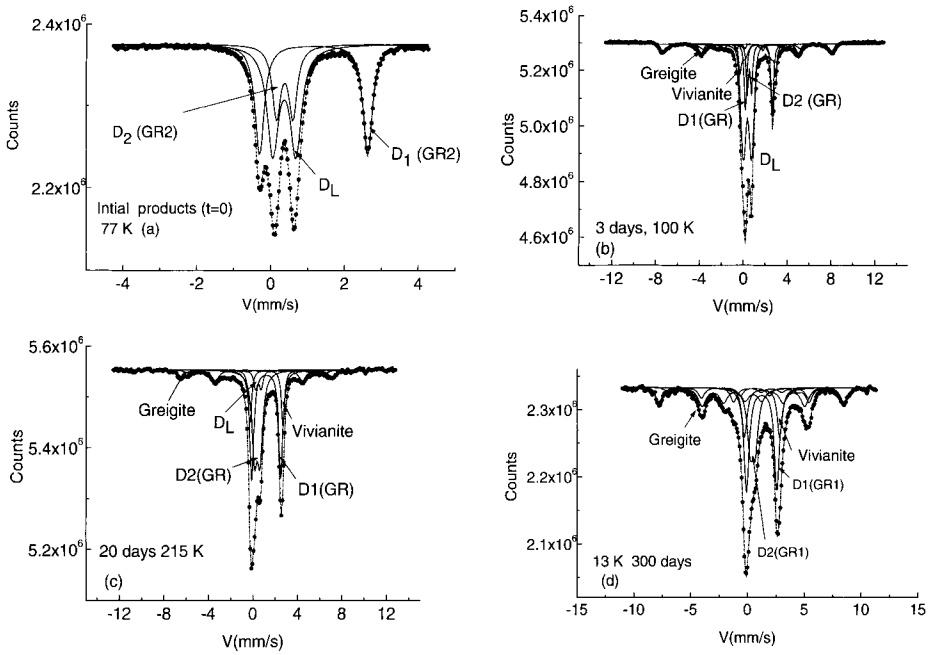

Figure 2 Mössbauer spectra of the products with various incubation periods.

with a primitive hexagonal cell) along the C axis than for GR1 (a three-layer repeat yielding a rhombohedral structure). The XRD discriminate unambiguously both poly-types (GR1, GR2) when one has a mixture of these two phases. The monitoring versus time of the interaction of GR2(SO_4^{2-}) with the SRB is carried out by characterising the precipitates by XRD, TMS and TEM. Figure 1 shows the diffractograms measured at various incubation periods.

The XRD patterns of products obtained after 0 and 3 days of incubation (Figure 1a and b) exhibit lines of GR2 and lepidocrocite. However, the lines of GR2 are always observable but their intensity strongly decreased. A new reflection probably corresponding to vivianite appears. After 20 days (Figure 1c), one observes the total extinction of the peaks corresponding to the GR2 and lepidocrocite and growth of new lines ascribable to the GR1 whose intensity increases with the time of incubation (Figure 1d).

Mössbauer spectra of the filtered solids were collected between 215 and 13 K at different time of incubation. The corresponding hyperfine parameters are given in Table I. The spectrum recorded at 100 K reveals a distinct, rapid formation of new mineral phases by day 0 (Figure 2a). At day 3, a magnetic component appears (Figure 2b). In spite of the appearance of a new iron component Fe(II) ascribable to vivianite, the total amount of Fe(II) is smaller than that of Fe(III) which correspond to two overlapping doublets (lepidocrocite and ferric of GR). After 20 days, the shape of the spectrum is similar to that obtained at 3 days of incubation, however the total quantity of paramagnetic Fe(III) decreased notably (Figure 2c). The absorption of lepidocrocite strongly decrease because of its probable dissolution by hydrogen sulphide [5], resulting from sulphate-reduction. When we continue incubation for a longer period (300 days), the paramagnetic components ascribable to vivianite and the GR are always present; in addition the intensity of the magnetically ordered component increased (Figure 2d). A potential candidate for this component is iron sulphide, which was identified as a greigite (Fe_3S_4), from the values of

the hyperfine fields of its two sextets (280 and 350 kOe). Greigite, Fe_3S_4, the sulphur analogue of magnetite Fe_3O_4 has a similar inverse spinel structure [6]. In spite of its clear observation by TMS, XRD does not indicate any additional phases other than GR1 and vivianite. This suggests that this iron sulphide is poorly crystallized. The TEM results (not shown) also confirm this observation. It consists of few areas that exhibit diffuse ring selected area diffraction (SAED) patterns, indicating a poor degree of crystallinity.

The analyses by XRD showed unambiguously the appearance of the GR1(CO_3^{2-}) to the detriment of the GR2(SO_4^{2-}) but the TMS and TEM identified, in addition of GR1(CO_3^{2-}), poorly crystallised greigite. TMS provided complementary data to understand the mineralogical and chemical evolution of the samples in agreement to structural analyses. Aqueous hydrogen sulphide and a part of aqueous ferrous iron species which is in equilibrium with the GR2(SO_4^{2-}) induces its dissolution and may then react and precipitate as iron sulphide. In addition, the precipitation from dissolved iron species and by incorporating the available dissolved surrounding anions such as carbonate (from lactate oxidation) leads preferentially to GR1(CO_3^{2-}).

4 Conclusion

The poorly crystalline Fe sulphides form as a result of the dissimilatory bacterial reduction of sulphate [7]. *D. alaskensis* can couple the oxidation of lactate to the reduction of sulphate ions incorporated in the biogenic GR2(SO_4^{2-}). Bicarbonate and hydrogen sulphide are reaction products [8].

In this study, it was suggested strongly that the interaction of iron reducing bacteria and sulphate reducing bacteria must be responsible for the catastrophic corrosion of steel in the marine environment [1]. Microbiologically Influenced Corrosion (MIC) proceeds in two steps: the reduction of ferric oxyhydroxides by DIRB to produce Fe^{2+}, which then form GR2(SO_4^{2-}), and the reduction of the sulphate ions trapped within the interlayers of the GR2(SO_4^{2-}) structure by SRB into sulphides and its subsequent reaction with Fe^{2+} to form ferrous sulphides.

References

1. Refait, P., Memet, J.-B., Bon, C., Sabot, R., Génin, J.M.: Corros. Sci. **45**, 833–845 (2003)
2. Zegewe, A., Ona-Nguema, G., Carteret, C., Huguet, L., Abdelmoula, M., Jorand, F.: Geomicrobiol. J. **22**, 389–399 (2005)
3. Huguet, L.: DEA Chimie et Microbiologie de l'eau. Université H. Poincaré (2004)
4. Bernal, J.O., Dasgupta, D.R., Mackay, A.L.: Clay Miner. Bull. **4**, 15–30 (1959)
5. Peiffer, S., Afonso, M.D.S., Wehrli, B., Gächter, R.: Environ. Sci. Technol. **2**, 2408–2413 (1992)
6. Lennie, A.R., Vaughan, D.: Mineral spectroscopic: A tribute to R. G. Burns (1996)
7. Neal, A.L., Techkarnjanaruk, S., Dohnalkova, A., McCready, D., Peyton, B., Geesey, G.G.: Geochim. Cosmochim. Acta **65**, 223–235 (2001)
8. Jørgensen, B.B., In: Krumbein, W.E. (ed.) Microbial Geochemistry, p. 91. Oxford (1983)

Hyperfine Interact (2006) 167:729–732
DOI 10.1007/s10751-006-9366-6

In situ ^{119}Sn Mössbauer spectroscopy used to study lithium insertion in c-Mg_2Sn

L. Aldon · C. M. Ionica · P. E. Lippens · D. Larcher · J.-M. Tarascon · J. Olivier-Fourcade · J.-C. Jumas

Published online: 14 November 2006

Abstract The electrochemical reactions of Li with c-Mg_2Sn have been investigated by in situ Mössbauer spectroscopy of ^{119}Sn and X-ray diffraction. The lithiation transforms initially c-Mg_2Sn part into Li_xMg_2Sn alloy (x<0.5). On further lithiation Mg is extruded from the structure with formation of Li_2MgSn ternary alloy. In situ Mössbauer spectroscopy provides valuable information on local environment of tin and swelling behavior and cracking of the particles during discharge and charge processes.

Key words in situ measurements · lithium-ion batteries · electrochemical behavior · Mössbauer spectroscopy of ^{119}Sn

1 Introduction

At the present time the lithium-ion technology is the preferable portable power source but the development of high energy and power batteries for other applications, such as portable power tools or hybrid vehicles, leads to intensive worldwide research about new electrode materials and electrolytes. Among the new anode materials, the tin-based alloys [1, 2] c-Mg_2Sn allows to insert 4.4 lithium atoms per formula unit at a potential of 0.45 V leading to a theoretical capacity of 704 Ah/kg.

We will show that use of ^{119}Sn as a local Mössbauer probe is of high interest for studying mechanisms induced by lithium insertion. Combined structural and electronic analysis from X-ray diffraction, ^{119}Sn Mössbauer spectrometry has allowed us to establish that lithium insertion induces a displacement reaction with Mg extrusion. Such

L. Aldon (✉) · C. M. Ionica · P. E. Lippens · J. Olivier-Fourcade · J.-C. Jumas
Laboratoire des Agrégats Moléculaires et Matériaux Inorganiques (UMR 5072 CNRS),
Université Montpellier II, CC 15, Place E. Bataillon, 34095 Montpellier Cedex 5, France
e-mail: laldon@univ-montp2.fr

D. Larcher · J.-M. Tarascon
Laboratoire de Réactivité et Chimie des Solides (UMR 6007 CNRS),
Université de Picardie Jules Vernes, 33 Rue St Leu, 80039 Amiens Cedex, France

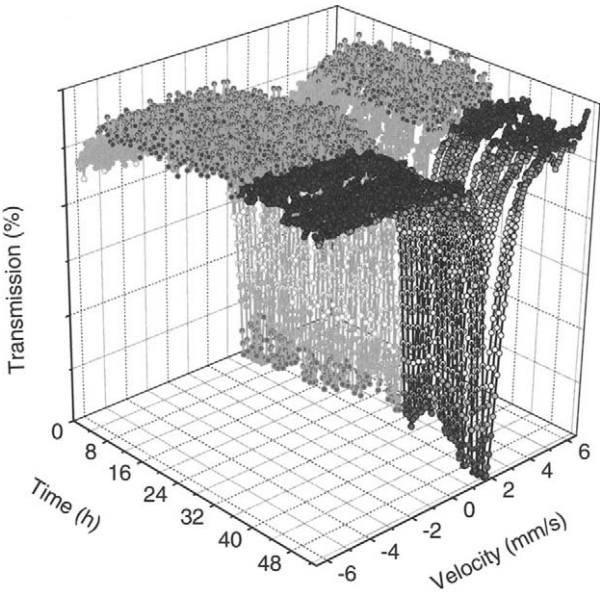

Figure 1 Evolution of ^{119}Sn Mössbauer spectra recorded under in situ condition during the first discharge and charge (C/10 rate, 1 spectrum/h).

displacement reaction definitively explains the well-defined plateau observed in the electrochemical potential curves.

2 Experimental

A batch of cubic Mg_2Sn was prepared by reacting stoichiometric amounts of elemental metallic powder (purity >99%) through a ball-milling process. Typically, for such a synthesis, 2 g of the mixed powders and a steel ball (7 g) were loaded into a stainless steel vial under an Argon atmosphere. Then, the sealed vial was sequentially shaken for various lengths of time in an SPEX8000 miller with 15 min of interruption every 30 min of shaking to release as much as possible of the shock-induced generated heat.

Electrochemical tests of c-Mg_2Sn have been done in thin plastic Li-ion cell PLIon™ developed by Bellcore[3].

3 Results and discussions

In Figure 1, we compare at the same velocity scale, in situ spectra of c-Mg_2Sn during lithium insertion (discharge) and extraction (charge). Each spectrum has been recorded for an hour. Variations of the baseline far from absorption lines are observed suggesting modification of the irradiated surface of the sample. Since this baseline is directly due to gamma rays going through the sample without absorption, the observed variation from a spectrum to another may be due to voids between the particles (increase of baseline level) or to the swelling of the particles themselves (decrease of baseline level). These voids are due to cracks formed during lithium insertion. In another hand, decrease of the baseline is mainly due to an increase of the number of absorbing nuclei. This observation is attributed to the swelling of the particles.

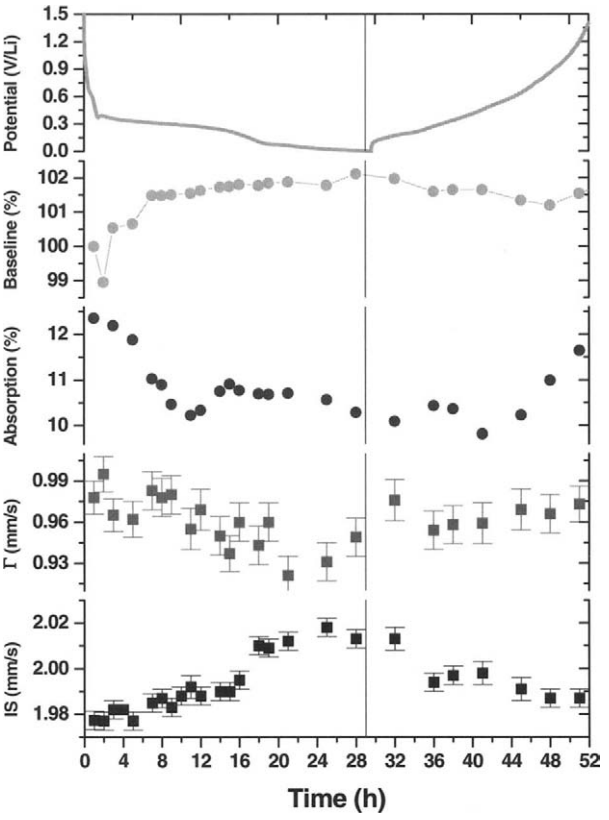

Figure 2 Discharge–charge curves of pristine c-Mg_2Sn upon Li-insertion compared to in situ ^{119}Sn Mössbauer results.

In Figure 2, we have drawn the baseline percent relative to those observed in the first spectrum. Hence, values lesser than 100% correspond to a more absorbing sample compared to pristine sample. Typical discharge/charge curves are shown in the upper part of Figure 2. The curve presents a sharp decrease of the potential at the very beginning of insertion process from 1.5 to 0.45 V. The well-defined plateau corresponding to a two-phase system is observed. Then, below 0.45 V a continuous decrease of the potential can be ascribed to a topotactic insertion of lithium atoms in the new phase.

In Figure 2, one can also see variations of hyperfine parameters. Isomer shift shows two main domains corresponding respectively to the formation of Li_2MgSn from Li_xMg_2Sn with extrusion of Mg (from 1.98 to 2.01 mm/s). The second domain show that tin atoms are not involved in the electrochemical process since isomer shift does not evolve and Li are then intercalated in Mg structure resulting in formation of Li_xMg.

Lithium insertion/extraction in c-Mg_2Sn induces baseline, absorption, linewidth and isomer shift that are in good agreement with the previously proposed mechanism starting from in situ XRD results [4].

$$1)\ Mg_2Sn + x\,Li \rightarrow Li_xMg_2Sn$$
$$2)\ Li_xMg_2Sn + (2-x)\,Li \rightarrow Li_2MgSn + Mg$$
$$3)\ Mg + x\,Li \rightarrow Li_xMg$$

The variations observed in Figure 2 during the first discharge in the baseline can be explained by the following. The initial contribution is mainly due to, in a first

approximation, the particles that are not joining together. So, γ-rays that are going through voids contribute to the baseline. The initial absorption close to 12.5% is characterizing the tightness of the Sn–Mg chemical bonding in the pristine material. The first steps of lithium insertion consist of topotactic mechanism in which swelling of particles is induced, reducing the voids between active particles. Hence baseline is decreasing as observed in the Mössbauer spectra. Absorption is also decreasing and reflects, through f-Lamb–Mössbauer factor, a decrease of the strength of Sn–Mg chemical bonding. This observation is in agreement with XRD cell parameters variation. Then, the increase of the baseline reaching asymptotically a saturating value is a fingerprint of crack formation, responsible of the irreversible capacity. More and more voids are present in the sample. The decrease of absorption to about 10.5% corresponds to a new phase formation (Li_2MgSn) while a part of Mg is extruded from the pristine structure.

4 Conclusions

In situ Mössbauer spectroscopy can be very useful to study lithium insertion mechanism in order to better understand the electrochemical behavior of the new electrode materials. We have shown how to use baseline variation to have a direct evidence of swelling of the active material particles in the battery which is a key issue for industrial applications.

Concerning Mg_2Sn, the electrochemical insertion of lithium in the pristine material leads to a topotactic insertion producing Li_xMg_2Sn. Then, this alloy is not stable and forms a new phase Li_2MgSn by extrusion of Mg from the initial structure. The conclusions deduced from Mössbauer are in a good agreement with those obtained from in situ X-ray diffraction measurements.

Now, this way of using Mössbauer spectroscopy provides a new tool to get deeper insight in characterizing Li-ion accumulators, even for the case in which X-ray diffraction pattern do not give information when amorphous or nanosized particles are formed.

Acknowledgements This work has been carried out in the framework of ALISTORE, Network of Excellence (contract no.: SES6-CT-2003-503532). The authors are grateful to the European Community for the financial support.

References

1. Grugeon, S., Laruelle, S., Dupont, L., Tarascon, J.-M.: Solid State Sci. **5**, 895 (2003)
2. Robert, F., Morato, F., Chouvin, J., Aldon, L., Lippens, P.E., Olivier Fourcade, J., Jumas, J.-C., Simon, B., Biensan, P.: J. Power Sources **119–121**, 581 (2003)
3. Tarascon, J.-M., Gozdz, A.S., Schmutz, C., Shokoohi, F., Warren, P.C.: Solid State Ionics **86–88**, 49 (1996)
4. Larcher, D., Prakash, A.S., Saint, J., Morcrette, M., Tarascon, J.-M.: Chem. Mater. **16**, 5502 (2004)

Hyperfine Interact (2006) 167:733–738
DOI 10.1007/s10751-006-9358-6

In situ ^{119}Sn Mössbauer spectroscopy study of Sn-based electrode materials

Abdelmaula Aboulaich · Florent Robert · Pierre Emmanuel Lippens · Laurent Aldon · Josette Olivier-Fourcade · Patrick Willmann · Jean-Claude Jumas

Published online: 8 November 2006

Abstract Sn-based composite materials were synthetized by a conventional melt-quenching method, and studied by X-ray diffraction, electrochemistry and *in situ*^{119}Sn Mösssbauer spectroscopy. Tin was dispersed *ex situ* into a matrix formed from B_2O_3:P_2O_5. XRD and ^{119}Sn Mössbauer spectroscopy show the formation of an interface between the active species (Sn^0) and the matrix. This amorphous interface acts as a "buffer-zone" which compensates volume changes during the tin–lithium alloy formation and avoids aggregation of tin particles.

Key words Li-ion batteries · tin-based composite materials · *in situ* Mössbauer spectroscopy

1 Introduction

Recently, there has been a considerable interest in finding new electrode materials with high capacity for new applications of Lithium-ion batteries. Many alloy based anode materials have been studied to overcome the limited capacity of graphite, but they undergo severe volume expansion/contraction during alloying and de-alloying reactions, which finally leads to the pulverisation of the electrodes. Sn-based oxides [1, 2] or Sn-based glasses [3] have attracted considerable attention because these materials exhibit very promising performances (high specific capacity, large reversibility, good safety). The choice of BPO_4 as a matrix for the dispersion of the active species is justified by its good thermal and electrochemical stability and its good ionic conductivity.

A. Aboulaich (✉) · F. Robert · P. E. Lippens · L. Aldon · J. Olivier-Fourcade · J.-C. Jumas
Laboratoire des Agrégats Moléculaires et Matériaux Inorganiques (UMR 5072-CNRS),
Université Montpellier II, CC015, Place Eugène Bataillon, 34095 Montpellier cedex 5, France
e-mail: abdelmaula.aboulaich@univ-mont2.fr

P. Willmann
Centre National d'Études Spatiales, 18 avenue Edouard Bellin, 31401 Toulouse cedex 9, France

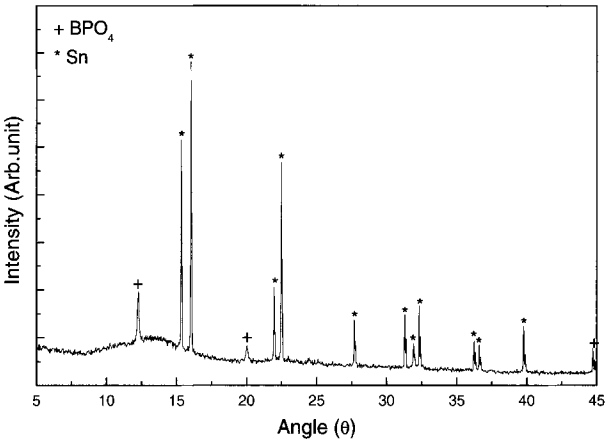

Figure 1 XRD Powder patterns of Sn/BPO_4 composite.

In this work, we report a study of such Sn-based composite materials based on X-ray diffraction, electrochemical tests and *in situ* ^{119}Sn Mössbauer spectroscopy.

2 Experimental

The Sn/BPO_4 composite was prepared by a conventional melt-quenching method. The active species (βSn) were homogeneously dispersed into the matrix formed by B_2O_3:P_2O_5 with an optimized composition [4]. Stoichiometric amounts of βSn (Aldrich, diameter <10 μm) and BPO_4 (synthesized from $NH_4H_2PO_4$ and H_3BO_3 as phosphoric and boric precursor, respectively) were ground and heated in a vitrous carbon heating boat inside a horizontal tube furnace at 500°C. This mixture was heated for 5 h in a constant flow of nitrogen and quenched to room temperature by removing the boat from the furnace. The solid formed gives a grey powder after grinding.

X-ray diffraction (XRD) powder patterns were recorded with a Philips instrument, using $CuK_{\alpha 1}$ radiation (λ=1.54051 Å). ^{119}Sn Mössbauer spectra were recorded by transmission (transmission Mössbauer spectroscopy, TMS) in the constant acceleration mode using a conventional EG&G spectrometer. Conversion electron Mösssbauer spectroscopy (CEMS) measurements were carried out by means of a standard Mössbauer spectrometer with a constant acceleration movement and using a gas flow (94% He, 6% methane) proportional counter to detect the internal conversion electrons emitted after resonant absorption of gamma rays. The source was ^{119m}Sn in a $CaSnO_3$ matrix and all spectra were collected at room temperature.

Electrochemical tests were carried out using a Swagelock™ cell employing a lithium foil as counter electrode and utilizing 1 M $LiPF_6$ in mixed organic solvents as the electrolyte. The cell was assembled in Ar-filled glove box. The discharge–charge tests were carried out by means of a Mac Pile system operating in a galvanostatic mode, between 1.2 and 0.1 V vs Li^+/Li^0.

3 Results and discussion

The XRD pattern of Sn/BPO_4 is shown in Figure 1. The observed diffraction peaks correspond to crystalline β-Sn and BPO_4 and the broad halo between 10 and 17° θ to an amorphous phase. The lattice parameters of the observed crystalline phases for BPO_4

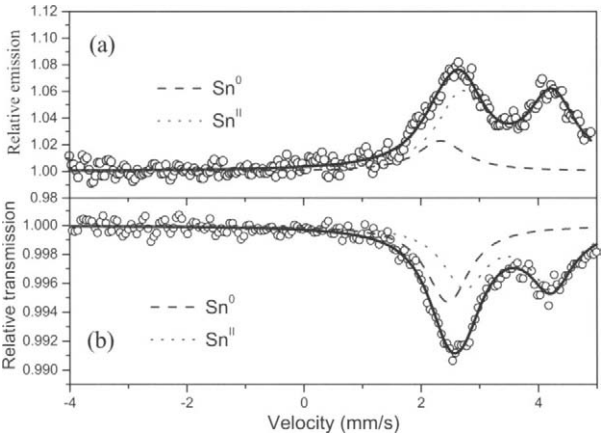

Figure 2 ^{119}Sn Mössbauer spectra at room temperature of Sn/BPO_4 composite obtained by (a) CEMS and (b) TMS.

Table I Hyperfine parameters obtained for the Sn/BPO_4 composite at 300 K: isomer shift δ relative to $BaSnO_3$, quadrupole splitting Δ and line width at half-maximum Γ

	Tin sites	Contribution (%)	δ (mm/s)	Δ (mm/s)	Γ (mm/s)
TMS	$Sn^{(0)}$	60	2.37	0	0.889
	$Sn^{(II)}$	40	3.39	1.47	0.889
CEMS	$Sn^{(0)}$	17	2.25	0	0.985
	$Sn^{(II)}$	83	3.38	1.54	0.985

(a=b=4.341 Å and c=6.635 Å) and β-Sn (a=5.830 Å and c=3.181 Å) are in good agreement with previously published values [5, 6].

^{119}Sn Mössbauer spectroscopy gives us further information about the Sn local environment in this composite material. Figure 2 shows both the experimental data and the fitted curves of the Mössbauer spectra recorded in transmission mode (TMS, Figure 2a) and in emission mode (CEMS, Figure 2b). The hyperfine parameters are given in Table I.

The spectrum obtained in transmission mode (Figure 2a) was fitted by considering two different contributions: Sn^{II} and Sn^0. The hyperfine parameters of the Sn^{II} doublet (δ= 3.39 mm/s, Δ=1.54 mm/s) are in the same range of values than those of amorphous tin oxides [7] and can be attributed to the amorphous phase observed by XRD. The hyperfine parameters of Sn^0 are close to those of βSn, which confirms the existence of βSn in the composites as observed by XRD. The relative quantities of the two species have been evaluated from the values of the Lamb–Mössbauer factor at 300 K (f≈0.4 for Sn^{II} and f≈ 0.04 for β-Sn) [8]. The composite is formed by about 95% of βSn and 5% of Sn^{II}-based amorphous phase. The spectrum obtained by CEMS (Figure 2b) is formed by an asymmetric doublet which was also fitted with two components due to Sn^0 and Sn^{II}. The hyperfine parameters are close to those obtained in transmission mode, which confirms that the two types of tin detected by CEMS can be assigned to the same species (Table I). The relative amounts obtained by considering the f factors are 80% for βSn and 20% for the Sn^{II}-based amorphous phase. The comparison between the relative contributions obtained in the two modes (TMS and CEMS) clearly shows that the Sn^{II} atoms are located in thin layers. Since the amorphous phase comes from the reaction of BPO_4 with βSn, we conclude that the composite is formed by particles of BPO_4 and βSn with an interface formed by the Sn^{II} based amorphous phase.

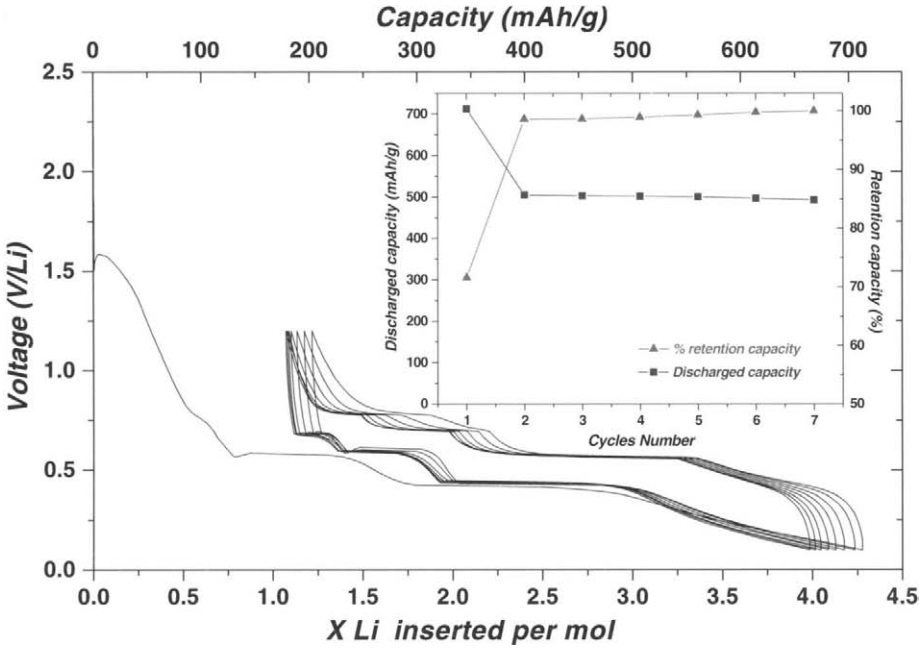

Figure 3 Voltage profile of Sn/BPO_4 composite between 1.2 and 0.1 V. The cell was cycled at a rate of C/20.

Figure 3 shows discharge/charge profiles of the $Sn\text{-}BPO_4$ composite at C/20 rate. The material exhibits a capacity of 712 mAh/g at the end of the first discharge. The capacity retention is 71% at the first cycle and increases to 100% at the seventh cycle. The lithium insertion/extraction mechanism has been characterized by *in situ* Mössbauer spectroscopy in TM with a battery assembled using the plastic technology [9]. The cell was discharged to 0.1 V and charged to 1.2 V with a constant current of 10 mA/g (C/30 rate). Each spectrum was recorded during 6 h, which corresponds to the insertion of 0.2 Li in the electrode.

Figure 4a shows the experimental *in situ* ^{119} Sn Mössbauer spectra at different depths of the first discharge and charge. The first spectrum obtained for the reaction of 0.2 Li with the composite material (point a) is close to the spectrum obtained for the pristine material (Figure 4b). For 0.4 Li (point b), the Sn^{II} atoms belonging to the interface layer were completely reduced into Sn^0. At the end of the discharge (point c), most of the β Sn particles were transformed into Li_7Sn_2 nano-alloys and at the end of the first charge (point d), the Li_7Sn_2 alloy is back-transformed into β Sn. The first discharge corresponds to a certain reorganization of the starting material. We can suppose that a very small amount of Li is inserted into the BPO_4 matrix improving its conductivity [10]. During the charge, the successive potential plateaus observed in Figure 3 are similar to those observed for β Sn [11]. Thus, the proposed mechanism for Sn/BPO_4 composite materials consists in two steps:

1) Reduction of the Sn^{II} atoms of the amorphous interface between BPO_4 and βSn and restructuring of the composite,
2) Reversible formation of Li_xSn alloys:

$$Sn + 3.5\,Li \leftrightarrow {}^1/_2\,Li_7Sn_2$$

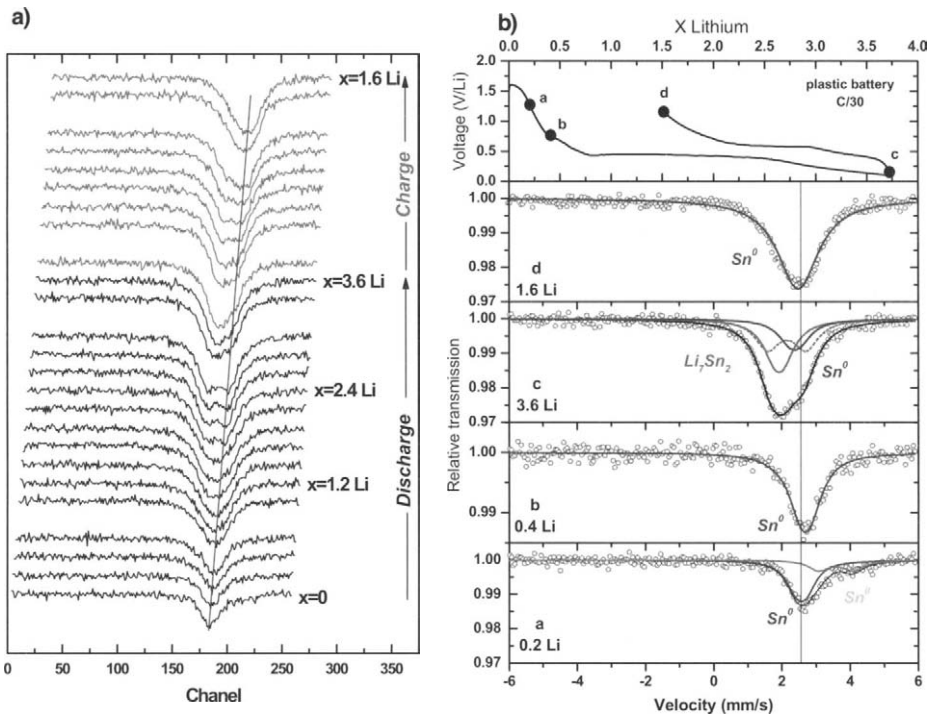

Figure 4 *In situ* [119] Sn Mössbauer spectra of Sn/BPO_4 composite at C/30 rate in TMS (a) recorded during the first discharge and charge, and (b) at different depths of the first discharge and at the end of the first charge.

The dispersion of tin particles (Sn^0) in the borophosphate matrix allows dissipating the mechanical stress induced by large volume changes in alloying and de-alloying reactions and avoiding an aggregation of tin particles.

4 Conclusion

Dispersion of tin particles in borophosphate matrix substantially improves the cycling performances of anode. The composite material shows high reversible initial capacity and high capacity retention. This could be correlated to the structural stability of the amorphous interface between tin and the crystalline BPO_4 matrix.

Acknowledgments The authors acknowledge Mathieu Morcrette from the CNRS Benchmarking Unit (LRCS, Amiens, France) for the plastic battery assembling and are grateful to CNES (Toulouse, France) for financial support (Contract no. 04/1756/00).

References

1. Courtney, I.A., Dahn, J.R.: J. Electrochem. Soc. **144**, 2045 (1997)
2. Chouvin, J., Branci, C., Sarradin, J., Olivier-Fourcade, J., Jumas, J.-C., Simon, B., Biensan, P.: J. Power Sources **81–82**, 277 (1999)

3. Idota, Y., Kubota, T., Matsufiji, A., Maekawa, Y., Miyasaka, T.: Science **276**, 1395 (1997)
4. Jumas, J.-C., Robert, F., Lippens, P.E., Olivier-Fourcade, J., Willman, P.: Patent n°FR2873855
5. Lee, J.A., Raynor, G.V.: Proc. Phys. Soc. Lond. B **67**, 737 (1954)
6. Shulze, G.E.R.: Z. Phys. Chem. B **25**, 215 (1934)
7. Robert, F., Morato, F., Chouvin, J., Aldon, L., Lippens, P.E., Olivier-Fourcade, J., Jumas, J.-C., Simon, B., Biensan, P.: J. Power Sources **119–121**, 581 (2003)
8. Robert, F., Lippens, P.E., Olivier-Fourcade, J., Jumas, J.-C., Morcrette, M.: J. Power Sources **146**, 492 (2005)
9. Gozdz, A.S., Schmutz, C.N., Tarascon, J.-M., Warren, P.C.: Pat. Coop. Treaty Appl. PCT/US 94/08772, (1994)
10. Kelder, E.M., Jak, M.J.G., De Lange, F., Schoonman, J.: Solid State Ionics **85**, 285 (1996)
11. Olivier-Fourcade, J., Jumas, J.-C., Simon, B., Godiveau, O.: Chem. Phys. Lett. **308**, 135 (1999)

Hyperfine Interact (2006) 167:739–746
DOI 10.1007/s10751-006-9350-1

Influence of Cu and Ni on the morphology and composition of the rust layer of steels exposed to industrial environment

L. M. Ocampo C. · O. R. Mattos · I. C. P. Margarit-Mattos · J. D. Fabris · M. C. Pereira · H. R. Rechenberg · D. L. A. de Faria

Published online: 5 December 2006

Abstract Four samples of steels with alloying elements were exposed to an industrial environment during 1,955 days, aiming to elucidate the effect of the alloying elements Cu and Ni on the resistance of weathering steels to corrosion processes. The samples were characterized with optical microscopy, scanning electron microscopy (SEM), powder X-ray diffraction (XRD), saturation magnetization measurements and with energy dispersive (EDS), infrared, Mössbauer and Raman spectroscopies. All the steels originated orange and dark corrosion layers; their thicknesses were determined from the SEM images. EDS data

L. M. Ocampo C.
Facultad de Minas, Escuela de Ingeniería de Materiales, Universidad Nacional de Colombia, M3 050 Medellín, Colombia
e-mail: lmocampo@unalmed.edu.co

O. R. Mattos
EE/COPPE/PEMM, Federal University of Rio de Janeiro, P.O. Box 68501, CEP 21945-970 Rio de Janeiro, Brazil
e-mail: hercilio@macbeth.if.usp.br

I. C. P. Margarit-Mattos
Department of Inorganic Processes, School of Chemistry, Federal University of Rio de Janeiro, 91949-900 Rio de Janeiro, RJ, Brazil
e-mail: margarit@metalmat.ufrj.br

J. D. Fabris (✉) · M. C. Pereira
Department of Chemistry, ICEx, Federal University of Minas Gerais, Campus Pampulha, 31270-901 Belo Horizonte, Minas Gerais, Brazil
e-mail: jdfabris@ufmg.br

M. C. Pereira
e-mail: mcpqui@ufmg.br

H. R. Rechenberg
Institute of Physics, University of São Paulo, P. O. Box 66318, 05315-970 São Paulo, SP, Brazil
e-mail: hercilio@macbeth.if.usp.br

D. L. A. de Faria
Institute of Chemistry, University of São Paulo, P. O. Box 26077, 05513-970 São Paulo, SP, Brazil

of such rust layers showed that the alloying element content decreases from the steel core towards the outer part of the rust layer. Moreover, in the dark rust layer some light-gray regions were identified in the W and Cu-alloy steel, where relatively higher Cr and Cu contents were found. XRD patterns, infrared, Raman and Mössbauer spectra (298, 110 and 4 K) indicated that the corrosion products are qualitatively the same, containing lepidocrocite (γ FeOOH; hereinafter, it may be referred to as simply L), goethite (αFeOOH; G), feroxyhite (δ'FeOOH; F), hematite (αFe_2O_3; H) and magnetite (Fe_3O_4; M) in all samples; this composition does not depend upon the steel type, but their relative concentrations is related to the alloying element. Mössbauer data reveal the presence of (super)paramagnetic iron oxides in the corrosion products. Saturation magnetization measurements suggest that feroxyhite may be an occurring ferrimagnetic phase in the rust layer.

Key words low alloy steels · iron oxides · corrosion

1 Introduction

The knowledge of the resistance of steels to corrosion is very important for metallurgy industries. The weathering steel, also known as low alloy steel, does contain small proportions of alloying elements, typically not more than 1 mass% of, for instance, Cu, Cr, Ni or P. In some cases, the weathering steel is preferable to the mild steel, due to the formation of an adherent and compact rust layer known as "patina," which tends to decrease its corrosion rate. The formation of the patina is favored by the presence of alloying elements, and also of SO_2 and humid–dry cycles of the industrial atmosphere. The exposition time to such conditions tends to increase the patina layer. According to the literature, the alloying elements tend mainly to decrease the size of the corrosion thickness [1, 2]. However, in those works, contents of the alloying elements were used in higher proportions than that of the weathering steel [3–6], and they were combined with other elements [7], making it difficult to infer about their individual contribution to the resistance of the steel to corrosion. The main objective of this work was to study specifically the role of Cu and Ni as alloying elements on the morphology and composition of the rust layer of the corresponding weathering steels.

2 Experimental procedures

Four different steels were used: (1) a commercial weathering steel; (2) a matrix without alloying elements and two special alloys, prepared by addition of (3) 1 mass% Cu and (4) 1 mass% Ni, respectively. The chemical composition of these steels shown in the Table I was selected basing on the works of Larrabee and Coburn [8] and Horton [9].

The steels were exposed to the atmosphere of an industrial area in the city of Ipatinga, state of Minas Gerais, Brazil, during 1,955 days. The corrosion rate of these steels was evaluated from mass loss measurements, in accordance to the ASTM G-90 standard. The optical microscopy (Olympus model MIC-D) was used to monitor the coloration of the rust layer and the SEM (Jeol Model JSM 6460 LV with EDS of Thermo Noran Systems Six model 200) images to obtain information about the morphology and thickness of the rust layer. The rust materials were prepared for spectroscopic techniques by removing the non-adherent corrosion products, with a stylet; the separated fractions were then homogenized and strained. The corrosion products in the rust layer were first characterized with powder

Table I Chemical composition of the studied steel samples (in mass%)

Steels	C	Mn	S	P	Si	Al sol	Cu	Cr	Ni
Weathering (WS)	0.1	0.37	0.009	0.07	0.36	_	0.37	0.56	0.33
Matrix (M)	0.043	0.30	0.015	0.019	0.024	0.047	0.003	0.018	0.015
Cu-alloy (Cu)	0.048	0.28	0.020	0.019	0.024	0.045	1.01	0.007	0.017
Ni-alloy (Ni)	0.040	0.27	0.015	0.020	0.020	0.050	<0.02	<0.02	1.000

Table II Corrosion rate and thickness of the rust layer of the steels

Steels	Ni	Cu	W	M
Corrosion rate/mm year^{-1}	0.02	0.022	0.026	0.032
Thickness of the rust layer/μm	59	66	82	126

XRD (Rigaku Geigerflex with CoKα radiation and nickel filter at 40 kv/30 mA), to identify the crystalline compounds, and with EDS, to estimate the distribution of the alloying elements in the rust layer. The infrared (Nicolet Magna-IR 760, operating in transmission mode, and KBr pellets) data were used to identify the amorphous compounds. Raman measurements (Renishaw Raman Microscope system 3000, using the 514.5 nm laser of an Ohmnichrome Ar^+ source, under 2 mW at the sample, to avoid thermal or photochemical degradation) and Mössbauer (conventional transmission mode, with a ^{57}Co/Rh source with ~10 mCi, at room temperature (RT; ~298 K), 110 and 4, 2 K) provided the experimental bases to identify and quantify the corrosion products. To analyze the Mössbauer spectra, the velocity scale was calibrated with a metallic Fe (αFe) foil; the isomer shift values are quoted relatively to this reference. Data were numerically treated with the least-square NORMOS [10] fitting program. The saturation magnetization measurements were made with a portable soil magnetometer with a fixed field of 0.3 T [11], in an attempt to detect the presence of ferrimagnetic iron oxides, particularly magnetite, maghemite or feroxyhite.

3 Results and discussion

The corrosion rate was lower for the Ni and Cu-alloys, followed by the WS and M steels (Table II). The optical microscopy images revealed that a rust layer, with orange (outer) and dark (inner) corrosion products, was formed in all steels. From SEM images, it was observed cracks in all rust layers. However, in the steels with lower corrosion rate (Ni and Cu), these cracks were thinner, less frequent and closer to the surface of the rust layer. The steel matrix appeared heterogeneous in color, granularity and thickness. The decrease in the thickness of the rust layer (Table II) corresponded to a decrease in the corrosion rate. These results evidence that Cu and Ni contribute to the formation of a thinner rust layer.

In Figure 1, from left to right, they can be seen the resin support (darker area), the rust layer and the steel (lighter area) matrix. The vertical line in the linescan shows the interface between the rust layer and the steel. It was observed that the alloying element contents decrease progressively from the steel matrix towards the outer layer. In the Cu and Ni-alloys there was an accumulation of Cu and Ni at the interface. However in the Ni-alloy the distribution of Ni was more uniform than Cu is in the Cu-alloy. The weathering steel presented some light-gray areas, in the dark region of the rust layer, for which the Cr and Cu contents are higher. The Cu-alloy also presented such light-gray areas, in which the Cu content was found to be higher.

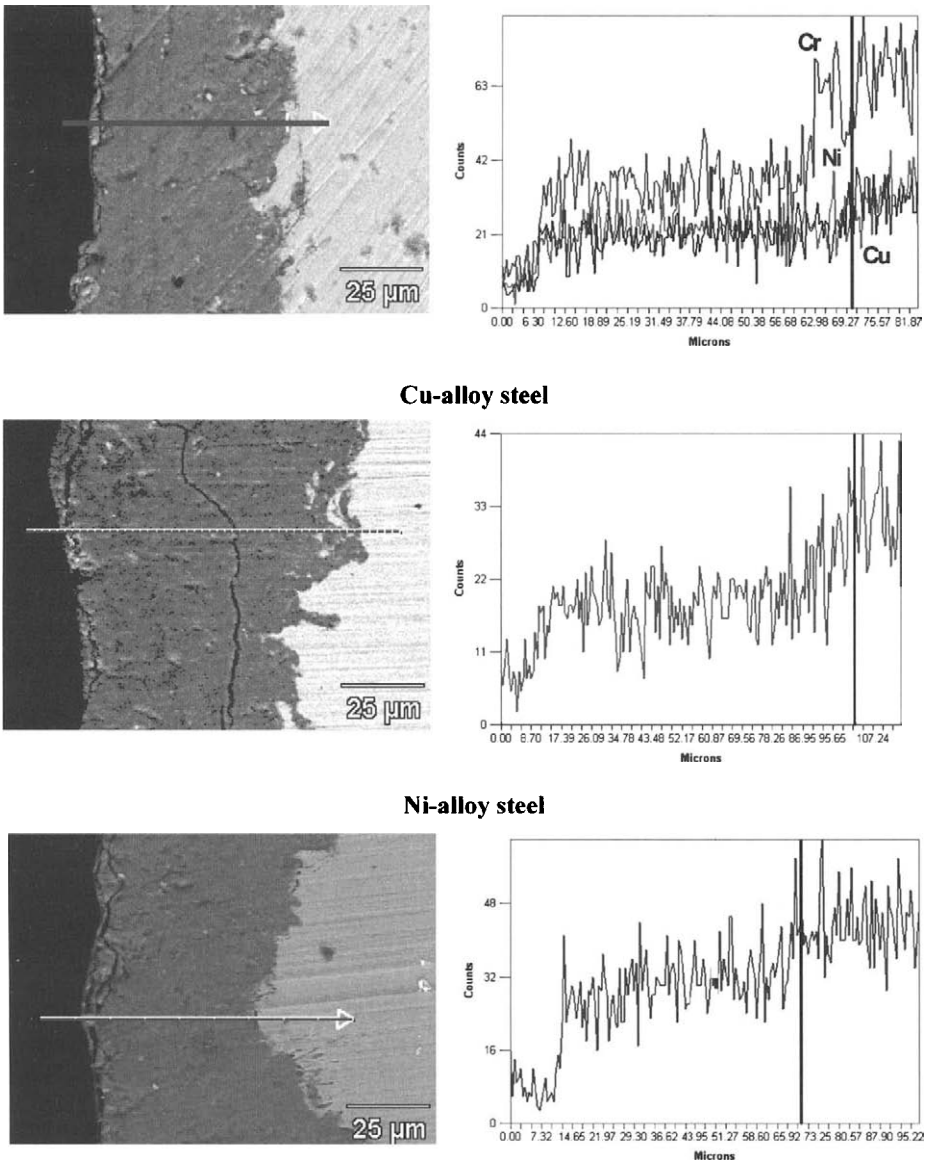

Figure 1 EDS linescan patterns (*right column*) along the horizontal lines of the rust layers of the steels (*left column*).

Figures 2a and b show the powder XRD patterns and the medium infrared spectra of the corrosion products of these steels, respectively; the diffractograms and infrared spectra were very similar for all steels. From these data, the identified corrosion products are actually lepidocrocite, goethite, feroxyhite and hematite.

Figures 3a and b show the Mössbauer spectra at 110 and 4.2 K, respectively. Once again, the spectra are very similar for all steels. In the RT (not shown) and 110 K Mössbauer spectra, it was observed incipient sextets, probably due to goethite and hematite and a doublet assignable to (super)paramagnetic compounds in the rust layers.

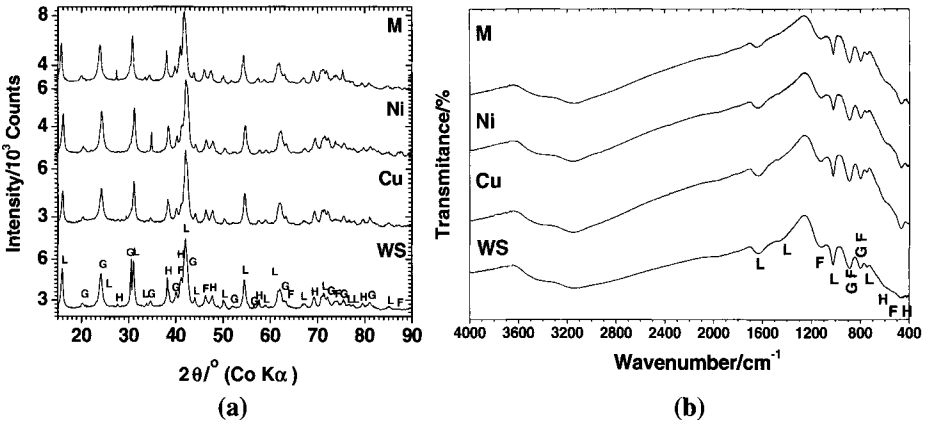

Figure 2 **a** Powder XRD patterns and **b** medium infrared spectra of the corrosion products of the rust layer of the steels.

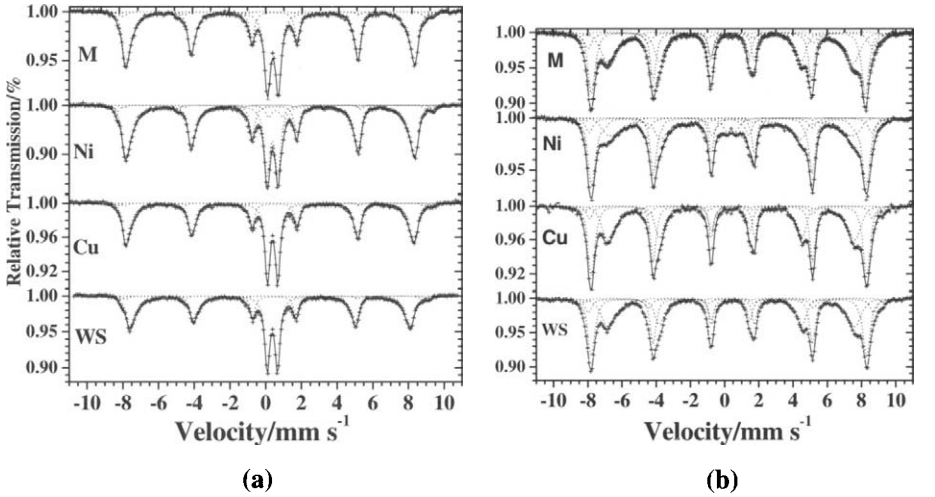

Figure 3 (**a**) 110 K and (**b**) 4.2 K Mössbauer spectra for the corrosion products from the steels.

The 4.2 K Mössbauer spectra were fitted with a hyperfine field distribution. The analysis of the 4.2 K Mössbauer spectra reveals the presence of lepidocrocite, goethite, feroxyhite and hematite. This hematite underwent the Morin transition. For the Ni-alloy steel it is observed a paramagnetic doublet of Fe^{3+} probably due to lepidocrocite. The fitting parameters of the 4.2 K Mössbauer spectra are presented in Table III. From this table, it can be seen that, for all steels, lepidocrocite and goethite are the main corrosion products, followed by feroxyhite and hematite. The proportions of lepidocrocite and hematite are comparable, for all steel, whereas those of goethite and feroxyhite change, depending upon the steel.

It was observed that a decrease of the corrosion rate follows an increase of the proportion of goethite (Figure 4a). These results agree with data reported in the literature: more protective steels have higher goethite relative concentration [1, 2, 13]. It was also observed that an increase of the corrosion rate is accompanied by an increase of the relative

Table III Fitted parameters of the 4.2 K Mössbauer spectra of the steel samples

Steel	Oxide	δ/mm s^{-1}	ε, Δ/mm s^{-1}	B_{hf}/T	Γ/mm s^{-1}	Ar/%	f	Ar/f	CAr/%
WS	L	0.501(3)	0.033(7)	45.5(2)	0.31[a]	39.9(2)	0.82(5)	48.66(6)	36.567(2)
	G	0.498(2)	−0.23[a]	50.6(5)	0.32[a]	45.2(2)	0.80(5)	56.50(6)	42.459(2)
	F	0.494(7)	0[a]	51.68(8)	0.50(3)	12.5(2)	0.49(3)	25.51(6)	19.170(3)
	H	0.49[a]	0.39[a]	54.1	0.32(7)	2.4(2)		2.4(2)	1.80(8)
Cu	L	0.506(5)	0.035(9)	45.4(3)	0.33[a]	42.2(2)	0.82(5)	51.46(6)	39.658(2)
	G	0.505(2)	−0.234(6)	50.5(3)	0.30[a]	46.6(2)	0.80(5)	58.25(6)	44.890(2)
	F	0.50(1)	0[a]	51.2(2)	0.42(6)	8.5(2)	0.49(3)	17.35(7)	13.371(4)
	H	0.49[a]	0.39[a]	54.1(2)	0.30(8)	2.7(2)		2.7(2)	2.08(7)
Ni	L	0.507(7)	0.04(2)	45.0(6)	0.31[a]	33.7(2)	0.82(5)	41.10(6)	31.110(2)
	G	0.502(2)	−0.229(4)	50.3(4)	0.30[a]	49.0(2)	0.80(5)	61.25(6)	46.363(2)
	F	0.482(9)	0[a]	51.2(1)	0.51(4)	11.0(2)	0.49(3)	22.45(6)	16.993(3)
	H	0.49[a]	0.39[a]	53.8(2)	0.31(1)	1.7(2)		1.7(2)	1.3(1)
	Fe^{3+}	0.52[a]	0.52[a]		0.56[a]	4.6(2)	0.82(3)	5.61(6)	4.25(1)
M	L	0.476(4)	0.020(9)[a]	45.4(2)	0.31[a]	41.2(2)	0.82(5)	50.24(6)	37.334(2)
	G	0.477(2)	−0.23[a]	50.3(3)	0.32[a]	42.6(2)	0.80(5)	53.25(6)	39.570(2)
	F	0.47(1)	0[a]	51.6(1)	0.56(5)	14.3(2)	0.49(3)	29.18(6)	21.684(3)
	H	0.49[a]	0.39	54.1	0.37(1)	1.9(2)		1.9(2)	1.4(1)

[a] Fixed parameter during the fitting procedure. WS=weathering steel, Cu=Cu-alloy steel, Ni=Ni-alloy steel and M=matriz steel. L=lepidocrocite, G=goethite, F=feroxhyte and H=hematite, δ=the isomer shift relative to the αFe, ε=quadrupole shift, Δ=quadrupole splitting, B_{hf}=maximum probability magnetic hyperfine field, Γ=line width; Ar is the Mössbauer subspectral area, f is the recoilless fraction [12] and CAr=$(Ar/f)_i/\Sigma(Ar/f)_i$ that correspond to the fraction de Fe present in each iron oxide in the rust layer of the steels.

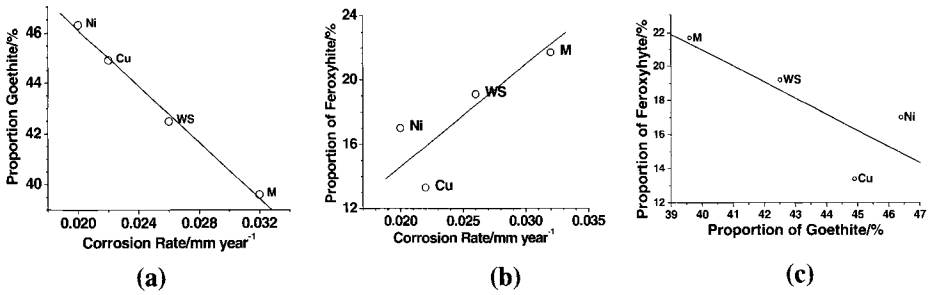

Figure 4 Correlation between **a** the proportion of goethite and the corrosion rate; **b** the proportion of feroxyhite and the corrosion rate and **c** the proportions of feroxyhite and goethite in the steel samples.

amount of feroxyhite (Figure 4a), resulting that, as a general trend, an increase of goethite is accompanied by a decrease of the relative concentration of feroxyhite (Figure 4c).

Feroxyhite is the only ferrimagnetic iron oxide present in the rust layers of these steels and it responds for the saturation magnetization values in all steels: 1.5; 2.5; 3.3 and 4.0 J T^{-1} kg^{-1} for Cu, Ni, WS and M, respectively. It was observed that an increase of saturation magnetization values was accompanied by an increase of corrosion rates.

Results of powder X-ray diffraction, infrared and Mössbauer spectroscopies indicate that the corrosion products are virtually the same for all steels, but Mössbauer data show that the alloying elements influence the relative concentration of the corrosion products.

Raman spectroscopy was confirmed to be a powerful tool on the identification of the corrosion products [1, 14]: lepidocrocite is the main compound present in the orange rust layer, followed, in a lesser extent, by goethite (Figure 5a). In the light gray area, where Cu

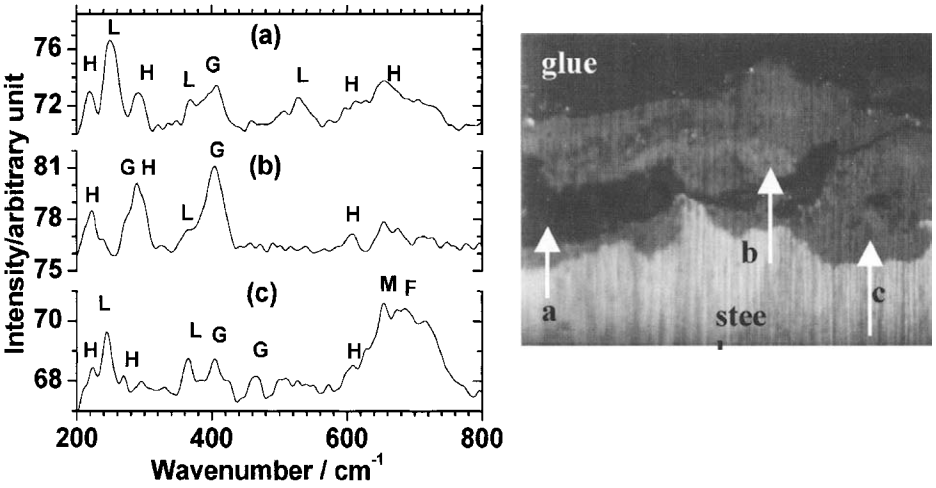

Figure 5 Raman spectra of **a** *red* island; **b** *light-gray* area and **c***dark-gray* layer of the Cu-alloy.

and Cr contents were found to be high, goethite and hematite bands dominated the spectrum (Figure 5b). The Raman spectrum of darker gray regions (Figure 5c) showed a broad band, centered at ca. 680 cm^{-1} and overlapped several narrow bands, as the major feature. Both magnetite and feroxyhite present bands in this spectral region and it is very likely that these two compounds are present in the studied rust area. It is surprising that magnetite was only detected by Raman spectroscopy and a possible reason is that magnetite could form an adherent layer, not easily scratched out and then it is in small quantities in the rust layers of the steels.

4 Conclusions

The alloying elements Cu and Ni influence the corrosion rate, the rust layer thickness, the saturation magnetization values, and the way they are distributed in the rust layer, which presents orange and dark corrosion products. The identified compounds, namely lepidocrocite, goethite, feroxyhite and hematite, appear in all studied steels, but Cu and Ni influence further the relative quantity of the corrosion products. The major compounds are lepidocrocite, goethite, followed by the feroxyhite and hematite. Magnetite is only detected with Raman spectroscopy as it occurs in very small quantities in these loose rust layer and it is hardier identified with the other techniques used in this work. It is also found that an increase of the corrosion rate is accompanied by a decrease of the proportion of goethite. An increase in the relative quantity of feroxyhite is accompanied by an increase in the corrosion rate and saturation magnetization values. From Raman spectroscopy it was found that the orange corrosion products are mainly constituted by lepidocrocite with minor quantity of goethite, feroxyhite and hematite, and the dark corrosion is constituted by goethite, feroxyhite, hematite and magnetite. The areas of the rust layer in which the Cu and Cr contents are higher contain higher proportions of goethite.

Acknowledgements The authors wish to express their gratitude to USIMINAS (the steel metallurgy industry in the state of Minas Gerais, Brazil), for providing the steel samples and to allow exposing some of them in its industrial environment and to the Brazilian agencies CNPq, CAPES, FAPERJ, FAPESP, FUJB and FAPEMIG for the financial support.

References

1. Oh, S.J., Cook, D.C., Towsend, H.E.: Corros. Sci. **41**, 1687 (1999)
2. Yamashita, M., Miyuki, H., et al.: Corros. Sci. **36**(2), 283 (1994)
3. Kamimura, T., Stratmann, M.: Corros. Sci. **43**, 429 (2001)
4. Stratmann, M., Bohnemkamp, K., Ramchandran, T.: Corros. Sci. **27**(9), 905 (1987)
5. Dillmann, P., Balasubramanian, R., Beranger, G.: Corros. Sci. **44**, 2231 (2002)
6. Balasubramanian, R., Kumar, A.V.R.: Corros. Sci. **45**, 2451 (2003)
7. Usami, A., Kihira, H., Kusonoki, T.: Nippon Steel technical Report 87 January (2003)
8. Larrabee, C.P., Coburn, S.K.: 1^0 ICMC, London, 276 (1961)
9. Horton, J.B.: Pittsburgh Regional Technical Meeting of American Iron and Steel Institute. Nov. 11, 1 (1965)
10. Brand, R.A.: Angewandte Physik. Universität Duisburg, Germany (1999)
11. Coey, J.M.D., Cugat, O., McCauley, J., Fabris, J.D.: Rev. Fis. Apl. Instrum. **7**(1), 25 (1992)
12. Oh, S.J., Cook, D.C.: J. Appl. Phys. **85**(1), 329 (1999)
13. Balasubramaniam, R., Cook, D.C., Townsend, H.E.: Hyperfine Interact. **141–142**, 369 (2002)
14. de Faria, D.L.A., Venâncio, S., de Oliveira, M.T.: J. Raman Spectrosc. **28**, 873 (1997)

Hyperfine Interact (2006) 167:747–751
DOI 10.1007/s10751-006-9351-0

Mossbauer investigations of corrosion environment influence on Fe valence states in oxide films of zirconium alloys

V. P. Filippov · V. I. Petrov · Yu. A. Shikanova

Published online: 14 November 2006

Abstract Mössbauer investigations about iron atom redistribution in oxide films of zirconium alloys subjected to corrosion at 500°C in pure *oxygen and water pair* have been analysed. The alloys were also subjected to autoclave conditions at a pressure of 10.0 MPa and autoclave conditions at 350°C and at a pressure of 16.8 MPa, using distilled water and water with additives of lithium and fluorine. It is shown that, depending on the corrosion environment, various compounds of iron, such as α-Fe_2O_3, Fe_3O_4, and FeO, as solid solutions of iron in ZrO_2 are formed in oxide films.

Key words alloy corrosion · Fe valence state · zirconium alloy

1 Introduction

The active use of zirconium alloys in the nuclear industry is related to a number of its positive properties, such as the low cross-section of thermal neutrons, plasticity, and high melting temperature. In order to improve its mechanical and corrosion properties, zirconium alloys use various dopants (iron, tin, niobium, nickel, chrome, and other atoms) [1, 2]. In this paper, numerous data relating to the change in iron atoms state in oxide films depending on corrosion conditions are analysed. A comparison of our data and those provided by other researchers is given.

2 Technique of alloy preparation

The techniques used to prepare the alloys for the corrosion and Mössbauer experiments are described in [3–6]. The Zr-1.3% Sn-1% Fe-0.5% Cr-0.12% O alloy was tested at 360°C in autoclave conditions (ð=16.8 MPa), in water with 10 ppm Li and 650 ppm B (as boric

V. P. Filippov (✉) · V. I. Petrov · Y. A. Shikanova
Moscow Engineering Physics Institute (State University),
31 Kashirskoe Shosse, Moscow 115409, Russia
e-mail: vpfilippov@mephi.ru

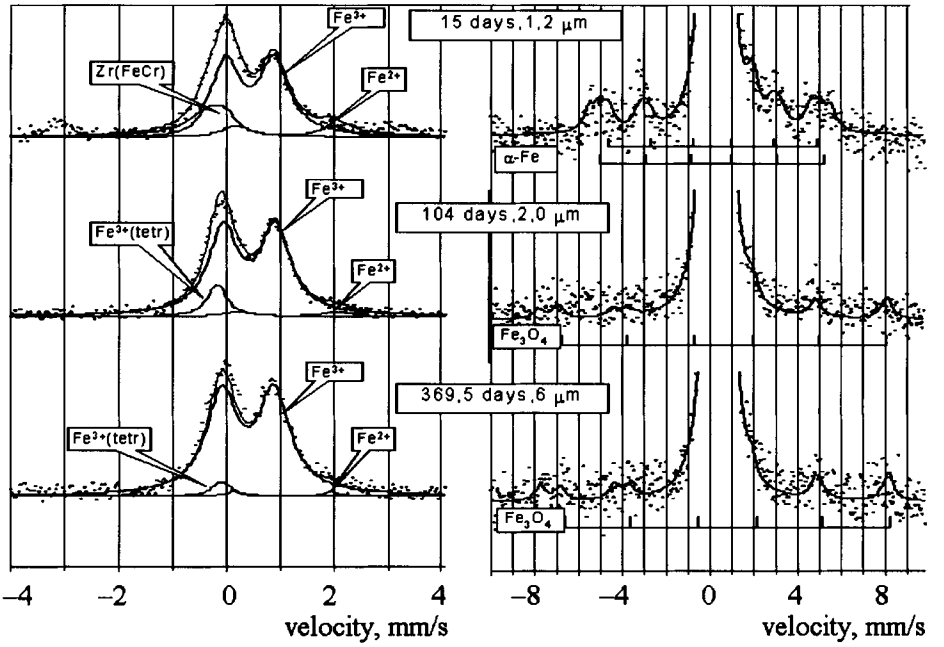

Figure 1 Fitings of ^{57}Fe CEMS spectra, taken at room temperature.

acid) (the concentrations are given in mass%). The duration of the corrosion tests was 370 days. The double alloys with (0.5÷1.5) mass% Fe concentration, also triple and four-fold alloys with (0.5÷1.5) mass% Fe, (0.5÷1.5) mass% Sn, (0.5÷0.7) mass% Cu, 0.5 mass % W, 0.5 mass% Cr were prepared. The corrosion tests were performed in stainless steel autoclave at 350 and 500°C. The corrosion test of Zr+1.5 mass% Fe in air were tested at 450 and 750°C. The oxide film was removed from the alloy both mechanically and chemically. The spectrometers were calibrated using a standard α-Fe absorber. The isomer shifts are given relative to α-Fe.

3 Experimental results

3.1 Spectra obtained after corrosion of alloys in water with B and Li

The spectra of oxide films of Zr-1.3% Sn-1% Fe-0.5% Cr-0.12% alloys were received in CEMS and transmission modes. Early research has shown that in the initial alloy, the iron atoms similar to those in Zr(Fe,Cr)2 intermetallic compound [4]. Figure 1 shows the CEMS spectra for several oxide film thicknesses. The left part of the figure shows the central part of the spectra, with the best resolution of lines of paramagnetic phases. In the right part of the figure, the spectra have been compressed along the velocity axis and stretched on along the intensity axis to better observe the lines of magnetic phases.

The spectra analysis shows that on 0.3–1.2 μm thick oxide films the paramagnetic phases Zr(Fe, Cr)$_2$ (with IS=−(0.15–0.25) mm/s, QS=0.22–0.32 mm/s), Fe^{3+} (with IS= 0.35–0.45 mm/s, QS=0.9–1.1 mm/s), and Fe^{2+} (IS=0.6–1.1 mm/s, QS=0.9–1.3 mm/s)

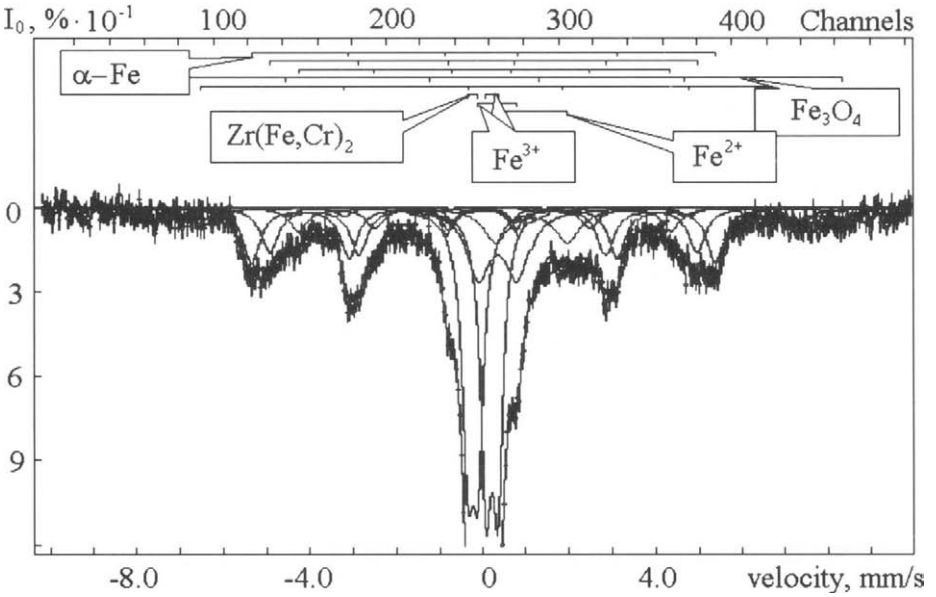

Figure 2 ^{57}Fe Mossbauer transmission spectra of oxide film of sample after 47 days of oxygenation (1.6 μm), taken at room temperature.

were found. Thus, in the initial corrosion stage in oxide film with the existence of Fe^{3+} and Fe^{2+}, the $Zr(Fe,Cr)_2$ particles are presented.

The traveling path for the conversion electrons of iron atoms is close to 0.3 μm. Therefore, for the 0.3 μm-thick oxide film, the $Zr(Fe,Cr)_2$ lines can be assigned to the precipitates which are located in the oxide film as well as in the metallic α-Zr matrix.

When the oxide film thickness increases, the intensities of both Fe^{2+} and $Zr(Fe,Cr)_2$ doublets decrease. This can be explained by the fact that the iron atom oxidises during corrosion. Taking into account [3, 4, 7], we can conclude that in the oxide films of these alloys the solid solutions of the Fe^{2+} and Fe^{3+} ions in ZrO_2 are formed. An analysis of the right part of Figure 1 shows the presence of lines due to hyperfine magnetic splitting of the magnetic phases in oxide films. The parameters of theses lines in the first spectra of the right part of Figure 1 are $B_{ef1} = (33.0 \pm 1.0)T$, and lines with $B_{ef2} = (30.5 \pm 1.0)T$ and $B_{ef3} = (27.5 \pm 1.0)T$. As it is shown in [4], these parameters correspond to the spectrum parameters of the Cr atom solid solution in α-Fe.

When the thickness of the oxide film increases, the intensity of metallic iron lines decreases and the lines of hyperfine magnetic splitting of Fe_3O_4 appear. It has been noticed that α-Fe lines are visible from the 1.2 μm thick oxide film, whereas the lines of a Fe_3O_4 compound are visible only after the thickness of the oxide film reaches 2.0 μm.

In order to investigate iron atom states for all oxide film thicknesses, the spectra of various-thickness separated films, from 0.3 up to 6.0 μm, have been collected. The spectra of 1.6 (Figure 2) and 6 μm (Figure 3) are shown to illustrate the change in iron chemical state as oxide film thickness increases.

In the transmission spectra of 1.6 μm thick oxide film (separated mechanically), intensive lines of quadruple splitting of paramagnetic phases can be observed. The fitting shows the lines of the $Zr(Fe,Cr)_2$ intermetallic particles. These particles were separated from the metallic part of the sample with oxide film.

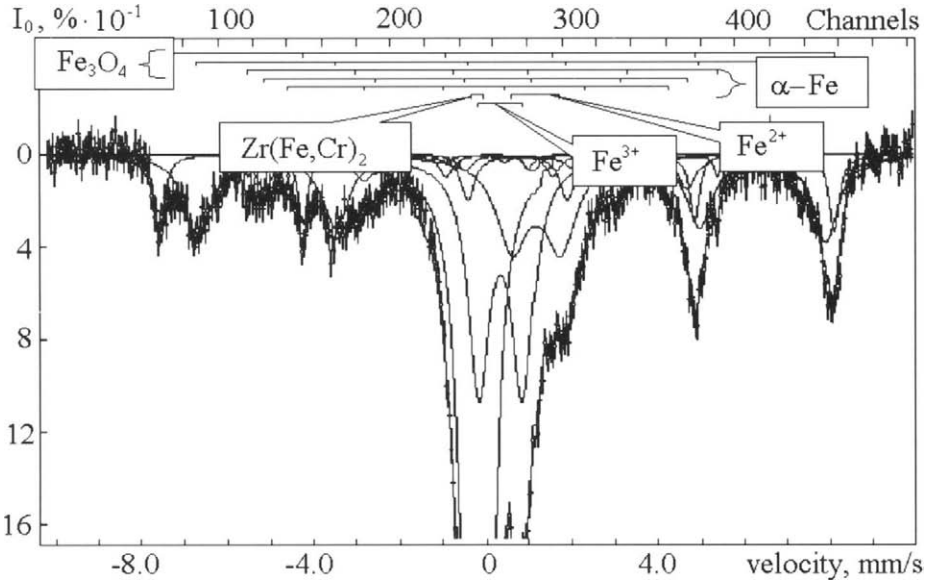

Figure 3 ^{57}Fe Mossbauer transmission spectra of oxide film of sample after 370 days of oxygenation (6.0 μm), taken at room temperature.

The 6 μm thick oxide film (Figure 3) was removed mechanically. Fitting shows the existence of Fe_3O_4, metallic α-Fe with Cr atoms. Fe^{+3} and Fe^{+2} ions are probably in solid solution in ZrO_2. The lines of the Fe_3O_4 compound have quite large intensities, and lines of the solid solution Cr in α-Fe are seen.

3.2 Corrosion in air

The spectra analysis [6] shows that under 0.1 MPa pressure at 750°C in oxide films, the α-Fe_2O_3, FeO and solid solutions of iron atoms in ZrO_2.compounds are formed. A decrease in temperature down to 450°C decreases the speed of corrosion, but in oxide films *complementary* metallic particles of α-Fe are formed. Low pressure (p=1.37 Pa, t=750°C) corrosion test of Zr-1.21 mass% Fe and Zr-1.21 mass% Fe-0.81 mass% Cu-0.42 mass% W alloys shows that in oxide films, α-Fe is formed, and its concentration increases with increasing oxide film thickness. After 17 h of corrosion, we can see the lines of Fe_3O_4 and lines which show the presence of a solid solution of iron atoms in hydrides (ZrH type). Low pressure corrosion of alloys doped by Cu and W gives slower oxidation than a binary alloy. It is important to note that the Fe_3O_4, compound was not detected in all stages of the corrosion process up to 20 h. This means that an interrelation between corrosion resistance and redistribution of iron atoms in ZrO_2 exists. The high α-Fe concentration in oxide films indicates the best corrosion resistance.

3.3 Corrosion in oxygen

Fitting of the spectra of oxide films of binary and multicomponent alloys [3, 5, 7] shows the lines of hyperfine magnetic splitting of α-Fe, α-Fe_2O_3, phases and the lines of paramagnetic phases, corresponding to FeO and solid solutions of Fe^{3+} and Fe^{4+} in ZrO_2 compounds [8].

The concentration of all phases, except Fe^{4+} solid solution in ZrO_2, increases. It was found that in binary alloys, the concentration of α-Fe is lower than in a multicomponent alloy.

It was shown that after transition to catastrophic corrosion, the concentration of α-Fe decreases and the concentration of α-Fe_2O_3 increases. Once again, these data show that there is an interrelation between the corrosion behavior of alloys and redistribution of iron atoms in ZrO_2. It was noted that in multicomponent alloys there is more α-Fe in ZrO_2, and the time of transition to catastrophic corrosion is longer.

3.4 Corrosion in autoclave

Analysis of spectra of oxide films obtained in an autoclave [3, 5, 7] shows the presence of the $Fe(OH)_3$, α-Fe_2O_3, and Fe^{3+} solid solutions in ZrO_2 compounds. The $Fe(OH)_3$ compound is unstable and under high temperature decays to α-Fe_2O_3 oxide and water. The great difference between water steam and autoclave corrosion is the following: in water steam, the Fe_3O_4 is formed on oxide film; in the autoclave, Fe_2O_3 is formed. It was found that the interrelation between redistribution of iron atoms in ZrO_2 and the alloy corrosion resistance exists both in autoclave and water steam corrosion.

4 Conclusion

1. The intermetallic compounds with iron in zirconium alloys during corrosion are destroyed, and iron atoms in oxide films form precipitates of metallic iron, iron oxides with various valences of iron, and solid solutions of Fe^{2+}, Fe^{3+}, Fe^{4+} in ZrO_2.
2. The valence state of iron atoms in oxide films depends on the corrosion environment. Oxygen and great pressure of water increase the relative concentration of α-Fe_2O_3; the presence of B and Li increases the probability of formation of Fe_3O_4.
3. The correlation between the iron atoms redistribution in oxide films and the alloy corrosion resistance was established. The alloys with more α-Fe content in oxide films have a greater corrosion resistance. Transition to catastrophic corrosion is linked to a decrease in concentration of α-Fe and an increase in concentration of iron oxides.

References

1. IAEA-TEC-DOC-996: Waterside Corrosion of Zirconium Alloys in Nuclear Power Plants. IAEA, Vienna (1998) (ISSN 1011-4289)
2. Lemoine, C., Fnidiki, A., Lemarshand, D., Teillet, J.: J. Phys., Condens. Matter **11**, 8341 (1999)
3. Babikova, Y.F., Gruzin, P.L., Ivanov, A.V., Filippov, V.P.: At. Energy (N.Y.N.Y.) **38**, 138 (1975)
4. Pecheur, D., Filippov, V., Bateev, A., Ivanov, Yu.: Thirteen international symposium. In: Moan, G. D., Ruling, P. (eds.) ASTM STP 1423, p. 135. ASTM, West Conshohocken, PA (2002)
5. Babikova, Y.F., Gruzin, P.L., Filippov, V.P., Khaikovskij, A.A., Abramtzev, V.N., Shtan, I.I., Ivanov, A.V.: Metallurgia. i metallovedenie chistych metallov **12**, 20 (1976)
6. Babikova, Y.F., Gruzin, P.L., Ivanov, A.V., Filippov, V.P.: Izv. Vyss. Ucebn. Zaved., Fiz. **74**, 70 (1981) (in Russian)
7. Babikova, Y.F., Gruzin, P.L., Filippov, V.P., Ivanov, A.V.: In: Zirconium and its Alloys, p. 70. Energoatomizdat, Moscow (1982)
8. Babicova, Yu.F., Ivanov, A.V., Filippov, V.P., Abramtsev, V.N.: Sov. Phys. Crystallogr. **27**, 236 (1982)

Hyperfine Interact (2006) 167:753–758
DOI 10.1007/s10751-006-9352-z

Atmospheric corrosion of mild steel in Oman

Abbasher Gismelseed · S. H. Al-Harthi · M. Elzain · A. D. Al-Rawas · A. Yousif · S. Al-Saadi · I. Al-Omari · H. Widatallah · K. Bouziane

Published online: 14 November 2006

Abstract A systematic study has been made of the initial corrosion products which form on mild steel capons exposed near the coastal region of Oman and at some industrial areas. The phases and compositions of the products formed at different periods of exposure were examined by using Mössbauer spectroscopy (295 and 78 K) and X-ray diffraction (XRD) techniques. The results show that lepidocorcite and maghemite are early corrosion products and goethite starts to form after 2 months of metal exposure to the atmosphere. Akaganeite is an early corrosion product but it forms in marine environments only, which reflects the role of chlorine effect in the atmosphere. The 12 months coupons showed the presence of goethite, lepidocorcite and maghemite, but no akaganeite being seen in the products of one of the studied areas.

Key words lepidocorcite · maghemite · akaganeite

1 Introduction

Metallic corrosion rates vary considerably with moisture and contaminant contents of atmosphere. Oman has a 1,700 km coastline that extends from the straits of Hormuz in the north to Salalah in the south. As a whole this region is characterised by high annual water evaporation, with high salinity ranging from 36.5 to 40.5 psu. Near the coastal regions, air is laden with increasing amounts of sea salt (in particular NaCl). Moisture exchange across the air–sea interface is enhanced by the extremely arid nature of the bordering lands. At industrial areas, such as Al-Rusail, Mina Al-Fahal and Sohar appreciable amounts of SO_2, which converts to sulfuric acid, and lesser amounts of H_2S, NO_2, NH_3 are encountered. Because of a very strong seasonal variation and inter-annual fluctuation in weather resulting from the reversal of south–west and north–east monsoons, Oman renders most climate conditions possible and offers a unique opportunity to study the influence of the

A. Gismelseed (✉) · S. H. Al-Harthi · M. Elzain · A. D. Al-Rawas · A. Yousif · S. Al-Saadi · I. Al-Omari · H. Widatallah · K. Bouziane
Department of Physics, College of Science, Box 36, Al-Khod 123, Oman
e-mail: abbasher@squ.edu.om

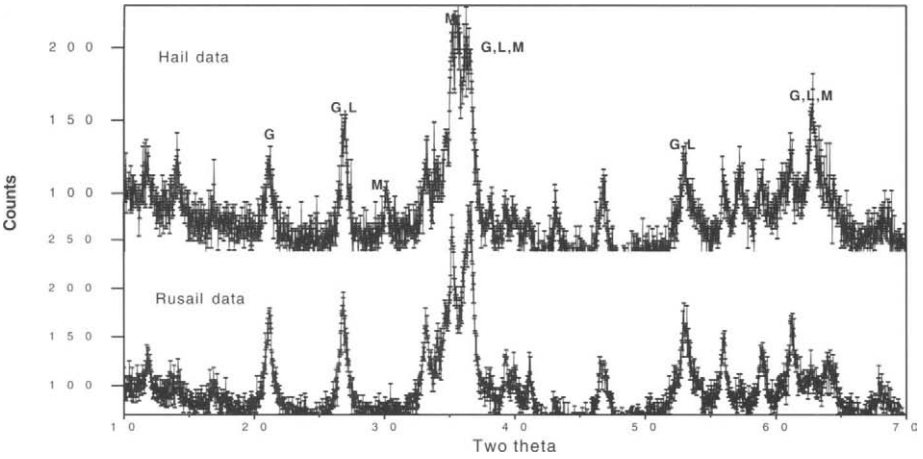

Figure 1 XRD spectra of Al-Hail and Rusail sites.

environment on the corrosion rates and the corrosion products of mild steel, copper, aluminum and zinc.

The present study is part of a strategic project aimed to produce the first corrosion maps of mild steel, copper, aluminum and zinc of Muscat region. The corrosion products formed on mild steel coupons exposed at two selected sites out of sixteen stations at different periods were identified by using Mössbauer spectroscopy and X-ray diffraction techniques.

2 Samples preparation and experimental methods

The commercial mild steel coupons of type C1010 were exposed Al-Hail (marine) site which is very close to Oman Gulf shore and at Al-Rusail (industrial area) site which is about 20 km off the shore. The formed corrosion products were carefully scrapped off from the surface of the coupons and prepared for XRD and Mössbauer measurements. However, due to hard filing considerable percentage of α-Fe appeared in the Mössbauer spectra of some samples. The powder X-ray diffraction (XRD) patterns of the samples were recorded on a Philips diffractometer (model pw 1820) with a Co Kα source. Mössbauer measurements were performed on the samples in a continuous liquid nitrogen flow cryostat using a 50 mCi ^{57}Co(Rh) source with a spectrometer in the transmission mode. The spectrometer was calibrated with α-Fe foil spectrum at room temperature.

3 Results and discussion

X-ray powder diffraction pattern for all samples were recorded in the angular range 10–70° to obtain a basic identification of the oxides present due to corrosion. Although, the relative peak intensities with the corresponding peaks of the detected oxides were different from coupon to coupon, all the X-ray diffraction patterns had mostly similar features independent of the exposure period and environment (see Figure 1). Goethite, lepidocorcite and maghemite were the main oxides identified with exclusion of akaganeite in each corrosion product. The phases were identified by performing multiple searches on a database using

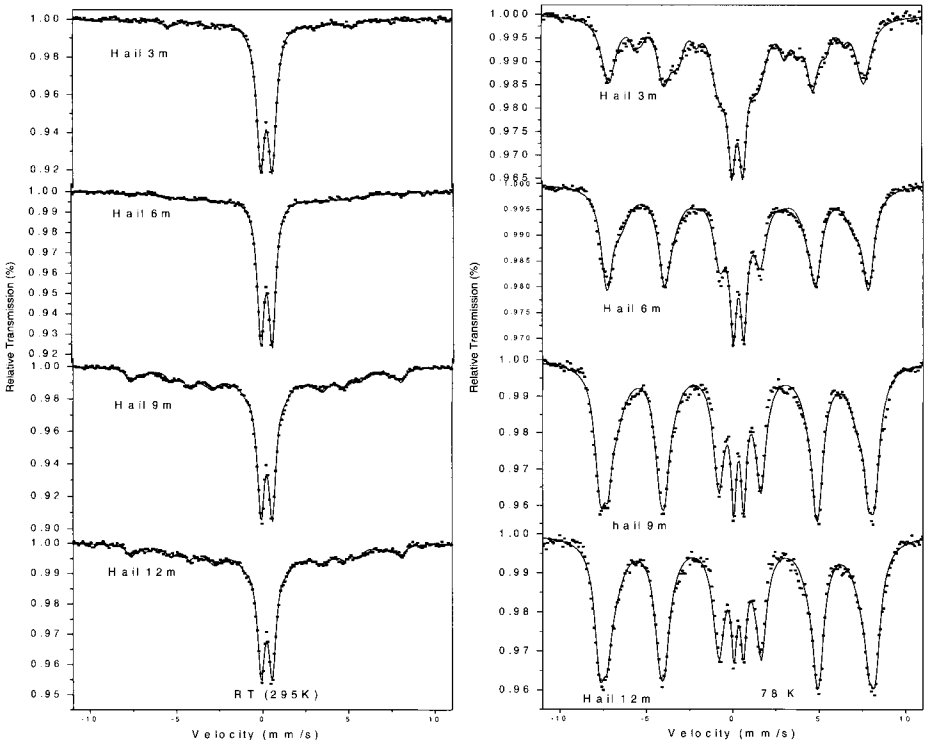

Figure 2 295 and 78 K Mössbauer spectra of the corrosion products on mild steel coupons exposed in Al-Hail site for 3, 6, 9, and 12 months.

PW 1876 PC-identify and PW 1877 APD (automatic Powder Diffraction) software programs.

To complete the identification of the detected oxides and to measure their partial fractions in each of the studied coupons, transmission Mössbauer measurement performed at room temperature and liquid nitrogen are presented in Figures 2 and 3 and their least square fitting parameters are collected in Table I.

The RT (295 K) spectra of Al-Hail site (Figure 2 left) consist of broadened magnetic component and a dominant paramagnetic doublet. The Mössbauer parameters of the doublet (δ=0.34 mm/s and ΔE_Q=0.65 mm/s) are in good agreement with those published for lepidocorcite and superparamagnetic component of goethite and maghemite at RT [1, 2], since the XRD data excluded the presence of akaganeite. The magnetic component of each spectrum were fitted to a distribution program with two /three subspectra since its field distribution is attributed to more than one phase and different particle sizes. One /two of the subspectra are assigned to magnetic goethite α-FeOOH and the third to magnetic maghemite γ-Fe_2O_3. As shown in Table I the maghemite (third component) is not yet crystallized during the first 3 months. It is well known that the magnetic hyperfine field of the well crystallized maghemite is in the range of 48–51 Tesla [1]. In order to identify the superparamagnetic components the Mössbauer spectrum of the samples was recorded at 78 K (Figure 2 right). The resolution of the magnetic component is much better compared to that of RT.

The spectrum was fitted with a doublet assigned for lepidocorcite and superparamagnetic goethite (SP) and three magnetic sub-spectra assigned as follows: magnetic goethite,

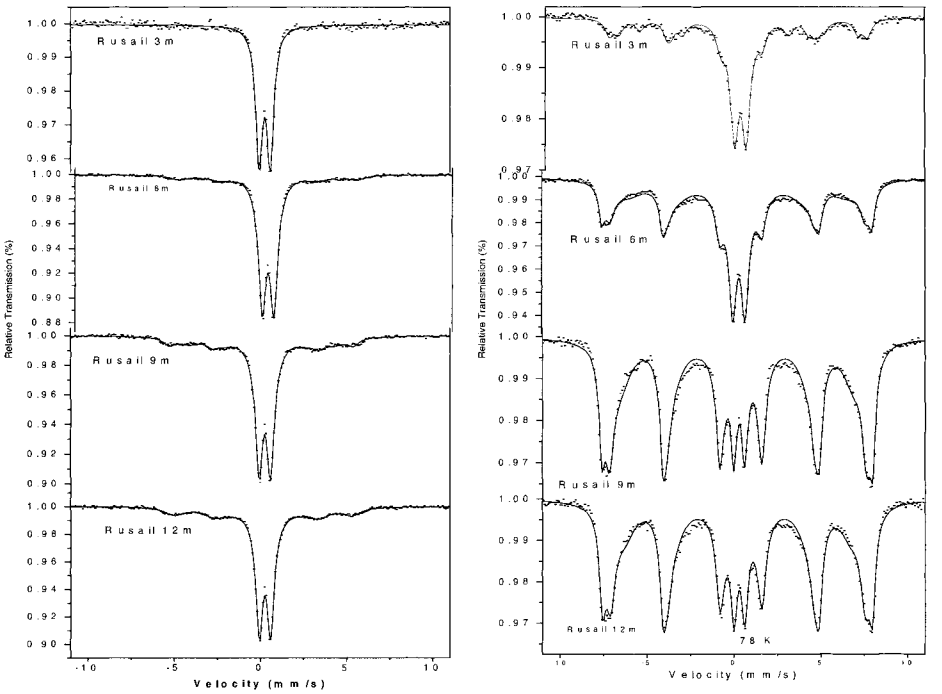

Figure 3 295 and 78 K Mössbauer spectra of the corrosion products on mild steel coupons exposed in Al-Rusail site for 3, 6, 9, and 12 months.

magnetically ordered goethite S2, and maghemite. The area percentages of each component are collected in Table II. In the table, P1 is attributed to lepidocorcite which is paramagnetic at both 295 and 77 K, while S1 is due to superparamagnetic (SP) goethite with particle size less than 8 nm [3]. The percentage of P1 is decreasing with time while S1 is almost constant.

A dominant doublet with weak intensity broadened magnetic component characterizes the Mössbauer spectra of Al-Rusail coupons produced at RT. The coupons are collected at the same periods of Al-Hail coupons. The hyperfine interaction parameters (Table I) obtained for the doublet are attributed to the superparamagnetic goethite, maghemite and lepidocorcite. The magnetic components were fitted to two subspectra with magnetic field in the range of 20–35 Tesla and are assigned to goethite with different particle size. In contrast to Al-Hail coupons there are no magnetic γ-Fe_2O_3 detected in Al-Rusail coupons. The shape of the spectrum at 78 K shows a tremendous change compared to the RT spectrum with a remarkable increase in the relative intensity of the magnetic component (see Figure 3. The 11% contribution of the paramagnetic component as obtained from the fitting results is attributed to the superparamagnetic component of goethite not yet resolved even at 78 K. According to Janot et al. [4] the persistence of this component at 78 K indicates that the size of its particle is below 8 nm. The fitting of the magnetic component at 78 K was achieved by assuming three magnetic sextets, two of them attributed to magnetic and magnetically ordered goethite and the third ascribed to magnetically ordered maghemite. The magnetically ordered superparamagnetic goethite S2 is increasing with time and then decreases leading to the growing of the maghemite γ-Fe_2O_3 component. The identification of the iron oxide phases in the samples as determined by the analysis of 78 K

Table I 295 K Mössbauer parameters of Al-Hail and A-Rusail sites corrosion products

	δ (±0.02) (mm/s)	Δ (±0.01) (mm/s)	B (±0.1) (T)	A (±1) (%)	δ (±0.02) (mm/s)	Δ (±0.01) (mm/s)	B (±0.1) (T)	A (±1) (%)
3 m	Al-Hail site					Al-Rusail site		
α-FeooH, γ-FeooH γ-Fe_2O_3	0.35	0.67		100	0.34	0.66		100
6 m								
α-FeooH, , γ-FeooH γ-Fe_2O_3	0.35	0.66		70	0.35	0.66		83
α-FeooH (m1)	0.38	−0.13	33.8	9	0.37	−0.13	32.2	14
α-FeooH (m2)	0.30	−0.09	25.0	17	0.37	−0.09	25.5	3
γ-Fe_2O_3	0.39	−0.14	48.6	4				
9 m								
α-FeooH, , γ-FeooH γ-Fe_2O_3	0.35	0.66		45	0.35	0.66		64
α-FeooH (m1)	0.30	−0.12	44.6	8	0.27	−0.17	33.2	13
α-FeooH (m2)	0.30	−0.13	27.0	36	0.28	−0.21	26.2	23
γ-Fe_2O_3	0.39	−0.14	48.8	11				
12 m								
α-FeooH, , γ-FeooH γ-Fe_2O_3	0.35	0.66		44	0.35	0.66		64
α-FeooH (m1)	0.31	−0.11	42.8	7	0.35	−0.17	31.9	25
α-FeooH (m2)	0.33	−0.13	26.5	37	0.34	−0.21	20.4	11
γ-Fe_2O_3	0.32	−0.14	48.6	12				

Table II Area percentage of Al-Hail and Al-Rusail coupons calculated from 78 K Mössbauer spectra

	γ-FeOOH P1	α-FeOOH S1 (SP)	α-FeOOH S2	α-FeOOH (magnetic)	γ-Fe_2O_3
Field range (T)[a]	0	0	39–42	43–46	48–51
Al-Hail site					
3 m	13	8	24	55	0
6 m	9	8	31	41	11
9 m	0	9	33	15	43
12 m	0	8	35	13	44
Al-Rusail site					
3 m	47	11	15	27	0
6 m	16	11	34	27	12
9 m	00	11	32	38	19
12 m	00	11	27	40	21

[a] Expected magnetic hyperfine field in Tesla for each component.

Mössbauer spectra are in good agreement with XRD data and their area percentages are collected in Table II.

4 Conclusions

Detailed investigation of the oxide concentration variation which are thought to occur within each exposed coupon will be helpful in explaining the environmental influence on

oxides formation as a function of time. The difference in the growing of α-FeOOH and γ-Fe_2O_3 in each site is of remarkably interest. Such studies will lead to improve selection of the materials and increase the overall understanding of the corrosion processes at the microscopic level.

Acknowledgement Financial support from Sultan Qaboos University under project no. SR/Sci/Phys/02/01 is gratefully acknowledged.

References

1. Cook, D.C., Oh, S.J., Balasubramanian, R., Yamashita, M.: Hyperfine Interact. **122**, 59–70 (1999)
2. Gismelseed, A., Elzain, M., Yousif, A. Al-Rawas, A., Al-Omari, I.A., Widatallah, H., Rais, A.: Hyperfine Interact. **156/157**, 487–492 (2004)
3. Oh, S.J., Cook, D.C., Townsend, H.E.: Corros. Sci. **41**, 1687–1702 (1999)
4. Janot, C., Gibert, H., Tobias, C.: Bull. Soc. Fr. Mineral. Cristallogr. **96**, 281 (1973)

Hyperfine Interact (2006) 167:759–765
DOI 10.1007/s10751-006-9353-y

Structural transformations in lithiated Mn_2Sb electrodes probed by Mössbauer spectroscopy and X-ray diffraction

L. Häggström · C. M. Ionica · J. C. Jumas · L. Aldon · P. E. Lippens · K. Edström

Published online: 16 November 2006

Abstract The electrochemical reactions of Li with Mn_2Sb and small amounts of MnSb have been investigated by Mössbauer spectroscopy and X-ray diffraction. The lithiation transforms initially the MnSb part and later the Mn_2Sb part into amorphous LiMnSb. On further lithiation the LiMnSb phase transforms to rather well crystallized Li_3Sb. In the X-ray diffraction pattern for the fully lithiated sample extruded nanocrystalline Mn is seen for the first time in these type of electrodes. The first delithiation of Li_3Sb results in a mixture of three phases Mn_2Sb, MnSb and LiMnSb. After several cycles (charges and discharges) of the electrode the Mn_2Sb phase disappears completely.

Key words Mössbauer spectroscopy · X-ray diffraction · nanocrystalline material

1 Introduction

A commercial Li-ion battery consists typically of a carbon based anode and a transition metal oxide as cathode. There is, however a great incentive to search for other anode material which can store more Li and function more safely than graphite. One aim has been to find anode compounds which can be cycled several times without loss in capacity, can take a high volumetric load of Li, are safer etc. Several binary intermetallic compounds have been studied with one constituent inactive and the other active. As active elements Sn and Sb have been favorites and as inactive e.g., Mn, Fe, Co, Ni, Cu have been used. *In situ*

L. Häggström (✉)
Department of Physics, Uppsala University, SE-751 21 Uppsala, Sweden
e-mail: lennart.haggstrom@fysik.uu.se

C. M. Ionica · J. C. Jumas · L. Aldon · P. E. Lippens
Laboratoire des Agrégats Moléculaires et Matériaux Inorganiques (UMR 5072 CNRS), Université Montpellier II, CC15 Place Eugène Bataillon, 34095 Montpellier Cedex 5, France

K. Edström
Department of Material Chemistry, Uppsala University, SE-751 21 Uppsala, Sweden

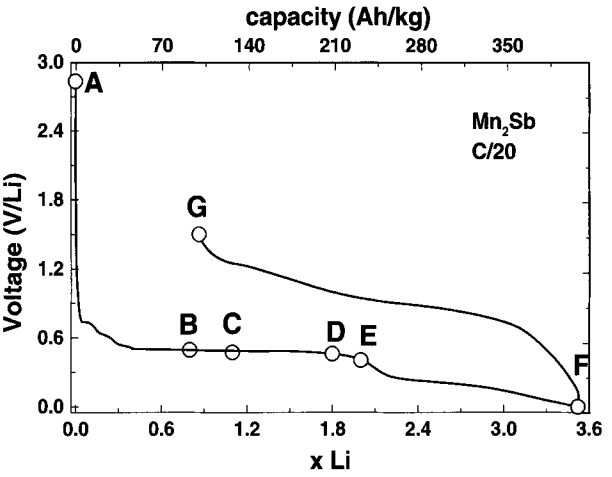

Figure 1 Discharge and charge curve for a representative Mn_2Sb cell. Letters *A* to *G* correspond to the samples used for X-ray diffraction and ^{121}Sb Mössbauer characterizations.

X-ray diffraction study of lithiated MnSb and Mn_2Sb was performed by Fransson et al. [1] followed up by a Mössbauer and X-ray study of MnSb by Ionica et al. [2]. They both found that the lithiation of the pristine material proceeds via an intermediate LiMnSb structure before transforming, with Mn extrusion, to Li_3Sb. This reaction seems to be reversible on delithiation to some extent due to the strong structural relationship between the involved compounds.

By contrast on lithiation of Mn_2Sb a direct transformation to Li_3Sb and on delithiation MnSb was formed and not Mn_2Sb [1].

In this paper, we report on the electrochemical reaction of lithium with Mn_2Sb and on the structural changes as determined by Mössbauer spectroscopy and X-ray diffraction.

2 Experimental

Mn_2Sb was synthesized by heating Mn and Sb metals with purities higher than 99% in alumina crucibles at 900°C under Ar for 25 h [1]. Mn_2Sb powder material was mixed with carbon black and PTFE (polytetrafluorethylene) binder in weight proportion of 84:8:8 and tested as negative electrode in a (Li/$LiPF_6$ (1M, PC:EC:DMC=1:1:3, v/v)/Sb-mixture) Swagelock cell. Discharges and charges were carried out for each cell under galvanostatic condition using a Mac Pile II system at 1/20 Li atom per mol Mn_2Sb and hour rate (C/20) between 0.0 and 1.5 V versus Li^+/Li. The discharge curves were, within experimental error the same for all cells, up to the points where the cell discharge was stopped (points B, C, D, E, F on Figure 1). One cell was, after being fully discharged, charged to a potential 1.5 V (point G on Figure 1).

The cells were opened in a glove box, Mössbauer absorbers and X-ray samples were prepared under Ar atmosphere. Mixtures of the electrode material and cellulose were placed in absorber holders, transparent for γ-rays and airtight closed with plastic covers. Parts of the electrode materials were also laid on glass plates covered by plastic covers for the X-ray measurements.

The pristine Mn_2Sb sample (point A in Figure 1) was ground to a fine powder and for the X-ray measurements placed on a glass plate while for the Mössbauer measurements the absorber was made with the powder mixed with grease.

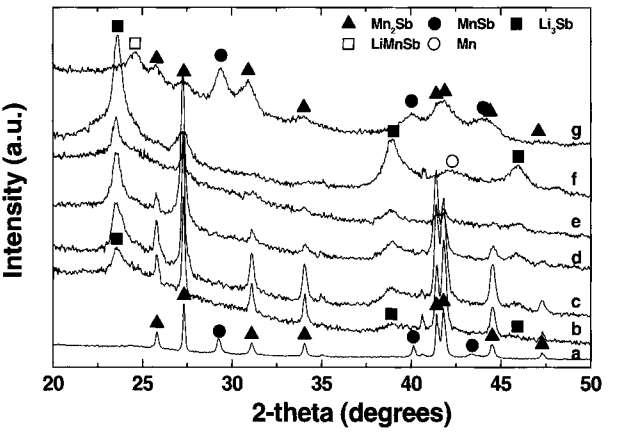

Figure 2 X-ray diffraction patterns of the Mn_2Sb electrode collected during discharge and charge.

^{121}Sb Mössbauer measurements were done in constant acceleration and transmission mode with both the source $Ba^{121m}SnO_3$ (0.2 mCi) and absorber held at 4.2 K. The isomer shifts δ later presented are referred to that source.

X-ray measurements were performed using a D8-Bruker diffractometer with monochromated Cu $K_{\alpha 1}$ radiation.

3 Results and discussions

The voltage profile for the first discharge and charge is shown in Figure 1. Upon discharge the voltage profile shows an immediate drop and a small step staircase behaviour typical for the formation of solid electrolyte interfaces, followed by a plateau similar to the one presented by Fransson et al. [1]. The cell is fully discharged for a Li content of about 3.5 atoms per Mn_2Sb unit. The charging curve follows the same behaviour as found in [1] and the cell is completely charged for a Li content $x \sim 0.9$.

The X-ray diffractograms and the Mössbauer spectra are presented in Figures 2, 3 and 4, respectively.

The Mössbauer spectra were analysed using a modified form of the fitting routine by Ruebenbauer et al. [3]. The source line width was fixed to 1.45 mm/s and the absorber line width Γ_a was kept the same for all lorentzian lines and fitted to on average 1.75 mm/s. In the fitting the electric quadrupole splitting Δ is defined as eQ_gV_{zz}, where Q_g is the electric quadrupole moment of the ^{121}Sb nucleus in its ground state and V_{zz} the electric field gradient. Figure 5 show the intensities of the different phases, as found from the fits of the the Mössbauer spectra.

3.1 Sample A

The X-ray diffractograms as shown in Figure 2 reveal that the pristine sample A can be composed of Mn_2Sb, MnSb and Sb. There is a strong overlap between the lines for MnSb and Sb and in the study by Fransson et al. [1] the MnSb specific line at 2θ=43.3° was hidden by the presence of stronger lines coming from the cell hardware. The presence of Sb is then only assured by the lines at 2θ=41.8 and 47.3° which however overlap with closely lying lines from Mn_2Sb. This means that the presence of Sb reported by Fransson et al. [1] can be questioned.

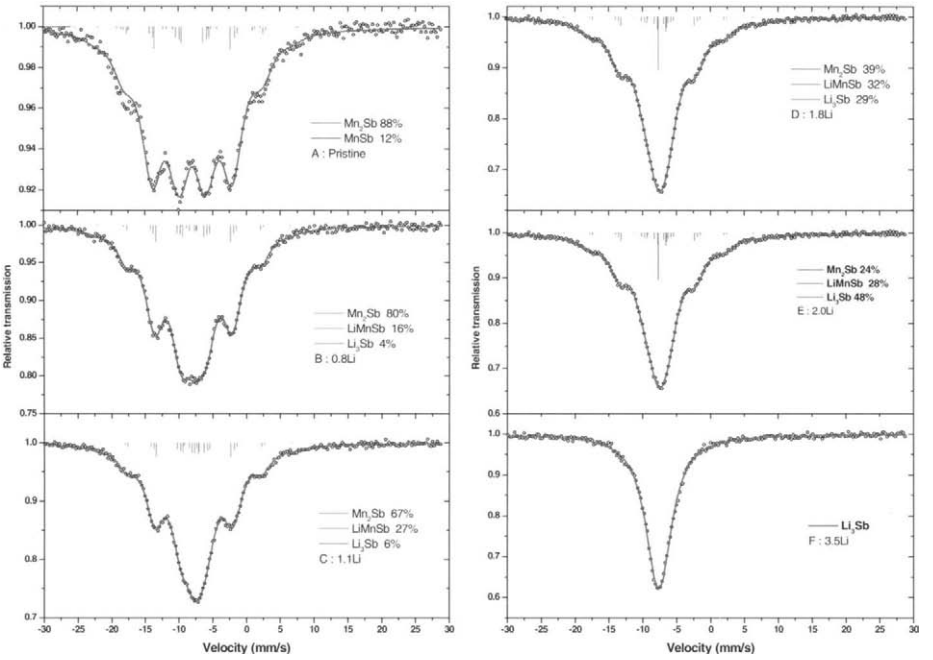

Figure 3 Mössbauer spectra of the samples *A–F* taken from the discharging process.

The Mössbauer spectrum for sample A could be reasonably well fitted using two magnetic patterns representing Mn_2Sb and MnSb. The magnetic moments and thus the magnetic hyperfine fields in Mn_2Sb are perpendicular to the c-axis below 240 K as found by Wilkinson et al. [4] and the charge symmetry around the Sb nuclei is such that the electric field gradient (efg) tensor has it main component along the crystallographic c-axis and its asymmetry parameter η equal to 0. Thus in the fitting procedure the angle between the magnetic hyperfine field B_{hf} and the efg z-axis was fixed to 90°. The isomer shift δ, quadrupole splitting Δ and magnetic hyperfine field B_{hf} were found to be −7.86(9) mm/s, 1.0(5) mm/s and 24.2(9) T, respectively, the latter value close to the value 25.12 T reported by Pinjare et al. [5] from NMR studies. The hyperfine parameters derived for MnSb (δ= −9.2(2) mm/s, Δ=2.6 (9) mm/s and B_{hf}=37(1) T) are in excellent agreement with the values in [2].

3.2 Samples B, C, D, E and F

X-ray diffractograms show that the phase MnSb (12% of the pristine sample A) is completely non-existing for all these samples. The intensity of the Li_3Sb lines grows steadily as a function of Li content while the Mn_2Sb diffraction lines become weaker and weaker. The diffraction lines of the Li_3Sb phase are much broader than the corresponding lines for Mn_2Sb reflecting the deformation of the crystal structures when Li atoms enter.

As also noted by Fransson et al. [1] the X-ray diffractograms do not reveal any lines characteristic for LiMnSb [6] in the discharging process. This phase is however seen in the subsequent delithiation process of Li_3Sb by Fransson et al. [1] and also in the electrochemical reactions of lithium with MnSb (Ionica et al. [2]). It has its most prominent line at 2θ=24.4°.

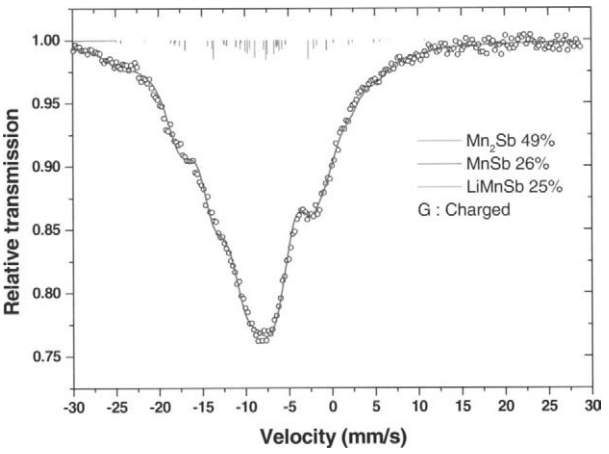

Figure 4 Mössbauer spectra of the sample *G* in the charged state.

The Mössbauer spectra for the samples B–E show patterns from Mn_2Sb, Li_3Sb and LiMnSb. The amount of pristine phase Mn_2Sb decreases, while the amount of the other phases increases as a function of Li content. Since the phase LiMnSb was not seen in the X-ray diffractograms but only in the Mössbauer spectra this phase must be amorphous with local ordering over short distances. The hyperfine parameters found for LiMnSb were $\delta = -8.0(2)$ mm/s and $\Delta = 8.7$ (9) mm/s.

The fully discharged sample F with nominally $x=3.5$ Li shows a simple X-ray diffraction pattern and a Mössbauer spectrum representative of Li_3Sb (Figures 2 and 3). Besides the rather broad X-ray peaks from Li_3Sb a very broad structure was found at $2\theta = 34.6°$ emanating from the cellulose in the cell and a broad line at around $2\theta = 42°$ which emanates from Mn. This is the first time electrochemically extruded nanocrystalline Mn has been detected. The Mössbauer spectrum was well fitted with a single line having an isomer shift δ of −7.65(5) mm/s in good agreement with the value −7.8 mm/s reported by Ionica et al. [2] for Li_3Sb.

3.3 Sample G

The X-ray diffractogram (Figure 2) and the Mössbauer spectrum (Figure 4) for this charged sample show the reappearance of Mn_2Sb and MnSb and the disappearance of Li_3Sb. Here the phase LiMnSb is largely crystalline and is clearly observed from the diffraction line at $2\theta = 24.4°$.

3.4 Phase formation processes

Lithiation process It seems that, on lithiation of the pristine material, Li ions first enter MnSb and an amorphous LiMnSb is formed (Figure 5). This process continues until all MnSb is "consumed." Above $x \approx 0.5$ Li ions also enter the Mn_2Sb phase and the process of forming amorphous LiMnSb from that phase takes over. This amorphous phase however starts to transform into the crystalline phase Li_3Sb on further lithiation and in the final stage when the discharge is complete all Sb atoms are in the phase Li_3Sb and all extruded Mn atoms are in a nanocrystalline phase as detected by the X-ray diffractogram.

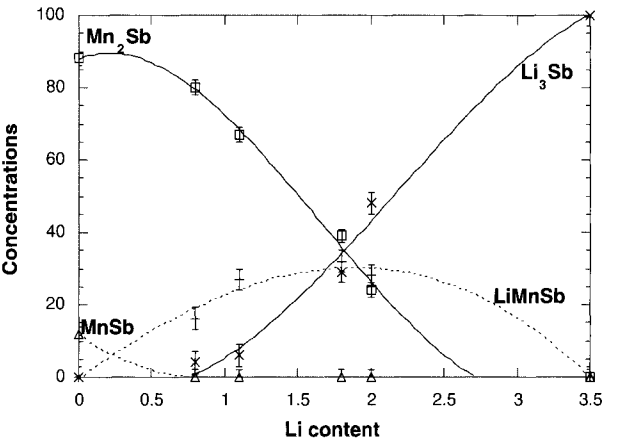

Figure 5 Intensities of the different phases versus Li content in the lithiation process as found from the fitting of the Mössbauer spectra.

The hypothesis put forward by Fransson et al. [1] that the transformation of Mn_2Sb to LiMnSb is more difficult to achieve than the MnSb-to-LiMnSb transition is thus proved by the present result.

Delithiation process Fully charged means in this case that the delithiation is not complete since some Li still exists in the cell. In our case we found $x \approx 0.9$. According to the Mössbauer result all Li in the fully charged state resides in the phase LiMnSb which now is better crystallized than when it was formed in the discharging process. Furthermore, upon delithiation of Li_3Sb, twice as much of the Mn_2Sb phase is formed as compared to MnSb. This may be due to the crystalline similarities between Li_3Sb and Mn_2Sb [1]. A transformation between Li_3Sb and MnSb is however also rather probable from structural considerations and on repeated cycling (20 times) it seems that the fully charged cell only consists of MnSb and LiMnSb while Mn_2Sb is absent [1].

4 Conclusions

Mn_2Sb (with small amounts of MnSb) electrodes operate in lithium cells in a complicated manner. On Li insertion the transformation into LiMnSb seems easier for the MnSb part of the electrode than for the Mn_2Sb part. This may be due to that the transformation of Mn_2Sb into LiMnSb also involves metal extrusion. In the fully lithiated cell the phase Li_3Sb is observed but also the extruded metal Mn as nanocrystalline material.

Upon further delithiation from Li_3Sb a completion between the formation of Mn_2Sb and MnSb seems to occur besides that all Li are not extruded being in the phase LiMnSb. Remaining traces of the Mn_2Sb structural framework results in twice as much Mn_2Sb phase as compared with the MnSb phase. Further cycling process however break up the Mn_2Sb structural skeleton and with 20 cycles only MnSb remains besides LiMnSb.

Acknowledgements This work has been carried out in the framework of ALISTORE, Network of Excellence (contract no.: SES6-CT-2003-503532). The authors are grateful to the European Community for financial support.

References

1. Fransson, L., Vaughey, J.T., Edström, K., Thackeray, M.M.: J. Electrochem. Soc. **150**, A86 (2003)
2. Ionica, C.M., Lippens, P.E., Olivier-Fourcade, J., Jumas, J.C.: J. Power Sources **146**, 478 (2005)
3. Ruebenbauer, K., Birchall, T.: Hyperfine Interact. **7**, 125 (1979)
4. Wilkinson, M.K., Gingrich, N.S., Schull, C.G.: J. Phys. Chem. Solids **2**, 289 (1957)
5. Pinjare, S.L., Rao, K.V.S.: J. Phys. F. Met. Phys. **14**, 2185 (1984)
6. Brauer, G., Zintl, E.: Z. Phys. Chem. **37**, 323(1937)

Hyperfine Interact (2006) 167:767–772
DOI 10.1007/s10751-006-9354-x

Mössbauer study on $LiFePO_4$ cathode material for lithium ion batteries

B. Hannoyer · A. A. M. Prince · M. Jean · R. S. Liu · G. X. Wang

Published online: 31 October 2006

Abstract Crystalline $LiFePO_4$ has been synthesized using solid-state, spray pyrolysis, and wet chemical methods. The crystal parameters were obtained from Rietveld's refinement methods of the X-ray diffraction patterns. A detailed investigation of the Fe valency carried out using Mössbauer spectroscopy at room temperature indicates that Fe is predominantly present in its bivalent state.

Key words lithium-ion batteries · cathode material · Mössbauer spectroscopy

1 Introduction

Rechargeable lithium-ion batteries are extensively used in numerous electronic devices. These batteries currently use various cathode materials such as $LiCoO_2$, $LiNiO_2$, $LiMn_2O_4$ and $Li_{1+x}Mn_{0.5}Cr_{0.5}O_2$, which have been previously tested; however, some of these electrodes are found to have poor charging and discharging characteristics and can be environmentally toxic and expensive to fabricate [1]. In the search for a good alternative cathode material, Goodenough's group discovered that lithium iron phosphate ($LiFePO_4$) could be an acceptable replacement [2]. Electrochemical studies of $LiFePO_4$ show that it has good specific capacity and high output voltage, properties which could be used for a wide range of applications in electronic devices [1].

B. Hannoyer (✉) · M. Jean
Institut des Matériaux, Université de Rouen, LASTSM, 76801 St. Etienne du Rouvray cedex, France
e-mail: beatrice.hannoyer@univ-rouen.fr

A. A. M. Prince
Department of Chemistry, Madras Christian College, Tambaram, 600 059 Chennai, Tamil Nadu, India

R. S. Liu
Department of Chemistry, National Taiwan University, Taipei 106 Taiwan, Republic of China

G. X. Wang
Institute for Superconducting & Electronic Materials, University of Wollongong, Wollongong, Australia

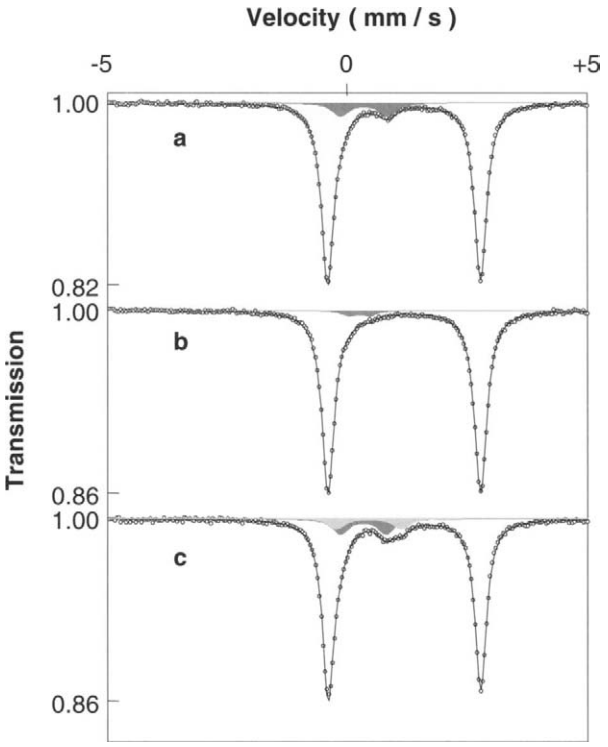

Figure 1 Room temperature Mössbauer spectra of samples A, B and C.

The olivine-based structure of $LiFePO_4$ consists of a polyoxyanionic framework containing FeO_6 octahedra and PO_4 tetrahedra. In addition, vacant interstitial sites available in the structure provide the Li^+ ions with more freedom to migrate. Moreover, it is electrochemically proven that Li^+ ions can be reversibly inserted into and extracted from the interstitial sites. This important property of $LiFePO_4$ has led many researchers to pursue investigations of this compound as a cathode material for lithium-ion batteries.

In order to accurately study the electrochemical characteristics of $LiFePO_4$, a pure compound must first be synthesized. It has been previously reported that $LiFePO_4$ can be prepared by hydrothermal or solid-state methods. $LiFePO_4$ powders obtained by hydrothermal routes were mostly amorphous and, in some cases, the presence of impurities could be identified by X-ray diffraction (XRD) studies. However a crystalline form of $LiFePO_4$ was obtained by annealing the amorphous sample at high temperature under an inert atmosphere [3]. In some reports, a pure and crystalline form of $LiFePO_4$ could be synthesized directly by the solid-state reaction method at high temperatures [10]. Unfortunately, the sample conductivity was measured to be between 10^{-9} and 10^{-10} S. cm^{-1}, which prevents its direct application as a cathode material. However, carbon addition during the synthesis is found to improve the electrical conductivity of $LiFePO_4$ materials [4–7]. Chung et al. [9], alternatively, found that doping $LiFePO_4$ with supervalent ions (Mg^{2+}, Al^{3+}, Ti^{4+}, Zr^{4+}, Nb^{5+} and W^{6+}) leads to a significant improvement in the conductivity, by a factor of ~10 [8]. Additionally, substitution by Mn, Mg, Ni, Co, Cu, Zn and Ge into the lattice sites of Fe has been observed to stabilize the crystalline structure. This class of conductive $LiFePO_4$ may be of interest for high-power, safe, rechargeable batteries for medical devices, and applications that currently use super capacitor technology [9].

Table I Room temperature hyperfine parameters of sample A (solid state reaction), sample B (spray pyrolysis) and sample C (wet chemical method)

Sample	IS (mm s^{-1})	QS (mm s^{-1})	Γ (mm s^{-1})	Relative area (%)
A	1.20	3.00	0.30	91.7
	0.43	0.91	0.40	9.3
B	1.21	2.96	0.30	97.0
	0.37	0.42	0.31	3.0
C	0.21	2.99	0.28	82.5
	0.41	0.89	0.38	7.2
	0.51	1.27	0.38	10.3
A*	0.43	0.91	0.40	100.0
C*	0.40	0.91	0.41	60.5
	0.53	1.23	0.41	39.5

A* and C* result from the adjustment of the spectra after extraction of the bivalent component.

In the present study, $LiFePO_4$ samples were prepared via solid-state, spray pyrolysis, and wet chemical methods. The samples where then characterized by several analytical methods, among them, Mössbauer spectroscopy which is well known to be much more sensitive than the diffraction analysis for detecting impurities with different valence states of Fe. An extensive Mössbauer study was carried out and some results of the room temperature study are presented and discussed.

2 Experimental section

A $LiFePO_4$ sample was prepared by solid-state reaction using LiOH, $Fe(II)C_2O_4.2H_2O$ and $(NH_4)_2HPO_4$ (sample A). Initially, the precursors were thoroughly mixed and loaded in to an alumina boat, heated at 350°C for 5 h under a reducing flow atmosphere consisting of 5% H_2 and 95% Ar and then cooled to room temperature. The sample was then reground and reheated at 700°C under the same conditions [11]. Sample B was synthesized by the spray pyrolysis method using the procedure reported by Bewlay et al. [12]. Amorphous $FePO_4$ was synthesized by spontaneous precipitation from an equimolar aqueous solution of Fe $(NH_4)_2(SO_4)_26H_2O$, $NH_4H_2PO_4$ and hydrogen peroxide as reported by Prosini et al. [13]. Amorphous $LiFePO_4$ (sample C) was obtained by chemical lithiation of amorphous $FePO_4$ by using LiI as a reducing agent. Crystalline $LiFePO_4$ was obtained by heating the latter amorphous compound in a tubular furnace at 550°C for 1 h under a reducing atmosphere.

All samples were characterized by XRD using a SCITAG (X1) diffractometer with Cu K_α radiation. Rietveld refinement was performed using the GSAS (General Structure Analysis System) program to determine the crystal structure parameters [14]. Fourier Transform Infrared spectra (FTIRS) were recorded with a Nicolet 710 instrument. This technique allows the user to identify easily the chemical bounding present in crystalline and non-crystalline compounds. The ^{57}Fe Mössbauer spectra were collected with a ^{57}Co γ-ray source. Velocity and isomer shift calibration was performed using Fe foil as the standard at room temperature. The sample thickness was adjusted so that the Fe content was ~10 mg/cm^2.

3 Results and discussion

For each sample, XRD indicated a pure single phase of $LiFePO_4$ with a crystalline olivine structure indexed by orthorhombic *Pnmb*. The cell parameters of the sample sample A a=

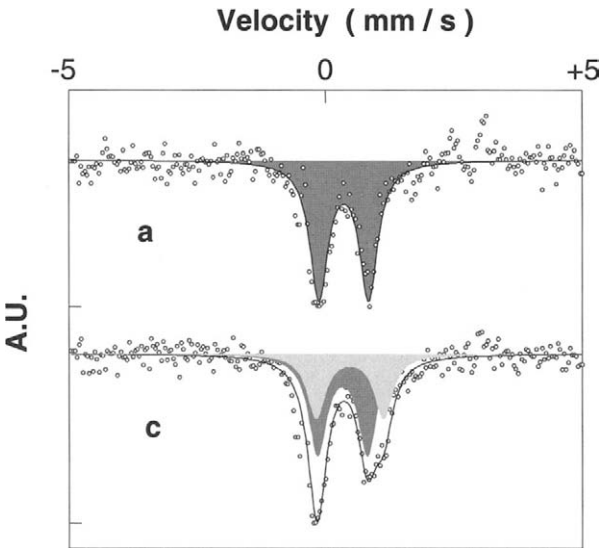

Figure 2 Room temperature Mössbauer spectra of the Fe^{3+} component in samples A and C.

10.3095 (7) Å, b=5.9993 (4) Å and c=4.6932 (3) Å obtained from the Rietveld refinement are in good agreement with previously reported values [11].

Infrared spectra are similar for the different samples and are in agreement with the structural data. The main absorption bands concern the PO_4 groups, with a strong split band appearing at ~1,060 cm^{-1}, which is attributed to the stretching vibration mode with splitting due to the distortion of the phosphate tetrahedra as observed from the structural results, and the bending mode appearing as a split signal at ~600 cm^{-1}.

Mössbauer spectroscopy measurements at room temperature of all samples are shown in Figure 1. The spectra were fitted with two or three doublets; a dominant symmetric doublet is observed in the case of naturally occurring mineral triphylite $LiFePO_4$[15]. In the room temperature data for paramagnetic $LiFePO_4$, two parameters are of importance: the isomer shift IS and the quadrupole splitting QS. The hyperfine parameters are reported in Table I. The doublet with IS=1.20–1.21 mm s^{-1}, present in each sample, is typical for Fe^{2+} in ionic compounds.

The exceptionally large quadrupole splitting value observed (QS=2.96–3.00 mm s^{-1}) is primarily explained by the asymmetry of the electrons surrounding (d^6 configuration), but also by the asymmetric local environment of the Fe atom. The Mössbauer parameters IS and QS for our samples are in good agreement with those of Li et al. [15] (IS=1.22 mm s^{-1}, QS=2.98 mm s^{-1}) and Andersson et al. [16] (IS=1.22 mm s^{-1}; QS=2.96 mm s^{-1}) obtained for natural triphylite.

In addition to the Fe^{2+} doublet, a small absorption area in the center of each of the Mössbauer spectra was also observed, with an isomer shift typical for Fe^{3+} (Table I). The nature of this Fe^{3+} phase could be due to amorphous or nanoparticules since it was not detected by XRD. Moreover, these parameters do not correspond to the characteristic of impurities of the type $FePO_4$ or $Li_3Fe_2(PO_4)_3$. In order to obtain further insight, the bivalent pattern of the spectrum was carefully removed. The resulting spectra presented in Figure 2 clearly show the presence of at least one or two doublets whose hyperfine parameters are indicated in Table I; these values were obtained without applying any constraints. The good agreement between the values obtained from the original spectra and these "subtracted" spectra provide an indication of the representativeness of such a subtraction.

The value of the electric field gradient at the Fe^{3+} nuclei (d^5 configuration) is caused by the distortion of the octahedral oxygen surrounding. The first one is more distorted than the second, so these two doublets correspond to Fe^{3+} in two inequivalent cation positions.

In the olivine structure, the phosphorous atoms occupy tetrahedral sites, while the iron and lithium atoms occupy octahedral sites (denoted M(2) and M(1), respectively). Sample A and B, obtained, respectively, by sol–gel route and solid-state reaction, have only one doublet which is poorly defined, whereas the wet chemical route sample is characterized by two more readily defined doublets. These latter doublets have parameters previously observed for trivalent iron in silicates [17], (IS=0.358 mm s^{-1}; QS=1.283 mm s^{-1}) and (IS= 0.423 mm s^{-1}; QS=0.614 mm s^{-1}) attributed, respectively, to M(1) and M(2) sites in $LiFePO_4$. Although it is presumed that $LiFePO_4$ has a very narrow composition range, Li vacancies can be accommodated in the olivine structure [18]. The Fe^{3+}can arise in the $LiFePO_4$ structure by composition variations such as $3Fe^{2+} \rightarrow 2Fe^{3+}$, leaving an iron vacancy in the M(2) site, or $LiFe^{2+} \rightarrow Fe^{3+}$, leaving a vacancy of Li in the M(1) site or Fe in the M(2) site [19] and Fe occupation of the M(1) site. The ionic radius of the high spin Fe^{3+} cation in octahedral coordination is 78.5 pm, and that corresponding to the hexacoordinated Li^+ ion is 90.0 pm; a reduction of the cell volume might therefore be expected with variation in the lithium stoichiometry. However, it must also be considered that if vacancies are introduced in Li^+ sites, repulsion between negatively charged ions could cause an expansion of the crystal.

Rietveld refinement of the entire sample set and Mössbauer measurements at low temperature are currently in progress in order to verify this assumption.

4 Conclusion

A crystalline form of $LiFePO_4$ has been prepared via solid-state reaction, spray pyrolysis and wet chemical methods. XRD refinement gives good agreement between experimental crystal parameters and reported values. As expected, analysis of room temperature Mössbauer spectra shows that Fe is predominantly present in its bivalent state. A weak Fe^{3+}subspectra could account for Fe^{3+} occupancy of cationic positions in an olivine structure.

References

1. Padhi, A.K., Nanjudaswamy, K.S., Goodenough, J.B.: J. Electrochem. Soc. **144**, 1188 (1997)
2. Padhi, A.K., Nanjudaswamy, K.S., Masquelier, C., Okada, S., Goodenough, J.B.: J. Electrochem. Soc. **144**, 1609 (1997)
3. Prosini, P.P., Carewska, M., Scaccia, S., Winiewski, P., Paerini, S., Pasquaali, M.: J. Electrochem. Soc. **149**, A886 (2002)
4. Yang, S., Song, Y., Zavalij, P.Y., Wittingham, M.S.: Electrochem. Commun. **4**, 239 (2002)
5. Rovert, N., Chouinard, Y., Magnan, J.F., Besner, S., Gauthier, M., Armand, M.: J. Power Sources **97**, 503 (2001)
6. Tarascon, J.M., Armand, M.: Nature **414**, 359 (2001)
7. Yamada, A., Chung, S.C., Hinokuma, K.: J. Electrochem. Soc. **148**, 224 (2001)
8. Huang, H., Yin, S.C., Nazar, L.F.: Electrochem. Solid-State Lett. **4**, 170 (2001)
9. Chung, S.Y., Bloking, J.T., Chiang, Y.M.: Nature Mater. **1**, 123 (2002)
10. Chen, Z., Dahn, J.R.: J. Electrochem. Soc. **149**, 1184 (2002)
11. Prince, A.A.M., Mylswamy, S., Chan, T.S., Liu, R.S., Hannoyer, B., Jean, M., Shen, C.H., Huang, S.M., Lee, J.F., Wang, G.X.: Solid State Commun. **132**, 455 (2004)
12. Bewlay, S.L., Konstantino, K., Wang, G.X., Dou, S.X., Liu, H.K.: Mater. Lett. **58**, 1788 (2004)

13. Prosini, P.P., Carewska, M., Scaccia, S., Wisniewski, P., Passerini, S., Pasquali, M.: J. Electrochem. Soc. **149**, 886 (2002)
14. Larson, A.C., von Dreele, R.B.: General Structure Analysis System. Los Alamos National Laboratory, Los Alamos, NM, (1994)
15. Li, Z., Shinno, I.: J. Mineral. **19**, 99 (1997)
16. Andersson, A.S., Kalska, B., Haggstrom, L., Thomas, J.O.: Solid State Ionics **130**, 41 (2000)
17. Amthauer, G., Lottermoser, W., Redhammer, G., Tippelt, G.: Hyperfine Interact. **113**, 219 (1998)
18. Goni, A., Lezema, L., Arriortua, M.I., Barberis, G.E., Rojo, T.: J. Mater. Chem. **10**, 423 (2000)
19. Fransolet, A.M., Antenucci, D., Speetjens, J.M.: Miner. Mag. **48**, 373 (1984)

Hyperfine Interact (2006) 167:773–778
DOI 10.1007/s10751-006-9355-9

Evaluation of structural and electrochemical properties of the MnSb–Li system as anode for Li-ion batteries

Costana Mihaela Ionica-Bousquet · Manfred Womes · Pierre-Emmanuel Lippens · Josette Olivier-Fourcade · Bernard Ducourant · Alan V. Chadwick

Published online: 14 November 2006

Abstract The electrochemical reaction mechanisms between lithium and cystalline MnSb are investigated by X-ray diffraction, ^{121}Sb Mössbauer spectroscopy, and X-ray absorption spectroscopy (XAS). The analysis of the experimental data at different depths of the electrochemical discharge process reveals a complex reaction mechanism comprising two steps. The main reaction of the first step corresponds to the dispersion of lithium in the MnSb matrix with formation of the intermediate compound LiMnSb. The second step corresponds to a Li–Sb alloying process with formation of Li_3Sb.

Key words intermetallics · lithium reaction mechanism · ^{121}Sb Mössbauer spectroscopy

1 Introduction

In recent years "Li-ion" batteries have become essential part of many portable electronic devices (computers, cellular phones, wireless tools). They are also considered as promising candidates for energy storage in electric vehicles. The electrodes of these batteries are composed of insertion materials in which lithium ions are inserted and extracted during the charge/discharge cycle. Currently, graphite or hard carbons are used as anode materials due to their advantageous properties concerning safety and reversibility of the lithium insertion and extraction [1–3]. However, alternative materials offering higher capacities and doubled energy densities will be demanded for next generation batteries.

The binary lithium-metal systems Li–Sn and Li–Sb have been considered as such alternatives and were thus studied intensively. They give high capacities during the first

C. M. Ionica-Bousquet (✉) · M. Womes · P.-E. Lippens · J. Olivier-Fourcade · B. Ducourant
LAMMI (CNRS UMR 5072), Université Montpellier II,
CC 015, Place E. Bataillon, Montpellier Cedex 5 34095, France
e-mail: ionica@univ-montp2.fr

A. V. Chadwick
Functional Materials Group, School of Physical Sciences,
University of Kent, Canterbury Kent CT2 7NR, UK

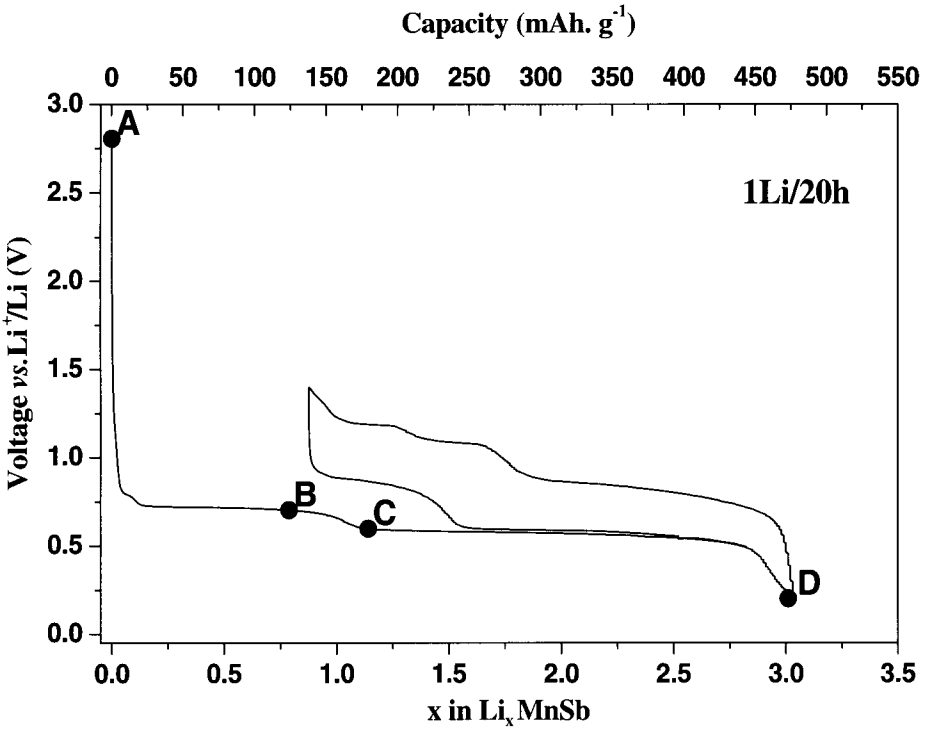

Figure 1 Charge/discharge curves of a MnSb electrode tested in a Swagelok™ cell between 0.2 and 1.4 V versus Li^+/Li at a C/20 rate.

discharge run, but show poor cyclability due to large volume changes during lithium insertion and extraction. Improved cyclability was observed for the newly proposed intermetallic materials M–Sn and M–Sb (M = transition metal), in which M plays the role of an inactive matrix buffering the volume changes during cycling [4–6]. In the present study the intermetallic compound MnSb was tested as anode material with the aim to combine the large reversible storage capability of antimony with the inactive matrix effect of manganese in order to improve the cycle performance.

Lithium insertion in intermetallic compounds M–Sb takes place via complex multi-phase mechanisms. The identification of the various phases is complicated by the poor crystallinity and small particle size of the discharged electrode material. X-ray diffraction alone is thus insufficient to elucidate the reaction mechanisms; the use of alternative techniques providing insight to the electrochemical reaction mechanisms on an atomic scale becomes necessary. In the present study we used ^{121}Sb Mössbauer spectroscopy and X-ray absorption spectroscopy at the Mn K edge in order to complete data from X-ray diffraction.

2 Experimental aspects

MnSb was synthesised by heating a stoichiometric mixture of the elements in an alumina crucible under an Ar (5% H_2) atmosphere for 10 h to 680°C. The crucible was then slowly cooled under the same Ar atmosphere. Finally, the sample was annealed at an appropriate temperature in order to obtain a single-phased intermetallic compound.

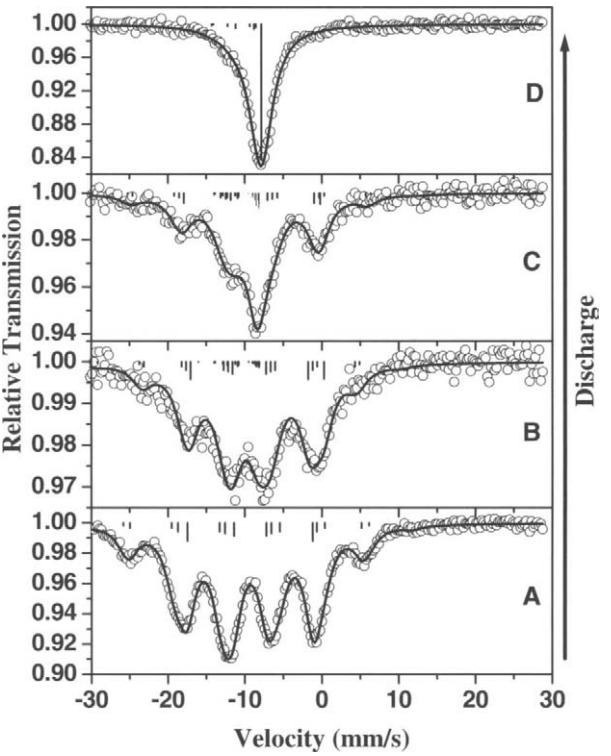

Figure 2 Evolution of the ^{121}Sb Mössbauer spectrum of MnSb during a complete discharge run down to 0.2 V at a C/20 rate. The velocity scale has not been corrected for InSb reference (δ=−8.72 mm/s relative to the source).

The electrochemical behaviour was tested using two-electrode Swagelok™ cells of the Li 1M Li PF_6 (PC:EC:DMC=1:1:3, v/v) | MnSb type. Electrodes containing 80 wt.% sample, 10 wt.% PTFE binder and 10 wt.% carbon black were pressed to pellets of a diameter of 7 mm. The electrochemical curves were recorded on a MacPile II system at a C/20 rate (a molar ratio Li/MnSb equal to unity was reached in 20 h) for both charge and discharge between 0.2 and 1.4 V *versus* Li^+/Li. The electrode materials were analysed *ex situ* at several depths of discharge and charge. For this purpose the Swagelok™ cells were opened inside an argon filled glove box and the electrode materials containing the active material were placed in specific sample holders transparent for γ and x-rays.

^{121}Mössbauer spectra were recorded on an EG&G spectrometer in a constant acceleration mode and in transmission geometry. The source of a nominal activity of 0.5 mCi consisted of $Ba^{121m}SnO_3$. During the measurements, both source and absorbers were cooled to 4 K in order to increase the fraction of recoil-free absorption and emission processes. Isomer shifts are given with respect to the source compound.

XAS experiments were performed in transmission mode on beam-line 7.1 of the Synchrotron Radiation Department, CCLRS Daresbury Laboratory (England). The beam-line was equipped with a Si(111) double crystal monochromator.

3 Results and discussions

The discharge curve of MnSb, shown on Figure 1, presents the following characteristics: a fast drop from the open circuit voltage of 2.8 to 0.8 V, associated with the formation of a

Table I ^{121}Sb Mössbauer parameters obtained from spectra recorded at points A to D of the discharge curve of Figure 1

Sample	Composition Li_xMnSb	δ (mm s^{-1})	eQV_{zz} (mm s^{-1})	Γ (mm s^{-1})	H_{hf} (T)	C (%)	Identification
A	x=0 (2.84 V)	−9.49 (3)	1.88 (8)	1.21 (8)	37.9	100	MnSb
B	x=0.8 (0.70 V)	−9.41 (5)	1.91	1.52	34.2	73 (2)	MnSb
		−8.42 (1)	2.84	1.52	–	12 (1)	LiMnSb
		−11.80 (2)	10.48	1.52	–	8 (1)	Li_xMnSb_y
		0.68[a]	−3.68[a]	1.52		7 (2)	Sb_2O_5
C	x=1.1 (0.59 V)	−9.49	3.41 (2)	1.43 (1)	36.4	49 (2)	MnSb
		−8.40 (2)	2.80 (4)	1.43 (1)	–	34 (1)	LiMnSb
		−11.84 (2)	10.62(1)	1.43 (1)	–	12 (1)	Li_xMnSb_y
		0.68[a]	−3.68[a]	1.43 (1)		5 (2)	Sb_2O_5
D	x=3 (0.20 V)	−7.82 (7)	–	1.81 (2)	–	88 (2)	MnSb
		−10.42 (9)	19.22 (1)	1.81 (2)	–	12 (2)	Li_3Sb

All isomer shifts are relative to the $Ba^{121m}SnO_3$ source

δ isomer shift, eQV_{zz} quadrupole coupling, Γ linewidth, H_{hf} hyperfine magnetic field, C relative contribution.

[a] Sb_2O_5 contribution

passivating film on the carbon particles as a result of the reduction reaction between lithium and the electrolyte, followed by two plateaus, a first one at 0.78 V *versus* Li^+/Li ending at point B, and a second at 0.55 V *versus* Li^+/Li beginning at point C. The discharge process is completed when the voltage reaches the value of 0.2 V (point D). The sample composition at this point corresponds to the formula $Li_{3.03}MnSb$.

The calculated specific capacity for this composition is 460 Ah kg^{-1}. The voltage profile reveals an important loss in capacity for the first cycle; the obtained reversible capacity value is 330 Ah kg^{-1}. Cycling tests carried out by Fransson et al. [7] indicate a good cyclability for 25 cycles.

Figure 2 shows ^{121}Sb Mössbauer spectra recorded at the four points A to D of the discharge curve shown on Figure 1. The corresponding refined values of the hyperfine parameters isomer shift δ (IS) and quadrupole splitting (eQV_{zz}) derived from the analysis of the experimental data using a transmission integral procedure [8] are reported in Table I.

The spectrum of sample A shows four broadened peaks each containing three unresolved lines and two small satellites each containing two unresolved lines. The refinement of this spectrum reveals a strong magnetic field of 37.9 T with a small quadrupole interaction on the antimony sites. The refined values of the hyperfine parameters evidence the occurrence of Sb on a single crystallographic site, in agreement with the NiAs type structure of MnSb [9].

The Mössbauer spectra of samples B and C reveal the formation of LiMnSb as a new phase while the potential decreases to 0.6 V. The hyperfine parameters of this phase derived from the spectra, δ=−8.42 m s^{-1}, eQV_{zz}=2.84 m s^{-1}, are in good agreement with calculated values using the density functional theory (DFT). The formation of LiMnSb has also been observed in a previous study by X-ray diffraction [10]. The presence of Sb_2O_5 in small amounts is attributed to oxidation during sample transfer from the glove box to the Mössbauer spectrometer and during the X-ray diffraction measurement. The amount of pristine MnSb decreases during the discharge run, while the amount of LiMnSb increases. A fourth contribution of a spectral weight of 10% was attributed to the formation of a metastable, antimony-rich phase of a Li-Sb type, due probably to the electrochemical reaction kinetics.

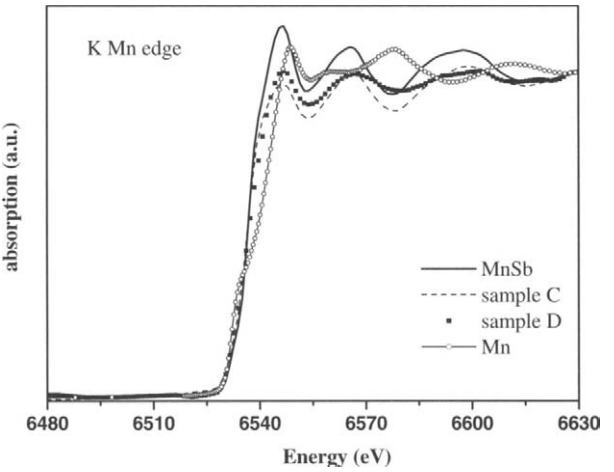

Figure 3 Mn K XANES of pristine, partially (*C*) and completely (*D*) discharged MnSb and of Mn metal.

The spectrum of the completely discharged sample D (Figure 2) reveals the occurrence of cubic Li_3Sb as the main phase, accompanied by a small amount of a second phase which is assigned to a highly dispersed antimony-poor Li_xMnSb_y phase (δ=−10.42 mm s^{-1}) formed electrochemically.

Spectra of the X-ray absorption near edge structure were recorded at the Mn K edge (Figure 3). The spectrum of the partially discharged sample C bears still close resemblance to that of the pristine material, indicating that the major part of manganese is still present in the form of MnSb. The spectrum of the fully discharged sample D differs from that of the starting material insofar as the intensity of the oscillations above 6560 eV is strongly reduced. A comparison of the spectra of MnSb and elemental Mn shows that above 6560 eV a maximum of the former coincides with a minimum of the latter and *vice versa*. The spectrum could therefore be considered as the sum of the spectra of MnSb and metallic Mn the formation of which would be expected from a reaction mechanism MnSb + 3Li → Li_3Sb + Mn. However, X-ray diffraction gave no indication of the presence of crystalline elemental manganese. Moreover, the shape of the Mn K edge spectrum resembles still more that of MnSb than that of Mn. We therefore conclude that manganese is present in finely dispersed form, with an important fraction of atoms in contact with the Li_3Sb phase via Mn–Sb bonds, forming in this way the antimony-poor Li_xMnSb_y phase seen in the Mössbauer spectrum of sample D.

4 Conclusions

Experimental and theoretical results are combined in order to better understand the electrochemical process. Considering the overall characterisations, we are able to confirm the displacement of Sb atoms during lithium insertion which leads to the formation of an intermediate material. As the amount of lithium insertion into the active matrix increased, Li_3Sb alloy was formed which remains in interaction with the Li_xMnSb_y matrix.

Acknowledgement C.M. Ionica acknowledges ADEME, France and SAFT Bordeaux, France (contract N° 752295/00) for the financial support. The XAS measurements were realised in the framework of ALISTORE Network of Excellence (contract no. SES6-CT-2003-503532) founded by the EC.

References

1. Dahn, J.R., Zheng, T., Liu, Y., Xue, J.S.: Science **270**, 590 (1995)
2. Sato, K., Nouguchi, M., Demachi, A., Oki, N., Endo, M.: Science **264**, 556 (1994)
3. Tarascon, J.-M., Armand, M.: Nature **414**, 359 (2001)
4. Grugeon, S., Laruelle, S., Dupont, L., Tarascon, J.-M.: Solid State Sci. **5**, 895 (2003)
5. Aldon, L., Garcia, A., Olivier-Fourcade, J., Jumas, J.-C., Fernandez-Madrigal, F.J., Lavela, P., Vincente, C.P., Tirado, J.L.: J. Power Sources **5362**, 1 (2003)
6. Ionica, C.M., Aldon, L., Lippens, P.E., Jumas, J.-C., Olivier-Fourcade, J.: Hyperfine Interact. **156/157**, 555–561 (2004)
7. Fransson, L.M.L., Vaughey, J.T., Edström, K., Thackeray, M.M.: J. Electrochem. Soc. **150**(1), A86-A91 (2003)
8. Rubenbauer, K., Birchall, T.: Hyperfine Interact. **7**, 125 (1979)
9. Zheng, J.-C., Davenport, J.W.: Phys. Rev. B **69**, 144415 (2004)
10. Ionica, C.M., Lippens, P.E., Olivier-Fourcade, J., Jumas, J.-C.: J. Power Sources **146**, 478–481 (2005)

Hyperfine Interact (2006) 167:779–784
DOI 10.1007/s10751-006-9356-8

Iron ions in ZSM-5 zeolite: Fe^{3+} in framework, Fe^{2+} in extra-framework positions in catalytic N_2O decomposition

K. Lázár · O. Pozdnyakova · A. Wootsch · P. Fejes

Published online: 27 October 2006

Abstract Fe-ZSM-5 samples containing a combination of $^{57}Fe^{3+}$ in framework (FW) and regular iron in extra-framework (EFW) sites were prepared by introducing ^{57}Fe in hydrothermal synthesis, then exchanging Fe^{2+} of natural isotope composition into the lattice. The stability for one part of Fe^{2+} and $Fe^{2+} \leftrightarrow Fe^{3+}$ reversibility for the other part in catalytic decomposition of N_2O is demonstrated by *in situ* Mössbaer measurements. Formation of dinuclear Fe_{FW}–O–Fe_{EFW} pairs is not prevailing.

Key words Fe^{2+} and Fe^{3+} simultaneously · N_2O decomposition

1 Introduction

Specific oxidation reactions may be carried out by applying Fe-ZSM-5, e.g., active "α-oxygen" can be generated by loading O to specific Fe sites with decomposing N_2O [1]. Presence and role of highly dispersed extra-framework (EFW) Fe^{2+} is experimentally demonstrated in these processes [1, 2]. Existence of higher oxidation state (Fe^{4+}) can also be proposed as model calculations suggest either for di- [3] or mononuclear centres [4]. Highly dispersed EFW iron can be generated by removal of framework (FW) iron from Fe-ZSM-5 (prepared by hydrothermal synthesis with iron in the synthesis gel) by high temperature treatment [1] or by steaming at lower temperatures [2]. Direct introduction of EFW iron from aqueous media is less preferred, due to hydrolysis of Fe^{3+}. Instead, non-aqueous solvents can be used [5] or evaporating $FeCl_3$ into the zeolite lattice can be applied [6].

In the present communication we demonstrate the simultaneous presence of FW and EFW iron. In the first step enriched ^{57}Fe is introduced to FW sites in hydrothermal synthesis (in $Si/^{57}Fe \approx 200$ ratio). In the second step Fe^{2+} with regular isotope composition is

K. Lázár (✉) · O. Pozdnyakova · A. Wootsch
Institute of Isotopes, CRC, HAS, Budapest P. O. B. 77, 1525, Hungary
e-mail: lazar@iki.kfki.hu

P. Fejes
Department of Applied and Environmental Chemistry, University of Szeged, 6720 Szeged, Hungary

exchanged from methanolic media to EFW position (Si/Fe≈67). Since modest temperatures are used (T<750 K) for treating the Fe-ZSM-5, the original FW and EFW siting and oxidation states are mostly maintained. Paramagnetic Fe^{3+} ions located in FW sites exhibit spin-lattice relaxation phenomena (due to their low concentration in the lattice) [7, 8], whereas diamagnetic EFW Fe^{2+} ions do not interact with Fe^{3+}. After oxidation of EFW Fe^{2+} to Fe^{3+} the collapse of relaxing spectral shape can be expected (due to the onset of spin-spin relaxation as a result of the increased amount of Fe^{3+}). This phenomena might particularly occur in the case of direct coupling, namely with occasional formation of dinuclear $Fe_{FW}-O-Fe_{EFW}$ pairs.

The Fe-ZSM-5 samples were exposed to N_2O atmospheres—the catalytic property is manifested in a test reaction of N_2O decomposition. *In situ* Mössbauer spectra under reaction conditions demonstrate in part the stability of Fe^{2+}, and for the other part the $Fe^{2+} \leftrightarrow Fe^{3+}$ reversible transformation. The anticipated collapse of the paramagnetic feature does not prevail, thus formation of dinuclear Fe_{FW}–O–Fe_{EFW} pairs is not dominant.

2 Experimental

2.1 Sample preparation

Fe-ZSM-5 was prepared in four stages. First, hydrothermal synthesis was performed with enriched ^{57}Fe, with Si/^{57}Fe≈200 ratio. The details of the synthesis are described in [9]. In the second step tetrapropyl-ammonium bromide template was removed at modest temperature (620 K) by treatment in ozone resulting in (H^+, Na^+) form of ZSM-5. In the third step NH_4^+ form was obtained by ion exchange in NH_4OH. In the following step Fe^{2+} of regular isotope abundance was exchanged from methanolic solution of $FeSO_4$, under continuous stream of argon—to prevent formation and hydrolysis of Fe^{3+}.

Iron content was determined by total dissolution of Fe-ZSM-5 and measuring the amount of iron by atomic absorption. Iron content of Si/Fe≈50 ratio was found, in average. Thus, the nominal ratio of Fe_{FW}/Fe_{EFW} is 1:3. For interpreting the spectra it is important to emphasize that the ^{57}Fe abundances are different for the FW and EFW iron parts (100 and 2.2%, respectively), thus the apparent nominal proportion for the FW and EFW with respect to the Mössbauer-active ^{57}Fe is 15, i.e., approximately only 6% of spectral area might be originated from the contribution of exchanged FW Fe^{2+} component.

2.2 Mössbauer measurements

The measurements were performed in an *in situ* cell, spectra were obtained at 77, 300 and 620 K. The latter spectrum was obtained in a 6 h treatment in N_2O. Fe-ZSM-5 samples were evacuated at 620 and 720 K for 2 h in 10^{-2} Pa. Isomer shift values are relative to metallic α-iron.

2.3 Catalytic performance

Catalytic performance of Fe-ZSM-5 (50 mg) was tested in a temperature programmed reaction in a flow of 10% N_2O/He mixture (40 ml/min) with a temperature ramp of 10 K/min up to 770 K. Activity was measured by detecting the amount of formed oxygen (MRU gas analyser, Delta 65-3).

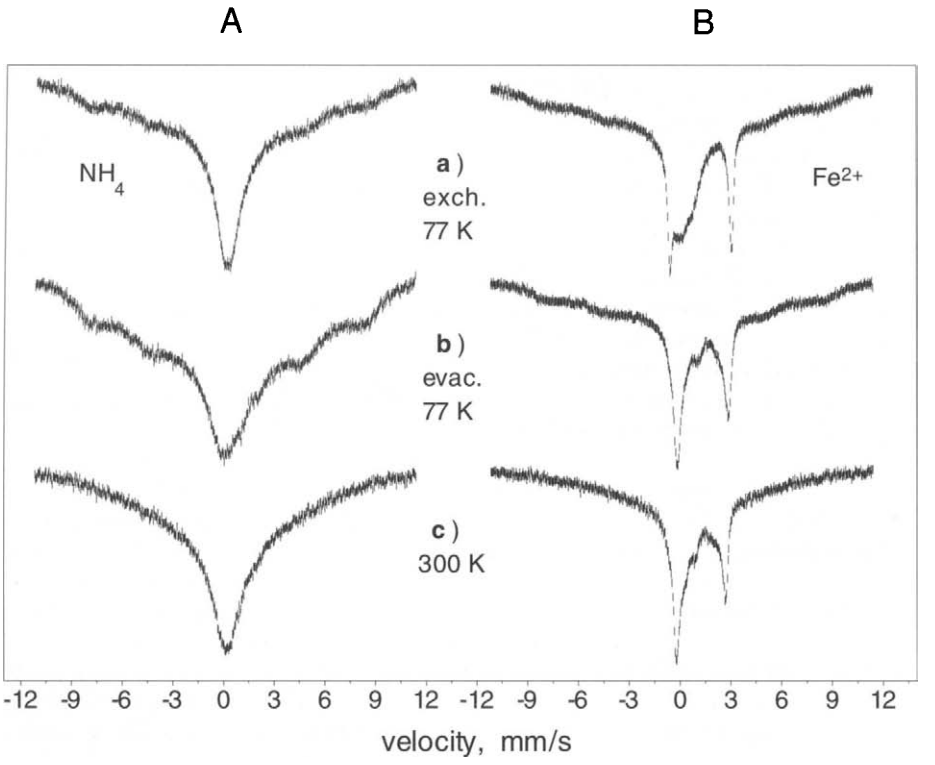

Figure 1 Spectra of ^{57}Fe-ZSM-5 after hydrothermal synthesis. (**A**) NH_4^+ exchange, (T_m=77 K) (*a*); evacuation 670 K (T_m=77 K) (*b*); same as *b* measured at T_m=300 K (*c*) (*left side*). Sample **A** after additional $FeSO_4$ exchange and after the same treatments (**B**) (*right side*).

3 Results and discussion

3.1 ^{57}Fe isomorphous substitution

Spectra of samples (Si/^{57}Fe=200) recorded after the hydrothermal synthesis followed by removal of TPABr template by ozone at 350°C and a subsequent exchange with 0.5 M NH_4NO_3 solution are shown in Figure 1A. The main feature of the spectra is the temperature dependent relaxation phenomena attesting the dominance of spin-lattice relaxation of isolated Fe^{3+} ions. Removal of water and NH_3 from the NH_4^+ form of zeolite (Figure 1Aa) results in weakened coupling with lattice vibrations, the spin relaxation time is longer after evacuation, i.e., the magnetic features are more expressed (Figure 1Ab). Upon increasing the temperature of measurement to 300 K the magnetic structure collapses to a broad central line (Figure 1Ac).

3.2 Ion exchange of Fe^{2+}

Spectra recorded on the sample after the $FeSO_4$ ion exchange in methanolic media are shown in Figure 1B. The spectrum recorded after drying at 350 K can apparently be combined from Figure 1A and an Fe^{2+} component. Thus, as expected, there is no magnetic interaction between the relaxing Fe^{3+} and diamagnetic Fe^{2+} in spite of the four-fold increase

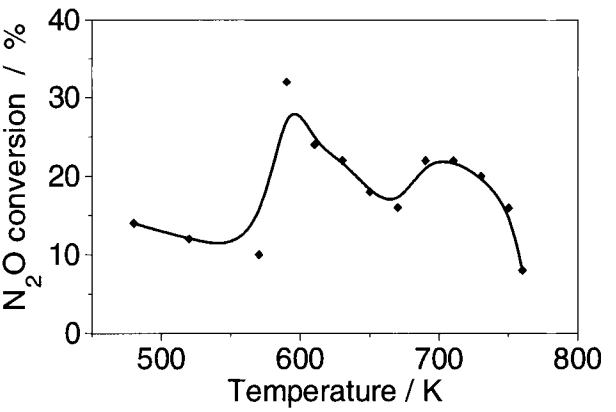

Figure 2 Temperature programmed decomposition of N_2O at a temperature ramp of 10 K/min.

of the iron content in the sample. The contribution of the Fe^{2+} to the spectral area is 7% (very close to the expected ~6% as mentioned in the Experimental part). This component exhibits IS=1.30 mm/s and QS=3.60 mm/s. Similarly to Figure 1Ab, the evacuation results in the decrease of the intensity of the central singlet. The environment of Fe^{2+} is also modified, IS=1.40 mm/s and QS=3.01 mm/s can be obtained from the spectrum of Figure 1Bb. Collection of the spectrum at 300 K results in a collapse of magnetic side peaks to a broadened central line. The separate dominant Fe^{2+} contribution is characteristic (IS= 1.27 mm/s, QS=2.90 mm/s).

3.3 Catalytic performance

The catalytic performance of FeZSM-5 was tested in the temperature-programmed-reaction of decomposing N_2O. Namely, 10% N_2O in He was flown above the sample in ramping the temperature in the 450–820 K range. The conversion of N_2O in dependence of temperature is shown in Figure 2. The highest activity for the decomposition of N_2O is found around 600 K, attesting that the Fe-ZSM-5 studied exhibits noticeable catalytic activity. The presented dependence of activity on temperature is similar to that reported in other communications for Fe-ZSM-5 (see e.g., [10]).

3.4 Effect of N_2O as reflected in the *in situ* spectra

In order to study the effect of N_2O on iron a second series of measurements was performed on an other portion of the Fe^{2+} exchanged sample. The spectrum of the starting sample (evacuated at 720 K) is similar to that shown in Figure 1Bb - it is composed from a broadened relaxing Fe^{3+} and a separated Fe^{2+} doublet (IS=1.35 mm/s, QS=3.05 mm/s in 14% spectral area, Figure 3a). Decomposition of N_2O via $2\ N_2O \rightarrow 2\ N_2+O_2$ is prevailing in 570–620 K region [1]. Hence, *in situ* spectrum was collected at 620 K during a 6 h treatment in N_2O (Figure 3b). A broad Fe^{3+} relaxing component is present with Fe^{2+} superimposed (IS=1.07 mm/s, QS=2.46 mm/s in 6.5% spectral area). This spectrum directly demonstrates that Fe^{2+} exists at reaction conditions. After cooling the sample to 77 K in N_2O/N_2 mixture the spectrum of Figure 3c is collected with Fe^{2+} in 9% spectral area (IS=1.38 mm/s, QS=3.05 mm/s). A repeated evacuation at 720 K practically restores the starting spectrum (Figure 3a), Fe^{2+} is present in 16% spectral contribution (IS= 1.39 mm/s, QS=2.99 mm/s) besides Fe^{3+}. It is worth referring here to the change of the Fe^{2+} portions in the series measured at 77 K: 14% in vacuum at the start, 9% in N_2O and

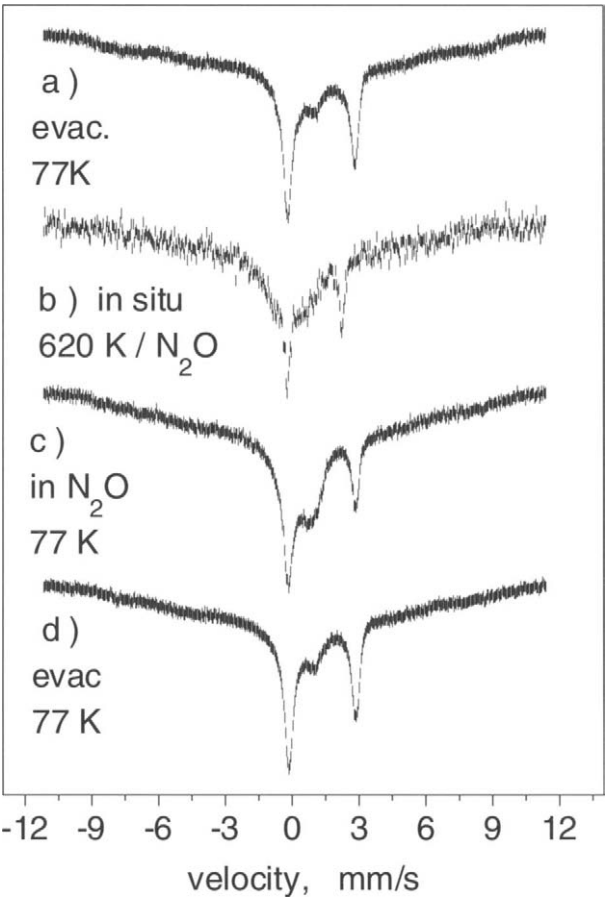

Figure 3 Series of subsequent spectra of Fe-ZSM-5 with combination of framework Fe^{3+} and extra-framework Fe^{2+}, obtained after Fe^{2+} exchange and evacuation at 670 K (**a**); *in situ* spectrum recorded during N_2O decomposition at 620 K (**b**); cooled to 77 K in N_2O (**c**); after evacuation at 670 K and cooled to 77 K in vacuum (**d**).

16% at the final evacuation. These numbers show that reversible $Fe^{2+} \rightarrow Fe^{3+} \rightarrow Fe^{2+}$ conversion proceeds on a significant part of EFW iron.

With regard to the other aspect, the occasional formation of dinuclear Fe_{FW}–O–Fe_{EFW} pairs, the process is not manifested in a significant extent. Namely, treatment in N_2O resulted in $Fe^{2+} \rightarrow Fe^{3+}$ oxidation for a significant part of EFW iron. At the same time however, the relaxing background originated from the isolated FW Fe^{3+} ions is retained, i.e., the number of dinuclear Fe_{FW}–O–Fe_{EFW} pairs with directly coupled spins should be limited.

Acknowledgements The authors are indebted to Gabriella Pál-Borbély for the determination of iron content of Fe-ZSM-5 and I. Kiricsi for the low-temperature removal of template from the synthesized Fe-ZSM-5 in ozone.

References

1. Dubkov, K.A., Ovanesyan, N.S., Shteinman, A.A., Starokon, E.V., Panov, G.I.: J. Catal. **207**, 341 (2002)
2. Taboada, J.B., Overweg, A.R., Koyman, P.J., Arends, I.W.C.E., Mul, G.: J. Catal. **231**, 56 (2005)

3. Yakovlev, A.L., Zhidomirov, G.M., van Santen, R.A.: J. Phys. Chem. B **105**, 12297 (2001)
4. Heyden, A., Peters, B., Bell, A.T., Keil, F.J.: J. Phys. Chem. B **109**, 1857 (2005)
5. Joyner, R., Stockenhuber, M.: J. Phys. Chem. B **103**, 5963 (1999)
6. Voskoboinikov, T., Chen, H.-Y., Sachtler, W.M.H.: Appl. Catal. B **19**, 279 (1998)
7. Blume, M.: Phys. Rev. Lett. **14**, 96 (1965)
8. Morup, S., Knudsen, J.E., Nielsen, M.K., Trumpy, G.: J. Chem. Phys. **65**, 536 (1976)
9. Fejes, P., Kiricsi, I., Lázár, K., Marsi, I., Rockenbauer, A., Korecz, L., Nagy, J.B., Aiello, R., Testa, F.: Appl. Catal. A **242**, 247 (2003)
10. El-Malki, El-M., van Santen, R.A., Sachtler, W.M.H.: Microporous Mesoporous Mater. **35–36**, 235 (2000)

Hyperfine Interact (2006) 167:785–790
DOI 10.1007/s10751-006-9357-7

^{119}Sn Mössbauer study of nickel–tin anodes for rechargeable lithium-ion batteries

S. Naille · P. E. Lippens · F. Morato · J. Olivier-Fourcade

Published online: 27 October 2006

Abstract ^{119}Sn Mössbauer spectrometry has been carried out on Ni–Sn alloys (Ni_3Sn LT, Ni_3Sn_2 LT and Ni_3Sn_4) and combined with *ab initio* calculations. Lithium insertion/extraction mechanisms of the most interesting compound (Ni_3Sn_4) have been studied from ^{119}Sn Mössbauer measurements. The first discharge shows a plateau close to 0.0 V, which can be attributed to the formation of the Li_7Sn_2 alloy.

Key words ^{119}Sn Mössbauer spectrometry · lithium-ion batteries · intermetallic compounds · lithium insertion mechanism

1 Introduction

Fifteen years ago, rechargeable "Li-ion" batteries appeared on the market, using graphite or hard carbons as anode for their safety and high reversibility during electrochemical lithium insertion/extraction [1–3]. With the soar of portable electronics, aerospace applications, etc., the relatively low capacity of these lithium cells (372 mAh/g with graphitic anode) makes that alternative anode materials must be found. In recent times, a number of binary alloy systems (Li–Sn, Li–Si, Li–Sb) were investigated as alternatives [4, 5], but a tremendous volume change occurs during cycling, inducing a weak cyclability [6, 7]. In order to avoid this volume change, several studies were made on tin-based lithium alloys using intermetallic host materials, where the transition metal is expected to buffer the expansion, such as nickel in Ni_3Sn_4 [8] or copper in Cu_6Sn_5 [9].

^{119}Sn Mössbauer spectrometry has been used in order to study local tin environment of pristine materials and to follow lithium insertion/extraction in intermetallic compounds for a better mechanism understanding. Moreover, electron structure calculations have been performed, using the linearized-augmented-plane-wave (LAPW) method [10], to evaluate hyperfine parameters of pristine materials.

S. Naille (✉) · P. E. Lippens · F. Morato · J. Olivier-Fourcade
Laboratoire des Agrégats Moléculaires et Matériaux Inorganiques (CNRS UMR 5072),
Université Montpellier II, CC 015, Place E. Bataillon, 34095 Montpellier cedex 5, France
e-mail: sebastien.naille@univ-montp2.fr

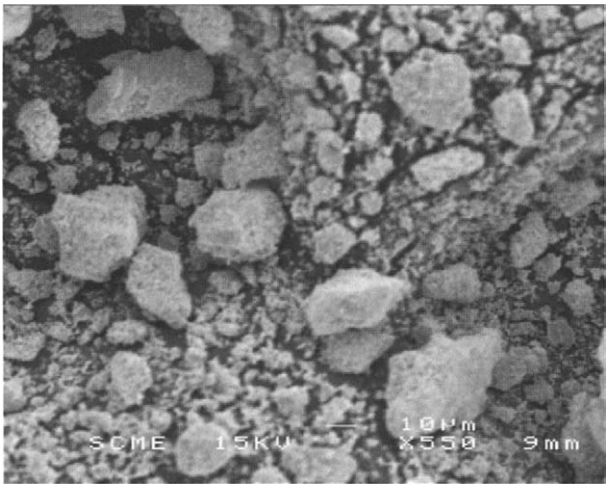

Figure 1 SEM picture of Ni_3Sn_4.

2 Experimental

The pristine materials, Ni_3Sn LT, Ni_3Sn_2 LT were synthesized by direct synthesis from pure elements in silica tubes sealed under vacuum. After annealing 10 days at 800°C for Ni_3Sn LT and 10 days at 500°C for Ni_3Sn_2 LT, the tubes samples were slowly cooled to room temperature in the furnace. As for Ni_3Sn_4, initial components in stoechiometric ratio were mechanically milled under argon atmosphere for 10 min before fired in a tube type furnace under controlled atmosphere for 4 h at 500°C.

The different phases were characterized by X-ray diffraction, for phase identification and purity. The powder morphology was investigated by Scanning Electron Microscopy (SEM). ^{119}Sn Mössbauer spectra were recorded by transmission in the constant acceleration mode using an EG&G spectrometer, the source was ^{119m}Sn in a $CaSnO_3$ matrix. The velocity scale was calibrated using the magnetic sextuplet of a high purity iron foil absorber as a standard, using ^{57}Co (Rh) as the source.

Electrochemical lithium insertion/extraction tests were performed in Swagelok™-type cells assembled in argon-filled glove box. Positive electrodes were prepared by mixing 80 wt.% pristine powder, 10 wt.% carbon black and 10 wt.% PTFE binder and pressed in 7 mm diameter pastilles. The electrolyte was 1M $LiPF_6$ in EC/PC/DMC (1:1:3 v/v). The lithium insertion/extraction experiments were performed galvanostatically, using a Mac Pile II system, within a voltage window of 0.0–1.2 V. ^{119}Sn Mössbauer measurements were done *ex situ* at several depths of discharge and charge, always in avoiding the air pollution.

3 Results and discussion

The different synthesized alloys were identified like single-phase compounds. The unit cell parameters refinement leads to hexagonal Ni_3Sn LT with a=5.298 (4) Å and c=4.250 (2) Å as compared with the literature data [11] and to orthorhombic Ni_3Sn_2 LT with a=7.118 (5) Å, b=5.194 (2) Å and c=8.132 (8) Å, which is in good agreement with the data reported

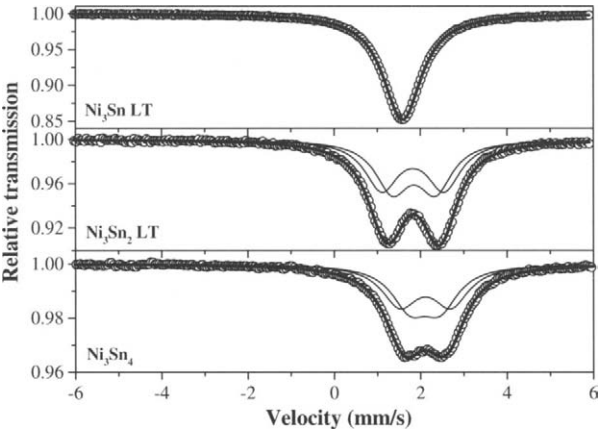

Figure 2 Room temperature ^{119}Sn Mössbauer spectra of Ni_3Sn LT, Ni_3Sn_2 LT and Ni_3Sn_4.

Table I ^{119}Sn Mössbauer parameters for Ni_3Sn LT, Ni_3Sn_2 LT and Ni_3Sn_4

Compound	Site	Experiment		Theory (±0.05)	
		δ (mm/s)	Δ (mm/s)	δ (mm/s)	Δ (mm/s)
Ni_3Sn LT		1.50	0.15	1.40	0.20
Ni_3Sn_2 LT	1	1.75	1.03	1.70	1.20
	2	1.73	1.50	1.70	1.55
Ni_3Sn_4	1	2.01	0.70	2.05	0.70
	2	2.02	1.18	2.05	1.15

δ is the isomer shift relative to $BaSnO_3$ and Δ is the quadrupole splitting.

in the literature [12]. Ni_3Sn_4 crystallizes in the monoclinic system with a=12.187 (13) Å, b= 4.055 (5) Å, c=5.216 (7) Å and β=105.19 (5)° which is within the homogeneity range reported in the literature [13]. The average particle size is of about 10 μm as shown in Figure 1 for Ni_3Sn_4.

The ^{119}Sn Mössbauer spectra obtained at room temperature are shown in Figure 2. As shown previously, the experimental data obtained for Ni_3Sn_2 LT and Ni_3Sn_4 can be roughly fitted with one component corresponding to an average site [14]. We have considered here a more accurate treatment by taking into account the different tin crystallographic sites. The hyperfine parameters were first evaluated from LAPW calculations as in [15, 16] and were used as starting values in the non-linear-least-square fitting procedure. The results are summarized in Table I.

Figure 3 shows the galvanostatic first cycle of the most interesting compound (Ni_3Sn_4), due to the high quantity of Sn per formula, at current density of 2.06 mA/g. 12.5 Li were inserted during the first discharge, corresponding to a capacity of 515 mAh/g. We can furthermore observe the existence of a biphasic plateau right above 0.0 V. It can be also seen that Li-extraction capacity is 282 mAh/g, which means that 6.85 Li were restored. X-ray diffraction pattern of the discharge electrode only shows the amorphisation of Ni_3Sn_4 but no presence of any Li_xSn phase, corresponding either to a formation of nanocrystalline or amorphous phases.

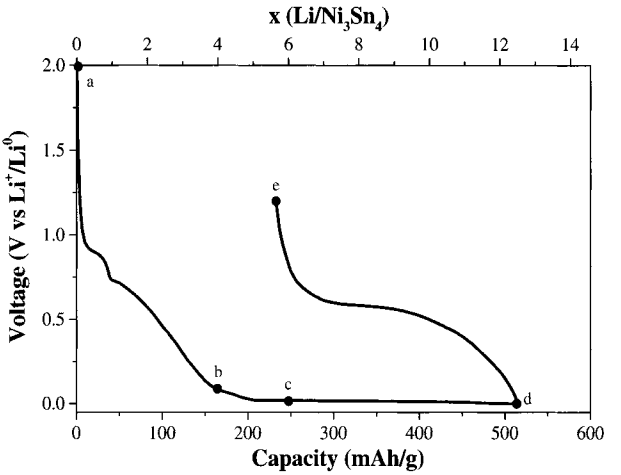

Figure 3 Galvanostatic discharge/charge of Ni_3Sn_4 electrode materials. *Ex situ* ^{119}Sn Mössbauer measurements were done at the points *a*, *b*, *c*, *d* and *e*.

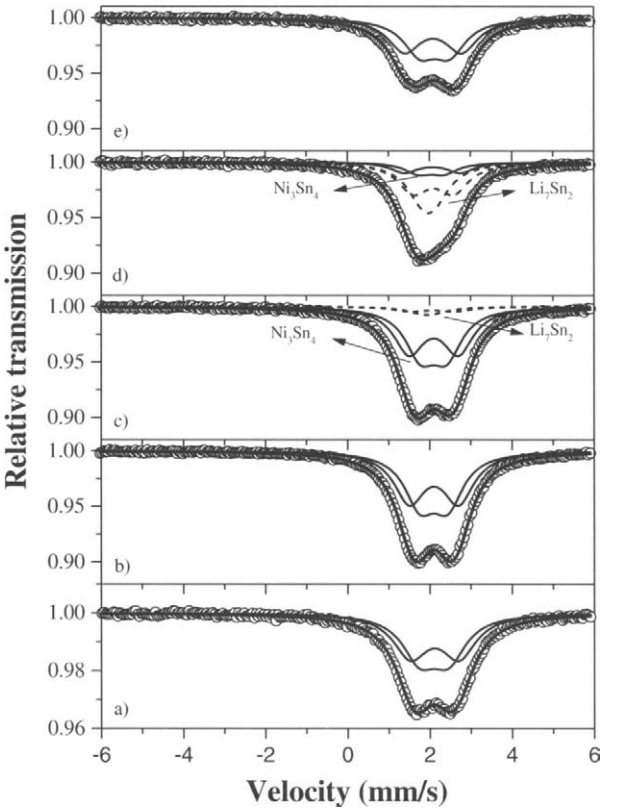

Figure 4 *Ex situ* ^{119}Sn Mössbauer spectra of the points shown in Figure 3: **a** the pristine compound Ni_3Sn_4 and the electrode **b** after 4 Li inserted, **c** after 6 Li inserted, **d** at the end of the first discharge and **e** at the end of the first charge.

The *ex situ* ^{119}Sn Mössbauer spectra of Ni_3Sn_4 samples recorded on the plateau cannot be fitted with the only Ni_3Sn_4 contribution (Figure 4c and d). Two doublets can fit the additional contribution (10% when 6 Li were inserted and 76% for the discharge electrode) with hyperfine parameters (Table II) close to those found for Li_7Sn_2 [17]. However, no

Table II ^{119}Sn Mössbauer parameters of (a) the pristine compound Ni_3Sn_4 and the electrode (b) after 4 Li inserted, (c) after 6 Li inserted, (d) at the end of the first discharge and (e) at the end of the first charge

Sample	Site	Ni_3Sn_4			Li_7Sn_2		
		δ (mm/s)	Δ (mm/s)	I (%)	δ (mm/s)	Δ (mm/s)	I (%)
(a)	1	2.01	0.7	50			
	2	2.02	1.18	50			
(b)	1	2.01	0.68	50			
	2	2.01	1.20	50			
(c)	1	2.00	0.64	45	1.98	1.10	5
	2	1.98	1.37	45	1.86	0.24	5
(d)	1	1.95	0.63	12	2.00	0.97	38
	2	1.98	1.37	12	1.88	0.29	38
(e)	1	2.04	0.72	50			
	2	2.00	1.39	50			

δ is the isomer shift relative to $BaSnO_3$, Δ is the quadrupole splitting and I is the relative intensity of the component.

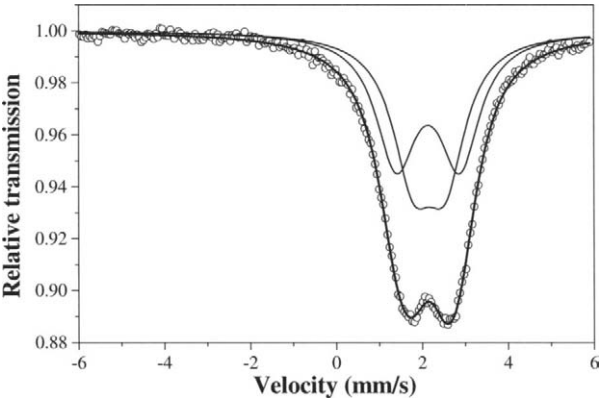

Figure 5 ^{119}Sn Mössbauer spectrum of the charged electrode at 75 K.

significant changes can be observed until 4 Li (Figure 4b) which means that the formation of Li_7Sn_2 occurs during the plateau. This shows that Ni_3Sn_4 reacted with lithium to form Li_7Sn_2 by the reaction proposed here:

$$Ni_3Sn_4 + 14Li \rightarrow 3Ni + 2Li_7Sn_2.$$

The Mössbauer spectrum obtained at the end of the first charge (Figure 4e) is close to that obtained for the pristine material (Figure 4a). Similar values of the Mössbauer parameters are obtained in the two cases except for the quadrupole splitting Δ_2 (Table II). Yet an asymmetry appears; experiment for the charged electrode was thus done at 75 K in order to eliminate the hypothesis of *in situ* β-Sn formation (Figure 5). Due to the weak recoilless factor of β-Sn at room temperature ($f_{(300k)} = 0.045$) [18], the asymmetry should increase as temperature decreases, that not happened. This suggests that only the contribution of Ni_3Sn_4 appears at 1.2 V. The observed small difference of hyperfine

parameters between this sample and the pristine material could be due to the slightly disordered structure of the reformed nanosized Ni_3Sn_4.

4 Conclusions

We have studied alloying mechanisms in Ni–Sn crystalline phases at the nanoscale whilst lithium insertion/extraction. First, ^{119}Sn Mössbauer spectrometry and *ab initio* calculations were combined for an accurate determination of the Mössbauer parameters. Then, we have found that the most attractive compound, Ni_3Sn_4, reacts electrochemically with lithium to form Li_7Sn_2 with a capacity of 515 mAh/g. In a near future, we will focus on nanostructured Ni_3Sn_4 in order to improve the electrochemical performances.

Acknowledgements This work has been carried out in the framework of ALISTORE Network of Excellence (contract no. SES6-CT-2003-503532). The authors are grateful to the European Community for the financial support.

References

1. Sato, K., Noguchi, M., Demachi, A., Oki, N., Endo, M.: Science **264**, 556 (1994)
2. Dahn, J.R., Zheng, T., Liu, Y., Xue, J.S.: Science **270**, 590 (1995)
3. Johnson, B.A., White, R.E.: J. Power Sources **70**, 48 (1998)
4. Huggins, R.A.: J. Power Sources **81–82**, 13 (1999)
5. Chouvin, J., Olivier-Fourcade, J., Jumas, J.C., Simon, B., Godiveau, O.: Chem. Phys. Lett. **308**, 413 (1999)
6. Wachtler, M., Besenhard, J.O., Winter, M.: J. Power Sources **94**, 189 (2001)
7. Winter, M., Besenhard, J.O.: Electrochim. Acta **45**, 31 (1999)
8. Cheng, X.Q., Shi, P.F.: J. Alloys Compd. **391**, 241 (2005)
9. Kepler, K.D., Vaughey, J.T., Thackeray, M.: Electrochem. Solid-State Lett. **2**, 307 (1999)
10. Blaha, P., Schwarz, K., Luitz, J.: WIEN97. Vienna University of Technology (1997) (improved and updated Unix version of the original copyright WIEN code, which was published by P. Blaha, K. Schwarz, P. Sorantin, and S.B. Trickey, Comput. Phys. Commun. 59 (1990) 399)
11. Lyubimtsev, A.L., Baranov, A.I., Fischer, A., Kloo, L., Popovkin, B.A.: J. Alloys Compd. **340**, 167 (2002)
12. Fjellvag, H., Kjekshus, A.: Acta Chem. Scand., A **40**, 23 (1986)
13. Jeitschko, W., Jaberg, B.: Acta Crystallogr., B **38**, 598 (1982)
14. Mildenberger, R., Venskutonis, A., Aubertin, F., Breme, J., Schwitzgebel, G.: Hyperfine Interact. **112**, 151 (1998)
15. Lippens, P.E., Olivier-Fourcade, J., Jumas, J.C.: Hyperfine Interact. **126**, 137 (2000)
16. Lippens, P.E., Jumas, J.C., Olivier-Fourcade, J.: Hyperfine Interact. **156/157**, 327 (2004)
17. Robert, F., Lippens, P.E., Fourcade, R., Jumas, J.C., Gillot, F., Morcrette, M., Tarascon, J.M.: Hyperfine Interact. (2006, this volume)
18. Bahgat, A.A.: Phys. Status Solidi. B **97**, K129 (1980)

Hyperfine Interact (2006) 167:791–796
DOI 10.1007/s10751-006-9359-5

Phase composition and distribution of corrosion products grown on galvanised steel in contact with hot water

G. Palombarini · M. Carbucicchio

Published online: 16 November 2006

Abstract The composition of localised corrosion products formed on galvanised steel in contact with hot water was determined using X-ray diffraction, electron probe microanalysis, Raman and Mössbauer spectroscopies. Iron carbonate, a Zn–Fe mixed carbonate, goethite, lepidocrocite and akaganeite were identified together with some Fe-free components. The necessity of using different, complementary techniques of analysis is emphasised and some features of the corrosion mechanism are discussed.

Key words corrosion products · galvanised steel · hot water · Mössbauer spectroscopy

1 Introduction

Iron oxides and oxyhydroxides are common compounds forming on iron and steel components working in contact with aqueous environments, soil, humid and aggressive atmospheres. The identification and characterisation of all compounds are of main importance in order to understand the corrosion mechanisms and undertake remedies suitable to prevent further damages. However, considerable difficulties may arise in many practical cases due to the complex and sometime synergic effects of several factors: type of iron alloy (composition, microstructure, surface state, etc.), environment and exposure conditions, and corrosion products (number, particle size, morphology, crystallinity, lattice defectivity, phase transformations [1–7]). In this regard, a determining approach involves the use of different and complementary techniques of analysis, especially for corrosion products in the form of small particles [8–10].

In the present work, the attention was addressed to the corrosion of components realised in galvanised carbon steel, working in contact with hot water in large household heating

G. Palombarini
Institute of Metallurgy, University of Bologna, Bologna, Italy

M. Carbucicchio (✉)
Department of Physics, University of Parma, Parma, Italy
e-mail: carbucicchio@fis.unipr.it

systems. As known, these components can undergo heavy corrosion when the in-service temperature exceeds a critical value (about 60°C), leading zones of the base steel to become anodic vs. the zinc coating, localised losses of metal to occur with formation of tubercles of oxidised corrosion products and the underlying steel to become gradually thinner up to perforation of the metal wall.

2 Experimental details

Samples of corrosion products were removed from ~3 mm thick specimens of galvanised low carbon steel, taken from two different positions in the heating system (in-service time ~1 year), selected for the considerable differences in the extent of local corrosion. On the wall of a tank, the tubercles of rust were somewhat extended in the vertical direction (gravity effect) but limited in thickness. Therefore, the samples of rust removed in the form of powder contained all the corrosion products (sample A). In contrast, some thick tubercles grew within a pipe, allowing the outer part (sample BE) and the inner part (sample BI) of the products to be removed separately from an almost perforated metal zone. Each sample was carefully mixed and homogenised, characterised by scanning electron microscopy (SEM) for morphological features and analysed by electron probe microanalysis (EPMA) in energy dispersion mode (EDS) for elemental composition. X-ray diffraction patterns (XRD) were recorded using a computer-controlled goniometer and CoK_{α} radiation, with a 0.01 2θ angular step and 2 s counting time. Transmission Mössbauer spectra (TMS) were detected using a 20 mCi ^{57}Co/Rh source. A least squares minimisation routine with a combination of linear and non-linear regressions was used to fit the spectra as a superposition of Lorentzian lines and to obtain the distribution of the hyperfine magnetic fields (H_{hf}). The isomer shift is referred to α-Fe. Raman spectra (RS) were recorded using a μ-Raman spectrometer incorporating an Ar^{+} laser (514.5 nm wavelengyh, 0.3 mW power).

3 Results and discussion

Figure 1a shows an XRD pattern measured for the sample A. It shows a prevailing contribution from $FeCO_3$ (siderite), and very small contributions from iron-free compounds, i.e., $(Ca,Mg)CO_3$ (calcite) and $Zn_5(CO_3)\cdot 2H_2O$ (hydrozincite). In agreement, EDS spectra showed the presence of significant amounts of calcium and zinc in this sample. The presence of calcite can be reasonably due to a deposition process from water, while hydrozincite may well be a product of zinc-water interaction. The Mössbauer spectrum measured for the same sample (Figure 2a) can be interpreted as the superposition of four doublets: doublet I (IS=1.22 mm s^{-1}, Δ_{EQ}=1.82 mm s^{-1}) due to siderite, doublet II (IS= 1.20 mm s^{-1}, Δ_{EQ}=2.22 mm s^{-1}) ascribed to $(Zn,Fe)CO_3$ mixed carbonate [11, 12], doublet III (IS=0.37 mm s^{-1}, Δ_{EQ}=0.94 mm s^{-1}) ascribed to β-FeOOH, akaganeite, and doublet IV (IS=0.36 mm s^{-1}, Δ_{EQ}=0.56 mm s^{-1}) attributable to γ-FeOOH, lepidocrocite, and partially to akaganeite [1, 13–15].

This interpretation is supported by the presence in the XRD pattern of low intensity peaks at 2θ=16.34, 31.28 and 42.52° attributable to lepidocrocite. The low intensity and large XRD peaks characterising the pattern measured for a commercial lepidocrocite (Figure 3a) indicate the tendency of this oxyhydroxide to form as poorly crystallised, small-sized particles. Akaganeite, in turn, could contribute to the XRD pattern with the very small

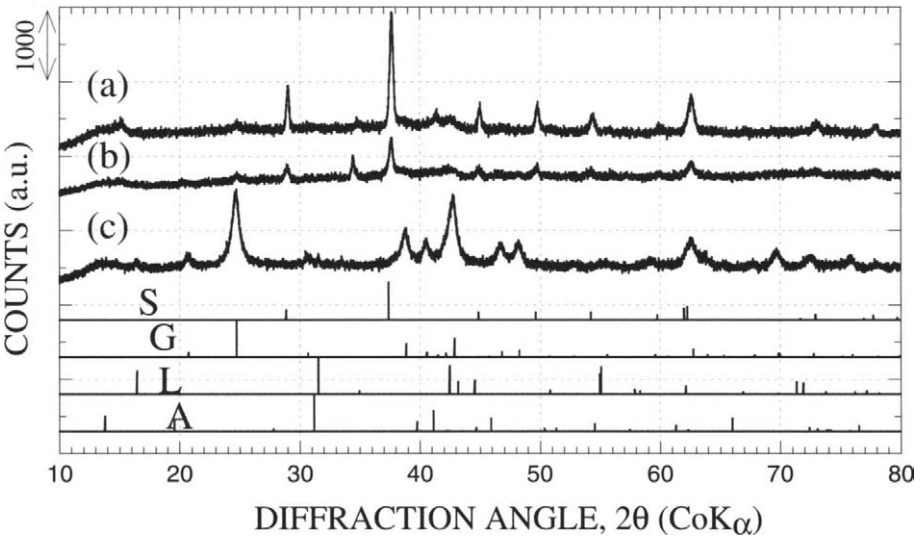

Figure 1 XRD patterns for (*a*) sample A, low thickness tubercle, all products analysed, (*b*) sample BI, thick tubercle, inner part, and (*c*) sample BE, same thick tubercle, outer part. *S* Siderite, *G* goethite, *L* lepidocrocite, *A* akaganeite.

peaks at 2θ=13.32 and 31.28°, which are not far from two of the three more intense reflections expected for this compound. It is worth noting that the formation of akaganeite is favoured by the presence of Cl^- or F^- ions in solution [1, 16]. In effect, EDS measurements have shown the presence of chlorine in some particles of the sample.

The XRD pattern in Figure 1a also shows a low intensity peak at 2θ=24.69°, a position corresponding to the maximun intensity peak of goethite. Reasonably, the content of this compound in sample A is too low to significantly contribute to the Mössbauer spectrum.

Figures 1b and 2b show respectively the XRD pattern and the Mössbauer spectrum measured for sample BI (inner part of a largely sized tubercle). Both spectra are similar to those measured for sample A (Figures 1a and 2a); therefore, also BI sample contains siderite, a Zn–Fe mixed carbonate, lepidocrocite and akaganeite as the main corrosion products. On the other hand, the comparison also shows that sample BI exhibits:

- XRD with less intense and more broadened peaks (indicating poorer cristallinity and smaller particle size) and a relatively higher contribution from goethite;
- a Mössbauer spectrum with a magnetic contribution (α in Figure 2b, main magnetic field H_{hf}=205 kOe). This contribution can be attributed to goethite (appreciably contributing to XRD) with particle size that can be evaluated to be around 15 nm considering the relation existing between goethite hyperfine magnetic field and particle size [17, 18].

Figure 1c shows the XRD pattern measured for the outer part of the same largely sized tubercle (sample BE). It shows a prevailing contribution from goethite and a small contribution from lepidocrocite. In agreement, the Raman spectrum shows distinctive peaks of goethite and, for some particles, also the maximum intensity peak of lepidocrocite (Figure 4).

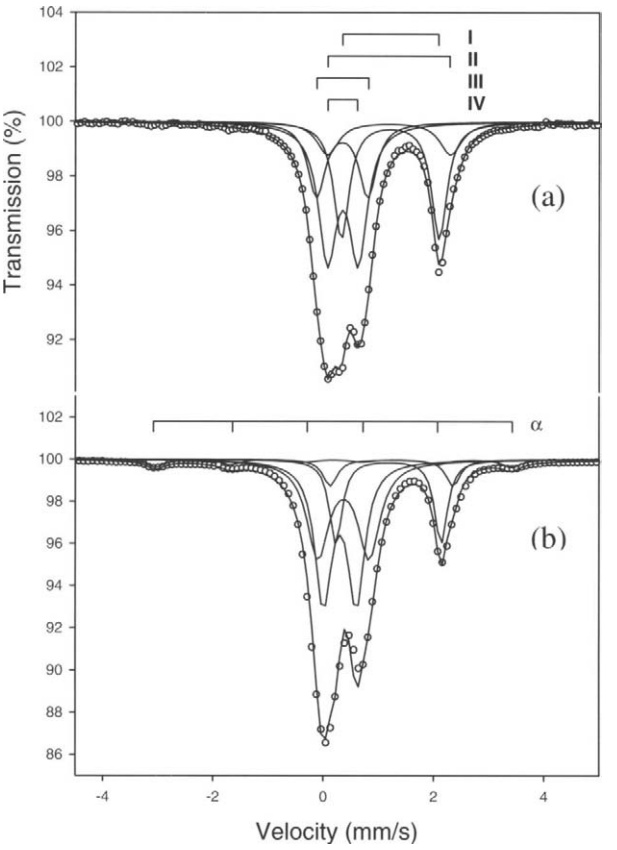

Figure 2 Transmission Mössbauer spectra for (*a*) sample A, low thickness tubercle, all products analysed, and (*b*) sample BI, thick tubercle, inner part. (I) $FeCO_3$, siderite; (II) Zn–Fe mixed carbonate; (III) β-FeOOH, akaganeite; (IV) γ-FeOOH, lepidocrocite (and, partially, akaganeite); α) α-FeOOH, goethite in particles around 15 nm in size.

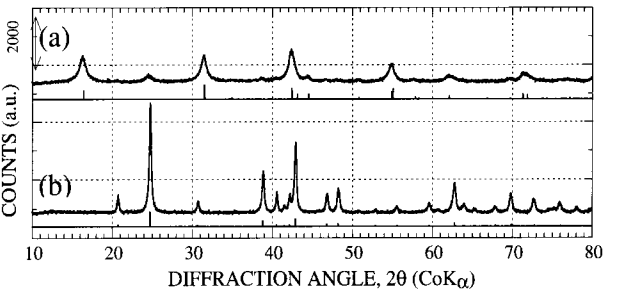

Figure 3 XRD patterns for commercial powders: (*a*) lepidocrocite; (*b*) goethite.

The Mössbauer spectrum for the same sample (Figure 5a) can be interpreted as the superposition of doublet V (IS=0.38 mm s^{-1}; Δ_{EQ}=0.92 mm s^{-1}) and doublet VI (IS=0.37 mm s^{-1}; Δ_{EQ}=0.54 mm s^{-1}). Doublet V and, partially, doublet VI can be attributed to akaganeite. As for doublet VI, it can be attributed to lepidocrocite and, taking into account the XRD results, also to goethite in the form of very small particles (<15 nm) [14, 17, 18]. In agreement, the particle size of this goethite, as determined from XRD line broadening using the Scherrer formula, is 13±1 nm.

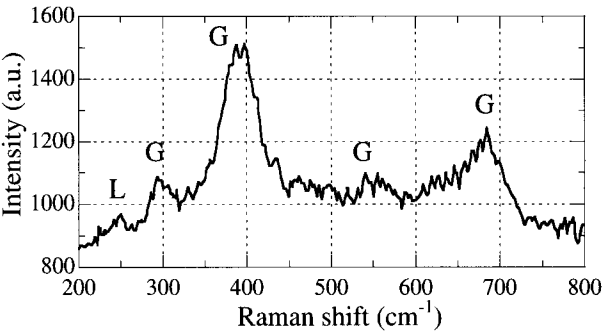

Figure 4 Raman spectrum typical of particle aggregates of sample BE (thick tubercle, outer part) containing goethite, *G*, and small amounts of lepidocrocite, *L*.

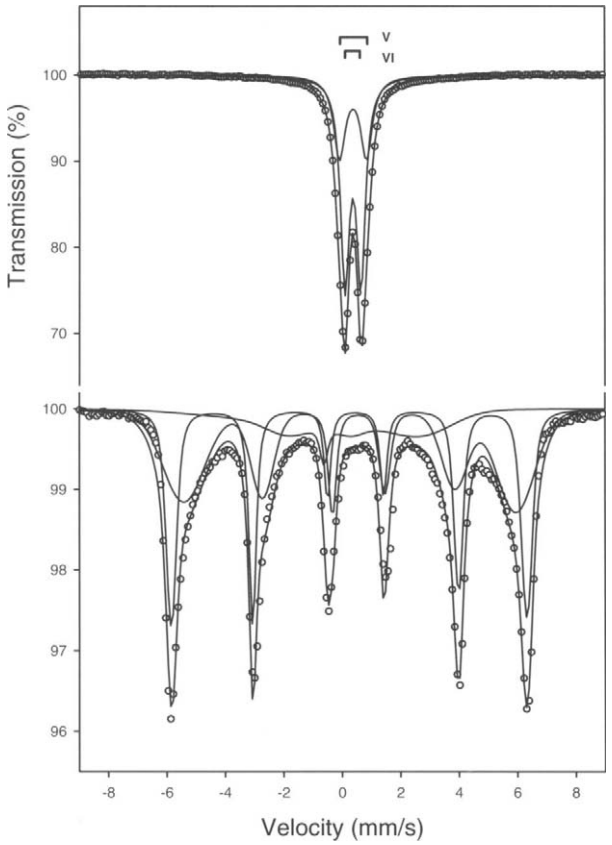

Figure 5 Transmission Mössbauer spectra for (*a*) sample BE, thick tubercle, outer part, and (*b*) commercial goethite. (*V*) β-FeOOH, akaganeite; (*VI*) γ-FeOOH, lepidocrocite (and, partially, akaganeite); and α-FeOOH, goethite in particles less than 15 nm in size.

For comparison, Figures 3b and 5b show the XRD and Mössbauer measurements carried out for a commercial goethite. The Mössbauer spectrum shows a predominant six-line contribution due to well crystallised, large particles of goethite and, superimposed, two series of sextets that can be attributed to small particles of goethite displaying a partial superparamagnetic relaxation. The analysis of the XRD pattern allowed a mean particle size of 44 nm to be evaluated for this sample.

The above results point out that an exhaustive identification of corrosion products formed on iron alloys in contact with aqueous environments only can be achieved using different and complementary techniques of analysis. In particular, without the support of Mössbauer measurements lepidocrocite and akaganeite hardly could have been unambiguously identified in XRD spectra exhibiting some prevailing contribution from other compounds (e.g. siderite in sample A, goethite in sample BE). On the other hand, without the support of XRD and Raman analyses, goethite in the form of small particles might not have been identified only on the basis of the Mössbauer spectra.

A conclusive point regards some features of the corrosion process under investigation. The presence of Fe^{2+} as carbonate is not surprising within corrosion products formed in contact with water of adequate hardness, generally giving rise to the formation of insoluble, impervious and protective layers of calcium carbonate on the galvanised steel. By the way, in different conditions of exposure Fe^{2+} can also be present within Fe_3O_4, especially on steel components working in contact with very hot water [10, 19]. Subsequently, Fe^{2+} in iron carbonate can be oxidised to Fe^{3+} in the form of goethite [20]. Goethite might also be formed by transformation of akaganeite [16]. In general, oxyhydroxides of Fe^{3+} can precipitate directly from aqueous solutions containing iron complexes produced by iron–water interactions [19], the formation of akaganeite being favoured by the presence in solution of chlorine or fluorine ions.

Acknowledgements The experimental support for Raman measurements given by F. Ospitali, University of Bologna, Italy, is gratefully acknowledged.

References

1. Murad, E., Johnston, J.H.: Iron oxides and oxyhydroxides. In: Long, G.J. (ed.) Mössbauer Spectroscopy Applied to Inorganic Chemistry, chapter 12, vol. 2, pp. 507–584. Plenum (1987)
2. Vanderberghe, R.E., Barrero, C.A., da Costa, G.M., Van San, E., De Grave, E.: Hyperfine Interact. **126**, 247–259 (2000)
3. Johnston, J.K., Norrish, K.: Aust. J. Soil Res. **19**, 231–237 (1981)
4. Olowe, A.A., Refait, P., Gènin, J.M.R.: Corros. Sci. **32**, 1003–1020 (1991)
5. Oh, S.J., Cook, D.C., Townsend, H.E.: Corros. Sci. **41**, 1687–1702 (1999)
6. Marco, J.F., Gracia, M., Gancedo, J.R., Martin-Luengo, M.A., Joseph, G.: Corros. Sci. **42**, 753–771 (2000)
7. Lin, J., Ellaway, M., Adrien, R.: Corros. Sci. **43**, 2065–2081 (2001)
8. Graham, M.J.: Corros. Sci. **37**, 1377–1397 (1995)
9. Glotch, T.D., Morris, R.V., Christensen, P.R., Sharp, T.G.: J. Geochem. Res. **109**, 1–18 (2004)
10. Carbucicchio, M., Palombarini, G., Rateo, M., Zini, F.: Characterisation of corrosion products on iron in contact with hot water. In: Gracia, M., Marco, J.F., Plazaola, F. (eds.) Industrial applications of the Mössbauer effect, pp. 73–78. AIP Conf. Proc., vol. 765 (2004)
11. Ahmed, M.A., Vanderberghe, R.E., De Grave, E., Eissa, N.A., Ibarra, J.V.: Fuel **78**, 453–457 (1999)
12. Price, D.C., Johnson, C.E., Maartens, I.: J. Phys. C. Solid State Phys. **10**, 4843–4853 (1977)
13. Chanbaere, D., Govaert, A., De Sitter, J., De Grave, E.: Solid State Commun. **26**, 657–659 (1978)
14. Johnston, J.K., Metson, J.B., Childs, C.W., Penhale, H.R.: Aust. J. Soil Res. **16**, 215–227 (1978)
15. Olowe, A.A., Gènin, J.M.R.: Corros. Sci. **32**, 1021–1028 (1991)
16. Stahl, K., Nielsen, K., Jiang, J., Lebech, B., Hanson, J.C., Norby, P., Van Lanschot, J.: Corros. Sci **45**, 2563–2575 (2003)
17. Cabral-Prieto, A., Reyes-Felipe, A.A., Siles-Dotor, M.G.: NanoStruct. Mater. **10**, 311–326 (1998)
18. Cook, D.C., Oh, G.J., Balasubramanian, R., Yamashita, M.: Hyperfine Interact. **122**, 59–70 (1999)
19. Musić, S., Nowik, I., Ristić, M., Orehovec, Z., Popović, S.: Croatica Chem. Acta **77**, 141–151 (2004)
20. Govaert, A., Dauwe, C., Plinke, P., De Grave, E., De Sitter, J.: J. Phys. **37**, 825–827 (1976)

Hyperfine Interact (2006) 167:797–801
DOI 10.1007/s10751-006-9360-z

Mechanosynthesis and characterisation of the Li–Sn system

Florent Robert · Pierre Emmanuel Lippens · Robert Fourcade · Jean-Claude Jumas · Frederic Gillot · Mathieu Morcrette · Jean-Marie Tarascon

Published online: 8 November 2006

Abstract Intermetallic phases Li–Sn were synthesized by ball-milling and characterized for their structures and electrochemical performances. All phases in Li–Sn binary phase diagram were identified by ^{119}Sn Mössbauer spectroscopy, used as reference materials for the study of lithium insertion into tin-based electrode materials. The observed spectra show two distinct environments of tin; the Sn-rich phases and the Li-rich phases. An example of electrochemical properties of these phases is proposed for $Li_{22}Sn_5$. Irreversibility of the first cycle is related to the structural change (3D→2D) of this phase.

Key words ^{119}Sn Mössbauer spectrometry · ball milling · Li–Sn alloys electrochemical performance

1 Introduction

The increasing demand of electric energy for many applications motivates an intensive research on batteries. Li-ion batteries have created a true revolution, allowing an improvement in electric performance in terms of mass and volume capacity. Lithium forms extensively alloys with tin, to a limiting stoichiometry of $Li_{22}Sn_5$ [1], which corresponds to a specific capacity of 991 mAh/g, considerably higher than those of graphite and coke which are 372 and 200 mAh/g, respectively [2].

F. Robert (✉) · P. E. Lippens · R. Fourcade · J.-C. Jumas
Laboratoire des Agrégats Moléculaires et Matériaux Inorganiques (CNRS UMR 5072), Université Montpellier II, CC 015, Place E. Bataillon, 34095 Montpellier Cedex 5, France
e-mail: frobert@univ-montp2.fr

F. Gillot · M. Morcrette · J.-M. Tarascon
Laboratoire de Réactivité et de Chimie des Solides (CNRS UMR 6007), Université d'Amiens, 33 rue Saint Leu, 80039 Amiens, France

Unfortunately, the Li-insertion mechanism is mainly based on the formation of Li–Sn alloys which leads to volume variations of the particles on cycling and therefore strongly limits the reversibility.

This leads us to study the Li–Sn system; the objective is to synthesize the intermetallic phases Li–Sn by mechanical alloying [3, 4]. The purpose of the study of these phases is to better understand the electrochemical mechanisms in anodic materials based on tin.

2 Experimental

Pure elemental Sn rod (99.9% Aldrich) and Li foil (99.9% FMC) were mixed together. Powder mixtures were sealed for 48 h under argon atmosphere, samples were milled in SPEX 8000. Starting materials were charged in stoichiometric amounts into hardened steels vials with two steel balls in a glove box under argon atmosphere. Then the mechanically alloyed powder was fired in a tube type vacuum furnace.

After ball milling experiments, phase purity and crystallinity of the powders were examined by X-ray diffraction on a D8 Brucker diffractometer (CoKα radiation, θ–θ geometry, psd detector) using a hermetically closed sample holder.

Electrochemical lithium tests were performed in Swagelok™-type cells assembled in an argon-filled glove box. The cells consist in a composite positive electrode containing the active material mixed with 10% acetylene black, a Li metal disk as the negative electrode, and a whattman borosilicate glass microfiber separator with $LiPF_6$ (1M) in PC/EC/DMC as electrolyte. The discharge/charge curves were measured by means of Mac Pile system operating in the galvanostatic or potentiostatic mode.

^{119}Sn Mössbauer spectra were recorded by transmission in the constant acceleration mode using an EG&G spectrometer. The source was ^{119m}Sn in a $CaSnO_3$ matrix. The velocity scale was calibrated using the magnetic sextet of a high purity iron foil absorber as a standard, using ^{57}Co (Rh) as the source. The spectra were fitted to Lorentzien profiles by least-squares method using the G.M.5.S.I.T program [5]. Isomer shift values are given relative to a $BaSnO_3$ spectrum recorded at room temperature. The absorbers containing 1–2 mg of ^{119}Sn per square centimeter were prepared by mixing powder samples and Apiezon grease inside the glove box, and sealed with parafilm to avoid contact with air.

3 Results and discussion

Room temperature ^{119} Sn Mössbauer effect spectra for Li–Sn alloys are shown in Figure 1. Spectra of this phases were fitted to various combinations of doublets in accordance with the results of the X-ray diffraction study.

The XRD analysis revealed that the : LiSn, $Li_{13}Sn_5$, Li_7Sn_2 and $Li_{22}Sn_5$ phases are rather pure and the structural parameters agree with those reported in the JCPDS files. The Mössbauer spectrum of Li_2Sn_5 was fitted to two doublets to account for the two inequivalent Sn sites present in this structure, and a single subspectrum corresponding to a small amount of βSn-like impurity. These results confirm that mechanical alloying provides rather pure and well crystallized Li_xSn phases.

Majority of these phases show two tin distinct environments; the Sn-rich phases (Li_2Sn_5, LiSn) with a higher symmetry (Δ small) and a significant number of Sn–Sn bonds (δ large), the Li-rich phases (LiSn, Li_5Sn_2, Li_7Sn_3, $Li_{13}Sn_5$, Li_7Sn_2, $Li_{22}Sn_5$) with low symmetry (Δ

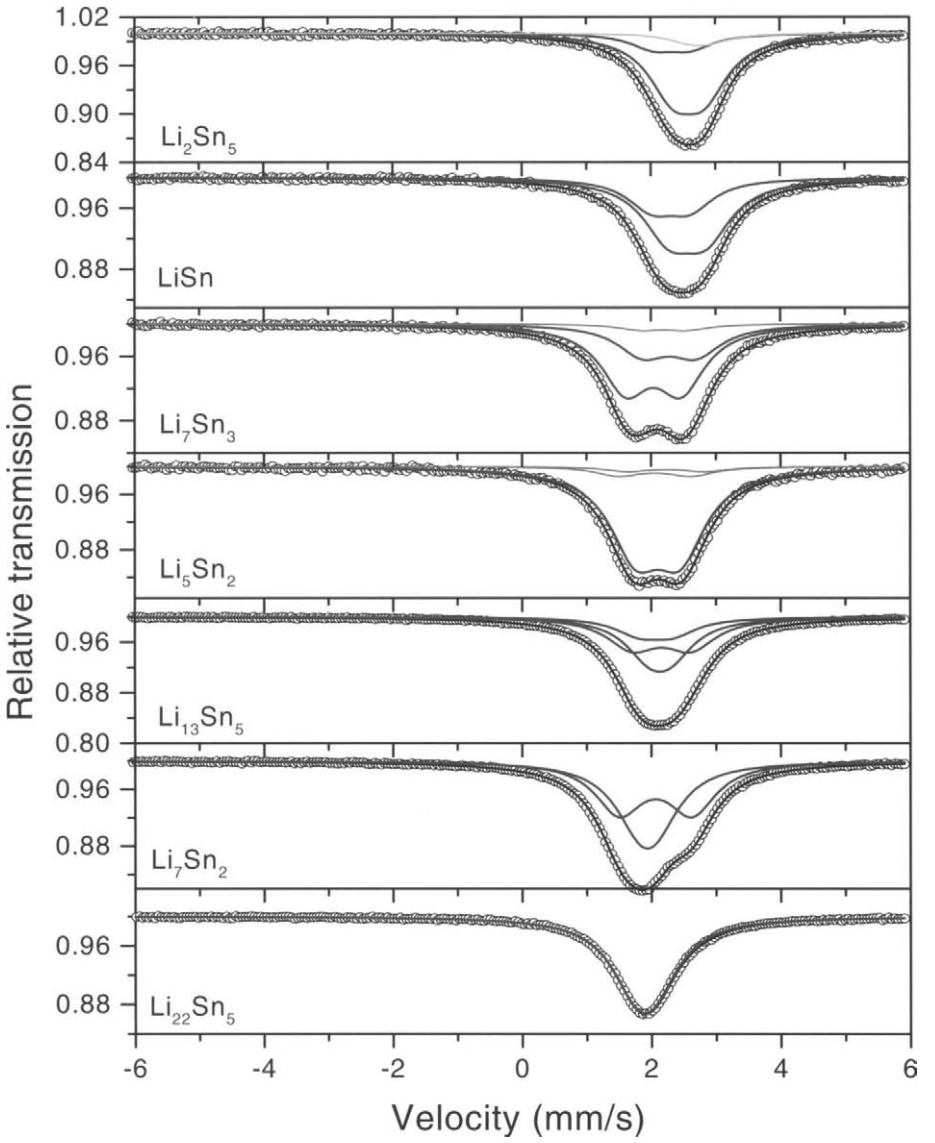

Figure 1 ^{119}Sn Mössbauer spectra of Li–Sn system.

large) and a low number of Sn–Sn bonds (δ low). Two types of variations of the isomer shift as a function of Li content can be related to changes in the Sn local environment. The Sn crystallographic sites are mainly formed by Sn atoms in Sn-rich phases and by Li atoms in Li-rich phases.

The ball-milled $Li_{22}Sn_5$ sample was tested in a Li-half cell that was cycled between 0.1 and 1 V at a Li/20 h rate in potentiostatic mode. As shown in Figure 2, the voltage-composition curves of $Li_{22}Sn_5$/Li cells exhibit three plateaus in charge (e.g., oxidation) located at 0.60, 0.73 and 0.80 V with the three corresponding ones situated near 0.67, 0.55

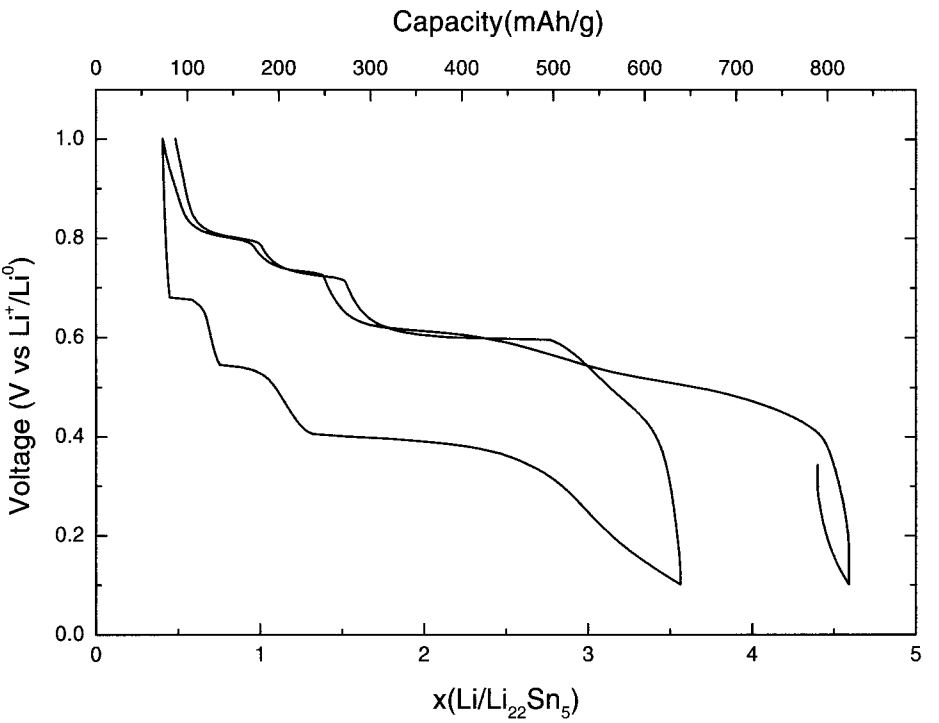

Figure 2 Voltage composition curve for a $Li_{22}Sn_5$/Li cell cycled between 0.1 and 1 V. The cell was cycled at a rate of Li/20 h in the potentiostatic mode.

and 0.4 V in discharge (e.g., reduction) indicative of the existence of three reversible two-phase processes. Several staircase steps show the existence of single-phase materials [6] in agreement with the previously reported phase diagram. The large volume changes occurring during lithium insertion and de-insertion are responsible for irreversible capacity loss in the first cycle because the Li_xSn alloy phases structurally differ with either 2D or 3D structures.

4 Conclusions

We further demonstrated the advantage of ball-milling to easily prepare single phases Li_xSn in the binary Li–Sn system. Rather pure Li–Sn crystalline phases have been obtained from ball-milling synthesis. They can be used as reference materials for the study of Li insertion into tin based electrode materials.

Although very attractive on a gravimetric capacity, Li–Sn phases were conditioned by cyclability issues due to large Li-driven volume swings inducing an electronic loss of connectivity.

Acknowledgements This work has been carried out in the framework of ALISTORE, Network of Excellence (contract no. SES6-CT-2003-503532). The authors are grateful to the European Community for the financial support.

References

1. Wang, J., Raistrick, I.D., Huggins, R.A.: J. Electrochem. Soc. **133**, 457 (1986)
2. Dahn, J.R., Fong, R., Sponn, M.J.: Phys. Rev., B. **42**, 6424 (1990)
3. Proceedings of the International Symposium on Metastable, Mechanically Alloyed and Nanocrystalline Materials (ISMANAM), Mater. Sci. Forum, 1995, 179–181; 1996, 225–227; 1997, 235–238; 1998, 269–272
4. Tarascon, J.M., Morcrette, M., Saint, J., Aymard, L., Janot, R.: CR Chimie **8**, (2005)
5. Ruebenbauer, K., Birchall, T.: Hyperfine Interact. **7**, 175 (1979)
6. Dunlap, R.A., Small, D.A., Mac Neil, D.D., Obravac, M.N., Dahn, J.R.: J. Alloys Compd. **289**, 135 (1999)

Hyperfine Interact (2006) 167:803–807
DOI 10.1007/s10751-006-9361-y

Chemical stability of hydroxysulphate green rust synthetised in the presence of foreign anions: carbonate, phosphate and silicate

C. Ruby · A. Géhin · R. Aissa · J. Ghanbaja · M. Abdelmoula · J.-M. R. Génin

Published online: 16 November 2006

Abstract Hydroxysulphate green rust $\{GR(SO_4^{2-})\}$ species were precipitated in the presence of various anions. $GR(SO_4^{2-})$ is stable at ~pH 7 and is transformed into a mixture of magnetite and ferrous hydroxide when the pH raised at ~12. In the presence of carbonate species, $GR(SO_4^{2-})$ is partially transformed into a mixture of magnetite and siderite at ~pH 8.5. This transformation is stopped when silicate anions are present in the solution. As already observed for phosphate anions, the adsorption of silicate anions on the lateral faces of the $GR(SO_4^{2-})$ crystals may explain this stabilization effect. Sulphate anions are easily exchanged by carbonate species at ~pH 10.5. In contrast, anionic exchange between sulphate and phosphate anions was not observed.

Key words green rust · Mössbauer spectroscopy · carbonate · phosphate · silicate

1 Introduction

Mixed Fe^{II}–Fe^{III} hydroxysalts green rust of general chemical formula $\left[Fe^{II}_{(1-x)}Fe^{III}_{x}(OH)_2\right]^{x+}$. $[(x/n)\ A^{n-},\ y\ H_2O]^{x-}$ are members of the layered double hydroxides (LDH) family and consists of brucite like sheets separated by anions A^{n-} and water molecules. They were observed as corrosion products on the surface of various materials: water pipes [1], steel sheet piles [2] and granular iron [3]. Due to the presence of Fe^{II}, these compounds are very reactive and are easily oxidized into ferric oxyhydroxides. In anoxic aqueous solutions, hydroxysulphate green rust $(GR(SO_4^{2-}))$ was shown to be a metastable compound compared to mixtures of magnetite and ferrous hydroxide [4] and the transformation of hydroxycarbonate green rust $\{GR(CO_3^{2-})\}$ into a mixture of magnetite and siderite was observed [5]. The reaction was stopped in the presence of phosphate anions that adsorb specifically on the lateral faces of the green rust crystals [6]. In this work, the

C. Ruby (✉) · A. Géhin · R. Aissa · J. Ghanbaja · M. Abdelmoula · J.-M. R. Génin
Laboratoire de Chimie Physique et Microbiologie pour l'Environnement, UMR 7564 CNRS-Université Henri Poincaré-Nancy 1, Equipe Microbiologie et Physique and Département Matériaux et Structures, ESSTIN, 405 rue de Vandoeuvre, 54600 Villers-lès-Nancy, France
e-mail: ruby@lcpme.cnrs-nancy.fr

Table I Concentrations of the species used for the coprecipitation experiments

Type of foreign anions	Iron concentration	Foreign anions concentrations	Basic solution
Carbonate	$[Fe]=6.7\times10^{-2}$ M	$0<[Na_2CO_3]<1.3\times10^{-1}$ M	Na_2CO_3
Silicate	$[Fe]=6.7\times10^{-2}$ M	$[Na_2SiO_3]=10^{-2}$ M	Na_2CO_3
Phosphate	$[Fe]=4\times10^{-1}$ M	$0<[Na_3PO_4]<1.3\times10^{-1}$ M	NaOH

coprecipitation in anoxic aqueous solution of dissolved sulphated Fe^{II} and Fe^{III} salts is studied in the presence of various anions. As it will be seen, $GR(SO_4^{2-})$ precipitates in a first step independently of the presence of these anions. However, $GR(SO_4^{2-})$ is not always chemically stable and several transformations will be observed.

2 Materials and methods

$FeSO_4{\cdot}7H_2O$ and $Fe_2(SO_4)_3{\cdot}5H_2O$ salts were dissolved in 600 ml of demineralised water and introduced in a gas-tight reactor. A ferric molar fraction $n(Fe^{III})/[n(Fe^{II})+n(Fe^{III})] = 33\%$ was chosen. If necessary, low quantity of $Na_3PO_4{\cdot}12H_2O$ or Na_2SiO_3 salts were introduced into the initial mixture and details concerning the various species present in the solution are given in Table I. Anoxic conditions were maintained by a continuous nitrogen bubbling. A basic solution (Na_2CO_3 or NaOH) was added progressively into the initial mixture at a flow of 0.5 ml min^{-1} and the pH was monitored to follow the steps of the coprecipitation reaction. The precipitates were analyzed with transmission electron microscopy coupled with an energy dispersive X-ray analyser (TEM–EDX) and with transmission Mössbauer spectroscopy (TMS). Isomer shifts were calculated by using the TMS spectrum of an α-Fe foil at 300 K as a reference. Lorentzian shape lines were used to fit the spectra.

3 Transformation of hydroxysulphate green rust and role of the carbonate species

Influence of the pH $GR(SO_4^{2-})$ is easily synthesised by adding a NaOH solution to the dissolved salts at a ratio $R = n(OH^-)/n(Fe) = 2$. The shape of the titration curve that represents the evolution of the pH as a function of the ratio R is presented in the inset of Figure 1a. It was previously discussed [7] : ferric species precipitate before the first equivalent point and $GR(SO_4^{2-})$ forms during the second pH plateau. For R=2, the pH is situated around 7 and the TMS of $GR(SO_4^{2-})$ consists of one ferrous doublets D_1 and one ferric doublet D_2. Hyperfine parameters are given in Table II.

In the absence of anions other than SO_4^{2-}, $GR(SO_4^{2-})$ was stable during several months when the suspension was maintained in anoxic condition. In contrast, when an excess of NaOH was introduced in the solution, a pH value of 12 was reached and $GR(SO_4^{2-})$ was fully transformed into a mixture of magnetite and ferrous hydroxide (Figure 1b). This is in agreement with previous thermodynamic predictions [4]: it was demonstrated that magnetite is more stable than $GR(SO_4^{2-})$ in alkaline solution.

Influence of the carbonate species The sulphated dissolved salts were precipitated by an Na_2CO_3 solution. The precipitation of $GR(SO_4^{2-})$ was observed at a pH around 8.5 at the second equivalent point of the titration curve (Figure 1c). This result was not expected because it is often reported that carbonated LDH compounds easily form. The

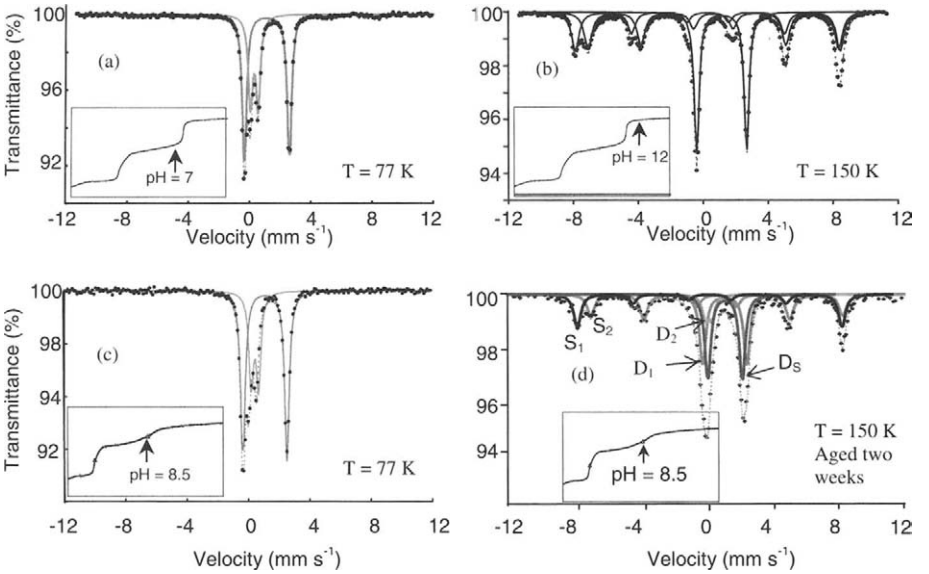

Figure 1 Mössbauer spectra of various precipitates: (a) precipitated with NaOH, (b) Fe_3O_4+$Fe(OH)_2$ precipitated with NaOH, (c) precipitated with Na_2CO_3, (d) sample **c** aged during two weeks in anoxic conditions.

Table II Hyperfine parameters of the Mössbauer spectra

Figure	Compound		δ	Δ or ε	H	RA (%)
1a	$GR(SO_4^{2-})$	D_1	1.3	2.93	–	65
		D_2	0.49	0.5	–	35
1b	$Fe(OH)_2$	D_1	1.29	3.06	–	37
	Fe_3O_4	S_1	0.41	0	507	28
		S_2	0.75	0	479	35
1c	$GR(SO_4^{2-})$	D_1	1.31	2.91	–	66
		D_2	0.49	0.47	–	34
1d	$GR(SO_4^{2-})$	D_1	1.29	2.85	–	18
		D_2	0.49	0.45	–	9
	$FeCO_3$	D_S	1.31	2.21	–	27
	Fe_3O_4	S_1	0.22	0	501	18
		S_2	0.66	0	477	24

δ Isomer shift (mm s^{-1}); Δ or ε quadrupole splitting or shift (mm s^{-1}); H hyperfine field (kOe); RA relative abundance (%)

transformation of $GR(SO_4^{2-})$ into $GR(CO_3^{2-})$ was only observed when an excess of carbonated species was added (~pH 10.5). The Mössbauer spectrum of $GR(CO_3^{2-})$ (not shown) consists of two ferrous doublets and one ferric doublet. At lower pH (~8.5), $GR(SO_4^{2-})$ was transformed partially into a mixture of magnetite and siderite after a 2 weeks aging of the suspension in anoxic condition (Figure 1d).

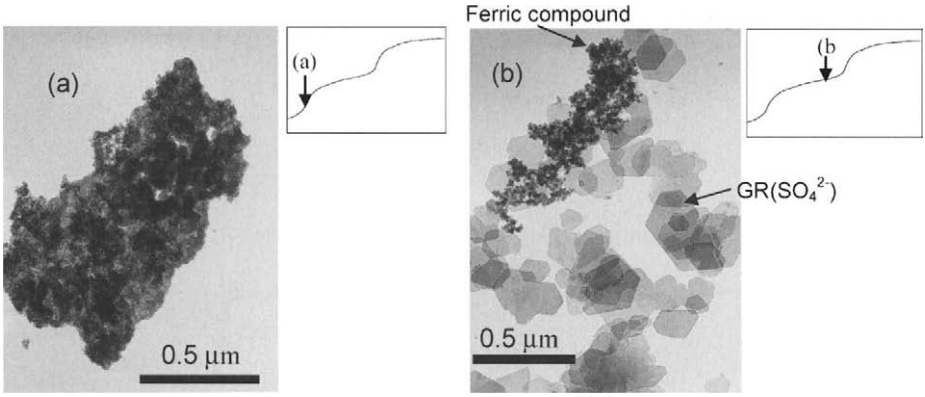

Figure 2 TEM images of the precipitates taken at different stages of the coprecipitation of Fe^{II} and Fe^{III} species in the presence of phosphate anions: (a) Badly crystallized ferric compound that contain Fe, O and P atoms; (b) and remaining ferric compound.

4 Stabilization of hydroxysulphate green rust by phosphate and silicate anions

Influence of the phosphate species Various amounts of a Na_3PO_4 salt were dissolved into the sulphated Fe^{II}–Fe^{III} solution and precipitated with a NaOH solution. The precipitate was ~100% of $GR(SO_4^{2-})$ when a ratio $R = 2 - (3 \times [Na_3PO_4]/[Fe])$ was introduced into the solution. This result suggests that the Fe species were neutralized by both basic solutions, i.e., NaOH and Na_3PO_4. For a ratio $[Na_3PO_4]/[Fe] = 1/6$, the TEM image of the sample taken at the first equivalent point (R=1/2) consists of agglomerated particles (Figure 2a). Fe, O and P atoms were identified with EDX and the estimated atomic relative abundance was, respectively, 22, 65 and 13%. At this stage of the reaction, the phosphate species are chemically bound with Fe^{III} ions. The TEM images of the sample taken at R=3/2 consist essentially of hexagonal $GR(SO_4^{2-})$ crystals, but small amounts of the initially formed ferric particles were sometimes observed. EDX analyses performed on the $GR(SO_4^{2-})$ crystals confirm the presence of Fe, O and S atoms. Anionic exchange between PO_4^{3-} and SO_4^{2-} anions did not occur and the absence of P atoms was verified with EDX. This result differs from previously reported data presented by Hansen and Poulsen [8]. It was reported that the reactivity of PO_4^{3-} with $GR(SO_4^{2-})$ occurred very slowly and several months were necessary to convert $GR(SO_4^{2-})$ into a mixture of vivianite $Fe_3(PO_4)_2$ and a badly crystallized ferric oxyhydroxide. The stability of $GR(SO_4^{2-})$ for such a long period was not verified in our experiments.

Influence of the silicate species The sulphated dissolved salts were mixed with a fixed amount of a Na_2SiO_3 salt and the mixture was precipitated with a Na_2CO_3 solution. The previously observed transformation of $GR(SO_4^{2-})$ into the mixture $\{Fe_3O_4, FeCO_3\}$ by aging did not occur and $GR(SO_4^{2-})$ remains stable during several weeks. Similarly to what was observed for phosphate anions for $GR(CO_3^{2-})$ [6], this stabilization effect may be explained by the adsorption of silicate anions on the lateral faces of the of $GR(SO_4^{2-})$ crystals. The concentration of P in solution was measured with ICP-AES and it was of the same order of magnitude than the relative number of surface sites present on the lateral

faces of the $GR(CO_3^{2-})$ crystals [6]. Here, direct evidence is difficult to perform with TEM–EDX because the (0001) faces of the $GR(SO_4^{2-})$ are always almost parallel to the copper grid. In contrast, the transformation of $GR(SO_4^{2-})$ into $GR(CO_3^{2-})$ observed at ~pH 10.5 was not stopped by the presence of silicate anions.

5 Conclusion

The coprecipitation of dissolved sulphated ferric and ferrous salts was studied in the presence of various foreign anions. Hydroxysulphate green rust $\{GR(SO_4^{2-})\}$ precipitated quickly even in the presence of carbonate species. However, $GR(SO_4^{2-})$ is a metastable compound and transforms either into hydroxycarbonate green rust at ~pH 10.5 or into a mixture of magnetite Fe_3O_4 and siderite $FeCO_3$ at lower pH. This last reaction is stopped in the presence of silicate anions that may adsorb on the lateral faces of the $GR(SO_4^{2-})$ crystals preventing their transformation. $GR(SO_4^{2-})$ is stable in the presence of low quantity of phosphate species and anionic exchange between phosphate and sulphate anions did not occur in our experimental conditions.

Acknowledgement We would like to thank the Conseil Regional de Lorraine for financing the thesis grant of Antoine Géhin.

References

1. Stampfl, P.P.: Corros. Sci. **9**, 185 (1969)
2. Refait, Ph., Memet, J.-B., Bon, C., Sabot, R., Génin, J.-M.R.: Corros. Sci. **45**, 833 (2003)
3. Ritter, K., Odziemkowski, M.S., Gillham, R.W.: J. Contam Hydrol. **55**, 87 (2002)
4. Refait, Ph., Géhin, A., Abdelmoula, M., Génin, J.-M.R.: Corros. Sci., **45**, 659 (2003)
5. Benali, O., Abdelmoula, M., Refait, P., Génin, J.-M.R.: Geochim. Cosmochim. Acta **65**, 1715 (2001)
6. Bocher, F., Géhin, A., Ruby, C., Ghanbaja, J., Abdelmoula, M., Génin, J.-M.R.: Solid State Sci. **6**, 117 (2004)
7. Ruby, C., Géhin, A., Abdelmoula, M., Génin, J.-M.R., Jolivet, J.-P.: Solid State Sci. **5**, 1055 (2003)
8. Hansen, H.C.B., Poulsen, I.F.: Clays Clay Miner. **47**, 312 (1999)

Hyperfine Interact (2006) 167:809–813
DOI 10.1007/s10751-006-9362-x

Mössbauer characterization of calcium–ferrite oxides prepared by calcining Fe_2O_3 and CaO

Daisuke Hirabayashi · Yoichi Sakai · Takeshi Yoshikawa · Kazuhiro Mochizuki · Yoshihiro Kojima · Kenzi Suzuki · Kazumasa Ohshita · Yasuo Watanabe

Published online: 14 November 2006

Abstract Calcium ferrite oxides were prepared by calcining a mixture powder of iron- and calcium oxide. The ^{57}Fe-Mössbauer spectra of the calcium ferrites oxides were measured, revealing that the products should be $Ca_2Fe_2O_5$ and $CaFe_2O_4$, the ratio of which was dependent of the Fe/Ca atomic ratio of the mixture powder.

Key words calcium ferrite · $Ca_2Fe_2O_5$ · $CaFe_2O_4$ · calcining of Fe_2O_3 and CaO · ^{57}Fe-Mössbauer characterization

1 Introduction

As strengthening the regulation of emission of exhausted gas of motor bicycles from a viewpoint of environment protection, there have been a lot of efforts to develop catalysts to decompose hazardous compounds such as carbon monoxide and hydrocarbons. Noble-metal based catalysts such as Pt and Pd catalysts are extensively adopted to reduce such emission gas, which have an advantage to ensure a long term use but is costly limited due to their rare amount as natural resources. We have paid attention to calcium–ferrite based catalyst for the purpose. Before our recent study on calcium–ferrite catalyst [1] revealing that the catalytic activity of propylene oxidation over $Ca_2Fe_2O_5$ was almost same as over a Pt-supported catalyst, few preceding reports have been published [2]. Calcium ferrite is environmentally safe, chemically stable, costly cheep and greatly abundant as the resource

D. Hirabayashi · T. Yoshikawa · K. Mochizuki · Y. Kojima · K. Suzuki
EcoTopia Science Institute, Nagoya University,
Nagoya 464-8603, Japan

Y. Sakai (✉) · K. Ohshita · Y. Watanabe
Department of Chemistry, Daido Institute of Technology,
Nagoya 457-8530, Japan
e-mail: yocsakai@daido-it.ac.jp

Y. Watanabe
Crystals Division, Saint-Gobain K.K.,
Tokyo 102-0083, Japan

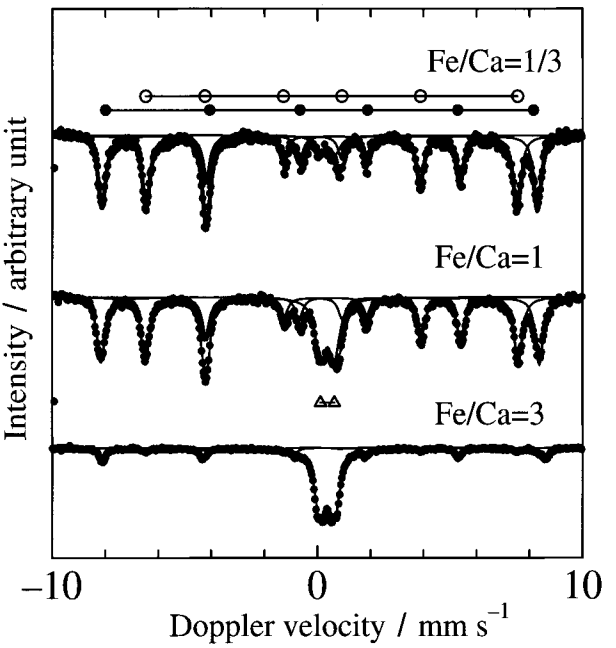

Figure 1 ^{57}Fe-Mössbauer spectra at 293.0 K of calcium ferrites prepared from the mixtures of Fe_2O_3 and CaO with mixing atomic ratio (Fe/Ca) of 1/3, 1 and 3. Two sets of sextet set for brownmillerite-type $Ca_2Fe_2O_5$; *closed circles* for the octahedral-site Fe^{3+} while *open* ones for the tetrahedral-site Fe^{3+}. The doublet component marked by *triangles* was assigned to $CaFe_2O_4$.

because it is by-product slug in iron-manufacture industry. In the present work, calcium–ferrite catalysts were characterized by means of ^{57}Fe-Mössbauer spectroscopy.

2 Experimental

The samples were prepared by calcining a physical mixture of Fe_2O_3 and CaO with an atomic ratio of Fe to Ca from 1/3 to 3 at 1,000°C for 3 h in air. Details of the procedure are referred to our previous report [1]. Mössbauer measurements were performed in an ordinary mode with Mössbauer spectrometers of Model MD-22B and MGF-500F, fabricated by Topologic Systems, Inc., with a ^{57}Co(Rh) source. Measurement temperature was ranged from 78.0 to 293.0 K regulated by using an Oxford cryostat DN-1726 with a temperature controller ITC-601. Each spectrum was measured for the running time of 1 or 2 days. The curve fitting of spectra was carried out by using of a commercially available Mössbauer analysis program named MossWinn 3.0i. The isomer shift and Doppler velocity scale were calibrated with respect to metallic iron at 293.0 K.

3 Results and discussion

Typical ^{57}Fe-Mössbauer spectra at 293.0 K measured for calcium ferrites are shown in Figure 1, where the mixing atomic ratios (Fe/Ca) in the starting mixtures are 1/3, 1, and 3 for the spectra at the top, middle and bottom, respectively. It was revealed by our analysis of the Mössbauer spectra that a main product in the samples with Fe/Ca=1/3 and 1 should be brownmillerite-type $Ca_2Fe_2O_5$ with two ferric ion sites of tetrahedral and octahedral. Calcium ferrite $Ca_2Fe_2O_5$ appears in the spectra of Figure 1 as two sets of sextet with an almost identical intensity, although their absorptions look too small to find out clearly for

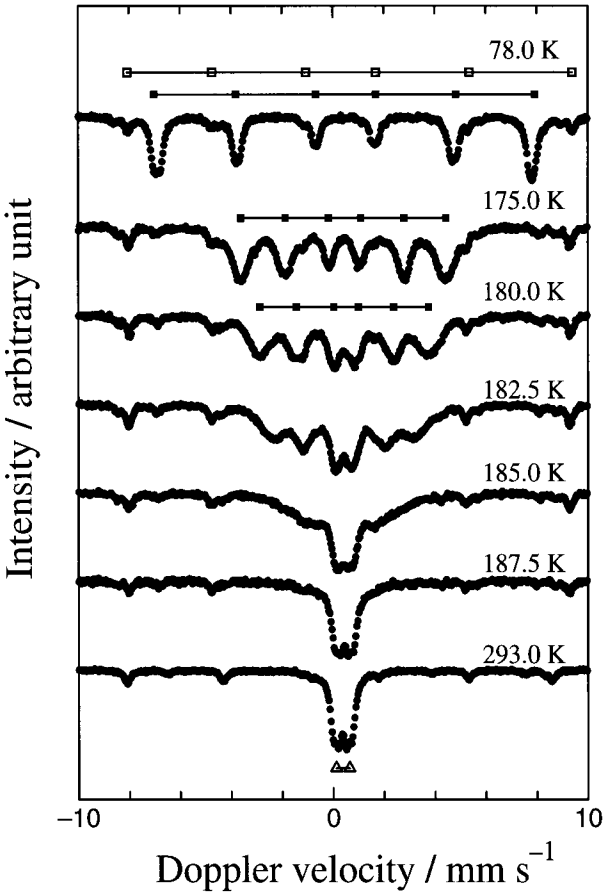

Figure 2 Temperature-dependence of ^{57}Fe-Mössbauer spectra for calcium ferrite prepared from the mixtures of Fe_2O_3 and CaO with a mixing atomic ratio (Fe/Ca) of 2. A set of sextet marked by *open squares* was ascribable to un-reacted Fe_2O_3, while a sextet by *closed squares* to $CaFe_2O_4$. With a transition temperature around 190 K, the sextet was found to change drastically to a doublet *line-shape* marked by *triangles*.

the sample with Fe/Ca=3. The two sextets are indicated by the markers in the figure, where closed and open circles set for Fe^{3+} occupied at octahedral and tetrahedral sites, respectively, in the brownmillerite-type structure; the isomer shift, quadrupole splitting, internal field were evaluated to be 0.35 mm/s, −0.52 mm/s, and 50.7 T for the octahedral site, and then 0.18 mm/s, 0.72 mm/s and, 43.2 T for the tetrahedral site. These Mössbauer parameters at 293.0 K agreed to those at 300 K previously reported by Randhawa and Sweety [3]; 0.37 mm/s, −0.52 mm/s, and 50.4 T for the octahedral site, and 0.18 mm/s, 0.72 mm/s and, 42.9 T for the tetrahedral site of $Ca_2Fe_2O_5$.

It was suggested that other calcium–ferrite species could be $CaFe_2O_4$, which was recorded at 293.0 K as a doublet with IS=0.37 mm/s and QS=0.51 mm/s in Figure 1 as pointed by triangle-markers, on the base of our recent X-ray diffraction study [1] and the Mössbauer data (IS=0.36 mm/s and QS=0.49 mm/s) by Simmons and Music [4]. In order to confirm such an assignment, the Mössbauer spectra of the product with Fe/Ca=2 were measured over the temperature range from 78.0 to 293.0 K as shown in Figure 2. It was clearly found that there was a drastic change of line-shape for $CaFe_2O_4$. The sextet component (marked by closed squares) with an internal magnetic field (H_f) of 46.2 T at 78.0 K was dramatically changed to the paramagnetic doublet marked by triangles at 293.0 K, corresponding to disappearing of magnetic ordering with increasing of temperature. This finding is due to a transition from antiferromagnetic to paramagnetic

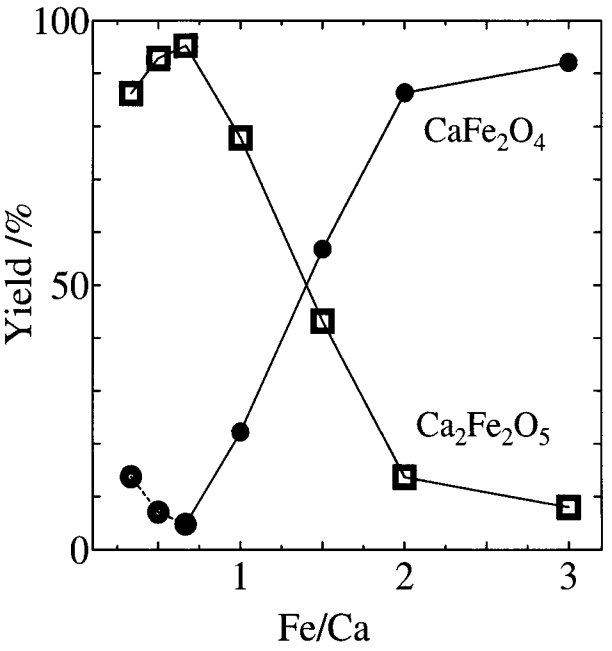

Figure 3 Atomic ratio (Fe/Ca)-dependence of product yield (%) obtained from Mössbauer spectra. *Symbol of square sets* for $Ca_2Fe_2O_5$, *closed circle* for $CaFe_2O_4$, and *double circle* for unknown Fe^{3+} species.

with a Neel temperature of ca. 190 K close to that (200 K) for $CaFe_2O_4$ in the literature [5], confirming that it should be ascribable to $CaFe_2O_4$. For the samples with Fe/Ca=1/3 and Fe/Ca=1, the Mössbauer spectra were measured at 78.0 K, which showed that the spectrum of Fe/Ca=1/3 was observed to be almost the same as that at 293.0 K while there was found a pronounced change in the spectrum for the Fe/Ca=1 sample; the doublet disappeared and changed to a set of sextet with H_f=45.5 T being ascribed to $CaFe_2O_4$. These observations imply that the ferric species observed for the Fe/Ca=1/3 was not $CaFe_2O_4$, unfortunately not identifying what chemical species it is exactly now although it is clarified to be paramagnetic Fe^{3+} species.

The product yields of $Ca_2Fe_2O_5$ and $CaFe_2O_4$ are plotted against the mixing atomic ratio of Fe/Ca in Figure 3, which were obtained from the Mössbauer absorption area of each component at 293.0 K. Since the doublet component for Fe/Ca<1/2 might probably be some Fe^{3+} species but not $CaFe_2O_4$ as described above, the marks were depicted by a double circle. For the spectra for the samples with Fe/Ca=2 and Fe/Ca=3, the non-reacted Fe_2O_3 component with an area percentage of 11.8 and 39.8%, respectively, was observed as well as calcium ferrites, $Ca_2Fe_2O_5$ and $CaFe_2O_4$. The plotted yield values for Fe/Ca=2 and 3 in the figure were corrected by eliminating the non-reacted Fe_2O_3 component from the total percentage. Figure 3 shows that below the ratio of Fe/Ca=1, a main product was $Ca_2Fe_2O_5$ while it was $CaFe_2O_4$ above the ratio=1. It should be a reasonable observation that the iron-richer ferrite-product of $CaFe_2O_4$ was easily yielded with increasing of iron content in the starting reaction mixture.

References

1. Hirabayashi, D., Yoshikawa, T., Mochizuki, K., Suzuki, K., Sakai, Y.: Catal. Lett. **110**, 155 (2006)
2. Isupova, L.A., Tsybulya, S.V., Kryukova, G.N., Budneva, A.A., Paukshtis, E.A., Litvak, G.S., Ivanov, V. P., Kolomiichuk, V.N., Pavlyukhin, Yu.T., Sadykov, V.A.: Kinet. Catal. **43**, 122 (2002)

3. Randhawa, B.S., Sweety, K.: Bull. Mater. Sci. **23**, 305 (2000)
4. Simmons, G.W., Music, S.: Characterization of Electric Arc Furnace Dust by Mössbauerr Spectroscopy. Lehigh University., Bethlehem, PA (1981)
5. Bertaut, E.F., Chappert, J., Apostolov, A., Semenov, V.: Bull. Soc. Fr. Mineral. Cristallogr. **89**, 206 (1966)

Hyperfine Interact (2006) 167:815–818
DOI 10.1007/s10751-006-9363-9

Relative Lamb–Mössbauer factors of tin corrosion products

M. T. Sougrati · S. Jouen · B. Hannoyer

Published online: 14 November 2006

Abstract Variable temperature ^{119}Sn Mössbauer spectroscopy was used to obtain relative Lamb–Mössbauer factors for three tin corrosion products: hydrated stannic oxide $SnO_2{\cdot}xH_2O$, abhurite $Sn_{21}O_6Cl_{16}(OH)_{14}$, and tin hydroxysulfate $Sn_3OSO_4(OH)_2$. Their hyperfine parameters have also been investigated.

Key words Lamb–Mössbauer factor · tin · corrosion products

1 Introduction

The use of tin in many industrial fields has become increasingly important. Thin tin coatings are used in solders, marine equipments, roofing, gasoline tanks, exhaust pipes and, more widely, coating of steel in canning industry. As a consequence of this usage, the tin comes in contact with an innumerable variety of environments [1]. Thus, the understanding of the corrosion mechanism is required to develop any protection protocol. Mössbauer spectroscopy can provide precious information on the corrosion process. It allows the characterisation of the phases resulting on the tin corrosion [2], and permits their quantification [3]. The identification of the corrosion products is deduced from the hyperfine parameters. The quantification is conditioned by the knowledge of the Lamb–Mössbauer factors e.g., *f*-factor. Therefore, reliable analysis of the corrosion layer requires an accurate determination of both the hyperfine parameters and the Lamb–Mössbauer factors of the formed phases. The hyperfine parameters have been published for the principle tin compounds. Unfortunately, only few *f*-factor values are available for tin compounds and the essential published results concern metallic tin and tin oxides. Also, for the same compound the value of Lamb–Mössbauer factor varies following the preparation method. The work of Collins and his collaborators, [4], illustrates clearly the impact of the crystallinity on both the Mössbauer parameters and the *f*-factor of tin oxides.

M. T. Sougrati · S. Jouen (✉) · B. Hannoyer
Laboratoire d'Analyse Spectroscopique et de Traitement de Surface des Matériaux Institut des Matériaux, Université de Rouen, B.P. 12, Saint Etienne du Rouvray Cedex 76801, France
e-mail: samuel.jouen@univ-rouen.fr

Table I Hyperfine parameters at RT for $SnO_2{\cdot}xH_2O$, $Sn_3OSO_4(OH)_2$ and $Sn_{21}O_6Cl_{16}(OH)_{14}$

Compounds	$\delta \pm 0.005$ mm s^{-1}	$\Gamma \pm 0.01$ mm s^{-1}	$\Delta \pm 0.01$ mm s^{-1}
$SnO_2{\cdot}xH_2O$	−0.001	1.02	0.61
$Sn_3OSO_4(OH)_2$	3.030	1.05	2.12
$Sn_{21}O_6Cl_{16}(OH)_{14}$	3.244	0.91	1.72

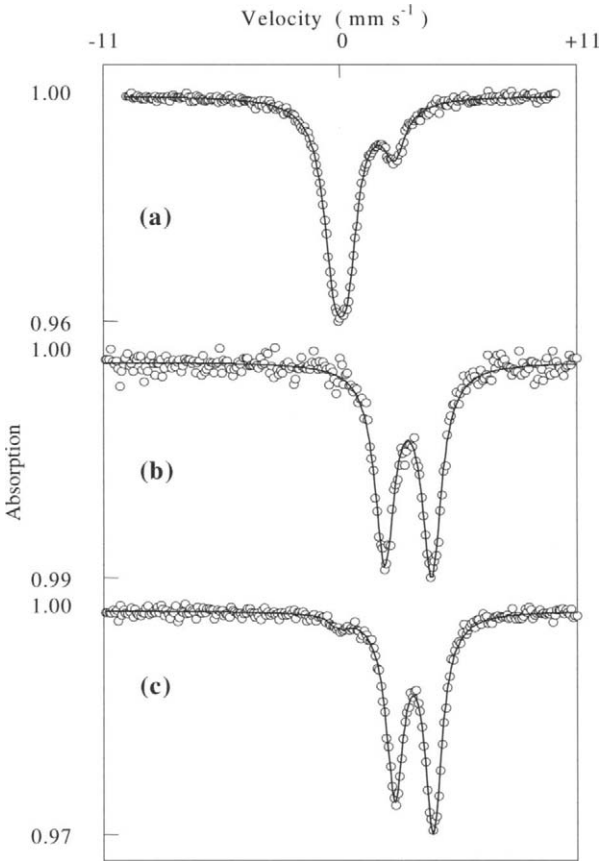

Figure 1 Mössbauer spectra at RT; (a) $SnO_2{\cdot}xH_2O$, (b) $Sn_3OSO_4(OH)_2$ and (c) $Sn_{21}O_6Cl_{16}(OH)_{14}$.

The purpose of this work is to give a complete Mössbauer study of three tin corrosion products. The hydrated stannic oxide $SnO_2{\cdot}xH_2O$ is formed during outdoor corrosion of metallic tin and tin bronzes [5], the abhurite $Sn_{21}O_6Cl_{16}(OH)_{14}$ has been detected as a corrosion product of tin formed in seawater [6] and tin hydroxysulfate $Sn_3OSO_4(OH)_2$ which is expected to form in atmospheres containing notable amount of sulphur dioxide [7].

2 Experimental

In the ideal case, only natural corrosion products must be investigated. However, except for natural hydrated stannic oxide, it was not possible to get sufficient amount of natural compounds for Mössbauer measurements. Hence, electrochemically synthesised tin hydroxysulfate and abhurite have been used. XRD examination shows that the resulting

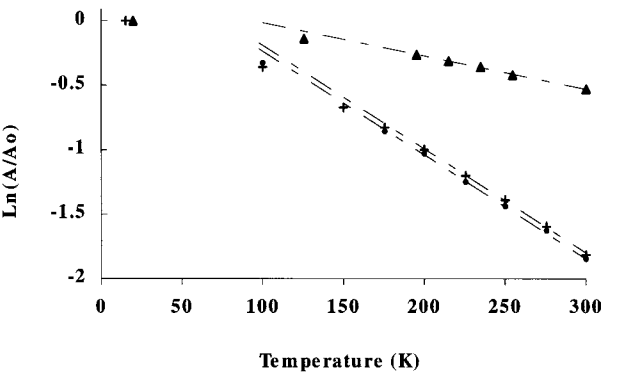

Figure 2 Temperature dependence of the normalised area under the resonance curve. $SnO_2{\cdot}xH_2O$ (*filled triangle*), $Sn_3OSO_4(OH)_2$ (*filled circle*) and $Sn_{21}O_6Cl_{16}(OH)_{14}$ (*plus symbol*).

products are of high crystallinity with orthorhombic and trigonal system respectively for tin hydroxysulfate and abhurite.

The variable temperature Mössbauer experiments were carried out in the 15–300 K temperature range on powdered samples. The source used was a ^{119m}Sn ($CaSnO_3$) source (10 mCi) with a conventional constant acceleration spectrometer. The analysed samples contain 10 mg cm^{-2} of natural tin nuclei. The chemical isomer shift data are quoted relative to the centroid of $BaSnO_3$ spectrum at room temperature.

3 Results

3.1 Hyperfine parameters

The Mössbauer hyperfine parameters obtained at room temperature for $SnO_2{\cdot}xH_2O$, Table I, are in good agreement with literature data [8, 9]. The data obtained for $Sn_3OSO_4(OH)_2$ are slightly different from those found by Davies and Donaldson [10] (δ=2.57 mm s^{-1}, Δ= 2.00 mm s^{-1}). No data have been found in the literature for $Sn_{21}O_6Cl_{16}(OH)_{14}$.

A typical spectrum for each compound is shown in Figure 1. Spectrum (a) contains, in addition to $SnO_2{\cdot}xH_2O$ sub-spectrum, a second component at δ=2.508 mm s^{-1} which is assigned to metallic tin. $Sn_3OSO_4(OH)_2$ spectrum consists on a single asymmetric doublet (b). $Sn_{21}O_6Cl_{16}(OH)_{14}$ spectrum is also an asymmetric doublet. The small peak observed around δ=0.0 mm s^{-1} indicates the formation of Sn(IV) compound (c). The relative area of this peak is less than 2% of the spectrum.

3.2 Lamb–Mössbauer factor (*f*-factor)

When the corrosion products are clearly identified, Mössbauer spectroscopy can be used for quantitative analysis. For this purpose, relative Lamb–Mössbauer factors are required. In the case of thin absorber, the temperature dependence of the Lamb–Mössbauer factor can be represented by the temperature dependence of the area under the resonance curve [11]. In the Debye model and in the high-temperature limit, one can write [8]:

$$\frac{d}{dT}(\ln A) = \frac{d}{dT}(\ln f) = \frac{-6E_R}{k_B\theta_M^2}$$

Where A is the area under the resonance curve, E_R=2.572 meV is the recoil energy for ^{119}Sn, θ_M is the Debye temperature of the solid and k_B is the Boltzmann constant.

Table II Experimental *f*-factors and θ_M for SnO_2, $SnO_2{\cdot}xH_2O$, $Sn_3OSO_4(OH)_2$ and $Sn_{21}O_6Cl_{16}(OH)_{14}$

Compounds	θ_M (K)	*f*-factor at RT
$Sn_{21}Cl_{16}(OH)_{14}O_6$	148.8	0.09_8
$Sn_3OSO_4(OH)_2$	147.0	0.09_3
$SnO_2{\cdot}xH_2O$	265.3	0.45_8
SnO_2industrial	310.3	0.56_5
SnO_2anhydrous	313.0	0.57*
SnO_2amorphous	243.0	0.40*

*Deduced from θ_M given in reference [4].

Figure 2 displays the temperature dependence of the area, normalised to the area at T_0= 15 K, for $SnO_2{\cdot}xH_2O$, $Sn_3OSO_4(OH)_2$ and $Sn_{21}O_6Cl_{16}(OH)_{14}$. The logarithmic dependence of the area under the Mössbauer spectra shows the shape expected by Debye model: linear at high temperature. The slope of this curve at high temperature permits the determination of the Debye temperature and therefore the *f*-factor. Table II recapitulates the obtained results.

The *f*-factor of crystalline industrial SnO_2 has also been determined, see Table II, the obtained value is in good agreement with literature data [4]. The significant difference between this value and that obtained for $SnO_2{\cdot}xH_2O$ (17%) shows that *f*-factor values obtained using industrial compounds can not be used for accurate quantitative analysis for corrosion products. Since the *f*-factor can be different for a same compound following its growth condition, it is necessary to determine systematically this factor for any quantitative purpose. Furthermore, the *f*-factor of tin compounds being low, it is pertinent to carry out Mössbauer measurement at low temperature in order to increase the sensitivity.

As regards to the *f*-factors found in this work, it appears difficult to detect small amount of $Sn_3OSO_4(OH)_2$ or $Sn_{21}O_6Cl_{16}(OH)_{14}$ compounds if they are mixed with stannic oxide. The detection limit of Mössbauer spectroscopy is commonly defined as the amount corresponding to a sub-spectrum of at least 1% of the Mössbauer spectrum area. In this case, the detection limit, at room temperature, of sulfate and chloride mixed with $SnO_2{\cdot}xH_2O$ can be evaluated to 1.5 mol%.

4 Conclusions

Three tin corrosion products have been investigated by Mössbauer spectroscopy. The Lamb–Mössbauer factors of these compounds have been determined. The obtained *f*-factor values are notably different. Consequently, the quantitative interpretation of the Mössbauer spectrum of a mixture of tin compounds must take into account this fact.

References

1. Huang, B.X., Tornatore, P., Li, Y.-S.: Electrochim. Acta **46**(5), 671 (2001)
2. Zapponi, M., Pérez, T., Ramos, C., Saragovi, C.: Hyperfine Interact. **148**, 145 (2003)
3. Muir, A.H.: Mössbauer effect and methodology. In: I. J. Gruverman (ed), vol. 4, p. 75. Plenum, New York (1968)
4. Collins, G.S., Kachnowski, T., Benczer-Koller, N., Pasternak, M.: Phys. Rev. B **19**, 1369 (1979)
5. Jouen, S., Hannoyer, B., Piana, O.: Surf. Interface Anal. **34**, 192 (2002)
6. Dunkel, S.E., Craig, J.R., Rimstidt, J.D., Lusardi, W.R.: Can. Mineral. **41**, 659 (2003)
7. Jouen, S.: Thesis, Université de Rouen, 2000
8. Shibuay, M., Endo, K., Endo, K., Sano, H.: Bull. Chem. Soc. Jpn. **51**(5), 1363 (1978)
9. Lefebvre, I., Szymanski, M.A., Olivier-Fourcade, J., Jumas, J.C.: Phys. Rev. B **58**, 1896 (1998)
10. Davies, C.G., Donaldson, J.D.: J. Chem. Soc., A 946 (1968)
11. Herber, R.H., Hazony, Y.: Techniques of Chemistry. In: Weissberger, A., Rossiter, B.W. (eds.),vol. I, p. 278ff. Wiley, New York, (1972)

Hyperfine Interact (2006) 167:819–823
DOI 10.1007/s10751-006-9364-8

Study of the electrochemical properties in substituted $Li_2Ti_3O_7$ ramsdellite

Michèle Van Thournout · Manfred Womes · Josette Olivier-Fourcade · Jean-Claude Jumas

Published online: 31 October 2006

Abstract Substituting the ramsdellite compound $Li_2Ti_3O_7$ has been considered in order to improve the structure stability and performances for its use as electrode material for Li-ion accumulators. Two substitutions have been carried out, Ti/Fe and (Ti, Li)/(Fe,Ni). The presence of ^{57}Fe as a local Mössbauer probe is interesting for studying its local environment and the electrochemical mechanisms induced by lithium insertion.

Key words lithium insertion mechanism · titanium oxides · metal substitution · ^{57}Fe Mössbauer spectroscopy

1 Introduction

Li-ion batteries are important energy storage devices, useful for high power applications such as portable power tools or hybrid vehicles. A considerable part of the work is focussed on new anodic electrodes with the aim to improve the performances and the security [1]. Since several years lithium titanates, based on the Ti^{IV}/Ti^{III} redox couple, are intensively studied as new Li^+ ion insertion materials. They have an ideal structure with vacant sites allowing lithium intercalation and a higher working potential versus lithium (1–2 V), compared to carbon anode materials, improving the security. Among these compounds, the spinel $Li_4Ti_5O_{12}$ (theoretical capacity 175 mA h g^{-1}) has already been selected for new commercialized lithium-cells. By heating the spinel compound above 1,000°C the metastable ramsdellite compound $Li_2Ti_3O_7$ is obtained. The ramsdellite structure has channels, partially filled with Li atoms according to the $(Li_{1.72}\square_{2.28})_e[Ti_{3.43}Li_{0.57}]_fO_8$

M. Van Thournout · M. Womes · J. Olivier-Fourcade · J.-C. Jumas (✉)
Laboratoire des Agrégats Moléculaires et Matériaux Inorganiques (UMR 5072), Université Montpellier II, CC015, Place Eugène Bataillon, 34095 Montpellier Cedex 5, France
e-mail: jumas@univ-montp2.fr

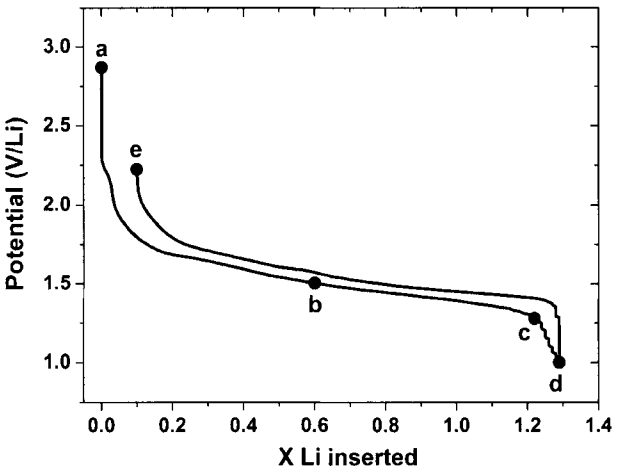

Figure 1 Discharge/charge curve of Fe/Ni-doped $Li_2Ti_3O_7$, showing the different samples *a*, *b*, *c*, *d*, *e* investigated by ^{57}Fe Mössbauer spectroscopy.

structural formula (□ = vacancies, *c*=channel, *f*=framework) [2]. The vacancies in the channels allow Li^+ ion insertion/extraction in agreement with a one-phase system:

$$(Li_{1.72\square\ 2.28})_c[Ti_{3.43}Li_{0.57}]_fO_8 + xLi \rightarrow (Li_{1.72+x})_c[Ti_{3.43}Li_{0.57}]_fO_8$$

The insertion of 2.28 Li^+ ions per formula unit corresponds to a capacity value of 198 mA h g^{-1}. However, capacity values are limited due to electrostatic repulsions between Li atoms in the structure [3]. Improved charge capacity requires thus a better Li^+ ion accessibility to the vacant sites.

To ensure better cycling performances, additional vacant sites can be created by substituting Fe^{III}/Ni^{II} on Ti^{IV}/Li framework sites [4–7]. Moreover, introducing ^{57}Fe as a local Mössbauer probe gives valuable informations concerning its local environment and makes it possible to study the electrochemical behaviour of iron in the ramsdellite structure during cycling [5, 6].

Lithium insertion in the ramsdellite compound $Li_2Ti_3O_7$ is based on the Ti^{IV}/Ti^{III} redox couple. The results of electrochemical tests of Fe doped $Li_2Ti_3O_7$ reveal a second redox reaction between 2.2 and 1.8 V characteristic for the reduction of Fe^{III} to Fe^{II}. Capacities were not improved but this composition showed an excellent cycling behaviour and was obtained at a lower synthesis temperature (<1,000°C) [4].

Aldon et al. investigated the Fe-containing $Li_2Ti_3O_7$ by ^{57}Fe Mössbauer spectroscopy. All iron atoms are located on octahedral sites with oxidation state Fe^{III}. During Li^+ insertion they observed the total Fe^{III}/Fe^{II} reduction between 2.2 and 1.8 V [5, 6].

By substituting Fe and Ni, Fe^{III}/Fe^{II} reduction is limited and improved capacities are obtained [7]. In this paper the redox process analyzed by ^{57}Fe Mössbauer spectroscopy will be discussed.

2 Experimental

The ramsdellite $Li_2Ti_3O_7$ phase is obtained by ceramic synthesis from pure oxides (Li_2CO_3 and TiO_2) in stoichiometric amounts. After a high temperature treatment (above 1,000°C) the final product is quenched in air to obtain the metastable ramsdellite phase. For the substitution of 5% Ti^{IV} by Fe^{III}/Ni^{II} with ratio 1:4, a two-step process (sol-gel and ceramic)

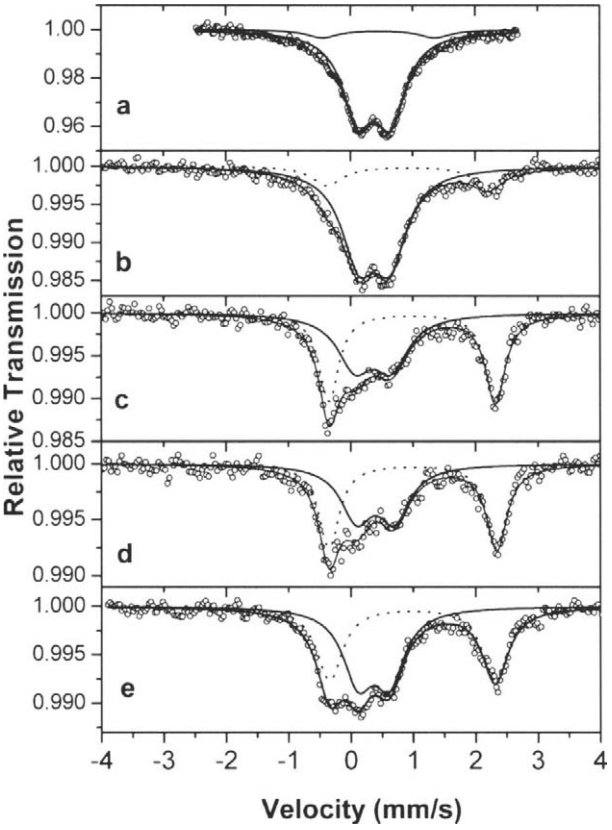

Figure 2 ^{57}Fe Mössbauer spectra of Fe/Ni-doped $Li_2Ti_3O_7$ before Li-insertion (a), after various discharge depths (b, c, d) and at Li-extraction (e).

Table I ^{57}Fe hyperfine parameters of $Li_2Ti_3O_7$/(Fe,Ni)

Sample	x	δ (mm/s)	ΔEq (mm/s)	2Γ (mm/s)	A (%)	Attribution
a	0	0.38 (1)	0.52 (1)	0.60 (1)	91	Fe^{III} octa
		0.45 (4)	1.80 (6)	0.60 (12)	9	Fe^{III} octa
b	0.6	0.38 (1)	0.50 (1)	0.66 (2)	83	Fe^{III} octa
		0.92 (3)	2.58 (4)	0.61 (6)	17	Fe^{II} tetra
c	1.2	0.36 (1)	0.59 (2)	0.67 (4)	50	Fe^{III} octa
		0.99 (1)	2.67 (1)	0.38 (1)	50	Fe^{II} tetra
d	1.3	0.37 (1)	0.59 (2)	0.63 (4)	52	Fe^{III} octa
		0.96 (1)	2.68 (1)	0.43 (2)	48	Fe^{II} tetra
e	0.1	0.36 (1)	0.50 (1)	0.59 (2)	52	Fe^{III} octa
		0.98 (1)	2.66 (1)	0.50 (2)	48	Fe^{II} tetra

x The number of lithium electrochemically inserted; δ isomer shift relative to α-Fe; ΔEq quadrupole splitting; 2Γ line width at half maximum; A contribution of subspectra to the spectrum.

was used. First the formed gel, precipitated from solutions of titanium *iso*-propoxide and iron metal powder enriched in the isotope ^{57}Fe, was calcined at 450°C resulting in (Fe)–TiO_2. The powder was then ball-milled in presence of Li_2CO_3 and NiO and treated at high temperatures (980°C).

X-ray powder diffraction (XPD) showed that the doped compounds conserve the ramsdellite structure.

Electrochemical lithiation was performed in Swagelok™ test cells with configuration: Li/$LiPF_6$ 1 M (EC:PC:3DMC)/ $Li_2Ti_3O_7$ (substituted) + carbon black + binder, assembled in an argon filled glove box. Galvanostatic discharge/charge curves were obtained using a McPile II system with cycling rates of 1 Li/10 h.

In order to study the lithium insertion mechanism, iron doped materials at several depths of discharge and charge have been analyzed by ^{57}Fe Mössbauer spectroscopy at room temperature in transmission mode using ^{57}Co in a Rh matrix as the γ-ray source. The electrochemically inserted samples were measured *ex situ* from Swagelok™ electrodes. ^{57}Fe hyperfine parameters are determined by fitting Lorentzian curves to the experimental data.

3 Results and discussion

Figure 1 shows one cycle of the electrochemical behaviour of $Li_2Ti_3O_7$: (Fe/Ni). Mössbauer spectra, shown in Figure 2, were recorded at different discharge/charge depths labelled a, b, c, d, e in Figure 1.

Before lithium insertion (Figure 2a) the isomer shift values (δ=0.38 mm/s and δ= 0.45 mm/s) of the fitted subspectra (Table I) indicate the presence of Fe^{III} on octahedral sites (full line subspectra); in agreement with a substitution mechanism Ti/Fe. The quadrupole splitting (ΔEq) is correlated with the symmetry of the charge distribution around the iron nucleus. The large values observed indicate a distortion of the octahedra. The large values of the line width at half maximum are correlated to symmetry modifications of the probed Fe atoms due to multiple environmental differences. During the first discharge one can observe a partial Fe^{III}/Fe^{II} reduction, in agreement with the occurrence of a small irreversible plateau in Figure 1. The values of the isomer shift ($0.9<\delta<1$) indicate a migration of Fe^{II} to tetrahedral channel sites (dot line subspectra). This phenomenon was previously observed in thiospinels where Fe^{II} migrates from octahedral 16d sites to tetrahedral 8a sites [8]. At the end of the discharge half of the iron atoms are reduced and their location within the channels forms pillars to the structure, which avoid volume changes during lithium insertion/extraction. No iron oxidation occurs upon lithium extraction (point e).

4 Conclusion

The (Ti, Li)/(Fe,Ni) substitution in $Li_2Ti_3O_7$ facilitates the synthesis, improves the structure stability and the electrochemical cyclability. The investigation of the redox process by Mössbauer spectroscopy reveals changes of the cation distribution during lithium insertion/ extraction by migration of Fe from octahedral to tetrahedral sites.

Acknowledgements The authors are grateful to SAFT (France) and UMICORE (Belgium) for financial support, under contract CNRS-UMII-SAFT-UMICORE no. 752964/00.

References

1. 3rd Lithium Battery Discussions, LiBD-3, Arachon, France, May 22–27 2005
2. Morosin, B., Mikkelsen, J.C.: Acta Crystallogr. **B35**, 798–800 (1979)
3. Garnier, S., Bohnke, C., Bohnke, O., Fourquet, J.L.: Solid State Ionics **83**, 323–332 (1996)

4. Ma, S., Noguchi, H.: Electrochemistry **69**(7), 526–529 (2001)
5. Aldon, L., Kubiak, P., Picard, A., Lippens, P.E., Olivier-Fourcade, J., Jumas, J.-C.: Hyperfine Interact. **156/157**, 497–503 (2004)
6. Aldon, L., Van Thournout, M., Strobel, P., Isnard, O., Olivier-Fourcade, J., Jumas, J.-C.: Solid State Ionics. **177**, 1185–1191 (2006)
7. Van Thournout, M., Picard, A., Womes, M., Olivier-Fourcade, J., Jumas, J.-C.: J. Phys. Chem. Solids. **67**, 1355–1358 (2006)
8. Branci, C., Sarradin, J., Olivier-Fourcade, J., Jumas, J.-C.: J. Power Sources **81–82**, 282–285 (1999)

Hyperfine Interact (2006) 167:825–831
DOI 10.1007/s10751-006-9365-7

A Mössbauer spectroscopic study of an industrial catalyst for dehydrogenation of etylbenzene to styrene

K. Y. Jiang · Q. Fan · Z. J. Zhao · L. S. Mao · X. L. Yang

Published online: 16 November 2006

Abstract Iron oxide catalyst with spinel structure used for dehydrogenation of ethylbenzene is one kind of important catalyst in petrochemical industry. In this work several series of industrial catalyst were prepared with different components and different manufacturing processes. Mössbauer Spectroscopy has been used to determine the optimal components and the better manufacturing process for spinel structure formation. The results may prove useful for producing the industrial dehydrogenation catalyst with better catalytic property.

Key words Mössbauer spectroscopy · iron oxide catalyst · dehydrogenation

1 Introduction

Styrene, which is widely used as a starting material of synthetic rubber and resins, is an important product in petrochemical industry. At present, most commercial styrene in the world is produced by ethylbenzene dehydrogenation using potassium-promoted iron oxide catalysts [1–3]. The GS series of potassium-promoted iron oxide catalyst produced by Shanghai Research Institute of Petrochemical Technology exhibit higher selectivity and higher catalytic activity. The maximum selectivity is about 95% and the maximum conversion is about 77%. We have found that when the catalysts are prepared, different components, their content, especially the content of K [4], and different manufacturing process will effect to the properties of catalysts. In this work, the content of the components (various oxides and cohesive agent) of catalyst or manufacturing process were changed to prepare seven new catalysts.

K. Y. Jiang (✉) · Z. J. Zhao · X. L. Yang
Department of Physics, East China Normal University, Shanghai 200062, China
e-mail: keyujiang@yahoo.com

Q. Fan · L. S. Mao
Shanghai Research Institute of Petrochemical Technology, Shanghai 201800, China

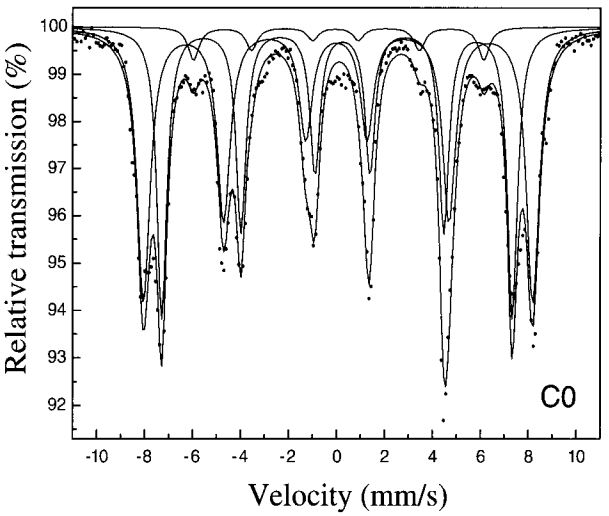

Figure 1 Mössbauer spectrum of sample C0.

Table I Mössbauer parameters (the magnetic hyperfine field H is in Tesla and the area of sub-spectra S is in percent)

Sample number	Fe_2O_3		$KFe_{11}O_{17}(1)$		$KFe_{11}O_{17}(2)$		$KFe_{11}O_{17}(3)$	
	H (T)	S (%)	H (T)	S (%)	H (T)	S (%)	H (T)	S (%)
C0			48.5(2)	55(2)	43.6(5)	42(2)	36.7(12)	3(1)
C190	51.5(2)	85(2)			44.8(25)	15(2)		
C280	51.7(2)	47(1)	47.1(3)	26(3)	42.1(20)	27(2)		
C290	51.8(2)	30(1)	47.7(6)	38(2)	42.7(9)	32(2)		
C380	51.7(2)	36(1)	47.2(11)	30(2)	42.0(18)	34(2)		
C390	51.7(4)	17(1)	47.8(7)	46(3)	42.7(9)	33(2)		
C478	51.7(1)	68(1)			44.2(15)	32(2)		
C482	51.9(5)	12(1)	48.0(6)	44(2)	43.9(7)	22(2)	39.8(15)	22(2)
C486			48.1(6)	62(3)	43.5(10)	21(2)	40.3(19)	17(2)
C490			48.0(5)	60(2)	43.5(7)	22(2)	40.3(13)	18(2)
C578	51.7(3)	15(1)	47.5(2)	47(2)	43.1(1)	19(1)	39.1(12)	19(1)
C580	51.6(5)	9(1)	47.6(5)	47(2)	43.3(7)	22(2)	39.6(14)	22(2)
C582			47.9(7)	63(3)	43.2(8)	20(2)	39.5(15)	17(2)
C586			47.7(6)	62(2)	43.1(7)	20(2)	39.6(12)	20(2)
C590			47.9(4)	56(2)	43.4(6)	22(2)	40.1(13)	22(2)
C680	51.7(4)	9(1)	47.7(5)	50(2)	43.3(6)	20(2)	39.5(12)	21(2)
C682			47.8(5)	57(2)	43.2(7)	22(2)	39.6(13)	21(2)
C690			47.9(4)	55(2)	43.4(6)	23(2)	40.1(12)	22(2)
C778			47.9(8)	62(2)	43.2(12)	22(3)	39.2(19)	16(2)
C780			47.9(6)	58(2)	43.3(9)	21(2)	39.7(18)	21(2)
C790			47.8(8)	53(2)	43.6(12)	30(3)	39.8(17)	17(2)

In our previous investigation using Mössbauer Spectroscopy, it was determined that the fresh catalysts of potassium-promoted iron oxide contain a certain amount of potassium ferrite $KFe_{11}O_{17}$ [5] with the spinel structure, which can be considered as the predecessor of the catalytic active phase. It is also mentioned in patents [6, 7]. In this work, Mössbauer spectroscopy was used to study the components of the products, especially to study the dependence between the formation of the Fe–K spinel structure and the new components or

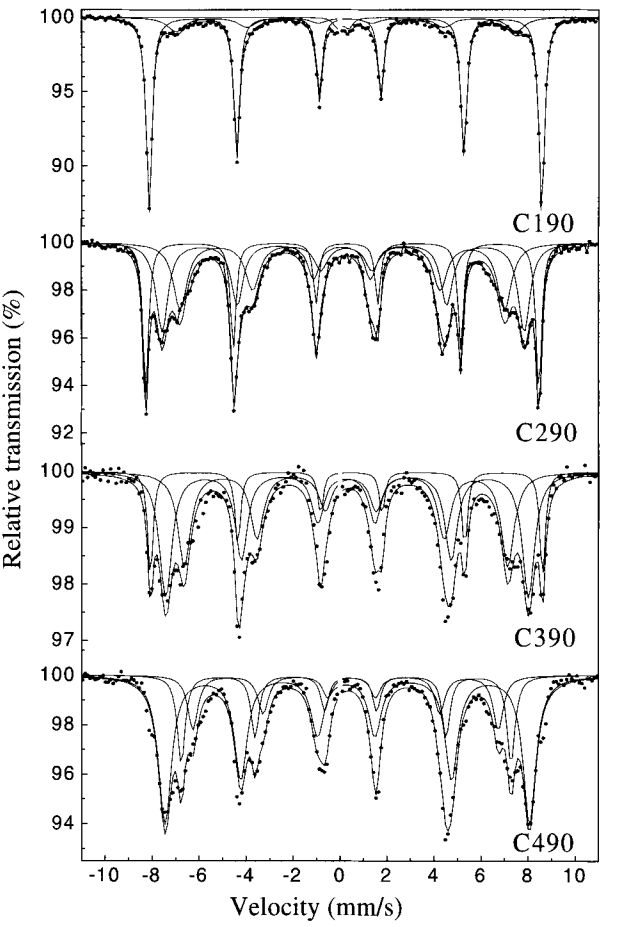

Figure 2 Mössbauer spectra of samples C190, C290, C390, C490.

the new manufacturing process. Combining the Mössbauer spectroscopic results and a catalytic property of samples, the optimal components and the better manufacturing process could be determined.

The main composition of the industrial catalyst is ferric oxide (α-Fe_2O_3) and an important promoter, potassium carbonate (K_2CO_3). Other oxides, such as magnesium oxide [5], cerium oxide [8], molybdenum oxide and some trace elements are also contained in the catalyst [9]. The cohesive agent (such as cement) is added for shaping catalyst. All raw materials are mixed together and shaped up, then calcined under a certain temperature.

In our first stage of research work, the catalyst with only two components, α-Fe_2O_3 and K_2CO_3 (without any other oxides), were studied and a sample C0 with lower content of K was selected [4]. Now the real industrial catalysts C1–C7 were investigated.

2 Experimental

All other components of industrial catalyst (except α-Fe_2O_3 and K_2CO_3) were added into C0 becoming samples C1–C7, in which the content of one of different components was changed in C1–C5, respectively (the detail does not mentioned for commercial secret). And C5 plus a part of another cohesive agent becomes C6. Another manufacturing process was

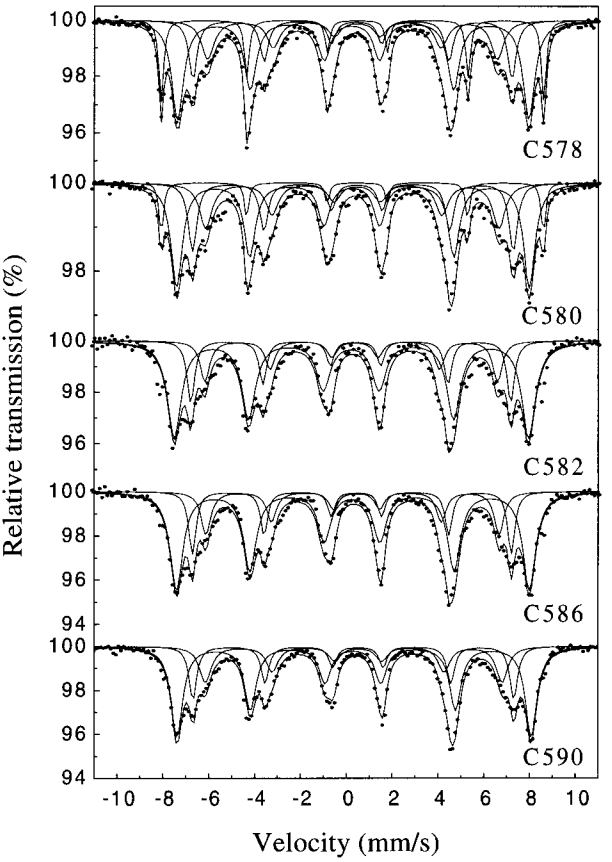

Figure 3 Mössbauer spectra of C5 series.

used in C5 for producing sample C7. Each sample was calcined for 4 h at seven temperatures from 780 to 900°C with increment of 20°C. Therefore, seven single samples became seven series of samples, respectively. Combining the sample number C1–C7 and the first two figures of its calcining temperature, the new sample numbers were named. For example, sample C280 means sample C2 calcined at 800°C and so on.

^{57}Fe Mössbauer spectra were recorded at room temperature using a constant acceleration spectrometer with a 9.2×10^{8} Bq ^{57}Co(Pd) source in transmission geometry. Spectral parameters were obtained from computer fitting and the isomer shift was calculated with respect to a α-Fe foil of 25 μm thick.

An isothermal stainless steel reactor with 2.5 cm inner diameter was used for measuring the catalytic selectivity in laboratory. Amount 100 ml of catalyst was placed in the reactor. Catalyst reacted under the following conditions: temperature 620°C, atmosphere pressure, liquid hourly space velocity (LHSV) 1.0 h^{-1} and steam to ethylbenzene ratio by weight 2:1. The reactive products were analyzed by gas spectrograph.

3 Results and discussion

Figure 1 shows the Mössbauer spectrum of sample C0, which consists with three sub-spectra of $KFe_{11}O_{17}$. In the lattice of the stoichiometric $KFe_{11}O_{17}$, there are four crystallographially identifiable Fe sites, namely, two octahedral sites (12k and 2a) and

Table II half-width of Mössbauer spectra and catalytic selectivity of three samples

Sample	Half-width of spinel peaks (mm/s)			Selectivity (%)
	Sub-spectrum1	Sub-spectrum 2	Sub-spectrum 3	
C5	0.30	0.22	0.33	91.27
C6	0.32	0.21	0.33	92.68
C7	0.35	0.22	0.35	94.78

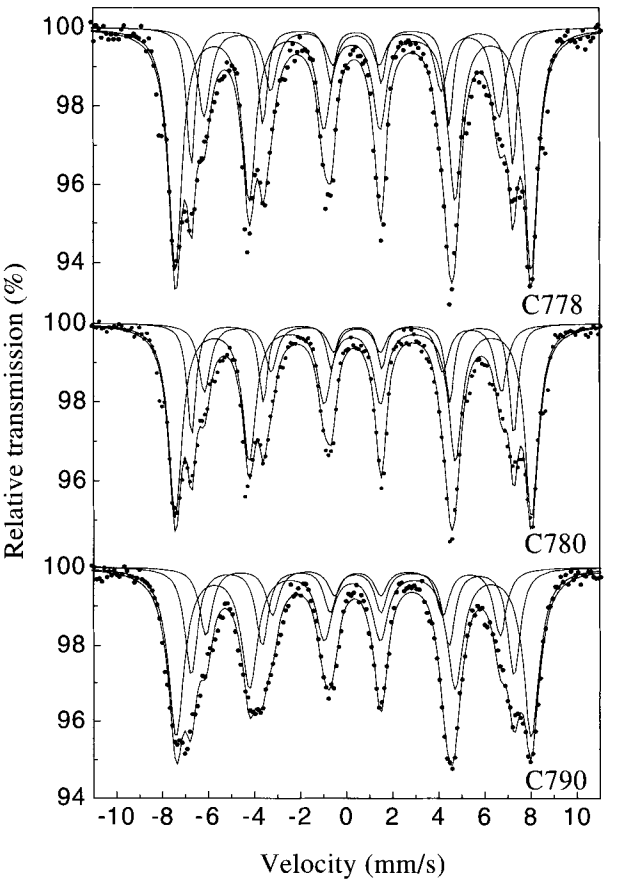

Figure 4 Mössbauer spectra of C7 series.

two tetrahedral sites [10–12]. Our Mössbauer spectrum of this potassium ferrite was analyzed with three sub-spectra: H_1=47.1–48.5 T for the contribution of Fe^{3+} on both tetrahedral sites and H_2=42.0–44.8 T for that from the octahedral sites 12 k. There exists the third sub-spectra H_3=36.7–40.3 T in spectra of most samples. It is considered as the contribution of Fe^{3+} on those octahedral sites with imperfect crystal lattice [4].

The Mössbauer parameters of all samples are shown in Table I. The Mössbauer spectra of C1–C4 calcined at the same temperature of 900°C are shown in Figure 2. The results show that the formation of $KFe_{11}O_{17}$ can be changed due to different content of components. For C1 series, the main spectrum is one sextet with $H \approx 52$ T, which is characteristic of α-Fe_2O_3 with its area percentage 85%. For C2 and C3 series, α-Fe_2O_3 remains 30 and 17%, respectively. It means that α-Fe_2O_3 does not completely change to the

predecessor of the catalytic active phase $KFe_{11}O_{17}$. For C4 series, iron compound is only $KFe_{11}O_{17}$ at 900°C. In fact, the formation of $KFe_{11}O_{17}$ will be effected by different calcining temperature, too. The lowest calcining temperature for C4 is 860°C, at which all α-Fe_2O_3 already react to K_2CO_3 and become $KFe_{11}O_{17}$.

Figure 3 shows five sets of spectra for samples C5 series calcined at different temperature, respectively. From the view of saving energy we want to find the lowest (critical) calcining temperature. The spectra of both C578 and C580 consist of three sub-spectra of $KFe_{11}O_{17}$ and one sextet of α-Fe_2O_3. The content of $KFe_{11}O_{17}$ increases with the raising of the calcining temperature. Iron compound is only $KFe_{11}O_{17}$ when the calcining temperature is equal and above 820°C. So the lowest calcining temperature of 820°C was selected as its critical calcining temperature, which is lower about 40°C than that of C4.

A part of new cohesive agent was used in sample C6. We want know whether agent can also effect to the formation of $KFe_{11}O_{17}$ except oxides components. Its magnetic hyperfine field H of $KFe_{11}O_{17}$ are very similar to C5 series, there only is $KFe_{11}O_{17}$ at equal and above 820°C. It means that changing the agent has little effect to H of $KFe_{11}O_{17}$, but we will compare their half-width of $KFe_{11}O_{17}$ and catalytic selectivity later.

The formation of $KFe_{11}O_{17}$ will also be effected by different manufacturing process. The traditional manufacturing process was superseded by a new manufacturing process, which was expected to improve the catalytic properties in sample C7. The Mössbauer spectra for samples of C7 series calcined at different temperature are shown in Figure 4, respectively. All spectra consist with three sub-spectra of $KFe_{11}O_{17}$ and there is no α-Fe_2O_3 at any choice calcining temperatures. It means that the catalyst can be calcined at lower temperature (780°C) relative to the catalysts C5 and C6.

Now three relative better samples of C5, C6 and C7 have been selected preliminary from the view of formation of $KFe_{11}O_{17}$.

Generally, the line width of Mössbauer spectrum of $KFe_{11}O_{17}$ in catalyst will be noticeably broadened due to Fe ions are substituted by the nearby randomly distributed potassium or other non-magnetic ions. It is found that the broader the width of peaks is, the more disperse the active phase of catalyst, which enhances the selectivity of the catalyst [5]. For samples of C5, C6, C7, their half-width of Mössbauer spectrum and the selectivity are listed in Table II. We can see that the selectivity increases with the increasing of average half-width of the sub-spectra.

In conclusion, above results prove that selecting suitable content of the components (C5), adding a part of another cohesive agent (C6) and using new manufacturing process (C7) are effective to improve catalyst properties and Mössbauer Spectroscopy is a quite useful approach for studying industrial dehydrogenation catalyst with spinel structure.

Acknowledgments This work was supported by Shanghai Rising Star program (04QMX1422) and the Emphasis Project of Shanghai Nano-technology Promotion Center (no.: 0452nm055).

References

1. Lee, E.H.: Catal. Rev. **8**(2), 285–305 (1973)
2. Hirano, T.: Appl. Catal. **26**, 65–79 (1986)
3. Yang, X.L., Weng, S.H., Jiang, K.Y., Mao, L.S., Euang, Y.T., Jing, K.: Hyperfine Interact. **69**, 863–866 (1991)
4. Jiang, K.Y., Yang, X.L., Yuan, Y.T., Mao, L.S., Yang, D.P.: Hyperfine Interact. **139/140**, 97–105 (2002)
5. Jiang, K.Y., Yang, J.X., Hu, B.Y., Yang, X.L., Mao, L.S., Yuan, Y.T., Zhang, G.L.: Hyperfine Interact. **111**, 45–49 (1998)

6. Watson, J.M., Crabbe, D.: Conrsen: JR.T.S. US Patent 4,963,343, 16 Oct 1990
7. Watson, J.M., Crabbe, D.: Conrsen: JR.T. S. US Patent 4,975,267, 4 Dec 1990
8. Hu, B.Y., Zeng, Z., Yang, X.L., Mao, L.S., Euang, Y.T.: Nucl. Instrum. Methods Phys. Res. **B76**, 178–179 (1993)
9. Hirano, T.: Bull. Chem. Soc. Jpn. **59**, 1653–1655 (1986)
10. Romanov, V.P., Candela, G.A., Roth, R.S., Swartzendruber, L.J.: J. Appl. Phys. **50**, 6455–6458 (1979)
11. Howe, A.T., Dudley, G.J.: J. Solid State Chem. **18**. 149–153 (1976)
12. Howe, A.T., Dudley, G.J.: J. Solid State Chem. **30**, 157–170 (1979)

Hyperfine Interact (2006) 167:833–838
DOI 10.1007/s10751-006-9368-4

Generation of long-lived isomeric states via bremsstrahlung irradiation

Yao Cheng · Bing Xia · Chuanxiang Tang · Yinong Liu · Qingxiu Jin

Published online: 7 December 2006

Abstract A method to generate long-lived isomeric states effectively for Mössbauer applications is reported. We demonstrate that this method is better and easier to provide highly sensitive Mössbauer effect of long-lived isomers (>1 ms) such as ^{103}Rh. Excitation of (γ,γ) process by synchrotron radiation is painful due mainly to their limited linewidth. Instead, (γ,γ') process of bremsstrahlung excitation is applied to create these long-lived isomers. Isomers of ^{45}Sc, ^{107}Ag, ^{109}Ag, and ^{103}Rh have been generated from this method. Among them, ^{103}Rh is the only one that we have obtained the gravitational effect at room temperature.

Key words long-lived Mössbauer effect · bremsstrahlung excitation

1 Introduction

We report the experimental observation of effective generation of Mössbauer emission by bremsstrahlung excitation and its particular Mössbauer effect. Since Mössbauer discovered the recoilless photon emitted from nuclei in 1958 [1], over a hundred isotopes have been investigated mainly using radioactive decay. Among them, ^{67}Zn has been considered to be one of the most sensitive isotopes producing the Mössbauer effect [2]. The natural linewidth Γ_0 is defined by the lifetime τ_0 according to the principle of uncertainty as:

$$\Gamma_0 = \frac{\hbar}{\tau_0} \tag{1}$$

Y. Cheng (✉) · B. Xia · C. Tang · Y. Liu · Q. Jin
Department of Engineering Physics, Tsinghua University, Beijing, China
e-mail: yao@tsinghua.edu.cn

Y. Cheng
Key Laboratory of Atomic and Molecular Nanosciences, Tsinghua University, Beijing, China

Table I The features of the isomeric states of four isotopes

Isotope	E_γ(keV)	Γ_0(eV)	$t_{1/2}$(s)	a(%)	Estimated f (%) recoilless factor			α
					300 K	77 K	0 K	
^{45}Sc	12.4	1.43×10^{-15}	0.318	100	77	90	93	400
^{107}Ag	93.1	1.03×10^{-17}	44.3	51.4	1×10^{-5}	0.1	4	20
^{109}Ag	88.0	1.15×10^{-17}	39.6	48.6	8×10^{-5}	0.4	6	20
^{103}Rh	39.8	1.35×10^{-19}	3,366	100	45	70	74	1,350

E_γ Mössbauer transition energy, Γ_0 energy linewidth of the Mössbauer level, $t_{1/2}$ half life of the Mössbauer level, a nature abundance, f the Lamb-Mössbauer factor, α internal conversion coefficient

We describe total linewidth Γ including broadening Γ_b of the natural linewidth as

$$\Gamma = \Gamma_0 + \Gamma_b, \tag{2}$$

which is assumed due to various impacts affecting the nuclear state. Γ of ^{67}Zn approached an ultra-fine level of 75 peV corresponding to a Q-value of 10^{15} to these 93 keV Mössbauer quanta [2]. Here the Q-value is

$$Q = \frac{E_\gamma}{\Gamma} \tag{3}$$

with corresponding gamma energy of E_γ. We arrange the stable Mössbauer isotopes in a sequence according to their Γ_0 as resolution from low to high, i.e., ^{73}Ge, ^{181}Ta, ^{67}Zn, ^{45}Sc, ^{109}Ag, ^{107}Ag, and ^{103}Rh. The sequence remains the same by arranging them in terms of Q-value as sensitivity. The last four isotopes have isomeric lifetimes of the first excited states longer than millisecond. ^{103}Rh studied in this report has Γ_0 of 0.1 aeV and E_γ of 39.8 keV that correspond to a Q-value in the order of 10^{24}.

2 Mössbauer spectroscopy with higher resolution

Higher sensitivity of Mössbauer effect beyond ^{67}Zn is to be achieved by exploring the isomeric transition listed above, but almost no Mössbauer experiment applying these transitions have been carried out successfully. The dilemma predicament is twofold, i.e., poor sample features and poor experimental methodology. No reliable Mössbauer source is available to extend the experimental methodology from present limitations to further possibilities.

The low-lying isomeric state of ^{45}Sc was discovered in 1964 [3]. It aroused interest worldwide because of its potential high Lamb-Mössbauer factor and high sensitivity. Although ^{45}Sc is superior to ^{67}Zn in many aspects, it was never successfully applied due to many problems, i.e., poor efficiency of generating Mössbauer photon from β decay, inner bremsstrahlung induced from β decay, and high internal conversion coefficient [3]. By choosing isotopes for experiments, the measurement sensitivity and the ease of measuring process are two issues of particular concern. In this work, we report a method that successfully addresses these two issues. As considered at the beginning of this study, the sensitivity increase is meaningless, if new methodologies have not been developed. ^{45}Sc shall be the first choice for us. However, our ^{45}Sc excitation was successful several times but not repeatable. In the course of this study, we have recently found out the highly

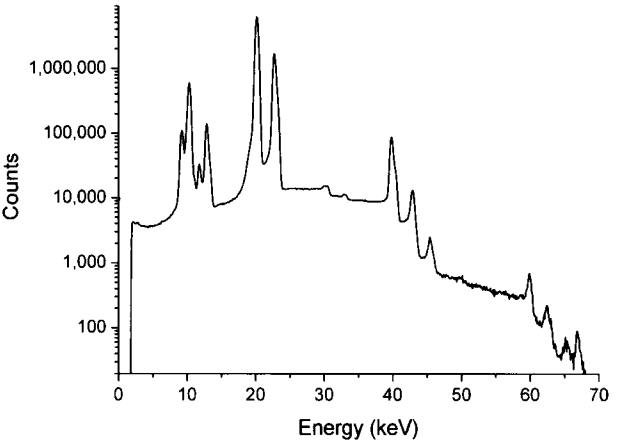

Figure 1 Measured spectrum of the emissions from ^{103}Rh isomers excited by bremsstrahlung irradiation from a 6 MeV linac for 120 min. The pile-up rejection system is off.

speed-up decay of ^{45}Sc is probably due to the entangled Mössbauer emission. This report concentrates on the excitation of ^{103}Rh.

The characteristics of interested long-lived isomers used in this work are listed in the Table I. They have smaller Γ_0 than feV. We first noticed that the experimental condition was extremely tough for such a narrow linewidth. For example, it is difficult to perform the measurement with the corresponding Doppler-scan. The gravitational redshift significantly comes into play. Consequently, new measurement concepts are to be developed for this ultimate sensitivity. It seems that many extreme conditions such as vibration, homogeneity, and temperature etc. are necessary to preserve the natural linewidth. However, our observation on gravitational effect of ^{103}Rh at room temperature leads us to think that many of these obstacles are not insuperable, which opens up new paths for Mössbauer spectroscopy. Generating such Mössbauer photon emission is just the beginning of the story. A good and easy-to-operate source becomes the major step for our future study.

3 Excitation by bremsstrahlung

A direct excitation with synchrotron radiation (SR) to generate Mössbauer photons with (γ,γ) process was suggested by Ruby in 1974 [4]. Ten years later, the excitation of ^{57}Fe was carried out at the DORIS ring [5] and later became the well-known nuclear resonant scattering. Leupold et al. summarized the experimental results for many isotopes other than iron studied at the third generation synchrotrons such as ESRF, APS, and Spring 8 [6]. The most sensitive sample of their studies was ^{181}Ta which was reported with less Γ comparing to the radioactive samples prepared by ion bombardment. This observation is extremely important for the long-lived isomers; otherwise their natural linewidths would no longer contribute to the sensitivity. In any case, to increase the number of the photons in the excitation band is the baseline of an accurate measurement, but this flux increase is limited by Γ_0.

Ruby considered isotopes with Γ_0 ranging from 10^{-7} to 10^{-9}eV [4]. The long-lived isomers mentioned in the last paragraph have much smaller Γ_0. Is there any other effective method to achieve isomeric excitation? Coulomb excitation [7], (γ,γ') of the bremsstrahlung excitation [8-11], (γ,γ') of the photo-activation [12], and (n,γ) of the neutron

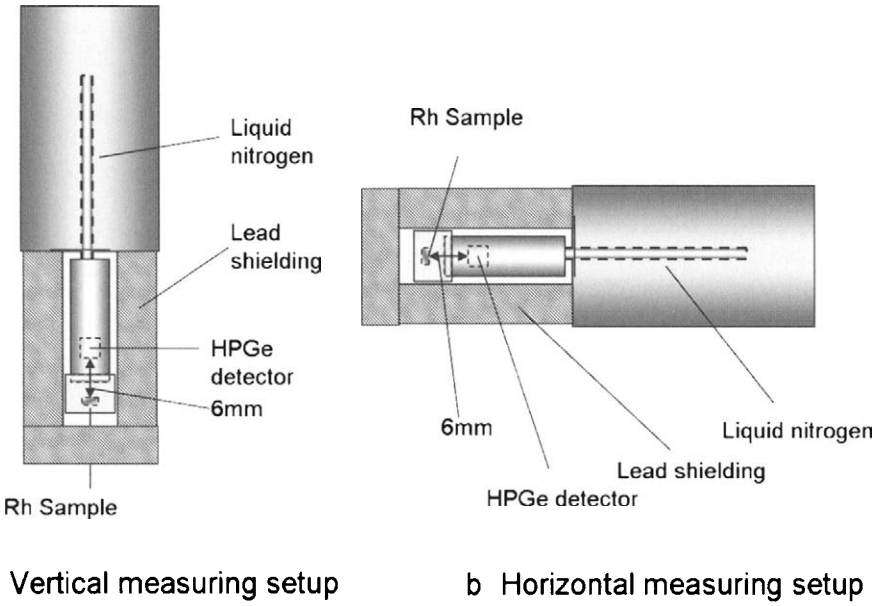

Figure 2 **a** *Vertical* measuring setup. **b** *Horizontal* measuring setup. Configurations of rhodium sample and detector in the experiment of time-resolved spectroscopy. Setup **b** was directed in the E–W direction.

excitation [13] are possible methods. Neutron excitation has the complication of generating radioactive isotope [13]. Two methods of (γ,γ') are considered to be more suitable for our application, since coulomb excitation generates more heat in samples. It is noted that ^{107}Ag [8-10, 12], ^{109}Ag [8, 10, 12], ^{103}Rh [11-13] created by (γ,γ') and (n,γ) have been reported, but not within the realm of the Mössbauer effect. ^{45}Sc has been observed only by nuclear decay. An issue of whether these four isotopes might exhibit Mössbauer effect was next raised. A recent observation of gravitational redshift using ^{109}Ag prepared from radioactive decay of ^{109}Cd [14] provides positive encouragement. Alpatov et al. applied an experimental arrangement developed from the experience of decades of research. Surprisingly, their reported Γ was only with the factor of 1~3 larger than Γ_0 [14]. We have understood the reason to obtain such a small broadening during the progress of this study, recently.

4 Experiment and results

We have carried out the isomeric excitation of ^{45}Sc, ^{107}Ag, ^{109}Ag, and ^{103}Rh using a 6 MeV standing-wave linac as the bremsstrahlung source [15]. The silver sample is a 999-purity ϕ-5 cm coin of 3 mm in thickness and its natural abundance data are shown in Table I. The scandium and rhodium samples (99.9% purity) purchased from Goodfellow are 0.1 mm-thick (1 mm-thick) and have a 2.5×2.5 cm^2 area. The irradiation time on ^{103}Rh was 120 min for the particular excitation illustrated in Figure 1. Three main emissions, i.e. 39.8, 20, and 23 keV are identified to be the E3 isomeric transition and its associated internal conversions. Figure 1 shows all of the possible pile-ups with the pile-up rejection system

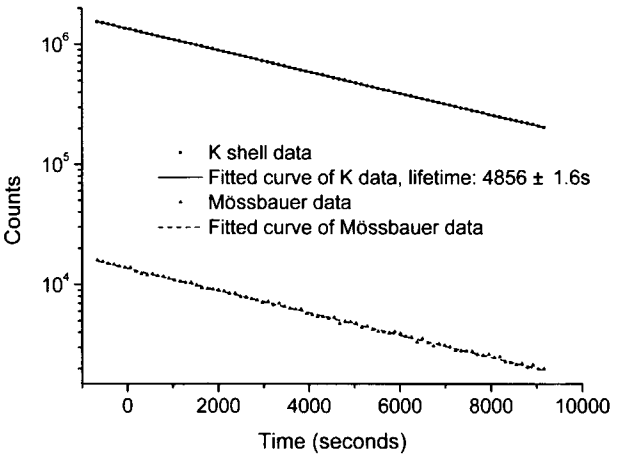

Figure 3 K-shell and Mössbauer emissions measured in periods of 2 min. The detector was rotated from Figure 2b to a at time zero. Mössbauer photon presents a speed-up decay.

purposefully turned off. Two unknown peaks around 66 keV are systematic [18]. The other two escape peaks of 10 and 13 keV are the features of our CANBERRA HPGe detector. Energy, pile-up time, dead time and the other system parameters are calibrated against ^{109}Cd source.

5 Gravitational impact

^{103}Rh is chosen for our experiment of gravitational redshift due to its reasonable Lamb-Mössbauer factor at room temperature [15]. Here, we want to point out that the reported second order Doppler effect shall inhibit the resonant absorption [16]. Nevertheless, the Lamb-Mössbauer factor of rhodium at room temperature still exists from this extraordinary observation. The HPGe detector of CANBERRA BE3830 mounted on an in situ object counting system is selected for our purpose, since it performs the freedom of setting any measurement angle corresponding to gravity (Figure 2).

Figure 3 illustrates the measured K-shell X-rays and Mössbauer photons [15]. Data were accumulated every 2 min. The measured K X-rays in Figure 3 behave as a nice exponential curve without significant dynamics. The fitted lifetime is 4,856 s (Canberra DSP MCA, Inspector-2000, trapezoid shaping with 5.6/0.8μs as rise/flat-top time), almost the same as the tabled one [17]. However, Mössbauer photons decay faster (4712 ± 22 s). Speed-up decay of Mössbauer photons was found in series of experiment [15], by promptly rotating the detector from Figure 2b to Figure 2a. This enhanced decay is a function of excitation density as well as configuration corresponding to gravitation [15]. The anisotropic internal conversion rate demonstrates the anisotropic emission in two positions as shown in Figure 2. Through detail examination of the pile-up peaks in Figure 1, we found that the triple pile-up does not obey the statistic rule of photons [18]. Most of the observations including gravitational effect in the previous report [15] are related to this particular mechanism. The in-depth report on this new phenomenon is detailed in [18].

Acknowledgements We thank Qiong Su and Jianping Cheng for the HPGe detector. Yao Cheng thanks Dr. Yaw-Wen Yang at NSRRC Taiwan for his carefully proofreading and Dr. Hognfei Wang at institute of Chemistry, Chinese Academy of Sciences for his intuitive advices. Yao Cheng thanks Professor Yuzheng Lin and his accelerator team in our department, for many efforts and his encouragement to study the reported issues. Yao Cheng thanks U. Van Bürck for fruitful discussions.

References

1. Mössbauer, R.L.: Z. Phys. **151**, 124 (1958)
2. Katila, T., Riski, K.J.: Phys. Lett. **83A**, 51 (1981)
3. Yntema, J.L., Satchler, G.R.: Phys. Rev. **134**, B976 (1964)
4. Ruby, S.L.: J. Phys. (Paris). **35-C6**, 209 (1974)
5. Gerdau, E., Rüffer, R., Winkler, H., Tolksdorf, W., Klages, C.P., Hannon, J.P.: Phys. Rev. Lett. **54**, 835 (1985)
6. Leupold, O., Chumakov, A.I., Alp, E.E., Sturhahn, W., Baron, A.Q.R.: Hyperfine Interact. **123**, 611 (1999)
7. Alder, K., Bohr, A., Huus, T., Mottelson, B., Winther, A.: Rev. Mod. Phys. **28**, 432 (1956)
8. Wolicki, E.J., Waldman, B., Miller, W.C.: Phys. Rev. **82**, 486 (1951)
9. Benwell, R.M., Mathieson, E.: Proc. Phys. Soc. **82**, 803 (1963)
10. Tonchev, A.P., Harmon, J.F., Brey, R.: Nucl. Instrum. Methods Phys. Res., Sect. A, Accel. Spectrom. Detect. Assoc. Equip. **422**, 926 (1999)
11. Sáfár, J., Kaji, H., Yoshihara, K.: Phys. Rev., C Nucl. Phys. **44**, 1086 (1991)
12. Yoshida, E., Kobayashi, T., Kojima, Y., Shizuma, K.: Nucl. Instrum. Methods Phys. Res., Sect. A, Accel. Spectrom. Detect. Assoc. Equip. **449**, 217 (2000)
13. Alpatov, V.G., Bayukov, Yu.D., Davydov, A.V., Isaev, Yu.N., Kartashov, G.R., Korotkov, M.M., Samoylov, V.M.: JETP Lett. **78**, 611 (2003)
14. Alpatov, V.G., Bayukov, Yu.D., Gelis, V.M., Davydov, A.V., Isaev, Yu.N., Kartashov, G.R., Korotkov, M.M., Milyutin, V.V., Samoylov, V.M.: Laser Phys. **10**, 952 (2000)
15. Cheng, Y., Xia, B., Liu, Y.-N., Jin, Q.-X.: Chin. Phys. Lett. **22**, 2530 (2005)
16. Pound, R.V., Rebka, G.A.: Phys. Rev. Lett. **4**, 274 (1960)
17. Firestone, R.B. (ed.): Table of Isotopes, 8. edn. Wiley, New York (1999)
18. Cheng, Y., Xia, B., Li, J.: Chin. Phys. Lett. **23**, 826 (2006); **23**, 2348 (2006) [erratum]

Hyperfine Interact (2006) 167:839–844
DOI 10.1007/s10751-006-9369-3

Magnetic and thermal Mössbauer effect scans: a new approach

G. A. Pasquevich · P. Mendoza Zélis · F. H. Sánchez · M. B. Fernández van Raap · A. Veiga · N. Martínez

Published online: 8 November 2006

Abstract Mössbauer transmission recorded at fixed photon energies as a function of a given physical parameter such as temperature, external field, etc. (Mössbauer scan), is being developed as a useful quantitative tool, complementary of Mössbauer spectroscopy. Scans are performed at selected energies, suitable for the observation of a given physical property or process. It is shown that one of main advantages of this approach is the higher speed at which the external physical parameter can be swept, which allows the recording of quasi-continuous experimental response functions as well as the study of processes which occur too fast to be followed by Mössbauer spectroscopy. The applications presented here are the determination of the temperature dependence of the ^{57}Fe hyperfine field in $FeSn_2$, the thermal evolution and nanocrystallization kinetics of amorphous $Fe_{73.5}Si_{13.5}Cu_1Nb_3B_9$ and

G. A. Pasquevich · P. Mendoza Zélis · F. H. Sánchez (✉) · M. B. Fernández van Raap · A. Veiga · N. Martínez
Dep. Física, FCE. Universidad Nacional de La Plata, 49 y 115, CC 67, 1900, La Plata, Argentina
e-mail: sanchez@fisica.unlp.edu.ar

G. A. Pasquevich
e-mail: gpasquev@fisica.unlp.edu.ar

P. Mendoza Zélis
e-mail: pmendoza@fisica.unlp.edu.ar

M. B. Fernández van Raap
e-mail: raap@fisica.unlp.edu.ar

A. Veiga
e-mail: veiga@fisica.unlp.edu.ar

N. Martínez
e-mail: nmartinez@fisica.unlp.edu.ar

G. A. Pasquevich · P. Mendoza Zélis · F. H. Sánchez · M. B. Fernández van Raap
IFLP, CONICET, La Plata, Argentina

N. Martínez
CICpBA, La Plata, Argentina

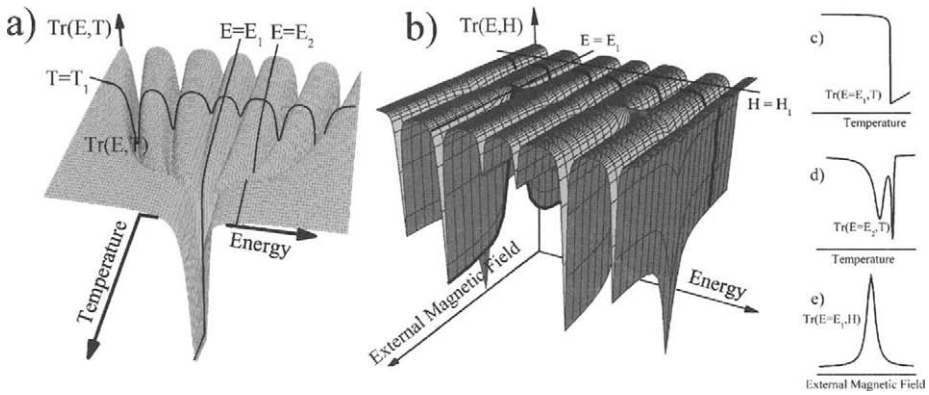

Figure 1 Gamma-ray transmission surface Tr(E, x) for $x = T$ (a) and $x = H$ (b). Intersects with planes E_C = const. correspond to scans (c, d, e). In the two simulated examples, Tr(E_C, x) reflects the hyperfine field-temperature dependence, and the evolution of the average hyperfine field orientation with the intensity of the applied field, respectively.

the measurement of the dynamic response of Fe magnetic moments in nanocrystalline $Fe_{90}Zr_7B_3$ to an external *ac* field.

Key words Mössbauer effect · scans · phase transitions · magnetic response

1 Introduction

Soon after the discovery of the Mössbauer effect, thermal scans performed at a fixed Doppler energy (usually zero energy) were explored in order to rapidly obtain information on magnetic ordering and other characteristic temperatures [1–4]. Nonetheless, to our knowledge, no attempts to formalize this methodology as a fully quantitative analytical tool were carried out until recently [5]. Here, we present experiments which were chosen to demonstrate the usefulness of Mössbauer scans, when they are performed at especially selected photon energies and appropriately combined with Mössbauer spectroscopy. They include the studies of the temperature dependence of the Fe hyperfine magnetic fields in $FeSn_2$ and Fe_3Si, of the thermal evolution and the kinetics of nano-crystallization in an amorphous *Finemet*®-precursor alloy, and of the magnetic dynamics in $Fe_{90}Zr_7B_3$ nanocrystalline alloys. In all cases ^{57}Fe 14.4 keV gamma-rays from a ^{57}Co*Rh* source were used.

A common problem in Mössbauer research is the study of resonant gamma ray transmission spectra as a function of temperature T, intensity of an applied field H, time t elapsed since the start of a phase transition or chemical reaction, etc. The information from such experiments can be represented by a gamma-ray transmission surface Tr(E, x), where E is the photon energy relative to the sample, and $x = T, H, t$, etc., (see Figure 1a, b). Intersects of this surface with planes x_C= const. are the spectra, while intersects with planes E_C= const. correspond to scans (Figure 1c, d). In the two simulated examples, Tr(E_C, x) reflects the hyperfine field-temperature dependence, and the evolution of the average hyperfine field orientation with the intensity of the applied field, respectively. The last effect follows from the well known dependence of ^{57}Fe nuclear transition probabilities on the angle between hyperfine field and gamma-ray directions. Scans allow a quasi-continuous study of material properties

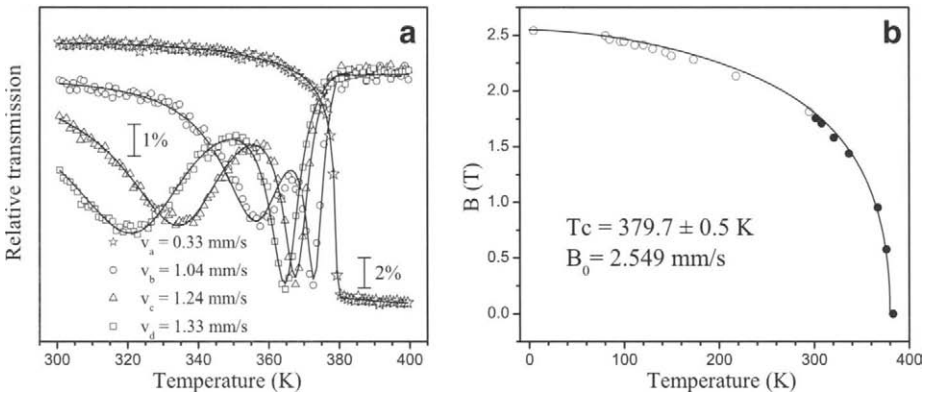

Figure 2 (a) Four scans carried out to determine the quasi-continuous temperature dependence of the Fe hyperfine field $B(T)$ in the antiferromagnet $FeSn_2$. (b) The *solid line* is the $B(T)$ evolution obtained from the simultaneous fit of the results of part (a); *circles* are discrete $B(T)$ values obtained from spectra recorded at fixed temperatures.

dependence upon x and, when time is a limiting factor, may become the only possible Mössbauer approach to study rapidly developing processes.

Saturation effects, even in absorbers nominally thin, influence noticeably the quantitative analysis of scans [5], therefore, the usual thin absorber approximation is not appropriate. For this reason, in order to retrieve information in a reliable quantitative way, the scans were analytically described with the integral expression of the Mössbauer absorption [6].

2 Experiments

As a first experimental example, a set of four scans carried out to determine the quasi-continuous temperature dependence of the Fe hyperfine field $B(T)$ in the antiferromagnet $FeSn_2$ are shown in Figure 2a, [5]. They were recorded at energies which correspond to positions near the spectrum center, and between the room temperature (RT) location of the fourth and fifth spectral lines, using a temperature ramp of 0.125 K/min. The first scan is especially suitable to determine accurately the Nèel temperature T_N, but with the whole set enough information is obtained to deduce the hyperfine field evolution for $T \leq T_N$. In this example, the importance of analyzing the data with the integral expression of the Mössbauer absorption becomes especially clear: saturation effects show a noticeable dependence on temperature, varying very rapidly in the neighbourhood of the Nèel point, where the $FeSn_2$ six lines pattern collapses into a singlet (see Figure 4 of [5]). For their analysis, physical models for the temperature dependence of isomer shift, effective absorber thickness, and the hyperfine field itself were explicitly introduced into the fitting analytic expression [4]. The $B(T)$ evolution obtained from the simultaneous fit of the results of Figure 2a are shown in Figure 2b along with discrete values measured from spectra recorded at fixed temperatures; a remarkable agreement between the two sets of results is observed. A similar approach was used to determine $B(T)$ at each of the two Fe sites of the $D0_3$ structure of ferromagnetic Fe_3Si [7].

Our second example is the thermal evolution of the amorphous ferromagnet $Fe_{73.5}Si_{13.5}Cu_1Nb_3B_9$ (*Finemet*® precursor) and of its nanocrystallisation kinetics [8]. Figure 3a, b show spectra taken at different temperatures and scans recorded between RT and 873 K at an

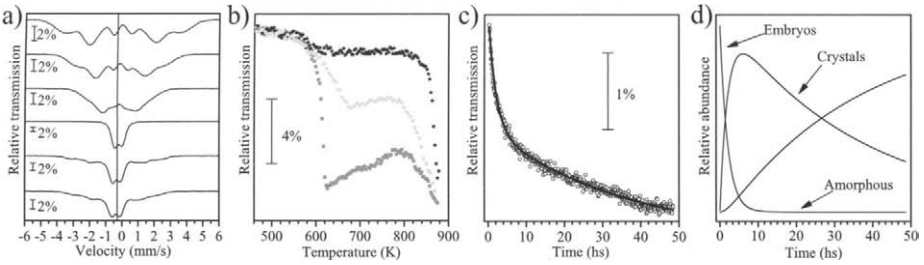

Figure 3 (a) Spectra from amorphous $Fe_{73.5}Si_{13.5}Cu_1Nb_3B_9$ measured at temperatures (*from top to bottom*) of 302, 508, 589, 637, 787, and 803 K. (b) Scans recorded between RT and 873 K at the energy near the spectrum center indicated in (a) by a solid vertical line. (c) Mössbauer transmission vs. time measured during nanocrystallisation at 823 K recorded at a constant energy coincident with one of the principal crystalline absorption lines. (d) Time evolution of the relative amounts of Fe in amorphous phase, crystal embryos and grown up nanocrystals, during nanocrystallisation at 823 K.

energy near the spectrum center (see vertical line in Figure 3a). Scans reflect the different physical processes the material undergoes as temperature increases: ferromagnetic–paramagnetic evolution of the original amorphous phase, nanocrystallisation, and ferromagnetic–paramagnetic evolution of the crystalline Fe–Si nanoparticles. The successive scans performed by heating and cooling back and forth the sample at constant rates of 2 K/min reveal changes in the relative fractions of Fe in amorphous and crystalline environments and a consequent modification of the amorphous phase composition and Curie temperature. The kinetics of nanocrystallisation was observed at 823 K recording the Mössbauer transmission as a function of time at a constant energy coincident with one of the most prominent crystalline absorption lines (Figure 3). The time evolution of the relative amounts of Fe in amorphous phase, crystal embryos and grown up nanocrystals was obtained (Figure 3c) using the hyperfine parameters of each component, obtained from a few Mössbauer spectra. It is worth mentioning that a real time determination of such evolution by Mössbauer spectroscopy is not possible at 823 K (though it can be done at lower temperatures, see Fig. 6 of [8]) because crystallization occurs too rapidly to allow recording of a good quality spectrum representative of a given intermediate state of transformation.

As a final example we present, for the first time, an on going experiment designed to study the dynamic response to an applied *ac* field, of Fe magnetic moments at different phases of $Fe_{90}Zr_7B_3$ ribbons in the nanocrystalline state. In this state, 15–20 nm Fe(Zr) crystals (nanocrystalline phase), which occupy 80–85% of the materials volume, are embedded in an amorphous Fe–Zr–B phase. A sketch of the experimental setup is shown in Figure 4. A triangular waveform was used to drive the current through the Helmohltz coils and to address the recording of the Mössbauer transmission to successive channels of a multi scaler. The Helmholtz coils provide an oscillating magnetic field parallel to the ribbon surface with a maximum intensity of about 75 Oe. For the preliminary experiments presented here the field was driven at 10^{-3} Hz. This low frequency enables a direct comparison between scans and spectra, which is important to test this new experimental approach. An investigation of the magnetic scan-frequency dependence in this material is currently on the way. To obtain information on the responses of the nanocrystalline and amorphous phases, data was recorded at two fixed photon energies where the relative absorption from both phases is different. The arrows in Figure 5a indicate these fixed energies E_i (i=5 and 6) and Figure 5b, c, show the results $Tr_i = Tr(E_i,H)$, which exhibit quite different H-dependences for i=5 and 6. Tr_6, where almost only the nanocrystalline contributions (both from crystals interior and surface) should

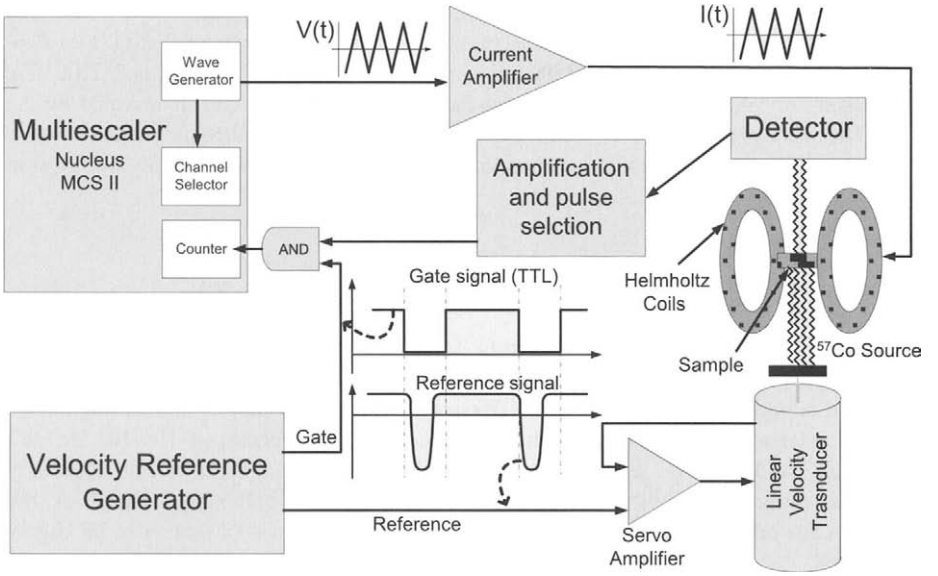

Figure 4 Sketch of the experimental setup for magnetic scans.

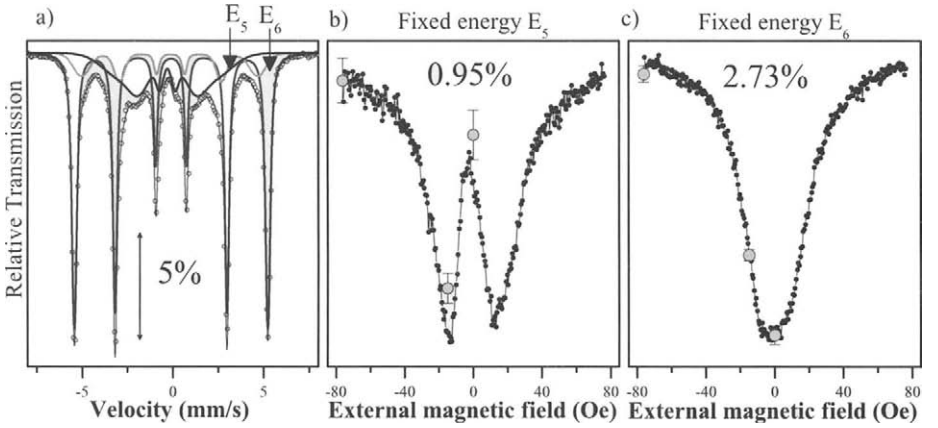

Figure 5 (a) Mossbauer spectrum of amorphous $Fe_{90}Zr_7B_9$ recorded for H=0, showing the contributions from nanocrystals interior (sextet with larger and sharper absorption lines), nanocrystals surface (intermediate average hyperfine field sextet) and amorphous phase. (b) and (c) Mössbauer transmission $Tr_I = Tr(E_i,H)$ as a function of applied field H recorded at the fixed energies E_i (i=5 and 6) indicated by *arrows* in (a). *Full circles* are $Tr(E_i,H)$ obtained from Mössbauer spectra taken at the corresponding fields.

be present [9], has the expected qualitative behaviour, i.e., an increase of transmission with increasing intensity of the applied field, with a tendency for saturation at high fields (see also Figure 1d). Tr_5, instead, has a complex behaviour. Opposite contributions from nanocrystals (fifth lines from crystals interior and surface) and amorphous (sixth line) are expected here, because transition intensities corresponding to lines five and six have opposite dependences on the hyperfine field direction. However, taking into account the amorphous relative amount, its effect would be too small as to justify the observed pattern at that energy. This

complex behaviour could be related to polarization effects which appear in thick absorbers [10]. To confirm this behaviour, a few spectra were recorded under external fields (H_j=−70.6, −15.3 and 0 Oe). In Figure 5b,c, the full circles are the values Tr(E_5,H_j) and Tr(E_6,H_j), respectively obtained from the spectra, and they agree with the behaviour revealed by the scan. The analysis of the physics beneath these results is left for a forthcoming article, but we found worthily to remark that its observation was possible by performing only one scan at energy E_5.

3 Conclusion

In conclusion, we have proved here, that the Mössbauer effect thermal and magnetic scans constitute a powerful tool, complementary of Mössbauer spectroscopy, for studying a variety of condensed matter phenomena. We are currently carrying out new developments of scans. Magnetic scans can be readily extended up to frequencies of 10^3–10^4 Hz, and applied *ac* fields can be substantially increased. Using velocity waveforms especially designed, and/or feedback mechanisms to vary velocity parameters based of the instantaneous outcome of an ongoing experiment, the applications of scans can be largely extended.

Acknowledgements We wish to acknowledge Prof. Teruo Bitoh for kindly providing us with the high quality $Fe_{90}Zr_7B_3$ amorphous ribbons and Prof. Elisa Baggio Saitovitch for kindly allowing one of us (G.A.P.) to use a high vacuum–high temperature device to perform the nanocrystallization of these ribbons. We are also grateful for encouraging discussions of G.A.P. with Profs. Bitoh and Baggio-Saitovich. This work has been done under financial support from CONICET and UNLP.

References

1. Preston, R.S., Hanna, S.S., Heberle, J.: Phys. Rev. **128**, 2207 (1962)
2. Gonser, U., Meechan, C.J., Muir, A.H., Wiedersich, H.: J. Appl. Phys. **34**, 2373 (1963)
3. Wagner, H.-J., Gonser, U.: J. Magn. Magn. Mater. **31–34**, 1343 (1983)
4. Chien, C.L.: Phys. Rev., B. **18**, 1003 (1978)
5. Mendoza Zélis, P., Pasquevich, G.A., Sánchez, F.H., Martínez, N., Veiga A.: Phys. Lett., A. **298**, 55 (2002)
6. Vèrtez, A., Korecz, L., Burger, K., In: Mössbauer Spectroscopy and Transition Metal Chemistry, p.31. Elsevier, Ámsterdam (1979)
7. Pasquevich, G.A., Mendoza Zélis, P., Fernández van Raap, M.B., Sánchez, F.H.: Physica. B **354**, 369 (2004)
8. Sánchez, F.H., Pasquevich, G.A., Mendoza Zélis, P., Cabrera, A.F., Ying-feng, L., Vázquez, M.: J. Metastable Nanocryst. Mater. **22**, 39 (2004)
9. Miglierini, M., Greneche, J.M.: J. Phys.: Condens. Matter **9**, 2321 (1997)
10. Williams, J.M., Brooks, J.S.: Nucl. Instrum. Methods **128**, 363 (1975)

Hyperfine Interact (2006) 167:845–850
DOI 10.1007/s10751-006-9370-x

Velocity calibration for *in-situ* Mössbauer data from Mars

David G. Agresti · M. Darby Dyar · Martha W. Schaefer

Published online: 14 November 2006

Abstract Beginning in August 2004, raw data acquired by the Mössbauer spectrometers on the Mars Exploration Rovers (MERs) have been released to the science community as Experimental Data Records (EDRs) for each Martian day (sol) on which measurements were made. To provide convenient direct access to the EDR data, to enable independent assessment and analysis, and to allow confirmation of MER-team scientific conclusions, a new Windows-based computer program, *MERView*, has been developed. Direct inspection of the binary structure of an EDR file, conversion of the binary data to decimal column format for display or export, and full-screen graphical displays are included, allowing, in a highly transparent and user-friendly manner, immediate and thorough overview of the entire EDR data set. *MERView* also includes automated procedures for velocity calibration. Correction for non-linearity is done using the EDR-provided drive error signal, a phase shift, and the requirement that the two halves of a reference spectrum must overlap exactly when plotted on a correct velocity scale. Absolute velocity calibration (mm/s) is then accomplished by comparing each reference spectrum with known peak positions of standard reference materials.

Key words Mössbauer data · Mars · velocity calibration · methodology · *MERView*

D. G. Agresti (✉)
Department of Physics, University of Alabama at Birmingham, Birmingham, AL 35294-1170, USA
e-mail: agresti@uab.edu

M. D. Dyar
Department of Astronomy, Mount Holyoke College, 50 College St., South Hadley, MA 01075, USA
e-mail: mdyar@mtholyoke.edu

M. W. Schaefer
Department of Geology and Geophys., E235 Howe-Russell,
Louisiana State University, Baton Rouge, LA 70803, USA
e-mail: schaefer@geol.lsu.edu

1 Introduction

Since January 2004, Mössbauer spectrometers [1] have been making measurements on Mars as a component of the Athena instrument suite because the technique can "yield information about early Martian environmental conditions" and can help in "identifying minerals formed in hot, watery environments that could preserve fossil evidence of Martian life" (from an early Athena web site; cf. [2]). The spectrometers are mounted on the instrument deployment arms of two Mars Exploration Rovers, MER-A (Spirit) and MER-B (Opportunity), where they have access to a wide range of rocks and soils. Initial measurements at the Spirit site showed that surface samples contained primarily basaltic minerals with weathering by physical processes [3], while mineralogy inferred from data acquired at the Opportunity site provided evidence for past aqueous processes [4]. More recently, Mössbauer spectroscopy has identified goethite at Columbia Hills [5] and contributed to an understanding of the nature of Martian atmospheric dust and its implications for the history of water on Mars [6].

It is important that MER-team results be verified and expanded upon. Since August 2004, Mars Mössbauer and related data, with supporting documentation, have been made available to the science community via the Planetary Data System (PDS) at the MER Analyst's Notebook download site (http://www.anserver1.eprsl.wustl.edu/) and at the PDS Geosciences Node (http://www.pds-geosciences.wustl.edu/). New data are released at regular intervals in the form of Experimental Data Records (EDRs), essentially as received from Mars, typically one file for each sol (Mars day) on which measurements were made, with up to 65 Mössbauer spectra and other pertinent data in compressed binary format. There are also channel-to-velocity conversion tables at the PDS nodes. Another resource is the web site, http://www.ak-klingelhoefer.chemie.uni-mainz.de/, which presents EDRs in their geological context and makes available for download the *MIMView* program, which extracts data from the EDR and does related graphics.

We have developed the Windows-based computer program *MERView* to facilitate analyses of the unprocessed Mars data [7]. It reads an EDR file, converts the binary data to decimal column format, and provides a graphical overview of the entire data set. Procedures are fully explained and the user interacts straightforwardly via drop-down and pop-up menus and dialog and information boxes. Correction for velocity non-linearity is performed by adjusting the size of the EDR-provided error signal and adding a channel offset (phase shift) while maximizing overlap of the two halves of a reference spectrum plotted versus velocity. A calibration factor may then be applied to obtain the velocity scale in millimeters per second, based on fits to EDR spectra of the reference absorbers (or their components), which are different for MER-A and MER-B.

In what follows we discuss the capabilities of *MERView* and how it computes the velocity, including the use of "pseudo values," which were found to be necessary to correct for the non-linearity in the MER velocity.

2 The *MERView* program

To begin program operation, an EDR file, with its associated label file, must be downloaded from the web and opened by *MERView*. The principal output modes are:

(1) An indexed display of the EDR contents in binary (hexadecimal) format
(2) Tables of values extracted from the EDR, displayed as decimal columns

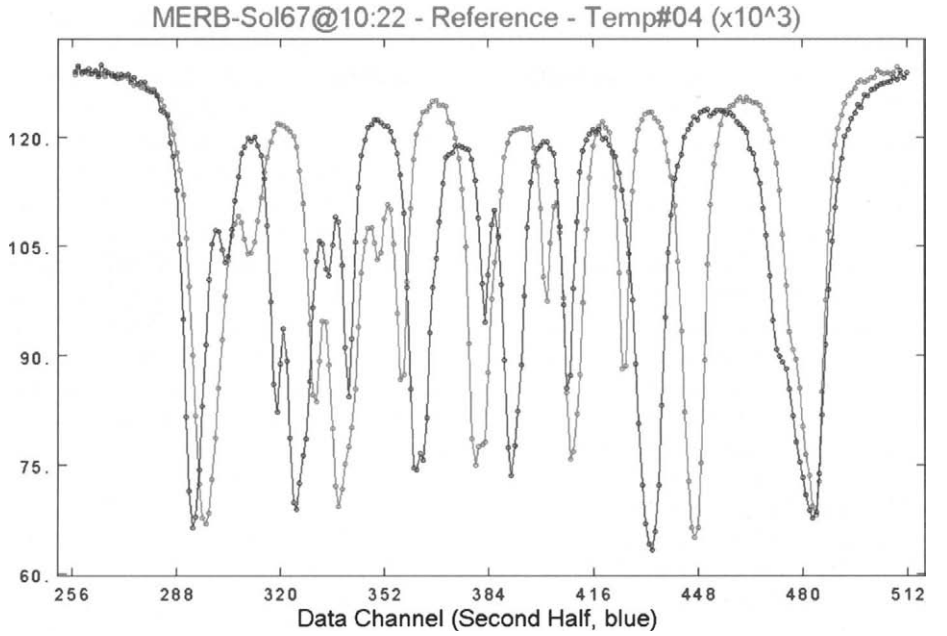

Figure 1 Example of a reference spectrum overlapped at mid channel and plotted versus channel. Second half is to the *left*.

(3) Tables of values exported to an external file
(4) Full-screen graphical displays

Displayed, exported, and graphical data include: Mössbauer sample and reference spectra; detector energy spectra; drive error signal; and temperature variation during measurement on a particular sol. The exported data are in column format, suitable for input to spreadsheet or other analysis programs.

For each text or graphical display screen, pressing the right mouse button opens a popup menu that allows direct selection of an action or defines special keys for manipulating screen contents, such as: changing what is displayed; moving to another part of the display; and zooming a graph. More sophisticated interactions are accomplished with use of dialog boxes, which in turn may open a secondary box for additional input or information display. Tabular and graphical output of *MERView*, and its operation through menus and dialog boxes, are discussed and illustrated in [7].

3 Velocity calibration

During measurement, a 512-channel transmission Mössbauer spectrum of the internal reference absorber (a mixture of ^{57}Fe-enriched α-iron, hematite, and magnetite (Klingelhöfer and Squyres, 2005, personal communication, received August 9, in response to an inquiry for information from M.D. Dyar, M.W. Schaefer, and D.G. Agresti) is acquired at the same time as the backscatter spectrum of a surface target. Because Mössbauer sources are employed at opposite ends of the drive shaft, velocity scales for the surface and reference spectra are negatives of each other. For each sol, a drive error signal is

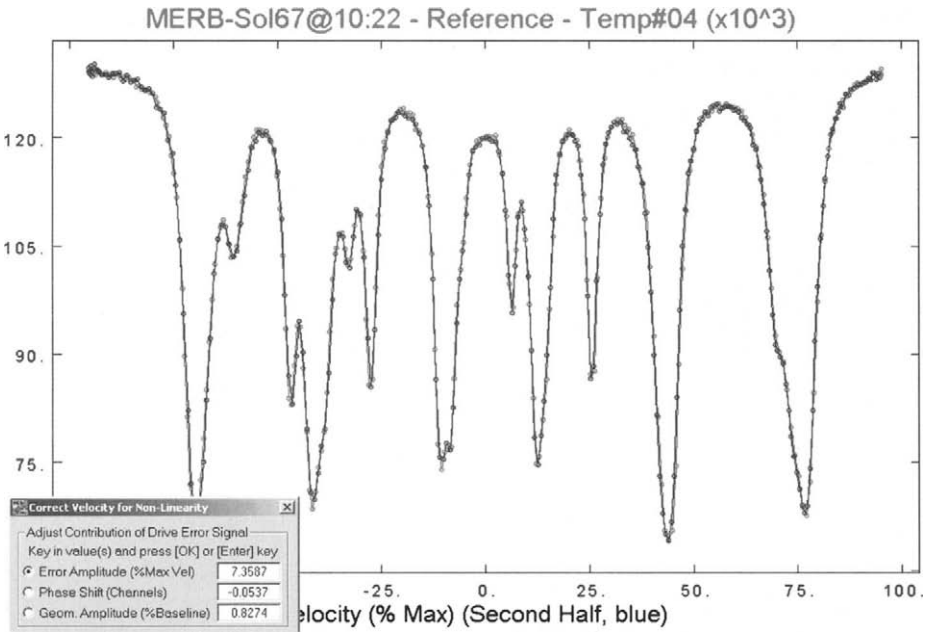

Figure 2 Data for Figure 1 plotted versus a velocity scale corrected for non-linearity. The geometric effect has been removed.

acquired electronically by differencing a pickup signal proportional to the actual velocity and an ideal "linear" velocity.

For the reference spectrum, the linear velocity waveform is a V-shape defined by Vlin(c)=+Vmax at c=0.5 to Vlin(256.5)=−Vmax, back to Vlin(512.5)=+Vmax, where c= channel number. In Figure 1 we plot a MER-B reference spectrum as counts versus channel, with the first half folded about the mid-channel point, equivalent to plotting versus linear velocity. Because the two halves do not overlap, and mirrored peaks from the two halves must be at the same velocity, it is clear that the velocity is highly non-linear. Thus we employ a simple requirement: *When two halves of a spectrum are displayed on the same graph versus a properly calibrated velocity scale, the halves must overlap perfectly.*

MERView corrects for non-linearity by adjusting the magnitude ErrAmp of the drive error signal $E(c)$ and applying a channel offset CShift until overlap of the two halves is maximized. First $E(c)$ is scaled to give the function $e(c)$ with average of zero and mean amplitude around zero velocity of ±1. Then, $\mathrm{Vpickup}(c) = \mathrm{Vlin}(c) + \mathrm{ErrAmp} \times e(c)$ and $\mathrm{Vtrue}(c) = \mathrm{Vpickup}(c - \mathrm{CShift})$ are defined. Interpolation of Vpickup(c) is required, since $c - \mathrm{CShift}$ is not generally an integer. In this way, a perfect overlap may be achieved, as shown in Figure 2, where the curved baseline, $\mathrm{Geom}(c) = \mathrm{GeomAmp} \times \int_1^c \mathrm{Vtrue}(c')dc'$, has been removed before overlapping the two halves. The integral is scaled so that GeomAmp gives the maximum deviation as percent of a computed baseline, while Vmax is assigned a value of 100%.

Adjustment of the three parameters is controlled by a dialog box that allows: (1) Direct entry of parameter values; (2) Stepwise adjustment according to selectable increments; or (3) Automatic stepwise adjustment until maximum overlap is achieved. Automation requires a numerical criterion, for *MERView* minimization of Q^2 = sum of weighted squared

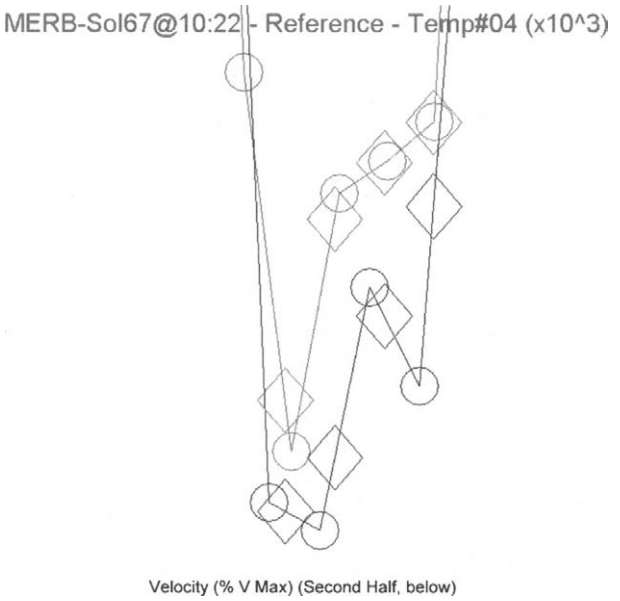

Figure 3 Relationship between pseudo data (*diamonds*) and true data (*circles*). The *diamonds* line up vertically and are always centered on a line connecting a pair of *circles*.

differences of the two halves, which also allows definition of χ^2 and other statistical quantities. However, because of the non-linearity, the channels do not line up when plotted in velocity space and Q^2 cannot be computed directly from the MER raw data. Therefore, *MERView* works with "pseudo values." First, a set of equally spaced velocities is defined, typically with increments of 0.8% Vmax, resulting in ~250 pseudo velocity values. Then pseudo data values are defined by interpolation (Figure 3) of the EDR raw data, whose velocities are Vtrue(c). Finally, χ^2 is minimized with respect to the pseudo data.

Experience in correcting velocity with *MERView* has shown the calibration to vary for MER-A and MER-B as function of temperature and from sol to sol. For the example of Figures 1 and 2, (ErrAmp, CShift)=(7.359, −0.054), while for MER-B, sol 48, window #4, (ErrAmp, CShift)=(7.696, 1.340), where a significant channel shift is required for perfect overlap. For MER-A, sol 58, window #5, (ErrAmp, CShift)=(0.926, −0.180). The velocity scale provided at the Geosciences Node does not allow for possible sol-to-sol variation. Therefore, for highest precision, the user should correct the drive velocity for each distinct reference spectrum.

Converting the velocity scale in percent Vmax to millimeter per second is less straightforward since "Measurements as function of temperature for the flight reference targets have not been done on Earth, only measurements at room temperature" (Klingelhöfer and Squyres, 2005, personal communication, received August 9, in response to an inquiry for information from M.D. Dyar, M.W. Schaefer, and D.G. Agresti). Work is underway to automate *MERView* determination of the velocity scale with reference to standard values for the α-iron and hematite line positions.

4 Conclusion

A new Windows-based program for MER Mössbauer data, *MERView*, provides an immediate overview of the entire EDR data set and writes output files in a format suitable

for further analysis. It is flexible, transparent, and easy to use. Rapid automated correction for drive non-linearity (seconds per sol) allows velocity calibration to be carried out independently of MER-team analysis. Data processed using this program are posted at www.mtholyoke.edu/go/mars. A copy of the *MERView* program may be obtained by request from author DGA at agresti@uab.edu.

References

1. Klingelhöfer, G., Morris, R.V., Bernhardt, B., Rodionov, D., de Souza, P.A. Jr., Squyres, S.W., Foh, J., Kankeleit, E., et al.: J. Geophys. Res. **108**(E12), 8067 (2003), doi:10.1029/2003JE002138
2. Wade, M.L., Agresti, D.G., Wdowiak, T.J., Armendarez, L.P., Farmer, J.D.: J. Geophys. Res. **104**(E4), 8489–8507 (1999)
3. Morris, R.V., Klingelhöfer, G., Bernhardt, B., Schröder, C., et al.: Science **305**, 833–836 (2004)
4. Klingelhöfer, G., Morris, R.V., Bernhardt, B., Schröder, C., et al.: Science **306**, 1740–1745 (2004)
5. Klingelhöfer, G., Rodionov, D.S., Morris, R.V., et al.: Lunar Planet. Sci. **36**(2349) (CD-ROM) (2005)
6. Goetz, W., Bertelsen, P., Binau, C.S., Gunnlaugsson, H.P., et al.: Nature **436**, 62–65 (2005)
7. Agresti, D.G., Dyar M.D., Schaefer, M.W.: Lunar Planet. Sci. **36**(1941) (CD-ROM) (2005)

Hyperfine Interact (2006) 167:851–854
DOI 10.1007/s10751-006-9380-8

A simple model to extract hyperfine interaction distributions from Mössbauer spectra

H. P. Gunnlaugsson

Published online: 8 November 2006

Abstract The general problem of finding a distribution in hyperfine interaction parameters from experimental Mössbauer spectra is outlined. Existing methods may lack flexibility to be easily applicable to simple problems. A line shape for hyperfine parameter distributions is given, which is based on linear segments in the probability function. This method is applied in the analysis of samples containing iron in a silicate glass.

Key words hyperfine parameter distribution

1 Introduction

Numerous effects can lead to a line broadening in Mössbauer spectroscopy. To obtain a meaningful analysis of the spectral data, one is often forced to use line shapes, which are based on distributions in hyperfine interaction parameters. Two main concepts are usually applied: (1) Calculation of hyperfine parameter distributions directly from the experimental data, e.g., the Window method [1] or the Hesse-Rübartsch method [2]. (2) Making assumptions about the distribution, possibly based on knowledge of the system, and applying line shapes based on the convolution of the natural Lorentzian shape with a hyperfine parameter distribution [3–5].

In the former case, it may be difficult to estimate whether features observed in the obtained distribution are significant or not. Methods for error estimates exist [6, 7], but may require additional calculations based on the obtained solution that are beyond the scope of the problem. In the latter case, obviously, if the assumptions on the physics are incorrect, the results may also be incorrect.

In this paper, a different approach is applied which is somewhat in-between the two concepts described above. The general philosophies behind this method are: (1) To analyse the data with as few free parameters as possible, still allowing for the shape of the obtained

H. P. Gunnlaugsson (✉)
Institute of Physics and Astronomy, Aarhus University,
Ny Munkegade, 8000 Århus C, Denmark
e-mail: hpg@phys.au.dk

hyperfine parameter distribution not to be predefined to too large extent. The number of free parameters that can be applied to describe the distribution will depend on the statistics of the experimental spectrum (2) Use a simple and crude description of the distribution function, that can still take into consideration the statistical accuracy of the spectrum and (3) to maintain simple error analysis based on the χ^2 value (see e.g. [8]).

The method described here is based on linear segments in the hyperfine parameter distributions. Though unphysical, it is still powerful enough to describe the experimental data with sufficient accuracy. The statistics of the spectrum will determine how many segments can be applied to describe the distribution function. Furthermore, the obtained line shape can be calculated analytically thus allowing for a fast analysis of spectra.

2 The model

A Lorentzian line centred around a Doppler velocity $v=v_0$ can be written in normalised form as

$$L(v, v_0, \Gamma) = \frac{2}{\pi\Gamma} \frac{1}{1 + \left(\frac{v-v_0}{\Gamma/2}\right)^2} \tag{1}$$

where Γ is the line width (FWHM). In the case of a singlet, the centre position v_0 has the meaning of an isomer shift, δ. Distributions based on linear segments, can generally be written as probability functions $P(x)=ax+b$, where x denotes a hyperfine interaction parameter. The line position will depend on x, generally as $v_0=c_0+c_1x$ where c_0 and c_1 are constants depending on the hyperfine interactions parameters. The line shape will be an integral over the probability distribution and the Lorentzial line shape, and for convenience we define

$$\begin{aligned} f(v, \Gamma, c_0 c_1, a, b, x_i, x_{i+1}) &= \int_{x_i}^{x_{i+1}} L(v, c_0 + c_1 x, \Gamma)(ax + b)\mathrm{d}x \\ &= \frac{1}{4\pi c_1^2}\left[(ac_0 - bc_1 - av)\left(\tan^{-1}\left(\frac{2(c_0 - v + c_1 x_i)}{\Gamma}\right)\right.\right. \\ &\quad \left.\left. - \tan^{-1}\left(\frac{2(c_0 - v + c_1 x_{i+1})}{\Gamma}\right)\right)\right] \\ &\quad + \frac{a\Gamma}{4\pi c_1^2} \ln\left(\frac{(c_0 - v + c_1 x_{i+1})^2 + (\Gamma/2)^2}{(c_0 - v + c_1 x_i)^2 + (\Gamma/2)^2}\right) \end{aligned} \tag{2}$$

Note that the case of $c_1=0$ has to be dealt with separately. Integration over velocity yields $I = a\left(x_{i+1}^2 - x_i^2\right)/2 + b(x_{i+1} - x_i)$, which can be used for normalisation.

A quadrupole splitting distribution $P(Q)$, can be simulated with N_Q linear segments each from Q_i to Q_{i+1}, $1 \le i < N_Q + 1.$, where Q is a shorthand notation for the quadrupole splitting ΔE_Q. Assuming a coupling between the isomer shift and the quadrupole splitting of the form $\delta=\delta_0+\delta_1 Q$, the distribution for the ith segment is then written using the function defined above as

$$\begin{aligned} D_i(v, \Gamma, \delta_0, \delta_1, a, b, Q_i, Q_{i+1}) &= f(v, \Gamma, \delta_0, \delta_1 - 1/2, a, b, Q_i, Q_{i+1}) \\ &\quad + f(v, \Gamma, \delta_0, \delta_1 + 1/2, a, b, Q_i, Q_{i+1}) \end{aligned} \tag{3}$$

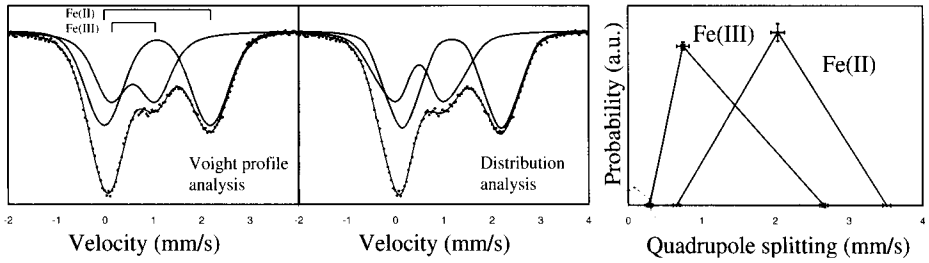

Figure 1 Mössbauer spectrum of Black tektite from Beloc obtained at 80 K analysed with Voight profiles (*left*) or linear segment distributions (*middle*, *right*).

The left component has the obvious meaning of the left component of the quadrupole distribution.

The problem of distributions in magnetic hyperfine fields in ^{57}Fe Mössbauer spectroscopy is analogous to that of quadrupole interaction distributions and couplings between hyperfine parameters can easily be constructed, and the final line shape written in terms of the f function defined above.

3 Examples of results

One class of samples, where the Mössbauer spectra may be analysed in terms of quadrupole interaction distributions, is that of iron in natural silicate glasses. Tektite from the Cretaceous/Tertiary boundary has been shown to contain unusually high amounts of ferric iron [9]. It has been disputed whether this is due to a real high ferric/ferrous ratio of the glass, or whether there are in-homogeneities in the samples [10]. Spectra of this kind are often analysed in terms of symmetric Voight profiles, i.e., Gaussian-broadened Lorentzian lines, however, this may lead to an incorrect determination of the hyperfine parameters.

As an example, Figure 1 shows the spectrum of black Beloc tektite (Haiti) recorded at 80 K.

In the distribution analysis we have assumed symmetric components (i.e., $\delta_1=0$), and that the qudrupole distribution consist of two linear segments. This gave χ^2 value that did not allow increasing the number of fitting variables (in this case 13). In the Voight profile analysis (11 fitting variables), the spectra were analysed with two symmetric profiles assigned to ferric and ferrous iron.

Visual inspection of the spectra in Figure 1 does not allow to state that one analysis is better than the other. However, the χ^2 value is significantly higher in the case of the Voigt profile analysis, and this alone should cause caution. On the other hand, the results obtained are significantly different in terms of the two quadrupole-split components as can be see in the arrangement of the left-hand quadrupole components in Figure 1.

From the data given here, it is difficult to determine which analysis is more reliable. However, at lower temperatures, the Fe(III) component shows magnetic interactions, i.e., a sextet splitting, and the remaining centre part of the spectra becomes dominated by the Fe (II) component, thus the two spectral components are much better resolved. In the Voight profile analysis, the isomershift of the Fe(II) component shows an unphysical jump at the temperatures where the Fe(III) component becomes magnetically ordered, while the isomerhift obtained from the distribution analysis follows the second order Doppler shift. We therefore favour the distribution analysis.

4 Discussion and conclusions

Some precautions have to be applied when using the model proposed here. In order to interpret the results correctly, one should start out with applying as few parameters as possible to describe the distribution and increase the number of segments one by one until the χ^2 value does not show appreciable decrease. Features such as drifting of segment points towards each other and obviously non-physical distributions are clear indications that the number of segments is too high. When this is taken properly into account, the method is powerful in extracting the information that is held within the spectral data.

Often, rather large values of the Lorentzian line width, Γ_E, are obtained, significantly larger than the natural line width, Γ_N. This is due to the sharp edges in the hyperfine parameter distributions. The distribution profile that simulated the spectrum is therefore a convolution between the obtained profile and a Lorentzian profile of width Γ_E–Γ_N. Such a convolution smoothens to some degree the sharp edges from the obtained distribution and can easily be evaluated.

The method presented here does not replace the direct methods, such as the Hesse-Rübartsch method, but these methods can supplement each other. The Hesse-Rübartsch method can give hints of how to build up the first guess of the hyperfine parameter distribution before fitting.

The method applied for obtaining hyperfine parameter distribution has to reflect the problem at hand, and which questions are sought answers to. The analytical form of the hyperfine distribution presented here gives a fast evaluation of hyperfine parameters and statistical errors, and is suitable for evaluating extended datasets, e.g., temperature series. Detailed analysis of a single measurement may need refinement in terms of different methods that describe the physics in a not too crude way.

References

1. Window, B.: J. Phys. E **4**, 401 (1971)
2. Hesse, J., Rübartch, A.: J. Phys. E **7**, 526 (1974)
3. Sharon, T.E., Tsuei, C.C.: Phys. Rev., B **5**, 1047 (1972)
4. Rancourt, D.G., Ping, J.Y.: Nucl. Instrum. Methods Phys. Res., B **58**, 85 (1991)
5. Hansen, M.F., Koch, C.B., Mørup, S.: Phys. Rev., B. **62**, 1124 (2000)
6. Dou, L., Hodgson, R.J.W., Rancourt, D.G.: Nucl. Instrum. Methods Phys. Res., B **100**, 511 (1995)
7. Metsova, O.M., Ageev, A.L., Vorina, E.V.: Nucl. Instrum. Methods Phys. Res., B **187**, 132 (2002)
8. Press, W.H., Teukolsky, S.A., Vetterling, W.T., Flannery, B.P.: Numerical Recipes in C, 2nd edn., Cambridge University Press, New York, pp. 689 (1992)
9. Óskarsson, N., Helgason, Ö., Sigurdsson, H. In: Ryder, G., Fastovsky, D., Gartner, S. (eds.) The Cretaceoous – Tertiary Event & Other Catastrophes in Earth History, Geological Soc. of America, paper 307, 445 (1996)
10. Bender Koch, C., Gunnlaugsson, H.P. (manuscript in preparation)

Hyperfine Interact (2006) 167:855–859
DOI 10.1007/s10751-006-9381-7

Dynamical beats of forward-scattered resonant synchrotron radiation as a nuclear polariton effect

M. Haas · H. Winkler

Published online: 27 October 2006

Abstract The decay of the nuclear exciton (immobile collective excitation), created by a pulse of synchrotron radiation, is analyzed. It is shown that in the later phases of the decay, the exciton becomes localized at the sample's frontal surface. Inside the sample, the secondary gamma-quanta, emitted by the contracting exciton, are converted into polaritons (mobile nuclear excitations) characterized by different frequencies and equal group velocities. On the sample's back surface, the polariton interference causes a beating structure of the transmitted radiation, observed in experiments.

Key words polariton · synchrotron radiation · nuclear resonant forward scattering

Abbreviations
NP nuclear polariton
NE nuclear exciton
SR synchrotron radiation

1 Introduction

In a resonant medium, a stationary flux of the electromagnetic radiation creates polaritons – coherently coupled pairs of a photon and a delocalized material excitation. The Mössbauer nuclei – almost ideal two-level systems, are potential sources of pronounced polariton effects in gamma-spectroscopy (nuclear polaritons – NP). The properties of new quasiparticles and primary photons may differ significantly when the polariton frequency approaches the resonance ($\omega \rightarrow \omega_r$). About 99.999% of the polariton energy is concentrated in the exciton component of NP (an ensemble of nuclear multipoles, performing forced

M. Haas (✉)
Institute of Physics, University of Tartu, Riia 142, 51014 Tartu, Estonia
e-mail: haas@fi.tartu.ee

H. Winkler
Institut für Physik, Universität zu Lübeck, 23538 Lübeck, Germany

oscillations) and a drastic decrease of the polariton group velocity takes place ($v_g \sim 10^2$–10^3 cm/sec). A series of polariton effects are known in optics where the strong delay of the light propagation has recently become an actual field of research [1, 2]. One such effect – the delay of prolonged pulses, emitted by a radioactive Mössbauer source – has also been experimentally observed [3]. Recently, the polariton origin of the cooperative effects, arising at the propagation of the synchrotron radiation (SR) in the perturbed two-target resonant systems, has been pointed out in [4]. In this paper, some polariton aspects of SR propagation will be discussed. The case of a conventional one-target system and a single Mössbauer transition will be considered.

2 Contracting nuclear exciton

A photon–polariton conversion takes place during the finite time interval $t_p \sim |\omega - \omega_r|^{-1}$ (at SR propagation in thick resonant targets $t_p > 10^{-9}$ s). The pulses of the primary SR are too short ($\sim 10^{-12}$ s) for an immediate photon–polariton conversion; thus, a "pure" nuclear exciton (NE, an immobile ensemble of freely oscillating multipoles) arises in the sample. The evolution of NE has been discussed in [5–8]. The authors have pointed out the decisive role of the strong coherent radiation field, generated by the nuclear ensemble. The evolution itself is considered to consist in a fast (in the scale of the nuclear life-time) damping of multipole oscillations. Such a simple model explains the fast attenuation of the secondary radiation emitted by NE in the first phase of its decay, but it fails to interpret the later deceleration of the process accompanied by beating phenomena (dynamical beats). A more detailed analysis shows the NE evolution to be a more complicated process, whereby important factors (field inhomogeneity inside the sample and the transfer of energy between nuclei) have been neglected in [5–8]. A more complicated character of the NE decay has also been pointed out in [9].

Indeed, in the coherent radiative channel, the evolution of NE is defined via basic equations:

$$\dot{U}_e(z,t) = bU_{ph}(z,t), U_{ph}(z,t) = (-1/d)\int_0^z dz' U_e\left(z',t\right) \tag{1}$$

($b = T_M\gamma/4$, d and T_M are the thickness and the dimensionless Mössbauer thickness of the sample, γ is the natural width of the excited level). The functions $e^{-\gamma t/2}U_e(z,t)$ and $e^{-\gamma t/2}U_{ph}(z,t)$ are the normalized amplitudes of the nuclear polarization and the coherent field in the sample (the factor $e^{-\gamma t/2}$ describes the decay in incoherent channels and will be omitted in the further discussions). Inside the sample, the amplitudes vary along the z-axis (beam direction), whereby $0 \le z \le d$. As the solutions of the Eq. 1

$$U_e(z,t) = J_0(\xi), U_{ph}(z,t) = -2(z/d)J_1(\xi)/\xi, \tag{2}$$

($\xi = 2\sqrt{(z/d)bt}$, $J_{0,1}$, are the Bessel functions) [9].

In the first phase of the evolution ($t < 1/b$), Eq. 1 describe the decay of a nuclear ensemble due to the reaction of the coherent radiation emitted by the nuclei. According to Eq. 1, such reaction represents an external braking (non-damping) force [$\sim U_{ph}(z,t)$], strongly varied over the sample from the very beginning of the process (Figure 1, curve 1).

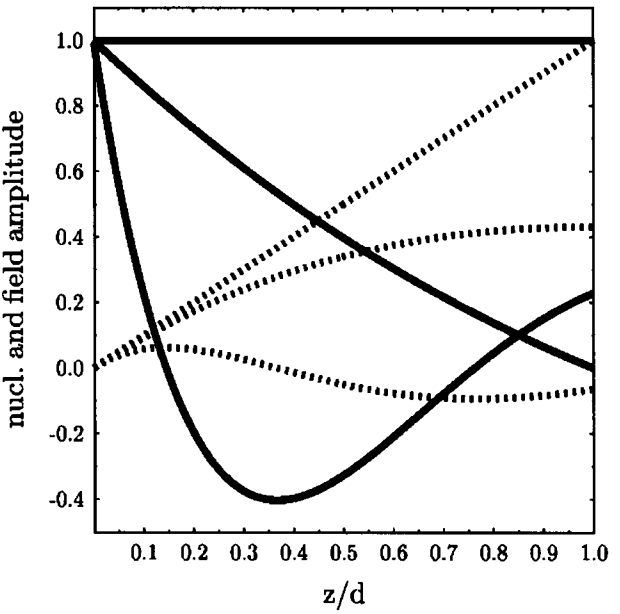

Figure 1 Nuclear ($U_e(z,t)$, solid line) and field ($-U_{ph}(z,t)$, dashed line) amplitude distribution in the sample (1 – t=0; 2 – t=1.445/b; 3 – t=10/b, z<0.14 d – exciton zone, z>0.15 d – polariton zone).

Thereby,

$$U_e(z,t) \approx 1 - btz/d + \ldots, U_{ph}(z,t) = -(z/d)(1 - btz/2d + ..). \quad (3)$$

According to Eqs. 2 and 3, each layer of the sample is characterized by its own nuclear de-excitation rate. In a concrete layer, the nuclear de-excitation proceeds almost twice as fast as the field attenuation $\left(\dot{U}_e \Big/ U_{ph} \approx 2\right)$. At the same time, the internuclear phase relations (phase memory) remain unaltered.

At $t \sim 1/b$ qualitative changes take place at the back surface of the sample ($z \sim d$). Here the strong reaction forces stop the nuclear multipole oscillators at the moments t_{cr} (z) (non-exponential decay, $U_e(z,t_{cr}) = J_0\left(2\sqrt{bzt_{cr}/d}\right) = 0, U_{ph}(z,t_{cr}) \neq 0$, on the back surface $t_{cr}(d) = 1.446/b$). A further evolution of the stopped oscillators consists in their re-excitation by the coherent field (energy transfer and NP formation). Due to the changed phases, the re-excited nuclei fall out of the initial ensemble (NE contraction).

In the second phase of the decay, at $t > t_{cr}$, NE contraction continues. The exciton is localized at the frontal surface ($0 < z < z_0(t), z_0(t) \approx 1.446d/bt$; Figure 1, curve 3). As before, the evolution is defined by approximate formulae (3). Due to the weak field in the region, NE decay decelerates (decay rate is $\sim 1/t$). The effective spectral width of the photon packet, emitted by the contracting NE, decreases also as $|\omega - \omega_r| \leq \Delta_{act}(t) \cong bz_0/d = 1/t$.

3 Dynamical beats as a polariton effect

In order to leave the sample, the coherent secondary radiation, emitted by a contracting NE, must penetrate a layer of the resonant matter ($z_0 < z \leq d$, polariton region) by creating nuclear polaritons (narrow NP packets) in it. Originally the polaritons, created at the time moment $t_0 \cong t_{cr}$, are localized on the boundary of the contracting exciton at z_0 (t_0)<< d. They belong

to two different polariton branches and have different frequencies $(\omega_r + \Delta_n(t_0))$ and wave numbers $(\omega_r/c + k_n(\Delta_n(t_0)))$, but an equal group velocity $v_g(t_0) = c\Delta_{act}^2(t_0)(d/cb)$ $(\Delta_n(t) = (-1)^n\Delta_{act}(t), k_n d = b/\Delta_n, n=1,2$, c – velocity of light in the vacuum). Further such polaritons travel slowly through the sample and reach the back surface at $t = d/v_g(t_0) >> t_0 \left(t_0 = (t/b)^{1/2}\right)$. Thereby, interference effects and a smearing of the initial packets take place. Note that NP characteristics change in accordance with the changes of the spectral characteristics of the secondary photons, emitted by the contracting NE.

Indeed, in the spectral representation the field amplitude $U_{ph}(d,t) = -J_1(2\sqrt{bt}/\sqrt{bt} = (2\pi b)^{-1}\cdot\int_{-\infty}^{\infty} d\Delta \exp[-i(\Delta t + b/\Delta)]$. At $t>>b^{-1}$, the Fourier integral can be calculated in the stationary phase approximation [3]. As a result

$$U_{ph}(d,t) \approx U_{ph}^{(pol)} = \sum_n u_n^{(ph)}(t_0)\exp[-i(k_n(t_0)d + \Delta_n(t_0)t)], \tag{4}$$

$\left(u_n^{(ph)} \approx \sqrt{1/4\pi(bt)^{3/2}}\exp\left((-1)^{n+1}i\pi/4\right)\right)$. Eq. 4 represents the field amplitude as a superposition of two polariton packets, centered on the back surface at $t=d/v_g$. A similar expression can be derived for the polarization amplitude ($U_e(d,t) \approx U_e^{(pol)}$, the amplitudes $u_n^{(e)} = i(-1)^n(bt)^{1/2}u_n^{(ph)}$). After summation

$$\begin{aligned} U_{ph}^{(pol)} &= \sqrt{1/\pi(bt)^{3/2}}\cos\left(2\sqrt{bt} + \pi/4\right), \\ U_e^{(pol)} &= \sqrt{1/\pi(bt)^{1/2}}\sin\left(2\sqrt{bt} + \pi/4\right) \end{aligned} \tag{5}$$

According to the asymptotic expansions of the Bessel functions [10], $\left|U_{e,ph} - U_{e,ph}^{(pol)}\right| < 3/16\sqrt{bt} << 1$ if $t>>1/b$, i.e., the model of interfering NP fits the results of the multiple scattering theory (Eqs. 1 and 2). At the same time, this model reveals the origin of the quasiharmonic oscillations of the field and the polarization amplitudes (Eq. 5) and explains the reason of the beating structure of the transmitted SR (intensity of the transmitted SR $I_{tr}(t) \sim \left|U_{ph}(d,t)\right|^2$). The described model of interfering polaritons also explains more complicated beating phenomena in the media, characterized by a remarkable splitting of nuclear levels. Thereby, the increase of the number of interfering polaritons and the more complicated dispersion relations of polariton wave vectors and group velocities must also be taken into account. The corresponding SR time-domain spectra, including the valuable information about the electron structure of resonant atoms, exhibit simultaneously strong dependences on the sample thickness [11].

Acknowledgements The authors are indebted to Prof. V. Hizhnyakov for helpful discussions. One of the authors (M. Haas) thanks the Universität zu Lübeck and the Estonian Science Foundation (Grant No. 5549) for support.

References

1. Phillips, D.F., Fleischhauer, A., Mair, A., Walsworth, R.L., Lukin, M.D.: Phys. Rev. Lett. **86**, 783 (2001)
2. Aleksandrov, E.B., Zapaskii, V.S.: Usp. Fiz. Nauk **174**, 1105 (2004)
3. Haas, M., Hizhnyakov, V., Realo, E., Jõgi, J.: Phys. Status Solidi, B Basic Res. **149**, 283 (1988)
4. Smirnov, G.V., van Bürck, U., Potzel, W., Schindelmann, P., Popov, S.L., Gerdau, E., Shvydko, Y., Rüter, H.D., Leupold, O.: Phys. Rev. **A71**, 023804 (2005)

5. Kagan, Y., Afanasiev, A.M., Kohn, V.: J. Phys. C. Solid State Phys. **12**, 615 (1979)
6. Kagan, Yu.: Hyperfine Interact. **123/124**, 83 (1999)
7. Hannon, J.P., Trammel, G.T.: Physica B **159**, 161 (1989)
8. Hannon, J.P., Trammel, G.T.: Hyperfine Interact. **123/124**, 127 (1999)
9. Smirnov, G.V.: Hyperfine Interact. **123/124**, 31 (1999)
10. Gradshtein, I., Ryzhik, I. (eds.): Tables of Integrals, Series and Productions. Academic, New York (1965)
11. Haas, M., Realo, E., Winkler, H., Meyer-Klaucke, W., Trautwein, A.X., Leupold, O., Rüter, H.D.: Phys. Rev., B **56**, 14082 (1997)

Hyperfine Interact (2006) 167:861–867
DOI 10.1007/s10751-006-9382-6

Multipurpose spectrometer TERLAB for depth selective investigation of surface and multilayer

S. M. Irkaev · V. G. Semenov · V. V. Panchuk · N. A. Makarov

Published online: 7 December 2006

Abstract The multipurpose spectrometer for nondestructive, depth selective investigation of physical and chemical properties of a surface and bulk is described. It realizes opportunities of Mössbauer and X-ray Fluorescence Spectroscopy in normal and TER-conditions, Mössbauer and X-ray diffractometry and also Mössbauer and X-ray Reflectometry. Some analytical characteristics and capabilities of a spectrometer are illustrated as an example of research with a model sample.

Key words total external reflection · surface · hyperfine field · TXREF · GIMS

1 Introduction

Nowadays different industrial technologies require the knowledge of physical and chemical properties of the surface, thin films and multilayer artificial structures. That is why the study is directed to the creation of new techniques and improvement of the existing ones. Special attention is given to the nondestructive methods, which allow carrying out the depth selective element, phase and structural analysis of the ultrathin surface layers in nanometer range.

The use of the total external reflection (TER) phenomenon in various spectrometric methods based on the interaction of the electromagnetic radiation with matter produced a true revolution and sharply increased sensitivity of these methods.

The process of total external reflection (TER) of electromagnetic radiation is inherently surface sensitive [1–4].

It is known that the variation of the angle of the incidence radiation in the range near TER leads to the change of penetration depths in the investigated surface. This allows us to

S. M. Irkaev (✉)
Institute for Analytical Instrumentation, RAS, 198103 St. Petersburg, Russia
e-mail: sobir_irkaev@mail.ru

V. G. Semenov · V. V. Panchuk · N. A. Makarov
St. Petersburg State University, 199164 St. Petersburg, Russia

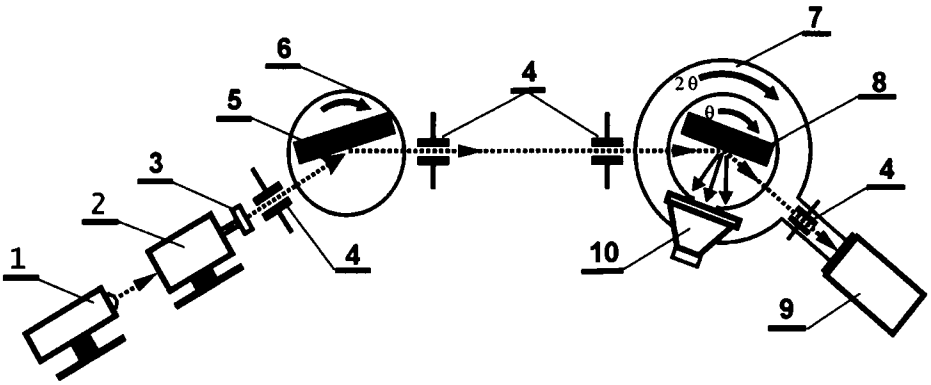

Figure 1 Optical scheme of the spectrometer. *1* – X-ray tube, *2*. – Doppler modulator, *3* – Mössbauer source, *4* – slit collimators, *5* – monochromator, *6* – two-circle goniometer, *7* – automated two-circle goniometer, *8* – sample, *9* – detector of speculary reflected radiation, *10* – detector of secondary radiation, *11* – slit collimator.

receive information about physics and chemistry of surface at different depths. A modern approach in carrying investigation includes simultaneous application of several methods, which would allow us to receive fuller information about the analyzed object.

The X-ray and Mössbauer Reflectometry allow us to determine the depth profile of electron and nuclear susceptibility and also the thickness of film and surface roughness. X-ray fluorescence spectroscopy in TER condition (TXREF) gave us a chance to extract information about the depth profile of elements. Grazing incidence Mössbauer spectroscopy (GIMS) allows to establish the phase, and electronic and magnetic states. The methods of X-ray and Mössbauer diffraction are valuable for the determination of the crystal and magnetic structure of the surface.

The multipurpose spectrometer TERLAB realizes in its scheme the above-mentioned techniques. The choice of these methods is caused by the fact that they all are based on the use of electromagnetic radiation with wavelengths lying in the same range. Due to the similarity of TER angles (from 0.071 to 0.154 nm), various information about element, phase and structure is extracted from the same depths of surface layers. Moreover, the similarity of schemes is supplemented by identical registration, control equipments and processing systems.

2 Block-diagram of spectrometer

The optical scheme of the spectrometer, based on the Bragg–Brentano focusing system is shown in Figure 1.

Monochromatization of radiation, which is necessary for the selection of this or that spectral line from the complex X-ray tube or radioactive source energy spectra, is maintained by monochromator 5, where pyrolitic graphite is used. The narrow plane–parallel radiation necessary for carrying out the experiments is formed by the slit collimators 4, which restrict the divergence of the beam within the limits ±0.2 mrad. The exact setting of the angles of incidence and reflection are provided by the automated two-circle goniometer 7, where the investigated sample and detector are installed.

The Si-PIN diode is used as a detector 10 for the measurement of X-ray-fluorescence spectra, its active area is 13 mm^2 and its energy resolution – 200 keV. In the Mössbauer mode the sample under investigation is placed inside the electron chamber of the detector so that the surface of interest faces the working volume of the chamber where a gas mixture of He+8% CH_4 fed through a nipple, flows at a rate of 2 cm^3/min. The anode of this chamber consists of three tungsten wires (20 μm in diameter) attached to the insulating base. The working gas used for detection of gamma- and X-rays is a mixture of Ar+8% CH_4 fed through the nipple at a rate of 2 cm^3/min. The detector is provided with an additional beryllium window so that the detector can also be used in the conventional backscattering geometry [5]. The specularly reflected radiation is detected by the Xe gas proportional counter 9.

The 50 W air-cooled tubes with copper and molybdenum anodes are used as a source of X-ray radiation. The ribbon type radioactive isotope ^{57}Co(Rh) is used as a source 3 of Mössbauer radiation.

The analytical bench of the spectrometer ensures the easy and reliable establishment of the grazing angles, the convenience of regulation of the incidence radiation, the possibility to change the type of the sample without the change of the experimental geometry.

The electronic system of the spectrometer consists of a power amplifier, control systems for step motors, two channel high voltage power supply, Doppler modulation and processing system of Mössbauer channel, control system of semiconductor detector, processing system of X-ray fluorescence channel, laser source power supply and operation module and power supply for the X-ray tube.

The operation of the two-circle goniometer step motors is controlled by the PC via LPT port. Two modes of operation are available: independent and dependent operation of step motors. Independent operation is necessary for adjustment of the zero positions of the optical scheme. The dependent mode ensure work in the geometry, which is necessary for registration of the specular reflection curves as well as for the accumulation of X-ray fluorescence and Mössbauer spectra in grazing incidence geometry.

The electronics are installed in PC via ISA ports.

The software was developed for the spectrometer operation.

3 Investigation procedure

The investigation procedure comprises several stages.

The first stage is the alignment of the optical scheme. For the alignment of the scheme and for determination of zero positions of the sample under investigation and the registration devices the optical method with a laser source of radiation is used.

In the second stage the X-ray fluorescence and Mössbauer spectra are measured at the normal (90°) angle of radiation at the specimen. That allows us to extract the preliminary determination of elements in sample and its Mössbauer parameters (isomer shift, quadrupole splitting, hyperfine fields).

The third stage consists of the reconstruction of the depth profile of real and imaginary parts of the electron susceptibility of the investigated surface. The profile could be determined as a result of mathematical processing of specularly reflected curves, using the data about elemental and phase content, received at the second stage.

The fourth stage determines the range and the step value of angle variation. These parameters can be determined by the penetration depth of excited radiation, which is extracted from the profile of electronic susceptibility.

At the final step, we measure a series of X-ray fluorescence and Mössbauer spectra at grazing incidence determined at the previous stage. Execution of these four stages allows us to determine the depth profile of elements and phase distribution.

4 Numerical simulation of analytical signals

In order to extract analytical information we used a model of interaction of radiation with a medium carried out in [6, 7]. On the base of this model fitting algorithms of experimental data were developed. We used a model of anisotropic multilayer medium. In that case, the surface is divided into several layers. Within the range of each layer the value of electronic and nuclear susceptibility are considered constant. It should be taken into account that the radiation field at the surface includes not only the incident wave but also the specularly reflected wave.

For the modeling of secondary radiation emission which is an analytical signal in X-ray fluorescence and Mössbauer spectroscopy it is necessary to determine the total intensity of radiation in every layer depending on the angle of incidence of primary radiation. Besides, it was necessary to take into consideration the absorption of secondary radiation during transmission through the above lying layers. As a result of solving these tasks, the algorithm of formation of analytical signal for X-ray fluorescence and Mössbauer spectroscopy with registration of the secondary electrons was developed.

5 Fitting of experimental data

The fitting package consists of four programs.

The first two programs are intended for treatment of X-ray fluorescence and Mössbauer spectra. In the case of X-ray fluorescence, one can determine the energy of spectral line and its intensity, which allows to carry out the multi-element analysis.

For Mössbauer spectra the values of isomer shifts, quadrupole splittings and hyperfine magnetic fields are determined.

The third program is intended for determination of the hyperfine interaction parameter in Mössbauer spectra. The necessity of creation of such a program is caused by the fact that spectral lines in Mössbauer spectra of thin films produce poor resolution.

The treatment of specularly reflected curves and intensity of secondary radiation versus the angle of incidence are carried out by fitting of the theoretical model to experimental data with the help of variation of the parameters we are looking for. In order to solve this task the fourth program was developed. The majority of parameters used for fitting of experimental data are fundamental parameters. These parameters are e.g.,: electronic susceptibility, mass absorption coefficient for definite wavelength, energy, etc.

All the programs are mutually coordinated. Information received from one program is used in all other programs.

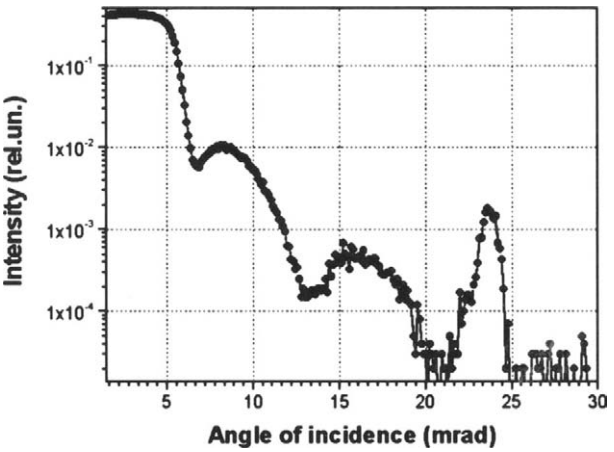

Figure 2 X-ray reflectivity curve (CuKα, λ=0.154 nm).

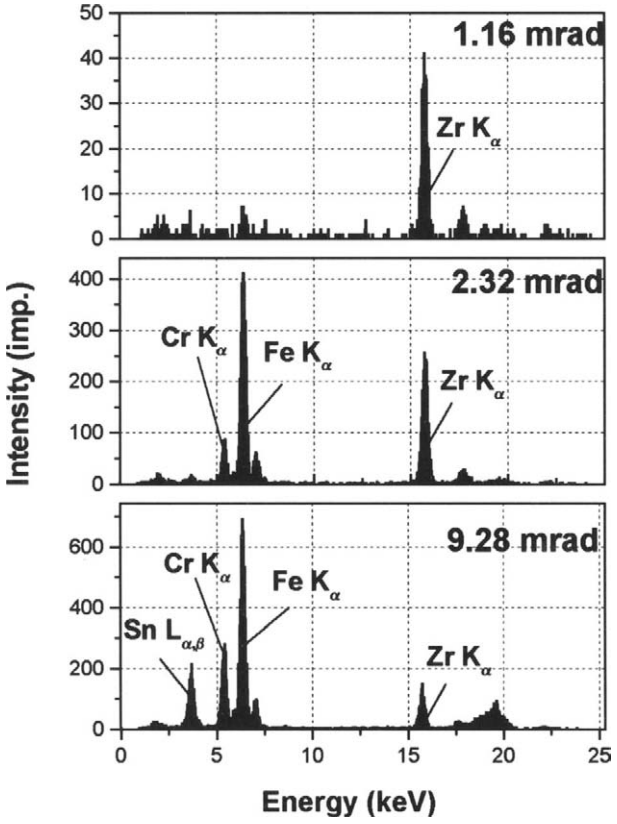

Figure 3 X-ray fluorescence spectra of multilayer $Zr_{9.5\ nm}$/[$Cr_{0.49\ nm}$/$Fe_{0.91\ nm}$]×26/$Cr_{50\ nm}$/glass.

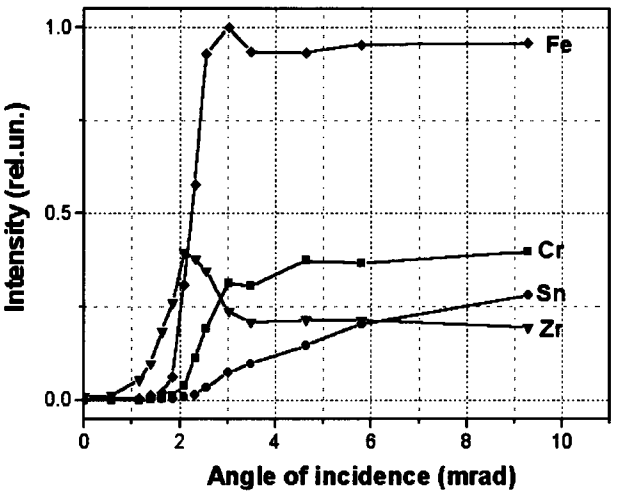

Figure 4 Depth profile of elements in multilayer structure $Zr_{9.5\ nm}/[Cr_{0.49\ nm}/Fe_{0.91\ nm}]\times 26/Cr_{50\ nm}$/glass.

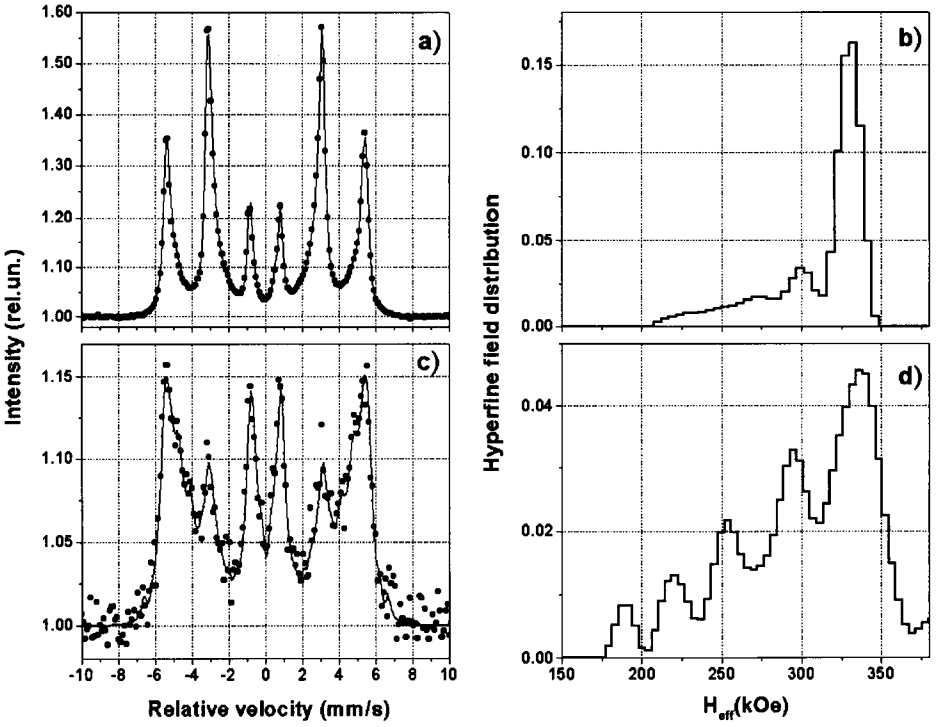

Figure 5 Experimental backscatter Mossbauer spectrum (*dots*) **a** and processing result (*line*), **b** function of hyperfine fields distribution, **c** conversion electron spectrum at the angle of 13.53 mrad and **d** distribution of hyperfine fields.

6 Example

The capabilities of the spectrometer are demonstrated by the investigation of artificial multilayer structure $Zr_{9.5\ nm}/[Cr_{0.49\ nm}/Fe_{0.91\ nm}]\times 26/Cr_{50\ nm}$/glass.

During the first stage, the specularly reflected curve was measured (Figure 2). According to the results of the processing of this curve the distribution of depth profile of electron density was determined. The Bragg maximum in the reflection curves shows that the period of separate layer is 3.3 nm.

At the next stage, the measurements of X-ray fluorescence spectra in the range of TER angles were carried out (Figure 3).

The results of processing of these spectra allowed us to determine the change of intensity of characteristic radiation versus the angle of incidence for all structural elements (Figure 5).

The fitting of theoretically calculated dependencies of fluorescence line intensity versus grazing incidence to experimental data allowed to restore the deviation of element concentration with depth (Figure 4).

Measurements of Mössbauer spectra in the range of total external reflection angles let us to define the portion of Fe atoms and evaluate the most probable neighbors of these atoms in the interface region.

Figure 5a present a Mössbauer spectrum measured in the backscatter mode. Processing of this spectrum (Figure 5b) gives the distribution function of the hyperfine interactions, which shows that the most of Fe atoms (about 60%) forms the iron layer, while the rest (40%) are located at the boundaries between the iron and chromium layers. The Mössbauer spectrum measured at the Bragg angle (Figure 5c) allowed an increase the contribution of the interface atoms to Mössbauer spectrum due to forming in the multilayer the standing waves. The processing of this spectrum (Figure 5d) allowed us to restore the most probable neighbors of Fe atoms in the interface region.

Acknowledgments The authors would like to thank M.A. Andreeva for helpful discussions, N.N. Salaschenko for providing the multilayer structure, J. G. Sevostianov and his colleagues for the creation of producing technology of the ribbon type Mössbauer source. We are also pleased to acknowledge Russian Foundation of Basic Research and the Foundation for Assessment to Small Innovative Enterprises for financial support of this work (Grant No. 02-02-0829).

References

1. Yoneda, Y.: Phys. Rev. **113**, 2010 (1963)
2. Stoev, K.N., Sakurai, K.: Spectrochim. Acta, Part B **54**, 41 (1999)
3. Klockenkamper, R.: Total-reflection X-ray fluorescence analysis. Chem. Anal. **140** (1997)
4. Irkaev, S.M., Andreeva, M.A., Semenov, V.G. et al.: Nucl. Instrum. Methods **B74**, 545 (1993)
5. Irkaev, S.M., Semenov, V.G.: Scientific Instrumentation **10**(1), 94 (2003)
6. Irkaev, S.M., Andreeva, M.A., Semenov, V.G., et al.: Nucl. Instrum. Methods **B74**, 554 (1993)
7. Andreeva, M.A., Irkaev, S.M., Semenov, V.G.: Hyperfine Interact. **97/98**, 605 (1996)

Hyperfine Interact (2006) 167:869–873
DOI 10.1007/s10751-006-9371-9

Automated Mössbauer spectroscopy in the field and monitoring of fougerite

D. Rodionov · G. Klingelhöfer · B. Bernhardt · C. Schröder · M. Blumers · S. Kane · F. Trolard · G. Bourrie · J.-M. R. Génin

Published online: 14 November 2006

Abstract A special experimental setup for in-field applications was developed at Mainz. It incorporates hardware for automated positioning of the Mössbauer sensor head, a Plexiglas tube, and a modified version of the space proven Miniaturized Mössbauer Spectrometer MIMOS II (Klingelhöfer et al., *Science*, 306:1740–1745, 2004; Klingelhöfer et al., *J. Geophys. Res.*, 108(E12):8067, 2003; Klingelhöfer et al., *Hyperfine Interact.* 144/145:371–379, 2002; Génin et al., *Solid State Sci.*, 7:545–572, 2005). MIMOS operates in backscattering geometry, thus no sample preparation is required. Also dedicated software for running measurement sequences (e.g., different depth positions at different times etc.) was developed. The setup can work autonomously up to several weeks in the field. Preliminary results confirm that fougerite mineral found in hydromorphic soils is Fe^{II-III} hydroxycarbonate green rust.

Key words methodology · hydromorphic soil · MIMOS II · environment · fougerite · green rust

D. Rodionov · G. Klingelhöfer (✉) · C. Schröder · M. Blumers
Institut Inorganic and Analytical Chemistry, Johannes Gutenberg-University Mainz,
Staudinger Weg 9, Mainz 55128, Germany
e-mail: klingel@mail.uni-mainz.de

B. Bernhardt
von Hoerner und Sulger, Schwetzingen, Germany

S. Kane
School of Physics, D.A. University, Khandwa Road Campus, Indore 452017, India

F. Trolard · G. Bourrie
UR Géochimie des Sols et des Eaux, INRA, BP 80, Aix-en-Provence 13545, France

J.-M. R. Génin
LCPME, UMR 7564, CNRS-Université Henri Poincaré,
405 rue de Vandoeuvre, 54600 Villers lès Nancy, Nancy, France

1 Introduction

Current applications for in situ soil monitoring in the field as well as the investigation of bore holes and extracted drill cores (up to a few meters long) will be discussed.

In particular in the case of soil monitoring both soil solutions and solid phases can be simultaneously analysed by in situ Moessbauer spectroscopy, thus enabling direct identification of iron-bearing phases and quantitative measurement of the distribution of iron oxidation states. Fast mineralogical transformations were observed at well defined points in soil, as evidenced by Fe^{II}/Fe^{III} ratio variations when Mössbauer spectra were acquired at different times at the same depth. Variations of the watertable level, of pE and pH of the soil solution were simultaneously observed explaining these mineralogical transformations.

2 The instrument and experimental setup

2.1 The instrument MIMOS II

The Mössbauer spectrometer MIMOS II, which is designed and fabricated at the University Mainz [1, 2], was originally developed for the exploration of the surface of the planet Mars and other planetary surfaces. It is intrinsically simple, rugged, and has sufficient radiation shielding to protect personnel and other instruments.

The instrument MIMOS II (Figure 1) is operating in backscattering geometry measuring the scattered 14.41 keV Mössbauer radiation and the 6.4 keV Fe X-rays. In backscattering geometry no sample preparation is needed. Measurements will be done by placing the detector head against the rock or soil to be analyzed, or by positioning it in front of the sample having physical contact via support structures like the Plexiglas tube described in this paper. The field of view of the instrument is circular (diameter ~1 to 2 cm). The average information depth for Mössbauer data is of the order of 150–300 μm, assuming basaltic rock composition.

The main parts of the instrument are the gamma- and X-ray detector system, the ^{57}Co Mössbauer source, which is embedded in a solid rhodium metal matrix attached to a titanium holder, the radiation collimator, the Mössbauer drive and its control unit, and the data acquisition and spectrometer control unit. The detector system consists of Si PIN-diodes, charge sensitive pre- and filter amplifiers, and single channel analyzers. The miniaturized Mössbauer drive is of the double loudspeaker type and has weight of about 50 g (Figure 1).

The spectrometer control and data acquisition system generates the velocity reference signal and collects the data. The data are stored in its own on-board memory, but can be transferred at any time via a standard serial interface to a computer. The instrument can be configured in different ways. For the field tests with the Rocky-7 rover [3] the whole instrument, with two detectors, including all the electronics, was assembled in a single housing with dimensions of about 90×65×45 mm and a total mass of less than 500 g.

2.2 Experimental setup for in-field applications

The instrument developed for terrestrial applications, e.g., in soils, is split into two parts: (a) the sensor head and (b) the printed circuit board carrying the digital electronics for instrument control, communication, data acquisition and storage. The sensor head has

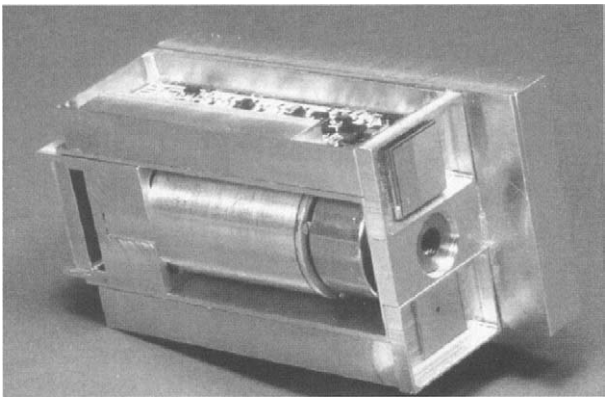

Figure 1 MIMOS II sensor head (two-detector version for terrestrial applications). Dimensions are about 80 mm in length, and 45×30 mm width.

Figure 2 Plexiglas tube with the electronics box on *top*. The length of the tube is about 2 m, with a diameter of about 20 cm.

incorporated two detector systems for the backscattering mode, and no reference channel. Therefore only one Mössbauer source is installed, with typically an initial activity of 100–150 mCi. The weight of the sensor head is about 300 g. The power consumption of the instrument is in the order of 2 W, so it can be operated easily over an extended period by battery. The MIMOS II instrument is mounted into a Plexiglas tube (Figure 2) which is installed in an hydromorphic soil in the field permitting investigations down to about 1.6 m depth. The mobile platform runs down with a distance of 1.75 mm per turn. A motor driller is used to bore a hole with a diameter a little smaller as the tube to achieve good contact between the outer wall of the tube and the soil. In this way the structure of the soil itself is not disturbed.

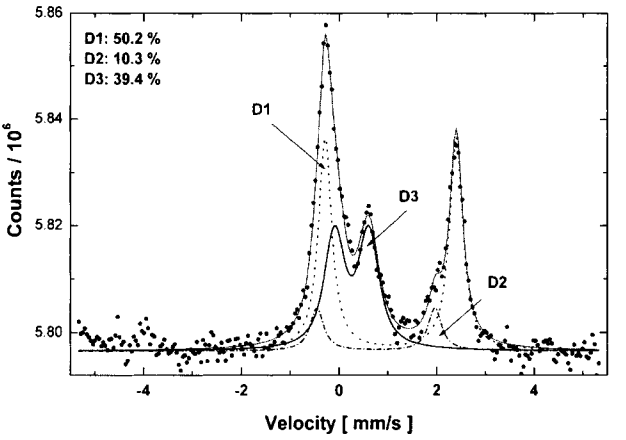

Figure 3 Example of in situ measurements (1.5 days).

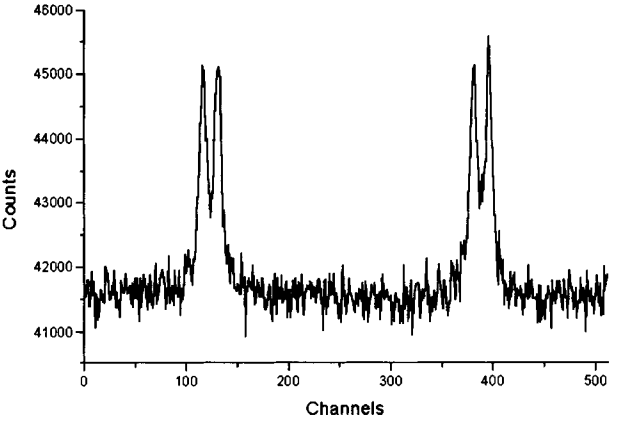

Figure 4 Example of a calibration spectrum (pyrite, 24 h, 2 mCi source, room temperature (lab measurement), target is mounted on the *outer side* of the tube).

The sensor head on the movable platform consists of the miniaturized Mössbauer drive and two PIN diode detector channels (up to four detectors can be used with the actual electronics). All digital electronics and motor arrangement is mounted in a waterproof box on top of the tube. Data can be downloaded from the instruments electronics at an RS-232 interface without opening the box. Also provided are diagnostic modes like pulseheight analysis of the detectors and acquisition of the Mössbauer drive velocity error signal (typically 1–3‰ non-linearity) in digital format. Two temperature sensors acquire a temperature log file of the ambient temperature in the box and at the sensor head parallel to the Mössbauer spectra.

Positioning of the sensor head to different depths is done by a stepping motor arrangement. The reproducibility of the measured spot is better than 0.1 mm. The position is calibrated using an end switch at the top hard stop.

A portable PC can be connected via COM port to the board. Special software has been developed to control and program measurements. It includes built-in firm-ware (which receives commands from the external PC and performs all operations with MIMOS and the movement unit) and external control program. Using this software it is possible to perform calibration (using a special calibration "switch," which is located at the top part of tube), to position the MIMOS sensor head at the desired depth (precision is better than 0.1 mm), to collect Mössbauer spectra, and to run automatic sequences in the so-called "scan" mode.

In the "scan" mode, the instrument acquires up to 13 Mössbauer spectra at different depths. Acquisition times and depths are programmable parameters which are sent to the instrument before starting a new session. From then on all operations run autonomously without any connection to PC. No additional human interference is required after programming – the setup will work autonomously up to several weeks (or longer, if a solar battery setup is used). The setup has a power failure protection. Backups of the main memory (including all instrument parameters and science data) to a non-volatile EEPROM memory is done on a regular basis (every 10 min). In case of power failure all data can be safely restored.

3 First results

With a total iron concentration at about 4% in the bulk soil, spectra are obtained after 1–2 days of count accumulation. An in situ Mössbauer spectrum measured at field temperature is displayed in Figure 3. Also, calibrations were done in the lab. One example is present at Figure 4. It demonstrates that the instrument can acquire Mössbauer spectra with reasonable statistics even with low intensity sources. The spectrum (Figure 3), which displays three quadrupole doublets D_1, D_2 and D_3, is that of the fougerite mineral [4] encountered in gley soils and responsible for its bluish-green colour where D_1 and D_2 with a large quadrupole splitting are attributed to Fe^{II} state and D_3 to Fe^{III}. Intensities of the peaks that are found to be 50, 10 and 40% from computer fitting are consistent with the Fe^{II-III} hydroxycarbonate green rust where at stoichiometry intensity ratios are 1/2:1/6:1/3.

Acknowledgements This work was funded by the German Space Agency DLR, PROSE/PNSE programs (CNRS-INRA, France) and the Brittany Region, France.

References

1. Klingelhöfer, G., Morris, R.V., Bernhardt, B., Schröder, C., Rodionov, D.S., de Souza Jr., P.A., Yen, A., Gellert, R., Evlanov, E.N., Zubkov, B., Foh, J., Bonnes, U., Kankleit, E., Gütlich, P., Ming, D.W., Renz, F., Wdowiak, T., Squyres, S.W., Arvidson, R.E.: Science **306**(5702), 1740–1745 (2004)
2. Klingelhöfer, G., Morris, R.V., Bernhardt, B., Rodionov, D., de Souza Jr., P.A., Squyres, S.W., Foh, J., Kankeleit, E., Bonnes, U., Gellert, R., Schröder, Ch., Linkin, S., Evlanov, E., Zubkov, B., Prilutski, O.: J. Geophys. Res. **108**(E12), 8067 (2003)
3. Klingelhöfer, G., Bernhardt, B., Foh, J., Bonnes, U., Rodionov, D., de Souza, P.A., Schröder, Ch., Gellert, R., Kane, S., Gütlich, P., Kankeleit, E.: Hyperfine Interact. **144/145**, 371–379 (2002)
4. Génin, J.-M. R., Aissa, R., Gehin, A., Abdelmoula, M., Benali, O., Ernstsen, V., Ona-Nguema, G., Upadhyay, C., Ruby, C.: Solid State Sci. **7**, 545–572 (2005)

Hyperfine Interact (2006) 167:875–879
DOI 10.1007/s10751-006-9372-8

New in-beam Mössbauer spectroscopy station at the Budapest Research Reactor

T. Belgya · K. Lázár

Published online: 8 November 2006

Abstract We report about a new in-beam Mössbauer station which is intended to utilize the cold neutron source and guide system installed on the 10th beam line of the Budapest Research Reactor. This new in-beam facility enables us to broaden the number of nuclides accessible for Mössbauer studies in various materials. In this article we describe our new system and summarize the possibilities of its application to Mössbauer spectroscopy.

Key words In-beam Mössbauer spectroscopy · Mössbauer effect · neutron beam excitation

1 Introduction

Mössbauer spectroscopy provides information about chemical bonds, oxidation states, geometrical location and magnetic state of the Mössbauer isotope as influenced by its surrounding atoms.

The Mössbauer effect was observed on 82 isotopes of 44 elements, but only a few of them are used in practice. The ^{57}Fe and ^{57}Co pair is used in 80% of the cases, while ^{119}Sn and all the others share the remaining 20% equally. The rare usage of the other Mössbauer nuclei is due to difficulty in their production or the short half-life of the exciting radioactive nuclei or their small abundance.

A way to increase the number of usable Mössbauer nuclei is to produce them in-beam. In 1965, Hafemeister and Brooks Shera [1] demonstrated the Mössbauer effect of the 29.4-keV neutron capture gamma ray of ^{40}K in a neutron beam of 2.4×10^6 cm^{-2}s^{-1}. They concluded that the recoilless fraction is not greatly impaired by the displacement of the ^{40}K atom due to neutron capture. The Mössbauer effect was also observed in neutron capture reaction on ^{56}Fe by Berger [2] and more recently a new in-beam facility was installed in Japan at the JRR-3M reactor with a neutron flux of 5×10^7 n·cm^{-2}·s^{-1}. This instrument has been

T. Belgya (✉) · K. Lázár
Institute of Isotopes, Chemical Research Center (CRC),
Hungarian Academy of Sciences (HAS), 1525 POB. 77, Budapest, Hungary
e-mail: belgya@iki.kfki.hu

demonstrated to be useful in studying neutron capture induced chemical changes in solid iron disulfide (FeS_2) [3].

2 The new in-beam Mössbauer facility

After the installation of the cold neutron source in the year of 2001 [4], it became possible to widen our experimental possibilities at the Budapest Neutron Center (BNC). From a number of possibilities the in-beam Mössbauer spectroscopy has been selected and the realization is in progress.

It has been under construction at the Budapest Research Reactor. The station is operated by researchers of the Institute of Isotopes, HAS in the framework of the BNC. After the commissioning the equipment will be part of the EU FP6 MNI3 [5] program, which makes it easily accessible for EU users. The instrument can be used on line, but during reactor shutdown, activated short lived Mössbauer sources will also be utilized. During the on line operation a beam of guided cold neutrons produce the Mössbauer transitions continuously.

The cold neutron flux, transmitted by a focused supermirror guide is measured to be about 10^9 n cm^{-2} s^{-1} at the target position. The beam shutter is installed at the beginning of the 7 m long guide section to avoid the high radiation caused by the closed beam shutter. The experimental area is shielded by concrete walls from the rest of the guide system on both at the entering and at the leaving sides. Near the guide end a collimator system made of lead and Li-6 enriched polyethylene is placed in the hole of the shielding concrete walls to minimize the unwanted radiations. The diameter of the beam, passing through this collimator system, at the target position is about 1×1 cm^2. The neutron beam enters through a thin vertical window (made of Mylar and beryllium) into the cryostat and leaves on its opposite side. The cryostat can be operated in the 3–360 K temperature range with liquid helium or nitrogen cooling. The maximum areas of the Mössbauer source and absorber are about 1 cm^2 thus the available maximum source strength is about 1 GBq. The sample holder is fixed to the end of a steel tube, which holds the moving rod mechanics as well as the absorber at its bottom. The Mössbauer transducer (Wissel MVT 1,000) is fitted to the top of the specifically modified cryostat (Konti-IT-Cryostat-Spektro-He product of CryoVac) and an aluminum moving rod connected to the transducer moves the Mössbauer source up and down in the beam.

For the acquisition of the Mössbauer spectra two detectors, a Na(Tl) and a HPGe, can be used in absorption geometry. The HPGe detector enables us to study the low energy prompt gamma spectrum in high resolution in order to be able to select the energy window for the Na(Tl) detector. The detectors can be mounted below the cryostat and perpendicular with their axis to the impinging neutron beam. The data acquisition system is equipped with an 8 K channel Wissel CMCA-550 USB pulse height and Mössbauer analyzer, which can be connected to a personal computer with USB port. Transducer driving electronics, a function generator and high voltage power supplies, all placed in a NIM Bin, complete the system. A schematic drawing of the equipment is given in Figure 1.

3 Expected performance of the system and fields of applications

Prospective prompt-gamma nuclei for in-beam excitation are identified in cooperation with Rick B. Firestone (LBL). The best candidates are (^{40}K, ^{56}Fe, ^{66}Zn, Gd, Er, Dy, Yb, Hf, W). Below we present the most characteristic data for these nuclei in Table I. We have estimated

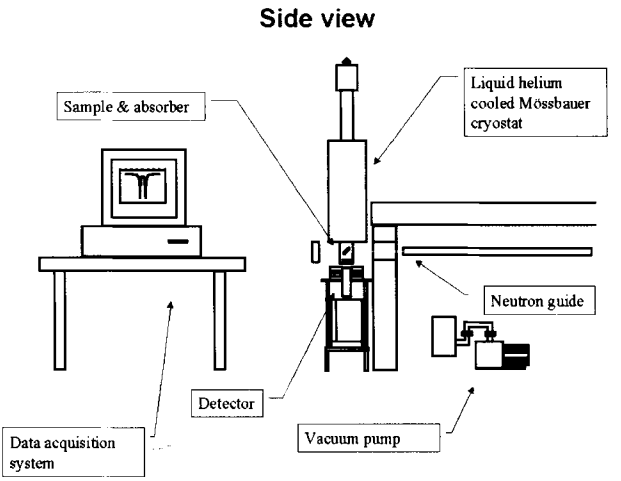

Figure 1 Schematic drawing of the in-beam Mössbauer equipment.

Table I Expected rates for experiment length of 10^5 s

Target nuclide	E_γ (keV)	σ_γ (b)	Rate [a] (s^{-1})	Rate [b] (s^{-1})	Percent [c]
^{157}Gd	79.00	4,010	28 757	717 180	0.009
^{155}Gd	88.97	1,380	9 896	203 390	0.014
^{167}Er	79.80	18.2	131	3 512	0.14
^{161}Dy	80.66	13.3	95	9 576	0.32
^{177}Hf	93.18	13.3	95	9 576	0.32
^{163}Dy	73.39	1.37	10	986	1.01
^{179}Hf	93.33	0.8	5.7	576	1.32
^{171}Yb	78.74	0.67	4.8	482	1.45
^{154}Gd	86.54	0.57	4.1	410	1.6
^{173}Yb	76.47	0.4	2.9	288	1.9
^{160}Dy	25.65	0.27	1.9	194	2.3
^{182}W	46.48	0.192	1.4	138	2.7
^{182}W	99.08	0.155	1.1	112	3.0
^{160}Dy	74.57	0.086	0.62	62	4.0
^{56}Fe	14.41	0.149	0.8	107	4.26
^{66}Zn	93.31	0.0344	0.23	25	7.0
^{39}K	29.83	1.38	0.069	994	144

[a] Rate of Mössbauer effect

[b] Rate of Mössbauer gamma ray

[c] Uncertainty of the rate ratios in percentage

the expected event rates with the parameters of our Mössbauer system. For the mass of Mössbauer nuclei in the source and absorber we used 0.001 mol, while for the recoilless fractions we assumed 0.1 for both of them. The Mössbauer absorption cross-section was set to 10^{-19} cm^2 in all cases. For both the source and absorber nuclei the natural abundance were taken into account. The natural elemental gamma ray production cross-sections σ_γ were taken from our experimental results [6]. It can be clearly seen that the rare earth elements give the smallest uncertainty for the same length of measurements. Some of the light elements can also be studied, however in the case of potassium enriched absorber would be needed to achieve better statistics.

Beside the prompt gamma sources we can make use of the short-lived continuously activated sources. The corresponding Mössbauer nuclei are ^{153}Er, ^{166}Er, ^{175}Lu, ^{186}Os, ^{191,192}Ir, ^{195}Pt and ^{197}Au. They can also be used in-beam similarly to the prompt gamma rays. Their characterization, however, is more complicated and is outside the scope of this short paper.

Longer half-life nuclei can be activated in the reactor and used during the reactor shutdown periods (^{141}Pr, ^{127}I, ^{129}I, ^{181}Ta, ^{182}W).

Fields of applications include: biological systems (^{40}K prompt excitation), catalysts (^{193}Ir, ^{196}Pt, ^{197}Au short-lived continuous activation), HTC superconductors (^{141}Pr reactor shutdown, Dy prompt activation), geological samples and magnetic layers (Gd, Er, Dy, Yb prompt and short-lived activation), the chemical behavior of the nuclear waste of ^{129}I (^{127}I reactor shutdown), corrosion in nuclear and traditional power plants (^{57}Co reactor shutdown) or in-beam produced ^{57}Fe to study chemical changes induced by radiation in solid states as described by Kubo et al. for all of the in-beam reactions.

Acknowledgements One of the authors (TB) would like to thank the support of the Bolyai Scholarship of the Hungarian Academy of Sciences. The contributions of R.B. Firestone and A. Vértes, E. Kuzmann and Z. Klencsár are greatly acknowledged. We also salute to late Gábor Molnár for his great effort and enthusiasm in starting up this project.

Appendix

The following formulas were used to estimate the rate for the Mössbauer effect in the absorption geometry:

$$R_{M\_\mathrm{effect}} = \frac{d_s}{M_s} N_A \Phi \sigma_{\gamma\mathrm{elem}} f_s \left(1 - \exp\left(-\frac{d_a}{M_a}\frac{N_A}{A_a}\sigma_0 \theta_a\right)\right) f_a \Delta\Omega_a \Delta\Omega_{\mathrm{det}} \varepsilon_{\mathrm{det}}$$

The first part (ending with f_s) describes the Mössbauer source rate for the specified gamma energy in thin sample approximation, while the second part describes the effect of the Mössbauer absorber and the geometry. We used the following values in the estimation:

Table II

Table II Values used in Mössbauer effect estimation.

Variable	Value	Description
d_s, d_a	0.001 M_s	Mol weight used in the estimation
M_s, M_a		Mol weight of element (s and a indices for source and absorber
N_A	6 10^{23}	Avogadro number
Φ	10^9 n cm^{-2} s^{-1}	neutron flux hitting the target (source)
$\sigma_{\gamma elem}$	Variable	Gamma ray production cross section
f_s, f_a	0.1	Recoilless fraction
A_a	1 cm^2	Surface of the absorber
σ_0	10^{-19} cm	Mössbauer absorption cross section
θ_a	Variable	Isotopic ratio of the absorber nucleus
$\Delta\Omega_a$	0.994	Absorber geometrical efficiency
$\Delta\Omega_{\mathrm{det}}$	0.0012	Detector geometrical efficiency
$\varepsilon_{\mathrm{det}}$	1	Detector intrinsic efficiency

References

1. Hafemeister, D.W., Brooks Shera, E.: Phys. Rev. Lett. **14**, 593–595 (1965)
2. Berger, W.G.: Z. Phys. **225**, 139–165 (1969)
3. Kubo, M.K., Kobayashi, Y., Yamada, Y., Nomoto, Y., Saito T., Sakai, Y., Shoji, H., Yonezawa, C., Matsue, H., Nakada, M.: Industrial applications of Mössbauer effect. In: Gracia,M., Marco, J.F., Plazaola, F. (eds) AIP CP vol. 765, p. 348. Springer, Berlin Heidelberg New York (2005)
4. Rosta, L., Cser, L., Révay, Zs.: Appl. Phys., A Mater. Sci. Process. **74**, S292 (2002)
5. http://www.bnc.hu/
6. Révay, Z., Firestone, R.B., Belgya, T., Molnár, G.L.: Prompt Gamma-ray Spectrum Catalog. In: Molnár, G.L. (ed) Handbook of Prompt Gamma Activation Analysis with Neutron Beams, pp. 173–366. Kluwer, Boston, (2004)

Hyperfine Interact (2006) 167:881–885
DOI 10.1007/s10751-006-9373-7

Effects of trapped electrons on the line shape in emission Mössbauer spectra

Yu. D. Perfiliev · V. S. Rusakov · L. A. Kulikov · A. A. Kamnev · K. Alkhatib

Published online: 14 November 2006

Abstract To explain line broadening in emission Mössbauer spectra as compared to the corresponding absorber measurements, the model of trapped electrons has been proposed. Auger electrons (emitted, e.g. after electron capture by ^{57}Co or after the converted isomeric transition of ^{119m}Sn), as well as secondary electrons, may be trapped in the proximity to the nucleogenic ion. Electrons captured by lattice traps at different distances from the daughter ion induce an asymmetric distribution of quadrupole splitting in the resulting emission spectra, as shown in a few examples. This model is supported by estimates of quadrupole splitting values which may be caused by such trapped electrons located at specified distances from the nucleogenic atom.

Key words trapped electrons · line broadening · emission Mössbauer spectroscopy · quadrupole splitting distribution function

1 Introduction

Resonant lines in emission Mössbauer spectra can be significantly broadened as compared to those in transmission spectra. Line broadening in emission spectra is observed for many

Y. D. Perfiliev (✉) · L. A. Kulikov
Department of Radiochemistry, Faculty of Chemistry, M.V. Lomonosov Moscow State University, 119992 Moscow, Russia
e-mail: perf@radio.chem.msu.ru

V. S. Rusakov
Department of General Physics, Faculty of Physics, M.V. Lomonosov Moscow State University, 119992 Moscow, Russia

A. A. Kamnev
Laboratory of Biochemistry of Plant–Bacterial Symbioses, Institute of Biochemistry and Physiology of Plants and Microorganisms, Russian Academy of Sciences, 410049 Saratov, Russia

K. Alkhatib
Laboratory of Inorganic Chemistry, Department of Chemistry, Albaath University, Homs, Syria

isotopes, but more often and with more evidence in experiments with ^{57}Co [1, 2] and ^{119m}Sn [3] in solids. Note that in both the two types of nuclear decay for ^{57}Co and ^{119m}Sn (via electron capture and converted isomeric transition, respectively), an electron vacancy in an internal shell of the daughter atom is formed. Filling in this vacancy results in the emission of X-ray radiation or electrons owing to the Auger effect. For electron emission, while an electron hole moves to the outer levels, the more Auger transitions take place, the higher the degree of ionization of the atom. The emitted electrons induce numerous physical and chemical processes within the environment of the daughter atom [4, 5], leading to the broadening of resonant lines, especially in molecular and non-crystalline compounds.

Line broadening is often ascribed to the states of the nucleogenic atoms featured by various slightly different microenvironments. A possible reason for their appearance was proposed for ^{57}Co in CoO [2] as a consequence of electron capture by Fe^{4+}, formed owing to the Auger ionisation, from a neighbouring Co^{2+}, producing Co^{3+}. Thus, a wide range of local environments could be produced resulting in small differences in the field at the Fe nuclei. However, line broadening was later shown [6] to be caused by the presence of defects in the initial CoO. This mechanism cannot account for line broadening in more complex molecular compounds. Attempts were also made [7] to explain line broadening by the formation of various chemical forms of the nucleogenic ion.

In our earlier work [8], the disappearance of the hyperfine magnetic structure in emission Mössbauer spectra was observed, which was interpreted as a consequence of the formation of trapped electrons participating in spin exchange with the daughter ion. In this work, a deeper analysis of emission Mössbauer spectra has been performed in order to find the evidence for such trapped electrons.

2 Materials and methods

The ^{57}Co-containing systems under study were: sample 1, a dry complex of anthranilic (*o*-aminobenzoic) acid with $^{57}Co^{2+}$ (carrier-free; 3.7×10^7 Bq); sample 2, a dry complex of indole-3-acetic acid with $^{57}Co^{2+}$ (also carrier-free; samples 1 and 2 were obtained by drying 1.0 ml of 1 mCi $^{57}Co^{2+}$-containing aqueous solution of a corresponding acid, taken in a large excess with regard to $^{57}Co^{2+}$, in air); sample 3, a solution of $^{57}CoCl_2$ in ethanol (containing also 4 M carbon tetrachloride) rapidly frozen in liquid nitrogen. The ^{119m}Sn-containing system (sample 4) was represented by ethanolic solutions of $^{119m}SnCl_2$ with different concentrations of $CrCl_2$ (added as an electron scavenger) rapidly frozen in liquid nitrogen. Other details of emission Mössbauer measurements and statistical treatment of the experimental data were described elsewhere [8–11].

3 Results and discussion

Emission (^{57}Co) Mössbauer spectra measured at T=293 K (sample 1) and at the temperature of liquid nitrogen (samples 2 and 3), are presented in Figure 1a–c. Each of the three spectra shows a superposition of two doublets related to $^{57}Fe^{2+}$ and $^{57}Fe^{3+}$ ions forming from the parent $^{57}Co^{2+}$ ions owing to competitive reactions of non- or weakly bound electrons in the medium [9]. The components of the spectra are essentially broadened and are typical for locally non-uniform systems [12, 13]. Processing and analysis of

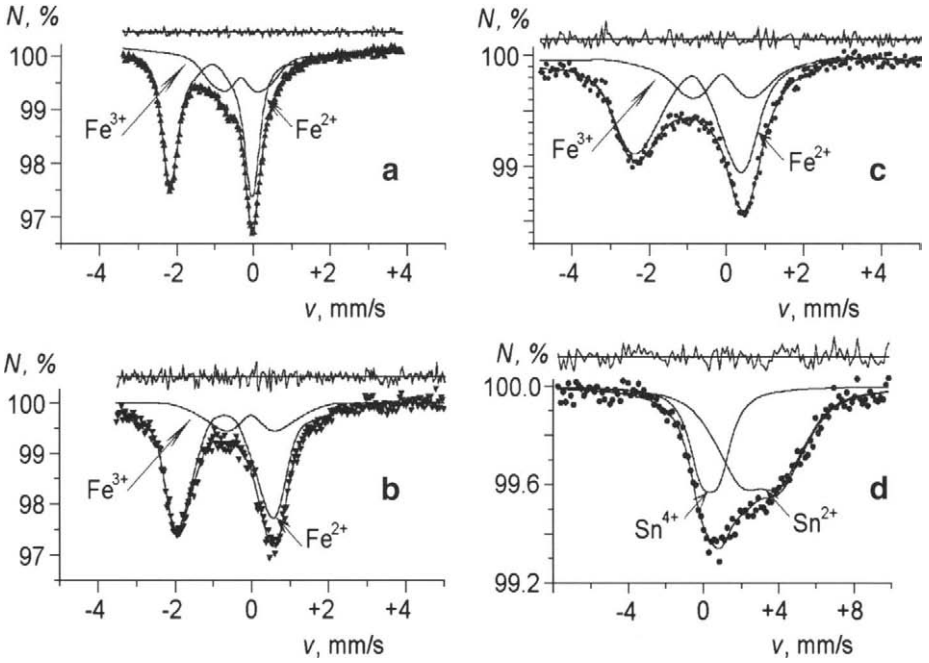

Figure 1 Emission Mössbauer spectra of $^{57}Co^{2+}$-containing complexes of **a** anthranilic acid and **b** indole-3-acetic acid in the dry state, as well as **c** $^{57}CoCl_2$ solution in ethanol with 4 M CCl_4 and **d** $^{119m}SnCl_2$-containing ethanol solution with $CrCl_2$ added as an electron scavenger (see text) rapidly frozen in liquid nitrogen. *N* Transmission (%), *v* velocity (mm/s); measured at T=293 K for **a** and at T=80 K for **b**–**d**.

the spectra were carried out by extracting two independent distribution functions $p(\Delta)$ of quadrupole splitting Δ for excited nuclear levels of the ^{57}Fe nucleus with the spin 3/2 [13] using the program DISTRI from the program complex MSTools [12].

The results of extraction of the distribution functions $p(\Delta)$ corresponding to $^{57}Fe^{2+}$ and $^{57}Fe^{3+}$ ions are presented in Figure 2. All the distribution functions are featured by asymmetric dome-shaped curves with a somewhat less steep slope at larger Δ values, which is more expressed for $^{57}Fe^{3+}$ ions (see the left-side upper plot in Figure 2). Such a shape of the $p(\Delta)$ function can be induced by charged particles located in the vicinity of Fe atoms at various distances from them. Considering the processes of post-decay relaxation of the system, electrons can be the most probable charged particles capable of creating a large electric field gradient.

The above model is supported by estimations of Δ values that could be created by a single electron located at distances 2, 1.5 or 1 Å from Fe ions (see the numbers at the vertical dashed lines in Figure 2). Calculation of the electric field gradient was carried out on the assumption of point localization of charges using the program LATTICE [12]. The quadrupole moment value of a ^{57}Fe nucleus in the excited state, Q=0.146 b [14], and the Sternheimer antishielding factors for Fe^{3+} ($\gamma_\infty = -9.14$) and for Fe^{2+} ($\gamma_\infty = -11.5$) [15] were used. According to these estimations, such a trapped electron can induce alterations in the electric field gradient. Thus, trapped electrons located at different distances from the nucleogenic atom can induce an asymmetric distribution of Δ. As an alternative to such trapped electrons, one may consider the formation of radicals near Fe atoms, or ion-radicals

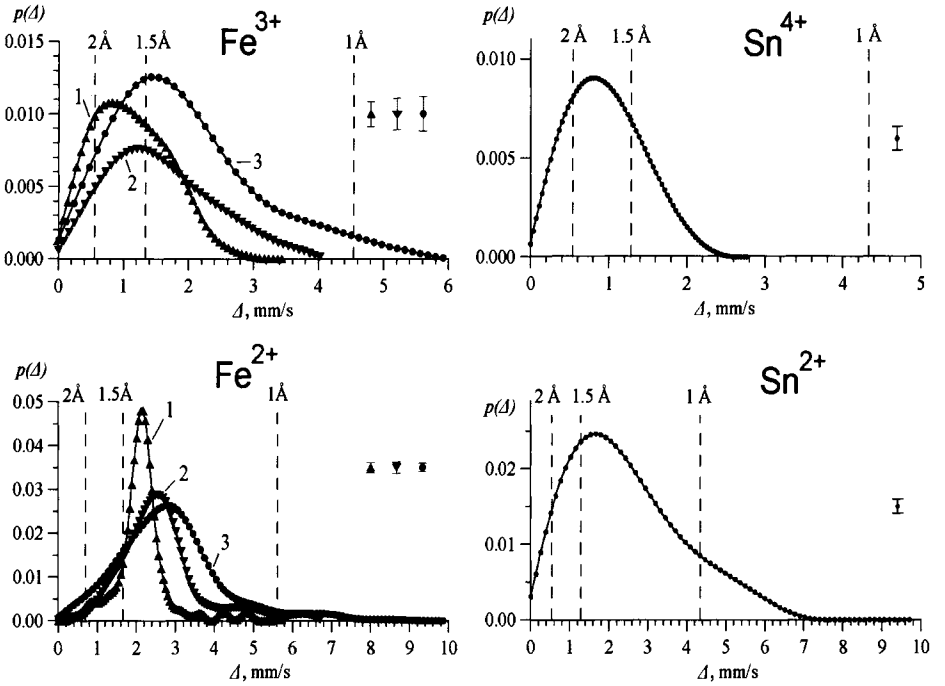

Figure 2 Distribution functions $p(\Delta)$ of quadrupole splitting (Δ) calculated for the components of emission (^{57}Co) Mössbauer spectra a–c presented in Figure 1 (see text) for the nucleogenic $^{57}Fe^{2+}$ (*left-side lower plot*) and $^{57}Fe^{3+}$ (*left-side upper plot*), as well as for the components of emission (^{119m}Sn) Mössbauer spectrum d presented in Figure 1 (see text) for Sn^{2+} (*right-side lower plot*) and Sn^{4+} (*right-side upper plot*). For the *vertical dashed lines*, see text.

more strongly influencing the electric field gradient. However, this seems less probable as, first, such radicals can form not in all systems and, second, electrons therein are valent with more delocalised wave functions and would therefore induce smaller electric field gradients. Note also that in the transmission Mössbauer spectra of the similar complexes containing Fe^{2+} and/or Fe^{3+} ions [16, 17], the line width values can be considered as normal considering the thickness of the samples, and the distribution of quadrupole splittings was symmetric.

A similar asymmetric distribution of Δ was also observed in emission spectra involving the isotope ^{119m}Sn. In Figure 1 (plot d), a spectrum is given of frozen ethanol solution containing $^{119m}SnCl_2$. For improving the statistics, the spectrum was obtained by summing up several spectra of the same type [10] in the presence of different concentrations of $CrCl_2$ which had been added as an electron scavenger. The large line width values observed for both Sn^{2+} and Sn^{4+} are indicative of non-uniformity of the system. In this case, the distributions of Δ are also asymmetric (Figure 2; right-side plots) and less steep at larger Δ values. In Figure 2 (right-side plots), dashed lines also represent the results of calculation of Δ according to the model used in the ^{57}Co emission experiments (see above and Figure 2, left-side plots). The quadrupole moment of the ^{119}Sn nucleus in the excited state, Q= −0.109 b [18], and the Sternheimer antishielding factor for Sn^{2+}, $\gamma_\infty = -21$ [15], were taken for calculations (the same value of γ_∞ was used for Sn^{4+} owing to the lack of relevant data in the literature for Sn^{4+}).

4 Conclusions

Line broadening in emission Mössbauer spectra can be caused by the formation of trapped (solvated, hydrated) electrons. Electrons trapped at various distances from the daughter ion induce distortions of the line shape which is described by an asymmetric distribution function for quadrupole splitting. Thus, the line shape may serve as a basis for estimating the distribution of trapped electrons in the vicinity of the daughter ion. Broadening is more strongly expressed for disordered systems which contain many traps for electrons.

Acknowledgements This work was supported in parts by the Russian Foundation for Basic Research (Grant 05-03-33079), NATO (Grants LST.NR.CLG.981092 and CPB.NR.NREV.981748), as well as under the Agreement on Scientific Cooperation between the Russian and Hungarian Academies of Sciences for 2002–2004 and 2005–2007.

References

1. Ladriere, J., Apers, D.: J. Phys. (Paris) **37**, 913 (1976)
2. Wertheim, G.K.: Phys. Rev. **124**, 764 (1961)
3. Ishiba, S., Yamada, M., Negita, H.: J. Phys. (Paris), **Colloque C2, 40**(Suppl. 3), 428 (1979)
4. Friedt, J.M., Danon, J.: At. Energy Rev. **184**, 893 (1980)
5. Perfiliev, Y.D.: Izv. Ross. Akad. Nauk. Ser. Fiz. (Bulletin of the Russian Academy of Science. Ser. Phys., in Russian) **63**, 1383 (1999)
6. Perfiliev, Y.D.: Zhurn. Fiz. Khimii (in Russian) **60**, 1057 (1986)
7. Kobayashi, T., Makita, T., Fukumura, K.: Hyperfine Interact. **56**, 1533 (1990)
8. Vrabchic, P., Perfiliev, Y.D., Kulikov, L.A.: Fiz. Tverdogo Tela (Solid State Phys., in Russian) **21**, 3151 (1979)
9. Perfiliev, Y.D., Kulikov, L.A., Bugaenko, L.T., Babeshkin, A.M., Afanasov, M.I.: J. Inorg. Nucl. Chem. **36**, 2145 (1976)
10. Perfiliev, Y.D., Kulikov, L.A., Byakov, V.M., Stepanov, S.V., Alkhatib, K., Bugaenko, L.T.: Khim. Vysokikh Energii (High Energy Chem., in Russian) **37**, 390 (2003)
11. Kamnev, A.A., Antonyuk, L.P., Kulikov, L.A., Perfiliev, Y.D.: BioMetals **17**, 457 (2004)
12. Rusakov, V.S.: Izv. Ross. Akad. Nauk. Ser. Fiz. (Bulletin of the Russian Academy of Science. Ser. Phys., in Russian) **63**, 1389 (1999)
13. Rusakov, V.S.: Mössbauer Spectroscopy of Locally Non-uniform Systems. Scientific Press Dept. of the Institute of Nuclear Physics, Natl. Nuclear Centre of the Republic of Kazakhstan, Almaty, 2000 (in Russian)
14. Rusakov, V.S., Khramov, D.A.: Izv. Ross. Akad. Nauk. Ser. Fiz. (Bulletin of the Russian Academy of Science. Ser. Phys., in Russian) **56**, 201 (1992)
15. Marathe, V.R., Trautwein, A.X.: Calculation of charge density, electric field gradient and internal magnetic field at the nuclear site using molecular orbital cluster theory. In: Thosar, B.V., Lyengar, P.K. (eds.) Advances in Mössbauer Spectroscopy, Chapter 7, pp. 398–454. Elsevier, Amsterdam (1983)
16. Kamnev, A.A., Kuzmann, E., Perfiliev, Y.D., Vankó, G., Vértes, A.: J. Mol. Struct. **482–483**, 703 (1999)
17. Kamnev, A.A., Shchelochkov, A.G., Perfiliev, Y.D., Tarantilis, P.A., Polissiou, M.G.: J. Mol. Struct. **563–564**, 565 (2001)
18. Haas, H., Menninger, M., Andreasen, H., Damgaard, S., Grann, H., Pedersen, F.T., Petersen, J.W., Weyer, G.: Hyperfine Interact. **15/16**, 215 (1983)

Hyperfine Interact (2006) 167:887–892
DOI 10.1007/s10751-006-9374-6

Development of a new method of the analysis mossbauer spectra of systems with nuclear heterogeneity

A. I. Pikulev · V. A. Semenkin · O. B. Milder · E. G. Novikov

Published online: 12 December 2006

Abstract At present there are two main rival fitting approaches to mossbauer spectra: restoration of hyperfine parameter distribution and discrete deconvolution one. Use of the parallel circuit of processing in which computing procedure the exchange of the calculated values between continuous and discrete algorithms is used for the first time is offered.

Key words mossbauer spectroscopy · fitting algorithm

1 Introduction

Now the scientific and practical interest is aimed at application mossbauer spectroscopy for research of systems with local nuclear heterogeneity. Such objects are amorphous matter, spin glasses, invar alloys, many minerals and meteorites. Prominent feature of such systems is presence of nonequivalent environments of resonant nucleus. In this connection mossbauer spectra of systems with local nuclear heterogeneity represent superposition of the great number subspectra and contain a minimum of the aprioristic information. Mathematical processing and physical interpretation of parameters of such spectra demand long computing procedures. At the present moment a plenty of methods and algorithms for processing and interpretations spectra has been developed.

The diagram of the basic existing methods and algorithms of processing shows their variety, both in mathematical approaches, and in ways of realization of algorithms (Figure 1). However, as is evident from the experience of application of the various approaches, resulting reliability of processing of experimental spectra of systems with local nuclear heterogeneity does not allow to receive an unequivocal model of physical interpretation of parameters.

The purpose of the present work is creation of a uniform universal technique of the analysis mossbauer spectra for various systems with nuclear local heterogeneity. Synthesis

A. I. Pikulev (✉) · V. A. Semenkin · O. B. Milder · E. G. Novikov
Faculty of Experimental Physics, Ural State Technical University, Ekaterinbrug,
Mira, 19 620002, Russia
e-mail: pikulev@uvtb.ru

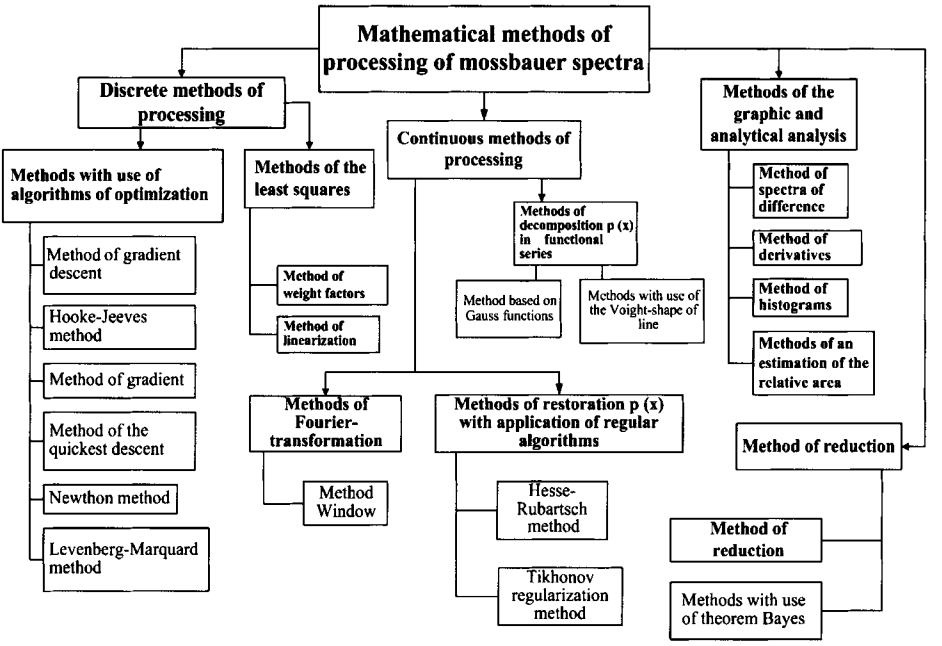

Figure 1 Classification of methods of spectra processing.

of discrete and continuous ways of the description of the form of a spectrum which bases on modern algorithms of optimization and search of decisions of incorrect problems is put in a basis of a method.

The discrete way of the description of a resonant line represents the form of mossbauer spectrum line as superposition of discrete component [1]:

$$I(v) = I(\infty)\left[1 - \sum_{p}\sum_{i,j}^{k} \frac{A_p}{\left(1 + \frac{4}{\Gamma_p^2}\left(v - B_p H_i - \delta - C_p \Delta E_{Q_j}\right)^2\right)}\right], \quad (1)$$

where i, j – number of mossbauer subspectra line; p – number of nonequivalent components in spectrum; A_p – ratio of intensity lines of spectrum; B_p – the factors which are taking into account hyperfine magnetic structure of power levels of ^{57}Fe nucleus; C_p – the factors which are taking into account hyperfine electric structure of ^{57}Fe power levels; ΔE_{Qj} – quadrupole splitting; H_i – hyperfine magnetic field; δ_j – isomer shift; Γ – half-width of mossbauer subspectra lines; $I(v)$ – intensity of resonant line; $I(\infty)$ – intensity in absence of resonance.

The problem of interpretation of a spectrum in this case consists in finding of a vector of discrete parameters $x=\{x_1, x_2,..., x_n\}$. As x_n parameter acts isomer shift δ, hyperfine magnetic field on nucleus H_{eff}, quadrupole splitting ΔE_Q and amplitude of lines A_p.

At the continuous description a resonant line is represented as function $p(x)$ of density of hyperfine parameters distribution [2]:

$$I(v) = I(\infty)\left[1 - \int_{x_{\min}}^{x_{\max}} p(x) f(x, v) dx\right], \quad (2)$$

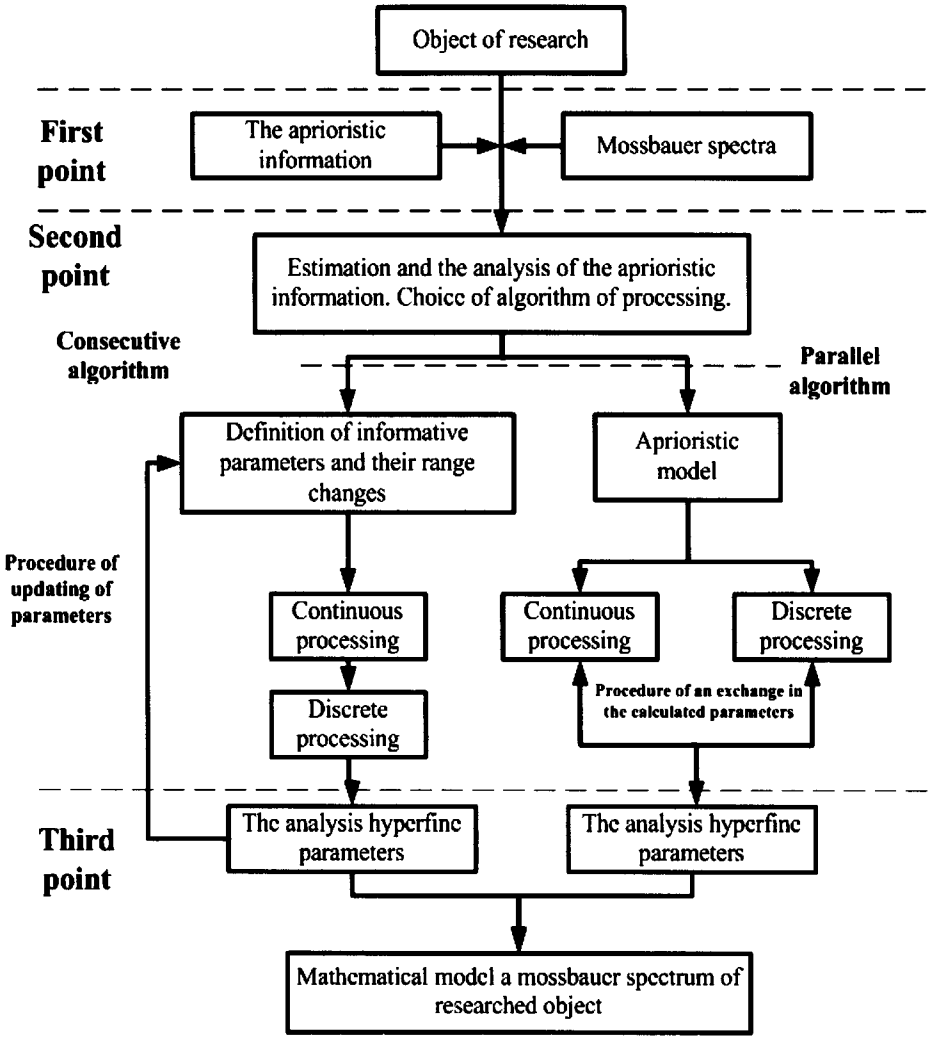

Figure 2 The block diagram of the developed method of processing.

where v – speed; $[v_{min}, v_{max}]$ – the speed change interval; $I(v)$ – intensity of resonant absorption; $p(x)$ – function of density of hyperfine parameter x probability; $[x_{min}, x_{max}]$ – interval on which the hyperfine parameter is determined.

In that case spectrum interpretation is reduced to the decision of the integrated Eq. 2 concerning unknown $p(x)$ function. The received functions of distribution for each parameter allow to receive estimations of their most probable values of hyperfine parameters.

2 New method of the analysis mossbauer spectra

Let's consider the developed procedure of decoding a spectrum (Figure 2). At the first point the analysis of the aprioristic information on a structure of researched object will be carried out: presence of phases, their crystal structure, type of nuclear and magnetic ordering, a

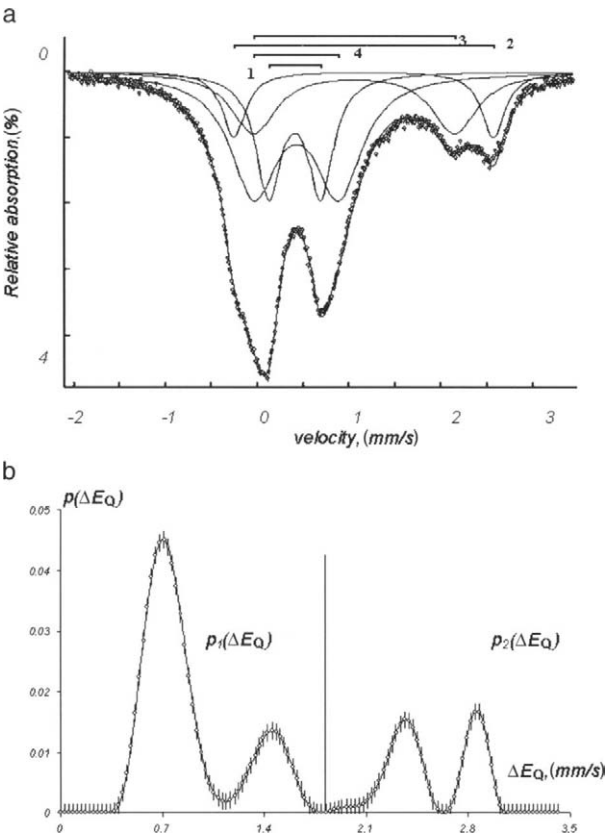

Figure 3 Results of application of parallel algorithm for processing spectra of ceramic: (a) Discrete processing. (b) Continuous processing.

dynamic condition etc. The aprioristic information allows to construct preliminary analytical models to formulate criteria of selection of more exact model from set approached. As a source of the similar information are considered theoretical calculations (g-factors of the basic and excited condition resonant nuclear, nuclear volume, parameters of a crystal lattice) and previous experimental researches in which some elements and parameters of the future model (the X-ray analysis, the neutron diffraction analysis, the electron diffraction investigation) were already estimated. Thus the estimation of quantity of phases is made, informative hyperfine parameters are allocated, probable ranges of change of hyperfine parameters are determined.

At the second point construction of initial mathematical models is made. By results of the analysis of the aprioristic information of models we offer two algorithms of processing a spectrum: parallel and consecutive (Figure 2).

At the minimum of the aprioristic information it is offered to use widespread consecutive algorithm of processing. It consists in consecutive construction of continuous and discrete models of an experimental spectrum. In a case when aprioristic representations about object are sufficient, we offer to use the parallel algorithm consisting in simultaneous construction of continuous and discrete models of a resonant spectrum and having high speed of convergence. Thus in a new method procedure of an exchange by the calculated values between continuous and discrete algorithms for the first time is used. Such procedure

Table I Values of hyperfine parameters of an mossbauer spectrum of a sample of archeological ceramics

Component	δ (mm/s)		ΔE_Q (mm/s)	
	Discrete processing	Continuous processing	Discrete processing	Continuous processing
1 – Fe^{2+}	0.378±0.001	0.375±0.001	0.795±0.002	0.807±0.002
2 – Fe^{3+}	1.166±0.002	1.167±0.001	1.944±0.002	1.871±0.001
3 – Fe^{3+}	1.132±0.001	1.122±0.001	2.820±0.002	2.767±0.002
4 – Fe^{2+}	0.500±0.001	0.481±0.001	1.565±0.002	1.568±0.002

allows the decoding problem converges faster. One more advantage of the developed algorithm is the opportunity of conducting correlations between hyperfine parameters. The parameters of correlation determined for discrete model, are taken into account at construction of continuous model. Function of required parameter distribution can be represented as several functions, each of which describes the appropriate component a spectrum and is determined on the interval of hyperfine parameter.

Computing procedures of discrete algorithm are realized with the help of a Levenberg–Marquard optimization method [3, 4]. For the decision of a return problem at restoration of hyperfine parameters distribution functions it is used modified Tikhonov regularization method [2]. Feature of used numerical algorithms for the decision of a return problem mossbauer spectroscopy has allowed to increase speed of convergence of fitting process in some times.

At the third point the analysis of the received results will be carried out. Thus specification of parameters is made by correction of initial parameters, change of intervals of existence of required parameters, construction of distribution of other functions of hyperfine parameter distribution. Result of application of the analysis is reception of analytical model of spectrum hyperfine structure.

3 Application of the developed method

The developed method was applied to processing mossbauer spectra of various objects. Mössbauer spectra have been measured on SM2201 Mössbauer spectrometer which is purposely meant for solving precision problems. The experiments were carried out according to the gamma-optical scheme with the constant acceleration moving absorber, at room temperature using the cobalt-57 in chromium matrix source.

As an example of application of parallel algorithm results of the analysis mossbauer spectra of a series of ceramic samples of archeologic monuments of Western Siberia are submitted. Mossbauer spectra of samples had the similar kind given on Figure 3. Numerous researches of similar objects allow to speak about sufficient volume of the aprioristic information [5, 6]. Discrete processing of spectra is carried out by superposition several quadrupole the doublets appropriate Fe^{2+} and Fe^{3+}. As a result of approximation the four-componental model a mossbauer spectrum (Figure 3) is received.

The continuous description of spectra is carried out with the help of two functions of quadrupole splittings distribution, accordingly for two and trivalent iron (Figure 3). Values of position of maxima (the most probable values quadrupole splittings) were compared to results of discrete approximation (Table I).

4 Conclusion

The method of processing the mossbauer spectra, based on new algorithm of a combination of discrete and continuous ways of the resonant line description is developed. Use of the parallel circuit of processing in which computing procedure the exchange of the calculated values between continuous and discrete algorithms is used for the first time is offered. Correlation dependences are entered into computing procedures between hyperfine parameters. Examples of use of a new method for interpretation mossbauer spectra are given.

References

1. Woodhams, F.W.: J.Phys. E **21**, 1067–1070 (1988)
2. Tikhonov, A.N., Arsenin, V.A.: Solutions of Ill-posed Problems. Winston, Washington (1977)
3. Levenberg, K.: Q. Appl. Math. **2**, 164–168 (1944)
4. Marquard, D.: SIAM J. Appl. Math. **11**, 431–441 (1963)
5. Cohen, R. L. (ed.): Applications of Mossbauer Spectroscopy, vol. 1. Academic, NY, San Francisco, London (1976)
6. Eissa, N.A., Sallam, H.A., Keszthelyi, L.: Acta Physiol. Hung. **34**, 337 (1973)

Hyperfine Interact (2006) 167:893–896
DOI 10.1007/s10751-006-9375-5

Radio-frequency controllable quantum interference in Mössbauer spectroscopy

E. K. Sadykov · V. V. Arinin · G. I. Petrov · A. V. Pyataev · F. G. Vagizov · O. A. Kocharovskaya

Published online: 8 November 2006

Abstract The role of quantum interference (QI) in spectra of the resonant Mössbauer scattering is investigated. As a mechanism ensuring the QI conditions, the radio-frequency (RF) mixing of the spin sublevels of the excited nuclear state is considered. It is shown that QI leads to a significant intensity redistribution of the elastic and Raman scattering.

Key words Mössbauer gamma optics

1 Introduction

Mössbauer spectroscopy is a very effective but not the unique application of the Mössbauer effect. *Mössbauer gamma optics* represents another interesting field. The basic purpose of research in that case is to change the properties of gamma (Mössbauer) radiation due to its interaction with the nuclear system, but not to study the material structure. It should be noted, that since the early 1960s [1] the Mössbauer effect has been used as a tool to solve the gamma optics problems (in particular, the *gamma laser problem*). The latest discoveries in the field of optical quantum interference (QI) have also stimulated progress in this area and it has especially been shown that the *quantum interference* (QI) mechanism makes it possible to control the intensity of Mössbauer transitions [2]. The idea of QI and its experimental confirmation have always been essential [3–6]. In this work we study the effects of QI in spectra of Mössbauer resonant scattering under coherent nuclear spin dynamics conditions caused by the resonant RF field. As shown below, the QI, in this case, leads to the enhancement of Raman scattering intensity.

E. K. Sadykov (✉) · V. V. Arinin · G. I. Petrov · A. V. Pyataev · F. G. Vagizov
Kazan State University, Kremlyovskaya Street 18, 420008 Kazan, Russia
e-mail: esad@ksu.ru

F. G. Vagizov · O. A. Kocharovskaya
Physics Department, Texas A&M University, College Station, TX 77840, USA

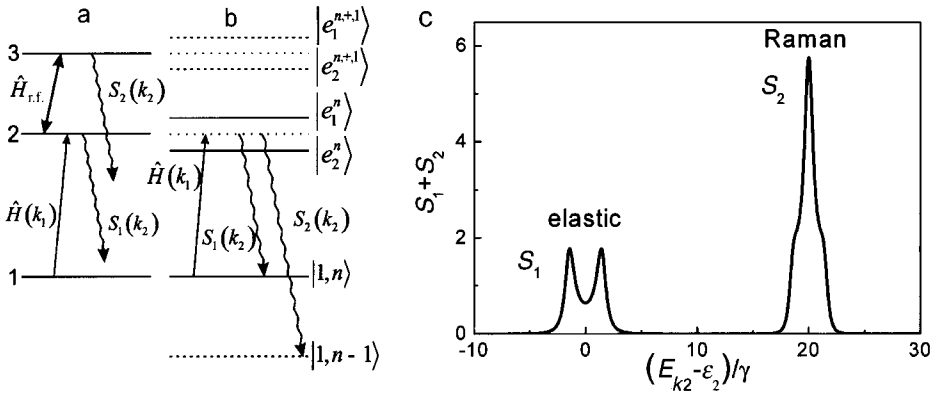

Figure 1 **a** Three-level model system; **b** Equivalent scheme using dressed states; **c** Expected spectra of resonant scattering (Ω_r=1.5, Γ=1, $E_{k0}=\varepsilon_2$ are used).

2 Resonant fluorescence of Mössbauer radiation in the regime of RF resonance in excited nuclear state

Let us consider a three-level model system (Figure 1a). Level 1 represents the ground nuclear state; 2 and 3 represent the excited nuclear spin substates. A strong RF field of frequency $\omega_0(\omega_0 = \omega_{32} = \varepsilon_3 - \varepsilon_2)$ is set up in exact resonance to transition 2–3. In these conditions two excited states form the pair of dressed states (Figure 1b) [6]:

$$e_1^n(t) = \exp\left(-iE_1^n t - \mathrm{in}\omega_0 t\right)\frac{1}{\sqrt{2}}\left(-|2,n\rangle + \exp(i\varphi)|3,n-1\rangle\right), \tag{1}$$

$$e_2^n(t) = \exp\left(-iE_2^n t - \mathrm{in}\omega_0 t\right)\frac{1}{\sqrt{2}}\left(\exp(-i\varphi)|2,n\rangle + |3,n-1\rangle\right), \tag{2}$$

where $|j,n\rangle \equiv |j\rangle|n\rangle$, $|j\rangle$ – jth spin sublevel, $|n\rangle$ – n-photon state of RF field, $E_{1,2}^n = \mp\Omega_r + \varepsilon_2$ – quasienergy, $\Omega_r = |\Omega_0|\sqrt{n}$ – Rabi frequency, $\Omega_0 = |\Omega_0|\exp(i\varphi)$, Ω_0 – the constant of the nucleus–RF mode interaction. Furthermore, we suppose $n \approx \bar{n}$, where $\bar{n}$ is the mean number of photons in the classical RF mode.

We used the scattering amplitudes in the dressed state representation (second order perturbation of the nuclear interaction with the gamma field $\hat{H}_\gamma(k)$) [7]:

$$A_{i,f} \sim \sum_q \int_0^\infty dt \exp(-\Gamma t/2)\langle f(t)|\hat{H}_\gamma\left(\vec{k}_2\right)\left|e_q^n(t)\right\rangle\left\langle e_q^n(0)\right|\hat{H}_\gamma\left(\vec{k}_1\right)|i(0)\rangle, \tag{3}$$

where Γ – the natural width of the Mössbauer level, $|i(0)\rangle = |i(t=0)\rangle = |1\rangle|n\rangle|k_1\rangle$ and $|f(t)\rangle = \exp\left(-iE_f t\right)|1\rangle|n'\rangle|k_2\rangle$ – initial and final states of the system, with total energies $E_i = \varepsilon_1 + n\omega_0 + E_{k1}$ and $E_f = \varepsilon_1 + n'\omega_0 + E_{k2}$, k_1 and k_2 are the wave vectors of the incident and scattered gamma quantum.

The probability of Mössbauer scattering is described by the expression [7]:

$$S_{i,f} \sim \int dE_{k1}\left|A_{i,f}\right|^2 \delta\left(E_f - E_i\right) f_L(E_{k1} - E_{k0}). \tag{4}$$

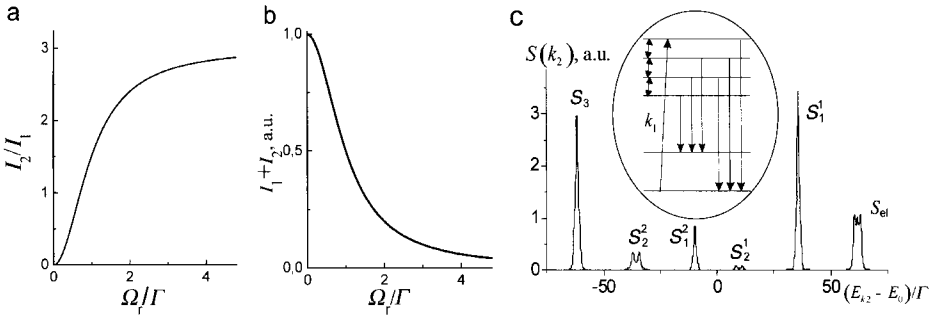

Figure 2 **a** Ratio of line intensities; **b** total scattering intensity; **c** expected spectrum of resonant scattering on isotope Fe^{57} in the condition of the RF resonance on excited nuclear state; E_0 – the Mössbauer level. The *probing line* is tuned to the *sixth line* of the Zeeman sextet, S_{el} – the line of elastic scattering, (S_1^1, S_1^2), (S_2^1, S_2^2) and S_3 – Raman lines of the *first*, *second* and *third order*, respectively. *Superscripts 1 and 2* indicate the different hyperfine components of Raman line.

In this expression the averaging over the gamma photon energies from the Mössbauer source E_{k1} is carried out using the line form function (usually of Lorentz type) $f_L(E_{k1}-E_{k0})$.

According to the expressions (3) and (4) two possible scattering channels (elastic S_1 and Raman S_2) indicated in Figure 1b may be written ($E_{k0}=\varepsilon_2$):

$$S_1(k_2) = S_{k1n,k2n} \sim \left|\frac{1}{ip-\Omega_r}+\frac{1}{ip+\Omega_r}\right|^2 f_L(E_{k2}-\varepsilon_2)\left|\langle 1|\widehat{H}(k_2)|2\rangle\langle 2|\widehat{H}(k_1)|1\rangle\right|^2, \quad (5)$$

$$S_2(k_2) = S_{k1n,k2n-1}$$

$$\sim \left|\frac{1}{ip-\Omega_r-\omega_0}-\frac{1}{ip+\Omega_r-\omega_0}\right|^2 f_L(E_{k2}-\varepsilon_2-\omega_0)\left|\langle 1|\widehat{H}(k_2)|3\rangle\langle 2|\widehat{H}(k_1)|1\rangle\right|^2, \quad (6)$$

$$p = -i(E_{k2}-\varepsilon_2)+\Gamma/2.$$

In Figure 1c the expected spectrum $S_1(k_2)+S_2(k_2)$ is presented according to the assumption that the matrix elements of transitions (1–2) and (1–3) are equal. It is easy to see that in expressions (5) and (6) the interference has both a constructive and destructive character at small values of Ω_r. In particular, S_2 tends to zero as Ω_r tends to zero. However with the growth of Ω_r ($\Omega_r > \Gamma/2$), the character of the interference in (5) and (6) (at the same condition $E_{k0}=\varepsilon_2$) will be reversed. Now at large enough values of Ω_r the intensity of the Raman line I_2 (I_2 is the area under the spectral form S_2) is more than that of the elastic scattering line I_1 (Figure 1c). In other words the nucleus excited to sublevel 2 in these conditions prefers to emit a gamma photon from level 3. Such preference in the scattering channel has been named by us as the "valve" effect.

The ratio I_2/I_1 (the measure of the "valve" effect) monotonously depends on the value of Ω_r (Figure 2a). However the total scattering intensity (I_1+I_2) decreases with increasing Ω_r (Figure 2b). Compromise condition for the experiment to be realized looks as $\Omega_r \approx \Gamma$. This is a condition of excitation by one photon in a phase correlated way of two dressed states interference in which the phenomenon under discussion occurs.

In Figure 2c the expected scattering spectrum for the isotope Fe^{57} is presented [8]. The "valve" effect will take place again if the nuclear excited sublevels are mixed by the RF field. The intensity of the elastic scattering will be reduced due to destructive interference. The intensity of the Raman lines increases, if the line is formed when an odd number of RF photons (n) participates in the process and decreases at an even number of photons. The possibility of observing the effect in Fe^{57} in magnetic materials is confirmed by RF Mössbauer absorption experiments [9, 10]. From the experimental spectra [9] it is easy to estimate the amplitude of the RF hyperfine field induced on a nucleus as h_1=88 kOe, which corresponds to a Rabi frequency Ω_r=1.5 leading to the expected spectrum in Figure 2c.

Acknowledgements This work was supported by the RFBR #04-02-16939, AFOSR, CRDF CGP #RP1-2560-KA-03, NIOKR RT #06-6.1-2003/2005(F).

References

1. Rivlin, L.A.: Questions of radio electronics **6**, 43 (1963)
2. Coussement, R., Van den Bergh, M., S'heeren, G., et al.: Phys. Rev. Lett. **71**, 1824 (1993)
3. Kocharovskaya, O., Kolesov, R., Rostovtsev, Yu.: Phys. Rev. Lett. **82**, 3593 (1999)
4. Sadykov, E.K., Zakirov, L.L., Yurichuk, A.A.: Laser Phys. **11**, 409 (2001)
5. Coussement, R., Rostovtsev, Y., Odeurs, J., et al.: Phys. Rev. Lett. **89**, 107601 (2002)
6. Sadykov, E.K., Arinin, A.A., Vagizov, F.G.: JETP Lett. **82**, 431 (2005)
7. Bashkirov, Sh. Sh., Beljanin, A.L., Sadykov, E.K.: Phys. Status Solidi (b) **93**, 437 (1979)
8. Sadykov, E.K., Arinin, V.V., Zakirov, L.L.: Proceedings of the SPIE, vol. 5402, 463 (2004)
9. Vagizov, F.G.: Hyperfine Interact. **61**, 1359 (1990)
10. Tittonen, I., Lippmaa, M., Ikonen, E., et al.: Phys. Rev. Lett. **69**, 2815 (1992)

Hyperfine Interact (2006) 167:897–901
DOI 10.1007/s10751-006-9376-4

Radio-frequency Mössbauer spectra of the "easy"-plane type magnetic system ($FeBO_3$)

E. K. Sadykov · A. A. Yurichuk · V. Yu. Lyubimov · G. I. Petrov

Published online: 27 October 2006

Abstract The theory of formation of the RF Mössbauer spectra for the "easy"-plane type magnetics ($FeBO_3$) and for various types of RF field polarization is presented. Experiments using both linearly and circularly polarized external RF fields were carried out at different temperatures. At room temperature the experimental spectra for both cases are well described by switching hyperfine (hf) field model. At temperatures close to the Neel temperature (335 K), the spectra in the oscillating and rotating RF field were obtained and their forms are described by models of switching and rotating hf field, respectively.

Key words Mössbauer spectroscopy · magnetic materials · gamma-optics

1 Introduction

Mössbauer radio frequency (RF) experiments on magnetic materials have long been of great interest. Two effects are usually observed in Mössbauer spectra in this case: *the collapse of the hyperfine structure* [1] and *the sideband effect* [2]. The sideband effect has a magnetostriction as well as a magnetization dynamics origin. The collapse effect occurs if fast magnetization reversal regime is achieved under the RF field. Spectra of a more complicated structure are expected if frequency of the RF field is equal to, or less than, the nuclear Larmor frequency, or (and) the fields of magnetic anisotropy (or external fields) inhibit the full magnetization reversal process. In this work, the results of RF Mössbauer measurements under these conditions for the "easy"-plane type $FeBO_3$ and for various types of polarization of the RF field are presented. The theoretical model includes possible relaxation jumps of magnetization, formation of ultrasonic sidebands due to magnetostriction and the self-absorption effect for thick (or isotope-enriched) samples [3–5].

E. K. Sadykov (✉) · A. A. Yurichuk · V. Y. Lyubimov · G. I. Petrov
Kazan State University, Kremlevskaya str.18, 420008 Kazan, Russia
e-mail: esad@ksu.ru

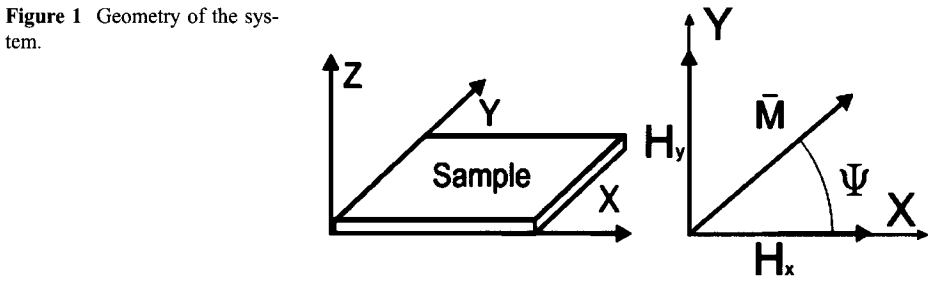

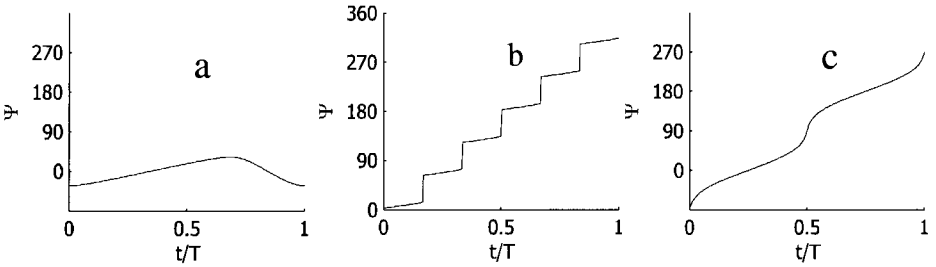

Figure 2 Magnetization behavior for: (a) "weak field" mode, (b) "stepwise motion" mode, (c) "strong field" mode.

2 Physical model

The theoretical model used [3–5] is based on two assumptions:

1. The magnetization lies in the "easy" plane and its direction (angle Ψ) may be determined by minimizing (1) a free energy E_f of the system, consisting of the magnetic anisotropy (2) and the external RF field (3) terms, with respect to the angle Ψ (Figure 1).

$$\frac{dE_f}{d\Psi} = 0; \quad E_f = E_H + E_A \tag{1}$$

$$E_H = -MH(t) = -H_0^x \cos(\omega t) M \cos\Psi - H_0^y \cos(\omega t - \phi_0) M \sin\Psi \tag{2}$$

$$E_A = -K_1 \cos^2 3(\Psi - \phi_1) - K_2 \cos^2(\Psi - \phi_2) \tag{3}$$

(Above) M—the magnetization of the sample, $H(t)$—the external RF field, K_1 and K_2—characteristic parameters of the magnetic anisotropy, Ψ—the angle in plane between the x axis and M (Figure 1).

The anisotropy energy (E_A) takes into account: (a) the crystalline anisotropy resulting from the hexagonal structure of $FeBO_3$ (in this case we have three "easy" axes in the plane with characteristic parameter K_1) and (b) the additional uniaxial anisotropy in the sample plane (with parameter K_2) which most likely has a technological origin. Three modes of magnetization time behavior are expected (Figure 2):

> The "weak field" mode is expected at amplitudes of the RF field which are lower than those of the anisotropy fields. In this case, magnetization oscillates near the minimum energy and its direction is slightly modified.

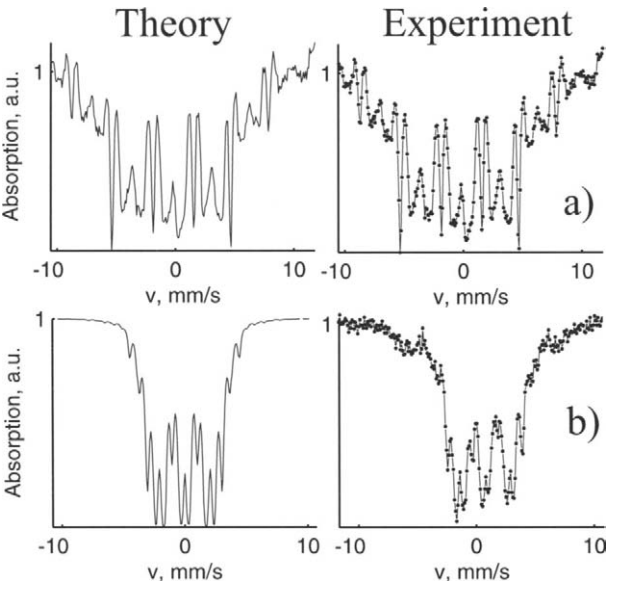

Figure 3 Theoretical spectra for "switching" hf field dynamics for various values of the hf field but at the same value of the ratio R: (a) H_{hf}=330 kOe, f=20 MHz; (b) H_{hf}=170 kOe, f=10 MHz.

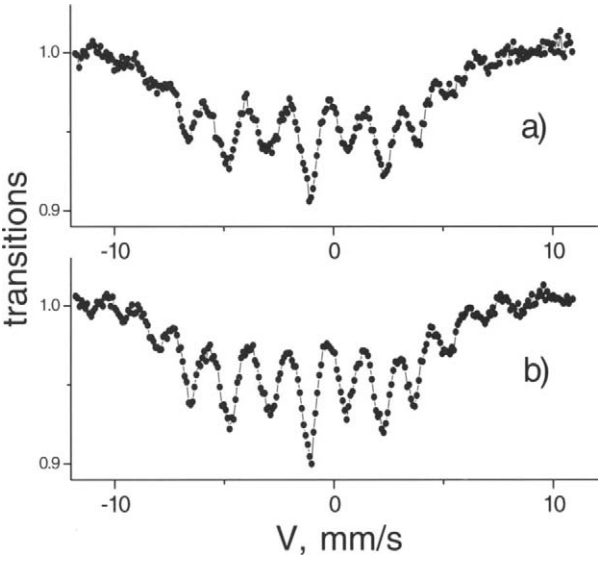

Figure 4 Experimental spectra at room temperature (T=293 K) for rotating (a) and oscillating (b) RF field mode, f=20 MHz, H_{hf}= 330 kOe, H_{RF}=8 Oe.

The "stepwise motion" mode takes place when the RF amplitude is comparable to the anisotropy fields. The stepwise motion of the magnetization is proper to this mode. It means that minimum, in which the magnetic moment resides, at some point vanishes and the magnetization moves to a nearby minimum.

The "strong field" mode is achieved when the RF field amplitude is much greater than that of the anisotropy field. In this case there is usually only one minimum driven by the external RF field.

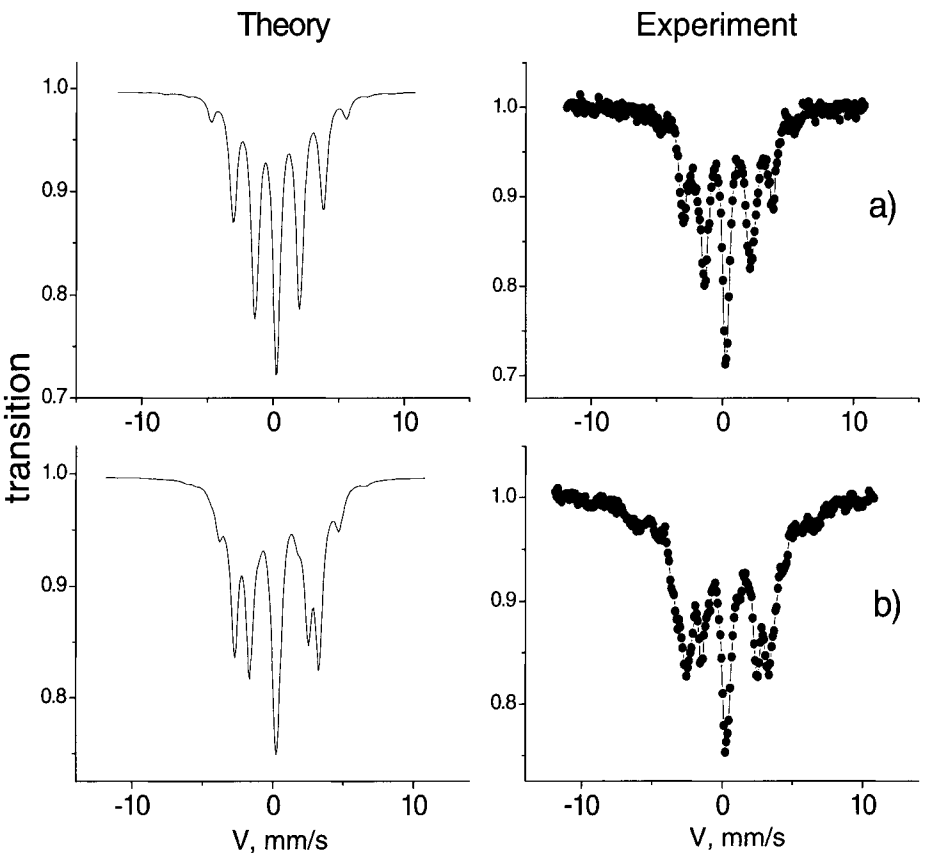

Figure 5 Temperature of sample close to Neel point (T=335 K) (a) oscillating and (b) rotating RF field; f= 20 MHz, H_{hf}=170 kOe, (a) H_{RF}=10 Oe, (b) H_{RF}=7 Oe.

2. Then, we assume that the hf field on the nucleus is strongly correlated with magnetization. This means that we ascribe the time dependence of the magnetization direction to the direction of the hf field. The magnitude of the hf field H_0 is supposed to be constant. Behavior of the hf field in the oscillating and rotating RF fields is reduced to *switching* and *rotating hf field* dynamics in the "strong field" limit, respectively. The spectra have been calculated numerically using super-operator formalism.

3 Features of theoretical spectra

We have studied the 10–30 MHz frequency range, which is interesting because, in this case, the RF field significantly modifies the spectrum, but its frequency is not high enough to achieve the collapse of the hf structure. Besides, the shape of the spectrum depends on the type (*rotating* or *switching*) of the hf field dynamics.

So, for a given type of hf field dynamics, the structure of spectrum is the same if the ratio $R = \omega_{hf}/\omega_{RF}$ of the hf splitting (ω_{hf}) to the RF frequency (ω_{RF}) is maintained constant. In this case, the scale of the spectrum is modified but its structure remains the same (Figure 3).

4 Experimental results

The external RF field of arbitrary polarization (at frequencies 7–30 MHz) is created by two coils. The sample is located where the axes cross, so the field always lies in the easy plane. The thickness of the sample ($FeBO_3$) was 60 μm. The RF amplitude was chosen to be large enough (~10 Oe) to overcome the magnetic anisotropy fields (at least those of crystallographic origin) in the easy plane. Experiments were carried out using both oscillating RF field and rotating RF field. Without RF field, the spectrum was a Zeeman sextet. We expected the observation of Mössbauer spectra corresponding to two types (switching and rotating) of magnetization dynamics. At room temperature, however, the experimental spectra for both cases display the switching hf field dynamics (Figure 4a, b), i.e., the rotating external RF field (Figure 4a) does not lead to a rotating hf field.

The key point of our investigation was a measurement of samples near the Neel temperature (347 K). So at 335 K, the spectra in an oscillating and a rotating RF field were obtained. The shapes of these spectra (Figure 5) are described by switching (a) and rotating (b) hf field dynamics, respectively.

In our model, it was implied that a magnetic sample had a single domain structure, and interactions in the multi-domain structure have not been taken into account. In our opinion, this might be a cause of discrepancy between theory and the experiment at room temperature. At high temperatures, it is possible to assume applicability of the single-domain behavior of magnetization under the RF field [6, 7].

5 Conclusion

RF Mössbauer investigations are stimulated from a gamma optics point of view. RF controllable Mössbauer susceptibility of materials can be used for a purposeful change in the gamma-radiation properties.

Acknowledgement The authors are grateful to G.V. Smirnov for providing the samples.
The work was supported by the grants CRDF CGP #RP1-2560-KA-03, RFBR #04-02-16939 and NIOKR RT 06-6.1-203/2005 (F)

References

1. Pfeiffer, L.: J. Appl. Phys. **42**, 1725 (1971)
2. Pfeiffer, L., Heiman, N.D., Walker, J.C.: Phys. Rev., B **6**, 74 (1972)
3. Sadykov, E.K., Zakirov, L.L., Yurichuk, A.A., Petrov, G.I.: Izv. RAN **65**, 46 (2001)
4. Sadykov, E.K., Skvortsov, A.I.: Phys. Status Solidi, B **158**, 685 (1990)
5. Afanas'ev, A.M., Chuev, M.A., Hesse, U.: JETP **113**, 1001 (1999)
6. Stoner, E.C., Wolfarth, E.P.: Phil. Trans. Royal Soc. A **240**, 599 (1948)
7. Rancourt, D.G., Julian, S.R., Daniels, J.M.: JMMM **51**, 83 (1985)

Hyperfine Interact (2006) 167:903–904
DOI 10.1007/s10751-006-9481-4

ERRATUM

Radio-frequency Mössbauer spectra of the "easy"-plane type magnetic system ($FeBO_3$)

E. K. Sadykov · A. A. Yurichuk · V. Yu. Lyubimov · G. I. Petrov

Published online: 12 December 2006

Due to an unfortunate turn of events this article was published online October 27th 2006 with an erroneous version of Figure 3. That same version is published on the preceding pages. The following printed Figure 3 however is the correct version and should be regarded by the reader as the final version.

The online version of the original article can be found at: http://dx.doi.org/10.1007/s10751-006-9376-4.

E. K. Sadykov (✉) · A. A. Yurichuk · V. Y. Lyubimov · G. I. Petrov
Kazan State University, Kremlevskaya str.18, 420008 Kazan, Russia
e-mail: esad@ksu.ru

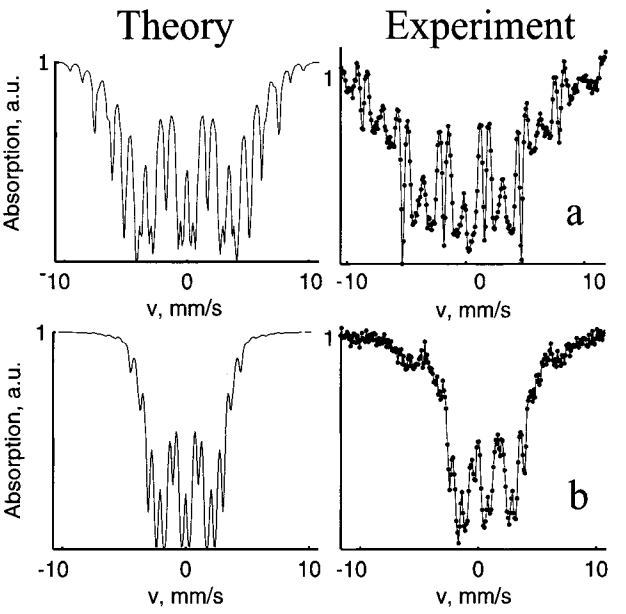

Figure 3 Theoretical spectra for "switching" hf field dynamics for various values of the hf field but at the same value of the ratio R: (a) $H_{hf} = 330$ kOe, $f = 20$ MHz; (b) $H_{hf} = 170$ kOe, $f = 10$ MHz.

Left (theoretical) and *right* (experimental) spectra of the top (a) of this figure are qualitatively similar, but at the same time they differ from each other in details. The same spectra of Figure 3 in the paper DOI: 10.1007/s10751-006-9376-4 are wrongly represented by the same (*solid line*) spectrum.

Hyperfine Interact (2006) 167:905–909
DOI 10.1007/s10751-006-9377-3

Advances in constant-velocity Mössbauer instrumentation

A. Veiga · N. Martínez · P. Mendoza Zélis · G. A. Pasquevich · F. H. Sánchez

Published online: 27 October 2006

Abstract A prototype of a programmable constant-velocity scaler is presented. This instrument allows the acquisition of partial Mössbauer spectra in selected energy regions using standard drivers and transducers. It can be fully operated by a remote application, thus data acquisition can be automated. The instrument consists of a programmable counter and a constant-velocity reference. The reference waveform generator is amplitude modulated with 13-bit resolution, and is programmable in a wide range of frequencies and waveforms in order to optimize the performance of the transducer. The counter is compatible with most standard SCA, and is configured as a rate-meter that provides counts per selectable time slice at the programmed velocity. As a demonstration of the instrument applications, a partial Mössbauer spectrum of a natural iron foil was taken. Only positive energies were studied in 512 channels, accumulating 20 s per channel. A line width of 0.20 mm/s was achieved, performing with an efficiency of 80%.

Key words Mössbauer · instrumentation · spectrometer · constant-velocity · MCS

1 Introduction

Electromechanical devices of the double loudspeaker type for Mössbauer experiments were first described 40 years ago [1], and since then have experienced only few modifications. These transducers are usually controlled with servo amplifiers optimized for operation with a triangular velocity reference, with a fundamental component around the self resonant frequency of the transducer. This constant-acceleration technique is widely used, but in

A. Veiga (✉) · N. Martínez · P. M. Zélis · G. A. Pasquevich · F. H. Sánchez
Departamento de Física–FCE, UNLP, La Plata, Argentina
e-mail: veiga@fisica.unlp.edu.ar

P. M. Zélis · G. A. Pasquevich · F. H. Sánchez
IFLP, CONICET, La Plata, Argentina

N. Martínez
CICPBA, La Plata, Argentina

particular cases has some disadvantages and limitations. Data obtained with this method is always centered in null velocity, which is unnecessarily time consuming when only a reduced range of the spectrum, far from the center, is under study. Its main limitation arises when the effect of a fast varying parameter must be measured, as in the case of the spectrum dependence with the frequency of an applied magnetic field.

Constant-velocity spectrometers for standard electromechanical devices use a square velocity reference [2, 3] to obtain data for a single energy. These instruments are difficult to automate because they require some re-tuning when the velocity changes, mainly due to the high frequency content of the square reference. That makes them difficult to use when several velocities of the spectrum must be recorded simultaneously.

An alternate method to generate the required velocity reference is using end-of-run sensors to change the sign of the velocity [4]. In this method the harmonic content of the reference depends on the velocity, incorporating lower frequencies as lower velocities are set. This necessarily implies a redesign of the servo amplifier, considering that standard devices are usually AC coupled to avoid erratic displacements due to not null mean value of the velocity reference and offset drifts.

A low cost constant-velocity programmable scaler is presented that partially overcomes these difficulties by limiting the harmonic content of the velocity reference. Using standard SCA, transducers and servo amplifiers, a high-quality constant-velocity Mössbauer spectrometer can be built.

2 Constant-velocity strategy

In order to allow automation, the frequency response of the system must remain nearly constant all over the required velocity range. A simple way to do this is to limit the harmonic content of the reference. The proposed design works with a fixed waveform strategy, initially assuring the same harmonic content for all the range. Changes in the velocity are obtained by a change in the amplitude of the reference waveform. A programmable generator is provided in order to optimize the tuning of different transducers by selecting an appropriate waveform for each particular case. Figure 1a shows some of the available options, assuming a limit in the faster velocity that can be used for returning, that in this particular example is three times the maximum velocity of the spectrum. Reduced frequency components using the sinusoidal returns are evidenced, in expense of a shorter constant-velocity time. Defining the duty-cycle d of the generator as the relation between the flat time F and the period T, this parameter will increase when hard returns are selected, as shown in the figure.

The overall efficiency of the instrument not only depends on the duty-cycle of the reference, but also on the settling time of the velocity error imposed by the high frequency response of the system. The event counting must be disabled, not only for the return, but also during a programmable time at the start of the velocity period, where the transient response occurs. Figure 1b shows the effective counting time F' that results from selecting only the flat region of the signal provided by the pickup coil. In this context, the efficiency e of the instrument may be calculated as F'/T. The settling time effect will be more important for velocity references with higher harmonic content, like the square waveform of Figure 1a, reducing its efficiency. Softer waveforms, like the sinusoidal, will require a longer time for the return but might present shorter, or even null, transient responses. In this way a better efficiency could be reached.

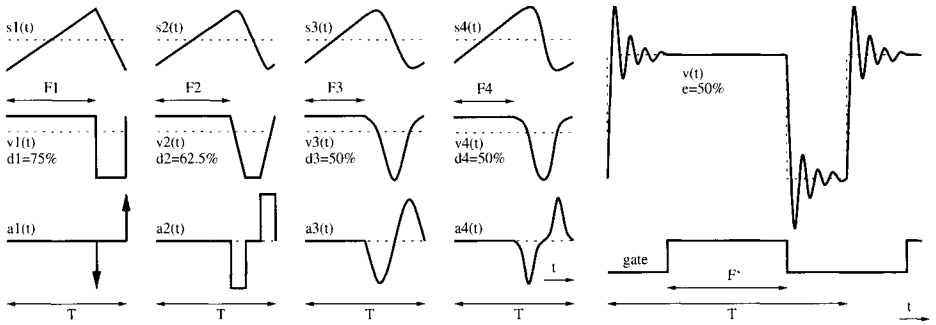

Figure 1 (a) Displacement $s(t)$, velocity $v(t)$ and acceleration $a(t)$ for four different velocity waveforms, evidencing the descending harmonic content in expense of the duty-cycle d. (b) Gate calibration in the case of a transducer and servo amplifier that present an overshoot transient response (*full line*) in presence of a square velocity reference (*dotted line*).

The selection of the best waveform, duty-cycle and efficiency for a particular case is hardly dependent on the performance of the transducer and the servo amplifier, but the following rules should be applicable to all cases. The harmonic content of the reference will be reduced if $F/(T–F)$ is an integer. In addition, the velocity control will perform better if the fundamental frequency of the return waveform of the reference $1/(T–F)$ is close to the natural oscillating frequency of the double loudspeaker system. The duty-cycle is limited by the velocity limits of the transducer. Finally, reference $v_4(t)$, as shown in Figure 1a, is an option that provides a continuous variation of the acceleration during all the period, so it will not require abrupt variations in the applied force; the use of this waveform is advisable if problems arise with the transient response of the driving coil.

3 General design considerations and operation

A single board prototype for the scaler, with standard RS-232 interface to PC is presented. A dual microcontroller architecture with internal bus serves mainly as rate meter and programmable waveform generator. Figure 2 presents an schematic diagram of the scaler. The two main blocks will be briefly described.

The main CPU consists of an analog devices ADuC841 microcontroller, operating with a 50 ns instruction period. This device is an 8051 compatible core with several analog and digital peripherals included, like two 12-bit digital to analog converters (DAC), real time clock, flash memory and watchdog timer. This device operates with a 16-bit counter and a 16-bit timer configured as programmable rate meter, which is enabled in each cycle by the waveform generator by the Gate signal, only when the required constant-velocity is stabilized. This main CPU provides also the RS-232 interface of the scaler. Dead time for the counter is 100 ns and is optimized to operate with fast negative NIM pulses from an standard SCA. The time slice is measured with 50 ns resolution. The two embedded 12-bit DAC are used to select the positive or negative amplitude of the velocity waveform, through a precision instrumentation amplifier, resulting in 8,192 different channels.

An auxiliary microcontroller is used to implement the velocity waveform and gate generator. In this case any 8051 compatible core can perform properly. Atmel AT89C51 is used for this implementation. This CPU handles an analog devices AD7547 high precision 12 bit multiplying DAC. The reference input of this DAC is driven by the two embedded DAC of the main CPU, providing channel selection. The auxiliary CPU generates the Gate

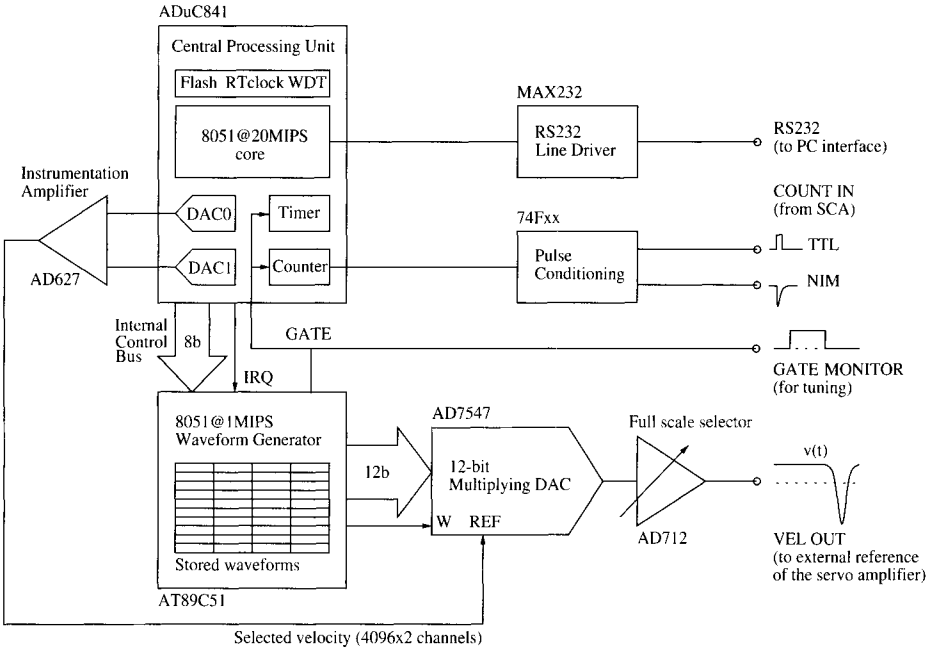

Figure 2 Schematic diagram of the constant-velocity scaler.

signal associated with each waveform, required to inhibit the main CPU rate meter during the return and settling time. Different waveforms, stored in memory tables, can be selected by the main CPU through an 8-bit internal control bus, as well as other waveform parameters like frequency, duty-cycle and efficiency. All these parameters are stored in the main CPU flash memory. The auxiliary CPU is configured at boot time with the stored parameters.

The scaler was implemented as a NIM module, which is the standard in our laboratories. It can be manually operated through the standard RS-232 interface or automatically using a PC application. All of the experiment parameters can be set, including shape, frequency, duty cycle and gate for the velocity reference, and counting time and channel for the counter. The gate adjustment must be performed using a scope. For optimum resolution, a manual control of the last channel velocity is provided through the gain of the output amplifier. Since there are no real time restrictions in the communication with the PC, any high level language that handles RS-232 links can be used for building the application program. Matlab is preferred in our case, because of its post-processing capabilities.

4 Experimental results and further work

An available CMTE transducer, model MA250, together with its servo amplifier and an Ortec 551 SCA were used to test this equipment. It was found to perform better with sinusoidal return waveforms. As this transducer accepts high return velocities, a duty-cycle of 90% could be used, resulting in an efficiency better than 80% for all the range from −10 to 10 mm/s. As a direct estimation of the performance, a partial Mössbauer spectrum of a natural iron foil was repeatedly taken. Positive energies were recorded in 512 channels ranging from 0 to 10 mm/s, accumulating 20 s per channel. A line width of 0.20 mm/s was

achieved in all cases, what is equivalent to the line width of the spectrum taken with the same transducer, servo amplifier and SCA, using a constant-acceleration technique with a nucleus MCS-II multi channel scaler. Long term stability proved to be satisfactory. This equipment has been also used to determine magnetic hyperfine field temperature dependences [5, 6], crystallization kinetics [7] and Fe magnetic moments dynamics [8].

Some limitations arise when attempting to produce a large and sudden change of the velocity, because of the previously mentioned DC rejection implemented in standard servo amplifiers. Direct coupling is under study, implying that some kind of displacement feedback must be implemented.

References

1. Kankeleit, E.: Rev. Sci. Instrum. **35**, 194 (1964)
2. Vértes, A., Korecz, L., Burger, K.: In: Mössbauer Spectroscopy, p. 106. Elsevier, Amsterdam (1979)
3. Veiga, A., Mayosky, M.A., Martínez, N., Spinelli, E., Mendoza Zélis, P., Pasquevich, G., Sánchez, F.: Rev. Sci. Instrum. **73**, 3579 (2002)
4. Seberini, M.: J. Phys., E J. Sci. Instrum. **21**, 641 (1988)
5. Mendoza Zélis, P., Pasquevich, G., Sánchez, F.H., Martínez, N., Veiga, A.: Phys. Lett. A **298**, 55 (2002)
6. Pasquevich, G.A., Mendoza Zélis, P., Fernández van Raap, M.B., Sánchez, F.H.: Physica B **354**, 369 (2004)
7. Saccone, F.D., Rodríguez Torres, C.E., Pasquevich, G.A., Fernández van Raap, M.B., Sánchez, F.H.: Physica B **354**, 237 (2004)
8. Mendoza Zélis, P., Pasquevich, G., Sánchez, F.H., Martínez, N., Veiga, A.: These proceedings

Hyperfine Interact (2006) 167:911–915
DOI 10.1007/s10751-006-9378-2

Optimization of the filter technique

K. Szymański · L. Dobrzyński

Published online: 8 December 2006

Abstract A technique of the resonant filtering is used in the Mössbauer spectroscopy for receiving polarized radiation. Two main contributions suppress the filter quality: unwanted small absorption line located at the resonance energy and large unwanted absorption line located far from the resonance energy. Both contributions can be parametrized by a single small parameter r. The optimal effective thickness is proportional to $1/r^2$, while the departure of the maximum polarization degree from the unity is proportional to r.

Key words Mössbauer spectroscopy · polarization · absorption line

Polarisation by the filter technique has been known since the papers of [1–4]. Recently, monochromatic sources of polarized radiation have been constructed from commercially available radioactive sources [5, 6]. The filter acts as a thick absorber, which is permanently in resonance with the emission line of the source and absorbs photons selectively with one polarization only. Although the theory of transmission of gamma-rays through resonantly absorbing medium was formulated [7], a sophisticated description allows for numerical simulations rather than for a discussion of the optimal conditions for the filter construction. On the other hand, the simplest model of the resonant filter consisting of only one absorption line results in unphysical behaviour of the predicted polarization degree P on the thickness t: $P \to 1$ when $t \to \infty$. Below, we propose a more reliable, simple model of the resonant filter.

1. The source of unpolarized radiation is characterised by the Lamb-Mössbauer factor f_s and emits an intensity N_0, composed of the fraction $f_sN_0/2$ of resonant photons with the polarization $\xi=+1$ and the $f_sN_0/2$ with the polarization $\xi=-1$; the $(1-f_s)N_0$ photons

K. Szymański (✉)
Institute of Experimental Physics, University of Białystok, 15-424 Białystok, Poland
e-mail: kszym@alpha.uwb.edu.pl

L. Dobrzyński
The Sołtan Institute for Nuclear Studies, 05-400 Otwock-Świerk, Poland

belong to the nonresonant radiation. The polarization $\xi=\pm1$ denotes one of two orthogonal photon polarizations and in this report two circular or two linear polarizations will be considered. The resonant radiation has the normalized energy distribution:

$$p(E) = \frac{\Gamma}{2\pi} \frac{1}{(E - E_\gamma)^2 + (\Gamma/2)^2}, \tag{1}$$

2. The main absorption line of the filter (with the polarization $\xi=+1$ and a relative weight A_ξ defined later in Eq. 3 is centered at the emission line of the source.
3. Because of not perfect alignment of the hyperfine field in the filter, there is a nonzero probability of the absorption of photon with the polarization $\xi=-1$ at the energy $E = E_\gamma$. We assume that the relative weight $A_{-1} \ll A_1$ (in a case of the ideal filter $A_{-1}=0$, $A_1=1$).
4. There is an unwanted absorption line for the photon polarization $\xi=-1$. Its relative weight is B_{-1}. Only a tail of this line causes unwanted absorption because the transition energy $E_B \gg \Gamma$ (in the case of an ideal filter $E_B \to \infty$ or $B_{-1} \to 0$). There may be some additional absorption lines with the polarization ξ, located far away from the region between E_A and E_B. The absorption of these lines is neglected for simplicity.

The energy distribution, $p_\xi(E)$, of the fraction of photons with the polarization ξ which passes the polarizer is:

$$p_\xi(E) = \frac{\Gamma}{2\pi} \frac{1}{(E - E_\gamma)^2 + (\Gamma/2)^2} \cdot e^{-t\sigma_\xi(E)}, \tag{2}$$

where t is the effective thickness [8] and $\sigma_\xi(E)$ is the resonant cross-section for the polarization ξ:

$$\sigma_\xi(E) = \frac{A_\xi \Gamma^2/4}{(E - E_\gamma)^2 + \Gamma^2/4} + \frac{B_\xi \Gamma^2/4}{(E - E_B - E_\gamma)^2 + \Gamma^2/4}. \tag{3}$$

The weights of the resonant transitions are normalized, e.g., the sum of all weights with the polarization ξ is equal one. The integrated intensity of the resonant radiation with the polarization ξ passing through the filter is proportional to [8]:

$$N_\xi = \frac{1}{2} f_s N_0 \int_{-\infty}^{+\infty} p_\xi(E) dE. \tag{4}$$

The polarization degree of the resonant radiation P is defined as usual:

$$P = \frac{N_{-1} - N_1}{N_{-1} + N_1}. \tag{5}$$

The parameters A_ξ, B_ξ, E_B are the intrinsic properties of the material and can be controlled to some extent by a selection of the material used for filter, thermo-chemical processing and an external magnetic field. In contrast, the effective thickness t can be tuned

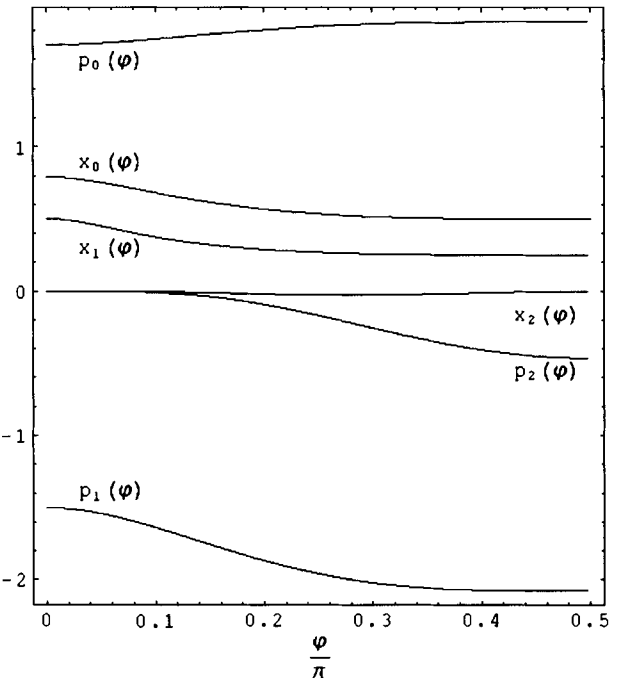

Figure 1 The dependence of the coefficients x_i and p_i of the series expansion on the parameter φ.

easily during the filter preparation, so the polarization degree P can be optimised. It is convenient to introduce parameters:

$$u = A_{-1}/A_1,\ x = tA_1/2, s = B_{-1}/A_1, \quad b = 2E_B/\Gamma. \tag{6}$$

In the following, we shall set B_1 to zero, because the tail of the absorption line separated by a large Doppler velocity disturbs negligibly the absorption of the main line with the amplitude A_1. Using the identity [9]:

$$\frac{1}{\pi}\int_{-\infty}^{+\infty} \frac{1}{y^2+1} \cdot e^{\frac{-A}{y^2+1}} dy = e^{-A/2} I_0(A/2)\,, \tag{7}$$

where I_n is the Bessel function of the imaginary argument, we get the expression for the polarization degree:

$$P(x) = \frac{\frac{1}{\pi}\int_{-\infty}^{+\infty} \frac{1}{y^2+1} e^{\frac{-2ux}{y^2+1} + \frac{-2sx}{(y-b)^2+1}} dy - e^{-x} I_0(x)}{\frac{1}{\pi}\int_{-\infty}^{+\infty} \frac{1}{y^2+1} e^{\frac{-2ux}{y^2+1} + \frac{-2sx}{(y-b)^2+1}} dy + e^{-x} I_0(x)}. \tag{8}$$

The optimum thickness x_{opt}, at which $P(x)$ attains its maximum, is obtained from the condition $\partial P/\partial x = 0$. To the best of our knowledge, there are no explicit results for the

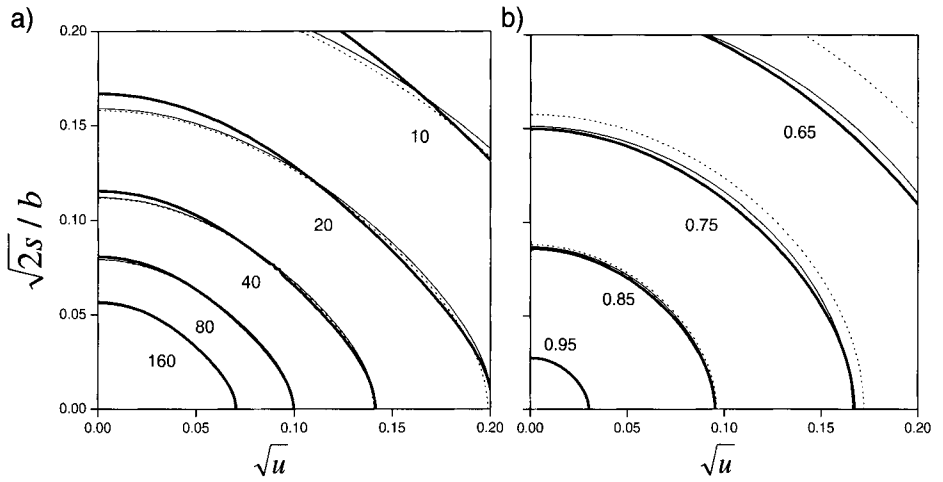

Figure 2 Contours showing constant values of a) the optimal thickness x_{opt} and b) the maximum polarization degree P_{max}. The *thick lines* - exact result (8) for s=1.3 satisfying condition $\partial P/\partial x$=0. The *dotted lines* approximate results including terms with the x_0, p_0 coefficients, *thin lines* approximate results including terms with the $x_0 \div x_2$, $p_0 \div p_2$ coefficients in Eq. 10.

integrals present in Eq. 8. We have shown [10] that Eq. 8 can be expanded in small parameter r:

$$r = \sqrt{u + \frac{2s}{b^2}}, \tag{9}$$

yielding a series for the optimal value of x (abbreviated here by x_{opt}) and the maximal polarization degree (P_{max}=$P(x_{opt})$):

$$\begin{aligned} x_{opt} &= \frac{x_0}{r^2} + x_1 + \frac{x_2}{s} + \ldots \\ P_{max} &= 1 - p_0 r + \tfrac{1}{2} \cdot p_0^2 r^2 + \left(p_1 + \tfrac{p_2}{s}\right) r^3 + \ldots \end{aligned} \tag{10}$$

The coefficients x_i and p_i in Eq. 10 are slowly varying functions of the only one parameter, namely an angle φ, defined as

$$\varphi = \operatorname{arctg} \sqrt{\frac{2s}{ub^2}}, \tag{11}$$

see Figure 1. The explicit form of x_i and p_i is given in [10].

The quality of the approximations Eq. 10 can be checked by a numerical integration of Eq. 8 and finding x_{opt} for which $P(x)$ has a maximum, see Figure 2. Our approximation works well when the intrinsic parameters, u and b, permit to achieve a high polarization of the beam.

Using initial parameters, for which the model of the filter was introduced and neglecting higher order terms in Eq. 10, the explicit results are:

$$r = \sqrt{\frac{A_{-1}}{A_1} + \frac{B_{-1}\Gamma^2}{2A_1 E_B^2}},\ \operatorname{tg}\varphi = \sqrt{\frac{B_{-1}}{2A_{-1}}}\frac{\Gamma}{E_B},\ t_{opt} \approx \frac{2x_0}{A_1 r^2},\ P_{max} \approx 1 - p_0 r. \tag{12}$$

As discussed in the model assumptions, two main mechanisms influence the filter quality. The first one is connected with a non-ideal orientation of the hyperfine fields (the h. m.f. or the electric field gradient), resulting in the appearance of the weak absorption line active for the $\xi=-1$ polarization state. The second mechanism comes from the presence of a strong absorption line, which although is separated by a quite large Doppler velocity, has a tail which causes unwanted absorption of photons with the $\xi=-1$ polarization. The role of both mechanisms is reflected in the form of and the value of a single small parameter r. The optimal thickness of the filter is proportional to r^{-2}. Thus, when intrinsic quality of the material increases (r tends to zero), the filter may be thicker while giving polarization degree smaller than one by a factor proportional to r. The proportionality constants x_0 and p_0 in Eq. 12 depend weakly on the angle φ, whose value indicates which of the two mechanisms is dominating in tuning of the filter quality.

To illustrate practical use of the presented approach, let us estimate properties of the system used in [5], where one of the two inequivalent iron sites (D-site) has the hyperfine field of 20 T and a property of the accidental coincidence of its third absorption line with the emission line of ^{57}Fe in Cr matrix. The unwanted absorption line with the opposite polarization (4rd line of the Zemann sextet) is located at a distance of 1.02 mm/s. Thus, the value of $b=21$. The best alignment, which was achieved, is monitored by a suppression of the intensities of the lines 2 and 5 to the level smaller than 1%. This implies that the unwanted absorption line intensity at zero Doppler velocity corresponds to $u=0.01$.

The contribution from the tail of the unwanted line, entering into (3) is much smaller than the contribution from the nonperfect alignment. Both contributions lead to parameter $r=0.12$ and we may estimate that the optimal $x_{opt}=42$. If we assume that all atoms from D-site (fraction of 2/3) were active in resonant filtering, we estimate that $A_1=1/4\cdot 2/3$ and $t_{opt}=504$. This value corresponds to approximately 31 mg/cm^2 (assuming 90% enrichment). The polarization degree related to this value is 0.81. The polarizer used in [5] contains 34 mg/cm^2 and the polarization degree was reported to be 80%.

References

1. Shtrikman, S.: Solid State Commun. **5**, 701 (1967)
2. Shtrikman, S., Somekh, S.: Rev. Sci. Instr. **40**, 1151 (1969)
3. Stampfel, J.P., Flinn, P.A.: Mössbauer Eff. Methodol. **6**, 95 (1971)
4. Varret, F., Imbert, P., Jehanno, G., Saint-James, R.: Phys. Status Solidi, (A) **27**, K99 (1975)
5. Szymański, K., Dobrzyński, L., Prus, B., Cooper, M.J.: Nucl. Instr. Meth. **B119**, 438 (1996)
6. Jäschke, J., Rüter, H.D., Gerdau, E., Smirnov, G.V., Sturhahn, W., Pollmann, J.: Nucl. Instr. Meth. **B155**, 189 (1999)
7. Gonser, U., Fischer, H.: In: Gonser, U. (ed.) Mössbauer Spectroscopy II, p. 99. Springer, Berlin Heidelberg New York (1981)
8. Margulies, S., Ehrman, J.R.: Nucl. Instr. Meth. **12**, 131 (1961)
9. Mössbauer, R.L., Wiedemann, W.H.: Zeitschrift fur Physik **159** (1960)
10. Szymański, K.: Nucl. Instr. Meth. **B243**, 429 (2006)

Hyperfine Interact (2006) 167:917–921
DOI 10.1007/s10751-006-9379-1

Experimental observation of vibrations produced by pulsed laser beam in MgO:^{57}Fe

Farit Vagizov · Roman Kolesov · Silviu Olariu · Yuri Rostovtsev · Olga Kocharovskaya

Published online: 7 December 2006

Abstract We report the first observation of a laser-produced vibration with the aid of Mössbauer techniques. Thin platelets of MgO single crystals were doped by diffusion of ^{57}Fe atoms. The illumination of the MgO:^{57}Fe sample with a pulsed Nd:YAG laser produced a significant broadening of the Mössbauer spectrum. In order to find out what caused these changes, we performed a series of time-domain experiments, in which the Mössbauer spectra were collected only during a 2.5 μs gate interval. This gate interval was swept from 5 μs to 190 μs over the time interval between the two laser pulses. After laser irradiation, the position of the Mössbauer line was found to be changing in time as a decaying oscillations of well-defined frequency, which can be due to the vibration of the sample induced by the laser pulse.

Key words MgO:^{57}Fe · Mössbauer spectroscopy · pulsed laser beam

1 Mössbauer spectroscopy, laser-induced effects

The Mössbauer spectroscopy is a powerful method for the investigation of atomic motion. Many other methods are available, including optical methods, but when we intend to study the motions taking place inside a sample, they are not effective because they depend on the

F. Vagizov (✉) · R. Kolesov · S. Olariu · Y. Rostovtsev · O. Kocharovskaya
Physics Department, Texas A&M University, College Station, TX 77840, USA
e-mail: vagizov@jewel.tamu.edu

F. Vagizov
Kazan State University, Kazan 420008, Russia

R. Kolesov · Y. Rostovtsev · O. Kocharovskaya
Institute of Applied Physics of the Russian Academy of Sciences,
Nizhny Novgorod 603600, Russia

S. Olariu
National Institute of Physics and Nuclear Engineering,
077125 Magurele, Bucharest, Romania

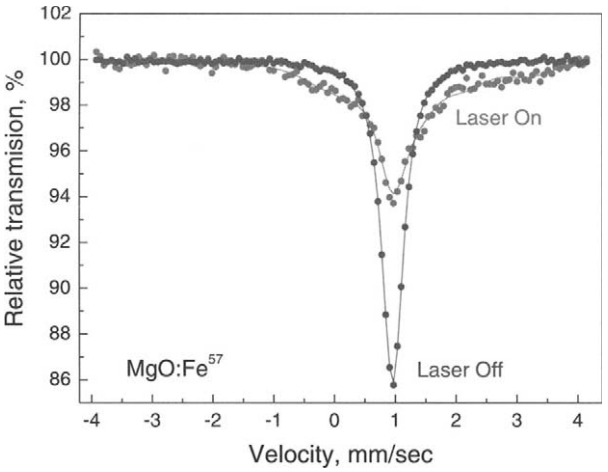

Figure 1 MgO:^{57}Fe Mössbauer spectra with and without laser radiation, T=RT.

scattering from the surface of the sample, whereas the Mössbauer spectrum gives information about the atoms in the volume of the sample. Laser-produced vibrations have been observed in the past with conventional ultrasound techniques [1]. Moreover, vibrations produced in thin ferromagnetic foils by magnetostriction have been extensively studied by Mössbauer spectroscopy [2].

In this paper we report the first observation of a laser-produced vibration with the aid of Mössbauer techniques. Previously we have observed that the illumination of samples with a pulsed laser produced a significant broadening of the Mössbauer spectrum [3, 4].

Thin platelets of MgO single crystals (obtained from MTI Corporation), with the axis orientation <100>, were doped by diffusion of ^{57}Fe atoms. The transverse dimensions of samples were 10×10 mm^2. Absorbers were prepared by rubbing $^{57}Fe_2O_3$ powder (95% enriched in ^{57}Fe, Cambridge Isotope Lab) into the surface of 0.5 mm thick platelets of MgO substrate until the surface had a slightly reddish appearance. Subsequently, the iron was diffused at 750°C in air for a week. This process was repeated several times and tested by Mössbauer spectroscopy. As a result, iron diffused into the MgO plate in di- and trivalent state. The next step in sample preparation was annealing in hydrogen atmosphere at 1,100°C for 20 h. The resulting sample contained only divalent iron, all trivalent iron impurities were reduced to a divalent state. The ^{57}Fe concentration was estimated to be roughly equivalent to 0.08 wt% Fe_2O_3 (or about 0.04 at.% Fe). The appearance of the sample was dark green–blue.

Conventional electromechanical Mössbauer drive systems operating in constant acceleration mode have been used for measurements. The source was 50 mCi ^{57}Co in a Rh matrix. The isomer shift values and velocity were calibrated to metallic iron at room temperature. We have developed a special technique to measure the position of the Mössbauer line as a function of time. This technique allows us to get a Mössbauer spectrum at successive intervals of 2.5 μs after the laser pulse shot. A Nd:YAG laser (ESI3570, Electro Scientific Industries) was used to illuminate the absorber. The 1064 nm wavelengths laser beam with energy per pulse of the order of 2 mJ and a repetition rate of 2.5 kHz was focused onto the sample down to a spot about 4 mm in diameter. It corresponds to the Mössbauer aperture used in the experiment. The duration of the pulses was about 70–100 ns.

A Mössbauer spectrum of MgO:^{57}Fe sample without laser radiation consisted of a broadened single line, as shown in Figure 1. Its width at room temperature was 0.46 mm/s

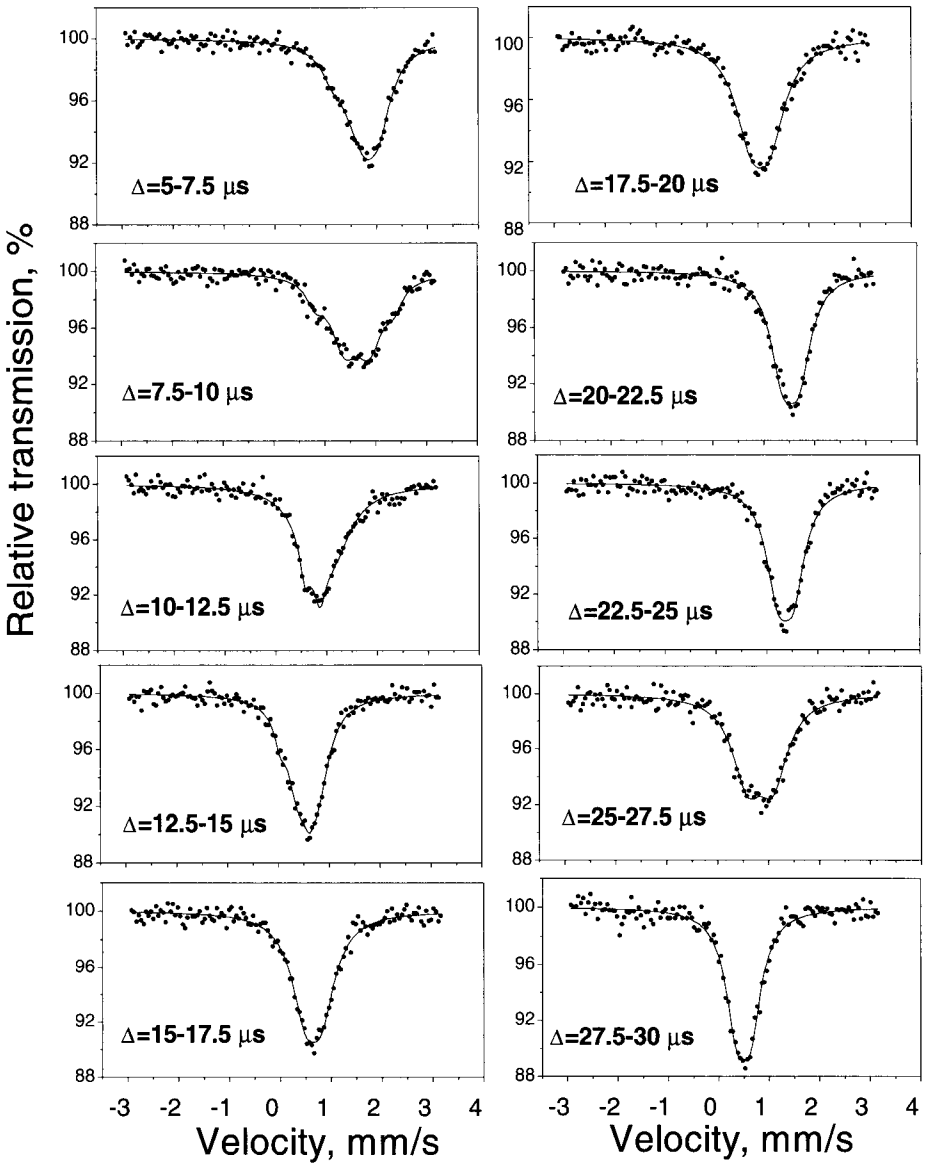

Figure 2 MgO:^{57}Fe Mössbauer spectra collected at different time gate.

and its isomer shift was 1.04 mm/s relative to α-Fe. The temperature Mössbauer measurements have revealed that the dependence of the center of gravity of the Fe^{2+} line and the reduction of Mössbauer absorption profile area, $A(T)/A$ (295 K), follow the Debye model, with Θ_D=420 K for the isomer shift dependence and Θ_D=428 K for the area reduction.

The illumination of the sample by pulsed laser radiation leads to major changes in the Mössbauer spectrum. In Figure 1, MgO:^{57}Fe Mössbauer spectra without and with laser radiation are shown. It can readily be seen that the last one is sufficiently broader and has broad wings at the both tails of Mössbauer line.

Our sample showed a strong dependence of the isomer shift and line width on its temperature. The isomer shift reduces as the temperature becomes higher while the line

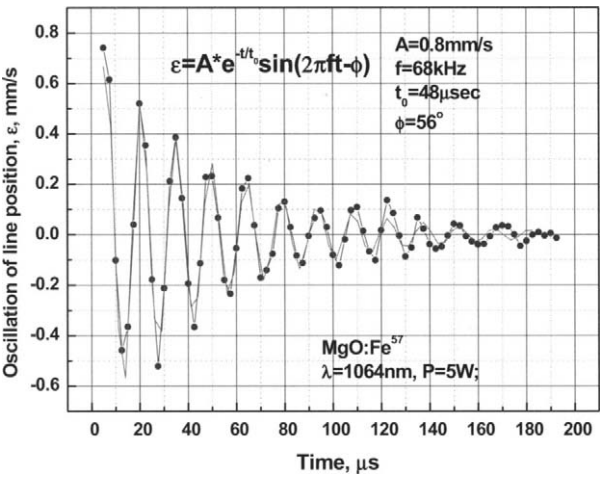

Figure 3 Spectral center-of-mass oscillations after the pulse action. Both the experimental data and the fitting curve are shown.

width decreases. Thus, the laser heating of the sample would affect the Mössbauer spectrum. In order to diminish the laser heating effect we have used a pulse laser radiation. A pulsed Nd:YAG laser operated at 1,064 nm wavelength. This wavelength corresponds to the phonon wing of Fe^{2+} electronic absorption into ^5E_g state. The pulse repetition rate was ~6.9 kHz (T=145 μs), and the laser average power was about 9 W. The time interval between the two subsequent pulses, T, was split into two parts – just after the pulse, T_1, and before the pulse, T_2. The Mössbauer data collection system was synchronized with the laser pulse arrival, and the spectra were collected by two acquisition cards (CMCA-550) alternately. The Mössbauer spectrum formed by gamma-ray quanta collected during the time interval T_1 was called "laser on" while the spectrum collected during the time T_2 was called "laser off". The described procedure allowed us to avoid heating effect since the estimated temperature difference between the "laser on" and "laser off" spectra was less than 1 K and could not lead to any measurable changes in the Mössbauer spectrum. The center shift of "laser on" and "laser off" Mössbauer spectra was almost same within the limits of experimental error, i.e., 0.95±0.03 mm/s and 0.97±0.02 mm/s for "laser on" and "laser off" Mössbauer spectra, respectively. Furthermore, Mössbauer spectral area of the spectra was essentially conserved. Therefore, we could conclude that "laser on" and "laser off" Mössbauer spectra are collected at almost the same temperature.

The wings of "laser on" spectrum are spread out at broad band of ~2 mm/s near the position of Mössbauer line center. In order to find out what caused these changes; we performed a series of time-domain experiments. The Mössbauer spectra were collected only during the 2.5 μs gate interval. The latter was swept from 5 μs to 190 μs over the time interval between the two laser pulses. In other words, we collected the Mössbauer spectrum only during the time gate whose position was varied within the pulse period. This was done in order to study the temporal behavior of the Mössbauer spectrum after the laser pulse hits the sample. After laser irradiation the position of the Mössbauer line was found to be changing in time, as one can see in Figure 2. The shape of the Mössbauer spectrum is complex. We can obtain a wholly satisfactory spectrum fit using the expression

$$f(v) = \int_{t_1}^{t_2} \frac{A\left(\Gamma/2\right)^2 dt}{\left(v - V_0 - v_0 \exp\left(-t/t_0\right) \sin\left(2\pi ft + \varphi_o\right)\right)^2 + \left(\Gamma/2\right)^2},$$

where v is the velocity, V_0 the position of Mössbauer line before laser pulse, and Γ is the width of the line at half height.

In particular, we have studied the spectral center-of-mass position as a function of time after the laser pulse. The result is shown in Figure 3. One can see decaying oscillations of rather well-defined frequency. The analysis of the experimental data allowed us to determine the amplitude A, the frequency and the relaxation time t_0 of this oscillatory curve as v_0=0.8 mm/s, f=68 kHz and t_0=48 μs.

According to the sample preparation procedure, iron ions should be located near one of the bigger surfaces of the sample, the one they were diffused from. This fact was confirmed by means of electron-conversion Mössbauer spectroscopy. In the first experiment the iron-containing surface of the sample was faced towards the Mössbauer source and the laser beam was coming to the sample roughly from the side of the Mössbauer source. In the second experiment the laser beam was coming from the opposite side of the sample. Finally, in the third experiment we flipped the sample so that the iron-containing surface faced outwards the Mössbauer source, but the laser illumination was arranged as in the first experiment. For the first two experiments the results were qualitatively the same, but in the third case the initial phase of the center-of-mass oscillations flipped. That was clear indication that we are dealing with mechanical effects, but not the electronic ones. Furthermore, it becomes clear that the membrane-like oscillations of the sample were excited due to the rapid laser heating from inside, not from the surface of the sample. Finally, the estimated amplitude of the sample surface oscillations was ~1–2 nm.

The oscillation after the laser irradiation of the position of the Mössbauer line can be attributed to the vibration of the sample induced by the laser pulse. The frequency of the vibrations of a thin rectangular plate are of the order of f=const×$(d/L)f_0$, where L is the side length and d the thickness of the plate, and f_0=v/2L is the frequency of the longitudinal vibrations, for a velocity v of the longitudinal oscillations. [5] The constant depends on the boundary conditions. For d=0.5 mm and L=1 cm, and for v=9.1×10^3 m/s, we have f_0= 4.5×10^5 Hz, and f=const×22.5 kHz, which gives the right order of magnitude of the vibration frequency.

This is the first observation of a laser-produced vibration with the aid of Mössbauer techniques. As with the ultrasound and magnetostrictive techniques, the Mössbauer detection of laser-produced vibrations may find applications for the study and diagnosis of the mechanical properties in the bulk of samples.

Acknowledgments We are grateful to Elena Kuznetsova for the help in preparing the present manuscript for publication. We also acknowledge the financial support of NSF, AFOSR, and CRDF.

References

1. Mason, W.P., Thurston, R.N. (ed.): Physical Acoustics, vol. XVIII. Academic (1988)
2. Heiman, N.D., Pfeiffer, L., Walker, J.C.: J. Appl. Phys. **40**, 1410 (1969)
3. Vagizov, F., Kolesov, R., Kocharovskaya, O.: J. Mod. Opt. **51**, 2579 (2004)
4. Kocharovskaya, O., Kolesov, R., Rostovtsev, Y.: Phys. Rev. Lett. **82**, 3593 (1999)
5. Landau, L.D., Lifshitz, E.M.: Theory of Elasticity. Pergamon, London, p. 113. (1959)

Hyperfine Interact (2006) 168:923–928
DOI 10.1007/s10751-006-9398-y

Characterization of products emanating from conventional and microwave energy roasting of chalcopyrite ($CuFeS_2$) concentrate

Antoine F. Mulaba-Bafubiandi

Published online: 5 December 2006

Abstract Chalcopyrite concentrate (83% $CuFeS_2$, 3% FeS_2 and 14% ZnS) which is a typical feed to the matte smelting process for copper extraction via pyro metallurgical route has been roasted with microwaves. Comparison of mineralogical phases obtained was made with the case of conventional roasting. Resulting calcines were characterised with Mössbauer spectroscopy and XRD. It was observed that complete oxidation (dead roasting) of the chalcopyrite was achieved after 10 min with microwaves while 20 min were required in the conventional route. The mineralogical phases found in the dead-roasted calcines produced from microwave roasting of this chalcopyrite concentrate were the hematite (Fe_2O_3), franklinite ($ZnFe_2O_4$), copper-rich ferrite ($Cu_{1-x}Zn_xFe_2O_4$, $x \leq 0.5$), and copper ferrite ($CuFe_2O_4$). The findings of this work indicated that it was technologically feasible to oxidize the chalcopyrite with microwaves using a 2.45 GHz multimode applicator.

Key words microwave and conventional roasting · chalcopyrite concentrate · ferrites formation

1 Introduction

Chalcopyrite ($CuFeS_2$) is the most abundant copper mineral on the earth. It is often found in association with sphalerite (ZnS). A typical sphalerite concentrate may contain up to 10% Fe either in chalcopyritic form or as pyrite (FeS_2). Chalcopyrite concentrate is used as feed to the matte smelting process for copper production via pyrometallurgical route. The matte smelting is convenient as the roast–leach–electrowin sequence usually used for

A. F. Mulaba-Bafubiandi (✉)
Extraction Metallurgy Department, Faculty of Engineering and the Built Environment, University of Johannesburg, P.O. Box 526, Wits 2050 Johannesburg, South Africa
e-mail: Mulaba@twr.ac.za

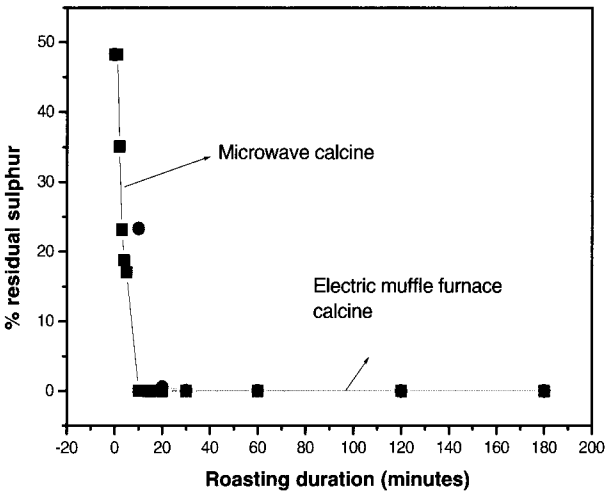

Figure 1 Percentage of retained sulphur in the electric muffle furnace and microwave produced calcines.

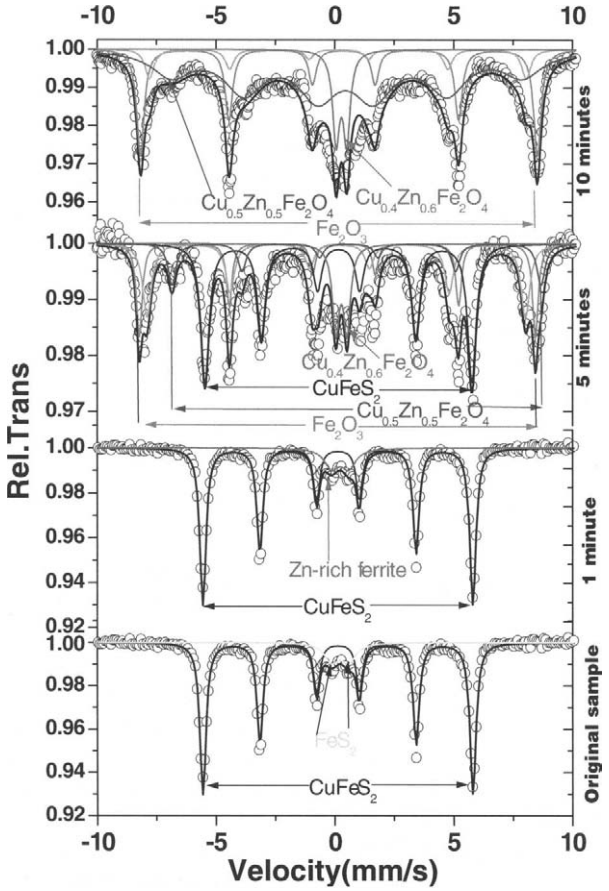

Figure 2 Mössbauer spectra of a microwave roasted chalcopyrite concentrate. Different roasting durations were used. *Solid lines* are theoretical fits to the data (*open circles*). The sextet extending from −6 to 6 mms^{-1} is attributed to chalcopyrite. The outermost sextet extending from −8 to 8 mms^{-1} is hematite.

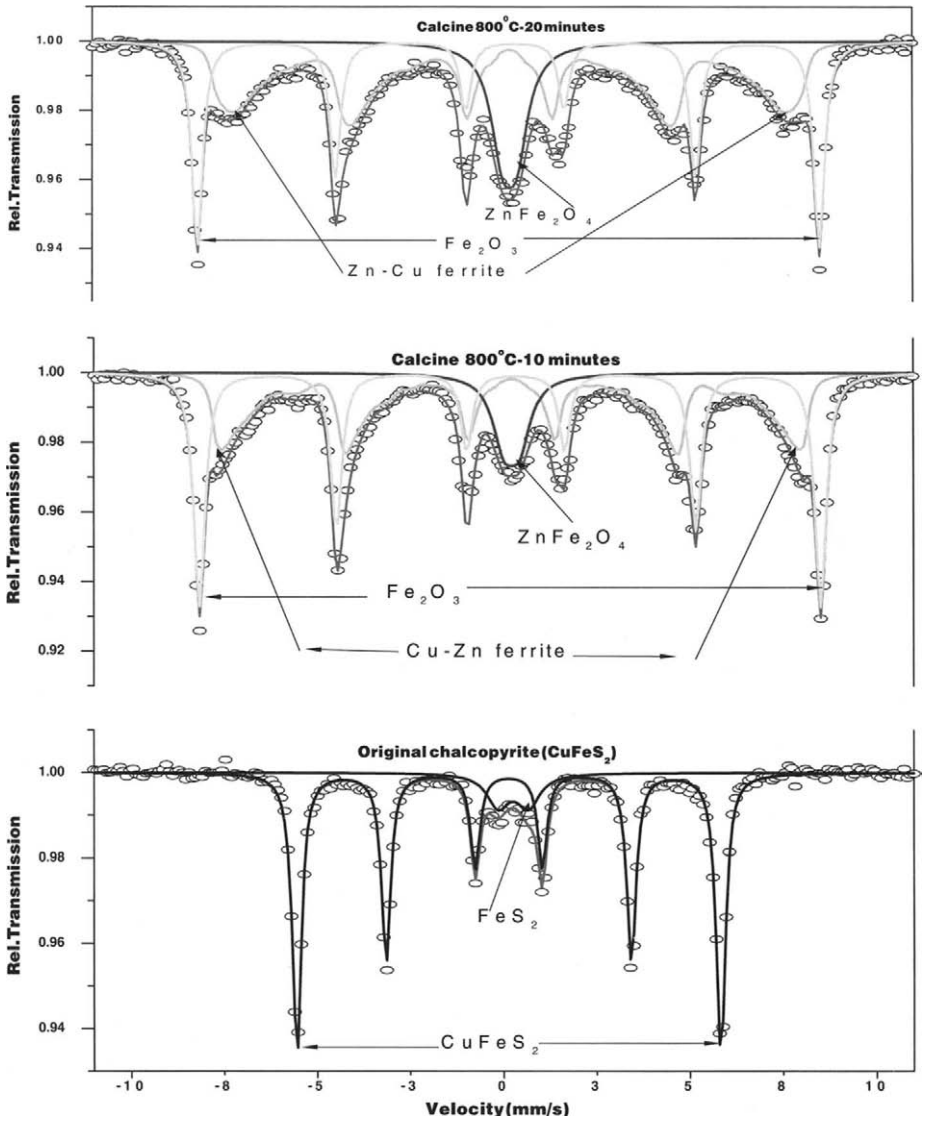

Figure 3 Room temperature Mössbauer spectrum of the calcines obtained at 800°C.

metal extraction from sulfides has been complicated by the formation of metal ferrites difficult to leach in commonly used leaching reagents (H_2SO_4, HNO_3, aqua regia, HCl) [1, 2] thus locking up residual metal leading to a metal loss in the leaching process. Moreover to obtain leachable products one may need to roast for a relatively longer time and at an adequate temperature [3]. As different minerals have different dielectric properties and they respond differently to microwaves, and as microwaves heating starts from the inner of the bulk of the material, it was suggested to investigate the possibility of roasting chalcopyrite concentrate with microwaves, characterise the calcines produced and ascertain

Table I Experimental hyperfine interaction parameters of the spectral components in the spectrum of calcines produced after 1, 5 and 10 min at 2.45 GHz – 1 KW

Microwave roasting duration (min)	Spectral Component	Γ, line width (mm/s)	δ/Fe (mm/s)	QS (mm/s)	Bhf (T)	[a]Abundance (%)
1	Chalcopyrite ($CuFeS_2$)	0.30 (2)	0.24 (2)	0.20	35.00	88(3)
	Pyrite	0.71	0.34 (2)	0.73 (2)	–	12
5	Chalcopyrite ($CuFeS_2$)	0.50 (2)	0.29(2)	0.21	34.81	38
	Hematite: Fe_2O_3	0.31	0.36(2)	−0.20 (2)	51.40 (2)	26
	Cu-rich ferrite ($Cu_{1-x}Zn_xFe_2O_4$, $x<0.5$)	0.43–60	0.43(2)	0.30–0.46	45.4 (1)	10
	Franklinite ($ZnFe_2O_4$)	0.35 (fixed)	037(2)	0.43	–	12
	Cu–ferrite ($CuFe_2O_4$)	0.42–0.60	0.33(2)	0.02 (2)	48–49.5	14
10	Hematite: Fe_2O_3	0.25–0.38	0.38(1)	−0.20 (2)	51.8 (2)	23
	Cu-rich ferrite ($Cu_{1-x}Zn_xFe_2O_4$, $x<0.5$)	0.60–1.95	0.32(2)	−0.20–0.59	45.4 (1)	61
	Franklinite ($ZnFe_2O_4$)	0.35 (fixed)	0.37(2)	0.43	–	9
	Cu–ferrite ($CuFe_2O_4$)	0.30–0.45	0.42(1)	0 (2)	49.00	7

Statistical error indicated in parenthesis

[a] From the integrated area under the sub-spectrum

the viability of the process. The present paper a reports mainly on the characterisation of products formed during both roasting processes.

2 Experimental

2.1 Materials and roasting process

20 g of chalcopyrite concentrate containing 83% $CuFeS_2$, 3% FeS_2 and 14% ZnS (i.e. a total of 48% S) was roasted in both i.e. an electrical muffle furnace (700–1,000°C) for different durations and in a multimode microwave applicator (2.45 GHz, 1,000 W) for varying roasting durations (1, 2, 3, 4, 5, 10, 15, 20, 20 and 40 min). Although the sample surface temperature was not measured during the microwave assisted roasting, resulting calcines were characterised using, X-ray Diffraction (XRD) and Mössbauer Spectroscopy (MS) techniques in conjunction with the determination of the residual sulphur. In the sulphur test the gravimetric method determination of sulphur was used.

2.2 Characterisation techniques

XRD patterns were collected using a Phillips PW 1,830 diffract meter with a CuKα cathode. The diffractometer was operated at a generator voltage of 40 KV and a current of 20 mA while the goniometer was scanning 2θ values from 10 to 70° at a scan rate of 1.0 s/step (step size=0.020° 2θ). Mössbauer spectra were recorded in the normal transmission geometry. A constant acceleration motor was used to scan the velocity range of interest, with a $^{57}Co(Rh)$ source (~10 mCi) at room temperature. Each spectrum was measured for about 30–60 h duration and was recorded in 1,024 channels. Each spectrum comprising 512

Table II Experimental hyperfine interaction parameters of the spectral components in the spectrum of the calcines conventionally produced at different temperatures and times

Calcines	Spectral component	Γ, line width (mm/s)	δ/Fe (mm/)	QS (mm/s)	B_{ht} (T)	[a]Abundance (%)
600°C – 30 min	Chalcopyrite	0.30	0.24	0.0005	35.3(5)	8(3)
	Hematite	0.34	0.36	−0.2	51.2(2)	22(2)
	Franklinite, Zn-rich ferrites*	0.40	0.33	0.45	–	18(2)
700°C – 30 min	Ferrites*	0.32*	0.36	0.14	10–50*	52(2)
	Hematite	0.30	0.38	−0.2	51.8(1)	51(2)
	Franklinite, Zn-rich ferrites	0.68	0.29	0.46	−FS	9(2)
	Ferrites* (Cu–Zn ferrites)	0.29*	0.30	−0.03	10–50*	40(2)
800°C – 10 min	Hematite	0.36	0.36	−0.2	51.7(2)	44(2)
	Franklinite, Zn-rich ferrites	0.72	0.34	0.42	–	11(2)
	Ferrites*	0.30*	0.31	−0.03	10–50*	*45(3)*
800°C – 20 min	Hematite	0.34	0.37	−0.2	51.8(2)	33(2)
	Franklinite, Zn-rich ferrites	0.73	0.32	0.39	–	16(2)
	Ferrites*	0.30*	0.31	−0.02	10–50*	*51(3)*
800°C – 30 min	Hematite	0.34	0.37	−0.19	51.7(1)	31(2)
	Franklinite, Zn-rich ferrites	0.66	0.34	0.44	–	18(2)
	Ferrites*	0.30*	0.33	−0.01	10–50*	*51(2)*
800°C – 60 min	Hematite	0.34	0.37	−0.19	51.7(2)	31(2)
	Franklinite, Zn-rich ferrites	0.65	0.32	0.44	–	19(2)
	Ferrites*	0.30*	0.30	−0.01	10–50*	*50(3)*
800°C –	Hematite	0.34	0.36	−0.18	51.6(2)	29(2)
120 min	Franklinite, Zn-rich ferrites	0.68	0.33	0.43	–	18(2)
	Ferrites*	0.30*	0.30	−0.02	10–50*	*53(3)*
800°C –	Hematite	0.34	0.26	−0.19	51.6(2)	30(2)
180 min	Franklinite, Zn-rich ferrites	0.64	0.30	0.46	–	18(2)
	Ferrites*	0.30*	0.30	−0.01	10–50*	*52(3)*

Statistical error indicated in parenthesis

[a] From the integrated area under the sub-spectrum

* Fitted with a distribution of magnetic hyperfine fields with a fixed line width

channels was analyzed using the non-linear least squares fitting program NORMOS-90, and mineral attributions were made using the Mossbauer minerals handbook [4].

3 Results and discussion

The chalcopyrite concentrate subjected to microwave roasting converted from greenish to dark-grey/black (charcoal) color. The residual sulphur determination test, showed a 65% sulphur reduction after only 5 min of microwave roasting. It was observed that roasting chalcopyrite for more than 10 min, the amount of residual sulphur was substantially reduced to zero. While for the muffle products similar values were observed at 800°C, after 30 min. As depicted in Figure 1, heating at 600 and 700°C for 30 min still left, respectively, 32 and 21% residual sulfur.

When characterised with X ray diffraction technique, Figures 2 and 3, it is observed that copper mixed oxides started to form from 5 min roasting. The formation of hematite is noticed. It could be formed either from the pyrite Figure 2:

The broad sextet in the spectra of the calcines produced after 5 and 10 min, Tables I and II, is attributed to copper-rich ferrite $Cu_{1-x}Zn_xFe_2O_4$ ($x<0.5$) and/or Zn–ferrite ($Zn_xFe_{3-x}O_4$, $x<0.8$), whereas the central doublet is supposed to be zinc-rich ferrite $Cu_{1-x}Zn_xFe_2O_4$ ($x>0.5$) and/or Franklinite $ZnFe_2O_4$.

4 Conclusions

In the case of roasting chalcopyrite concentrate with microwaves for 5 min the minerals detected using Mössbauer spectroscopy are hematite, copper–ferrite Cu_2FeO_4, copper-rich ferrite and zinc-rich–ferrite with respective abundances (23±2) and (7±2)%, (61±6) and (9±2)%. This is in agreement with results obtained with XRD. In the MS spectra, typically a sextet with broad line widths has been used to model possible cases of Zn or Cu-depleted ferrites $Zn_xFe_{3-x}O_4$, $Cu_xFe_{3-x}O_4$ and/or $Cu_{1-x}Zn_xFe_2O_4$ with $x<0.5$. Whereas a central doublet has been used to represent Zn-rich ferrites, Franklinite, $Zn_xFe_{3-x}O_4$ ($x\sim1$) and/or $Zn_xCu_{1-x}Fe_2O_4$ ($x>0.5$) which, are paramagnetic at room temperature. Mössbauer spectroscopy alone cannot easily distinguish between these ferrites, i.e., $Zn_xFe_{3-x}O_4$, $Cu_xFe_{3-x}O_4$ and/or $Cu_{1-x}Zn_xFe_2O_4$, because they may have overlapping Mössbauer parameters for a range of compositions (x values). MS of conventionally produced calcines from chalcopyrite concentrate showed mainly zinc rich ferrites. It seemed that selected Zn–Cu ferrites could be preferentially produced if an appropriate mix of microwave energy levels and exposure time was used.

Acknowledgements The author is thankful to Kumba Resources (Zincor), South Africa, for providing with the chalcopyrite concentrate used in this work. Yves Kinkie was involved in the early stage of the project. The author acknowledges the financial supports from the South African National Research Foundation (NRF) and the Technikon Research Committee from the former Technikon Witwatersrand during the first part of the project.

References

1. Rangarajan, V.S., Acharjee, D.K., Gupta, P.S.: Indian J. Technol. **18**, 8 (1980)
2. Jain, R.C., Madhavan, S., Acharjee, D.K., Gupta, P.S.: Can. J. Chem. Eng. **60**, 516 (1982)
3. Bandyopadhyay, D., Singru, R.M., Biswa, A.K.: Min. Eng. J. **13**(8–9), 973–978 (2000)
4. Stevens, J.G., Khasanoy, A.M., Miller, J.W., Pollak, H., Li, Z.: Mössbauer Effect Data Centre, 1998

Hyperfine Interact (2006) 168:929–935
DOI 10.1007/s10751-006-9461-8

Mössbauer analysis and magnetic properties of Invar Fe–Ni–C and Fe–Ni–Mn–C alloys

V. M. Nadutov · Ye. O. Svystunov · S. G. Kosintsev · V. A. Tatarenko

Published online: 5 December 2006

Abstract The saturation magnetization and the hyperfine magnetic field of different f.c.c. Fe–Ni based alloys containing nearby 29 at .% Ni were studied as a function of temperature and for different Carbon and Manganese contents. We have observed abnormal behaviors that are explained in terms of mixed exchange interactions between atomic spins: $J_{\mathrm{NiNi}}(r_i) < 0$, $J_{\mathrm{FeFe}}(r_i) > 0$, $J_{\mathrm{NiFe}}(r_i) < 0$.

Key words Mössbauer spectroscopy · magnetic susceptibility · saturation magnetization · exchange interaction

1 Introduction

The Invar f.c.c. Fe-36at % Ni alloys show anomalously low thermal expansion in the temperature range of 4.2–300 K [1]. Alloying with carbon is considered as undesirable due to the loss of Invar properties [2]. But as shown in [3], the positive or negative effect of C on the Invar behavior of the f.c.c. Fe–Ni–C alloys depends on Ni concentration. In the Fe–Ni–C alloys containing lower Ni concentration (30 at.% Ni) than in standard Invar (Fe-36 at.% Ni) carbon reduces thermal expansion at 110–300 K by approximately one order. The physical reason of such an effect of C is still opened. As assumed, the interstitial carbon changes the magnetic state of alloys resulting from the increase of interatomic distances and variations of the short-range atomic order. As previously shown, carbon in f.c.c. Fe–Ni alloys increases the hyperfine magnetic fields [4], the Curie temperature [4–6] and the intensity of the small-angle neutron scattering [7]. The study of the temperature-dependent saturation magnetization and hyperfine magnetic fields in the f.c.c. Fe–Ni, Fe–Ni–C and Fe–Ni–Mn–C alloys is the aim of this work.

V. M. Nadutov (✉) · Ye. O. Svystunov · S. G. Kosintsev · V. A. Tatarenko
G. V. Kurdyumov Institute for Metal Physics of the National Academy of Sciences of Ukraine, Kiev, Ukraine
e-mail: nadvl@imp.kiev.ua

Table I Chemical composition and Curie point[a] of alloys

Ni (at %)	Mn (at %)	C (at %)	Fe	$T_C(\chi_{ac})$ K	$T_C(M)$ K
28.18	–	–	Balance	335	402[b]
27.63	–	5.85	Balance	454	496
28.77	0.63	–	Balance	322	398[b]
28.80	0.43	5.51	Balance	438	489
29.93	1.06	6.62	Balance	422	–
33.55	–	–	Balance	512	546
33.99	–	2.82	Balance	546	594

[a] $T_C(\chi_{ac})$ and $T_C(M)$ were determined from variations of the magnetic susceptibility and saturation magnetization, respectively;

[b] T_C was obtained at cooling.

2 Experimental

The chemical compositions of the f.c.c. Fe–Ni, Fe–Ni–C, Fe–Ni–Mn–C alloys are listed in Table I. The C concentration was determined by chemical analysis and the concentration of substitution elements by X-ray fluorescence. Samples were annealed in vacuum at 1,373 K during 30 min and subsequently quenched in oil. The X-ray diffraction data show that alloys were in austenitic state.

Mössbauer measurements have been carried out on the MS1101E spectrometer in the constant acceleration mode at temperatures in the range 163–413 K. ^{57}Co (Cr) of 1.8 MBq was the source of γ-radiations. The magnetization was measured within the temperature range of 77–780 K by means of ballistic magnetometer with the magnetic field H = 800 kA·m^{-1}, which is sufficient for saturation of a Fe–Ni sample [5, 6, 8]. The low field alternating current (ac) magnetic susceptibility was measured at temperatures between 77 and 560 K. The magnitude of the magnetic field and the frequency were 400 A·m^{-1} and 1 kHz, respectively.

3 Results and discussion

The martensitic transformation is observed for carbon-free alloys. The values of the martensitic point (M_S) obtained from the magnetic susceptibility (Figure 1a,c) and from the saturation magnetization (Figure 2a) are different. The applied external magnetic field, which is greater in the case of magnetization measurements, increases M_S [9, 10]. This is interpreted theoretically in [11]. The martensitic transition is suppressed by addition of carbon (decreasing of M_S), which results in the reversibility of the magnetization and magnetic susceptibility curves at cooling and heating (Figures 1b, d, and 2b).

The values of the magnetic transition temperatures, T_C, evaluated from the temperature-dependent magnetic susceptibility, $T_C(\chi_{ac})$, (Figure 1) and from the saturation magnetization, $T_C(M)$, (Figure 2) are listed in Table I. $T_C(M)$ is 10–20% greater than $T_C(\chi_{ac})$ (Table I). This is due to the effect of the rather large external magnetic field (800 kA·m^{-1}). The increase of T_C in f.c.c. Fe–Ni–Co–Cu–Ti alloys under applied magnetic field was previously observed and interpreted in terms of the $\Delta T_C \sim H^{2/3}$ law in [9].

However, the observed main trend is the increase of the magnetic transition temperature ($T_{>C}(\chi_{ac})$ or $T_C(M)$) with Ni concentration and this does not depend on the experimental

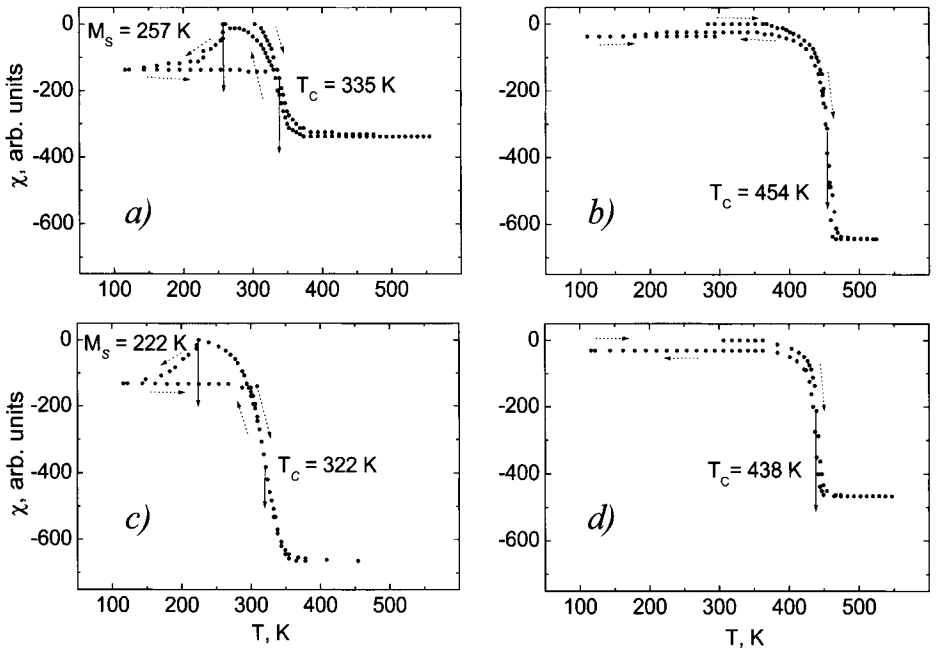

Figure 1 Temperature-dependent magnetic susceptibility of Fe-28.18% Ni (**a**), Fe-27.63% Ni-5.85% C (**b**), Fe-28.77% Ni-0.63% Mn (**c**), Fe-28.80% Ni-0.43% Mn-5.51% C (**d**). M_s is the martensitic point, T_C is the Curie temperature.

technique. The ac susceptibility data show that T_C increases by 177 K with increasing Ni content from 28.18 up to 33.55 at.% in the binary Fe–Ni alloys (Table I). Alloying with 5.85at % C (≅ 1 wt.%) of the alloy containing ~29at % Ni results in the increase of T_C by 119 K, which is consistent with the data of [4–6]. The value of T_C for the Fe-33.99at % Ni-2.82at % C alloy containing carbon is greater than that of the Fe-33.55at % Ni alloy (Table I), however this increase is smaller than in the case of lower Ni content and does not confirm the data obtained in [5]. Thus, the Curie point strongly depends on the presence of carbon in f.c.c. Fe–Ni alloys and this effect is related to the Ni concentration. The addition of 0.63at % Mn has an opposite effect on T_C which decreases by 13 K with respect to the binary Fe–Ni alloy (Table I). Simultaneous alloying with 0.43at % Mn and 5.51at % C reduces T_C at a value lower than the Curie point of the Fe-27.63at % Ni-5.85at % C alloy. Increasing Mn content in the Fe-29.93at % Ni-1.06at % Mn-6.62at % C alloy decreases T_C by about 32 K. The decrease of T_C with addition of Mn for Fe–Ni and Fe–Ni–C alloys was previously observed in [4]. This effect does not depend on the experimental technique of measurements and shows that Mn reduces the influence of C and Ni. This can be attributed to the decrease of the thermodynamical activity of C by Mn in austenite resulting in atomic clustering [12]. Moreover, Mn is the source of antiferromagnetic ordering.

The magnetization curves, $M(T/T_C)/M_0$, were plotted using the values of $T_C(\chi_{ac})$. M_0 was obtained from the extrapolation of the experimental data to zero temperature (Figure 2). The behavior of $M(T/T_C)/M_0$ curves (Figure 3a, b) depends on the Ni content and the presence of C. Both the increase of 5.37at % Ni concentration from 28.18 to 33.55at % in binary Fe–Ni alloys and the increase of 5.85at % C in the Fe-27.63at % Ni-5.85at % C alloy lead to the increase of the magnetization (Figures 2b, and 3a). Similar changes are observed for the Fe–Ni–Mn–C alloys (Figures 2b, 3b). The largest magnetization is

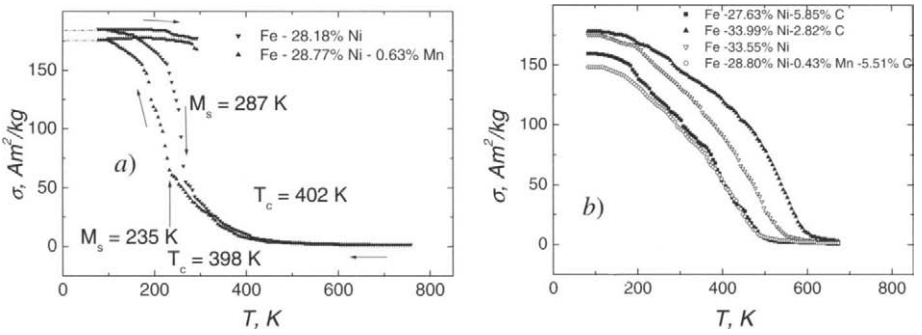

Figure 2 Temperature-dependent saturation magnetization for Fe-28.18 at % Ni, Fe-28.77at % Ni-0.63at % Mn alloys after heating and following cooling (**a**) and Fe-33.55at % Ni, Fe-27.63at % Ni-5.85at % C, Fe-33.99at % Ni-2.82at % C, Fe-28.80at % Ni-0.43at % Mn-5.51at % C (**b**, heating curves). M_s is the martensitic point, T_C is the Curie temperature.

observed for the alloy with 33.99at % Ni and 2.82at % C, which however remains lower than $M(T/T_C)/M_0$ relating to pure Ni.

In order to explain the influence of C the exchange interaction parameters were estimated from the variations of the Curie point with the concentration by using the $T_C(C_{Ni}, C_C)$ values of Table I and [4–6], and from the references listed in [13]. This approach is based on statistical-thermodynamic self-consistent field approximation [14]. The expression of T_C for a disordered f.c.c. $Fe_{1-c_{Ni}}Ni_{c_{Ni}}$ alloy was considered in [13, 14]. The exchange interaction energies for the nearest interatomic distances r_i were estimated using the relationship: $J_{\alpha\alpha'}(r_1 = a/\sqrt{2}) \cong \tilde{J}_{\alpha\alpha'}(0)/12$, where a is the f.c.c. unit cell parameter, $\tilde{J}_{\alpha\alpha'}(k)$ are the Fourier-components of the exchange interaction energies for wave vector $\boldsymbol{k} = \boldsymbol{0}$.

The different signs of the exchange integrals, $J_{NiNi}(r_i) < 0$, $J_{FeFe}(r_i) > 0$, $J_{NiFe}(r_i) < 0$ (Table II), indicate the existence of mixed exchange interactions in the f.c.c. Fe–Ni alloys: the ferromagnetic (FM) Fe–Ni and Ni–Ni and the antiferromagnetic (AF) Fe–Fe interspin interactions. This is qualitatively consistent with the data of [15, 16]. The addition of C saves the mixed character of interspin interactions by weakening the Ni–Ni FM and increasing the Fe–Ni FM and Fe–Fe AF interspin interactions (Table II).

Using the $\tilde{J}_{\alpha\alpha'}(k)$ values (Table II) and the most realistic spin values $s_{Fe} = 3/2$ and $s_{Ni} = 1/2$ [1] we have simulated the temperature dependence of the reduced magnetization for the Fe-28at % Ni and Fe-28at % Ni–C systems:

$$\frac{M}{M_0} = \frac{\sigma_{Fe}{}^{s}{}_{Fe}{}^{c}{}_{Fe} + \sigma_{Ni}{}^{s}{}_{Ni}{}^{c}{}_{Ni}}{\sigma_{Fe}^{T\to 0}{}^{s}{}_{Fe}{}^{c}{}_{Fe} + \sigma_{Ni}^{T\to 0}{}^{s}{}_{Ni}{}^{c}{}_{Ni}},$$

where σ_{Fe} and σ_{Ni} are the partial (per atom) magnetizations of Fe and Ni in the f.c.c. Fe–Ni alloy, which are given by the Brillouin's functions [14]:

$$\sigma_{Fe} = B_{S_{Fe}}\left(-\frac{1}{(1-c_{Ni})k_BT}\left\{\tilde{J}_{FeFe}(0)(1-c_{Ni})^2 s_{Fe}^2\sigma_{Fe} + \tilde{J}_{FeNi}(0)c_{Ni}(1-c_{Ni})s_{Fe}s_{Ni}\sigma_{Ni}\right\}\right)$$

$$\sigma_{Ni} = B_{S_{Ni}}\left(-\frac{1}{c_{Ni}k_BT}\left\{\tilde{J}_{NiNi}(0)c_{Ni}^2 s_{Ni}^2\sigma_{Ni} + \tilde{J}_{FeNi}(0)c_{Ni}(1-c_{Ni})s_{Fe}s_{Ni}\sigma_{Fe}\right\}\right)$$

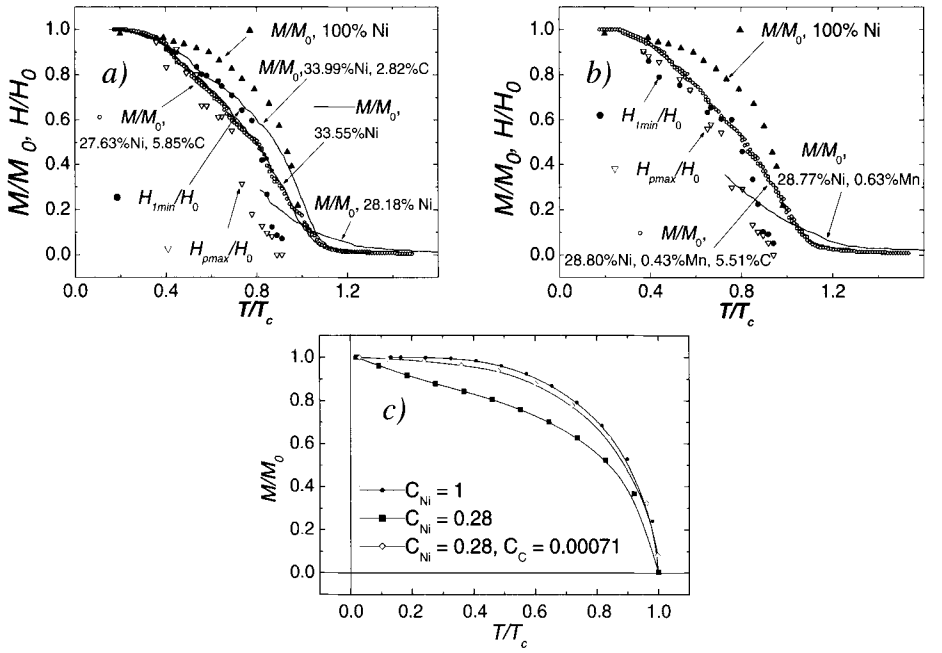

Figure 3 Reduced saturation magnetization and hyperfine magnetic field vs. reduced temperature for Fe-33.35 at % Ni, Fe-27.63 at % Ni-5.85 at % C, Fe-33.99 at % Ni-2.82 at % C (**a**) and Fe-28.80 at % Ni-0.43 at % Mn-5.51 at % C (**b**) (heating curves) and for Fe-28.18 at % Ni (**a**) and Fe-28.77 at % Ni-0.63 at % Mn (**b**) (cooling curves). Calculated $M(T/T_C)/M_0$ curves vs. reduced temperature (**c**). ▲ denotes M/M_0 for pure Ni [2].

Table II Fourier-components of exchange interaction energies $\tilde{J}_{\alpha\alpha'}(k)$ (eV) and relevant exchange integrals for nearest spins interaction $J_{\alpha\alpha'}(r_1)$ (meV) for two low-spin states of Ni and Fe atoms in disordered f.c.c. Fe–Ni and Fe–Ni–C alloys

c_C	s_{Ni}	s_{Fe}	$\tilde{J}_{NiNi}(0)$	$J_{NiNi}(r_1)$	$\tilde{J}_{FeFe}(0)$	$J_{FeFe}(r_1)$	$\tilde{J}_{NiFe}(0)$	$J_{NiFe}(r_1)$
–	1/2	3/2	−0.211	−17	0.074	6	−0.240	−20
0.00071	1/2	3/2	−0.186	−15.5	0.262	21.8	−0.314	−26

Signs of $J_{NiNi}(r_i) < 0$, $J_{FeFe}(r_i) > 0$, $J_{NiFe}(r_i) < 0$ are opposite to those obtained in [15, 16] that is associated with the initial definition of the exchange interaction energy and remains the correct determination of FM and AF ordering.

One can notice the deviation of the calculated $M(T/T_C)/M_0$ function for the Fe–Ni system from the curve of Ni metal (Figure 3c). Addition of carbon raises the magnetization curve, which however remains lower than that for pure Ni. The Mössbauer spectra of the Fe-27.63at % Ni-5.85at % C and Fe-28.80at % Ni-0.43at % Mn-5.51at % C alloys has a smeared shape with broadened components (Figure 4). The hyperfine magnetic field lies within the interval of 3–40 T at 293 K and the distribution of values $p(H)$ differs from the rather narrow function for C-free Fe–Ni alloys [4]. The broadened distribution of fields is attributed to fluctuations of spin density at Fe nuclei in different atomic configurations of Fe with C and Ni (Mn). The asymmetric shape of the spectra is due to the wide distribution of

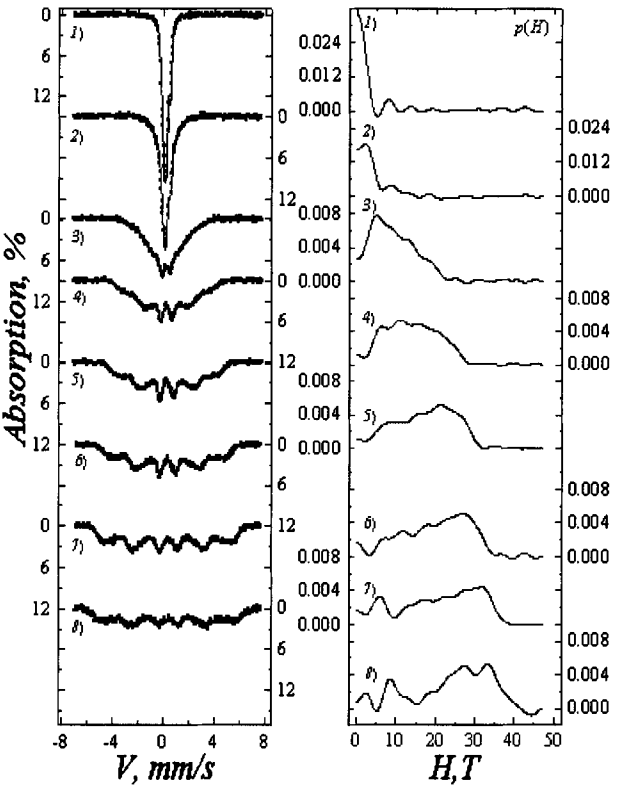

Figure 4 Temperature-dependent Mössbauer spectra of the Fe-28.80 at % Ni-0.43 at % Mn-5.51 at % C alloy at different temperatures: 413 K *(1)*, 403 K *(2)*, 373 K *(3)*, 333 K *(4)*, 293 K *(5)*, 253 K *(6)*, 193 K *(7)*, 163 K *(8)* and distribution of hyperfine magnetic fields p (H).

isomer shifts, $p(\delta)$ [13]. Increasing the temperature in the range of 163–413 K narrowed the Mössbauer spectra and the magnetic splitting collapsed as the temperature achieved T_C (Figure 4). The observed doublets in the spectra are due to quadruple interactions and are usually observed for γ-Fe–C solid solution [12]. The temperature-dependent Mössbauer spectra of the Fe-27.63at % Ni-5.85at % C alloy are given in [13].

The H_{1min} values were evaluated from the minimum of the first derivative on the right slope of the p (H) function and the H_{Pmax} values from the maximum. H_0 was obtained from the extrapolation of the experimental $H(T/T_C)$ points to zero temperature. For this procedure we have considered $H(T/T_C)/H_0 = 0.91–0.96$ for the Fe–Ni–C and Fe–Ni–Mn–C alloys at $T/T_C = 0.35–0.40$ (the lowest temperatures in our experiments) by assuming that values are close to those of Invar Fe–Ni alloys: 0.89–0.95 [17, 18].

One can notice the drastic decrease of H_{1min}/H_0 and H_{Pmax}/H_0 at temperatures lower than $T_C(\chi_{ac})$ (Figure 3a,b). The estimated temperatures T_C $(H) = 407 \pm 15$ K and T_C $(H) = 402 \pm 15$ K for the Fe-27.63at % Ni-5.85at % C and Fe-28.80at % Ni-0.43at % Mn-5.51at % C alloys, respectively, are lower than those determined from ac susceptibility and magnetization measurements (Table I) because they were obtained without external magnetic field. It is also worth noticing that the relationship $H = A <M> + B\mu_{Fe}$ (where A and B are constants) [19] cannot be used for C-containing Invar alloys. For example, $B/A = 1.24$ kOe/μ_B at low temperature and $B/A = 0.19$ kOe/μ_B nearby T_C for the Fe-27.63 at.% Ni-5.85at % C alloy. We think that deviation of H($<M>$) from the linear relationship can be related to the activation by the C atoms of different contributions to H at the Fe nuclei ($H_{cp} < 0$, $H_{sp} > 0$, $H_n < 0$, [20]) and at different temperatures.

4 Conclusions

The values of the hyperfine magnetic fields in f.c.c. Fe–Ni–C and Fe–Ni–Mn–C alloys are distributed in a broad range which depends on the temperature. This shows a considerable inhomogeneity in the magnetic order. The values of the magnetization and hyperfine magnetic field in the f.c.c. Fe–Ni–C and Fe–Ni–Mn–C alloys containing ~29 at.% Ni strongly decrease with increasing temperature compared to magnetization of pure Ni. Increase of Ni content by 5.37at % Ni or addition of 5.85at % C into ~29at % Ni alloys leads to the increase of the magnetization. We have also shown that Curie temperature depends on the method of measurements in the following order: $T_C(H) < T_C(\chi_{ac}) < T_C(M)$. The mixed exchange interactions between the atomic spins: $J_{NiNi}(r_1) < 0$, $J_{FeFe}(r_1) > 0$, $J_{NiFe}(r_1) < 0$ in Fe–Ni and Fe–Ni–C alloys are of great importance for both the magnetic order and the anomalous behaviour of the temperature-dependent saturation magnetization.

Acknowledgments This work was financially supported by STCU (the no. 2412 project). Authors thank to T.V. Efimova and O. Babij for magnetic measurements.

References

1. Physics and Applications of Invar Alloys (Honda Memorial Series on Materials Science, Maruzen Company, Ltd, Tokyo) No. 3, p. 646 (1978)
2. Zakharov, A.I.: Physics of Precision Alloys with Special Thermal Properties (in Russian, Metallurgija, Moscow), p. 238 (1986)
3. Nadutov, V.M., Svystunov, Ye.O.: Metallofiz. Novejs. Tehnol. (in Ukrainian) **24**(12), 1639 (2002)
4. Nadutov, V.M., Svystunov, Ye.O., Efimova, T.V., et al.: In: Mashlan, M., Miglierini, M., Schaaf, P. (eds.) Material Research in Atomic Scale by Mössbauer Spectroscopy, NATO Science Series, Math. Phys. Chem., vol. 94, p. 105 (2003)
5. Georgieva, I.Ya., Maksimova, O.P.: Fiz. Met. Metalloved. (in Russian) **24**, 574 (1967)
6. Kalinin, V.M., Beskachko, V.P.: Fiz. Met. Metalloved. (in Russian) **36**(1), 73 (1973)
7. Nadutov, V.M., Garamus, V.M., Willumeit, R., et al.: Mat. Sci. Forum **443–444**, 251 (2004)
8. Asano, H.: J. Phys. Soc. Jpn. **27**(3), 542 (1969)
9. Chernenko, V.A., Kokorin, V.V., Minkov, A.V.: Phys. Status Solidi **134**, 193 (1992)
10. Kakeshita, T., Shimizu, K., Kijima, S., et al.: Trans. Jpn. Inst. Met **26**(9), 630 (1985)
11. Krivoglaz, M.A., Sadovskij, V.D.: Fiz. Met. Metalloved. (in Russian) **18**(4), 502 (1964)
12. Bugaev, V.N., Gavrylyuk, V.G., Nadutov, V.M., et al.: Fiz. Met. Metalloved. (in Russian) **68**(5), 931 (1989)
13. Nadutov, V.M., Svystunov, Ye.O., Kosintsev, S.G., et al.: Izvestiya RAN, Ser. Fiz. (in Russian) **69**(10), 1475–1481 (2005)
14. Tatarenko, V.A., Radchenko, T.M., Nadutov, V.M.: Metallofiz. Novejs. Tehnol. (in Ukrainian) **25**(10), 1303 (2003)
15. Dubé, M., Heron, P.R.L., Rancourt, D.G.: JMMM, A **147**(1), 122 (1995)
16. Dang, M.-Z., Dubé, M., Rancourt, D.G.: JMMM, B **147**(1), 133 (1995)
17. Tomiyoshi, S., Yamamoto, H., Watanabe, H.: J. Phys. Soc. Jpn. **30**(6), 1605 (1971)
18. Makarov, V.A., Puzey, I.M.: Fiz. Met. Metalloved. (in Russian) **38**(1), 161 (1974)
19. Shiga, M., Maeda, Y., Nakamura, Y.: J. Phys. Soc. Jpn. **37**(2), 363 (1974)
20. Turov, E.A. (ed.) Hyperfine Interactions in Solids (in Russian, Mir, Moscow), p. 368 (1970)

Hyperfine Interact (2006) 168:937–942
DOI 10.1007/s10751-006-9399-x

Phase coexistence in mechanicallly alloyed iron–manganese powders

V. V. Tcherdyntsev · L. Yu. Pustov · S. D. Kaloshkin · E. V. Shelekhov · G. Principi

Published online: 8 November 2006

Abstract Iron–manganese alloys with Mn concentration of 6–30 at.% were prepared by mechanical alloying. Structure and phase composition of the samples were investigated by X-ray diffraction and Mössbauer spectroscopy. Mechanical alloying results in the formation of b.c.c. and f.c.c. solid solutions with high concentration of structure defects and refined grains. A single b.c.c. phase was observed in Fe–Mn alloys a Mn concentration less than $\leq$8 at.% and, for higher Mn contents, a mixture of b.c.c. and f.c.c. phases was observed. The main features of phase composition of as-prepared alloys consisted in significant widening of single phase concentration range.

Key words mechanical alloying · phase composition · X-ray diffraction · Mössbauer spectroscopy

1 Introduction

Iron-rich alloys of Fe–Mn systems belong to the martensitic class. b.c.c. and/or h.c.p. phases appear through non-diffusional martensitic mechanism by cooling from the temperature range of f.c.c. phase stability [1]. Temperature starting and end points of martensite transformation are sensitive to the parameters of the alloy structure determined by the method of preparation and treatment – including deformation. These questions have been always discussed in review papers as ref. [2]. However, a particularly strong influence on the martensitic points can be achieved using methods of alloy preparation far from equilibrium. For example, a significant decrease in the martensitic points of Fe–Ni alloys was obtained

V. V. Tcherdyntsev (✉) · L. Yu. Pustov · S. D. Kaloshkin · E. V. Shelekhov
Moscow State Institute of Steel and Alloy, Leninsky prosp., 4, Moscow 119049, Russia
e-mail: vvch@misis.ru

G. Principi
Settore Materiali and INFM, Dipartimento di Ingegneria Meccanica, Università di Padova, via Marzolo 9, 35131 Padova, Italy

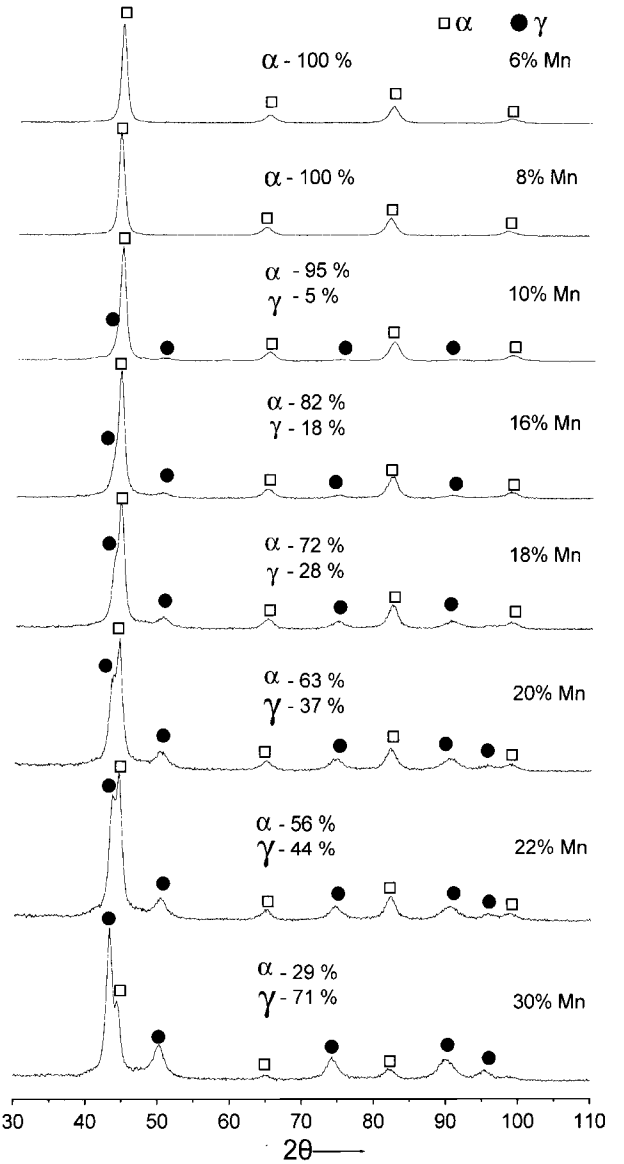

Figure 1 X-ray diffraction patterns of Fe-Mn powders after ball milling. The phase composition of samples is indicated in correspondence to each pattern.

by rapid quenching from the melt [3, 4]. Mechanical alloying, which is one application of the most general high energy ball milling technique, is one of the most severe mechanical treatments of materials at relatively low temperature. Due to the very high degree of induced material deformation, this method allows to obtain non-equilibrium and very defective structures. For instance, the Fe–Ni alloys preparation by ball-milling also results in a significant lowering of the martensitic points [5, 6].

We recently studied the phase compositions of mechanically alloyed Fe–Mn [7, 8] and Fe–Ni [9, 10] systems in wide composition ranges. We also reported about a significant retardation, compared to the equilibrium alloys, of martensitic transformation in Fe–Ni alloys obtained by ball milling of elemental powder mixtures [11, 12]. In this work we

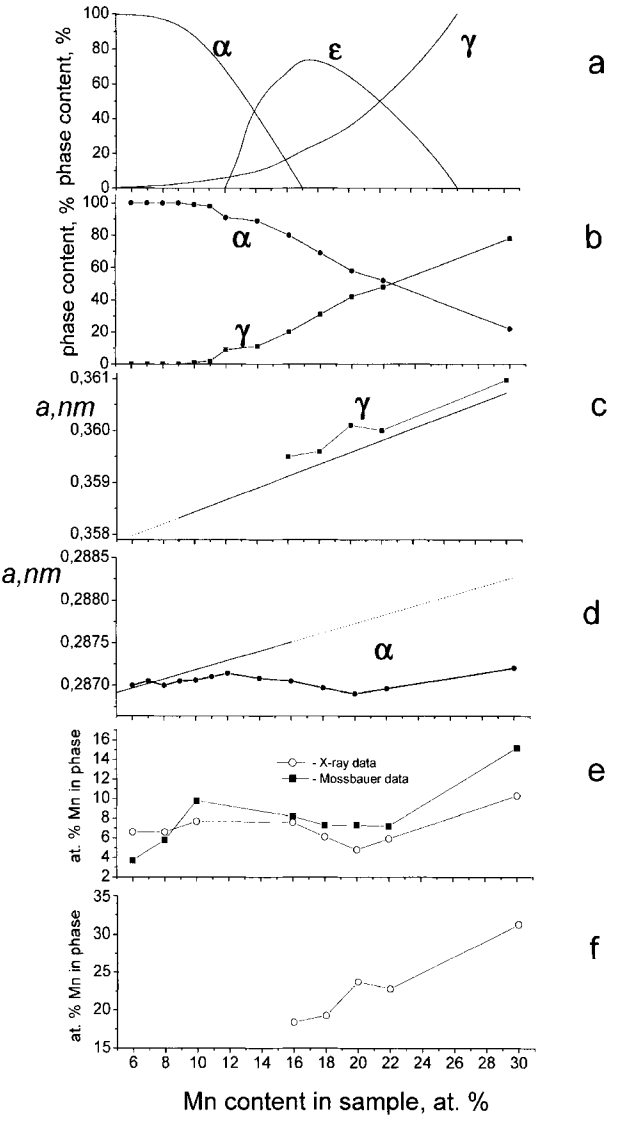

Figure 2 Behaviour vs. Mn content of: phase composition according to data [13] for metastable cast alloys (**a**) and for as-milled Fe-Mn samples (**b**); of lattice parameter for b.c.c. (**c**) and f.c.c. phases (**d**) (our data are indicated with lines and symbols, literature data [14] are indicated with straight lines) and of chemical composition of b.c.c. (**e**) and f.c.c. phase (**f**).

investigate the influence of mechanical alloying on the phase composition of the Fe–Mn system.

2 Experimental

Ball milling of powder mixtures of carbonyl iron (99.95%) and electrolytic manganese (99.5%) was carried out in the planetary ball mill AGO-2U for the preparation of binary alloys $Fe_{100-x}Mn_x$ (x=6, 8, 10, 14, 16, 18, 20, 22, 30 at.% Mn). Fifteen grams of material and 150 g of 7.8 mm-diameter steel balls were loaded into hermetic 160-cm^3 steel vials. The milling process was conducted in argon atmosphere. X-ray diffraction analysis was performed with a DRON-3 diffractometer using the CuK_α radiation. Room temperature

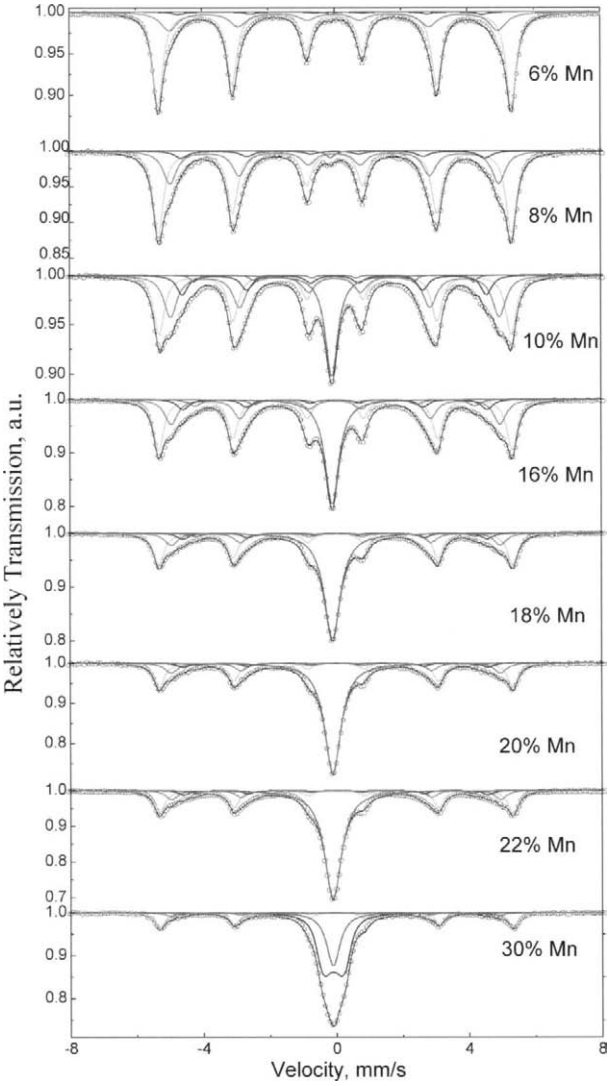

Figure 3 Mössbauer spectra of Fe-Mn powders after ball milling.

Mössbauer measurements were carried out by means of a constant acceleration spectrometer with a ^{57}Co:Rh source. The isomer shifts were calculated with respect to the centroid of the α-Fe spectrum. Conventional minimization routines were used to obtain the best fit of the spectra.

3 Results and discussion

X-ray patterns of as-milled samples in Figure 1 show that mechanical alloying leads to the formation of b.c.c. (α-Fe) and f.c.c. (γ-Fe) solid solutions. A single b.c.c. phase is observed in similar alloys with manganese concentration $x \leq 8$ at.%, while both b.c.c. and f.c.c.

phases are present for $10 \leq x \leq 30$ at. 57 %. Figure 2 shows the results of X-ray diffraction data analysis. Comparison of the phase composition of as-milled alloys (Figure 2b) with literature data for metastable cast alloys (Figure 2a) [13] evidences that mechanical alloying results in significant expansion of the concentration range of the single-phase b.c.c. solid solution. No h.c.p. phases were observed in any studied alloys. Figures 2c and 2d report the values of lattice parameter for our as-milled alloys compared with literature data of Fe–Mn b.c.c. and f.c.c. alloys [14] represented as linear behaviours and extrapolated to the two-phases area of the phase diagram.

The chemical composition of coexisting phases in mechanically alloyed samples (Figure 2e and f), calculated from our X-ray data, show that the Mn solubility in α-Fe based b.c.c. phase increases threefold compared to the equilibrium phase diagram, while in the f.c.c. phase increases by about 10%.

Figure 3 shows Mössbauer spectra of as-milled samples. The spectra may be fitted with a number of sextets, each one corresponding to a lattice site with a number of Mn atoms in the b.c.c. phase with a central component, which consist of collapsed sextet related to antiferromagnetic f.c.c. phase and with a singlet which, as it was proposed in [15], may be associated with Fe atoms in stacking faults of f.c.c. structure. Indeed, our previous investigations show that stacking faults concentration in the f.c.c. phase of mechanically alloyed Fe–Mn alloys is about 4–9%, depending on the chemical composition of the sample [8]. By using the Mössbauer data, we have calculated the content of Mn in b.c.c. phase (for the procedure see [8, 15]). The results are presented in Figure 2e and are in rough agreement with the values obtained from X-ray data.

For single-phase alloys (total Mn concentration ≤ 8 at.%), the calculated Mn content in b.c.c. phase was well in line with the nominal one. For the two-phase samples (total Mn concentration $10 \leq \times \leq 30$ at.%), the b.c.c. phase was enriched with Fe and f.c.c. phase was enriched with Mn in relation to the total sample composition. This difference is appropriate for cast alloys, but for the mechanically alloyed ones, special attention is necessary. It was reported [16–18] that for mechanically alloyed binary systems, the chemical composition of the two coexisting phases is the same and is equal to the total chemical composition of powder. However, in our case, the chemical composition of the coexisting phases in ball-milled alloys follows not so closely the values predefined by classical thermodynamics of binary systems. The behaviour of the chemical composition of coexisting phases in mechanically alloyed powders will be a topic for future research.

Acknowledgements This study was supported by RFBR project 05-03-32780.

References

1. Houdremont, E.: Handbuch der Soderstahlkunde. Springer, Berlin Heidelberg New York (1956)
2. Thatnani, N.N., Meyers, M.A.: Progr. Mater. Sci. **30**, 1 (1986)
3. Inokiti, Y., Cantor, B.: Scripta Met. **10**, 655 (1976)
4. Inokiti, Y., Cantor, B.: J. Mater. Sci. **12**, 946 (1977)
5. Kuhrt, C., Schultz, L.: J. Appl. Phys. **73**, 1975 (1993)
6. Kuhrt, C., Schultz L.: J. Appl. Phys. **73**, 6588 (1993)
7. Tcherdyntsev, V.V., Kaloshkin, S.D., Tomilin, I.A., Shelekhov, E.V., Baldokhin Y.V.: Z. Metallk. **90**, 747 (1999)
8. Uhrmacher, M., Kulinska, A., Baldokhin, Y.V., Tcherdyntsev, V.V., Kaloshkin, S.D., Maddalena, A., Principi, G.: Intermetallics **10**, 571 (2002)
9. Baldokhin, Yu.V., Tcherdyntsev, V.V., Kaloshkin, S.D., Kochetov, G.A., Pustov, Yu.A.: J. Magn. Magn. Mater. **203**, 313 (1999)

10. Tcherdyntsev, V.V., Kaloshkin, S.D., Tomilin, I.A., Shelekhov, E.V., Baldokhin, Yu.V.: Nanostr. Mater. **12**, 139 (1999)
11. Kaloshkin, S.D., Tcherdyntsev, V.V., Baldokhin, Yu.V., Tomilin, I.A., Shelekhov, E.V.: J. Non-Cryst. Solids **287**, 329 (2001)
12. Kaloshkin, S.D., Tcherdyntsev, V.V., Tomilin, I.A., Baldokhin, Y.V., Shelekhov, E.V.: Physica. B. **299**, 236 (2001)
13. Volynova, T.F.: Vysokomargantsovistye stali I splavy. Metallurgiyad, Moscow (1988)
14. Li, C.-M., Sommer, F., Mittemeijer, E.J.: Mater. Sci. Eng., A. **325**, 307 (2002)
15. Tcherdyntsev, V.V., Kaloshkin, S.D., Tomilin, I.A., Shelekhov, E.V., Baldokhin, Yu.V.: Phys. Met. Metallogr. **94**, 391 (2002)
16. Hong, L.B., Fultz, B.: J. Appl. Phys. **79**, 3946 (1996)
17. Schilling, P.J., He, J.H., Tittsworth, R.C., Ma, E.: Acta Mater. **47**, 2525 (1999)
18. Schilling, P.J., Palshin, V., Tittsworth, R.C., He, J.H., Ma, E.: Phys. Rev. B **68**, 224204 (2003)

Hyperfine Interact (2006) 168:943–949
DOI 10.1007/s10751-006-9383-5

Synthesis and characterization of $Fe_3AlC_{0.5}$ by mechanical alloying

W. Barona Mercado · M. Fajardo · G. A. Pérez Alcázar · H. Sánchez Sthepa

Published online: 7 December 2006

Abstract Double iron and aluminum carbides were prepared by mechanical alloying from elemental powders, with a ball-to-powder weight ratio 20:1. The samples were milled for 1, 3, 5, 10, 15, 20 and 25 h. The alloy progress for each milling time was evaluated by X-ray diffraction (XRD) and ^{57}Fe Mössbauer spectroscopy. Once the alloy was consolidated two sorts of paramagnetic sites and a magnetic distribution were detected according to the Mössbauer fit. The majority doublet could correspond to $Fe_3AlC_{0.5}$ carbide as X-ray diffraction suggest, and the other could be $Fe_3AlC_{0.69}$; the magnetic distribution corresponding to Fe_3Al phase, Fe_7C_3 and Fe_5C_2 single carbides. The hyperfine parameters are reported.

Key words double carbide · mechanical alloying · Mössbauer spectroscopy

1 Introduction

The structure of metallic carbides is generally governed by the ratio of the atomic radius between the metal and the carbon atoms (Hägg's rule). Starting with the close-packed lattice of the metallic elements, the successive incorporation of the smaller C atoms into octahedral sites results in the development of structures with various sequences of occupied carbon layers, such as: MC, M_2C, M_3C_2, M_3C, M_6C, M_7C_3 and $M_{23}C_6$ [1].

Carbon forms double carbides too, requiring the integration of two metals to be stable. It is favored when one of the two metals is a stronger carbide former than the other one. Two

W. B. Mercado (✉)
Universidad Santiago de Cali, A.A. 4102 Santiago de Cali, Colombia
e-mail: william.barona00@usc.edu.co

M. Fajardo · G. A. P. Alcázar
Departamento de Física, Universidad del Valle, A.A. 25360 Cali, Colombia

W. B. Mercado · H. S. Sthepa
Escuela Ingeniería de Materiales, Universidad del Valle, A.A. 25360 Cali, Colombia

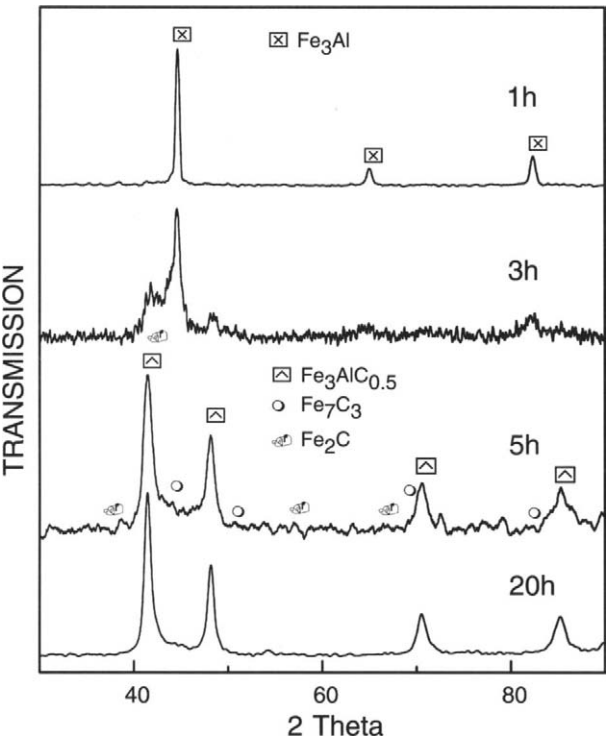

Figure 1 X-ray diffraction patterns showing the formation of the $Fe_3AlC_{0.5}$ double carbide by mechanical alloying from elemental powders of Fe, Al and C. *Symbols* show the different obtained phases.

closely related structural sub-types exist, denoted by η_1 and η_2. These differ in the relative proportions of smaller and larger atoms: $\eta_1 = A_2B_2C$ or A_3B_3C and $\eta_2 = A_2B_4C$, where A can be Ni, Co, Fe, Mn, Cr and even V, and possible Ti and B can be Mo, W, Nb, Zr, Ta and possible Hf. The lattice dimensions of η_2 are thus always larger than those of η_1. There are double carbide types $\eta = A_xB_yC$, where A is a transition metal and B is other metal such as: Al, Mg, Sn or Zn. These double carbides have their distinctive crystal structures and properties. One of the most interesting types is that of the cubic perovskite structure such as: $Fe_3AlC_{0.5}$, which has been reported previously [2, 3, 4].

Double carbides are very hard compounds conferring improved abrasion, wear resistance and superior high temperature properties to the materials in which they are embedded. Y. Minamino et al. [3] have carried out an investigation of the microstructure and mechanical properties of bulk nanocrystalline Fe Al C alloys made by mechanical alloying with subsequent spark plasma sintering. They have reported that the castings with fine precipitates of $Fe_3AlC_{0.5}$ exhibit superior mechanical properties (strength, rupture strain and Vickers hardness) than those of ordinary Fe_3Al. J. Yang et al. [2] reported that Fe_3Al composites materials with 40, 60 and 80 wt.% $Fe_3AlC_{0.5}$ have good wear resistance, high hardness and bending strength, especially with 60 and 80 wt.% $Fe_3AlC_{0.5}$.

Mechanical alloying (MA) is a solid-state powder processing technique involving repeated welding, fracturing, and rewelding of powder particles in a high-energy ball mill [5]. MA has been used to synthesize equilibrium and non-equilibrium phases using elementary or prealloyed powders. Carbides prepared by MA have been reported in several previous works [6, 7, 8].

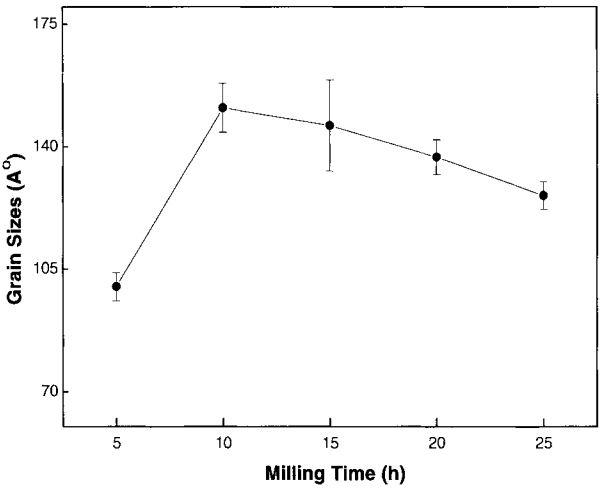

Figure 2 $Fe_3AlC_{0.5}$ grain size vs. milling time, determined from the (111) reflection of the XRD patterns.

A process control agent (PCA) is generally added to powder mixture during milling when the powder mix involves a substantial fraction of a ductile component. The PCAs are absorb on the surface of the powder particles and minimize cold welding between powder particles and lower the surface tension of the solid material. PCAs are mostly organic compounds, such as: stearic acid, hexane, oxalic acid, methanol, etc. [5]. For this alloy the carbon powder that is one constituent acts as PCA. This work reports the synthesis and characterization of $Fe_3AlC_{0.5}$ from elemental powders by mechanical alloying.

2 Experimental procedure

Pure Fe, Al, and graphite powders were weighted in a 3:1:1 atomic ratio; these powders were mixed in a flask, then they were transferred into the anvils made of hardened Cr steel with balls of the same composition and treatment; the ball-to-powder weight ratio was 20:1. The powder mixtures were milled under an argon atmosphere in a planetary ball mill type Fritsch Pulverisette 5. The planetary mill was worked at 280 rpm. So the jars run at about 730 rpm. The milling was interrupted for 1 h every hour in order to dissipate the thermal energy.

It was used 10 balls of 20 mm diameter and 10 of 11 mm diameter. The samples were milled for 1, 3, 5, 10, 15, 20 and 25 h. The alloy progress for each milling time was evaluated by X-ray diffraction (XRD) and ^{57}Fe Mössbauer spectroscopy. The XRD patterns were performed with a D8 Bruker AXS diffractomer, using the Cu–Kα radiation (λ= 1.54056 Å). Mössbauer procedure was carried out by the transmission geometry with a 20 mCi (57 Co/Rh) source using a ranger MS 1200 Spectrometer in the constant acceleration mode at room temperature. The spectra were fitted by using MOSFIT program [9].

3 Results and discussions

In order to discuss the powder structural changes undergone when milled for 1, 3, 5, 20 and 25 h, the XRD patterns are presented in Figure 1. As seen from the pattern up to the first milling hour the powders are not well alloyed yet. The Fe_3Al peak is present. The 3 h

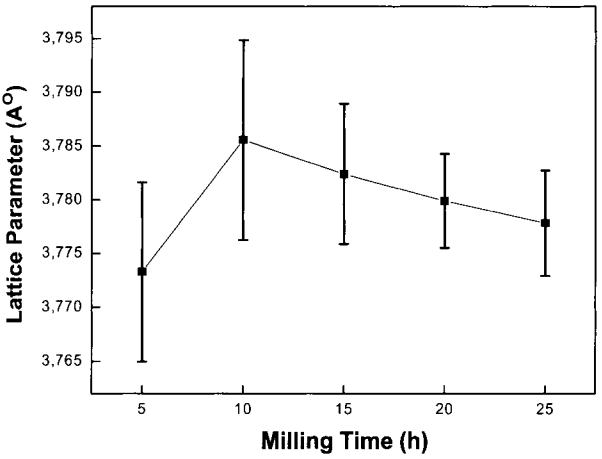

Figure 3 Lattice parameter vs. milling time of the $Fe_3AlC_{0.5}$ double carbide.

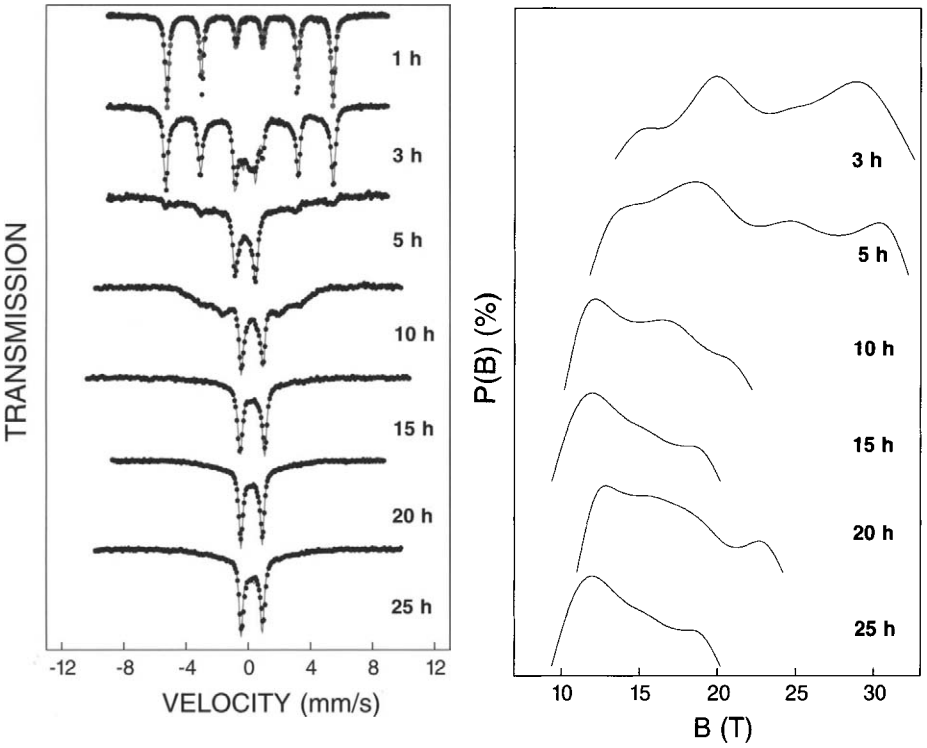

Figure 4 Mössbauer spectra and their corresponding hyperfine field distributions for the milled samples during the different times.

pattern shows that the $Fe_3AlC_{0.5}$ double carbide begins to appears, while that of the Fe_3Al is diminished. The Fe_3Al phase and the single carbides Fe_2C and Fe_3C_7, which although are difficult to observe, could be present in minor quantities. At 5 h the consolidation of the $Fe_3AlC_{0.5}$ double carbide is almost complete, while the Fe_3Al peak has practically disappeared.

Table I Hyperfine parameters for the milled samples at different times

Milling time (h)	Sites	δ (mm/s)	Γ (mm/s)	ΔE_Q (mm/s)	B_{HF} (T)	R.A. (%)
1	S	−0.064	0.15	−0.016	32.867	88.27
	D1	0.169	0.15	1.259	–	4.07
	D2	0.065	0.20	−0.390	–	7.66
3	S	0.073	0.17	0.039	32.189	28.90
	D1	−0.152	0.25	1.120	–	23.26
	D2	−0.018	0.20	−0.339	–	11.67
	MD	−0.017	–	0.231	17.028	36.17
5	D1	−0.182	0.18	1.272	–	55.42
	D2	−0.188	0.20	−0.468	–	10.67
	MD	0.119	–	0.921	9.544	33.91
10	D1	−0.195	0.15	1.290	–	60.99
	D2	−0.224	0,20	−0.501	–	16.21
	MD	−0.154	–	0.716	3.722	22.80
15	D1	−0.182	0.18	1.282	–	65.58
	D2	−0.150	0.20	−0.342	–	10.79
	MD	−0.134	–	0.805	3.936	23.63
20	D1	−0.176	0.17	1.286	–	63.89
	D2	−0.171	0.20	−0.323	–	11.50
	MD	−0.131	–	0.784	4.011	24.61
25	D1	−0.100	0.20	1.319	–	56.79
	D2	−0.025	0.25	−0.220	–	8.50
	MD	−0.025	–	0.993	5.902	34.71

δ data are given relative to α-Fe

S Sextet; *D1* doublet 1; *D2* doublet 2 and *MD* Magnetic Distribution

Single iron carbides, Fe_3C, Fe_5C_2, Fe_3C_7 and Fe_2C whose lines are overlapped because of broaden of the diffractograms [10], must be present.

The 20 and 25 h patterns show that the double carbides are totally consolidated. The single iron carbides, Fe_7C_3 and Fe_5C_2 might be still present, although the peaks are narrower.

Figure 2 presents the $Fe_3AlC_{0.5}$ grain size vs. milling time, as calculated from the Scherer's formula [11] along (111) direction, as the carbide $Fe_3AlC_{0.5}$ is synthesized. Up to 10 h the milling process might be similar to that of ductile materials, due to the welding and fracturing of he particles, the grains could increase or diminish. After the complete consolidation of the $Fe_3AlC_{0.5}$ carbide, the grain tendency is to diminish according with its brittle character.

Figure 3 summarizes the behavior of the lattice parameter vs. milling time, once the $Fe_3AlC_{0.5}$ carbide is formed. The peaks were fitted with Lorentzian curves to determine 2θ angles, and using the Bragg's law, the lattice parameter was calculated.

Figure 3 shows that within the experimental error, this parameter remains practically constant, and corresponds to the fact that they are very hard materials difficult to deform plastically. Its value, 3.77 A°, is very similar to that reported by the chart 29-0044 [12].

Figure 4 shows the ^{57}Fe Mössbauer spectra and the corresponding hyperfine field distributions (HFD) for the milled samples during the times consider above, the hyperfine parameters are listed in Table I. The isomer shift data are given relative to α-Fe.

The spectrum corresponding to one milling hour was fitted with a sextet and two doublets. The sextet was associated with Fe_3Al phase which is formed at the beginning of

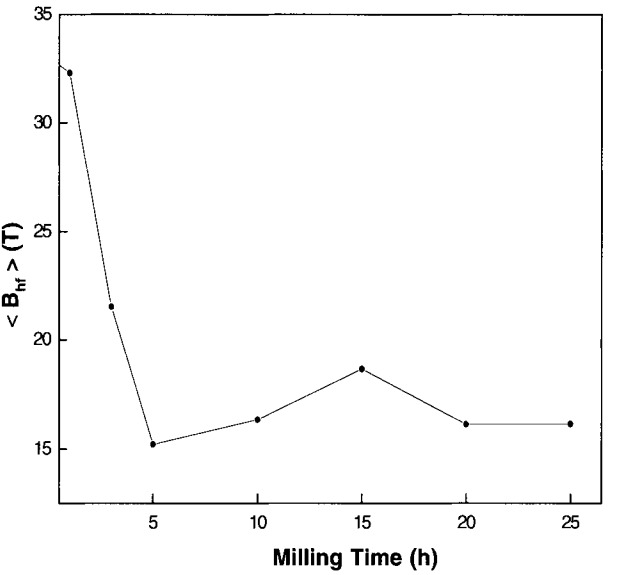

Figure 5 Milling time dependence of the average hyperfine field $\langle\beta\rangle_{magn}$.

the milling operation and seems to act as a precursor of the other species, and that's why it disappears as the milling time proceeds. The doublets were associated with the paramagnetic phases corresponding to $Fe_3AlC_{0.5}$ and $Fe_3AlC_{0.69}$ double carbides. These phases aren't defined in the corresponding XRD spectra.

The 3 h spectrum was fitted using a sextet, corresponding to the Fe_3Al site, two doublets associated with $Fe_3AlC_{0.5}$ and $Fe_3AlC_{0.69}$ double carbides and a HFD, This HFD which must represent single iron magnetic carbides; these phases are difficult to observe in the XRD diffractograms. The quadrupole splitting of the sextets for 1 and 3 h spectra fluctuates because of the disturbance of the crystal lattice by carbon atoms [13]. The 5 h milling spectrum maintains the impure Fe_3Al component by carbon atoms, which was considered in the HFD, and characterized by hyperfine fields from 25.8 to 33.9 T, besides the single iron carbides. From 10 to 25 h the fit of the spectra require two doublets and one HFD; each doublet is associated with each of the double carbides $Fe_3AlC_{0.5}$ and $Fe_3AlC_{0.69}$. The HFD, as former discussed, are due the single iron carbides, whose magnetic hyperfine field ranges from 8.0 to 22.6 T, as shown in Figure 4. These values are in agree with literature, taking into consideration that these carbides must be unpurified by aluminum atoms [10, 13].

Figure 5 shows the variation of the mean hyperfine field of the magnetic distribution. The behavior is in accordance with the milling process, indicating that as the milling time goes on, the mean hyperfine field diminishes.

4 Conclusions

With the present milling conditions the $Fe_3AlC_{0.5}$ double carbide was obtained after a milling time of 10 h. As a product, the $Fe_3AlC_{0.69}$ double carbide was also obtained, as Mössbauer spectroscopy reveals. These carbides are characterized by two doublets, D1 and D2, with the following hyperfine parameters: δ for D1 from −0.100 to 0.169 mm/s; δ for D2 from −0.025 to 0.065 mm/s; and quadrupole splitting ΔQ for D1 from 1.120 to 1.319 mm/s and ΔQ for D2 from −0.501 to −0.220 mm/s.

Acknowledgements This work was been carried out with the Colciencias support, the Universidad del Valle and the Universidad Santiago de Cali to whom the authors are greatly indebted.

References

1. Swain, M.: Structure and Properties of Ceramics, vol. 11, pp. 101–112, 187–189. VCH, Weinheim (1994)
2. Yang, J., La, P., Liu, W., Hao, Y.: Mater. Sci. Eng. A **382**, 8 (2004)
3. Minamino, Y., Koizumi, Y., Tsuji, N., Hirohata, N., Mizuuchi, K., Ohkanda, Y.: Sci. Technol. Adv. Mater. **5**(I–2), 133 (2004)
4. Radhakrishna, A., Baligidad, R.G., Sarma, D.S.: Scr. Mater. **45**, 1077 (2001)
5. Suryanarayana, C.: Prog. Mater. Sci. **46**, 1 (2001)
6. Yang, X.Y., Huang, Z.W., Wu, Y.K., Ye, H.Q.: Mater. Sci. Eng. A **300**, 278 (2001)
7. Matteazzi, P., Le Caër, G., Mocellin, A.: Ceram. Int. **23**, 39 (1997)
8. Umemoto, M., Todaka, Y., Takaschi, T., Li, P., Tokumiya, R., Tsuchiya, K.: Mater. Sci. Eng. A **375–377**, 881 (2004)
9. Varret, F., Teillet, J.: Unpublished MOSFIT program. Université du Maine, France
10. Tukumitsuan, K., Umemoto, M.: Mat. Sci. Forum **386–388**, 479 (2002)
11. Martín, V.E., Garcia-Escorial, A., Martín, A., Cebolledo, F., Carmona, F., Aveda, P., Gonzalez, J.M.: J. Phys. C **51**(4)
12. Smith, D., et al.: Penn State University, University Park, PA, USA, ICDD-in-Aid (1976)
13. Nadutov, V.M., Morduyk, B.N., Prokopenko, G.I., Gavrilenko, I.S.: Ultrasonics **42**, 47 (2004)

Hyperfine Interact (2006) 168:951–957
DOI 10.1007/s10751-006-9393-3

Mössbauer and X-ray diffraction characterization of $Fe_{60}Al_{40}$ coatings prepared by thermal spraying

Catherine Cordier-Robert · Thierry Grosdidier · Gang Ji · Jacques Foct

Published online: 8 November 2006

Abstract Microstructured (atomized) and nanostructured (milled) $Fe_{60}Al_{40}$ powders together with their corresponding coatings synthesized by High Velocity Oxy-fuel (HVOF) or Atmospheric Plasma Spray (APS) thermal spraying techniques have been characterized by Mössbauer Spectroscopy (MS) and X-ray Diffraction (XRD). The evolution of the microstructure and the atomic ordering degree in the powders and coatings are discussed at the light of the various processing conditions. The operational correlation between the parameters of the duplex morphology of coatings and the processing parameters is discussed.

Key words iron alloys · coatings · High Velocity Oxy-fuel (HVOF) · Atmospheric Plasma Spray (APS) thermal spraying · nanostructure · order–disorder · Mössbauer spectroscopy

1 Introduction

The good chemical and physical properties of iron aluminides make them attractive for high temperature industrial applications in spite of the bulk $Fe_{60}Al_{40}$ material is too brittle to be machined without Zr additions [1, 2]. Ultra fine grain materials have improved mechanical and physical properties and an important issue is now to fabricate massive components ready to be used. Mechanical milling of FeAl powder leads to the disordering of the initial B2 ordered phase into a metastable and nanostructured bcc phase [3–5]. Using

C. Cordier-Robert (✉) · J. Foct
LMPGM, UMR CNRS 8517, USTL, 59655 Villeneuve d'Ascq Cedex, France
e-mail: catherine.cordier@univ-lille1.fr

T. Grosdidier · G. Ji
LETAM, UMR CNRS 7078, Université de Metz, Ile de Saulcy, 57045 Metz Cedex 01, France

G. Ji
LERMPS, Université de Technologie de Belfort-Montbéliard, Site de Sévenans, 90000 Belfort, France

this type of milled powder, nanostructured Fe–40Al based coating having improved corrosion resistance/hardness balance were recently synthesized by HVOF thermal spraying [6, 7].

The purpose of the present paper is to shed more light on our understanding of the microstructure of the Fe–40Al coatings obtained by HVOF or APS spraying from milled and atomized powders. In HVOF and APS, which are thermo-mechanical processes, the initial state of the Fe–40Al powder is supposed to affect the nature of the nanostructure retained in the coating. It is the reason why the first part of this paper is devoted to the thermal stability of the disordered nanostructured powder. In the second part, the complex microstructure of the treated surfaces obtained by HVOF and APS from as-atomized or milled Fe–40Al powders and the atomic ordering state in Fe–Al phases which constitute the coatings are characterized and compared. Long range order (LRO) and short range order (SRO) parameters are quantified and discussed.

2 Experimental method

The material, of nominal composition Fe–40Al–0.05Zr (at.%) with 50 ppm B, was atomized under argon atmosphere. These atomized powders were milled with yttrium additions as described in [6] to produce a non-equilibrium microstructure in the powder particles and to create about 1 wt.% of finely dispersed Y_2O_3 reinforcing particles [8, 9]. The HVOF and APS thermal spraying conditions used to build up the coatings were already given elsewhere [6, 10]. Several passes of the torch were made to produce coatings having an average thickness of about 300 μm. The coating microstructure depends on the nature of the starting feedstock powder particles, on their interaction with the flame in transit and, finally, on the interaction of each particle with the substrate to form the individual splats that are the building blocks of the coatings. Under controlled HVOF processing conditions, which lead to the presence in the coating of unmelted powder particles, the microstructure of the milled nanostructured powder particles can be sufficiently preserved to form nanostructured coatings [11]. It is the reason why this study is devoted to the characterization of atomized microstructured and milled nanostructured powders and of corresponding "microstructured" and "nanostructured" coatings produced by thermal spraying.

Phase identification by XRD was carried out with the Co K_α radiation. X-ray line broadening analysis was used to obtain the size of the coherently diffracting domains (D_{eff}). Details of the XRD analysis can be found elsewhere [6, 12]. The relative LRO parameter was estimated from the X-ray diffraction peaks by comparing the intensities of the superlattice S(100) and fundamental F(200) lines [6, 12]. MS measurements were carried out at room temperature in the conventional constant-acceleration mode with a ^{57}Co source. The spectra were fitted to Lorentzian lines, in using Le Caër's Program [13], and Mössbauer hyperfine parameters of each Fe environment obtained. The fraction of paramagnetic material (f_p) was determined by comparing double and single (paramagnetic) peaks with sextuplet magnetic sites, as detailed elsewhere [4]. According to Gialanella's model [4], the LRO parameters, $S_{<H>}$ and S_{f_p}, can be evaluated from MS spectra thanks to the mean hyperfine magnetic field $<H>$ and the paramagnetic ordered fraction (f_p), respectively. The average LRO parameter noted S_M is defined as being the average value between $S_{<H>}$ and S_{f_p}. Fitting the Mössbauer spectra gives rise to quantification of SRO parameter which corresponds to the f_p fraction in FeAl phases according to Le Caër [4].

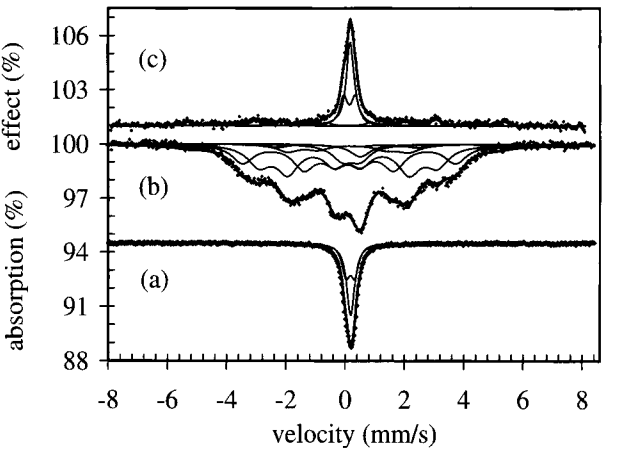

Figure 1 Room temperature transmission Mössbauer spectra of as-atomized (*a*) and milled (*b*) $Fe_{60}Al_{40}$ powders. X-reflection Mössbauer spectrum (*CXMS*) of coatings resulting from APS of atomized powders (*c*). Calculated subspectra are shown in comparison with experimental spectra.

3 Results and discussion

XRD and MS spectra obtained for the as-atomized and milled powders show that the microstructural states of these powders are very different. Mössbauer spectra of atomized and milled powder look rather similar to the room temperature Mössbauer spectra recorded by Gialanella et al. [4]. As depicted by Mössbauer spectroscopy (Figure 1) and XRD analyses, the main result of the milling process is the transformation of the $Fe_{60}Al_{40}$ atomized powder initially under the paramagnetic B2 ordered state (LRO parameter=0.8) into a disordered bcc ferromagnetic state (LRO parameter=0.1). At the same time, the Mössbauer peak are broadened (the peak widths are 0.91 and 0.84 mm/s, respectively, compared to 0.23 mm/s for α-iron standard). This is consistent with the loss of order in the B2-FeAl structure induced by the milling process observed in several studies [4]. Successive breaks and agglomerations during the milling process do reduce the size of coherently diffracting domains from above 100 nm in the atomized powder down to 9 nm in the final milled $Fe_{60}Al_{40}$ powder (Table I). An idea of the atomic order state in milled powders can be obtained by using the assumption of a quasi-regular solid solution. The mean hyperfine magnetic field, $\langle H \rangle$, was determined to be about 180 kG, which corresponds to a fully disordered state [4, 13]. The comparison of the SRO parameter values of the atomized and milled powders, given in Table I, nicely depicts the effect of the milling process.

The milled powder microstructure is thermodynamically unstable. The main reason is the high strain level and high specific surface of grain boundaries that are the driving forces for recrystallization and reordering. As revealed by the combination of XRD, Differential Scanning Calorimetry (DSC), Transmission Electron Microscopy (TEM) and MS analyses, the reordering phenomena in the milled powder starts at 175°C and is completed at 700°C while recrystallization is not completely achieved after 15 min at 850°C [14]. During the reordering phenomena, the short range reordering first occurs prior to be extended to long range distances. As confirmed by MS and XRD investigations, after the various heat-treatments, the SRO parameters are always smaller than the LRO ones. The B2 ordered fraction in the annealed powders increases with increasing annealing temperature and the S_M values cover the range from 0 to 0.77, for the disordered milled powder and the atomized $Fe_{60}Al_{40}$ powder. TEM experiments revealed that the grain size in the deformed matrix remains nanometric (<100 nm) over the range annealing temperature. In XRD

Table I Summary of XRD and Mössbauer parameters for both $Fe_{60}Al_{40}$ powders and sprayed coatings

	XRD results		Mössbauer results				
	D_{eff} (nm)	LRO (or S_d) parameter	f_p	S_{f_p}	$<H>$ (kG)	$S_{<H>}$	$S_M = (S_{f_p} + S_{<H>})/2$
Atomized powder (as-prepared)	>100	0.8	1	0.80	–	–	0.77
Milled powder (as-prepared)	9	0.1	0.05± 0.05	0.05	180	~0	~0
Milled powder (175°C)			0.27± 0.05	0.23	151±6	0.06	0.14±0.05
Milled powder (275°C)			0.37± 0.07	0.30	79±5	0.42	0.36±0.06
Milled powder (390°C)			0.67± 0.05	0.54	36±2	0.64	0.59±0.05
Milled powder (700°C)			0.85± 0.05	0.68	10±2	0.78	0.73±0.05
HVOF coating from atomized powder	28	0.6	0.77± 0.04	0.62	66.5±2	0.48	0.55±0.03
HVOF coating from milled powder	23	0.4	0.67± 0.04	0.54	88.7±2	0.37	0.46±0.03
APS coating from atomized powder	51	0.6	0.87± 0.04	0.69	26±2	0.69	0.69±0.03

D_{eff} is the coherently diffracting domain size, *LRO* the long range order parameter, f_p the fraction of paramagnetic material, $<H>$ the mean hyperfine magnetic field. $S_{<H>}$ and S_{f_p} are long range order parameters evaluated from Mössbauer spectra thanks to $<H>$ and f_p, respectively. The average long range order (LRO) parameter noted S_M is defined as being the average value between $S_{<H>}$ and S_{f_p}

patterns, only broad peaks of the bcc structure were detected at 175 and 275°C, as in the milled powder. From 390°C, the width of these peaks decreased and the superlattice reflection peaks showed up [14]. As shown in Table I, the Mössbauer spectra features a mixture of B2 ordered and bcc disordered FeAl phases whatever the annealing temperature in the range 175–700°C. The ordered fraction (f_p) increased with increasing temperature (Table I).

In the HVOF coatings obtained from milled powder, three different zones were identified by Scanning Electron microscopy (SEM), TEM and Energy Dispersive Spectroscopy (EDX) analyses: (1) disordered bcc FeAl retained in unmelted milled particles, (2) ordered (or partly ordered with antiphase boundaries) B2 zones in the melted splats and (3) Fe_3Al and oxide regions essentially present at the splat periphery. The presence of these various phases was confirmed by XRD and SM investigations [14], along with some oxides identified by TEM experiments being as amorphous [7] or of the $FeAl_2O_4$ spinel type [14]. As shown in Table I, compared to the original powder of the feedstock, the thermal cycle imparted to the powder during the spraying process reduces the atomic order in the coating consolidated from the atomized powder and promotes atomic reordering for the milled powder. For HVOF coatings, the D_{eff} values of the coatings obtained from atomized and milled powders are very similar (~25 nm). They are intermediate between the D_{eff} values obtained from atomized and milled starting powders. For the APS coating, the D_{eff} value is found to be higher (~52 nm).

Despite the strong differences in the initial structure of the feedstock powders, the f_p values being 1 in atomized powders and 0 in milled powders, the "microstructured" (atomized powder) and "nanostructured" (milled powder) coatings present very similar aspect through Mössbauer spectra [14]. After the HVOF spraying, the relative amount of ordered FeAl phase, f_p, was 0.77 and 0.67 in the "microstructured" and "nanostructured" coatings, respectively. For the APS coating, the microstructure also consisted of B2 ordered and disordered FeAl phases, but the fraction of ordered phase was the highest (87.5%). In the case of the APS coating, the much higher heating source temperature (12,000°C) and lower powder velocity (300 m/s) associated with the plasma spraying process resulted in a complete melting of the powder particles [10]. For the HVOF process, the lower temperature (3,000°C) and higher velocity values (1,400 m/s) could result in powder particles that kept an unmelted core and were melted only at the periphery. Indeed, even if the variation in temperature is high in these processes, the time of interaction between powder particles and the flame is very short, i.e. of the order of a few microseconds. In fact, because of the stochastic nature of the process, SEM and TEM analyses revealed that the microstructure of the HVOF coatings was the result of the deposition from fully melted, semi-melted or almost completely unmelted powders. Therefore the aspect of the coating microstructure was a mixture of fully flatten splats corresponding to zones that melted completely in the flame and unmelted parts of powder particles that were retained as compact blocks. Therefore, the HVOF coating obtained from milled powder can be described as consisting of a fraction of unmelted powder particles, retained in a disordered state and trapped in zones that melted properly. Comparatively, the HVOF coating obtained from the atomized powder consists of the same type of melted zones within, which are unglued ordered powder particles. Unmelted fraction value of particles and the order parameter in it superficial melted zone can be estimated from order parameters. By definition, we consider that f_s is unmelted particle fraction then $(1-f_s)$ is the melted fraction. Since the processing conditions and size fraction of the starting sieved feedstock-powders were the same for both coatings, it seems reasonable to assume that the amount of retained unmelted powder particles (f_s) is the same for both coatings. Ω parameter is the small range ordering (SRO) parameter in melted region. The SRO parameter values in the milled and atomized powders being known (0.05 and 1 respectively) and the size of coherently diffracting domains (D_{eff}) being similar for both coatings (Table I). The composite nature of coatings can be depicted by the following equations and the Ω and f_s parameters are determined as being f_s=10.5% and Ω=0.74.

- For the coating obtained from atomized powder: $1 f_s + \Omega(1 - f_s) = 0.77$
- For the coating obtained from milled powder: $0.05 f_s + \Omega(1 - f_s) = 0.67$

For an easier understanding of the SRO variations in each coating, a schematic description of the microstructure showing not fully melted particles and the corresponding SRO evolution are drawn in Figure 2, assuming that all particles have the same size and sustained the same thermal cycle. It is interesting to note that the estimation of the amount of unmelted powder particle fraction is consistent with the fraction determined by analysis of SEM images from the same coating (12.3±3.1%) [7]. The SRO parameter of the melted regions for the HVOF processing is lower than that obtained for the APS coating (fully melted with SRO=0.87, as seen in Table I). This is also consistent with the fact that the HVOF technique leads to higher solidification rates and improved cooling efficiency during the solidification of the melted splats. In addition, as suggested recently [16], it is possible that the peening imparted by the unmelted powder particles hitting the already deposited

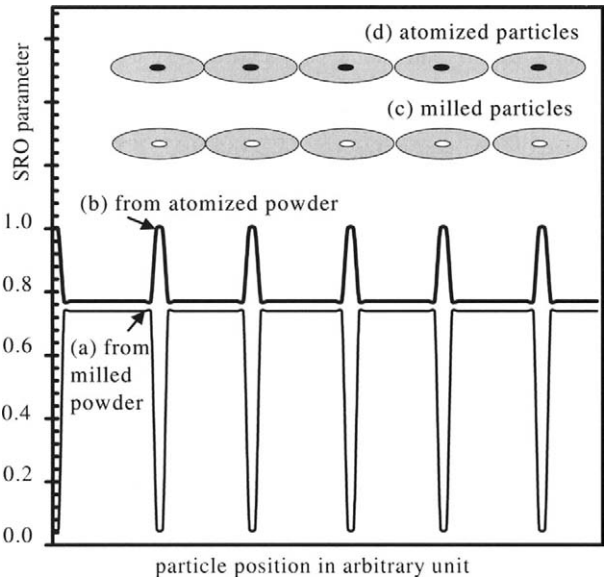

Figure 2 Schematic evolution of the short range order (*SRO*) parameter in the HVOF coatings elaborated from (*a*) milled and (*b*) atomized powders, and (*c*, *d*) corresponding sketches of several splats presenting melted areas (*grey*) and unmelted cores. The cores are there atomically ordered (*dark*) or disordered (*white*), depending on the either atomized or milled state of the starting powders.

layers at several hundreds of meter per second generates structural defects. This would also contribute to a lower SRO value in melted areas of the HVOF coatings compared to the APS one.

The ideal structure of a perfectly ordered, defect free, equiatomic FeAl alloy is of B2-type with an iron sublattice (corner positions of bcc unit cell) and an aluminum sublattice (center position), named α and β, respectively. The unit cell of the DO_3–Fe_3Al alloy involves eight centered cubes in which four types of equivalent sites are defined [15]. In ideal DO_3–Fe_3Al structure, β site is subdivided into two different β sites noted β_1 and β_2 and α site is splitted into α_1 and α_2 equivalent subsites. In stoichiometric perfectly ordered Fe_3Al alloys, only iron atoms occupy α ($\alpha = \alpha_1 + \alpha_2$) and β_2 positions and aluminum atoms are in β_1 centered positions. Each iron atoms is surrounded by four Fe and four Al atoms. Eight nearest (n.n.) and six next nearest (n.n.n.) Fe neighbors are located around each aluminum atom. From LRO parameter determined by X-ray diffraction analyses (denoted LRO or S_d in Table I), the type of atomic order (B2 or DO_3) is determined in $Fe_{1-x}Al_x$ (with x=0.4) atomized and milled powders. The assumption that the number of Fe–Al bonds is maximized; Al atoms only occupy β site and Fe atoms α+β sites; in ordered B2–FeAl structure S_d = 1; the probabilities of "i" site occupation (i=α or β) by "j" atoms (j=Fe or Al) is noted P_j^i. In $Fe_{1-x}Al_x$ alloy, where 0.25<x<0.5, all α sites are occupied by Fe atoms $P_{Fe}^{\alpha} = 1$, β sites by (1–2x) Fe atoms and (2x) Al atoms which can be written as $Fe_1^{\alpha}Fe_{(1-2x)}^{\beta}Al_{(2x)}^{\beta}$. The LRO parameter (noted S_{B2} in ordered B2 structure assumption), P_{Al}^{β} and P_{Fe}^{β} probabilities are expressed as a function of $F_{S(100)}/F_{F(200)}$. From XRD diffractograms, $F_{S(100)}/F_{F(200)}$ and S_{B2} values were extracted and S_{B2} are compared to S_d (or LRO) parameters in Table I. These S_{B2} and S_d values are in good agreement which confirms the B2 order rather than DO_3 order in powder particles.

4 Conclusion

This study was devoted to Fe–Al coatings elaborated by HVOF and APS thermal spraying of Fe–40Al powders on metallic substrates. LRO and SRO parameters were quantified in both powders and coatings. In particular, the composite nature of the HVOF coatings, which consists of a mixture of fully flattened splats and retained unmelted blocks could be depicted. The non-homogeneous atomic order state in coatings depends on the initial powder microstructure in the feedstock. Core is more ordered than surface in the case of the atomized $Fe_{60}Al_{40}$ powder and vice versa for the milled $Fe_{60}Al_{40}$ powder. The same HVOF and APS thermal spraying conditions are leading to identical results. It is estimated that coatings consist of 10.5% unmelted zones, while the short range order (SRO) parameter in the melted zones of the HVOF coatings is estimated as 0.74. Finally, the calculation of S_{LRO} and S_{B2} order parameters confirm the B2 ordered structure in atomized and milled powders.

References

1. Frangini, S., De Cristofaro, N.B., Mignone, A., Lascovitch, J., Giorgi, R.: Corros. Sci. **39**, 1431 (1997)
2. Tortorelli, P.F., Natesan, K.: Mater. Sci. Eng. A. **258**, 115 (1998)
3. Enzo, S., Frattini, R., Gupta, R., Macrì, P.P., Principi, G., Schiffini, L., Scipione, G.: Acta Mater. **44**, 3105 (1996)
4. Gialanella, S., Amils, X., Barò, M.D., Delcroix, P., Le Caër, G., Lutterotti, L., Suriñach, S.: Acta Mater. **46**, 3305 (1998)
5. Morris-Muñoz, M.A., Dodge, A., Morris, D.G.: Nanostruct. Mater. **11**, 873 (1999)
6. Grosdidier, T., Tidu, A., Liao, H.L.: Scr. Mater. **44**, 387 (2001)
7. Ji, G., El-Kedim, O., Grosdidier, T., Coddet, C.: Surf. Coat. Technol. **190**, 406 (2005)
8. Valshe, G., Botton, G.A., Brown, L.M.: Acta Mater. **47**, 2303 (1999)
9. Yavari, A.R., Negri, D., Navarro, E., Derui, A., Hemando, A., Botta, W.J.: J. Metastable Nanocryst. Mater. **2–6**, 229 (1999)
10. Ji, G., Grosdidier, T., Liao, H.L., Morniroli, J.P., Coddet, C.: Intermetallics. **13**, 596 (2005)
11. Ji, G., Morniroli, J.P., Grosdidier, T.: Scr. Mater. **48**, 1599 (2003)
12. Ji, G., Morniroli, J.P., Tidu, A., Coddet, C., Grosdidier, T.: J. Phys. IV **12**, 509 (2002), France, Pr6
13. Le Caër, G.: thèse d'état, Ecole des Mines de Nancy, France (1974)
14. Ji, G.: PhD thesis. Université de Technologie de Belfort-Montbéliard (UTBM), France (2003)
15. Athanassiadis, G., Le Caër, G., Foct, J., Rimlinger, L.: Phys. Stat. Sol. (a) **40**, 425 (1977)
16. Totemeier, T.C., Wright, R.N., Swank, W.D.: Intermetallics. **12**, 1335 (2004)

Hyperfine Interact (2006) 168:959–964
DOI 10.1007/s10751-006-9396-0

Formation of Mn-doped iron silicides by ball milling

J. Desimoni · S. M. Cotes · M. A. Taylor · R. C. Mercader

Published online: 19 December 2006

Abstract Using X-ray diffraction (XRD) and Mössbauer spectroscopy, we have studied the sequence of phase formations in the solid Mn-doped iron silicide series $Fe_{1-x}Mn_xSi_2$, with $0.00 \leq x \leq 0.12$, in samples prepared by mechanical alloying from the pure elements. The milling was carried out at room temperature in Ar atmosphere in a horizontal mill for 15 h. The XRD patterns display broad lines, which can be ascribed to stable and metastable iron silicides like β-$FeSi_2$, ε-FeSi, α-$FeSi_2$, MnSi, and Si. The set of hyperfine parameters obtained support the coexistence of β-$FeSi_2$, α-$FeSi_2$ and ε-FeSi, in agreement with the XRD results. No replacement of Fe by Mn atoms in the regular sites of β-$FeSi_2$ has been observed.

Key words iron silicides · mechanical alloying · phase doping

1 Introduction

The Fe–Si system is complex because several stable and metastable phases can be produced depending on the synthesis conditions. Non-equilibrium preparation methods, like mechanical alloying, allow the formation of compounds and metastable phases which are not accessible by conventional techniques. In particular, among the nine types of iron silicides, semiconducting β-$FeSi_2$ disilicide has attracted the attention in the last years due to its technological potential in the field of optoelectronics and as a material for thermoelectric conversion [1].

For device applications, the control of the electrical conductivity regime of the system is critical. Additives like V, Cr, Mn and Al turn the material into an *n*-type semiconductor. In particular, the doping with Mn poses intriguing fundamental issues related to the occurrence of metastable phases due to the structural difference between iron and

J. Desimoni (✉) · S. M. Cotes · M. A. Taylor · R. C. Mercader
Departamento de Física, Facultad de Ciencias Exactas, IFLP, CONICET,
Universidad Nacional de La Plata, C. C. no. 67, 1900 La Plata, Argentina
e-mail: desimoni@fisica.unlp.edu.ar

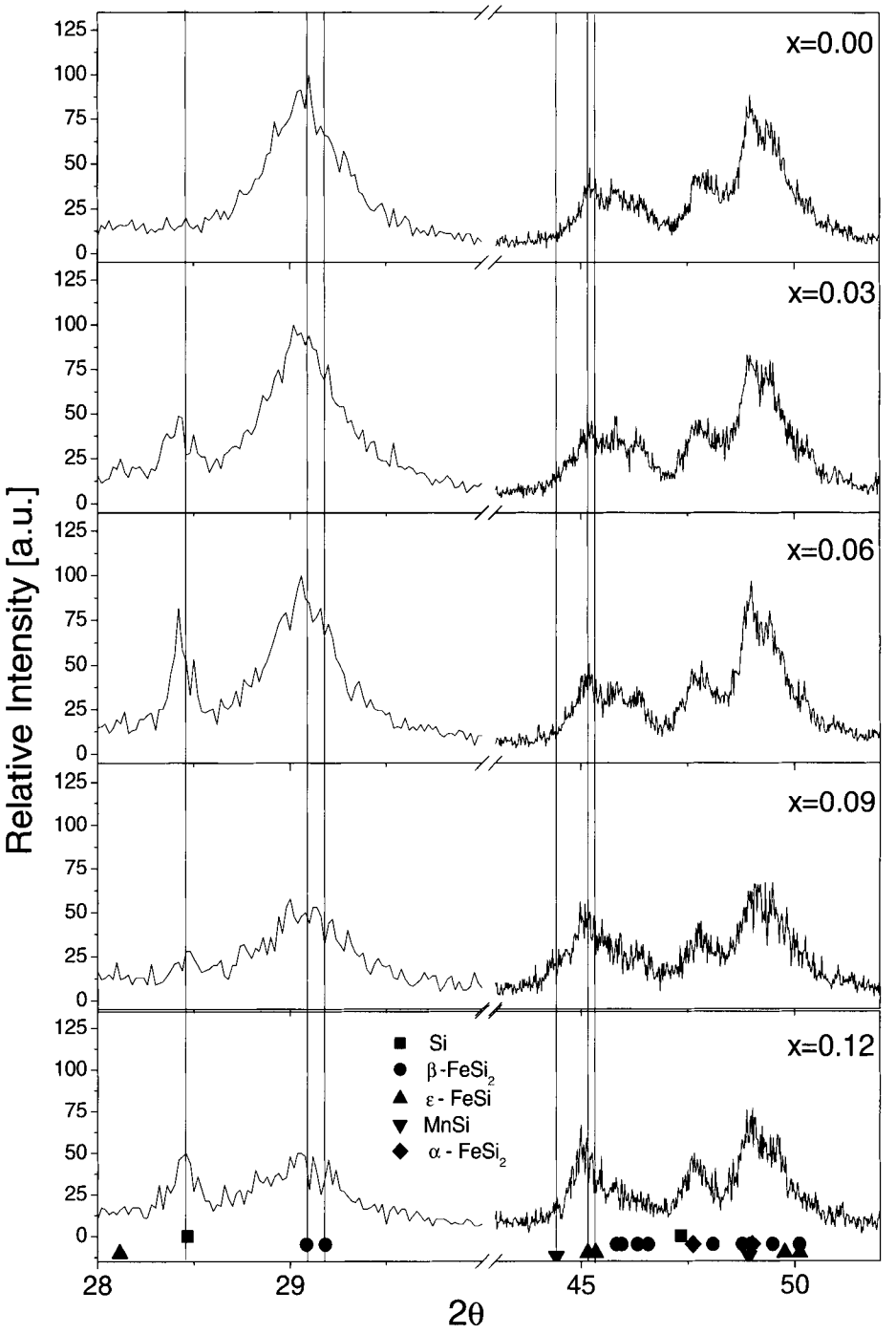

Fig. 1 X-ray diffractograms of $Fe_{1-x}Mn_xSi_2$ samples

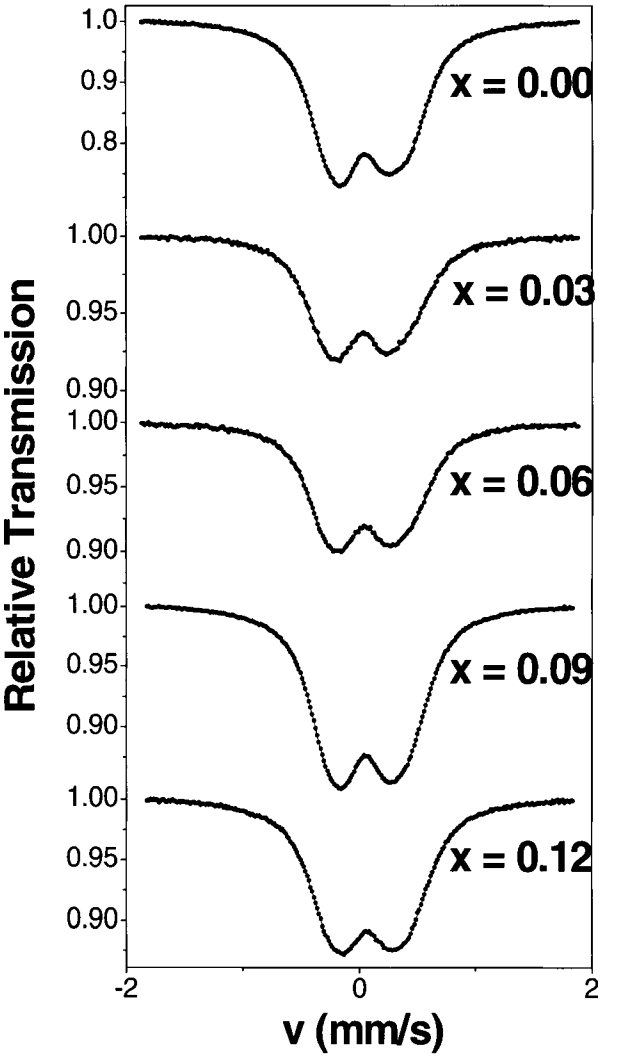

Fig. 2 Mössbauer spectra of $Fe_{1-x}Mn_xSi_2$ samples. The *solid line* results from the fitting process described in the text

manganese silicides and also related to the occupancy of the two non-equivalent Fe sites in the β-$FeSi_2$ structure [2].

In this frame, we have carried out a study of the sequence of phase formations of stoichiometric $Fe_{1-x}Mn_xSi_2$ ($0.00 \leq x \leq 0.12$) mixtures prepared by mechanical alloying from small pieces of the pure elements. In this work we report the preliminary results obtained by Mössbauer Spectroscopy and X-ray diffraction.

2 Experimental

We have mechanically alloyed mixtures (0.700 g) of stoichiometric amounts of elemental Fe (99.999% purity) and Si (99.99%) for pure silicides and Fe, Si and Mn (99.95%) for $Fe_{1-x}Mn_xSi_2$. We have used a Retsch MM2 horizontal mill which operated at 33 Hz, at

Table 1 Hyperfine parameters of the three quadrupole interactions I_1, I_2, I_3 that fit the spectra

	I_1				I_2				I_3			
x	Δ	δ	Γ	f	Δ	δ	Γ	f	Δ	δ	Γ	f
0.00	0.52_1	0.25_1	0.43_1	57_2	0.51_1	0.06_1	0.37_1	38_1	0.69_1	0.30_1	0.26_3	5_1
0.03	0.52_3	0.22_2	0.47_2	52_8	0.53_1	0.05_1	0.36_1	37_6	0.69_2	0.29_2	0.29_6	10_5
0.06	0.53_2	0.25_1	0.44_1	51_4	0.53_1	0.06_1	0.38_1	42_3	0.72_2	0.29_1	0.29_5	8_4
0.09	0.52_1	0.26_1	0.42_1	54_1	0.52_1	0.07_1	0.37_1	42_1	0.74_1	0.30_1	0.22_1	3_1
0.12	0.52_1	0.27_1	0.43_1	56_2	0.53_1	0.07_1	0.39_1	42_2	0.79_1	0.31_1	0.29_3	2_1

Isomer shifts δ (mm/s), referred to α-Fe at room temperature, quadrupole splittings Δ (mm/s), line widths Γ (mm/s) and relative fractions f (%) obtained from the Mössbauer spectra. The fitting errors are quoted as sub-index

room temperature and under Ar atmosphere. The ball-to-powder ratio was 10:1 and the milling time was 15 h.

Samples were characterised by X-ray diffraction (XRD) in a Philips PW1710 diffractometer using graphite monochromatised Cu $K\alpha$ radiation. Data were recorded in the range $10° \leq 2\theta \leq 110°$ in steps of 0.02° with a counting time of 2 s per step. The identification of phases was performed using the Powder diffraction files [3].

Mössbauer spectra were taken in transmission geometry using a ^{57}Co*Rh* source of approximately 5 mCi activity and recorded in a standard 512 channels conventional constant acceleration spectrometer in the velocity ranges −2 to +2 mm/s and −8 to +8 mm/s. Velocity calibration was performed against a 12 μm thick α-Fe foil. All spectra were fitted to Lorentzian line shapes with a non-linear least-squares program with constraints. Isomer shifts were referred to α-Fe at 298K.

3 Results and discussion

Figure 1 shows the diffractograms corresponding to the as-milled samples with different Mn concentrations. The patterns show broad lines probably due to the grain crumbling and lattice internal strain. An admixture of stable and metastable iron silicides like β-$FeSi_2$, α-$FeSi_2$ and ε-FeSi, MnSi [3] was identified. The presence of Si lines [3] was also detected. The formation of Si clusters could be related with the formation of Fe and Mn silicides having a Si/metallic atoms ratio lower than two. Segregation of Fe and Mn was not observed.

The high velocity range Mössbauer spectra (not shown here) do not show any signal that might be assigned to the presence of remnant Fe. The Mössbauer spectra plotted in Fig. 2, recorded in the −2 to +2 velocity range, are characterised by two broad lines which had to be necessarily fitted using three quadrupole interactions, I_1, I_2 and I_3, as reported in Table 1. Due to the large line width, it was not possible to perform an unambiguous association of the hyperfine interactions with known phases [4]. However, if we consider the average values of the reported hyperfine parameters [4], and compare them with those reported in Table 1, it is possible to conclude that the fitted set of hyperfine parameters is in correspondence with the presence of ε-FeSi, β-$FeSi_2$ and α-$FeSi_2$. This conclusion is also in agreement with the present X-ray results.

In agreement with previous results obtained on Pt doped β-$FeSi_2$ milled under the same conditions [5], the main contribution to the spectra comes from the ε-FeSi phase (I_1, see Table 1). The isomer shift of the second interaction (I_2) is close to the average value of the isomer shift of both Fe sites of the β-$FeSi_2$ phase [4]. We assume that the main contribution to this interaction (I_2) comes from the β phase. However, the quadrupole splitting reported in Table 1 (≈0.5 mm/s) is larger than the average values corresponding to the β-$FeSi_2$ phase (≈0.4 mm/s). Since this quantity is strongly sensitive to small local distortions from crystal symmetry, we conclude that it is very likely that this interaction arises from disordered β-$FeSi_2$. In a similar way, the last interaction (I_3) can be associated to disordered α-$FeSi_2$. Since the relative area of the I_3 subspectra decreases smoothly with the Mn concentration, it is possible that the formation of Mn silicides takes place at the expense of α-$FeSi_2$.

Taken into account the fact that XRD patterns have broad lines and Mössbauer signals are overlapped, the formation during the milling process of a certain amount of amorphous material cannot be discarded, as has been previously suggested by Gaffet et al. [6].

It is well known that mechanical alloying leads to the formation of Fe/Si interfaces and to the decrease in the crystallite size, then favouring the welding of the elemental powders. Hence, as in the case of MBE [7] and ion implantation [8], the highly negative heat of formation of the silicides favours the formation of compounds. The formation of a high amount of ε-FeSi may be due to its more negative enthalpy of formation (ΔH=−26 kJ/mol [9]) than that of $FeSi_2$ (ΔH=−12 kJ/mol [9]). Once the $FeSi_2$ local atomic concentration is achieved, the formation of β-$FeSi_2$ disilicide is more favourable than α-$FeSi_2$. However, deviations from the ideal stoichiometry and/or the defects created by the mechanical alloying could be responsible for the presence of the metastable α-$FeSi_2$ phase.

Finally, the segregation of Mn silicides under the present experimental conditions could be associated with their highly negative heat of formation (−40 kJ/mol < ΔH < −27 kJ/mol [9]) if compared with those of Fe silicides [9], indicating the preponderance of chemical forces over diffusional and energy transfer processes.

4 Conclusions

On Mn doping of β-$FeSi_2$, the replacement of the Fe atoms in the regular β-$FeSi_2$ sites by the Mn atoms, was not clearly observed, even for the lowest Mn samples. The formation of Mn silicides, due to its more negative heat of formation compared with those of iron silicides, hampered the formation of Mn-doped β-$FeSi_2$.

The present results indicate that the chemical driving forces outweigh the mechanically induced non-equilibrium mechanisms in the present experimental conditions, as it happened when doping with Pt atoms. Further experiments are in progress in order to overcome the problem.

Acknowledgement Authors thank F. Sives for helping during Mössbauer measurements.

References

1. Cho, W.-S., Choi, S.W., Park, K.: Mater. Sci. Eng., B **66**, 116 (1999)
2. Rundqvist, S.: Acta Chem. Scand. **16**, 1 (1962)
3. Powder diffraction files of the Joint Committee on Powder diffraction data. Georgia Institute of Technology, Atlanta, GA (1966)
4. Desimoni, J., Sánchez, F.H.: Hyperfine Interact. **122**, 277 (1999)

5. Desimoni, J., Sánchez, F.H.: J. Phys., Condens. Matter. **13**, 2737 (2001)
6. Gaffet, E., Malhouroux, N., Abdellaoui, M.: J. Alloys Compd. **194**, 339 (1993)
7. Degroote, S., Kobayashi, T., Dekoster, J., Vantomme, A., Langouche, G.: Mater. Res. Soc. Symp. Proc. **337**, 685 (1994)
8. Santos, D.L., de Souza, J.L., Amaral, L., Boudinov, H.: Nucl. Instrum. Methods Phys. Res., B **103**, 56 (1995)
9. Boer, F.R., Boom, R., Mattens, W.C., Miedema, A.R., Niessen, A.K.: In: Cohesion in Metals. North-Holland, Amsterdam (1988)

Hyperfine Interact (2006) 168:965–971
DOI 10.1007/s10751-006-9397-z

Calculation of absolute concentrations and probability of resonant absorption for iron-bearing precipitates in zirconium alloys

V. P. Filippov · V. I. Petrov · D. E. Lauer · Yu. A. Shikanova

Published online: 14 November 2006

Abstract In order to find the absolute concentrations and the probability of resonant absorption, the theoretical dependence of effective thickness from Mössbauer absorption line area has been obtained. Calculations of absolute concentrations of secondary phase precipitate in zirconium alloys with natural iron and with iron enriched with Mössbauer isotopes were carried out.

Key words Mössbauer spectroscopy · iron–niobium doped zirconium alloys absolute concentrations

1 Introduction

It is known that corrosion stability of zirconium alloys depends on a physical and chemical state of iron and tin atoms in alloys and their oxide films [1, 2]. Formed iron phases and precipitates in oxide films have small concentration: from 0.02 up to 0.4 mass%. The absolute concentration calculation of iron-bearing precipitates represents the important scientific and practical interest, as there is an interrelation between concentration of alloying elements precipitates and corrosion stability of zirconium alloys [1, 2].

Today, Mössbauer spectroscopy is a unique method which allows us to define the physical and chemical state of iron and tin atoms in compounds with small concentration of phases and precipitates (~0.02%). The analysis processing and the interpretation of experimental Mössbauer spectra of precipitates with low iron concentrations are difficult tasks. Carrying out the quantitative phase analysis is one of the difficulties and this is due to the absence of adequate theoretical dependence of the resonant absorption line area from effective thickness of the sample. Bearing this fact in mind, it is possible to define the absolute concentration of a phase or probability of resonant absorption. The existing dependences described in works [3] and [4] are coordinated among them, and theoretical

V. P. Filippov (✉) · V. I. Petrov · D. E. Lauer · Y. A. Shikanova
Moscow Engineering Physics Institute (State University), 31, Kashirskoe shosse
Moscow, Russia 115409
e-mail: vpfilippov@mephi.ru

deductions of such dependencies contain plenty of discrepancies. Therefore the aim of the given work is to deduce the theoretical dependence of the resonant absorption line area from effective thickness of the sample and use it to calculate values of absolute concentration of the phases contained in zirconium alloys.

2 Theoretical dependence

In order to find the absolute concentrations or the probability of resonant absorption the theoretical dependence of the resonant absorption line area from effective thickness of the sample has been obtained. To deduce that equation, the resonant absorption line area S is obtained from the effect of resonant absorption $\varepsilon(v)$ in velocity region as:

$$S = \int_{-\infty}^{+\infty} \varepsilon(v)dv \tag{1}$$

The effect of resonant absorption depends on the source emission $W(E)$ and resonant absorption, characterized by cross-section $\sigma(E)$, of photons with energy E and calculated as [3–5]:

$$\varepsilon(v) = \int_{-\infty}^{+\infty} W(E,v)\left(1 - e^{-nf'\sigma(E)}\right)dE \tag{2}$$

with n being the number of resonant atoms in the surface unit and f' the probability of resonant absorption.

It was assumed that at greater speeds of a source movement the cross-section of resonant absorption σ becomes equal to zero and the lines of emission and absorption have the Lorenz form:

$$W(E,v) = \frac{f \cdot \Gamma_0}{2\pi} \cdot \frac{1}{[E - E_0(1 - v/c)]^2 + (\Gamma_0/2)^2}; \; \sigma(E) = \frac{\sigma_0(\Gamma_0/2)^2}{(E - E_a)^2 + (\Gamma_0/2)^2} \tag{3}$$

In those equations f – the probability of resonant emission, Γ_0 – the natural line width, E_0 – the energy of resonant emission, σ_0 – the maximum cross-section of resonant absorption, E_a – the energy of resonant absorption, c – the speed of light.

The following theoretical dependence of the resonant absorption line area from effective thickness of the sample has been obtained substituting Eqs. 2 and 3 in Eq. 1 and integrated:

$$S(\lambda) = \frac{\pi \cdot \Gamma o \cdot f \cdot c}{2 \cdot E_0} \cdot \lambda \cdot e^{\frac{-\lambda}{2 \cdot B}} \cdot \left(I_0\left(\frac{\lambda}{2B}\right) + I_1\left(\frac{\lambda}{2B}\right)\right)$$

where $\lambda = \sigma_o f' n$, $I_0(\lambda)$, $I_1(\lambda)$ – the modified Bessel functions of the first kind of zero and first orders, respectively, from real argument:

$$I_0\left(\frac{\lambda}{2B}\right) = \frac{1}{\pi}\int_0^{\pi} e^{\frac{\lambda}{2B}\cos\theta}d\theta; \; I_1\left(\frac{\lambda}{2B}\right) = \frac{1}{\pi}\int_0^{\pi} \cos\theta \cdot e^{\frac{\lambda}{2B}\cos\theta}d\theta;$$

B – the broadening coefficient, calculated as: $B = \frac{\Gamma - \Gamma_S}{\Gamma_0}$, where Γ – experimental line width at half maximum, Γ_s – width of source line.

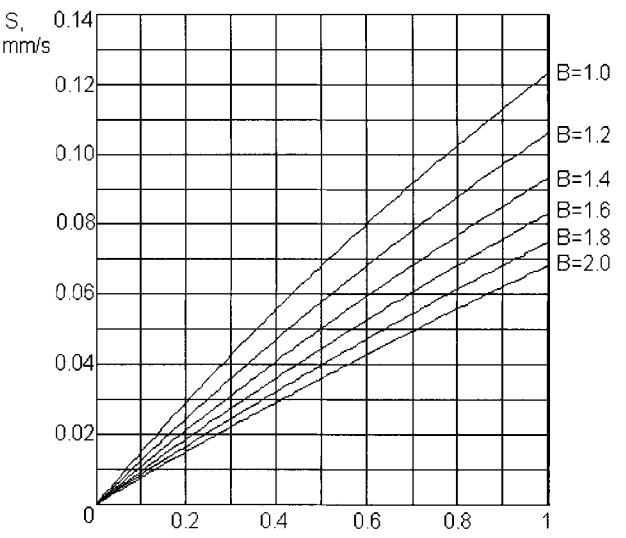

Figure 1 The theoretical dependence of Mössbauer absorption line area from effective thickness.

This equation can be used to calculate the absolute concentration of phases or probability of resonant absorption.

Thus, calculations are based on the following algorithm:

1. The Mössbauer absorption line area is calculated from experimental spectrum as $S_e = \frac{\pi \cdot \varepsilon \cdot \Gamma/2}{f \cdot \mathrm{K}_f}$, where ε – the effect magnitude, Γ – the experimental line width, æf – the probability of resonant emission of photon by source, K_f – the background coefficient.
2. The broadening coefficient B is calculated.
3. The effective thickness λ is determined by graph of the theoretical dependence of Mössbauer absorption line area S from effective thickness λ (Figure 1).
4. The absolute concentration of atoms of respective Mössbauer elements is determined from equation $n = \lambda/(f' \cdot \sigma_0)$.
5. Knowing the effective thickness λ and absolute concentration of a corresponding Mössbauer element, it is possible to also find the probability of resonant absorption $f' = \lambda/(n \cdot \sigma_0)$.

It was established that experimental calculation error is mainly connected with exactness of obtaining of experimental area value and exactness of determining of sample thickness.

The obtained dependence was checked on a test sample of metallic iron foil (α-Fe) at room temperature, which revealed that the received from experiment probability of resonant absorption for α-Fe is $f' = (0.79 \pm 0.05)$. Within the limits of an experimental error, this value coincides with that obtained by other experiments $(f' = 0.72 \pm 0.07)$ [6] and theoretically calculated (f'=0.79) using equation deduced in paper [7], such as:

$$-\ln f' = A \frac{T}{Tm} V^{2/3}$$

Where A – constant (for ^{57}Fe A=0.38), T – temperature of calculation, Tm – temperature of melting, V – volume of gram-atom $V = Am/\rho$, Am – mass of atom, ρ – density of material.

Using the obtained results, calculation of the absolute concentration of iron secondary phase precipitates in zirconium alloys has been carried out.

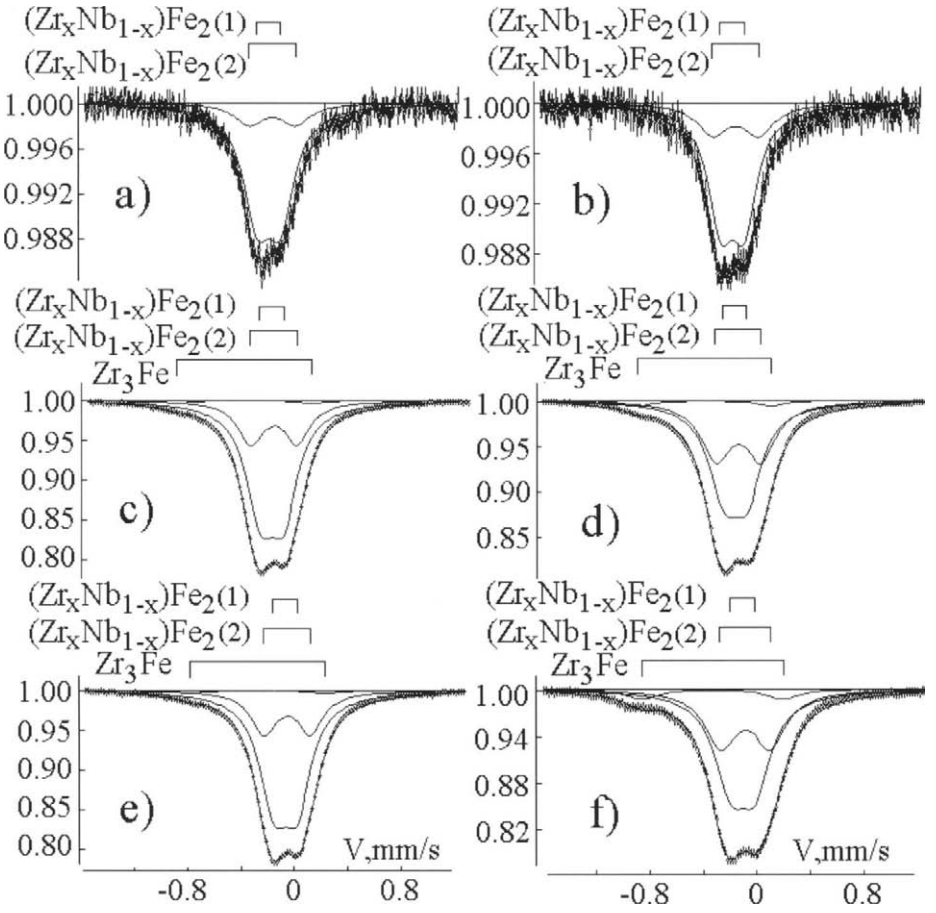

Figure 2 Spectra of samples of NSF alloy **a** rolled, without isotopes, T=300 K, **b** annealed, without isotopes, T=300 K, **c** rolled, with isotopes, T=298 K, **d** annealed, with isotopes, T=298 K, **e** rolled, with isotopes, T=78 K, **f** annealed, with isotopes, T=78 K.

3 Results of investigations

Investigations of alloy samples with chemical composition as E635 (Zr-0.39%–1.1%Sn-1.0%Nb) and NSF (Zr-0.34%–1.2%Sn-1.0%Nb) type after rolling and annealing, containing natural iron and iron enriched with Mössbauer isotopes are carried out.

The spectra of samples with isotopes were obtained at both room and liquid nitrogen temperatures. The fitting of spectra was carried out with the UNIVEM and DISCVERW programs [5]. The form of spectra and their computer fitting are plotted in Figures 2 and 3.

To describe the spectra, the model including three system lines of quadrupole splitting has been chosen. This model was constructed due to the following reasons.

Spectra of all alloy samples of NSF type with Mössbauer isotopes have strong asymmetry in the central part, hence, they should be described by the system including, at least, two lines of quadrupole splitting. (As zirconium has a hcp lattice, the existence of single lines is excluded). There is also an asymmetry expressed in the left part – the more

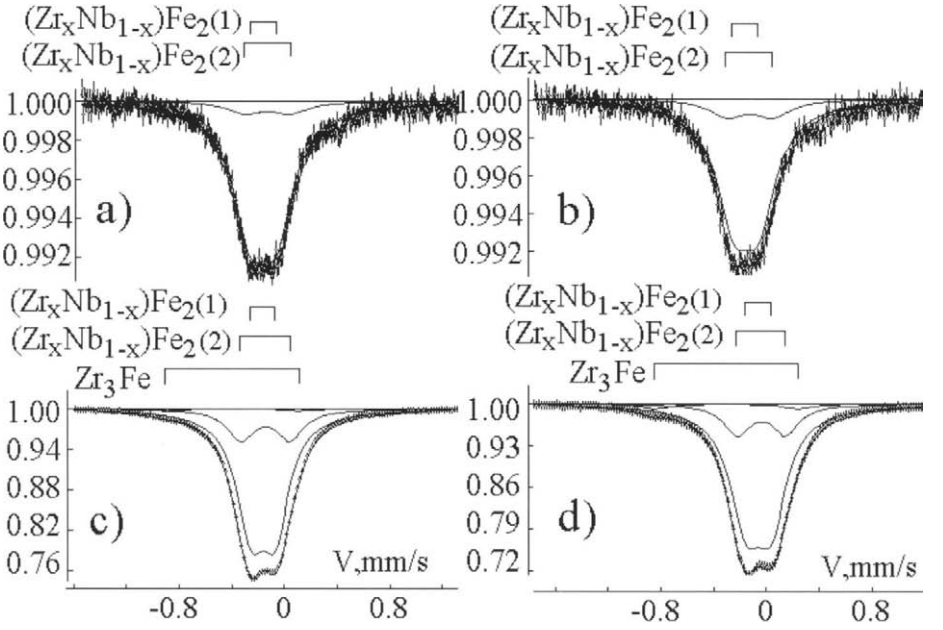

Figure 3 Spectra of samples of E635 alloy **a** rolled, without isotopes, T=300 K, **b** annealed, without isotopes, T=300 K, **c** rolled, with isotopes, T=298 K **d** rolled, with isotopes, T=78 K.

"flat" part – of a spectrum. This asymmetry can be better observed on the spectrum, which was obtained at liquid nitrogen temperature. In the central part of the spectrum, increase or reduction in asymmetry is not observed.

It is important to note that if both above-mentioned asymmetries are ascribed to lines of the same phases, the parameters of this phase ($\delta \sim -0.56$ mm/s, $\Delta E \sim 0.62$ mm/s) are not interpreted with any of the phases, found by TEM ore other researchers, basically because of big isomer shift. Therefore, the spectrum should be described by, at least, three systems lines of quadrupole splitting.

In the chosen model, the asymmetry of the left part of a spectrum is ascribed to Zr_3Fe precipitates with big isomer shift ($\delta \sim -0.4$ mm/s) and quadruple splitting ($\Delta E \sim 1.04$ mm/s). The asymmetry of the central part of a spectrum is described by two states of precipitates $(Zr_xNb_{1-x})Fe_2$ with Mössbauer parameters $\delta 1 \sim -0.17$ mm/s, $\Delta E1 \sim 0.20$ mm/s and $\delta 2 \sim -0.15$ mm/s, $\Delta E2 \sim 0.36$ mm/s.

The given model was applied for spectra fitting for all investigated samples.

It is necessary to note that relative areas of precipitates $(Zr_xNb_{1-x})Fe_2$, determined from the spectra obtained at two temperatures, hardly differ. The relative areas of precipitates Zr_3Fe determined from spectrum at liquid nitrogen temperature are almost three times more than the relative areas of these precipitates determined from spectrum at room temperature. This can be explained by the difference in probability of resonant absorption for the found phases at different temperatures.

The spectra of alloy samples with natural iron are described by a model including two quadrupoles corresponding to two states of precipitate $(Zr_xNb_{1-x})Fe_2$. The lines corresponding to Zr_3Fe precipitates of these alloys were not revealed on these spectra. It can be caused by small concentration of iron in the precipitates.

Table I Probabilities of resonant absorption of iron phases finding in NSF and E635 alloys

Temperature Phase	T=78 K	T=298 K
Zr_3Fe	0.81±0.05	0.54±0.05
$(Zr_xNb_{1-x})Fe_2$	0.78±0.13	0.70±0.19
$(Zr_xNb_{1-x})Fe_2$	0.78±0.06	0.70±0.14

Table II Absolute concentrations of phase (mg/sm^2)

Alloy	Phase	Alloy with isotopes		Alloy without isotopes
		spectra obtained at T=78 K	spectra obtained at T=298 K	spectra obtained at T=300 K
NSF, rolled	Zr_3Fe	0.0042±0.0010	0.004±0.001	–
	$(Zr_xNb_{1-x})Fe_2$	0.047±0.008	0.0460±0.010	0.0062±0.0008
	$(Zr_xNb_{1-x})Fe_2$	0.028±0.006	0.0274±0.007	0.0018±0.0006
	Total concentration of iron	0.080±0.015	0.077±0.018	0.0082±0.0014
	Chemical analysis	0.087±0.002	0.087±0.002	0.008±0.002
NSF, annealed	Zr_3Fe	0.004±0.009	0.002±0.001	–
	$(Zr_xNb_{1-x})Fe_2$	0.047±0.007	0.058±0.009	0.00768±0.0009
	$(Zr_xNb_{1-x})Fe_2$	0.028±0.006	0.021±0.007	0.0014±0.0007
	Total concentration of iron	0.084±0.014	0.0813±0.026	0.0082±0.0016
	Chemical analysis	0.087±0.002	0.087±0.002	0.008±0.002
E635, rolled	Zr_3Fe	0.0024±0.0090	0.0021±0.0010	
	$(Zr_xNb_{1-x})Fe_2$	0.085±0.014	0.090±0.012	0.0055±0.0009
	$(Zr_xNb_{1-x})Fe_2$	0.017±0.005	0.019±0.010	0.0009±0.0004
	Total concentration of iron	0.105±0.028	0.110±0.023	0.0064±0.0013
	Chemical analysis	0.123±0.003	0.123±0.003	0.006±0.002

On the basis of the received areas of experimental lines, the probabilities of resonant absorption niobium-containing phases and absolute concentration of all the phases of iron found were determined. The obtained values of resonant probabilities are listed in Table I.

4 Discussion of results

The analysis of the received data has shown that the probability of resonant absorption of iron atoms in α-Fe, received using deduced theoretical dependence, within the limits of an error of measurement, coincides with the value obtained by other researchers and theoretical accounts. The probabilities of resonant absorption for identical iron-bearing phases in various samples of alloys within the limits of an error of measurements are equal. The probabilities of resonant absorption received at liquid nitrogen temperature are much higher than those received at room temperature, which corresponds to theoretical representations about Mössbauer effect. Besides, the sum of absolute concentration of all iron-containing phases coincides with absolute concentration of iron determined by the chemical analysis within the limits of experimental error for all researched alloys (Table II). The phase absolute concentrations hardly change when the measuring temperatures vary. This is due to the temperature stability of the phase structure.

On the basis of the above-mentioned results, it was concluded that the obtained data are in good agreement with the theoretical assumptions. Consequently, it is possible to use them for further analysis of alloy behavior. The deduced ratio can also be used to determine the probability of resonant absorption and absolute concentration of Mössbauer elements from experimental spectra.

5 Conclusions

1. The theoretical dependence of Mössbauer absorption line area from effective thickness of sample has been obtained.
2. The experimental check of the deduced dependence on a standard absorber α-Fe is carried out.
3. The probabilities of resonant absorption in iron–niobium containing phases formed in zirconium alloys are determined.

References

1. Babikova, Yu.F., Gruzin, P.L., Ivanov, A.V., Filippov, V.P.: Izvestiya VUZ Fizika. **1**, 70 (1981)
2. Pecheur, D., Filippov, V., Baateev, A., Ivanov, Yu. In: Gerry D., Moan ad Petr Ruling (eds.) Thirteen International Symposium. ASTM STP 1423. ASTM international. West Conshohocken. PA 2002, p.135
3. Bykov, G.A., Hien, P.Z.: JETP. **16**(3), 646–651 (1963)
4. Goldanskii, V.I., Makarov, E.F.: Chemical Application of Mössbauer Spectroscopy, Academic, New York/ London, p. 102 (1968)
5. Afanas'ev, A.M., Chuev, M.A.: JETP. **80**, 560–567 (1995)
6. Foster, N.M., Iranchev, N.P.: Bolgarsky physichesky Journal, **6**(5), 540–544 (1979)
7. Alekseev, L.A., Gruzin, P.L., Shtan, I.I., Radionov, Yu.L. In: Problemi Metallovedeniya i Phisiki Metallov, Metallurgizdat, Moscow, p.101 (1969)

Hyperfine Interact (2006) 168:973–977
DOI 10.1007/s10751-006-9384-4

Mössbauer spectroscopy and X-ray diffraction study of the $Fe_{3-x}Ti_xAl$ ternary alloys

Krzysztof Brząkalik · Janusz E. Frąckowiak

Published online: 16 November 2006

Abstract Mössbauer spectroscopy and X-ray diffraction have been applied to study the structural and magnetic properties of $Fe_{3-x}Ti_xAl$ alloy system. The distribution of nearest neighborhood of iron atoms as a function of the Ti concentration and formation of the Heusler phase with $L2_1$ type of structure were investigated.

Key words Fe–Ti–Al alloys · Heusler phase · Mössbauer spectroscopy

1 Introduction

The $Fe_{3-x}M_xAl$ ternary alloys based on Fe_3Al iron aluminides doped with 3d-M elements are considered to be potential high-temperature structural materials because of their high strength combined with excellent oxidation and corrosion resistance [1]. The Ti addition improves the high temperature strength of Fe_3Al by stabilization of the DO_3 ordered structure and leads to some extreme change in physical properties, than others elements. The substitution of Fe atoms by Ti atoms yields the Fe_2TiAl Heusler phase with $L2_1$ structure and increases the critical temperature T_C for $DO_3/L2_1 \leftrightarrow B2$ transition [2–4]. According to the established isothermal sections of the Fe–Al–Ti phase diagram at 1073 K the two phase equilibrium ($L2_1$–Fe_2TiAl+hexagonal Laves phase with C14 structure) is expected in the iron rich alloys [5]. Mössbauer investigations on quenched $Fe_{3-x}Ti_xAl$ alloys indicate that in the wide range of Ti concentration the α-Fe, Fe_2Ti and Fe_2TiAl phases are in coexistence [6]. In this paper, the Mössbauer spectroscopy and X-ray diffraction were applied to explain the structural and magnetic properties of annealed $Fe_{3-x}Ti_xAl$ alloys in the range of titanium concentration x from 0.2 to 1.0.

K. Brząkalik · J. E. Frąckowiak (✉)
Institute of Materials Science, University of Silesia, 12 Bankowa Street, 40-007 Katowice, Poland
e-mail: jfrack@us.edu.pl

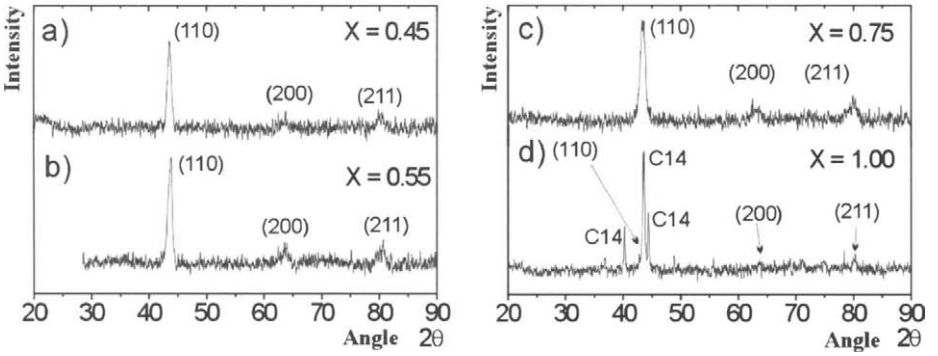

Figure 1 The X-ray diffraction patterns for $Fe_{3-x}Ti_xAl$ alloys.

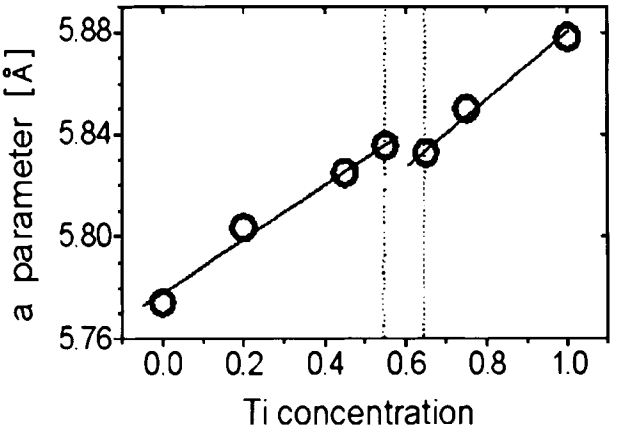

Figure 2 Dependence of lattice parameter (a) on the Ti concentration (x) for investigated $Fe_{3-x}Ti_xAl$ alloys.

2 Experimental

The investigated compounds $F_{3-x}Ti_xAl$ (x=0.2, 0.45, 0.55, 0.65, 0.75, 1) were prepared by arc melting in high purity argon atmosphere. After melting the samples were mechanically crashed and annealed at 1173 K for 1 h and next at 673 K for 4 h followed by furnace cooling. The ^{57}Fe Mössbauer spectra were recorded at room temperature using a constant acceleration spectrometer with ^{57}Co(Rh) source with an activity of 50 mCi. All of investigated alloys were measured in two ranges of velocity: (±3) mm/sec and (±8) mm/sec. The spectra were analyzed by MOSMOD computer program which is a direct implementation of Voigt-based fitting method of Rancourt and Ping [8]. A least-squares method program using the Gauss–Legendre technique for evaluation of the transmission integral was used for fitting the non-magnetic component of Mössbauer spectra. The X-ray measurements were made at room temperature on powder samples using a high-resolution Simens D-5000 diffractometer with a graphite monochromator.

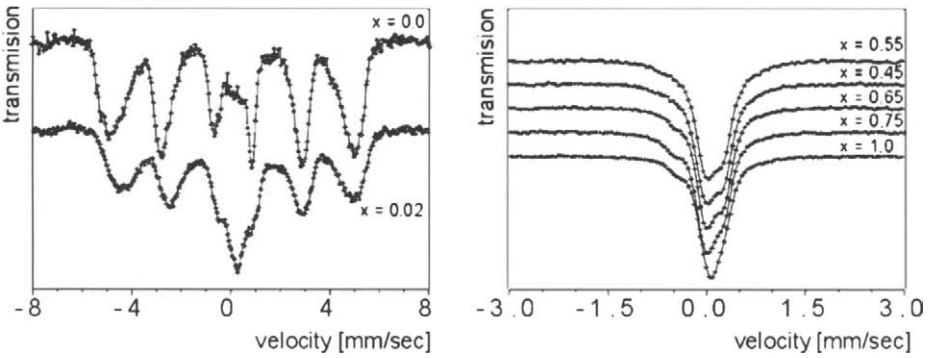

Figure 3 The Mössbauer spectra of $Fe_{3-x}Ti_xAl$ alloys.

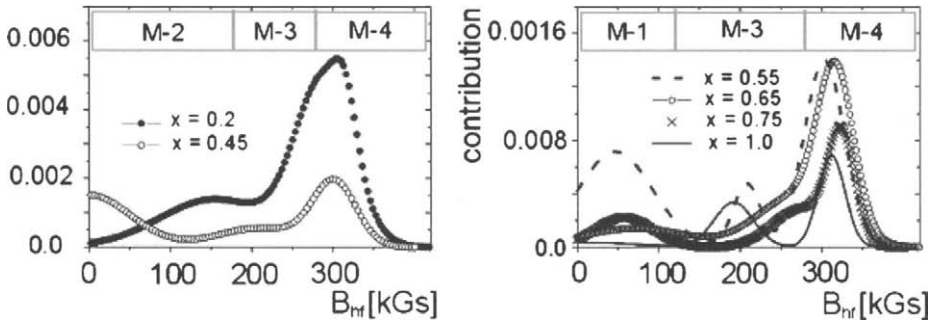

Figure 4 The hyperfine field distributions $P(B_{hf})$ of the magnetic component.

3 Results and discussion

The X-ray diffraction patterns (Figure 1) reveal the predominant reflection of the $DO_3/L2_1$ structure, although a small amount of Fe_2Ti phase with C14 structure was found for the nominal Heusler concentration Fe_2TiAl.

The lattice parameter (a), as is presented in Figure 2, increases with increasing x but for $x>0.55$ the significant change in the slope is observed. It is a result of the distinctive stabilization of the DO_3 phase for $x<0.55$ and formation of $L2_1$ phase for $x\geq0.55$.

The Mössbauer spectra (Figure 3) show both magnetic and non-magnetic components.

The contribution of non-magnetic component in the form of a broadened line increases with Ti concentration and for $x\geq0.45$ dominates in the spectra. The magnetic component of the Mössbauer spectra can be resolved on the four magnetic Zeeman's sextets (M-1 to M-4) with different values of hyperfine field. (see Figure 4).

The M-2 subspectrum arises from the iron atoms surrounded by the four Fe atoms and the four Al atoms (the DO_3 intermediate phase). The M-3 subspectrum with the average value of magnetic field (150÷250) kGs is connected with the disordered phases contained mainly iron and titanium atoms localized at the antiphase boundaries. The M-4 subspectrum with the average value of hyperfine magnetic field equal about of 300 kGs is a natural consequence of site occupation of Fe atoms in the fine grain boundaries, while the M-1

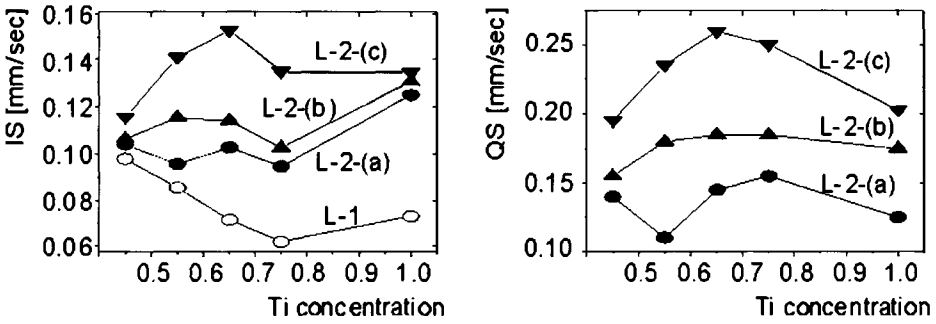

Figure 5 Isomer shift (IS) and quadruple splitting (QS) of the L-subspectra as the function of the Ti concentration.

subspectrum is attributed to Fe_2Ti Laves phase formed in the range of Ti concentration from $x=0.55$ to $x=1.0$.

The detailed analyze based on the Monte Carlo simulation [7] shows that as a result of the strong preference of Ti atoms to Fe sites, the non-magnetic component of the Mössbauer spectra attributed to $L2_1$ structure is a superposition of a single line (L-1) and a three quadrupole dublets (L-2(a), L-2(b) and L-2(c)) which represent Fe atoms having the nearest neighbor configurations: (4Al,4Ti), (4Al,3Ti+1Fe), (4Al,2Ti+2Fe) and (4Al,1Ti+3Fe), respectively. The dependence of the isomer shift (IS) and quadrupole splitting (QS) on the Ti concentration for the L-subspectra is shown in the Figure 5.

The L-1 single line with IS=0.07 mm/s represents the ordered Heusler phase with $L2_1$ structure, while the partial disorder within ordered domains is reflected by L-2 quadrupole dublets. The observed dependence in IS and QS values with Ti concentration indicates that for $x \geq 0.65$ the long range atomic ordering within the Heusler phase is established. It can be point out that due to stable number of 4Al atoms in the neighborhood of a central Fe atoms the value of IS linearly depends on the number of Ti atoms in the first coordination sphere. The change in value of isomer shift per the one Ti atom was estimated as $\Delta IS=(-0.015\pm 0.003)$ mm/sec, what is in the good relation to value reported in [9].

4 Conclusions

Analysis of X-ray and Mössbauer results shows that in the $Fe_{3-x}Ti_xAl$ system the Heusler phase with $L2_1$ structure is formed for Ti concentration $x>0.45$, however the long range atomic order is established for $x>0.65$. The Mössbauer spectra include both magnetic and non-magnetic components. The presented model applied for Mössbauer spectra decomposition based on the results of the Monte Carlo computer simulation well describes the evolution of $L2_1$ ordering in investigated alloys.

References

1. Ohnuma, I., Schön, C.G., Kainuma, R., Iden, G., Ishida, G.K.: Acta Mater. **46**, 2083 (1998)
2. Stein, F., Schneider, A., Frommeyer, G.: Intermetallics **11**, 71 (2003)
3. Buckley, R., Kaviani, S.: Mater. Sci. Eng. **A258**, 173 (1998)

4. Kato, M., Nishino, Y., Mizutani, U., Watanabe, Y., Asano, S.: J. Phys., Condens. Matter **12**, 9153 (2000)
5. Raghavan, V.J.: Phase Equil. **23**, 367 (2002)
6. Brząkalik, K., Frąckowiak, J.E.: Nukleonika **48S**, 13 (2003)
7. Brząkalik, K., Frąckowiak, J.E.: J. Alloys Compd., submitted.
8. Rancourt, D.G., Ping, J.Y.: Nucl. Instrum. Methods Phys. Res. **B44**, 199 (1989)
9. Mahmood, S., Gharaibeh, M., Saleh, A.: Solid State Commun. **95**, 263 (1995)

Hyperfine Interact (2006) 168:979
DOI 10.1007/s10751-006-9482-3

ERRATUM

Mössbauer spectroscopy and X-ray diffraction study of the $Fe_{3-x}Ti_xAl$ ternary alloys

Krzysztof Brząkalik · Janusz E. Frąckowiak

Published online: 20 December 2006

Due to an unfortunate turn of events this article was published online November 16th 2006 with an erroneous version of Figure 1. That same version is published on the preceding pages. The below printed Figure 1 however is the correct version and should be regarded by the reader as the final version.

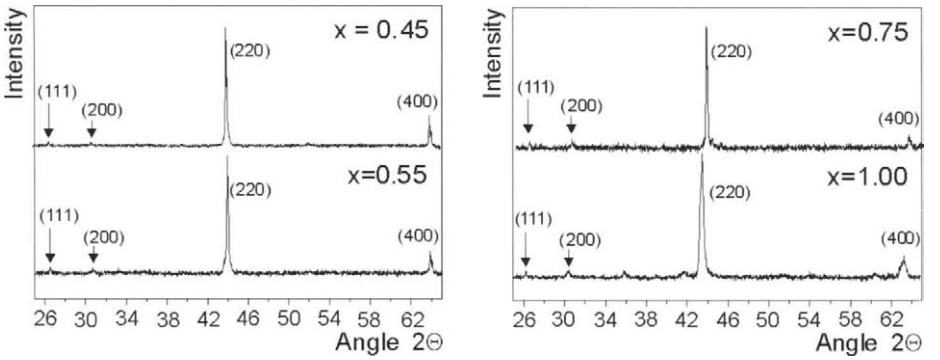

Figure 1 The X-ray diffraction patterns for $Fe_{3-x}Ti_xAl$ alloys.

The online version of the original article can be found at: http://dx.doi.org/10.1007/s10751-006-9384-4.

K. Brząkalik · J. E. Frąckowiak (✉)
Institute of Materials Science, University of Silesia, 12 Bankowa Street, 40-007 Katowice, Poland
e-mail: jfrack@us.edu.pl

Hyperfine Interact (2006) 168:981–987
DOI 10.1007/s10751-006-9460-9

Complexes based on ethylene- and propylene-bridged-pentadentate-Fe(III)-units allow interplay between magnetic centers and multistability investigated by Mössbauer spectroscopy

F. Renz · P. Kerep · D. Hill · M. Klein

Published online: 14 December 2006

Abstract The propylene-based ^{5}3,3-L=[*N*,*N*'-Bis(1-hydroxy-2-benzylidene)-1,7-diamino-4-azaheptane] and ethylene-based pentadentate ligand ^{5}2,2-L=[*N*,*N*'-Bis(1-hydroxy-2-benzylidene)-1,5-diamino-3-azapentane] has been prepared. Complexation with Fe(III) yields high-spin (S=5/2) complexes of [Fe^{III}(^{5}2,2-L)Cl] and [Fe^{III}(^{5}3,3-L)Cl]. Such precursors were combined with $[M(CN)_x]^{y-}$ (M=W(IV), Mo(IV), Ru(II), Co(III)) and heptanuclear and nonanuclear clusters of $[M\{(CN\text{-}Fe^{III}(^5\text{2,2-L})\}_x]Cl_y$ and $[M\{(CN\text{-}Fe^{III}(^5\text{3,3-L})\}_x]Cl_y$ resulted. Such starshaped hepta- and nonanuclear compounds are high-spin systems at room temperature. On cooling to 20 K in all presented ethylene compounds the iron(III) centers switch to a second high-spin state as proven by Mössbauer spectra with a yield of about 30%, i.e., multiple electronic transitions. The propylene compounds, however, perform a high-spin to low-spin transition. Mössbauer spectra taken during green light irradiation indicate changes in the population of the different electronic states, i.e. concerted inorganic reaction.

Key words heptanuclear · nonanuclear · high-spin molecule · Fe(III)–W(IV) · Fe(III)–Mo(IV) · Fe(III)–Ru(II) · Fe(III)–Co(III) · multiple electronic transition

1 Introduction

The heptanuclear Fe^{III}_6–Fe^{II} system exhibits an S=6 ground state [1], while the Fe^{III}_6–Co^{III} reveals multistability, a thermally induced multiple spin transition [2]. This is the first example for a heptanuclear compound with spin transition. Extending this approach to nonanuclear systems was fruitful. The Fe^{III}_8–Mo^{IV} compound is the first nonanuclear compound showing spin transition [3]. Recently, we have presented the first tetranuclear compound (Fe^{III}_3–Cr^{III}) that shows spin transition [4]. The topology of the compound enables magnetic interactions between the iron centers and the chromium.

F. Renz (✉) · P. Kerep · D. Hill · M. Klein
Institut für Anorganische Chemie und Analytische Chemie, Johannes Gutenberg-Universität, Duesbergweg 10-14, 55099 Mainz, Germany
e-mail: Franz.Renz@uni-mainz.de

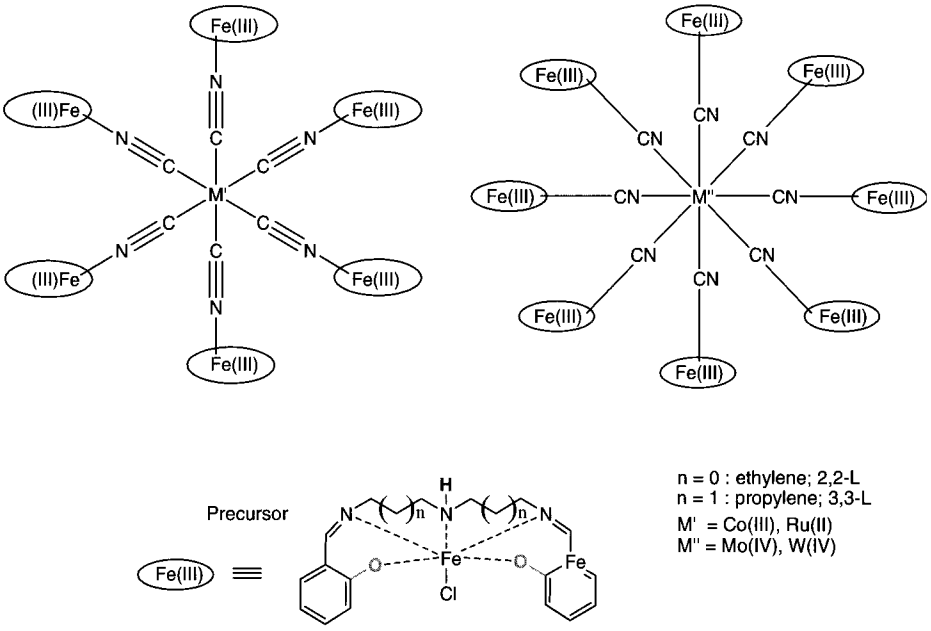

Figure 1 Topology of the *star-shaped* hepta- and nonanuclear compounds based on the iron(III) precursors [Fe(^{5}2,2-L)Cl] and [Fe(^{5}3,3-L)Cl].

In the present work, our approach is extended to compare the effect of chain length in the back-bone of the ligand. A new series of propylene and ethylene chains forming the pentadentate ligands will be compared and their electronic effect for the hepta- and nonanuclear compounds investigated (see Figure 1).

2 Experimental

The main strategy for the synthesis was performed in analogy to the literature [2, 3]. The pentadentate ligand ^{5}3,3-L (*N,N'*-bis(1-hydroxy-2-benzylidene) 1,7 diamino 4-azaheptane), the resulting iron-precursor and the Mo- and Co-complexes were prepared as described in the literature [2, 3].

2.1 Ligand: ^{5}2,2-L

^{5}2,2-L (*N,N'*-bis(1-hydroxy-2-benzylidene)-1,5-diamino-3-azapentane) was prepared by Schiff base condensation of salicylaldehyde (50 mmol) with bis(2-aminoethyl)amine (25 mmol) both dissolved in methanol (20 cm^3). The mixture was heated under reflux for 10 min. The resulting solution was used for the preparation of the precursor.

2.2 Precursor [Fe^{III}(^{5}2,2-L)Cl]

A solution of anhydrous iron(III) chloride (25 mmol) in methanol (50 cm^3) was added to the freshly prepared solution of ^{5}2,2-L. The mixture was boiled and then triethylamine

(50 mmol) was added. The resulting solution was then heated under reflux for 1 h. After cooling, crystals precipitated. They were collected and recrystallized in methanol and dried in vacuum.

Yield: 88% rel. to Fe (M=401 g/mol). Analysis calculated for $C_{18}H_{18}ClFeN_3O_2$(%): C (53.96), N(10.49), H(4.78); with 0.7 CH3OH C(53.21) N(9.96) H(4.97); found: C(52.74), N(10.45), H(5.00). IR (KBr): ν(cm^{-1})=3,256 cm^{-1} (N–H, val.), 2,920 cm^{-1} (CH_2, val.), 1,627 cm^{-1} (C=N, val.), 1,500–1,600 cm^{-1} (aromat. C=C, val.), 750–760 cm^{-1} (C–H, o. o. p.); FD MS m/z=365.1 (96.01%, ^{5}2,2-LFe)$^+$

2.3 Multinuclear complexes [(^{5}2,2-LFe^{III}NC)$_8$Mo^{IV}]Cl$_4$, [(^{5}2,2-LFe^{III}NC)$_8$W^{IV}]Cl$_4$, [(^{5}2,2-LFe^{III}NC)$_6$Co^{III}]Cl$_3$, [(^{5}2,2-LFe^{III}NC)$_6$Ru^{II}]Cl$_2$

The complexes were each prepared following a universal recipe. One millimole of the precursor is dissolved in methanol (150 cm^3) and an aqueous methanol (1:1) solution (15 cm^3) of the appropriate cyanide (1/8 mmol for the octacyanides $K_4[Mo(CN)_8].2H_2O$ and $K_4[W(CN)_8].2H_2O$; 1/6 mmol for the hexacyanides $K_4[Ru(CN)_6]$ and $K_3[Co(CN)_6]$) were added dropwise. After 1 h of stirring at room temperature the solution was reduced under pressure to 50 cm^3 (below 35°C). Addition of 150 cm^3 distilled water precipitates the product, which was slowly filtered off on the frita funnel. The product was washed with distilled water and diethylether and dried under vacuum for 24 h.

[(^{5}2,2-LFe^{III}NC)$_8$Mo^{IV}]Cl$_4$ Yield: 28% rel. to Mo (M=3,362.5 g/mol). Analysis calculated for $C_{152}H_{152}Cl_4Fe_8MoN_{32}O_{16}$(%): C(54.21), N(13.31), H(4.55); with 2.9 CH3OH 4.7 KCl C(48.82) N(11.76) H(4.33); found: C(48.40), N(13.09), H(5.64). IR (KBr): ν(cm^{-1})=3,421 cm^{-1} (N–H, val.), 2,925 cm^{-1} (CH_2, val.), 2,129 cm^{-1} (C≡N, val.), 1,628 cm^{-1} (C=N, val.), 1,600–1,500 cm^{-1} (aromat. C=C, val.), 760–750 cm^{-1} (C–H, o. o. p.)

[(^{5}2,2-LFe^{III}NC)$_8$W^{IV}]Cl$_4$ Yield: 24% rel. to W (M=3,450.4 g/mol). Analysis calculated for $C_{152}H_{152}Cl_4Fe_8WN_{32}O_{16}$(%): C(52.83), N(12.97), H(4.43); found: C(47.18), N(12.87), H(5.14). IR (KBr): ν(cm^{-1})=3,418 cm^{-1} (N–H, val.), 2,928 cm^{-1} (CH_2, val.), 2,107 cm^{-1} (C≡N, val.), 1,625 cm^{-1} (C=N, val.), 1,600–1,500 cm^{-1} (aromat. C=C, val.), 760–750 cm^{-1} (C–H, o. o. p.)

[(^{5}2,2-LFe^{III}NC)$_6$Co^{III}]Cl$_3$ Yield: 27% rel. to Co (M=2,512.7 g/mol). Analysis calculated for $C_{114}H_{114}Cl_3Fe_6CoN_{24}O_{12}$(%): C(54.49), N(13.38), H(4.57); with 0.1 CH3OH 5.1 KCl C(47.59) N(11.68) H(4.00); with 11.8 KCl C(40.36) N(9.91) H(3.39); found: C(38.98), N(15.29), H(4.47). IR (KBr): ν(cm^{-1})=3,422 cm^{-1} (N–H, val.), 2,925 cm^{-1} (CH_2, val.), 2,129 cm^{-1} (C≡N, val.), 1,628 cm^{-1} (C=N, val.), 1,600–1,500 cm^{-1} (aromat. C=C, val.), 760–750 cm^{-1} (C–H, o. o. p.)

[(^{5}2,2-LFe^{III}NC)$_6$Ru^{II}]Cl$_2$ Yield: 32% rel. to Ru (M=20,590.3 g/mol). Analysis calculated for $C_{114}H_{114}Cl_2Fe_6RuN_{24}O_{12}$(%): C(52.86), N(12.98), H(4.44); with 6.4 KCl 5.4 CH3OH C(45.25) N(10.61) H(4.31); found: C(44.89), N(11.76), H(5.46). IR (KBr): ν(cm^{-1})=3,421 cm^{-1} (N–H, val.), 2,927 cm^{-1} (CH_2, val.), 2,062 cm^{-1} (C≡N, val.), 1,623 cm^{-1} (C=N, val.), 1,600–1,500 cm^{-1} (aromat. C=C, val.), 760–750 cm^{-1} (C–H, o. o. p.)

2.4 Mössbauer spectroscopy

A conventional spectrometer has been used for measuring the Mössbauer spectra between liquid helium and room temperature (^{57}Co/Rh source, calibration at α-Fe at room temperature; isomer shifts are relative to the source).

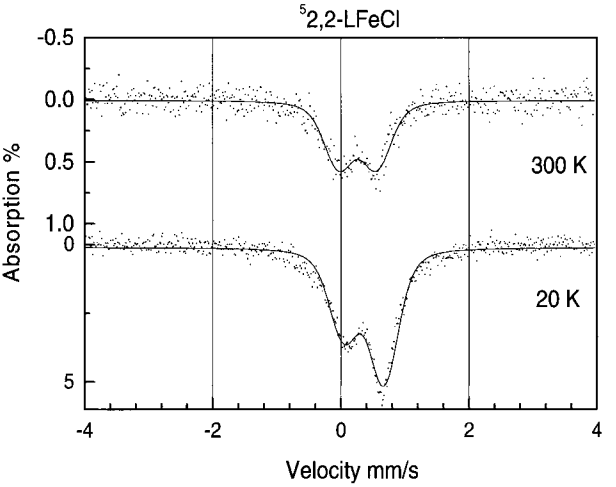

Figure 2 Mössbauer spectra of the precursor [Fe^{III}(^{5}2,2-L)Cl)] at 300 and 20 K.

Table I Mössbauer parameters of the precursors with ethylene [Fe^{III}(^{5}2,2-L)Cl)] and propylene [Fe^{III}(^{5}3,3-L)Cl)] at 300 and 20 K

Iron precursor Mössbauer parameters 300 K	δ (mm/s) State 1	Δ (mm/s)	mol%
^{5}2,2-LFeCl	0.26	0.593	100
^{5}3,3-LFeCl	0.256	0.716	100
Mössbauer parameters 20 K	State 1		
^{5}2,2-LFeCl	0.355	0.628	100
^{5}3,3-LFeCl	0.364	0.701	100

3 Results and discussion

Figure 2 and Table I show the temperature-dependent Mössbauer data and spectra of the [Fe^{III}(^{5}2,2-L)Cl)] and the [Fe^{III}(^{5}3,3-L)Cl)] precursor compounds. At 300 and 20 K the Mössbauer spectra exhibit a quadrupole doublet indicative for Fe(III) in the HS state (S= 5/2) [2, 3]. The Mössbauer parameters follow the thermal progression down to 20 K.

The prepared hepta- and nonanuclear complexes are characterized by IR spectrum and M+ peaks in ESI mass spectroscopy. No evidence for a splitting of the characteristic C–N stretching vibration band indicates a highly symmetric coordination sphere around the central Co(III), Ru(II), W(IV), and Mo(IV) atom (see Figure 1), i.e. either all eight or none of the cyanides are bridged. The shift of the CN-band for all product compounds indicates a bridged coordination.

Figure 3 and Table II show temperature dependence of the Mössbauer spectra of the hepta- and nonanuclear compounds for ethylene and propylene. At 300 K a quadrupole doublet is detected, which is indicative for Fe(III) in the HS state (S=5/2) [2, 3]. In opposite to the precursor compound the product spectra are symmetric.

In comparison to the precursor the isomer shifts (IS) of the ethylene compounds are moved downwards by 0.001–0.042 mm/s, except the IS of Co(III), which shifts upwards by 0.022 mm/s. The IS of propylene compounds shift by −0.048 and 0.022 mm/s for Mo(IV) and Co(III), respectively. Hence, the IS of the ethylene systems overshoot the IS of the

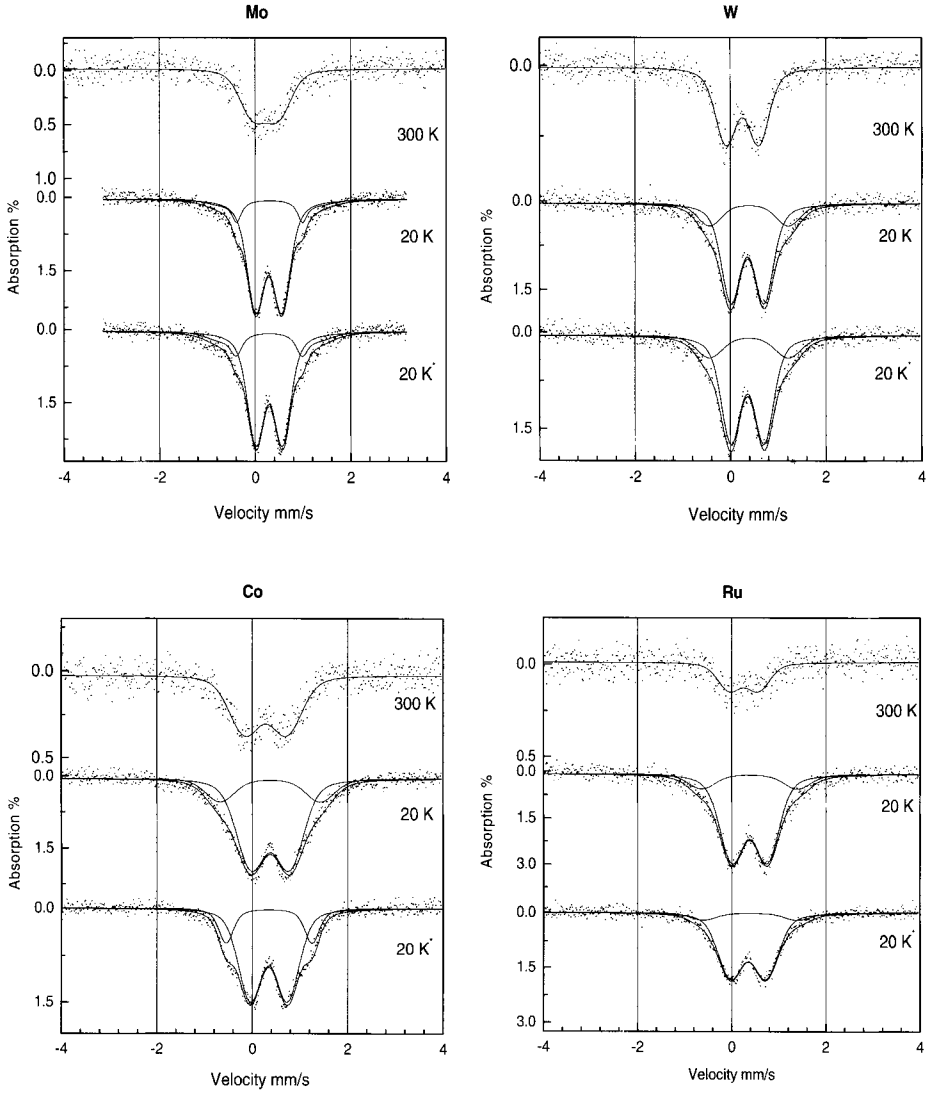

Figure 3 Mössbauer spectra of the multinuclear complexes Mo(IV), W(IV), Co(III), Ru(II) based on [Fe^{III}(^{5}2,2-L)Cl)] units at 300, 20, and at 20 K during light irradiation (25 mW/cm^2 at 514.5 nm; Ar-ion laser).

propylene, which is not the case for the quadrupole splitting. The quadrupole splittings for the ethylene compounds are moved by about 0.279, 0.092, 0.092, and −0.051 mm/s for Co (III), W(IV), Ru(II), and Mo(IV), respectively, while they change for the propylene compounds by about −0.136 and 0.059 mm/s for Mo and Co, respectively.

At 20 K the Mössbauer spectrum shows, in addition to the Fe(III) in the HS state, a second doublet appearing which is characteristic of Fe(III) in the low-spin state [2, 3] for the propylene compounds. The second doublet for the ethylene compounds shows a significant wider quadrupole splitting in comparison to the HS state, but the IS does not change significantly as expected for different electronic states, as in case of a transition between HS and LS states [2, 3].

Table II Mössbauer parameters of the multinuclear complexes at 300 and 20 K

Complex Mössbauer parameters 300 K	δ (mm/s) State 1	Δ (mm/s)	mol%	δ (mm/s) State 2	Δ (mm/s)	mol%
$[(^5$2,2-LFeNC)$_8$Mo]Cl$_4$	0.218	0.538	100	–	–	–
$[(^5$3,3-LFeNC)$_8$Mo]Cl$_4$	0.208	0.580	100	–	–	–
$[(^5$2,2-LFeNC)$_8$W]Cl$_4$	0.251	0.685	100	–	–	–
$[(^5$2,2-LFeNC)$_6$Co]Cl$_3$	0.282	0.872	100	–	–	–
$[(^5$3,3-LFeNC)$_6$Co]Cl$_3$	0.278	0.775	100	–	–	–
$[(^5$2,2-LFeNC)$_6$Ru]Cl$_4$	0.259	0.619	100	–	–	–
Mössbauer parameters 20 K	State 1			State 2		
$[(^5$2,2- LFeNC)$_8$Mo]Cl$_4$	0.286	0.539	82.7	0.297	1.425	17.3
$[(^5$3,3-LFeNC)$_8$Mo]Cl$_4$	0.337	0.695	68.1	0.161	2.283	31.9
$[(^5$2,2- LFeNC)$_8$W]Cl$_4$	0.376	0.689	77.3	0.403	1.685	22.7
$[(^5$2,2-LFeNC)$_6$Co]Cl$_3$	0.375	0.804	78.7	0.375	2.100	21.3
$[(^5$3,3-LFeNC)$_6$Co]Cl$_3$	0.356	0.700	65.7	0.267	2.470	34.3
$[(^5$2,2-LFeNC)$_6$Ru]Cl$_4$	0.376	0.746	83.8	0.383	2.029	16.2

Table III Mössbauer parameters of the multinuclear complexes at 20 K during light irradiation (25 mW/cm^2 at 514.5 nm; Ar-ion laser)

Mössbauer parameters 20 K	State 1			State 2		
Complex	δ (mm/s)	Δ (mm/s)	mol%	δ (mm/s)	Δ (mm/s)	mol%
$[(^5$2,2- LFeNC)$_8$Mo]Cl$_4$	0.293	0.551	78.8	0.290	1.496	21.2
$[(^5$3,3-LFeNC)$_8$Mo]Cl$_4$	0.324	0.763	69.8	0.189	2.387	30.2
$[(^5$2,2- LFeNC)$_8$W]Cl$_4$	0.359	0.715	82.3	0.392	1.700	17.7
$[(^5$2,2-LFeNC)$_6$Co]Cl$_3$	0.348	0.780	78.8	0.352	1.800	21.2
$[(^5$3,3-LFeNC)$_6$Co]Cl$_3$	0.360	0.722	100.0	–	–	–
$[(^5$2,2-LFeNC)$_6$Ru]Cl$_4$	0.350	0.750	88.9	0.396	2.000	11.1

The temperature dependence of the area fraction of the respective doublets A(Fe^{III}-S1):A(Fe^{III}-S2) indicates that all the Fe(III) centers in the ethylene hepta- and nonanuclear complexes perform a thermally induced electronic switching between HS and HS states, e.g. multistability. The ethylene W, Mo, Co, and Ru switch about 22, 21, 17, and 16% between the HS states. For the propylene compounds, the Co and Mo switch between HS to LS state by about 34 and 32%, respectively. Therefore, we attribute a HS to LS spin transition for the propylene compounds and a HS to HS transition for the ethylene compounds.

Table III shows the Mössbauer parameters of the multinuclear complexes taken at 20 K during light irradiation (25 mW/cm^2 at 514.5 nm; Ar-ion laser). The population between the two electronic states can be altered by about 5% for the ethylene systems. This indicates a light induced HS to HS transition. The propylene system, however, is not affected by light.

In conclusion, the ethylene-based ligand is less flexible arranged around the Fe(III) centers. Nevertheless it allows a HS to HS transition as well as a reversible light induced switching effect. The propylene compound however appears to be more flexible in the arrangement and allows sterical alterations such as a thermal induced HS to LS transition in the Fe(III) units.

Acknowledgements This work was partly funded by the University of Mainz ("Forschungsfond"; MWFZ) and the "Deutsche Forschungsgemeinschaft" (DFG: Re-1627/1-3).

References

1. Gembicky, M., Boca, R., Renz, F.: Inorg. Chem. Commun. **3**, 662–665 (2000)
2. Renz, F., Kerep, P.: Polyhedron **24**, 2849–2851 (2005)
3. Renz, F., Kerep, P.: Hyperfine Interact. **156**, 371–377 (2004)
4. Herchel, R., Boča, R., Gembickỳ, M., Koižiŝek, J., Renz, F.: Inorg. Chem. **43**, 4103–4105 (2004)

Hyperfine Interact (2006) 168:989–994
DOI 10.1007/s10751-006-9385-3

Hyperfine interactions, structure and magnetic properties of nanocrystalline Co–Fe–Ni alloys prepared by mechanical alloying

E. Jartych · J. K. Żurawicz · D. Oleszak · M. Pękała

Published online: 8 November 2006

Abstract Mechanical alloying method was used to prepare nanocrystalline $Co_{50}Fe_{40}Ni_{10}$, $Co_{52}Fe_{26}Ni_{22}$ and $Co_{65}Fe_{23}Ni_{12}$ alloys. X-ray diffraction proved that during milling Co–Fe-based solid solution with *b.c.c.* lattice was formed in the case of $Co_{50}Fe_{40}Ni_{10}$, while for $Co_{52}Fe_{26}Ni_{22}$ and $Co_{65}Fe_{23}Ni_{12}$ compositions Co–Ni-based solid solutions with *f.c.c.* lattice were obtained. Mössbauer spectroscopy revealed similar values of the average hyperfine magnetic fields for all alloys, e.g. 32.17, 32.24 and 31.21 T for $Co_{50}Fe_{40}Ni_{10}$, $Co_{52}Fe_{26}Ni_{22}$ and $Co_{65}Fe_{23}Ni_{12}$ alloys, respectively. Magnetization measurements allowed to determine the effective magnetic moment, Curie temperature, saturation magnetization and coercive field for the obtained alloys.

Key words nanocrystalline Co–Fe–Ni alloys · mechanical alloying · Mössbauer spectroscopy

1 Introduction

Co–Fe–Ni ternary alloys are materials exhibiting good soft magnetic properties. Alloys prepared by electrodeposition as thin films have extremely high saturation magnetization of about 2.1 T and low coercivity around 1 Oe. [1, 2]. In this work we propose the mechanical alloying (MA) method as the potential technology of production of bulk Co–Fe–Ni alloys with good soft magnetic properties. The compositions of alloys: $Co_{50}Fe_{40}Ni_{10}$,

E. Jartych (✉) · J. K. Żurawicz
Department of Experimental Physics, Institute of Physics, Technical University of Lublin,
ul. Nadbystrzycka 38, 20-618 Lublin, Poland
e-mail: e.jartych@pollub.pl

D. Oleszak
Faculty of Materials Science and Engineering, Warsaw University of Technology,
ul. Wołoska 141, 02-507 Warsaw, Poland

M. Pękała
Department of Chemistry, Warsaw University, Al. Żwirki i Wigury 101, 02-089 Warsaw, Poland

$Co_{52}Fe_{26}Ni_{22}$ and $Co_{65}Fe_{23}Ni_{12}$ were chosen on the basis of the data reported in [1, 2]. The structure and some magnetic properties of these alloys were determined using X-ray diffraction (XRD), Mössbauer spectroscopy (MS) and magnetization measurements.

2 Experimental details

Co, Fe and Ni elemental powders (purity of 99.9%, initial dimensions of particles 3–10 μm) were subjected to the mechanical alloying process in a Fritsch P5 planetary ball mill with stainless-steel vial and balls. MA processes were performed under an argon atmosphere.

XRD measurements were carried out using a Philips PW 1830 diffractometer working in a continuous scanning mode with CuK_α or CoK_α radiation. The Williamson–Hall approach was used for determination of the average grain sizes, D, and the mean level of internal strains, ε, [3]. The volume fraction of the grain boundaries, C_{gb}, was estimated on the basis of the coherent polycrystal model and assuming that the average grain boundary thickness is 1 nm ([4] and references therein).

MS studies were performed at room temperature in standard transmission geometry using a source of ^{57}Co in a rhodium matrix.

Temperature dependencies of magnetization were measured on a Faraday balance in magnetic fields up to 1.5 T. The hysteresis loops measurements were performed using a vibrating sample magnetometer PAR Model 155 at room temperature in fields up to ±1.6 T.

3 Results and discussion

XRD studies proved that alloys started to form after 20 h of milling. Figure 1a shows patterns obtained for the final products of milling. Detailed analysis of XRD results allowed to state that during MA process of $Co_{50}Fe_{40}Ni_{10}$ system the solid solution with *b.c.c.* (body centred cubic) lattice was formed, while for $Co_{52}Fe_{26}Ni_{22}$ and $Co_{65}Fe_{23}Ni_{12}$ compositions solid solutions with *f.c.c.* (face centred cubic) lattice were obtained. These results agree well with the phase-diagram for the bulk Co-rich Co–Fe–Ni alloys obtained by melting [5]. Moreover, the obtained alloys are disordered, e.g. Co, Fe and Ni atoms occupy the lattice sites randomly. Table I summarizes structural data for the final products of MA processes. The lattice parameters of the obtained alloys are similar to those reported for electro-deposited binary Co–Fe and Co–Ni alloys [6, 7]. It may be supposed that in the mechanically synthesized $Co_{50}Fe_{40}Ni_{10}$ solid solution the Co–Fe alloy is the matrix, in which Ni atoms dissolve, while in the case of $Co_{52}Fe_{26}Ni_{22}$ and $Co_{65}Fe_{23}Ni_{12}$ solid solutions, the matrix is Co–Ni alloy, in which Fe atoms dissolve.

Mössbauer spectra of all the mixtures for various milling periods were the six-line patterns. Figure 1b presents results of MS measurements for the final products of milling. The spectra of the samples milled up to 10 h were characteristic for α-iron what confirmed XRD results that the process of alloys formation did not start yet. The spectral lines of the samples milled between 20 and 100 h (or 80 h) were systematically broadened testifying the alloy formation. Moreover, in the case of $Co_{50}Fe_{40}Ni_{10}$ and $Co_{65}Fe_{23}Ni_{12}$ milled for 20 and 50 h besides the six-line component, the paramagnetic doublet was revealed. This doublet was attributed to a partially oxidized iron phase formed during the manipulation of the samples. The hyperfine interaction parameters of this doublet (the isomer shift, IS, of about 0.35 mm s^{-1} and the quadrupole splitting, QS, of about 0.65 mm s^{-1}) were very similar to

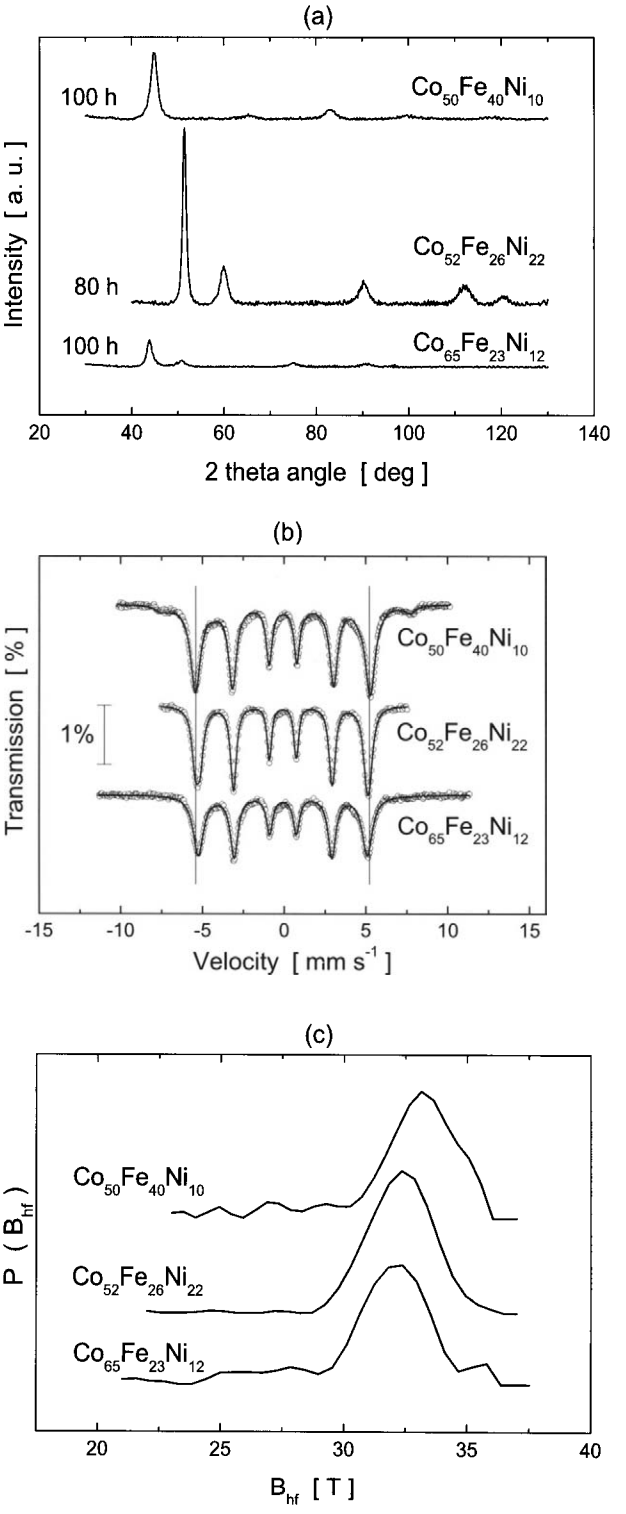

Figure 1 **a** XRD patterns of the mechanosynthesized Co–Fe–Ni alloys measured with CuK_α ($Co_{50}Fe_{40}Ni_{10}$ and $Co_{65}Fe_{23}Ni_{12}$) and CoK_α ($Co_{52}Fe_{26}Ni_{22}$) radiation; **b** room-temperature Mössbauer spectra of the Co–Fe–Ni alloys; vertical lines denote the positions of the spectral lines of α-iron; **c** hyperfine magnetic field distributions, $P(B_{hf})$ – probability in arbitrary units.

Table I Structural data for the mechanically synthesized Co–Fe–Ni alloys

Composition	Lattice	D (nm)	ε (%)	C_{gb} (%)	a (nm)
$Co_{50}Fe_{40}Ni_{10}$	*b.c.c.*	15(1)	1.30(5)	19(1)	0.2843(4)
$Co_{52}Fe_{26}Ni_{22}$	*f.c.c.*	24(1)	0.72(5)	12(1)	0.3575(1)
$Co_{65}Fe_{23}Ni_{12}$	*f.c.c.*	10(1)	0.58(5)	27(1)	0.3581(10)

D – average grain sizes, ε – mean level of internal strains, C_{gb} – volume fraction of the grain boundaries, a – lattice parameter

Table II Magnetic data for the mechanically synthesized Co–Fe–Ni alloys

Composition	$<B_{hf}>$ (T)	B_{max} (T)	(Co, Fe, Ni) configuration	μ_{eff} (μ_B)	T_C (K)	B_s (emu g^{-1})	H_c (Oe)
$Co_{50}Fe_{40}Ni_{10}$	32.17	33.13	(4, 3, 1)	1.65	798	159.9	67
$Co_{52}Fe_{26}Ni_{22}$	32.24	32.34	(7, 3, 2)	1.63	1000	158.3	15
$Co_{65}Fe_{23}Ni_{12}$	31.21	32.37	(9, 2, 1)	1.62	749	144.3	54

$<B_{hf}>$ – average hyperfine magnetic field, B_{max} – most probable value, μ_{eff} – effective magnetic moment per formula unit, T_C – Curie temperature, B_s – saturation magnetization, H_c – coercive field

the data for the iron oxide reported in [8]. The prolonged milling up to 100 h caused disappearing of the iron oxide in the case of $Co_{65}Fe_{23}Ni_{12}$ alloy, while the spectrum of $Co_{50}Fe_{40}Ni_{10}$ alloy revealed two additional sextets (see Figure 1b) with high values of the hyperfine magnetic fields, B_{hf}, (e.g. 47.5 and 46.4 T). These sextets were attributed to the magnetite Fe_3O_4 (the hyperfine interaction parameters were similar to the data reported in [9]). However, the relative contribution of the magnetite to the whole spectrum, which was estimated from the area of the spectral lines, was rather small (about 8%).

The Mössbauer spectra for the final products of MA processes were fitted using the hyperfine magnetic field distribution, $P(B_{hf})$, as suggested by the relatively high values of the width of the spectral lines and disordered structure of the alloys. The linear correlation between B_{hf} and IS as well as between B_{hf} and QS was assumed in the fitting procedure. The B_{hf} values ranged from about 22 to 37 T (see Figure 1c). The average values of the B_{hf} obtained from the distributions are listed in Table II. The possible atomic configuration around ^{57}Fe isotopes was analysed under the assumption that only the first nearest neighbours (NN) contribute to the hyperfine field at ^{57}Fe site. The probabilities of the various (Co, Fe, Ni) configurations in the NN shell were calculated using the extended binomial distribution [10]. The maximum values of these probabilities obtained for the suitable (Co, Fe, Ni) configurations were attributed to the most probable field values, B_{max}, which are listed in Table II.

Figure 2 shows the dependencies of magnetization on the temperature and the applied magnetic field for the final products of MA processes. The values characterizing magnetic properties of the Co–Fe–Ni alloys are summarized in Table II. The Curie temperatures, T_C, are significantly lower than those for pure cobalt as well as for bulk Co–Fe and Co–Ni alloys. The reduced Curie temperature of the investigated Co–Fe–Ni alloys may be caused by the relatively high value of the lattice strains as well as by the large amount of atoms located in strongly disordered grain boundaries. The B_s and H_c values obtained from the hysteresis loops are of the same order of magnitude as those observed for Co–Fe–Ni thin films [5].

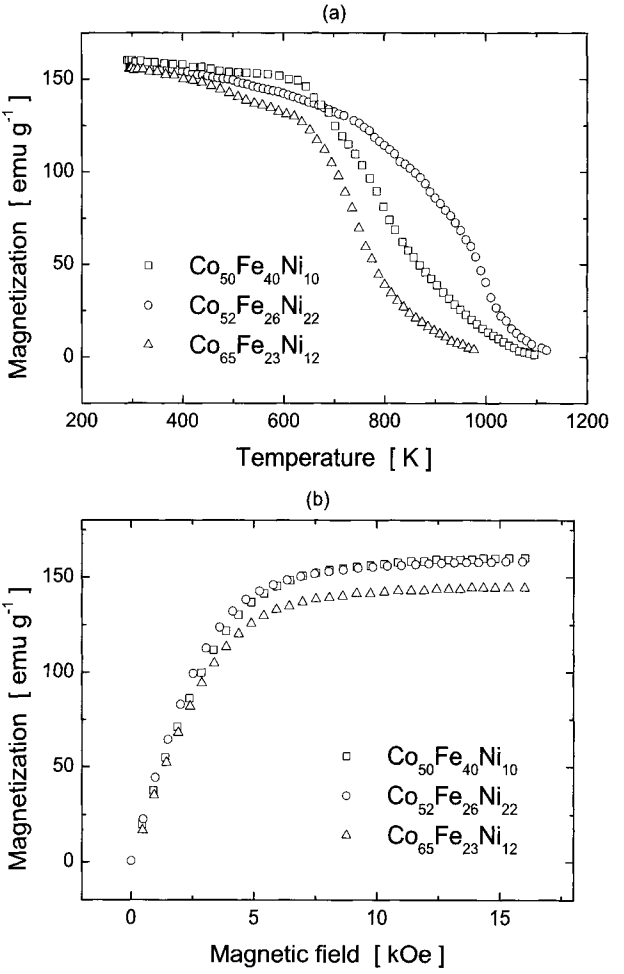

Figure 2 Magnetization of the mechanosynthesized Co–Fe–Ni alloys as a function of **a** temperature and **b** magnetic field.

4 Conclusions

XRD, MS and magnetization studies proved that during MA process the nanocrystalline $Co_{50}Fe_{40}Ni_{10}$, $Co_{52}Fe_{26}Ni_{22}$ and $Co_{65}Fe_{23}Ni_{12}$ alloys were formed. In the case of $Co_{50}Fe_{40}Ni_{10}$ and $Co_{65}Fe_{23}Ni_{12}$ alloys, Mössbauer and magnetic measurements revealed a small contamination of the powders with a second phase, possibly an iron oxide, which can have occurred during the powder handling. The obtained alloys were characterized by the hyperfine magnetic field distributions. The most probable configurations, (Co, Fe, Ni), of atoms in the nearest neighbourhood of ^{57}Fe isotopes was deducted on the basis of the binomial distributions. They are as follows: (4 Co, 3 Fe, 1 Ni), (7 Co, 3 Fe, 2 Ni) and (9 Co, 2 Fe, 1 Ni) for $Co_{50}Fe_{40}Ni_{10}$, $Co_{52}Fe_{26}Ni_{22}$ and $Co_{65}Fe_{23}Ni_{12}$ alloys, respectively.

The alloys have the saturation magnetization of the order of 1.6–1.7 T and relatively small coercive fields that allows to consider that mechanically synthesized Co–Fe–Ni alloys are good soft magnetic materials.

References

1. Osaka, T.: Electrochim. Acta **45**, 3311–3321 (2000)
2. Liu, X., Zangari, G., Shen, L.: J. Appl. Phys. **87**, 5410–5412 (2000)
3. Williamson, G.K., Hall, W.H.: Acta Metall. **1**, 22–31 (1953)
4. Song, H.W., Guo, S.R., Hu, Z.Q.: Nanostruct. Mater. **11**, 203–210 (1999)
5. Jen, S.U., Chiang, H.P., Chung, C.M., Kao, M.N.: J. Magn. Magn. Mater. **236**, 312–319 (2001)
6. Jartych, E., Zurawicz, J.K., Budzynski, M.: J. Phys., Condens. Matter **5**, 927–934 (1993)
7. Jartych, E., Olchowik, J., Zurawicz, J.K., Budzynski, M.: J. Phys., Condens. Matter **5**, 8921–8926 (1993)
8. Marest, G., Skoutarides, C., Barnavon, Th., Tousset, J., Fayeulle, S., Robelet, M.: Nucl. Instrum. Methods **209/210**, 259–265 (1983)
9. da Costa, G.M., De Grave, E., de Bakker, P.M.A., Vandenberge, R.E.: J. Solid State Chem. **113**, 405–412 (1994)
10. Gerstenkorn, T., Śródka, T.: In: Kombinatoryka i rachunek prawdopodobieństwa, p. 170. PWN, Warszawa (1974) (in Polish)

Hyperfine Interact (2006) 168:995–999
DOI 10.1007/s10751-006-9386-2

Metallurgical behaviour of iron in brass studied using Mössbauer spectroscopy

Saeed Kamali-M · Lennart Häggström · Tore Ericsson · Roger Wäppling

Published online: 14 November 2006

Abstract The behaviour of small amounts of Fe in brass is investigated using Mössbauer spectroscopy. Different samples, made from the same ingot material, but run through different annealing temperatures and duration times and then quenched to room temperature, have different amount of γ-Fe. The present work shows that a suitable heat treatment can increase the amount of these precipitations and, that a heat treatment at 650°C is the optimal one for having the highest amount of this phase.

Key words brass · Mössbauer spectroscopy · precipitates · heat treatment

1 Introduction

In some industrial applications of brass, the precipitation of Fe, either in form of γ-Fe or α-Fe, is desired or unwanted as the mechanical but also other properties are strongly altered. The precipitation of Fe atoms, as an example, not only attract the other impurities but also vacancies and as a result the electric conductivity will increase [1]. The aim of this study is to determine the structure of Fe in thin brass foils containing 86% copper and 13% zinc. Although the Fe content is only 0.8%, it is expected to precipitate and build up γ-Fe with the same crystal structure as the brass matrix itself, or even ferromagnetic α-Fe having the bcc structure.

2 Experimental

All the samples are made from the same ingot material, but run through different annealing processes. First, every sample was annealed at 1,000°C for 10 min. Then they were quenched to an intermediate temperature between 750 and 600°C, held at

S. Kamali-M (✉) · L. Häggström · T. Ericsson · R. Wäppling
Department of Physics, Uppsala University, Box 530, SE-751 21 Uppsala, Sweden
e-mail: s.kamali.m@gmail.com

this temperature for 10, 30 or 100 s and afterwards quenched to room temperature. The samples are denoted as $S(T,t)$, where the first parameter is the intermediate temperature and the second parameter is the time during which the sample was heat treated at the intermediate temperature. For comparison one of the samples was quenched directly from 1,000°C to room temperature which will be denoted quenched. The amount of precipitated and dissolved Fe in the samples were then determined using transmission Mössbauer spectroscopy. For ^{57}Fe Mössbauer spectroscopic measurements, radioactive ^{57}Co in a Rh matrix was used at room temperature as source. The spectra were calibrated by using the six lines of α-Fe, the center of which was taken as zero center shift (CS). The Mössbauer spectra were fitted using Lorentzian lines. The question to be answered is, if precipitation of γ-Fe or α-Fe takes place as a result of the annealing process. The samples studied are 50 μm thick brass-foils of 1.5×1.5 cm^2 area. The samples were prepared at Outokumpu Fabrication Technology using standard methods followed by chemical analysis (Jorgen.Eriksson@outokumpu.com). Brass is a copper–zinc alloy having a wide solid solution range. The phase diagram [2] shows a brass α-phase with fcc structure, thermodynamically stable up to about 900°C for Zn$\leq$ 40 at.%. For the composition studied here the melting point is about 1,030°C. There is no phase transition in brass during the sample-preparation process. Pure Fe has different crystallographic structures depending on temperature e.g. an α-phase (bcc structure and stable below 910°C) and γ-phase (fcc-structure and stable between 910 and 1,390°C). The iron α-phase is ferromagnetic, and the γ-Fe is weakly antiferromagnetic. The solubility of Fe in copper is very low; even 0.2 wt.% of Fe can give precipitations of γ-Fe [3] having the same structure as the Cu matrix. However, these precipitates may undergo a transition to α-Fe under plastic deformation or aging, when the size of grains is large enough. The same behaviour may also be expected for Fe in brass. Experimental results for brass alloys with 5% Zn and 0.1 or 1.0% Fe [4] show no differences in the Mössbauer spectra. The aging process is simulated with the annealing process for the present samples, thus one could expect some α-Fe to show up in the Mössbauer spectra, and the amount is to be determined by fitting the spectrum and comparing the related spectral intensities. The samples are quite thick (50 μm) for transmission Mössbauer measurements. The linear atomic absorbtion for 14.4 keV in brass is 72 mm^{-1} thus only about 2.7% of 14.4 keV photons will transmit, when no Mössbauer effect is taken into consideration. (The alternative backscattering CEMS method was not applied since the Fe content was low.)

3 Result and discussion

Mössbauer spectra for nine samples (Figure 1) were recorded in the velocity range of $\pm$1.5 mm/s and also, in order to search for any α-Fe, in a wider range of $\pm$7.0 mm/s. The fitting results are given in Table I. The Fe atoms, depending on the heat treatment, can have two extreme surroundings. The first extreme case is when the Fe atoms are simply dissolved in brass i.e. there are essentially only Cu and Zn atoms in the near neighbourhood. The subspectrum is then a single line with a CS of about 0.25 mm/s [5]. If an Fe atom has another Fe atom as nearest neighbour, then the symmetry is broken and a quadrupole splitting (QS) appears. The Fe atom

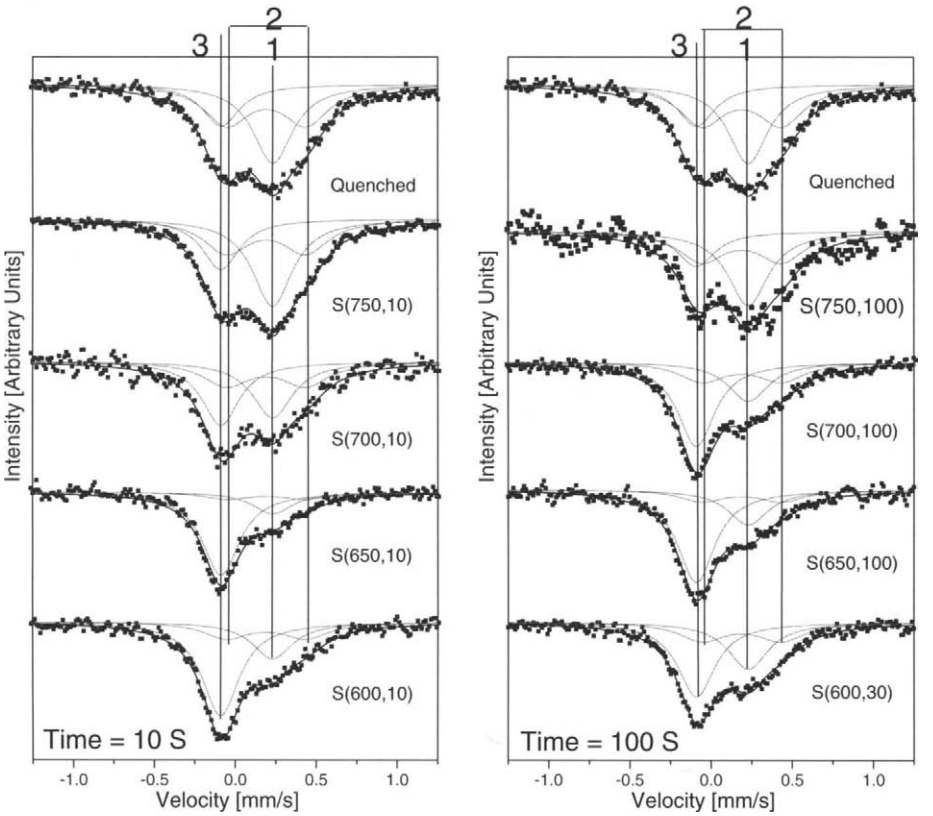

Figure 1 All the Mössbauer spectra for different annealing temperatures and different times; 10 s (*left*) and 100 s (*right*) except for *S*(600,30) sample. The numbers 1 and 3 refer to the singlets and 2 refers to the doublet discussed in the text. The same components in the subspectra are indicated by *lines*.

under study can have more than one Fe atom as nearest neighbour which might increase or decrease the QS depending on the actual atomic configuration. In the other extreme case, an Fe atom is surrounded only by other Fe atoms forming clusters. These clusters probably adopt the fcc structure of brass and, thus, locally forming γ-Fe which is known to have a single absorption line with CS ≈ -0.09 mm/s. These clusters might also form α-Fe, known to be ferromagnetic if they are big enough. No traces of magnetically splitted Mössbauer patterns could however be observed in the present samples. For small clusters of α-Fe superparamagnetism may occur, leading to a Mössbauer pattern with a single line at 0 mm/s. Here, this seems to us not very reasonable, as the particles sizes large enough to change the iron lattice structure to bcc, should be able to show hyperfine field close to 33 T. Thus one may fit the spectra with two single lines and one doublet. The line width of the absorbtion lines is however larger than the natural line width as a result of the variation of the surroundings.

The singlet which is due to the precipitation of γ-Fe increases in intensity as the intermediate temperature is decreased reaching a maximum at 650°C.

Table I The peak positions in the nine low-range samples

Components	1			2			3		
Samples	CS	QS	I	CS	QS	I	CS	QS	I
Quenched	0.23	0.00	38	0.19	0.49	43	−0.09	0.00	19
S(600,10)	0.23	0.00	23	0.19	0.49	22	−0.09	0.00	55
S(600,30)	0.23	0.00	30	0.19	0.49	26	−0.09	0.00	44
S(650,10)	0.23	0.00	19	0.19	0.49	13	−0.09	0.00	68
S(650,100)	0.23	0.00	24	0.19	0.49	17	−0.09	0.00	59
S(700,10)	0.23	0.00	33	0.19	0.49	32	−0.09	0.00	35
S(700,100)	0.23	0.00	25	0.19	0.49	26	−0.09	0.00	49
S(750,10)	0.23	0.00	42	0.19	0.49	36	−0.09	0.00	22
S(750,100)	0.23	0.00	43	0.19	0.49	38	−0.09	0.00	19

The CS is given versus α-Fe. The FWHM of all peaks was fixed to be around 0.31 mm/s and the same for all lines. The errors in CS and QS is ±0.02 mm/s and in I is ±3%.

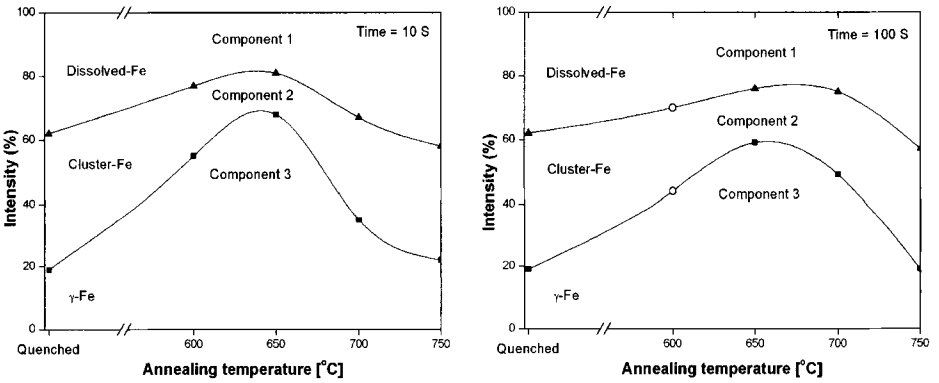

Figure 2 The amount of the different Fe phases as function of temperature for different annealing times; 10 s (*left*) and 100 s (*right*) except for *S*(600,30) where the time is 30 s and is indicated by *open circles* in the figure.

Component 1 has an average isomer shift of 0.23 mm/s, in between the values for iron in zinc and iron in copper and closer to the latter [6]. It represents Fe atoms dissolved in the brass matrix. Component 2 originates from Fe atoms with one or more Fe atoms as nearest neighbour (NN) and component 3 represents Fe atoms surrounded by almost only Fe atoms as NN. There are a number of zinc-rich phases in the Fe–Zn phase diagram. However the values of the hyperfine parameters rule out $FeZn_x$ for all reported values x=13, 10, 4 and 3.33 [7]. As can be seen in Figure 2 the amount of γ-Fe is largest for an annealing temperature of 650°C. The annealing times of 10–100 s are obviously enough to influence the amount of Fe precipitations. Under the same conditions the amount of Fe dissolved in brass has its lowest value. Thus it seems quite clear that clustering of Fe atoms most easily take place under these conditions.

4 Conclusion

The tiny amount of Fe shows different character in brass samples made from the same ingot, but run through different annealing processes. The amount of Fe atoms which precipitate to γ-Fe has the highest value when the intermediate temperature is about 650°C. No α-Fe has been observed.

References

1. Yamauchi, T., Takayanagi, K., Yamaguchi, H.: J. Phys. Soc. Japan **54**, 4621 (1985)
2. Hansen, M., Anderko, K.: Constition of Binory Alloys. McGraw-Hill, New York (1958)
3. Window, B.: J. Phys. C: Metal Phys. Suppl. **3**, 323 (1970)
4. Window, B.: J. Phys. C: Metal Phys. **1**, 533 (1971)
5. Cathey, W.N., Norris, B.D.: Phys. Lett., A **42**, 331 (1972)
6. Qaim, S.M.: Proc. Phys. Soc. **90**, 1065 (1967)
7. Gu, Y., et. al.: Metal. Trans. **21A**, 273 (1990)

Hyperfine Interact (2006) 168:1001–1007
DOI 10.1007/s10751-006-9457-4

Chemical tuning of high-spin complexes based on 3- and 4-hydroxy-pentadentate-Fe (III) complex-units investigated by Mössbauer spectroscopy

M. Klein · F. Renz

Published online: 14 December 2006

Abstract The pentadentate ligands 3-OH-^{5}L=[*N*,*N*′-Bis(1,3-dihydroxy-2-benzylidene)-1, 7-diamino-4-azaheptane] and 4-OH-^{5}L=[*N*,*N*′-Bis(1,4-dihydroxy-2-benzylidene)-1,7-diamino-4-azaheptane] has been prepared by a Schiff base condensation between 1,7-diamino-4-azaheptane and the dihydroxybenzaldehyde. Complexation with Fe(III) yields high-spin (S=5/2) complexes of [Fe^{III}(3-OH-^{5}L)Cl] and [Fe^{III}(4-OH-^{5}L)Cl]. These precursors were combined with $[M(CN)_x]^{y-}$ (M=W(IV), Mo(IV), Ru(II), Co(III)) and heptanuclear and nonanuclear clusters of $[M\{(CN\text{-}Fe^{III}(3\text{-}OH\text{-}^5L)\}_x]Cl_y$ and $[M\{(CN\text{-}Fe^{III}(4\text{-}OH\text{-}^5L)\}_x]Cl_y$ resulted. Such starshaped hepta- and nonanuclear compounds are high-spin systems at room temperature. On cooling to 10 K some of the iron(III) centers switch to a second high-spin state as proven by Mössbauer spectra, i.e. multiple electronic transitions. Parts of the compounds perform a high-spin to high-spin transition.

Key words heptanuclear · nonanuclear · high-spin molecule · Fe(III)–W(IV) · Fe(III)–Mo(IV) · Fe(III)–Ru(II) · Fe(III)–Co(III) · multiple electronic transition

1 Introduction

Recently, molecular switchability has been observed in star shaped compounds. Such compounds exhibits multistability, e.g. multiple spin transition: (1) the heptanuclear $Fe^{III}{}_6$–Co^{III} [1], (2) the nonanuclear $Fe^{III}{}_8$–Mo^{IV} [1, 2], and (3) the tetranuclear $Fe^{III}{}_3$–Cr^{III} [3].

In the present work, our approach is to study the effect of OH-substitution in both the [N-H-^{5}LFe^{III}Cl] precursors and its hepta- and nonanuclear analogous compounds. The question is whether the effect of the hydroxy group results in a sterical or electronic contribution to the magnetic and electronic behaviour of the multistability.

M. Klein · F. Renz (✉)
Institut für Anorganische Chemie und Analytische Chemie, Johannes Gutenberg-Universität, Duesbergweg 10-14, 55099 Mainz, Germany
e-mail: Franz.Renz@uni-mainz.de

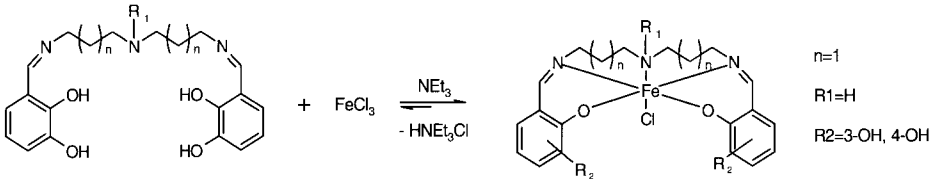

Figure 1 Synthesis and structure of the iron precursors [Fe(3-OH-^{5}L)Cl], [Fe(4-OH-^{5}L)Cl].

2 Experimental

The main strategy for the synthesis was performed in analogy to the literature [1, 2].

2.1 Ligands: 3-OH-^{5}L, 4-OH-^{5}L

The pentadentate ligands 3-OH-^{5}L=*N,N'*=-Bis(1,3-hydroxy-2-benzylidene)-1,7-diamino-4-azaheptane, 4-OH-^{5}L=*N,N'*-Bis(1,4-hydroxy-2-benzylidene)-1,7-diamino-5-azaheptane were each formed in a Schiff base condensation. The 1,7-diamino-4-azaheptane (0.025 mol) and the appropriate dihydroxybenzaldehyde (0.05 mol) are dissolved in methanol (25 cm^3) and slowly mixed, refluxed for 10 min, and the yellow mixture was used without any purification for the preparation of the precursor.

2.2 Precursors [Fe(3-OH-^{5}L)Cl], [Fe(4-OH-^{5}L)Cl]

A solution of anhydrous iron(III) chloride (0.025 mol) in methanol (50 cm^3) was added to the freshly prepared solution of the pentadentate ligand. The mixture was boiled and then triethylamine (50 mmol) was added (see Figure 1). The resulting solution was then heated under reflux for 1 h. After cooling, crystals precipitated. These were collected dried 24 h in vacuum.

[Fe(3-OH-^{5}L)Cl]: Yield: 71% rel. to Fe (M=462 g/mol). Analysis calculated: for $C_{20}H_{25}ClFeN_3O_4$ (%): C (51.91), N (7.66), H (5.45); with 6.2 mol CH3OH: C:47.58 N:6.35 H:7.59 found: C (45.82), N (7.68), H(5.64). IR (KBr): ν(cm^{-1})= 1,647 cm^{-1} (–C=N–), 787 cm^{-1} (aromat. H) MALDI-ToF MS m/z=425.0 ([Fe(3-OH-^{5}L)Cl]$^+$)

[Fe(4-OH-^{5}L)Cl]: Yield: 66% rel. to Fe (M=462 g/mol). Analysis calculated: for $C_{20}H_{25}ClFeN_3O_4$ (%): C (51.91), N (9.08), H (5.45); with 3.80 CH3OH 0.1 (C2H5)3NCl 1.10 FeCl3 C(37.74) N(5.59) H(5.41); found: C (37.95), N (5.39), H(5.26). IR (KBr): ν(cm^{-1})=1,648 cm^{-1} (–C=N–), 853 cm^{-1} (aromat. H), 760–770 cm^{-1} (C–H, out of plane= o.o.p.). FD MS m/z=425 ([Fe(4-OH-^{5}L)Cl]$^+$).

2.3 Multinuclear complexes [W^{IV}{(CN) Fe^{III}(3-OH-^{5}L)}$_8$]Cl$_4$, [W^{IV}{(CN) Fe^{III}(4-OH-^{5}L)}$_8$]Cl$_4$, [Mo^{IV}{(CN) Fe^{III}(3-OH-^{5}L)}$_8$]Cl$_4$, [Mo^{IV}{(CN) Fe^{III}(4-OH-^{5}L)}$_8$]Cl$_4$, [Ru^{II}{(CN) Fe^{III}(3-OH-^{5}L)}$_6$]Cl$_2$, [Ru^{II}{(CN) Fe^{III}(4-OH-^{5}L)}$_6$]Cl$_2$, [Co^{III}{(CN) Fe^{III}(3-OH-^{5}L)}$_6$]Cl$_3$, [Co^{III}{(CN) Fe^{III}(4-OH-^{5}L)}$_6$]Cl$_3$

The complexes were each prepared following a universal precept. 0.001 mol of the precursor were dissolved in methanol (100 cm^3) and an aqueous methanol (1:1) solution

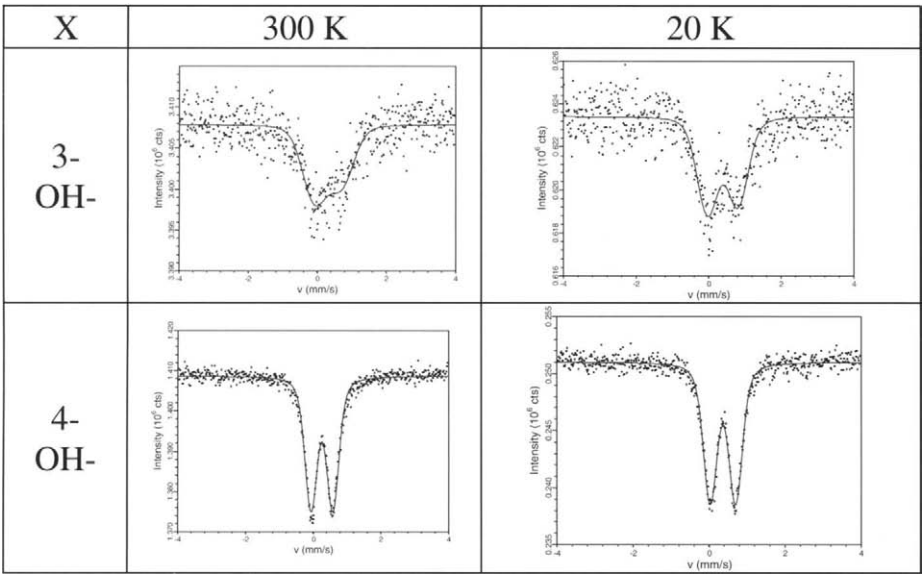

Figure 2 Mössbauer spectra of the precursors $[Fe^{III}(X\text{-}^5L)Cl]$ at 300 and 20 K.

(10 cm^3) of the appropriate cyanide ($K_4[Mo(CN)_8]$).$2H_2O$, $K_4[W(CN)_8]\cdot 2H_2O$, $K_4[Ru(CN)_6]$, $K_3[Co(CN)_6]$) 0.125 mmol for octacyanids (and 0.17 mmol for hexacyanids) was added dropwise. After 30 min of stirring at room temperature the solution was reduced to 50 cm^3 (below 35°C in vacuum). Addition of 150 cm^3 distilled water precipitated the product, which was slowly filtered off on the frita funnel. The product was washed with distilled water and diethylether and dried under vacuum for 24 h. Note that too low carbon content is commonly observed and based on incomplete decomposition to CO_2 due to formation of stable metal carbides.

$[Mo^{IV}\{(CN)\ Fe^{III}(3\text{-}OH\text{-}^5L)\}_8]Cl_4$: Yield: 29% rel. to Mo (3,754.42 g/mol). Analysis calculated for $C_{160}H_{184}\ Cl_4Fe_8MoN_{32}O_{32}$ (%): C(52.44), N(11.65), H(4.82); with KCl C (43.47) N(10.14) H(4.20); found: C(45.22), N(3.70), H(1.40). IR (KBr): $\nu(cm^{-1})$=2,103 (–C≡N–); 1,650 (–C=N–); 1,500–1,600 cm^{-1} (aromat. C=C, val.), 750–760 cm^{-1} (C–H, o. o. p.)

$[Mo^{IV}\{(CN)\ Fe^{III}(4\text{-}OH\text{-}^5L)\}_8]Cl_4$: Yield: 77% rel. to Mo (3,754.42 g/mol). Analysis calculated for $C_{160}H_{184}Cl_4Fe_8MoN_{32}O_{32}$ (%): C(52.44), N(11.65), H(4.82); with 1.87 KCl 0.51 CH3OH C(37.35) N(8.44) H(3.88); found: C(33.72), N(8.83), H(4.26). IR (KBr): $\nu(cm^{-1})$=2,109 (–C≡N–); 1,643 (–C=N–); 1,500–1,600 cm^{-1} (aromat. C=C, val.), 750–760 cm^{-1} (C–H, o. o. p.)

$[W^{IV}\{(CN)\ Fe^{III}(3\text{-}OH\text{-}^5L)\}_8]Cl_4$: Yield: 86% rel. to W (3,942.33 g/mol). Analysis calculated for $C_{160}H_{184}Cl_4Fe_8WN_{32}O_{32}$ (%): C(51.27), N(11.39), H(4.71); with 5.5 KCl C (45.22) N() H5.90; found: C(45.07), N(), H(5.92). IR (KBr): $\nu(cm^{-1})$=2,099 (–C≡N–); 1,649 (–C=N–); 1,500–1,600 cm^{-1} (aromat. C=C, val.), 750–760 cm^{-1} (C–H, o. o. p.)

$[W^{IV}\{(CN)\ Fe^{III}(4\text{-}OH\text{-}^5L)\}_8]Cl_4$: Yield: 45% rel. to W (3,942.33 g/mol). Analysis calculated for $C_{160}H_{184}Cl_4Fe_8WN_{32}O_{32}$ (%): C(51.27), N(11.39), H(4.71); with 11×KCl C (41,17) N(9,6) H(3.97); found: C(33.54), N(10.21), H(4.15). IR (KBr): $\nu(cm^{-1})$=2,105 (–C≡N–); 1,642 (–C=N–); 1,500–1,600 cm^{-1} (aromat. C=C, val.), 750–760 cm^{-1} (C–H, o. o. p.)

Table I Mössbauer parameters of the iron precursors

Iron precursors	δ (mm/s)	Δ (mm/s)	mol%
Mössbauer parameters 300 K	State 1		
3-OH-^{5}LFeCl	0.311	0.785	100
4-OH-^{5}LFeCl	0.258	0.645	100
Mössbauer parameters 20 K	State 1		
3-OH-^{5}LFeCl	0.389	0.833	100
4-OH-^{5}LFeCl	0.363	0.669	100

$[Ru^{II}\{(CN)\ Fe^{III}(3\text{-}OH\text{-}^5L)\}_6]Cl_2$: Yield: 82% rel. to Ru (2,808.48 g/mol). Analysis calculated for $C_{120}Cl_2RuH_{138}Fe_6N_{24}O_{24}$ (%): C(52.55), N(11.67), H(4.83); with 14 CH3OH 5.4 KCl C (43.99) N (9,19) H (5.34); found: C(43.70), N(10.07), H(6.21). IR (KBr): $\nu(cm^{-1})$=2,054 (–C≡N–), 1,648 (–C=N–), 1,500–1,600 cm^{-1} (aromat. C=C, val.), 750–760 cm^{-1} (C–H, o. o. p.)

$[Ru^{II}\{(CN)\ Fe^{III}(4\text{-}OH\text{-}^5L)\}_6]Cl_2$: Yield: 41% rel. to Ru (2,808.48 g/mol). Analysis calculated for $C_{120}Cl_2RuH_{138}Fe_6N_{24}O_{24}$ (%): C(52.55), N(11.67), H(4.83); with 7.3 KCl C (39.65) N(9.25) H(3.83); found: C(31.99), N(7.37), H(4.45). IR (KBr): $\nu(cm^{-1})$=2,046 (–C≡N–), 1,646 (–C=N–), 1,500–1,600 cm^{-1} (aromat. C=C, val.), 750–760 cm^{-1} (C–H, o. o. p.)

$[Co^{III}\{(CN)\ Fe^{III}(3\text{-}OH\text{-}^5L)\}_6]Cl_3$: Yield: 26% rel. to Co (2,802.79 g/mol). Analysis calculated for $C_{120}Cl_3CoH_{138}Fe_6N_{24}O_{24}$ (%): C(52.68), N(11.70), H(4.84); with 7.70 KCl C (42.71) N(9.96) H(4.12) ; found: C(39.19), N(7.24), H(5.40). IR (KBr): $\nu(cm^{-1})$=2,124 (–C≡N–), 1,648 (–C=N–), 1,500–1,600 cm^{-1} (aromat. C=C, val.), 750–760 cm^{-1} (C–H, o. o. p.)

$[Co^{III}\{(CN)\ Fe^{III}(4\text{-}OH\text{-}^5L)\}_6]Cl_3$: Yield: 39% rel. to Co (2,802.79 g/mol). Analysis calculated for $C_{120}Cl_3CoH_{138}Fe_6N_{24}O_{24}$ (%): C(52.68), N(11.70), H(4.84); with 10.8 KCl C (38.97) N(9.32) H(3,86); found: C(32.26), N(8.82), H(4.95). IR (KBr): $\nu(cm^{-1})$=2,126 (–C≡N–), 1647 (–C=N–), 1,500–1,600 cm^{-1} (aromat. C=C, val.), 750–760 cm^{-1} (C–H, o.o.p.)

2.4 Mössbauer spectroscopy

A conventional spectrometer has been used for measuring the Mössbauer spectra between liquid helium and room temperature (^{57}Co/Rh source, calibration at α-Fe at room temperature; isomer shifts are relative to the source).

3 Results and discussion

Figure 2 and Table I show the temperature-dependent Mössbauer data and spectra of the [Fe (3-OH-^{5}L)Cl] and the [Fe(4-OH-^{5}L)Cl] precursor compounds. At 300 K the Mössbauer spectra exhibit a quadrupole doublet which is common for Fe(III) in the HS state (S=5/2) [1, 2]. In opposite to 3-OH the 4-OH compound is symmetric. At 20 K the same quadrupole doublet as at room temperature is observed.

The prepared hepta- and nonanuclear complexes has been characterized by IR spectrum and M+ peaks in ESI mass spectroscopy. No evidence for a splitting of the characteristic C–N stretching vibration band indicates a highly symmetric coordination sphere around the central Co(III), Ru(II), W(IV), and Mo(IV) atom, i.e. either all eight or none of the cyanides are bridged. The shift of the CN-band for all compounds indicates a bridged coordination.

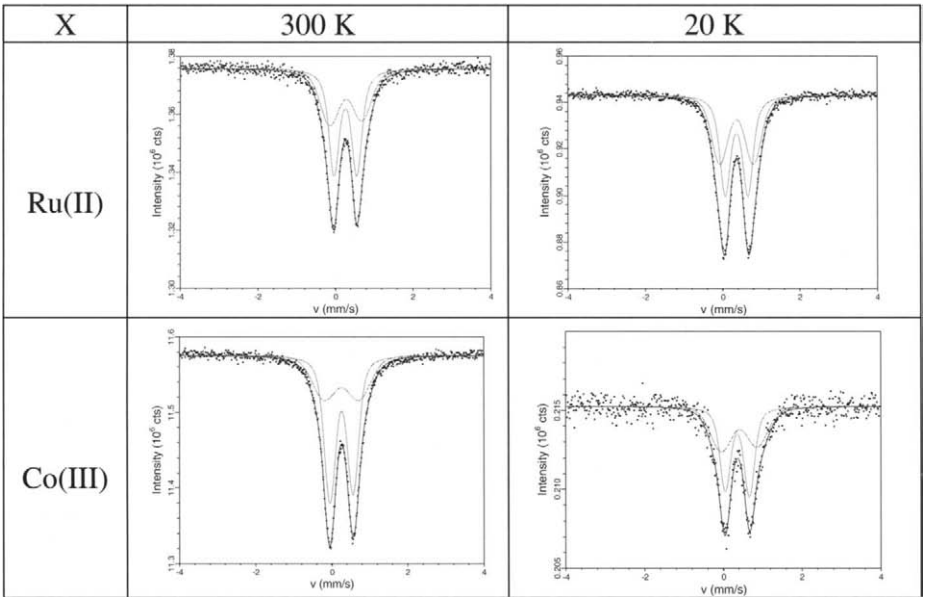

Figure 3 Mössbauer spectra of the *star-shaped* heptanuclear compounds $[Ru^{II}\{(CN)\ Fe^{III}(4\text{-}OH\text{-}^5L)\}_6]^{2+}$ and $[Co^{III}\{(CN)\ Fe^{III}(4\text{-}OH\text{-}^5L)\}_6]^{3+}$ at 300 and 20 K.

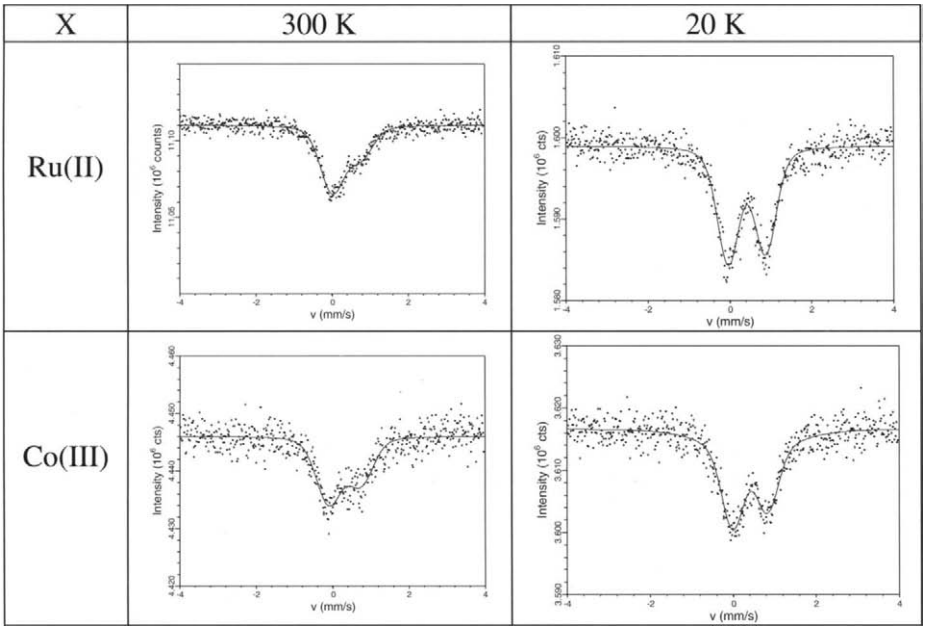

Figure 4 Mössbauer spectra of the *star-shaped* heptanuclear compounds $[Ru^{II}\{(CN)\ Fe^{III}(3\text{-}OH\text{-}^5L)\}_6]^{2+}$ and $[Co^{III}\{(CN)\ Fe^{III}(3\text{-}OH\text{-}^5L)\}_6]^{3+}$ at 300 and 20 K.

Table II Mössbauer parameters of the hepta- and nonanuclear compounds at 300 K

Mößbauer parameters 300 K	State 1			State 2		
Complex	δ (mm/s)	Δ (mm/s)	mol%	δ (mm/s)	Δ (mm/s)	mol%
$[(3\text{-Hydroxy-}^5\text{3,3-LFeNC})_8\text{Mo}]^{4+}$	0.344	0.804	100	–	–	–
$[(3\text{-Hydroxy-}^5\text{3,3-LFeNC})_6\text{Co}]^{3+}$	0.322	0.837	100	–	–	–
$[(3\text{-Hydroxy-}^5\text{3,3-LFeNC})_8\text{Mo}]^{4+}$	0.339	0.816	100	–	–	–
$[(3\text{-Hydroxy-}^5\text{3,3-LFeNC})_6\text{Ru}]^{2+}$	0.381	0.751	100	–	–	–
$[(4\text{-Hydroxy-}^5\text{3,3-LFeNC})_8\text{W}]^{4+}$	0.257	0.620	75.1	0.290	1.100	24.9
$[(4\text{-Hydroxy-}^5\text{3,3-LFeNC})_6\text{Co}]^{3+}$	0.257	0.611	63.3	0.260	0.905	36.7
$[(4\text{-Hydroxy-}^5\text{3,3-LFeNC})_8\text{Mo}]^{4+}$	0.261	0.604	100	–	–	–
$[(4\text{-Hydroxy-}^5\text{3,3-LFeNC})_6\text{Ru}]^{2+}$	0.256	0.589	54.5	0.266	0.829	45.5

Table III Mössbauer parameters of the hepta-and nonanuclear compounds at 20 K

Mößbauer parameters 20 K	State 1			State 2		
Complex	δ (mm/s)	Δ (mm/s)	mol%	δ (mm/s)	Δ (mm/s)	mol%
$[(3\text{-Hydroxy-}^5\text{3,3-LFeNC})_8\text{W}]^{4+}$	0.408	0.840	91,7	0,354	1,950	8,3
$[(3\text{-Hydroxy-}^5\text{3,3-LFeNC})_6\text{Co}]^{3+}$	0.408	0.842	100	–	–	–
$[(3\text{-Hydroxy-}^5\text{3,3-LFeNC})_8\text{Mo}]^{4+}$	0.421	0.916	100	–	–	–
$[(3\text{-Hydroxy-}^5\text{3,3-LFeNC})_6\text{Ru}]^{2+}$	0.415	0.911	100	–	–	–
$[(4\text{-Hydroxy-}^5\text{3,3-LFeNC})_8\text{W}]^{4+}$	0.364	0.651	74.0	0.399	1.160	26.0
$[(4\text{-Hydroxy-}^5\text{3,3-LFeNC})_6\text{Co}]^{3+}$	0.357	0.613	53.0	0.405	0.910	47.0
$[(4\text{-Hydroxy-}^5\text{3,3-LFeNC})_8\text{Mo}]^{4+}$	0.360	0.624	73.0	0.367	1.100	27.0
$[(4\text{-Hydroxy-}^5\text{3,3-LFeNC})_6\text{Ru}]^{2+}$	0.361	0.588	50.6	0.363	0.868	49.4

Figures 3, and 4 and Tables II, and III show the Mössbauer spectra of the hepta- and nonanuclear compounds. At 300 K a quadrupole doublet is detected, which is common for Fe(III) in the HS state (S=5/2) [1, 2].

In comparison to the precursors the isomer shifts are moved upwards by 0.01–0.07 mm/s upon coordination to the 3-OH compounds. For the 4-OH compounds there is only a faint deviation between −0.01 and 0.03 mm/s. The quadrupole splitting of the 3-OH compounds is moved upwards by about 0.02–0.05 mm/s for the Mo(IV), W(IV), and Co(III), respectively, while the quadrupole splitting of the Ru(II) compound moves downwards. The quadrupole splittings of the 4-OH compounds are all shifted downwards by 0.02–0.06 mm/s.

In addition a second doublet occurs for the 4-OH compounds, except for Mo(IV), which is characteristic for an Fe(III) in the high-spin state.

At 20 K the Mössbauer spectra show in addition to the Fe(III) in the HS state a second doublet appearing which is characteristic of Fe(III) in high-spin state [1–3], but with slightly wider quadrupole splitting. Only the W(IV)-3-OH compound deviates with an exceptional large quadrupole splitting.

This may be attributed to a structural change close to the coordination sphere. The isomer shifts for the 3-OH compounds little alter from 0.02 to +0.03 mm/s, while the 4-OH compounds remain almost constant with 0.001 to −0.006 mm/s.

The quadrupole splitting for 3-OH exhibits a jump between 0.007 and 0.009 mm/s for W (IV) and Co(III), to 0.083 mm/s for Mo(IV) and 0.07 mm/s for Ru(II). The same is true for Ru(II)-4-OH with 0.081 mm/s, Co(III) with 0.056 mm/s, Mo(IV) with 0.045 mm/s, and W (IV) with 0.018 mm/s.

The temperature dependence of the area fraction of the respective doublets A(Fe^{III}-S1):A (Fe^{III}-S2) indicates that several Fe(III) centers in the hepta- and nonanuclear complexes perform a thermally induced electronic switching between HS and HS states, e.g., multistability. For the 3-OH only the W(IV) may switch with about 8.3% between 300 and 20 K. The 4-OH, however, show 1.1% for W(IV), 3.9% for Ru(II), 10.3% for Co(III) and 27% for Mo(IV).

4 Conclusion

In conclusion, the 3-OH and 4-OH substitutions in the salicylic aldehyde do not favour thermally induced HS to LS transition in the Fe(III) units. There is however a HS to HS transition and a significant stronger bonding in the 4-OH octahedron.

Acknowledgements This work was partly funded by the University of Mainz ("Forschungsfond"; MWFZ) and the "Deutsche Forschungsgemeinschaft" (DFG: Re-1627/1-3).

References

1. Renz, F., Kerep, P.: Polyhedron **24**, 2849–2851 (2005)
2. Renz, F., Kerep, P.: Hyperfine Interact. **156**, 371–377 (2004)
3. Herchel, R., Boèa, R., Gembicky, M., Koisek, J., Renz, F.: Inorg. Chem. **43**, 4103–4105 (2004)

Hyperfine Interact (2006) 168:1009–1015
DOI 10.1007/s10751-006-9387-1

Determination of the chromium concentration of phase decomposition products in an aged duplex stainless steel

Hisashi Kuwano · Hisanao Imamasu

Published online: 7 December 2006

Abstract A commercial duplex stainless steel has been aged at 673 K for up to 55,000 h. The aging results in the phase decomposition of the ferrite in duplex stainless steel. The end products of the phase decomposition are a Fe-rich and a Cr-rich phase. The chromium concentration of these phases is determined by measuring the hyperfine magnetic field and the isomer shift using Mössbauer effect. The experimental results are compared with a phase diagram calculated for Fe–Cr–Ni ternary system at 673 K.

Key words spinodal decomposition · Fe-rich phase · Cr-rich phase · PWR · isomer shift · hyperfine magnetic field

1 Introduction

Duplex stainless steels are important materials used for the primary coolant water piping systems in the nuclear power plant. The metallurgical structure of the stainless steel is composed of a paramagnetic austenite and a ferromagnetic ferrite phase. The Cr content in the ferrite is about 25 mass%. Because of the high Cr content, the ferrite finally decomposes into an Fe-rich phase and a Cr-rich phase by spinodal decomposition, when aged around 593 K which is the typical operation temperature of the pressurized water reactor (PWR). Various properties such as anti-corrosion, ductility and toughness are degraded due to the phase decomposition. It is necessary to know the compositions of the phase decomposition products for a better understanding of the degradation mechanism. Mössbauer spectroscopy is one of the useful techniques to determine the Cr concentration. However, as the Cr-rich phase and the austenite are paramagnetic at room temperature, the detection of the paramagnetic peak due to the Cr-rich phase becomes difficult by the interference of the austenite phase, unless the volume fraction of the Cr-rich phase is large enough. Moreover, in order to determine the Cr content of the Fe-rich phase, a very long term aging is required to attain the completion of the phase decomposition. For these reasons, the Cr concentration

H. Kuwano (✉) · H. Imamasu
Muroran Institute of Technology, 27-1 Mizumoto, Muroran, Hokkaido 050-8585, Japan
e-mail: kuwano@mmm.muroran-it.ac.jp

Table I Chemical compositions of CF3M grade duplex stainless steel (mass%)

	Cr	Ni	Mo	Mn	Si	C
Bulk	19.9	9.98	2.42	0.69	1.2	0.018
Ferrite	24.0	5.48	3.73	0.47	1.24	–
Austenite	19.4	9.11	2.47	0.55	1.09	–

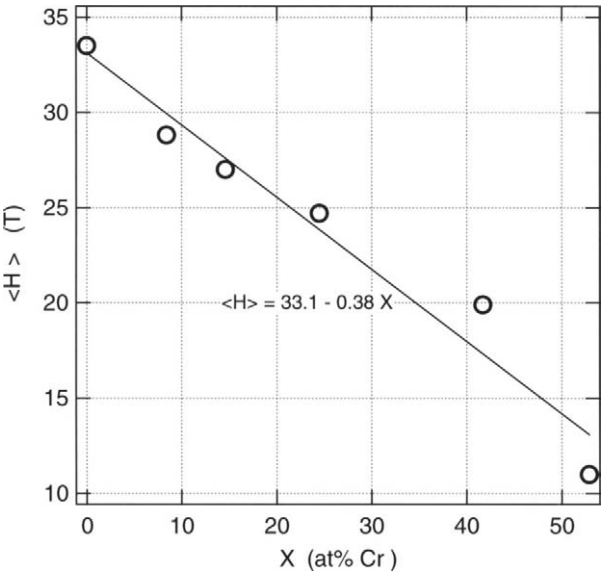

Figure 1 Average hyperfine magnetic field of ^{57}Fe as a function of Cr concentration in Fe–Cr–Ni–Mo alloys.

of the two phases has been left unknown at the low temperatures. In the present experiment, a duplex stainless steel has been aged for long times to complete the phase decomposition. The present study aims to determine the Cr concentrations of the Cr-rich phase and the Fe-rich phase by Mössbauer spectroscopy.

2 Experimental

A duplex stainless steel of CF3M grade, which contains 25% of ferrite in the austenite matrix, is melted followed by casting. Bulk chemical compositions of the duplex stainless steel are chemically analyzed as presented in Table I. Chemical compositions of the ferrite phase analyzed by energy dispersion spectroscopy are also listed in Table I together with the austenite phase. The ferrite composition is characterized by 24 mass% Cr, 5.5 mass% Ni and 3.7 mass% Mo. Mössbauer measurements have been carried out on thin foil of 30 μm in thickness using a ^{57}Co(Rh) source at room temperature. The Doppler velocity is changed from −10 to 10 mm/s and −1.8 to 2 mm/s for the measurements of the hyperfine magnetic field and the isomer shift, respectively. Hyperfine magnetic field distributions (hereafter called P(H) curve) are calculated in the hyperfine magnetic field range from 0 to 40 T using

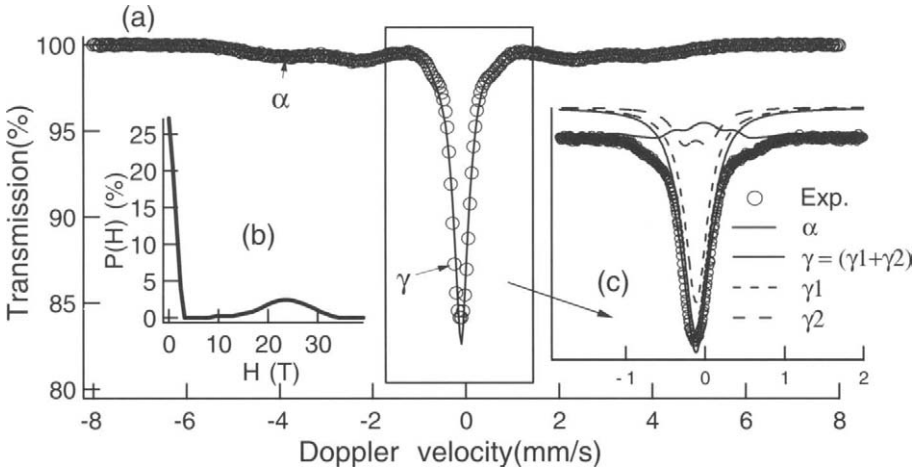

Figure 2 Room temperature Mossbauer spectrum (a), P(H) curve (b) and paramagnetic peak (c) for the unaged duplex stainless steel.

a program made by Le Caer and Dubois [1]. Phase diagrams for a Fe–Cr–Ni ternary system have been calculated by Chung and Chang [2]. The binodal lines for the ferrite phase at 673 K are calculated by us using the program and thermodynamic parameters reported in the reference [2].

3 Results and discussion

3.1 Cr concentration of the iron-rich phase

(1) Relation between hyperfine magnetic field and chromium concentration in Fe–Cr–Ni–Mo alloys.
In order to examine a relationship between the average hyperfine magnetic field <*H*> of ^{57}Fe and the Cr content x in Fe–Cr–Ni–Mo alloys, x is varied from x=0 to 49 mass % Cr (53 at.% Cr), whereas the Ni and the Mo content are adjusted to 5.4±0.6 mass% Ni and 3.1±1.2 mass% Mo, respectively. As shown in Figure 1, <*H*> decreases linearly with increasing x as expressed by an empirical relationship,

$$\langle H \rangle = 33.1 - 0.38x. \quad (1)$$

The equation allows us to estimate the Cr content in the ferrite by the measurement of <*H*>.

(2) Phase decomposition in duplex stainless steel.

The Mössbauer spectrum of the unaged duplex stainless steel is characterized by the superposition of a paramagnetic peak and a ferromagnetic spectrum as shown in Figure 2a. The former is associated with Fe atoms in the austenite phase (γ) which is paramagnetic, and the latter with Fe atoms in the ferrite (α) which is ferromagnetic at room temperature. The corresponding P(H) curve shown in Figure 2b is characterized by the two peaks

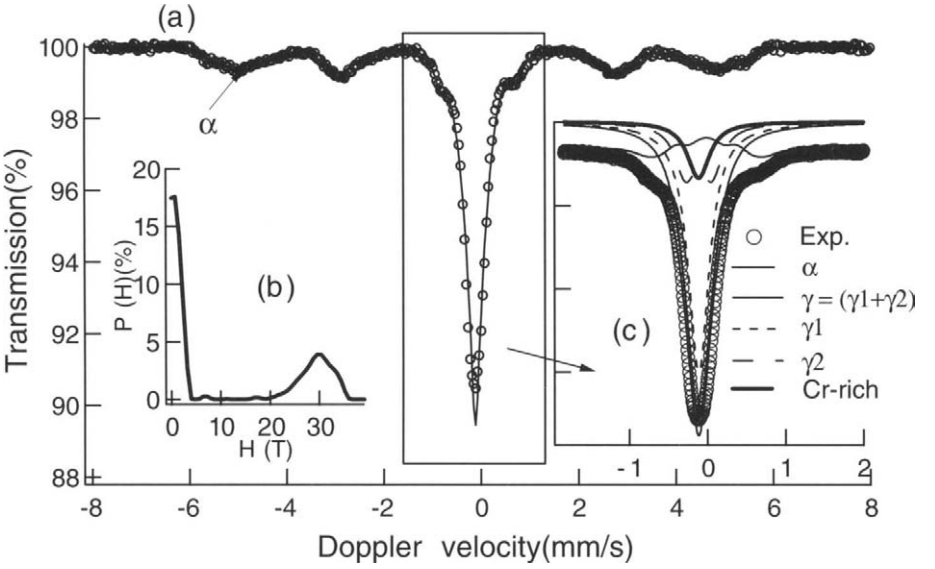

Figure 3 Room temperature Mossbauer spectrum (a), P(H) curve (b) and paramagnetic peak (c) for the duplex stainless steel aged at 673 K for 55000 h.

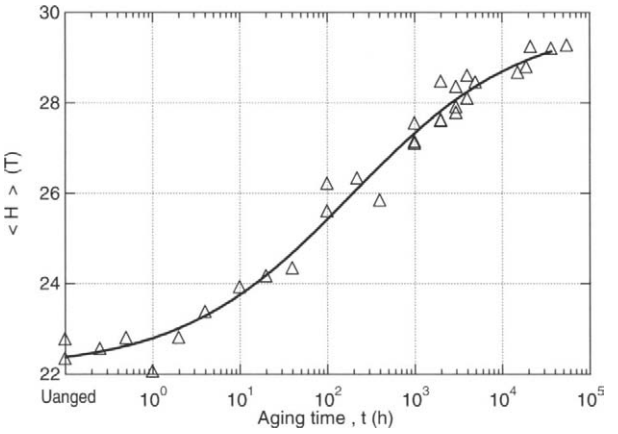

Figure 4 Variation of the average hyperfine magnetic field of ferrite in a duplex stainless steel as a function of aging time at 673 K.

existing in H<5 T and 5 T<H<40 T, which are concerned with the austenite and the ferrite phase, respectively. The P(H) curve for the ferrite(α) makes a maximum at H=23.5 T.

The Mössbauer spectrum after the aging at 673 K for 55,000 h is presented in Figure 3a. The distance between the two outermost peaks of the ferromagnetic spectrum is larger than that of the unaged steel spectrum, and the peak position of P(H) curve for the ferrite shifts to H=30 T after the aging. These results indicate that the aging results in the increase in <H> for the ferrite.

A variation of <H> with aging time is given in Figure 4, showing a gradual increase in <H> with increasing aging time. The increase in <H> corresponds to the decrease in the Cr concentration in Eq. 1. So, the aging results in the decrease in the Cr content of the ferrite.

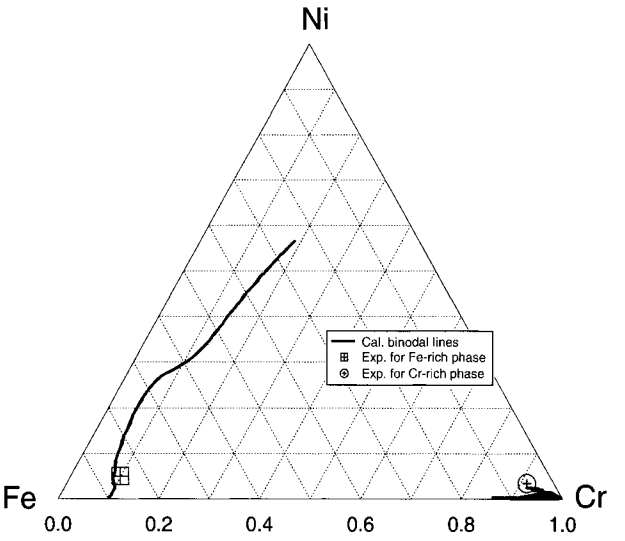

Figure 5 Calculated Fe–Cr–Ni phase diagram showing binodal lines for the ferrite phase at 673 K.

The ferrite depleted with Cr atom is usually called as the Fe-rich phase. Since there is very little change of $\langle H \rangle$ between 20,000 and 55,000 h of the aging time, it is interpreted that the phase decomposition has been almost completed at the aging time of 20,000 h. The maximum value of $\langle H \rangle$ is 29.3 T at 55,000 h. Inserting the value into Eq. 1, x is obtained as 10 at.% Cr which is the Cr concentration of the Fe-rich phase.

According to a phase diagram calculation [2], there is a miscibility gap of the ferrite in the Fe–Cr binary and Fe–Cr–Ni ternary system at low temperatures. We have calculated the phase diagram using a program and thermodynamic parameters reported in the reference [2]. One of the examples of the calculated results for the binodal lines at 673 K is shown in Figure 5. One of the binodal lines locate near a 10 at.% Cr line in the iron rich side, and the other lies along the Fe–Cr basal axis in the chromium rich side. Supposing that very small change in the Ni concentration is accompanied by the aging, the above measured chromium concentration is plotted in Figure 5, indicating that the experimental result is consistent with the calculated result in the iron-rich side.

3.2 Cr concentration of the chromium-rich phase

As for the paramagnetic peak, its peak position shifts to the negative Doppler velocity accompanied by the broadening of the peak width after the 673 K aging. It was unable to fit the paramagnetic peak after the aging by two components of $\gamma 1$ and $\gamma 2$ appearing in the spectrum of the unaged steel. There is little possibility that the austenite phase undergoes the phase transformation at 673 K. So if we assume that there is no change in the parameters for $\gamma 1$ and $\gamma 2$ before and after the aging, there is a high possibility that the third paramagnetic peak coexists with the two original paramagnetic peaks as shown in Figure 3c. The isomer shift of the newly appeared paramagnetic peak is $-0.127(\pm 0.007)$ mm/s. The isomer shift is ascribed to the Cr-rich phase which is one of the final phases of the phase decomposition of the ferrite, because the isomer shift is comparable with a value

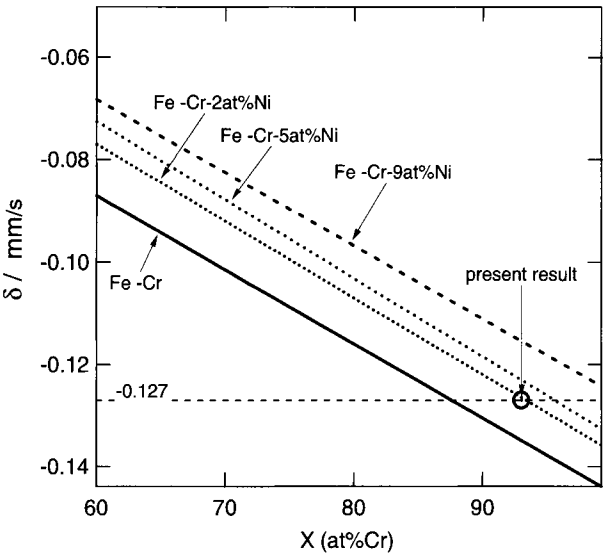

Figure 6 Isomer shift of ^{57}Fe as a function of Cr and Ni content in Fe–Cr–Ni alloys.

of −0.122 mm/s for an Fe–80Cr–3Mo–5Ni alloy [3] rather than −0.09 mm/s for the austenite phases [3].

Empirical relationships between the isomer shift and the Cr content in bcc Fe–Cr and bcc Fe–Cr–Ni alloys have been reported elsewhere [4], and reproduced in Figure 6. The isomer shift of ^{57}Fe decreases linearly with increasing Cr concentration with a slope of −0.0016 mm/s/at.% Cr. On the other hand, the addition of Ni to Fe–Cr alloys increases the isomer shift of Fe by 0.002 mm/s /at.% Ni. The result is nearly equivalent with a value of 0.0023 mm/s measured by Vincze and Campbell [6]. According to Figure 6, the isomer shift of −0.127 mm/s corresponds to 87 to 100 at.% Cr depending on the Ni content. In order to determine the Cr concentration of the Cr-rich phase, it is necessary to estimate the Ni content.

Ishikawa and Yoshimura [5] have investigated distributions of Cr, Ni, Mo in the ferrite in the CF3M duplex stainless steel aged at 723 K for 10,000 h by position sensitive atom probe (POSAP). The Cr-rich phase was detected as the regions where the Cr concentration is more than 50 at.% Cr, whereas the Fe-rich phase as the regions less than 12 at.% Cr. Though the Cr content in the Cr-rich phase has not been determined precisely by POSAP, detailed information has been obtained for the distributions of Ni, Mo and Si. Mössbauer effect is not effective to measure these elements. Mössbauer effect and POSAP seems to be complementary each other. According to the POSAP study, Mo and Si are excluded either from the Cr-rich regions or the Fe-rich regions to be concentrated somewhere. As the result, the Mo content in the Cr-rich regions is depleted less than 1 at.%. Though the addition of Mo to pure iron decreases the isomer shift of ^{57}Fe by −0.001 mm/s/at.% Mo [6], its contribution to the isomer shift of the Cr-rich phase is so small that can be negligible in the present case. The POSAP study has also revealed that Ni atoms have a tendency to be depleted from the Cr-rich regions. The Ni concentration in the Cr-rich region is about 2 at. % Ni, or less. If we adopt the result, the isomer shift of −0.127 mm/s corresponds to the Cr content of 93 (±5) at.% Cr. The present result is roughly consistent with the calculated result of the binodal line in the chromium-rich side of the ternary phase diagram shown in Figure 5.

4 Conclusion

The ferrite in a duplex stainless steel decomposes into a ferromagnetic phase and a paramagnetic phase by aging at 673 K. The ferromagnetic phase has a mean hyperfine magnetic field of 29.3 T after 55,000 h aging time. The mean hyperfine magnetic field corresponds to the Cr concentration of 10 at.% Cr. The isomer shift for the paramagnetic phase is −0.127 mm/s. The Cr concentration of the paramagnetic phase is estimated about 93 at.% Cr, supposing that its Ni content is 2 at.%.

References

1. Le Caer, G., Dubois, J.M.: J. Phys. E. **12**, 1083 (1979)
2. Chung, Y.-Y., Chang, Y.A.: Metall. Trans. **18A**, 733 (1987)
3. Solomon, H.D., Levinson, L.M.: Acta Metall. **26**, 429 (1978)
4. Ito, K., Kuwano, H., Yoshimura, T., Ishikawa, Y.: J. Japan. Inst. Metals(in Japanese) **58**, 1113 (1994)
5. Ishikawa, Y., Yoshimura, T.: Mater. Trans., JIM **35**, 895 (1994)
6. Vincze, I., Campbell, I.A.: J. Phys. F. Met. Phys. **3**, 647 (1973)

Hyperfine Interact (2006) 168:1017–1022
DOI 10.1007/s10751-006-9400-8

Mössbauer spectroscopy study of mechanically alloyed Fe_2O_3–(Al, Co and WC) systems

Antoine F. Mulaba-Bafubiandi

Published online: 14 December 2006

Abstract Mössbauer spectroscopy revealed that a central hyperfine interaction doublet and an additional sextet characterized the appearance of new phases in the mechanically alloyed Fe_2O_3–Al and Fe_2O_3–Co systems. In the Fe_2O_3–Al system, the intensity of the central super paramagnetic doublet which represents small particles of iron, increased with increasing milling time from 5 to 30 h of mechanical alloying. The magnetic sextet characterizing hematite vanished in the room temperature Mössbauer spectra of samples produced after 25 h of mechanically alloying the 50% Fe_2O_3 and 50% Al system. In general XRD peak broadening was observed as a result of extensive material structural distortion and formation of small particles. Fe, Al_2O_3 and mixed iron–aluminium oxide phases were identified in the XRD patterns with a small persistence of the iron oxide up to 20 h of mechanically alloying the 1:1 system Al–Fe_2O_3. In the 50% Co–50% Fe_2O_3 system, a 55% abundant new phase $CoFe_2O_4$ was observed, from the Mössbauer spectra of the system. The presence of this new phase was confirmed by the XRD analysis. The high energy ball milling of WC–Fe_2O_3 revealed a more effective grinding compared to hematite alone. The hematite particles were reduced to nanosized particles.

Key words Mössbauer spectroscopy · hematite ore · cobalt · WC · aluminum · mechanical alloying

1 Introduction

Mechanical alloying was originally used as a novel manufacturing technique. It was subsequently tried in minerals processing and extraction of metals [1]. Work relating to hematite ore or fines discards have been reported in the literature. Several authors [2] managed to mechano-thermally extract metals from their ores using this technique e.g. iron

A. F. Mulaba-Bafubiandi (✉)
Extraction Metallurgy Department, Faculty of Engineering and the Built Environment, University of Johannesburg, P.O. Box 526, Wits 2050, South Africa
e-mail: Mulaba@twr.ac.za

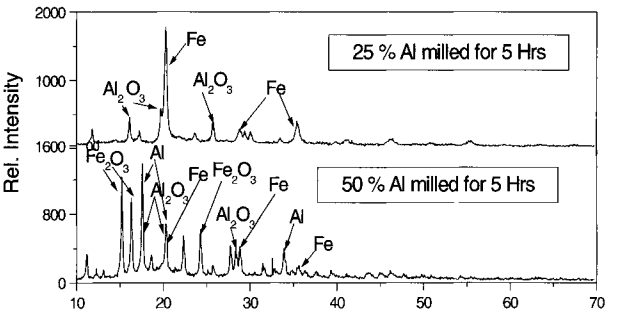

Figure 1 XRD patterns comparing the effect of milling time on phase transformation of a mixture of 75% hematite and 25% aluminium and 50% hematite and 50% aluminium mechanically alloyed for 5 h.

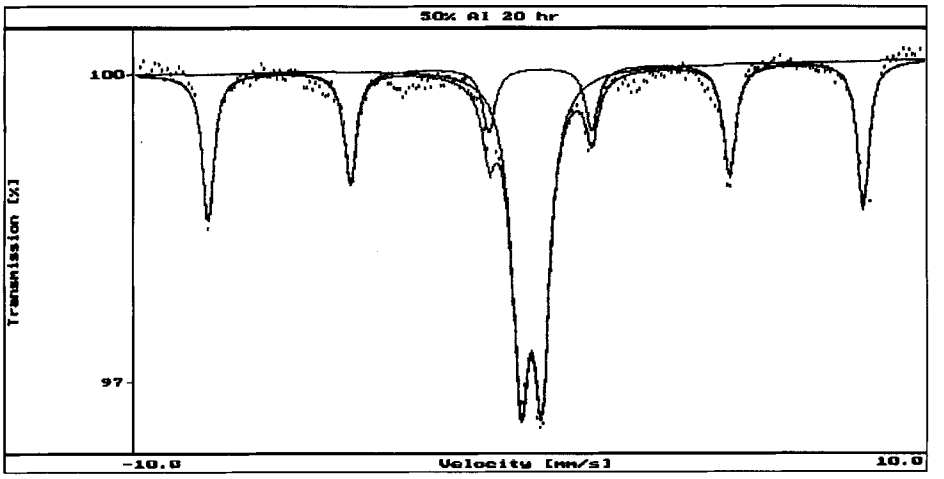

Figure 2 The Mössbauer spectrum showing the effect of milling time on phase transformation of a mixture of 50 wt% hematite and 50 wt% aluminum mechanically alloyed for 20 h.

was produced from hematite using aluminium as a reducing agent while others [3] demonstrated that the ball milling of hematite ore and WC–Co lead to the formation of intermetallics and mixed oxides. The present paper is a follow up on the above mentioned pieces of work.

2 Materials and methods

A run off mine (ROM) hematite ore crushed in the laboratory was subsequently high energy ball milled with 50 wt% aluminium and 50 wt% cobalt i.e. in a ratio of 1:1 for up to 30 h. A subsequent milling of a 20% WC–80% Fe_2O_3 was conducted. A planetary ball mill (PM400/2) containing 50 balls of average weight 7 g each i.e. a ball to powder ratio of 10:1 was used without inert atmosphere i.e. argon nor nitrogen. The effect of milling time on the products formed was monitored. During a total milling time of 30 h, samples were collected at 5 h intervals. The collected sample was characterized with transmission Mössbauer spectroscopy (MS) at room temperature and major observations were confirmed with XRD

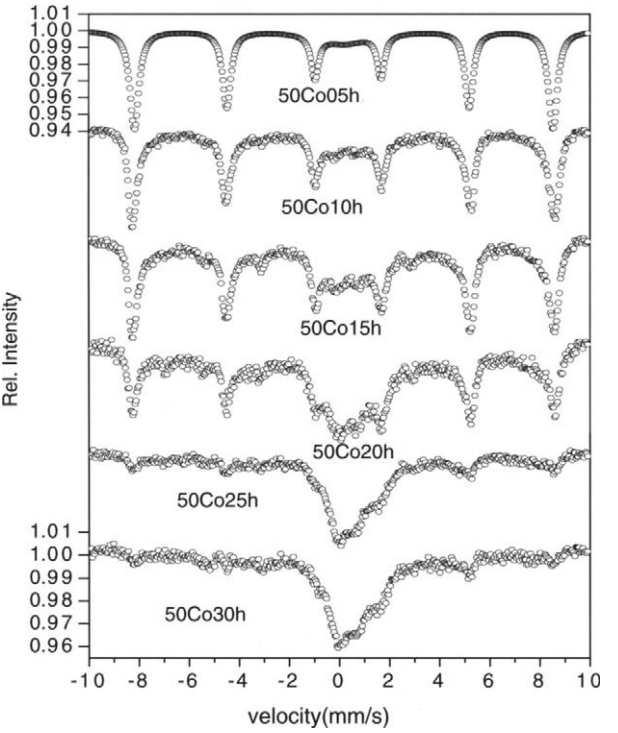

Figure 3 MS spectra of 50% Co+50% hematite ore milled at different times.

(CuKα). MS experiments were carried out with about 20 mg/cm^2 of sample and a Co (Rh) source. The hyperfine parameters are reported with respect to α-Fe.

3 Results and discussion

When milling hematite ore with aluminium, a sextet of hematite (Fe_2O_3) and a central paramagnetic doublet of iron (Fe) are observed in the Mössbauer spectrum of a mixture milled for 5 h. The sextet corresponding to a magnetically ordered iron is not observed in the MS spectra because iron present in the sample is already fine and forms nanoparticles as the system is being ball milled. The value of the measured magnetic field decreases as particles' size decreases with milling time. The intensity of the central doublets increases after 10 h and continues to do so up to 30 h as the fraction of the produced nanoparticles of iron increases in the sample. The sextet corresponding to a magnetically ordered iron continues to decrease in samples mechanically alloyed for durations between 10 and 20 h. This sextet disappears completely after 25 h where all the hematite present in the system has been reduced into iron, while aluminium has been oxidized into aluminium oxide. Hematite and aluminium systems mechanically alloyed for more than 25 h displayed only a central paramagnetic doublet characteristic of the presence of nanoparticles. This observation confirms the results obtained from the XRD analysis presented in Figure 1 showing that milling, only for 5 h, aluminium and hematite system, where aluminium content has been increased from 25% to 50%, still leaves un-reacted some of the hematite

Table I Mössbauer hyperfine interaction parameters of a mixture of 50% Co+50% hematite mechanically alloyed for various times

Milling time (h)	Hyperfine interaction parameters				
	$\delta/_{Fe}$ (mm/s)	Δ (mm/s)	Bhf (T)	Γ (mm/s)	RA (%)
5	0.38	−0.17	51.76	0.38	100
10	0.38	−0.18	52.20	0.36	46
	0.41	−0.21	49.31	1.18[a]	27
	0.59	1.66	–	2.50[a]	27
15	0.38	−0.19	52.08	0.39	34
	0.37	−0.52	47.67	1.68[a]	38
	0.05	−0.11	33.22	0.43	7
	0.41	0.69	–	0.60[a]	5
	0.74	2.14	–	1.56[a]	16
20	0.39	−0.19	52.13	Fixed	22
	0.49	−0.17	45.58	1.82[a]	26
	0.06	−0.13	32.60	1.40[a]	30
	0.40	0.82	–	0.73[a]	7
	0.97	1.59	–	1.09[a]	16
25	0.36	−0.17	52.02	0.35	8
	0.47	−0.30	46.68	2.28[a]	36
	0.37	0.75	–	1.02[a]	36
	0.89	1.64	–	1.07[a]	20
30	−0.05	0.71	51.59	Fixed	7
	0.69	−0.23	45.81	1.98[a]	55
	0.41	0.77	–	0.67[a]	19
	0.91	1.24	–	0.87[a]	19

$\delta/_{Fe}$ Isomeric shift (with respect to α-Fe); Δ quadrupole splitting; Γ full width at half maximum; *RA* relative absorbance

[a] Too wide a doublet

and some of the aluminium although a production of Fe and Al_2O_3 would be noticed. It was noticed that aluminium will completely reduce hematite to iron after 25 h of mechanical alloying in the 50% Fe_2O_3 and 50 % Al composition. Figure 2 shows that a milling of the above system for a period of 20 h still leaves about 15% of residual hematite and produces about 85% of super paramagnetic doublet attributed to nano particles of iron.

All hematite contained in the stoichiometric composition has been reduced to iron in the first 5 h of mechanical alloying. In the 1:1 ratios, an excess of hematite was observed still present in the products after 5 h (and even after 20 h) of mechanical alloying. It was observed that the relative abundance of Fe and Fe_2O_3 phases in the mechanically alloyed mixture of 50% Fe_2O_3 and 50% Al_2O_3 went from 87% hematite and 13% doublet, after 5 h milling to 0% hematite sextet to 100% superparamagnetic doublet after 25 h milling.

MS spectra of mechanically alloyed 50% Co+50% hematite are presented in Figure 3. The corresponding hyperfine interaction parameters are summarized in Table I. When milling 80 wt% hematite + 20 wt% Co systems, a new phase was observed in samples produced after milling for 5 h. The new phase was characterized by a doublet with hyperfine interaction parameters of Δ=1.850 mm/s and δ=0.710 mm/s [3] while in the 50 wt% hematite and 50 wt% Co sample the new phase, also a doublet, (δ=0.592 mm/s, Δ =1.667 mm/s) started to appear after 10 h. This indicated the occurrence of a possible phase transformation in the material. A second sextet appeared after 10 h of milling in both

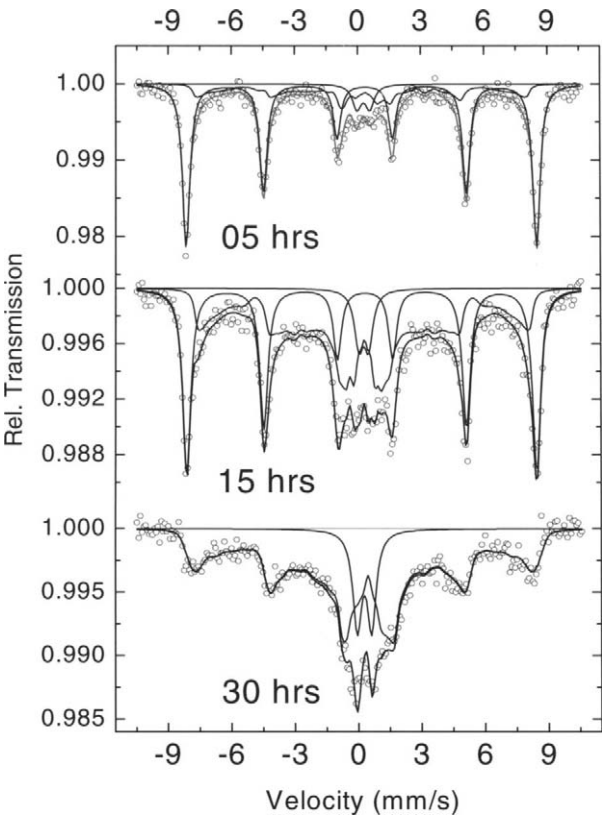

Figure 4 Mössbauer spectra of mechanically alloyed 50% WC+ 50% α-Fe_2O_3 milled for different times.

samples (Figure 3). This sextet would be attributed to the presence of an additional iron bearing new phase. This phase has approximately the same hyperfine magnetic field in both samples ranging between 45 and 49 T. It is lower than that of hematite (51 T) and higher than that of α-Iron (33 T). The observed slightly higher value (~52 T) of the hyperfine magnetic field (Bhf) of hematite would be caused by the contamination of hematite with cobalt and new-formed phases. Possible new phases would include the following: $CoFe_2O_4$, Co_2FeO_4 and $Co_{2.5}Fe_{0.5}O_4$. The $Co_{2.5}Fe_{0.5}O_4$ was reported to be nonmagnetic while $CoFe_2O_4$ and Co_2FeO_4 were magnetic [3]. Although no hyperfine interaction parameter values were reported for these compounds, their MS spectra resemble those observed in this study.

When milling WC and hematite systems, the MS spectra of samples produced could be fitted with a distribution of magnetic fields and paramagnetic doublets (Figure 4). The sextet component is considered to be bulk crystalline hematite largely unaffected by the milling. The component modelled as a distribution of magnetic fields, taken in conjunction with the XRD results, is considered to be hematite with a distribution of particle sizes down to the ~10 nm range. The central doublet is then considered to represent the smaller (superparamagnetic) particles each bigger than ~10 nm. The observed distribution of magnetic fields and/or doublet could also be attributed to amorphous iron–oxide phases which are not visible in the XRD patterns. Such amorphous phases will also tend to exhibit collapsed internal magnetic fields. At milling times of 15 h and more, the Mössbauer

spectra of the WC–hematite mixtures tend to show more resonance intensity in the central region than the hematite-only spectra. This suggests that more effective milling occurs in the WC–hematite mixtures, the WC likely acting as an effective abrading or grinding agent. There is evidence of bulk crystalline hematite (largely unaffected by milling) up to 15 h of milling, but at 30 h such a crystalline component cannot be superimposed on the spectrum. This suggests that all of the hematite has been reduced in size from original bulk dimensions, and that an appreciable volume fraction is in the 10–30 nm and near to super paramagnetic size range.

4 Conclusions

Mechanical alloying of a mixture of hematite and aluminium resulted in the formation of new phases. It is possible to reduce iron oxide to iron by aluminium using mechanical alloying. It is advised to adhere to the stoichiometric ratio when reducing hematite by aluminum using mechanical alloying as the aimed results are obtained in a short time compared to the 50:50 ratios. Iron peaks dominated the spectra in the last 25 and 30 h. The peaks for other phases were very small, almost invisible in the last 25 and 30 h of milling. The presence of iron-bearing phases was confirmed by Mössbauer spectroscopy. Emerging new phases are characterized by a central hyperfine interaction doublet and an additional sextet. The Mössbauer results confirms that hematite is completely reduced to iron after 25 h of mechanical alloying in the 50% Fe_2O_3 and 50% Al composition. The doublet which represent small particles of iron increases from 5 to 30 h of mechanical alloying. Hematite sextet decreases from 5 h and diminishes after 25 h. In the milling of individual powders WC, Co and hematite no phase transformation occurred due to mechanical alloying as revealed by both XRD and MS. High energy ball milling of WC–hematite mixture resulted in reduction of particle size to less than 10 nm for the same duration of time as the individual powders. No new phases were observed due to mechanical alloying. Mechanical alloying of a mixture of α-Fe_2O_3 and Co was found to yield $CoFe_2O_4$ with a crystallite sizeof less than 4 nm. High energy ball milling of α-Fe_2O_3 alone also resulted only in the formation of nanosize crystallites of hematite. The formation of $CoFe_2O_4$ means that the cobalt, which holds the WC grains together, will be depleted from the matrix leaving the drill bit susceptible to mass loss and brittle fracture. As the binder material is lost to the cobalt ferrite phase the drill bit loses its toughness and strength.

References

1. Takacs, L.: Mater. Lett. **13**, 119 (1992)
2. Waanders, F.B., Mulaba-Bafubiandi, A.F.: AIP Conf. Proc. **765**(1), 362 (2005)
3. Banganayi, C., Mulaba-Bafubiandi, A.F., Luyckx, S.: Int. J. Refract. Met. Hard Mater. **24**, 177 (2006)

Hyperfine Interact (2006) 168:1023–1027
DOI 10.1007/s10751-006-9388-0

Mössbauer study of the invar Fe–Ni and Fe–Ni–C alloys in magnetic field

V. M. Nadutov · T. Ericsson · S. G. Kosintsev · S. M. Bugaychuk · Ye. O. Svystunov · H. Annersten

Published online: 8 November 2006

Abstract F.C.C. Fe–30.3%Ni and Fe–30.5%Ni–1.5%C (wt.%) alloys were studied by means of Mössbauer spectroscopy in external magnetic field B_{ext}=2.5, 5, 7 T parallel to the gamma-beam. It is shown that distribution of effective magnetic field in the alloys is broad and that carbon expands the range of B_{eff}. The external magnetic field increases B_{eff} in the Fe–Ni alloy and decreases it more evidently in the Fe–Ni–C alloy. Antiferromagnetic spin coupling along the ferromagnetic component is proposed to explain data.

Key words Mössbauer spectroscopy · Fe–Ni and Fe–Ni–C alloys · hyperfine magnetic field · external magnetic field

1 Introduction

One of the models describing the Invar behavior of the classical f.c.c.–Fe–36%Ni alloy is based on the existence of large volume high moment (HM) and low volume low moment phases (LM) [1]. In order to support or exclude this idea, recent papers focused on Mössbauer measurements of Fe–Ni alloys in external magnetic field. Mössbauer spectroscopy measurements in longitudinal external magnetic fields up to 7 T have been reported on ball milled γ-$Fe_{100-x}Ni_x$ (x=21, 24, 27 at.%Ni) alloys after annealing at 923 K showing two LM paramagnetic Fe-rich phases and Ni-rich clusters of a ferromagnetically ordered HM phase [2]. Other authors [3] using Mössbauer spectroscopy in a magnetic field of 1.1 T and a polarized γ-beam came to the conclusion that there are two kinds (large and small) of iron magnetic moments in the f.c.c.–$Fe_{100-x}Ni_x$ (x=35, 30, 25) alloys (bulk

V. M. Nadutov (✉) · S. G. Kosintsev · S. M. Bugaychuk · Y. O. Svystunov
G.V. Kurdyumov Institute for Metal Physics, The National Academy of Sciences of Ukraine,
36 Acad. Vernadsky Blvd, UA-03680 Kiev, Ukraine
e-mail: nadvl@imp.kiev.ua

T. Ericsson · H. Annersten
Department of Earth Sciences, Uppsala University, Villavagen 16, SE-75236 Uppsala, Sweden

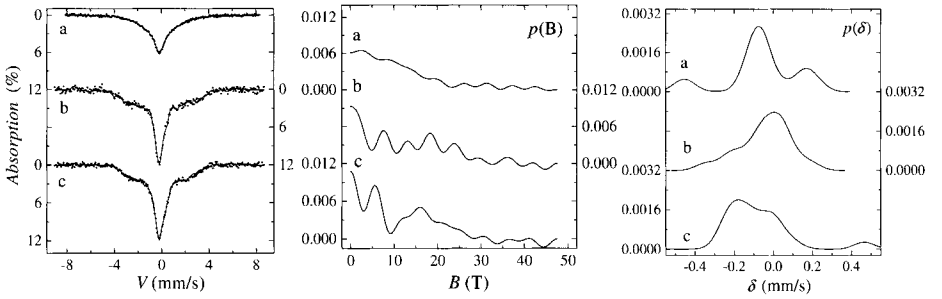

Figure 1 Mössbauer spectra of the Fe–30.3%Ni alloy after homogenization at 1,373 K measured in magnetic fields: without field (*a*), at B=2.5 T (*b*) and at 7 T (*c*). The distributions of the HMF, $p(B)$, and IS, $p(\delta)$, are also shown (the δ values are given with respect to α-Fe).

material). The applied magnetic field causes reorientation of magnetic moments only and the hyperfine magnetic fields (HMF) distribution remains unchanged.

The f.c.c.–Fe–Ni alloy containing about 30%Ni does not usually show Invar behavior since the martensitic transformation inhibits it. However, an addition of C considerably reduces the martensitic point, which results in low thermal expansion approaching the value for standard Invar (Fe–36%Ni) [4]. As established in [5, 6], carbon impurity in a solid solution leads to the decrease in elastic moduli and lowers the Debye temperature in the f.c.c.–Fe–Ni–C alloys due to strong negative magnetic contribution into the ultrasonic velocity. As shown by Mössbauer spectroscopy [4, 7], the HMF distribution resembles a typical Invar $p(B)$ function showing the complex inhomogeneous magnetic order in the Fe–Ni–C alloys. Intensive small-angle neutron scattering (SANS) has been observed in the Fe–Ni–C alloy as a result of inhomogeneous magnetic order [8]. The SANS intensity was considerably reduced by means of an applied magnetic field of 2.5 T [9].

In this work, in order to support the idea that ferromagnetic and antiferromagnetic interactions coexist in Fe–Ni–C-Invar alloys, the f.c.c. Fe–30.3%Ni and Fe–30.5%Ni–1.5% C (wt.%) alloys were studied by means of Mössbauer spectroscopy in external magnetic field B_{ext}=2.5, 5, 7 T parallel to the gamma-beam.

2 Experimental details

The Fe–30.3%Ni, Fe–30.5%Ni–1.5%C (wt.%) alloys were melted in vacuum induction furnace in protective argon atmosphere. The ingots were aged at 1,273 K in vacuum during 3 h. The samples were 20–25 μm thick foils obtained by chemical etching of metal plates with 80–90 μm thickness. The foils were annealed at 1,373 K during 30 min and subsequently quenched in oil. After quenching, the alloys were austenitic as obtained by X-ray analysis. The carbon concentration was determined by chemical analysis and the content of nickel was obtained by means of X-ray fluorescence analysis.

Mössbauer spectra in different magnetic fields were measured on a constant acceleration spectrometer at Uppsala University. A Cryogenic Ltd. closed cycle refrigerator superconducting magnet with a central field homogeneity of 99% was used for in field Mössbauer spectroscopy measurements. The applied magnetic fields of 2.5, 5 and 7 T were parallel to the gamma beam. ^{57}Co in Rh matrix was used as gamma quantum source. The spectra were stored in a multichannel scaler with 512 channels. All spectra (of 256

Table I The hyperfine magnetic fields in the Fe–30.3%Ni and Fe–30.5%Ni–1.5%C alloys obtained by fitting of the Mössbauer spectra

Alloy (wt.%)	B_{ext} (T)	B_L, (T)		B_M, (T)		B_H, (T)		B_{eff}, (T)
		Interval of B_L	$B_L^{max\,a}$	Interval of B_M	$B_M^{max\,a}$	Interval of B_H	$B_H^{max\,a}$	
Fe–30.3%Ni	0	0–6.3	2.5	6.3–11.9	–	11.9–23.4	–	21.5
	2.5	0–4.9	–	4.9–10.6	7.6	10.6–32.6	18.3	25.4
	7	0–3.0	–	3.0–9.2	5.6	9.2–33.8	16.0	26.7
Fe–30.5%	0	0–3.1	–	3.1–8.2	6.9	8.2–33.4	22.7	29.4
Ni–1.5%C	2.5	0–3.0	–	3.0–8.4	6.2	8.4–32.8	25.8	30.4
	0, ϕ=54.7°	0–3.4	–	3.4–12.4	9.3	12.4–32.6	23.9	30.2
	7	0–4.1	–	4.1–10.2	6.8	10.2–27.2	19.0	24.6

B_L is the low-field component of hyperfine magnetic field (HMF); B_M is the middle-field component of HMF; B_H is the high-field component of HMF; B_{eff} is the effective value of HMF; ϕ is the magic angle between the normal to a sample plane and the γ-beam direction

[a] The field at maximum in a selected section of the $p(H)$ function

channels) were fitted using the Window method [7] and the distributions of the hyperfine magnetic fields (HMF) and isomer shifts (IS) were deduced. The IS are given with respect to α-Fe.

3 Results and discussions

The Mössbauer spectrum of the Fe–30.3%Ni alloy obtained at B_{ext}=0 T as a broad singlet (Figure 1) can be fitted with a distribution of HMF from 23.4 T to lower values, with the B_{eff}=21.5 T (Table I) determined on the minimum of the first derivative of the $p(B)$ function. Under an applied external magnetic field of 2.5 T the spectrum of the alloy is split and there is a broad distribution of the HMF from 32.6 T to smaller values. The maxima of $p(B)$ are nearly 7.6 and 18.3 T (Table I). The B_{eff} increases to 25.4 T. For B_{ext}=7 T, the $p(B)$ function shows a higher value of B_{eff}=26.7 T and lower values for maxima: B_M^{max}=5.6 T and B_H^{max}=16.0 T. This indicates that the effective internal fields are parallel and anti-parallel to the external field.

The shape of the Mössbauer spectrum of the Fe–30.5%Ni–1.5%C alloy after annealing at 1,373 κ obtained at B_{ext}=0 T considerably differs from that of the Fe–30.3%Ni alloy (Figure 1a and Figure 2a). The Fe–30.5%Ni–1.5%C sample gives a very broad magnetic spectrum. The distribution of B_{eff} extends from 33.4 T to smaller values and shows two peaks at B_M^{max}=6.9 T and B_H^{max}=22.7 T (Table I).

The effective field components in the spectrum of the carbon-containing alloy were not considerably changed under the B_{ext}=2.5 T: B_{eff} increases from 29.4 to 30.4 T. However, at higher applied external magnetic field B_{ext}=7 T, the marked reduction of B_{eff} (24.6 T) and high-field component (B_H^{max}=19.0 T) is observed (Table I). The B_M^{max} is changed slightly and a low-field component still exists at B_{ext}=7 T (Figure 2, Table I). The obtained data indicate the existence of antiparallel coupling of spins in the alloy and the coexistence of spins in paramagnetic and ferromagnetic states. Thus, this experiment confirms the mixed exchange interaction in the Fe–Ni and Fe–Ni–C alloys and shows that carbon enhances this "magnetic decomposition" that was predicted in calculations [10]. The mixed exchange

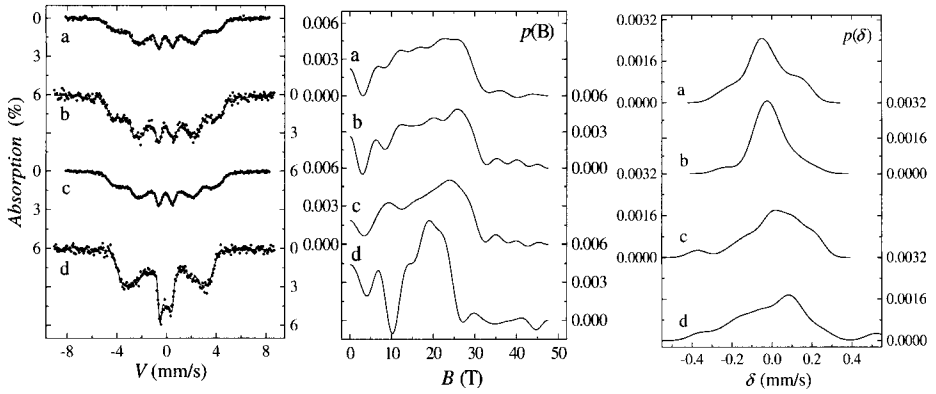

Figure 2 Mössbauer spectra of the Fe–30.5%Ni–1.5%C alloy after homogenization at 1,373 K measured in magnetic fields: without field (*a*), 2.5 T (*b*), angle 54.7° (*c*), 7 T (*d*). The calculated HMF, $p(B)$, and IS, $p(\delta)$, distributions are also shown (the δ values are given with respect to α-Fe).

interaction in the alloys results in inhomogeneous magnetic order as seen in SANS studies [9].

The measurements at a 54.7° angle from the normal to the sample with respect to the gamma beam direction did not change the shape of the spectrum. This indicates the absence of texture in the alloy.

It is to be noticed, that the isomer shift for the Fe–Ni–C alloy slightly increases under applied external magnetic field (Figure 2), and this does not occur for the Fe–Ni alloy (Figure 1). This means that the *s*-electron density decreases under the applied field being the result of a redistribution of electronic charge and an enhancement of screening effect by magnetic *d*-electrons.

4 Conclusions

When $B_{ext}=0$ the distribution of the effective magnetic field is broad in the Fe–Ni and Fe–Ni–C alloys containing ≈30%Ni. Alloying with carbon increases the effective field up to 33.4 T, whereas in carbonless alloy it is extended only to 23.4 T.

The applied external magnetic fields of 2.5 and 7 T result in a small decrease of B_M^{max} and B_H^{max} with the simultaneous increase of effective field B_{eff} in the Fe–30.3%Ni alloy.

The interstitial carbon enhances the effect of external magnetic fields. More marked changes in HMF are observed for the Fe–30.5%Ni–1.5%C alloy in $B_{ext}=7$ T. The decrease of B_{eff} and B_H^{max} and weak changes of the low-field and middle-field components under B_{ext} occur, indicating the presence of ferromagnetic and antiferromagnetic alignment of spins.

The data confirm the existence of mixed exchange interaction in the Fe–Ni and Fe–Ni–C alloys.

Acknowledgment The Science and Technology Center in Ukraine (project #2412, 2001-2004) and the Fundamental Research Program of the National Academy of Sciences of Ukraine "Nanosystems, nanomaterials and nanotechnologies" (2005) supported this work.

References

1. Rancourt, D.G.: Phase Transit. **75**, 201 (2002)
2. Abdu, Y.A., Annersten, H., Ericsson, T., Norblad, P.: J. Magn. Magn. Mater. **280**, 243 (2004)
3. Satuła, D., Szymański, K., Dobrzyński, L., et al.: Nukleonika **48**, S71 (2003)
4. Nadutov, V.M., Svystunov, Ye.O.: Metallofiz. Novejs. Tehnol. **24**, 1639 (2002) (in Ukrainian)
5. Nadutov, V.M., Zaporozhec, O.I., Dordienko, M.A., Svystunov, Ye.O.: Metallofiz. Novejs. Tehnol. **25**, 533 (2003) (in Ukrainian)
6. Nadutov, V.M., Golub, T.V., Hymenyuk, O.V.: Funct. Mater. **11**, 496 (2004)
7. Nadutov, V.M., Svystunov, Ye.O., Efimova, T.V., Gorbatov, A.V.: Hyperfine magnetic structure and magnetic properties of invar Fe–Ni–C alloys. In: Mashlan, M., Miglierini, M., Schaaf, P. (eds.) Material Research in Atomic Scale by Mossbauer Spectroscopy, pp. 105–116. Kluwer, Dordrecht, The Netherlands (2003)
8. Nadutov, V.M., Garamus, V.M., Willumeit, R., Svystunov, Ye.O.: Metallofiz. Novejs. Tehnol. **24**, 717 (2002) (in English)
9. Nadutov, V.M., Willumeit, R., Garamus, V.M., Semenov, D.V.: Funct. Mater. **11**, 501 (2004)
10. Tatarenko, V.A., Radchenko, T.M., Nadutov, V.M.: Metallofiz. Novejs. Tehnol. **25**, 1303 (2003) (in Ukrainian)

Hyperfine Interact (2006) 168:1029–1035
DOI 10.1007/s10751-006-9389-z

Mössbauer study of Mg–Ni(Fe) alloys processed as materials for solid state hydrogen storage

P. Palade · G. Principi · S. Sartori · A. Maddalena · S. Lo Russo · G. Schinteie · V. Kuncser · G. Filoti

Published online: 8 November 2006

Abstract Mg–Ni–Fe magnesium-rich intermetallic compounds were prepared following two distinct routes. A $Mg_{88}Ni_{11}Fe_1$ sample (A) was prepared by melt spinning Mg–Ni–Fe pellets and then by high-energy ball milling for 6 h the obtained ribbons. A $(MgH_2)_{88}Ni_{11}Fe_1$ sample (B) was obtained by high-energy ball milling for 20 h a mixture of Ni, Fe and MgH_2 powders in the due proportions. A SPEX8000 shaker mill with a 10:1 ball to powder ratio was used for milling in argon atmosphere. The samples were submitted to repeated hydrogen absorption/desorption cycles in a Sievert type gas–solid reaction controller at temperatures in the range 520÷590 K and a maximum pressure of 2.5 MPa during absorption. The samples were analysed before and after the hydrogen absorption/desorption cycles by X-ray diffraction and Mössbauer spectroscopy. The results concerning the hydrogen storage properties of the studied compounds are discussed in connection with the micro-structural characteristics found by means of the used analytical techniques. The improved kinetics of hydrogen desorption for sample A, in comparison to sample B, has been ascribed to the different behaviour of iron atoms in the two cases, as proved by Mössbauer spectroscopy. In fact, iron results homogeneously distributed in sample A, partly at the Mg_2Ni grain boundaries, with catalytic effect on the gas–solid reaction; in sample B, instead, iron is dispersed inside the hydride powder as metallic iron or superparamagnetic iron.

Key words ball milling · melt spinning · hydrogen storage · catalytic effect

P. Palade · G. Principi (✉) · S. Sartori · A. Maddalena
Settore Materiali, DIM, Università di Padova, via Marzolo 9, 35100 Padova, Italy
e-mail: giovanni.principi@unipd.it

S. Lo Russo
Dipartimento di Fisica, Università di Padova, via Marzolo 8, 35100 Padova, Italy

P. Palade · G. Schinteie · V. Kuncser · G. Filoti
Solid State Magnetism Department, National Institute for Materials Physics, Atomistilor 105 bis, 077125 Bucharest–Magurele, P.O. Box MG-7, Romania

1 Introduction

Very promising materials for hydrogen storage in the solid state, as an alternative to the storage in high pressure vessels or in cryostats, are based on light metal hydrides as MgH_2 having theoretically a hydrogen storage capacity of 7.6 wt.%. Unfortunately, MgH_2 shows slow kinetics of hydrogen absorption/desorption (a/d) and a too low plateau pressure (as displayed in pressure-composition-temperature diagrams) at ambient temperature. This means that to release H_2 gas with a pressure higher than 0.1 MPa (1 atm) it is necessary to raise the temperature above 550 K. Several authors have tried to improve the hydrogen a/d kinetics by ball milling mixtures of MgH_2 with transition metals [1] or transition metal oxides [2]. Other many attempts have been done in order to improve the thermodynamics introducing particular elements into the MgH_2 lattice. Again, ball-milling results a useful preparation method [3], but also melt spinning can help to this purpose [4].

These two preparation methods have been applied in the present work to the Mg–Ni–Fe system, which results interesting on the basis of previous studies [5]. Samples obtained by short time ball milling Mg–Ni–Fe melt spun ribbons have been compared to samples obtained by long time ball milling a MgH_2, Ni and Fe powder mixture. Hydrogen a/d kinetics and thermodynamics of hydride dissociation have been also studied and discussed on the basis of ^{57}Fe Mössbauer spectroscopy measurements aimed to determine the changes of iron local structure during the different stages of sample processing.

2 Experimental

$Mg_{88}Ni_{11}Fe_1$ ribbons were prepared by melt-spinning. Sample A was obtained by milling the ribbons using a SPEX8000 shaker mill with a ball to powder weight ratio of 10/1 and a milling time of 6 h. Sample B, having similar composition, was obtained by ball milling for 20 h in the same conditions commercial powders of MgH_2, Ni, Fe in the proportion $(MgH_2)_{88}Ni_{11}Fe_1$. The preparation details of samples studied in the present work are described elsewhere [6]. Due to the different preparation routes, it is expected that sample A would present a more homogeneous distribution of the alloyed elements than sample B. This is expected to affect the hydrogen a/d kinetics, too.

Hydrogen a/d kinetics, were measured using a AMC (Pittsburgh) volumetric Sievert apparatus. Room temperature Mössbauer spectra were measured using a ^{57}Co:Rh source and a constant acceleration drive. Some measurements were performed also to 80 K. All milling operations and samples handling were performed in a protective argon atmosphere.

3 Results and discussions

As described elsewhere [6], the starting ribbons appear mainly amorphous with overlapped sharp peaks of Mg and metastable Mg_6Ni phase, while milled ribbons as sample A are crystalline exhibiting Mg and Mg_2Ni phases. No evidence of metallic iron or iron phases can be seen in the XRD patterns of as spun and milled ribbons. As milled sample B is crystalline with broad peaks indicating a grain size of about 10 nm and the detected phases are mainly β-MgH_2 and Mg_2NiH_4 with a small contribution of α-Fe. The XRD patterns of A and B hydrogenated samples exhibit mainly the presence of β-MgH_2 and Mg_2NiH_4, but small quantities of MgO and α-Fe are also present.

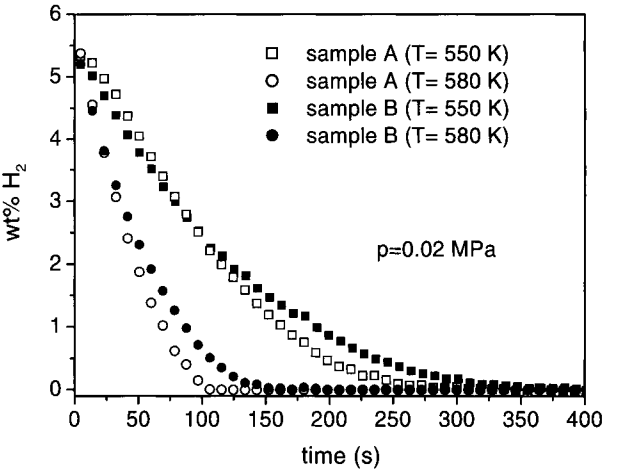

Figure 1 Hydrogen desorption kinetics at 550 and 580 K under a hydrogen pressure of 0.02 MPa for samples A and B.

Sample A displays a better hydrogen desorption kinetics than that sample B (Figure 1): at 580 K the desorption of all stored hydrogen occurs in less than 120 s, while in sample B it occurs completely after 150 s. At 550 K the difference is even more evident, since all stored hydrogen is released in 250 s by sample A, and in 350 s by sample B.

The room temperature Mössbauer spectra of as melt spun, milled and hydrogenated ribbon are shown in Figure 2a, b, d, respectively. The spectrum of as prepared ribbon is rather broad and resembles that of an amorphous iron compound, with two maxima around 3 and 20 T in the hyperfine magnetic field distribution. This broad shape was well fitted only with a distribution of magnetic hyperfine fields, while the spectra of milled and hydrogenated ribbons could be well fitted both with discrete components and hyperfine field distributions. The hyperfine parameters obtained by fitting the experimental data are given in Table I. The spectrum of milled ribbon (Figure 2b) exhibits a magnetic sextet of about 20 T (dotted line), a paramagnetic doublet (solid line) with isomer shift, δ, of 0.15 mm/s and quadrupole splitting, Δ, of 0.94 mm/s and two minor components (two sextets of about 27 T (dashed line) and 33 T (solid line)). The hyperfine field distribution corresponding to the milled ribbon looks almost similar to that obtained for as melt spun ribbon (Figure 2a, b). This suggests a substantial increase of crystallinity during milling (supported by XRD data [6]), but preserving the local environment of iron unchanged. Additionally, the hyperfine field distribution of milled ribbon shows a peak at 33 T due to the presence of metallic iron.

The pattern of hydrogenated milled ribbon shown in Figure 2d exhibits mainly α-Fe (solid line sextet of 33 T) and another sextet of about 20 T (dotted line). Two doublets with $\Delta \cong 1$ mm/s (solid line) and $\Delta \cong 0.5$ mm/s (dotted line) appear in the central region of the spectrum. The origin of these spectral components associated to different iron environments will be discussed in the following.

Considering that ball milling and melt spinning are non-equilibrium processes which can overpass the immiscibility between Mg and Fe at the equilibrium [7], none of the following possibility can be excluded in principle for sample A: Mg dissolved in Fe clusters, Fe in Mg, Fe in Mg_2Ni, some kind of Fe–Ni compound. The interpretation of the main components in the Mössbauer spectra can be made with a perusal of literature data for Fe–Mg compounds obtained by non-equilibrium techniques: mechanical alloying [8], ion implantation [9], or vacuum deposition [10]. It has been shown that, for low iron concentrations, Mg–Fe compounds exhibit a paramagnetic doublet with $\delta = 0.03 \div 0.18$ mm/s and $\Delta = 0.45 \div 0.6$ mm/s [9, 10], while at iron concentrations above 80 at.%, the Mössbauer pattern is an

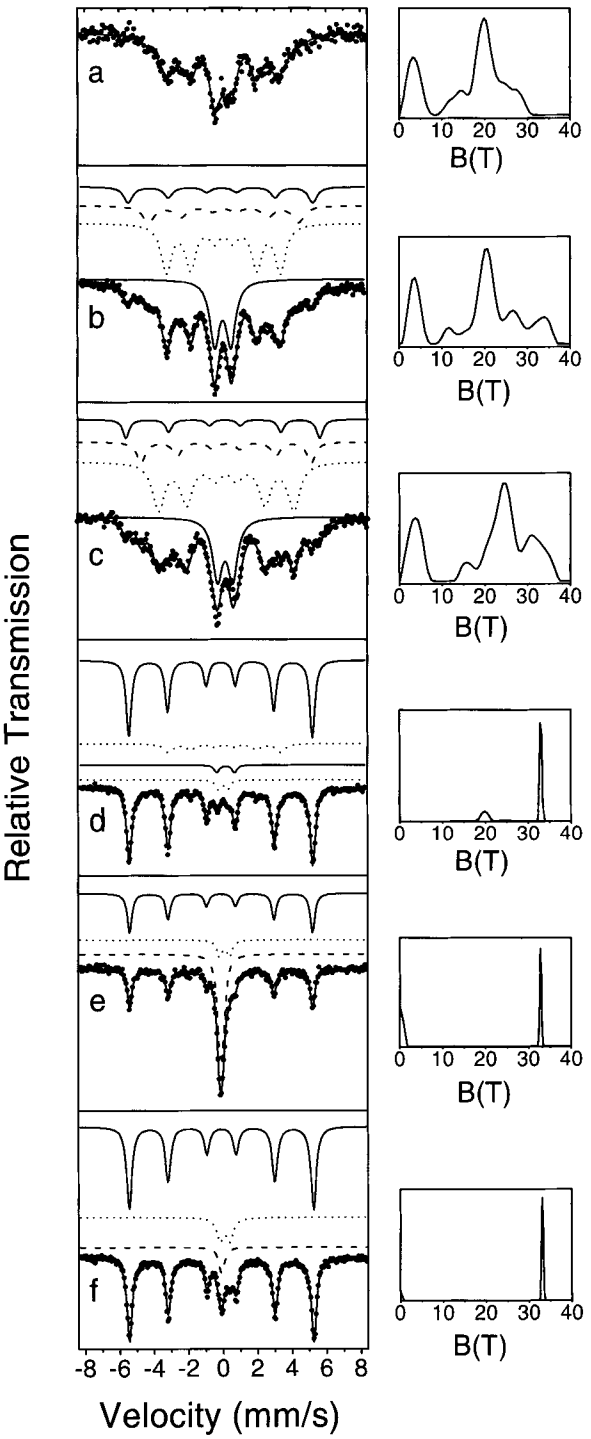

Figure 2 Mössbauer spectra of sample A: **a** as melt spun (RT), **b** milled (RT), **c** milled (80 K), **d** milled and hydrogenated (RT) and of sample B: **e** as milled (RT), **f** milled and hydrogenated (RT). In the *right side* the corresponding hyperfine field distributions are displayed.

Table I Mössbauer hyperfine parameters: δ (isomer shift, referred to metallic iron), Δ (quadrupole splitting), B_{hf} (hyperfine magnetic field) for samples A and B before and after hydrogenation

Sample	Phase	δ (mm/s)	Δ (mm/s)	B_{hf} (T)	Relative area (%)
A (RT)	α-Fe	0.03(2)	0.06(5)	33.2(2)	12(2)
	Fe–Ni(Mg)	0.18(1)	0.02(1)	20.5(1)	47(1)
	$FeNi_3$(Mg)	0.21(3)	0.04(4)	27.0(3)	16(2)
	Mg_2Ni(Fe)	0.15(1)	0.94(2)	–	25(1)
A (80 K)	α-Fe	0.09(3)	0.09(6)	34.5(4)	11(3)
	Fe–Ni(Mg)	0.31(3)	0.03(2)	24.3(2)	50(3)
	$FeNi_3$(Mg)	0.33(3)	0.02(5)	30.6(4)	15(3)
	Mg_2Ni(Fe)	0.26(2)	0.89(3)	–	24(2)
A hydrogenated (RT)	α-Fe	0.002(2)	0.002(2)	33.03(2)	76(1)
	Fe–Ni(Mg)	0.19(3)	0.06(5)	20.3(3)	15(1)
	Mg_2Ni(Fe)	0.28(3)	1.03(6)	–	4(1)
	Fe^{3+} oxide	0.13(3)	0.53(5)	–	5(1)
B (RT)	α-Fe	0.005(4)	0.005(5)	32.95(4)	46(2)
	Fe superparamagnetic	0.00(1)	0.2(1)	–	43(3)
	Fe^{3+} oxide	0.20(5)	0.6(2)	–	11(4)
B hydrogenated (RT)	α-Fe	0.002(2)	0.005(3)	33.16(2)	80(1)
	Fe superparamagnetic	0.00(4)	0.0(3)	–	7(3)
	Fe^{3+} oxide	0.20(3)	0.56(4)	–	13(3)

hyperfine magnetic sextet of about 30 T, indicating the presence of Mg dissolved into the bcc α-Fe lattice (Mg atoms nn of Fe atoms have the effect of depressing the magnetic field) [8]. As shown in Figure 2a), the main peak of the hyperfine field distribution of as obtained ribbon is located at about 20 T, therefore the presence of Mg dissolved inside iron clusters has to be excluded. The same could be valid for sample A (milled ribbon), which gives a main magnetic sextet of 20 T (dotted line in Figure 2b). In sample A, also dissolution of Fe into the Mg structure can be excluded, because the doublet has a Δ of about 0.94 mm/s, higher than that reported for Fe dissolved in Mg [9, 10]. Another possibility to be ruled out is to assign the main magnetic component of 20 T to Fe dissolved into Mg_2Ni, which is paramagnetic at room temperature [11]. Regarding Fe–Ni compounds, $FeNi_3$, $Fe_{0.5}Ni_{0.5}$ and $Fe_{1-x}Ni_x$ invar (x=0.35) have hyperfine magnetic fields of 27.9 T [12], 31.4 T [13], and 23÷24 T [14, 15], respectively, all higher than 20 T. However, considering that, due to the preparation method and the overall composition of the samples, Mg atoms may be dissolved into grains of a Fe–Ni alloy, depressing the internal field, it is reasonable to attribute the 20 T component to a structure of this kind. The other two minor magnetic components which appear in the Mössbauer spectrum of sample A (Figure 2b) are attributed to metallic iron (33 T) and a $FeNi_3$-like phase (27 T). They may be due to Fe separation from the Mg_2Ni during ball milling. Concerning the doublet with $\Delta \cong 0.9$ mm/s, it could belong either to Fe atoms dissolved in Mg_2Ni grains or, most probably, to Fe atoms located at Mg_2Ni boundary, where a highly distorted structure may justify the high value of Δ.

At 80 K (Figure 2c) the fitted spectral components for $Mg_{88}Ni_{11}Fe_1$ milled ribbon (sample A) are the same as at 293 K (Figure 2b). By lowering the temperature, the hyperfine field of Fe–Ni(Mg) and $FeNi_3$(Mg) increases of about 3÷4 T, a too little increment to explain a relaxation process, while the isomer shifts follow a regular variation of second order Doppler shift (Table I). As a consequence, according to Mössbauer data, neither phase nor magnetic transitions occurred in the range 80÷293 K.

As seen in Figure 2d, in the hydrogenated milled ribbon the main part of Fe segregates from Fe–Ni compounds, giving rise to the α-Fe sextet of 33 T (solid line). This segregation forms α-Fe particles large enough to be detected by XRD. Small Fe quantities remain dissolved inside the Fe–Ni alloy (dotted line sextet of 20 T) or located at Mg_2NiH_4 grain boundary (solid line doublet of $\Delta \cong 1.0$ mm/s) or as a Fe^{3+} compound (dotted line doublet). Moreover, the corresponding hyperfine field distribution, obtained disregarding the central doublets, shows a small peak around 20 T besides the main sharp peak of metallic iron. Fe dissolved into Fe–Ni alloy has the same hyperfine parameters after hydrogenation (Table I), not affected by the presence of hydrogen. The isomer shift of Fe located at Mg_2Ni grain boundary increases very slightly with the hydrogenation ($Mg_2Ni \rightarrow Mg_2NiH_4$) (Table I), while the quadrupole splitting remains practically unchanged, suggesting the same strength of local distortion of Fe environment at the Mg_2Ni or Mg_2NiH_4 grain boundaries. Taking into account the isomer shift and quadrupole splitting values of Table I, the Fe^{3+} doublet can be assigned to Fe dissolved into Mg or to some Fe complex with cationic vacancies in MgO matrix [16] or still to some Fe^{3+} oxide in superparamagnetic relaxation state. The last two assignments are more probable, because in hydrogenated samples Fe tends to segregate from Mg–Ni matrix and to form metallic iron. The same assumption is supported also by the presence of a similar Fe^{3+} doublet in the Mössbauer pattern of sample B (Figure 2e, f) before and after hydrogenation, which was obtained by ball milling of powders.

The Mössbauer spectrum of sample B before hydrogenation shows mainly the presence of α-Fe sextet (solid line) and of a singlet (dashed line) with almost equal intensity (Table I). The sharp hyperfine field distribution, very different from the broad one of sample A, indicates that ball milling alone is not able to produce an amorphous-like Fe–Ni(Mg) structure, contrary to melt spinning. After hydrogenation the intensity of the singlet strongly decreases. The isomer shift of the singlet, $\delta \cong 0$ mm/s, can be assigned to superparamagnetic iron or/and to iron in Mg_2FeH_6, both exhibiting similar Mössbauer patterns at room temperature [17]. The superparamagnetic relaxation may be due to the grain size decrease during ball milling, which leads to loss of the long range atomic order. Moreover, high energy milling of MgH_2 mixed with Fe may produce Mg_2FeH_6, according to Huot et al. [18]. Mössbauer spectroscopy proves the increase of the amount of α-Fe after hydrogen a/d cycles (Table I). This may be either due to increase of iron grain size or caused by partial decomposition of Mg_2FeH_6 into α-Fe and MgH_2. Taking into account the relatively small time of milling (20 h) compared to the 60 h of Huot et al. [18], more probably the singlet can be assigned to superparamagnetic iron, not to Mg_2FeH_6. A small doublet (dotted in Figure 2e, f), previously assigned to Fe^{3+} in some Fe–MgO complex or to superparamagnetic Fe^{3+}oxide in relaxation state, is present before and after hydrogenation and is practically unaffected by hydrogen a/d cycles.

What is very important to draw from the Mössbauer measurements is that Fe does not give rise to a Fe–Ni phase nor gets dissolved at Mg_2Ni grain boundary during ball milling if the starting material is a mixture of commercial powders, contrary to what happens using as starting material melt spun ribbons.

4 Conclusions

Mg–Ni–Fe compounds obtained by melt spinning and subsequently ball milling show a better kinetic of hydrogen desorption than similar samples obtained by milling a mixture of MgH_2, Ni and Fe commercial powders. This may be explained, as proved by Mössbauer spectroscopy, by the presence in former samples of Fe at the Mg_2Ni grain boundaries, with

catalytic effect on the gas–solid reaction. In the last sample, Fe is dispersed inside the hydride powder as metallic iron and superparamagnetic iron.

It is clearly shown that during a/d hydrogen cycles of melt spun and subsequently ball milled samples the main part of Fe separates from Mg_2NiH_4.

References

1. Liang, G., Huot, J., Boily, S., Van Neste, A., Schulz, R.: J. Alloys Compd. **292**, 247 (1999)
2. Oelerich, W., Klassen, T., Bormann, R.: J. Alloys Compd. **315**, 237 (2001)
3. Liang, G.: J. Alloys Compd. **370**, 123 (2004)
4. Spassov, T., Lyubenova, L., Köster, U., Baró, M.D.: Mater. Sci. Eng. A **375–377**, 794 (2004)
5. Bobet, J.L., Grigorova, E., Khrussanova, M., Khristov, M., Radev, D., Peshev, P.: J Alloys Compd. **45**, 280 (2002)
6. Palade, P., Sartori, S., Maddalena, A., Principi, G., Lo Russo, S., Lazarescu, M., Schinteie, G., Kuncser, V., Filoti, G.: J. Alloys Compd. **415**, 170 (2006)
7. Burylev, B.P.: In: Moffatt, W.G. (ed.) The Handbook of Binary Phase Diagrams, p. 466. General Electric Comp., Schenectady, NY (1978)
8. Hightower, A., Fultz, B., Bowman R.C. Jr.: J Alloys Compd. **252**, 238 (1997)
9. Reuther, H., Betzl, M., Matz, W., Richter, E.: Hyperfine Interact. **112**, 165 (1998)
10. van der Kraan, A.M., Buschow, K.H.J.: Phys. Rev. B **25**, 3311 (1982)
11. Schlapbach, L., Stucki, F., Seiler, A., Seigmann, H.C.: J. Magn. Magn. Mater. **15–18**, 1271 (1980)
12. Heilmann, A., Zinn, W.: Z. Metallkd. **58**, 113 (1967)
13. Jeandey, C., Peretto, P.: J. Phys. **36**, 1103 (1975)
14. Müller, J.B., Hesse, J.: Z. Phys. B **54**, 43 (1983)
15. Shiga, M., Nakamura, Y.: J. Magn. Magn. Mater. **40**, 319 (1984)
16. Hayashi, N., Sakamoto, I., Toriyama, T., Wakabayashi, H., Okada, T., Kuriyama, K.: Surf. Coat. Technol. **169–170**, 540 (2003)
17. Didisheim, J.J., Zolliker, P., Yvon, K., Fischer, P., Schefer, J., Gubelmann, M., Wiliams, A.F.: Inorg. Chem. **23**, 1953 (1984)
18. Huot, J., Boily, S., Akiba, E., Schulz, R.: J. Alloys Compd. **280**, 306 (1998)

Hyperfine Interact (2006) 168:1037–1040
DOI 10.1007/s10751-006-9390-6

Characterizing the ordering of thermomechanically processed high-Si steel by Mössbauer effect techniques

D. Ruiz · R. E. Vandenberghe · T. Ros-Yañez · E. De Grave · Y. Houbaert

Published online: 14 November 2006

Abstract The processing of high-Si steels remains challenging. The development of ordered phases is the reason for the deteriorated workability which makes not feasible its production. The influence of the hot and the cold work on the order degree in high-Si steel is investigated by TMS (Transmission Mössbauer spectroscopy) and ILEEMS (Integrated low-energy electron MS). The Si-addition favors the creation of an order gradient in the hot rolled sheets; this accounts as an extra strengthening mechanism. In order to have a successful cold rolling the degree of order must be as low as possible; this is difficult to obtain when the Si-content is too high.

Key words electrical steel · thermomechanical processing · ILEEMS · order–disorder

1 Introduction

Si-steel is used to make most of the cores of transformers and electrical motors. The reason lies in the enhanced magnetic properties which reduce the power losses of the corresponding device. Although a very good compromise between the different magnetic properties is obtained for a Si-content around 12 at.% Si, mass production by conventional rolling techniques keeps restricted to Si-levels below 7 at.%. Atomic ordering phenomena are the main reason for the very poor cold ductility which makes the material impossible to cold roll. However, there is still an opened discussion about the type of order present in Fe–Si alloys in the 6–12 at.% Si range [1, 2]. Within this context it has been recently

D. Ruiz (✉) · T. Ros-Yañez · Y. Houbaert
Department of Metallurgy and Materials Science, Ghent University,
Technologiepark 903, B-9052 Ghent, Belgium
e-mail: Daniel.Ruiz@UGent.be

D. Ruiz · R. E. Vandenberghe · E. De Grave
Department of Subatomic and Radiation Physics, Ghent University,
Proeftuinstraat 80, B-9000 Ghent, Belgium

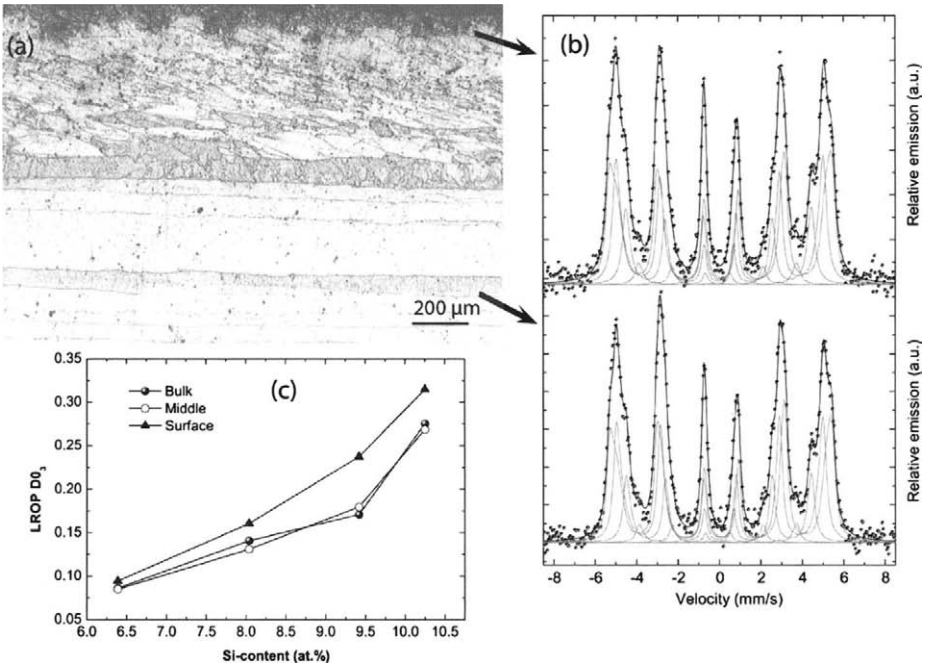

Figure 1 **a**: SEM micrograph of 10.3 at.% Si-steel after the hot rolling. **b**: Fitted ILEEMS spectra of the *surface* and the *center* of the same sample. **c** $D0_3$ long-range order parameters deduced from the ILEEMS spectra (*surface* and *middle*) and transmission spectra (Bulk).

shown that following an adequate thermomechanical route it is possible to reduce the degree of order and make the cold rolling feasible in steels up to 10.5 at.% Si [3, 4]. In the present work the existence of an order gradient through the hot rolled plates is analyzed by ILEEMS (Integrated low-energy electron Mössbauer spectroscopy). In addition a detailed view of the effect of cold working on the ordering of high Si-steel is presented. A better knowledge of the ordering phenomena occurring in high Si-steel can be of a great help in order to improve the processing conditions for its production.

2 Experimental

Five different Si-steels were laboratory cast. The contents of Si in atomic percent were 6.4, 8.1, 8.8, 9.4 and 10.5. They were reheated at 1,100°C for 1 h and then they were hot rolled in four to six passes up to a thickness of 1.5 mm. Chemical etching was used to remove the surface oxide layer and then they were analyzed by ILEEMS. In addition, ILEEMS was carried out on the center of the sample after mechanical grinding and chemical etching. Another series of as-cast specimens were uniaxially deformed in a computer-driven servo-hydraulic machine designed to compute and maintain a constantly reducing velocity profile that assures a constant rate of deformation during the whole test. Testing was carried out at a constant rate of strain of 0.5 sec^{-1}. The 8.8 at.% Si-steel was plane strained to different deformations at a strain rate of 1 sec^{-1}.

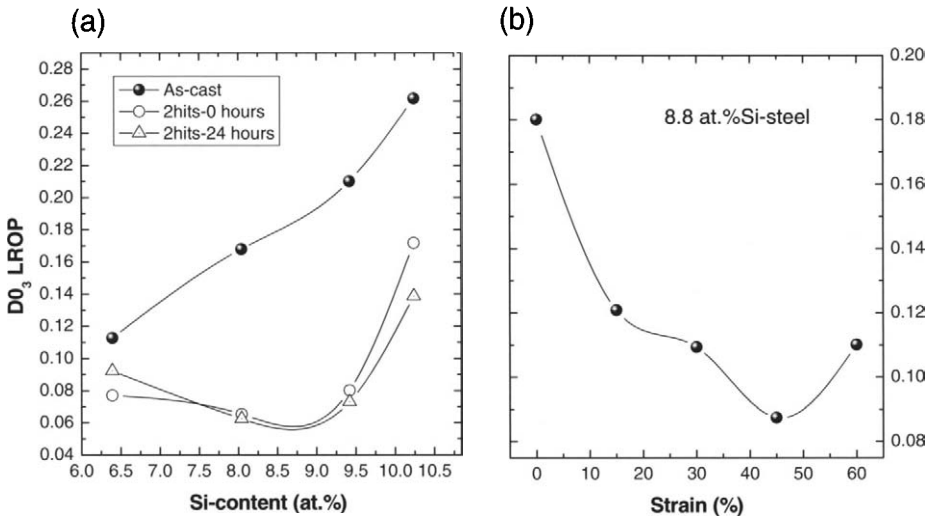

Figure 2 **a**: $D0_3$ LROP of as-cast and uniaxially deformed Si-steels by double-hit. Zero and 24 h mean the delay time between the two. **b**: Evolution of the $D0_3$ LROP with the applied strain in a 8.8 at.% Si-steel.

3 Results and discussion

Figure 1a shows the microstructure of the 10.5 at.% Si-steel after hot rolling and air cooling. The center of the sample is characterized by coarse elongated grains in the middle whereas small elongated grains are found near the surface. A subgrain structure is detected within the coarse grains what can be a sign of recovery after heavy deformation. On the right hand Figure 1b presents ILEEMS spectra corresponding to the surface and the middle of the sample. They were fitted with the help of a special fitting routine based on a modified binomial distribution depending on the order parameters [5]. First and second neighbors are taken into account using a quadratic decrement in the hyperfine field with the number of first neighbors. Steels with 6.4, 8.1 and 9.4 at.% Si-steel present a structure which is a mixture of $Fe_{15}Si$ and $D0_3$ types of order whereas 10.3 at.% Si-steel posses a mixture of $D0_3$ and B2 orderings [5]. Figure 1c gives the $D0_3$ long-range order parameter (LROP) of the surface and the middle of every hot rolled steel obtained from the ILEEMS spectra. They are compared with the ones obtained with standard transmission Mössbauer spectroscopy (bulk). It is seen that the degree of order is always higher in the surface and this effect is more pronounced for higher Si-contents. In addition the ILEEMS values in the middle coincide with the transmission results, which is an indication for the validity of the results.

Figure 2a presents the influence of the deformation and the Si-content on the degree of order of high Si-steel. The alloys were heavily deformed in two passes and with or without delay time (24 h) between the two hits. This was done to study the observed room temperature aging behavior in these materials [6]. It is seen that cold deformation suppresses a high amount of order, especially for higher Si-contents. The order parameters must be reduced to a very low value in order to reach a high cold deformation. In the case of 10.5 at % Si this is not possible and for this reason the alloy presented a brittle behavior. On the other hand, Figure 2b presents the $D0_3$ order parameter of 8.8 at.% Si-steel after plain deformation at different strain levels. For higher deformations, lower values of the degree of

order are obtained, except for the highest deformation where the tendency is reverted. This can be related to change of deformation mechanism towards twinning mode [3].

4 Conclusions

$D0_3$ order is present in Si-steels for Si contents as low as 6.4 at.%. In the hot rolled plates, a gradient in order degree is found through their thickness. This gradient is more pronounced when the Si-content is increased. A hot band annealing is then recommended after the hot rolling in order to homogenize the order. The key in order to perform a successful cold working is suppressing as much order as possible, which seems complicated for the very high Si-levels. It is advisable to start the cold rolling with already low amounts of order.

References

1. Swann, P.R., Grånäs, L., Lehtinen, B.: Met. Sci. **9**, 90 (1975)
2. Kilfrich, H., Kölker, W., Petry, W., Schärpf, O., Nembach, E.: Scripta. Met. et Mater. **24**, 39 (1990)
3. Ros, T., Houbaert, Y., Fischer, O., Schneider, J.: IEEE Trans. Magn. **37**, 2321 (2001)
4. Ruiz, D., Ros-Yáñez, T., Vandenberghe, R.E., Houbaert, Y.: Steel Res. Int. **76**(6), 21 (2005)
5. Ruiz, D., Ros-Yañez, T., Vandenberghe, R.E., Houbaert, Y.: AIP Conf. Proc. **765**, 331 (2005)
6. Ruiz, D., Rivera-Tovar, J.L., Segers, D., Vandenberghe, R.E., Houbaert, Y.: Mater. Sci. Eng. A (2006) (in press)

Hyperfine Interact (2006) 168:1041–1045
DOI 10.1007/s10751-006-9391-5

Effect of hydrogen on interatomic bonds in austenitic steels

V. Shivanyuk · V. Gavriljuk · J. Foct

Published online: 14 December 2006

Abstract Mössbauer spectroscopy was used to investigate the influence of dissolved hydrogen on the interatomic bonds in austenitic steels. It was carried out to prove the decohesion mechanism of hydrogen embrittlement (HE). It is shown that hydrogen increases Debye temperature, i.e., the interatomic bonds in hydrogenated austenitic steel becomes stronger.

Key words hydrogen · austenitic steel · Mössbauer effect

1 Introduction

Hydrogen-caused decohesion was one of the first mechanisms proposed to explain hydrogen-induced embrittlement in metals and alloys [1–3]. It has been often referred to (see e.g. [4–8]) but it has never been really proven. Interstitially solved in the crystal lattice, hydrogen is assumed to assist the creation and opening of cracks due to decreasing atomic bonds. An evidence for the hydrogen-caused decohesion can be sought in the effect of hydrogen on the elastic constants, atomic force constants derived from phonon spectra, measurements of the surface energy etc. Hydrogen in the bcc metals of the V group in the periodic table is known to increase the phonon frequencies corresponding to the atomic force constants [9]. This effect is noteworthy because it occurs despite the large increase in volume when hydrogen is dissolved in the bcc lattice. A somewhat different situation is observed in the fcc metals where hydrogen decreases the elastic constants, which is attributed to the increase in volume [9].

The purpose of this work is to contribute to this topic through the study of the effect of hydrogen on Debye temperature. In the Debye approximation vibrational properties give

V. Shivanyuk (✉) · V. Gavriljuk
Kurdjumov Institute for Metal Physics, NAS of Ukraine, 36 Vernadsky blvd., Kiev 03680, Ukraine
e-mail: shyva@imp.kiev.ua

J. Foct
LMPGM-UMR CNRS 8517, Universite de Lille1 Bât C6, 59655 Villeneuve d'ASCQ Cedex, France

Table I Chemical composition (mass %)

Steel	C	N	Cr	Ni	Mn	Si	S	P
$Cr_{18}Ni_{16}Mn_{10}$	0.03	0.066	18.48	16.3	9.64	0.45	0.04	0.008

information about atomic bonds. The material used for the service in hydrogen environment is austenitic stainless steel, therefore understanding the role of H on mechanical resistance is essential.

2 Experimental

The austenitic stainless steel $Cr_{18}Ni_{16}Mn_{10}$ has been studied. It was melted in the arc furnace in ingots about 20 kg. The chemical composition is given in Table I.

After hot forging to rods of about 8 mm in diameter and solution treatment at 1,100°C the samples were cold rolled with intermediate anneals to plates of 20–30 μm. Hydrogen charging was performed at room temperature and at 72°C in 1N H_2SO_4+125 $mg \cdot l^{-1}$ $NaAsO_2$ solution using the platinum anode at the current densities 50 mA/cm^2 during 72 and 6 h. In such conditions of hydrogen charging, the ratio c_H/c_{Me} is about 0.6 in this alloy.

Mössbauer spectra were measured using the MS 1101 E spectrometer ("Mosstech" Co., Russsia, Rostov-on Don) in the constant acceleration regime. ^{57}Co in the Rh matrix with an activity 25 mKu used as a source of γ-rays.

The MS1101E spectrometer was equipped with flow nitrogen cryostat that makes it possible to measure the Mössbauer spectra in the 80–300 K temperature range. The spectra were fitted using the UNIVEM software. This program allows us to fit an experimental spectrum with any set and number of monolines, doublets and sextets, based on the physical model.

3 Results and discussion

3.1 Debay temperature

An effect of hydrogen on the Debye temperature was studied using Mössbauer spectroscopy. An advantage of this experimental technique as compared to X-ray diffraction is that Mössbauer spectra are affected by the mean square amplitude of the atomic vibrations only and not by static displacements of atoms from their equilibrium positions, so that the lattice dynamics can be best studied. The Debye temperature was determined on the basis of the temperature dependence measurements of the area under the lines of the Mössbauer spectrum and that of the isomer shift. The first one is proportional to the recoilless fraction which depends on the mean square amplitude of the atomic vibration in the direction of γ-rays which is related to the Debye temperature [10]. The temperature dependence of $S(T)$ obtained in the experiment can be approximated by the following equation:

$$S(T) = S(0) \cdot \exp\left[-\frac{6R}{k\theta_D} \cdot \left[\frac{1}{4} + \left(\frac{T}{\theta_D}\right)^2 \int_0^{\theta_D/T} \frac{x dx}{e^x - 1}\right]\right] \quad (1)$$

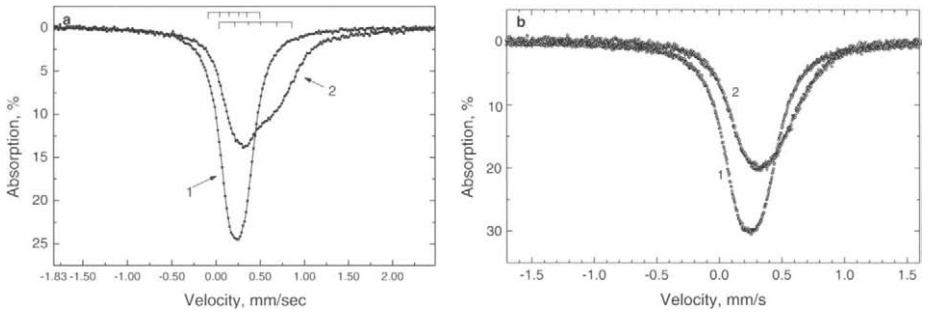

Figure 1 Mossbauer spectra of steel $Cr_{18}Ni_{16}Mn_{10}$, **a**—before hydrogen charging (1) and after hydrogen charging at 20°C, 50 mA/cm^2 for 72 h (2), positions of sextets lines of spectrum for the charged state is shown as example; **b**—before hydrogen charging (1) and after hydrogen charging at 72°C, 50 mA/cm^2 for 6 h (2). Measurements at 80 K.

where R and k are the recoil energy of the iron nuclei and the Boltzman constant, respectively; θ_D – the Debye temperature; $S(0)$ – the area under the experimental spectrum at T=0 K.

The vibrational properties can also be studied via the temperature red shift of the Mössbauer spectrum due to the fact that the second order Doppler effect is related to the θ_D by following equation [11]:

$$\frac{\delta E}{E} = -\frac{9kT}{4Mc^2} \cdot \left[\frac{1}{4} \cdot \frac{\theta_D}{T} + 2\left(\frac{T}{\theta_D}\right)^3 \cdot \int_0^{\theta_D/T} \frac{x^3 dx}{e^x - 1} \right] \tag{2}$$

The relative change of the spectrum line gravity centre is obtained from the experiment; therefore the approximation function for the temperature shift $\delta(T)$ acquires the following form:

$$\delta(T) = \delta(0) - \frac{9k}{4Mc} \cdot \left[\frac{1}{4} \cdot \frac{\theta_D}{T} + 2\left(\frac{T}{\theta_D}\right)^3 \cdot \int_0^{\theta_D/T} \frac{x^3 dx}{e^x - 1} \right] \tag{3}$$

where $\delta(0)$ – spectrum line gravity centre position at 0 K.

Determination of the Debye temperature from the temperature dependence of the isomer shift, resulting from the influence of the velocity squared in all directions was successfully used to study the dynamic displacements of iron atoms in different sites of the ε Fe–N solid solutions [12].

Mössbauer spectra of steel $Cr_{18}Ni_{16}Mn_{10}$ are presented in Figure 1. The spectrum of the specimen charged at room temperature is made up of two components which may result from a non-homogeneous distribution of hydrogen in the sample (Figure 1a). It is in agreement with previous X-ray diffraction studies on austenitic steels [13]. Charging at high temperature has led to a more homogeneous hydrogenation of the sample (Figure 1b).

A feature of Mössbauer lines for both the initial and the charged states is their broadening, so that no spectrum can be fitted with a single Lorentzian. We believe that this broadening is mainly is mainly due to magnetic effects because superparamagnetic clusters

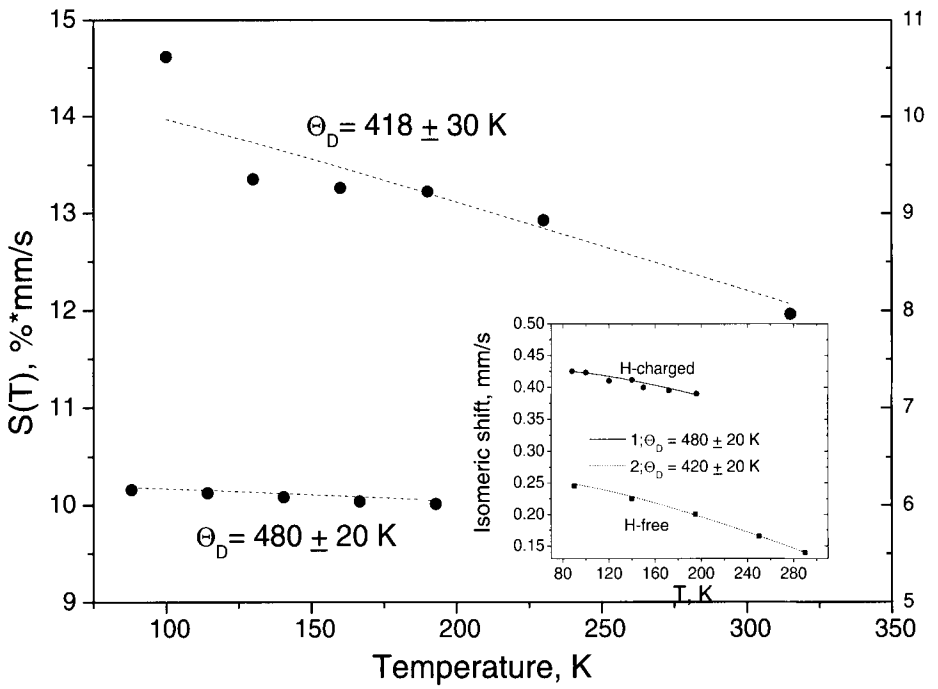

Figure 2 Effect of hydrogen on the temperature dependence of the area under Mossbauer spectra in steel $Cr_{18}Ni_{16}Mn_{10}$, hydrogen charging at 20°C. Temperature dependence of the isomer shift is shown in the insert, charging at 72°C.

exist in the studied steel. Single sextets with small hyperfine fields were used for the fitting of the spectra.

Hydrogen charging has increased the ferromagnetic broadening and caused the gravity centre to shift toward the positive velocities, which corresponds to the positive isomer shift of the nuclear levels, i.e. to a decrease in the charge density of s-electrons at the iron nuclei. Such a change in the isomer shift may be due either to the filling of the d-shell of the iron atoms with electrons coming from hydrogen, which results in the screening of the external s-electrons, or to a hydrogen-caused space redistribution of free electrons decreasing their densities at the nuclei.

Another distinctive feature of the Mössbauer spectrum from the sample charged at 20°C (Figure 1a) is its clear splitting into two components, which means that the hydrogen profile is rather sharp and the central area of the sample is not significantly affected by hydrogen. This spectrum was fitted with two sextets whose isomer shift values are 0.202 and 0.407 mm/s and whose hyperfine fields values are 0.96 and 1.42 T, respectively.

The temperature dependence of the area under the Mössbauer spectrum of the uncharged sample and that of the sextet belonging to the iron atoms in the hydrogen-saturated surface layer of the sample charged at room temperature are presented in Figure 2. Isomer shift data of the sample charged at 72°C and those of the H-free sample are shown in the insert.

It is seen that hydrogen charging decreases the temperature dependence of the area under the spectrum and that of isomer shift, which corresponds to higher values of the Debye temperature. Both methods give the same value of Θ_D. Thus, it is possible to conclude that hydrogen decreases the mean-square dynamic displacements of atoms in the crystal lattice

of austenitic steels and, therefore, in the Debye approximation, hydrogen enhances bonds between atoms. However, some comments about the applicability of the Debye approximation to interstitial solid solutions can be given based on the results obtained. Because of extremely high hydrogen concentration in the cathodically charged austenitic steels, it is possible to imagine that dynamic displacements of the host atoms can be just mechanically impeded by the hydrogen atoms occupying interstitial positions, which does not characterize interatomic bonds.

4 Conclusions

It is shown by means of Mössbauer spectroscopy that hydrogen increases the Debye temperature in the crystal lattice of the austenitic steel, i.e. hydrogen enhances interatomic bonds in the Debye approximation which are not in agreement with the decohesion hypothesis of hydrogen embrittlement.

References

1. Steigerwald, E.A., Schaller, F.W., Troiano, A.R.: Trans. Metall. Soc. AIME **218**, 832 (1960)
2. Oriani, R.A., Josephic, P.H.: Acta Metall. **22**, 1065 (1974)
3. Briant, C.L., Feng, H.C., McMahon, C.J., Jr.: Metall. Trans. **9A**, 625 (1978)
4. Ladna, B., Loxton, C., Birnbaum, H.K.: Acta Metall. **34**, 988 (1986)
5. Knott, J.F.: In: Proc. 5th Int. Conf. on Hydrogen Effects in Materials, Thompson, A.W., Moody, N.R. (eds.) Publ. TMS, p. 387 (1996)
6. Briant, C.L., Feng, H.C., McMagon, C.J., Jr.: Metall. Trans. **9A**, 625 (1978)
7. Rice, J.R.,Thomson, R.: Philos. Mag. **29**, 73 (1974)
8. Gerberich, W.W., Foecke, T.J.: In: Hydrogen Effects on Material Behavior, Moody, N.R., Thompson, A.W. (eds.) TMS, p. 687 (1990)
9. Springer, T.: In: Alefeld, G.P., Volkl, J. (eds.) Hydrogen in Metals I, p. 75. Springer, Berlin Heidelberg New York (1978)
10. Bykov, G.A., Khien, F.Z.: J. Exp. Theor. Phys. **43**, 909 (1962) (in Russian)
11. Maradudin, A.A.: In: Theoretical and Experimental Aspects of the Effects of Point Defects and Disorder on the Vibrations of Crystals, Solid State Physics, 18, p. 273. Academic, New York (1966) (19 1 (1966))
12. Foct, J., Rochegude, P.: C.R. Acad. Sci. Paris, t. 304, Serie 2, **20**, 1217–1220 (1987)
13. Gavriljuk, V.G., Tarasenko, A.V., Tereshchenko, A.S.: Acta Mater. **22**, 269 (1997)

Hyperfine Interact (2006) 168:1047–1050
DOI 10.1007/s10751-006-9392-4

Quadrupole interactions at ^{57}Fe and ^{119}Sn in 3d-metal antimonides

T. M. Tkachenka · V. A. Virchenko

Published online: 14 November 2006

Abstract 3d-metal antimonides: $Fe_{1+x}Sb$, $N_{1+x}Sb$, $Co_{1+x}Sb$ and the $(Ni_{1-y}Fe_y)Sb$ solid solution have been studied by the Mössbauer effect method at ^{57}Fe and ^{119}Sn. It was found that the quadrupole interactions at the Fe and Sn nucleus in 3d-metal antimonides are very sensitive to the filling of different crystallographic sites with metal atoms. The metal atoms in trigonal-bipyramidal sites have a strong effect on the quadrupole splitting of ^{119}Sn. They are nearest to anions (Sb or Sn) with the typical axial ratio of c/a=1.25. The QS(x) dependence of ^{119}Sn in 3d-metal antimonides in the $0 \le x \le 0.1$ concentration range can be used to determine x – the concentration of transition metal excess relative to the stoichiometric composition.

Key words 3d-metal antimonide · NiAs-type of crystal structure · octahedral site · trigonal-bipyramidal site · stoichiometric composition · concentration excess · property–composition correlation · Mössbauer effect · quadrupole splitting of Mössbauer spectrum

1 Introduction

The 3d-metal antimonides with NiAs-type of crystal structure have wide ranges of homogeneity close to a stoichiometric composition [1]. Metal atoms occupy the octahedral sites of the NiAs structure (so-called MeI). Being in excess, they may also partly occupy the trigonal-bipyramidal sites (MeII). Excess or a lack of 3d-metal in the compound, relative to Sb content, leads to a variety of physical characteristics within the one-phase limits [2]. As a result, it is difficult to exactly reach the composition–property conformity. Thus, the purpose of this work is to determine the influence of 3d-metal excess on Mössbauer parameters (for instance quadrupole splitting value) for the NiAs-type antimonides that could be helpful for a proper understanding of the composition–property correlation.

T. M. Tkachenka (✉) · V. A. Virchenko
Institute of Solid State and Semiconductor Physics of the National Academy of Sciences of Belarus, Minsk, Republic of Belarus
e-mail: lttt@ifttp.bas-net.by

Table I Mössbauer parameters of ^{57}Fe and ^{119}Sn for $Fe_{1+x}Sb$ system, $0 \leq x \leq 0.3$

Composition	^{57}Fe				^{119}Sn	
	Fe I		Fe II			
	IS (mm/s)	QS (mm/s)	IS (mm/s)	QS (mm/s)	IS (mm/s)	QS (mm/s)
FeSb	0.65	0.24	0.69	0.42	2.11	1.50
$Fe_{1.1}Sb$	0.66	0.23	0.70	0.43	2.16	1.47
$Fe_{1.2}Sb$	0.67	0.24	0.67	0.44	2.15	1.50
$Fe_{1.3}Sb$	0.70	0.25	0.72	0.43	2.16	1.51

The Mössbauer investigations have been carried out for the $N_{1+x}Sb$, $Co_{1+x}Sb$, $Fe_{1+x}Sb$ systems and the $(Ni_{1-y}Fe_y)Sb$ solid solution. By alloying 1 % at. of Sb, the atoms were replaced by ^{119}Sn stable isotopes. The $^{57m}Co/Rh$ and $Ca^{119m}SnO_3$ sources at 295 K were used. All the spectra were fitted and both the isomer shift (IS) and the quadrupole splitting (QS) values were determined within the accuracy of ±0.03 mm/s.

2 Results and discussion

2.1 $Fe_{1+x}Sb$ system, $0 \leq x \leq 0.3$

All the spectra of ^{57}Fe and ^{119}Sn for this system are quadrupole-split spectra. The parameters are given in Table I. There are two doublets in each spectrum of ^{57}Fe and only one doublet of ^{119}Sn. The spectrum parameters do not vary significantly as x changes. In each spectrum the orthorhombic $FeSb_2$ spectrum is presented. The $FeSb_2$ spectrum has the following parameters: IS=0.72 mm/s, QS=1.27 mm/s at ^{57}Fe; and IS=3.22 mm/s, QS=0.50 mm/s at ^{119}Sn. Though $x = 0$ in $Fe_{1+x}Sb$ (stoichiometric composition), some of the MeII positions in $Fe_{1+x}Sb$ are already occupied by metal atoms.

2.2 $Ni_{1+x}Sb$ and $Co_{1+x}Sb$ system, $-0.05 \leq x \leq 0.10$

All the ^{119}Sn spectra for these samples are also quadrupole-split spectra. In the concentration range from Ni-deficiency to stoichiometric state, the QS value for $Ni_{1+x}Sb$ remains the same. When x increases, the QS value also increases proportionally to x for both Co and Ni. More precisely, OS increases from 0.75 to 1.50 mm/s for $Ni_{1+x}Sb$, and from 0.83 to 1.56 mm/s for $Co_{1+x}Sb$.

The metal atoms in MeII sites are nearest to the Sn(Sb) atoms and determine the QS of ^{119}Sn, as this parameter is the most sensitive one to the resonance atom environment. It is supposed, that the metal atoms are randomly distributed on the MeII sites. The probability to find n atoms in the MeII positions near the Sb atom, $P(n)$ is:

$$P(n) = \left(\frac{5}{n}\right) x^n (1-x)^{5-n},$$

where $n = 0, 1...5$ – is the number of MeII sites filled if the concentration of transition metal excess relative to the stoichiometric composition is x. Obviously, the Sn(Sb) atom local environment is the most symmetric one if $x = 0$ and there is no atoms in MeII sites. This atomic configuration results in relatively small Electric Field Gradient (EFG) and QS value

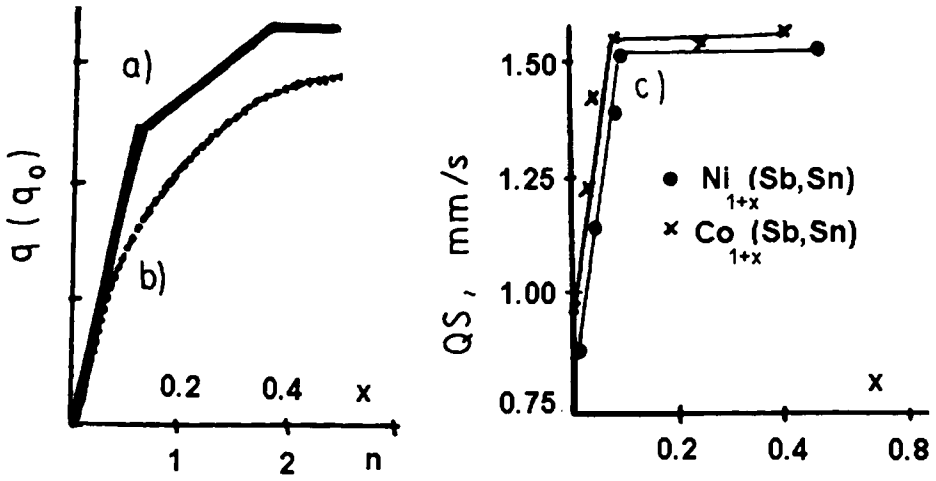

Figure 1 The Electric Field Gradient of the Sb(Sn) atom $q(q_0)$ *a* – vs. the number of MeII sites occupied, *b* – vs. the transition metal concentration *x* and *c* – the experimental Quadrupole Splitting value vs. transition metal concentration *x*.

of Sn. The appearance of some additional atoms in the Sn(Sb) local environment leads to the distortion of the local symmetry and to the increase in the EFG (QS) value. Within the point charge model it is possible to qualitatively evaluate the EFG value of the Sn(Sb) atom. One MeII atom with the *Z* charge produces the following EFG (q_i) at the Sn(Sb) atom site:

$$\vec{q_i} = \frac{2Z}{R^2}\frac{\left|\vec{R}\right|}{\vec{R}}$$

where $\vec{R}$ is the radius vector between the Sn(Sb) atom and the metal atom in MeII site. If there are a few atoms in MeII sites, the EFG is determined by their vector sum $\vec{q} = \sum \vec{q_i}$. Taking into account the probabilities of the corresponding configurations, the curves *a*, *b* are obtained. (see Figure 1).

It is seen that the experimental QS(*x*) dependence in the $0 \le x \le 0.1$ concentration range is stronger than the calculated one [3]. This peculiarity of $Ni_{1+x}Sb$ and $Co_{1+x}Sb$ Mössbauer data in the concentration range of $0 \le x \le 0.1$ allows us to solve the inverse problem, in other words, to find the concentration of metal excess of the unknown $Ni_{1+x}Sb$ or $Co_{1+x}Sb$ sample using the previously measured QS(*x*) dependence. There is no dependence of the same kind for ^{119}Sn spectra in $Fe_{1+x}Sb$ system as there always are some atoms in MeII positions.

2.3 $(Ni_{1-y}Fe_y)Sb$ solid solution, $0 < y \le 1$

X-ray Powder Difraction (XRPD) shows the NiAs-phase formation in this system. The lattice parameters – *a* and *c* – decrease when *y* increases. $FeSb_2$ is formed in each solid solution with $y > 0$, but the amount does not exceed 10 % mol. The spectra of ^{57}Fe and ^{119}Sn have a quadrupole splitted structure for all the *y* values. QS values monotonically increase in the range $0 \le y \le 0.6$ of both Fe and Sn. When $y \ge 0.7$, the low intensity doublet arises in the

^{57}Fe spectra. It is linked to the filling of some trigonal-bipyramidal positions with Fe atoms. At the same time, the QS value at Sn rises sharply, starting from the composition $y = 0.7$. QS = 0.87 mm/s for $y = 0.7$ and QS = 1.50 mm/s for $y = 1$. Increase in QS value of Sn is similar to that of Ni and Co antimonides and has the same nature.

3 Conclusions

1. The quadrupole interactions of Fe and Sn in 3d-metal antimonides are very sensitive to the filling of different crystallographic sites with metal atoms.
2. Metal atoms in trigonal-bipyramidal sites have the most significant effect on the quadrupole splitting of ^{119}Sn. They are nearest to the anions (Sb or Sn) at the typical axial ratio c/a=1.25.
3. The QS(x) dependence of ^{119}Sn in 3d-metal antimonides in the $0 \leq x \leq 0.1$ concentration range can be used to determine x – the concentration of transition metal excess relative to the stoichiometric composition.

References

1. Sirota, N.N.: Physical–Chemical Nature of the Variable Composition Phases, p. 68. Nauka i technika, Minsk (1970)
2. Teramoto, I., van Run, A.M.J.G.: J. Phys. Chem. Solids **29**, 347 (1968)
3. Vasilev, E.A., Tkachenka, T.M.: Cryst. Res. Technol. **32**, 931 (1997)

Hyperfine Interact (2006) 168:1051–1056
DOI 10.1007/s10751-006-9394-2

Effect of *N*-substitution in multinuclear complexes allows interplay between magnetic states and multistability investigated by Mössbauer spectroscopy

F. Renz · D. Hill · P. Kerep · M. Klein · R. Müller-Seipel · F. Werner

Published online: 5 December 2006

Abstract A series of pentadentate ligands N–X–$^5LH_2$ (X=H, Methyl, Benzyl)=N–X–saldptn (4-X-*N*,*N*′-bis(1-hydroxy-2-benzylidene)-1,7-diamino-4-azaheptane) has been prepared by a Schiff base condensation between 1,7-diamino-4-X-azaheptane and salicylaldehyde. Complexation with Fe(III) yields a series of high-spin (S=5/2) complexes of [Fe^{III}(N–X–^{5}L)Cl]. Such precursors were combined with $[Mo(CN)_8]^{4-}$ and a series of blue nonanuclear cluster compounds $[Mo^{IV}\{(CN)Fe^{III}(N–X–^5L)\}_8]Cl_4$ resulted. Such star-shaped nonanuclear compounds are high-spin systems at room temperature. On cooling to 10 K some of the iron(III) centers switched to the low-spin state as proven by Mössbauer spectra, i.e. multiple electronic transitions. Parts of the compounds perform a high-spin to high-spin transition. Under light irradiation the populations are altered slightly.

Key words nonanuclear complex · high-spin molecule · Fe(III)-Mo(IV) · multiple spin transition

1 Introduction

High-spin molecules bear a potential for development in the field of information storage. The class of high-spin molecules containing transition metals has been enriched considerably over the last decades [1–10].

One molecular building block, the pentadentate iron(III) precursor, shows a thermal induced spin crossover in the following topologies: (1) mononuclear [11–14], (2) binuclear [14], (3) tetranuclear [7], (4) heptanuclear [8], (5) nonanuclear [8, 9]. $^5LH_2$=saldptn=*N*,*N*′-bis(1-hydroxy-2-benzylidene)-1,7-diamino-4-azaheptane represents one of the candidates to function as a pentadentate blocking ligand.

In the present work, our approach is extended to study the effect of *N*-substitution in both the [N–X–^{5}LFe^{III}Cl] precursors and its nonanuclear analogous $Fe^{III}{}_8$-Mo^{IV} compounds. A

F. Renz (✉) · D. Hill · P. Kerep · M. Klein · R. Müller-Seipel · F. Werner
Institut für Anorganische Chemie und Analytische Chemie, Johannes Gutenberg-University, Duesbergweg 10-14, 55099 Mainz, Germany
e-mail: Franz.Renz@uni-mainz.de

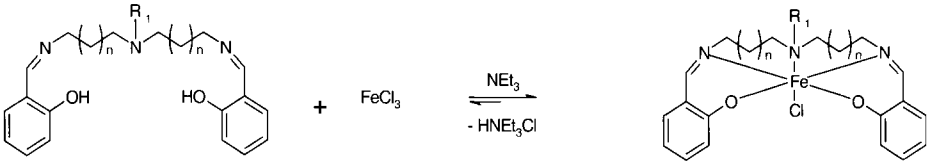

Figure 1 Synthesis and structure of the iron precursors [Fe(^{5}L)Cl], [Fe(*N*-Methyl-^{5}L)Cl] and [Fe(*N*-Benzyl-^{5}L)Cl] (with n=1; R_1=H, methyl, benzyl).

new series of pentadentate ligands N–X–$^5LH_2$ (X=H, Methyl, Benzyl)=N–X–saldptn (4-X-*N*,*N*′-bis(1-hydroxy-2-benzylidene)-1,7-diamino-4-azaheptane) has been prepared by a Schiff base condensation reaction between 4-X-1,7-diamino-4-azaheptane and salicylaldehyde.

The question is weather the effect of *N*-substitution results in a sterical or electronic contribution to the magnetic and electronic behaviour of the multistability in both the Fe (III) units and nonanuclear complex compounds.

2 Experimental

The main strategy for the synthesis was performed in analogy to the literature [8, 9].

2.1 Ligands: ^{5}L, *N*-Methyl-^{5}L and *N*-Benzyl-^{5}L

The pentadentate ligands ^{5}L=*N*,*N*′-bis(1-hydroxy-2-benzylidene)-1,7-diamino-4-azaheptane, *N*-Methyl-^{5}L=*N*,*N*′-bis(1-hydroxy-2-benzylidene)-1,7-diamino-4-methylazaheptane and *N*-Benzyl-^{5}L=*N*,*N*′-bis(1-hydroxy-2-benzylidene)-1,7-diamino-4-benzylazaheptane (see Figure 1) were each formed in a Schiff base condensation reaction of salicylaldehyde and the appropriate amine. Both, the salicylaldehyde (0.05 mol) and the amine (0.025 mol), were dissolved in methanol (20 cm^3), slowly mixed together, and heated under reflux for 10 min. The resulted yellow mixture was used without any purification for the preparation of the precursor.

2.2 Precursors [Fe(^{5}L)Cl], [Fe(*N*-Methyl-^{5}L)Cl] and [Fe(*N*-Benzyl-^{5}L)Cl]

A solution of anhydrous iron (III) chloride (25 mmol) in methanol (50 cm^3) was added to the freshly prepared solution of the pentadentate ligand. The mixture was boiled and then triethylamine (50 mmol) was added (see Figure 1). The resulting solution was then heated under reflux for 1h. After cooling, crystals precipitated. These were collected and recrystallized in methanol and dried in vacuum.

[Fe(^{5}L)Cl]: Yield: 71% rel. to Fe (M=428 g/mol). Analysis calculated: for $C_{20}H_{23}ClFeN_3O_2$ (%): C(56.03), N(9.80), H(5.41); with 0.2 CH3OH C(55.76) N(9.66) H(5.51); found: C(55.20), N(10.38), H(5.25). IR (KBr): ν(cm^{-1})=3,235 cm^{-1} (N–H, valence strech=val.), 2,927 cm^{-1} (CH_2, val.), 1,625 cm^{-1} (C=N, val.), 1,500–1,600 cm^{-1} (aromat. C=C, val.), 750–760 cm^{-1} (C–H, out of plane=o.o.p.). FD MS m/z=428.0 (3.2%, [Fe(^{5}L)Cl]$^+$), 393.1 (100.0%, [Fe(^{5}L)]$^+$).

[Fe(*N*-Methyl-^{5}L)Cl] Yield: 68% rel. to Fe (M=442 g/mol). Analysis calculated: for $C_{21}H_{25}ClFeN_3O_2$ (%): C(56.97), N(9.49), H(5.69); with 0.5 CH3OH C(56.29) N(9.16) H(5.93); found: C(55.48), N(10.79), H(5.84). IR (KBr): ν(cm^{-1})=2,927 cm^{-1} (CH_2, val.), 1,625 cm^{-1} (C=N, val.), 1,500–1,600 cm^{-1} (aromat. C=C, val.), 760–770 cm^{-1} (C–H, out

of plane=o.o.p.). FD MS *m/z*=442.9 (3.2%, [Fe(*N*-Methyl-^{5}L)Cl]$^+$), 408.0 (100.0%, [Fe(*N*-Methyl-^{5}L)]$^+$).

[Fe(*N*-Benzyl-^{5}L)Cl] Yield: 27% rel. to Fe (*M*=518 g/mol). Analysis calculated: for $C_{27}H_{29}ClFeN_3O_2$ (%): C(62.49), N(8.10), H(5.63); with 2.8 CH3OH C(58.54) N(6.87) H(7.09); found: C(57.86), N(7.25), H(5.71). IR (KBr): ν(cm^{-1})=2,923 cm^{-1} (CH_2, val.), 1,616 cm^{-1} (C=N, val.), 1,500–1,600 cm^{-1} (aromat. C=C, val.), 750–760 cm^{-1} (C–H, out of plane=o.o.p.). FD MS *m/z*=518.7 (1.6%, [Fe(*N*-Benzyl-^{5}L)Cl]$^+$), 483.3 (62.2%, [Fe(*N*-Benzyl-^{5}L)]$^+$).

2.3 Nonanuclear complexes [Mo^{IV}{(CN) Fe^{III}(^{5}L)}$_8$]Cl$_4$, [Mo^{IV}{(CN) Fe^{III} (*N*-Methyl-^{5}L)}$_8$]Cl$_4$ and [Mo^{IV}{(CN) Fe^{III}(*N*-Benzyl-^{5}L)}$_8$]Cl$_4$

The complexes were each prepared following a universal precept. 0.001 mol of the precursor were dissolved in methanol (100 cm^3) and an aqueous methanol (1:1) solution (10 cm^3) of $K_4[Mo(CN)_8]\cdot 2H_2O$ (0.25 mmol) was added dropwise. After 30 min of stirring at room temperature the solution was filtered and reduced under pressure to 50 cm^3 (below 35°C). Addition of 150 ml distilled water precipitates the product, which was slowly filtered off on the frita funnel. The product was washed with distilled water and diethylether and dried under vacuum for 24 h.

[Mo^{IV}{(CN) Fe^{III}(^{5}L)}$_8$]Cl$_4$: Yield: 35% rel. to Mo (*M*=3,586.5 g/mol). Analysis calculated for $C_{168}H_{184}Cl_4Fe_8MoN_{32}O_{16}$ (%): C(56.18), N(12.48), H(5.16); with 3.8 KCl C (51.97) N(11.54) H(4.78); found: C(51.43), N(13.37), H(5.73). Note that a too low carbon content is commonly observed and based on incomplete decomposition to CO_2 due to formation of stable metal carbides. IR (KBr): ν(cm^{-1})=3,420 cm^{-1} (N–H, val.), 2,925 cm^{-1} (CH_2, val.), 2,129 cm^{-1} (C≡N, val.), 1,628 cm^{-1} (C=N, val.), 1,500–1,600 cm^{-1} (aromat. C=C, val.), 750–760 cm^{-1} (C–H, o.o.p.).

[Mo^{IV}{(CN) Fe^{III}(*N*-Methyl-^{5}L)}$_8$]Cl$_4$: Yield: 24% rel. to Mo (*M*=3,698.5 g/mol). Analysis calculated for $C_{176}H_{200}Cl_4Fe_8MoN_{32}O_{16}$ (%): C(57.07), N(12.10), H(5.44); with 5.4 KCl C(51.47) N(10.91) H(4.91); found: C(50.98), N(12.90), H(5.67). IR (KBr): ν(cm^{-1})=3,425 cm^{-1} (N–H, val.), 2,924 cm^{-1} (CH_2, val.), 2,117 cm^{-1} (C≡N, val.), 1,625 cm^{-1} (C=N, val.), 1,500–1,600 cm^{-1} (aromat. C=C, val.), 750–760 cm^{-1} (C–H, o.o.p.).

[Mo^{IV}{(CN) Fe^{III}(*N*-Benzyl-^{5}L)}$_8$]Cl$_4$: Yield: 21% rel. to Mo (*M*=4,306.5 g/mol). Analysis calculated for $C_{224}H_{232}Cl_4Fe_8MoN_{32}O_{16}$ (%): C(62.38), N(10.39), H(5.42); with 0.1 CH3OH 4.6 KCl C (57.77) N (9.62) H (5.03); found: C(57.61), N(10.38), H(5.54). IR (KBr): ν(cm^{-1})=3,422 cm^{-1} (N–H, val.), 2,925 cm^{-1} (CH_2, val.), 2,114 cm^{-1} (C≡N, val.), 1,621 cm^{-1} (C=N, val.), 1,500–1,600 cm^{-1} (aromat. C=C, val.), 750–760 cm^{-1} (C–H, o.o.p.).

2.4 Mössbauer spectroscopy

A conventional spectrometer has been used for measuring the Mössbauer spectra between liquid helium and room temperature (^{57}Co/Rh source, calibration at α-Fe at room temperature; isomer shifts are relative to the source).

3 Results and discussion

Table I shows the temperature-dependent Mössbauer spectra of the [Fe(N–X–^{5}L)Cl] precursor compounds. At 300 K the Mössbauer spectra exhibit a quadrupole splitted

Table I Mössbauer parameters of the iron precursors

Iron precursors	State 1			State 2		
	δ (mm/s)	Δ (mm/s)	mol%	δ (mm/s)	Δ (mm/s)	mol%
Mössbauer parameters 300 K						
^{5}3,3-LFeCl	0.256	0.716	100	–	–	–
N-Methyl-^{5}3,3-LFeCl	0.255	1.494	100	–	–	–
N-Benzyl-^{5}3,3-LFeCL	0.269	0.812	100	–	–	–
Mössbauer parameters 20 K						
^{5}3,3-LFeCl	0.364	0.701	100	–	–	–
N-Methyl-^{5}3,3-LFeCl	0.354	1.502	100	–	–	–
N-Benzyl-^{5}3,3-LFeCL	0.378	0.806	73	0.352	1.660	27

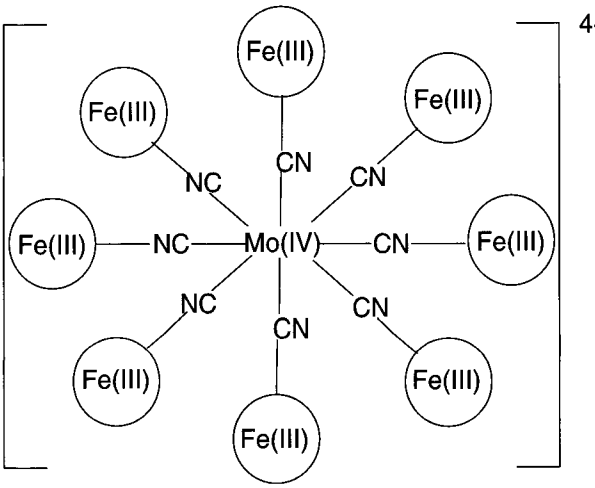

Figure 2 Schematic structure of $[Mo^{IV}\{(CN)\ Fe^{III}(^5L)\}_8]^{4+}$, $[Mo^{IV}\{(CN)\ Fe^{III}(N\text{-Methyl-}^5L)\}_8]^{4+}$ and $[Mo^{IV}\{(CN)\ Fe^{III}(N\text{-Benzyl-}^5L)\}_8]^{4+}$.

doublet which is slightly broadened due to an upcoming appearance of relaxation, common for Fe(III) in the HS state (S=5/2) [8, 9]. At 20 K the quadrupole splitted doublet is broadened due to relaxation and characteristic for Fe(III) in the HS state [8, 9]. For Fe(III) ions in the high-spin state ($^6A_{1g}$) the expected electronic contribution to the quadrupole splitting is expected to be zero. Nevertheless the Fe(III)-*N*-Methyl compound reveals an enormous 1.5 mm/s. That is doubled the value for analogous compounds. After assemblation into the nonanuclear units the 1.5 mm/s appear reduced to normal values. This indicates a transition between at least two structural deformations within the octahedral compound, the so-called high-spin high-spin transition. For the *N*-Benzyl compound a similar quadrupole splitted (1.66 mm/s) fraction occurs at 20 K.

The prepared nonanuclear complex has been characterized by IR spectrum and M+-peaks in mass spectroscopy. No evidence for a splitting of the characteristic C–N stretching vibration band indicates a highly symmetric coordination sphere around the central Mo(IV) atom (Figure 2), i.e. either all eight or none of the cyanides are bridged. The shift of the CN-band from 2,200 to 2,129, 2,117, and 2,114 cm^{-1} indicates a bridge.

Figure 3 and Table II show the temperature-dependent Mössbauer spectra of the nonanuclear compounds $[Mo^{IV}\{(CN)Fe^{III}(N\text{–}X\text{–}^5L)\}_8]Cl_4$. At 300 K a quadrupole splitted

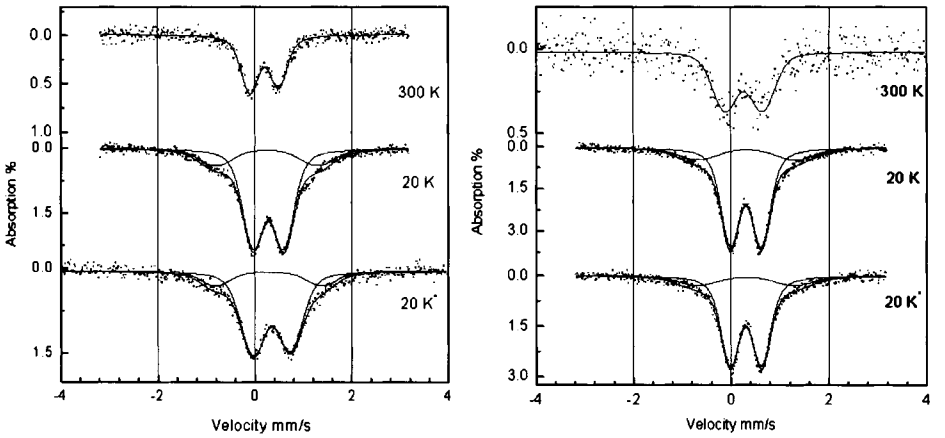

Figure 3 Mössbauer spectra of the nonanuclear compounds $[Mo^{IV}\{(CN)Fe^{III}(N\text{-Methyl-}^5L)\}_8]Cl_4$ (*left*) and $[Mo^{IV}\{(CN)Fe^{III}(N\text{-Benzyl-}^5L)\}_8]Cl_4$ (*right*) at 300 K, 20 K and at 20 K under light irradiation (25 mW/cm^2, 514.5 nm of green argon ion laser).

Table II Mössbauer parameters of the nonanuclear compounds at 300 K and 20 K

Complex	State 1			State 2		
	δ (mm/s)	Δ (mm/s)	mol%	δ (mm/s)	Δ (mm/s)	mol%
Mössbauer parameters 300 K						
$[(^5$3,3-LFeNC)$_8$Mo]Cl$_4$	0.208	0.580	100	–	–	–
[(*N*-Methyl-^{5}3,3-LFeNC)$_8$Mo]Cl$_4$	0.195	0.594	100	–	–	–
[(*N*-Benzyl-^{5}3,3-LFeNC)$_8$Mo]Cl$_4$	0.263	0.768	100	–	–	–
Mössbauer parameters 20 K						
$[(^5$3,3-LFeNC)$_8$Mo]Cl$_4$	0.337	0.695	68.1	0.161	2.283	31.9
[(*N*-Methyl-^{5}3,3-LFeNC)$_8$Mo]Cl$_4$	0.282	0.633	78.4	0.246	2.100	21.6
[(*N*-Benzyl-^{5}3,3-LFeNC)$_8$Mo]Cl$_4$	0.302	0.636	80.3	0.310	2.000	19.7

Table III Mössbauer parameters of the nonanuclear compounds at 20 K under light irradiation (25 mW/cm^2, 514.5 nm green argon ion laser)

Complex	State 1			State 2		
Mössbauer parameters 20 K	δ (mm/s)	Δ (mm/s)	mol%	δ (mm/s)	Δ (mm/s)	mol%
$[(^5$3,3-LFeNC)$_8$Mo]Cl$_4$	0.324	0.763	69.8	0.189	2.387	30.2
[(*N*-Methyl-^{5}3,3-LFeNC)$_8$Mo]Cl$_4$	0.349	0.773	82.3	0.284	2.200	17.7
[(*N*-Benzyl-^{5}3,3-LFeNC)$_8$Mo]Cl$_4$	0.300	0.643	82.9	0.300	2.000	17.1

doublet is observed which is slightly broadened due to relaxation, common for Fe(III) in the HS state (S=5/2) [8, 9]. In comparison to the precursors the isomer shifts are lowered by 0.05 for N–H and *N*-Methyl, but remains constant for *N*-Benzyl. The giant quadrupole splitting in the *N*-Methyl precursor compound of 1.494 dropped to 0.594 mm/s in the nonanuclear compound. For the *N*-Benzyl this change is faint with less than 0.04 mm/s.

At 20 K the Mössbauer spectrum shows in addition to the Fe(III) in the HS state a second doublet which is characteristic for a Fe(III) in the LS state [8, 9], for the N–H compound, in its quadrupole splitting while its isomer shift is quite close to the Fe(III)-HS state, for *N*-Methyl and *N*-Benzyl compound. This indicates that in the nonanuclear complexes $[Mo^{IV}\{(CN)Fe^{III}(N–X–^{5}L)\}_8]Cl_4$ a thermally induced transition occurs: a HS to LS transition and/or a HS to HS transition. The area fractions of the respective doublets A (Fe^{III}-S1)/A(Fe^{III}-S2) indicate that several Fe(III) centers switch, i.e. multiple electronic transitions.

Table III shows the effect of green light irradiation. The light slightly alters the population of both states reversibly.

Acknowledgments This work was partly funded by the University of Mainz ("Forschungsfond";"Material-Wissenschaftliches Forschungs-Zentrum" MWFZ) and the "Deutsche Forschungsgemeinschaft" (DFG: Re-1627/1-3).

References

1. McCusker, J.K., Schmitt, E.A., Hendrickson, D.N.: In: Gatteschi, D., Kahn, O., Miller, J.S., Palacio, F. (eds.) Magnetic Molecular Materials. NATO ASI Series, vol. 198, p. 297. Kluwer, Dordrecht (1991)
2. Kahn, O.: Molecular Magnetism. VCH, New York (1993)
3. Gatteschi, D.: Molecular magnetism. In: Coronado, E., Delhaes, P., Gatteschi, D., Miller, J.S. (eds.) From Molecular Assemblies to the Devices. NATO ASI Series, vol. 321, p. 141, 289. Kluwer, Dordrecht (1996)
4. Gütlich, P., Garcia, Y., van Koningsbruggen, P.J., Renz, F.: In: Palacio, F., Schweizer, J., Ressouche, E. (eds.) Introduction to Physical Techniques in Molecular Magnetism, Part I – Structural and Magnetic Methods. University Press, Zaragoza, Spain (2000)
5. Gütlich, P., van Koningsbruggen, P.J., Renz, F.: Struct. Bond. **107**, 27–75 (2004)
6. Gadet, V., Bujoli-Doeuff, M., Force, L., Verdaguer, M., ElMalkhi, K., Deroy, A., Besse, J.P., Chappert, C., Veillet, P., Renard, J.P., Beauvillain, P.: In Gatteschi, D., Kahn, O., Miller, J.S., Palacio, F. (eds.) Magnetic Molecular Materials. NATO ASI Series, vol. 198, p. 281. Kluwer, Dordrecht (1991)
7. Herchel, R., Boča, R., Gembicý, M., Kožišek, J., Renz, F.: Inorg. Chem. **43**, 4103–4105 (2004)
8. Renz, F., Kerep, P.: Polyhedron **24**, 2849–2851 (2005)
9. Renz, F., Kerep, P.: Hyperfine Interact. **156**, 371–377 (2004)
10. Gembicky, M., Boca, R., Renz, F.: Inorg. Chem. Commun. **3**, 662–665 (2000)
11. Matsumoto, N., Ohta, S., Yoshimura, C., Ohyoshi, A., Kohata, S., Okawa, H., Maeda, Y.: J. Chem. Soc., Dalton Trans. 2575 (1985)
12. Ohyoshi, A., Honbo, J., Matsumoto, N., Ohta, S., Sakamoto, S.: Bull. Chem. Soc. Jpn. **59**, 1611 (1986)
13. Ohta, S., Yoshimura, C., Matsumoto, N., Okawa, H., Ohyoshi, A.: Bull. Chem. Soc. Jpn. **59**, 155 (1986)
14. Boča, R., Fukuda, Y., Gembický, M., Herchel, R., Jaroščiak, R., Linert, W., Renz, F., Yuzurihara, J.: Chem. Phys. Lett. **325**, 411 (2000)

Hyperfine Interact (2006) 168:1057–1063
DOI 10.1007/s10751-006-9395-1

Mössbauer, X-ray diffraction and magnetization studies of Fe–Mn–Al–Nb alloys prepared by high energy ball milling

Ligia E. Zamora · G. A. Perez Alcazar · J. M. Greneche · S. Suriñach

Published online: 5 December 2006

Abstract $Fe_{60}Mn_{10}Al_{20}Nb_{10}$, $(Fe_{60}Mn_{10}Al_{30})_{95}Nb_5$ and $(Fe_{60}Mn_{10}Al_{30})_{90}Nb_{10}$ ball milled powdered alloys were investigated using X-ray diffraction, Mössbauer spectrometry, thermomagnetic (TGM) and magnetization measurements. We studied the influence of Nb content and of different milling times on the structural and magnetic properties. Two main features can be concluded: (1) the FeAlMn induces a BCC phase whatever the Nb content is, and (2) as both increasing Nb content and milling time give rise to an highly disordered state in conjunction with a decrease of the ferromagnetic behavior.

Key words ^{57}Fe Mössbauer spectrometry · X-ray diffraction · milled metallic powders · Nb alloys

1 Introduction

The FeAlMn system has been studied by several researchers using different techniques [1–5]. This system exhibits different magnetic and structural behaviors depending on both the type and concentration of the elements and on the temperature as well. It was proved that the $Fe_{60}Mn_{10}Al_{30}$ and $Fe_{55}Mn_{25}Al_{20}$ ternary alloys are ferromagnetic at room temperature and present a semi-soft magnetic character with coercive fields close to 80 Oe [5].

Otherwise, the effect of Nb in Fe containing alloys remains interesting. Indeed, FeAlNb alloys are studied and developed due to their excellent oxidation and high-temperature corrosion properties [6, 7]. FeNbB based alloys, with crystallite sizes less than 100 nm,

L. E. Zamora (✉) · G. A. Perez Alcazar
Physics Department, Universidad del Valle, A. A. 25360 Cali, Colombia
e-mail: lizamora@univalle.edu.co

J. M. Greneche
Laboratoire de Physique de L'Etat Condensé, UMR CNRS 6087, Université du Maine, 72085, Le Mans, Cedex 9, France

S. Suriñach
Facultad de Ciencias, UAB 08193, Barcelona, Spain

have attracted attention due to their magnetic properties such as effective permeability and saturation magnetic flux density. These properties indicate that these materials may have applications in magnetic parts and devices such as inductors, transformers, and motors [8].

It has been established that the presence of Nb atom in magnetic materials improves the soft magnetic behavior. Kobayashi et al. [9] showed that the total resulting magnetic moment decreases significantly in FeNb alloys, due to the presence of antiferromagnetic interactions induced by the increasing Nb content. When $Fe_{52}Nb_{48}$ and $Fe_{36}Nb_{64}$ alloys were mechanically alloyed [10], the milled powders exhibit an amorphous state and behave as a paramagnet at 300 K. Also the Fe_xNb_{100-x} samples with $x < 60$ are nonmagnetic at room temperature [11].

In order to improve the soft magnetic properties of FeMnAl melted alloys, it was introduced Nb in them, and the preliminary results were presented in [12].

In this work we report the results of the study of the magnetic and hyperfine properties of $Fe_{60}Mn_{10}Al_{20}Nb_{10}$, $(Fe_{60}Mn_{10}Al_{30})_{95}Nb_5$ and $(Fe_{60}Mn_{10}Al_{30})_{90}Nb_{10}$ systems, prepared by mechanical alloying for different milling times.

2 Experimental

Mechanical alloying was carried out in a planetary high-energy ball mill starting from elements with more than 99.8% purity and with a powder-to-ball weight ratio of 1:15. Both vials and balls used are made of hardened chromium steel. Powders with nominal compositions $Fe_{60}Mn_{10}Al_{20}Nb_{10}$ were milled for 12, 24 and 36 h, and $(Fe_{60}Mn_{10}Al_{30})_{95}Nb_5$ and $(Fe_{60}Mn_{10}Al_{30})_{90}Nb_{10}$ for 12 h. The milling was performed in Ar atmosphere in a pulverisette P7 Fritsch planetary ball mill.

The sample structures were determined by X-ray diffraction (XRD), the thermomagnetic measurements were carried out by thermal gravimetric analysis (TGA) in a temperature range from 300 to 800 K. The magnetic properties of the samples were studied at 300 K using a vibrating-sample magnetometer (VSM) with a maximum applied field (H) of 10 kOe. The structural and microstructural parameters were refined from the X-ray pattern using the MAUD procedure which is based on the Rietveld method combined with Fourier analysis: the grain size and the microstrain were evaluated by means of the Warren–Averbach procedure [13]. Mössbauer spectra were performed at 300 K using a conventional spectrometer with a ^{57}Co (Rh) source. The spectra were fitted using the MOSFIT program (unpublished MOSFIT program) including a hyperfine field distribution (HFD) and, in most of the cases, additional quadrupolar doublets, all components composed of lorentzian lines.

3 Results and discussion

3.1 $Fe_{60}Mn_{10}Al_{20}Nb_{10}$ powders milled for 12, 24 and 36 h

Figure 1a shows the XRD patterns obtained on the $Fe_{60}Mn_{10}Al_{30}$ alloy milled for 12 h and on the $Fe_{60}Mn_{10}Al_{20}Nb_{10}$ alloys milled for 12, 24 and 36 h. One observes that the ternary system is BCC at 12 h, while the Nb is not completely consumed, at this time, because of remaining peaks due to elemental Nb. Then, these peaks disappear as the milling time increases, while the BCC peaks are broadened. These results show that the $Fe_{60}Mn_{10}Al_{20}Nb_{10}$ system presents a tendency to reach a highly disordered state with the increasing

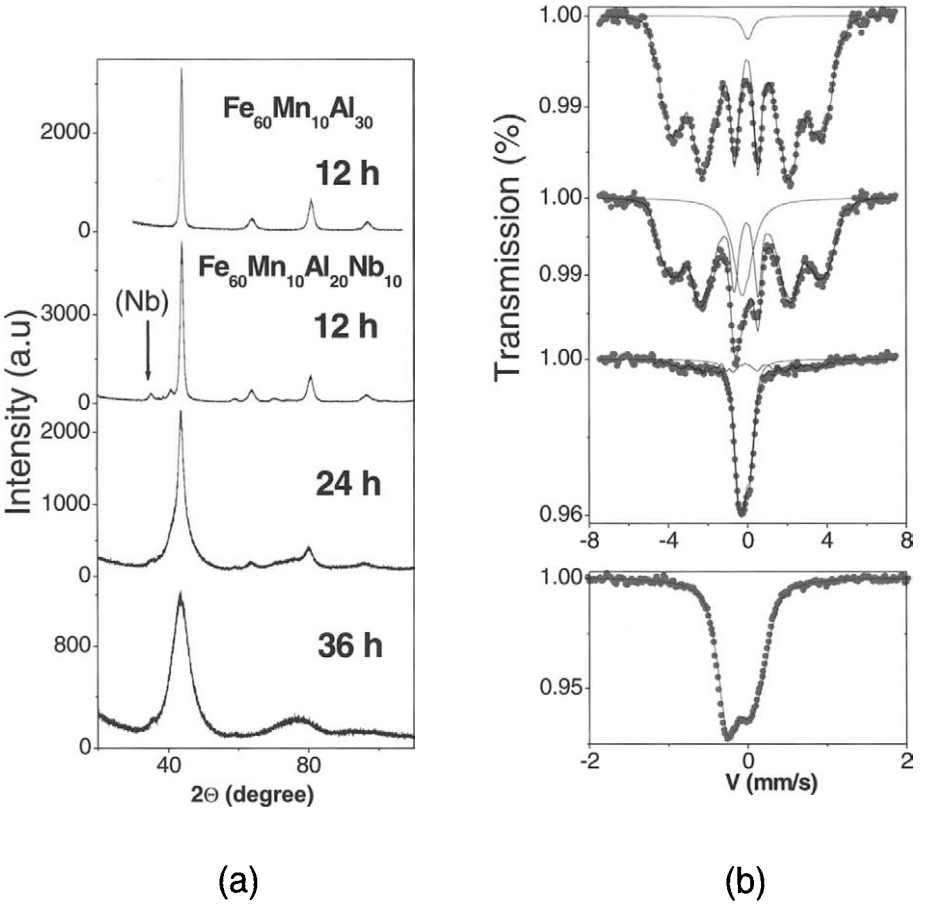

Figure 1 XRD patterns (**a**) and Mössbauer spectra (**b**) obtained on the $Fe_{60}Mn_{10}Al_{30}$ alloy milled for 12 h and on the $Fe_{60}Mn_{10}Al_{20}Nb_{10}$ alloys milled for 12, 24 and 36 h.

Table I Mössbauer data obtained for ($Fe_{60}Mn_{10}Al_{30}$) with 12 h of milling time and for ($Fe_{60}Mn_{10}Al_{20}Nb_{10}$) with 12, 24 and 36 h milling time

Nb	Milling time (h)	$<B_{hf}>$ (T) ±2	Paramagnetic area (%) ±2
0	12	20	2
10	12	18	13
10	24	5	70
10	36	0	100

milling time, either an amorphous state or a dense random packing of nanoclusters of about 2 nm diameters.

Corresponding Mössbauer spectra which are shown in Figure 1b, were fitted using a magnetic hyperfine field distribution and a quadrupolar splitting distribution, except the last one which can be described using only a quadrupolar splitting distribution. The averaged hyperfine field (resulting from both ferromagnetic and paramagnetic components) and the

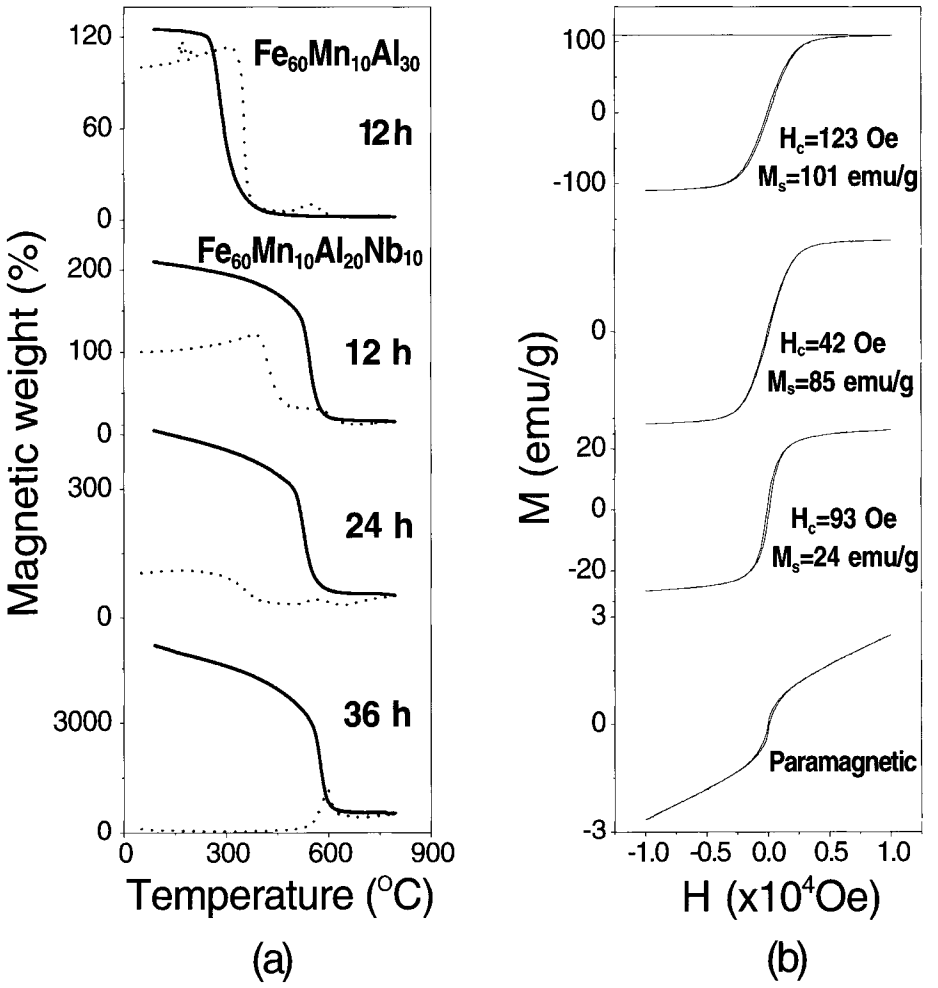

Figure 2 TGM (**a**) and hysteresis loops (**b**) obtained on the $Fe_{60}Mn_{10}Al_{30}$ alloy milled for 12 h and on the $Fe_{60}Mn_{10}Al_{20}Nb_{10}$ alloys milled for 12, 24 and 36 h.

fraction of paramagnetic phase were derived and reported in Table I. We can note that when Nb substitutes Al atoms in samples milled during 12 h, the mean hyperfine field decreases while the paramagnetic area increases. This result shows that the presence of Nb atoms originates a decrease of the ferromagnetic behavior, maybe as a consequence of its tendency to produce antiferromagnetic bonds, while the Al atoms decrease this behavior due its diluting character. Also, we can note that the ferromagnetic behavior is strongly affected in the system with Nb as the milling time increases.

In Figure 2a TGM heating (dashed line) and cooling (continuous line) curves are displayed for these samples. For all samples the curves heating show two transitions, at about 350 and 550°C. The first one, is associated to a ferro-to paramagnetic transition in agreement with previous reports for FeAl and FeMnAl disordered alloys [3, 14], and the second one to a chemical and/or structural reordering. The sample milled for 36 h presents

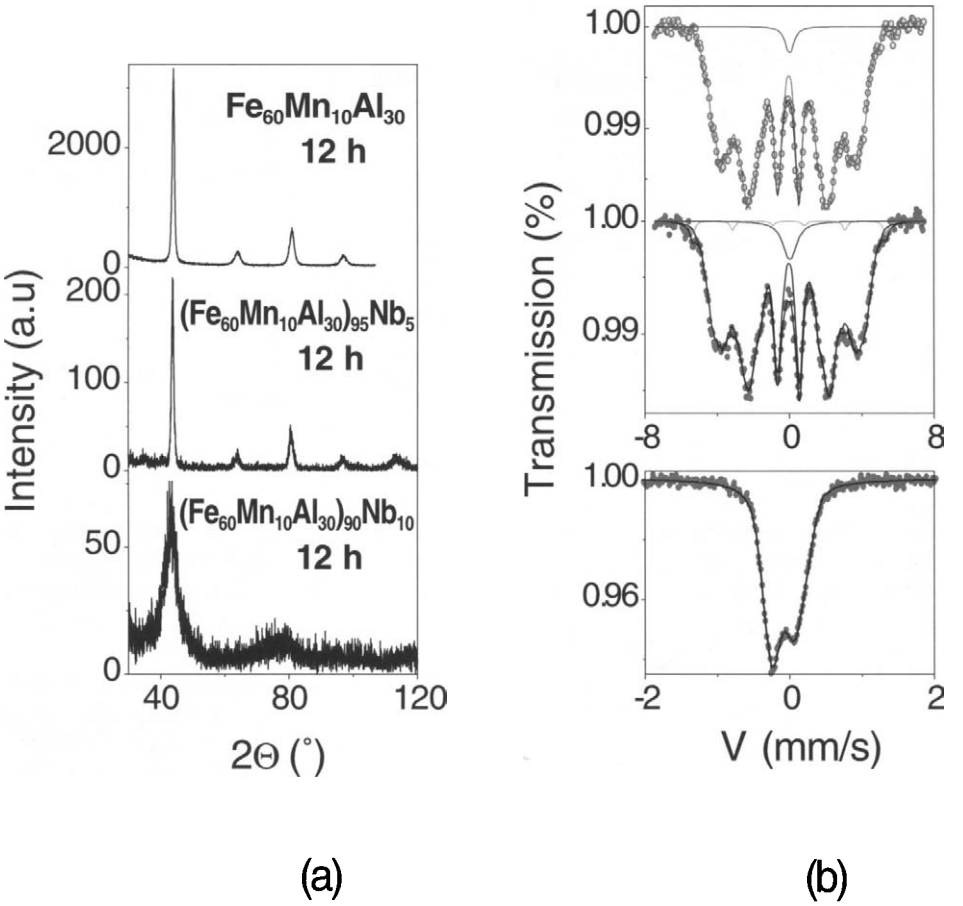

Figure 3 XRD patterns (**a**) and Mössbauer spectra (**b**) obtained on the $Fe_{60}Mn_{10}Al_{30}$ $(Fe_{60}Mn_{10}Al_{30})_{95}Nb_5$ and $(Fe_{60}Mn_{10}Al_{30})_{90}Nb_{10}$ alloys milled for 12 h.

only the second transition, in agreement with its paramagnetic character at room temperature. Thus, TGM curves completely confirm the Mössbauer results.

The cooling curves show, a transition F–P at about 300°C for the sample without Nb, while this transition approximately at the same value (near 560°C) for the samples with Nb is attributed to a para-ferromagnetic transition. Indeed, the emergence of ferromagnetic behavior is favored by the structural, which is a priori independent of the alloying conditions. Then, for heat-treated Nb containing samples, the ferromagnetic behavior is reinforced, while for the sample without Nb this behavior decreases. Some further experiments are now in progress in order to explain these results.

From the hysteresis loops at RT, showed in Figure 2b, the saturation magnetization, Ms, and the coercive field, Hc, were evaluated. Comparing the first and second graphs of this figure, it can be noted that the substitution of Nb by Al decreases the Ms value, from 101 to 85 emu/g. It can be also noted that the increase of milling time yields the decrease of the Ms value. The Hc value decreases from 123 to 42 Oe when Al atoms are substituted by Nb, improving in this way the soft magnetic character of the sample. However, it is not possible to see a clear tendency when the milling time changes.

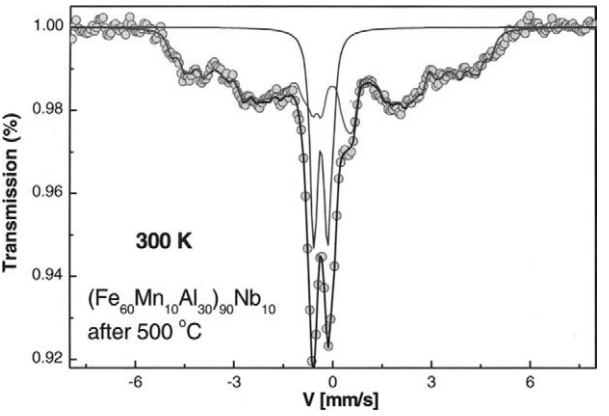

Figure 4 Mössbauer spectrum for after rapid heating up to 500°C for $(Fe_{60}Mn_{10}Al_{30})_{90}Nb_{10}$, 12 h.

3.2 $(Fe_{60}Mn_{10}Al_{30})_{100-x}Nb_x$ system with x = 0, 5 and 10 milled for 12 h

In Figure 3 are shown the results obtained from $(Fe_{60}Mn_{10}Al_{30})_{100-x}Nb_x$ system with x = 0, 5 and 10 and milling time of 12 h. In Figure 3a and b are shown both, the XRD pattern and Mössbauer spectra, respectively. It is possible to see that adding Nb to the system induces the structural disorder of the samples as in the case of previous powders, and that the magnetization disappears for x = 10 at 300 K.

Similar TGM curves were observed for these samples, suggesting thus that the behavior is very similar to that showed for the alloys with Nb of the previous system. The current samples were heating up to 800°C and all show a magnetic behavior when the samples were measured again after cooling. To prove this, we select the $(Fe_{60}Mn_{10}Al_{40})_{90}Nb_{10}$ alloy. In the original one (before heating) the Mössbauer spectrum shows a paramagnetic character (Figure 3). After a rapid heating up to 500°C, the 300 K Mössbauer spectrum (Figure 4) consists of a broad line sextet superimposed to a central quadrupolar doublet: such a feature confirms that a reordering occurs, originating thus a ferromagnetic behavior, even at 300 K, in the same way of previous samples.

4 Conclusions

This study clearly demonstrates that (1) the presence of Nb atoms in the FeMnAl alloys induces structural disorder and lowers ferromagnetic behavior, probably due to the antiferromagnetic nature of interactions, and (2) a subsequent annealing favors structural reordering of powders, giving rise thus to the reoccurrence of ferromagnetic behavior, whatever the milling time is and whatever the preparation conditions.

Acknowledgements The authors would like to thank Colciencias (Colombian Agency), Universidad del Valle and the French and Colombian Ecos–Nord exchange program (CF03P01) for financial support. We are grateful to A. M. Mercier from Laboratoire des Oxyfluorures of Université du Maine UMR CNRS 6010 for performing XRD measurements.

References

1. Kobeissi, M.A.: J. Phys.: Condens. Matter **3**, 4983 (1991)
2. Mohan Babu, T.V.S.M., Bansal, C.: Phys. Stat. Sol. (b) **193**, 167 (1996)

3. Zamora, L.E., Pérez Alcázar, G.A., Bohórquez, A., Marco, J.F., González, J.M.: J. Appl. Phys. **82**, 6165 (1997)
4. González, C., Pérez Alcázar, G.A., Zamora, L.E., Tabares, J.A., Greneche, J.M.: J. Phys., Condens. Matter **14**, 6531 (2002)
5. Restrepo, J., González, J.M., Pérez Alcázar, G.A.: J. Appl. Phys. **87**, 7425 (2000)
6. Morris, D.G., Requejo, L.M., Munoz-Morris, M.A.: Intermetallics **13**, 863–871 (2005)
7. Baligidad, R.G.: Mater. Sci. Eng. **A368**, 131–138 (2004)
8. Suñol, J.J., González, A., Taurina, J., Escoda, Ll., Bruna, P.: Mater. Sci. Eng. A **375–377**, 874–880 (2004)
9. Kobayashi, M., Kai, T., Takano, N., Ohashi, Y., Shiiki, K.: J. Magn. Magn. Mater. **166**, 329–333 (1997)
10. Jartych, E., Oleszak, D., Zurawicz, J.K.: Hyperfine Interact. **136**, 25–33 (2001)
11. Chien, C.L., Unruh, K.M., Liou, S.H.: J. Appl. Phys. **53**, 7756 (1982)
12. Zamora, L.E., Pérez Alcazar, G.A., Greneche, J.M., Valderruten, J.F.: Hyperfine Interact. **148/149**, 91–96 (2003)
13. Lutterotti, L., Scardi, P.: J. Appl. Crystallogr. **23**, 246 (1990)
14. Pérez Alcázar, G.A., Plascak, J.A., Galvão da Silva, E.: Phys. Rev. B **38**, 2816 (1988)

Hyperfine Interact (2006) 168:1065–1071
DOI 10.1007/s10751-006-9406-2

CEMS study on diluted magneto titanium oxide films prepared by pulsed laser deposition

K. Nomura · K. Inaba · S. Iio · T. Hitosugi · T. Hasegawa · Y. Hirose · Z. Homonnay

Published online: 5 December 2006

Abstract 6% ^{57}Fe doped titanium oxide films, prepared by pulsed laser deposition (PLD) on sapphire substrate at 650°C under various vacuum conditions, were characterized mainly by conversion electron Mössbauer spectrometry (CEMS). Two magnetic sextets with hyperfine fields 33 and 29 T, and one doublet were observed in the CEMS spectra of TiO_2 films prepared under $PO_2 = 10^{-6}$ and 10^{-8} torr, which showed ferromagnetism at room temperature, whereas only the doublet of paramagnetic Fe^{3+} species was observed for the film prepared under $PO_2 = 10^{-1}$ torr.

Key words Conversion Electron Mössbauer Spectroscopy (CEMS) · Dilute Magnetic Semiconductor (DMS) · Ti oxide doped with Fe · pulsed laser deposition

1 Introduction

Dilute magneto-semiconductors (DMS) are new materials with both semiconductor and magnetic properties [1]. They are prospected as materials for spin electronics. DMS of

K. Nomura (✉) · S. Iio
School of Engineering, The University of Tokyo, 7-3-1 Hongo, Bunkyo-ku, Tokyo 113-8656, Japan
e-mail: k-nomura@t-adm.t.u-tokyo.ac.jp

K. Inaba
Materials and Structures Laboratory, Tokyo Institute of Technology, Yokohama 226-8503, Japan

T. Hitosugi · T. Hasegawa
School of Science, The University of Tokyo, 7-3-1 Hongo, Bunkyo-ku, Tokyo 113-8656, Japan

T. Hasegawa · Y. Hirose
Kanagawa Academy of Science and Technology, 3-2-1 Sakato, Takastu-ku, Kawasaki 213-0012, Japan

Z. Homonnay
Research Group for Nuclear Methods in Structural Chemistry, HAS and Department of Nuclear Chemistry ELTE, 1117 Budapest Pázmány P. s. 1/A, Budapest, Hungary

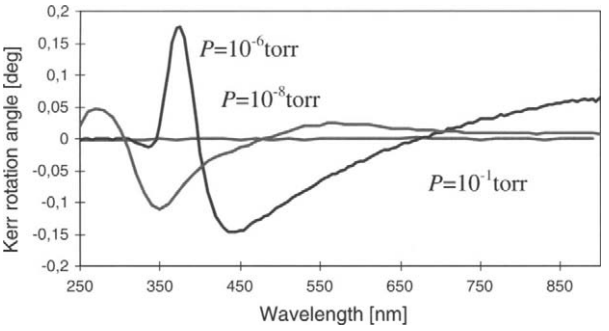

Figure 1 Relation between Kerr rotation angles and light wavelengths for 6% Fe doped TiO_2 films prepared at different oxygen pressures indicated.

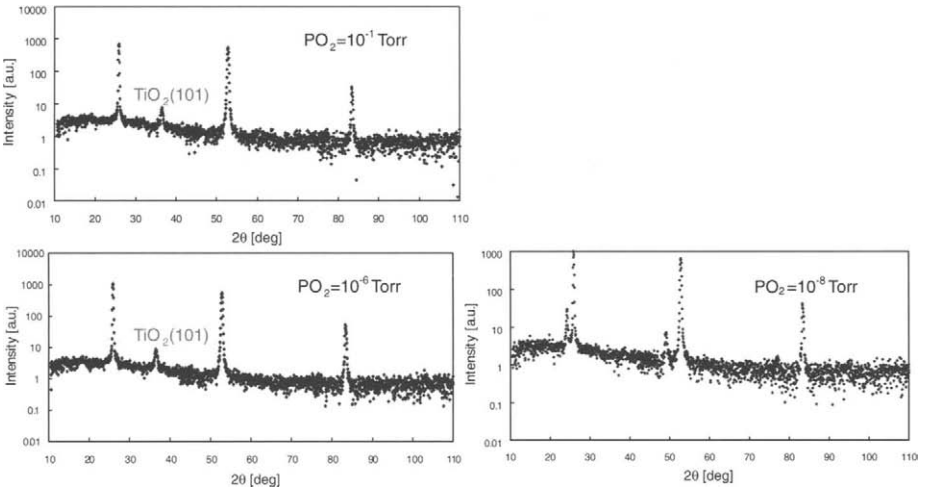

Figure 2 XRD patterns of TiO_2 films prepared under 10^{-1}, 10^{-6} and 10^{-8} torr by pulsed laser deposition. Three strong peaks are due to the substrate of γ Al_2O_3. TiO_2 peaks were observed together with three large peaks of sapphire substrate.

GaAs doped with Mn show ferromagnetism at low Curie temperatures ($Tc < 250$ K) [2]. It has been found recently that TiO_2 films doped with Co show transparent and ferromagnetic semiconducting properties at room temperature [3]. Wang et al. [4] showed that rutile type TiO_2 films doped with Fe show *p*-type semiconductivity, whereas anatase type TiO_2 films doped with Co are *n*-type semiconductors. H. M. Lee et al. [5] and Kim et al. [6] suggested, on the basis of transmission Mössbauer spectra of Fe doped TiO_2 powders that the ferromagnetism may be due to either electron carriers induced by substitution in the TiO_2 lattice or to the formation of granular magnetite. Inaba et al. [7] reported that Fe doped TiO_2 films prepared by PLD under $PO_2 = 10^{-6}$ torr and at the substrate temperature ranges of 600 to 675°C show the ferromagnetism and Kerr effect. In this paper, in order to make the chemical states of iron doped in TiO_2 films clear, these films were characterized by ^{57}Fe CEMS.

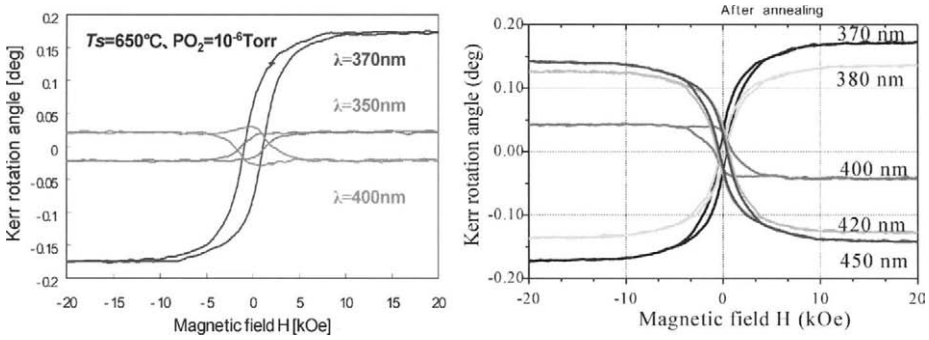

Figure 3 Hysteresis of the Kerr rotation angle on magnetic field and at various wavelengths before and after post-annealing at 300°C for 20 h in air and for 6 h in oxygen atmosphere.

2 Experimental

Titanium dioxide films with ca. 100 nm in thickness were prepared on sapphire substrates kept at 650°C under 10^{-1} to 10^{-8} torr by pulsed laser deposition (PLD) (KrF laser; wavelength: 248 nm, power: 5 J/cm^2, pulse: 6 ns, frequency: 2 Hz). The mixed pellet of 94 w/w%TiO_2 (of 99.9% purity) and 6 w/w% $^{57}Fe_2O_3$ (of 99.99% purity, ^{57}Fe: > 95%) was prepared by thermal treating at 1,200°C for 12 h in air, and was used as the target for PLD.

The as-prepared and post-annealed films were characterized by X-ray diffraction, scanning SQUID microscopy, magneto-optical measurements and Mössbauer spectrometry.

Conversion electron Mössbauer spectroscopy (CEMS) can provide us the characterization of a thin surface layer within ca.100 nm in thickness non-destructively and selectively. CEMS spectra of the TiO_2 films doped with 6% $^{57}Fe_2O_3$ were measured by using a home-made He + 5%CH_4 gas flow counter [8] and a gamma source of ^{57}Co(Cr) with the activity of 1.3 GBq. The Doppler velocity was calibrated using metallic iron foil.

3 Results and discussion

From the micro images by atomic force microscopy, the surface roughness over 25 nm^2 area increases from 0.47 to 1.9 nm with decreasing PO_2 from 1×10^{-1} torr to 1×10^{-8} torr. The ferromagnetic phases in the films prepared under 10^{-1}, 10^{-6} and 10^{-8} torr were observed by a scanning SQUID microscope. The scanning area was 200 × 200 μm. The films prepared under $PO_2 = 10^{-6}$ torr and at substrate temperature $T_s = 650$°C show strong Kerr effect as shown in Figure 1. Magnetic domain structures were clearly observed in ^{57}Fe doped TiO_2 films prepared in 10^{-6} torr, suggesting the presence of long range ordering of magnetic moment induced by Fe doping in these thin films.

It was confirmed by XRD as shown in Figure 2 that epitaxial (101) films of the rutile polymorph of TiO_2 were obtained for the samples prepared under 10^{-1} and 10^{-6} torr. On the other hand, other diffraction patterns, which might belong to TiO_2 with oxygen defects (i.e., Magneli, Ti_nO_{2n-1}), were observed for the films prepared under 10^{-8} torr. Inaba et al. [7] confirmed that the full width at half maximum (FWHM) of low angle peak is 0.4340, 0.4840, and 0.5230° for the films deposited for 10^{-4}, 10^{-6}, and 10^{-8} torr, respectively,

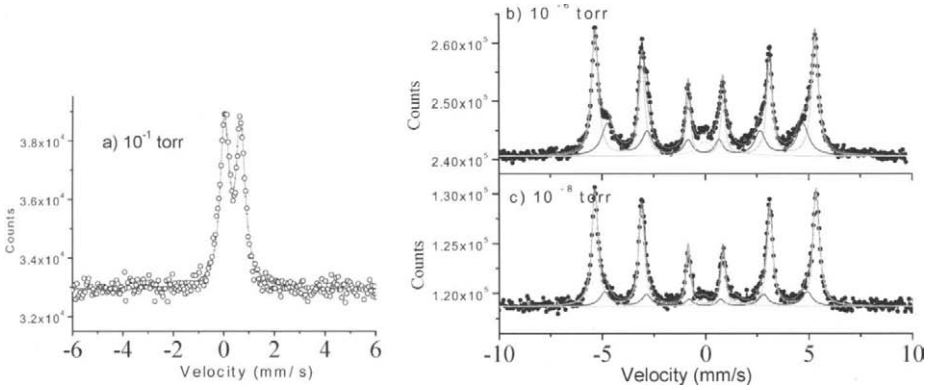

Figure 4 CEMS spectra of transparent titanium oxides deposited on sapphire heated at 650°C in **a** 10^{-1} torr, **b** 10^{-6} torr, and **c** 10^{-8} torr by pulsed laser ablation of 6%$^{57}Fe_2O_3$ + TiO_2 target. The substrate temperature: 650°C.

indicating that the lower crystallinity is obtained at the lower oxygen pressure. The distance between (101) faces increased with the decrease of the oxygen pressure (d = 0.2481, and 0.2517 nm) for 10^{-1}, and 10^{-6} torr, respectively, showing either higher oxygen defect concentration or incorporation of Fe species into the lattice (or both). These results lead to a conclusion that the crystallinity is not directly related to the ferromagnetism.

Hysteresis of the Kerr rotation angle on magnetic field and light wavelengths are shown in Figure 3, before and after post-annealing at 300°C for 20 h in air and for 6 h in oxygen atmosphere. The hysteresis curve became narrow by post-annealing, suggesting that the weaker magnetic fields can be applied.

As shown by the CEMS spectra in Figure 4, a doublet of paramagnetic Fe^{3+} was observed for transparent TiO_2 films prepared under the low vacuum condition of 10^{-1} torr. Two magnetic sextets and also a small amount of paramagnetic peaks were observed for the films prepared under 10^{-6} and 10^{-8} torr. The Mössbauer parameters are shown in Tables I and II. The parameters of paramagnetic peaks showing up together with the sextets were around isomer shift, δ = 0.37(2) mm/s and quadrupole splitting, Δ = 0.9(2) mm/s. It is assumed that the sextet with the larger magnetic field (B_{hf}) is due to metallic iron with δ = 0.0 mm/s and B_{hf} = 33.0 T (α-Fe). The other sextet with smaller B_{hf} = 29.5 T is ambiguous because it may be due to either finely dispersed metallic iron, Fe(Ti) alloy or high spin Fe^{4+} species incorporated in TiO_2 (the δ value of the latter is very close to 0). The assignment of this sextet will be further discussed later.

The peak intensities of the sextet with the smaller B_{hf} as well as those of the paramagnetic components were low for the TiO_2 films prepared under 10^{-8} torr. The question arises why the metallic iron detected in the samples prepared under 10^{-8} torr was not sensitive to scanning SQUID. It is assumed that, if the magnetic domains are much smaller than the probing scale of 5 μm in diameter, the vertical up and down magnetic moments due to spontaneous magnetization cancel each other and cannot be detected.

The internal relative peak intensities of the sextet with the smaller B_{hf} were different from those of the sextet with 33 T. The former indicates that the magnetic moments tend to align parallel to the surface by post annealing, whereas those with the large B_{hf} are rather random. If the sextet with a small B_{hf} is due to fine particles of metallic iron, post-annealing

Table I Mössbauer parameters of 6%Fe doped TiO_2 films prepared at 10^{-1} and 10^{-8} torr

Sample; 6% Fe + TiO_2 films	Partial	δ (mm/s)	Δ (mm/s)	B_{hf} (T)	Γ (mm/s)	Area (%)
650°C 1 × 10^{-1} torr	1	0.36	0.63	–	0.42	100
650°C 1 × 10^{-8} torr	1	0.00	0.06	30.0	0.60	17
	2	0.01	−0.00	33.2	0.36	80
	3	0.68	1.54	–	0.62	4

Table II CEMS parameters of 6%Fe doped TiO_2 films prepared at 650°C in 10^{-6} torr, and post-annealed at 300°C for various hours

Sample; 6% Fe + TiO_2 films	Partial	δ (mm/s)	Δ (mm/s)	B_{hf} (T)	Γ (mm/s)	Area (%)
As prepared	1	−0.02	0.10	29.5	0.58	29.4
	2	0.01	−0.03	33.0	0.35	63.6
	3	0.37	0.91	–	0.74	7.1
Post-annealed 300°C 20 h in air	1	0.02	0.04	29.4	0.59	31.4
	2	0.02	−0.03	32.9	0.34	59.5
	3	0.43	0.85	–	0.67	9.1
(*b*) + 300°C 3 h in O_2	1	0.04	0.13	29.5	0.57	30.4
	2	0.01	−0.01	33.0	0.33	57.8
	3	0.35	0.87	–	0.86	11.7
(*b*) + 300°C 6 h in O_2	1	0.01	0.06	29.7	0.66	32.6
	2	0.03	−0.02	32.9	0.32	55.0
	3	0.37	0.95	–	0.69	12.4
400°C 16 h in O_2	1	0.41	−0.14	48.3	1.18	31.6
	2	0.38	0.73	–	0.59	68.4

of the films may induce agglomeration of small particles to form large ones, or the easy oxidation of small particles. In the Mössbauer spectra, the subspectra with the smaller B_{hf} would disappear, and only the other sextet would be observed.

Therefore we applied thermal treatment of this sample in air and also in oxygen for several hours at 300°C. As shown in Figure 5, the intensity of the sextet of smaller B_{hf} did not change so much although the sextet with 33 T decreased a little and the doublet of Fe^{3+} increased. This suggests that the sextet with broad peaks and B_{hf} = 29.3 T may not be due to finely dispersed iron species. The sextets with 33 T and 29 T disappeared after heating on oxygen atmosphere at 400°C for 16 h, and a broad sextet with δ = 0.41 mm/s, Δ = −0.14 mm/s and B_{hf} = 48.3 was observed together with a doublet of Fe^{3+}. This broad sextet is considered to be due to hematite containing Ti atoms because the B_{hf} of the broad sextet was a little smaller than that of pure hematite. The area intensity of 31% was almost the same as that of the sextet with 29 T. It may suggest that the sextet with 29 T contained Ti atoms.

This point is of great importance considering that the magnetic sextet components are still present in the films annealed for long time at 300°C in air and oxygen i.e. in strongly oxidizing conditions. It is known that laser ablated species such as atoms, ions and clusters have high kinetic energy (<100 eV) as compared with that used in physical films deposited by a normal resistance heater (~0.1 eV). On the process of the film formation, the kinetic

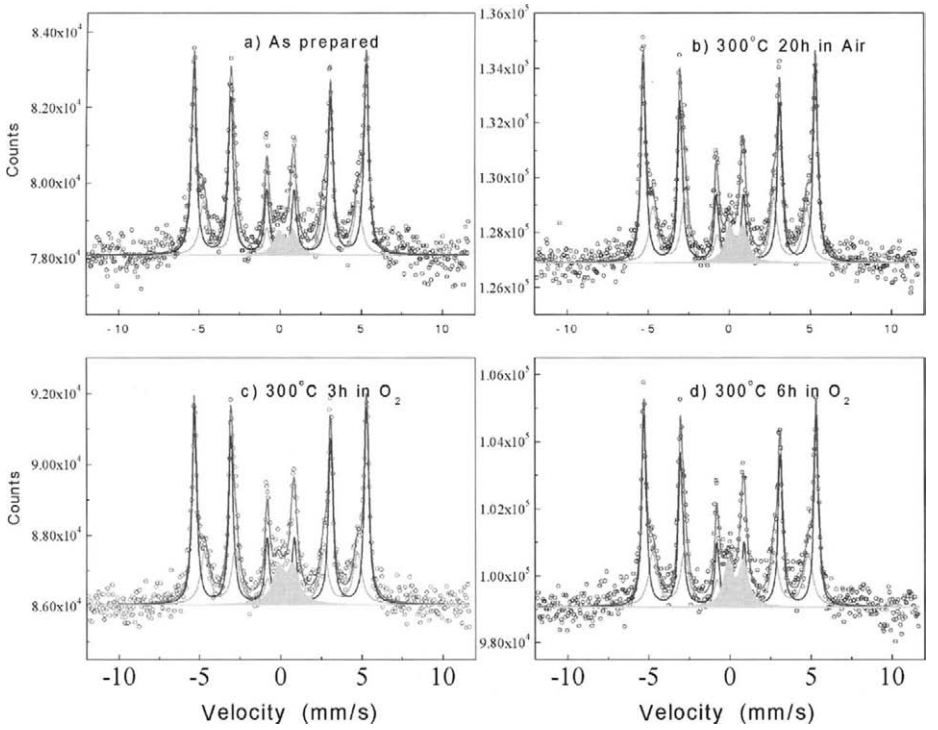

Figure 5 CEMS spectra of TiO_2 films after post-annealing at 300°C for various durations; **a** as prepared on substrate at 650°C, **b** annealing for 20 h in air, **c** treatment b followed by annealing for 3 h in O_2 atmosphere, and **d** treatment b followed by annealing for 6 h in O_2 atmosphere.

energy may affect the diffusion of element species. We have to mention here that the applied vacuum conditions are significantly different in the sense that at 10^{-1} torr, the mean-free path length of the evaporated atoms is much shorter than the target-sample distance, while at 10^{-6} and 10^{-8} torr, it is much longer. Thus at the lower vacuum not only the availability of oxygen is larger at the deposition, but also the deposited atoms or clusters of atoms have much lower kinetic energy when hitting the sample surface.

In order to check if the Mössbauer sextet with B_{hf} = 33 T can really be assigned to metallic iron, we performed one more experiment heating the sample in reductive ambient. CEMS spectra of the (previously already oxidized) samples did not show substantial change in the intensity of this sextet upon heat treatment at 400°C for 2 h in 5%H_2 + Ar atmosphere. This confirmed that, really, metallic Fe was incorporated into structure of the TiO_2 film.

A large part of the metallic iron must be due to oxygen loss during the high vacuum laser ablation process. Then it is logical to assume that TiO_2 might also have suffered some reduction and a small amount of metallic Ti formed. The sextet with 29 T may then be Fe alloy doped with Ti at the interface of TiO_2, which covers the metallic iron particles and may explain the strong corrosion resistance.

Inaba et al. [7] reported that low spin Fe^{3+} species were observed by XPS spectra and magneto-optical measurements. XPS observed only top surface of the films, which might correspond to the paramagnetic Fe^{3+} peaks observed in CEMS. We need to reconsider these

assignments further, taking into account of other mechanism such as those involving the role of delocalized electrons.

4 Summary

Fe doped TiO_2 epitaxial films prepared by PLD at 10^{-1}, 10^{-6} and 10^{-8} torr were characterized by CEMS. It was confirmed by Kerr magneto-optical measurement and scanning SQUID microscope that the films prepared under 10^{-6} torr show strong ferromagnetic behavior. Two magnetic components and one doublet were observed in CEMS spectra of the films prepared under the high vacuums, whereas only one doublet of Fe^{3+} was observed for the film prepared under 10^{-1} torr. Two sextet components of B_{hf} = 33 T and 29 T were stable against the post-annealing for long-term oxidation at 300°C. Tentatively, these subspectra may be largely due to metallic Fe, and Fe (Ti) alloy, produced in the transparent semiconductor of TiO_2. Further studies are needed to confirm these assignments.

References

1. Ohno, H.: Science **281**, 955 (1998)
2. Nazmul, A.M., et al.: Phys. Rev. Lett. **95**, 017201 (2005)
3. Matsumoto, Y., et al.: Science **291**, 854 (2001)
4. Wang, Z., et al.: J. Appl. Phys. **93**, 7870 (2003)
5. Lee, H.M., et al.: IEEE Trans. Magn. **39**, 2788 (2003)
6. Kim, Y.J., et al.: Appl. Phys. Lett. **84**, 3531 (2004)
7. Inaba, K., et al.: Jpn. J. Appl. Phys. **45**, L114 (2006)
8. Nomura, K., et al.: Spectrochim. Acta, Part B: Atom. Spectrosc. **59**, 1259 (2004)

Hyperfine Interact (2006) 168:1073–1077
DOI 10.1007/s10751-006-9404-4

Elastic properties of filled-Skutterudite compounds probed by Mössbauer nuclei

S. Tsutsui · J. Umemura · H. Kobayashi · T. Tazaki · S. Nasu · Y. Kobayashi · Y. Yoda · H. Onodera · H. Sugawara · T. D. Matsuda · D. Kikuchi · H. Sato · C. Sekine · I. Shirotani

Published online: 5 December 2006

Abstract We have carried out Mössbauer spectroscopy and nuclear resonant inelastic scattering to elucidate the lattice dynamics in filled-Skutterudite compounds, especially phosphides. The second-order Doppler shift obeys the Debye model in RFe_4P_{12}. Nuclear quadrupole interaction reveals an unusual temperature dependence in these compounds. An anomaly is observed in ^{57}Fe nuclear resonant inelastic scattering of these compounds. The

S. Tsutsui (✉) · Y. Yoda
Japan Synchrotron Radiation Research Institute, SPring-8, Mikazuki, Sayo, Hyogo 679-5198, Japan
e-mail: satoshi@spring8.or.jp

J. Umemura · H. Kobayashi
Graduate School of Materials Science, University of Hyogo, Kamigori, Hyogo 678-1297, Japan

T. Tazaki · S. Nasu
Graduate School of Engineering Science, Osaka University, Toyonaka, Osaka 560-8531, Japan

Y. Kobayashi
RIKEN, Wako, Saitama 351-0198, Japan

H. Onodera
Graduate School of Science, Tohoku University, Sendai, Miyagi 980-8578, Japan

H. Sugawara
Faculty of Integrated Arts and Sciences, University of Tokushima,
Tokushima, Tokushima 770-8502, Japan

T. D. Matsuda
Advanced Science Research Center, Japan Atomic Energy Research Institute,
Tokai, Ibaraki 319-1195, Japan

D. Kikuchi · H. Sato
Graduate School of Science, Tokyo Metropolitan University, Hachioji, Tokyo 192-0937, Japan

C. Sekine · I. Shirotani
Department of Electrical and Electronic Engineering, Muroran Institute of Technology, Muroran,
Hokkaido 050-8585, Japan

energy where the anomaly observed in $SmFe_4P_{12}$ agrees with the phonon excitation energy observed by ^{149}Sm nuclear resonant inelastic scattering. We have also performed the ^{99}Ru Mössbauer measurements of $SmRu_4P_{12}$.

Key words filled-Skutterudite · second-order Doppler shift · nuclear quadrupole interaction · nuclear resonant inelastic scattering

1 Introduction

Filled-Skutterudite compounds are interesting materials on the viewpoint not only of strongly correlated electron systems but also for industrial application. The chemical form of these materials are RT_4X_{12}, where R is a rare-earth, actinide, alkaline or alkaline-earth elements, T is a transition metal element, and X is a pnicogen element. They have a characteristic crystal structure. This contains an icosahedral cage structure consisting of 12 pnicogen atoms. This pnicogen cage includes an R element. They show superconductivity, magnetic order, heavy fermion behavior and so on at low temperature [1]. They are also expected to be thermoelectric devices. It has been believed that the atomic motion of R atoms correlates with their physical properties on both aspects. This motion is expected to be a local mode like an Einstein oscillator. The presence of the Einstein modes has been quantatively discussed by inelastic neutron scattering and nuclear resonant scattering of filled-Skutterudite antimonides [2–4]. Few studies have been performed in filled-Skutterudite phosphides.

Mössbauer techniques are useful tools to investigate the elastic properties at specific element. Some of Mössbauer parameters correlate with lattice dynamics. Second-order Doppler shift and/or recoil-free fraction provide with Debye temperature, temperature dependence of nuclear quadrupole interaction (QS value) obeys $T^{3/2}$ dependence in usual non-cubic metallic compounds [5]. Besides this, nuclear resonant inelastic scattering (NRIS) is a useful tool to investigate the phonon density of states at element specific sites directly [6].

We have carried out Mössbauer measurements and NRIS of these compounds to investigate their elastic properties. High Debye temperatures are obtained by second-order Doppler shift and recoil-free fraction. An anomalous behavior is observed in temperature dependence of the QS values at ^{57}Fe nuclei. The NRIS results suggest the possibility of a phonon–phonon interaction in RFe_4P_{12} unlike that in filled-Skutterudite antimonides [4].

2 Experimental procedure

The source used in the ^{57}Fe Mössbauer measurements is ^{57}Co in Rh. The source in ^{99}Ru is ^{99}Rh in Ru metal. The ^{99}Ru Mössbauer measurements were carried out in Wako branch of RIKEN. The Doppler velocity is calibrated by ^{57}Fe Mössbauer spectra of α-Fe at room temperature. The NRIS was carried out at BL09XU of SPring-8. The high resolution monochrometers used are reported in [7] and [8].

3 Experimental results

All the ^{57}Fe spectra of RFe_4P_{12} are a paramagnetic doublet. Since the temperature of the phase transition in RFe_4P_{12} is very low [1], the contribution of the electronic states in the

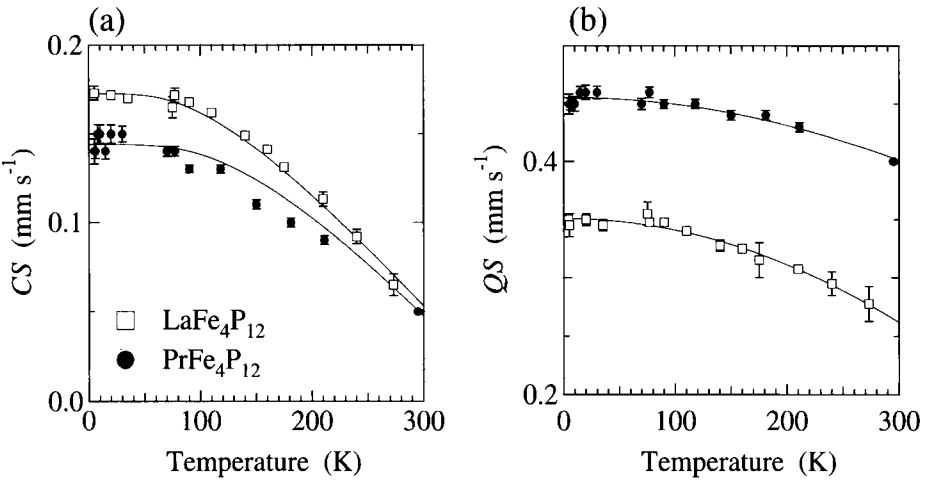

Figure 1 Temperature dependence of the ^{57}Fe Mössbauer parameters in $LaFe_4P_{12}$ [9] and $PrFe_4P_{12}$. **a** Temperature dependence of CS values. The solid lines are the curves calculated by Debye model. **b** Temperature dependence of QS values. The solid lines are the curve fitted by Eq. 2.

temperature dependence is expected to be small in every compound. The temperature dependences of the Mössbauer parameters are shown in Figure 1. The reported results are plotted in $LaFe_4P_{12}$ [9]. Both CS values in $LaFe_4P_{12}$ and $PrFe_4P_{12}$ obey the curves based on the Debye model. This demonstrates that the main contribution of CS values is due to second-order Doppler shift. The Debye temperature obtained in $LaFe_4P_{12}$ and $PrFe_4P_{12}$ are 450 ± 25 K and 600 ± 25 K, respectively. This indicates that the recoil-free fraction at Fe sites is close to one in these compounds.

An anomalous temperature dependence of the nuclear quadrupole interactions is observed at ^{57}Fe in RFe_4P_{12} as shown in Figure 1. As mentioned above, the temperature dependence of the nuclear quadrupole interactions in non-cubic alloys obeys the equation as follows:

$$QS(T) = QS(0)\left(1 - BT^{3/2}\right), \tag{1}$$

where QS(T) is nuclear quadrupole interaction at temperature T, QS(0) is a value extrapolated to $T = 0$ and B is a constant [5]. However, this temperature dependence is fitted by

$$QS(T) = QS(0)\left(1 - BT^{2}\right), \tag{2}$$

rather than Eq. 1. Equation 2 shows the low temperature limit of Eq. 1. The observation of T^2 dependence up to 295 K expects anomalous phonon dispersion.

To understand the T^2 dependence of the nuclear quadrupole interactions at ^{57}Fe nuclei, we carried out ^{57}Fe NRIS of RFe_4P_{12} at 295 K. Figure 2 shows the ^{57}Fe NRIS spectra of RFe_4P_{12}. We observed the dip in the spectra between 10 and 15 meV as indicated by arrows. The wing-shaped spectra demonstrate that Fe atoms play a role in the acoustic modes in these compounds. The spectra of the NRIS in low energy region usually obey the square of the excitation energy reflecting on the acoustic phonon density of states. Therefore, the dip observed by the ^{57}Fe NRIS is anomalous in phonon density of states.

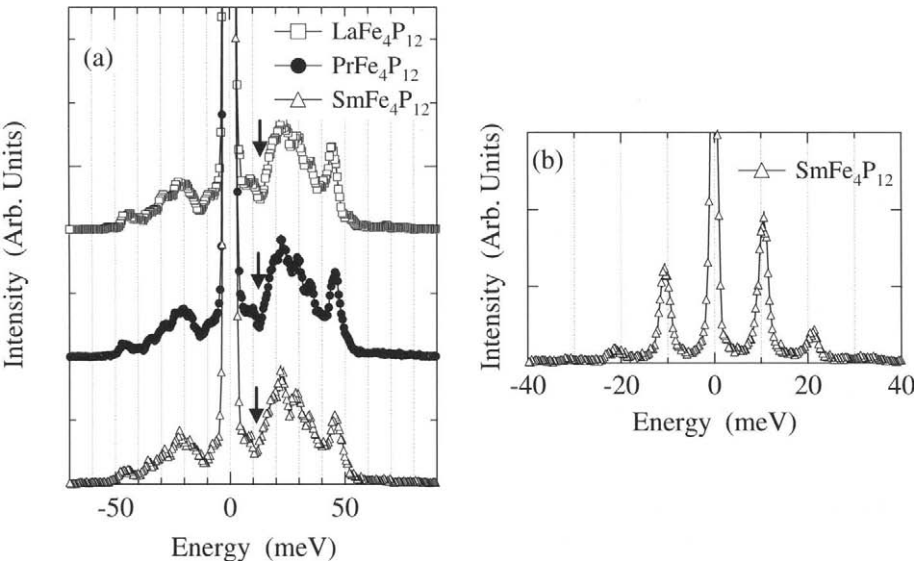

Figure 2 **a** ^{57}Fe NRIS spectra of RFe_4P_{12} (R = La, Pr and Sm) at 300 K by 3.5 meV resolution [7]. **b** ^{149}Sm NRIS of $SmFe_4P_{12}$ at 300 K by 1.5 meV resolution [8].

This indicates the presence of the interaction between the acoustic modes and the local mode as expected from their crystal structure. In addition, we measured the ^{149}Sm NRIS of $SmFe_4P_{12}$. Periodic excitations by every 11 meV are observed at 295 K as shown in Figure 2. This suggests the presence of a local mode like an Einstein oscillator. Surprisingly, the excitation energy in the ^{149}Sm NRIS spectra agrees with the energy of the dip obtained in the ^{57}Fe NRIS spectra of $SmFe_4P_{12}$. This is evidence that an Einstein-like mode at Sm sites interact with the acoustic modes observed by the ^{57}Fe NRIS.

We briefly mention the results of the ^{99}Ru Mössbauer measurements. We took the spectra of $SmRu_4P_{12}$ at 2, 5 and 77 K. The temperature dependence is small, although the energy of the ^{99}Ru Mössbauer resonance is 89.7 keV. This indicates that the Debye temperature is high at the Ru site in $SmRu_4P_{12}$ like that in RFe_4P_{12}.

4 Summary

We have carried out Mössbauer spectroscopy and nuclear resonant inelastic scattering of filled-Skutterudite phosphides. Experimental results are summarized as follows:

(1) The second-order Doppler shift obtained by the ^{57}Fe Mössbauer measurements and the recoil-free fraction obtained by ^{99}Ru Mössbauer measurements demonstrate that the lattice consisting of the cage structure contains a high Debye temperature in every filled-Skutterudite phosphide we investigated.
(2) The temperature dependence of the QS values shows a T^2 dependence and not the $T^{3/2}$ dependence which is the typical behavior in non-cubic metallic compounds.
(3) The ^{149}Sm and ^{57}Fe NRIS results show the presence of an interaction between an Einstein-like mode at rare-earth site and acoustic modes role-played by iron atoms.

The results of (2) and (3) seem to be common properties in filled-Skutterudite phosphides. These facts probably correlated with the unusual phonon dispersion and thermoelectricity of these compounds.

Acknowledgements The NRIS experiments were performed with the approval of JASRI (Proposal no. 2004A0589-ND3b-np and 2005A0369-ND3d-np). The present work was supported by a Grant-in-Aid for Scientific Research Priority Area "Skutterudite" of the Ministry of Education, Culture, Sports, Science and Technology, and a Grand-in Aid for Young Scientists from Japan Society for the Promotion of Science.

References

1. Sato, H., et al.: Phys. Rev., B **62**, 15125 (2000) (and references therein)
2. Keppens, V., et al.: Nature **395**, 876 (1997)
3. Long, G.J., et al.: Phys. Rev., B **60**, 7410 (1999)
4. Long, G.J., et al.: Phys. Rev., B **71**, 140302 (2005)
5. Christiansen, J., et al.: Z. Phys., B **24**, 177 (1976)
6. Seto, M., et al.: Phys. Rev. Lett. **74**, 3828 (1995)
7. Yoda, Y., et al.: Nucl. Instrum. Methods Phys. Res., A **467–468**, 715 (2001)
8. Tsutsui, S., et al.: J. Magn. Magn. Mater. **272–276**, 199 (2004)
9. Shenoy, G.K., et al.: J. Appl. Phys. **53**, 2628 (1982)

Hyperfine Interact (2006) 168:1079–1083
DOI 10.1007/s10751-006-9405-3

Mössbauer spectroscopy study of spin structure and its in-field and temperature dynamics in B2 ordered Fe(Al) alloys

E. V. Voronina · E. P. Yelsukov · A. V. Korolyov · A. E. Yelsukova

Published online: 17 November 2006

Abstract The experimental data from Mössbauer spectroscopy and magnetic measurements are presented as functions of the temperature and external magnetic field for a B2-type ordered $Fe_{66}Al_{34}$ alloy.

Key words ordered Fe(Al) alloys · magnetic structure · Mössbauer spectra · magnetic measurements

1 Introduction

Despite sixty-year history of study of the Fe(Al) system, it attracts great attention to the present day in the magnetic interactions and magnetic structure aspect. Being a natural magnetic lamellar, the B2-type ordered alloys exhibit abnormal magnetic characteristics for the Al concentration from 27 to 35 at.%. So, they differ from disordered ferromagnetic alloys whose magnetic properties are successfully explained in terms of a site-diluted Ising model [1]. Investigations of the magnetic properties anomalies led to controversial conceptions of magnetic structure of these alloys: mictomagnetic [2], reentrant spin glass [3], sperimagnetic [4], antiferromagnetic with ferromagnetic clusters [5, 6]. In [7] the magnetic properties of these alloys were interpreted from the dominant local magnetic anisotropy conception. At length, in [8] the incommensurate spin density waves (SDW) were found in B2-type

E. V. Voronina · E. P. Yelsukov (✉)
Physical-Technical Institute UrD RAS, Izhevsk, Russia
e-mail: yelsukov@fnms.fti.udm.ru

A. V. Korolyov
Institute of Metal Physics UrD RAS, Ekaterinburg, Russia

A. E. Yelsukova
Moscow State University, Moscow, Russia

ordered Fe-Al alloys. The ambiguity of the nature of their magnetic state motives to proceeding experimental researches.

2 Experimental

The sample of Fe with 34.1 at.% Al was melted from high-purity starting metals (Fe and Al of 99.99% purity) in purified He atmosphere using an induction furnace. The ingot was homogenized at 1100 K in an argon atmosphere for 8 h followed by filling, sieving and annealing at 1073 K during 1 h and 873 K during 32 h. Fe $K\alpha$-radiation X-ray diffraction was taken at room temperature. Chemical analysis was performed by wet chemistry and with the atomic emission spectrometer "Spectraflame-Modula-D" with inductive coupled plasma. Magnetic measurements were carried out with the SQUID-magnetometer SQUID-MPMS-XL-5 (Quantum Design) at temperature from 5 to 300 K in external magnetic field from 0 to 5 T. Mössbauer spectra were measured at $T = [5 - 300\ K]$ and in external magnetic field $B_{ext} = [0.03 - 2.6\ T]$ using the γ−ray source ^{57}Co in Cr. Mössbauer spectra were analyzed for the average hyperfine magnetic field $\overline{B_{eff}}$ and the fraction of a non-magnetic component P_0 depending on the temperature T and external magnetic field B_{ext}.

3 Results and discussion

X-ray diffraction patterns of the sample corresponds to a bcc B2-type superstructure with a lattice parameter a = 0.2883 nm and a mean grain size $< L > = 0.08\ \mu$m. The Al content was estimated equal to 34.1 at.%. Magnetization measurements show that magnetization curves do not saturate up to B_{ext} = 5 T. Hysteresis loops measured in a longitudinal magnetic field before and after cooling in field are symmetrical in relation to zero. The coercive force B_c decreases from 90 to 2.7 mT on increase of temperature from 5 to 80 K, and even at a room temperature a small coercive force B_c = 1.5 mT exists. It was shown [9] that the parameters of temperature hysteresis at B_{ext} <0.5T are determined by the magnetic hysteresis parameters. In paper [9], a prominent maximum at $T \approx 50$ K under low B_{ext} <0.8 T in FC and ZFC curves was also reported. The temperature dependence of AC susceptibility χ is characteristic of antiferromagnet, as well as its 90°-quadrature component χ'' that shows a sharp peak at $T \simeq 40$ K and a peculiarity at T>150 K, vanishing in external magnetic field, Figure 1a,b. The dependences of magnetization $\sigma(B/T)$ are identical for any temperatures above T = 150 K as it follows from Figure 1c. Low-temperature Mössbauer measurements indicate a rapid growth of P_0 in the temperature range from 21 to 45 K resulting in a decrease of the average hyperfine magnetic field $\overline{B_{eff}}$ by a step-like function, rather than the Brillouin law. The magnetic splitting vanishes at T $\simeq$ 80 K (see Figure 2a,b), but magnetization is not equal to 0 at this temperature and increases by 20 times on B_{ext} going up from 0.05 to 2.5 T. Comparing the magnetization and Mössbauer spectroscopy data gives an abnormally high value of the ratio $\overline{B_{eff}}/\overline{m} = 50 \div 70\ T/\mu_B$. Measurements under low B_{ext} indicate an essential growth of $\overline{B_{eff}}$ and appearance of the components with a magnetic splitting highly exceeding B_{ext}, as it is clearly seen in Figure 2a,c.

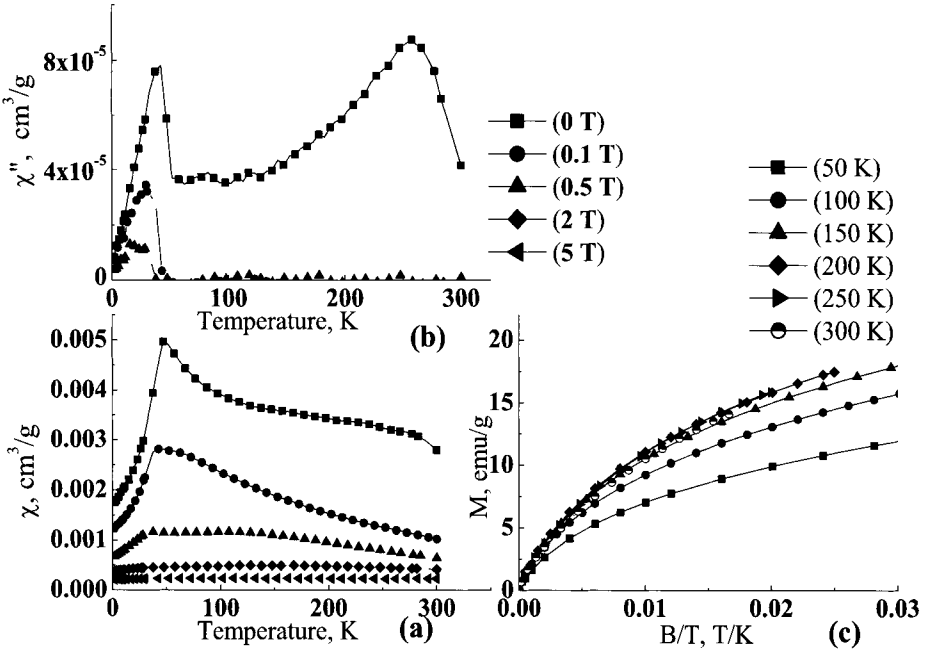

Figure 1 The temperature dependence of AC susceptibility $\chi(T)$-(**a**) and its 90°-quadrature component $\chi''(T)$-(**b**). The dependences of magnetization $\sigma(B)$ versus temperature T-(**c**).

The considerable difference in the temperature behaviour of $\overline{B_{eff}}$(T) and $\sigma(T)$ vanishes at low values of the applied magnetic field and these dependences get correlating. According to the data presented and available in the literature, the ground state (T = 0 K) of the alloy can not be classified as a pure ferromagnet, or antiferromagnet, or canonical spin glass or mictomagnetic. The features in χ(T), $\sigma(T)$ and $\overline{B_{eff}}(T)$ curves and the behaviour of Mössbauer spectra in magnetic filed evidence for collective magnetic moments fluctuations. An estimation of the Fe atoms number forming such fluctuating complexes from $\sigma(B/T)$ gives $\approx 10^2$, while the value of freezing temperature 130–150 K (starting from which the $\sigma(B)$ is a unique function of temperature) corresponds to much larger assemblies $\approx 10^4$ Fe atoms. The temperature and in-field dynamics of Mössbauer spectra parameters indicate time-dependent hyperfine interactions. Besides, the broadening and splitting of the Mössbauer spectra in external magnetic fields, clearly observed in Figure 2, indicate that the temperature of transition into the actual paramagnetic state is higher than 300 K. The data obtained can be interpreted within several models:

(1) system of magnetic moments is composed of two subsystems with randomly distributed antiparallel spins, the magnitude and sign of a certain magnetic moment being determined by the chemical local environment. This model, provided that magnetic moment m_{Fe} of the Fe atoms having more than four Al atoms in the nearest neighborhood is antiparallel to the local magnetization, gives the average $\overline{m}_{Fe}$ = 0.3 μ_B, fitting the experimental magnetization data. The magnetic moments of Fe atoms in the Al-rich environments degrade on increasing the temperature, which results in destroying Fe magnetic moments

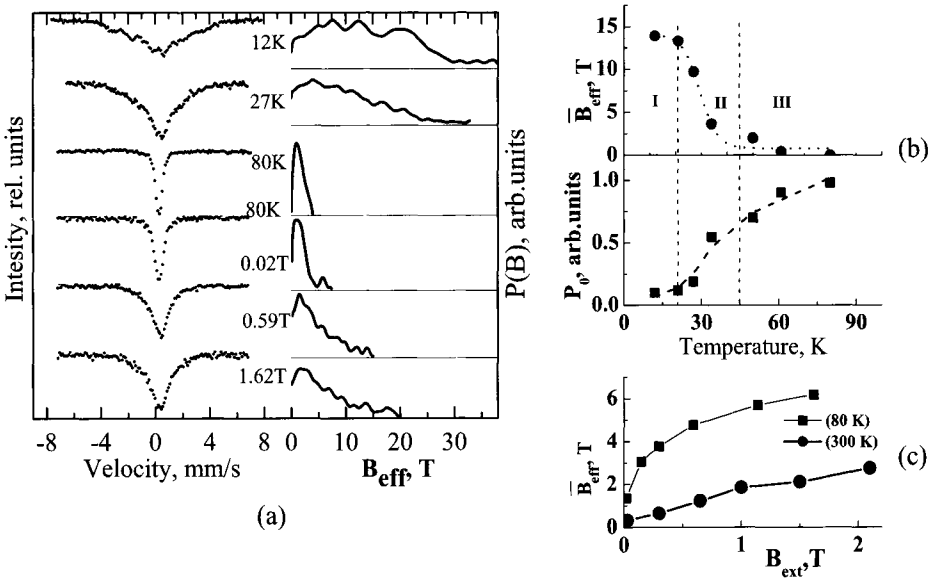

Figure 2 Mössbauer spectra and hyperfine magnetic field distributions P(B) versus temperature-(**a**); the average B_{eff} (upper part) and P_0 (lower part) versus temperature-(**b**); the average B_{eff} as a function of external magnetic field B_{ext} at T = 80 and 300 K-(**c**).

coupling. The clustered regions, consisting of the Fe atoms having less than four Al atoms, form. At the temperatures higher than 150 K, the Fe magnetic moments in these regions collectively fluctuate.

(2) system of magnetic moments consisting of two type of spins : collinear (Fe atoms in the Al-poor environment) and non-collinear, with a spin randomly oriented, (Fe atoms in the Al-rich environment). In this model, the non-collinearity is caused, mainly, by disorder of the local anisotropy axes. The temperature and in-field dynamics is governed by a metamagnetic-type transition.

(3) a particular state – the incommensurate SDW [8] found in B2-type ordered Fe-Al alloys that implies the interpretation of magnetic properties principally in terms of itinerant magnetism.

New experimental Mössbauer and theoretical studies promise to resolve this ambiguity.

Acknowledgement The authors thank Prof.A.Arzhnikov for the interest and effective discussions.

References

1. Perez Alcazar, G.A., Galvao da Silva, E.: J. Phys., F **17**, 2323–2335 (1987)
2. Shull, R.D., Okamoto, H., Beck, P.A.: Solid State Commun. **20**, 863–868 (1976)
3. Raymond, S., Bao, W., Shapiro, S.M., Motoya, K.: Physica, B **241–243**, 597–599 (1998)
4. Schneeweiss, O., Zak, T., Vondracek, M.: J. Magn. Magn. Mater. **127**, 33–66 (1993)
5. Danan, H., Gengnagel, H.: J. Appl. Phys. **39**, 678–679 (1968)

6. Cable, J.W., David, L., Parra, R.: Phys. Rev., B **16**, 1132–1137 (1977)
7. Takahashi, S., Li, X.G., Chiba, A.: J. Phys., Condens. Matter **8**, 11243–11257 (1996)
8. Noakes, D.R., Avott, A.S., Bells, M.G., Deevi, S.C., Huang, Q.Z., Lynn, J.W., Shull, R.D., Wu, D.: Phys. Rev. Lett. **91**, 217201-1-4 (2003)
9. Elsubov, E.P., Yelsukov, E.P., Voronina, E.V., Korolev, A.V., Gaczynski, P., Drulis, M.: Phys. Met. Metallogr. **98**, 469–474 (2004)

Hyperfine Interact (2006) 168:1085–1089
DOI 10.1007/s10751-006-9441-z

^{57}Fe Mössbauer spectra and magnetic data from the *kagomé* antiferromagnet H_3O-jarosite

P. Bonville · V. Dupuis · E. Vincent · P. E. Lippens · A. S. Wills

Published online: 26 October 2006

Abstract ^{57}Fe Mössbauer spectra are presented from $(H_3O)Fe_3(SO_4)_2(OH)_6$ (or H_3O-jarosite), which is a model *kagomé* antiferromagnet which features geometrical frustration and spin-glass-like behaviour. Dynamic scaling of the freezing temperature as a function of frequency is observed over a large frequency range, which indicates the presence of a spin-glass transition. A fast relaxation model between "up" and "down" states, separated by an energy gap, is presented to account for the shape of the Mössbauer spectra below the freezing temperature. From a calculation of the Electric Field Gradient tensor, it is suggested that H_3O-jarosite is an XY-Heisenberg antiferromagnet, where the Fe^{3+} moments lie in the *kagomé* planes.

Key words geometrical frustration · *kagomé* lattice · spin-glass · Mössbauer spectroscopy

P. Bonville (✉) · V. Dupuis · E. Vincent
C.E.A.- Saclay, Service de Physique de l'Etat Condensé, URA 2464 (CNRS),
91191 Gif-sur-Yvette, France
e-mail: bonville@spec.saclay.cea.fr

V. Dupuis
Laboratoire des Liquides Ioniques et Interfaces Chargées,
Université Pierre et Marie Curie, 75006 Paris, France

P. E. Lippens
Laboratoire des Agrégats Moléculaires et Matériaux Inorganiques, UMR 5072 (CNRS),
Université Montpellier II, 34095 Montpellier, France

A. S. Wills
Department of Chemistry, University College London,
20 Gordon Street, London WCIH 0AJ, UK

In $(H_3O)Fe_3(SO_4)_2(OH)_6$ (or H_3O-jarosite), the Fe^{3+} ions (S=5/2) are arranged in *kagomé* layers, i.e., they lie on a triangular network where the triangles are connected through shared vertices. The magnetic susceptibility shows a Curie–Weiss law with a large negative paramagnetic Curie temperature $\theta_p \simeq -780$ K, indicative of strong antiferromagnetic (AF) interactions between Fe^{3+} ions. No long range magnetic ordering is observed down to 2 K [1], which can be ascribed to the frustration of the AF nearest-neighbour exchange interactions on the *kagomé* lattice: no spin configuration can satisfy all AF bonds in such a triangular lattice. The ground state is then highly degenerate and short range correlations may prevail down to the lowest temperature [2]. An unexpected feature of H_3O-jarosite is the spin-glass-like behaviour of its Field Cooled (FC) and Zero Field Cooled (ZFC) dc magnetic susceptibilities below $T_g = 17.8$ K, and of its aging properties [3]. Indeed, spin-glass behaviour is expected in site-disordered materials, whereas our sample of H_3O-jarosite has an Fe^{3+} occupancy close to 97%. A short ^{57}Fe Mössbauer study in this compound has been published previously [4].

In this work, we performed extensive ^{57}Fe Mössbauer spectroscopy measurements in H_3O-jarosite and a calculation of the Electric Field Gradient (EFG) tensor at the Fe site, in order to obtain information on the Fe moment orientation. We also put forward a two-state dynamic model to account for the shape of the low temperature spectra. Finally, using the results of various techniques with very different characteristic frequencies, we check whether a spin-glass-like dynamic scaling is obeyed in the vicinity of T_g.

H_3O-jarosite crystallises into the space group $R\bar{3}m$, the Fe^{3+} ion being at the center of a slightly distorted O_6 octahedron (point symmetry $2/m$). The FeO_4 plane is at an angle of $\simeq 22°$ from the *kagomé* plane, which is the **(a, b)** plane of the hexagonal crystal. The ^{57}Fe Mössbauer spectra show a single quadrupolar doublet above 22 K, with a splitting $\Delta E_Q \simeq 1.15$ mm/s which shows practically no thermal variation. This points to the presence of Fe^{3+} alone in H_3O-jarosite. Below 22 K, the spectra broaden and show the six lines characteristic of a magnetic hyperfine interaction (see Figure 1 left). Their overall shape reflects the presence of a distribution of hyperfine fields, as often observed in spin-glasses [5]. The phenomenological fits using such a distribution (not shown) allow the average hyperfine field to be determined, and its thermal variation is represented in Figure 1 right top. The temperature $T_M \simeq 22$ K at which the mean hyperfine field vanishes cannot be considered as a Néel temperature, as no long range order is present in H_3O-jarosite [1]. It is instead a spin freezing temperature associated with the characteristic ^{57}Fe Mössbauer hyperfine Larmor frequency of 100 MHz.

In order to understand better the nature of this glassy magnetic phase, we have tried to obtain the orientation(s) of the Fe magnetic moment with respect to the crystal axes. The first step is to determine the orientation of the hyperfine field, antiparallel to the Fe^{3+} moment to a good approximation, in the principal axes OXYZ of the EFG tensor. This can be best done using the spectra near 18–20 K, where the magnetic hyperfine interaction is weak and of the same order of magnitude as the quadrupolar interaction. We find that only the polar angle between the hyperfine field and OZ can be reliably determined, and that it is $\theta = 75(5)°$. This angle is unique, which means that the orientation of the Fe moment with respect to the local XYZ axes is the same for the nine Fe sites in the unit cell. The second step is to determine the orientation of the principal EFG axes in the crystal frame. For

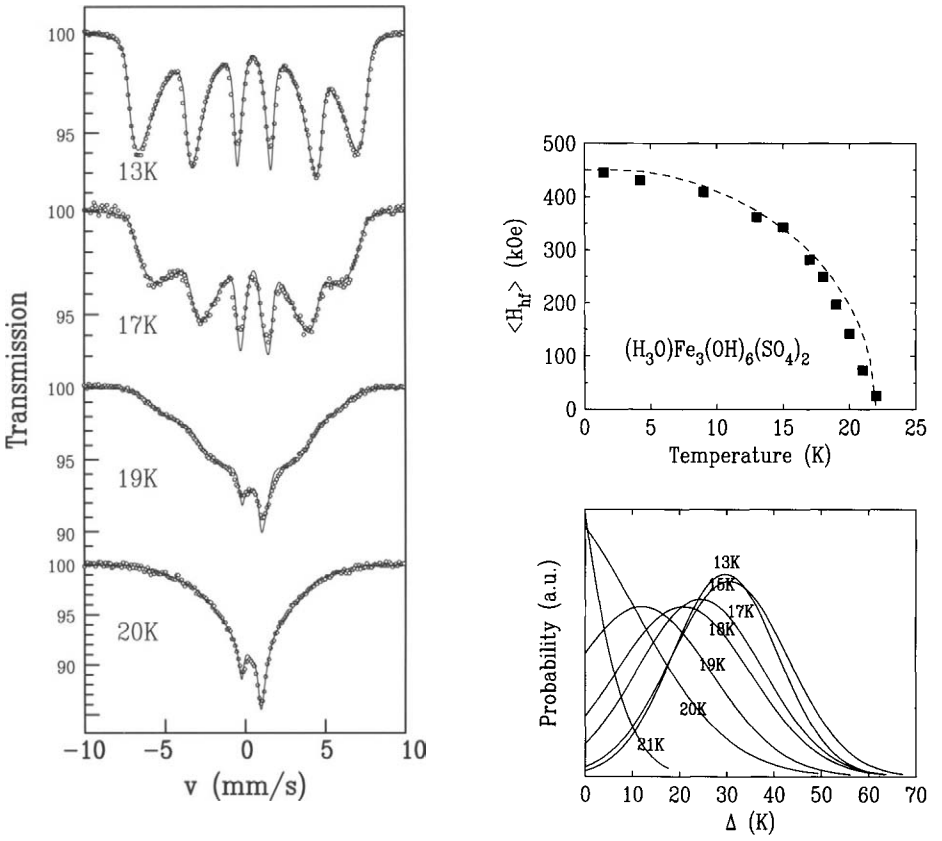

Figure 1 *Left:* ^{57}Fe Mössbauer spectra in H_3O-jarosite below the Mössbauer freezing temperature (22 K), fitted with a two-state dynamic model (see text). *Right top:* thermal variation of the average hyperfine field derived from fits using hyperfine field histograms. The *dashed line* is the mean-field law associated to S=5/2, with a critical temperature $T_M = 22$ K. *Right bottom:* variation with temperature of the distribution of "up-down" gaps in the two-state model proposed to account for the Mössbauer lineshape below the freezing temperature.

this purpose, we performed an ab initio calculation of the EFG at the Fe site in the non-magnetic approximation, and we obtain the following results: $\Delta E_Q \simeq 0.7$ mm/s (experimental value 1.15 mm/s), and the OZ axis is at an angle $\alpha = 22(2)°$ from **c** in the mirror plane (perpendicular to, say, **b**). These data do not allow the moment direction to be unambiguously determined, but they are compatible with an Fe moment perpendicular to *c*, i.e., lying in the *kagomé* plane.

The shape of the Mössbauer spectra below T_M can be accounted for by assuming that the exchange field experienced by an Fe^{3+} ion is distributed, and that it vanishes above T_M. This is the classical explanation in spin-glasses, but it overlooks the fact that, at least in H_3O-jarosite, the exchange interaction is much bigger than T_M, which is not a Néel temperature. We propose here another model, which could be labelled a dynamic two-state model: the short range correlated Fe moments fluctuate rapidly between the "up" and "down" configurations, which are separated by an energy gap $\Delta(T)$ whose values are distributed. Then the local equilibrium hyperfine field is given

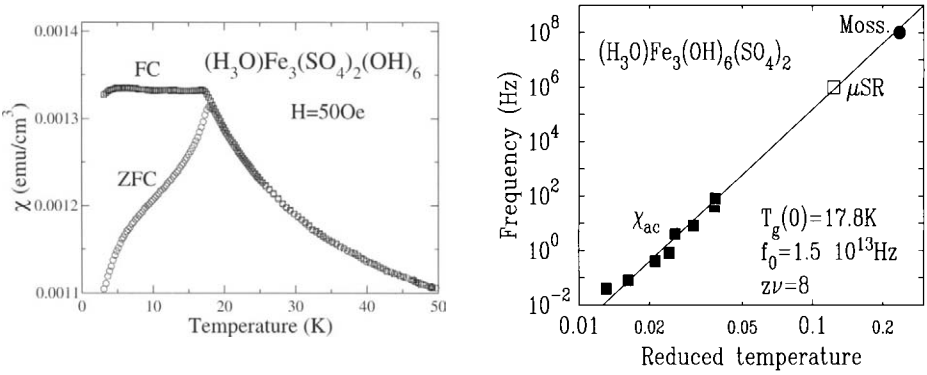

Figure 2 *Left:* Field Cooled (FC) and Zero Field Cooled (ZFC) branches of the magnetic susceptibility in H_3O-jarosite, after subtraction of a Curie-like paramagnetic contribution. *Right:* characteristic frequency f as a function of the reduced temperature t from ac susceptibility measurements (χ_{ac}), and muon spin rotation (μSR) [8] and ^{57}Fe Mössbauer spectroscopies (Moss). The *solid line* is the law: $f = f_0 t^{z\nu}$.

by: $H_{hf}(T) = H_0 \tanh \frac{\Delta(T)}{2k_B T}$, it is distributed in values and static on the Mössbauer timescale. Figure 1 right bottom represents the thermal variation of the distribution of Δ values corresponding to the fits of the spectra shown in Figure 1 left. Above T_M, the gap vanishes, and therefore it could be considered as an order parameter. Its physical origin can be the anisotropy of exchange [6] arising from the Dzyaloshinsky–Moriya interaction [7] or, more likely in the case of Fe^{3+}, from further neighbour contributions.

The dc magnetic susceptibility curves, as shown in [3], present an irreversibility between FC and ZFC branches below $T_g \simeq 17.8$ K, and show Curie-like upturns at low temperature. Here, we present FC/ZFC curves where we subtracted a Curie contribution, so that the corrected susceptibility shows the flat FC branch encountered in spin-glasses (Figure 2 left). The required correction corresponds to about 1% Fe^{3+} ions, which remain paramagnetic inside the spin-freezing region probably due to neighbouring defects or vacancies.

The in-phase ac susceptibility measured in the frequency range 0.04–80 Hz shows a peak at a freezing temperature $T_g(f)$ which increases as the frequency increases. A generic feature of spin-glasses is the critical scaling law: $f = f_0 t^{z\nu}$ expected for the characteristic frequency of the experiment, where $t = [T_g(f) - T_g(0)]/T_g(0)$ is the reduced temperature, f_0 is a microscopic frequency of the order of 10^{12} Hz, ν is the critical exponent describing the divergence of the spin correlation length ξ as $t \to 0$, and z is the dynamic exponent linking f and ξ: $f \propto \xi^{-\nu}$. Figure 2 right shows, on a log-log scale, the variation of f with the reduced temperature computed using $T_g(0) = 17.8$ K, the peak value obtained from the dc susceptibility data (Figure 2 left). In order to sweep a larger frequency range, we included the freezing temperatures measured by the μSR technique [8], which has a characteristic frequency of 1 MHz ($T_{\mu SR} = 20$ K) and by the present ^{57}Fe Mössbauer study, with a characteristic frequency 100 MHz ($T_M = 22$ K). The critical scaling is seen to be satisfactorily obeyed over 10 orders of magnitude for f, with reasonably physical values $f_0 = 1.5 \times 10^{13}$ Hz and $z\nu = 8$.

As a conclusion, our data suggest that the *kagomé* antiferromagnet H_3O-jarosite is an XY-Heisenberg frustrated system with the Fe moments lying in the *kagomé* plane, and they show that it undergoes a spin freezing transition analogous to that in spin-glasses, although the site-disorder appears to be very small. We note that the XY plane, that our measurements suggest the spins to be in, does not correspond to the local coordination plane of the Fe^{3+} ion, but instead to the *kagomé* plane. This would imply that the gap inducing anisotropy has its symmetry.

References

1. Wills, A.S., Harrison, A., Mentink, S.A.M., Mason, T.E., Tun, Z.: Magnetic correlation in deuteronium jorosite, a model $S = 5/2$ kagomé antiferromagnet. Europhys. Lett. **42**(3), 325–330 (1998)
2. Buschow, K.H.J. (ed.): Handbook of Magnetic Materials, vol. 13, p. 425. Elsevier, Amsterdam, The Netherlands (2001) (See Ramirez, A.P. for a review about geometrical frustration.)
3. Wills, A.S., Dupuis, V., Vincent, E., Hammann, J., Calemczuk, R.: Aging in a topological spinglass. Phys. Rev. B **62**, R9264 (2000)
4. Afanas'ev, A.M., Gorobchenko, V.D., Kulgawczuk, D.S., Lukashevich, I.I.: Nuclear γ-resonance in iron sulphates of the jarosite group. Phys. Status Solidi, A **26**, 697 (1976)
5. Meyer, C., Hartmann-Boutron, F., Gros, Y., Campbell, I.A.: Mössbauer effect measurements on *Au*Fe spin glass. J. Magn. Magn. Mater. **46**, 254 (1985)
6. Kuroda, A., Miyashita, S.: Existence of phase transition in Ising-like Heisenberg antiferromagnets on the kagomé lattice. J. Phys. Soc. Jpn. **64**, 4509 (1995)
7. Elhajal, M., Canals, B., Lacroix, C.: Symmetry breaking due to Dzyaloshinsky–Moriya interactions in the kagomé lattice. Phys. Rev. B **66**, 014422 (2002)
8. Harrison, A., et al.: μSR studies of the kagomé antiferromagnet $(H_3O)Fe_3(OH)_6(SO_4)_2$. Physica. B **289–290**, 217 (2000)

Hyperfine Interact (2006) 168:1091–1096
DOI 10.1007/s10751-006-9407-1

Structural evolution of ball-milled permalloy

K. Brzózka · D. Olekšáková · P. Kollár · T. Szumiata · B. Górka · M. Gawroński

Published online: 5 December 2006

Abstract Two series of $Fe_{19.8}Ni_{80.2}$ samples obtained by ball milling and differing in the form of starting material were investigated by Mössbauer spectroscopy. In the case of milled elemental powder, strong structural evolution was stated: both α and γ phases arise and a small amount of pure iron is present as well. The annealing of as-milled powder at 490°C causes faster forming of γ-(Ni–Fe) phase. Only slight changes in atomic order were stated in the series of milled polycrystalline ribbon.

Key words Mössbauer spectroscopy · Fe–Ni alloys · mechanical alloying

1 Introduction

Mechanical alloying (MA), which makes it possible to prepare nanostructured systems, offers a new opportunity to improve the properties of current magnetic materials [1, 2]. Although many metastable phases arise in the course of the milling procedure, they are often stable enough for some technical applications. In comparison to materials obtained by conventional methods, mechanical alloyed systems – owing to small-size grains, specific structure, large strains as well as significant density of defects and grain boundaries – usually exhibit different mechanical, thermal, electric and magnetic peculiarities, e.g. reduced density, enforced resistivity, higher specific heat and coercivity which highly depends on the grain diameter.

The structural evolution and properties of permalloy-type alloys obtained by long-time milling in the low-energy vibratory mill was the subject of this work. One can expect the creation of diverse phases with structural and magnetic characteristics depending on the proportions between the elements and hardly distinguished by diffraction methods. Due to

K. Brzózka (✉) · T. Szumiata · B. Górka · M. Gawroński
Department of Physics, Technical University, Malczewskiego 29, 26-600 Radom, Poland
e-mail: kbrzozka@poczta.fm

D. Olekšáková · P. Kollár
Department of Condensed Matter Physics, Institute of Physics, Faculty of Science,
P.J. Šafárik University, Park Angelinum 9, 041 54 Košice, Slovakia

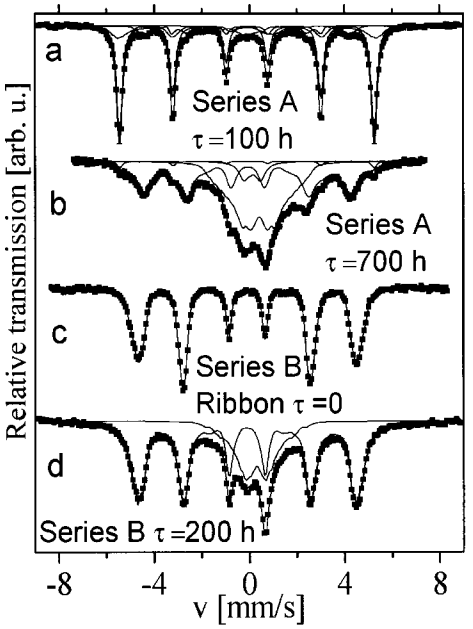

Figure 1 Mössbauer spectra of selected samples obtained for: **a**, **b** milled mixture of elements; **c**, **d** milled polycrystalline ribbon, for different milling time τ.

sensitivity to hyperfine fields, Mössbauer spectroscopy provides the possibility to study phase evolution in these systems and analyze it in terms of other effects induced by mechanical treatment, such as strong changes in magnetization and coercivity [3, 4].

2 Experimental

In this study, two series of Fe–Ni samples which were obtained by ball milling in a low-energy vibratory micro-mill (Pulverisette 0, Fritsch) under the argon atmosphere are investigated. They have the similar chemical content – i.e. 19.8 at.% of iron – and different kinds of initial material: in series A – a mixture of pure elements, and in series B – 5 mm-wide and 50 μm-thick microcrystalline ribbon obtained by melt spinning method. In both cases, initial purity of elements was equal to: Ni 99.98%, Fe 99.99%. The samples were milled for 30, 100, 200 and 700 h, using a vibration amplitude equal to 1.5 mm and powder to ball ratio: 25:1. Chemical analysis showed that the chemical content did not really change during milling since changes were smaller than 0.5%.

Transmission Mössbauer measurements were performed with temperatures ranging from −100 to 490°C using ^{57}Co(Rh) source of radiation, a nitrogen cryostat and a vacuum furnace with maximal pressure $2 \cdot 10^{-5}$ Torr. To analyze the Mössbauer spectra, the MOSFIT program was used (Teillet and Varret, unpublished). The Mössbauer results were compared to the magnetization results, which were obtained using vibrating sample magnetometer (VSM).

3 Phase evolution in milled elemental powder

Room temperature Mössbauer spectra reveal different structural evolutions of the samples belonging to both series (Figures 1, 2). In the case of milled elemental powder, except the

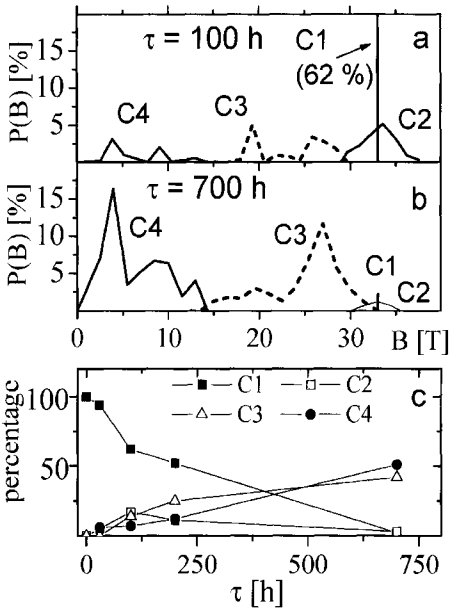

Figure 2 **a**, **b** Hyperfine field distribution derived for two samples of milled elemental powder, **c** relative intensities of individual components of spectra p_i vs. milling time.

sharp sextet with hyperfine magnetic field 33.0 T characteristic of pure iron (called C1), a smeared high-field component corresponding to the range: 30–37 T (called C2) was found. This component peaks after 100 h of milling and decreases at longer milling time. This is attributed to the bcc phase – both distorted Fe and Fe(Ni) solid solution [5]. Moreover, another distributed Zeeman sextet (C3) arises and grows during milling. This component, characterized by hyperfine fields from the range 15–33 T and mean hyperfine field 26–27 T, mainly originates from γ Ni–Fe phase and dominates in the spectrum after 700 h of milling although a small amount of nearly pure iron is still present. Besides, a growing low-field component of Mössbauer spectrum (C4) was found, the origin of which is discussed below. It should be pointed out that the intensities of subspectra p_i (shown in Figure 2c) are related to the proportion of iron atoms contributing to particular components. Therefore, the phases with no iron are not represented in the Mössbauer results. Also, the iron-poor phases are underestimated whereas the iron-rich ones are overestimated. Calculation of the volumetric fraction of phases c_i requires the knowledge of concentration of iron in individual phases x_i and in the whole sample x ($c_i = xp_i/x_i$). Unfortunately, we do not know x_i well enough. The approximate evaluations together with the balance of elements reveal, besides the above-mentioned phases, the significant contribution of pure nickel in samples belonging to the series A: from 75% after 30 h of milling to 50% after 200 h. In the case of sample milled for 700 h the relative content of nickel is equal to 3–5%, but the uncertainty of calculation of this contribution is high.

The low-field component C4 (called below paramagnetic component) increases from 6% for short-milled powders up to 54% after 700 h of milling and mainly comprises a Zeeman sextet with mean isomer shift 0.48 mm/s and hyperfine field from the range 0–13 T and also, in the sample milled for 700 h, a smeared doublet with isomer shift 0.22 mm/s and quadrupole splitting 0.63 mm/s. It seems, that various, quite different phases contribute to this constituent, namely: small amount of oxides, phases with about 30–35 at.% of nickel (invar alloys), grain boundaries and ultrafine particles with diverse compositions.

The changes in structure as well as strong distortions and spin relaxation effects occurring during milling cause a systematic increase in mean isomer shift and a reduction

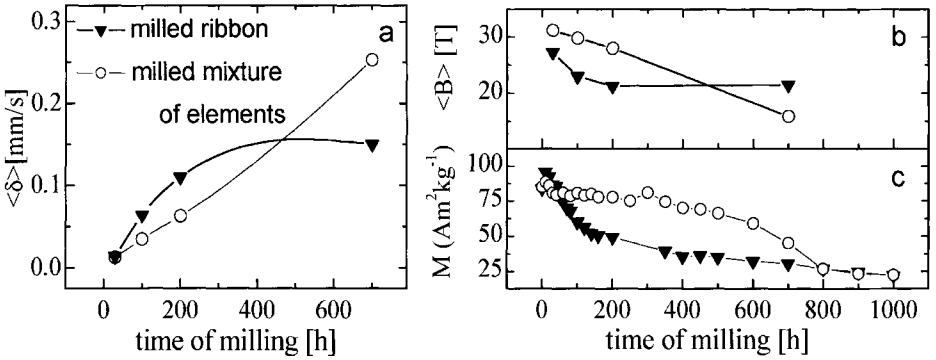

Figure 3 **a** Mean isomer shift <δ>, **b** mean hyperfine field <*B*>, **c** magnetic moment derived from VSM measurements vs. milling time.

of the mean magnetic hyperfine field illustrated in Figure 3a, b. The latter quantity is well correlated with the magnetic moment derived from VSM measurements and plotted in Figure 3c. Both quantities show a progressive decrease during milling due to an increasing amount of γ phases, powder size reduction as well as growing intensity of strain (for more details about magnetic measurements, please see [4]).

4 Atomic order in milled ribbon

In the case of milled ribbon, a component with distributed hyperfine field (mean value 28.6 T) representing γ-(Ni, Fe) with about 15–20 at.% of iron dominates in the spectra. The relative content of this constituent in the long-time milled samples is as high as 75%. As in a previous series, a low-field subspectrum is also present, although its intensity is distinctly smaller.

In binary alloys, the site positions may be occupied randomly or there may be some preferences in atom arrangement. The local environment model (LEM) was used to analyze the atomic order of the γ-(Ni, Fe) phase [6]. The related subspectrum is made up of many overlapping six-line patterns, each corresponding to a magnetic hyperfine field experienced by ^{57}Fe nucleus at a particular lattice site. The analysis of the intensities of these components gives information about atomic order and enables us to distinguish between the different types of chemical order. The Mössbauer spectra of milled ribbon were re-analyzed from a short-range order point of view. In LEM, magnetic hyperfine field noticed by an iron atom surrounded by m iron atoms in the first coordination shell and n iron atoms in the second one is a linear function of m and n:

$$B(m,n) = B(0,0) + m\,\Delta B_1 + n\,\Delta B_2$$

In our computations, we used the following values: B (0, 0) = 26.21 T, ΔB_1 = 1.07 T, ΔB_2 = 0.24 T [7]. Mössbauer spectra were fitted with a set of sextets applying fixed hyperfine field values calculated by LEM in the first coordination shell approximation. The relative intensities of sextets vs. m are presented in Figure 4. We can see that the atomic arrangement does not really change during milling (only small shift towards the lower m is visible) but it slightly differs from the theoretical predictions based on random atomic distribution. The quantitative analysis of these discrepancies can be done using the short

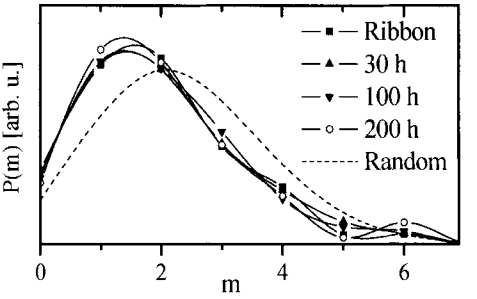

Figure 4 Comparison between the random distribution in the occupied sites of the first coordination shell around a Mössbauer probe by iron atoms and the experimental ones obtained for the permalloy ribbon milled at different times.

range order Warren–Cowley parameter [8, 9] for iron atoms in the first coordination shell (which describes deviation of the real atomic arrangement from the random one), defined as follows:

$$\alpha_1 = \frac{< m > - Z_1 x}{Z_1(1-x)} \qquad < m > = \sum mP(m,n)$$

With x being the iron concentration, $< m >$ the average number of iron atoms in the first coordination shell and Z_1 the coordination number in the first coordination shell; for fcc lattice $Z_1 = 12$.

Both in the case of ribbon and powder, the Warren–Cowley parameter α_1 has a small negative value of about (-0.05). This means that there are more nickel atoms in the vicinity of an iron atom than in the random solid solution, which reveals a slight tendency for ordering, probably towards the $FeNi_3$ structure.

5 Temperature investigations

The results presented in chapter 3 reveal rather difficult alloying of elemental powders during milling – after 200 h there was still over 50% of pure elements in the mixture. In order to evidence the effect of the subsequent heat treatment, the sample obtained after 200 h of milling has been annealed in vacuum for 24 h at 490°C and then slowly cooled down. Room temperature Mössbauer spectrum collected after annealing shows a significant growth (from 22 up to 70%) of the component representing the γ-(Fe, Ni) phase, compared to as-milled sample (Figure 5b, c). Besides, a sharp single line arises. It is located almost in the centre of the spectrum and is attributed to low-spin iron state in the invar alloy with 30 at.% of Ni. Temperature measurements of the annealed sample carried out at 300 and 490°C reveal a significant increase in the paramagnetic component (Figure 5d, e). The results of earlier magnetic investigations [4] suggested that a portion of the smallest powder particles may show superparamagnetic behavior. Although the observed evolution of the Mössbauer spectra is not typical for superparamagnetism, we cannot exclude the relaxation effects of the magnetic moments of finest powder particles. The contribution of temperature relaxations is indicated by the gradual increase in the paramagnetic component with milling time as well as with growing temperature. This hypothesis is also supported by a small but marked decline of the paramagnetic component in the spectrum collected at liquid nitrogen temperature (LNT) compared to room temperature (RT) spectrum (as-milled sample, Figure 5a, b). However, due to the large dispersion of particle sizes as well as

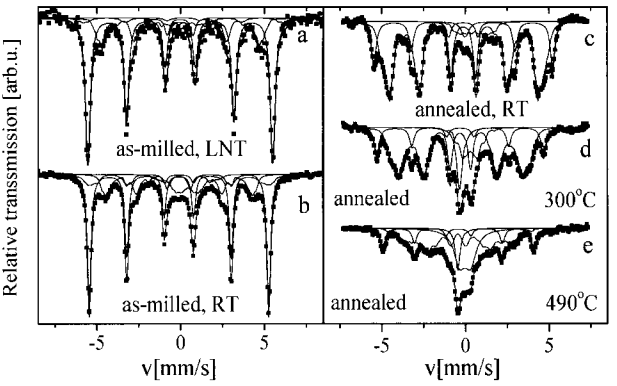

Figure 5 Mössbauer spectra obtained for mixture of elemental powders milled for 200 h: **a** as-milled sample, LNT spectrum, **b** as-milled sample, RT spectrum, **c** after annealing at 500°C, RT spectrum, **d**, **e** after annealing at 500°C, spectra collected at 300 and 490°C.

possible interactions between the magnetic moments, we do not observe typical superparamagnetic evolution of Mössbauer spectra.

6 Summary

It was stated that low-energy milling of mixture of elemental powders leads to the formation of both α and γ phases with various chemical compositions although small amount of pure elements is still present in the final product. Annealing the as-milled powder leads to fast formation of γ Fe–Ni phase. Paramagnetic component grows during milling and originates from: small amount of oxides, phases with about 30–35 at.% of nickel, grain boundaries and (possibly) relaxation effects of ultrafine particles of diverse composition. Short range atomic order in milled ribbon and also in the initial one slightly deviates from the random arrangement and tend to localize the Ni atoms in the first coordination shell around Fe atom.

Acknowledgement This work was supported by the Science and Technology Assistance Agency under the contract no. APVT-20-008404 and by the Scientific Grant Agency of Ministry of Education of Slovak Republic and Slovak Academy of Sciences under the contract no. 1/1021/04.

References

1. Inoue, A.: NanoStruct. Mater. **6**, 53 (1995)
2. Suryanarayana, C., Ivanov, E., Boldyrev, V.V.: Mater. Sci. Eng., A **304–306**, 151 (2001)
3. Brzózka, K., Olekšáková, D., Górka, B., Gawroński, M., Szumiata, T., Kollár, P.: Czechoslov. J. Phys. **54**, D145 (2004)
4. Olekšáková, D., Füzer, J., Kollár, P., Švec, T., Kováč, J., Briančin, J., Polánski, K.: Czechoslov. J. Phys. **54**, D93 (2004)
5. Wijn, H.P. (ed.): Landolt-Börnstein, New Series vol. III/19a. Springer, Berlin Heidelberg New York (1986)
6. Wertheim, G.K., Jaccarino, V., Wernick, J.H., Buchanan, D.N.E.: Phys. Rev. Lett. **12**, 24 (1964)
7. Drijver, J.W., van der Woude, F., Radelaar, S.: Phys. Rev. B **16**, 985 (1977)
8. Cowley, J.W.: Phys. Rev. **77**, 669 (1950)
9. Cowley, J.W.: Phys. Rev. **120**, 1648 (1960)

Hyperfine Interact (2006) 168:1097–1102
DOI 10.1007/s10751-006-9408-0

^{57}Fe Mössbauer and magnetic studies of $DyFe_{12-x}Ta_x$ compounds

J. L. Wang · S. J. Campbell · J. M. Cadogan · A. V. J. Edge

Published online: 14 November 2006

Abstract Refinements of the X-ray diffraction patterns show that $DyFe_{12-x}Ta_x$ compounds with $x = 0.5$–0.7 crystallise in the $ThMn_{12}$-type structure and that the Ta atoms occupy the 8i sites. Spin reorientations have been detected by ac magnetic susceptibility for all compounds below room temperature. First the moments shift direction from easy axis to easy cone at T_{sr1}, then to easy plane at T_{sr2}. Both T_{sr1} and T_{sr2} increase with increasing Ta content up to $x = 0.65$ before decreasing with further increase in Ta content. Analyses of the Mössbauer spectra indicate that the individual Fe site hyperfine fields derived at 4.5 K for $DyFe_{11.35}Ta_{0.65}$ are $B_{hf} = 37.4$ T, 32.2 T and 27.6 T for the 8i, 8j and 8f sites, respectively.

Key words spin reorientation · Mössbauer effect · magnetic susceptibilities

1 Introduction

Given that the Curie temperature T_C and the saturation magnetization M_s of the $RFe_{12-x}M_x$ intermetallics decrease as the x concentration is increased [1], it is important to synthesize compounds in this series with the minimum amount of the stabilizing M element. Recently, Piquer et al. [2, 3] reported that the Ta-stabilized phase of $RFe_{11.5}Ta_{0.5}$ only forms with the heavier rare-earth elements Tb, Dy, Ho, Er and Lu. Vert et al. [4] found that pure single-phase samples do not form but that all samples included α-Fe and/or Fe_2Ta as impurity phases and approximately single phase samples of $RFe_{12-x}Ta_x$ were stabilised for $x = 0.5$–0.7 [4]. Later, the magnetic structure of $ErFe_{11.5}Ta_{0.5}$ was determined by neutron

J. L. Wang · S. J. Campbell (✉) · A. V. J. Edge
School of Physical, Environmental and Mathematical Sciences, The University of New South Wales, The Australian Defence Force Academy, Canberra, ACT 2600, Australia
e-mail: stewart.campbell@adfa.edu.au

J. M. Cadogan
School of Physics, The University of New South Wales, Sydney, NSW 2052, Australia

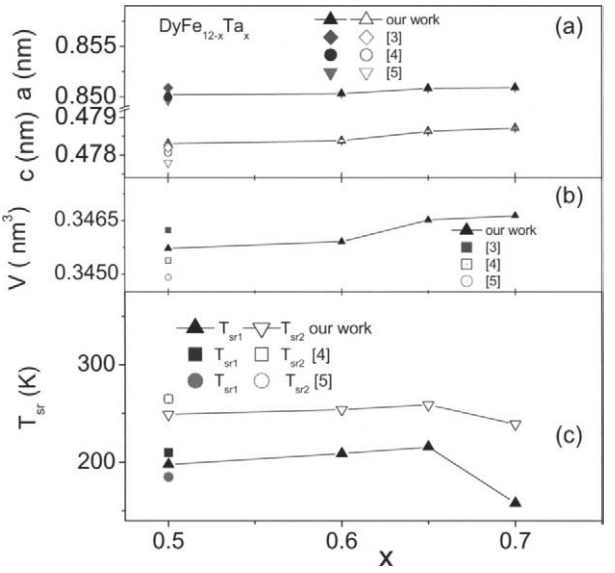

Figure 1 Dependence of: **a** the lattice parameters a and c; **b** unit cell volume V; **c** spin reorientation temperatures T_{sr1} and T_{sr2} of $DyFe_{12-x}Ta_x$ on Ta composition.

powder diffraction measurements and a spin reorientation detected from easy axis to easy cone at T_{sr} = 40 K [2, 3] or 49 K [5] with decreasing temperature.

As outlined previously [1], a significant feature of these compounds is that a range of spin reorientation temperatures has been reported by different authors – even for $DyFe_{12-x}M_x$ compounds containing the same M element and the same nominal M content. For $DyFe_{11.5}Ta_{0.5}$, Piquer et al. reported different values for T_{sr2} (T_{sr2} = 210 K in [3] and T_{sr2} = 185 K in [2]) – they attributed the difference to the fact that the change in the easy magnetization direction from cone to the basal plane is first-order but takes place gradually as the conical and basal phases may coexist with the volume ratio of one phase varying progressively with respect to the other as the temperature is lowered [3]. Recently it has been reported that T_{sr} depends sensitively on composition in $RFe_{1-x}Nb_x$ and $RFe_{12-x}Ti_x$ for R = Tb and Dy whereas for $ErFe_{1-x}Nb_x$ it has been found that T_{sr} remains essentially constant over the same concentration range [6, 7]. In order to clarify the question of the compositional dependence of the magnetocrystalline anisotropy in the $RFe_{12-x}Ta_x$ system, we have investigated the structural and magnetic properties of $DyFe_{12-x}Ta_x$ (x = 0.5, 0.6, 0.65 and 0.7).

2 Experimental

The alloys $DyFe_{12-x}Ta_x$ (x = 0.5–0.7) were prepared by arc-melting 99.9% purity materials in argon atmosphere. The quality of the samples was checked by X-ray diffraction with Cu–K_α radiation and the phase transition temperature determined by ac magnetic susceptibility. ^{57}Fe Mössbauer spectra were obtained between 4.5 and 298 K using a standard constant-acceleration spectrometer and a ^{57}CoRh source.

3 Results and discussion

Analysis of the X-ray diffraction patterns showed that all samples are essentially single phase and have the $ThMn_{12}$-structure as expected; samples exhibited typically less than 4 wt.% of α-Fe and Fe_2Ta as impurity phases, similar to earlier findings [2, 4]. The data were refined by Rietveld analysis using the FULLPROF program. As shown in Figure 1, the lattice parameters increase slightly with increasing Ta content, consistent with the larger radius of Ta compared with Fe and similar to the behaviour of $HoFe_{12-x}Ta_x$ [4]. We also find that the Ta atoms occupy only the 8i sites in all of the compounds; this can be understood in terms of enthalpy effects and metallic radii as for the $RFe_{12-x}Nb_x$ system [6]. We have calculated the Wigner-Seitz cell (WSC) volumes with the BLOKJE program [8] for all the crystallographic sites in $DyFe_{11.35}Ta_{0.65}$ by using the structural and positional parameters and the 12 coordinate metallic radii of 1.8, 1.26 and 1.49 Å for Dy, Fe and Ta, respectively. The calculated WSC volumes for the 2a, 8i, 8j and 8f sites are 30.03, 12.66, 11.80 and 11.34 Å^3, respectively, with the same sequence occurring in the other compounds [7].

Below room temperature, two anomalies (marked by arrows in Figure 2a) are detected in the χ-T curves. Based on the similarity to $DyFe_{12-x}T_x$ with T = Nb [6], T = Ti [9], and T = W [10], the anomalies can be ascribed to the effects of spin reorientation. With decreasing temperature from room temperature (as confirmed by neutron powder diffraction measurement [3]), the easy magnetization direction of the $DyFe_{12-x}Ta_x$ compounds changes from easy axis at T_{sr1}, via an easy-cone range, to easy plane at T_{sr2}.

According to crystal-field theory and using standard notation [1], the total anisotropy constant K_1^{tot} can be expressed, in a first-order approximation, as

$$K_1^{tot} = K_1^{Fe} + K_1^R = K_1^{Fe} - \frac{3}{2}\alpha_J A_{20} < O_{20} >< r^2 > . \quad (1)$$

where the second-order crystal-field coefficient A_{20} depends on the crystal structure and composition of a given compound. According to [1], A_{20} is negative in this system. For Dy^{3+}, $\alpha_J < 0$; this means that the second-order contribution of the Dy-sublattice to the anisotropy is planar. Since the temperature dependences of the anisotropies of the Dy-sublattice and Fe-sublattice are different, the competition between the Dy-sublattice and the Fe-sublattice with increasing temperature leads to a spin reorientation at a certain temperature below Curie temperature, consistent with the χ-T curves. It was reported that in $RFe_{12-x}T_x$ with T = Ti or V, A_{20} shifts towards a more negative value with decreasing x [11–13]. By estimating the individual CEF terms, Kuzmin [11] reported that the second-order term is the dominant contribution (~85%) to the shift of T_{sr} in $DyFe_{12-x}Ti_x$ compounds ($dT_{sr}/dx \sim -130$ K) and that the shift of A_{20} to positive values plays a critical role in the decrease of T_{sr} with increasing x. Moreover, in $RFe_{12-x}T_x$, the overall anisotropy constant K_1(Fe) is the sum of contributions from three sites:

$$K_1^{Fe}(tot) = K_1^{Fe}(8i) + K_1^{Fe}(8j) + K_1^{Fe}(8f). \quad (2)$$

It is known that the three anisotropy constants do not have the same magnitude [1] and normally it is found that the Fe ion at the 8i site gives the largest contribution to the overall 3d anisotropy [1, 9]. On the other hand it was recently reported that in $DyFe_{11}Mo_1$, the 8f site plays the largest role [14]. Thus the total Fe anisotropy constant is the result of the interplay between these three contributions. It should also be noted that Ta occupies the 8i site in $DyFe_{12-x}Ta_x$ and modifies the K_1^{tot}(Fe) contribution. So, the increase in Ta content

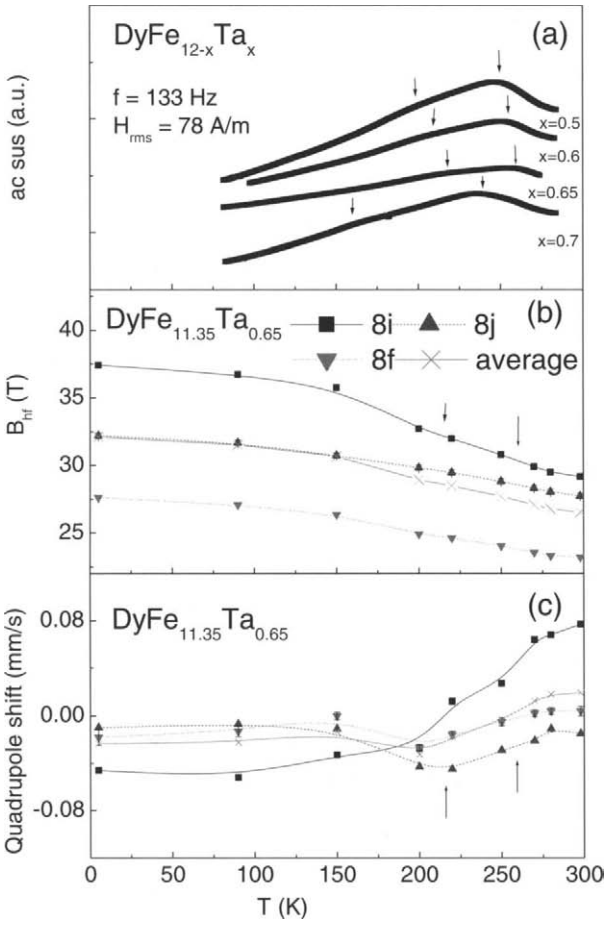

Figure 2 Temperature dependence of: (a) the ac magnetic susceptibility χ for $DyFe_{12-x}Ta_x$; and the temperature dependence of the hyperfine parameters of $DyFe_{11.35}Ta_{0.65}$: (b) magnetic hyperfine field B_{hf} and (c) quadrupole interaction QI.

not only decreases the contribution of the total Fe-sublattice to the anisotropy, but also leads to a change of the crystal parameter A_{20} which influences the contribution of the Dy-sublattice. As discussed below, the compositional dependence of T_{sr} in $DyFe_{12-x}Ta_x$ can be understood in terms of the competition between these two influences.

The Mössbauer spectra of $DyFe_{11.35}Ta_{0.65}$ at selected temperatures are shown in Figure 3 as examples of the spectra obtained in this study. Since the iron atoms in $DyFe_{12-x}Ta_x$ occupy three inequivalent 8i, 8j, and 8f crystallographic sites and the Ta atoms occupy only the 8i sites, we use six sextets [7] to fit the Mössbauer spectra, taking into account the random distribution of the Ta atoms in the neighbourhood of the three iron sites. Full details of the fit procedure are described in [7]. The Mössbauer relative intensities of the α-Fe and Fe_2Ta contributions can be deduced from the fit to the room temperature spectrum, as their contributions are clearly distinguishable [14]. Following [7, 9, 14, 15] the order of $B_{hf}(8i) > B_{hf}(8j) > B_{hf}(8f)$ is assumed for the hyperfine fields of the three Fe sites of the $ThMn_{12}$ structure depending on both the number of Fe nearest neighbours and the corresponding interatomic Fe–Fe distances. The temperature dependence of the hyperfine parameters for $DyFe_{11.35}Ta_{0.65}$ (Figure 2b and c) shows that the hyperfine fields B_{hf} increase with

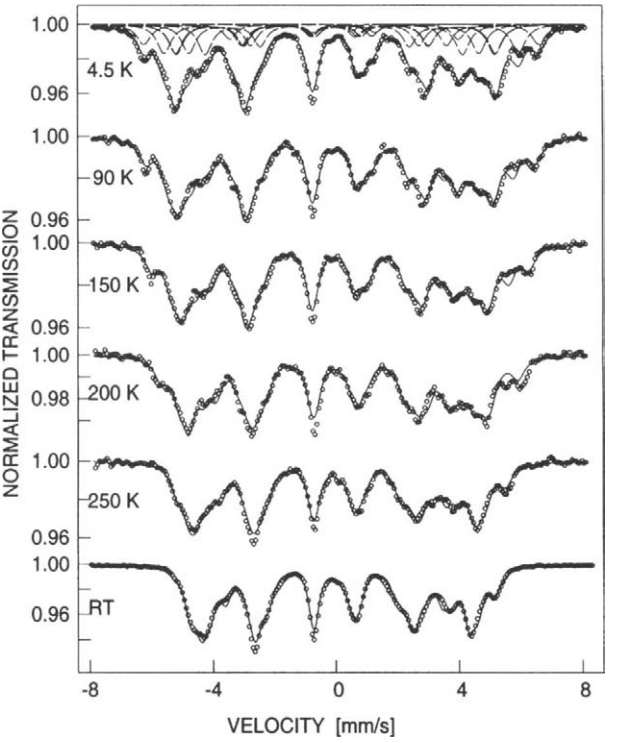

Figure 3 Mössbauer spectra of $DyFe_{11.35}Ta_{0.65}$ over the temperature range 4.5 to 300 K.

decreasing temperature as expected. Moreover, the sequence of the isomer shift magnitude is $\delta(8i) > \delta(8j) \cong \delta(8j)$ over the whole temperature range – this can be understood as the consequence of the order of the average Fe–Fe distances for each Fe ion site ($d_{Fe-Fe}(8i) > d_{Fe-Fe}(8j) \geq d_{Fe-Fe}(8f)$ [7, 14, 15]. The correlation between the isomer shifts and the WSC volume has been observed in many R–T compounds [14–16]. Given that the quadrupolar interaction (QI) is connected with the change of angle between the easy axis of magnetization and the electric field gradient, a change of QI is expected around the spin reorientation temperature (QI from negative to positive, Figure 2c).

Assuming a field-moment conversion coefficient of 15.6 T/μ_B [9], our individual site hyperfine field values of B_{hf} = 37.4, 32.2 and 27.6 T at 4.5 K for $DyFe_{11.35}Ta_{0.65}$ correspond to μ_{Fe} = 2.4, 2.1 and 1.8 μ_B for the 8i, 8j and 8f sites, respectively. This leads to an average Fe moment of 2.05 μ_B at 4.5 K. For the other compositions the temperature dependences of the hyperfine parameters have the same order and tendency.

Acknowledgement This work is supported in part by a Discovery Grant from the Australian Research Council leading to the award of a Research Associateship to JLW.

References

1. Li, H.S., Coey, J.M.D.: In: Buschow, K.H.J. (ed.) Handbook of Magnetic Materials, vol. 6, p. 1. North Holland, Amsterdam (1991)
2. Piquer, C., Artigas, M., Rubın, J., Bartolome, J.: J. Phys., Condens. Matter **10**, 11055 (1998)

3. Piquer, C., Palacios, E., Artigas, M., Bartolome, J., Rubın, J., Campo, J., Hofmann, M.: J. Phys., Condens. Matter **12**, 2265 (2000)
4. Vert, R., Bououdina, M., Fruchart, D., Gignoux, D., Kalychak, Y.M., Skolozdra, R.V.: J. Alloys Compd. **287**, 38 (1999)
5. Cadogan, J.M., Ryan, D.H., Swainson, I.P., Gagnon, R.: J. Phys., Condens. Matter **11**, 8975 (1999)
6. Wang, J.L, Tang, N., Shen, Y.P., Yang, D., Fuquan, B., Wu, G.H., Yang, F.M., de Boer, F.R., Brück, E., Buschow, K.H.J.: J. Appl. Phys. **91**, 2165 (2002)
7. Wang, J.L., Campbell, S.J., Cadogan, J.M., Tegus, O., Edge, A.V.J.: J. Phys., Condens. Matter **17**, 3689 (2005)
8. Gelato, L.: J. Appl. Crystallogr. **14**, 151 (1981)
9. Hu, B.P., Li, H.S., Gavigan, J.P., Coey, J.M.D.: J. Phys., Condens. Matter **1**, 755 (1989)
10. Plugaru, N., Rubın, J., Bartolome, J., Piquer, C., Artigas, M.: Phys. Rev., B **65**, 134419 (2002)
11. Kuzmin, M.D.: J. Appl. Phys. **88**, 7217 (2000)
12. Stefanski, P., Ivanov, V.: J. Alloys Compd. **219**, 199 (1995)
13. Wang, J.L., Garcia-Landa, B., Marquina, C., Ibarra, M.R., Yang, F.M., Wu, G.H.: Phys. Rev., B **67**, 014417 (2003)
14. Le Breton, J.M., Duc, N.H., Hien, V.T., Thuy, N.P., Teillet, J.: J. Magn. Magn. Mater **262**, 452 (2003)
15. Piquer, C., Isnard, O., Grandjean, F., Long, G.J.: J. Magn. Magn. Mater. **265**, 156 (2003)
16. Piquer, C., Grandjean, F., Isnard, O., Pop, V., Long, G.J.: J. Appl. Phys. **95**, 6308 (2004)

Hyperfine Interact (2006) 168:1103–1107
DOI 10.1007/s10751-006-9409-z

Gol'danskii–Karyagin effect and induced fields in rare earth-transition metal stannides

A. C. McGrath · J. D. Cashion

Published online: 8 November 2006

Abstract The asymmetric doublet obtained in earlier ^{119}Sn Mössbauer measurements of ternary stannides is re-interpreted as being due to the Gol'danskii–Karyagin effect instead of a β-Sn impurity included in the structure. Measurements in applied magnetic fields show that the conduction electron polarization at the Sn(2) site of $ErRh_{1.1}Sn_{3.6}$ is of the opposite sign to that of $PrRh_xSn_y$ and $PrCo_xSn_y$.

Key words Mössbauer spectroscopy · stannides · Gol'danskii–Karyagin effect · hyperfine field · conduction electron polarization

1 Introduction

The large family of ternary stannides of the type RT_xSn_y [1], (R = rare earth, Y, Sc, Ca, Sr; T = Rh, Ir, Ru, Os) have provided the basis for a wide variety of physical experimentation because of their interesting superconducting and magnetic properties and also the diverse crystallography which includes a multiplicity of phases, non-stoichiometry, twinning and rare earth-tin substitution. $ErRh_{1.1}Sn_{3.6}$ was one of the earliest examples of a re-entrant superconductor [1]. Because the crystals of the family were commonly grown from a tin solvent, inclusions of tin could occur, as well as aiding other effects such as the varying degrees of non-stoichiometry. This resulted in values of many of the parameters being sample dependent, with the best established values for the transitions in $ErRh_{1.1}Sn_{3.6}$ were that it became superconducting at T_c = 1.36 K and then ferromagnetic below T_m = 0.46 K, at which point the superconductivity was destroyed. However a range of values for both parameters was observed [1, 2], with some samples having no superconducting transition and consequently the highest magnetic transition.

In an earlier ^{119}Sn Mössbauer study of $ErRh_{1.1}Sn_{3.6}$ [3], an asymmetrical doublet was observed at room temperature, which was attributed to a small amount of included elemental β-tin. We have taken ^{119}Sn Mössbauer spectra of $ErRh_{1.1}Sn_{3.6}$, $PrRh_{1.33}Sn_{3.9}$ and

A. C. McGrath · J. D. Cashion (✉)
School of Physics, Monash University, Melbourne, Victoria 3800, Australia
e-mail: john.cashion@sci.monash.edu.au

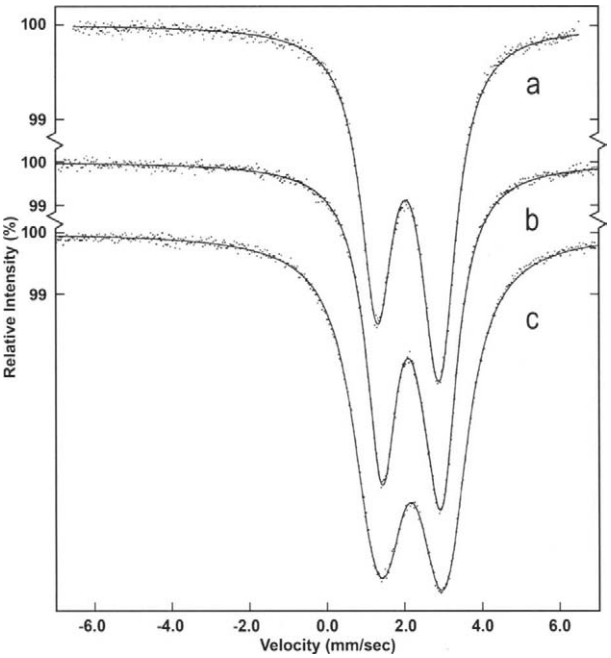

Figure 1 ^{119}Sn Mössbauer spectra of (a) $ErRh_{1.1}Sn_{3.6}$ at room temperature, (b) $PrRh_{1.33}Sn_{3.9}$ at 5 K and (c) $ErRh_{1.1}Sn_{3.6}$ at 5 K.

$PrCo_xSn_y$ in order to clarify the assignment of the asymmetry and also to probe the magnetic behaviour.

2 Experimental

The samples used in this investigation were original $ErRh_{1.1}Sn_{3.6}$, $PrRh_{1.33}Sn_{3.9}$ and $PrCo_xSn_y$ material produced in the Bell Laboratories, Murray Hill, NJ in 1980 and so the results are directly comparable to that used in other investigations at that time, including reference [3]. The crystals were crushed to <38 μm and 20 mg/cm^2 placed in perspex absorber holders with approximately 50 mg of BN. No traces were found of flattened pieces of β-tin as had been observed in other samples from this family. Mössbauer spectra were taken at room temperature, 82 and 5 K, the latter including spectra in an applied magnetic field of 8 T. In order to eliminate the possibility of preferred orientation (texture), sets of four room temperature spectra were also taken with the plane of the absorber tilted at the magic angle of 54.7° to the gamma ray beam and the absorber being rotated by 90° between successive spectra. These spectra were then summed to eliminate any texture effect [4].

3 Results

At room temperature, the ^{119}Sn Mössbauer spectra of all three samples were very similar, consisting mainly of an asymmetrical doublet as shown for $PrRh_{1.33}Sn_{3.9}$ in Figure 1a. The texture-free asymmetry, as determined from the sets of magic angle spectra, were 1.37 for $PrRh_{1.33}Sn_{3.9}$, 1.30 for $PrCo_xSn_y$ and 1.27 for $ErRh_{1.1}Sn_{3.6}$. As the temperature was lowered, the asymmetry decreased and the 5 K spectra of the two praseodymium

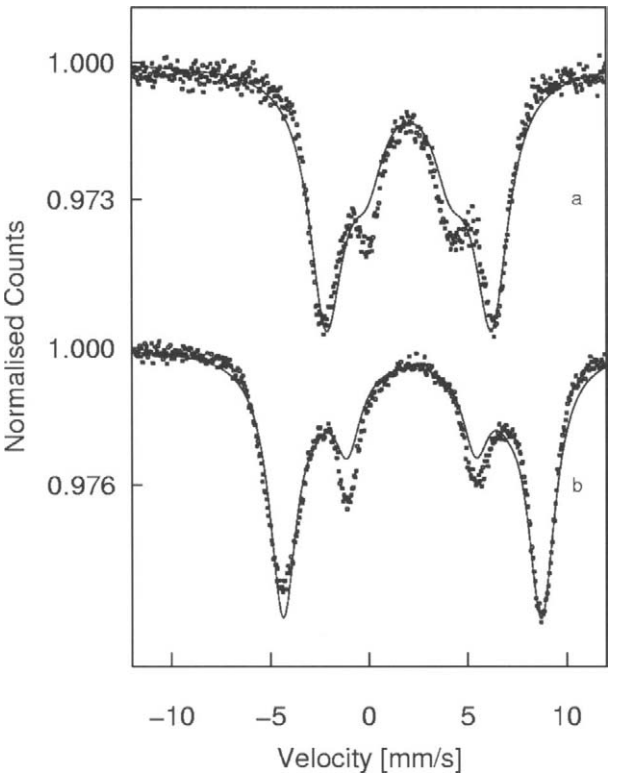

Figure 2 ^{119}Sn Mössbauer spectra of (a) $ErRh_{1.1}Sn_{3.6}$ and (b) $PrRh_{1.33}Sn_{3.9}$, both taken at 5 K and in an external longitudinal magnetic field of 8.0 T.

compounds were almost identical, with an asymmetry of 1.12 (Figure 1b). The spectrum of the $ErRh_{1.1}Sn_{3.6}$ had started to broaden at this stage (Figure 1c), but not as much as in the 1.5 K spectrum shown in Shenoy et al. [3].

The 77 K spectrum in [3] is very similar to those in Figure 1a and b and was fitted to the sum of two doublets corresponding to the Sn(1) and Sn(2) sites and a single line at 2.5 mm/s ascribed to undissolved β-tin from the excess tin flux. Our spectra could also be fitted this way, but an equally good fit could be obtained from only two doublets if the principal doublet was allowed to be asymmetrical. It is this fit which is shown in Figure 1a and b.

Figure 1c could be reasonably well fitted by assuming a hyperfine field of 1.5 T collinear to the electric field gradient (EFG) principal axis, but an improved fit was obtained with a field of only 0.42 T at an angle of approximately 70° to the EFG axis, with a family of acceptable fits in between these values.

The spectra of the praseodymium compounds at 5 K in a longitudinal applied field of 8.0 T were almost identical and that of $PrRh_{1.33}Sn_{3.9}$ is shown in Figure 2b, together with the spectrum of $ErRh_{1.1}Sn_{3.6}$ in Figure 2a, taken under the same conditions. Lines 2 and 5 of the sextets have disappeared, showing that the magnetization is parallel to the gamma ray direction. The asymmetry of the spectra, together with the known presence of two sites, the Gol'danskii–Karyagin effect and averaging over different angles between the applied field and the EFG principal axis, made them very difficult to fit. Since we do not have an unambiguously correct fit, we have chosen a simple, one site fit for Figure 2, with the angle between the field and the EFG equal to zero. This gives the average quadrupole splitting as

zero and enables us to obtain the hyperfine magnetic field as 9.7 T for the praseodymium compounds and 6.3 T for the erbium compound.

4 Discussion

The assumptions made when fitting poorly resolved spectra, such as those in Figure 1, have a considerable bearing on the resulting parameters and hence the interpretations. There are several reasons why we have rejected the interpretation involving included β-tin. First, the asymmetry remained remarkably constant between different samples of the same compound, and between different samples in the series, including also dysprosium, thulium and ytterbium rhodium stannides, in addition to the three described here. Second, the asymmetry decreases with temperature and if it was caused by β-tin, this would require the stannides to have a significantly lower Debye temperature than β-tin, which we regard as being unlikely. The third reason, which is consistent with a re-interpretation in terms of the Gol'danskii–Karyagin effect, is the measurement of the vibrational anisotropy of the Sn(2) atoms of the phase 1, $SnYbRh_4Sn_{12}$ member (or $YbRh_{1.33}Sn_{4.33}$ in our terms) by Hodeau et al. [5]. They obtained r.m.s. values for the thermal ellipsoid at room temperature of 0.0158, 0.0095 and 0.0082 nm, with the largest value being directed at about 15° to the Sn(1)–Sn(2) bond.

The Sn(2) atoms lie on mirror planes, each of which contains its single very close Sn(2) neighbour and the Sn(1) to which both are bonded. One principal axis of the EFG must be perpendicular to the mirror plane, with the other two axes in the plane probably being parallel and perpendicular to the Sn(2)–Sn(2) bond. This last direction is almost parallel to the major principal axis of the thermal ellipsoid and, if we assume that this is also the principal EFG direction, then we can use the method of Herber and Chandra [6] to calculate the expected asymmetry of the quadrupole doublet due to the Gol'danskii–Karyagin effect. The resulting value of 1.28 agrees well with our observed room temperature values.

The elimination of the β-tin component increases the uncertainty of the right hand member of the Sn(1) doublet. However, this uncertainty does not alter the conclusion in [3] that the Sn(1) and Sn(2) atoms are chemically different, in agreement with the crystal chemistry. Chenevas et al. [7] pointed out that the Rh–Sn(2) distance in the phase 1 structure of the stannides is too short to correspond to a metallic bond, so it must have some ionic-covalent character. Considering this, with the observation by Vandenberg [8] of the similarity of the structure of the Sn(2) atoms in phase III to that of the covalent α-tin, we note that the isomer shift of the principal doublet in all of these compounds (2.1–2.2 mm/s) is much closer to that of α-tin (2.03 mm/s) than it is to β-tin (2.55 mm/s).

Our measurements of the hyperfine fields in Figure 2 show a difference of 1.7 T between the measured values and the applied field, but with opposite sign. This can be explained as follows. The small field observed at 1.5 K at the Sn(2) site in $ErRh_{1.1}Sn_{3.6}$ was attributed [3] to a transferred hyperfine field generated by the erbium spin polarizing the conduction electrons and thus creating a spin density at the Sn(2) site. Such a field is usually negative and we see that, even with a relatively large applied field, the sign of the conduction electron polarization is determined by the erbium magnetization and not by the applied field. However, in the praseodymium compounds, the conduction electron polarization is created by the applied field and is parallel to it, thus giving an enhanced field in these samples.

Acknowledgement We are pleased to acknowledge the financial support of the Australian Research Council and a Monash Graduate scholarship for A. C. McG.

References

1. Remeika, J.P., Espinosa, G.P., Cooper, A.S., Barz, H., Rowell, J.M., McWhan, D.B., Vandenberg, J.M., Moncton, D.E., Fisk, Z., Woolf, L.D., Hamaker, H.C., Maple, M.B., Shirane, G., Thomlinson, W.: Solid State Commun. **34**, 923–926 (1980)
2. Ott, H.R., Odoni, W., Fisk, Z., Remeika, J.P.: In: Shenoy, G.K., Dunlap, B.D., Fradin, F.Y. (eds.) Ternary Superconductors, pp. 251–254. North-Holland, New York (1981)
3. Shenoy, G.K., Pröbst, F., Cashion, J.D., Viccaro, P.J., Niarchos, D., Dunlap, B.D., Remeika, J.P.: Solid State Commun. **37**, 53–55 (1980)
4. Grenèche, J.M., Varret, F.: J. Physique, Lett. **43**, L233–L237 (1982)
5. Hodeau, J.L., Chenavas, J., Marezio, M., Remeika, J.P.: Solid State Commun. **36**, 839–845 (1980)
6. Herber, R.H., Chandra, S.: J. Chem. Phys. **52**, 6045–6048 (1970)
7. Chenevas, J., Hodeau, J.L., Collomb, A., Marezio, M., Remeika, J.P., Vandenberg, J.M.: In: Shenoy, G.K., Dunlap, B.D., Fradin, F.Y. (eds.) Ternary Superconductors, pp. 219–224, North-Holland, New York (1981)
8. Vandenberg, J.M.: Mater. Res. Bull. **15**, 835–847 (1980)

Hyperfine Interact (2006) 168:1109–1114
DOI 10.1007/s10751-006-9410-6

Thermal equilibrium defects in iron-based alloys

Jan Chojcan

Published online: 27 October 2006

Abstract The Mössbauer spectra of ^{57}Fe were measured for the thermal equilibrium b.c.c. $Fe_{0.947}V_{0.053}$ and $Fe_{0.956}Co_{0.044}$ solid solutions being at temperature ranging from 300 to 1,000 K. The obtained data were analysed in terms of concentration of unoccupied sites in the 14-site surroundings of an ^{57}Fe Mössbauer probe in a b.c.c. sample. It turned out that the probe detects unoccupied sites in its neighbourhood when the temperature of the material studied does not exceed about 900 K. This result suggests that the Mössbauer spectroscopy "sees" the pre-vacancy effect revealed by the positron annihilation spectroscopy in the early 1960s.

Key words thermal equilibrium defects · iron alloys · Mössbauer spectroscopy

1 Introduction

Thermal equilibrium studies with positron annihilation spectroscopy show that an increase in the temperature of a metal goes together with prolonging of the positron lifetime in the material [1]. This can be explained as a result of two processes – thermal expansion of the crystalline lattice and creation of vacancies in the lattice. The latter is observed for iron crystal when its temperature is higher than about 1,070 K. Simultaneously, for the temperatures not exceeding 1,070 K, the positron lifetime τ_p in iron increases with temperature at the rate α_p about three times larger than one could expect having known that in the first approximation τ_p is proportional to the reciprocal of the "free" electron density, determined by thermal expansion of the crystalline lattice. The unexpected large value of α_p speaks in favour of the suggestion that an increase in the temperature of iron is accompanied by creation of some low-electron-density regions that attract positrons and prolong their lifetime. It seems that the regions arise due to thermal distortions (dilatations) of the crystalline lattice leading only to a transient increase of the distance between a certain number of neighbouring atoms and not resulting in creation of a stable vacancy. This so-

J. Chojcan (✉)
Institute of Experimental Physics, University of Wrocław, Pl. M. Borna 9, 50-204 Wrocław, Poland
e-mail: chojcan@ifd.uni.wroc.pl

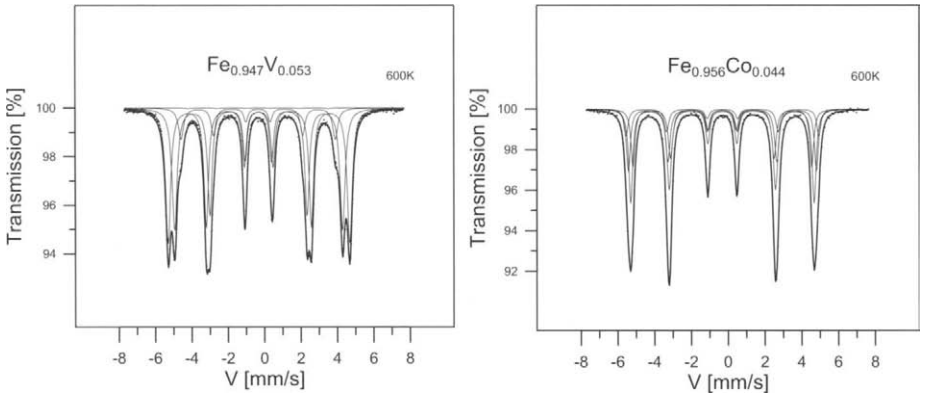

Figure 1 The Mössbauer spectra of ^{57}Fe for the $Fe_{0.947}V_{0.053}$ and $Fe_{0.956}Co_{0.044}$ alloys being at 600 K.

called prevacancy effect was observed for the first time on In, Cd and Zn in the early 1960s [2] but its intensively studies began in the middle of 1970s [3] and lasted for approximately two decades [1–7].

In recent years it appeared that such "low-temperature" distortions in the crystalline lattice can be observed also with the ^{57}Fe Mössbauer spectroscopy [8–10]. According to our simplified interpretation of the Mössbauer spectrum for a binary iron-based solid solution, the ^{57}Fe probe is sensitive to any change in the number of its neighbouring atoms located in the first or in the first and second coordination shells (determined by the kind of the non-iron atoms in the solution). Thanks to that the probe can detect simultaneously both the real vacancies as well as distortions of the crystalline lattice leading to a displacement of one or more neighbouring atoms outside the first or the second coordination shell of the probe. Moreover, the two different kinds of defects are seen by the probe in the same way – as unoccupied sites or vacancies in its neighbourhood, for example. That is why the Mössbauer nuclei detect vacancies created at temperatures for which probabilities of formation of "clear" (Schottky) vacancies as well as vacancies forming the separate interstitial-vacancy (Frenkel) pairs are negligibly small. The "low-temperature" vacancies or pseudo-vacancies, detected by ^{57}Fe nuclei, seem to be the low-electron-density regions that attract positrons so they can be explored independently with these two different nuclear probes.

In this paper we present results obtained for the thermal equilibrium study of pseudo-vacancies in two solid solutions $Fe_{0.947}V_{0.053}$ and $Fe_{0.956}Co_{0.044}$.

2 Experimental and results

The samples of iron-vanadium and iron-cobalt alloys were prepared by melting the Johnson–Matthey vanadium of spectral purity as well as the Aldrich 99.999% pure iron and 99.995% pure cobalt in an arc furnace filled with argon. Resulting ingots were forged and cold-rolled to the final thickness of about 0.04 mm and then the foils were annealed in vacuum at about 1,270 K for 4 h and slowly furnace cooled to room temperature for 6 h. Under these conditions, diffusion effectively stops at about 700 K [11], so the observed distributions of atoms in the annealed specimens should be the frozen-in state

Table I The best-fit parameters of the assumed model of the ^{57}Fe Mössbauer spectrum measured for the $Fe_{0.947}V_{0.053}$ alloy being at different temperatures

T (K)	B_0 (T)	ΔB (T)	IS_0 (mm/s)	ΔIS (mm/s)	c_1	c_2
300	33.479(3)	−2.578(4)	+0.0012(4)	−0.0188(5)	0.415(2)	0.111(1)
400	32.867(3)	−2.514(4)	−0.0675(4)	−0.0195(5)	0.419(2)	0.112(2)
500	32.090(4)	−2.443(5)	−0.1343(4)	−0.0193(5)	0.421(2)	0.112(2)
600	31.087(4)	−2.354(5)	−0.2003(4)	−0.0181(5)	0.423(2)	0.108(2)
650	30.489(4)	−2.304(6)	−0.2325(4)	−0.0190(6)	0.424(2)	0.107(2)
700	29.813(4)	−2.238(5)	−0.2646(4)	−0.0186(5)	0.423(2)	0.105(2)
750	29.043(5)	−2.173(6)	−0.2987(5)	−0.0192(6)	0.421(2)	0.106(2)
800	28.116(5)	−2.073(6)	−0.3328(5)	−0.0175(6)	0.412(2)	0.106(2)
850	27.039(5)	−1.969(6)	−0.3665(5)	−0.0182(6)	0.408(3)	0.107(2)
900	25.730(5)	−1.827(7)	−0.3995(5)	−0.0183(6)	0.404(3)	0.109(2)
950	24.111(6)	−1.625(8)	−0.4357(5)	−0.0147(7)	0.398(3)	0.117(3)
1,000	22.196(13)	−1.150(14)	−0.4688(7)	−0.0099(7)	0.352(5)	0.220(4)

corresponding to 700 K whereas concentration of vacancies should approach the equilibrium concentration of vacancies at room temperature (practically zero). The atomic composition of the samples were checked by an analysis of the energy distribution of X-rays (EDX) induced by the 20 keV electron beam. The EDX data showed that the studied Fe–V and Fe–Co alloys contained 5.3 ± 0.2 at.% of vanadium and 4.4 ± 0.2 at.% of cobalt, respectively. The measurements of the ^{57}Fe Mössbauer spectra were performed for the samples heated in a vacuum CYGNUS furnace, having a stability of about 0.2 K by using the controller TERMOS and a chromel–alumel thermocouple. The spectra were recorded in transmission geometry by means of a constant-acceleration POLON spectrometer of standard design. The 14.4 keV gamma rays were provided by a ^{57}Co:Rh source. Some spectra are presented in Figure 1.

The spectra measured for temperatures ranging from 300 to 1,000 K were analysed as in our previous papers (see [8–10] for example) in terms of four six-line patterns corresponding to different hyperfine fields B at ^{57}Fe nuclei generated by different numbers of iron and non-iron (D) atoms located in the vicinity of the probing nuclei, assuming that the effect of non-iron atoms on B is additive and independent of their positions in the surroundings of the probe. Moreover, it was accepted that for a given temperature the field (and the corresponding centre shift IS of the subspectrum) is a linear function of the number n of non-iron neighbours of ^{57}Fe with the form: $B_n = B_0 + n\Delta B$, where B_0 and ΔB are fitted parameters; ΔB stands for the change of B with one D atom in the neighbourhood of the Mössbauer probe. Finally, it was assumed that the three line widths Γ_{16}, Γ_{25} and Γ_{34} as well as the two line area ratios I_{16}/I_{34} and I_{25}/I_{34} are the same for all six-line components of the given spectrum. The fits obtained under these assumptions are satisfied – see Figure 1, and the found values of the best-fit parameters ΔB and ΔIS (displayed in Tables I and II) are in good agreement with corresponding data given in the literature; e.g., in [12] one can find that at room temperature ΔB amounts to −2.43 T for D = V and for D = Co it is 0.96 T.

As the main result of the analysis the relative areas c_1 and c_2 of the second and third spectrum components were determined. The components are related to the existence of one D atom and two D atoms in the neighbourhood of ^{57}Fe, respectively. Assuming that the Lamb–Mössbauer factor is independent of the configuration of atoms in the surroundings of the ^{57}Fe nucleus (quite reasonable for a metal [13]), the c_1 and c_2 values describe intensities of the components mentioned above. The results are listed in Tables I and II.

Table II The best-fit parameters of the assumed model of the ^{57}Fe Mössbauer spectrum measured for the $Fe_{0.956}Co_{0.044}$ alloy being at different temperatures

T (K)	B_0 (T)	ΔB (T)	IS_0 (mm/s)	ΔIS (mm/s)	c_1	c_2
300	32.658(17)	0.848(11)	+0.0022(5)	0.0018(4)	0.375(7)	0.270(6)
400	32.060(18)	0.833(12)	−0.0683(5)	0.0012(4)	0.391(8)	0.257(6)
500	31.173(17)	0.835(10)	−0.1369(5)	0.0016(4)	0.407(7)	0.270(6)
600	30.263(22)	0.786(14)	−0.2031(6)	0.0020(4)	0.390(9)	0.257(7)
650	29.630(19)	0.810(12)	−0.2371(6)	0.0014(4)	0.394(8)	0.277(6)
700	28.939(22)	0.821(14)	−0.2714(7)	0.0020(5)	0.396(8)	0.271(7)
750	28.145(21)	0.855(14)	−0.3030(7)	0.0010(5)	0.407(9)	0.275(7)
800	27.279(21)	0.848(15)	−0.3394(7)	0.0018(5)	0.405(9)	0.252(7)
850	26.102(23)	0.849(15)	−0.3725(7)	0.0025(5)	0.394(8)	0.268(7)
900	24.258(31)	0.958(14)	−0.4047(11)	0.0012(6)	0.390(9)	0.291(7)
950	22.963(23)	0.937(14)	−0.4456(9)	0.0038(6)	0.376(10)	0.291(8)
1,000	20.878(22)	1.012(14)	−0.4788(9)	0.0045(6)	0.375(9)	0.286(7)
1,060	16.976(22)	1.427(16)	−0.5269(11)	0.0078(11)	0.344(9)	0.312(8)

The c_1 and c_2 values for the samples at 300 K were used to calculate the binding energy E_b for pairs of D atoms (V or Co) in the studied materials. The computations were performed, as in our earlier papers [8–10], on the basis of the modified Hrynkiewicz–Królas formula [14, 15]. The E_b values obtained for the investigated samples $Fe_{0.947}V_{0.053}$ and $Fe_{0.956}Co_{0.044}$ at 300 K are 26(2) and −78(6) meV, respectively, and they are in qualitative agreement with those obtained in our previous studies [15]. These values of E_b were used to estimate the concentration of vacancies (real vacancies and/or pseudo-vacancies – see Introduction) in the specimens being at temperature higher than 300 K according to the idea given in [8]. The idea is based on the assumption that a creation of vacancies in iron-based solid solutions $Fe_{1-x}D_x$ goes together with a certain decrease in the effective number N of neighbours having a direct influence on the Mössbauer probe and the decrease of N is responsible for a change in relative intensities of the ^{57}Fe Mössbauer spectrum components observed on heating of a specimen. For the investigated alloys, the maximum value of N is 14 (the total number of the lattice sites in the first and second coordination shells of an atom in the bcc lattice). The number N for samples at different temperatures was determined assuming that the value of E_b for a given sample is temperature independent and applying the following equation [10]:

$$N = 0.5 \cdot \left\{ 3x - 1 + (1-x)[1 + 8 \cdot (1 + 2 \cdot c_2/c_1) \cdot (c_2/c_1) \cdot \exp(+E_b/(kT_d))]^{0.5} \right\} / x. \quad (1)$$

Having known the N value one can calculate the concentration $c_V = (14 - N)/14$ of vacancies or unoccupied sites in the 14-site neighbourhood of the ^{57}Fe probe atom. The results of such calculations are presented in Figure 2.

As it is seen in Figure 2, the Mössbauer study of thermal equilibrium vacancies give reasonable results i.e. positive or zero values for concentration c_V of the defects, if the study are performed at temperatures from a limited range only. In the case of the $Fe_{0.947}V_{0.053}$ alloy $c_V \geq 0$ when $T \leq 900$ K whereas for the $Fe_{0.956}Co_{0.044}$ alloy $c_V \geq 0$ when $T \leq 800$ K. The observation for the $Fe_{0.947}V_{0.053}$ specimen agrees very well with our previous findings concerning the $Fe_{0.948}Cr_{0.052}$ alloy [10]. It seems that the temperature limit exists because

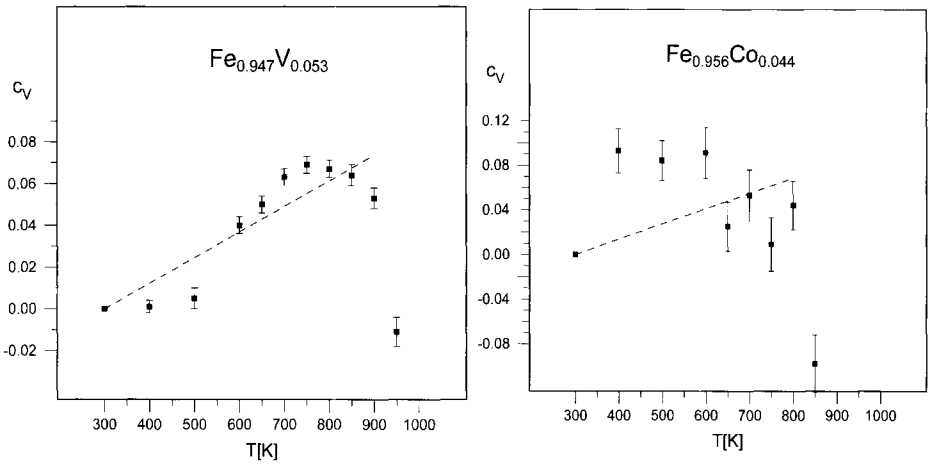

Figure 2 The temperature dependence of concentration c_V of vacancies detected by the ^{57}Fe Mössbauer probes in the b.c.c. $Fe_{0.947}V_{0.053}$ and $Fe_{0.956}Co_{0.044}$ alloys. The *dashed lines* are plots of the function $f(T) = \beta + \alpha T$, fitted by the least-squares method to the c_v values for $T \leq 900$ K in the case of the $Fe_{0.947}V_{0.053}$ alloy ($\alpha = 1.23(12) \times 10^{-4}$ K^{-1}) and for $T \leq 800$ K in the case of the $Fe_{0.956}Co_{0.044}$ alloy ($\alpha = 1.4(6) \times 10^{-4}$ K^{-1}).

the spectrum, measured at too high temperature, is not resolved enough to obtain credible information about intensities of the spectrum components delivering the information on the vacancies located in the investigated material. However, the data for the $Fe_{0.956}Co_{0.044}$ sample suggests that such explanation of the temperature limit may not be fully correct. In the case of the sample, spectrum components are badly resolved at any temperature and in spite of that the resulting temperature dependence of c_V, in general, is very similar to that for the $Fe_{0.948}Cr_{0.052}$ and $Fe_{0.947}V_{0.053}$ specimens with relatively well resolved spectrum components.

Although the $c_V(T)$ dependencies for the studied samples are similar in general – both reach maximum (see Figure 2), it is impossible to say that they are linear for the range of temperatures where c_V values increase with T as it was found in the case of the $Fe_{0.948}Cr_{0.052}$ alloy [10]. Moreover, the shape of the curve $c_V(T)$ for the $Fe_{0.956}Co_{0.044}$ sample is revealed with less precision than for the $Fe_{0.947}V_{0.053}$ specimen due to essential differences in uncertainty of the corresponding c_V values. In these circumstances it seems obvious that one should concentrate on the conclusions resulting from the curve shape for the $Fe_{0.947}V_{0.053}$ specimen only. This is worth noticing that the shape is similar to the letter S; based on its details one can conclude that detectable creation of pseudo-vacancies starts at about 500 K and the process probably saturates at about 700 K. It is too early to draw more quantitative conclusions on the parameters of the pseudo-vacancy formation because such detailed "low-temperature" dependence of c_V has been measured for the first time and the obtained results should be verified by further studies of the kind presented in this paper.

3 Final conclusion

The findings of this paper support our earlier suggestion [8] that the Mössbauer spectroscopy of ^{57}Fe gives exceptionally wide information concerning different types of thermal defects, existing in some binary iron-based solid solutions. In particular, the

spectroscopy seems to detect also the pre-vacancy effect discovered by the positron annihilation spectroscopy. The latter suggests that existing of the effect is a natural feature of metals and it is not created by a special behaviour of positrons in the materials [4–7].

Acknowledgement This work was supported by the University of Wroclaw under the Grant 2016/IFD/2004.

References

1. Schaefer, H.-E.: Phys. Status Solidi, A **102**, 47 (1987)
2. MacKenzie, I.K.: In: Coleman, P.G., Sharma, S.C., Diana, L.M. (eds.) Positron Annihilation, p. 179. North Holland, Amsterdam (1982)
3. Smedskjaer, L.C.: In: Brandt, W., Dupasquier, A. (eds.) Positron Solid-State Physic, p. 597. North Holland, Amsterdam (1983)
4. Seeger, A.: In: Jain, P.C., Singru, R.M., Gopinathan, K.P. (eds.) Positron Annihilation, p. 48. Word Scientific, Singapore (1985)
5. Seeger, A., Banhart, F.: Mat. Sci. Forum **105–110**, 825 (1992)
6. Seeger, A.: Mat. Sci. Forum **255–257**, 1 (1997)
7. Seeger, A.: Phys. Status Solidi, A **167**, 289 (1998)
8. Chojcan, J.: J. Alloys Compd. **337**, 25 (2002)
9. Chojcan, J.: Acta Phys. Pol., A **100**, 723 (2001)
10. Chojcan, J.: J. Alloys Compd. **373**, 33 (2004)
11. Cranshaw, T.E.: J. Phys., Condens. Matter **1**, 829 (1989)
12. Vincze, I., Campell, I.A.: J. Phys., F **3**, 647 (1973)
13. Bogner, J., Steiner, W., Reissner, M., Mohn, P., Blaha, P., Schwarz, K., Krachler, R., Ipser, H., Sepiol, B.: Phys. Rev., B **58**, 14922 (1998)
14. Hrynkiewicz, A.Z., Królas, K.: Phys. Rev., B **28**, 1864 (1983)
15. Chojcan, J.: J. Alloys Compd. **264**, 50 (1998)

Hyperfine Interact (2006) 168:1115–1119
DOI 10.1007/s10751-006-9411-5

Study of the $[Fe(OMe)(dpm)_2]_2$ dimer in the presence of a magnetic field by using Mössbauer spectroscopy

L. Cianchi · F. Del Giallo · M. Lantieri · P. Moretti · G. Spina

Published online: 16 November 2006

Abstract We present a Mössbauer study of a $S = 0$ ground state magnetic Fe(III)-dimer in the presence of an applied 5 T longitudinal magnetic field, between 7.6 and 33 K. The values obtained for the isomer shift and the quadrupolar splitting are comparable with the ones of Fe(III) ions coordinated to eight oxygen ions. Regarding the spin dynamics, both intramultiplet and intermultiplet transitions are considered. In the chosen temperature range the rate of the former transitions is constant, within the errors, while the rate of the latter ones quickly increases with the temperature.

Key words nanomagnets · Mössbauer · spin dynamics

In the $[Fe(OMe)(dpm)_2]_2$ cluster (Figure 1), the two Fe(III) ion spins ($s = 5 / 2$) are antiferromagnetically coupled via oxomethil bridges, so that its spin can assume six possible values from 0 to 5 in order of increasing energy. Moreover, the presence of an axial magnetic anisotropy has to be taken into account so that the spin Hamiltonian is:

$$H_S = J\boldsymbol{S}_1 \cdot \boldsymbol{S}_2 + \boldsymbol{S}_1 \underline{\Lambda}\, \boldsymbol{S}_2 + D\left[S_\zeta^2 - \frac{1}{3}S(S+1)\right] - g\mu_B \boldsymbol{S} \cdot \boldsymbol{B}$$

L. Cianchi (✉) · F. Del Giallo · P. Moretti
Istituto dei Sistemi Complessi, CNR, via della Madonna del Piano 10, 50019 Sesto Fiorentino (FI), Italy
e-mail: luciano.cianchi@isc.cnr.it

M. Lantieri
Dipartimento di Chimica, Università di Firenze, via della Lastruccia 5, 50019 Sesto Fiorentino (FI), Italy

G. Spina
Dipartimento di Fisica, Università di Firenze, via G. Sansone 1, 50019 Sesto Fiorentino (FI), Italy
INFM, Sesto Fiorentino (FI), Italy

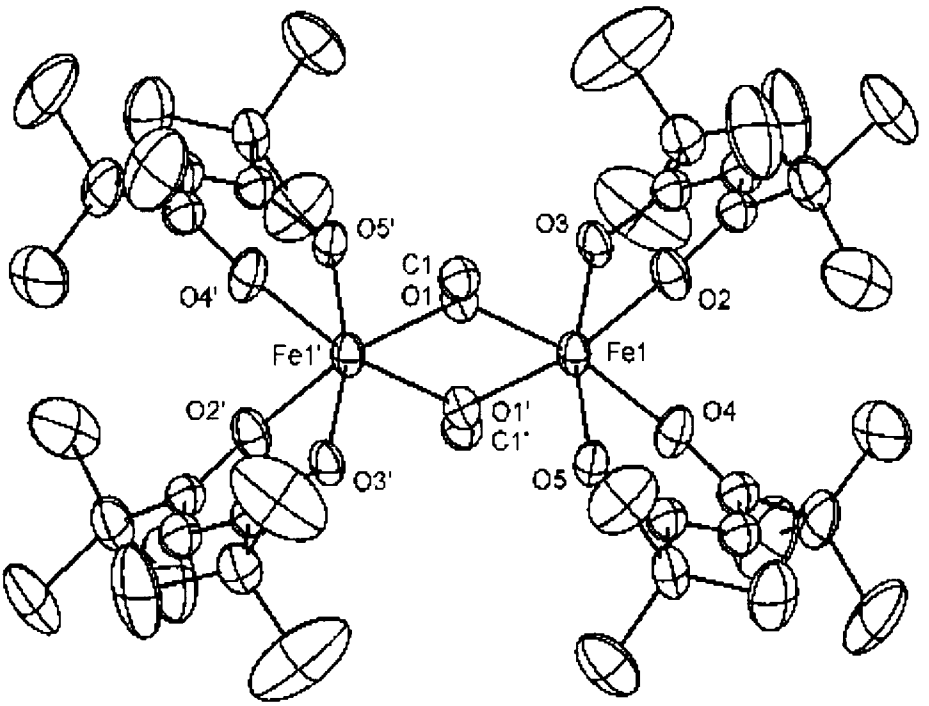

Figure 1 ORTEP view of the complex $[Fe(OMe)(dpm)_2]_2$.

where D is the magnetic-anisotropy constant, ζ denotes the anisotropy direction, J and $\underline{\Lambda}$ ($|D|$, $\Lambda << J$; $J > 0$) denote the isotropic and anisotropic exchange parameters, respectively. Lastly, the other symbols have the usual meanings.

In a previous paper [1] a Mössbauer study of the spin dynamics between 6.5 and 288 K in the absence of any external magnetic field was performed on the basis of fast relaxation limit. Although for $T < 40$ K spectra were not suitable to evaluate the relaxation rate, in the range from 60 to 200 K a quasi-flat trend of this parameter was found. Similar behaviours had been already observed in other $S = 0$ ground state ring-shaped iron clusters (i.e. Fe6 [2]).

In the present work we study the same dimer in the presence of a 5 T applied longitudinal magnetic field $\boldsymbol{B_0}$ ($\boldsymbol{B} = \boldsymbol{B_0} + \boldsymbol{B_{hyp}}$), in the temperature range from 7.6 to 33 K.

In the absence of any applied magnetic field, we found that the 15 K spectrum consists of a quadrupolar doublet, the lines of which show a little intensity difference that disappears by collecting the spectrum with the sample oriented at the magic angle 54.7°: this means that crystallographic texture is present in our sample [3].

By fitting these spectra (see Figure 2) the isomer shift (δ), the two independent EFG components (Q, η) and the direction and intensity of the magnetic anisotropy can be evaluated.

Regarding the spin dynamics, intramultiplet and intermultiplet spin transitions are considered. The former ones are described by a phenomenological Hamiltonian of the form: $H_d = F S_x$, where F is a stochastic real function of time. Unlike the intramultiplet transitions, the latter ones have to be described in terms of the single irons spin components. The mechanism of the intermultiplet transitions might consist of anisotropic modulations of the

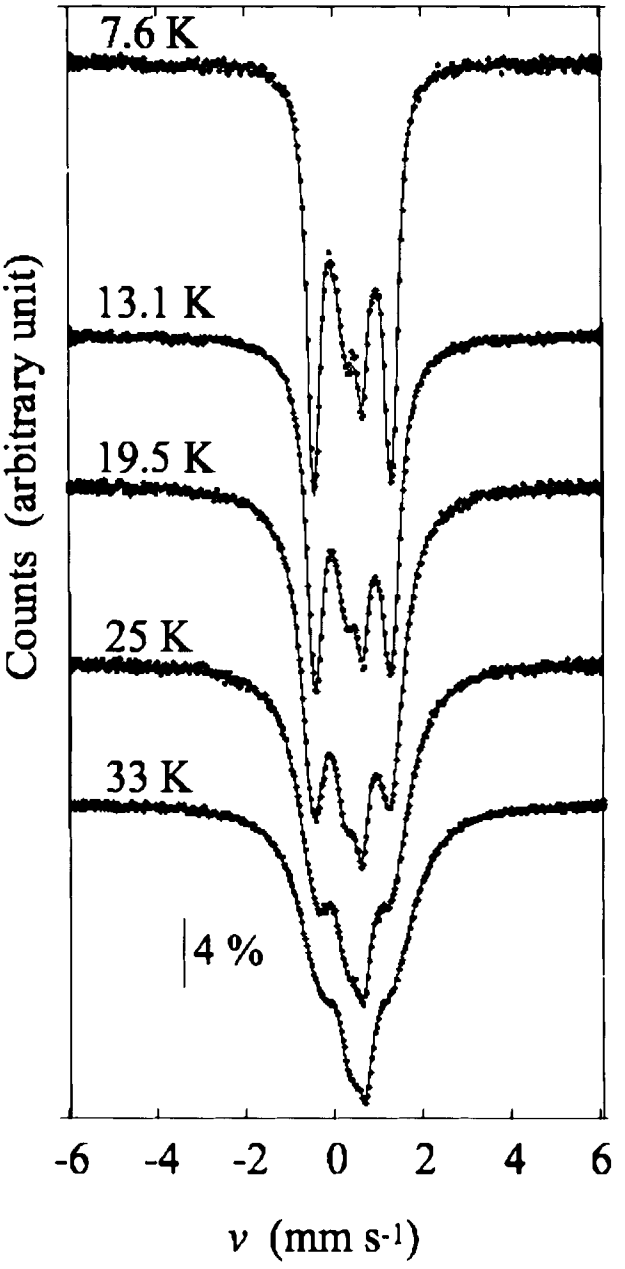

Figure 2 Spectra collected from 7.6 to 33 K. The *solid lines* represent the fits obtained as described in the text.

exchange interaction due to the thermal atomic motions. For the sake of simplicity, we considered only $\Delta S = 1$ and $|\Delta M| = 1$ transitions, so that the interaction Hamiltonian takes the form:

$$H_i = \Lambda(t)\left[(1-i)(S_1^+ S_{2z} - S_2^+ S_{1z}) + (1+i)(S_1^- S_{2z} - S_2^- S_{1z})\right]$$

where $\Lambda(t)$ is a stochastic time function.

Table I The usual hyperfine parameters are reported from the second to the fourth column

T (K)	Q (mm/s)	η	δ (mm/s)	B_{hyp} (T)	J_{rel} (10^7 s^{-1})	W_{01} (10^6 s^{-1})	$\Delta\Gamma$ (mm/s)
7.6	0.40(1)	0.71(5)	0.43(1)	40(10)	–	0	–
13.1	0.40(1)	0.74(1)	0.43(1)	39.9(1)	1.3(1)	0.44(5)	–
19.5	0.40(1)	0.74(9)	0.43(1)	40(4)	0.9(3)	1.59(2)	–
25.0	0.40(1)	0.9(4)	0.43(1)	40(30)	–	2(1)	0.1(1)
33.0	0.40(1)	0.8(2)	0.43(1)	40(14)	–	8.8(5)	0.1(1)

J_{rel} denotes the FT of the F correlation function, W_{01} the probability per unit time of the transition $S = 0 \rightarrow S = 1$ and $\Delta\Gamma$ extra-line width introduced in order to take into account the transitions towards the $S = 2$ multiplet

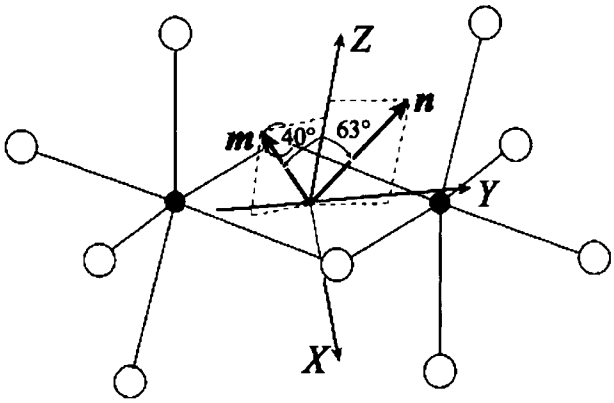

Figure 3 Orientations of texture axis n and magnetic anisotropy axis m with respect to the dimer EFG principal axes.

The spectrum shapes were obtained by means of the usual relaxation theory. Moreover, the micro-crystals in the sample look like to thin chips. On the other hand, the sample was made by mixing the material with Eicosano wax and by pressing the mixture inside a copper ring: during the compression an orientation of the grains occurs, so that a weighted average on the angles of B_0 with respect to the EFG principal axes is needed.

Some physical parameters obtained from the fitting of the spectra are shown in Table I. The quadrupolar splitting Q and the isomer shift δ are constant in our temperature range. Regarding the asymmetry parameter, the value around 0.7 is the most reliable because the low temperature spectra (7.6 and 13.1 K) contain more information than the other ones. The rather low value of the hyperfine field should denote a delocalization of the iron magnetic moment [4]. Only the intermediate-temperature spectra (13 and 19 K) give information about the intramultiplet relaxation parameter J_{rel}. In fact, in the lowest temperature spectrum the contributions of the $S \neq 0$ levels are negligible, and for $T > 19$ K the spin-thermal bath interaction mixes the ground state with the excited multiplets. Lastly, the trend of W_{01} versus T shows a rather steep increasing.

As far as the exchange constants are concerned, we obtained $\Lambda = 0$ and $J = 25(3)$ k_B, in agreement (within the errors) with 27.4 k_B deduced from susceptibility measurements [2].

The orientation angles of the magnetic anisotropy (Figure 3), referred to the EFG principal axes, as they came out from the fitting are $\theta = 0.7(2)$ rad, $\phi = 4.8(7)$ rad. Moreover, the anisotropy constant $D = -8(3)$ k_B coincides (within the errors) with the one deduced from previous Mössbauer measurements in the absence of any applied magnetic field [1].

Texture features are described by the angular distribution $n(\alpha)$ of the thin-chip-shaped grains with respect to texture symmetry axis $\boldsymbol{n}$ according to

$$n(\alpha) = \frac{C_T}{\sqrt{1 + C_T \cos^2(\alpha)}}$$

where C_T is a fitting constant and α is the angle between $\boldsymbol{n}$ and the field $\boldsymbol{B_0}$. It depends on the polar angles θ_T and ϕ_T formed by n with the EFG principal axes. We obtained C_T -1, that means that all the grains are parallel to each other, and $\theta_T = 1.1(1)$ rad, $\phi_T = 1.5(5)$ rad.

References

1. Cianchi, L., Del Giallo, F., Lantieri, M., Moretti, P., Spina, G., Caneschi, A.: Phys. Rev., B **69**, 014418 (2004)
2. Caneschi, A., Capaccioli, M., Cianchi, L., Del Giallo, F., Gatteschi, D., Moretti, P., Pieralli, F., Spina, G.: Hyperfine Interact. **116**, 215 (1998)
3. Greneche, J.M., Varret, F.: J. Phys. C: Solid State Phys. **15**, 5333 (1982)
4. Baruah, T., Kortus, J., Pederson, M.R., Wesolowski, R., Haraldsen, J., Musfeldt, J.L., Micah North, J., Zipse, D., Dalal, N.S.: Phys. Rev., B **70**, 214410 (2004)

Hyperfine Interact (2006) 168:1121–1125
DOI 10.1007/s10751-006-9480-5

Distribution of electric and magnetic hyperfine fields in Fe-rich gallo-germanates

S. Constantinescu

Published online: 12 December 2006

Abstract The crystal field disorder in some tetragonal and trigonal Ca-gallo-germanates, i.e., $A_2Fe_2ZO_7$ and $A_2LnFe_3Ge_3O_{14}$, with A=Ba or Sr, Ln=La or Nd and Z=Ge or Si, has been studied by ^{57}Fe Mössbauer spectroscopy. The observed distribution of the hyperfine fields is analysed from a theoretical model based on the additive perturbation approximation of crystal fields, a rigid lattice of ionic point charges and the random substitution of Fe^{3+}/Z^{4+} and A^{2+}/Ln^{3+}.

Key words hyperfine field distribution · gallo-germanates

1 Introduction

Mössbauer spectroscopy has been used to study strontium and barium iron-rich Ca-gallo-germanates (CGGO) with tetragonal (Tt) and trigonal (Tr) structures. Such crystalline structures are made up of successive layers of small (tetrahedrons) and large (Thompson cubes and octahedrons) oxygen polyhedrons and show intrinsic structural disorder, due to the random substitution of heterovalent ions on the tetrahedral (T1, T2) and octahedral (Oh) cationic sites: T1 and T2 for Tt-CGGO, T1 and Oh for Tr-CGGO, [1–3]. The intrinsic structural disorder leads to a distribution of crystal fields and, as a consequence, to the heterogeneous broadening of the optical transitions, which dominates the homogeneous one, even at 300 K. Over the last 15 years, efforts have been made to find new materials producing a tuneable stimulated emission with metal or lanthanide activators [4–6] and new piezoelectric crystals which show high piezoelectric coupling, low acoustic loss and high temperature stability [7–9]. It has been recently possible to obtain intrinsic disordered crystalline materials containing Mössbauer probes (iron, europium) and to study them from high-energy resolution Mössbauer spectroscopy [10, 11]. These materials show an hyperfine field distribution due to the diversity of the Fe environments arising from the random substitution of ions. The present work concerns a refined analysis of the hyperfine

S. Constantinescu (✉)
National Institute of Materials Physics, P.O. Box Mg-07, Bucharest, Romania
e-mail: sconst14061945@yahoo.com

Table I List and structures of the CGGO samples studied in this work

Structure	Sample	
Fe-Tetragonal gallo-germanate (Tt-CGGO)	$Ba_2Fe_2GeO_7$ $Sr_2Fe_2GeO_7$ $Sr_2Fe_2SiO_7$	$< A >_2 [Fe_{x1}, Z_{1-x1}]^{T1}[Fe_{x2}, Z_{1-x2}]_2^{T2}O_7$
Ln- and Fe-Trigonal gallo-germanate (Tr-CGGO)	$Ba_3Fe_2Ge_4O_{14}$ $Sr_3Fe_2Ge_4O_{14}$ $Sr_2LaFe_3Ge_4O_{14}$ $Sr_2NdFe_3Ge_4O_{14}$	$< A, Ln >_3 \{Fe_{x2}Ge_{1-x2}\}^{Oh}[Fe_{x1}, Ge_{1-x1}]_3^{T1}[Ge]_2^{T2}O_{14}$

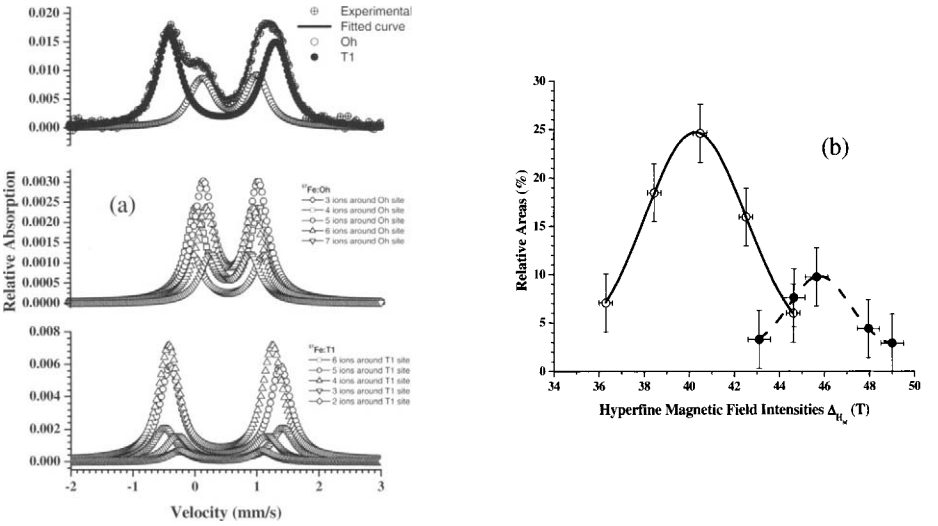

Figure 1 **a** ^{57}Fe Mössbauer spectrum of $Sr_2NdFe_3Ge_4O_{14}$ at room temperature and the different subspectra used to fit the experimental data. **b** Magnetic hyperfine field distribution for $Sr_2NdFe_3Ge_4O_{14}$ at liquid helium temperature, Fe:T1 (*open circles*) and Fe:Oh (*circles*) experimental values, fitted Gaussain curves for Fe:T1 (*solid line*) and Fe:Oh (*dashed line*).

field distribution in CGGO obtained from ^{57}Fe Mössbauer spectroscopy and based on a simple theoretical model of the random substitution of heterovalent ions.

2 Experimental results

The CGGO-type polycrystalline samples studied in this work are listed in Table I. They were prepared by solid phase synthesis and characterized by XRD [1–3]. The ^{57}Fe Mössbauer spectra were obtained in a large temperature range — between 4.2 K and 300 K (±0.5 K) — using a conventional constant acceleration transmission spectrometer and ^{57}Co: Cr (or Rh) source at room temperatures. Low-temperature measurements were made with a continuous flow Oxford Instruments cryostat. The experimental data were fitted to a sum of doublets and/or sextets of Lorentzian peaks, with the same line width *s* and intensity ratios 1:1 (doublets) and 3:2:1 (sextet).

Table II Mössbauer hyperfine parameters of $Sr_2NdFe_3Ge_4O_{14}$ at room and liquid helium temperatures (centre shift, δ_{Rh}, quadrupole splitting, Δ_Q, or shift, ε_Q, magnetic hyperfine field, H_{hf}, half linewidth, Γ, and relative area, A)

	Oh sites					*T*1 sites				
Subspectra	1	2	3	4	5	6	7	8	9	10
δ_{Rh} [mm/s]±0.02 mm/s	0.55	0.54	0.59	0.57	0.58	0.47	0.49	0.42	0.44	0.42
Δ_Q [mm/s]±0.04 mm/s	1.36	1.03	0.89	0.77	0.64	1.91	1.79	1.68	1.44	1.34
Γ[mm/s]±0.02 mm/s	0.40	0.39	0.39	0.37	0.38	0.43	0.41	0.42	0.43	0.42
A[%]±2%	4.17	8.16	10.31	7.68	3.97	8.07	21.91	27.20	6.03	2.49
δ_{Rh} [mm/s]±0.02 mm/s	0.62	0.61	0.60	0.60	0.60	0.54	0.54	0.54	0.54	0.54
ε_Q [mm/s]±0.02 mm/s	0.36	0.36	0.36	0.35	0.34	0.08	0.08	0.08	0.08	0.07
H_{hf}(T)±0.3 T	43.10	44.64	45.65	47.95	49.00	36.30	38.44	40.49	42.52	44.61
A[%]±2%	3.28	7.59	9.75	4.39	2.90	5.59	14.65	19.50	12.65	4.76

The different samples and their structures are given in Table I. For simplicity, only the Mössbauer spectrum of $Sr_2NdFe_3Ge_4O_{14}$ at room temperature is shown in Figure 1a. Ten different subspectra (doublets) were considered to fit the experimental data by considering the substitution of the Fe atoms on the T1 and Oh sites. The values of the Mössbauer parameters of $Sr_2NdFe_3Ge_4O_{14}$ at room and liquid helium temperatures are given in Table II. The values of the hyperfine parameters for the other compounds can be found in [12].

3 Discussion

The observed Mössbauer spectra are formed by a large number of subspectra that can be divided into two groups, corresponding to Fe^{3+} in T1 and T2, respectively, for Tt-CGGO (or Fe^{3+} in T1 and Oh for Tr-CGGO, more details can be found in [10, 11]). Magnetic hyperfine fields iare observed for Tt-CGGO, and for Ln-Tr-CGGO but at temperature lower than 30 K. Variations of the relative area of the subspectra as a function of the hyperfine field values show the overlapping of two distributions that can be assigned to the above-mentioned two groups (Figure 1b). They were fitted to Gaussian distributions and the largest line width s were found for Fe^{3+}:T1 in Tt-CGGO and Fe^{3+}:Oh in Tr-CGGO structures, respectively. Moreover, the overlapping degree is stongly dependent on the type and the number of ions on A and T sites. The location of the ions with smaller volume and higher ionicity in Thomson cube (<Ba^{2+}>→<Sr^{2+}>→<Sr^{2+}, La^{3+}>→<Sr^{2+}, Nd^{3+}>) and in T2 tetrahedrons ([Ge^{4+}]→[Si^{4+}]) leads to the broadening of the Gaussian components and a slight increase in the distance between their positions.

By assuming a direct relation between the distribution of hyperfine fields and the broadband tuneable selected emission from laser activators (Ln^{3+}, Cr^{3+}, etc.) it is of high interest to find a simple model that helps in the analysis and the prediction of the crystalline field distribution starting from the observed dispersion by Mössbauer spectroscopy.

The present theoretical model is based on the following approximations:

(a) the additive perturbation model for the hyperfine fields distribution [13] (in our case of Δ_Q and Δ_{Hhf}). Each nearest-neighbour substituting ion determines a perturbation $\partial\Delta_\alpha$ of the electric and magnetic hyperfine fields at ^{57}Fe, $\Delta_o\alpha$, and the effect of many substituting ions can be evaluated from the superposition of the individual perturbations. In our case, a linear decrease/increase in the hyperfine parameters Δ_Q/

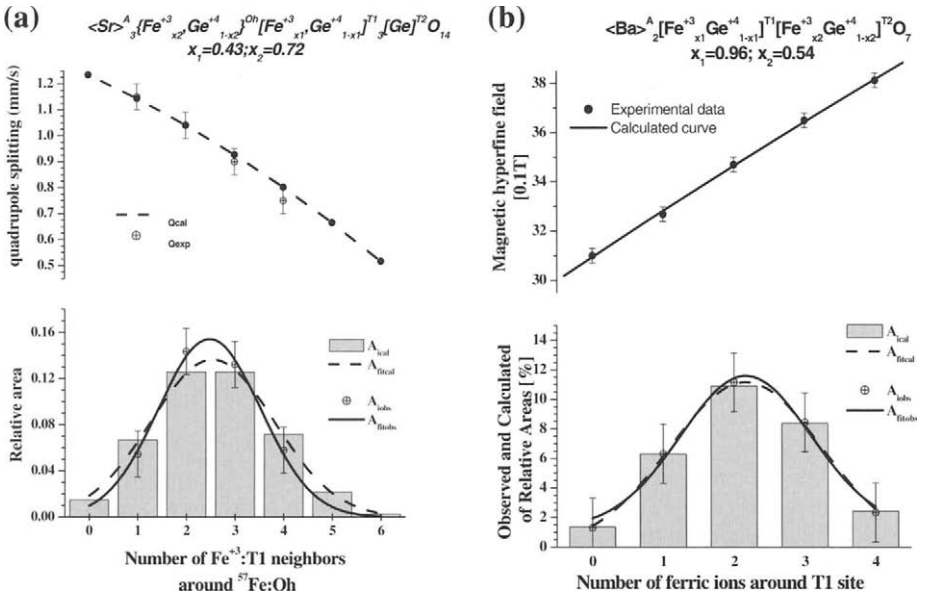

Figure 2 Quadrupole splitting vs. the number of trivalent ions around ^{57}Fe in $Sr_3Fe_2Ge_4O_{14}$ at room temperature (**a**) and magnetic hyperfine fields in $Ba_2Fe_2GeO_7$ at liquid helium temperature (**b**).

Δ_{Hhf} is expected with the increase in the number trivalent ions around the Mössbauer probe. Thus, the observed quadrupole doublets and magnetic sextets in Mössbauer spectra are related to the number of the trivalent ions

$$\Delta\alpha = \Delta\alpha o + \sum_{i=1}^{Nr.Shells} k_i \partial\Delta_\alpha; \alpha = Q, H_{hf} \tag{1}$$

(b) the relative areas of the observed subspectra are assumed to be linearly dependent on the probability to find a given number and a given type of cations around the ^{57}Fe probe. The individual binomial probability of random substitution $p(k_i,m_i;x)$ of k_i heterovalent cations in a given shell with m_i possible sites and x_i occupancy is given by

$$p(k_i, m_i; x_i) = \binom{m_i}{k_i} x_i^{k_i} (1 - x_i)^{m_i - ki} \tag{2}$$

and for different ^{57}Fe environments [14] by:

$$P_s(k, m; x_1, x_2, x_3 \ldots) = \prod_{i=1}^{Nr.shell} \binom{m_i}{k_i} x_i^{k_i} (1 - x_i)^{m_i - ki}; k = \sum_{i=1}^{Nr.shell} k_i; m = \sum_{i=1}^{Nr.shell} m_i;$$
$$P(k,m;x_1, x_2, x_3 \ldots) = \sum_{s=1}^{N_k} P_S(k, m; x_i, x_2, x_3 \ldots); N_k = \text{distinct vicinities of k ions} \tag{3}$$

The occupancies are obtained from the relative areas of 4- and 6- coordinated ^{57}Fe by

$$\begin{cases} x_1 = \frac{2a_{T1}}{a_{T1}+a_{T2}}; x_2 = \frac{a_{T2}}{a_{T1}+a_{T2}} \text{ for Tt} - \text{CGGO} \\ x_1 = \frac{(2+x_3)}{3} \cdot \frac{a_{T1}}{a_{T1}+a_{Oh}}; x_2 = (2 + x_3) \frac{a_{Oh}}{a_{T1}+a_{Oh}} \text{ for Tr} - \text{CGGO} \end{cases} \tag{4}$$

(c) the rigid lattice with fractional ionic point charges (electrostatic model), obtained by valence summation procedure (for oxygen polyhedron surrounding the cationic sites) [10], has been considered to evaluate the EFG^{lat}.

The hyperfine field distribution was calculated for the first and second cationic shells of ^{57}Fe in the T1 and T2 sites of Tt-CGGO and in the Oh sites of Tr-CGGOfrom the software: H(yperfine) F(ield) D(istribution) P(rogram) A(ssemblage) [15]. Figure 2 shows the distribution of quadrupole splittings in $Sr_3Fe_2Ge_4O_{14}$ at room temperature and the distribution of magnetic hyperfine fields in $Ba_2Fe_2GeO_7$ at liquid helium temperature obtained from experimental data and the present theoretical model. The observed correct agreement confirms that the additive perturbation approximation for the distribution of hyperfine fields and the electrostatic model are good approximations for the present intrinsic disordered crystalline materials. Moreover, the observed relative areas of the subspectra are in line with the combinatorial probabilities for the random substitution of heterovalent ions in the cationic shells surrounding the Mössbauer probes (<1 nm) in both Tt-CGGO and Tr-CGGO structures.

4 Conclusions

Because of the narrow line width of the Mössbauer peaks and the location of Mössbauer probes in Tt-CGGO and Tr-CGGO it has been possible to investigate the distribution of hyperfine fields in Fe-rich gallo-germanates. The good agreement between observed and calculated distributions confirms the validity of the proposed theoretical model and shows that both the intensity and the broadening of the crystal field dispersion can be evaluated as a function of the number of heterovalent ions randomly distributed on the different sites. This gives additional information about the broadening of the optical transitions and the broadband tuneable selected emission of laser activators (Ln^{3+}: A, Cr^{3+}: Oh, etc.).

References

1. Belokoneva, E.L., Simionov, N.A., Butashin, A.V., Mill, B.V., Belov, N.V.: Dokl. Akad. Nauk UzSSR **225**, 1099 (1980)
2. Belokoneva, E.L., Belov, N.V.: Dokl. Akad. Nauk UzSSR **260**, 1363 (1981)
3. Mill, B.V., Butashin, A.V., Kpdzhabagyan, G.G., Belokoneva, E.L., Belov, N.V.: Dokl. Akad. Nauk UzSSR **264**, 1385 (1982)
4. Budgor A.B., Esterowicz L., DeShazer L.G. (eds): Taneable Solid-State Lasers, Vol. 2, Springer, Berlin Heidelber, New York (1987)
5. Kaminskii, A.A.: In: Jezowzka-Trzebiatowska, B., Legendziewicz, J., Strek, W. (eds.) Proceedings of the 1st International School on Excited States of Transition Elements, Ksiaz Castle, 1988, World Scientific Singapore, p. 649 (1989)
6. Grinberg M., Macfarlane P.I., Henderson B., Holliday K.: Phys. Rev. **52**, 3917 (1995)
7. Mill, B.V.: Proceedings of the 2000 IEEE/EIA International Frequency Control Symposium and Exibition **1**, 139 (2000)
8. Mill B.V., Fukuda T.: J. Inorg. Chem. **43**, 470 (1998)
9. Mill, B.V., Belokoneva, E.L., Fukuda, T.: J. Inorg. Chem. **43**, 1168 (1998)
10. Constantinescu S., Tarina D.: Eur. Phys. J., B **13**, 75 (2000)
11. Constantinescu, S.: Rom. Rep. Phys. **56**, 56 (2004)
12. Constantinescu, S.: Rom. Rep. Phys. **57**(1), 83 (2005)
13. Fultz, B.: In: Long, G.J., Grandjean, F. (eds.) Mössbauer Spectroscopy Applied to Magnetism and Material Science. Plenum, New York, "Chemical Systematics of Iron-57 Hyperfine Magnetic Field Distributions in Iron Alloys," vol. 1, 1 (1993)
14. Barb, D., Constantinescu, S., Tarina, D.: Hyperfine Interact. **96**(73), 83 (1995)
15. Constantinescu, S.: Rom. Rep. Phys. **57**, 99 (2005)

Hyperfine Interact (2006) 168:1127–1132
DOI 10.1007/s10751-006-9458-3

Mössbauer effect studies on the formation of iron oxide phases synthesized via microwave–hydrothermal route

P. P. Bakare · S. K. Date · Y. B. Khollam · S. B. Deshpande · H. S. Potdar · S. Salunke-Gawali · F. Varret · E. Pereira

Published online: 16 November 2006

Abstract Microwave–hydrothermal (MH) route was employed to synthesize various iron oxide phases in ultra-fine crystalline powders by using ferrous sulphate and sodium hydroxide as starting chemicals. All chemical reactions were carried out under identical MH conditions, namely, at 190°C, 154 psi, 30 min, by varying the molar ratio (MR) of $FeSO_4$/NaOH in the aqueous solutions. The variation of MR has a dramatic effect on the crystallization behavior of various phases of iron oxides under MH processing conditions. For example, spherical agglomerates of Fe_3O_4 powder were obtained if MR equal to 0.133 (pH>10 sample A). On the other hand non-stoichiometric Fe_3O_4 powders (Sample B) were obtained for all higher MR of $FeSO_4$/NaOH between 0.133 and 4.00 (6.6<pH<10). However, when MR was equal to 4.0 (pH≅6.6) a varied distribution of shapes and sizes of agglomerates of α-Fe_2O_3 powders (sample C) were produced. Fe^{57} Mössbauer spectra were recorded for all the three sets of samples at room temperature. In the case of sample B, temperature dependent Mössbauer spectra were recorded in the range of 77–300 K to understand the non-stoichiometric nature of Fe_3O_4 powders. All these results are discussed in the present paper.

Key words microwave–hydrothermal synthesis · iron oxide phases · Mössbauer spectroscopy

P. P. Bakare · S. K. Date · Y. B. Khollam · S. B. Deshpande · H. S. Potdar
Physical Chemistry Division, National Chemical Laboratory, Pune 411 008, India

S. Salunke-Gawali · F. Varret
Laboratorie de Magnetisume d' Optique, CNRS UMR 8634, Universite de Versailles, 78035 Versailles Cedex, France

S. Salunke-Gawali · E. Pereira
REQUIMTE / Departmento de Quimica, Universidade do Porto, Porto, Portugal

Present Address:
S. K. Date (✉)
Department of Physics, University of Pune, Pune 411 007, India
e-mail: date@physics.unipune.ernet.in

1 Introduction

Chemically derived magnetic particles are of great interest basic research point of view because their properties differ considerably from those of corresponding bulk materials [1–4]. In addition, these particles are extensively studied in recent years due to numerous present and future potential technological applications such as digital storage media, computation, communication networks etc. At finite temperatures, magnetic particles with dimensions in the range of (5–20 nm) often exhibit super paramagnetic relaxation i.e. thermal fluctuation of the magnetization vector among the easy directions of magnetizations. In thin films of magnetic materials, the intimate coupling of magnetization with elastic strain fields, surface spin canting and thermally activated processes result in modifying the magnetic properties from those of corresponding particulate media. The relaxation processes is currently being studied by a number of experimental techniques such as AC/DC susceptibility measurements, neutron diffraction, FMR, Mössbauer spectroscopy etc.

In past 10 years, the microwave–hydrothermal (MH) route is well established for the synthesis of various types of inorganic/organic materials like multi-component oxides, phosphates, zeolites, metal powders etc. having controlled physical and chemical characteristics. The use of MH route over the conventional hydrothermal (CH) is found to be growing in the recent years because of its inherent advantages like rapid heating, faster kinetics of crystallization, phase purity, higher yield, better reliability and reproducibility and fine control over the morphological characteristics of particles [5]. The synthesis of Fe-oxide is the subject of interest of present investigation. Several routes have been reported for the synthesis of Fe-oxide fine particles [6]. The MH synthesis of α-Fe_2O_3 particles using $FeCl_3$ as Fe precursor in the range of 164–194°C at acidic condition is reported in literature. However, it is not yet explored for the synthesis Fe-oxide particles using ferrous salts under alkaline conditions. In this respect, an attempt is made here to see the effect of variation of pH on the formation of Fe-oxide particles of different phases (e.g. Fe_3O_4, α-Fe_2O_3 etc.) during the MH treatment on the ferrous salt. Further, the low temperature Mössbauer studies were also carried to understand non-stiochiomertic nature in these particles.

2 Experimental

Precursor solutions of $FeSO_4 \cdot 7H_2O$ (0.04 M) and NaOH (0.30, 0.10, 0.06, 0.02 and 0.01 M) were prepared in distilled water. It gives different values for the molar ratios (MR) of $FeSO_4$/NaOH=0.133, 0.400, 0.667, 2.000 and 4.000 and covers pH range from 10 (alkaline) to 6.6 (slightly acidic). All microwave–hydrothermal (MH) reactions were carried out in a microwave-accelerated reaction system: MARS-5 [CEM Corpn., USA, f=2.45 GHz, P=1200 W (0–100%), T=300°C max., P=800 psi max.]. The system can be controlled by temperature/pressure/standard control. The mixture: $FeSO_4$ (10 ml) and NaOH (19 ml) was treated in 50 ml capacity lined digestion vessel (XP-1500 plus, double walled consisting of a teflon TFM inner liner and cover surrounded by high strength vessel shell made from advanced composite materials). Further, 190°C, 154 psi and 30 min were chosen as MH conditions for all the synthesis in order to get highest yield in the resultant oxide powders. The resultant powders were washed with distilled water several time to remove the Na^+ contamination and dried under ambient conditions. The powder samples with MR=0.133, 0.400 and 4.000 are identified as A, B and C, respectively. The phase analysis of powders was carried out by X-ray diffractometer (Cu – K_α radiation, Ni filter).

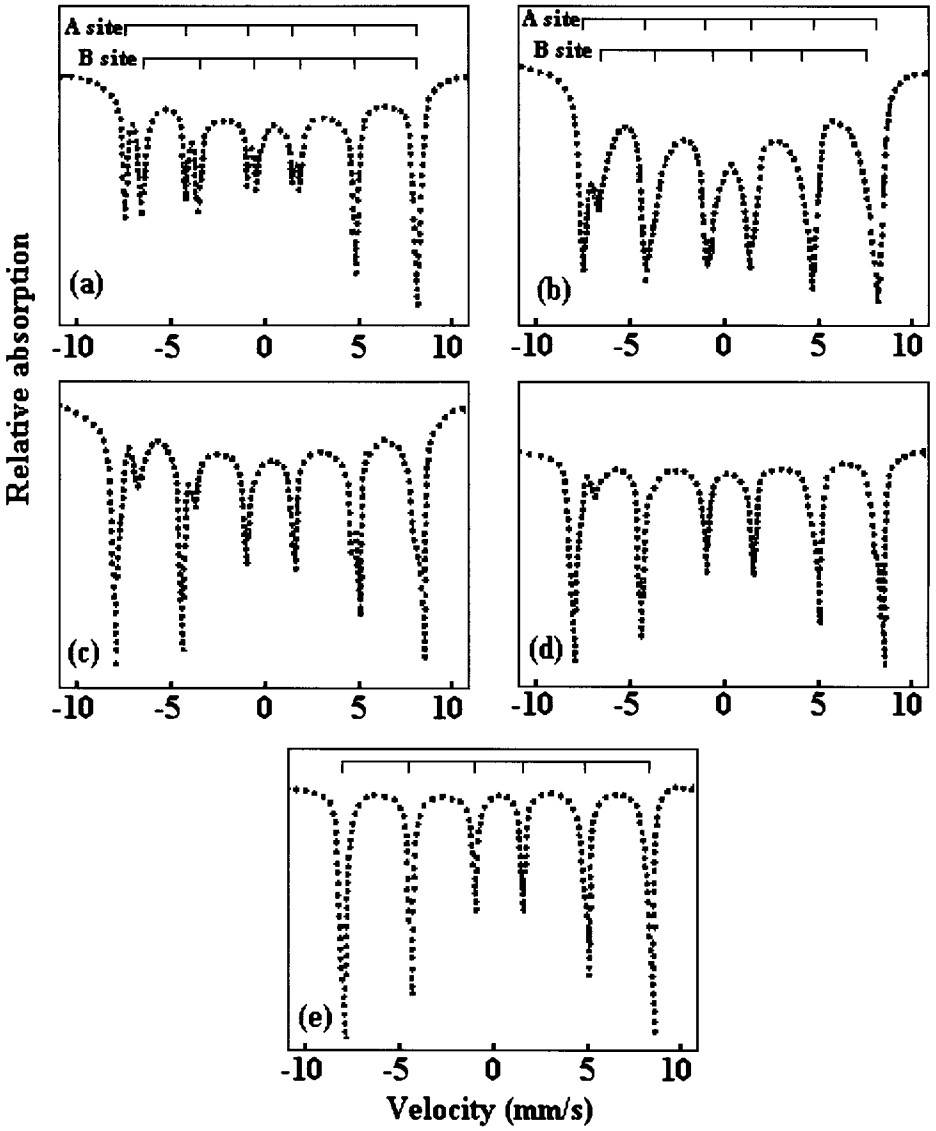

Figure 1 ^{57}Fe Mössbauer spectra of powders synthesized at different MR equal to **a** 0.133, **b** 0.400, **c** 0.667, **d** 2.000 and **e** 4.000.

At room temperature, Fe^{57} Mössbauer spectra were recorded to obtain information on the existence of inequivalent sites by studying the different components arising from the different sites in powder samples. Scanning electron microscopy was used to estimate particle size, nature of agglomerates and the morphology in the resultant powders.

3 Results and discussion

There is no difference between the XRD patterns (not shown here) of the powders prepared at different MR equal to 0.133, 0.400, 0.667 and 2.000. Patterns could be indexed to cubic

Table I Mössbauer hyperfine interaction parameters for different samples

Figure	Site		H_n		I.S.		Q.S.		Temp.	Sample
1(a)	A	B	484	455	0.35	0.72	0.00	0.02	RT	A
1(b)	A	B	491	445	0.35	0.46	0.03	−0.15	RT	B
1(d)	–	–	511	–	0.41	–	−0.07	–	RT	C
2(a)	A	B	525	492	0.46	0.47	0.10	−0.06	77	B
2(b)	A	B	521	485	0.46	0.47	0.09	−0.06	100	B
2(c)	A	B	522	464	0.45	0.51	0.09	−0.04	150	B
2(d)	A	B	508	446	0.41	0.49	0.06	−0.09	200	B

H_n (±5 kOe), I.S. (±0.02 mm/s), Q.S. (±0.02 mm/s)

spinel structure with lattice parameter of a_o=8.392 Å. This lattice parameter and the calculated *d* values are found to be very close to the reported data for Fe_3O_4 phase [5–7]. However, the XRD pattern for powder with MR=4.00 could be indexed to α-Fe_2O_3 as the entire calculated *d* values match perfectly with the data reported for α-Fe_2O_3 [5–7]. The SEM studies of these powders showed the formation of spherical agglomerates (0.15–4 μm) with varied size distribution having primary crystallites in the range of nanometers [5, 6].

Figure 1a, b, c, d and e show the room temperature Mössbauer spectra recorded in the constant acceleration mode for powders with MR equal to 0.133, 0.400, 0.667, 2.000 and 4.000, respectively. The spectra shown in Figure 1a–d exhibit magnetically hyperfine splitting and a finite line broadening observed in the line shapes indicates the presence of Fe^{2+} in lattice.

These spectra could be resolved each in two sub-spectra indicating thereby the presence of Fe^{3+} at A (tetrahedral) and B (octahedral) sites of Fe_3O_4. The derived hyperfine Mössbauer resonance parameters for spectra 1(a) and (b) are given in the Table I, which indicate the crystallization of Fe_3O_4 very well [5, 8–11].

The resonance parameters for spectra 1(c) and (d) (not given here) are also found to close to that given for the spectra 1(b) indicating thereby the formation of Fe_3O_4. However, there is a marked difference in the asymmetry of the outer lines of the magnetically split spectra given in Figure 1a–d. The changes in the (1) intensity and (2) line broadening are taking place in the outer lines of each spectrum. The difference in the broadening of Figure 1b–d compared to Figure 1a indicated the cation deficiency in occupied sites in case of powder samples with MR=0.400, 0.667 and 2.000. In the case of powder sample with MR=0.133 (Figure 1a), the relative intensity ratio of two sub-spectra is similar to that for stoichiometric Fe_3O_4 [5, 8–11]. On the other hand, the relative intensity ratio (Figure 1b–d) of the magnetic sextets for powders with MR=0.400, 0.667 and 2.000 is found to be similar to that of non-stoichiometric Fe_3O_4 [5, 8–11]. The relative intensity of B site to A site spectral lines decreases continuously as we go from Figure 1a to d. It indicates the increase in B site vacancies corresponding to Fe^{2+} ions. It has been also reported that the relative intensity ratio of B site to A site spectrum decreases if non-stoichiometric Fe_3O_4 [5, 8–11] is formed as is in the case of samples with MR=0.400, 0.667 and 2.000 [Figure 2b–d]. Further, corresponding data given Table I is consistent with spectral and hyperfine interaction data reported on the stoichiometric and non-stoichiometric Fe_3O_4 [5, 6, 8–11]. All the above observations indicate that with increase in MR (decreasing pH from ≥10 to

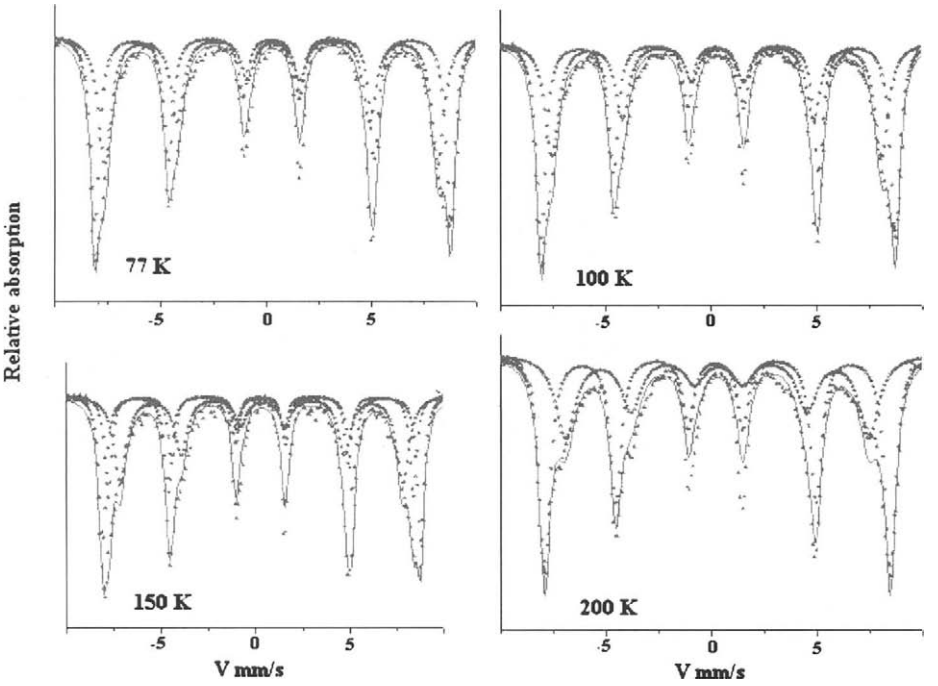

Figure 2 Mössbauer spectra for sample B at different temperatures.

6.6 in the solution), there is increase in B site vacancies corresponding to the Fe^{+2} ions leading to formation of more and more non-stoichiometric Fe_3O_4. Finally, when MR became (pH~6.6) equal to 4.00, a single sextet is obtained as shown in Figure 1e. The derived hyperfine interaction parameters given in Table I match very well with data reported for single-phase α-Fe_2O_3 [5, 8–11]. The powder sample with MR=0.4 is further selected for low temperature Mössbauer studies. Figure 2 shows the Mössbauer spectra for sample B (non-toichiometric Fe_3O_4) at various temperatures between 77 and 300 K.

The hyperfine interaction parameters are computed and given in Table I. It is clear from the analysis it matches well with those reported for the oxygen deficient Fe_3O_4 [8–11]. Recently, we have synthesis successfully nanometric spherical magnetite powder by DC, thermal-arc plasma route [12]. The hyperfine interaction parameters are very similar even though the methods of preparation are far different in many respects. The only difference is the microscopic chemical homogeneity and stoichiometry. This is predominantly reflected in the line shapes and intensities of the outermost lines in the spectra. In addition, broad unresolved components are seen in the center of Mössbauer spectra, which is most likely due to the paramagnetic relaxation effects. Further studies at low temperatures (~4 K) and high magnetic fields (5 T) will resolve the essential details of the magnetic phases. In summary, it has been shown that the magnetic particles of various phases in the Fe–O system are successfully synthesized via MH route.

Acknowledgements One of us (SKD) wishes to thank Alexander Von Humboldt foundation for the financial support. SKD also wishes to thank Duisburg Mössbauer Group (Prof Dr Werner Kenne) for all the necessary technical support.

References

1. Ichinose, N., Ozaki, Y., Kashu, S.: Superfine Particle Technology. Springer, Berlin Heidelberg New York (1992)
2. Gleiter, H.: Prog. Mater. Sci. **33**, 223 (1989, and references therein)
3. Matijevic, P.E.: In: Hench, L.L., Ulrich, D.B. (eds.) Colloid Science of Composites System, Science of Ceramic Chemical Processing, pp. 463. Wiley, New York (1986)
4. Osterhout, V.: In: Craik, D.S. (ed.) Magnetic Oxides, pp. 700. Wiley, New York (1975)
5. Khollam, Y.B., Dhage, S.R., Potdar, H.S., Deshpande, S.B., Bakare, P.P., Kulkarni, S.D., Date, S.K.: Mater. Lett. **56**, 571 (2002)
6. Dhage, S.R., Khollam, Y.B., Potdar, H.S., Deshpande, S.B., Bakare, P.P., Sainkar, S.R., Date, S.K.: Mater. Lett. **57**, 457 (2002)
7. JCPDS card nos. Fe_3O_4 [19–629] and α-Fe_2O_3 [16–653]
8. Simmons, G.W., Leidheiser, H., Jr.: In: Cohen, R.L. (ed.) Application of Mössbauer Spectroscopy, vol. 1, pp. 106. Academic, New York (1976)
9. Visalakski, G., Venkateswaran, G., Kulshreshtha, S.K., Moorthy, P.H.: Mater. Res. Bull. **28**, 829 (1993)
10. Wang, S., Xin, H., Qian, Y.: Mater. Lett. **33**, 113 (1997)
11. Coey, J.M.D., Morrish, A.H., Sawatzky, G.A.: J. Phys. **32**, C1–C271 (1971)
12. Balasubramanian, C., Khollam, Y.B., Banerjee, I., Bakare, P.P., Date, S.K., Das, A.K., Bhoraskar, S.V.: Mater. Lett. **58**, 3958 (2004)

Hyperfine Interact (2006) 168:1133–1137
DOI 10.1007/s10751-006-9412-4

Magnetic behavior of the bond random mixed compound $FE(BR_xI_{1-x})_2(x = 0.9)$ with Mössbauer spectroscopy

Nai-Li Di · T. Tamaki

Published online: 14 November 2006

Abstract The bond random mixed compound $Fe(Br_{0.9}I_{0.1})_2$ has been studied by magnetization and Mössbauer measurements. Although the zero-field cooled and field-cooled magnetization variations are not like a typical spin glass one, the Mössbauer spectrum below Néel temperature shows a hyperfine field distribution. It implies that the 10% FeI_2 mixed in $FeBr_2$ can be induced by the bond random effect which causes the sample to exhibit a spin glass-like behavior.

Key words bond random magnet · $Fe(Br_xI_{1-x})_2$ · Mössbauer study · magnetization

1 Introduction

Most theoretical studies on spin-glass are for bond random systems. Up to the present, most of the experimental studies on Ising spin-glass systems have been made for the site random systems [1–3]. In order to compare theoretical and experimental studies, we were motivated to study the bond-random mixed compound $Fe(Br_xI_{1-x})_2$. The pure sample of $FeBr_2$ as well as FeI_2 have a CdI_2-type crystal structure and show antiferromagnetism at Néel temperature (T_N) of 14.2 and 9.3 K, respectively [4, 5]. Both of them show the hexagonal c-axis as the magnetic easy axis. The Fe^{2+} spins in $FeBr_2$ arrange ferromagnetically in the c-plane and antiferromagnetically between the c-planes, while in FeI_2 they are partially coupled ferromagnetically and partially antiferromagnetically both in and between the c-planes. We

N.-L. Di (✉)
State Key Laboratory of Magnetism, Institute of Physics, Chinese Academy of Sciences,
Beijing 100080, China
e-mail: dinaili@aphy.iphy.ac.cn

T. Tamaki
Department of General Studies II, Faculty of Engineering, Gunma University, 4-2, Aramaki, Maebashi,
Gunma 371-8150, Japan

T. Tamaki
Mathematical Assist Design Laboratory, 54-2, Kamisadori, Maebashi, Gunma 371-0816, Japan

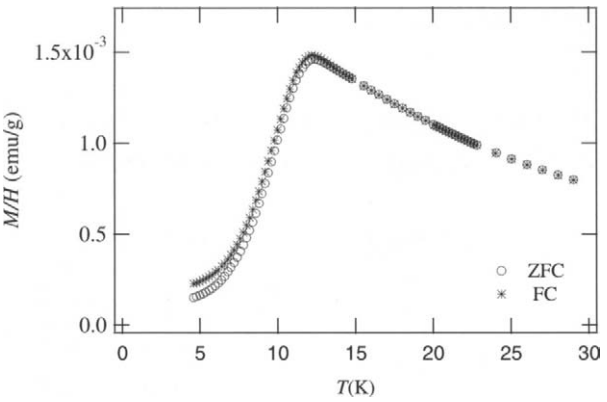

Figure 1 Temperature dependence of the magnetizations observed with 10 Oe applied field parallel to the *c*-axis of Fe $(Br_{0.9}I_{0.1})_2$ single crystal.

expected the random distribution of two kinds of anions to create exchange frustration among Fe^{2+} spins.

In a previous paper, we reported the experimental studies of $Fe(Br_{0.6}I_{0.4})_2$ [6]. In that case, the $x = 0.6$ sample showed a spin glass-like behavior by magnetization measurements. The Mössbauer spectrum observed at 1.6 K showed a large hyperfine field distribution (H_{hf}). The $x = 0.8$ sample also shows a similar behavior as the $x = 0.6$ one according to the results of the magnetization and Mössbauer measurements. The distribution of H_{hf} suggests that the antiferromagnetic and ferromagnetic bonds randomly distribute as expected. In this paper, we report the magnetic behavior of the $x = 0.9$ sample.

2 Experimental

The $Fe(Br_{0.9}I_{0.1})_2$ compound was prepared by mixing the powders of $FeBr_2$ and FeI_2 in pure water at a determined chemical composition. The mixed sample was prepared to form a single crystal by the Bridgman method. $FeBr_2$ and FeI_2 are hygroscopic and react with moisture changing to hydrated compounds, therefore the handling of the sample and measurements were done in a dry box or in vacuum state.

Magnetization measurements were carried out using a SQUID magnetometer in an applied field of 10 Oe parallel to the *c*-axis under zero-field cooled (ZFC) and field-cooled (FC) conditions.

For the Mössbauer measurement, an absorber was prepared by the 50 μm-thick single crystal sample. The absorber was mounted on a cryostat so that the incident γrays were perpendicular to the *c*-plane. A constant-acceleration Mössbauer spectrometer was used in a transmission arrangement. The measurement was performed at a 1.6–77 K temperature with a ±0.01 K accuracy.

3 Results and discussion

Figure 1 shows magnetization of ZFC and FC in 10 Oe applied field parallel to the *c*-axis of the single crystal. As the temperature decreases, the ZFC magnetization (M_{ZFC}) and FC magnetization (M_{FC}) show a cusp at 12.2 K. If the transition temperature T_N is taken as the temperature where dm/dT has a maximum in $M(T)$, then T_N is near 10 K. Although the

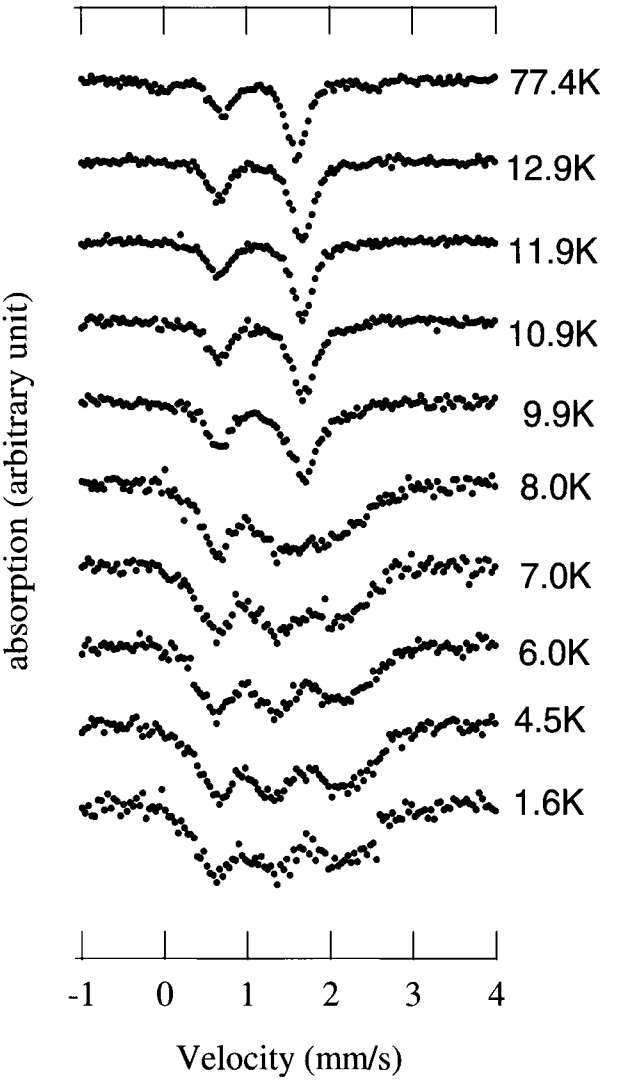

Figure 2 Temperature variation of Mössbauer spectrum of Fe $(Br_{0.9}I_{0.1})_2$ single crystal.

difference between M_{FC} and M_{ZFC} exists, it is not so obvious compared to that of the x = 0.6 and 0.8 samples which show a spin glass-like behavior.

In order to understand the effect of the x = 0.9 sample in microcosmic view, Mössbauer measurements were performed at 1.6–77 K temperatures for the single crystal sample. Figure 2 shows the temperature variation of Mössbauer spectra of $Fe(Br_{0.9}I_{0.1})_2$. Because the γrays were parallel to the c-axis, the absorption lines corresponding to Δm = 0 transition between the sublevels of the 14.4 keV excited state and those of the ground state of the ^{57}Fe nucleus are forbidden. Thus, the lines in the spectra are lines 1, 3, 4 and 6; the line intensities have a 3:1 ratio as showed in the figure. The spectra above T_N reveal a paramagnetic doublet with a narrow line width. As temperature decreased below 10 K, the right-hand side absorption line becomes broader showing the onset of magnetic splitting. However, at 1.6 K – the lowest temperature of the experiment – no sharp magnetic splitting spectrum is observed. In any case, the Mössbauer spectrum at 1.6 K for the x = 0.9 sample

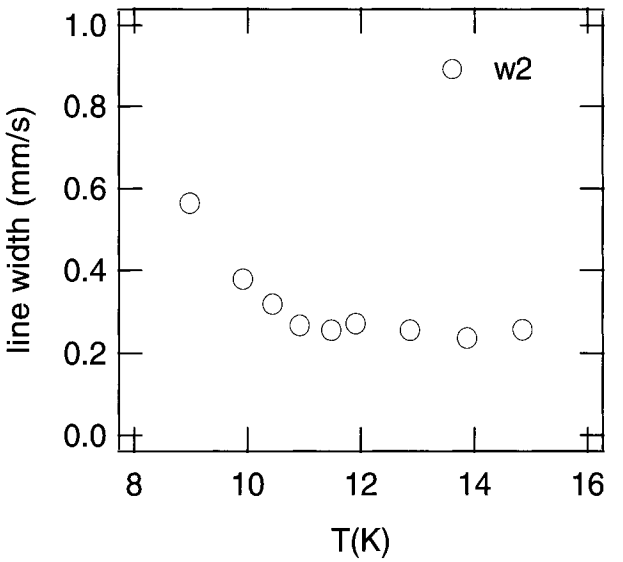

Figure 3 Temperature variation of the line width (line 1 or line 6).

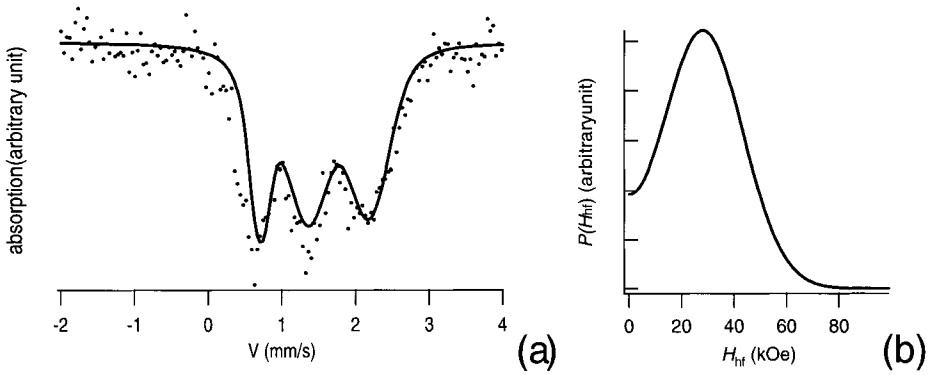

Figure 4 The best fit spectrum shown by the *solid line* (**a**) and the distribution of H_{hf} (**b**) at 1.6 K.

was not like those observed in the x = 0.6 and 0.8 samples at similar temperatures. Although the spectrum of the x = 0.9 sample shows some distribution, a split of H_{hf} was observed in the spectrum at 1.6 K. The broadened spectra below T_N imply that the H_{hf} has a distribution. A detailed analysis of the x = 0.9 spectrum was carried out using the same method as for the x = 0.8 sample, i.e. using a H_{hf} distribution to fit the spectrum. The fitting parameters are H_{hf}, the H_{hf} distribution $P(H_{hf})$, quadrupole splitting (ΔE_Q) and centre shift (δ). The line width is generally fixed at 0.26 mm/s from 77 to 1.6 K. On the basis of these parameters, a good fitting is obtained as shown below.

The temperature variation according to the line width – line width of the right-hand side absorption – is shown in Figure 3. The line width begins to rapidly increase near 10 K which is the T_N temperature. This implies that a magnetic transition in the Mössbauer measurement also occurs at T_N. Furthermore, the temperature variation of H_{hf} also reveals the same result; the H_{hf} becomes 0 at 10 K.

Figure 4 shows the fitting results at 1.6 K. The H_{hf} is distributed from 0 to 80 kOe. The maximum of $P(H_{hf})$ is about 28 kOe which is equal to the value of the H_{hf} of $FeBr_2$ at 4.5 K. The Gaussian width is 15.3 kOe lower than that of the $x = 0.8$ sample which is 27.5 kOe. The values of ΔE_Q and δ at 1.6 K are 1.13 and 1.11 mm/s. As a comparison, $FeBr_2$ is 1.11 mm/s (ΔE_Q) and 0.99 mm/s(δ) at 4.5 K, respectively [7].

4 Summary

The bond random mixed compound $Fe(Br_{0.9}I_{0.1})_2$ has been performed by magnetization and Mössbauer measurements. An antiferromagnet-like behavior was shown by magnetization measurements. The results do not show an obvious difference between M_{FC} and M_{ZFC}. But the Mössbauer spectra below T_N show a distribution of the H_{hf} which is rather different from that of the antiferromagnet one. It implies that the antiferromagnetic and ferromagnetic bonds distribute randomly because of the random distribution of the two types of anions. The analysis suggests that the 10% FeI_2 mixed in $FeBr_2$ induced the bond random effect which causes the sample to show a spin glass-like behavior.

Acknowledgment Both authors thank the Doctoral Research Course in Human Culture, Ochanomizu University for making Mössbauer experiments. All of the work was done at Ochanomizu University.

References

1. Dutta, P., Horn, P.M.: Rev. Mod. Phys. **53**, 497 (1981)
2. Wong, P.z., von Molnar, S., Palstra, T.T.M., Mydosh, J.A., Yoshizawa, H., Shapiro, S.M., Ito, A.: Phys. Rev. Lett. **55**, 2043 (1985)
3. Yoshizawa, H., Mitsuda, S., Aruga, H., Ito, A.: Phys. Rev. Lett. **59**, 2364 (1987)
4. Fert, A.R., Carrara, P., Lanusse, M.C., Mischler, G., Redoules, J.P.: J. Phys. Chem. Solids **34**, 223 (1973)
5. Fert, A.R., Gelard, J., Carrara, P.: Solid State Commun. **13**, 1219 (1973)
6. Di, N.L., Tamaki, T., Ito, A.: Il Nuovo Cimento, Conference Proceedings "ICAME95" **50**, 303–306 (1996)
7. Di, N.-L., Morimoto, S., Ito, A.: J. Phys., Condens. Matter **16**, 3725 (2004)

Hyperfine Interact (2006) 168:1139–1144
DOI 10.1007/s10751-006-9413-3

Mössbauer studies of the layered compound 1T-TAS_2

A. Djedid · J. G. Mullen

Published online: 21 December 2006

Abstract We report the temperature dependence in Tantalum Disulfide 1T-TaS_2 of the elastic and inelastic intensities of the first order satellite (1.285, 0, 0.333) and (3, 0, 0.21) near the Bragg peaks (1, 0, 0) and (3, 0, 0), respectively. The phason temperature factor has been measured as a function of temperature from 70 to 295 K using Mössbauer *gamma*-ray scattering. The high-energy resolution provided by this technique allowed experimental separation of the elastic scattering from the inelastic thermal diffuse scattering. The first order satellite is found to be 15% inelastic. The results were compared with those found by Chapman and Colella obtained by X-ray method (Moret and Colella, Phys. Rev. Lett. 52:652, 1984).

Key words layered compound 1T-TAS_2 · Mössbauer *gamma*-ray scattering · charge density waves (CDW)

1 Introduction

1T-TaS_2 Tantalum disulfide (1T) is one of a family of layered compounds which exhibit charge density waves (CDW). A comprehensive study of the physical properties of this transition metal dichalcogenide has been reported in the review by Wilson et al. [1]

These materials consist of stacks of covalently bounded atomic sandwiches of TaS_2 held together by weak Van deer Waals' forces between the sandwich layers. The unit cell of 1T-TaS_2 exhibits the octahedral coordination of the metal atom, where each sandwich in this compound is three atom layers and consists of multiple repetitions of this unit cell arranged to give a close-packed plane of metal atoms between two close-packed of sulphur atoms. The 1T polytype displays the strongest charge density waves. The electrical properties and

A. Djedid (✉)
Department of physics, Annaba University, Annaba, Algeria
e-mail: djedid_ammar@hotmail.com

J. G. Mullen
Department of physics, Purdue University, West Lafayette, Indiana 47907, USA

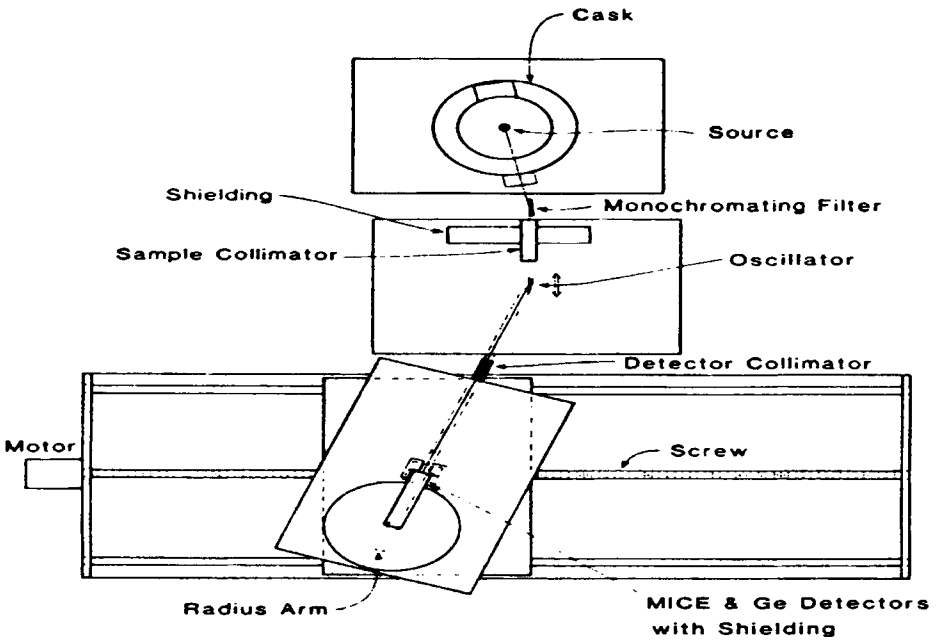

Fig. 1 General view of the QUEGS instrument. A radius arm pivoted at the sample axis to keep the detector collimator precisely directed toward the sample as 2 is changed

diffraction patterns of this crystal indicate a phase transition in the CDW's structure at 352 and 200 K. The phase between 550 and 352 K is an incommensurate CDW phase. From 352 to 200 K the phase is characterized by a quasicommensurate CDW with noticeably streaking in the X-ray pattern. Below 200 K the phase is commensurate.

Using Microfoil Conversion Electron (MICE) spectroscopy, J.R. Stevenson and J.G. Mullen (1981) [2] observed a peaking in the inelastic intensity at the phase transition which was interpreted as an inelastic critical scattering when they looked at the (100) reflection in 1T-TaS_2. Moret and Colella [3] observed, using direct X-ray diffraction measurements, that all Bragg peak intensities exhibit a discontinuous jumping in the Debye-Waller factor at the 352 K transition which was explained as being due to a sudden change of the displacement amplitude at this first order transition.

In this work we quantify the curve shape observed by J.R. Stevenson and J.G. Mullen. We also report the observation of a structural change in the charge density waves across the transition; further we measure the elastic intensity of the first order CDW's satellite around the (100) and (300) Bragg peaks. From this we derive the phase temperature factor, using the unique energy resolution of the Mössbauer instrument at the Missouri Research Reactor [4].

2 Experimental arrangement

The crystal used in this experiment was selected from crystals prepared by F Disalvo at AT&T Bell laboratories. Its dimensions were approximately 1 cm × 1.3 cm × 20 μm. The

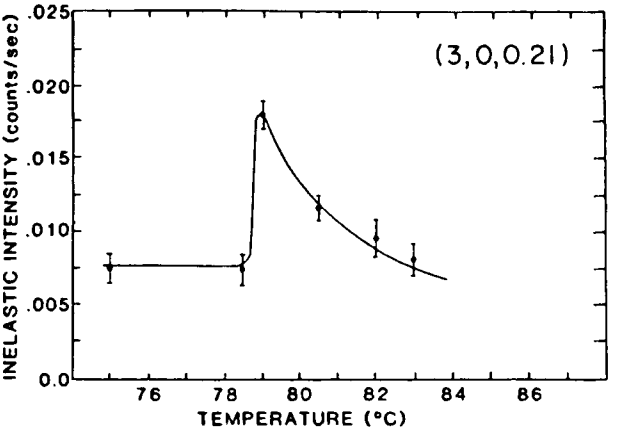

Fig. 2 Inelastic scattering intensity measured at (3,0,0.21), near the (300) Bragg peak in 1T-TaS_2 as a function of temperature. The *line* drawn through the inelastic intensity does not have a theoretical significance. It is just used to indicate the trend in the data

crystal was mounted in a transmission furnace which was electrically heated. In order to avoid stress and prevent strain due to thermal expansion, only one small area at the edge was glued to the furnace. The other end was left to expand freely under a strip of Mylar stretched across the crystal face. The temperature was measured and regulated by the use of a chromel–alumel thermocouple attached near the edge of the crystal. Regulation of temperature to better than 0.3°C was obtained between 60 and 170°C, and the transition temperature itself, as determined by a Bragg shift, was used to calibrate the thermometry.

The measurements were performed using the Mossbauer gamma-ray diffractometer, described in Fig. 1. This investigation used the intense 46.5 keV gamma ray line emitted by ^{183}Ta source produced by double neutron capture at the Missouri University Research Reactor (M.U.R.R). This line has a Mossbauer width of 4.6×10^{-6} eV. This high energy resolution provides a unique method of separating the truly elastic intensity from the truly inelastic intensity to within 10^{-6} eV which is clearly an advantage over conventional X-ray scattering methods, where the energy resolution is too poor to differentiate elastic from inelastic scattered photons. The use of high intensity source, 70 Ci, allowed good angular resolution, better than the X-ray experiment [3]

A LiF (200) monochromating crystal filter was used to reduce background by preventing other gamma and X-ray from reaching the germanium and MICE detectors. The absorbers were mounted on a rotary stage. Four absorbers of enriched ^{183}W powder in a plastic matrix were mounted in a paddle wheel arrangement on a vertical axis rotor as in [4]. These absorbers were driven at two constant speed values from 0.4 to 19.2 cm/s. This speed range is necessary to measure on-resonance, off-resonance rates for the rather broad intrinsic Mössbauer effect width (3.1 cm/s) of the 46.5 keV transition.

The parameters of the resonance were determined using a least square fit to a Lorentzian absorption curve, which was adequate for this experiment, although it is a very inadequate approximation in line shape measurements. The true line shape analysis would have improved the results, but this was not available when this investigation was carried out. The resonance absorption fraction $P_{el}(0)$ observed from the nearly 100% elastic LiF (200) is given by:

$$P_{el}(0) = \frac{I(\infty) - I(0)}{I(\infty) - B} \tag{1}$$

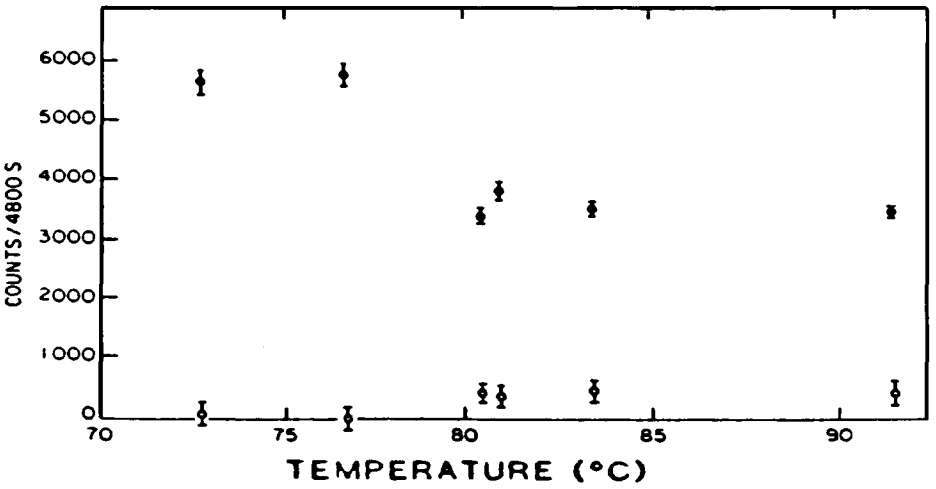

Fig. 3 Temperature dependence of the elastic and the inelastic intensity of the first order satellite, (1.285,0,0.333): *full circles* are elastic intensity while *open circles* are inelastic intensity

Where the $I(\infty)$ is the counting rate far from the resonance peak, $I(0)$ is the counting rate for a zero velocity absorber, and B is the background counting rate. The elastic fraction was determined by:

$$R_{el} = \frac{1}{P_{el}(0)} \left(\frac{a}{b}\right) \frac{I(n) - I(r)}{I(n) - B} \tag{2}$$

Where $I(n)$ is the intensity observed at the off resonance velocity, which at 19.2 cm/s is six times greater than the natural line width, and $I(r)$ is the intensity of the on resonance velocity which is 0.64 cm/s. This non-zero velocity was necessary since the rotor arrangement produced a variable absorber thickness which required accumulating data for an integral number of rotor revolution. The constants a and b are given by the following equations:

$$a = \frac{[I(\infty) - I(0)]}{I(n) - I(r)} \tag{3}$$

and

$$b = \frac{[I(\infty) - B]}{[I(n) - B]} \tag{4}$$

Which are the necessary corrections due to the finite velocities at resonance and far from resonance. The background B, principally derived from high energy down-scattered photons, was determined by using a 0.075 cm thick cadmium foil which was inserted after the monochromator. This thickness attenuated 99.99% of the 46.5 keV intensity, but allowed the higher energy photons to reach the sample and the detector. Contributions from the lower energy X-rays are also attenuated but they were filtered quite well by the LiF crystal. The relative intensities can then be determined from:

$$I_{el} = a[I(n) - I(r)] \tag{5}$$

$$I_{in} = P_{el}(0)b[I(n) - B] - I_{el} \tag{6}$$

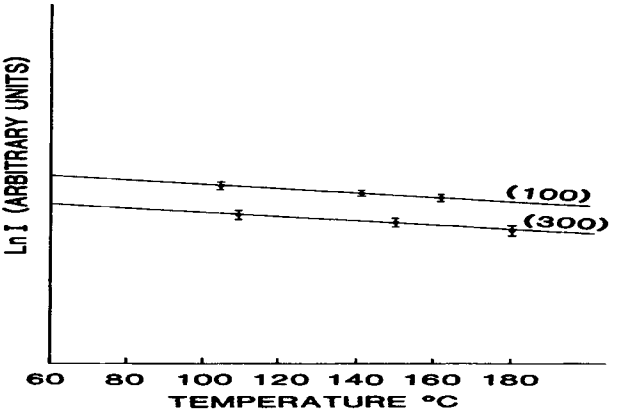

Fig. 4 Temperature dependence of the logarithm of the integrated intensity of the first order satellites: (1.285,0,0.333), and the (2.72,0,−0.333) around the (100) and the (300) Bragg peaks, respectively

3 Experimental results

The full width at half maximum of a Bragg reflection from 1T-TaS_2 was in our case typically 0.3°, compared to 0.6° for the X-ray diffraction experiment of Moret and Colella [3]. This advantage was used to detect the 2–3% shift in the bragg position for the (102) peak and to calibrate the thermometry relative to the transition temperature.

Our result agreed with those of [3] concerning the effect of the temperature on the bragg peak across the transition temperature $T = 352$ K, where we observed a 6.1% jump in the elastic intensity. We also looked 2° off the (300) Bragg reflection in the transverse direction which corresponds to (3, 0, 0.21) in (h, k, l) space, searching for the Q-space location of the discontinuity of the inelastic intensity in the (100) 1T-TaS_2, at the phase transition seen by Stevenson and J.G. Mullen.

In Fig. 2 we show a very interesting feature of the inelastic intensity: a sharp increase and a rapid fall off the inelastic intensity just at the transition.

This effect is roughly exponential in character; the peak has a width of about about 3°C. The result shown in Fig. 2 is the best of many complete runs which show the same qualitative behaviour and shape. This result is in agreement with the findings of Stevenson and Mullen which were too imprecise to identify the shape of the anomaly. The above authors suggest that the observed critical phenomenon might be evidence for a softening of a phason mode associated with the CDW in this system.

We expected the observed enhancement of the inelastic intensity to maximize near or on one of the satellites, or even at the Bragg peaks themselves, especially when a Kohn anomaly was observed in the longitudinal phonon mode propagating in the (100) direction [5]. This search did not yield a very well defined peak. We found that the intensity at the Bragg peaks and the satellite is almost 100% elastic. The fluorescence of the tantalum in the sample added to the background, thus making the experiment difficult.

A similar investigation was done at the second order satellite in the (hk0) plane. There the sudden drop in the count rate at the transitions coupled with the thickness of the sample, which was one-fourth of the 1 / e optimum thickness, reduces the scattering intensity and further added to the experimental difficulties.

The temperature dependence of the elastic intensities of the first order satellite, (1.285, 0, 0.333) 1T-TaS_2 revealed two important results:

1. The elastic intensity across the transition decreased by almost 30% for the first order satellite around the (100) Bragg peak as seen in Fig. 3 this is a totally different

behaviour as compared to the Bragg peak elastic intensity which jumped from 6.3% for the (300) reflection to 175% for the (500) Bragg reflection [5].

2. The inelastic intensity across the transition increased from 0 below 79 to 15% above 79°C, when we looked at the first order satellite(1.285, 0, 0.333) of the (100) Bragg peak. This inelastic component stayed constant for the range of the scanned temperature which was 90 to 170°C.

The publication by Chapman and Colella [6] shows the absence of the usual k^2 dependence expected from the Debye-Waller factor when looking at the first order satellite around the Bragg peaks. Their result reflects a dependence consistent with the phason model of A.W. Overhauser [7], i.e., a k dependence instead of the usual k^2 dependence in phonon scattering. Their experiment was repeated using the high energy resolution (4×10^{-6} eV) of the Mössbauer technique to separate the truly elastic intensity from the inelastic contribution to within the above energy resolution. A plot of logarithm of the elastic temperature dependence is displayed in Fig. 4. This investigation of the temperature dependence of the first order satellite (1.285, 0, 0.333), and the (2.72, 0, −0.333) around the corresponding (100) and (300) Bragg peak, respectively, yielded a factor $C = 2.0(3) \times 10^{-3}\ \mathrm{K}^{-1}$, in good agreement with $C = 1.8 \times 10^{-3}\ \mathrm{K}^{-1}$ found by Chapman and Colella, where e^{-ct} is the usual phason temperature factor.

4 Conclusion

We conclude that the intensity of the first order satellite is 15% inelastic even though this is large, it is nearly constant and thus does not alter the basic conclusion of Chapman and Colella. Also we should mention here that we did not do an absolute intensity measurement, and we cannot preclude possible temperature dependence of the phason amplitude, as was done by Chapman and Colella.

References

1. Wilson, Zibeck, J.A., Dorner, B., Striling, W.G., Schollhorm, R.: J. Phys. **F7**, 1139 (1977)
2. Stevenson, J.R., Mullen, J.G.: Solid State Commun. **39**, 319 (1981)
3. Moret, R., Colella, R.: Phys. Rev. Lett. **52**, 652 (1984)
4. Yelon, W.B., Schupp, G., Crow, M.L., Holmes, C., Mulles, J.G.: Nucl. Instrum. Methods **B14**, 341 (1986)
5. Crow, M.L., Schupp, G., Yelon, W.B., Djedid, A.: Acta Crystallogr. **A443**, 638 (1987)
6. Chapman, L.D., Colella, R.: Phys. Rev. Lett. **52**, 652 (1984)
7. Overhausser, A.W.: Phys. Rev. **167**, 691 (1968)

Hyperfine Interact (2006) 168:1145–1149
DOI 10.1007/s10751-006-9414-2

^{57}Fe Mössbauer spectroscopy studies of $Sr_2Fe_{1-x}Cr_xMo_{1-x}W_xO_6$ double perovskite compounds

A. P. Douvalis · I. Panagiotopoulos · A. Moukarika · T. Bakas · V. Papaefthymiou

Published online: 8 November 2006

Abstract Polycrystalline double perovskites $Sr_2Fe_{1-x}Cr_xMo_{1-x}W_xO_6$ with x = 0, 0.05, 0.10, 0.15, 0.20, and 0.30 have been prepared by sold state reactions. *A* continuous decrease of the tetragonal unit cell parameters α and c with increasing x values is observed. The highest Curie temperature T_C = 426 K is recorded for the x = 0.10 compound. ^{57}Fe Mössbauer spectroscopy measurements indicate a non-integral electronic configuration of ~$3d^{5.3}$ for the Fe ions at the ordered double perovskite structure for $x \leq 0.20$, which reaches ~$3d^{5.4}$ for x = 0.30. Fe–Mo/W anti-site and anti-phase boundary defects are observed in all samples in equal concentrations of around 3% of the total number of Fe ions in their structure.

Key words double perovskites · Mössbauer spectroscopy · $Sr_2Fe_{1-x}Cr_xMo_{1-x}W_xO_6$

1 Introduction

Half-metallic materials are in the centre of both basic and applied scientific interest for the last years thanks to their unique magneto-electronic properties [1]. An important category of these materials are members of the family of double perovskite (DP) oxides, which have general formula $A_2MM'O_6$, where *A* accounts for alkaline earths (Sr, Ba, Ca) and M, M′ for transition metals (M = Fe, Cr,; M′ = Mo, Re, W). Large values of low field magneto-resistance (MR) at room temperature (RT), combined with Curie temperatures (T_C) above 400 K are characteristics which ascribe to some of these compounds very important value as candidate materials for realizing novel devices for spin-electronic applications [2, 3]. Sr_2FeMoO_6 is one of – if not – the most important member of these series, and it has be shown that partial substitution of Mo by W [4], and of Fe by Cr [5] independently, can lead

A. P. Douvalis (✉) · I. Panagiotopoulos
Department of Materials Science and Engineering, University of Ioannina,
P.O. Box 1186, 45110 Ioannina, Greece
e-mail: adouval@cc.uoi.gr

A. Moukarika · T. Bakas · V. Papaefthymiou
Physics Department, University of Ioannina, P.O. Box 1186, 45110 Ioannina, Greece

Table I Unit cell parameters and T_c values found for the $Sr_2Fe_{1-x}Cr_xMo_{1-x}W_xO_6$ compounds

x	a (Å)	c (Å)	$1 - (a\sqrt{2}/c)$	T_c (K)
0	5.5711(2)	7.9038(4)	0.00317	420(1)
0.05	5.5693(2)	7.8988(3)	0.00286	424(1)
0.10	5.5685(2)	7.8963(3)	0.00269	426(1)
0.15	5.5679(2)	7.8945(3)	0.00257	422(1)
0.20	5.5680(1)	7.8924(3)	0.00229	422(1)
0.30	5.5677(2)	7.8908(4)	0.00214	408(1)

Errors are indicated in parentheses and refer to the last digit for each value

to an increase of T_C for the resulted compounds relative to the T_C of the undoped material, without major loss of the high MR values at RT.

In this work we are studying the influence of the combined substitution of Mo and Fe by equal amounts of W and Cr, respectively, on the structural, electronic and magnetic properties of Sr_2FeMoO_6, using ^{57}Fe Mössbauer spectroscopy, X-ray diffraction (XRD) and magnetization measurements. We decided to confine the Cr and W doping to low values (up to 30%) in order to see the effect of substitution without altering strongly the crystal, electronic and magnetic structure of the original compound.

2 Experimental

$Sr_2Fe_{1-x}Cr_xMo_{1-x}W_xO_6$ compounds with x = 0, 0.05, 0.10, 0.15, 0.20, and 0.30 were prepared in bulk polycrystalline form by solid state reactions using the encapsulation technique [6]. In particular stoichiometric amounts of high purity (>99.99%) $SrCO_3$, α-Fe_2O_3, Cr_2O_3, MoO_3, and WO_3 where well mixed, pelletized and heated in air at 900°C for 15 h. The resulted materials were reground, pelletized, sealed in evacuated silica tubes together with Fe grains (>99.9%) placed in a separate compartment of the tube, and heated at 1150°C for 145 h, followed by rapid cooling on a large bronze plate at RT. XRD diagrams of powder samples, crashed from the prepared pelletized samples, were collected using Cu Kα radiation on a Bruker AXS D8 diffractometer. The crystal structure of the phases present in the samples was determined by analyzing the XRD patterns with the Rietveld method using the GSAS package [7]. ^{57}Fe Mössbauer spectra (MS) were collected at RT (≈299 K) and 77 K, using a constant acceleration spectrometer equipped with a ^{57}Co (Rh) source kept at RT, and a liquid N_2 bath cryostat (Oxford Instruments). Velocity calibration of the spectrometer was done using α-Fe at RT and 77 K. IS, 2ε, Γ / 2, B_{hf}, and A denote the isomer shift (relative to α-Fe at RT), quadrupole shift ($e^2qQ(3\cos^2\theta - 1)/4$), half line width, hyperfine magnetic field, and relative absorption area of the components used to fit the experimental MS. T_C values were determined from magnetization measurements made with a LakeShore 7300 magnetometer equipped with a high temperature furnace.

3 Results and discussion

Rietveld refinement results using the tetragonal I 4/m (no. 87) space group for the DP phase, show that all samples are single phase materials, with the indication of only a minor amount of $SrMoO_4$ (less than 0.8 wt.%) present for the x = 0 and x = 0.30 samples. There is

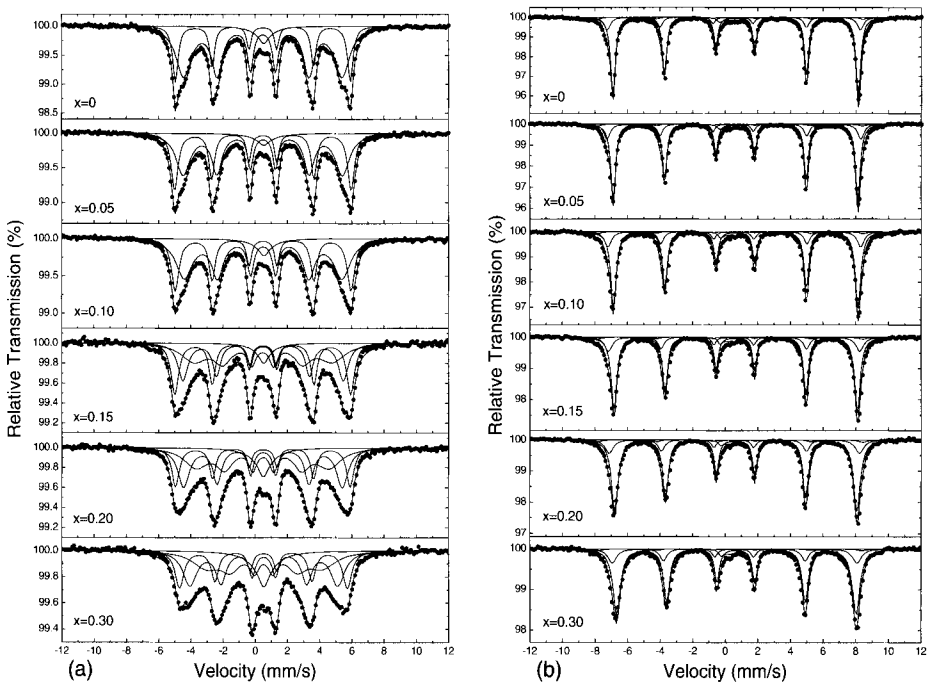

Figure 1 Mössbauer spectra of the $Sr_2Fe_{1-x}Cr_xMo_{1-x}W_xO_6$ compounds recorded at 299 K (**a**) and 77 K (**b**). Cycles correspond to experimental points and the continuous lines to the theoretical components used to fit the spectra.

a tendency of continuous decrease for both unit cell parameters α and c, as x increases from 0 to 0.30 (see Table I). This results mainly due to the lower Cr^{3+} ionic radius (0.615 Å) compared to that of substituted formally Fe^{3+} ions (0.645 Å), as the difference in the ionic radius of W^{5+} (0.62 Å) or W^{6+} (0.60 Å) when substituting the formally Mo^{5+} (0.61 Å) is lower [8]. The crystal structure seems to become more 'symmetric' with increasing Cr and W doping, as the value of the quantity $[1 - (\alpha\sqrt{2}/c)]$ decreases continuously with increasing x (see Table 1). The refined occupancy factors for the B and B′-sites of the $A_2BB'O_6$ DP structure indicate the presence of Fe/Cr–Mo/W anti-site (AS) defects [4, 9].

Magnetization measurements made from 300 K to 483 K in applied field of $\mu_0H = 0.1$ T reveal an initial increase in the T_C value of the doped materials, which peaks at $x = 0.10$, followed by a subsequent decrease for $x = 0.20$ and 0.30 (Table I).

MS of the samples collected at 299 and 77 K are shown in Figure 1. At RT all spectra show broad lines, and the broadening increases as the x value increases specially above $x = 0.10$. We used a combination of magnetic components (MC) and one paramagnetic single-line (PC) component in order to fit the RT spectra of all samples. To model correctly the broadening, a distribution of B_{hf} values (ΔB_{hf}) was added to the MCs. The resulted average values of the Mössbauer parameters (MP) are listed on Table II. Line broadening comes as a consequence of increased disorder in the immediate cationic environment of the iron ions, caused by W and Cr doping, as also by decrease of the T_C values for the higher doped compounds. This behaviour for the room and elevated temperatures MS, and the simultaneous appearance of both MCs and PCs, specially in the temperature region below T_C, is a striking characteristic of pure, as also Fe-, or Mo-substituted Sr_2FeMoO_6 [4, 5, 9, 10].

Table II Mössbauer parameters as resulted from the best fits of the $Sr_2Fe_{1-x}Cr_xMo_{1-x}W_xO_6$ MS at 299 K and 77 K

299 K				77 K		
Comp.	MCs/PC	MCs	MCs[a]/PC	(a)/(b)/(c)/(d)	(a)/(b)/(c)/(d)	(a)/(b)/(c)/(d)
x	<IS> (mms^{-1}) <2ε> (mms^{-1})	<B_{hf}> (T)	A (%)	IS (mms^{-1}) 2ε (mms^{-1})	B_{hf} (T) ΔB_{hf} (T)	A (%) Γ / 2[$] ($mms^{-1}$)
0	0.58/0.64 0.00	31.6	94/6	0.73/0.61/0.52/0.26 0.00/0.02/−0.24/0.15	46.9/48.4/50.8/3.6 0.2/0.5/0.8/0.3	78/16/3/3 0.14
0.05	0.59/0.65 −0.01	32.3	95/5	0.73/0.62/0.52/0.30 0.00/0.03/−0.24/0.16	46.8/48.5/50.7/4.0 0.2/0.5/1.0/0.2	75/19/3/3 0.14
0.10	0.60[a]/0.65 0.01	31.8	94/6	0.73/0.64/0.52/0.19 0.01/0.02/−0.25/0.15	46.8/48.3/50.8/2.9 0.3/0.6/1.2/0.0	75/19/3/3 0.15
0.15	0.59[a]/0.64 0.00	30.4	95/5	0.74/0.64/0.52/0.16 0.01/0.01/−0.25/0.12	46.6/48.0/50.8/2.8 0.4/0.8/1.2/0.0	75/19/3/3 0.14
0.20	0.59[a]/0.61 0.02	29.6	91/9	0.74/0.64/0.52/0.18 0.01/0.02/−0.25/0.10	46.3/47.9/50.8/2.6 0.6/0.9/1.0/0.1	78/17/3/2 0.15
0.30	0.64[a]/0.64 0.01	27.7	88/12	0.77/0.67/0.52/0.20 0.02/0.02/−0.26/0.08	45.8/46.8/50.3/2.6 0.8/1.0/1.2/0.0	76/18/3/3 0.16

Typical errors are ± 0.02 mms^{-1} for IS and 2ε, ± 0.01 mms^{-1} for Γ / 2, ± 0.5 T for B_{hf} and ΔB_{hf}, and 3% for A.

[a] Total area of MCs,
[$] common for all components.

The average IS of the MCs at RT has a slight increase tendency with increasing x, which is more pronounced above x = 0.20. The corresponding average B_{hf} values show a small increase up to x = 0.05, but are reduced with further increasing x values. These results are consistent with the behaviour of the corresponding MPs observed for the $Sr_2FeMo_{1-x}W_xO_6$ compounds [4], and reflect the effect of additional electronic charge on the electronic configuration of iron ions in the B-sites of the DP structure, which results from W doping. The increase in the absorption area of the PCs with x values indicates increase in disorder or in the amount of AS defects present on the DP structure. However this remains to be cleared by the analysis of the 77 K MS. All MCs have 2ε values very close to zero at RT.

At 77 K the MS have quite narrower resonant lines compared to RT. However these spectra show characteristics for the appearance of Fe–Mo/W antisite defects, which manifest themselves specially by the asymmetric 'structure' of the extreme left resonant line for each spectrum [4, 9]. Three MCs corresponding to three groups of iron ions: (a) on the 'correct' B-sites with 6 Mo/W first cation neighbours, (b) on the 'correct' B-sites with 5 Mo/W and 1 Fe/Cr cation neighbours, and (c) on the 'wrong' B′-sites with 6 Fe/Cr cation neighbours were used to fit the spectra accordingly. Following [9] the resulted IS and B_{hf} values for these components are in accordance with a non-integral electronic configuration of about $3d^{5.3}$ for the Fe ions corresponding to (a)-case for $x \leq 0.20$, which increases slightly to $3d^{5.4}$ for x = 0.30, in agreement with the corresponding behaviour of these MPs at RT.

A slightly decreased electronic configuration from that of the ions of the (a)-case is observed for the ions of the (b)-case in all samples. Fe ions corresponding to (c)-case show pure ferric ($3d^{5.0}$) character. The amount of AS defects present in each sample can be determined from the relative values of the absorption areas of the MCs corresponding to the

ions of (b)- and (c)-cases. This amount seems to be quite similar for all samples showing no dependence on Cr and W doping, averaging to about 3%. This comes in general agreement with the results of site-occupancy factors found from Rietveld refinements of the corresponding XRD patters. A forth minor MC with quite low IS and B_{hf} values was necessary to be included in the theoretical model in order to describe correctly the part of each MS at 77 K around zero velocity. This component is attributed to iron ions on anti-phase boundaries (APB) ((d)-case), and appears in similar spectra observed for Sr_2FeMoO_6 samples synthesised by the same preparation route [11]. The A values for this component are relatively constant and a concentration of ~3% of the total amount of Fe ions can be estimated to participate to the APB [12] defects.

4 Conclusions

Doping of Sr_2FeMoO_6 with equal amounts of Cr and W up to 30% has a small effect on T_C values, which increase up to 426 K for 10% doping, and on the unit cell parameters which reduce continuously. The electronic configuration of iron ions on the correct B-sites of the $Sr_2Fe_{1-x}Cr_xMo_{1-x}W_xO_6$ double perovskite structure is non-integral, ~$3d^{5.3}$ for all compounds with $x \leq 0.20$, and is slightly altered for $x = 0.30$ to ~$3d^{5.4}$. Anti-site defects and anti-phase boundaries appear in all samples, and their population is estimated to be ~3% of the total amount of iron ions in each compound.

Acknowledgments This research was funded by the program "Pythagoras I" of the Operational Program for Education and Initial Vocational Training of the Hellenic Ministry of Education under the 3rd Community Support Framework and the European Social Fund.

References

1. Ziese, M., Thornton, M.J. (eds.): Spin Electronics. Springer, Berlin Heidelberg New York (2001)
2. Kobayashi, K.I., Kimura, T., Sawada, H., Terakura, K., Tokura, Y.: Nature **395**, 677 (1998)
3. Kobayashi, K.I., Kimura, T., Tomioka, Y., Sawada, H., Terakura, K.: Phys. Rev. B **59**, 11159 (1999)
4. Douvalis, A.P., Venkatesan, M., Coey, J.M.D., Grafoute, M., Greneche, J.-M., Suryanarayanan, R.: J. Phys., Condens. Matter **14**, 12611 (2002)
5. Kim, J.H., Ahn, G.Y., Park, S.I., Kim, C.S.: J. Magn. Magn. Mater. **282**, 295 (2004)
6. Yamamoto, T., Liimatainen, J., Linden, J., Karppinen, M., Yamauchi, H.: J. Mater. Chem. **10**, 2342 (2000)
7. Von Dreele, R.B., Larson A.C.: General Structure Analysis System, University of California (2001)
8. Shannon, R.D.: Acta Crystallogr. **A32**, 751 (1976)
9. Douvalis, A.P., Venkatesan, M., Coey, J.M.D.: Hyperfine Interact. (C) **5**, 131 (2003)
10. Menendes, N., Garcia-Hernandez, M., Sanchez, D., Tornero, J.D., Martinez, J.L., Alonso, J.A.: Chem. Mater. **16**, 3565 (2004)
11. Linden, J., Karppinen, M., Shimada, T., Yasukawa, Y., Yamauchi, H.: Phys. Rev. B **68**, 174415 (2003)
12. Greneche, J-M., Venkatesan, M., Suryanarayanan, R., Coey, J.M.D.: Phys. Rev. B **63**, 174403 (2001)

Hyperfine Interact (2006) 168:1151–1157
DOI 10.1007/s10751-006-9415-1

Magnetic and Mössbauer study of $Mg_{0.9}Mn_{0.1}Cr_xFe_{2-x}O_4$ ferrites

M. Elzain · H. Widatallah · A. Gismelseed · K. Bouziane · A. Yousif · A. Al Rawas · I. Al-Omari · A. Sellai

Published online: 31 October 2006

Abstract The ferrites $Mg_{0.9}Mn_{0.1}Cr_xFe_{2-x}O_4$ $(0 \leq x \leq 0.9)$ were prepared using the conventional double sintering method. The XRD showed that the samples maintain a single spinel cubic phase. The Mössbauer measurements were carried out at room and liquid nitrogen temperatures. From the area ratios of the A and B sites, it was found that the Fe cation population of the A and B sites decreases in proportion to Cr concentration. The contact hyperfine fields at the A and B sites were found to decrease with increasing Cr contents. This was found to be in approximate agreement with the results of magnetization measurement. The distributions of Mg and Mn cations versus Cr concentration were also determined using the Mössbauer and magnetization results. The Curie temperatures were determined and found to agree with the reported values. As the Cr contents increases the relative magnetization, was found to increase at low temperatures and decreases at higher temperatures.

Key words Mössbauer spectroscopy · Neel temperature · ferrites · magnetization

1 Introduction

Ferrite materials remain interesting for their various technological applications and their rich underlying fundamental theoretical picture. The ferrite's physical characteristics make them useful in computer memories, digital electronics, microwave devices and several other areas. The spinel ferrites are described by the formula AB_2O_4, where A and B represent cations at the tetrahedral and octahedral sites, respectively. The basic theoretical properties are modeled through the superexchange interactions J_{AB}, J_{AA} and J_{BB}. In Neil's model the intersite antiferromagnetic coupling J_{AB} dominates the intrasite interactions J_{AA} and J_{BB} leading to collinear ferrimagnetism. Deviations from collinear ferrimagnetism were

M. Elzain (✉) · H. Widatallah · A. Gismelseed · K. Bouziane · A. Yousif · A. Al Rawas · I. Al-Omari · A. Sellai
Department of Physics, College of Science, Sultan Qaboos University, Box 36, Al Khod 123, Oman
e-mail: elzain@squ.edu.om

observed with cation substitutions leading to uniform or local spin canting as reviewed in [1].

Magnesium ferrites, $MgFe_2O_4$, are partially inversed spinels, where Mg^{2+} cations are distributed among the A and B sites as $(Mg^{2+}_{\eta}Fe^{3+}_{1-\eta})[Mg^{2+}_{1-\eta}Fe^{3+}_{1+\eta}]O_4$. Here the curly and square brackets stand for A and B sites, respectively. The inversion parameter η depends on the preparation conditions and was found to vary from about 0.1 to about 0.25 with the quenching rate of the hot materials [2]. The measured magnetic moments were found to depend on this inversion ratio. On the other hand, in Mn ferrites the Mn^{2+} cations were found to reside mostly in the A site with an inversion ratio of about 0.8 [2, 3]. The magnesium–chromium ferrites were also intensively studied [4–8]. With inclusion of Mn, the ferrites $Mg_{0.9}Mn_{0.1}Cr_xFe_{2-x}O_4$ were studied against Cr concentration [7, 8]. It was found that the spinel structure with decreasing lattice constant is maintained as the Cr concentration increases [6]. The magnetization measurements showed that the average magnetic moment and Neel temperature decrease with increasing Cr concentration. Using Mössbauer spectroscopy the contact hyperfine field was also found to decrease with increasing Cr contents [4, 5]. In general Cr occupies the B site replacing Fe there; however, both X-ray and Mössbauer studies showed that the concentration of Fe in the A site decreases, while that of Mg increases as more Cr enters the B site. Moreover, the order of inversion η was found to increase with temperature [5].

In this study we have measured the saturated magnetizations and the hyperfine fields of $Mg_{0.9}Mn_{0.1}Cr_xFe_{2-x}O_4$ ferrites. Both quantities were found to agree with the reported trends at room temperature. However, we found that, contrary to the common belief, the saturation magnetization at low temperatures may increase with increasing Cr contents. We report the relative magnetization and discuss the results in terms of Neel's model. It is proposed that spin canting should be included to reach agreement between experiment and theory. In the following section we present the experimental procedures and discuss the results in Section 3.

2 Experimental procedures

Single-phase $Mg_{0.9}Mn_{0.1}Cr_xFe_{2-x}O_4$ (x = 0.1, 0.3, 05, 0.7 and 0. 9) ferrites were prepared by the standard solid-state reaction method. High purity powders of $MgCO_3$, $MnCO_3$, α-Fe_2O_3 and Cr_2O_3, in the desired stoichiometric ratios, were mixed, ground and calcined in air at 900°C (12 h) and allowed to slow cool in the furnace. The calcined mixtures were pressed into pellets and sintered at 1,200°C (12 h) in similar conditions. This preparation approach is close to that used in [8].

X-ray powder diffraction (XRD) data were recorded with a Philips PW1820 diffractometer in the reflection mode using *CuKα* radiation. The program PowderCell was used to analyze the XRD data. The DC magnetic measurements were performed on a DMS 1660 vibrating sample magnetometer (VSM) in a temperature range from 77 to 770 K. The temperature dependent measurements of magnetization were carried out by, heating or cooling the sample under an applied field of 13.5 kOe. The saturation magnetization was determined from the hysteresis loop and the isotherms measurements.

The Mössbauer measurements were performed on the samples in a continuous liquid nitrogen flow cryostat using a 50 mCi ^{57}Co(Rh) source with a spectrometer in the transmission mode. The spectrometer was calibrated with α-Fe foil spectrum at room temperature.

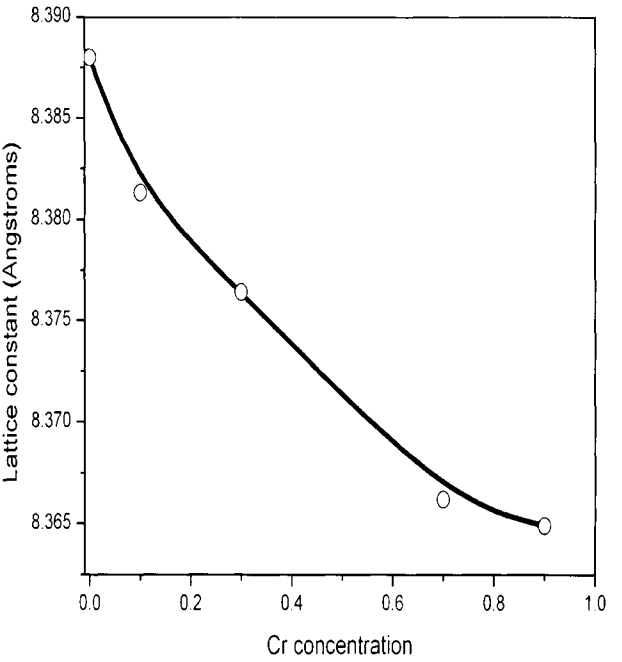

Figure 1 The lattice constant versus chromium concentration measured at *RT*.

3 Results and discussion

The samples were scanned from $2\theta = 20°$ to $2\theta = 80°$ in steps of 0.02°. The XRD data shows that the samples retain the cubic spinel structure as more Cr is added in agreement with the results in [5–8]. The measured lattice constants decrease with increasing Cr concentration as shown in Figure 1. This is expected since the larger Fe^{3+} cations (of 0.067 nm ionic radius) are being replaced by the smaller Cr^{3+} cations (of 0.063 nm ionic radius) and agrees with the observed trends in [6–8].

The Neel temperature T_N was determined for each sample from magnetization measurement versus temperature at low external fields. The Neel temperature was found to decrease with increasing x as shown in Figure 2. The sample with $x = 0.9$ did not show ferrimagnetism at temperatures above liquid nitrogen (LNT). The magnetization was also measured for all samples from above T_N to liquid nitrogen in an external field of 13.5 kOe. The relative magnetization isotherms were determined for each x. The relative magnetization, m_r, is defined as the measured magnetization for each sample scaled by the corresponding magnetization of Cr-free sample. The results are shown Figure 3. The room temperature (RT) curve shows that m_r decreases with increasing Cr concentration in a fashion not unlike the results found in [7, 8] for saturation magnetization. Higher temperature curves follow the same trends. However, the LNT curve exhibits the opposite trends; the relative magnetization increases with increasing Cr contents. The latter behavior is unexpected on the ground that the Cr^{3+} cations with smaller magnetic moment (3 μ_B) are replacing the Fe^{3+} cations with the larger magnetic moment (5 μ_B) as x increases.

In the Neel model the magnetization depends on the distribution of cations in the A and B sites. Since a Mn^{2+} cation has magnetic moment of 5 μ_B, it is not distinguishable from an Fe^{3+} cation. The magnetic moment per formula unit according to Neel model is then $0.5 + 9\eta(x, T) - 2x$. By comparing this relation to the experimental results of m_r, it is

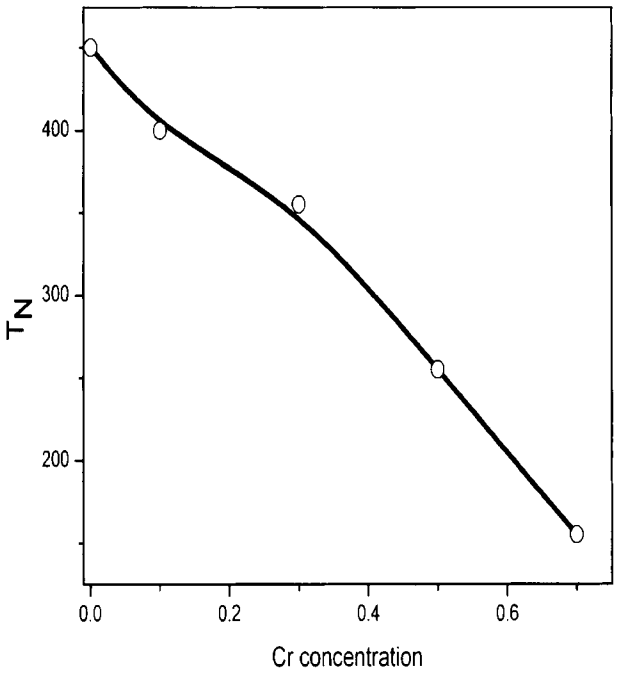

Figure 2 The Neel temperature T_N in C against chromium concentration.

possible to determine the dependence of η on x and T. In obtaining these relations we assume that η is independent of T for Cr-free systems for T less than about 200°C [5]. The actual value taken for η in this case does not affect the observed trends. The resulting trends are illustrated in Figure 4. Figure 4a shows the dependence of η on x for fixed T, while Figure 4b shows the dependence on T for x equal to 0.1 and 0.3. For all T the inversion parameter η increases with increasing x, whereas it decreases with increasing T for fixed x. The increase of the inversion ratio with Cr concentration is in agreement with the results obtained using XRD in [6]. However, the decrease of η with increasing temperature contradicts the reported trends [5]. We note that this latter result is obtained when fitting the magnetization obtained using the collinear Neel model to the experimental data. To resolve this contradiction, we suggest the replacement of the collinear Neel model by spin canting models.

The Mössbauer spectroscopy determines the Fe occupation of the A and B sites. We have carried out the Mössbauer measurements on the samples at LNT and RT. The Mössbauer parameters were found to agree with those reported for cubic spinels. The data was fitted to two sextets corresponding to the A and B sites. The quadruple splitting is zero and the respective isomer shifts at the A and B sites, relative to α-Fe, vary from about 0.25 to 0.3 mm/s and 0.35 to 0.4 mm/s with Cr contents. The magnetic hyperfine fields were found to decrease with increasing Cr concentration as shown in Figure 5. The Fe contents of the A and B sites were determined from the area ratios of the two sites. The line width of the A site increases with Cr addition indicating the existence of more than a single local environment. In general the Fe occupations of both A and B sites were found to decrease with increasing Cr concentration. The rate at which this Fe occupation decreases determines the trends of magnetic moments. When both occupations decrease at similar rates, the magnet moments increases with Cr concentration, whereas faster decrease at the B site leads to reduction in magnetic moment. The results of Mössbauer measurements at LNT

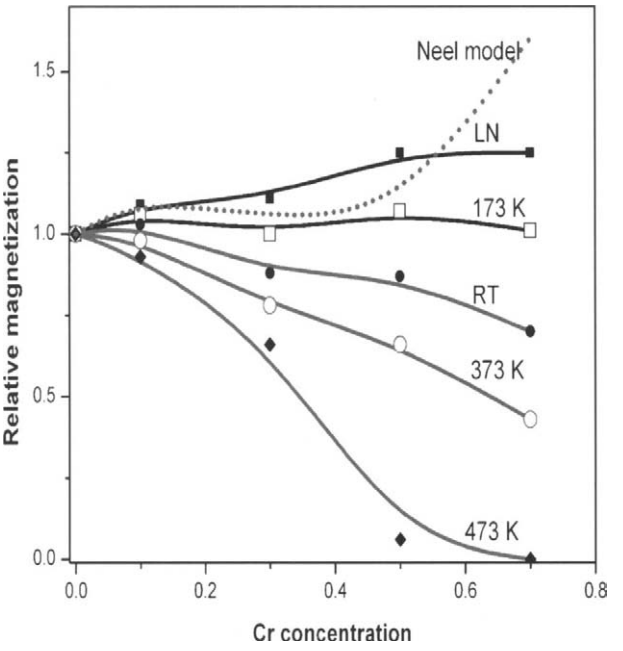

Figure 3 The relative magnetization m_r against chromium concentration for liquid nitrogen (*LN*) temperature, room temperature (*RT*) and other indicated temperatures. The *dotted curve* gives the result of application of the Neel model using the fractions Fe occupation at A and B sites as determined by Mössbauer spectroscopy at *LN* temperature.

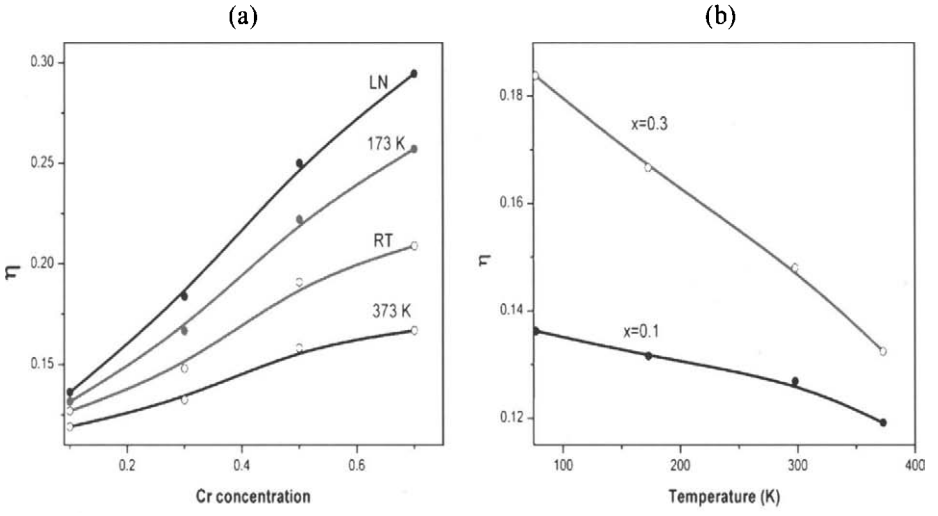

Figure 4 **a** The inversion parameter η versus chromium concentration for different temperatures obtained by fitting Neel model to experimental data; **b** The inversion parameter versus temperature for chromium concentration of 0.1 and 0.3 obtained by fitting Neel model to the experimental data.

give similar reduction in Fe occupation at A and B sites and hence to increasing magnetic moment. The relative magnetization calculated using the Mössbauer LNT data within Neel model is shown in Figure 3. We note that at higher Cr concentration m_r becomes relatively large. To achieve the required reduction in magnetic moment at higher temperatures, the Fe occupation of the B site should decrease at a higher rate. This would mean that on addition

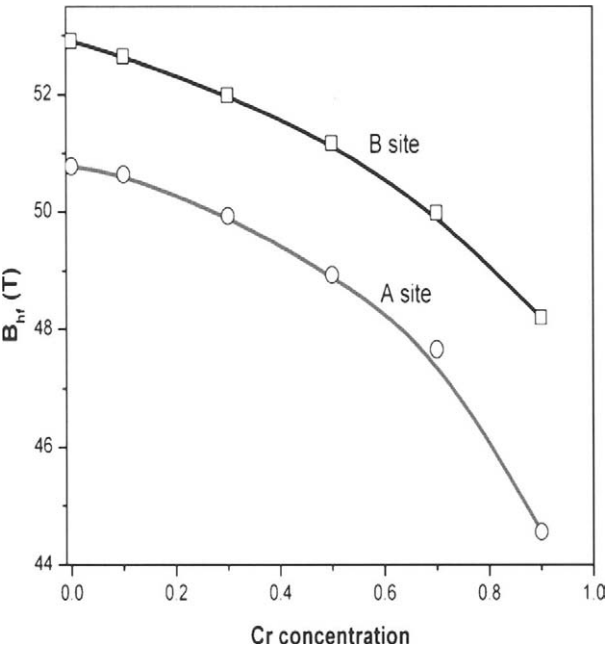

Figure 5 The magnetic hyperfine field at Fe in the A and B sites against chromium concentration measured at liquid nitrogen temperature.

of Cr more Fe migrates from the A site to the B site at low temperatures than at higher temperatures in disagreement with reported results of Lee et al. [5]. Such observation is physically unacceptable and calls for replacing the collinear Neel model. In our view the experimental results could be reconciled with theory if spin canting is allowed. It is well documented that addition of Cr leads to spin canting [9,10]. The presence of spin canting will reduce the large value of m_r at high Cr concentration for low temperatures. In addition, the spin canting should be accompanied by faster vibration of Cr moments as temperature increases. This will reduce the average contribution of Cr to the magnetic moment and leads to further reduction in m_r at higher temperatures. A detailed study of these features is currently underway.

In summary, we have characterized the $Mg_{0.9}Mn_{0.1}Cr_xFe_{2-x}O_4$ as cubic spinels. The relative magnetization was found to increase (decrease) with increasing Cr concentration at low (high) temperatures. The Fe occupations at the A and B site as determined from the Mössbauer measurement at liquid nitrogen temperature indicate that the relative magnetization should increase with increasing Cr contents in Neel model although the corresponding magnetic hyperfine fields decrease. It was proposed that spin canting and faster vibration of Cr moment would explain the results.

References

1. Dormann, J.L., Nogues, M.: J. Phys., Condens. Matter **2**, 1223 (1990)
2. Sawatzky, G.A., van der Woude, F., Morrish, A.H.: Phys. Rev. **157**, 747 (1969)
3. Kriessman, C.J., Harrison, S.E.: Phys. Rev. **103**, 857 (1956)
4. Balaev, A.D., Bayukov, O.A., Savitskii, A.F.: Phys. Status Solidi, B **152**, 639 (1989)
5. Lee, S.W., An, S.Y., Ahn, G.Y., Kim, C.S.: J. Appl. Phys. **87**, 6238 (2000)
6. Kawade, V.B., Bichile, G.K., Jadev, K.M.: Mater. Lett. **42**, 33 (2000)

7. Singh, M., Sud, S.P.: Mater. Sci. Eng., B **83**, 180 (2001)
8. Lakshman, A., Rao, K.H., Meniratta, R.G.: J. Magn. Magn. Mater. **250**, 92 (2002)
9. Vandenberghe, R.E., De Grave, E.: In: Long, G., Grandjean, D. (eds.) Mössbauer Spectroscopy Applied to Inorganic Chemistry, vol. 3, p. 59. Plenum, New York (1989)
10. Chappert, J., Frankel, B.: Phys. Rev. Lett. **19**, 570 (1967)

Hyperfine Interact (2006) 168:1159–1163
DOI 10.1007/s10751-006-9416-0

Theoretical investigation of Mössbauer hyperfine interactions in ordered FeNi and disordered Fe–Ni alloys

Diana Guenzburger · Joice Terra

Published online: 14 November 2006

Abstract Electronic structure spin-polarized calculations were performed for 79-atoms embedded clusters representing the ordered intermetallic compound FeNi, the fcc Fe-rich disordered alloy $Fe_{85}Ni_{15}$ in an antiferromagnetic (AFM) configuration, and the ferromagnetic (FM) disordered alloy $Fe_{50}Ni_{50}$. The spin-polarized discrete variational method (DVM) in Density Functional theory was employed. Spin magnetic moments, as well as the ^{57}Fe Mössbauer hyperfine parameters isomer shift and magnetic hyperfine fields, were obtained from the calculations. For FM $Fe_{50}Ni_{50}$, the effect of pressure on the hyperfine field and on the isomer shift was investigated, for three different local atomic configurations surrounding the ^{57}Fe probe atom. In the case of the isomer shift, the calculated values were compared to reported experimental data.

Key words Fe–Ni alloys · hyperfine interactions · electronic structure · magnetic moments

1 Introduction

Fe–Ni alloys have great technological importance due to their structural, magnetic and mechanical properties. The fcc (or γ) phase that is present at lower temperatures is known to exist in different magnetic states [1], similar to pure γ-Fe. At low Ni concentrations, an antiferromagnetic (AFM) phase has been characterized at low temperatures, which is present in meteorites [2] and may also be obtained by synthetic means [3]. An ordered form of Fe–Ni 50–50 named tetrataenite is also found in meteorites [4], and may be obtained in the laboratory by irradiation of the disordered 50–50 alloy with neutrons or electrons [5].

Ferromagnetic (FM) Fe–Ni alloys at the composition range of 30–40 at% Ni present vanishing thermal expansion coefficients, a phenomenon known as INVAR. There is a clear correlation between molar volume and the average magnetic moment in fcc Fe–Ni alloys, as there is in fcc Fe. Experiments have been reported in which the lattice constants of Fe–Ni

D. Guenzburger (✉) · J. Terra
Centro Brasileiro de Pesquisas Físicas, rua Xavier Sigaud 150, 22290-180 Rio de Janeiro, RJ, Brazil
e-mail: djr64gue@cbpf.br

alloys were determined at different pressures [6]; on the other hand, Mössbauer spectroscopy studies reported the effect of pressure on the magnetic hyperfine field (HF) and the isomer shift (IS) of ^{57}Fe in such alloys [7].

Calculations with first-principles electronic structure methods give detailed information on the magnetic and hyperfine properties of Fe–Ni alloys, which, coupled to the experimental results, will contribute to elucidate their origin. We present results of electronic structure calculations for some Fe–Ni systems. Magnetic moments (μ), magnetic hyperfine fields (HF) and isomer shifts (IS) are obtained. In particular, calculations were performed for the disordered fcc FM alloy $Fe_{50}Ni_{50}$, at different lattice parameters corresponding to different applied pressures; this allowed to derive the trends of IS and HF of Fe with pressure.

2 Theoretical method

First-principles self-consistent-field (SCF) spin-polarized electronic structure calculations, employing the numerical Discrete Variational method (DVM) [8, 9], were performed for 79-atoms clusters embedded in the potential of the external solid, representing the Fe–Ni systems. The local spin-density approximation in Density Functional theory (DFT) was employed. The Kohn–Sham equations of DFT are solved numerically in a three-dimensional grid of points. The cluster orbitals, from which the electronic charge density $\rho(\boldsymbol{r})$ is constructed, are expanded on a basis of numerical atomic orbitals. An Fe atom is at the center of the clusters, where all the local properties are obtained.

Spin magnetic moments are calculated by the integration of the spin density $[\rho_{\uparrow}(\boldsymbol{r}) - \rho_{\downarrow}(\boldsymbol{r})]$ inside the Wigner–Seitz cell of the central Fe atom, where the term in brackets is the difference between the electronic charge density for spin up and spin down. The Mössbauer hyperfine parameters [10] isomer shift (IS), electric-field gradient (V_{zz}) and quadrupole shift (ε), and magnetic hyperfine field (HF), were calculated at the nucleus of the central Fe atom of the cluster, utilizing the self-consistent spin and total electronic density obtained from the calculations for the clusters.

3 Results and discussion

The ordered FeNi 50–50 compound (tetrataenite) is formed by alternating layers of Fe and Ni. Spin magnetic moments on Fe in FeNi 50–50 were found to be larger than in FM bcc Fe ($2.6\mu_B$, as compared to $2.2\mu_B$). Calculated magnetic moments on Ni are $0.6\mu_B$. The calculations reveal that there is an electronic charge transfer from the Fe layers to the Ni layers, which is responsible for the electric field gradient (V_{zz}) found experimentally on Fe. The calculated V_{zz} at the Fe nucleus is positive; this result, coupled to the positive sign measured for the quadrupole shift ε, indicates that the direction of magnetization in FeNi is perpendicular to the layers. The value of the quadrupole shift ε in ^{57}Fe obtained from the calculations is +0.35 mm/s. The magnetic hyperfine field at the Fe nucleus obtained was −241 kOe (perpendicular to the layers) and −262 kOe (parallel); these values may be compared to −288 kOe and −327 kOe obtained experimentally [5]. The difference between the values of parallel and perpendicular HF is seen to be due mainly to the rather large contribution from the electron spin-dipolar hyperfine field (also calculated here), originating from non-negligible spin-density anisotropy.

Table I Calculated values of the magnetic moment μ and hyperfine parameters of Fe in AFM $Fe_{85}Ni_{15}$, for different lattice constants a and configurations A and B

Alloy	a (Å)	μ (μ_B)	HF (kOe)[a]	IS (mm/s)[b]
$Fe_{85}Ni_{15}$(A)	3.58	1.59	−75	−0.05
	3.48	1.17	−56	−0.12
	3.39	0.61	−30	−0.20
$Fe_{85}Ni_{15}$(B)	3.58	1.96	−139	−0.02
	3.48	1.58	−113	−0.08
	3.39	1.04	−78	−0.16
AFM γ-Fe	3.39	0.24	−35	−0.22

[a] Contact contribution only

[b] Relative to ordered FeNi (tetrataenite); $\alpha = -0.23$ mm/s a_o^{-3}

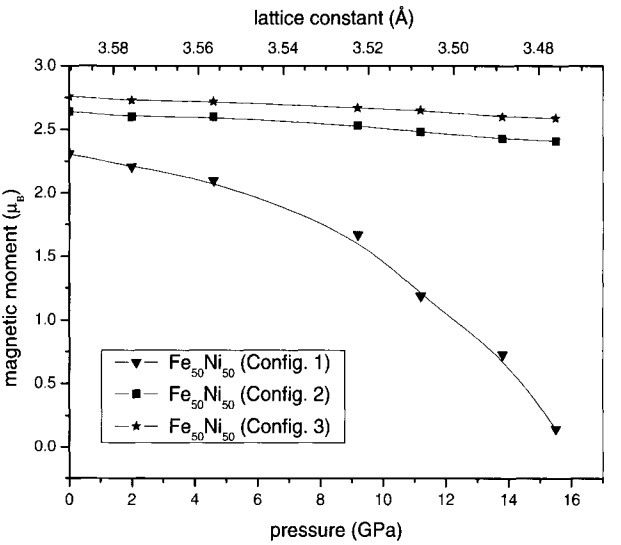

Figure 1 Calculated values of μ against pressure. *Lines* drawn are to guide eye.

The same methodology was applied in calculations for 79-atoms embedded clusters representing the Fe-rich fcc disordered alloy $Fe_{85}Ni_{15}$ [11]. An AFM configuration of alternating spin-up and spin-down layers was adopted; two local distributions of the Ni atoms were considered, one in which the central Fe atom has no Ni nearest-neighbors (configuration A), and another in which it has two Ni nearest-neighbors (configuration B). Three lattice parameters were considered (see Table I), starting with the same lattice parameter of ordered FeNi (3.58 Å) and decreasing its value, since the lattice parameter of AFM γ-Fe is known to be considerably smaller than FM γ-Fe. During the SCF iterations, the initial alternating AFM configuration was broken by the Ni atoms: their spin magnetic moments changed sign, in order to maximize the number of FM-coupling bonds with its Fe nearest-neighbors. Therefore, these calculations predict that the AFM character of this alloy is restricted to local clusters of Fe.

In Table I are given the calculated values for the spin magnetic moments μ, HF and IS of Fe in the clusters modelling the AFM alloy $Fe_{85}Ni_{15}$, for the two different local

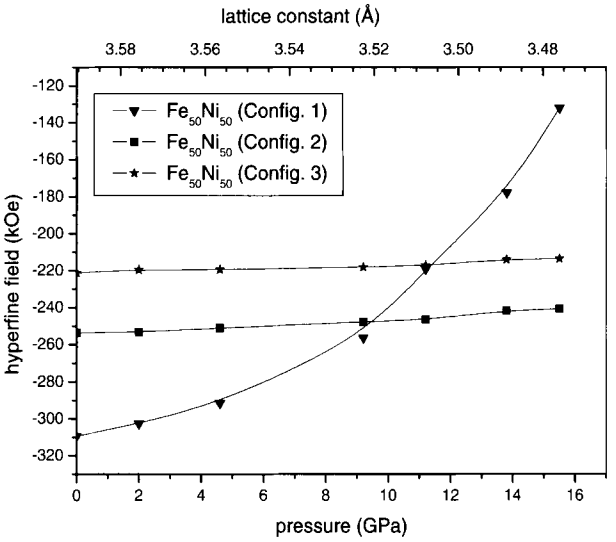

Figure 2 Calculated values of HF against pressure. *Lines* drawn are to guide the eye.

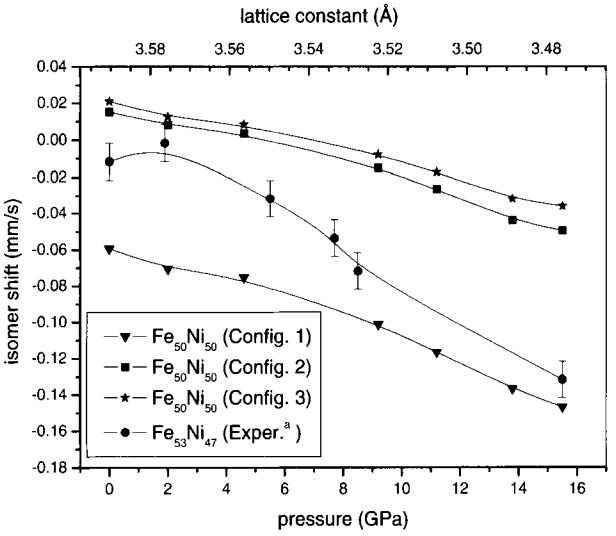

Figure 3 Calculated and experimental values of IS against pressure. *Lines* drawn are to guide the eye. [a]Experimental values from [7], corrected for SOD (θ_D = 380 K [12], SOD = −0.2433 mm/s). All values of IS are relative to ordered FeNi (tetrataenite) [12].

configurations A and B, and three values of the lattice constant. It is seen that magnetic moments and magnitudes of HF decrease with lattice compression. Comparing configurations A and B, it is seen that the effect of Ni first-neighbours of Fe is to increase μ and the magnitudes of HF. It is concluded that only a smaller lattice constant may explain the low values of IS in these alloys [3, 12], as compared to ordered FeNi and FM disordered alloys.

Analogous calculations were performed for 79-atoms clusters representing the FM fcc disordered alloy $Fe_{50}Ni_{50}$ in three different local configurations around the central Fe atom. In Configuration 1, the central Fe atom has 12 Fe nearest-neighbours (NN) atoms, in Configuration 2 it has 8 Ni and 4 Fe NN atoms, and in Configuration 3 the central Fe atom has 12 Ni NN atoms. In Figure 1 are shown the values of the spin magnetic moment at the

central Fe atom, at several values of the applied pressure (which correspond to different values of the lattice constant [6]). It is seen that for Config. 1, the magnetic moment collapses with pressure, which is not the case for Configs. 2 and 3. Therefore, we conclude that the Fe moment is unstable when this atom is surrounded by Fe NN. In all configurations and all pressures, the moment on Ni remains remarkably close to $\sim 0.6\mu_B$.

In Figure 2 the values of the hyperfine field HF at the central Fe is given for several pressures (corresponding to several values of the lattice constant). It may be observed that, although at lower pressures the magnetic moments for Config. 1 are smaller (see Figure 1), the magnitudes of HF are larger, as compared to Configs. 2 and 3. This is due to the following: for Config. 1, the core and valence contributions to HF have the same sign, and so their magnitudes are added; on the contrary, for Configs. 2 and 3 the core and valence contributions to HF have opposite signs, and so they cancel each other partially, resulting in smaller magnitudes of HF.

In Figure 3 are shown the values of the IS for different pressures for Configs. 1–3, as well as experimental values from [7]. It is seen that the calculations reproduce the correct trend of the IS with pressure, in which increasing the pressure (decreasing the lattice constant) leads to lower values of the IS. Since the calibration constant α that relates IS to the electronic density at the nucleus is negative for ^{57}Fe, lower values of IS correspond to higher values of the electron density at the nucleus. At lower pressures, results for Configs. 2 and 3 are closer to experiment.

References

1. Hopfe, W.D., Goldstein, J.I.: Meteorit. Planet. Sci. **36**, 135 (2001)
2. de Grave, E., Vandenberghe, R.E., de Bakker, P.M.A., van Alboom, A., Vochten R., van Tassel, R.: Hyperfine Interact. **70**, 1009 (1992)
3. Abdu, Y.A., Ericsson, T., Annersten, H.: J. Magn. Magn. Mater. **280**, 395 (2004)
4. Danon, J., Scorzelli, R.B., Souza Azevedo, I., Christophe-Michel-Levy, M.: Nature **281**, 469 (1979)
5. Gros, Y., Pauleve, J.: J. Phys. **31**, 459 (1970)
6. Dubrovinsky, L., Dubrovinskaia, N., Abrikosov, I.A., Vennström, M., Westman, F., Carlson, S., van Schilfgaarde, M., Johansson, B.: Phys. Rev. Lett. **86**, 4851 (2001)
7. Abdu, Y.A., Annersten, H., Dubrovinsky, L.S., Dubrovinskaia, N.A.: Hyperfine Interact. **156/157**, 389 (2004)
8. Ellis, D.E., Painter, G.S.: Phys. Rev., B **2**, 2887 (1970)
9. Ellis, D.E., Guenzburger, D.: Adv. Quantum Chem. **34**, 51 (1999)
10. Greenwood, N.N., Gibb, T.C.: Mössbauer Spectroscopy. Chapman & Hall, London (1971)
11. Guenzburger, D., Terra, J.: Phys. Rev., B **72**, 024408 (2005)
12. Rancourt, D.G., Lagarec, K., Densmore, A., Dunlap, R.A., Goldstein, J.I., Reisener, R.J., Scorzelli, R.B.: J. Magn. Magn. Mater. **191**, L255 (1999)

Hyperfine Interact (2006) 168:1165–1169
DOI 10.1007/s10751-006-9417-z

Tin-doped spinel-related oxides of composition M_3O_4 (M = Mn, Fe, Co)

Orn Helgason · Frank J. Berry · Thomas Moyo · Xiaolin Ren

Published online: 8 November 2006

Abstract Tin-doped compounds of spinel-related M_3O_4 (M = Fe, Mn, Co) have been studied by ^{119}Sn and ^{57}Fe Mössbauer spectroscopy in the temperature range of 20–600 K. The ^{119}Sn Mössbauer spectra recorded down to 20 K from the non-iron-containing compounds of Co_3O_4 and Mn_3O_4 contained only doublets showing no transfer of magnetic properties from cobalt or manganese to the dopant tin ions. In contrast, the tin-doped-$(FeCo)_3O_4$ and $(FeMn)_3O_4$ gave ^{119}Sn and ^{57}Fe Mössbauer spectra, which showed magnetic hyperfine interactions. The Curie temperature has been estimated for the former sample.

Key words Mössbauer spectroscopy · tin-doped spinel-related oxides · Curie temperature

1 Introduction

Compounds of the type M_3O_4 (M = Fe, Mn, Co) all adopt the cubic spinel-related structure. Mn_3O_4 and Co_3O_4 are normal spinels containing M^{2+} ions in tetrahedral sites and M^{3+} in octahedral sites whilst Fe_3O_4 is an inverse spinel in which the tetrahedral sites are occupied by Fe^{3+} and the octahedral sites by both Fe^{2+} and Fe^{3+}.

We have, in recent years, been interested in the structural and magnetic effects, which result from the doping of tin into Fe_3O_4 [1–4]. Although the existence of mixed metal spinel-related structures is known [5, 6], there appears to have been less activity in the doping of these materials by tin. We have, therefore, initiated a study of tin-doped oxides of formula M_3O_4 (M = Mn, Fe, Co) and report here on their structural properties as

O. Helgason (✉)
Science Institute, University of Iceland, Dunhagi 3, Reykjavik IS-107, Iceland
e-mail: ornh@hi.is

F. J. Berry · T. Moyo · X. Ren
Department of Chemistry, The Open University, Walton Hall, Milton Keynes MK7 6AA, UK

T. Moyo
School of Pure and Applied Physics, University of Kwa-Zulu Natal, Durban 4041, South Africa

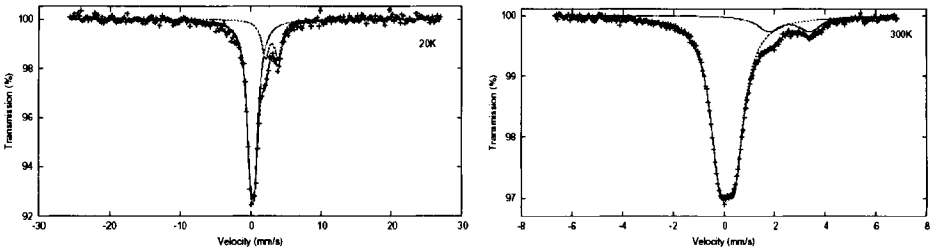

Figure 1 ^{119}Sn Mössbauer spectra of 6.6% tin-doped Mn_3O_4 recorded at 20 and 300 K.

revealed by X-ray diffraction and their magnetic properties as elucidated by Mössbauer spectroscopy.

2 Experimental

Tin-doped compounds of the type M_3O_4 (M = Mn, Fe, Co) were prepared by mixing an aqueous solution of tin (II) chloride dihydrate with an aqueous solution of manganese (II) chloride tetrahydrate, iron (III) chloride hexahydrate or cobalt (II) chloride hexahydrate (or mixtures of these). Excess ammonia was added and the solutions boiled under reflux for 3 h. The precipitates were removed by filtration, washed with 95% ethanol and dried under an infrared lamp. For materials of the type Sn/Mn_3O_4 and Sn/Co_3O_4 the infrared-dried solid was subsequently heated at 250°C for 12 h in air.

X-ray powder diffraction patterns were recorded at 298 K with a Siemens D5000 diffractometer using Cu-K_α radiation.

^{57}Fe and ^{119}Sn Mössbauer spectra were recorded with a constant acceleration spectrometer using 400 MBq ^{57}Co/Rh and 400 MBq $Ca^{119m}SnO_3$ sources. The line width (FWHM) of the calibration spectrum was 0.24 mms^{-1} for the ^{57}Fe spectra and 1.00 mms^{-1} for ^{119}Sn spectra. The chemical isomer shift data are quoted relative to the centroid of the metallic iron spectrum at 298 K in all cases.

3 Results and discussion

X-ray powder diffraction showed the formation of single phase materials. The patterns recorded from tin-doped Co_3O_4, $(FeCo)_3O_4$, Mn_3O_4 and $(FeMn)_3O_4$ were typical of spinel-related structures.

The compositions determined by ICP analysis were 6.2% Sn/Co_3O_4, 6.4% $Sn/Fe_{2.03}Co_{0.97}O_4$, 6.6% Sn/Mn_3O_4, 6.5% $Sn/Fe_{2.03}Mn_{0.97}O_4$.

3.1 6.2% tin-doped Co_3O_4 and 6.6% tin-doped Mn_3O_4

The ^{119}Sn Mössbauer spectra recorded at 20 and 300 K from these samples were very similar and even at 20 K showed no transfer of magnetic properties from cobalt and manganese to the dopant tin ions (Figure 1). In both cases the ^{119}Sn Mössbauer spectra recorded at 20 and 300 K showed the superposition of two quadrupole split absorptions characteristic of a composition containing ca. 90% Sn^{4+} and 10% Sn^{2+}. The isomer shifts

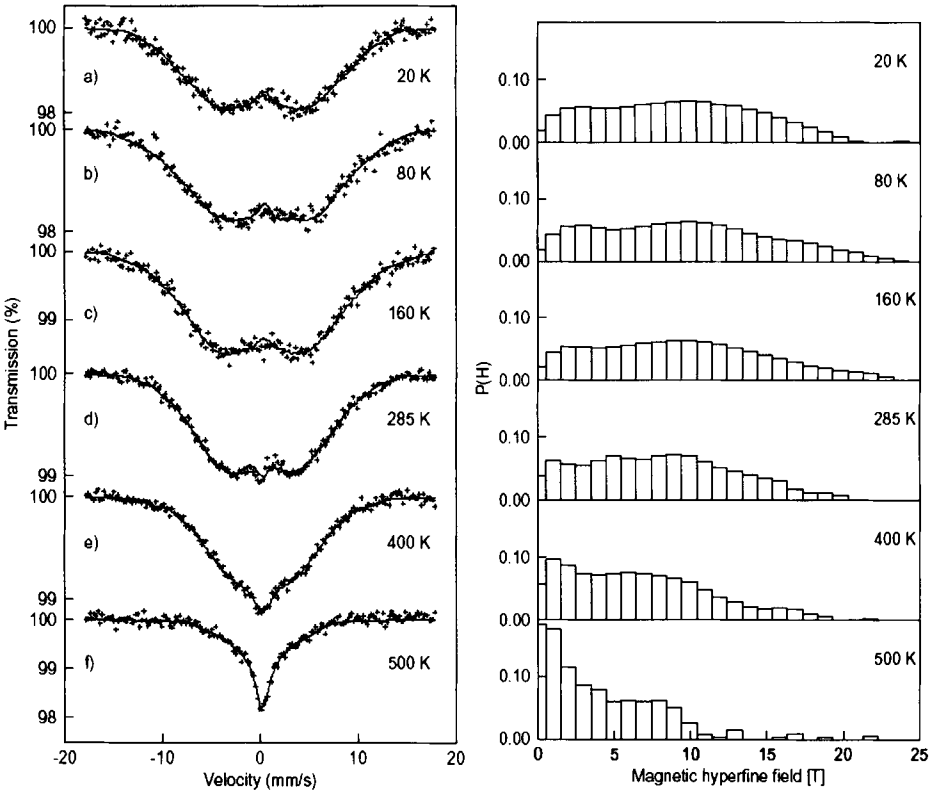

Figure 2 ^{119}Sn spectra of 6.4% tin-doped ($Fe_{2.03}Co_{0.97}O_4$) to the *left* and to the *right* the magnetic field distribution analysed from the same spectra.

were 0.2 and 2.6 mms^{-1} (±0.2) respectively, and the quadrupole splittings, 0.6 and 1.5 mms^{-1} (±0.2) respectively.

3.2 6.4% tin-doped ($Fe_{2.03}Co_{0.97}O_4$)

The ^{119}Sn Mössbauer spectra (Figure 2) recorded between 20 and 500 K showed an extremely broad distribution of hyperfine magnetic fields. At temperatures between 20 and 160 K the maximum hyperfine field approached ca. 20–22 T, which was similar to that observed in tin-doped Fe_3O_4 [2, 7]. At 284 K the largest component was ca. 18 T and at 500 K ca. 10 T. From 20 to 284 K about 90% of the spectral area could be assigned to the magnetic phase and at 500 K some 60% of the spectral area corresponded to the magnetic component. The material became paramagnetic when heated at 600 K.

The ^{57}Fe Mössbauer spectra (Figure 3a) recorded at 20 and 80 K were composed of two well defined magnetic sextets with slightly different isomer shifts, δ (0.4 and 0.5 mms^{-1} (±0.1) at 20 K, zero quadrupole shift and magnetic hyperfine fields of 51.0 and 53.5 T (±0.5 T) respectively. At 295 K the overlap of the sextets become more evident together with increasing superparamagnetism. At 500 K about 50–60% of the area could be associated with the paramagnetic doublet. A crude estimate of the Curie temperature based on the three first spectra indicated a T_c between 600–750 K.

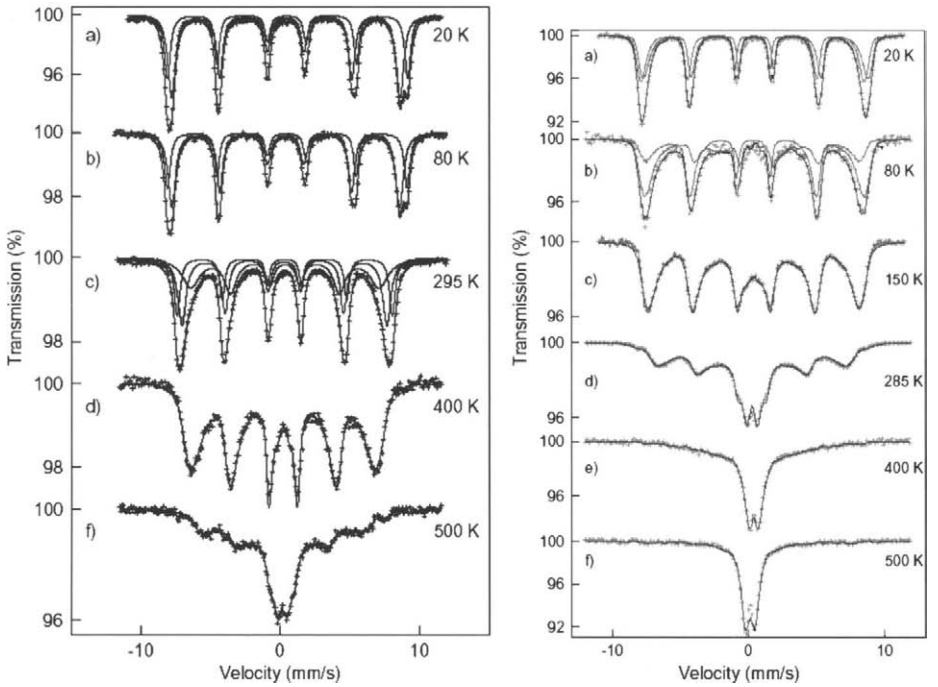

Figure 3 ^{57}Fe spectra of **a** 6.4% tin-doped ($Fe_{2.03}Co_{0.97}O_4$) to the *left* and of **b** 6.5% tin-doped ($Fe_{2.03}Mn_{0.97}O_4$) to the *right*.

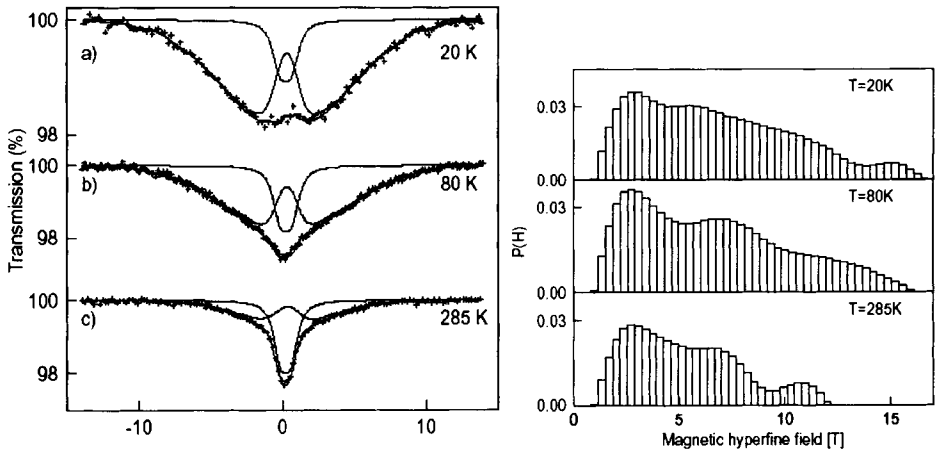

Figure 4 ^{119}Sn spectra of 6.5% tin-doped ($Fe_{2.03}Mn_{0.97}O_4$) to the *left* and to the *right* the corresponding magnetic field distribution.

3.3 6.5% tin-doped ($Fe_{2.03}Mn_{0.97}O_4$)

The ^{119}Sn Mössbauer spectra (Figure 4) showed magnetically split components at temperatures of 284, 80, and 20 K indicative of iron inducing magnetic order in the structure. The spectrum at 20 K could be best fitted with a broad hyperfine magnetic field

distribution up to ca. 15 T (90% of the area) and a doublet with a quadrupole splitting of ca. 0.7 mms^{-1} and a chemical isomer shift of ca. 0.2 mms^{-1}. At 80 K the distribution was shifted slightly to lower field and accounted for ca. 80% of the area whilst the doublet increased to account for ca. 20% of area without any significant changes in the hyperfine parameters. At 285 K the area of the magnetic and paramagnetic parts were approximately equal. The parameters of the doublet were the same and the main magnetic field distribution was largely diminished to ca. 2–8 T.

The ^{57}Fe Mössbauer spectra (Figure 3b) recorded between 20 and 284 K showed magnetically split spectra with a doublet characteristic of paramagnetic species appearing in the spectra recorded at higher temperatures. At 20 K the spectrum was composed of two well defined magnetic sextets with slightly different δ 0.4 and 0.5 mms^{-1} (±0.1), no quadrupole shift, and magnetic hyperfine fields of 50.0 and 52.0 T (±0.5 T) respectively. At 80 K there were signs of paramagnetic relaxation in the spectrum. The two main sextets were reduced by ca. 1 T and a third sextet of very broad line width and with a magnetic hyperfine field of 43 T was required to fit the spectrum. At 150 K the magnetic hyperfine field of the main sextets was further reduced and a paramagnetic doublet emerged. At 295 K the sextets could not be separated and were best fitted to a magnetic field distribution with a maximum at ca. 41 T and with $\delta = 0.35$ mms^{-1} (±0.05) accounting for ca. 75% of the spectral area and a quadrupole split absorption (δ = ca. 0.34 and Δ = ca. 0.75 mms^{-1}) accounting for ca. 25% of the area.

4 Conclusions

The ^{119}Sn Mössbauer spectra recorded down to 20 K from tin-doped Co_3O_4 and Mn_3O_4 show no evidence for the transfer of magnetic properties from cobalt and manganese to the dopant tin ions. In contrast, both the tin-doped $(FeCo)_3O_4$ and $(FeMn)_3O_4$ gave ^{119}Sn and the ^{57}Fe Mössbauer spectra which showed magnetic hyperfine interactions. In the case of tin-doped ($Fe_{2.03}Co_{0.97}O_4$) a crude estimate of the Curie temperature could be made but, for the $(FeMn)_3O_4$ sample, paramagnetic relaxation due to the particle size distribution hindered an estimation of T_c.

References

1. Berry, F.J., Helgason, O., Jonsson, K., Skinner, S.J.: J. Solid State Chem. **122**, 353 (1996)
2. Berry, F.J., Skinner, S.J., Helgason, O., Bilsborow, R., Marco, J.F.: Polyhedron **17**, 149 (1998)
3. Berry, F.J., Greaves, C., Helgason, O.: J. Mater. Chem. **9**, 227 (1999)
4. Moore, E.A., Bohorquerz, A., Berry, F.J., Helgason, O., Marco, J.F.: J. Phys. Chem. Solids **62**, 1277 (2001)
5. Derbyshire, W.D., Xearian, H.J.: Phys. Rev. **112**, 1603 (1958)
6. Guillemot-Fritsch, S., Viguié, S., Rousset, A.: J. Solid State Chem. **146**, 245 (1999)
7. Berry, F.J., Helgason, O., Moore, E.A., Mosselmans, F., Ren, X.: J. Phys., Condens. Matter **16**, 5119 (2004)

Hyperfine Interact (2006) 168:1171–1174
DOI 10.1007/s10751-006-9418-y

Mössbauer study of 1/8 anomaly in $La_{2-x}Ba_xCuO_4$

Kazuhiro Hikosaka · Juichiro Arai

Published online: 5 January 2007

Abstract The measurements of Mössbauer effect, magnetic susceptibility and muon spin relaxation have been carried out for the high-T_c superconductor $La_{2-x}Ba_xCuO_4$. The intensity of Mössbauer doublet spectrum of the sample of x~1/8 begins to decrease rapidly at a certain temperature T_m, which we define as a magnetic transition temperature $T_{Möss}$. This temperature almost agrees with $T_{\mu SR}$ determined from muon spin relaxation. The quadrupole doublet disappears at low temperature below T_m but a clearly splitted spectrum is not observed even at 4.2 K, which indicates a peculiar magnetic state with a wide distribution of internal magnetic field. Around x~1/8, the superconducting critical temperature T_c and T_m are competed each other. In conclusion, superconductivity disappears around 1/8 hole concentration and a peculiar magnetic state such as spin density wave appears.

Key words high-T_c superconductor · 1/8 anomaly

1 Introduction

The superconducting critical temperature T_c in La-214 high-T_c superconductors is known to be strongly suppressed near hole concentration 1/8(0.125), which is referred to as the 1/8 anomaly. Although much effort has been devoted to this problem, a clear solution has not been found. Neutron diffraction experiments have revealed the existence of a peculiar magnetic order such as spin density wave (SDW) in $La_{1.48}Nd_{0.4}Sr_{0.12}CuO_4$ which shows the 1/8 anomaly [1]. We have investigated the 1/8 anomaly in $La_{2-x}Sr_xCuO_4$ (LSCO) and $La_{2-x}Ba_xCuO_4$ (LBCO) by μSR experiment [2]. The destruction of superconductivity seems to be closely connected with the appearance of the peculiar magnetic order. In order to study the relationship between superconductivity and magnetic order, we carried out

K. Hikosaka · J. Arai (✉)
Department of Physics, Faculty of Science and Technology, Tokyo University of Science,
2641 Yamazaki, Noda, Chiba 278-8510, Japan
e-mail: arai@ph.noda.tus.ac.jp

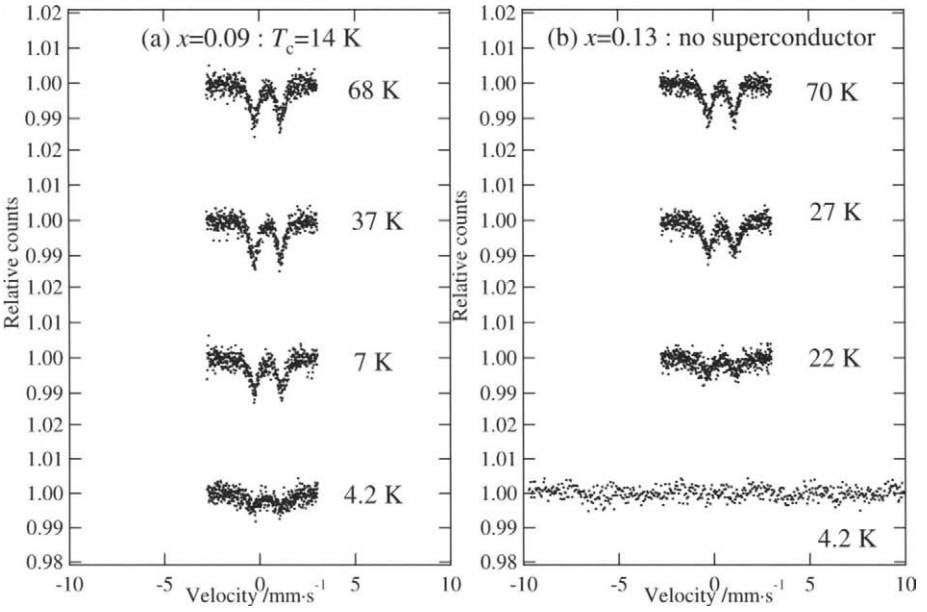

Fig. 1 Mössbauer spectra for samples $x = 0.09$ and 0.13 sample, respectively

measurements of susceptibility, Mössbauer effect and μSR (Fe-free sample) for the samples of $La_{2-x}Ba_xCu_{0.99}{}^{57}Fe_{0.01}O_4$ ($x = 0.09$–0.15).

2 Experimental

The polycrystalline samples of $La_{2-x}Ba_xCu_{0.99}{}^{57}Fe_{0.01}O_4$ (for Mössbauer) and $La_{2-x}Ba_xCuO_4$ (for μSR) were prepared using dried powder of La_2O_3, $BaCO_3$, CuO with 99.99% purity and $^{57}Fe_2O_3$(enriched 95.1%) by a usual solid state reaction method and were confirmed to be a single phase by *X*-ray diffraction. Mössbauer experiments have been performed in the temperature range 4.2 K < T < 300 K using a liquid-He cryostat. Mössbauer source of 50 mC-^{57}Co in Rh matrix was used. The superconducting critical temperature T_c was chosen in relation to the magnetic susceptibility measurements using a SQUID magnetometer. A μSR experiment was carried out at Muon Science Laboratory of High Energy Accelerator Research Organization in Japan.

3 Results and discussion

Figure 1 shows the Mössbauer spectra for (a) $x = 0.09$ and (b) $x = 0.13$ in the samples of $La_{2-x}Ba_xCu_{0.99}{}^{57}Fe_{0.01}O_4$. The sample of $x = 0.09$ shows superconductivity with $T_c = 14$ K but that of $x = 0.13$ does not. Except at 4.2 K, the Mössbauer spectra for both samples are simple and sharp doublet spectra due to quadrupole splitting. This means that the Mössbauer probe ^{57}Fe are found into only Cu sites and are in paramagnetic state except for 4.2 K. Figures 2a and b show temperature dependence of the relative absorption area of the doublet spectra and quadrupole splitting (Q.S.) value, respectively for $x = 0.13$ sample.

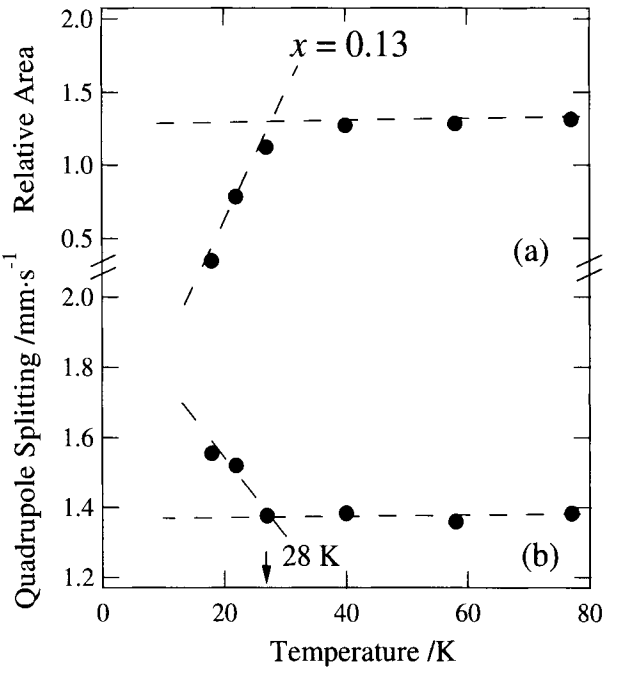

Fig. 2 Temperature dependence of the relative absorption area and the quadupole splitting (Q.S.) value for the sample when $x = 0.13$

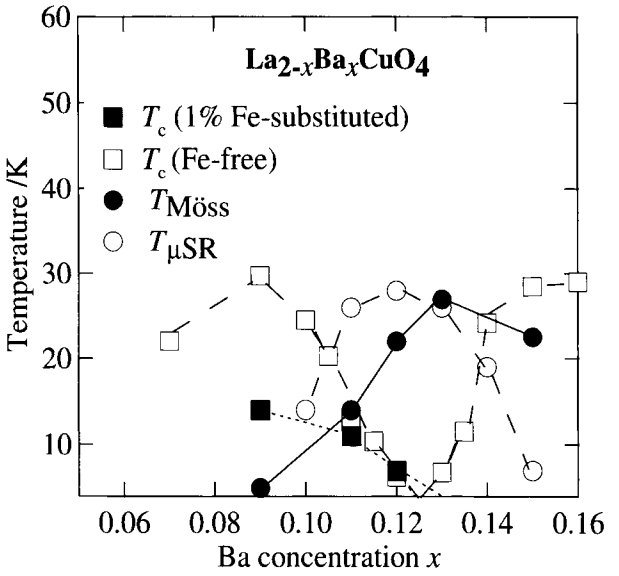

Fig. 3 Concentration x dependence of T_c (1% Fe-substituted, Fe-free), $T_{Möss}$ and $T_{\mu SR}$

Here we notice a marked change in their temperature dependence at a certain temperature T_m. The determined temperatures T_m are 28 and 6 K for $x = 0.13$ and 0.09, respectively. This suggests that below the temperature T_m(Möss), Fe-spin fluctuation rapidly slows down and some structural changes may take place at the same time, which implies the onset of a

peculiar magnetic order accompanied by some topological changes. Then we define $T_{Möss}$ as a magnetic transition temperature. Finally as can be seen at 4.2 K for (b) $x = 0.13$, the doublet spectrum completely disappears but a sextet spectrum due to magnetic splitting can be hardly observed. This means that although ^{57}Fe probes replace Cu ions, which are all equivalent in CuO_2 plane, each ^{57}Fe Mössbauer probe feels different hyperfine field at each site. Consequently, a sextet spectrum can never be observed because of a wide distribution of internal magnetic field. The anomalous Mössbauer pattern at 4.2 K possibly indicates the presence of a peculiar magnetic order. In this figure, we also plot the temperature $T_{\mu SR}$ where a peculiar magnetic order starts, which was determined from μSR experiment in the Fe-free samples. Both temperatures – $T_{Möss}$ and $T_{\mu SR}$ – exhibit the same behaviour but a different peak position because Mössbauer probe Fe^{+3}-substitution for Cu^{+2} reduces 1% hole carriers and consequently, the peak of $T_{Möss}$ shifts to higher concentration by 1% compared to $T_{\mu SR}$. Therefore, both temperatures must detect the same origin although the probes are different; Fe-spin for Mössbauer and μ-spin for μSR. Here we also notice that near $x = 1/8$, superconductivity disappears and the magnetic order occurs, indicating that T_m and T_c are compete with each other. As already mentioned above, unsplitted Mössbauer pattern at 4.2 K significantly below $T_{Möss}$ means a peculiar magnetic order with a wide hyperfine field distribution. With respect to the quadupole splitting (Q.S.), we must pay attention to the increase in Q.S. value below $T_{Möss}$ in Fig. 2b. P.M. Singer et al. have reported [3] that the value of frequency ν_Q in NQR experiment changes significantly at the temperature where charge density wave (CDW) occurs in the sample of Nd-substituted LaNdSrCu, in which the existence of spin density wave (SDW) and CDW were already confirmed by neutron diffraction experiment. Therefore, it is reasonable to consider that the abrupt rise in the Q.S. value should correspond to the occurrence of CDW since the appearance of CDW influences the electric field gradient at ^{57}Fe probes via charge displacement. This peculiar magnetic order must be the state of SDW accompanied by CDW. It can be concluded that when superconductivity is inhibited, near 1/8 hole concentration, SDW and CDW are observed (Fig. 3).

References

1. Tranquada, J.M., et al.: Nature **375**, 15 (1995)
2. Arai, J., et al.: Low Temp. Phys. **131**, 375 (2003)
3. Hunt, A.W., et al.: Phys. Rev., B **60**, 15345 (1999)

Hyperfine Interact (2006) 168:1175–1179
DOI 10.1007/s10751-006-9419-x

^{237}Np and ^{57}Fe Mössbauer study of $NpFeGa_5$

Y. Homma · M. Nakada · A. Nakamura · S. Nasu · D. Aoki · H. Sakai · S. Ikeda · E. Yamamoto · Y. Haga · Y. Ōnuki · Y. Shiokawa

Published online: 16 November 2006

Abstract ^{57}Fe and ^{237}Np Mössbauer Ōmeasurements have been performed for $NpFeGa_5$, which is one of the so-called neptunium 1-1-5 compounds. The ^{57}Fe Mössbauer spectra below T_N = 118 K show the magnetically ordered state. The magnitude of the hyperfine magnetic field at the ^{57}Fe nucleus is determined to be 1.98 ± 0.05 T at 10 K. From the ^{237}Np Mössbauer spectrum at 10 K, the hyperfine magnetic field at the ^{237}Np nucleus is 203 T and the hyperfine coupling constant is determined to be 237 T/μ_B using the Np atomic magnetic moment of 0.86 μ_B determined by the neutron diffraction study.

Key words $NpFeGa_5$ · ^{237}Np Mössbauer spectroscopy · ^{57}Fe Mössbauer spectroscopy · hyperfine magnetic field · hyperfine coupling constant

1 Introduction

The discovery of superconductivity in $PuCoGa_5$ and $PuRhGa_5$ has provided a new perspective on the physics of transuranium compounds with 5*f* electrons [1, 2]. It is obviously important to study experimentally the electronic and the magnetic states of transuranium compounds including Pu and Np. Colineau et al. [3, 4] reported the magnetic and electronic properties of the $NpCoGa_5$ and $NpRhGa_5$ polycrystalline samples and their microscopic magnetism was studied by ^{237}Np Mössbauer spectroscopy. Recently, we

Y. Homma (✉) · S. Nasu · D. Aoki · Y. Shiokawa
Institute for Materials Research, Tohoku University, Sendai, Japan
e-mail: yhomma@imr.tohoku.ac.jp

M. Nakada
Nuclear Science and Engineering Directorate, Japan Atomic Energy Research Institute, Tokai-mura, Japan

A. Nakamura · S. Nasu · H. Sakai · S. Ikeda · E. Yamamoto · Y. Haga · Y. Ōnuki · Y. Shiokawa
Advance Science Research Center, Japan Atomic Energy Research Institute, Tokai-mura, Japan

Y. Ōnuki
Graduate School of Science, Osaka University, Osaka, Japan

reported the magnetic and the electronic properties of $NpTGa_5$ (T = Fe, Rh, Ni and Co) using the high-quality single crystals [5, 6]. Magnetic structures of $NpTGa_5$ have been proposed by Metoki et al. from neutron diffraction data of these crystal [7, 8]. Nevertheless, there are no reports concerning the Mössbauer spectroscopy for $NpFeGa_5$ and $NpNiGa_5$. In this study we performed the ^{57}Fe and ^{237}Np Mössbauer measurements for $NpFeGa_5$ in order to understand its magnetic properties. $NpFeGa_5$ shows antiferromagnetic order below T_N = 118 K and another magnetic transition at T^* = 78 K. The magnetic moments were derived as 0.24 μ_B/Fe and 0.86 μ_B/Np, respectively, from neutron study. The magnetic structure of $NpFeGa_5$ exhibits in-plane AFM and inter-plane FM interaction, whereas those of $NpCoGa_5$ are totally opposite. The magnetic propagation q = (1/2 1/2 0) is proposed for $NpFeGa_5$.

2 Experimental

A high-quality single crystal of $NpFeGa_5$ with a tetragonal structure was prepared by the Ga-flux method and the crushed powder was sealed in epoxy resin (Staicast). Sealed specimens were used for the ^{57}Fe Mössbauer measurements and also for the ^{237}Np Mössbauer measurements. For the ^{57}Fe Mössbauer measurements, a gas-flow type cryostat (CF500, Oxford) was used to cool the specimen, ^{57}Co source in Rh was set on the head of transducer at room temperature. For the ^{237}Np Mössbauer measurements, a closed-cycle refrigerator was used to cool down both of the source (^{241}Am in metal matrix) and the specimen powder. The velocity scale is calibrated relative to α-Fe at 300 K for the ^{57}Fe Mössbauer measurements and for ^{237}Np Mössbauer spectroscopy by using a laser interferometer attached on the Mössbauer drive.

3 Results and discussion

Figure 1 shows the ^{57}Fe Mössbauer spectra obtained from $NpFeGa_5$ at 298, 77 and 10 K. The $NpFeGa_5$ is a paramagnet at 298 K and its ^{57}Fe Mössbauer spectrum shows a clear singlet absorption line superposed a weak doublet line. This impurity component with quadrupole splitting QS is about 3% of the total absorption. The origin of the satellite line may be due to the small amounts of an impurity phase, but the details are not yet clear. At 77 K well below T_N = 118 K, $NpFeGa_5$ shows a magnetically ordered state and the ^{57}Fe Mössbauer spectrum is magnetically broadened and asymmetric. Origin of the asymmetry of the spectral shape is most probably due to a small perturbation from an electric quadrupole interaction on the magnetic hyperfine pattern, although in the paramagnetic state of 298 K the spectral shape is completely symmetric. Since the magnetically broadened spectrum is again symmetric at the lower temperature of 10 K and the spectrum has been analyzed by a single magnetic component, the magnetically induced lattice strain might not be an origin of the quadrupole interaction appearing just below the Néel temperature and further investigation is necessary to understand this phenomenon. We measured a detailed temperature dependence of the hyperfine interaction parameters at the ^{57}Fe nucleus; B_{hf} (the hyperfine magnetic field), IS (the value of isomer shifts), QS (the effective quadrupole splitting) and FWHM (the full width at half-maximum of the spectrum) and we did not observe any anomaly around T^* = 78 K. By the computer fit using a single set of

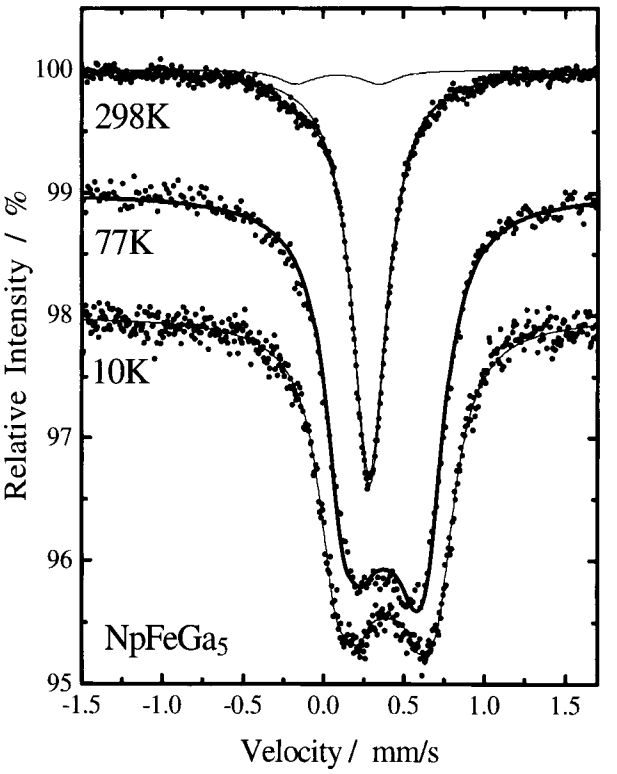

Figure 1 The ^{57}Fe Mössbauer spectra of $NpFeGa_5$ at 298, 77 and 10 K. Velocity is relative to α-Fe at 300 K.

the magnetically split pattern for the spectrum at 10 K, the magnitude of the hyperfine magnetic field at ^{57}Fe nucleus in $NpFeGa_5$ was determined to be 1.98 ± 0.05 T at 10 K. Using an atomic magnetic moment of 0.24 μ_B/Fe determined by the neutron diffraction study [6], the hyperfine-coupling constant of the ^{57}Fe nucleus in $NpFeGa_5$ was determined to be 8.3 ± 0.2 T/μ_B which is smaller than the value for the ferromagnetic α-Fe (15 T/μ_B). The reason why the ^{57}Fe in $NpFeGa_5$ has a small hyperfine coupling constant is not yet clear, but we have to consider the direct (dipolar) and the indirect (conduction electron polarization) contributions from the magnetic Np atoms to the hyperfine fields at ^{57}Fe nucleus in this compound.

Figure 2 shows the ^{237}Np Mössbauer spectrum obtained from $NpFeGa_5$ at 10 K. The spectrum was magnetically splitted. A single set of hyperfine parameters was derived with the magnetic hyperfine fields B_{hf} = 204 T perpendicular to the main component of the electric field gradient, the quadrupole interaction e^2qQ = +3.4 mm/s and the isomer shift value IS = 5.5 mm/s. Using an atomic magnetic moment of 0.86 μ_B/Np determined by the neutron diffraction study [6], the hyperfine-coupling constant of ^{237}Np in $NpFeGa_5$ was determined to be 236 T/μ_B which fairly agrees with the value of 215 T/μ_B reported previously [7]. The temperature dependence of the hyperfine interaction parameters of the ^{237}Np Mössbauer spectroscopy is very important to understand the magnetism of this compound, but the measurements of the ^{237}Np Mössbauer spectra from 10 K up to the temperatures above the Néel temperature of 118 K has not yet been finished. Contrast to the negative sign of the effective quadrupole interaction at the ^{237}Np nucleus in $NpCoGa_5$, the sign of the effective quadrupole interaction at the ^{237}Np nucleus in $NpFeGa_5$ is positive. The difference of the sign in the observed effective quadrupole interactions is due to the

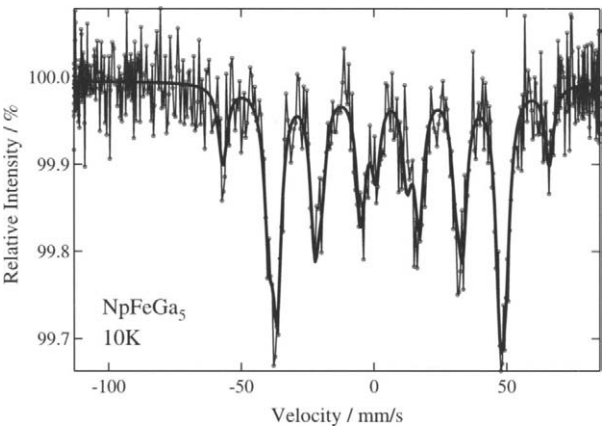

Figure 2 The ^{237}Np Mössbauer spectrum of $NpFeGa_5$ at 10 K. Velocity scale is calibrated by using a laser interferometer.

difference in the magnetic structures of $NpCoGa_5$ and $NpFeGa_5$. From the neutron diffraction study as mentioned in previous section, the direction of the Np atomic moments in $NpFeGa_5$ is perpendicular to the *c*-axis in spite of the parallel to the *c*-axis in $NpCoGa_5$. Therefore, the sign of the observed quadrupole splitting depends on the angular factor between the magnetic moment direction and the main component of the electric field gradient. A detailed temperature dependence of the hyperfine interaction parameters of $NpFeGa_5$ and the ^{237}Np Mössbauer measurements for $NpNiGa_5$ which have not performed yet are very important and necessary to understand the magnetic and electronic properties of the neptunium 1-1-5 compounds.

4 Conclusion

^{237}Np and the ^{57}Fe Mössbauer measurements for $NpFeGa_5$ that is one of the so-called neptunium 1-1-5 compounds have been performed. The magnitude of the hyperfine magnetic field at the ^{57}Fe nucleus in this compound is determined to be 1.98 ± 0.05 T at 10 K. The hyperfine magnetic field at the ^{237}Np nucleus at 10 K is 204 T in $NpFeGa_5$ and the hyperfine-coupling constant of ^{237}Np nucleus in this compound is determined to be 236 T/μ_B.

References

1. Sarrao, J.L., Morales, L.A., Thompson, J.D., Scott, B.L., Stewart, G.R., Wastin, F., Rebizant, J., Boulet, P., Colineau, E., Lander, G.H.: Nature **420**, 297 (2002)
2. Wastin, F., Boulet, P., Rebizant, J., Colineau, E., Lander, G.H.: J. Phys., Condens. Matter **15**, S2279 (2003)
3. Colineau, E., Javorsky, P., Boulet, P., Wastin, F., Griveau, J.C., Rebizant, J., Sanchez J.P., Stewart, G.R.: Phys. Rev., B **69**, 184411 (2004)
4. Colineau, E., Wastin, F., Boulet, P., Javorský, P., Rebizant, J., Sanchez, J.P.: J. Alloys Compd. **386**, 57 (2005)
5. Aoki, D., Homma, Y., Shiokawa, Y., Sakai, H., Yamamoto, E., Nakamura, A., Haga, Y., Settai, R., Ōnuki, Y.: J. Phys. Soc. Jpn. **73**, 2608 (2005)

6. Aoki, D., Homma, Y., Shiokawa, Y., Yamamoto, E., Nakamura, A., Haga, Y., Settai R., Takeuchi, T., Ōnuki, Y.: J. Phys. Soc. Jpn. **73**, 1665 (2004)
7. Honda, F., Metoki, N., Kaneko, K., Aoki, D., Homma, Y., Yamamoto, E., Shiokawa, Y., Ōnuki, Y., Colineau, E., Bernhoeft, N., Lander, G.H.: Physica B **359–361**, 1147 (2005)
8. Metoki, N., Kaneko, K., Colineau, E., Javorský, P., Aoki, D., Homma, Y., Boulet, P., Wastin, F., Shiokawa, Y., Bernhoeft, N., Yamamoto, E., Ōnuki, Y., Rebizant, J., Lander, G.H.: Phys. Rev., B. **72**, 014460 (2005)
9. Dunlap, B.D., Lander, G.H.: Phys. Rev. Lett. **33**, 1046 (1974)

Hyperfine Interact (2006) 168:1181–1184
DOI 10.1007/s10751-006-9420-4

The study of superexchange interaction of ordered $Li_{0.5}Fe_{1.0}Rh_{1.5}O_4$

Kun Uk Kang · Chul Sung Kim

Published online: 14 November 2006

Abstract $Li_{0.5}Fe_{1.0}Rh_{1.5}O_4$ has been studied by X-ray diffraction, Mössbauer spectroscopy. The crystal structure is characterized by the additional reflection (200) that is described by 1:1 ordered structure of Li, Fe at tetrahedral (A) site and can be assigned to the space group $F\bar{4}3m$. The lattice constant (a_0) is 8.4348 Å. The temperature dependence of the magnetic hyperfine field is analyzed by the Néel theory of ferrimagnetism. The inter-sublattice superexchange interaction is found to be antiferromagnetic with a strength of $J_{A-B} = -3.78\ k_B$ while the intra-sublattice superexchange interactions are ferromagnetic with strengths of $J_{A-A} = 5.40\ k_B$ and $J_{B-B} = 7.39\ k_B$. The Debye temperatures of the tetrahedral and octahedral sites are determined to be 388 and 464 ± 3 K, respectively, and the Néel temperature has been found to be 260 ± 3 K.

Key words Superexchange interaction · Mössbauer spectroscopy · Debye temperature · Lithium ferrites

1 Introduction

Li iron spinel related to spinel structure AB_2O_4 has been reported by a number of authors [1–3]. Its electric, crystallographic and magnetic properties have attracted increasing attention because of its technical application in microwave devices. The magnetic properties depend on their characteristic structure related to the ordering mechanism. $Li_{0.5}Fe_{2.5}O_4$ is known to two crystalline forms corresponding Fd3m (disordered phase) and $P4_332$ (ordered phase) [4]. Also, the various transition metal doped (Al, Ti, etc.) lithium ferrites and lithium gallates have an isostructure of the ordered lithium ferrite, too. The magnetic properties that the intra-sublattice interactions are comparable to inter-sublattice interaction by cation ordering on the

Kun Uk Kang · Chul Sung Kim (✉)
Department of Physics, Kookmin University, Seoul 136-702, Korea
e-mail: cskim@phys.kookmin.ac.kr

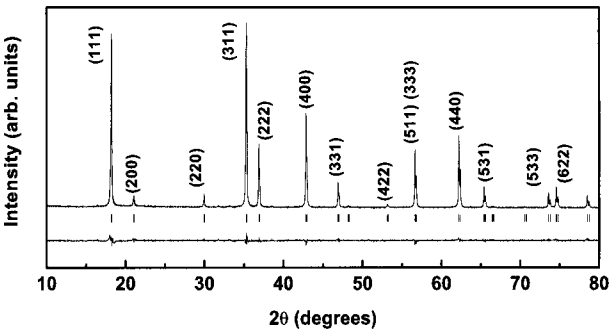

Figure 1 X-ray diffraction pattern of $Li_{0.5}Fe_{1.0}Rh_{1.5}O_4$ at room temperature.

octahedral sites have been reported [5]. The ordering distribution of the tetrahedral site rarely reported in spinel oxides have revealed in thiospiels – $Cu_{0.5}Fe_{0.5}Cr_2S_4$, $Cu_{0.5}Fe_{0.5}Rh_2S_4$, etc. Neutron diffraction showed that the copper and iron ions order onto two interlocking face-centered cubic sublattices consisting of tetrahedral sites [6]. In this work, the microscopic magnetic hyperfine structures and superexchange interaction between each sublattice of $Li_{0.5}Fe_{1.0}Rh_{1.5}O_4$ with the cation ordering on the tetrahedral site have been studied by Mössbauer spectroscopy.

2 Experiments

$Li_{0.5}Fe_{1.0}Rh_{1.5}O_4$ sample was prepared by the following ceramic method. The starting materials were Li_2CO_3 (99.999%), Fe_2O_3 (99.999%), Rh_2O_3 (99.95%), and ^{57}Fe enriched Fe_2O_3 (99.999%). The powder of materials dried at 350°C for 2 h. Mixtures of the correct proportions of the compounds were pre-sintered in air at 700°C for 12 h and heated at 950 °C for 24 h, and then rapidly quenched into water. In order to obtain homogeneous material, it was necessary to grind the samples after the first firing and press the powder into pellets before heating it for a second time to 950°C for 24 h. The sample was ^{57}Fe enriched to 3 at.% of the metal atoms for Mossbauer measurements. X-ray diffraction patterns were obtained with Cu Kα radiation. A Mössbauer spectrometer of the electromechanical type was used in the constant-acceleration mode. External magnetic field was applied parallel to the direction of γ-ray propagation using a solenoid type superconductor cryostat. A ^{57}Co source in a rhodium matrix was used at room temperature.

3 Results and disscussion

The X-ray diffraction pattern of $Li_{0.5}Fe_{1.0}Rh_{1.5}O_4$ is shown in Figure 1 and has been analyzed by the Rietveld refinement method. The X-ray pattern is characterized by the additional reflection at (200) plane that is described by 1:1 ordered structure of Li, Fe at tetrahedral (A) site which indicate symmetry reduction to $F\bar{4}3m$. The ordering splits the oxygen site into two positions noted in Table I: Fe1 ion connected only to O1 whilst Li ion is bonded to O2.

The bond angles reveal no significant distortion from ideal structure. The lattice constant a_0 was 8.4348 Å. Mössbauer spectra were taken at the various absorber

Table 1 Structural parameters, bonding angles and bonding lengths for $Li_{0.5}Fe_{1.0}Rh_{1.5}O_4$ at room temperature (space group: $F\bar{4}3m$, lattice constant $a_0 = 8.4347(6)$ Å)

Atom	Position	x	y	z
Fe1	4a	0	0	0
Li	4d	0.75	0.75	0.75
Fe2, Rh	16e	0.3762	0.3762	0.3762
O1	16e	0.1350	0.1350	0.1350
O2	16e	0.6161	0.6161	0.6161
Bond lengths (Å)	Fe1–O1	Li–O2	Fe2–O1	Fe2–O2
	1.972	1.956	2.039	2.026
Bond angles (degree)	Fe2–O1–Fe2	Fe2–O2–Fe2	Fe1–O1–Fe2	
	95.2	93.6	121.5	

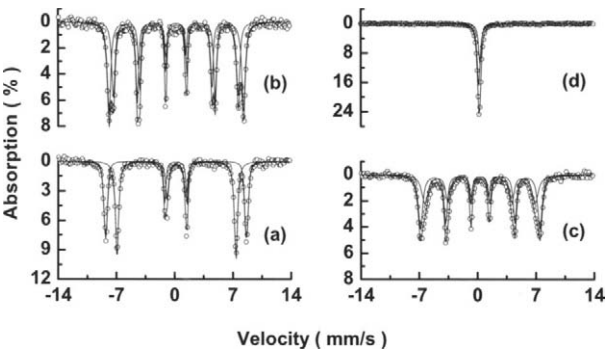

Figure 2 The Mössbauer spectra of sample at various temperatures: (*a*) 4.2 K, under 6 T, (*b*) 4.2 K, (*c*) 120 K, and (*d*) 260 K.

temperatures from 4.2 K to room temperature. To investigate the spin structure, the spectra were measured under 6 T external field parallel to the γ-ray direction. Figure 2 shows some of the spectra. The spectra at 4.2 K show that the iron ions occupy both A and B sites and the second and the fifth absorption lines of the spectra taken under 6 T external field at 4.2 K vanish. This vanishing effect explains that the sample has the collinear ferrimagnetic spin structure. The isomer shift values at room temperature are found to be the same value 0.25 mm/s relative to the iron metal for both sites, which is consistent with Fe^{3+} [7] . Figure 3a shows the reduced magnetic hyperfine field H(T)/H(0) for the tetrahedral site and octahedral site as a function of the reduced temperature τ=T/T_N, where the Néel temperature T_N of the sample is found to be 260 K. In order to get information on the superexchange interactions from Figure 3a, the temperature dependence of the magnetic hyperfine field was analyzed based on the Néel theory of ferrimagnetism about two sublattice model. The detailed theoretical procedures are published in [8]. From the best fit result between the experimental data and the theoretical values, the intersublattice superexchange interaction was found to be antiferromagnetic with a strength of $J_{A-B} = -3.78\,k_B$, while the intrasublattice A–A interaction and B–B interaction were found to be ferromagnetic with a strength of $J_{A-A} = 5.40\,k_B$ and $J_{B-B} = 7.39\,k_B$, respectively. k_B is the Boltzmann constant. Considering that the strength

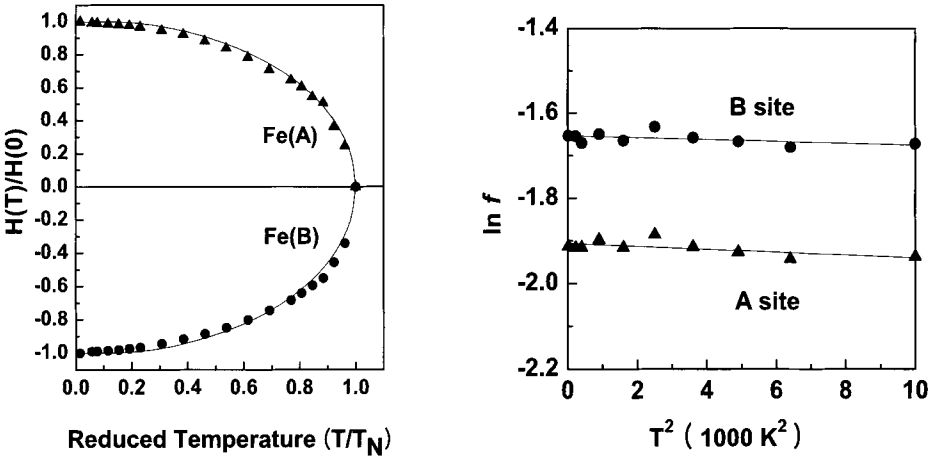

Figure 3 **a** Reduced magnetic hyperfine fields H(T)/H(0) for tetrahedral site and octahedral site as a function of reduced temperature τ. **b** National logarithm of the resonant absorption area as a function of T^2 for samples at tetrahedral sites and octahedral sites.

of the intersublattice interaction is usually larger than that of the intrasublattice interaction, it is noteworthy that the ferromagnetic intrasublattice interactions are stronger than the antiferromagnetic intersublattice interaction. Figure 3b shows the temperature dependence of the resonant absorption area. The absorption area as a function of temperature is analyzed by using the recoil free fraction developed by the Debye model [9, 10]. The Debye temperatures calculated for the tetrahedral and the octahedral site are found to be 388 and 464 K, respectively. This suggests a larger inter-atomic binding force for the B site than for A site with the ordered cations.

Acknowledgement This study has been supported by the Korea Research Foundation grant no. (KRF- 2005-070-C00050).

References

1. Gupta, N., Kashyap, S.C., Dube, D.C.: J. Magn. Magn. Mater. **288**, 307 (2000)
2. Xu, Z.C.: J. Appl. Phys. **93**, 4726 (2003)
3. Kang, K.U., Oak, H.N., Kim, C.S.: J. Appl. Phys. **97**, 10F102 (2005)
4. An, S.Y., Shim, I.-B., Kim, C.S.: J. Appl. Phys. **97**, 10Q909 (2005)
5. Oak, H.N., Baek, K.S., Yu, K.S.: J. Phys. Condens. Matter. **10**, 131 (1998)
6. Palmer, H.M., Greaves, C.: J. Mater. Chem. **9**, 637 (1999)
7. Kum, J.S., Kim, S.J., Shim, I.B., Kim, C.S.: Hyperfine Interact. **156/157**, 169 (2004)
8. Kim, S.J., Lee, S.W., Kim, C.S.: Jpn. J. Appl. Phys. **40**, 4987 (2001)
9. Kim, C.S., Shim, I.B., Choi, H., Ha, M.Y., Sur, J.C.: J. Korean Phys. Soc. **23**, 166 (1990)
10. Ok, H.N., Kim, Y.K.: Phys. Rev. **B36**, 5120 (1987)

Hyperfine Interact (2006) 168:1185–1190
DOI 10.1007/s10751-006-9421-3

Amorphous Fe–Mg alloy thin films: magnetic properties and atomic vibrational dynamics

B. Sahoo · W. Keune · E. Schuster · W. Sturhahn · T.S. Toellner · E.E. Alp

Published online: 26 October 2006

Abstract Amorphous (a-) Fe_xMg_{1-x} alloys are interesting materials for the investigation of non-Debye-like low-energy vibrational excitations. We have prepared a-Fe_xMg_{1-x} alloy thin films ($0.3 \leq \times \leq 0.7$) by vapour quenching. The amorphous state was confirmed by conversion electron Mössbauer spectroscopy between 4.2–300 K, and the x- and temperature-dependence of the isomer shift and hyperfine magnetic field was measured. For x= 0.6 and 0.7, magnetic ordering occurs below ~150 K. The atomic vibrational density of states, g(E), was determined by nuclear resonant inelastic scattering, providing clear evidence for the non-Debye-like low-energy vibrational excitations.

Key words conversion electron Mössbauer spectroscopy · nuclear resonant inelastic X-ray scattering · Fe–Mg amorphous alloys · magnetic properties · atomic vibrational dynamics

1 Introduction

The atomic vibrational dynamics of amorphous and disordered systems is a subject of continuing interest because of their anomalous behavior in the low energy part of the vibrational density of states (VDOS) [1, 2]. In particular, the phenomenon of the so called 'boson peak' in the reduced VDOS, $g(E)/E^2$, which appears as an excess contribution to the VDOS in comparison with the usual Debye law ($g(E)/E^2$ = constant) of the crystalline materials, is a topical subject [3]. The microscopic origin of the boson peak is still a matter of debate [3–8]. After the pioneering work of

B. Sahoo (✉) · W. Keune · E. Schuster
Laboratory of Applied Physics, University of Duisburg-Essen, 47048 Duisburg, Germany
e-mail: balaram_sahoo@uni-duisburg.de

W. Sturhahn · T. S. Toellner · E. E. Alp
Advanced Photon Source, Argonne National Laboratory, Argonne, IL 60439, USA

three different groups [9–11] nuclear resonant inelastic X-ray scattering (NRIXS) has emerged as a unique method to explore the atomic vibrational properties of condensed matter, see, e.g., ref. [12–20]. The frequency (or energy) distribution of atomic vibrations, g(E), for the vibrating resonant isotope in the crystalline or amorphous state, can be directly measured by NRIXS. The VDOS is a fundamental quantity from which important thermodynamic properties may be deduced [12–20]. Because only small quantities of materials are needed, NRIXS is suitable for the study of lattice dynamics in thin films, at interfaces and in multilayers [21–31].

After a comprehensive investigation of the amorphous (a-) Fe_xTb_{1-x} thin film system [28], here we report on the magnetic and vibrational properties of a-Fe_xMg_{1-x} alloy thin films. We expect that the difference in atomic mass, atomic radius and electron affinity modifies the amplitude (height) and energy of the boson peak. Besides X-ray and other diffraction techniques, Mössbauer spectroscopy is an excellent method for the qualitative characterization of the amorphous state via the hyperfine parameters. In particular, we report on the electric and magnetic hyperfine properties of amorphous (a-) Fe_xMg_{1-x} alloy thin films studied by conversion electron Mössbauer spectroscopy (CEMS) over a wide concentration and temperature range. Preliminary magnetoresistance results are also presented. Our NRIXS results provide the compositional dependence of g(E) and $g(E)/E^2$, and prove the existence of a composition-dependent boson peak in these amorphous thin films.

2 Experimental

Amorphous 800– Å thick a-$^{57}Fe_xMg_{1-x}$ alloy thin films with nominal composition in the range $0.3 \leq x \leq 0.7$ have been prepared in ultrahigh vacuum (UHV) by thermal evaporation of metallic ^{57}Fe (95% isotopic enrichment) and Mg onto oxidized Si(001) substrates held at −140°C. The details of the preparation and characterization via X-ray diffraction of the a-Fe–Mg alloy films are described elsewhere [32]. The CEM spectra were measured at different temperatures in a bath cryostat by using a channeltron detector with the film surface perpendicular to the incident 14.4 keV γ-ray of the ^{57}Co source (Rh-matrix). For the least-squares fitting of the CEM spectra, the computer program *NORMOS* by R. A. Brand [33], was used. The magnetoresistance measurement was performed in a split-coil superconducting magnet cryostat with the magnetic field perpendicular to the film plane by using a standard four-point probe method. The NRIXS experiments were performed at room temperature (RT) at the undulator beamline 3-ID of the Advanced Photon Source in Argonne (USA), with an energy bandwidth (FWHM) of 1 meV for the 14.4125 keV X-ray beam [32]. Details of the NRIXS technique and the data evaluation procedure are described elsewhere [9–16, 34].

3 Results and discussion

3.1 Magnetism

The CEM spectra of a-$Fe_{0.7}Mg_{0.3}$ measured at different temperatures are shown in Figure 1a. The 4.2 K spectrum indicates complete magnetic ordering with a wide

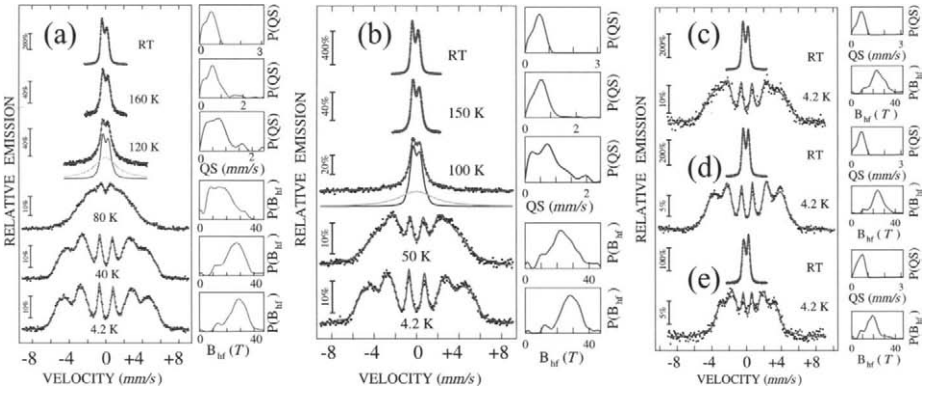

Figure 1 CEM spectra of a-Fe_xMg_{1-x} alloy thin films measured at different temperatures: (**a**) x= 0.7, (**b**) x= 0.6, (**c**) x= 0.5, (**d**) x= 0.4, (**e**) x= 0.3. The spectra were fitted by a hyperfine field distribution $P(B_{hf})$ at low temperatures, by a distribution of quadrupole splittings P(QS) at high temperatures, and with a distribution P(QS) combined with a broad *single line* at 100 and 120 K. The corresponding distributions are shown at the *right-hand side* of each spectrum.

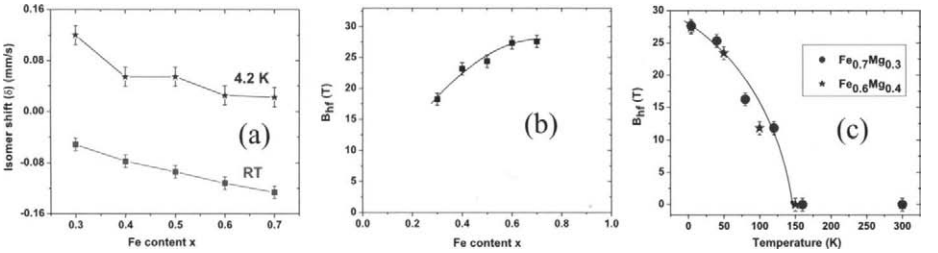

Figure 2 (**a**) Isomer shift (= *center line shift*) δ measured at RT and 4.2 K, and (**b**) average hyperfine field B_{hf} at 4.2 K, of a-Fe_xMg_{1-x} alloy thin films versus Fe content x. (**c**) T-dependence of average hyperfine field B_{hf} for a-$Fe_{0.7}Mg_{0.3}$ (*circles*) and a-$Fe_{0.6}Mg_{0.4}$ (*asterisks*). (The *drawn lines* are guides for the eye).

distribution of magnetic hyperfine fields, $P(B_{hf})$, typical for amorphous materials. With increasing measurement temperature the average magnetic hyperfine field B_{hf} is found to decrease and to collapse below ~160 K. At and above ~160 K we observe electric quadrupole-split doublets with a wide distribution of quadrupole splittings, P(QS), typical for amorphous alloys. The T-dependence of the spectra of a-$Fe_{0.6}Mg_{0.4}$ (Figure 1b) is similar to that of a-$Fe_{0.7}Mg_{0.3}$. The CEM spectra at two different temperatures (RT and 4.2 K , respectively,) for a-$Fe_{0.5}Mg_{0.5}$, a-$Fe_{0.4}Mg_{0.6}$ and a-$Fe_{0.3}Mg_{0.7}$ are shown in Figures 1c, d and e, respectively. All samples are found to be magnetically ordered at 4.2 K and paramagnetic at RT. The fitting of all the spectra measured at 4.2 K results in a line intensity ratio R_{23} of ~2.0 (R_{23}= intensity ratio of the 2nd (or 5th) and 3rd (or 4th) Mössbauer line), which suggests that the Fe spins are not oriented in the film plane, but rather randomly oriented, indicating a spin-glass type of magnetic ordering. The average isomer shift (= center shift, relative to the ^{57}Co (Rh-matrix)-source) at RT and 4.2 K(Figure 2a) decreases with increasing Fe-content x, indicating an increase of s-electron density at the ^{57}Fe

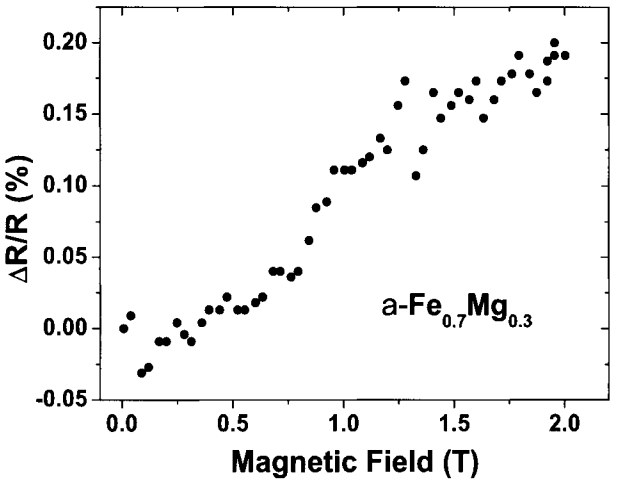

Figure 3 Magnetoresistance ratio ($\Delta R/R = (R_m - R_0)/R_0$) of the a-$Fe_{0.7}Mg_{0.3}$ alloy thin film measured at 4.2 K up to an applied field of 2 T at 1 mA current. (R_m (R_0) is the resistance in non-zero (zero) magnetic field).

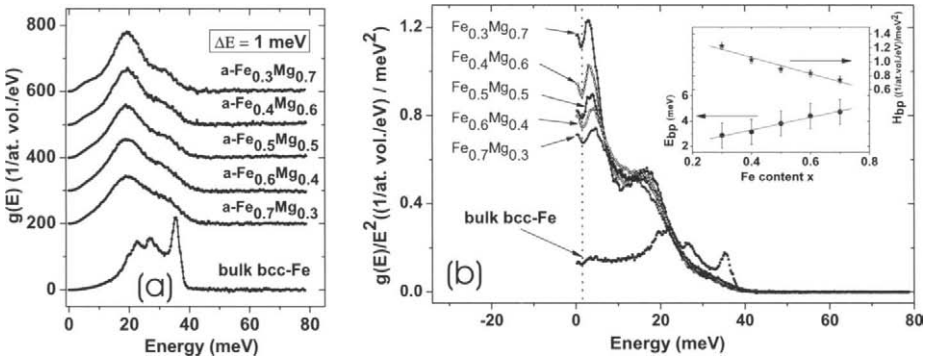

Figure 4 (**a**) Partial vibrational density of states, g(E), at RT of 800–Å thick a-Fe_xMg_{1-x} alloy thin films. (Energy resolution $\Delta E = 1.0$ meV). The VDOS for bulk bcc-Fe is also shown. For clarity, g(E) of a-$Fe_{0.7}Mg_{0.3}$ was displaced upwards by 200 /at.vol./eV, and neighboring a-Fe_xMg_{1-x} *curves* were vertically displaced by 100 /at.vol./eV. (**b**) Reduced partial VDOS, $g(E)/E^2$, for different compositions x and for bulk bcc-Fe. Data below the instrumental resolution (1 meV, the *vertical dotted line*) are physically irrelevant. Insert: The boson peak height H_{bp} (*asterisks*) and boson peak energy E_{bp} (*filled circles*) versus Fe content x. The *straight lines* are least-squares fits to the data points.

nucleus with x. The average magnetic hyperfine field B_{hf} at 4.2 K is found to increase with rising Fe content(Figure 2b). From the T-dependence of B_{hf} (Figure 2c) a magnetic ordering temperature of 150–160 K may be estimated for $x = 0.6$ and 0.7. The Mössbauer spectral parameters are similar to those observed earlier by van der Kraan and Buschow [35].

The magnetoresistance (Figure 3) is observed to be small and increases with rising external field. This suggests that the in-plane anisotropy is not very strong and that the material perhaps has spin-glass type ordering with Fe spins following weakly the external field.

3.2 Vibrational dynamics

The VDOS (Figure 4a) of a-$^{57}Fe_xMg_{1-x}$ alloy thin films were obtained from the excitation probability measured by NRIXS [32]. The low-energy modes in g(E) below ~10 meV in Figure 4a are of particular interest because of the boson peak phenomenon. In Figure 4b we have plotted the reduced VDOS, $g(E)/E^2$, versus E. In this representation strict Debye-like behavior is reflected by a horizontal line which intersects the $g(E)/E^2$ axis at a value that is proportional to c_s^{-3} (c_s= average sound velocity) as in case of bulk bcc-Fe in Figure 4b. For decreasing E, a striking and unambiguous rise in $g(E)/E^2$ below ~10 meV and a peak at ~3–5 meV, identified as the boson peak, is observed for all the amorphous alloy films. Its peak height H_{bp} is found to increase with decreasing Fe content x. By contrast, Debye-like behavior in bulk bcc-Fe is observed in $g(E)/E^2$ below ~15 meV, where $g(E)/E^2$ remains constant at ~0.15 $(at.vol)^{-1}$ $(eV)^{-1}$ $(meV)^{-2}$ [25]. The boson peak height, H_{bp}, and the boson peak position, E_{bp}, are found to depend linearly on the Fe content x (Figure 4b, insert). (H_{bp} was measured from $g(E)/E^2=0$ in Figure 4b). Apparently, the anomalous low-energy excitations in these amorphous Fe-alloys are related to vibrational modes induced by the non-ferrous atoms. Similar behavior was observed earlier for a-Fe_xTb_{1-x} alloy films [28].

Acknowledgements Work at Duisburg was supported by Deutsche Forschungsgemeinschaft (GRK 277 and SFB 491). Work at Argonne was supported by the US department of energy, Basic Energy Sciences, Office of Science, under Contract No. W-31-109-Eng-38.

References

1. Phillips, W.A. (ed.): Amorphous Solids – Low Temperature Properties. Springer, Berlin Heidelberg New York (1981)
2. Dianoux, A.J., Petry, W., Richter, D. (eds.): Dynamics of Disordered Materials. II. North-Holland, Amsterdam (1993)
3. Chumakov, A.I., Sergueev, I., van Bürck, U., Schirmacher, W., Asthalter, T., Rüffer, R., Leupold, O., Petry, W.: Phys. Rev. Lett. **92**, 245508 (2004)
4. Finkemeier, F., von Niessen, W.: Phys. Rev. B **66**, 087202 (2002)
5. Schirmacher, W., Diezemann, G., Ganter, C.: Phys. Rev. Lett. **81**, 136 (1998)
6. Schirmacher, W., Diezemann, G., Ganter, C.: Physica. B **284-288**, 1147 (2000)
7. Mauer, E., Schirmacher, W.: J. Low Temp. Phys. **137**, 453 (2004)
8. Suck, H.B., Rudin, H.: In: Beck, H., Güntherodt, H.J. (eds) Glassy Metals II (Topics in Applied Physics), vol. 53, p 217. Springer, Berlin Heidelberg New York(1983)
9. Seto, M., Yoda, Y., Kikuta, S., Zhang, X.W., Ando, A.: Phys. Rev. Lett. **74**, 3828 (1995)
10. Sturhahn, W., Toellner, T.S., Alp, E.E., Zhang, X.W., Ando, M., Yoda, Y., Kikuta, S., Seto, M., Kimball, C.W., Dabrowski, B.: Phys. Rev. Lett. **74**, 3832 (1995)
11. Chumakov, A.I., Rüffer, R., Grünsteudel, H., Grünsteudel, H.F., Grübel, G., Metge, J., Leupold, O., Goodwin, H.A.: Europhys. Lett. **30**, 427 (1995)
12. Chumakov, A.I., Sturhahn, W.: Hyperfine Interact. **123/124**, 781 (1999)
13. Alp, E.E., Sturhahn, W., Toellner, T.S.: J. Phys. Condens. Matter **13**, 7645 (2001)
14. Alp, E.E., Sturhahn, W., Toellner, T.S.: Hyperfine Interact. **135**, 295 (2001)
15. Alp, E.E., Sturhahn, W., Toellner, T.S., Zhao, J., Hu, M., Brown, D.E.: Hyperfine Interact. **144/145**, 3 (2002)
16. Sturhahn, W.: J. Phys. Condens. Matter **16**, S497 (2004)
17. Parak, F., Achterhold, K.: Hyperfine Interact. **123/124**, 825 (1999)
18. Grünsteudel, H., Paulsen, H., Winkler, H., Trautwein, A.X., Toftlund, H.: Hyperfine Interact. **123/124**, 841 (1999)
19. Lubbers, R., Grünsteudel, H.F., Chumakov, A.I., Wortmann, G.: Science **287**, 1250 (2000)

20. Seto, M., Kobayashi, Y., Kitao, S., Haruki, R., Mitsui, T., Yoda, Y., Nasu, S., Kikuta, S.: Phys. Rev. B **61**, 11420 (2000)
21. Sturhahn, W., Röhlsberger, R., Alp, E.E., Ruckert, T., Schrör, H., Keune, W.: J. Magn. Magn. Mater. **198/199**, 590 (1999)
22. Keune, W., Sturhahn, W.: Hyperfine Interact. **123/124**, 847 (1999)
23. Ruckert, T., Keune, W., Sturhahn, W., Hu, M.Y., Sutter, J.P., Toellner, T.S., Alp, E.E.: Hyperfine Interact. **126**, 363 (2000)
24. Cuenya, B.R., Keune, W., Sturhahn, W., Toellner, T.S., Hu, M.Y.: Phys. Rev., B **64**, 235321 (2001)
25. Ruckert, T., Keune, W., Sahoo, B., Sturhahn, W., Toellner, T.S., Alp, E.E., Röhlsberger, R.: Hyperfine Interact. **144/145**, 65 (2002)
26. Ruckert, T., Keune, W., Sturhahn, W., Alp, E.E.: J. Magn. Magn. Mater. **240**, 562 (2002)
27. Gómez, J.A., Guenzburger, D., Ellis, D.E., Hu, M.Y., Alp, E., Baggio-Saitovitch, E.M., Passamani, E.C., Ketterson, J.B., Cho, S.: Phys. Rev., B **67**, 115340 (2003)
28. Keune, W., Ruckert, T., Sahoo, B., Sturhahn, W., Toellner, T.S., Alp, E.E., Röhlsberger, R.: J. Phys. Condens. Matter **16**, S379 (2004)
29. Walterfang, M., Keune, W., Schuster, E., Zayak, A.T., Entel, P., Sturhahn, W., Toellner, T.S., Alp, E.E., Jochym, P.T., Parlinski, K.: Phys. Rev., B **71**, 035309 (2005)
30. Röhlsberger, R., Sturhahn, W., Toellner, T.S., Quast, K.W., Hession, P., Hu, M., Sutter, J., Alp, E.E.: J. Appl. Phys. **86**, 584 (1999)
31. Handke, B., Kozlowski, A., Parliński, K., Przewoźnik, J., Ślęzak, T., Chumakov, A.I., Niesen, L., Kąkol, Z., Korecki, J.: Phys. Rev., B **71**, 144301 (2005)
32. Sahoo, B., Keune, W., Sturhahn, W., Toellner, T.S., Alp, E.E.: J. Phys. Chem. Solids **66**, 2263 (2005)
33. Brand, R.A.: Nucl. Instrum. Methods B **28**, 398 (1987)
34. Sturhahn, W.: Hyperfine Interact. **125**, 149 (2000)
35. van der Kraan, A M., Buschow, K.H.J.: Phys. Rev., B **25** 3311 (1982)

Hyperfine Interact (2006) 168:1191–1195
DOI 10.1007/s10751-006-9422-2

Neutron diffraction and Mössbauer study on $FeGa_xCr_{2-x}S_4$

Sam Jin Kim · Bae Soon Son · In-Bo Shim · Bo Wha Lee · Chul Sung Kim

Published online: 8 November 2006

Abstract Ga doped sulphur spinel $FeGa_xCr_{2-x}S_4$ ($x = 0.1$ and 0.3) have been studied with X-ray, neutron diffraction, and Mössbauer spectroscopy. Rietveld refinement of X-ray, neutron diffraction, and Mössbauer spectroscopy lead to the conclusion that the samples are in inverse spinel type, where most Ga ions are present at octahedral site (B). The neutron diffractions on $FeGa_xCr_{2-x}S_4$ ($x = 0.1$) above 10 K show long range interaction behaviors and reveal a ferrimagnetic ordering, with the magnetic moment of Fe^{2+}(−3.45 μ_B) aligned antiparallel to Cr^{3+} (+2.89 μ_B) at 10 K. Fe ions migrate from the tetrahedral (A) site to the octahedral (B) site with an increase in Ga substitutions. The electric quadrupole splittings of the A and B sites in Mössbauer spectra give direct evidence that Ga ions stimulate an asymmetric charge distribution of Fe ions in the A site.

Key words neutron diffraction · magnetic structure · charge structure · cation distribution · Mössbauer spectroscopy

1 Introduction

Since the discovery of the colossal magnetoresistance (CMR) effect perovskite manganite, investigating these ferromagnetic compounds has been of great interest. There are many interesting results on Cr-based chalcogenide materials. Ramirez et al. reported the existence of CMR effect in Cr-based chalcogenide spinel such as $FeCr_2S_4$ [1]. Tsurkan et al. reported a spin-glass-like anomaly from a structural lattice transformation [2]. Fichtl et al. reported orbital freezing and orbital glass state in $FeCr_2S_4$, while Ogasawara et al. reported the spin-orbit coupling in a dominant interaction for this material [3, 4]. Authors published on anomalous magnetic behaviors of ferrimagnetic properties on Ga-doped sulphur spinel by

S. J. Kim · B. S. Son · I.-B. Shim · C. S. Kim (✉)
Department of Physics, Kookmin University, Seoul 136-702, Korea
e-mail: cskim@phys.kookmin.ac.kr

B. W. Lee
Department of Physics, Hankuk University of Foreign Studies, Yongin, Kyungki 449-791, Korea

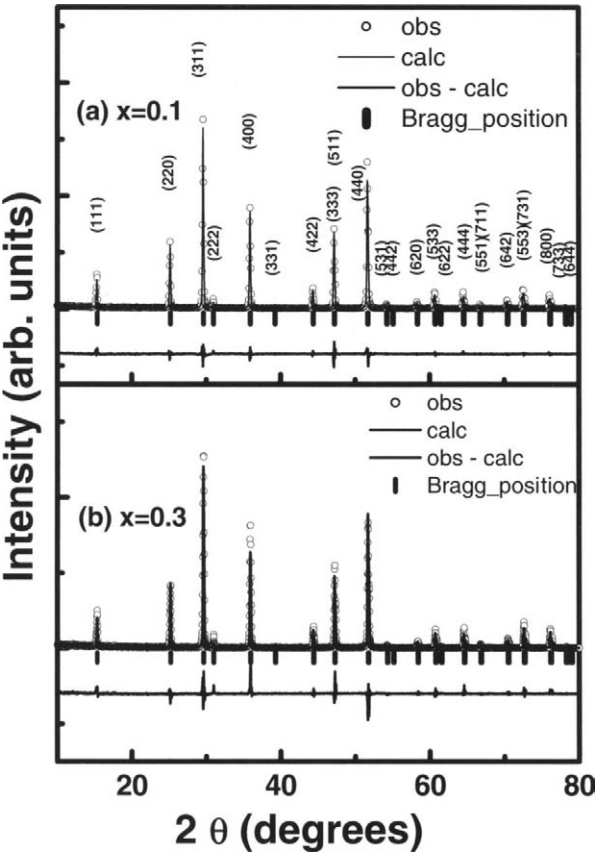

Figure 1 Refined X-ray diffraction pattern of the $FeGa_xCr_{2-x}S_4$ (**a**) $x = 0.1$, (**b**) $x = 0.3$ at 295 K. *Tick marks* show the Bragg positions.

Table I Results of refinement parameters of X-ray diffraction on $FeGa_xCr_{2-x}S_4$ ($x = 0.1$ and 0.3) [*Fd3m*: Fe, Ga (8a); Fe, Ga, Cr (16d); S(32e (*u, u, u*))]

	$x = 0.1$	$x = 0.3$
a/Å	10.0067(3)	9.9962(3)
u (S)	0.7401(3)	0.7409(3)
Fe (A)-occ	0.98	0.90
Ga (A)-occ	0.02	0.10
Fe (B)-occ	0.02	0.10
Ga (B)-occ	0.08	0.20
R_B	2.66%	7.39%

magnetoresistance studies [5]. Recently, Hemberger et al. published on multiferroic properties, on which magnetic and electric order coexist, in $CdCr_2S_4$ [6]. Here, we present the results of X-ray, neutron diffraction Mössbauer experiments on Ga doped sulphur spinel compounds.

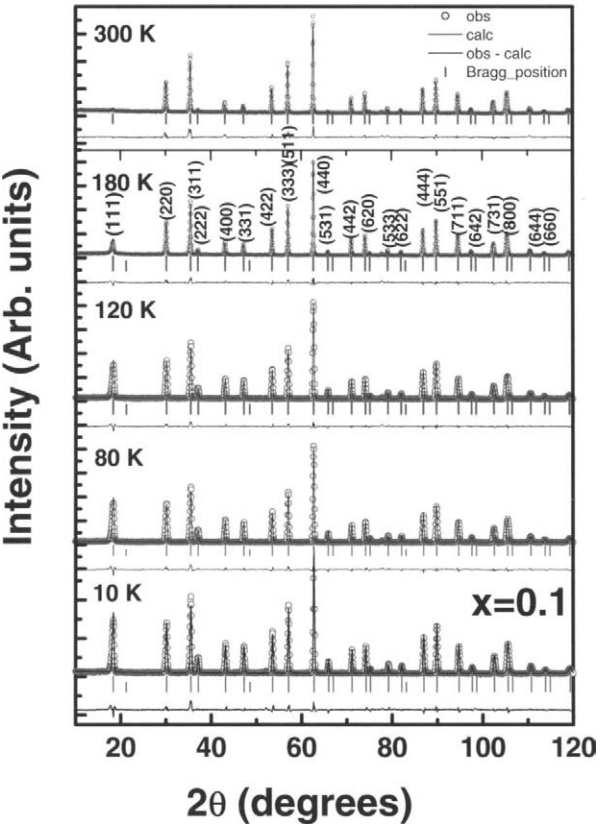

Figure 2 Neutron diffraction patterns of $FeGa_{0.1}Cr_{1.9}S_4$ at various temperatures. *Upper and lower tick marks* show the Bragg and magnetic reflection positions.

2 Experiments

$FeGa_xCr_{2-x}S_4$ ($x = 0.1$ and 0.3) were prepared by the direct reaction of the following high-purity elements Fe, Cr, Ga and S in an evacuated quartz tube. The crystal structures of the samples were examined by X-ray diffractometer with Cu Kα radiation. The magnetic structures of the samples were examined with a neutron diffractometer at the Korea Atomic Energy Research Institute HANARO HRPD (high resolution powder diffractometer, $\lambda = 1.8348$ Å) reactor. The Mössbauer spectra were recorded using a conventional spectrometer with a ^{57}Co source in a rhodium matrix.

3 Results and discussion

Figure 1(a) and (b) show the results of Rietveld refinement of the X-ray diffraction for the $FeGa_{0.1}Cr_{1.9}S_4$ ($x = 0.1$) and $FeGa_{0.3}Cr_{1.7}S_4$ ($x = 0.3$), at 295 K, respectively. We could not find any different positions of peaks other than cubic spinel in Figure 1(a) and (b).

Crystal structure is determined to be *Fd3m*. The determined lattice constants a_0, oxygen parameter u, cation occupancy, and Bragg factor R_B are listed in Table I. The Cr ions enter the B site with strong preference of the octahedral symmetry. It is noticeable that Ga ions

Table II Results of refinement parameters of neutron diffraction on $FeCr_{1.9}Ga_{0.1}S_4$

T (K)	Fe (μ_B)	Cr (μ_B)	Net (μ_B)
10	−3.45	2.87	2.04
80	−3.86	3.12	2.07
120	−3.58	2.86	1.86
180	−2.28	1.62	0.79
300	0	0	0

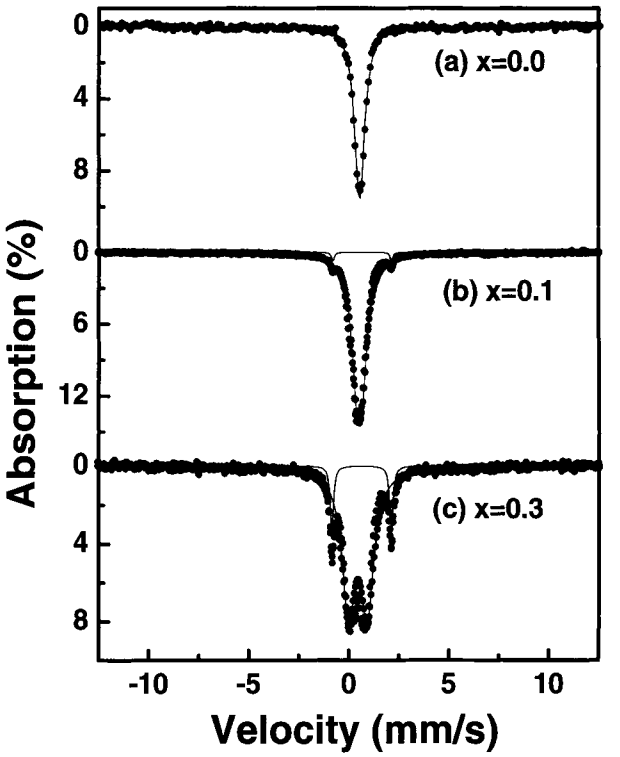

Figure 3 Mössbauer spectra of $FeGa_xCr_{2-x}S_4$ (**a**) $x = 0.0$, (**b**) $x = 0.1$, and (**c**) $x = 0.3$ at 295 K.

enter both sites, the same amounts of Fe ions simultaneously migrate from the A to the B site.

In order to examine crystallographic and magnetic structure in $FeGa_{0.1}Cr_{1.9}S_4$ ($x = 0.1$), we obtained neutron diffraction patterns from 10 to 300 K. Magnetic structure is determined by Rietveld refinement of the Fullprof program. Figure 2 shows the results of refined neutron diffraction patterns for $FeGa_{0.1}Cr_{1.9}S_4$, at various temperatures. Below 300 K, a significant increase in the intensity of the inner Bragg reflections – (111), (220), (222), and (331) – was observed when temperature was lowered, which indicates strong magnetic contribution to these reflections. As shown in Figure 2, the diffraction peaks happened to remain very sharp, which shows the presence of magnetic long-range order (LRO) in this sample. The observed magnetic moments of Fe^{2+}(A) and Cr^{3+}(B) as well as net magnetic moments of $FeGa_{0.1}Cr_{1.9}S_4$ are listed in Table II. Neutron diffraction at 10 K

revealed a cubic spinel structure of ferrimagnetic ordering, with magnetic moments of Fe^{2+}(A) ($-3.45\ \mu_B$), Cr^{3+}(B) ($2.89\ \mu_B$), and net moment ($2.04\ \mu_B$), respectively.

The Mössbauer spectra were collected from 12 to 295 K. Figure 3(a),(b) and (c) show the Mössbauer spectra for the sample $x = 0.0$, 0.1, and 0.3, respectively, at room temperature. $FeCr_2S_4$ ($x = 0.0$) has a single line at room temperature, while both spectra on Figure 3(b) and (c) consist of two doublets at room temperature. The first one corresponds to the iron ions at the A sites (inner doublet), the other corresponds to the iron ions at the B sites (outer doublet). The electric quadrupole splitting of the outer and inner sets are 0.30 and 2.93 mm/s, for the sample $x = 0.1$, respectively. While, they are 0.83 and 2.94 mm/s, for the sample $x = 0.3$, respectively. The isomer shifts and area ratio of the A and B sites, for the $x = 0.1$, are 0.53 and 0.66 mm/s, 98.0 and 2.0%, respectively. While, those of the sample $x = 0.3$ are 0.50 and 0.65 mm/s, 89.7 and 10.3%, respectively.

The Mössbauer absorption area ratio is in agreement with the results of the X-ray diffraction refinement, too. The covalence of the A site is lager than that of the B site in spinel structure. Therefore the isomer shift of the A site is smaller than that of the B site. In addition, the crystal symmetry of the octahedral site is slightly tilted. So, a large quadrupole splitting in B sites can be identified. Due to the fact that $FeCr_2S_4$ has a single line at room temperature, it is unusual that it has large quadrupole splitting [7]. We notice that the quadrupole splitting of the A site significantly increases when the number of non-magnetic Ga ions increase, compared to that of the B site. These results are in agreement with enhancement of electric quadrupole interaction. Finally, it shows severely distorted asymmetric Mössbauer absorption lines. It gives direct evidence that Ga ions stimulate asymmetric charge distribution of Fe ions of the A site in $FeGa_xCr_{2-x}S_4$ ($x = 0.1$ and 0.3).

4 Conclusion

$FeGa_xCr_{2-x}S_4$ ($x = 0.1$ and 0.3) have been studied with X-ray, neutron difraction and Mössbauer spectroscopy. The neutron diffractions on $FeGa_xCr_{2-x}S_4$ ($x = 0.1$) above 10 K show an antiferromagnetic ordering, with the magnetic moment of Fe^{2+}($-3.45\ \mu_B$) aligned antiparallely to Cr^{3+} ($+2.89\ \mu_B$) at 10 K. The electric quadrupole splittings of the A and B sites in Mössbauer spectra give direct evidence that Ga ions stimulate asymmetric charge distribution of Fe ions in the A site.

Acknowledgement This study was supported by the KRF-2005-070-C00050.

References

1. Ramirez, A.P., Cava, R.J., Krajewski, J.: Nature **386**, 156 (1997)
2. Tsurkan, V., Hemberger, J., Klemm, M., Klimm, S., Loidl, A., Horn, S., Tidecks, R.: J. Appl. Phys. **90**, 4639 (2001)
3. Fichtl, R., Tsurkan, V., Lunkenheimer, P., Hemberger, J., Fritsch, V., Krug von Nidda, H.-A., Scheidt, E.-W., Loidl, A.: Phys. Rev. Lett. **94**, 027602 (2005)
4. Ogasawara, T., Ohgushi, K., Tomioka, Y., Takahashi, K.S., Okamoto, H., Kawsaki, M., Tokura, Y.: Phys. Rev. Lett. **94**, 087202 (2005)
5. Son, B.S., Kim, S.J., Lee, B.W., Kim, C.S.: J. Appl. Phys. **95**, 6828 (2004)
6. Hemberger, J., Lunkenheimer, P., Fichtl, R., Krug von Nidda, H.-A., Tsurkan, V., Loidl, A.: Nature **434**, 364 (2005)
7. Kim, S.J., Kim, W.C., Kim, C.S.: J. Appl. Phys. **91**, 7935 (2002)

Hyperfine Interact (2006) 168:1197–1200
DOI 10.1007/s10751-006-9423-1

^{57}Fe Mössbauer spectroscopy on the cyclic spin-cluster $Fe_6(tea)_6(CH_3OH)_6$

J. Kreitlow · J. Litterst · S. Süllow · B. Pilawa

Published online: 26 October 2006

Abstract We present ^{57}Fe Mössbauer spectroscopy experiments on the cyclic spin-cluster $Fe_6(tea)_6(CH_3OH)_6$ (tea = triethanolaminato(-3)). In former studies, the spin cluster has been treated as a homogenous, quasi-one-dimensional spin $S = 5/2$ Heisenberg antiferromagnet. Our experiments reveal spectra, which consists of two different quadrupolar doublets. In consequence, there are two different Fe sites among the hexanuclear iron spin-cluster.

Key words ^{57}Fe Mössbauer spectroscopy · cyclic spin-cluster · quadrupolar doublets

PACS 33.45.+x · 75.50.Xx

1 Introduction

Antiferromagnetically coupled cyclic clusters, viz., spin carrying ions on ring-like structures, are a class of molecule based magnets. By now, in inorganic chemistry it is possible to synthesize almost perfect cyclic clusters containing 6, 8, 10, 12 or even 18 metal ions. Because of only intra-molecular antiferromagnetic coupling of the spins, this class is neither a representative of para- nor bulk magnetism. Efforts to tune the magnetism in these compounds by changing the ligands or bringing in an alkali metal in the middle of the ring [1] lie at the base of the wide scientific field of these "ferric wheels."

J. Kreitlow (✉) · J. Litterst · S. Süllow
Institut für Physik der Kondensierten Materie, TU Braunschweig,
38106 Braunschweig, Germany
e-mail: j.kreitlow@tu-bs.de

B. Pilawa
Physikalisches Institut, Universität Karlsruhe (TH), 76128 Karlsruhe, Germany

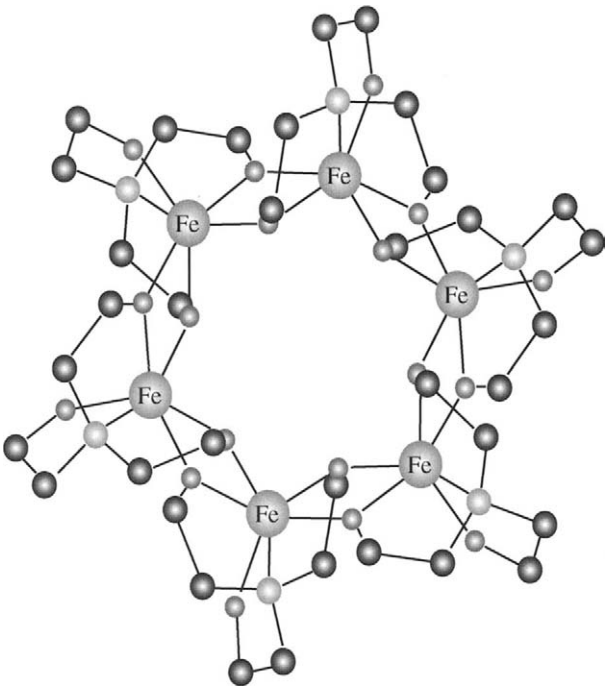

Figure 1 Structure of the hexanuclear iron spin-cluster $Fe_6(tea)_6$. The intra-molecular exchange is antiferromagnetic.

$Fe_6(tea)_6$ is one such ferric wheel, with a structure as shown in Figure 1. The intra-molecular exchange coupling between the Fe spins has previously been determined by measurements of the magnetic susceptibility $\chi(T)$ [1]. For a polycrystalline sample $\chi(T)$ has been interpreted in terms of a quasi-one-dimensional spin $S = 5/2$ Heisenberg antiferromagnet, with an exchange interaction of $J/k_B = -31.5$ K [2].

Further, a pronounced anisotropy of $\chi(T)$ has been attributed to a zero field splitting of the Fe^{III}. As yet, however, neither the ionic state of the iron has unambiguously been determined, nor have (magneto)elastic effects been considered. Therefore, in order to address these open issues we have carried out a detailed Mössbauer spectroscopy study. From our data we observe no long range order in this temperature range. However, we find that the spectra contain two different quadrupole split pairs of lines.

2 Experimental results

^{57}Fe Mössbauer spectroscopy experiments have been performed in a standard low-temperature Mössbauer set-up at temperatures ranging from 5 to 300 K (source: ^{57}Co-in-Rh matrix at room temperature; half width half maximum: 0.12(1) mm/s).

First attempts to interpret the output of our readings by means of only one quadrupole splitting were discarded, as they resulted in insufficient χ^2. Especially the asymmetry of the 300 K spectrum of our powder sample is an argument for our assumption of two splittings. The spectra have been evaluated using the Mössbauer fitting program Recoil [3] in the thin absorber approximation. The measured data

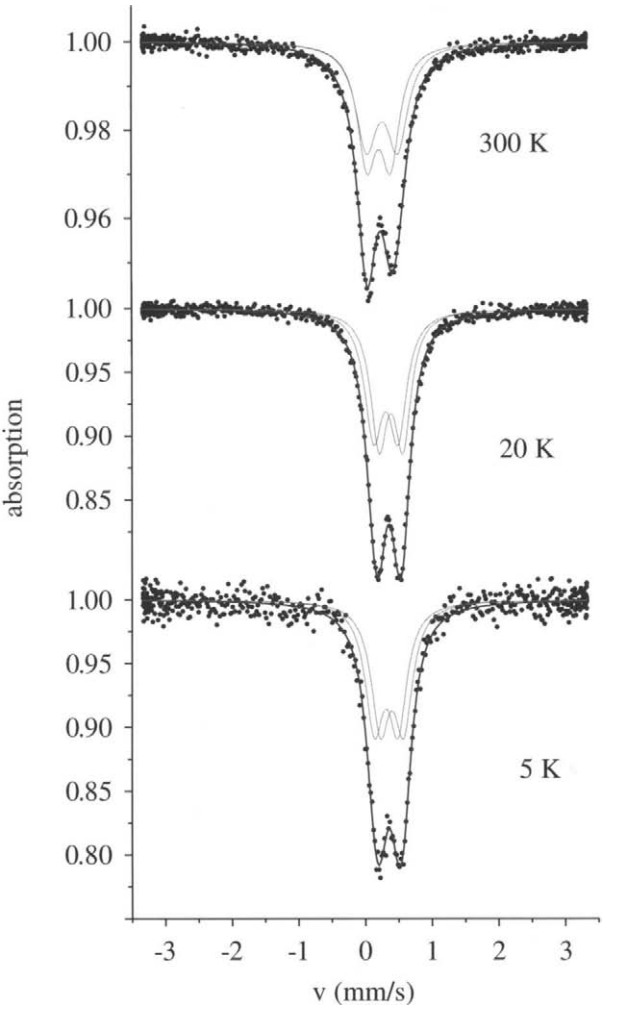

Figure 2 ^{57}Fe Mössbauer spectroscopy spectra of $Fe_6(tea)_6$ at different temperatures.

were modelled as Lorentzian lines in the presence of an electric field gradient (see Figure 2). We obtain fit results for the center shifts (relative to the ^{57}Co-in-Rh source ($CS_{1,2}$)), the quadrupole splittings ($QS_{1,2}$) and the linewidths (half width at half maximum ($HWHM_{1,2}$)) as shown in Table I. The size of the center shifts and the quadrupole splittings is typical for Fe^{III} [4]. The two sub spectra imply that for the six iron ions locally there are two different electronical environments in the molecule. Both iron sites show a weak temperature dependence regarding *CS*, *QS* and *HWHM*. At 5 K the values of the quadrupole splittings and the linewidths are nearly the same. In other words, the sub spectra differ only in the center shifts.

The data for 250 K seem to behave somewhat exceptionally, since the highest values of the linewidths and an unexpected decrease of the center shift for one of the sub spectra are observed. At this point of the investigation there is not yet a ready explanation at hand for this behavior.

Table I Fit results for the Mössbauer spectra in Figure 2 and additional measurements

T (K)	$CS_{1,2}(mm/s)$	$QS_{1,2}(mm/s)$	$HWHM_{1,2}(mm/s)$	χ^2
300	0.222	0.354	0.171	1.17
	0.273	0.467	0.194	
250	0.186	0.396	0.216	1.29
	0.364	0.432	0.216	
100	0.282	0.375	0.179	1.12
	0.419	0.402	0.175	
20	0.319	0.367	0.162	1.15
	0.398	0.358	0.151	
7	0.319	0.356	0.178	1.01
	0.396	0.370	0.166	
5	0.314	0.354	0.164	1.16
	0.402	0.349	0.165	

The values for the center shift (CS) are relative to the ^{57}Co-in-Rh source.

3 Conclusion

From our present data we conclude that $Fe_6(tea)_6$ is not a homogeneous cyclic spin-cluster, but that on the ring there is additional structure. For the near future, very detailed structural investigations are planned, in order to directly detect local structural deviations from a homogeneously coupled Fe ring and to study its relevance for the magnetic properties of the material.

Acknowledgement This work was supported by the Deutsche Forschungsgemeinschaft DFG under project number SU/6-1.

References

1. Waldmann, O., Koch, R., Schromm, S., Müller, P., Bernt, I., Saalfrank, R.W.: Phys. Rev. Lett. **89**, 246–401 (2002)
2. Pilawa, B., Desquiotz, R., Kelemen, M.T., Weickenmeier, M., Geisselmann, A.: J. Magn. Magn. Mater. **177–181**, 748–749 (1997)
3. Lagarec, K.: Department of Physics University of Ottawa, Version 1.02 (1998)
4. Wegener, H.: Der Mössbauer-Effekt und seine Anwendung in Physik und Chemie. Bibliographisches Institut, Mannheim (1965)

Hyperfine Interact (2006) 168:1201–1206
DOI 10.1007/s10751-006-9424-0

Mössbauer spectroscopic study of half-Heusler compounds

V. Ksenofontov · K. Kroth · S. Reiman · F. Casper · V. Jung · M. Takahashi · M. Takeda · C. Felser

Published online: 14 November 2006

Abstract The family of half-Heusler compounds offers a variety of half-metallic ferromagnetic materials. We have applied the Mössbauer spectroscopy to study the atomic order, local surroundings and hyperfine fields to several half-Heusler compounds. ^{121}Sb Mössbauer study of the compound CoMnSb revealed the presence of two nonequivalent antimony positions in the elementary cell and enabled to identify the structure. ^{119m}Sn, ^{155}Gd and ^{197}Au Mössbauer spectroscopic studies were used to characterize the properties of ferromagnetic granular material based on the half-Heusler ferromagnet MnAuSn in the antiferromagnetic GdAuSn matrix.

Key words half-Heusler compounds · half-metallic ferromagnets · granular ferromagnets

1 Introduction

The family of half-Heusler compounds offers a variety of half-metallic ferromagnetic materials. Half-Heusler phases *XYZ* (*X* and *Y* are different transition metals, *Z* denotes a *sp* element) can be formally deduced from the Heusler phases X_2YZ by removing one of two *X* atoms, leaving structural voids [1]. The increase of the distance between *X* neighbours leads to a weaker overlap between 3*d* wave functions, enhanced magnetic moments and to the presence of gaps in the density of states [2]. These peculiarities give rise to a large variety of electronic and magnetic properties of half-Heusler compounds starting from nonmagnetic semiconductors (CoTiSb) to ferromagnetic half-metals (NiMnSb) with a complete spin polarization of electrons at the Fermi level. The half-Heusler-type structure easily allows for structural disorder, either by the occurrence of vacancies, interchange of atoms

V. Ksenofontov (✉) · K. Kroth · S. Reiman · F. Casper · V. Jung · C. Felser
Institut für Anorganische Chemie und Analytische Chemie, Johannes Gutenberg Universität, 55099 Mainz, Germany
e-mail: v.ksenofontov@uni-mainz.de

M. Takahashi · M. Takeda
Department of Chemistry, Faculty of Science, Toho University, Miyama 2-2-1, Funabashi, Chiba 274-8510, Japan

(*X* and *Y*) or partial addition of atoms to the structural voids. This feature complicates the structural analysis of half-Heusler compounds. Due to the close electronic density of *X* and *Y* transition elements, in many cases X-ray powder diffraction is not informative to the disorder. Using the fact that hyperfine fields are very sensitive to the disorder, Mössbauer characterization could be very useful for the structural characterization of half-Heusler compounds. Unique possibility appears when two or all constituent atoms of the half-Heusler probe are the Mössbauer probes. Recently, several groups have shown that certain granular ferromagnets exhibit giant magnetoresistances [3]. Such granular ferromagnets are produced by cosputtering or comelting two materials which are immiscible, and of which one is ferromagnetic. The properties of resulting materials can be essentially different from those of the pure single phases. We applied the Mössbauer spectroscopy to characterize the novel granular material, which is based on the half-Heusler ferromagnet MnAuSn and antiferromagnetic GdAuSn.

2 Experimental

The half-Heusler compounds CoMnSb, NiMnSb and CoTiSb have been synthesized by arc-melting of proper amounts of the constituents under purified argon atmosphere [4, 5]. The same preparation procedure has been used to produce the polycrystalline samples of GdAuSn, MnAuSn and the granular material consisting of their mixture. Magnetic characterization of the samples was performed using a Quantum Design MPMS-XL SQUID-magnetometer equipped with a high-temperature furnace. Structural information was obtained by powder diffraction in transmission mode using a Bruker D5000 diffractometer.

^{121}Sb Mössbauer measurements were done in a standard transmission geometry using a ^{121m}Sn ($CaSnO_3$) source. Both source and absorber were immersed in liquid helium in order to increase the recoil-free fraction. The spectra were analyzed with the program EFFI using the transmission integral [6]. As a constraint, the recoil-free fraction of the source was kept to 0.6. ^{119m}Sn Mössbauer measurements were carried out at 80 K in a transmission geometry using a ^{119m}Sn ($CaSnO_3$) source. The ^{155}Gd Mössbauer spectra were measured with a ^{155}Eu / $^{154}SmPd_3$ source. The ^{197}Au Mössbauer measurements were done with a ^{197}Pt / Pt source, produced by neutron irradiation of Pt foil. During the measurements both of the source and sample were kept at 12 K in a cryostat equipped with a closed cycle refrigerator. The ^{155}Gd and ^{197}Au Mössbauer spectra were computer-fitted using a MossWin software [7].

3 Results and discussion

De Groot et al. have shown that the half-Heusler compound NiMnSb has a gap at the Fermi energy in the minority band [2]. The half-Heusler ferromagnetic compound CoMnSb like NiMnSb is often referred to the category of half-metallic ferromagnets [8]. The compounds NiMnSb and CoTiSb crystallize in the $C1_b$ structure, space group $F\bar{4}3m$ [9]. According to our X-ray study, the structure of CoMnSb belongs to the space group $Fm\bar{3}m$. In contrast to NiMnSb, the crystal lattice of CoMnSb contains two antimony positions Sb1 and Sb2 at ratio 1 to 3. The position Sb1 is surrounded by six Mn and four Co atoms and possesses a central symmetry similar to the Sb position in NiMnSb with Mn and Ni atoms in the first

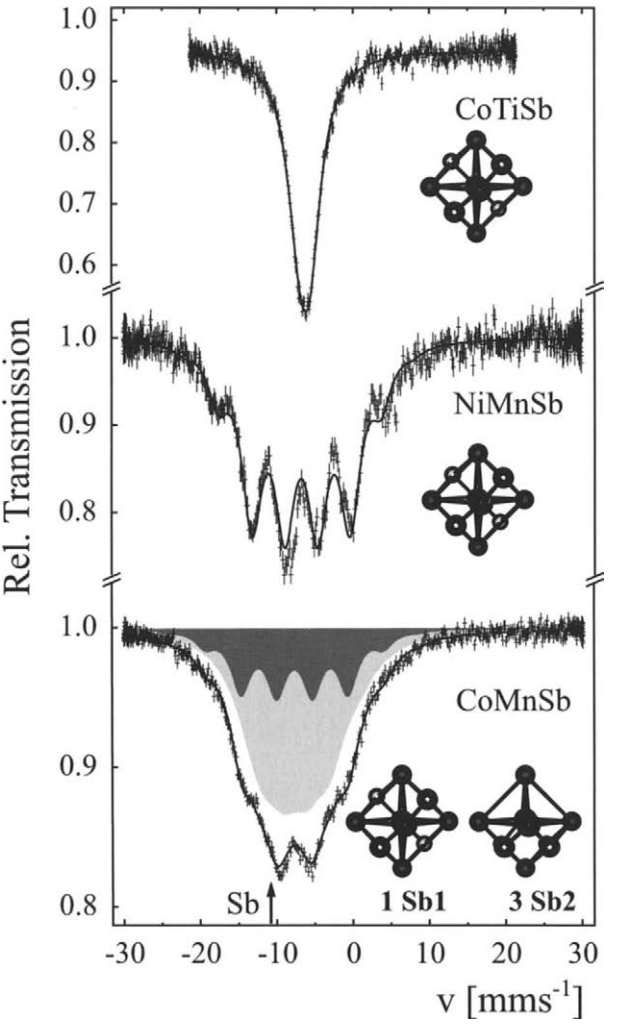

Figure 1 Mössbauer spectra of CoTiSb, NiMnSb and CoMnSb recorded at $T = 4.2$ K.

coordination sphere. The majority of antimony atoms (Sb2) in CoMnSb has a fourfold local symmetry axis. The first coordination sphere of Sb2 comprises four Co atoms and six Mn atoms.

To clarify the number of different antimony positions in CoMnSb, we applied ^{121}Sb Mössbauer spectroscopy. Simultaneously, for comparison reasons, CoTiSb and NiMnSb were studied, too. Mössbauer spectra of CoTiSb (**1**), NiMnSb (**2**) and CoMnSb (**3**) recorded at T = 4.2 K are shown in the Figure 1. The measurement of (**1**) reveals a paramahnetic spectrum with isomer shift $\delta(\mathbf{1}) = -6.34(2)$ mms^{-1} and line width $\Gamma(\mathbf{1}) = 3.62(2)$ mms^{-1} (herewith the IS values are quoted relative to $Ca^{121m}SnO_3$ at 4.2 K). The Mössbauer spectrum of (**2**) consists of one sextet with $\delta(\mathbf{2}) = -6.84(3)$ mms^{-1}, line width $\Gamma(\mathbf{2}) = 2.88(2)$ mms^{-1} and hyperfine magnetic field $H_{hf}(\mathbf{2}) = 25.0(5)$ T.

The Mössbauer spectrum of (**3**) reveals a magnetic hyperfine structure, which can be decomposed into two sextets **A** and **B** with partial intensities 27(1)% and 73(1)%, isomer shifts $\delta(\mathbf{3A}) = -7.74(2)$ mms^{-1} and $\delta(\mathbf{3B}) = -7.58(3)$ mms^{-1}, line widths $\Gamma(\mathbf{3A}) = 3.1$

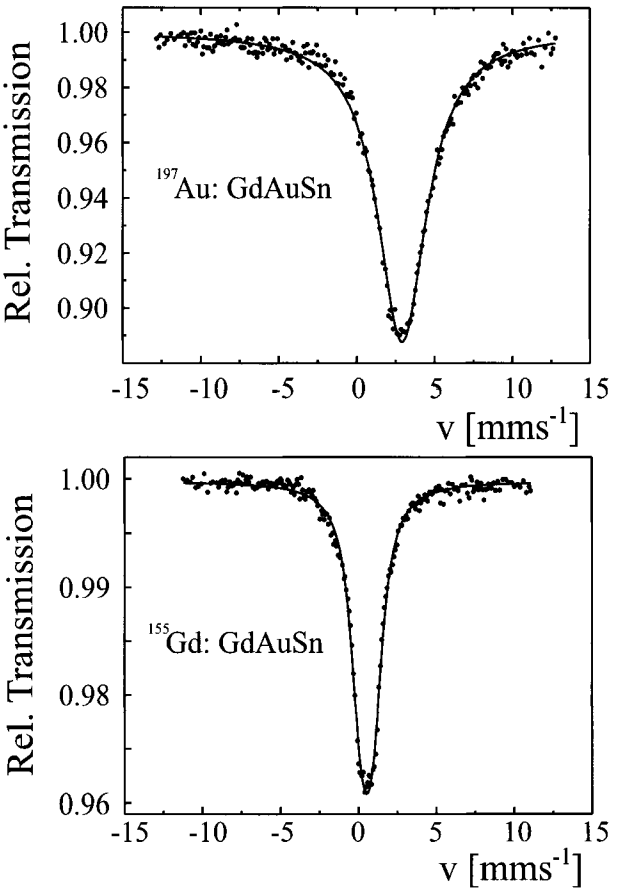

Figure 2 ^{197}Au and ^{155}Gd Mössbauer spectra of *GdAuSn*.

(2) mms^{-1} and Γ(**3B**) = 5.6(5) mms^{-1}, respectively. Site **A** with H_{hf}(**3A**) = 26.9(3) T with zero value of quadrupole coupling corresponds to the regular coordinated position of antimony. Site with H_{hf}(**3B**) = 16.3(5) T corresponds to the distorted local surrounding of the position **B** with a quadrupole splitting ΔE_Q(**3B**) = −2.54(5) mms^{-1}. The finding of two positions in the Mössbauer spectrum confirms the existence of two crystallographic sites of antimony following from the structural analysis. Taking into account the partial intensities of the subspectra, we attribute sites **A** and **B** to Sb1 and Sb2 positions, respectively.

Calculations of the hyperfine magnetic field at antimony sites in NiMnSb based on the APL + lo method [10] yield the value of 26.3 T, which is in good agreement with the experimentally measured one H_{hf}(**2**) = 25.0(5) T. In contrast, the calculation of the ordered structure fails to explain the hyperfine parameters in CoMnSb. The experimentally determined sign of the quadrupole splitting for the Sb2 position in CoMnSb is opposite to the expected one obtained from band structure calculations. Since the sign of the quadrupole moment for ^{121}Sb is negative [11], the experimentally found negative quadrupole splitting for Sb2 indicates the positive sign of the principal component of the electric field gradient in contradiction to the negative calculated value V_{xx} = $-8.37807 \cdot 10^{21}$ V/m^2. A possible explanation of this fact is partial disorder in Co and Mn positions. The disorder should strongly affect the local values of the hyperfine fields at antimony nuclei. The APW+lo calculations give the values of hyperfine fields H_{hf}(Sb1) ≅

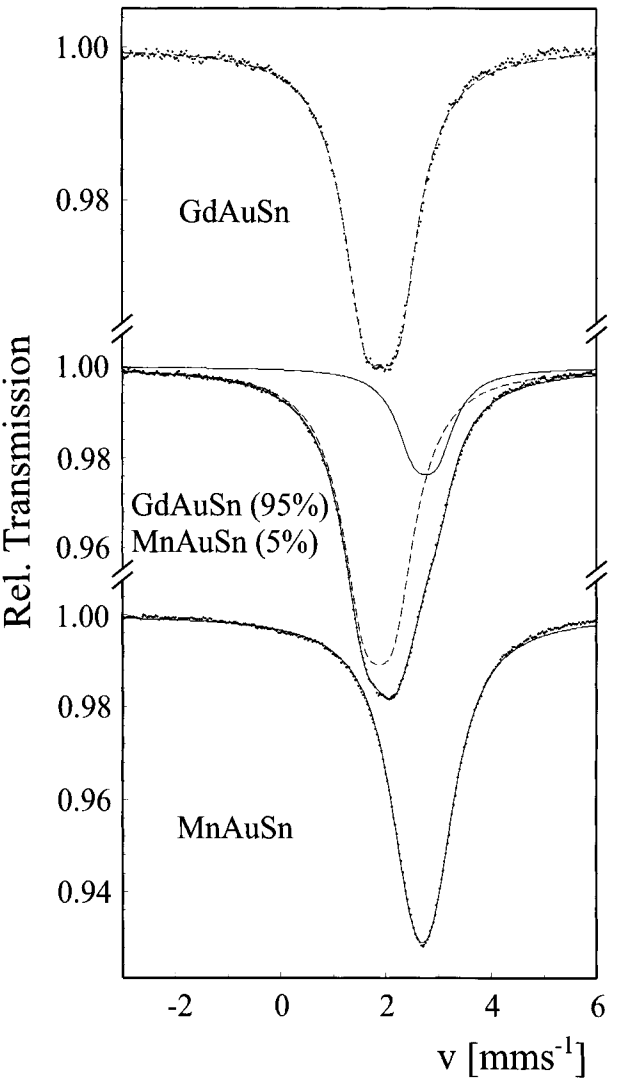

Figure 3 ^{119}Sn Mössbauer spectra of *GdAuSn*, *MnAuSn* and their 0.95/0.05 mixture.

23.1 T and $H_{hf}(Sb2) \cong 39.1$ T for the ordered structure. The partial substitution of magnetic Mn by nonmagnetic Co atoms decrease the value of the hyperfine magnetic field induced at Sb atoms. This argument can clarify, why the measured value $H_{hf}(Sb1) = 26.9(3)$ T exceeds the hyperfine field $H_{hf}(Sb2) = 16.3(5)$ T. One can suppose, that in addition to reported Mössbauer measurements a neutron diffraction study should elucidate details of disorder in CoMnSb.

Studies of the novel granular material based on half-Heusler ferromagnet MnAuSn with $T_C = 570$ K and antiferromagnetic GdAuSn with $T_N = 26$ K were carried out using the ^{119m}Sn, ^{155}Gd and ^{197}Au Mössbauer spectroscopy. GdAuSn crystallizes in the hexagonal LiGaGe structure ($P6_3mc$) [12], whereas MnAuSn crystallizes in the cubic half-Heusler AlLiSi structure $(F\bar{4}3m)$. The difference of the atomic radii of Mn and Gd hinders an appearance of the solid solution between two compounds. From other hand, this circumstance favours the creation of the ferromagnetic granular MnAuSn material in the

antiferromagnetic GdAuSn matrix. One need to notice that X-ray powder diffraction studies failed to detect the disorder effects in basic constituent and to provide the phase analysis of the granular system.

^{155}Gd and ^{197}Au Mössbauer spectra measured at T = 12 K are shown in Figure 2. The 77.34 keV ^{197}Au resonance at δ = 2.92(1) mms^{-1} shows the hyperfine magnetic field of 12 (1) T, presumably as a result of conduction electron polarization in antiferromagnetically ordered state. The ^{155}Gd spectrum with parameters δ = 2.92(1) mms^{-1} and H_{hf} = 1.98(5) T reveals the unique Gd site in the crystal lattice. This finding confirms the magnetic and structural homogeneity of the sample under study in contrast with results of the publication [13], where the magnetic nonhomogeneity of GdAuSn was observed.

Figure 3 shows ^{119m}Sn Mössbauer spectra measured at 80 K for GdAuSn, MnAuSn and granular compound containing 95 and 5% of basic components, respectively. The paramagnetic spectrum of GdAuSn reveals the only Sn site with following parameters: δ = 1.919(4) mms^{-1}, Γ = 0.51(1) mms^{-1} and ΔE_Q = 0.62(1) mms^{-1}. This finding confirms the homogeneity of the sample in comparison with one studied in [13]. From the fit of ^{119m}Sn spectrum of cubic half–Heusler compound MnAuSn the following parameters were extracted: δ = 2.696(3) mms^{-1}, Γ = 0.55(1) mms^{-1} and H_{hf} = 0.380(1) T. The Mössbauer spectrum of the granular compound is well represented by two subspectral components with parameters, corresponding to GdAuSn and MnAuSn. The remarkable fact that the partial intensity of MnAuSn subspectrum of 20% essentially exceeds the nominal amount of this phase of 5% one can explain by the difference off Debye-Waller factors of both compounds.

Acknowledgements This work is supported by DFG research project FE 633/1-1. We gratefully acknowledge the financial help from the Materialwissenschaftliches Forschungszentrum der Universität Mainz and Landes-Kompetenzzentrum "Elektronische Eigenschaften komplexer Festkörper-Materialien."

References

1. Helmholdt, R.B., de Groot, R.A., Mueller, F.M., van Engen, P.G., Buschow, K.H.J.: J. Magn. Magn. Mat. **43**, 249 (1984)
2. de Groot, R.A., Mueller, F.M., van Engen, P.G., Buschow, K.H.J.: Phys. Rev. Lett. **50** 2024 (1983)
3. Chien, C.L.: J. Appl. Phys. **69**, 5267 (1991)
4. Buschow, K.H.J.: J. Magn. Magn. Mater. **38**, 1 (1983)
5. Kouacou, M.A., Pierre, J., Skolozdra, R.V.: J. Phys., Condens. Matter **7**, 7373 (1995)
6. Spiering, H., Deak, L., Bottyan, L.: Hyperfine Interact. **125**, 197 (2000)
7. Klencsár, Z.: Nucl. Instrum. Methods B **129**, 527 (1997)
8. Galanakis, I.: J. Phys., Condens. Matter **14**, 6329 (2002)
9. Watanabe, K.: Trans. Jpn. Inst. Met. **17**, 220 (1976)
10. Blaha, P., Schwarz, K., Madsen, G.K.H., Kvasnicka, D., Luitz, J.: WIEN2k, An Augmented Plane Wave + Local Orbitals Program for Calculating Crystal Properties. Techn. Universtät, Wien, Austria (2001)
11. Stevens, J.G., Stevens, V.E.: Mössbauer Effect Data Index, p. 130 (1975)
12. Baran, S. et al.: J. Phys., Condens. Matter, **9**, 9053 (1997)
13. Bialic, D., Kruk, R., Kmieć, R., Tomala, K.: J. Alloys Compd. **257**, 49 (1997)

Hyperfine Interact (2006) 168:1207–1210
DOI 10.1007/s10751-006-9425-z

Mössbauer study of the martensitic transformation in a Ni–Fe–Ga shape memory alloy

J. Gutiérrez · P. Lázpita · J. M. Barandiarán · J. S. Garitaonandia · F. Plazaola · E. Legarra · V. A. Chernenko · T. Kanomata

Published online: 8 November 2006

Abstract We present the results of an extensive Mössbauer study of the magnetic and martensitic transformation at room temperature of a polycrystalline alloy with a $Ni_{55}Fe_{19}Ga_{26}$ nominal composition. From calorimetric measurements, we have determined the martensitic transformation temperature of T_M = 240 K, in good agreement with the one obtained by magnetic characterization. This sample has a Curie temperature of T_C = 287 K. Additional Curie temperatures, belonging to a γ phase, have been also detected. Mössbauer spectroscopy performed at different temperatures monitored all these transformations and the fitting of the obtained spectrum at the highest temperature allow us to give percentages of the different phases in the sample.

Key words ferromagnetic shape memory alloys · martensitic transformation · Mössbauer spectroscopy

1 Introduction

Fe-based Ferromagnetic Shape Memory Alloys (FSMAs) have attractive mechanical properties as compared with the classical Ni–Mn–Ga ones. Their enhanced ductility opens new ways for technical applications such as new magnetic sensors or actuators.

J. Gutiérrez · P. Lázpita (✉) · J. M. Barandiarán · F. Plazaola · E. Legarra
Departamento de Electricidad y Electrónica, Fac. Ciencia y Tecnología, Universidad del País Vasco/EHU, P.Box 644, E-48080 Bilbao, Spain
e-mail: weblaarp@lg.ehu.es

J. S. Garitaonandia
Departamento de Física Aplicada II, Fac. Ciencia y Tecnología, Universidad del País Vasco/EHU, P.Box 644, E-48080 Bilbao, Spain

V. A. Chernenko
Institute of Magnetism, Kyiv 03142, Ukraine

T. Kanomata
Department of Applied Physics and Informatics, Tohoku Gakuin University, Sendai 985-8537, Japan

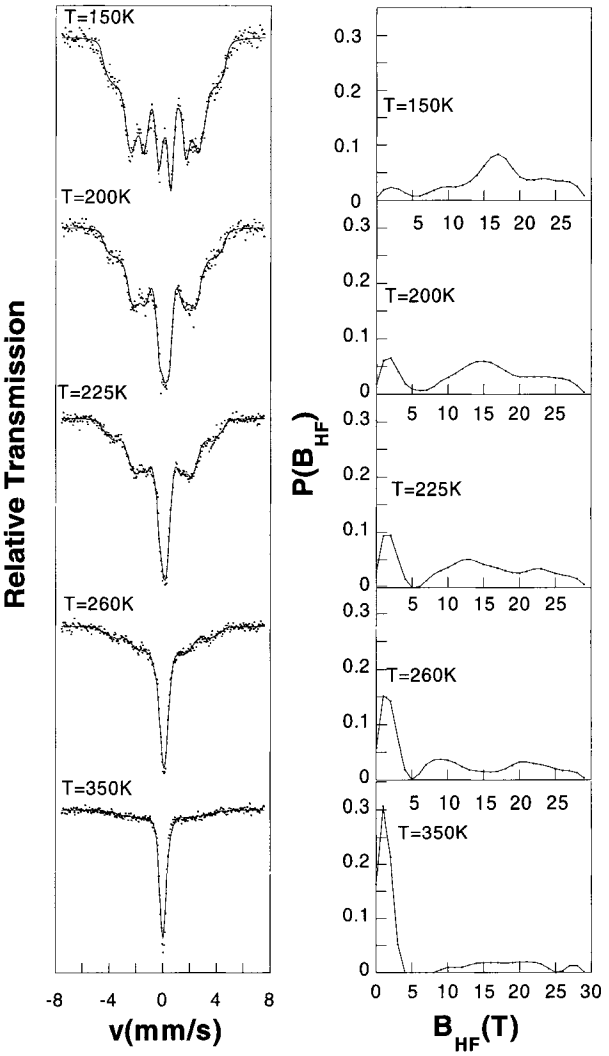

Figure 1 Experimental (*dots*) and fitted (*solid curves*) Mössbauer spectra for $Ni_{55}Fe_{19}Ga_{26}$ alloy (*left*), and their hyperfine field distributions $P(B_{HF})$ (*right*) at indicated temperatures.

The Ni–Fe–Ga Heusler alloys [1] are particularly promising FSMAs but so far, they have been little studied compared to those containing Mn.

Mössbauer spectroscopy is a useful tool to provide information about microscopic aspects of the martensitic transformation in these Fe-based alloys [2–4]. In this work, we present the results of an extensive Mössbauer study of the magnetic and martensitic transformation at room temperature of a polycrystalline alloy with a $Ni_{55}Fe_{19}Ga_{26}$ nominal composition.

2 Experimental methods

The alloy with a $Ni_{55}Fe_{19}Ga_{26}$ nominal composition was prepared by arc melting and suction casting from pure elements. Samples were polycrystalline and their average composition, as determined by EDX, matched the nominal one within 0.2 %at. Previous

Table I Fitted average hyperfine field (B_{HF}), average isomer shift (IS), and relative area of low B_{HF} for Ni55Fe19Ga26 sample at different temperatures

T(K)	IS(mm/s)	B_{HF}(mm/s)	Rel. area(%)
150	0.13 ± 0.02	16.7 ± 0.2	8 ± 1
200	0.10 ± 0.01	14.0 ± 0.2	20 ± 1
225	0.046 ± 0.004	12.5 ± 0.1	28 ± 1
260	0.022 ± 0.004	9.9 ± 0.4	44 ± 1
350	0.083 ± 0.003	5.6 ± 0.6	74 ± 1

calorimetric measurements showed a martensitic transformation temperature M_S 240 K. Magnetic measurements performed by a SQUID magnetometer at temperatures ranging from 150 to 350 K and by AC methods up to 450 K, showed a Curie temperature T_C = 287 K and T_M in agreement with DSC results. In addition, two higher Curie temperatures T'_C = 360 K, T''_C = 420 K are revealed by the magnetic measurements, which indicates the coexistence of (at least) two additional ferromagnetic phases in the alloys. These are likely to be γ phases that do not show martensitic transformation. ^{57}Fe Mössbauer spectroscopy measurements were carried out in the 150 to 350 K temperature range, in transmission geometry using a conventional spectrometer with a ^{57}Co–Rh source. Fittings with the obtained spectra were performed with NORMOS program developed by Brand et al. [5].

3 Results and discussion

Figure 1 shows Mössbauer spectra, recorded when warming the sample, below and above the martensite temperature transformation. The spectrum recorded at 150 K shows a six-line contribution arising from the ferromagnetic ordered martensitic phase, plus a certain contribution coming from the γ phases. At 350 K, the spectrum shows a typical single peak of the austenite phase in its paramagnetic state, plus a background contribution which still indicates the presence of some magnetically ordered phase(s). A continuous evolution occurs between these two temperatures. The spectra are fitted with a distribution of magnetic hyperfine fields, $P(B_{HF})$. From these fits, the existence of a paramagnetic phase corresponding to the $L2_1$ austenite phase, detected by other techniques like neutrons [6], is clearly evidenced (see Figure 1, right). Moreover, the amount of this phase in the sample continuously increases when temperature increases, monitoring so the transformation. The measured change ranges from 8% at 150 K to 74% at 350 K. On the other hand, at temperatures below 260 K, there is also a high hyperfine field value phase corresponding to the martensite plus γ phases. In fact, at the highest temperature of our measurements (over the Curie temperature of the $L2_1$ austenite phase), there is still about 26% of ferromagnetic contribution arising from the γ phase(s), as it was previously evidenced from our magnetic measurements. Table I summarizes the main results obtained from the fitting of the Mössbauer spectra.

4 Conclusions

The martensitic and magnetic transitions of the shape memory alloy with $Ni_{55}Fe_{19}Ga_{26}$ nominal composition have been investigated using bulk magnetization and Mössbauer

spectroscopy techniques, Mössbauer spectroscopy is particularly useful to monitor the transitions and to determine the evolution with temperature of the percentages of the different phases coexisting in the sample. This alloy has two phases: one of them transforms from a 14M martensite phase to a $L2_1$ austenite phase in a fraction of a 74%, plus other γ-fcc phase that remains unchanged during the heating process.

Acknowledgements This work was supported under ACTIMAT project, sponsored by the Industry Department of the Basque Government.

References

1. Oikawa, K., Ota, T., Sutou, Y., Ohmori, T., Kainuma, R., Ishida, K.: Mater. Trans., JIM **43**, 2360 (2002)
2. Akgun, I., Gedikoglu, A., Durlu, T.N.: J. Mater. Sci. **17**, 3479 (1982)
3. Durlu, T.N.: J. Mater. Sci. Lett. **11**, 702 (1992)
4. Kakeshita, T., Kuroiwa, K., Shimizu, K., Ikeda, T., Yamagishi, A., Date, M.: Mater. Trans., JIM **34**, 415 (1993)
5. Brand, R.A., Lauer, J., Herlach, D.M.: J. Phys. F. Met. Phys. **13**, 675 (1983)
6. Gutierrez, J., Lázpita, P., Siruguri, V., Barandiarán, J.M., Henry, P., Chernenko, V.A., Kanomata, T.: Int. J. Appl. Electromagn. Mech. **23**, 71 (2006)

Hyperfine Interact (2006) 168:1211–1215
DOI 10.1007/s10751-006-9426-y

The BM_5Se_9 phases: Mössbauer studies of the superconductors and the ferromagnets

A. Leblanc-Soreau · J. C. Jumas · L. Aldon

Published online: 5 December 2006

Abstract Syntheses performed in the A_3B/MSe_2 (A = Sb, Ga, Sn) (B = Nb, V, Ta) (M = V, Nb, Ta) systems lead to the formation of $B(M/A)_5Se_9$ phases which could be ferromagnets or superconductors. It has been shown that the presence of V modifies the superconducting exchanges and allows ferromagnetic couplings. Mössbauer spectroscopy of both ^{121}Sb and ^{119}Sn gives local electronic structure of the $SbNb_5Se_9$ superconductor and the $Sn_{0.94}Ga_{0.06}V_{0.30}Nb_{4.70}Se_9$ ferromagnet. For the latter compound, a complete study as a function of temperature is carried out showing that the Sn environment is not modified when the ferromagnetic transition occurs. The Debye temperature is calculated and compared to those obtained for other selenide compounds.

Key words ^{119}Sn and ^{121}Sb Mössbauer spectroscopy · Mössbauer temperature · superconductor · ferromagnet · selenide

1 Introduction

New superconductors, such as ferromagnets, could be obtained by dissolution of some A15 phases in lamellar metallic dichalcogenides, i.e. 2H-$NbSe_2$ and 1T-VSe_2 [1, 4]. The susceptibility of the $SnNb_5Se_9$ superconductor in the 2–300 K temperature range and the evolution of H_{c1}, H_{c2} and Tc values obtained in zero field-cooling mode at different field strengths have been measured with a SQUID magnetometer from Quantum Design Co. They exhibit a transition to the superconductor from 17.5 K under a 100 G field strength, and a significant anisotropy (1.2) when the applied field is $\perp$ c or // c. This anisotropy is smaller than the one observed in a pure $2H_a$-$NbSe_2$ but much bigger than that of Nb_3Sn [1, 4]. From the susceptibility measurements, an anomaly is noticed around 85–90 K, probably

A. Leblanc-Soreau (✉)
I.M.J.R.-CNRS, 2, rue de la Houssinière, BP 32229, 44322 Nantes Cedex 3, France
e-mail: leblanc@cnrs-imn.fr

J. C. Jumas · L. Aldon
LAMMI-CNRS, Place E. Bataillon, 34095 Montpellier Cedex 5, France

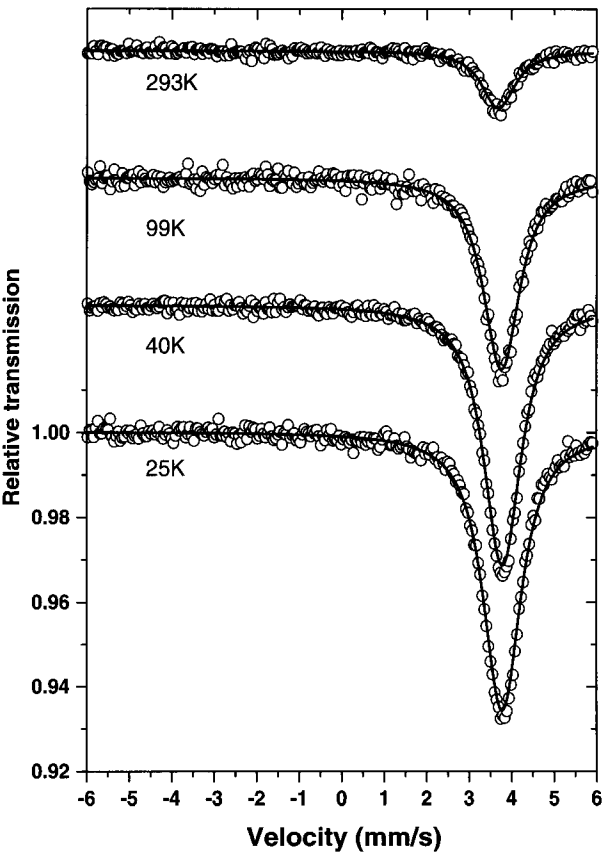

Figure 1 ^{119}Sn Mössbauer spectra of sample $Sn_{0.94}Ga_{0.06}Nb_{4.70}V_{0.30}Se_9$ recorded at various temperatures. Absorption and velocity scales are the same of all spectra.

indicating a condensation of conduction electrons in a charge-density-wave (CDW) state, as seen in $2H_a$-$NbSe_2$. However when non-stoichiometric $NbSe_2$ is used for the synthesis, non-superconducting $SnNb_5Se_9$ is obtained [4]. $SbNb_5Se_9$ is also a superconductor, but GaV_5Se_9 is a ferromagnet like all BM_5Se phases containing few V atoms, for example $Sn_{0.94}Ga_{0.06}Nb_{4.70}V_{0.30}Se_9$. For the $SnNb_5Se_9$ superconductor [2], three types of site exist which is corrected to two species of Sn. One site is for an Sn in an Nb environment (site 1), the two others for Sn^{II} in an Se environment (site 2 symmetrical and site 3 asymmetrical). A reversible dynamic process between sites 2 and 3 has been observed and is correlated to a modification of site 1 at 90 K. Thus given the susceptibility anomaly at 85–90 K and the temperature behaviors of the Mössbauer parameters, a possible CDW has been proposed [2].

The purpose of this work is to present the ^{119}Sn and ^{121}Sb Mössbauer studies of the $Sn_{0.94}Ga_{0.06}V_{0.30}Nb_{4.70}Se_9$ ferromagnet and the $SbNb_5Se_9$ superconductor.

2 Experimental

^{119}Sn Mössbauer spectra were recorded in constant-acceleration mode using an ELSCINT-AME40 spectrometer, equipped with a cryostat for the low temperature measurements. The γ-source was $Ba^{119m}SnO_3$. The velocity scale was calibrated with the magnetic sextet

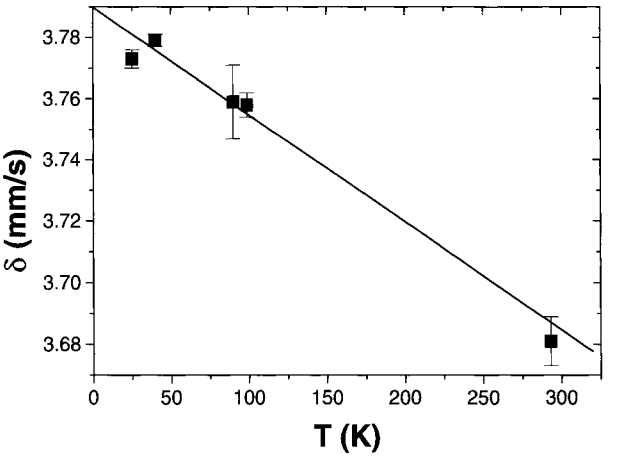

Figure 2 Evolution of the isomer shift vs temperature.

spectrum of a high purity iron foil absorber, using ^{57}Co(Rh) as source. The recorded spectra were fitted to Lorentzian profiles by the least squares method and the fit quality was controlled by the classical χ^2 tests [3]. The origin of the isomer shift was determined from the center of the $BaSnO_3$ spectrum recorded at room temperature.

The ^{121}Sb Mössbauer measurements were carried out in standard transmission geometry using as the source, the ^{121m}Sn isotope included in a $BaSnO_3$ matrix. During the measurements, both source and absorber were simultaneously cooled down to liquid helium temperature to increase the fraction of the recoil-free absorption and emission processes. The velocity scale was calibrated with the standard spectrum of an iron absorber obtained using a ^{57}Co source. The zero isomer shift was defined from the spectrum of the reference InSb (−8.70 mm/s relative to the $BaSnO_3$ source).

3 Results

3.1 $Sn_{0.94}Ga_{0.06}Nb_{4.70}V_{0.30}Se_9$ (ferromagnet)

^{119}Sn Mössbauer spectra have been recorded at different temperatures (Figure 1) in order to determine the vibrating effective mass and the Mössbauer temperature of the $Sn_{0.94}Ga_{0.06}Nb_{4.70}V_{0.30}Se_9$ compound.

This compound shows one asymmetric site with hyperfine parameters which is a feature of Sn(II) surrounded by Se. Its isomer shift variation according to temperature (Figure 2) shows no modification at Tc transition. So the Sn environment is not modified even if ferromagnetic couplings occur without any transferred field on Sn.

The temperature dependence of isomer shift leads to a value of $d\delta/dT = -3{,}65897.10^{-4}$ mm s^{-1} K^{-1} and gives an effective mass $M_{eff} = 4.141.10^{-2}/3.65897.10^{-4} = 113.7$ u.m.a. which is close to tin atomic mass (118.9 u.m.a.). The slope of absorption temperature dependence as shown in Figure 3 leads to a value of $d\ \ln A/dT = -6.18.10^{-3}$ K^{-1} and gives a Mössbauer temperature $\theta_M = (3.10^4 / (113.7 \times 6.18.10^{-3}))^{1/2} = 207$ K. These values are compared to those observed for various reference materials in Table I.

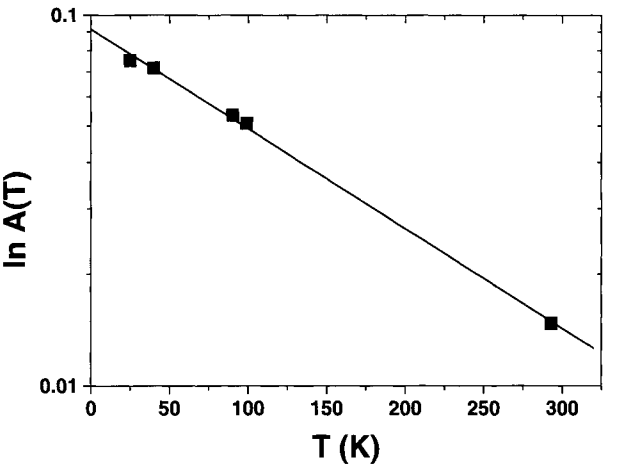

Figure 3 Variation of the absorption vs temperature in logarithmic scale.

Table I Hyperfine parameters of some selenide compounds presented in this work and reported in the literature

Compound	M_{eff} (u.m.a)	θ_M (K)	δ (mm/s)	Δ (mm/s)
$SnNb_5Se_9$ [4]	172	–	3.46	0.77
	150	–	3.63	0
"SGVN"	113	207	3.68	0.18
SnSe [5]	130	159	3.25	0.73
SnO [6]	168	229	2.64	1.31
$Cr_2Sn_3Se_7$ [7]	–	151	3.40	0.46
	–	234	1.46	0.35
Nb_3Sn [8]	119	228	1.52	0

Δ and δ (relative to $BaSnO_3$) are those observed at room temperature

SGVN $Sn_{0.94}Ga_{0.06}V_{0.30}Nb_{4.70}Se_9$ compound

3.2 $SbNb_5Se_9$ (superconductor)

For the $SbNb_5Se_9$ superconductor phase, dynamical study of the observed process is excluded since, with this isotope, Mössbauer spectrum is recorded at 4 K (both source and sample) in order to get valuable information. For this phase we observed a relative simple spectrum composed of only one site with a $\delta = -3.55$ mm/s isomer shift and a $\Delta = +8.5$ mm/s quadrupole splitting. These values are close to those reported for Sb_2Se_3 ($\delta = -6.28$ mm/s and $\Delta = +6.8$ mm/s) and are rather far from the values observed in intermetallics like MnSb ($\delta = -0.38$ mm/s and $\Delta = 0$ mm/s) or $CoSb_3$ ($\delta = -0.28$ mm/s and $\Delta = +9.3$ mm/s) [9]. In our case, hyperfine parameters for antimony suggest Sb(III) species surrounded by Se atoms. Another point is the non-zero value of the quadrupole splitting in agreement with the stereoactivity of the lone pair located on the Sb(III) specie. Since only one type of environment is observed, at this low temperature (4 K), a Sb–Nb environment are excluded. However it is difficult to draw conclusions on the possible exchange between the two sites (2) and (3) as observed in the case of Sn(II) for the $SnNb_5Se_9$ compound. In

addition, the quite high value of the line width (1.81 mm/s) does not allow us to make a distinction between the two Sb–Se which might be located in the structure.

4 Discussion

In the case of the $Sn_{0.94}Ga_{0.06}Nb_{4.70}V_{0.30}Se_9$ ferromagnet compound, the temperature behavior is rather different from that of the $SnNb_5Se_9$ compound. The presence of additional elements (Ga and V) seems to block the transition observed in the case of non-supraconducting $SnNb_5Se_9$. This behavior allows us to determine the Mössbauer temperature and the effective mass of tin in this compound. This compound is isostructural to the previously studied $SnNb_5Se_9$ phase [4]. All these features are compared to those obtained for the $Sn_{0.94}Ga_{0.06}V_{0.30}Nb_{4.70}Se_9$ ferromagnet compound whose vibrating mass exactly corresponds to Sn. The determined values are in agreement with those reported for the Sn–Se environments. The effective mass is in line with vibrating modes which are not as high as those of selenides. The bonds are more metallic than those observed for the SnSe compound.

Regarding the $SbNb_5Se_9$ compound, the recorded ^{121}Sb spectrum at 4 K do not clearly evidence the possible transition observed in the case of $SnNb_5Se_9$.

5 Conclusions

From ^{119}Sn Mössbauer data analysis of the $Sn_{0.94}Ga_{0.06}Nb_{4.70}V_{0.30}Se_9$ ferromagnet, only the contribution of Sn^{II} due to a Sn–Se environment is observed independently from the measurement temperature. From temperature dependence of both isomer shift and absorption, a 113.7 u.m.a. effective mass and a 207 K Mössbauer temperature have been determined. These values are in a good agreement with those previously obtained for reference materials such as SnSe or Nb_3Sn.

Finally, at 4 K, the $SbNb_5Se_9$ superconductor shows a Sb–Se environment that cannot be detected at higher temperatures since it is not possible to obtain a spectrum at room temperature for ^{121}Sb.

References

1. Molinié, P., Leblanc, A., Faulques, E., Ouilli, Z., Jumas, J.C., Ayache, C.: Spectroscopy of superconducting materials. In: Faulques, E. (ed.) American Chemical Society, Symposium series no. 730. Oxford University Press, Oxford (1999)
2. Leblanc-Soreau, A., Molinié, P., Jumas, J.C.: Physica B **321**, 138 (2002)
3. Ruebenbauer, K., Birschall, T.: Hyperfine Interact. **7**, 125 (1975)
4. Leblanc-Soreau, A., Molinié, P., Jumas, J.C.: Phys. Status Solidi (C) **1**(7), 1846 (2004) 3(9), 3081 (2006)
5. Fano, V., Ortalli, I.: J. Chem. Phys. **61**, 5017 (1974)
6. Herber, R.H.: Phys. Rev. B **27**, 4013 (1983)
7. Bodénan, F., Cajipe, V.P., Danot, M., Ouvrard, G.: J. Solid State Chem. **137**, 249 (1998)
8. Taylor, R.D., Graig, P.P.: Phys. Rev. **17**, 782 (1968)
9. Lippens, P.E.: Solid State Commun. **113**, 399 (2000)

Hyperfine Interact (2006) 169:1217–1222
DOI 10.1007/s10751-006-9427-x

Systematic study of mechanical deformation on $Fe_3Al_xSi_{1-x}$ powders by Mössbauer spectroscopy

E. Legarra · F. Plazaola · J. S. Garitaonandia · D. Martín Rodriguez · J. A. Jimenez

Published online: 14 November 2006

Abstract The Mössbauer technique has been used to measure hyperfine magnetic fields, isomer shifts and relative areas of ^{57}Fe atoms located at various sites in $Fe_3Al_xSi_{1-x}$ series with x=0, 0.3, 0.5, 0.7. Four samples were crushed; then they were annealed for 10 h at 1,023 K and cooled down at 3°/min in order to recover the DO_3 stable phase. Mössbauer studies revealed that annealed samples have a DO_3 structure, whereas deformed samples are partially disordered, with both ordered DO_3 and disordered A2 structures, even though X-rays measurements do not show superstructure peaks. The amount of disordered structure decreases with Si content.

Key words Fe–Al–Si alloys · DO3 ordered phase · Mössbauer spectroscopy

1 Introduction

Intermetallic Fe–Al alloys have DO_3 structure at room temperature over the 23–37 at.% Al range [1]. Figure 1 shows the DO_3 unit cell of Fe_3Al structure. It consists of four face-centred-cubic sublattices, A, B, C and D. Iron atoms occupy A, B and C sublattices while D is occupied by Aluminium. Iron atom at the A sublattice is denoted by Fe[A] and is equivalent to that at the site C, Fe[C]. Therefore, in the case of the stoichiometric composition studied in this work DO_3 structure has two Fe inequivalent positions which will be referred to as B8 (Fe surrounded by 8 Fe as nearest neighbours atoms) and A4 (Fe surrounded by 4 Fe and 4 Al as nearest neighbours atoms).

E. Legarra (✉) · F. Plazaola · D. M. Rodriguez
Dpto. Electricidad y Electrónica, UPV-EHU, C. P. 644, 48080 Bilbao, Spain
e-mail: weblesae@lg.ehu.es

J. S. Garitaonandia
Dpto. Física Aplicada II, UPV-EHU, C. P. 644, 48080 Bilbao, Spain

J. A. Jimenez
CENIM, Avda. Gregorio del Amo 8, 28040 Madrid, Spain

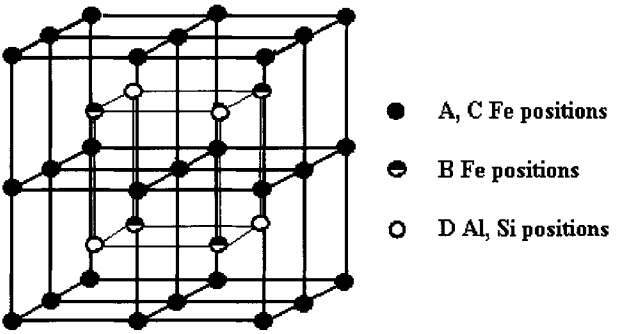

Figure 1 Unit cell of the ordered DO_3 structure.

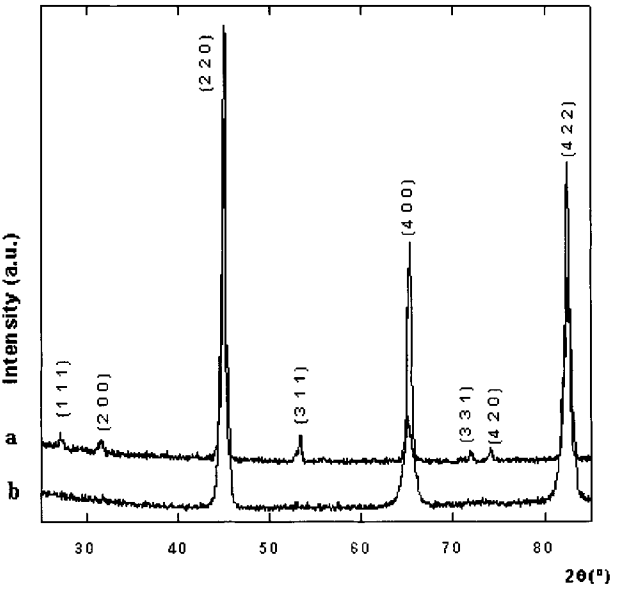

Figure 2 X-ray measurements for $Fe_3Al_{0.7}Si_{0.3}$ in **a** annealed, **b** deformed samples.

Fe–Al alloys have been extensively studied. Fnidiki et al. [2] found that it is possible to induce a magnetic splitting caused by atomic disorder by implantation of Al ions into $Fe_{0.6}Al_{0.4}$ alloys. More recently, Amils et al. [3] show that a paramagnetic to ferromagnetic transition linked to an order–disorder transition between ordered B2 structure (paramagnetic) and disordered A2 structure (ferromagnetic) can be observed after mechanical deformation in $Fe_{0.6}Al_{0.4}$. On the other hand, in $Fe_{0.7}Al_{0.3}$ an enhancement of the magnetism of the intermetallic alloy after order–disorder transition has been found [4, 5].

The phase diagram of Fe–Al alloys [1] shows that for Fe_3Al at temperatures above 833 K the equilibrium phase is B2 and above 1,023 K disordered A2. However, for Fe_3Si alloys the phase diagram [1] does not show B2 structure. Therefore, Al/Si substitution is expected to promote the stabilization of DO_3 structure in ternary alloys in respect to binary Fe–Al alloys.

Mössbauer spectroscopy is a powerful tool for studying local environment of Fe atoms. Therefore it is a good candidate to study the local environment of Fe and the magnetic properties of the alloys.

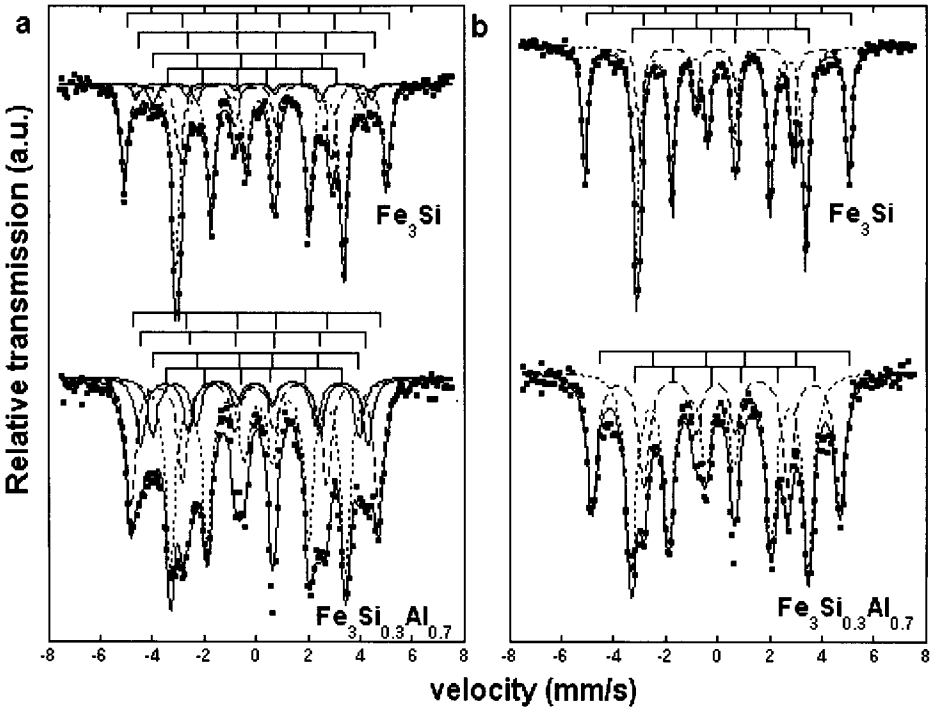

Figure 3 Mössbauer spectra of **a** deformed and **b** annealed Fe_3Si and $Fe_3Al_{0.7}Si_{0.3}$ alloys.

Table I Values of the internal fields, isomer shifts and relative areas of the annealed samples

Percent Si	Number of nearest neighbours Fe atoms					
	B8			A4		
	B_{HF} (T)	IS (mm/s)	Area (%)	B_{HF} (T)	IS (mm/s)	Area (%)
0.3	29.5	0.039	40	21.1	0.195	60
0.5	29.8	0.055	41	20.9	0.208	59
0.7	30.4	0.062	40	20.5	0.229	60
1	31.4	0.082	38	20.2	0.251	62

The purpose of this work is the systematic study of the influence of Al/Si substitution on the disordering of the alloys by Mössbauer spectroscopy and X-ray diffraction.

2 Experimental

Four $Fe_3Al_xSi_{1-x}$ alloys with x=0, 0.3, 0.5, 0.7 were prepared by induction melting in alumina crucibles and cast into ingots under a 40 kPa pressure of high purity argon. Iron, Aluminium and Silicon with a purity of 99.99, 99.99 and 99.999%, respectively were used. The mechanical deformation has been performed crushing the samples to obtain

Table II Values of the internal fields, isomer shifts and relative areas of the deformed samples

Percent Si	Number of nearest neighbours Fe atoms											
	B8			B7			A5			A4		
	B_{HF}	IS	Area	B_{HF}	IS	Area	B_{HF}	IS	Area	B_{HF}	IS	Area
0.3	29.5	0.048	29	27.1	0.035	15	24.8	0.097	13	20.9	0.179	43
0.5	29.6	0.055	30	27.2	0.026	10	24.8	0.104	10	20.6	0.202	50
0.7	30.0	0.058	31	27.5	0.002	8	24.6	0.120	9	20.3	0.224	52
1	31.2	0.080	31	28.0	0.031	5	25.1	0.187	7	20.1	0.250	57

homogeneous powders (with a diameter of about 10 μm). The ordered phases were obtained after annealing the samples for 10 h at 1,023 K and cooling down at 3°/min to room temperature to recover the DO_3 stable structure.

^{57}Fe Mössbauer spectroscopy measurements were carried out at room temperature in transmission geometry using a conventional spectrometer with a ^{57}Co-Rh source. The measured spectra were fitted using the NORMOS program developed by Brand et al. [6]. All the isomer shift values presented in this work are relative to metallic iron at room temperature.

XRD measurements were carried out in a Philips PW 1710 powder diffractometer using CuKα radiation.

3 Results and discussion

Figure 2 shows that X-ray measurements for $Fe_3Al_{0.7}Si_{0.3}$ annealed alloy exhibits well-defined superstructure peaks, whereas, for the deformed alloy, they do not appear. This is a clear indication that DO_3 structure has been recovered after annealing. This behaviour is also seen in the rest of the samples.

Figure 3 shows Mössbauer spectra obtained for annealed and deformed Fe_3Si and $Fe_3Al_{0.7}Si_{0.3}$ samples at room temperature, which are the samples with extreme compositions of this study.

3.1 Annealed samples

The spectra of $Fe_3Al_xSi_{1-x}$ annealed samples have been fitted with two subspectra related with the two inequivalent positions of the structure DO_3 (A and B positions in Figure 1).

Mössbauer parameters obtained from the fittings of the annealed samples are shown in Table I. Table I indicates that hyperfine fields at A positions increases linearly with increasing Al concentration, whereas the hyperfine fields at B positions decreases. This is in agreement with the results reported by Lin et al. [7].

The values of the isomer shifts at both positions decrease with increasing Al concentration (see Table I). Since Al has one p electron less than Si, as Al substitutes Si the charge transfer is reduced and this results in reduced shielding of s-like electrons. Therefore, the isomer shift becomes more negative as Al concentration increases.

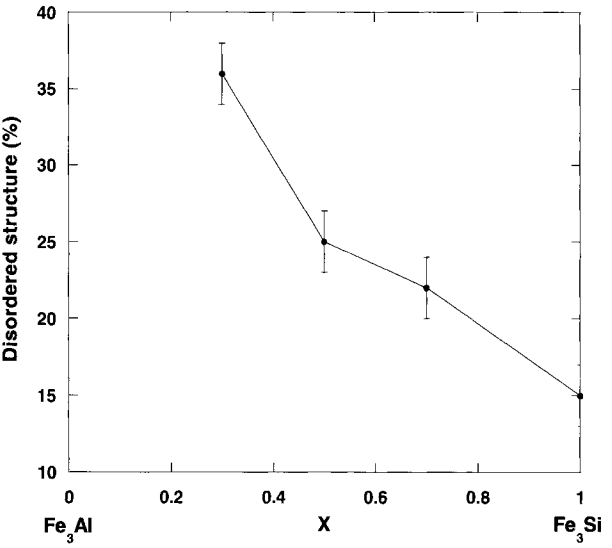

Figure 4 Evolution of the disordered structure with the amount of Al/Si.

3.2 Deformed samples

In order to fit the Mössbauer spectra of the deformed samples we make some assumptions about the expected disordering process of the alloys. The simplest assumption one could expect about disordering is that some Fe atoms in B8 positions are displaced to Al/Si positions and vice versa (see Figure 1). If this was true, instead of two inequivalent positions, there would be four inequivalent positions: B8, A4, B7 (Fe atom surrounded by 7 Fe and 1 (Al, Si) as nearest neighbour atoms) and A5 (Fe atom surrounded by 5 Fe and 3 (Al, Si) as nearest neighbour atoms).

Table II shows the data obtained from the fittings of the Mössbauer spectra of the deformed alloys with four subspectra. The largest and the smallest B_{HF} values are roughly the same as those obtained for the annealed alloys, so they must correspond to A4 and B8 positions; therefore under our assumption the new subspectra have B_{HF} related to the A5 and B7 positions. The quality of the fittings is fairly good and this points out that our assumption is also good.

Relative areas of these subspectra do not correspond neither to the binomial distribution expected for a disordered A2 structure nor to an ordered DO_3 structure, so it must be a mixture of both. X-ray measurements of deformed samples do not show superstructure peaks, however, Mössbauer spectra show that order has not completely disappeared. This is in agreement with Martin-Rodriguez et al. results reported in $Fe_{0.7}Al_{0.3}$ [4].

In order to obtain the amount of disordered structure in deformed alloys it has been taken into account that the ratio of the areas of the two Fe inequivalent positions in the ordered samples. The extra amount of B8 has been considered due to the disorder and therefore it has been added to the A5 and B7 relative areas. Figure 4 shows the amount of disordered structure versus Al/Si composition. As we expected in Fe_3Si the relative amount of disordered structure is small, this can be also observed from Mössbauer spectra (see Figure 3) where annealed and deformed spectra are quite similar; on the other hand annealed and deformed spectra of $Fe_3Al_{0.7}Si_{0.3}$ are quite different.

4 Conclusions

Even X-ray diffraction does not show superstructure peaks corresponding to ordered phase, Mössbauer spectroscopy shows that the mechanical deformation given to the samples is not able to produce a complete disorder of the alloys. The main part of the spectra still has a DO_3 phase and the disorder appears with two inequivalent positions with Fe surrounded by 7 Fe and 1 (Al, Si) and 5 Fe and 3 (Al, Si). Moreover, Si substitution prevents the disordering of the alloys.

Acknowledgements This work was undertaken under Project Nos. UPV 224.310-14553/2002 and MAT 2006-12743. One of the authors (E.L.) wishes to thank UPV-EHU for the fellowship.

References

1. Kubaschweski, O.: "Iron–Aluminium" and "Iron–Silicon" In: Iron Binary Phase Diagrams. Springer, Berlin Heidelberg New York 5–9 and 130–139 (1982)
2. Fnidiki, A., Eymery, J.P., Delafond, J.: J. Magn. Magn. Mater. **40**, 130 (1983)
3. Hernando, A., Amils, X., Nogués, J., Suriñach, S., Baró, M.D., Ibarra, M.R.: Phys. Rev., B **58**, 11864 (1998)
4. Apiñaniz, E., Plazaola, F., Garitaonandia, J.S., Martín, D., Jiménez, J.A.: J. Appl. Phys. **93**, 7649 (2003)
5. Martín-Rodriguez, D., Apiñaniz, E., Plazaola, F., Garitaonandia, J.S., Jiménez, J.A., Schmool, D.S., Cuello, G.J.: Phys. Rev. B **71**, 212408 (2005)
6. Brand, R.A. et al.: J. Phys. F: Met. Phys. **13**, 675 (1983)
7. Lin, Mou-Ching, Barnes, R.G., Torgeson, D.R.: Phys. Rev., B **24**, 3712 (1981)

Hyperfine Interact (2006) 169:1223–1230
DOI 10.1007/s10751-006-9428-9

Magneto-crystalline properties of $BaFe_{12-2x}M_xSn_xO_{19}$ (M = Sn, Ni, Zn) ferrite powders

A. Grusková · J. Lipka · J. Sláma · V. Jančárik · M. Papánová · M. Štofka · A. González · G. Mendoza

Published online: 5 December 2006

Abstract $BaFe_{12-2x}M_xSn_xO_{19}$ compounds, where $M=Sn^{2+}$, Ni^{2+} or Zn^{2+} ions, were synthesized by mechanical milling and partially by citrate precursor methods. Analysis of magneto-crystalline structure has been carried out by Mössbauer spectroscopy. The Sn^{4+} ions replace Fe^{3+} ions on 2b and slightly on $2a+4f_1$ sites, Zn^{2+} ions strongly prefer $4f_1$ sites, Sn^{2+} ions prefer $4f_1$ sites too and Ni^{2+} ions occupy $4f_2$ and 12k or 2a sites. The magnetic properties were evaluated by the vibrating sample magnetometry and the thermomagnetic analysis. A large variation of the intrinsic coercivity H_c (330 to 78 kA/m) and of temperature coefficient of coercivity of $\Delta H_c / \Delta \vartheta$ (0.39 to 0.22 kA/m°C) were achieved as a function of the (Zn–Sn) and (Sn–Sn) substitutions, respectively. The Curie temperature T_c decreased with the (Ni–Sn) substitution from 447 to 399°C.

Key words magnetic properties · substitutional effects · Mössbauer spectra · hexagonal ferrites

A. Grusková · M. Papánová
Department of Electrotechnology, Faculty of Electrical Engineering and Information Technology, Slovak University of Technology, Ilkovičova 3, 812 19 Bratislava, Slovak Republic

A. Grusková
e-mail: anna.gruskova@stuba.sk

J. Lipka (✉)
Department of Nuclear Physics and Technology, Faculty of Electrical Engineering and Information Technology, Slovak University of Technology, Ilkovičova 3, 812 19 Bratislava, Slovak Republic
e-mail: jozef.lipka@stuba.sk

J. Sláma · V. Jančárik · M. Štofka
Department of Electromagnetic Theory, Faculty of Electrical Engineering and Information Technology, Slovak University of Technology, Ilkovičova 3, 812 19 Bratislava, Slovak Republic

A. González · G. Mendoza
Cinvestav-Saltillo, Carr. Saltillo-Mty. Km. 13, P.O. Box 663, 25000 Saltillo, Coahuila, Mexico

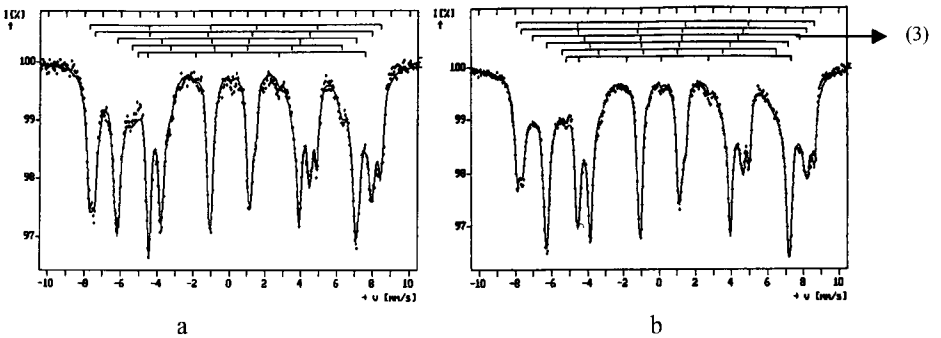

Figure 1 Mössbauer spectra for samples BaM_{Ni-Sn} (Sk) (a) and BaM_{Ni-Sn} (Mx) (b) for $x=0.3$, respectively.

1 Introduction

The fine particles of cationic substituted BaM are widely anticipated to be a suitable candidate for high-density perpendicular and magneto-optical recording in the near future [1]. High magnetic polarisation J and adequately low coercivity H_c is required for these materials. The magnetic properties of the final product are strongly dependent on the conditions of synthesis [2]. In our case H_c was controlled through the substitution of Fe^{3+} ions by the pair of the divalent and the tetra-valent ions. Several of combinations of substituents such as Zn–Zr, Co–Ti, Zn–Ti, Ni–Ti and others have been investigated and reported [3–6]. Co–Sn substituted BaM is a new kind of very promising particulate material for magnetic recording [7]. The different cationic combinations with Sn^{4+} ions were tested in our earlier research works [8, 9]. The goal of this paper is to compare the micro-structural and magnetic parameters of hexaferrites having substituted pairs of Sn^{4+} ions with Sn^{2+}, Ni^{2+} or Zn^{2+} ions, prepared by mechanical milling and the citrate precursor methods.

2 Experimental

Samples of $BaFe_{12-2x}M_xSn_xO_{19}$ with $0 \leq x \leq 0.3$, where $M=Sn^{2+}$ or Ni^{2+} ions, further denoted as BaM_{Sn-Sn} (Mx) or BaM_{Ni-Sn} (Mx), were produced by mechanical milling. $BaCO_3$, Fe_2O_3, (SnO or NiO), and SnO_2, all of purity of 98% and the Fe/Ba ratio of 10 [8] were used. After mechanical milling, the samples were annealed at 1050°C for 1.5 h. Samples of $BaFe_{12-2x}M_xSn_xO_{19}$ with $0 \leq x \leq 0.3$, where $M=Ni^{2+}$ ions, denoted as BaM_{Ni-Sn} (Sk) and further samples with $M=Zn^{2+}$ ions with $0 \leq x \leq 0.6$, denoted as BaM_{Zn-Sn} (Sk), were prepared by using of an organometallic precursor. $Ba(OH)_2.8H_2O$ $Fe(NO_3)_3.9H_2O$, $Ni(NO_3)_2.6H_2O$ or $Zn(CH_3COO)_2$, $SnCl_2.2H_2O$ and citric acid, all of purity of 99% and the Fe/Ba ratio of 10.8 [10] were used. The samples were subsequently annealed at temperatures of 700 and 1050°C for 1.5 h. The magnetic properties were studied using a vibrating sample magnetometer (VSM) with a maximum intensity of external magnetic field of 540 kA/m. The phase constitution was analysed by Mössbauer spectroscopy using a conventional constant acceleration mode with γ ray source of $^{57}Co/Rh$. The spectra were fitted using the NORMOS software package. The temperature dependencies of the magnetic susceptibility $\chi(\vartheta)$ were measured by the bridge method, while the samples were heated at a constant rate of 4°C/min. The Philips XL 30 scanning electron microscope (SEM) was used to obtain data on microstructure and morphology of particles.

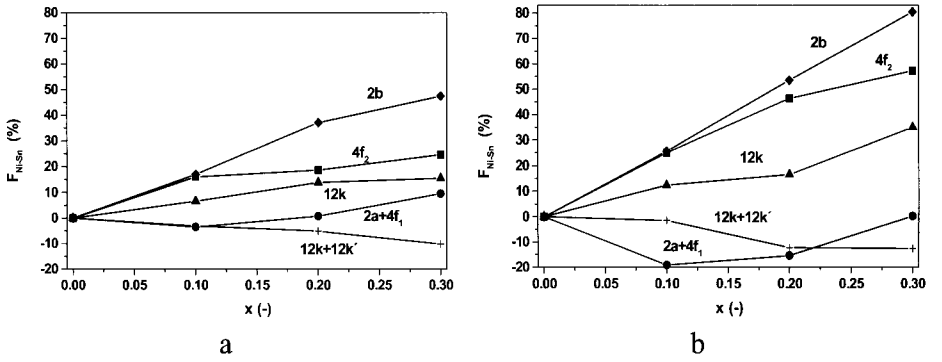

Figure 2 Factor of occupancy of F_{Ni-Sn} vs substitution x for the BaM_{Ni-Sn} (Sk) (a) and BaM_{Ni-Sn} (Mx) (b).

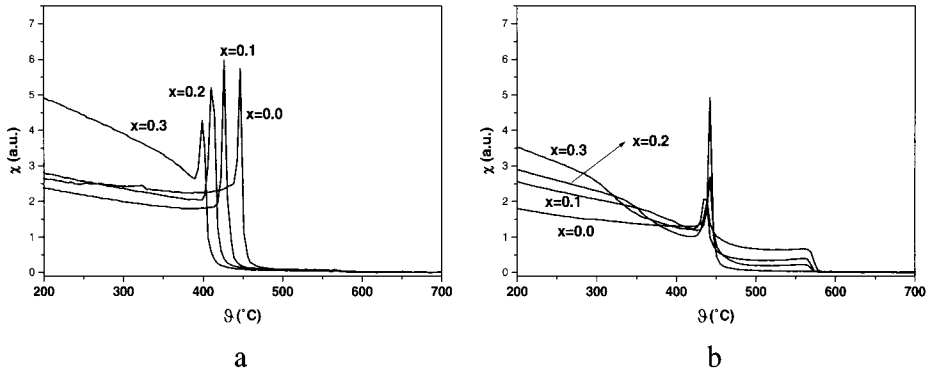

Figure 3 Temperature dependencies of $\chi(\vartheta)$ for BaM_{Ni-Sn} (Sk) (a) and BaM_{Ni-Sn} (Mx) (b) samples.

3 Results and discussion

An example of the Mössbauer spectrum of the sample with x=0.3 which has been prepared by precursor method (Sk) and was measured at room temperature, is given in Figure 1a. This spectrum was fitted by five sextets ($4f_2$, $2a+4f_1$, 12k, 12k′ and 2b). The Mössbauer spectrum of the sample prepared by mechanical milling (Mx) is in Figure 1b, for x=0.3. The evaluation shows that there is one more sextet, indicating the presence of an undesired phase. The third sextet from the six sextets this sample has; has the value of hyperfine splitting of B_{hf} (3)=45.9 T. Probably it is the position of Ni ferrite or magnetite (Fe_3O_4).

From the analysed Mössbauer spectra the values of the occupancy factor F, as described in [10] for the Ni^{2+}–Sn^{4+} ions have been estimated using the formula, given in [3]. In the Figure 2 it can be seen, that for the given substitution, the 2b, $4f_2$ and 12k positions are preferred for both methods of preparation. It should be noted, that there are quantitative differences in above-mentioned occupation sites. The latter probably could be caused by the fact, that the samples (Mx) contained also the secondary phase existing above the Curie temperature of 450°C of the BaM ferrite. The temperature dependencies of $\chi(\vartheta)$, given in Figure 3b, confirm that secondary phase has T_c around 585°C [8]. The amount of this phase raised with increasing of x, as evidently can be seen in Figure 3b. The $\chi(\vartheta)$ dependencies for the samples (Sk) are depicted in Figure 3a and can be interpreted as significantly simple-phase systems in the whole range of substitution (for x up to x=0.3). The Curie

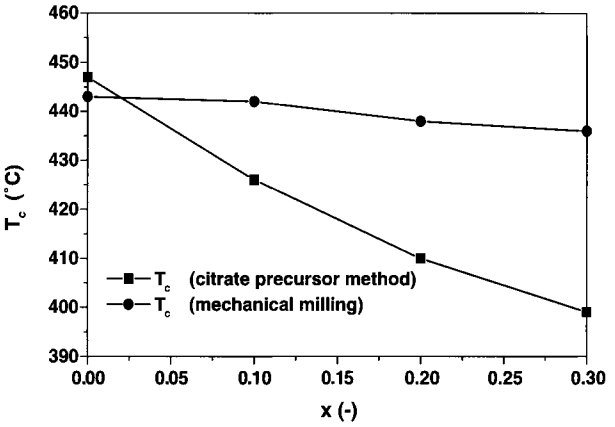

Figure 4 Curie temperature T_c vs substitution x of the BaM_{Ni-Sn} (Sk) and (Mx) samples.

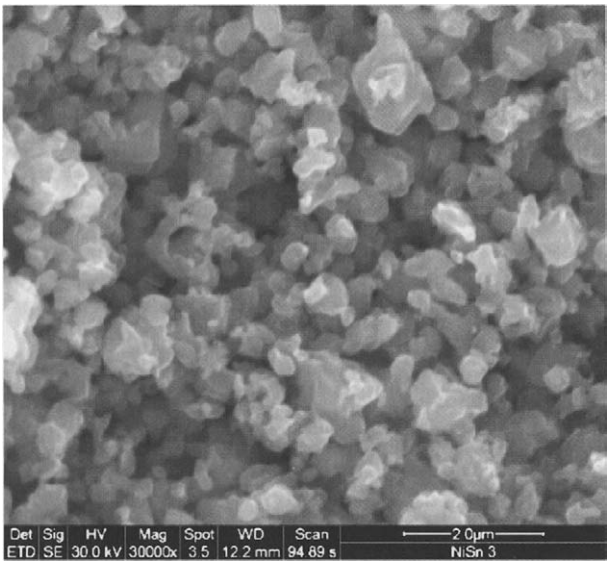

Figure 5 SEM micrograph of BaM_{Ni-Sn} sample with x=0.3.

temperature T_c of BaM_{Ni-Sn} ferrite decreases with x, (Figure 4). Almost linear drop for the samples (Sk) is connected with weakening of the superexchange interactions between Fe^{3+} ions and O^{2-} ions and rather milder drop in T_c (x) dependence for the samples (Mx) is most probably connected with the presence of the secondary phase.

The morphology and the particle size distribution of BaM_{Ni-Sn} sample can be seen on the micrograph in Figure 5. The grain size is well below 1 μm at x=0.3. The Mössbauer spectra of BaM_{Sn-Sn} ferrites are analysed in [9]. With the x rising, the site of 12k was splitting to 12k and 12k′ and this may be connected with changes in proximity of neighbouring Fe^{3+} ions in 12k, if the substitution is performed in R block. At considering of variations in ionic diameters of Sn^{2+} (0.112 nm) and Sn^{4+} (0.083 nm) it can be assumed, that the Sn^{2+} ions are replacing the Fe^{3+} ions in octahedral sites ($4f_2$ and 2a), while the Sn^{4+} preferably occupy tetrahedral $4f_1$ site and bipyramidal 2b site. The presence of substitution in the $4f_2$ site is evident also from increasing of the occupancy factor F_{Sn-Sn}, as given in

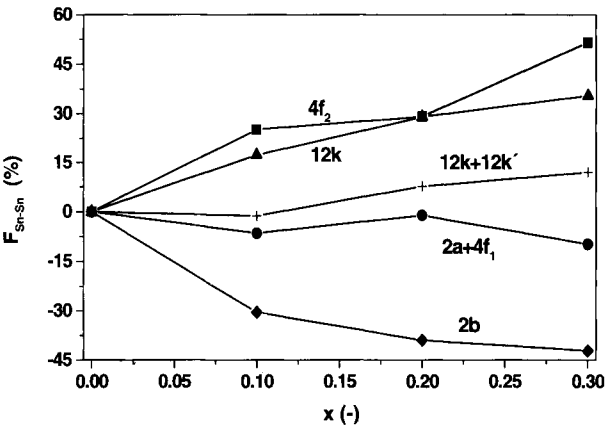

Figure 6 Factor of occupancy of F_{Sn-Sn} vs x for the BaM_{Sn-Sn} (Mx) samples.

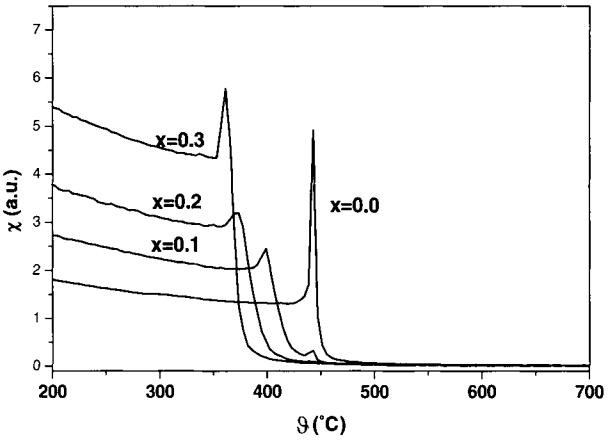

Figure 7 Temperature dependence of $\chi(\vartheta)$ for BaM_{Sn-Sn} (Mx) samples.

Figure 6. The measured temperature dependencies of magnetic susceptibility $\chi(\vartheta)$ depicted in Figure 7 exhibit rather sharp Hopkinson maximum, especially for the substitution measure up to of x=0.3. On the basis of analysis of Mössbauer spectra of BaM_{Zn-Sn} ferrites it can be assumed, that the Sn^{4+} ions enter preferably into bipyramidal site of 2b and $4f_2$ and into the spinel block of $2a+4f_1$, while the Zn^{2+} ions preferably enter into $4f_1$ site. In given combination of substituents, the Zn^{2+} ions can enter also into $4f_2$ site, due to their larger ionic diameter (0.074 nm), as compared with Sn^{4+} ions. The preferences in entering of particular ions into various sites is confirmed by the occupancy factor F_{Zn-Sn}, (Figure 8), where the substitution manifests itself most expressively especially in 2b site, but in the $4f_2$ site as well. The values of the Curie temperature T_c determined from $\chi(\vartheta)$, (Figure 9) decrease as a function of x. It can be explained by the substitution of the Fe^{3+} ions by the nonmagnetic Zn^{2+}, Sn^{4+} ions.

The experimental values of saturation and remnant mass magnetic polarisations (J_{s-m}, J_{s-r}), and of coercivity H_c and of $\Delta H_c/\Delta\vartheta$ for the samples of Ni–Sn, Sn–Sn and Zn–Sn substituted BaM samples are collected and given in Table I. It is obvious, that the maximum value of J_{s-m} for samples of BaM_{Ni-Sn} (Sk) and BaM_{Ni-Sn} (Mx) is reached at substitution value of x=0.2. Increasing of the values of J_{s-m} for BaM_{Sn-Sn} (Mx) sample within the whole substitution range, up to x=0.3, can be connected with the preference in the

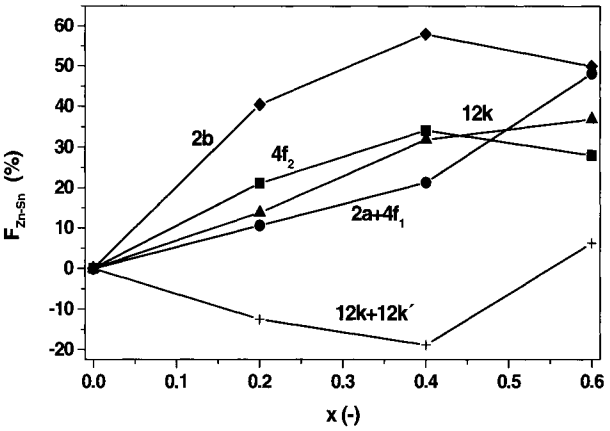

Figure 8 Factor of occupancy of F_{Zn-Sn} vs x for BaM_{Zn-Sn} (Sk) samples.

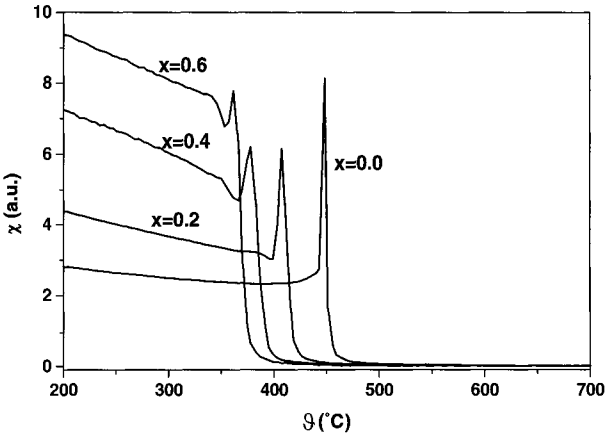

Figure 9 Temperature dependence of $\chi(\vartheta)$ for BaM_{Zn-Sn} (Sk) samples.

substituting of Sn^{2+} and Sn^{4+} ions into $4f_1$ and $4f_2$ sites, which are characteristic with inverted orientation of spins of Fe^{3+} ions with respect to other sites. Enhancing of values of J_{s-m} within the whole substitution range up to x=0.6 can be seen also for M_{Zn-Sn} (Sk) samples. The values of mass remnant magnetic polarisation J_{s-r} for BaM_{Ni-Sn} (Sk), BaM_{Ni-Sn} (Mx), BaM_{Sn-Sn} (Mx) and BaM_{Zn-Sn} (Sk) samples reach maxima already at substitution level of x=0.1. The existence of these maxima is presumably caused by the substitution of the nonmagnetic Sn^{4+} ions and Zn^{2+} ions into $4f_1$ site and by Sn^{2+} ions and the less-magnetic Ni^{2+} ions into $4f_2$ sites. The value of coercivity H_c decreases very rapidly to the value of 100 kA/m for the BaM_{Ni-Sn} (Mx) sample at x=0.3. This drop could be a consequence of magnetic anisotropy A_a and the presence of the secondary phase. The expressive drop in value of coercivity H_c for the BaM_{Sn-Sn} samples can by connected with the decreasing of value of the A_a. The substitution of Fe^{3+} ions in the 2b bipyramidal sites has the largest contribution to the anisotropy [9]. The most expressive change of coercivity H_c has been observed for the BaM_{Zn-Sn} (Sk) samples, where the value of coercivity H_c decreased from 330 kA/m down to 78 kA/m at x=0.6. Drop in values of $\Delta H_c/\Delta\vartheta$ with rising measure x of substitution has been measured according to [11] and it manifested itself for all measured BaM_{Ni-Sn}, BaM_{Sn-Sn} and BaM_{Zn-Sn} samples.

Table I Measured magnetic parameters of Ni–Sn, Sn–Sn and Zn–Sn substituted BaM samples

Sk					Mx				
x (–)	J_{s-m} ($10^{-6}Tm^3$ kg^{-1})	J_{s-r} ($10^{-6}Tm^3$ kg^{-1})	H_c (kA/m)	$\Delta H_c/\Delta\vartheta$ (kA/m °C)	x (–)	J_{s-m} ($10^{-6}Tm^3$ kg^{-1})	J_{s-r} ($10^{-6}Tm^3$ kg^{-1})	H_c (kA/m)	$\Delta H_c/\Delta\vartheta$ (kA/m °C)
Ni–Sn					Ni–Sn				
0.0	73.64	39.12	330	0.59	0.0	80.77	42.91	350	0.39
0.1	78.22	42.42	302	0.48	0.1	80.21	41.21	220	0.27
0.2	84.04	39.33	189	0.28	0.2	84.48	40.92	153	0.25
0.3	80.10	37.01	146	0.22	0.3	83.59	36.27	100	0.24
Zn–Sn					Sn–Sn				
0.0	73.60	39.10	330	0.59	0.0	80.77	42.91	350	0.39
0.2	86.90	42.58	202	0.38	0.1	88.75	43.74	236	0.34
0.4	87.80	38.51	120	0.31	0.2	88.81	40.89	161	0.32
0.6	90.78	32.34	78	0.24	0.3	89.77	35.36	93	0.22

4 Conclusions

We succeeded to synthesize Sn–Sn and/or Ni–Sn substituted barium hexaferrites by mechanical milling (Mx). The maximum mass magnetic polarisation J_{s-m} was increased slightly by ~9% for small levels of substitution of Sn–Sn and by ~3% for small levels of substitution of Ni–Sn. The increment of J_{s-m} was presumably due to the Sn^{4+} cations substituted Fe^{3+}, mainly on the bipyramidal 2b and partially on tetrahedral $4f_1$ site, whilst the Sn^{2+} ions preferably occupy the octahedral $4f_2$ and 2a sites. The expressive drop of H_c (fall of ~73%), as x increased was related to reduction of the magneto-crystalline anisotropy, due to the replacement of iron ions in bipyramidal sites. The measurements of magnetic susceptibility showed that with increasing of value of x, mass susceptibility χ increased, which is believed to be related to the disappearance of some of superexchange interactions. The diminution of T_c (drop of ~21%) demonstrates the gradual weakening of magnetic ordering. It was possible to synthesize Ni–Sn and/or Zn–Sn substituted Ba hexaferrites by citrate precursor method (Sk) while changing the substitution level of x. The coercivity H_c could be easily controlled without a significant reduction of the J_{s-m} value. The Sn^{4+} cations substitute Fe^{3+} ions mainly in the bipyramidal 2b and partially in tetrahedral $4f_1$ sites, whilst the Ni^{2+} ions prefer the octahedral $4f_2$ and $2a+4f_1$ sites at low and high as well substitution rates, respectively. Zn^{2+} ions strongly prefer the $4f_1$ sites. The 12k site splits into two sublattices of 12k and of 12k′, with the substitution of different ions. This may be a result of changes of the neighbours of the Fe^{3+} ions in the 12k site, when the substitutions take place in hexagonal blocks. The value of J_{s-m} reached a maximum at the value of $x=0.2$, as a consequence of substitution of the Sn^{4+} ions into the $4f_1$ and of less-magnetic ions of Ni^{2+} into the $4f_2$ sites, respectively. The lower value of temperature coefficient of coercivity of $\Delta H_c/\Delta\vartheta=0.22$ kA/m°C has been achieved in this case. The Zn^{2+}–Sn^{4+} substitution in the BaM ferrite results in a considerable diminution of particle size and decreasing of value of coercivity down to 78 kA/m at $x=0.6$, while the J_{s-m} values remain almost constant. Obtained results of samples with Sn^{2+}–Sn^{4+} substitution in the BaM ferrite, prepared by mechanical milling (Mx) show, that such materials can be useful for magnetic recording. The Ni^{2+}–Sn^{4+} substitution in BaM ferrite (Mx) has shown similar affecting the magnetic properties of samples as Sn^{2+}–Sn^{4+} substitution, at low measure of substitution of $x=0.3$. For the samples with the Ni^{2+}–Sn^{4+} and Zn^{2+}–Sn^{4+} substitutions into

BaM ferrite, prepared by the precursor method (Sk), similar magnetic properties can be achieved up to value of $x=0.3$, without the presence of the undesired phase, which was, on the other hand, observed in samples of BaM_{Ni-Sn} (Mx).

Acknowledgment We would like to thank to CONACyT – México for the support given to the project J28283U and to VEGA – Slovakia for the support of the projects no. G-1/3096/06 and G-1/3189/06, respectively. Many thanks belong to Ing. Tóth and Dr Dosoudil, for performing the Mössbauer and the B-H measurements, respectively, and to Dr Kevická for the preparation of samples.

References

1. Teh, G.B., et al.: J. Solid State Chem. **167**, 254 (2002)
2. Mendoza-Suárez, G., et al.: Mater. Res. Bull. **36**, 2597 (2001)
3. Li, Z.W., et al.: Phys. Rev. B, **62**(10), 6530 (2000)
4. Mendoza-Suárez, G., et al.: J. Magn. Magn. Mater. **234**, 73 (2001)
5. Wartewig, P., et al.: J. Magn. Magn. Mater. **193**, 83 (1999)
6. Turilli, G., Licci, L.: IEEE Trans. Magn. **24**(4), 2146 (1988)
7. Han, D.H., et al.: J. Magn. Magn. Mater. **137**, 191 (1994)
8. González-Angeles, A., et al.: J. Magn. Magn. Mater. **270**, 77 (2004)
9. González-Angeles, A., et al.,: Mater. Lett. **58**, 2906 (2004)
10. Grusková, A., et al.: Hyperfine Interact. **156–157**, 187 (2004)
11. Sláma, J., et al.: J. Magn. Magn. Mater. **272–276**, 385, (2004)

Hyperfine Interact (2006) 169:1231–1234
DOI 10.1007/s10751-006-9429-8

Mössbauer studies of the re-entrant spin-glass behaviour of Fe–Al alloys

D. Martín Rodríguez · F. Plazaola · J. S. Garitaonandia

Published online: 12 December 2006

Abstract Fe–Al alloys around the concentration of 30 at. % Al present re-entrant spin-glass behaviour at low temperatures. This behaviour is not completely understood and Mössbauer spectroscopy, combined with other experimental techniques, is useful to describe and explain this behaviour. Results show that the Mössbauer spectra coincide with the magnetic behaviour showed in literature and they can be explained as a magnetic cluster system whose magnetic clusters are getting smaller when the temperature is decreasing. When the temperature is reaching to the spin-glass transition at 92 K the spins in the paramagnetic matrix are moving slower and below this transition the spins are completely frozen.

Key words Mössbauer spectroscopy · spin-glass behaviour · magnetic cluster system

$Fe_{70}Al_{30}$ alloy presents an interesting magnetic behaviour. First, Cable et al. [1] showed the presence of magnetic clusters in this alloy using diffuse neutron scattering. The origin of these clusters was explained using the local environment effect. According to this work, the clusters are formed by Fe atoms with four or more Fe atoms as nearest neighbours, which have a larger magnetic moment than those with less than four Fe atoms as nearest neighbours. The reported cluster size had a mean diameter of 25 Å.

Alloys around 30 at. % Al also show re-entrant spin-glass behaviour at low temperature, when the spin-glass phase comes from a ferromagnetic phase. There are various models explaining the re-entrant spin-glass behaviour, e.g., the random field model proposed by Aeppli et al. [2]. In this model the ferromagnetic order

D. Martín Rodríguez · F. Plazaola
Elektrika eta Elektronika Saila, Universidad del País Vasco-Euskal Herriko Unibertsitatea,
644 P. K., 48080 Bilbao, Spain

J. S. Garitaonandia (✉)
Fisika Aplikatua II Saila, Universidad del País Vasco-Euskal Herriko Unibertsitatea,
48080 Bilbao, Spain
e-mail: garita@we.lc.ehu.es

weakens due to a random field, causing the formation of magnetic clusters until the ferromagnetic order disappears. Motoya et al. [3] showed that this model is the one that fits best for $Fe_{70}Al_{30}$ re-entrant spin-glass alloy. Mitsuda et al. [4] also observed the same fact using neutron depolarization technique.

Mössbauer spectroscopy, combined with other experimental techniques is very useful to describe and understand the re-entrant spin-glass behaviour in these alloys. However, there are few Mössbauer spectroscopy studies in these alloys [5, 6]. In this work Mössbauer spectroscopy was used at various temperatures in order to have a better insight of the re-entrant spin-glass phenomenon.

Alloy with 30 at. % Al was prepared by induction melting and cast into ingots in an Ar atmosphere; then a powder was obtained by mechanical crushing until the particles reach a mean diameter of 5 μm. In order to obtain D03 long range order, a long time heat treatment was applied. Powders were annealed at about 1,200 K for 2 h in order to homogenize them. After, they were cooled down at a rate of 20 K/h up to 825 K and from this temperature down to 625 K they were cooled at a rate of 1 K/h. Finally they were left to cool down to room temperature (RT).

^{57}Fe Mössbauer spectroscopy measurements were carried out for these powders at room temperature in transmission geometry using a conventional spectrometer with a ^{57}Co–Rh source. Fittings with the obtained spectra were performed with NORMOS program developed by Brand et al. [7]. For the fittings a continuous hyperfine field distribution was used. In the fitting procedure we considered that the quadrupole splitting is zero due to the cubic symmetry of the crystalline structure of the sample.

Figure 1 shows Mössbauer spectra taken at different temperatures and their corresponding hyperfine field distributions. At RT the Mössbauer spectrum shows an important nonmagnetic contribution together with a broad magnetic contribution. When temperature decreases the magnetic contribution becomes smaller and between 150–200 K the magnetic contribution disappears almost completely. However, the spectrum at about 100 K shows that the broad magnetic contribution appears again and in the spectrum at 77 K a discrete sextet starts to appear.

Hyperfine field distributions show two peaks at low magnetic fields (around 2 and 10–15 T). Evidently, the peak located at about 2 T must correspond to the nonmagnetic contribution while the other one at about 10–15 T must correspond to the broad magnetic contribution. The contribution at 10 T decreases as the temperature decreases while the contribution at 2 T increases. The broad magnetic contribution never disappears completely and between 100 and 150 K starts to increase again. The hyperfine field distribution of the Mössbauer spectrum at 77 K is completely different. The contribution at 2 T is much smaller than in the other spectra and new magnetic contributions at higher hyperfine fields (20 and 25 T) are present.

According to the work by Shull et al. [8], the magnetic behaviour of $Fe_{70}Al_{30}$ alloy at low temperatures shows two transition temperatures. The first one is at about 170 K, when the magnetic susceptibility starts to decrease. Shull et al. [8] called it inverse Curie temperature (T_c^{inv}) and assign it to a phase transition from ferromagnetic to superparamagnetic-like one. The second phase transition occurs at about 90 K, the freezing temperature (T_f), and corresponds to the spin-glass transition. At this temperature, spins start to freeze without any long range order.

The magnetic state of the $Fe_{70}Al_{30}$ can be explained as a magnetic cluster structure in a paramagnetic matrix [1]. Clusters' trend is to decrease in size with temperature

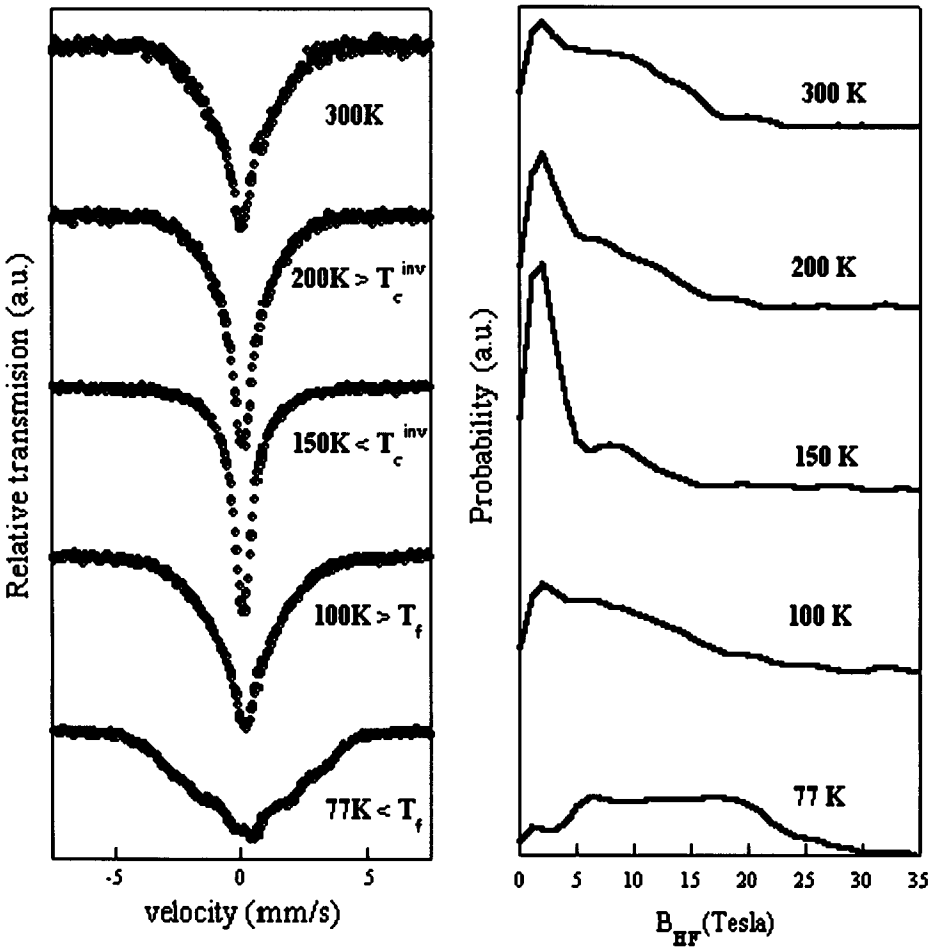

Figure 1 Mössbauer spectra of $Fe_{70}Al_{30}$ sample at selected temperatures and their corresponding hyperfine field distribution.

decrease. As the clusters are getting smaller, some of then are so small that start to behave superparamagnetically. The fraction of those superparamagnetic clusters increases as indicated by the increase of the nonmagnetic contribution and the decrease of the broad magnetic contribution. However, between 100–150 K the broad magnetic contribution increases while the nonmagnetic one decreases. This fact seems contradictory taking into account that the magnetization is still decreasing [8].

Spin-glasses have a short-range magnetic coupling between spins creating some kind of magnetic clusters that do not have to be fully ferromagnetic entities [9]. When the temperature is reaching to T_f the freezing of this kind of clusters makes the appearance of magnetic contributions. The results indicate that the freezing starts at higher temperatures than T_f. Canonical spin-glasses as Au–Fe diluted alloys also present the same behaviour [10] in which the freezing represents the appearance of magnetic contributions. When the temperature reaches T_f the magnetic contributions are greater and sextet-like features start to appear. This could be due to the

freezing of spins in paramagnetic matrix, but it could also be due to magnetic clusters not behaving superparamagnetically. However, Mössbauer spectroscopy do not distinguish those two facts, so it is needed to use another experimental techniques.

Finally, below T_f, and according to the random field theory [2], it is expected that the ferromagnetic clusters are getting smaller with decreasing temperature until they disappear.

The magnetic state of this alloy is a magnetic cluster structure embedded in a paramagnetic matrix. When temperature is decreasing, the magnetic clusters also decrease in size. When T_c^{inv} is reached the clusters become so small that behave superparamagnetically and Mössbauer spectroscopy almost cannot detect those clusters. However, decreasing the temperature further (between 100–150K) the magnetic contribution in Mössbauer spectra starts to appear again although the magnetization is still decreasing. This is interpreted as the spin motion in paramagnetic matrix is getting slower than the Mössbauer characteristic sensing time and finally, when T_f is reached, the spins in paramagnetic matrix are completely frozen. However, it is impossible to distinguish by Mössbauer spectroscopy if the matrix is freezing or if the magnetic clusters are freezing too. Below T_f it is expected that there is a mixed ferromagnetic-spin glass state in which the magnetic clusters are getting smaller due to a random molecular field until they disappear.

Acknowledgement This work was undertaken under projects MAT2002-4087-C02-01 and UPV 224.310-14553/2002. D. M. R. wishes to thank UPV-EHU for the fellowship.

References

1. Cable, J.W., David, L., Parra, R.: Phys. Rev. B **16**, 1132–1137 (1977)
2. Aeppli, G., Shapiro, S.M., Birgeneau, R.J., Chen, H.S.: Phys. Rev. B **28**, 5160 (1983)
3. Motoya, K., Shapiro, S.M., Muraoka, Y.: Phys. Rev. B **28**, 6183 (1983)
4. Mitsuda, S., Yoshizawa, H., Endoh, Y.: Phys. Rev. B **45**, 9788 (1992)
5. Huffman, G.P.: J. Appl. Phys. **42**, 1606–1607 (1971)
6. Takahashi, S., Onodera, H., Li, X.G., Miura, S.: J. Phys. Condens. Matter **9**, 9235–9249 (1997)
7. Brand, R.A., Lauer, J., Herlach, D.M.: J. Phys. F. Met. Phys. **13**, 675 (1983)
8. Shull, R.D., Okamoto, H., Beck, P.A.: Metall. Trans. **20**, 863–868 (1976)
9. Mydosh, J.A.: Spin Glasses: An Experimental Introduction. Taylor & Francis, London pp. 86–88 (1993)
10. Violet, C.E., Borg, R.J.: Phys. Rev. **149**, 540–551 (1966)

Hyperfine Interact (2006) 169:1235–1240
DOI 10.1007/s10751-006-9430-2

Mössbauer study on the magnetic field-induced insulator-to-metal transition in perovskite $Eu_{0.6}Sr_{0.4}MnO_3$

Shin Nakamura · Masami Sato · Shotaro Morimoto · Saburo Nasu · Yorihiko Tsunoda

Published online: 5 December 2006

Abstract We have investigated the spin dynamics of a distorted perovskite $Eu_{0.6}Sr_{0.4}MnO_3$ by means of Mössbauer spectroscopy. Below 70 K the exchange interaction grows gradually, and below 42 K the spins turn into a cluster glass state. The magnetic field-induced insulator-to-metal (IM) transition at low temperature is a transition from cluster glass to ferromagnet. The induced metallic phase seems to be still in non-uniform electronic state. On the other hand, at 80 K, just above T_c of the induced ferromagnet, a metamagnetic transition was observed.

Key words $Eu_{0.6}Sr_{0.4}MnO_3$ · magnetic field-induced insulator-to-metal transition · cluster glass · ferromagnet · metamagnetic transition

1 Introduction

A distorted perovskite $Eu_{0.6}Sr_{0.4}MnO_3$ is an insulator down to 5 K [1] but it shows magnetic field-induced insulator-to-metal (IM) transition at low temperature [2, 3]. The

S. Nakamura (✉) · M. Sato
Department of Science and Engineering, Teikyo University, Utsunomiya 320-8551, Japan
e-mail: shin@koala.mse.teikyo-u.ac.jp

S. Nakamura
Advanced Research Institute of Science and Engineering,
Waseda University,
Shinjuku-ku Tokyo 169-8555, Japan

S. Morimoto · S. Nasu
Graduate School of Engineering Science, Osaka University, Toyonaka, Osaka 560-8531, Japan

S. Morimoto
Radioisotope Research Center, Osaka University, Toyonaka, Osaka 560-0043, Japan

Y. Tsunoda
School of Science and Engineering, Waseda University,
3-4-1 Ohkubo,
Shinjuku-ku, Tokyo 169-8555, Japan

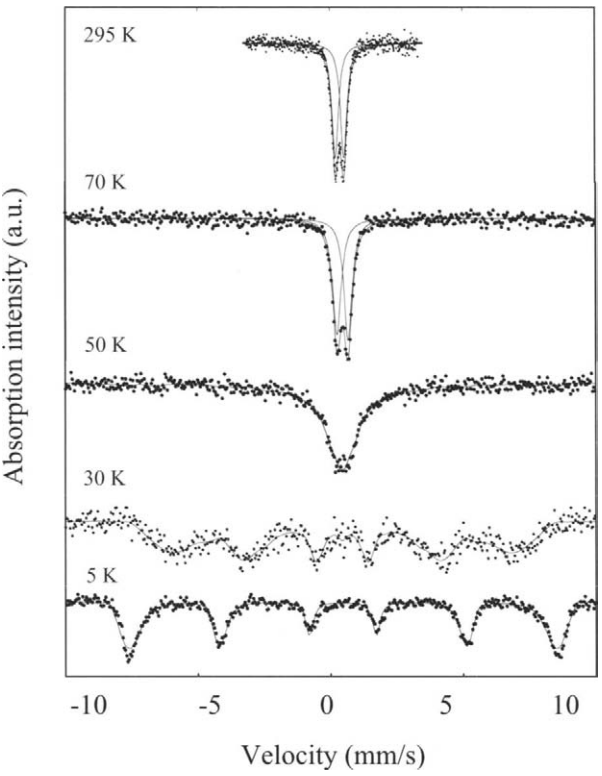

Figure 1 Mössbauer spectra of slightly ^{57}Fe-substituted $Eu_{0.6}Sr_{0.4}MnO_3$ specimen at several temperatures. The smooth curves for the sextet spectra are the result of $P(H_{hf})$ analysis.

transition field is about 2.1 T at 5 K. Once it has occured, the induced metallic and ferromagnetic state remains stable even in the absence of magnetic field, and is retained up to its Curie temperature (T_c) 75 K. There is no evidence in the resistivity (ρ) – temperature (T) curve that the charge order occurs. The IM transition is also accompanied by a transition from a low magnetization phase (1.1 μ_B) to a high magnetization phase (3.51 μ_B). The latter value is indicative of the ferromagnetic arrangement of Mn moments. In the insulator phase, the thermomagnetic curve in a weak magnetic field shows a cusp around 42 K (T_{cusp}) after being cooled without magnetic field (ZFC), while the curve shows a branching from the ZFC curve below T_{cusp} after being cooled with magnetic field (FC). This may be suggestive of a spin glass like state [2, 4]. On the other hand, above T_c, in the temperature range between 80 K and 160 K, a metamagnetic behavior is observed, which is also accompanied by a colossal magnetoresistence effect (CMR). The transition field is about 2 T at 80 K.

Synchrotron X-ray powder diffraction study [5, 6] also indicates that the charge order does not occur at low temperature. Both the insulator phase (in zero magnetic field) and the induced metal phase (in a magnetic field) have orthorhombic structure with the *Pnma* space group and thus, a change in the crystal symmetry does not occur through the IM transition. However, the lattice constants abruptly increase and the reflection intensities abruptly change through the IM transition, which suggests a rotation of the MnO_6 octahedron so as to increase Mn–O–Mn angles.

In order to further clarify the mechanism of the IM transition, an investigation on the spin dynamics is necessary. However, neutron scattering measurements could not be

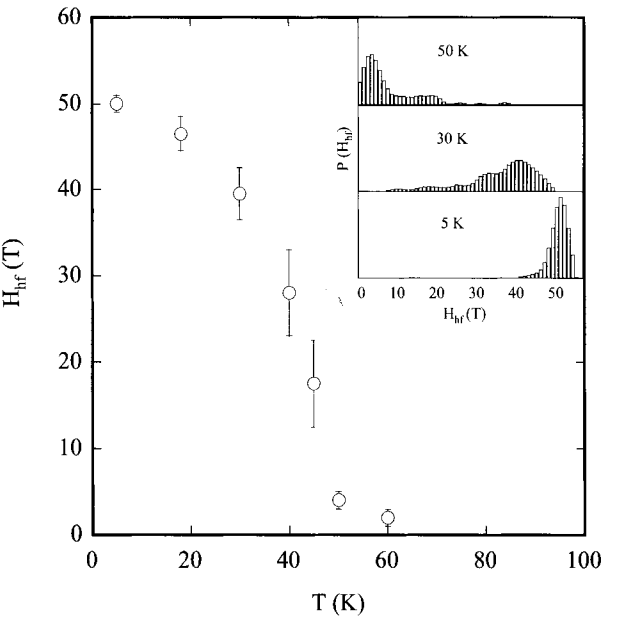

Figure 2 Temperature dependence of the average hyperfine field (H_{hf}). The insert indicates $P(H_{hf})$ at several temperatures.

correctly performed due to large absorption by Eu atoms. Here, we have applied ^{57}Fe Mössbauer spectroscopy to investigate the spin dynamics.

2 Experiments

A Slightly ^{57}Fe-substituted specimen (0.5% in Mn site) was used for the measurements. The specimen was prepared by using Eu_2O_3, $SrCO_3$, MnO_2, and $^{57}Fe_2O_3$ powders as starting materials. These powders were mixed, pressed into disks, and fired at 1,673 K for 12 hrs in air. The crystal structure is the same as the pure one, i.e., orthorhombic (*Pnma*) with a=5.438(5) Å, b=7.663(6) Å, and c=5.428(4) Å at room temperature. The magneto-transport properties were also confirmed to be almost identical to those of the pure one: transition field at 5 K, saturation magnetic moment at 5 K, and Curie temperature of the induced ferromagnetic phase are about 2.6 T, 3.52 μ_B, and 75 K, respectively. The resistivity of the induced metallic phase is several 10 Ωcm at 5 K. It is worth noting that further Fe-substitution drastically changes the magnetotransport properties, which indicates that the substitution significantly affects the electronic state of Mn ions.

Mössbauer spectra were obtained with usual transmission geometry by using ^{57}Co-in-Rh as the γ-ray source. The spectra in a magnetic field (up to 7 T) were also measured. The direction of the applied magnetic field was parallel to the incident γ-ray direction. Doppler velocity was calibrated with respect to Fe-metal foil. Lorentzian line shapes were assumed for the spectra analysis.

3 Results and discussions

In Figure 1, the Mössbauer spectra at several temperatures are shown. The room temperature values of isomer shift and quadrupole splitting are 0.364 mm/s and 0.322 mm/s,

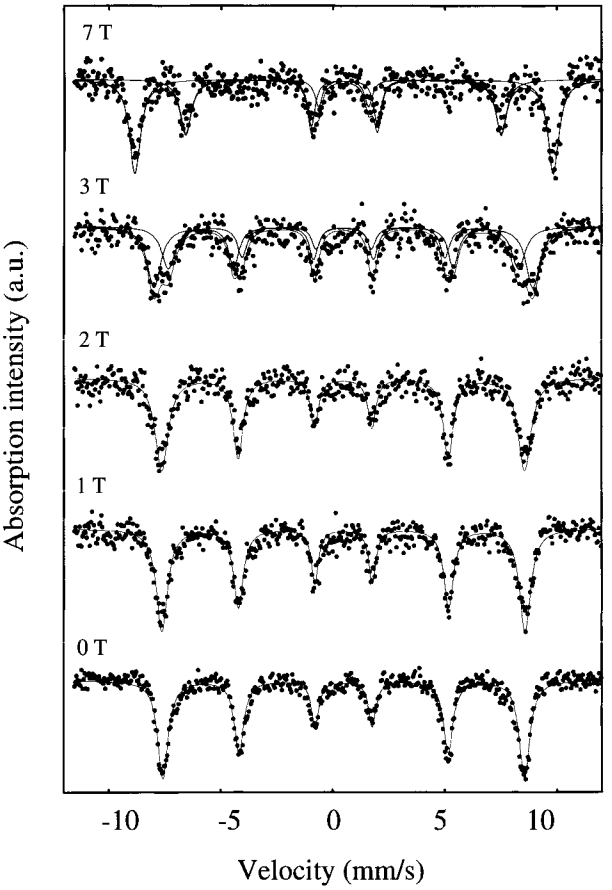

Figure 3 Mössbauer spectra in a magnetic field at 5 K. Simple Lorentzian line shape is tentatively used for the fitting.

respectively, indicating that ^{57}Fe ions are in 3+ states and successfully substituted in the Mn site. Thus we assume that the magnetic behavior of the $^{57}Fe^{3+}$ spins well represents that of Mn ion spins. Below 70 K, the absorption lines become noticeably broader. The hyperfine field is easily observed below 60 K. It grows slowly with decreasing temperature and then increases rather abruptly below around 45 K (just above T_{cusp}). Since the absorption lines of the sextet spectra are rather broad, the spectra were analyzed by a distribution of hyperfine field (Hesse method). The spectra can be well fitted assuming constant isomer shift and no quadrupole shift at each temperature. Temperature dependence of the average hyperfine field, estimated from its distribution $P(H_{hf})$, is shown in Figure 2. The insert shows $P(H_{hf})$ at several temperatures. The average hyperfine field and the isomer shift at 5 K are 50.3 T and 0.49 mm/s, respectively. The absence of the quadrupole shift in the sextet spectra may suggest that the angle between the magnetic moment and the principal axis of EFG is random.

The spectral change against applied magnetic field at 5 K is shown in Figure 3. Here, simple Lorentzian line shape is tentatively used for the fitting. In the insulating state ($H_{ex}<$ 2.6 T), the application of magnetic field broadens the absorption lines only, and does not change the absorption intensity of the 2- and 5-lines (3:2:1:1:2:3). Taking also into account that the quadrupole shift is absent, we conclude that the spins of the insulator phase are in a cluster glass state below 42 K (T_{cusp}). At H_{ex}=3 T, just above the transition field, the

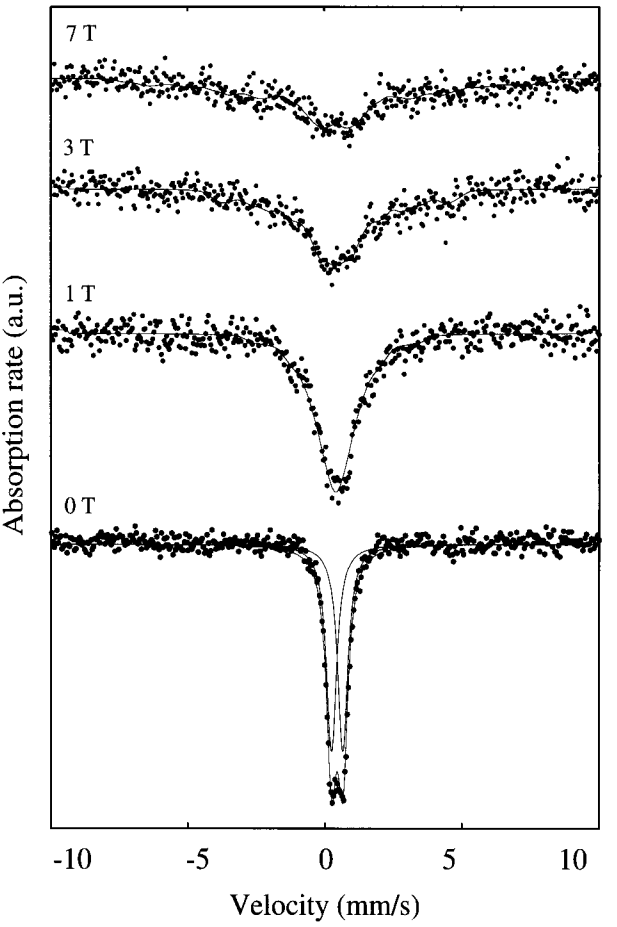

Figure 4 Mössbauer spectra in a magnetic field at 80 K. The smooth curves are the result of $P(H_{hf})$ analysis.

spectrum breaks down into two subspectra and the absorption intensity of the 2- and 5-lines decreases (3:1.5:1:1:1.5:3). The intensity ratio of the two subspectra is about 3:2. In the fully metallic state at H_{ex}=7 T, the two subspectra correctly break down and their 2- and 5-lines disappear. These subspectra correspond to the Fe^{3+} moments aligning antiparallel (observed field H_{obs}=58.0 T) and parallel (H_{obs}=43.7 T) to the external magnetic field, respectively. Bearing in mind that all Mn moments align parallel to the magnetic field and Fe^{3+} spins do not contribute to the double exchange interaction, we consider that there are two types of clusters (or regions) which have different superexchange interactions, or electron densities. Such non-uniform electronic state may be responsible for the rather high resistivity (several Ωcm at 5 K) of the induced metal phase.

The spectral change against applied magnetic field at 80 K is shown in Figure 4. The spectrum is noticeably broadened by the applied magnetic field, and at H_{ex}=7 T a hyperfine sextet is clearly observed. Moreover, by hyperfine field distribution analysis, H_{hf} is proved to range from 5 T to 40 T at H_{ex}=7 T. This indicates that the ferromagnetic state is induced by the applied magnetic field. Thus we can observe the metamagnetic transition at 80 K by Mössbauer effect.

In summary, the spins of $Eu_{0.6}Sr_{0.4}MnO_3$ are in a cluster glass state below 42 K. The IM transition at low temperature is a transition from cluster glass to ferromagnet. The induced

metal phase seems to be still in non-uniform electronic state. The metamagnetic transition just above T_c is also observed.

Acknowledgement This work is partly supported by the Foundation of Eno Science, Japan.

References

1. Tadokoro, Y., Shan, Y.J., Nakamura, T., Nakamura, S.: Solid State Ion. **108**, 261 (1998)
2. Sundaresan, A., Maignan, A., Raveau, B.: Phys. Rev. B **55**, 5596 (1997)
3. Nakamura, S., Tadokoro, Y., Shan, Y.J., Nakamura, T.: J. Phys. Soc. Jpn. **68**, 1485 (1999)
4. Eto, T., Oomi, G., Sampathkumaran, E.V., Sundaresan, A., Kosaka, M., Uwatoko, Y.: Physica. B **294–295**, 111 (2001)
5. Nakamura, S., Shimomura, S., Ikeda, N., Mizumaki, M., Ohsumi, H., Nimori, S., Takeuchi, T., Itoh, K.: J. Magn. Magn. Mater. **272–276**, 424 (2004)
6. Nakamura, S., Shimomura, S., Ikeda, N., Nimori, S., Takeuchi, T., Itoh, K.: J. Phys. Soc. Jpn. **73**, 3059–3063 (2004)

Hyperfine Interact (2006) 169:1241–1246
DOI 10.1007/s10751-006-9431-1

^{57}Fe and ^{151}Eu Mössbauer studies of magnetoresistive Europium based cobalt perovskites

Z. Németh · E. Kuzmann · A. Vértes · Z. Homonnay · Z. Klencsár · J. M. Grenèche · J. Hakl · K. Vad · S. Mészáros · B. Lackner · K. Kellner · G. Gritzner

Published online: 14 December 2006

Abstract $Eu_{0.8}Sr_{0.2}Fe_xCo_{1-x}O_{3-z}$ CMR perovskites with different iron concentrations (x= 0, 0.025, 0.075, 0.15, 0.3) were investigated by X-ray diffraction, AC magnetic susceptibility, magnetotransport, as well as ^{57}Fe and ^{151}Eu Mössbauer spectrometry. The valence state of europium ions was found to be trivalent, independently of the iron concentration. ^{57}Fe Mössbauer spectra and magnetic susceptibility of the investigated perovskites presented complementary results for the magnetic transitions.

Key words magnetoresistance · perovskite · doped transition metal compounds · Mössbauer spectrometry

1 Introduction

Colossal magnetoresistance (CMR), a promising key mechanism for the new generation of magnetic storage devices and magnetic sensors was found and extensively investigated in the

Z. Németh (✉) · A. Vértes · Z. Homonnay · Z. Klencsár
Department of Nuclear Chemistry, Eötvös Loránd University, 1518 Budapest, Hungary
e-mail: hentes@ludens.elte.hu

E. Kuzmann
Research Group for Nuclear Methods in Structural Chemistry, Hungarian Academy of Sciences, 1518 Budapest, Hungary

J. M. Grenèche
Laboratoire de Physique de l'Etat Condensé, UMR CNRS 6087 Université du Maine, 72085 Le Mans Cedex 9, France

J. Hakl · K. Vad · S. Mészáros
Institute of Nuclear Research of the Hungarian Academy of Sciences, 4001 Debrecen POB 51, Hungary

B. Lackner · K. Kellner · G. Gritzner
Institute for Chemical Technology of Inorganic Materials, Johannes Kepler University, Altenbergerstraße 69, 4040 Linz, Austria

last decade e.g., in several chalcogenide spinels, double perovskites and doped perovskite oxides. Examples for the latter family of compounds include $La_{0.67}Ca_{0.33}MnO_{3-z}$ manganate perovskites, in which the CMR effect was observed [1], and $La_{0.8}Sr_{0.2}CoO_{3-z}$ cobaltate perovskites, which showed high magnetoresistance not only around the Curie temperature, but the magnitude of their MR at low temperatures (below about 50 K) was also found to be colossal [2]. Moreover, mixing the different cations (i.e., cobalt, iron, manganese) at the transition metal site of these perovskite systems significantly altered the magnitude as well as the temperature at which magnetoresistance appeared (see e.g., [3] or [4]).

Recently it was suggested that the key mechanism of the colossal magnetoresistance around the magnetic transition temperature is the formation of nano-scale metallic and superparamagnetic clusters surrounded by an insulating and paramagnetic matrix (see e.g., [5, 6]). According to this theory, the size of the clusters and the intercluster magnetic interaction can be altered by an external magnetic field, thus resulting in the colossal change of electric resistance [5]. The effect of doping the transition metal site in the perovskite structure seems to play the dominating role in the formation of these clusters. However, the effect of rare earth site doping has not yet been investigated. Moreover, the observed low temperature magnetoresistance was attributed, on the basis of ^{57}Fe Mössbauer spectrometry [7], to the appearance of a spin cluster glass phase.

In the present work we report the results of magnetic transport, AC magnetic susceptibility, as well as ^{151}Eu and ^{57}Fe Mössbauer investigations on a novel family of cobalt perovskites: $Eu_{0.8}Sr_{0.2}Fe_xCo_{1-x}O_{3-z}$ (x=0, 0.025, 0.075, 0.15, 0.3), and we compare the present results with the properties of the analogous $La_{0.8}Sr_{0.2}Fe_xCo_{1-x}O_{3-z}$ ($0 \le x \le 0.3$) CMR perovskites [7, 10].

2 Experimental

The $Eu_{0.8}Sr_{0.2}CoO_{3-z}$ sample was the same as investigated in [8]. The $Eu_{0.8}Sr_{0.2}Fe_xCo_{1-x}O_{3-z}$ (x=0.025, 0.075, 0.15, 0.3) samples were prepared as follows: The respective amounts of Eu_2O_3, $SrCO_3$, Fe_2O_3 and Co_3O_4 were milled in a suspension of 2-propanol with zirconium dioxide balls (diameter 2 mm) in a planetary mill for 120 min. After removing the zirconium dioxide balls by a sieve the suspension was centrifuged and the 2-propanol was decanted. The remaining mixture was dried for 2 h at 150°C and then calcined in an alumina crucible at 800°C for 24 h. The product was then ground in an agate mortar. Into discs of a diameter of 10 mm, 0.4 g of the material was compacted at 750 MPa. The samples were sintered for 24 h at 1,100°C in air. Heating and cooling rates were 5 K min^{-1}. The phase purity was checked by X-ray diffractometry.

The temperature dependence of the real part of AC magnetic susceptibility (χ') of the $Eu_{0.8}Sr_{0.2}Fe_xCo_{1-x}O_{3-z}$ samples was measured at frequencies of 133 Hz, 1 kHz and 10 kHz using an AC magnetic field of 365 A/m in the temperature range of 7–250 K. Magnetotransport measurements were performed by the standard four point contact method.

^{57}Fe and ^{151}Eu Mössbauer measurements were carried out on powdered samples in transmission geometry. The low temperature ^{57}Fe Mössbauer spectra were recorded as a function of temperature in the range of 4.2 to 300 K. The samples were cooled down in a temperature controlled flow-through type liquid nitrogen cryostat (Leybold), and in a temperature controlled helium bath cryostat (Oxford). The γ-rays were provided by a ^{57}Co(Rh) source with 10^9 Bq activity and a $^{151}SmF_3$ source with 10^9 Bq activity. In the case of the spectrum of $Eu_{0.8}Sr_{0.2}Fe_xCo_{1-x}O_{3-z}$ taken at 40 K, the ^{57}Co(Rh) source was cooled to the

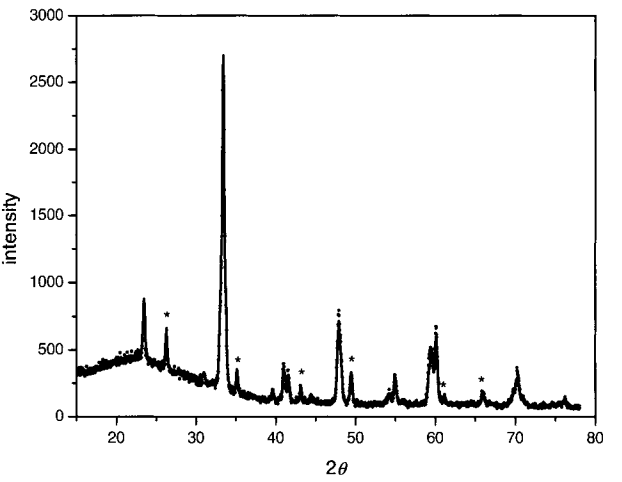

Figure 1 X-ray diffraction pattern of $Eu_{0.8}Sr_{0.2}Fe_{0.3}Co_{0.7}O_{3-z}$. The *hump* of the baseline between 15 and 40° occurred due to glass substrate during recording. The peaks marked with an *asterisk* do not appear in the X-ray diffractogram of the analogous $La_{0.8}Sr_{0.2}Fe_xCo_{1-x}O_{3-z}$ ($0 \leq x \leq 0.3$) perovskites.

same temperature. In all other experiments the source was maintained at room temperature. ^{57}Fe and ^{151}Eu isomer shift values are given relative to α-iron and EuF_3 at room temperature, respectively. Mössbauer spectra were analyzed with version 3.0 of the MossWinn program [9].

3 Results and discussion

Figure 1 shows a typical X-ray diffractogram of the produced $Eu_{0.8}Sr_{0.2}Fe_xCo_{1-x}O_{3-z}$ perovskites. Independently of the iron concentration x the relative intensities and the angles of the diffraction peaks were found to be quite similar. On the other hand, comparing the X-ray diffractogram of the $Eu_{0.8}Sr_{0.2}Fe_xCo_{1-x}O_{3-z}$ ($0 \leq x \leq 0.3$) family of compounds with those of the analogous $La_{0.8}Sr_{0.2}Fe_xCo_{1-x}O_{3-z}$ ($0 \leq x \leq 0.3$) perovskites [3, 7], a tendentious difference can be observed. Namely, in the case of the europium based perovskites some new peaks (marked with asterisks in Figure 1) appeared in the X-ray diffractogram but were absent in the lanthanum based perovskites. As the X-ray pattern of the investigated materials is not yet published in common databases, the origin of these new peaks is not clear yet. Thus, either the existence of a minor by-product in each sample or a change of the crystal structure due to the La–Eu exchange cannot be excluded. Further investigations are necessary to clarify this difference.

The AC magnetic susceptibility results are displayed in Figure 2b. The iron-free $Eu_{0.8}Sr_{0.2}CoO_{3-z}$ perovskite shows a narrow peak at around 96 K with a slightly broader left wing showing spin glass like behaviour below 96 K, and a small peak at 117 K. Samples with an iron stoichiometry of ≥0.025 shifted the susceptibility peaks to higher temperatures (e.g., the temperature of the main peak is $T_{peak} \cong 130$ K for $x=0.025$), but the further increase of x from 0.075 to 0.3 led to a decrease of T_{peak} and disappearance of the minor peak. Although the relation of decreasing magnetic transition temperature (here marked as T_{peak}) with increasing iron content may also be observed in the case of the analogous lanthanum based perovskites, the $La_{0.8}Sr_{0.2}CoO_{3-z}$ sample showed higher characteristic magnetic transition temperatures than its iron doped derivatives. This behaviour is in contrast with the present case of the analogous europium based perovskites. Moreover, in the case of the $Eu_{0.8}Sr_{0.2}Fe_xCo_{1-x}O_{3-z}$ ($x=0.075$, 0.15, 0.3) perovskites, only

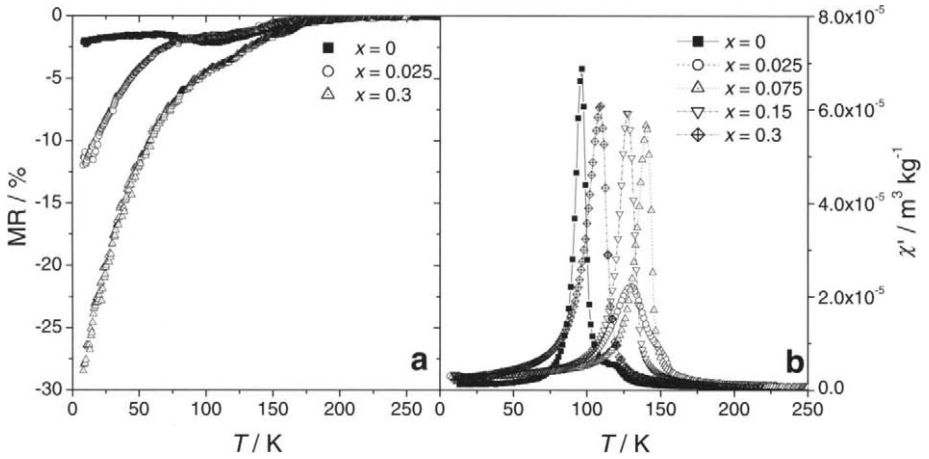

Figure 2 Magnetoresistance (**a**) and real part of the AC magnetic susceptibility recorded at 1 kHz (**b**) of $Eu_{0.8}Sr_{0.2}Fe_xCo_{1-x}O_{3-z}$ ($0 \le x \le 0.3$).

one magnetic transition can be observed in the AC magnetic susceptibility data, while $La_{0.8}Sr_{0.2}Fe_xCo_{1-x}O_{3-z}$ ($0 \le x \le 0.3$) showed two transitions [7, 10]. The reason for the different magnetic properties of the europium based cobalt perovskites is still unclear and needs further research.

The investigated $Eu_{0.8}Sr_{0.2}Fe_xCo_{1-x}O_{3-z}$ (x=0, 0.025, 0.3) perovskites showed strong magnetoresistance (MR, defined as $MR=(R_0-R_H)/R_0$, where R_0 is the resistance without external magnetic field, and R_H is the resistance in an applied external magnetic field, H), most pronounced in the low temperature regions, where MR decreases with decreasing temperature and increasing iron content (Figure 2a). Beside this MR, a smaller CMR peak around the magnetic transition temperature can also be observed. The temperature dependence of the magnetoresistance of the studied $Eu_{0.8}Sr_{0.2}Fe_xCo_{1-x}O_{3-z}$ perovskites is very similar to that of the lanthanum based analogous materials, but for a similar iron content the lanthanum based perovskites exhibit a higher negative MR than the europium based samples. For example, the lowest MR for $Eu_{0.8}Sr_{0.2}Fe_{0.3}Co_{0.7}O_{3-z}$ is about −30%, while for $La_{0.8}Sr_{0.2}Fe_{0.3}Co_{0.7}O_{3-z}$ it reaches about −80% [7, 10].

^{151}Eu Mössbauer spectrum of each $Eu_{0.8}Sr_{0.2}Fe_xCo_{1-x}O_{3-z}$ (x=0.025, 0.075, 0.15, 0.3) sample was adjusted with one quadrupole multiplet with 0.66 mm/s$\le\delta\le$0.69 mm/s, $-4.7\cdot10^{21}$ V/m$^2\le V_{zz}\le -4.3\cdot10^{21}$ V/m^2 and $0.54\le\eta\le0.69$, where δ is the isomer shift, V_{zz} is the component of the diagonalized electric field gradient with the highest absolute value, and η is the asymmetry parameter. A typical spectrum recorded at room temperature is displayed in Figure 3a. The above mentioned isomer shifts reveal that europium ions are exclusively in 3+ oxidation form. Moreover, the Mössbauer parameters of the examined europium ions did not exhibit a consistent dependency on the iron content, thus alteration of the transition metal network does not seem to affect the electronic structure of the ions in the rare earth site of the examined perovskite systems.

Room temperature ^{57}Fe Mössbauer spectra of the $Eu_{0.8}Sr_{0.2}Fe_xCo_{1-x}O_{3-z}$ (x=0.025, 0.075, 0.15, 0.3) samples show a broadened doublet with typical high-spin trivalent ^{57}Fe Mössbauer parameters. The isomer shift values (δ) are between 0.27 and 0.42 mm/s, while those of the quadrupole splitting (Δ) are between 0.28 and 0.40 mm/s. These values of the Mössbauer parameters are in accordance with those of the analogous lanthanum based

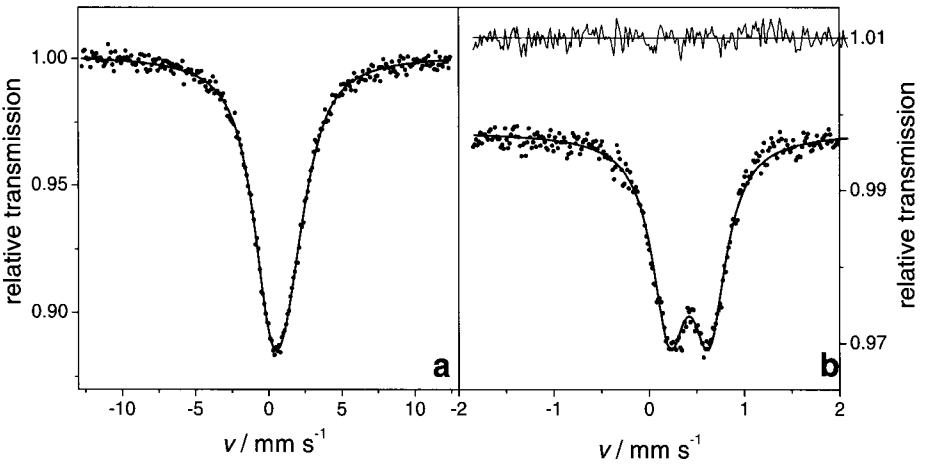

Figure 3 Room temperature ^{151}Eu Mössbauer spectrum (**a**) and ^{57}Fe Mössbauer spectrum recorded at 77 K (**b**) of $Eu_{0.8}Sr_{0.2}Fe_{0.3}Co_{0.7}O_{3-z}$. *Above* the *right* spectrum, the residual is displayed.

perovskites [7, 10], thus the change of the rare earth metal does not cause significant changes in the electronic state of the iron ions. A clear trend in the change of the ^{57}Fe Mössbauer parameters of the $Eu_{0.8}Sr_{0.2}Fe_xCo_{1-x}O_{3-z}$ (x=0.025, 0.075, 0.15, 0.3) samples as a function of Fe content x was also not observed.

The evolution of the ^{57}Fe Mössbauer spectra shows that in contrast to the lanthanum based cobalt perovskites, where the magnetic transitions revealed by the magnetic susceptibility measurements were in good accordance with the temperature dependence of the ^{57}Fe Mössbauer spectra [7, 10], well below the magnetic transition temperature of $Eu_{0.8}Sr_{0.2}Fe_{0.3}Co_{0.7}O_{3-z}$ (obtained by magnetic susceptibility measurement: $T_{peak}\approx 109$ K, Figure 2b) e.g., at 77 K the ^{57}Fe Mössbauer spectrum of this europium perovskite contains still only a paramagnetic doublet (Figure 3b). A magnetic structure with strong relaxation effect appears first at 60 K in the ^{57}Fe Mössbauer spectrum of $Eu_{0.8}Sr_{0.2}Fe_{0.3}Co_{0.7}O_{3-z}$, and it transforms into a broadened magnetic sextet at 4.2 K, which can be best fitted by a distribution of hyperfine magnetic fields (Figure 4). The magnetic transition shown by ^{57}Fe Mössbauer spectrometry resembles that of the analogous $La_{0.8}Sr_{0.2}Fe_{0.05}Co_{0.95}O_{3-z}$ perovskite, where the strong relaxation effect and so the observed evolution of the distribution of hyperfine magnetic fields was explained by a transition to a spin glass or spin cluster glass phase [7]. However, a more detailed series of ^{57}Fe Mössbauer measurements is required to elucidate this phenomenon. In the same way, a deeper understanding of the difference between the magnetic structures of the europium based and lanthanum based cobalt perovskites needs further detailed investigations.

In summary, $Eu_{0.8}Sr_{0.2}Fe_xCo_{1-x}O_{3-z}$ (x=0, 0.025, 0.075, 0.15, 0.3) samples were investigated by magnetic transport, AC magnetic susceptibility, as well as ^{151}Eu and ^{57}Fe Mössbauer spectrometry. The electronic state of europium and iron was determined as trivalent for both ions. Although the ^{57}Fe Mössbauer parameters related to the electronic structure of iron ions and the temperature dependence of the magnetoresistance of $Eu_{0.8}Sr_{0.2}Fe_xCo_{1-x}O_{3-z}$ ($0\leq x\leq 0.3$) were found to be similar to those of the analogous lanthanum based perovskites, the differences between the AC magnetic susceptibility response and X-ray diffraction pattern of the europium based and lanthanum based CMR

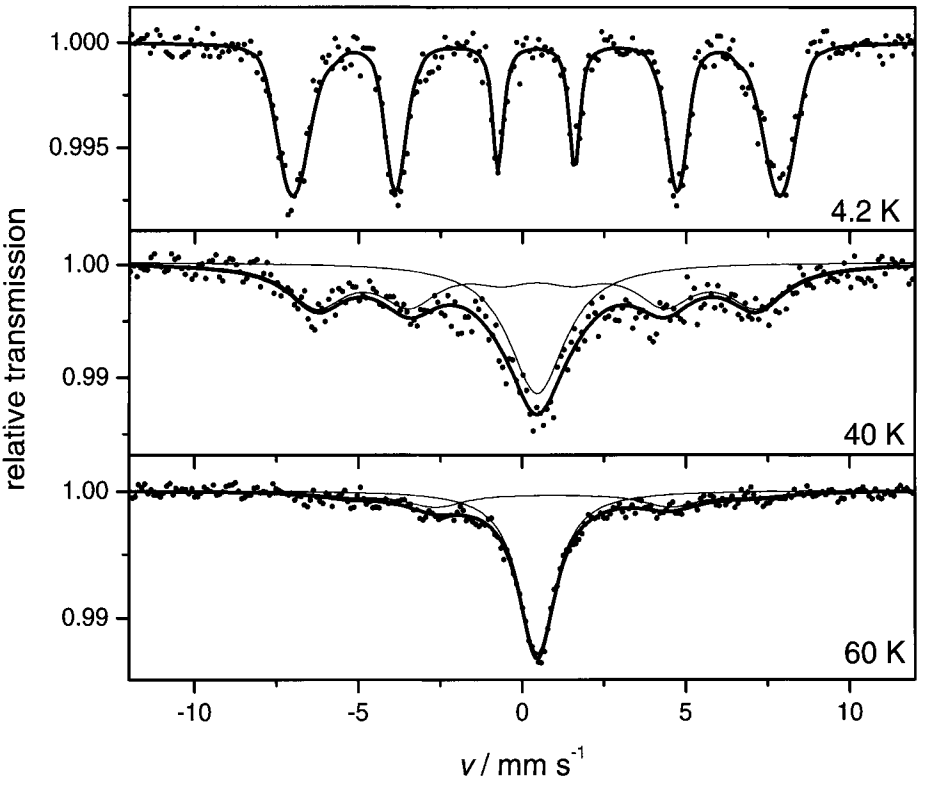

Figure 4 ^{57}Fe Mössbauer spectra of $Eu_{0.8}Sr_{0.2}Fe_{0.3}Co_{0.7}O_{3-z}$ at different temperatures.

perovskites, as well as the anomalies found in the magnetic transition of $Eu_{0.8}Sr_{0.2}Fe_{0.3}Co_{0.7}O_{3-z}$ require further studies on this new family of CMR perovskites.

Acknowledgements Support by the Hungarian Science Foundation OTKA (K 62691) and the Hungarian–French Intergovernmental S&T Cooperation Program (F-22/2005) is gratefully appreciated.

References

1. Fontcuberta, J.: Physics World, Feb. 1999
2. Golovanov, V., Mihály, L., Moodenbaugh, A.R.: Phys. Rev. B **53**, 8207 (1996)
3. Barman, A., Ghosh, M., Biswas, S., De, S.K., Chatterjee, S.: Appl. Phys. Lett. **71**, 3150 (1997)
4. Hannoyer, B., Marest, G., Greneche, J.M., Bathe, R., Patil, S.I., Ogale, S.B.: Phys. Rev. B **61**, 9613 (2000)
5. Zhang, S.: J. Appl. Phys. **79**(8), 4542 (1996)
6. Chechersky, V., Nath, A., Michel, C., Hervieu, M., Ghosh, K., Greene, R.L.: Phys. Rev. B **62**(9), 5316 (1999)
7. Németh, Z., Klencsár, Z., Kuzmann, E., Homonnay, Z., Vértes, A., Greneche, J.M., Lackner, B., Kellner, K., Gritzner, G., Hakl, J., Vad, K., Mészáros, S., Kerekes, L.: Eur. J. Phys. B **43**, 297 (2005)
8. Homonnay, Z., Klencsár, Z., Kuzmann, E., Németh, Z., Rajczy, P., Kellner, K., Gritzner, G., Vértes, A.: Sol. State Phen. **90–91**, 165 (2003)
9. Klencsár, Z., Kuzmann, E., Vértes, A.: J. Radioanal. Nucl. Chem. **210**, 105 (1996)
10. Németh, Z., Klencsár, Z., Kuzmann, E., Homonnay, Z., Vértes, A., Simopoulos, A., Devlin, E., Kallias, G., Greneche, J.M., Hakl, J., Vad, K., Mészáros, S., Cziráki, Á., De, S.K.: (in press)

Hyperfine Interact (2006) 169:1247–1251
DOI 10.1007/s10751-006-9432-0

Creation of ferromagnetic properties of V–Fe and Zr–Fe alloys by hydrogen absorption

A. Ostrasz

Published online: 17 November 2006

Abstract The results of investigations of $V_{1-y}Fe_yH_x$ and $Zr_{1-y}Fe_yH_x$ alloys by ^{57}Fe Mössbauer spectroscopy are presented and discussed in view of hydrogen ability to create ferromagnetic properties of the alloy. The results indicate two different possibilities of hydrogen influence on the hyperfine magnetic field. Hydrogen absorption causes the ferromagnetic behaviour of the alloys at significant lower iron concentration compared to the concentration of magnetic transition in binary alloys. The main reason for such behaviour is the anisotropic lattice expansion in hydrogenated V–Fe and Zr–Fe alloys as well as the decomposition of paramagnetic Zr-rich intermetallic compounds in the aftermath of the strong electron affinity of hydrogen for zirconium. These trends give rise to growth of magnetic clusters of Fe atoms so strong that they can participate in the overall magnetic properties of the system under investigation.

Key words ^{57}Fe Mössbauer spectroscopy · iron alloys · hydrogen absorption · magnetic ordering

1 Introduction

Discussing on the magnetic properties of metallic alloys two aspects have to be distinguished – the presence and the magnitude of atomic magnetic moments and the magnetic interactions between them. If the 3d transition metal is alloyed with a non-magnetic partner one can still speak of localised magnetic moments. However, the presence or absence of such localised moments in a given situation depends on the local environment of the magnetic atoms or partner atoms under consideration. The onset of magnetic moments localisation due to hydrogen absorption has been already observed in $V_{1-y}Fe_yH_x$ alloys ($y \leq 0.25$) by positron annihilation spectroscopy [1]. Taking into account the data of

A. Ostrasz (✉)
Institute of Experimental Physics, University of Wrocław,
Maksa Borna 9, 50-204 Wrocław, Poland
e-mail: ostrasz@ifd.uni.wroc.pl

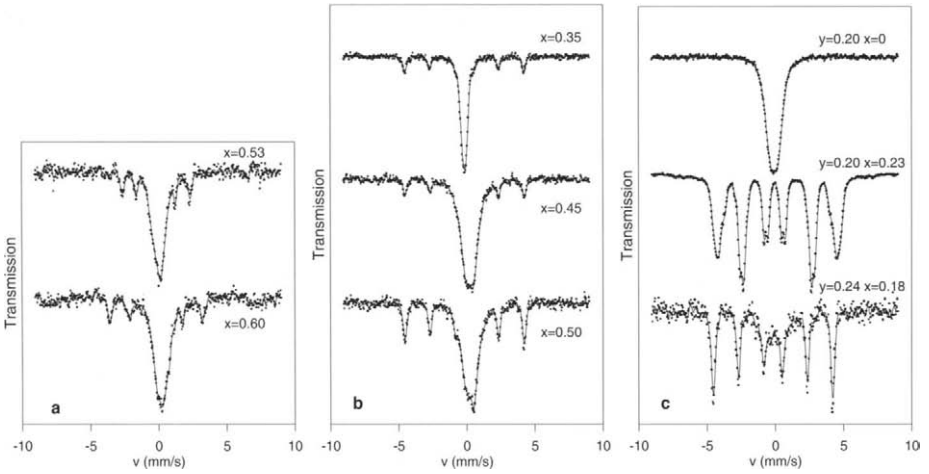

Figure 1 Mössbauer spectra at 4.2 K of ^{57}Fe in (a) $V_{0.96}Fe_{0.04}H_x$, (b) $V_{0.90}Fe_{0.10}H_x$, and (c) $V_{0.80}Fe_{0.20}$, $V_{0.80}Fe_{0.20}H_{0.23}$ and $V_{0.76}Fe_{0.24}H_{0.18}$.

magnetic susceptibility measurements [2] this phenomena was explained by assumption of localised d-like electron states in the vicinity of the Fermi energy capable of being occupied beyond a certain electron concentration of 4s- and 3d-like electrons equal to about n_e=5.6 electrons per atom, called thereafter the critical concentration. Unfortunately, contrary to expectation the hyperfine magnetic splitting was not observed in the room temperature ^{57}Fe Mössbauer spectra [3] probably because of the disturbance of interactions between magnetic moments of Fe atoms or iron clusters by thermal excitations. To exclude this effect the spectra were measured at 4.2 K for the samples with the mean electron concentration near the critical one.

Another problem is the material degradation phenomena. In the ternary hydrides of $A_mB_nH_{2x}$ type they would be decomposed into a hydride AH_x, B metal or AB_n compound and hydrogen gas. If B is a ferromagnetic metal, the formation of AB_n ferromagnetic compound can be easily monitored by Mössbauer spectroscopy. Regarding a strong electron affinity of hydrogen for many transition metals, the tendency to decomposition of A_mB_n ($m>n$) compounds into AH_2 and AB_n (n=1, 2, 3) should determine the disclosure of ferromagnetism in initially paramagnetic system such as $Zr_{1-y}Fe_y$ ($y\leq 0.6$).

2 Experimental details

All specimens of the binary alloys were prepared by melting appropriate amounts of alloy components in an arc furnace under argon atmosphere. To obtain Me–H (metal–hydrogen) system the alloys were exposed to hydrogen gas at a pressure up to ~10^5 Pa during slow cooling in the temperature range 1200–300 K. Finally, 11 different samples of hydrogen free and hydrogen charged $V_{1-y}Fe_yH_x$ alloys ($y = 0.04 \div 0.24$ and $x = 0.18 \div 0.60$) as well as 24 samples of $Zr_{1-y}Fe_yH_x$ alloys ($y = 0.05 \div 0.60$ and $x = 0.14 \div 1.26$) were meant for the ^{57}Fe Mössbauer spectra (MS) measurements. In the case of the vanadium alloys the ^{57}Fe MS were measured at 4.2 K. All spectra have been measured in a transmission geometry using a standard constant-acceleration spectrometer. The monoenergetic 14.4 keV γ-ray was provided by a 50 mCi activity source of ^{57}Co in a Cr matrix.

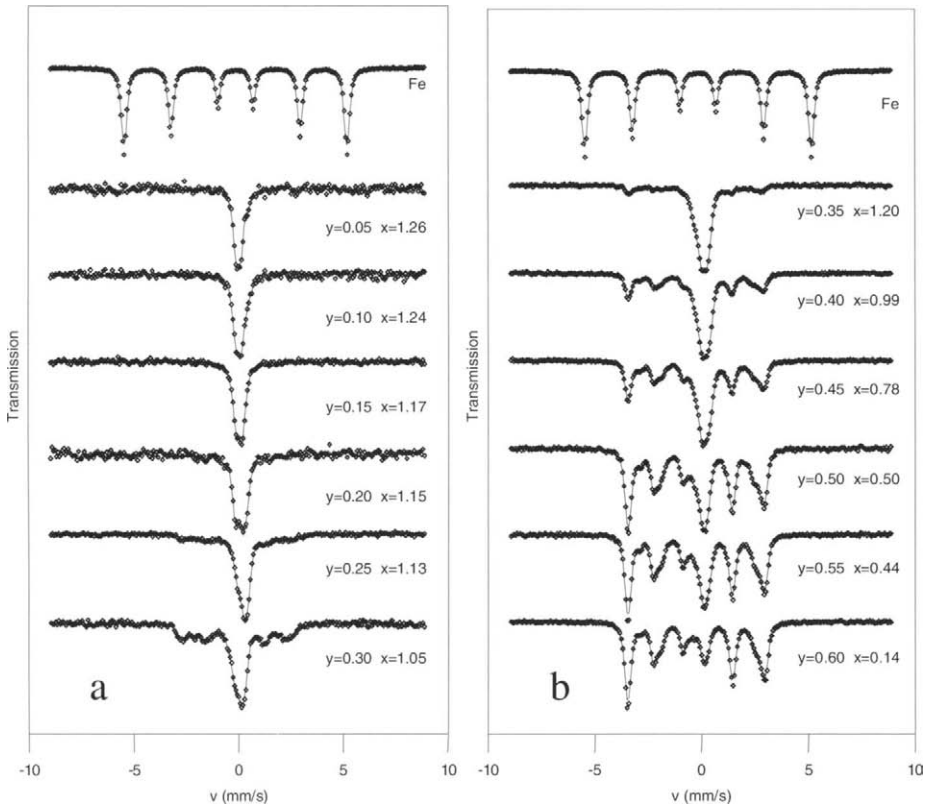

Figure 2 Mössbauer spectra at 300 K of ^{57}Fe in $Zr_{1-y}Fe_yH_x$ alloys in the range of iron concentration: (a) $y = 0.05 \div 0.30$ and (b) $y = 0.35 \div 0.60$.

3 Results and discussion

3.1 $V_{1-y}Fe_yH_x$ system

Some of measured ^{57}Fe MS are presented in Figure 1. As seen the obtained results confirm the property of the assumptions. The low temperature ^{57}Fe MS of hydrogenated $V_{1-y}Fe_y$ alloys clearly show a wide hyperfine splitting. Additionally, structural investigations by X-ray diffraction method supported the Mössbauer results. It was found that tetragonal deformation of the lattice is the main effect of hydrogen on the crystal structure of the alloy. It is worthwhile to add that an essential change of the lattice from cubic symmetry to tetragonal one takes place just above the critical electron concentration. The relative change in the atomic volume of hydrogenated alloys attains 11%. So, the anisotropic deformation of the lattice due to hydrogen absorption gives rise to increase in V–Fe distance and substantially loses the mutual contact between them. It is in agreement with the increase of the degree of 3d-like electron localisation at Fe atoms in the alloy estimated on the base of positron annihilation data [3] and can to explain the local ordering of magnetic moments.

Moreover, the simultaneous reduction of hybridization of the valence atomic orbitals of vanadium and iron atoms can be expected in the aftermath of volume effect. This is

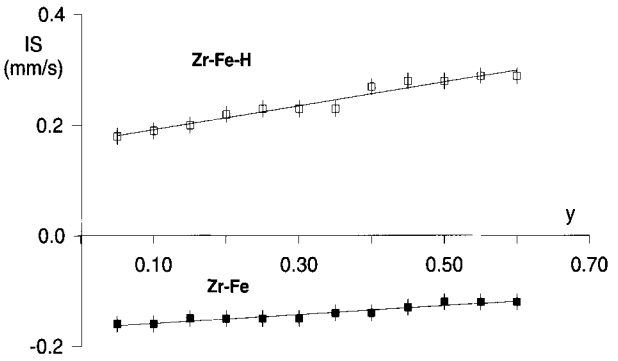

Figure 3 The ^{57}Fe isomer shift with respect to α-Fe in $Zr_{1-y}Fe_y$ alloys before (*filled square*) and after (*square*) hydrogenation *vs* iron concentration (y). The standard deviations of data presented are shown as vertical bars.

attributed to the intra-atomic exchange coupling or Coulomb repulsion of d-like electrons in Fe and should give rise of the energy splitting of localised d-like opposite spin orientation electron states, which eventually lowers the Fermi level and generates the local magnetic order. On the other hand, if the magnetic moments or magnetic clusters are formed as a result of the anisotropic rearrangement of Fe atoms, they may not have a distinct contribution to the average hyperfine magnetic field until the concentration of the magnetic impurity is too low. For this reason the growth of hyperfine magnetic splitting is most spectacular for the alloys with 20 and 24 at.% of Fe (Figure 1c).

3.2 $Zr_{1-y}Fe_yH_x$ system

The ^{57}Fe MS of the $Zr_{1-y}Fe_yH_x$ alloys (Figure 2) were analysed in compliance with possible phases formation in Zr–Fe alloys. It is worth to emphasize that for uncharged alloys the X–ray investigation reveals mainly the α-Zr (hcp ZrFe solid solution) and Zr_2Fe (D) (the diamond structure of $NiTi_2$ type) along with the trace of Zr_2Fe (C16), an orthorhombic Zr_3Fe and $ZrFe_2$ (C15) phases. After hydrogenation the increase in amount of $ZrFe_2$ was detected as the main phase along with α-Zr and ZrH_2 phases. In [4–6] has been already discussed that in hydrogenated $Zr_{1-y}Fe_y$ alloys there is a distinct growth of the $ZrFe_2$ phase ($ZrFe_2$ is a ferromagnetic at room temperature with the hyperfine field of 18.0±0.5 T [4]). Apart from the non-magnetic components the MS were also fitted with a view of $ZrFe_2$ intermetallic phase existence. They were analysed in terms of two sets of the six-line patterns corresponding to the low-field (B<18 T) and the high-field (B>18 T) components to determine the hyperfine field distribution. It was reasonable to consider the high-field component in P(B) as the contribution of $ZrFe_2$ compound that is enlarge in hydrogenated alloys through the commitment of zirconium atoms from Zr_2Fe and/or Zr_3Fe intermetallic compounds to ZrH_2 formation.

A severe problem that however closely concerns the overall magnetic properties of the system is the origin of the low-field contributions in hyperfine magnetic field distributions [7]. Now, it was assumed that hydrogen partly dissolves into α-Zr phase. This phase crystallize in a hexagonal lattice and hydrogen can lead to its anisotropic volume expansion which plays an essential role in rearrangement of the NN of certain Fe atoms in distorted matrix. It is well established that in metallic alloys and binary intermetallic compounds the isomer shift is almost a linear function of the fractional change in volume [8, 9]. Since the isomer shift reflects the change of interatomic distances it is useful to compare its concentration dependence in the case of hydrogen-free and hydrogenated Zr–Fe alloy (Figure 3). In most metallic compounds in which metal partners have a relatively high

electronegativity the atomic volume increases usually of order 20% upon hydrogen absorption [10]. Such volume effect corresponds to the positive change in the isomer shift. This change equals approximately 0.30 mm/s in relation to α-Fe [11] and it is only somewhat smaller than the average shift of $\langle \Delta IS \rangle \approx 0.35$ mm/s estimated in this work. Consequently, anisotropic lattice expansion is likely to help Fe–Fe pairs to generate localised moments and would give rise to growth of magnetic clusters, so strong that they can participate in the overall magnetic properties of the system under investigation.

4 Conclusion

In the alloys with too low Fe content to be ferromagnetic – as in the case of V–Fe alloys (<20 at.% Fe) – the local magnetic ordering can be induced owing to an increase of the magnetic interaction between magnetic moments of iron atoms as a result of anisotropic expansion of the lattice caused by hydrogen interstitials. The low temperature Mössbauer spectra revealed ferromagnetic properties of hydrogenated alloys. This result allows to confirm the d-like electron localisation phenomenon at Fe atoms in hydrogenated V–Fe alloys studied by positron annihilation spectroscopy. Apart from the volume effect the ferromagnetic behaviour of the system containing many intermetallic compounds, such as Zr_3Fe, Zr_2Fe, ZrFe and $ZrFe_2$ in Zr–Fe alloy, is generated by hydrogen due to decomposition of paramagnetic zirconium-rich compounds into the ferromagnetic $ZrFe_2$ one and the hydride ZrH_2 respectively.

Acknowledgements This work was supported by the University of Wrocław under the grant number 2016/ IFD/ 2004–2005.

References

1. Szuszkiewicz, M., Chojcan, J., Ostrasz, A.: Phys. Status Solidi, B **117**, 645 (1983)
2. Obermann, A., Wanzl, W., Mahning, M., Wicke, E.: J. Less-Common Met. **49**, 75 (1976)
3. Ostrasz, A., Szuszkiewicz, M.: Phys. Status Solidi, B **139**, 205 (1987)
4. Vincze, I., van der Woude, F., Scott, M.G.: Solid State Commun. **37**, 567 (1981)
5. Wertheim, G.K., Jaccarino, V., Wernick, J.H.: Phys. Rev., A **135**, 151 (1964)
6. Ghafari, M., Gonser, U. Wagner, H.G.: Nucl. Instrum. Methods **199**, 197 (1982)
7. Ostrasz, A., Szuszkiewicz, M.: Hyperfine Interact. **94**, 2287 (1994)
8. Ingalls, R., Drickamer, H.G., de Pasquali, G.: Phys. Rev. **155**, 165 (1967)
9. Ingalls, R.: Phys. Rev. **155**, 157 (1967)
10. Buschow, K.H.J., Châtel, P.F.: Pure Appl. Chem. **52**, 135 (1979)
11. Kalvius, G.M., Klein, U.F. Wortmann, G.: J. Phys. **35**, C6–C139 (1974)

Hyperfine Interact (2006) 169:1253–1258
DOI 10.1007/s10751-006-9433-z

Magnetic and structural properties of the $Nd_2(Fe_{100-x}Nb_x)_{14}B$ system prepared by arc melting

D. Oyola Lozano · L. E. Zamora · G. A. Pérez Alcázar · Y. A. Rojas · H. Bustos · J. M. Greneche

Published online: 16 November 2006

Abstract In this work the magnetic and structural properties are investigated by Mössbauer spectrometry, Vibrating Sample Magnetometry and X-ray diffraction of $Nd_2(Fe_{100-x}Nb_x)_{14}B$ powdered alloys with x=0, 2 and 4 prepared by arc melting. The Mössbauer spectra of the samples were fitted with several contributions from: $Nd_2Fe_{14}B$, α-Fe and a paramagnetic phase associated with $Nd_{1.1}Fe_4B_4$ for x=0 and additionally from NbFeB and Nd_2Fe_{17} for x=2 and x=4. The relative fractions of α-Fe and $Nd_2Fe_{14}B$ are smaller for x=4 than for x=0, indicating that the amount of these two phases is reduced with increasing Nb content, while the relative fraction of Nd_2Fe_{17} increases. The α-Fe grain size slightly decreases while that of the $Nd_2Fe_{14}B$ phase is increasing, when the Nb content increases. The hysteresis loops indicate that these samples behave as hard ferromagnets, with a coercive field which decreases when the Nb content increases, but with rather low remanent magnetization.

Key words hard and soft magnetic phases · Mössbauer spectrometry · permanent magnet iron57

1 Introduction

A possible method to improve the magnetic properties in permanent magnets is to use nanocomposites consisting of a mixture of hard and soft magnetic phases, where the soft phase contributes a high saturation magnetization and the hard phase a high coercive field. Kneller and Hawig [1] claim that a strong magnetic interaction between the hard and soft phases is achieved when the mean grain size of the phases is of the order of 10 nm,

D. Oyola Lozano (✉) · Y. A. Rojas · H. Bustos
Department of Physics, University of Tolima, A.A.546 Ibagué, Colombia
e-mail: doyola@ut.edu.co

L. E. Zamora · G. A. Pérez Alcázar
Department of Physics, University of Valle, A.A.25360 Cali, Colombia

J. M. Greneche
Laboratoire de Physique de l'Etat Condensé, UMR CNRS 6087, Université du Maine, 72085 Le Mans Cedex 9, France

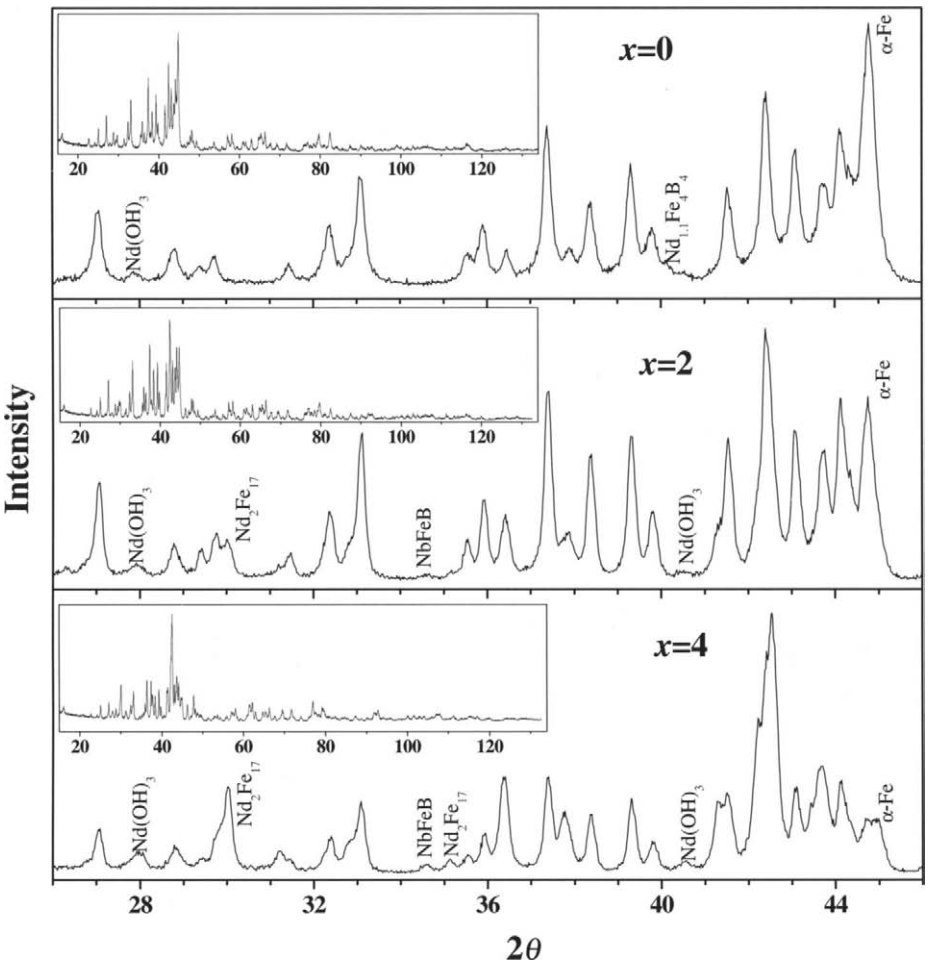

Figure 1 XRD pattenrs of $Nd_2(Fe_{100-x}Nb_x)_{14}B$ with x=0, 2 and 4. The insets show the whole 2θ range. The non indexed peaks are those of the $Nd_2Fe_{14}B$ phase.

corresponding to the ferromagnetic correlation length. Recently, Chen et al. [2] and Ahmed et al. [3] reported that the addition of Nb in the NdFeB system prevents the increase of the grain size of the α-Fe phase produced by the heat treatments.

Previous works report that the Nd–Fe–B system presents the phases $Nd_2Fe_{14}B$, major phase, a Nd-rich intergranular phase, in small quantity and the non-magnetic $Nd_{1.1}Fe_4B_4$ phase in a small quantity [4]. Further, when Nb is added the phase Nd_2Fe_{17} is present [5].

In this paper, we report the magnetic and structural properties of $Nd_2(Fe_{100-x}Nb_x)_{14}B$ powdered alloys with x=0, 2 and 4 prepared by arc melting.

2 Experimental procedure

Alloys of the $Nd_2(Fe_{100-x}Nb_x)_{14}B$ system with x=0, 2 and 4 were prepared by arc melting using Nd, Fe, B and Nb powders. The starting elements used were at least 99.9% pure.

Table I Mean grain sizes and proportions of the different phases estimated from XRD patterns and 300 and 77 K Mössbauer spectra

	Phase	RX			Mössbauer	
		Mean grain size (nm)±5	Volume percent±10	Percent Fe content±10	300 K Percent±5	77 K Percent±5
x=0	$Nd_2Fe_{14}B$	51	79	61	73	71
	α-Fe	47	17	38	23	27
	$Nd_{1.1}Fe_4B_4$	40	2	1	4	2
x=2	$Nd_2Fe_{14}B$	96	72	62	70	60
	α-Fe	45	9	22	12	20
	Nd_2Fe_{17}	55	13	14	15	18
	NbFeB	48	4	2	3	2
x=4	$Nd_2Fe_{14}B$	96	45	41	41	40
	α-Fe	40	4	10	3	7
	Nd_2Fe_{17}	72	39	44	50	49
	NbFeB	56	9	5	6	4

Initially the appropriate amounts of powders were compacted to 2500 psi, then were melted by arc melting in a high purity argon atmosphere. To ensure homogeneity the alloys were annealed in vacuum at 1000°C for 4 days followed by quenching into water. The Mössbauer spectra at 300 and 77 K were obtained with a conventional constant acceleration transmission spectrometer equipped with a ^{57}Co-/Rh source. The Mössbauer spectra of these samples were fitted with the Mosfit program [6] using α-Fe foil as calibration sample. X-ray-diffraction (XRD) experiments were performed at room temperature on powder samples using a diffractometer with the Cu K*a* radiation and the diffractograms were fitted using the Maud program [7], to determine the phase structure and the lattice constants. The hysteresis loops of the samples were obtained using vibrating sample magnetometer (VSM).

3 Results and discussion

The X-ray diffractograms of the $Nd_2(Fe_{100-x}Nb_x)_{14}B$ samples with x=0, 2 and 4 are shown in Figure 1. When x=0, the $Nd_2Fe_{14}B$, the $Nd(OH)_3$, the $Nd_{1.1}Fe_4B_4$ and the α-Fe phases are unambiguously identified. The presence of the $Nd(OH)_3$ phase is considered due to the quenching in water, like it reports in [4]. For the Nb containing samples, the X-ray diffraction pattern indicates the additional presence of the NbFeB and Nd_2Fe_{17} phases while $Nd_{1.1}Fe_4B_4$ is not detected, in agreement with a previous work [5]. In spite of the complexity of the X-ray patterns a quantitative analysis can be carried out and the results are reported in Table I. To better describe the broad line shape of the Bragg peaks, we have also refined carefully the size of the crystalline grains of each phase, assuming a spherical shape. It is clearly concluded that (1) the proportion and the mean grain size of the α-Fe phase decrease, (2) the proportion of the $Nd_2Fe_{14}B$ phase decreases, and (3) the proportion of the Nd_2Fe_{17} phase increases, when the Nb content increases, (4) the α–Fe mean grain size slightly decreases of 40 to 47 nm while that of the $Nd_2Fe_{14}B$ phase is increasing of 51 up to 96 nm, when the Nb content increases.

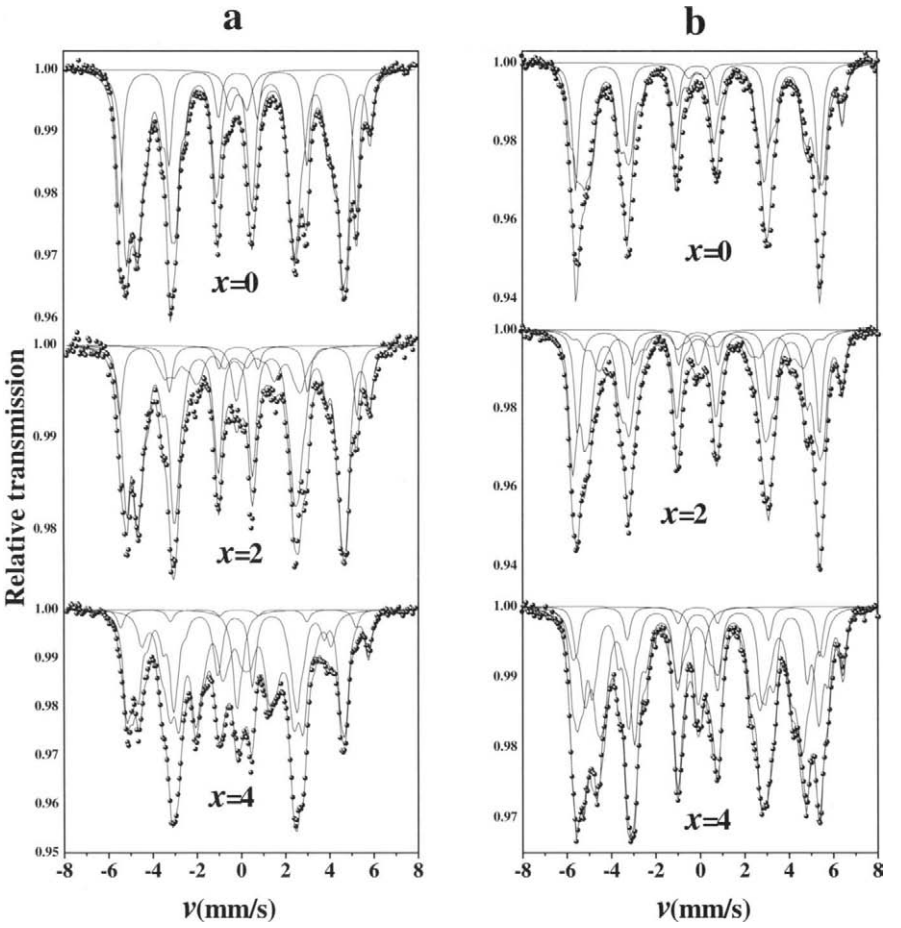

Figure 2 300 K (**a**) and 77 K (**b**) Mössbauer spectra of $Nd_2(Fe_{100-x}Nb_x)_{14}B$ samples prepared by arc melting.

Both the 300 and 77 K Mössbauer spectra of the $Nd_2(Fe_{100-x}Nb_x)_{14}B$ samples with $x=0$, 2 and 4 are shown in Figure 2a and b, respectively. They exhibit a complex hyperfine structure mainly composed of magnetic sextets. They can be well described using a model based on the presence of the components identified in the X-ray pattern. It is important to emphasize that the $Nd_2Fe_{14}B$ and Nd_2Fe_{17} phases exhibit crystallographic structures with six and seven different Fe sites, respectively. Thus, they give rise to rather complex hyperfine structures, preventing a refinement of all hyperfine parameters from the present experimental spectra. Hence in the fitting procedure, the values of isomer shift, quadrupole shift and hyperfine field were fixed with those found in the literature and the relative areas were constrained in agreement with the ideal crystallographic structures, assuming thus no lattice distortions due to atomic substitution but similar *f*-factor values for all Fe sites for each phase. We have here considered only lorentzian lines, and the values of hyperfine parameters proposed by Grandjean et al. [8] and by Long et al. [9] for the $Nd_2Fe_{14}B$ phase and Nd_2Fe_{17} phases, respectively, whereas the $Nd_{1.1}Fe_4B_4$ phase is fitted with a quadrupole doublet ($Q=0.7$ mm/s, IS=0.04) and the NbFeB phase with a single line.

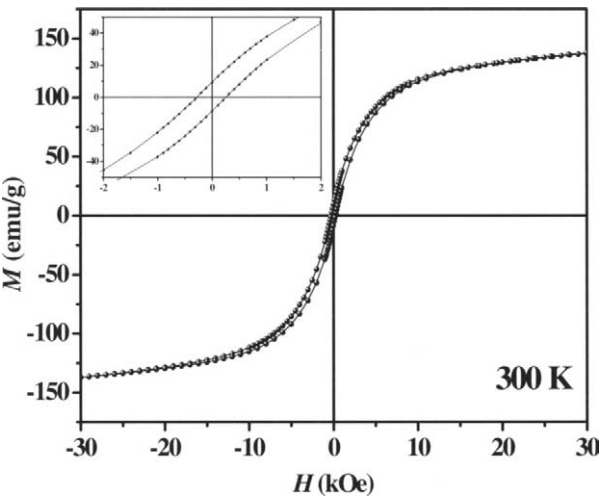

Figure 3 Typical hysteresis loop of $Nd_2(Fe_{100-x}Nb_x)_{14}B$ samples with x=0 prepared by arc melting.

For x=0, both the 300 and 77 K Mössbauer spectra were well fitted with three contributions: assigned to $Nd_2Fe_{14}B$, $Nd_{1.1}Fe_4B_4$ and α-Fe. This result suggests that the different phases exhibit ideal crystallographic structures. For the x=2 and 4 samples, the Mössbauer spectra were satisfactorily fitted with four contributions assigned to: $Nd_2Fe_{14}B$, α-Fe, Nd_2Fe_{17} and NbFeB. A good agreement was achieved providing that the hyperfine field values slightly differ from published values and lines are broadened. One thus concludes that Nb preferentially enters into Nd_2Fe_{17} and $Nd_2Fe_{14}B$. However, its presence at the periphery of the crystalline grains cannot be completely excluded. Finally, the Mössbauer percentages obtained at 300 and 77 K are compared in Table I to those obtained from X-ray diffraction after conversion into Fe atomic percent. The reasonable agreement supports our fitting procedures of both the X-ray patterns and the Mössbauer spectra.

A typical hysteresis loop for x=0 at 300 K is shown in Figure 3. The coercive field and the remanence are 22 kA/m and 9 emu/g, respectively, whereas for x=4, they are 11 kA/m and 5 emu/g.

4 Conclusions

Arc melting procedure has been used to produce $Nd_2(Fe_{100-x}Nb_x)_{14}B$ powdered samples, with x=0, 2 and 4. This system which contains hard, $Nd_2Fe_{14}B$ and Nd_2Fe_{17}, if x=2 and 4, and soft, α-Fe, magnetic phases, behaves as a semi-hard ferromagnet and exhibits high coercive field but low remanence. The addition of Nb atoms favors the occurrence of the Nd_2Fe_{17} phase. To improve the hard magnetic properties, the search for a better composition and optimal crystalline grain size of each phase is currently in progress.

Acknowledgements We are grateful to the Central Committee of Research of the University of Tolima for its financial support, to the Mössbauer Laboratory of the University of Valle, to the Laboratoire de Physique de l'Etat Condensé of Université du Maine in Le Mans – France and to COLCIENCIAS through the BOMPLAN and Ecos–Nord Program (CF03P01) and the support of the New Materials Excellent Center (CENM) for the achievement of this work. We are grateful to A. M. Mercier from Laboratoire des Fluorures of Université du Maine UMR CNRS 6010 for performing XRD measurements. We also thank to the CBPF Rio de Janeiro – Brasil for the VSM measurements.

References

1. Kneller, E.F., Hawig, R.: IEEE Trans. Magn. **27**, 3588 (1991)
2. Chen, Z., Zhang, Y., Ding, Y., Hadjipanayis, G.C., Chen, Q., Ma, B.: J. Magn. Magn. Mater. **125**, 420 (1999)
3. Ahmed, F.M., Ataie, A., Williams, A.J., Harris, I.R.: J. Magn. Magn. Mater. **157**, 59 (1996)
4. Edgley, D.S., Le Breton, J.M., Steyaert, S., Ahmed, F.M., Harris, I.R., Teillet, J.: J. Magn. Magn. Mater. **173**, 29 (1997)
5. Steyaert, S., Le Breton, J.M., Ahmed, F.M., Edgley, D.S., Harris, I.R., Teillet, J.: J. Alloys Compd. **264**, 227 (1998)
6. Bremers, H., Jarms, C., Hesse, J., Chajwasiliou, S., Efthiadis, K.G., Tsonkalas, Y.: J. Magn. Magn. Mater. **140**, 63 (1995)
7. Lutterotti, L., Scardi, P.: J. Appl. Crystallogr. **23**, 246 (1990)
8. Grandjean, F., Long, G.J., Tharp, D.E., Pringle, O.A., James, J.: J. Phys. **49**, C8 581 (1988)
9. Long, G.J., Pringle, O.A., Grandjean, F., Buschow, K.H.J.: J. Appl. Phys. **72**, 4845 (1992)

Hyperfine Interact (2006) 169:1259–1266
DOI 10.1007/s10751-006-9434-y

Mössbauer spectroscopic studies of Fe-20 wt.% Cr ball milled alloy

Brajesh Pandey · M. Ananda Rao · H. C. Verma · S. Bhargava

Published online: 16 November 2006

Abstract Interesting differences were noticed in the alloying process during ball milling of Fe-10 wt.% Cr and Fe-20 wt.% Cr alloys by ^{57}Fe Mössbauer spectroscopic studies. In both cases, there is almost no diffusion of Fe in Cr or vice versa up to 20 h of milling time. As the powders are milled for another 20 h substantive changes occur in the Mössbauer spectra showing atomic level mixing. But the two compositions behave differently with respect to alloying. Fe-20 wt.% Cr sample does not differ much in the hyperfine field distribution as it is milled from 40 to 100 h. On the other hand, the hyperfine field distribution keeps on changing with milling time for Fe-10 wt.% Cr sample even up to 100 h of milling. The average crystallite size is found to be 7.5 nm for Fe-10 wt.% Cr and 6.5 nm in Fe-20 wt.% Cr after milling.

Key words Mössbauer spectroscopy · mechanical alloying · ball milling · iron–chromium alloy

1 Introduction

A variety of equilibrium and non-equilibrium phases can be produced in alloys by mechanical alloying of elemental metallic powders. The mechanism of alloying during the mechanical milling process has been studied in great details [1–4]. The heavily dislocated structure formed due to the large scale deformation of individual or layered particles during their cold welding enhances the mutual solubility of elements and leads to their mixing at the atomic scale by progressively eliminating the concentration gradient between cold welded layered structures. Therefore, mechanical alloying is capable of producing powders in a non-equilibrium state by either accumulating mechanical energy or accelerating

B. Pandey · H. C. Verma (✉)
Department of Physics, I.I.T Kanpur, Kanpur 208016, India
e-mail: hcverma@iitk.ac.in

M. A. Rao · S. Bhargava
Department of Materials and Metallurgical Engg., I.I.T. Kanpur, Kanpur 208016, India

diffusion across the interface between unlike elements [4–6]. The grain size of the alloyed material also simultaneously decreases as a function of milling time and eventually reaches a nano-scale. In some cases the continuous milling of the powder may also lead to the formation of amorphous phase [1–4, 7]. The formation of mechanically alloyed end product, however, depends on many parameters such as milling conditions and thermodynamic properties of the milled system.

Several researchers have prepared different compositions of Fe–Cr alloys, starting from elemental powders by mechanical alloying approach [8–10]. These studies show that the mechanical alloying is indeed capable of producing a nano-scale structure with grain size of ~10 nm [10, 11]. Due to different magnetic properties of Fe and Cr and a strong composition dependence of magnetic properties in the Fe–Cr system, Mössbauer spectroscopy can be used to find the chemical inhomogeneity in the alloys synthesized and thus the progress of mechanical alloying. Mössbauer spectroscopy has thus been used by several research groups [8, 12–14] to study mechanically alloyed systems. In addition, SEM imaging technique suited to morphological studies such as dependence of grain shape on milling time, and of lamellar spacing on milling time. While SEM gives information at micron scale, the Mössbauer spectroscopy gives information at atomic scale in the immediate surrounding of ^{57}Fe atoms. We have earlier reported XRD, Mössbauer spectroscopic, SEM and AFM studies of Fe-10 wt.% Cr alloys produced by mechanical alloying [14]. In the present article we report our studies on Fe-20 wt.% Cr alloy made by the same procedure.

2 Experimental procedures

Iron and chromium powders of purity greater than 99.99% were used for the purpose of mechanical alloying. Powders had been sealed and stored in the argon glove box to ensure no oxygen contamination during their storage. Charge to ball ratio for each milling operation was maintained as 1:8 in a Retsch type planetary ball mill. The milling speed was kept at 250 rpm and size of the balls taken was 10 mm. To study the nature of milling and alloying we have taken out a portion of powder after 5, 10, 20, 40, 65 and 100 h.

To see the effect of milling on crystallite size we have used X-ray diffraction technique. X-ray diffraction was performed on a Seifert Iso-Debyeflex 2002 diffractometer with Cu target. The tube was operated at 30 kV and 10 mA. The radiation used was $Cu\ K_\alpha$ having wavelength of 1.54 Å. The peak broadening was used to estimate the crystallite size. In order to remove the effect of broadening due to instrumental interference, XRD pattern of a well crystalline silicon piece was recorded in the same experimental conditions as used with the milled powder samples. The FWHM obtained after removal of instrumental broadening effect, was input to Scherrer's equation to determine crystallite size.

Powder samples were sandwiched between two layers of cello tape in a copper ring of 13 mm inner diameter for the purpose of transmission mode Mössbauer spectroscopy. The data were recorded at room temperature in a transmission geometry using a conventional ^{57}Fe constant acceleration Mössbauer spectrometer employing a 25 mCi ^{57}Co/Rh source. The spectra were analyzed using least squares method assuming Lorenzian line shapes and the Magnetic Hyperfine Field (p–B) distribution were obtained using Windows approach [15]. Powder morphology of mechanically alloyed Fe–Cr powders was analyzed under a JOEL JSM 840A Scanning Electron Microscope (SEM). The milled powder morphologies were observed by dispersing the powders with acetone on finely polished brass stubs prepared especially for this purpose.

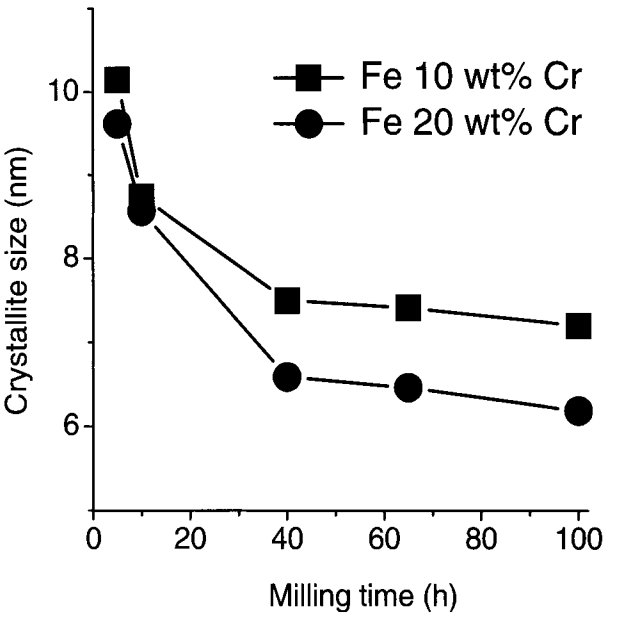

Figure 1 Crystallite size versus milling time for the ball milled alloys.

3 Results and discussions

3.1 X-ray diffraction

The effect of milling time on the crystallite size of Fe-20 wt.% Cr powder is shown in Figure 1. For comparison we have also included the data on Fe-10 wt.% Cr [14]. It can be seen that crystallites of the size as small as 10 nm are formed in the first 10 h itself. Subsequently the rate of decrease of crystallite size was found to be less rapid. Beyond the milling time of 40 h, the crystallite size was found to be almost constant. For the same time of milling the decrease of crystallite size in Fe-20 wt.% Cr is more rapid as compare to that in Fe-10 wt.% Cr. For 40 h of milling the crystallite size becomes around 6.5 nm for Fe-20 wt.% Cr samples, whereas it decreases only up to 7.5 nm for Fe-10 wt.% Cr sample.

3.2 Particle morphology

From the SEM micrographs the structural changes during milling can be visualized. The morphology of the 5-h milled samples show different particles sticking over one another and cold welded to form composite granules. The sizes of these granules are several tens of micrometers. In fact it increases initially with milling because of impact welding of particles. As the powder is milled for 20–40 h, these granules become elongated, work hardened and therefore they fracture. The shape of these granules changes drastically between 40 and 65 h of milling. Both for 65 and 100 h of milling, the shape of these granules are very flat and flaky (Figure 2). As the flattened granules become work hardened they resist further impact welding and the impact results only in further flattening and fracture.

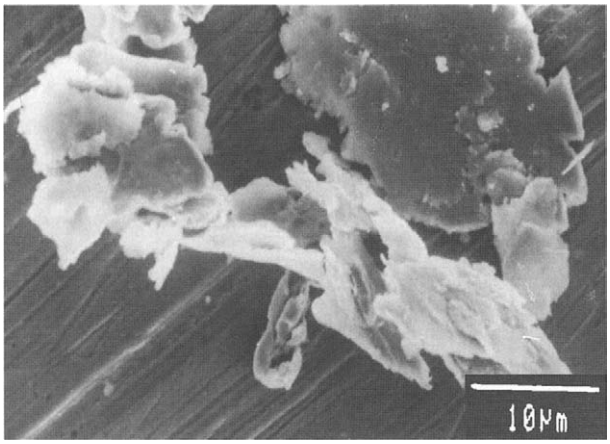

Figure 2 SEM micrographs of 100 h ball milled Fe-20 wt.% Cr powder.

3.3 Mössbauer spectroscopy

Figure 3 shows the Mössbauer spectra of the milled Fe-20 wt.% Cr powders. It is seen from that there is almost no interdiffusion of Cr and Fe into each other's crystal up to 20 h of milling as only a single six-line pattern characteristic of pure iron phase appears.

There is a drastic change in the shape of the spectrum as the milling time is increased to 40 h. A number of other six-line patterns appear showing that chromium has started entering in the Fe matrix on milling between 20 and 40 h. These observations are very similar to what has been seen with Fe-10 wt.% Cr alloys [14]. However there are differences in the few areas once the alloying started. The Mössbauer spectra of 100 h milled powder of Fe-20 wt.% Cr does not differ much from that of 65 h, whereas in Fe-10 wt.% Cr sample the spectra differ significantly, showing that alloying is faster in Fe-20 wt.% Cr than in Fe-10 wt.% Cr.

The above discussion is based on qualitative visual appearance of Mössbauer spectra. To get more quantitative information we have analyzed all the Mössbauer data in terms of a continuous variation of hyperfine magnetic field (HMF) B. The probabilities for different values of B were calculated using Window's approach [15]. The p–B distributions for different samples are shown in Figure 4.

As expected, the p–B distributions for samples up to 20 h of milling time show only a single peak at 33.0 T corresponding to no diffusion of chromium in the Fe matrix. The p–B distributions of 40, 65 and 100 h samples show multipeak structures showing that some of the other possible environments of Fe are growing. To further study the differences in the p–B distributions, we have fitted five Gaussians to each of the p–B distribution curves using PEAKFIT programme. The Gaussians are centered roughly around 33.0, 29.0, 24.0, 19.0 and 14.5 T. The first of these correspond to no chromium diffusion in the nn and nnn cell of iron and others correspond to gradually more chromium atoms diffusing in Fe matrix. The results are shown in Figure 5. For 5, 10 and 20 h milled samples of both the samples Fe-10 wt.% Cr and Fe-20 wt.% Cr only 33.0 T component exists corresponding to the fact that despite structural changes such as impact welding and fracturing, no significant mixing has occurred at the atomic level. Beyond 20 h, alloying takes place at different pace in the two systems. During 20–40 h of milling of Fe-20 wt.% Cr sample, the relative area under the 33.0 T Gaussian is reduced drastically (from 100 to about 20%) and all the other

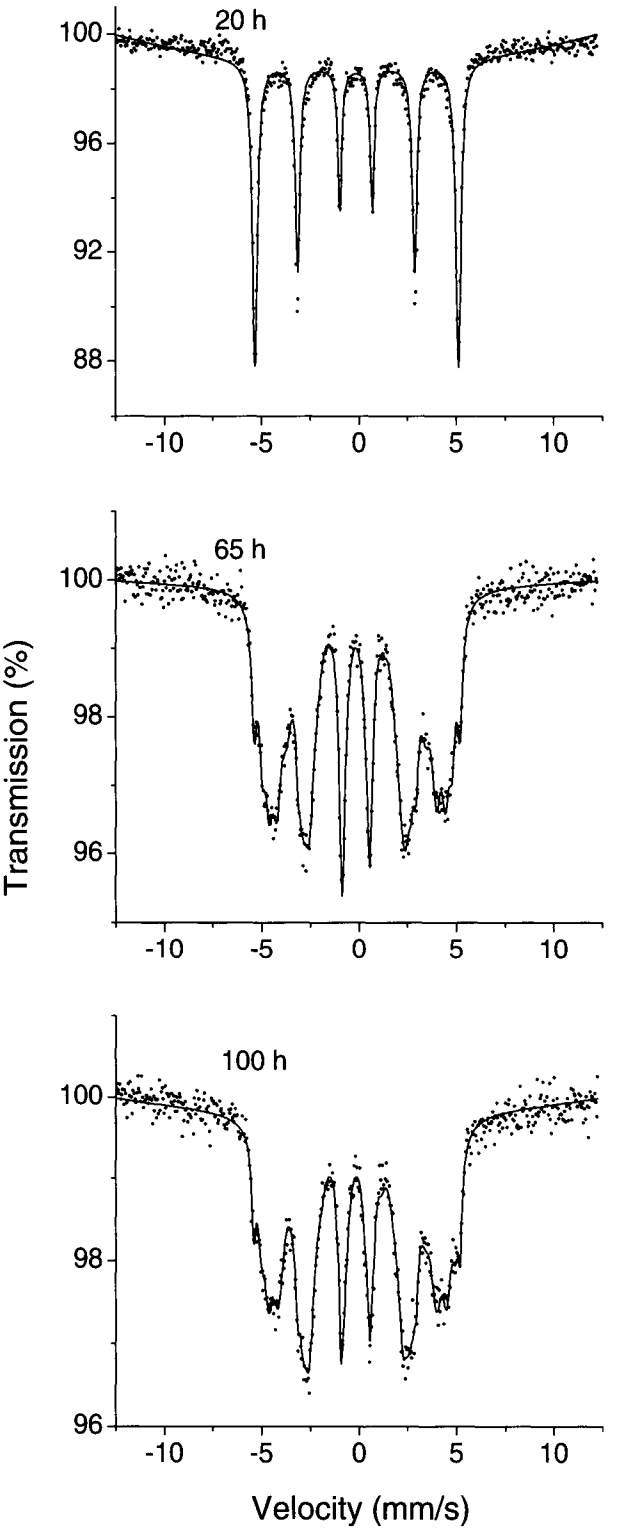

Figure 3 Mössbauer spectra of Fe-20 wt.% Cr ball milled alloys at various time of milling.

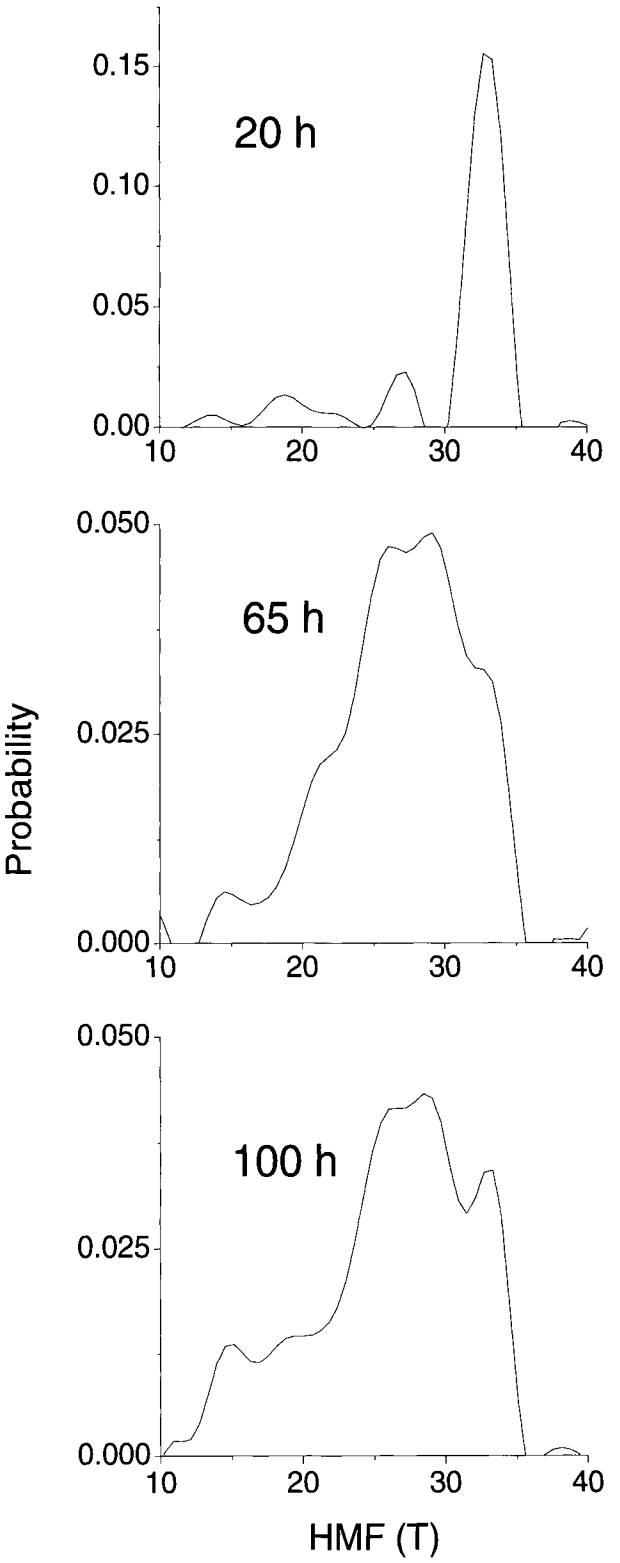

Figure 4 p–B distributions of Fe-20 wt.% Cr ball milled alloys at various time of milling.

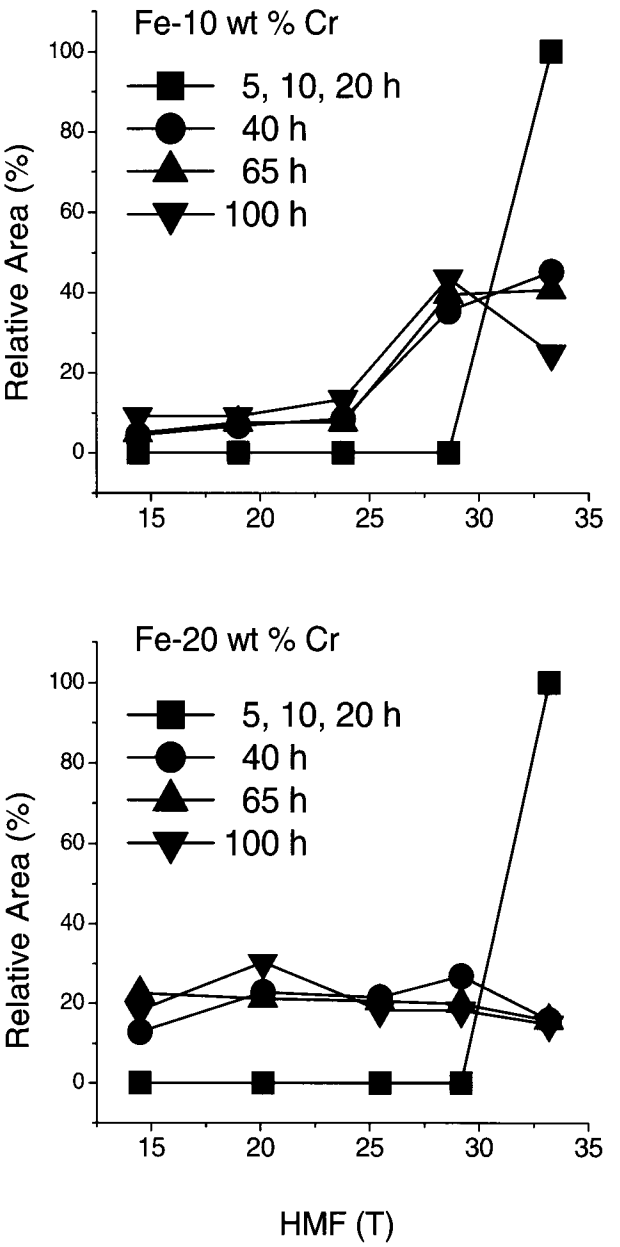

Figure 5 Relative area of different environments plotted against their HMF.

environments have grown, in almost equal proportion. On further milling there is not much change in the relative area showing no further mixing at atomic level. In contrast in Fe-10 wt.% Cr [14] the alloying is more gradual and continued till 100 h of milling.

However, even the p–B distributions of 100 h milled samples in both the cases are not very close to the simulated p–B distribution assuming a completely random solid solution, may be because of lots of defects introduced during the mechanical milling.

3.3.1 Preferential diffusion of Chromium atoms

Mössbauer spectra of the milled Fe–Cr sample do not show any single line component which should appear if Fe atoms diffuse in Cr lattice [8–10, 12, 16]. Though both Fe and Cr particles undergo the structural deformation such as flattening and fracturing, Cr atoms are preferentially diffusing in Fe lattice as against Fe atoms diffusing in Cr lattice.

4 Conclusion

A complete picture of the processes during mechanical alloying of Fe, Cr powders has been revealed by the complimentary information obtained through XRD, Mössbauer studies and SEM. It is observed that as the Cr concentration increases, the alloying process becomes easy. Most of the iron environments are created between 20 and 40 h of milling in the Fe-20 wt.% Cr alloy. In contrast to Fe-10 wt.% Cr alloy the environments keep changing over full range of milling time [14]. It is much easier for Cr to diffuse in the Fe lattice than the vice versa.

Reference

1. Suryanarayana, C.: Prog. Mater. Sci. **46**, 1 (2001)
2. Koch, C.C.: Processing of metals and alloys, vol. 15 of Materials science and technology – a comprehensive treatment, p. 193. In: Cahn R.W. (ed.) VCH, Weinheim, Germany (1991)
3. Lai, M.O., Lu, L.: Mechanical alloying. Kluwer, Boston, MA (1998)
4. Turnbull, D.: Metall. Trans. **12A**, 695 (1981)
5. Suryanarayana C. (ed.): Non-equilibrium processing of materials. Pergamon, Oxford (1999)
6. Anantharaman, T.R., Suryanarayana, C.: Rapidly solid metals – a technological overview. Trans Tech, Aedermannsdorf, Switzerland (1987)
7. Ermakov, A.E., Yurchikov, E.E., Barinov, V.A.: Phys. Met. Metallogr. **52**(6), 50 (1981)
8. Koyano, T., Takizawa, T., Fukunaga, T., Mizutani, U., Kamizuru, S., Kita, E., Tasaki, A.: J. Appl. Phys. **73**, 429 (1993)
9. Lemoine, C., Fnidiki, A., Lemarchand, D., Tellet, J.: J. Magn. Magn. Mater. **203**, 184 (1999)
10. Murugesan, M., Kuwano, H.: IEEE Trans. Magn. **35**, 3499 (1999)
11. Lemoine, C., Fnidiki, A., Lemarchand, D., Tellet, J.: J. Phys. Condens. Matter. **11**, 8341 (1999)
12. Petrov, Y.I., Shafranovsky, E.A., Krupyanskii Y.F., Essine, S.V.: J. Appl. Phys. **91**, 352 (2002)
13. Dubiel, S.M., Zukrowaski, J.: J. Magn. Magn. Mater. **23**, 214 (1981)
14. Pandey, B., Rao, M.A., Verma, H.C., Bhargava, S.: J. Phys. Condens. Matter. **17**, 7981 (2005)
15. Window, B.: J. Phys. E. Sci. Instrum. **4**, 401 (1971)
16. Cieślak, J., Dubiel, S.M., Sepiol, B.: J. Phys. Condens. Matter. **12**, 6709 (2000)

Hyperfine Interact (2006) 169:1267–1272
DOI 10.1007/s10751-006-9435-x

Magnetotransport and magnetic properties of sulfospinels $Zn_xFe_{1-x}Cr_2S_4$

Jae Yun Park · Kwang Joo Kim

Published online: 20 December 2006

Abstract Cr-based chalcogenide spinels, which do not have heterovalency and distortion-induced ions such as manganese oxides with perovskite structure, have demonstrated the existence of colossal magnetoresistance. In order to investigate the magnetotransport phenomena and magnetic properties of sulfospinels $Zn_xFe_{1-x}Cr_2S_4$, polycrystalline $Zn_xFe_{1-x}Cr_2S_4$ samples were synthesized in the $0 \leq x \leq 0.2$ range by a solid reaction method. The crystal structure for $x=0.05$, 0.1, and 0.2 turned out to be cubic at room temperature by X-ray diffraction measurement. In magnetoresistance measurement, $Zn_xFe_{1-x}Cr_2S_4$ samples indicate that this system is semiconducting below about 150 K. The temperature of maximum magnetoresistance is almost consistent with Curie temperature. The isomer shift and the electric quadrupole shift of $Zn_xFe_{1-x}Cr_2S_4$ samples by Mössbauer experiment show that Fe^{2+} ions occupy the tetrahedral site in the spinel structure. As the Zn ions are substituted for Fe ions, the Jahn–Teller relaxation slows down and the electric quadrupole shift increases. The magnetotransport phenomena of $Zn_xFe_{1-x}Cr_2S_4$ is related to Jahn–Teller effect and half-metallic electronic structure, which are different from the double exchange interactions of the manganite La–Ca–Mn–O system or the triple exchange interactions of sulfospinel $Cu_xFe_{1-x}Cr_2S_4$.

Key words sulfospinel · magnetotransport · Mössbauer spectroscopy

1 Introduction

Since von Helmolt et al. published the colossal magnetoresistance (CMR) in thin films of $La_{2/3}Ba_{2/3}MnO_3$ in 1993, intensive interest has arisen from both experimental and theoretical points of view in studying the mechanism of CMR property [1]. Recently,

J. Y. Park (✉)
Department of Materials Science and Engineering, University of Incheon,
Incheon 402-749, South Korea
e-mail: pjy@incheon.ac.kr

K. J. Kim
Department of Physics, Konkuk University, Seoul 143-701, South Korea

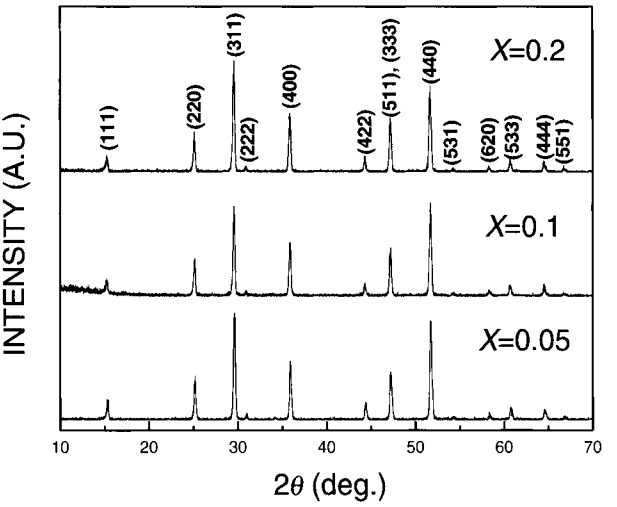

Fig. 1 X-ray diffraction patterns of $Zn_xFe_{1-x}Cr_2S_4$

CMR effect has been reported not only in manganite perovskites but also in sulfospinel $Cu_xFe_{1-x}Cr_2S_4$ [2–4]. CMR effect of manganites with perovskite structure is known to be associated with a double-exchange mechanism. On the otherhand CMR effect in the sulfospinel $Cu_xFe_{1-x}Cr_2S_4$, which is neither oxide nor perovskite, has opened a renewed interest for the further exploration of the magnetoresistance effect.

Mössbauer and magnetic properties on sulfospinel $FeCr_2S_4$ have been studied by many workers. $FeCr_2S_4$ is a ferrimagnetic semiconductor, crystallizing in the normal spinel structure. The Curie temperature T_c is about 177 K [5–8]. Both the metal-insulator transition and a negative magnetoresistance are observed around T_c. Much research on the conduction mechanism of sulfospinel compounds has been performed. And several models to explain CMR effect of these compounds have been suggested: the magnetic polaron model in $FeCr_2S_4$ [9], the half-metallic model [10], and the triple-exchange interaction [4]. The crystal structure of $ZnCr_2S_4$ is a normal spinel. $Zn_xFe_{1-x}Cr_2S_4$ has no heterovalence, which is different from both manganite perovskites and $Cu_xFe_{1-x}Cr_2S_4$. Moreover, there is no appreciable structural discontinuity around T_c. Here we investigate that Zn ion substitutions for Fe ions have effects on the magnetic properties and magnetoresistance properties of sulfospinel $Zn_xFe_{1-x}Cr_2S_4$ with X-ray diffraction (XRD), magnetoresistance measurement and Mössbauer spectroscopy.

2 Experimental

$Zn_xFe_{1-x}Cr_2S_4$ compounds (x=0–0.2) were prepared by the following solid state reaction method [11]. Mixtures of the proper portions of the high-purity elements (Fe, Zn, Cr, and S) sealed in evacuated quartz ampoules were heated to 480°C for a day and to 1,000°C for 4 days, and then slowly cooled down to room temperature at a rate of 10°C/h. In order to obtain homogeneous materials it was necessary to grind the samples after the first sintering and to press the powder into a pellet before annealing it for a second time to 1,000°C for 4 days in a evacuated and sealed quartz ampoule.

The crystal structure of $Zn_xFe_{1-x}Cr_2S_4$ samples was monitored by X-ray diffractometer in θ–2θ geometry with Cu K_α radiation. The electrical resistivity ρ and magnetoresistance

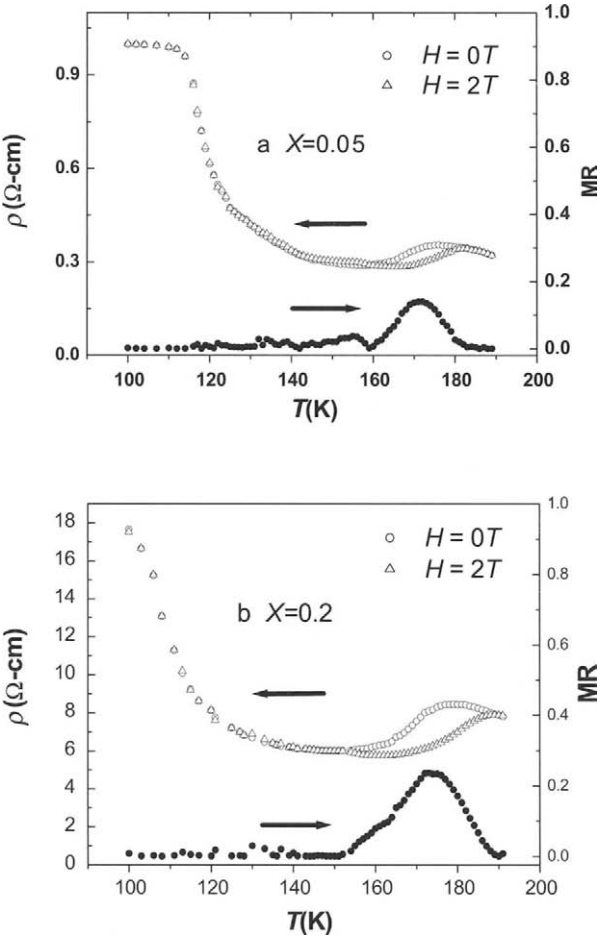

Fig. 2 Temperature dependence of the electrical resistivity ρ in magnetic field H=0, 2 T and magnetiresistance MR for $Zn_xFe_{1-x}Cr_2S_4$: (a) x=0.05, (b) x=0.2

were investigated by the 4-point probe method. The Mössbauer spectra were recorded using a conventional spectrometer of the electromechanical type with a single-line ^{57}Co source in a rhodium matrix.

3 Results and discussion

As shown in Fig. 1, the XRD results of $Zn_xFe_{1-x}Cr_2S_4$ exhibit the cubic spinel phase for all our samples, where both Zn and Fe ions occupy the tetrahedral sites and the Cr ions the octahedral sites. The lattice parameter for each composition was found by plotting $a(\theta)$ against the Nelson–Riley function and extrapolating to θ=90°. The lattice parameter is 9.993, 9.985, and 9.990 Å for x=0.05, 0.1, and 0.2, respectively. Zn substitutions have no strong effect on the crystal structure of sulfospinel $Zn_xFe_{1-x}Cr_2S_4$. This is explicable in the view of the fact that the ionic size of 0.74 Å for Zn^{2+} ions is almost equal to that of 0.76 Å for Fe^{2+} ions.

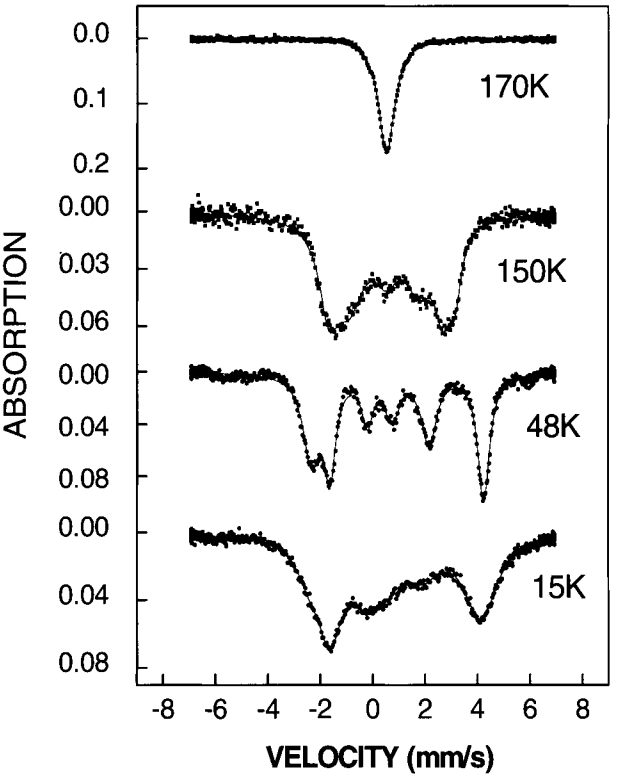

Fig. 3 Mössbauer spectra of $Zn_{0.05}Fe_{0.95}Cr_2S_4$ at various temperatures

Figure 2 exhibits the temperature dependence of the electrical resistivity ρ and magnetoresistance MR=$[\rho(0\ \mathrm{T})-\rho(2\ \mathrm{T})]/\rho(2\ \mathrm{T})$ of $Zn_xFe_{1-x}Cr_2S_4$ in the magnetic field H=0, 2 T. The spinel system is semiconducting below about 150 K. The metal-semiconductor transition can be found around T_c, which is due to polaron by Jahn–Teller effect [12]. MR of $Zn_{0.2}Fe_{0.8}Cr_2S_4$ is about 20%, which is relatively less than that of manganites. However, the temperature of maximum magnetoresistance is almost consistent with the Curie temperature. The magnetoresistance MR increases with increasing Zn composition.

Mössbauer spectra of $Zn_xFe_{1-x}Cr_2S_4$ were measured at various absorber temperatures from 16 K to room temperature. All samples are the pure spinel phase in the range $0 \leq x \leq 0.2$. Some of them are shown in Figs. 3 and 4. It is noted that the quadrupole shift vanishes above the Néel temperature T_N, indicating that Fe^{2+} ions occupy the tetrahedral site in the spinel structure because the local symmetry of a tetrahedral site is cubic T_d while that of an octahedral site is trigonal D_{3d} [6, 7]. On the other hand, the quadrupole shift below T_N increases steadily with decreasing temperature, implying a crystallographic distortion or a magnetically induced electric field gradient. The isomer shift 0.52±0.01 mm/s with respect to Fe metal indicates that the valence state of Fe ions is ferrous. The Néel temperature T_N increases with Zn composition x, suggesting that the superexchange interaction for the Zn–S–Cr link is stronger than that for Fe–S–Cr link. In the tetrahedral site, the ground state of Fe^{2+} ions is a degenerate orbital doublet ^5E_g. This state is unstable and must be resolved via a Jahn–Teller distortion, which may explain the appearance of the quadrupole shift below T_N. A dynamic Jahn–Teller distortion brings about the asymmetrical line broadening in Figs. 3 and 4. The results of asymmetrical line broadening is clearly seen around 15 and

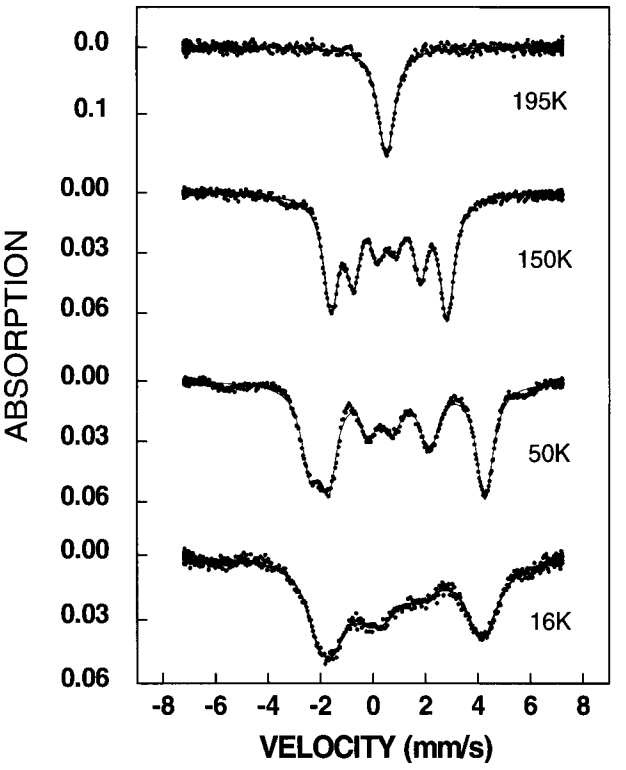

Fig. 4 Mössbauer spectra of $Zn_{0.2}Fe_{0.8}Cr_2S_4$ at various temperatures

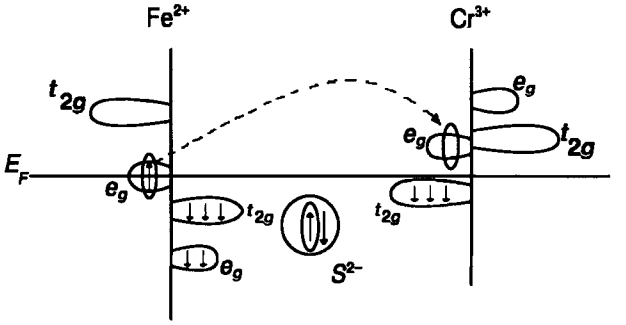

Fig. 5 Schematic energy diagram of half-metallic $FeCr_2S_4$

50 K. The difference between the first and sixth line, $\Gamma(1)$–$\Gamma(6)$, for x=0.05 and 0.2 is 0.3 and 0.4 mm/s around 15 K, respectively. It suggests that Jahn–Teller relaxation with increasing Zn composition slows down at low temperature.

As shown in Fig. 5, the e_g electrons of Fe^{2+} ions transit to the empty e_g level of Cr^{3+} ions in half-metallic band structure [12]. Such hopping is likely to happen due to the non-spin-flip nature of the transition. This CMR property could be explained in terms of the Jahn–Teller effect and half-metallic electronic structure, which are different from both the double exchange interactions of the manganite La–Ca–Mn–O system [10] and the triple exchange interactions of sulfospinels $Cu_xFe_{1-x}Cr_2S_4$ [4].

4 Conclusion

Zn substitutions have no effect on the crystal structure of sulfospinel $Zn_xFe_{1-x}Cr_2S_4$ samples. It is found that Zn^{2+} ions substitute Fe^{2+} ions at the tetrahedral site of the cubic spinel structure. As the Zn composition increases, the electric quadrupole shift, Jahn–Teller effect and the magnetoresistance effect increase. The CMR property might be interpreted in terms of the dynamic Jahn–Teller effect, and half-metallic electronic structure, which are different from manganites and sulfospinels $Cu_xFe_{1-x}Cr_2S_4$.

References

1. von Helmolt, R., Wecjer, J., Holzapfel, B., Schultz, L., Samwer, K.: Phys. Rev. Lett. **71**, 2331 (1993)
2. Ramirez, A.P., Caba, R.J., Krajewski, J.: Nature **386**, 156 (1997)
3. Kim, S.J., Kim, W.C., Kim, C.S.: J. Appl. Phys. **91**, 7935 (2002)
4. Palmer, H.M., Greaves, C.: J. Mater. Chem. **9**, 637 (1999)
5. Bouchard, R.T., Russo, P.A., Wold, A.: Inorg. Chem. **4**, 685 (1965)
6. Spender M.R., Morrish, A.H.: Can. J. Phys. **49**, 2659 (1971)
7. Spender M.R., Morrish, A.H.: Solid State Commun. **11**, 1417 (1972)
8. van Stapele, R.P.: In: Ferromagnetic Materials, vol. 3, p. 603. North-Holland, Amsterdam (1982)
9. Yang, Z., Tan, S., Chen, Z., Zhang, Y.: Phys. Rev. **B62**, 13872 (2000)
10. Millis, A.J., Shraiman, B.I., Mueller, R.: Phys. Rev. Lett. **77**, 175 (1996)
11. Ok, H.N., Back K.S., Kim, C.S.: Phys. Rev. **B26**, 4436 (1982)
12. Park, M.S., Youn, S.J., Min, B.I.: J. Korean Mag. Soc. **8**, 111 (1998)

Hyperfine Interact (2006) 169:1273–1277
DOI 10.1007/s10751-006-9436-9

Antiferromagnetic $TiFe_2$ in applied fields: experiment and simulation

T. B. Martins · H. R. Rechenberg

Published online: 16 November 2006

Abstract Mössbauer spectra of a powdered $TiFe_2$ sample were measured under different applied fields and the results were compared to simulated spectra obtained by minimizing the total energy of a two-sublattice antiferromagnet. In order to reproduce experimental results a highly textured distribution had to be assumed, the local anisotropy axis lying mostly perpendicular to the applied field. Thus, magnetic alignment of AF grains by an external field was demonstrated. In addition, exchange and anisotropy fields for $TiFe_2$ at $T \sim 0$ K have been determined.

1 Introduction

The intermetallic Laves phase compound $TiFe_2$ crystallizes in the C14 hexagonal structure and orders antiferromagnetically below T_N=280 K [1, 2]. Fe atoms occupy two sites in this structure, 6h and 2a. The Mössbauer spectrum below T_N is a superposition of a magnetic sextet and a quadrupolar doublet in the 3:1 ratio; from this result it was concluded that Fe (2a) is nonmagnetic [3]. We have recently undertaken a Mössbauer study of $TiFe_2$ in applied magnetic fields in order to determine whether Fe atoms at the 2a site carry a paramagnetic moment; the results have been reported elsewhere [4]. In this paper the magnetic hyperfine interaction of the 6h Fe site will be separately discussed. Mössbauer spectra of a powdered $TiFe_2$ sample were collected at T=4.2 K in various fields up to 12 T. The sample was prepared by arc melting, at the slightly nonstoichiometric composition $TiFe_{1.95}$ in order to prevent ferromagnetic clustering. Its single-phase quality was checked with X-ray diffraction. Some spectra are shown in Figure 1.

At increasing applied fields only a slight line broadening was observed and the sextet lines remained well resolved. Figure 2 displays the measured effective field vs applied field. The data accurately follow the relationship $B_{eff} = \left(B_{hf}^2 + aB^2\right)^{1/2}$, where B_{hf}=9.73 T is the intrinsic hyperfine field, B is the applied field, and a=0.867(4). Geometrically, this result implies that the B_{hf} vector was nearly perpendicular to the applied field. Such behavior would be expected for a single-crystalline AF sample with its anisotropy axis oriented

T. B. Martins · H. R. Rechenberg (✉)
Instituto de Física, Universidade de São Paulo, C. P. 66318, 05315-970 Sao Paulo, Brazil
e-mail: hercilio@macbeth.if.usp.br

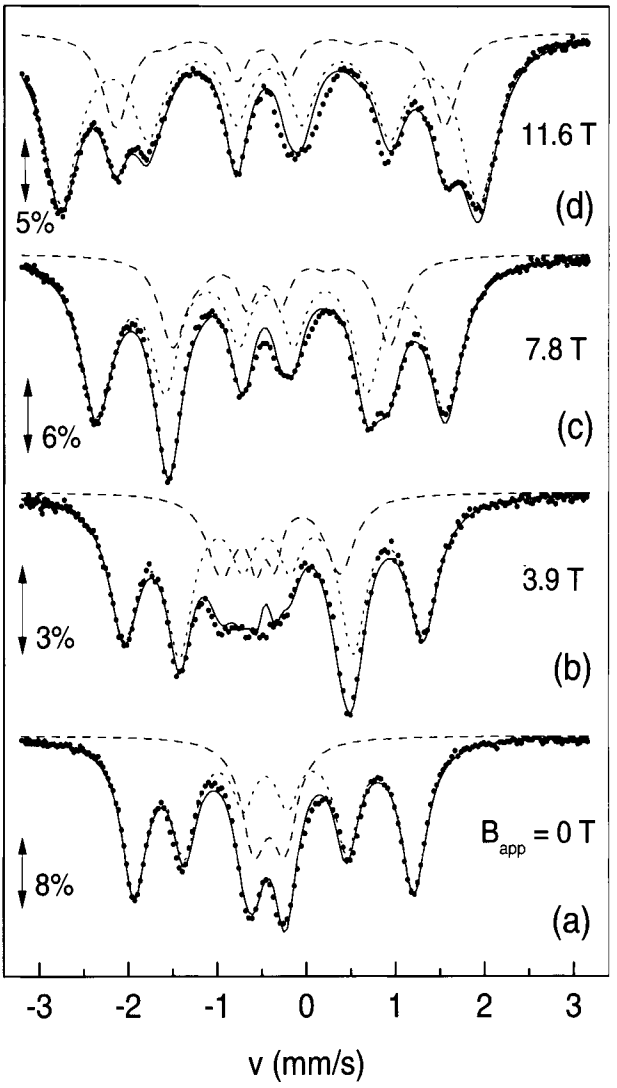

Figure 1 Mössbauer spectra of $TiFe_2$ at T=4.2 K and B=0 **a**, 3.9 T **b**, 7.8 T **c** and 11.6 T **d**. *Fitted curves* correspond to Fe (6*h*) site (*dotted*) and Fe(2*a*) site (*dashed*).

transversally, but not for a randomly oriented powder [5]. To understand this result, we carried out numerical simulations of the behavior of an AF polycrystal in arbitrarily large applied fields.

2 Model calculations

The total magnetic energy U of a two-sublattice antiferromagnet in applied field B is given by the classical expression:

$$u(\alpha_1, \alpha_2) = -B[\cos(\alpha_1 - \theta) + \cos(\alpha_2 - \theta)] + B_E \cos(\alpha_1 - \alpha_2) + \frac{1}{2} B_A(\sin^2 \alpha_1 + \sin^2 \alpha_2) \quad (1)$$

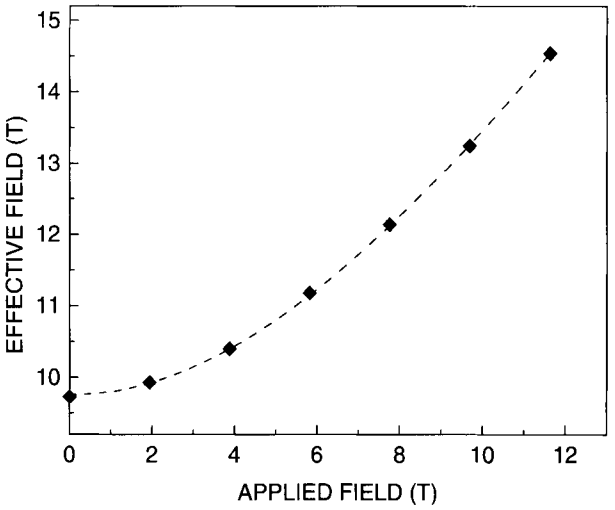

Figure 2 Effective hyperfine field vs applied field at 6*h* Fe site of $TiFe_2$ (T=4.2 K). *Dotted line* is a fitted curve.

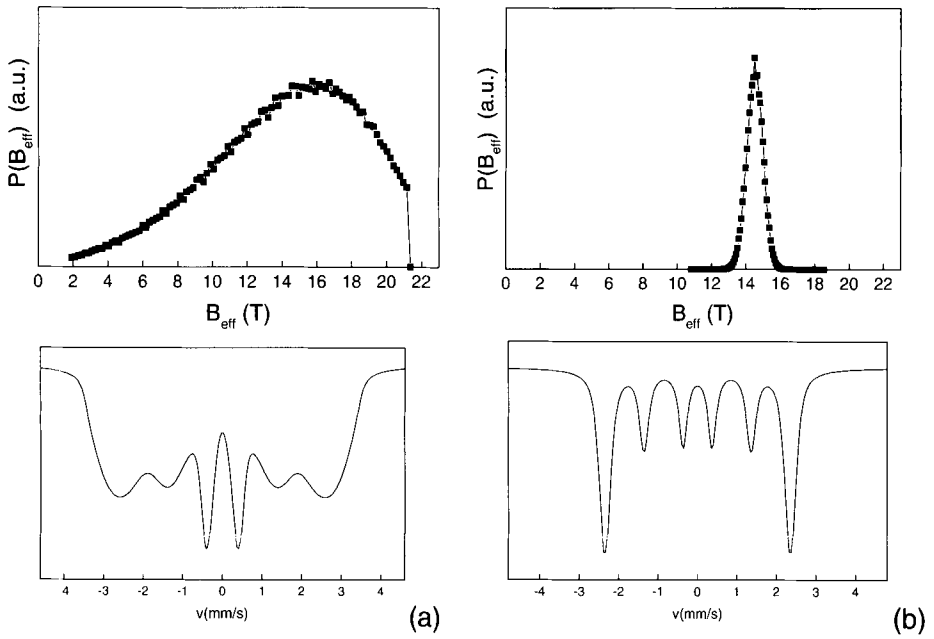

Figure 3 Calculated effective field distributions (*top*) and Mössbauer spectra (*bottom*), for **a** isotropic and **b** strongly textured powder. Parameters used for both calculations were B_E=72 T, B_A=2.2 T, B=11.6 T. For simplicity, spectra were calculated with null quadrupole interaction and Fe(2*a*) was not included.

In Eq. 1, $u = U/M_0$ where M_0 is the sublattice magnetization at T=0 K. Parameters B_E, B_A and θ are, respectively, the inter-sublattice exchange field, the anisotropy field, and the angle between B and the anisotropy axis. The free variables (α_1, α_2) are the angles between the axis and the magnetization vector of each sublattice. For a fixed set of parameters, the system's magnetic ground state is given by the angles that make the total energy a minimum. The minimization procedure was implemented with the gradient method. Once

α_1 and α_2 have been found, the effective hyperfine field for Fe nuclei in each sublattice can be obtained as a vector sum,

$$B_{eff}^{(i)} = \sqrt{B^2 + B_{hf}^2 - 2B \cdot B_{hf} \cos(\alpha_i - \theta)} \tag{2}$$

and a Mössbauer sextet can be constructed, proper account being taken of the line intensity ratios. To simulate the spectrum of a powder sample, such elementary spectra are summed over an ensemble of space orientations, weighted with a distribution function $w(\theta)$ [5]. The effective field distribution $P(B_{eff})$ was also calculated, as an alternative way of displaying the results.

The best choice of parameters, which yielded average B_{eff} values agreeing with the data of Figure 2 within experimental error, was B_E=72 T and B_A=2.2 T. These values are consistent with the spin–flop critical field $B_{SF} = [(2B_E - B_A)B_A]^{1/2}$ which is approximately 18 T for $TiFe_2$ [2]. The simulated spectra, however, showed exceedingly broad B_{eff} distributions if the distribution of crystallite orientations was assumed to be isotropic [i.e., if $w(\theta) = \frac{1}{2}\sin\theta$]. This is illustrated in Figure 3a.

Satisfactory simulations could only be achieved if, instead of random crystallite orientations, a narrow angular distribution around θ=90° was assumed. Specifically, $w(\theta)$ was taken to be a Gaussian function of width σ_θ=5°, yielding results such as those displayed in Figure 3b. The qualitative resemblance to the experimental spectra is much improved, for B=11.6 T (as shown) and for all other applied field values.

3 Discussion

The physical meaning of the result above is that our powder sample was substantially oriented by the external field. Magnetic alignment of ferro- or ferrimagnetic powders by application of a static field is a routine step in permanent magnets manufacturing. In such case, the magnetic torque on a particle of volume V is $\tau_F = M_s VB \sin\theta$. For an antiferromagnetic particle, the torque originates from the susceptibility anisotropy [6] and is given by

$$\tau_{AF} = \frac{1}{2\mu_0} V\left(\chi_\perp - \chi_\parallel\right) B^2 \sin 2\theta \tag{3}$$

(in this case, the perpendicular orientation has lowest energy). Thus, antiferromagnetic grains will rotate if the magnetic field is sufficiently large to overcome friction forces. This condition could be fulfilled in our experiments because the absorber sample was a loose powder. Incidentally, our measurements were done in order of decreasing fields, so the maximum alignment occurred at B=11.6 T and did not change during the subsequent experiments at lower fields.

The latter conclusion was corroborated by a later Mössbauer measurement in zero field, which showed that the magnetically induced texture persisted (at least partially) long after the first series of experiments, even upon heating to room temperature and moving the sample (Figure 4). The fitted Fe(6h) sextet had a 3:q:1 line intensity ratio with q=3.13, from which $\langle\sin^2\theta\rangle$=0.878, or $\theta_{av}\approx$70°, was obtained. It is also noticeable that the components of the Fe(2a) doublet (Δ=0.386 mm/s) have unequal intensities, which is an additional indication of preferred orientation. From the crystal symmetry it can be inferred that the Fe(2a) V_{zz} axis is parallel to the Fe(6h) magnetic axis. Thus, the doublet intensity

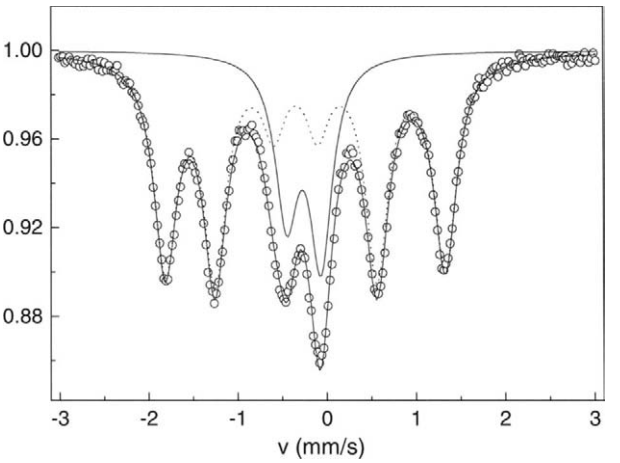

Figure 4 $TiFe_2$ spectrum at T= 4.2 K and zero applied field, measured after exposure to high fields. *Dotted curve* Fe(6*h*), *full curve* Fe(2*a*).

ratio could be calculated by the expression [8] $I_\sigma/I_\pi = \left(\frac{2}{3} + < \sin^2 >\right)/\left(2 - < \sin^2 \theta >\right)$; the obtained ratio was 1.38, in good agreement with the experimental value 1.40. Furthermore, the fact that the higher-velocity component had the larger intensity allows its identification as the σ (i.e., $\left|\pm\frac{1}{2}\right\rangle \rightarrow \left|\pm\frac{1}{2}\right\rangle$) transition; hence, $V_{zz}<0$ at the Fe(2a) site of $TiFe_2$, a previously unknown result [7].

4 Conclusions

We have measured Mössbauer spectra of a powdered sample of antiferromagnetic $TiFe_2$ under different applied fields, and the results were compared to simulated spectra. A theoretical model was constructed, by means of which the angular orientation of the two sublattice magnetizations was determined by minimizing the total energy. Spectra calculated by assuming random crystallite orientations failed to reproduce the experimental results. In order to obtain simulated spectra with the required narrow effective field distributions, a strongly textured distribution had to be assumed, the local anisotropy axis lying perpendicular to the applied field within ±5°. Thus, magnetic alignment of antiferromagnetic grains by an external field was demonstrated. Additionally, the exchange field B_E=72 T and the anisotropy field B_A=2.2 T have been determined for $TiFe_2$ at $T\approx0$ K.

Acknowledgement The $TiFe_2$ sample was prepared and characterized by Dr. L. Morellon (ICMA, Zaragoza). This work was financially supported by FAPESP and CNPq.

References

1. Nakamichi, T.: J. Phys. Soc. Jpn. **25**, 1189 (1968)
2. Brown, P.J., Deportes, J., Ouladdiaf, B.: J. Phys., Condens. Matter **4**, 10015 (1992)
3. Wertheim, G.K., Wernick, J.H., Sherwood, R.C.: Solid State Commun. **7**, 1399 (1969)
4. Rechenberg, H.R., Morellon, L., Algarabel, P.A., Ibarra, M.R.: Phys. Rev., B **71**, 104412 (2005)
5. Pankhurst, Q.A., Pollard, R.J.: J. Phys. Condens. Matter **2**, 7329 (1990)
6. Morrish, A.H.: The Physical Principles of Magnetism. Wiley, New York (1965)
7. Pelloth, J., Brand, R.A., Keune, W.: J. Magn. Magn. Mater. **140–144**, 59 (1995)
8. Greenwood, N.N., Gibb, T.C.: Mössbauer Spectroscopy. Chapman & Hall, London (1971)

Hyperfine Interact (2006) 169:1279–1283
DOI 10.1007/s10751-006-9437-8

Determination of Lamb–Mössbauer factors and lattice dynamics in some nitroprusside single crystals

V. Rusanov · S. Stankov · V. Gushterov · L. Tsankov · A. X. Trautwein

Published online: 5 December 2006

Abstract Mössbauer spectra have been recorded for sodium, guanidinium, barium and lithium nitroprussides single crystal cuts. The temperature dependence of the Lamb–Mössbauer fraction f, respectively, the mean-square nuclear displacement $\langle x^2 \rangle$ and the mean-square (of the total) velocity of the iron nucleus $\langle v^2 \rangle$ were analyzed on the basis of the Debye and Einstein lattice-vibration models. The characteristic temperatures of the two models, θ_D and θ_E, fitted to $\langle x^2 \rangle$ are considerably lower than those fitted to $\langle v^2 \rangle$. This effect seems to be typical for the iron complexes and was explained with the presence of low and high frequencies in the phonon vibration spectra and of low-temperature anharmonicity. The Lamb–Mössbauer fraction at 77 K in all principal crystal directions of sodium, guanidinium and barium nitroprussides has been determined. These values will be used for more precise studies of the population and the properties of the light-induced molecular states of the nitrosyl $[Fe(CN)_5NO]^{2-}$ anion.

Key words nitroprusside single crystals · Lamb–Mössbauer factors · lattice dynamics · Debye and Einstein characteristic temperatures

1 Introduction

Two long-lived, light-induced molecular states (SI and SII) have been observed in the sodium nitroprusside $Na_2[Fe(CN)_5NO]\cdot 2H_2O$ (SNP) [1]. The decay temperatures are

V. Rusanov (✉) · S. Stankov · V. Gushterov
Department of Atomic Physics, Faculty of Physics, University of Sofia,
5 James Bourchier Boulevard, 1164 Sofia, Bulgaria
e-mail: rusanov@phys.uni-sofia.bg

L. Tsankov
Department of Nuclear Engineering, Faculty of Physics, University of Sofia,
5 James Bourchier Boulevard, 1164 Sofia, Bulgaria

A. X. Trautwein
Institut für Physik, Universität zu Lübeck, Ratzeburger Allee 160, 23538 Lubeck, Germany

low: about 140 K for SII and about 200 K for SI. There is evidence that new materials with decay temperatures around room temperatures could be found and that such controlled and reversible photo-switching materials could be used for optical information storage with extremely high capacity. The structural changes related to SI and SII have been controversially debated in the recent years. For example, SI was described as inverted Fe–O–N bond compared to the Fe–N–O bond in the ground state. For SII a side-on bonding of the NO group to the iron atom is proposed [2]. These structural changes are not widely approved because other studies [3] do not indicate such changes. This controversy remains a challenge for future investigations. A summary of investigations on photochromatic effects and on SI and SII carried out by resonance methods can be found in [4] and a more general review in [5].

The nitroprussides $(CN_3H_6)_2[Fe(CN)_5NO]$ (GuNP), $Ba[Fe(CN)_5NO]\cdot 3H_2O$ (BaNP), and $Li_2[Fe(CN)_5NO]\cdot 4H_2O$ (LiNP), available as single crystals, are suitable for a study of the physical nature of SI and SII. Mössbauer parameters of the first two nirtoprussides are measured at room temperature (GuNP in [6] and BaNP in [7]). Population experiments and investigations of SI and SII are usually performed at 77 K. In the present contribution temperature dependent measurements of Mössbauer parameters with single crystal *a*-, *b*-, and *c*-cuts are described. The Lamb–Mössbauer factor f at 77 K has been determined. The temperature dependence of f and the isomer shift (second-order Doppler shift V_0) were analyzed on the basis of the Einstein and Debye lattice-vibration models [8, 9].

2 Experimental details and calculations

The raw material for the crystal growth was obtained by double cation exchange reaction from sodium nitroprusside as described in [10]. Dark red, well-faced single crystals with dimensions of several centimetres were grown by slow evaporation of saturated aqueous solutions at about 305 K. For the measurements single crystal *a*-, *b*-, and *c*-cuts with thickness in the range 240–500 μm have been used. Because of the high electron absorption in BaNP and the existence of an excellent cleavage plane the thinnest crystal, 240 μm, was used to study BaNP, and it was glued to a 1 mm supporting Plexiglas layer. All spectra were recorded with a spectrometer in constant acceleration mode and a ^{57}Co[Rh] source of about 20 mCi activity. The isomer shifts were related to the α-Fe standard at room temperature. The temperature dependent measurements were performed in a continuous flow cryostat from Oxford Instruments. The sample temperature was maintained stable in the range of ±0.2 K.

In the case of a single crystal the cross-sections for nuclear resonant absorption of the two absorption lines of the quadrupole doublet are polarization dependent [6]. In our analysis of cross-sections (f factors) we have considered this effect. The first nitroprusside single crystal studied in this way was $Na_2[Fe(CN)_5NO]\cdot 2H_2O$ (SNP) [11]. Within the harmonic approximation of lattice dynamics the mean-square displacement $\langle x^2\rangle$ along the vector k can be derived from $f = \exp\left(-k^2\langle x^2\rangle\right)$. The mean-square velocity of the nucleus $\langle v^2\rangle$ can be extracted from the source velocity at resonance, $V_0 = \delta_0 - \langle v^2\rangle/2c$, where δ_0 is the isomer shift that exists between the chosen standard and absorber at a definite temperature, c is the speed of light. Einstein (θ_E) and Debye (θ_D) temperatures, respectively, have been derived from the temperature dependence of $\langle x^2\rangle$ and $\langle v^2\rangle$ as described in [8, 9].

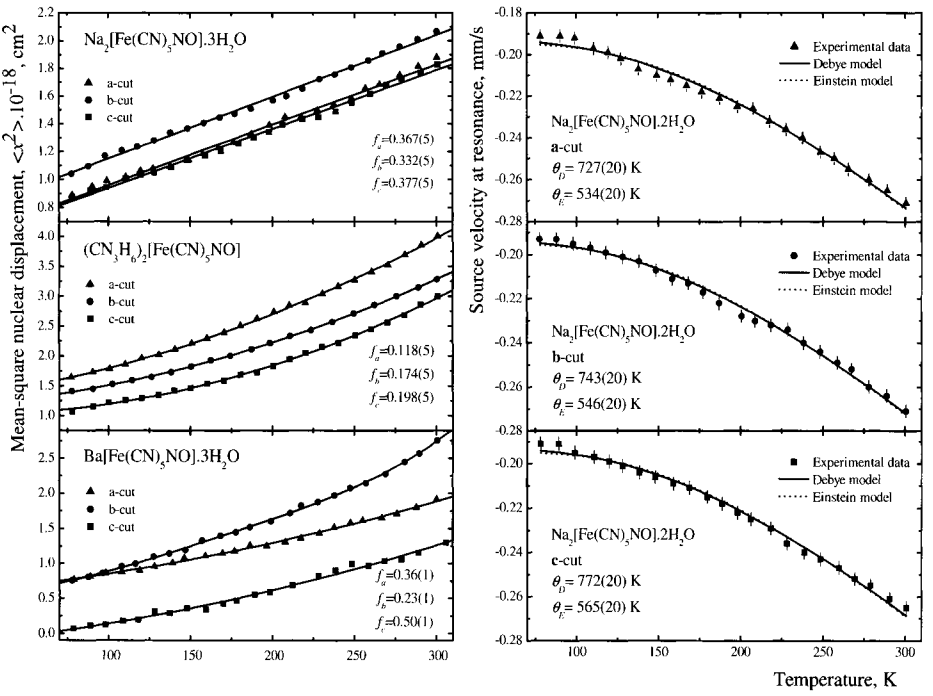

Figure 1 $\langle x^2 \rangle$ results (polarization and saturation effects are neglected) together with Lamb–Mössbauer factors f at room temperature for nitroprusside single crystal cuts (*left*); temperature dependence of the resonant source velocity V_0 together with Debye (θ_D) and Einstein (θ_E) temperatures for sodium nitroprosside single crystal cuts (*right*). The mean values are θ_D=747(20) K and θ_E=548(20) K. For the guanidinium and barium nitroprussides the mean values are θ_D=716(20) K, θ_E=527(20) K, and θ_D=717(20) K, θ_E=528 (20) K, respectively.

3 Results and discussion

Temperature dependent measurements of Mössbauer parameters of single crystal *a*-, *b*-, *c*-cuts of SNP, GuNP and BaNP were performed. Figure 1 (left) presents $\langle x^2 \rangle$ results (polarization and saturation effects, both about 5%, were neglected). In the harmonic approximation a linear behaviour of $\langle x^2 \rangle$ versus T is expected at high temperature with the straight-line asymptote intersecting the $\langle x^2 \rangle$-axes in the origin. Only SNP shows an approximately linear decrease of $\langle x^2 \rangle$ with decreasing temperature. For GuNP this behaviour is not linear. The vibrational anisotropy observed at room temperature remains down to 77 K. BaNP exhibits three significantly different $\langle x^2 \rangle$ values at room temperature for the three different crystal cuts. We want to emphasize that this vibrational anisotropy becomes axially symmetric with only two values of the Lamb–Mössbauer factor at 77 K. Such behaviour indicates low-temperature anharmonicity in the solid. After polarization and saturation effect corrections the set of values of $\langle x^2 \rangle$ as a function of temperature for each single crystal direction of the nitroprussides were fitted on the basis of the Debye and Einstein models, respectively. Both models have yielded practically the same fits. The calculated characteristic temperatures θ_D and θ_E are summarized in Table I.

The analysis of the temperature dependent $\langle v^2 \rangle$ data yields different θ_D and θ_E values, Figure 1 (right), compared to those derived from $\langle x^2 \rangle$ (Table I) by up to a factor of about 5.

Table I Characteristic temperatures θ_D and θ_E obtained from analyzing $\langle x^2 \rangle$-data (Figure 1 left) taking into account polarization and saturation effects. The error margin expressed in brackets corresponds to one standard deviation.

↓ Crystal	Crystal direction →		
	a-axis	*b*-axis	*c*-axis
SNP			
θ_D	203(3)	189(3)	205(3)
θ_E	117(2)	109(2)	118(2)
GuNP			
θ_D	142(3)	157(3)	166(3)
θ_E	82(2)	91(2)	96(2)
BaNP			
θ_D	208(3)	180(3)	280(3)
θ_E	120(2)	104(2)	161(2)

Table II Lamb–Mössbauer factors *f* at 77 K. The error margin expressed in brackets corresponds to one standard deviation

↓ *f* factor	Crystal direction →		
	a-axis	*b*-axis	*c*-axis
SNP	0.71(1)	0.66(1)	0.70(1)
GuNP	0.53(1)	0.59(1)	0.65(1)
BaNP	0.75(1)	0.77(1)	0.94(1)

The $\langle x^2 \rangle$-data present the mean value along the wave vector k and therefore are direction dependent, whereas $\langle v^2 \rangle$-data are averaged in all directions and therefore can have only a single value. The general trend in the behaviour of the characteristic temperatures is that θ_D and θ_E extracted from $\langle x^2 \rangle$ data are always many times lower than those extracted from $\langle v^2 \rangle$ data. This behaviour is due to the existence of two vibrational frequency regions: low-energy acoustical lattice vibrations with energy up to 30 meV, which affect more strongly $\langle x^2 \rangle$ values, and high-energy optical molecular vibrations with energy in the range 60–100 meV, on which the $\langle v^2 \rangle$ values depend considerably. This vibration specificity is especially true for Fe-complexes and indicates that results derived on the basis of Einstein and Debye models for nitroprussides have to be taken with caution. From the average value of the second-order Doppler shift between 77 and 293 K an effective recoil mass of about 138 g/mol was calculated, which as expected is nearly equal to the mass of the iron atom and its first neighbours (five carbon and one nitrogen atom) i.e. 131 g/mol [10].

The *f* factors derived at 77 K for SNP, GuNP and BaNP are summarized in Table II compared to those at room temperature listed on Figure 1 for nitroprussides with inorganic cations (Na, Ba) they are at least two times higher for all principal crystal directions, for the organic guanidinium cation about three to four times higher.

The LiNP is chemically unstable at room temperature (looses its crystal water). It was measured in the form of a powder sample with a nondefinite quantity of crystal water and therefore was not used in this presentation.

4 Conclusions

Temperature dependent Mössbauer studies have been performed on sodium, barium, guanidinium and lithium nitroprussides single crystal cuts. Lower sensitivity to temperature

than that expected from the harmonic approximation of lattice dynamics and low-temperature anharmonicity have been observed. Strongly differing characteristic temperatures θ_D and θ_E have been found from analyzing $\langle x^2 \rangle$- and $\langle v^2 \rangle$-data, respectively, which clearly indicates that results derived on the basis of the Einstein as well as Debye model have to be considered with caution. The Lamb–Mössbauer fraction at 77 K in all principal crystal directions of sodium, guanidinium and barium nitroprussides were determined. These values will be used for more precise studies of the population and properties of the light-induced molecular states of the nitrosyl $[Fe(CN)_5NO]^{2-}$ anion.

Acknowledgements We thank the Alexander von Humboldt Foundation, the special program Stability Pact for South Eastern Europe (Rusanov, V.) and the German Academic Exchange Office, DAAD (Stankov, S.) for the provided Research Fellowship Grants.

References

1. Hauser U., Oestreich V., Rohrweck H.D.: Z. Phys. A **280**, 17 (1977)
2. Carducci M.D., Pressprich M.R., Coppens P.: J. Am. Chem. Soc. **119**, 2669 (1997)
3. Schaniel D., Schefer J., Imlau M., Woike T.: Phys. Rev., B **68**, 104108 (2003)
4. Rusanov V., Stankov S., Trautwein A.X.: Hyperfine Interact. **144/145**, 307 (2002)
5. Coppens P., Novozhilova I., Kovalevsky A.: Chem. Rev. **102**, 861 (2002)
6. Rusanov V., Stankov S., Angelov V., Koop N., Winkler H., Trautwein A.X.: Nucl. Instrum. Methods, B **207**, 205 (2003)
7. Stankov S., Rusanov V., Angelov V., Haussühl S., Trautwein A.X.: Hyperfine Interact. **141/142**, 223 (2002)
8. Lafleur L.D., Goodman C.L.: Phys. Rev., B **4**, 2915 (1971)
9. Gibb,T.C.: Principles of Mössbauer Spectroscopy, p. 135. Charman and Hall, London (1976)
10. Rusanov V., Angelov V., Angelova J., Bonchev T., Woike T., Kim H., Haussühl S.: J. Solid State Chem. **123**, 39 (1996)
11. Grant R.W., Housley R. M., Gonser U.: Phys. Rev. **178**, 523 (1969)

Hyperfine Interact (2006) 169:1285–1290
DOI 10.1007/s10751-006-9438-7

Temperature dependent Mössbauer and neutron diffraction studies of $Cu_xFe_{1-x}Cr_2S_4$ compounds

Bae Soon Son · Sam Jin Kim · In-Bo Shim · Bo Wha Lee · Chul Sung Kim

Published online: 16 November 2006

Abstract The cation distribution and magnetic structure of $Cu_xFe_{1-x}Cr_2S_4$ (x=0.1, 0.2, 0.3, 0.4, and 0.5) has been studied by X-ray and neutron diffraction, vibrating sample magnetometer (VSM), and Mössbauer spectroscopy. The charge state of Fe is found to be ferrous (Fe^{2+}) for the x=0.1 sample; ferric (Fe^{3+}) for the x=0.5 sample; mixed state (Fe^{2+}, Fe^{3+}) for the x=0.2, 0.3, and 0.4 samples. The Mössbauer spectra of the x=0.1 sample show asymmetric line broadening, which is considered to be due to the Jahn–Teller effect of Cu^{2+} ions, and a symmetrical six-line pattern is shown for the x=0.5 sample. The valence state of the Cu ions for the x=0.1 and 0.5 samples is found to be divalent and monovalent, respectively. The magnetic structure of the samples was determined to be a ferrimagnetic structure with antiparallel alignment of the Fe and Cr ion magnetic moments.

Key words neutron diffraction · Mössbauer spectroscopy · sulphur spinel

1 Introduction

The discovery of the colossal magnetoresistance (CMR) phenomenon on sulphur spinel has been of great interest, due to its potential for technological applications and the interesting physical properties of materials [1, 2]. Ferroelectricity and colossal magnetocapacitive coupling in Cd-doped sulphur spinel have recently been reported. Cd-doped sulphur spinel has also been considered for its physical properties [3]. Studies on sulphur spinel compounds ($Fe_{1-x}Cu_xCr_2S_4$; x=0.0 and 0.5) have suggested that the conduction mechanism in these materials may not be the double exchange (DE) of carriers [4]. According to the octahedral (B) site preference of Cr^{3+}, the Mössbauer spectra of $FeCr_2S_4$ is believed to arise

B. S. Son · S. J. Kim · I.-B. Shim · C. S. Kim (✉)
Department of Physics, Kookmin University, Seoul 136-702, South Korea
e-mail: cskim@phys.kookmin.ac.kr

B. W. Lee
Department of Physics, Hankuk University of Foreign Studies, Yongin, Kyungki 449-791, South Korea

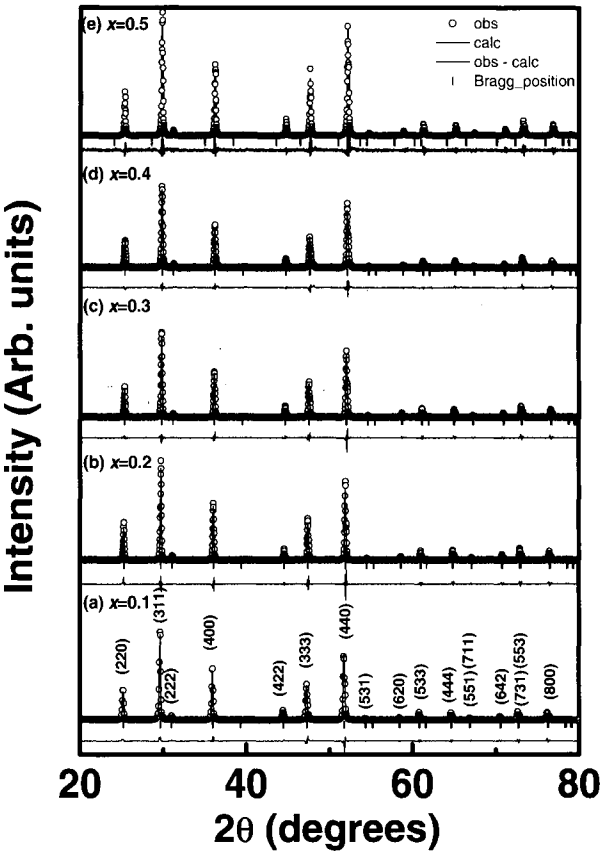

Figure 1 Refined X-ray diffraction patterns of $Cu_xFe_{1-x}Cr_2S_4$ at room temperature, **(a)** x=0.1, **(b)** x=0.2, **(c)** x=0.3, **(d)** x=0.4, and **(e)** x=0.5, respectively.

from the tetrahedral (A) site of the Fe^{2+} spectra. However, the Mössbauer spectra of $FeCr_2S_4$ were found to be dependent on the sample; furthermore some of the papers reported line broadening caused by an excess of B-site Fe^{2+}. Samples of $Cu_xFe_{1-x}Cr_2S_4$ ($x \leq 0.5$) have been studied extensively [5]. Lotgering et al. developed a monovalence model of Cu^+ ion, while Goodenough postulated the existence of divalent Cu^{2+} for the $0.5<x\leq1.0$ concentration range [6]. Also Palmer et al. and V. Fritsch et al. reported the triple exchange model and suggested the coexistence of Fe^{2+} and Fe^{3+} iron ions in the tetrahedral sites [7]. Therefore, it is essential to determine the valence state of iron ions in various sulphur spinel compounds to properly understand the underlying mechanism. We herein present the results for the temperature dependence of the Mössbauer experiments and compare them with the results of the X-ray, neutron diffraction and vibrating sample magnetometer (VSM) magnetization measurements for the sulphur spinel compounds of $Cu_xFe_{1-x}Cr_2S_4$ (x=0.0, 0.1, 0.2, 0.3, 0.4, and 0.5).

2 Experiments

Cu-substituted $Cu_xFe_{1-x}Cr_2S_4$ (x=0.1, 0.2, 0.3, 0.4, and 0.5) were synthesized in highly evacuated quartz tube. The X-ray diffraction (XRD) measurements were performed with Cu K_α radiation. Neutron diffraction was obtained at the Korea atomic energy research institute

Table I Results of parameters of X-ray diffraction refinement on $Cu_xFe_{1-x}Cr_2S_4$ (x=0.1, 0.2, 0.3, 0.4, and 0.5)

	x=0.1	x=0.2	x=0.3	x=0.4	x=0.5
a_0 (Å)	9.988	9.962	9.941	9.927	9.866
u (S)	0.741	0.741	0.741	0.741	0.741
d_{Fe-S} (Å)	2.312	2.306	2.301	2.298	2.299
d_{Cu-S} (Å)	2.312	2.306	2.301	2.298	2.299
d_{Cr-S} (Å)	2.414	2.406	2.403	2.399	2.376
R_{exp} (%)	4.28	6.08	5.32	5.29	4.64
R_B (%)	4.16	5.30	4.96	5.16	7.09

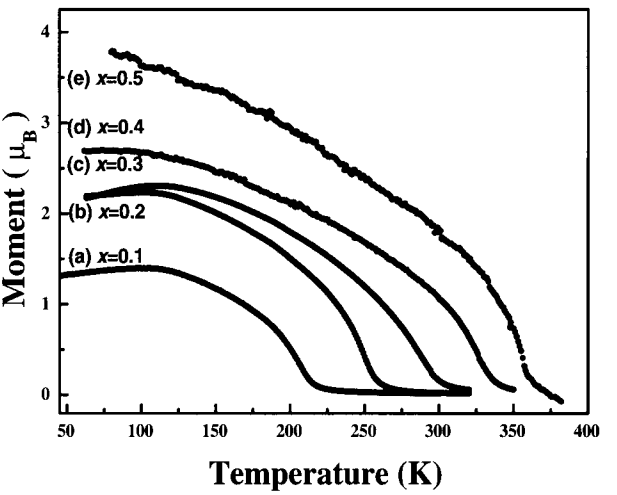

Figure 2 Temperature dependence of Bohr magnetization curves of $Cu_xFe_{1-x}Cr_2S_4$ under 5 kOe external magnetic field.

reactor HANARO HRPD (high resolution powder diffractomerter, λ=1.8348 Å). The magnetic properties were measured using vibrating sample magnetometer (VSM) in the 50≤ T≤380 K temperature range and in the 100 Oe and 5 kOe external field. The Mössbauer spectra were recorded using the conventional spectrometer with a ^{57}Co source in a rhodium matrix at temperatures ranging from 4.2 to 300 K.

3 Results and discussion

The XRD data of the single phase samples can be successfully fitted by the Rietveld refinement method, which gives the lattice constants a_0, anion parameter u, bond lengths d for the sulphur spinel system. It also indicates that the $Cu_xFe_{1-x}Cr_2S_4$ system crystallizes in normal spinel structure as shown in Figure 1, in which Cu/Fe and Cr occupy the tetrahedral (A) and octahedral (B) sites, respectively. The crystal space group is *Fd3m* (Fe, Cu (8*a*); Cr (16*d*); S (32*e*) (*u*,*u*,*u*)). The determined lattice constants a_0, anion parameter u, bond lengths d, and R-factor are listed in Table I. It is observed that the lattice constant decreases linearly when the Cu concentration increases (Vegard's law). As expected, the Cu/Fe–S (referred as A–S) and Cr–S (refereed as B–S) inter-atomic distance decrease remarkably due to the reduction of unit cell size.

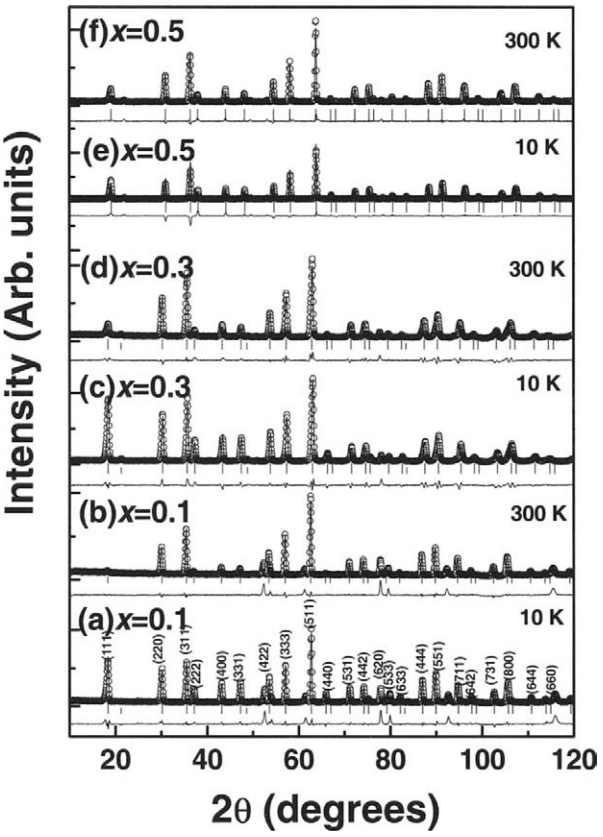

Figure 3 Neutron diffraction patterns of $Cu_xFe_{1-x}Cr_2S_4$ compounds, **(a)** at 10 K, **(b)** at 300 K, for the sample x=0.1; **(c)** at 10 K, **(d)** at 300 K, for the sample x=0.3; **(e)** at 10 K, **(f)** at 300 K, for the sample x=0.5, respectively.

The temperature dependence of the magnetic moment at a constant H=5 kOe magnetic field is indicated in Figure 2. The Néel temperature T_N increases with the Cu concentration x. Here, the Néel temperature is defined as the temperature of the maximum slope in dM/dT. According to the VSM results, both the magnetic moment and the Néel temperature increased with increasing Cu substitution. It is noticeable that the Néel temperature increased with the enhancement of superexchange interaction. The strength of superexchange interaction is inversely proportional to the bond length between the magnetic ions. So, an increase in the Néel temperature is due to the bond lengths as shown in Table I. It is observed that saturation magnetizations increase when Cu concentration increases. From this result, we can conclude that the relative spin arrangement of Fe ions in the A site and Cr ions in B site are coupled to be antiferromagnetic, whereas the A–A and B–B interactions are arranged to be ferromagnetic. In order to clarify the magnetic structure and microscopic interaction, we studied them with the neutron diffraction and Mössbauer spectroscopy.

Figure 3 shows some of the neutron diffraction patterns for $Cu_xFe_{1-x}Cr_2S_4$ (x=0.1, 0.3, and 0.5) at 10 and 300 K. The neutron diffraction for $Cu_xFe_{1-x}Cr_2S_4$ (x=0.1, 0.3, and 0.5) above 10 K showed that the magnetic peaks were overlapping on the nucleus peak. The magnetic peak decreases when temperature increases and it disappears at Néel temperature. According to the Néel theory two-sublattice model, both Fe and Cr sublattices are ferromagneticaly ordered, while the magnetic moment of Fe sublattice is antiparallel to that

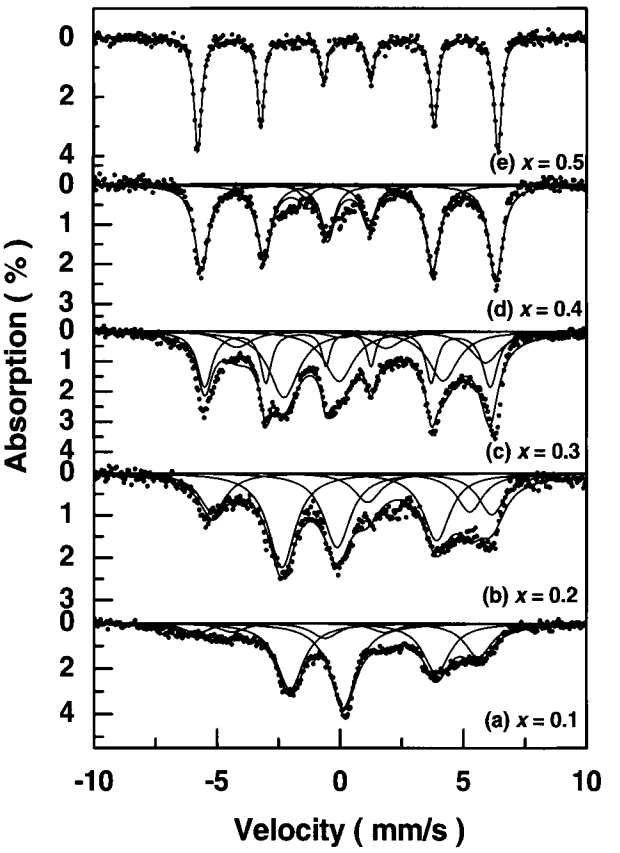

Figure 4 Mössbauer spectra of $Cu_xFe_{1-x}Cr_2S_4$ at 4.2 K, **(a)** x=0.1, **(b)** x=0.2, **(c)** x=0.3, **(d)** x=0.4, and **(e)** x=0.5, respectively.

of the Cr sublattice due to the magnetic coupling between these two sublattices. This is due to the fact that the net magnetic moment of the Cr sublattices is larger than that of the Fe sublattices. The results agree with those obtained by VSM.

The Mössbauer spectra were collected at temperatures ranging from 4.2 to 300 K. Figure 4 shows the Mössbauer spectra of the $Cu_xFe_{1-x}Cr_2S_4$ samples (x=0.1, 0.2, 0.3, 0.4, and 0.5) at 4.2 K with various Cu concentrations. The large asymmetrical line broadening of Mössbauer absorption line is shown for the x=0.1 samples at 4.2 K. It is related to the dynamic Jahn–Teller effect. The distorted line shape is due to the Jahn–Teller active ion. Bearing in mind that Fe^{2+} with $3d^6$ electrons is a Jahn–Teller active ion in the tetrahedral sites, the energy splitting of the ground state is due to a Jahn–Teller effect at the Fe sites corresponding to a degenerate orbital doublet E_g state of Fe^{2+} [9].

Asymmetrical six-line pattern is shown for the x=0.5 sample in Figure 4. It is interesting to note that nonzero quadrupole shift in $FeCr_2S_4$ is observed despite the fact that spatial symmetry of the Fe^{2+} ions is Td [10]. The obtained magnetic hyperfine field and isomer shift value of the x=0.1 and 0.5 samples are 170, 378 kOe at 13 K and 0.43, 0.20 mm/s at room temperature, respectively, which are typical values of Fe^{2+} and Fe^{3+} in Cr based sulphur spinel. We notice that the degree of asymmetrical line broadening is high up to x= 0.1 but it decreases above x=0.3. Then, a nearly symmetrical six-line pattern is shown for the x=0.4 sample. As for x=0.5 sample, a sharp sextet is observed. Furthermore, the magnetic hyperfine field is quite large compared to that of the x=0.1 sample. Remembering

that ferrous ions show large quadrupole shifts due to a large orbital angular contribution and that the ferric ion has a small quadrupole shift, we can carefully conclude that the charge states of the iron ions in the x=0.1 and 0.5 samples are ferrous and ferric, respectively. Moreover, the valence states of copper ions of the x=0.1 and 0.5 samples are divalent and monovalent, respectively, from charge neutrality. From the above discussion, we can conclude that the $Cu_xFe_{1-x}Cr_2S_4$ samples (x=0.2, 0.3, and 0.4) are mixed system of Fe^{2+} and Fe^{3+}. The portion of Fe^{2+} and Fe^{3+} ions for $Cu_xFe_{1-x}Cr_2S_4$ (x=0.3) is 80.7 and 19.3%, respectively, by Mössbauer absorption ratio.

4 Conclusion

In summary, samples of $Cu_xFe_{1-x}Cr_2S_4$ (x=0.1, 0.2, 0.3, 0.4, and 0.5) have been studied by using Mössbauer spectroscopy, X-ray diffraction, magnetization, and neutron diffraction. The magnetic structure is ferrimagnetic, the spins of Fe ions in the A sites and Cr ions in B sites are coupled to form an antiferromagnetic arrangement. The charge states of iron ions for the x=0.1 and x=0.5 samples are ferrous and ferric, respectively, while it is concluded that the $Cu_xFe_{1-x}Cr_2S_4$ samples (x=0.2, 0.3, and 0.4) are mixed system of Fe^{2+} and Fe^{3+}. The Mössbauer spectra of the x=0.1 sample show an asymmetric line broadening, which is due to dynamic Jahn–Teller relaxation.

Acknowledgments This work was supported by the Korea Research Foundation Grant no. (KRF-2005-070-C00050).

Reference

1. Jin, S., Tiefel, T.H., McCormack, M., Fastnacht, R.A., Ramesh, R., Chen, L.H.: Science **264**, 413 (1994)
2. Fichtl, R., Tsurkan, V., Lunkenheimer, P., Hemberger, J., Fritsch, V., Krug von Nidda, H.-A., Scheidt, E.-W., Loidl, A.: Phys. Rev. Lett. **94**, 027601 (2005)
3. Hemberger, J., Lunkenheimer, P., Fichtl, R., Krug von nidda, H.-A., Tsurkan, V., Loidl, A.: Nature **434**, 364 (2005)
4. Ramirez, A.P., Cava, R.J., Krajewski, J.: Nature **386**, 156 (1997)
5. Kang, J.S., Kim, S.J., Kim, C.S., Olson, C.G., Min, B.I.: Phys. Rev. B **63**, 144412 (2001)
6. Son, B.S., Kim, S.J., Lee, B.W., Kim, C.S.: J. Appl. Phys. **97**, 10D332 (2005)
7. Goodenough, J.B.: J. Phys. Chem. Solids **30**, 261 (1969)
8. Deb, A., Hiraoka, N., Itou, M., Sakurai, Y., Palmer, H.M., Greaves, C.: Phys. Rev. B **66**, 100407(R) (2002)
9. Kim, S.J., Kim, W.C., Kim, C.S.: J. Appl. Phys. **91**, 7935 (2002)
10. Yang, Z., Tan, S., Chen, Z., Zang, Y.: Phys. Rev. B **62**, 13872 (2000)

Hyperfine Interact (2006) 169:1291–1294
DOI 10.1007/s10751-006-9439-6

Mössbauer effect study of the decagonal quasicrystal $Al_{65}Co_{15}Cu_{20}$

Z. M. Stadnik · G. Zhang

Published online: 14 November 2006

Abstract The ^{57}Fe Mössbauer effect study at 5.0 K and in an external magnetic field of 9.0 T on a high-quality stable decagonal quasicrystal $Al_{65}Co_{15}Cu_{19.9}Fe_{0.1}$ is presented. It is shown that the iron atoms are located in two distinct classes of sites. The values of the principal component of the electric field gradient tensor and the asymmetry parameter at these sites are, respectively, $-1.90(10)\times10^{21}$ V/m^2, 0.97(15) and $-3.95(12)\times10^{21}$ V/m^2, 0.00(17).

Key words quasicrystal · decagonal alloy · electric field gradient

1 Introduction

One of the open questions in studies of quasicrystals (QCs) is to determine their atomic structure, which is a prerequisite to understand many unusual physical properties of these alloys [1]. In spite of significant progress in recent years, the complete determination of the structure of QCs has not yet been accomplished [2].

The first, and until now, the only quantitative X-ray diffraction (XRD) study of the structure of the decagonal Al–Co–Cu QC using the five-dimensional description of the structure of a decagonal QC was carried out by Steurer and Kuo [3, 4]. The difficulty with the five-dimensional approach is that only an average structure can be determined because disorder, which is clearly present in the decagonal Al–Co–Cu QC [5], cannot be treated properly. A relatively small number of Bragg reflections available [2] leads to some spurious atoms with unphysical inter-atomic separations in structural models. In addition, a problem of XRD analysis is that it is not possible to distinguish between the different transition metal (TM) atoms in the ternary Al–Co–Cu QC. It appears that the XRD

Z. M. Stadnik (✉)
Department of Physics, University of Ottawa, Ottawa, ON K1N 6N5, Canada
e-mail: stadnik@uottawa.ca

G. Zhang
Department of Radiation Oncology, University of Maryland, Baltimore, MD 21201, USA

investigations alone might not be able to solve the structure of the decagonal Al–Co–Cu QC.

Complimentary to the diffraction methods of structure determination are the local probes, such as extended X-ray absorption fine structure (EXFAS), nuclear quadrupole resonance (NQR), or Mössbauer spectroscopy (MS), which are element selective and sensitive to the local atomic structure. It has been recently demonstrated [6] how the combination of the complete set of the MS data and the calculations of the electric field gradients (EFGs) for several XRD-based structural models of the icosahedral Al-Cu-Fe QC led to the solution of the structure of this QC.

The main objective of the present study is to provide a complete set of the EFG parameters at the Cu sites in the decagonal Al-Cu-Co QC.

2 Experimental procedure

An ingot of nominal composition $Al_{65}Co_{15}Cu_{19.9}Fe_{0.1}$ was prepared by melting in an argon atmosphere of high-purity constituent elements using an arc furnace; the Fe metal used was enriched to 95.9% in the ^{57}Fe isotope. The ingot was annealed in vacuum at 1073 K for 48 h.

^{57}Fe MS measurements were performed using a standard Mössbauer spectrometer operating in a sine mode. Mössbauer spectra in zero external magnetic field and in an external magnetic field of 9.0 T parallel to the γ-ray propagation direction were measured with the $^{57}Co(Rh)$ source held at the same temperature as that of the sample. The spectrometer was calibrated with a 6.35-μm α-Fe foil (the surface density of 107×10^{-3} mg $^{57}Fe/cm^2$), and the spectra were folded. The full line width at half maximum of the inner pair of the α-Fe Zeeman pattern was 0.224(4) mm/s and this value can be regarded as the resolution of the Mössbauer spectrometer. The Mössbauer absorber was prepared by mixing the powdered alloy with powdered BN to ensure a uniform thickness of the absorber and the random orientation of sample particles. This mixture was then put into a plastic sample holder. The surface density of the Mössbauer absorber was 36×10^{-3} mg $^{57}Fe/cm^2$.

3 Results and discussion

The XRD analysis of the studied QC showed [7] that all the Bragg peaks could be indexed to the decagonal structure, with a quasilattice parameter a=7.185 Å perpendicular to the 10-fold axis and a quasilattice stacking periodicity c=4.129 Å along the 10-fold axis.

The low-temperature Mössbauer spectrum of the decagonal $Al_{65}Co_{15}Cu_{19.9}Fe_{0.1}$ QC (Figure 1), in contrast to Mössbauer spectra of icosahedral QCs which are in a form of a somewhat broadened single quadrupole doublet [8], exhibits a clear structure. It can be fitted unequivocally with two symmetric quadrupole doublets (Figure 1). Each doublet is characterized by a full line width at half maximum Γ, a relative area A, a centre shift δ (relative to α-Fe at 298 K), and a quadrupole splitting $\Delta = \frac{1}{2}eQ|V_{zz}|\left(1+\frac{1}{3}\eta^2\right)^{1/2}$ where e is the proton charge and Q is the electric quadrupole moment of the nucleus. The asymmetry parameter is $\eta = \left|\left(V_{xx}-V_{yy}\right)/V_{zz}\right|, (0 \le \eta \le 1)$, where V_{xx}, V_{yy}, and V_{zz} are the eigenvalues of the electric field gradient (EFG) tensor in order of increasing magnitude. The values of Γ, A, δ, Δ determined from the fit (χ^2=1.09) for each quadrupole doublet are, respectively, 0.313(9) mm/s, 63.0(2.6)%, 0.299(2) mm/s, 0.389(7) mm/s and 0.258 (10) mm/s, 37.0(2.5)%, 0.235(3) mm/s, 0.706(7) mm/s. The fact that the Mössbauer

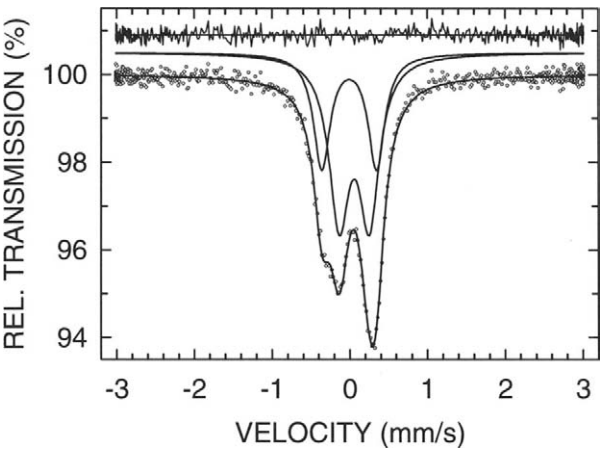

Figure 1 The ^{57}Fe Mössbauer spectrum of the decagonal $Al_{65}Co_{15}Cu_{19.9}Fe_{0.1}$ quasicrystal at 5.0 K fitted (*solid curve*) with two symmetric quadrupole doublets which are shown above the spectrum. The zero of the velocity scale is relative to the ^{57}Co (Rh) source at 5.0 K. The residuals are shown above the spectrum.

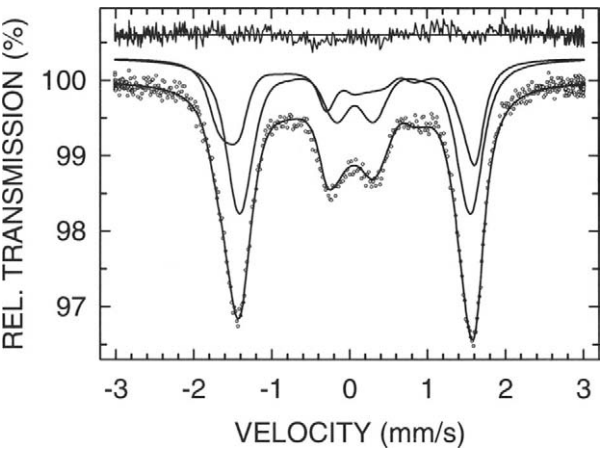

Figure 2 The ^{57}Fe Mössbauer spectrum of the decagonal $Al_{65}Co_{15}Cu_{19.9}Fe_{0.1}$ quasicrystal at 5.0 K in an external magnetic field of 9.0 T fitted (*solid line*) with two components which are shown above the spectrum. The zero velocity scale is relative to the ^{57}Co(Rh) source at 5.0 K. The residuals are shown above the spectrum.

spectrum of the decagonal $Al_{65}Co_{15}Cu_{19.9}Fe_{0.1}$ QC is indisputably composed of two quadrupole doublets (Figure 1) proves the existence of two distinct iron sites in this QC.

The fit of the zero-field Mössbauer spectrum in Figure 1 gives information on the magnitude of Δ, but not on the sign of the main component of the EFG, V_{zz}, or the value of η. The complete information of the sign of V_{zz} and the value of η can be obtained from the Mössbauer spectra measured in external magnetic fields such that the magnetic dipole interaction becomes of a similar magnitude as the electric quadrupole interaction. To determine the sign of V_{zz} and the value of η in the studied QC, a Mössbauer spectrum was measured in an external magnetic field of 9.0 T (Figure 2). The Mössbauer spectra exhibiting mixed hyperfine magnetic dipole and electric quadrupole interactions must be treated using the exact Hamiltonian. If texture effects are negligible one can assume, similarly to the case of powder samples, that the principal axes of the EFG tensor are randomly oriented with respect to the external magnetic field. The algorithm for calculating the spectra in such a case was given by Blaes et al. [9] and was used to fit the spectrum in Figure 2. As there are two classes of iron sites (Figure 1), it is clear that there are four possible combinations of signs for $q = \frac{1}{2}eQV_{zz}$: (+,+), (+,−), (−,−), and (−,+). The Mössbauer spectrum in Figure 2 was fitted with two components corresponding to these

four combinations of q signs; the value of Γ of two component subspectra was taken from the zero-field fit (Figure 1) and was fixed in the fit. The best fit ($\chi^2=1.24$) (Figure 2) was obtained for the following values of A, δ, q, η corresponding, respectively, to two iron sites: 59.5(2.7)%, 0.312(10) mm/s, −0.316(13) mm/s, 0.97(15) and 39.5(2.6)%, 0.236(12) mm/s, −0.658(15) mm/s, 0.00(17). Thus, V_{zz} is negative at two iron sites and has the value of $-1.90(10)\times10^{21}$ and $-3.95(12)\times10^{21}$ V/m^2. In converting from the measured q to V_{zz} we have used the value $Q=16$ fm^2, which is based on a systematic comparison of experimentally determined quadrupole splittings and calculated EFGs [10] and which has been confirmed by a nuclear shell-model calculations [11].

The analysis presented above enabled us to determine precisely the values of the EFG at the two classes of iron sites in the decagonal $Al_{65}Co_{15}Cu_{19.9}Fe_{0.1}$ QC. What is now required are ab initio calculations of the EFGs for the Al-Cu-Co QC for several available structural models of this QC. Comparing these calculated EFGs with the experimentally determined EFG here, similarly as has been done for the icosahedral Al-Cu-Fe QC [6], could lead to the solution of the structure of the decagonal Al–Co–Cu QC.

4 Conclusions

The ^{57}Fe Mössbauer effect study at 5.0 K and in an external magnetic field of 9.0 T on a high-quality stable decagonal quasicrystal $Al_{65}Co_{15}Cu_{19.9}Fe_{0.1}$ has been presented. The iron atoms are shown to be located in two distinct classes of sites. The values of the principal component of the electric field gradient tensor and the asymmetry parameter at these sites are determined to be, respectively, $-1.90(10)\times10^{21}$ V/m^2, 0.97(15) and $-3.95(12)\times10^{21}$ V/m^2, 0.00(17).

Acknowledgement This work was supported by the Natural Sciences and Engineering Research Council of Canada.

References

1. Stadnik, Z.M. (ed.): Physical properties of quasicrystals. Springer, Berlin Heidelberg New York (1999)
2. Steurer, W.: J. Non-Cryst. Solids **334–335**, 137 (2004)
3. Steurer, W., Kuo, K.H.: Acta Cryst. **B46**, 703 (1990)
4. Steurer, W., Kuo, K.H.: Philos. Mag. Lett. **62**, 175 (1990)
5. Frey, F., Steurer, W.: J. Non-Cryst. Solids **153–154**, 600 (1993)
6. Zijlstra, E.S., Kortus, J., Krajčí, M., Stadnik, Z.M., Bose S.K.: Phys. Rev., B **69**, 094206 (2004)
7. Stadnik, Z.M., Zhang, G.: J. Phys. Condens. Matter **17**, 6599 (2005)
8. Stadnik, Z.M. In Long, G.J., Grandjean, F. (eds.): Mössbauer Spectroscopy Applied to Magnetism and Materials Science, vol. 2, p. 125. Plenum, New York (1996)
9. Blaes, N., Fischer, H., Gonser, U.: Nucl. Instrum. Methods Phys. Res. B **9**, 201 (1985)
10. Dufek, P., Blaha, P., Schwarz, K.: Phys. Rev. Lett. **75**, 3545 (1995)
11. Martínez-Pinedo, G., Schwerdtfeger, P., Caurier, E., Langanke, K. Nazarewicz, W., Söhnel, T.: Phys. Rev. Lett. **87**, 062701 (2001)

Hyperfine Interact (2006) 169:1295–1299
DOI 10.1007/s10751-006-9440-0

Absence of charge fluctuations of europium in metallic single crystals of $EuCu_2Si_2$

Z. M. Stadnik · P. Wang · J. Żukrowski · B. K. Cho

Published online: 16 November 2006

Abstract The ^{151}Eu Mössbauer effect study in the temperature range 2.2–299.5 K on pulverized single crystals of $EuCu_2Si_2$ synthesized from an indium flux is presented. In contrast to previous studies on polycrystalline samples in which valence fluctuations for Eu were reported, we find that the Eu atoms are divalent in the whole temperature range. Therefore, there are no charge fluctuations of Eu in $EuCu_2Si_2$.

Key words valence fluctuation · divalent Eu

1 Introduction

The ternary alloy $EuCu_2Si_2$ is one of the first europium-based alloys in which intermediate valence behaviour was observed [1]. It is also one of the most well studied [2–5]. Previous ^{151}Eu Mössbauer studies of $EuCu_2Si_2$ [1, 4, 5] found that the effective valence of Eu changes from ~2.6 at room temperature to ~2.8 at lowest temperature.

Recently, single crystals of $EuCu_2Si_2$ were synthesized from an In flux and studied again [6, 7]. Surprisingly, magnetic susceptibility, electron-spin-resonance, and specific heat results [6, 7] are consistent with Eu being in stable divalent state. Here, we present the preliminary ^{151}Eu Mössbauer spectroscopy results on the single crystals of $EuCu_2Si_2$. We demonstrate that Eu in $EuCu_2Si_2$ is in the divalent state in the temperature range 2–300 K.

Z. M. Stadnik (✉) · P. Wang
Department of Physics, University of Ottawa, Ottawa, ON K1N 6N5, Canada
e-mail: stadnik@uottawa.ca

J. Żukrowski
Solid State Physics Department, AGH University of Technology, 30-059 Cracow, Poland

B. K. Cho
Department of Materials Science and Engineering, Gwangju Institute of Science and Technology (GIST), Gwangju 500-712, South Korea

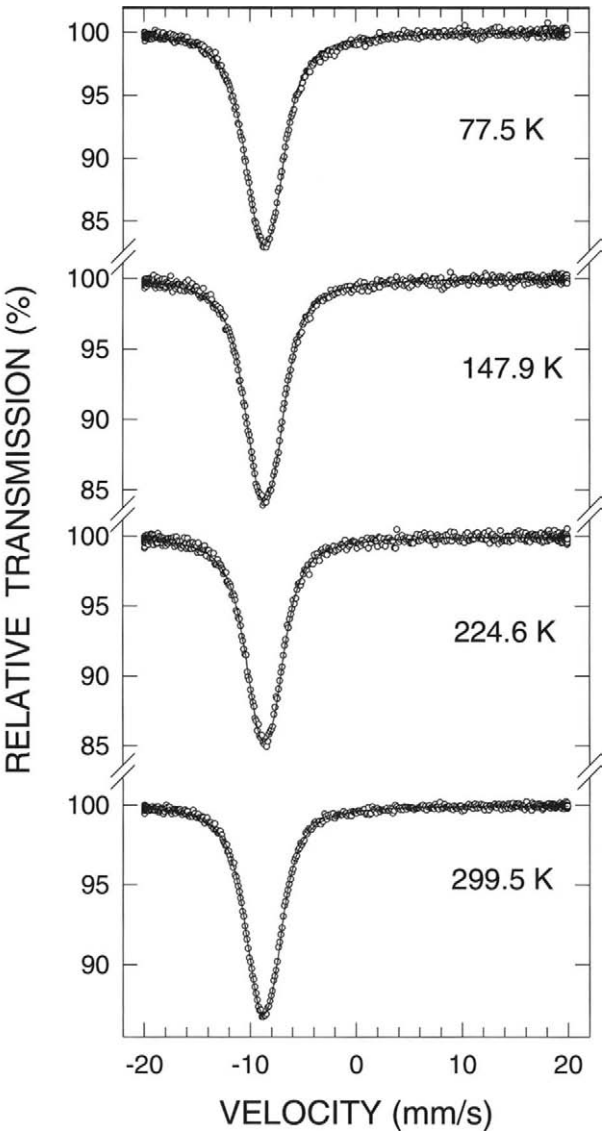

Figure 1 ^{151}Eu Mössbauer spectra of $EuCu_2Si_2$ at various temperatures above the magnetic ordering temperature. The zero of the velocity scale is relative to the $^{151}Sm(SmF_3)$ source at room temperature. The *solid line* is a least-squares fit, as described in the text.

2 Experimental procedure

Single crystals of $EuCu_2Si_2$ were synthesized from an In flux, as described in [7]. They were found to be single phase, crystallizing in the tetragonal $ThCr_2Si_2$ structure with lattice constants a=4.10 Å and c=9.93 Å [7].

^{151}Eu Mössbauer measurements were performed in the temperature range 2.2–299.5 K with a standard Mössbauer spectrometer operating in a sine mode using a 330 mCi $^{151}Sm(SmF_3)$ source kept at room temperature. The spectrometer was calibrated with a 6.35-μm α-Fe foil, and the spectra were folded. The Mössbauer absorber was prepared by mixing the

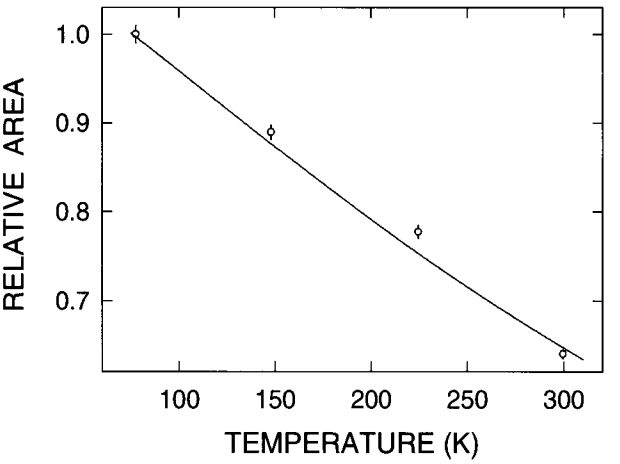

Figure 2 Temperature dependence of the normalized area under the resonance curve. The *solid line* is a least-squares fit based to the expression for the Lamb–Mössbauer factor within the Debye model of lattice vibrations.

pulverized crystals of $EuCu_2Si_2$ with powdered BN to ensure a uniform thickness of the absorber and the random orientation of sample particles. This mixture was then put into a plastic sample holder. The surface density of the Mössbauer absorber was 18.0 mg Eu/cm^2, which corresponds to the effective absorber thickness $8.1f_a$, where f_a is the absorber Lamb–Mössbauer factor.

3 Results and discussion

The Mössbauer spectra of $EuCu_2Si_2$ at selected temperatures above the antiferromagnetic ordering temperature T_N=8.5 K [8] are shown in Figure 1. In contrast to the Mössbauer spectra of a polycrystalline $EuCu_2Si_2$ [1, 4, 5], the spectra of the studied specimen consist of one line located at ~−8.65 mm/s. This shows that Eu is divalent and there are no signs of valence fluctuations in the temperature range 77.5–299.5 K.

The spectra in Figure 1 result from a pure electric quadrupole interaction. They were fitted with the transmission integral and the positions and relative intensities of absorption lines were calculated by numerical diagonalization of the hyperfine Hamiltonian [8]. The source $^{151}Sm(SmF_3)$ used is not a monochromatic source as ^{151}Sm nuclei are located in the SmF_3 matrix at the site of noncubic symmetry. By measuring the spectra of the cubic EuSe we determined [8] that the electric quadrupole coupling constant eQ_gV_{zz} in our source is −3.98(13) mm/s (Q_g=0.903 b [9]), which is very close to the value found in [10]. The precise shape of the source emission line was taken into account in the fits of the spectra in Figure 1.

The values of the electric quadrupole coupling constant eQ_gV_{zz} and the asymmetry paramer η obtained from the fits of the spectra in Figure 1 are temperature independent [8] and are, respectively, 6.11(8) mm/s and η=1.0(1). The temperature dependence of the area under the resonance curve (Figure 2) derives from the temperature dependence of f_a. The fit of the relative area to the expression for f_a within the Debye theory of lattice vibration gives the Debye temperature Θ_D=236(4) K. This value is close to the value of 210 K found from the specific heat data for the polycrystalline $EuCu_2Si_2$ [2].

The Mössbauer spectra of $EuCu_2Si_2$ at selected temperatures below and around T_N are shown in Figure 3. It is evident that these spectra are the spin relaxation spectra, even at the

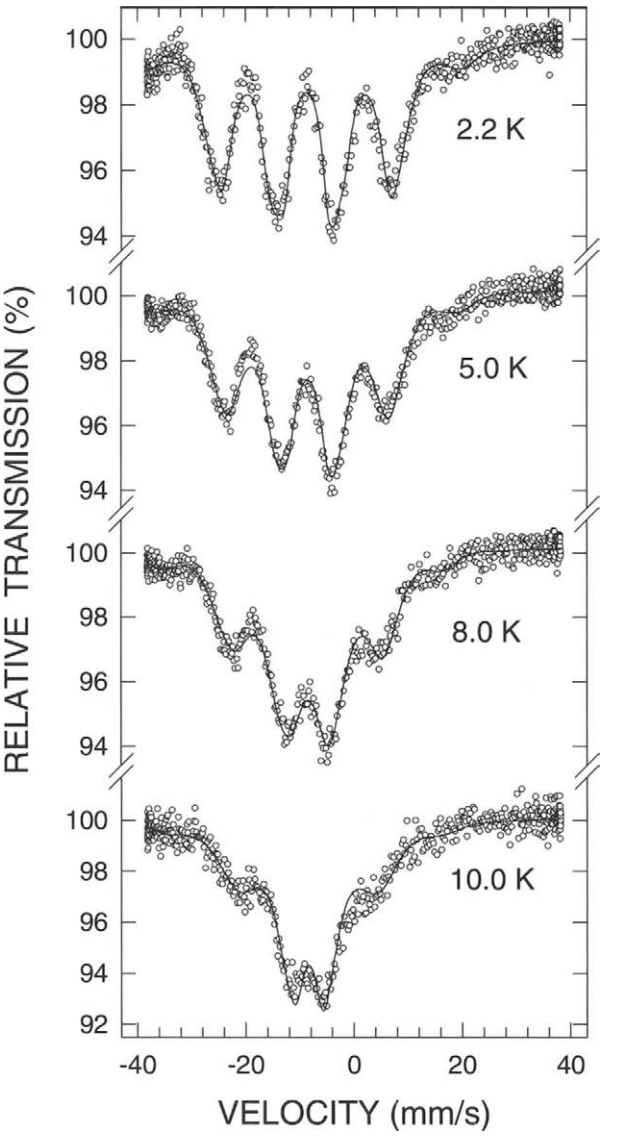

Figure 3 ^{151}Eu Mössbauer spectra of $EuCu_2Si_2$ at various temperatures below and around the magnetic ordering temperature. The zero of the velocity scale is relative to the ^{151}Sm (SmF_3) source at room temperature. The *solid line* is a least-squares fit, as described in the text.

lowest temperature of 2.2. K. They were fitted (Figure 3) using the line shape function given by Blume and Tjon [11]. The analysis of these relaxation spectra are discussed in detail elsewhere [8]. Here we notice that the isomer shift δ of these spectra is ~−8.68 mm/s. This demonstrates that the Eu atoms in the studied alloy are divalent.

The temperature dependence of δ of the spectra in Figures 1 and 3 is shown in Figure 4. It is evident that δ changes very little with temperature and its value proves that Eu in $EuCu_2Si_2$ is divalent in the temperature range 2.2–299.5 K. Consequently, there are no charge fluctuations of Eu in $EuCu_2Si_2$.

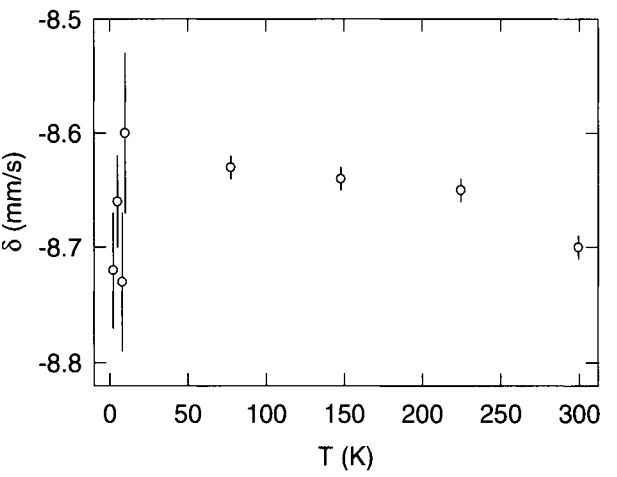

Figure 4 Temperature dependence of the ^{151}Eu isomer shift in $EuCu_2Si_2$.

4 Conclusions

The ^{151}Eu Mössbauer effect study in the temperature range 2.2–299.5 K on a ternary alloy $EuCu_2Si_2$ synthesized from an In flux has been presented. The values of the electric quadrupole coupling constant eQ_gV_{zz} and the asymmetry paramer η are, respectively, 6.11 (8) mm/s and η=1.0(1). The Debye temperature of the studied alloy is 236(4) K. The Eu atoms are in stable divalent state in the temperature range 2.2–299.5 K.

Acknowledgements This work was supported by the Natural Sciences and Engineering Research Council of Canada. The work at GIST was supported by ABRL program in Ewha Woman University funded by KRF, Korea.

References

1. Bauminger, E.R., Froindlich, D., Nowik, I., Ofer, S., Felner I., Mayer, I.: Phys. Rev. Lett. **30**, 1053 (1973)
2. Sales, B.C., Viswanathan, R.: J. Low Temp. Phys. **23**, 449 (1976)
3. Buschow, K.H.J., Campagna, M., Wertheim, G.K.: Solid State Commun. **24**, 253 (1977)
4. Röhler, J., Wohlleben, D., Kaindl G., Balster, H.: Phys. Rev. Lett. **49**, 65 (1982)
5. Abd-Elmeguid, M.M., Sauer, C., Zinn, W.: J. Phys. C **18**, 345 (1985)
6. Pagliuso, P.G., Sarrao, J.L., Thompson, J.D., Hundley, M.F., Sercheli, M.S., Urbano, R.R., Rettori, C., Fisk Z., Oseroff, S.B.: Phys. Rev., B **63**, 092406 (2001)
7. Rhyee, J.-S., Cho, B.K., Ri, H.C.: J. Appl. Phys. **93**, 8346 (2003)
8. Stadnik, Z.M., Wang, P., Żukrowski J., Cho, B.K. (to be published)
9. Tanaka, Y., Steffen, R.M., Shera, E.B., Reuter, W., Hoehn, M.V., Zumbro, J.D.: Phys. Rev. C **29**, 1830 (1984)
10. Nowik, I., Felner, I.: Hyperfine Interact. **28**, 959 (1986)
11. Blume, M., Tjon, J.A.: Phys. Rev. **165**, 446 (1968)

Hyperfine Interact (2006) 169:1301–1304
DOI 10.1007/s10751-006-9442-y

Debye temperature and magnetic ordering in $K_xBa_{1-x}Fe_2S_3$

M. Reissner · W. Steiner · J. Wernisch · H. Boller

Published online: 8 December 2006

Abstract ^{57}Fe Mössbauer measurements are reported for the series $K_xBa_{1-x}Fe_2S_3$, $x \leq 0.3$, at temperatures between 4.2 K $\leq$ T $\leq$ 294 K. A decrease of the Debye temperature from 435 to 405 K with x, indicates a weakening of the stiffness of the Fe sublattice. The ordering temperatures, taken from the appearance of magnetic hyperfine splitting in the spectra, are approximately 40 K lower for $x \geq 0.1$. The values of the centre shift and the small temperature dependence of the quadrupole splitting strongly supports that similar to the border compound $BaFe_2S_3$ also the K containing samples should be characterised as mixed valence compounds.

Key words ^{57}Fe Mössbauer measurements · Debye temperature · thioferrates

Polyanionic infinite $[Fe_2S_3]^{2-}$ double chains formed by edge-sharing $[FeS_4]$ tetrahedra are characteristic for the crystal structure of the thioferrate $BaFe_2S_3$ (space group Cmcm [1]). The Ba^{2+} cations are interspersed between these chains. Crystallographically only one Fe site is present, which should be divalent, Mössbauer investigations revealed, however, an isomer shift pointing to a mixture of di- and trivalent Fe atoms [2]. For isostructural KFe_2S_3, with cation charge +1, for Fe a valence state of 2.5 is expected, which may be realised by a random distribution of Fe^{2+} and Fe^{3+} at the same crystallographic site [3]. Quite unique for partially ionic compounds, $BaFe_2S_3$ and KFe_2S_3 form a continuous solid solution (Boller, unpublished). This offer the possibility to study the influence of the cation distribution on the magnetic properties and to gain information on the presently not well established character

M. Reissner (✉) · W. Steiner · J. Wernisch
Institut für Festkörperphysik, Technische Universität Wien, 1040 Wien, Austria
e-mail: reissner@ifp.tuwien.ac.at

H. Boller
Institut für Allgemeine und Anorganische Chemie, Universität Linz, 4040 Linz, Austria

Table I Lattice parameters and Debye temperatures of $K_xBa_{1-x}Fe_2S_3$

x	a [Å]	b [Å]	c [Å]	Θ_D [K]
0.00	8.795(2)	11.228(3)	5.285(2)	435
0.05	8.790(2)	11.216(3)	5.294(5)	418
0.1	8.808(2)	11.193(3)	5.305(1)	427
0.3	8.824(4)	11.171(5)	5.323(2	405

of the bonding between Fe and S within the tetrahedra. We started therefore with a systematic ^{57}Fe-Mössbauer investigation of the series $K_xBa_{1-x}Fe_2S_3$ [4, 5], a part of which is presented in this report.

The samples were prepared from stoichiometric mixtures of powdered BaS, $KFeS_2$, Fe, and S. Because of the high moisture sensitivity, they had to be handled under inert conditions (glove box). The educts were slowly heated up to 900°C in evacuated quartz tubes and then cooled to 300°C at a cooling rate of 20°C/h. The resulting samples consisted from compact reguli, which were highly oriented along the [001] direction. Phase purity of the products was checked by X-rays (Guinier photographs). The main contribution in the diffraction spectra belongs to reflection of the space group Cmcm, with lattice parameters increasing with x in a, c and decreasing in b direction (Table I). Depending on the K content, the presence of impurity phases is recognised. However, especially if not so well crystallised and in view of the relatively high background caused by iron fluorescence the determination of their structure and amount was not possible. The final concentration of the samples was checked by micro-probe analysis. Maximal deviations of 3 at % from the nominal composition (with no general trend for one of the constituent elements) were obtained. Generally it seems that avoidance of impurity phases in synthesising alkali thioferrates is extremely difficult [6].

^{57}Fe Mössbauer spectra were recorded in standard transmission geometry at temperatures between 4.2 and 300 K using a ^{57}Co**Rh** source, relative to which all centre shift data, CS, are given. Because of the sensitivity on moisture the powdered samples were embedded in wax and kept in helium atmosphere during the measurements. The temperature stability during measurement was ±0.5 K. The spectra were analyzed by solving the full Hamiltonian with both magnetic and quadrupole splitting taking sample thickness into account.

Despite of the impurities (shown by thin full lines in Figure 1) present in the sample of $BaFe_2S_3$ (relative intensity 0.16 [4]) the spectra recorded at 4.2 K could be described with only one well resolved subspectrum, pointing to a rather simple type of magnetic structure. For the K substituted compounds, however, complex spectra were obtained, which, after taking into account the different contributions of secondary phases (relative intensity of these subspectra 0.08, 0.25, and 0.03 for x = 0.05, 0.10, and 0.30, respectively), could only be analysed in a consistent way over the complete measured temperature interval by a superposition of several subspectra accepting still some remaining deviations (Figure 1). The appearance of magnetic order (characterised by a broad temperature interval in which the presence of subspectra with and without magnetic hyperfine splitting was obtained, for details see [4, 5] is strongly determined by the K content (Figure 2). Investigations on a sample with x = 0.2 are currently in progress to gain information on the steep

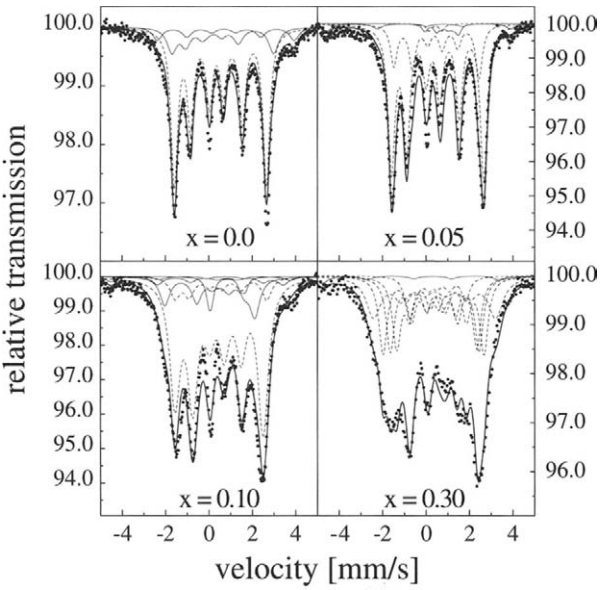

Figure 1 ^{57} Fe Mössbauer spectra of $K_xBa_{1-x}Fe_2S_3$ recorded at 4.2 K.

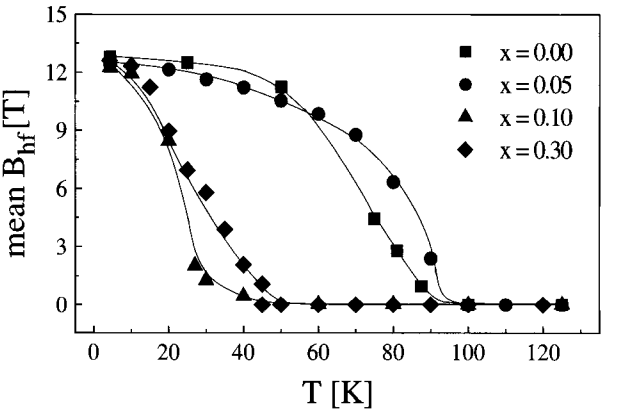

Figure 2 Temperature dependence of the mean hyperfine field in $K_xBa_{1-x}Fe_2S_3$. The *lines* are guides for the eyes.

decrease of the ordering temperature, although both X-ray and CS results strongly support the solid solution of K and Ba.

At higher temperatures for the K containing samples a superposition of at least two subspectra, with relative intensities roughly in accordance with the Ba to K ratio, was sufficient to obtain reasonable fits. For all samples the quadrupole splitting (mean values at room temperature $|eQV_{zz}/4|$ = 0.28, 0.29, 0.286, and 0.295 mm/s for x = 0.00, 0.05, 0.10, and 0.30, respectively) exhibits only a small temperature dependence, which can be explained by the change in interatomic distances with temperature. The value of the quadrupole splitting in the border compound KFe_2S_3 is practically the same [3]. Thus the difference in the electronic charge and size of the cations in the neighbourhood leads only to small asymmetries of the charge density around the Fe nucleus, although a strong dependence of the Fe–S polyhedron distortion parameter on the cation ionic radius was observed [6].

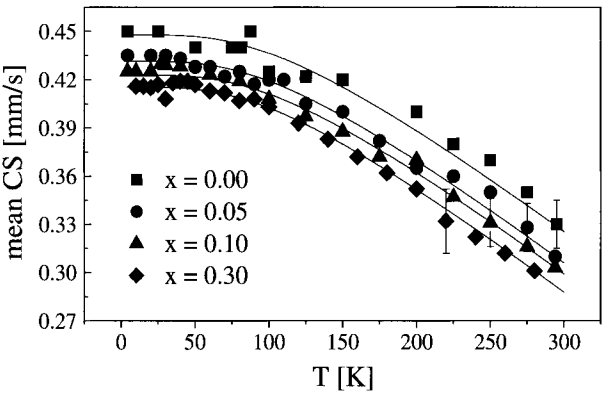

Figure 3 Temperature dependence of the mean centre shift of $K_xBa_{1-x}Fe_2S_3$. *Full lines*: fits according to the Debye model.

The decrease in CS with x reflects the alteration in charge density caused by the K substitution (Figure 3). Decomposing CS in a temperature independent term representing the charge density at the nucleus and the second order Doppler shift, allows the determination of the Debye temperature Θ_D from the latter. Θ_D decreases with x (Table I), which indicates a weakening in stiffness of the Fe sublattice with increasing K concentration and might be a hint to a change of the Fe–S bonds.

To sum up, for the presently investigated compounds of the series $K_xBa_{1-x}Fe_2S_3$ a decrease of approximately 40 K for $x \geq 0.1$ is found for the magnetic ordering temperature. Both the value of CS and the small dependence of the quadrupole splitting on temperature are indications, that, similar to the border compound $BaFe_2S_3$, the K containing samples should also be characterised as mixed valence compounds.

References

1. Hong, H.Y., Steinfink, H.: J. Solid State Chem. **5**, 93–104 (1972)
2. Reiff, W.M., Grey, I.E., Fan, A., Eliezer, Z., Steinfink, H.: J. Solid State Chem. **13**, 32–40 (1975)
3. Amthauer, G., Bente, K.: Naturwissenschaften **70**, 146-147 (1983)
4. Reissner, M., Steiner, W., Boller, H.: Hyperfine Interact. (C) **5**, 197–200 (2002)
5. Reissner, M., Steiner, W., Boller, H.: J. Alloys Compd. **383**, 131–134 (2004)
6. Mitchell, R.H., Ross, K.C., Potter, E.G.: J. Solid State Chem. **177**, 1867–1872 (2004)

Hyperfine Interact (2006) 169:1305–1308
DOI 10.1007/s10751-006-9443-x

Mössbauer investigation of $Fe_{0.5}In_{1.5}S_3$

M. Reissner · W. Steiner · Z. Seidov · G. Guseinov

Published online: 8 December 2006

Abstract ^{57}Fe Mössbauer measurements are reported on a cubic spinel with nominal composition $Fe_{0.5}In_{1.5}S_3$ in the temperature range 4.3 K to 295 K. An occupation ratio of 0.05:1 was determined for Fe in the tetrahedral A and octahedral B positions. Below 10 K evidence for the appearance of a spin glass state is obtained.

Key words $Fe_{0.5}In_{1.5}S_3$ · inverse cubic spinels · site occupation · magnetic order · quadrupole splitting · centre shift

The discovery of ferromagnetic order in semiconductors has renewed the research interest on iron containing thiospinels because of both the capability to develop devices in spintronics for signal processing as well as magnetic memories and the inherent magnetic properties of these compounds like site-dependent ferro- and antiferromagnetic exchange interactions, which allow the detailed study of the interplay between charge carriers and magnetic ions (e.g. [1]).

At ambient pressure stoichiometric In_2S_3 exists in three modifications. The disordered cubic α-phase (space group $Fd\bar{3}m$) is a defect spinel structure in which all the octahedral (B) sites are occupied, and 1/3 of the tetrahedral positions (A) remain empty in random arrangement. Thus the atomic configuration of In^{3+} can be represented by $(In_{0.67}\square_{0.33})^A(In_2)^BS_4$, where $\square$ denotes a vacancy. In cooling at 420°C a transition into a body-centred tetragonal supercell, containing 16 In_2S_3 formula units and an ordered arrangement of vacancies, the β-phase (space group $I4_1/amd$) appears. At 754°C the transition into the trigonal γ-phase (space group $P\bar{3}m1$) takes place [2–5]. For $FeIn_2S_4$ an almost complete cation inversion in the cubic

M. Reissner (✉) · W. Steiner
Institute of Solid State Physics, Vienna University of Technology, Vienna, Austria
e-mail: reissner@ifp.tuwien.ac.at

Z. Seidov · G. Guseinov
Institute of Physics, Azerbaijan National Academy of Science, Baku, Azerbaijan

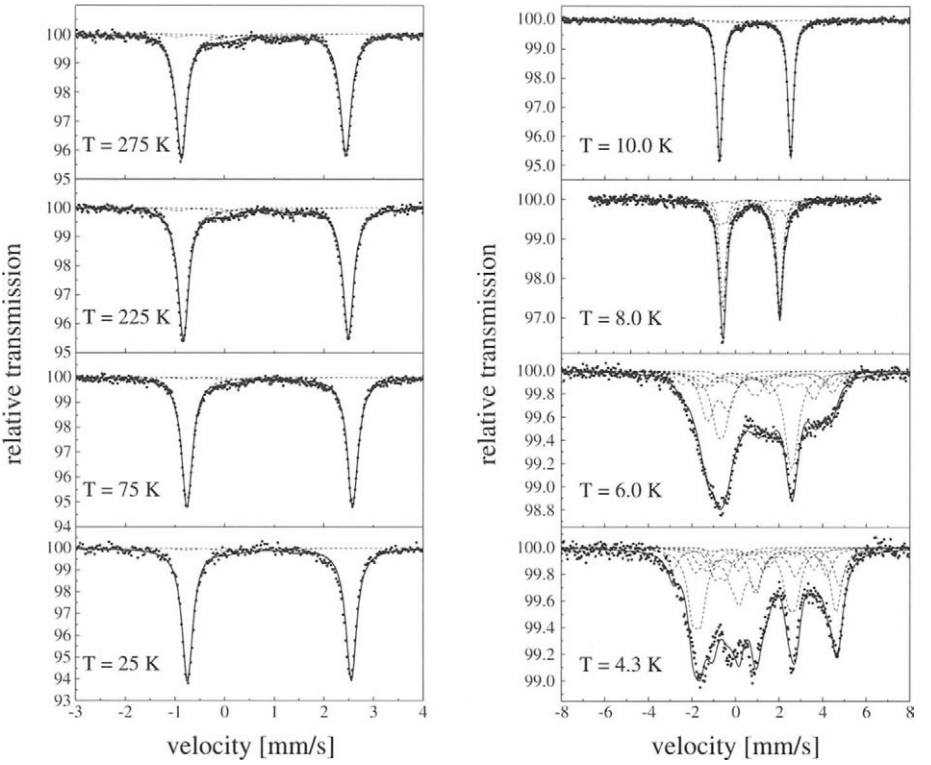

Figure 1 ^{57}Fe Mössbauer spectra of $Fe_{0.5}In_{1.5}S_3$.

spinel-structure was observed with Fe occupying the B-sites and In present at both the A- and the B-sites. From magnetic susceptibility measurements a spin-only value for divalent Fe was obtained, which is also confirmed by the isomer shift data [6–9]. The existence of a quadrupole splitting ($eQV_{zz}/2$ = 3.23 mm/s at room temperature) in an octahedral environment was taken as an indication for a trigonal distortion, which splits the triplet orbital ground state of Fe^{2+} in a doublet and a singlet [6, 9].

Very recently we could substitute approximately 25% of In by Fe in In_2S_3. Details of the sample preparation routine are described elsewhere [11]. The magnetic measurements revealed a spin glass state with freezing temperature of 5 K and X-ray and neutron diffraction investigations point to a description of the structure of this compound as a cubic spinel corresponding to $(Fe_{0.04}In_{0.89}\square_{0.07})^A(Fe_{0.72}In_{1.28})^BS_4$ with an almost complete cation inversion [11]. In parallel to those experiments we performed a detailed Mössbauer study, the result of which are presented in this report.

The spectra were recorded between 4.3 K and 295 K in transmission geometry with a constant acceleration spectrometer using a ^{57}Co**Rh** source (relative to which all centre shift, CS, data are given) and a continuous flow cryostat (temperature stability ± 0.5 K).

A small amount (mean relative intensity over all measurements for this subspectrum 0.025) of an impurity phase, although not detectable in the X-ray investigations,

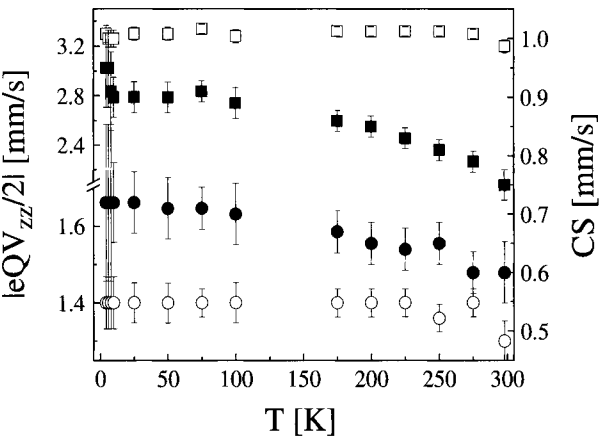

Figure 2 Temperature dependence of centre shift (*full symbols*) and quadrupole splitting (*open symbols*) for A (*open circles*) and B sites (*open squares*) in $Fe_{0.5}In_{1.5}S_3$.

is present in the recorded spectra (Figure 1). Despite this contribution, above 8 K all spectra could be satisfactorily analysed by a superposition of only two subspectra (mean area ratio over the whole temperature range 1:0.05) with room temperature values of $eQV_{zz}/2 = 3.20$ and 1.30 mm/s and CS = 0.75 and 0.60 mm/s, respectively. The line width of 0.26 mm/s for the subspectrum with the large relative intensity was only 8% larger than the one obtained for the Fe calibration spectra. For the spectrum with the small relative intensity the width was 0.40 mm/s, indicating a strong influence of the different Fe surroundings on this contribution. Considering the inverse spinel structure, on the A-site Fe is bonded to four sulfur anions, which by themselves are each bonded to three metallic cations on the B-sites, resulting in total to 35 different configurations. Since the distances to the tetrahedrally coordinated cations are only approximately 5% larger, the 15 possible different surroundings of the third neighbour shell should in addition be taken into account. On the other hand, it was observed [6–9] that the various possible environments of Fe located on the B-sites, influence $eQV_{zz}/2$ and CS only to a less extent. The main contribution to the quadrupole splitting of these sites results from a trigonal distortion of the sulfur octahedra, which for space reasons are pushed somewhat away along the four [111] directions. Thus the spectrum with the small relative intensity ratio and the large line width can be allocated to Fe embedded on the tetrahedral A-sites and the one with the large intensity and small line width to Fe on the octahedral B-sites. The observed values of $eQV_{zz}/2$ and CS (Figure 2) are in line with this allocation and agree well with those reported in literature [6–9]. From neutron and X-ray investigations a ratio of 0.055:1 is found for the occupation of Fe on A:B sites [11], which is in full agreement with the ratio determined in the present analysis of the Mössbauer spectra neglecting a possible difference in the f-factor as observed for these two sites in isostructural Fe_3O_4 [10]. Similar to the results found for $FeIn_2S_4$ [6] the temperature dependence of $eQV_{zz}/2$ for Fe on the B-sites is very small (Figure 2). The same small dependence is also present for the A-sites, although this subspectrum can only be seen as a superposition of the contributions resulting from different numbers of vacancies and In atoms in the Fe environment as discussed above. The lack of resolution (the experiments were performed with unenriched samples) allows, however, no decomposition of this subspectrum.

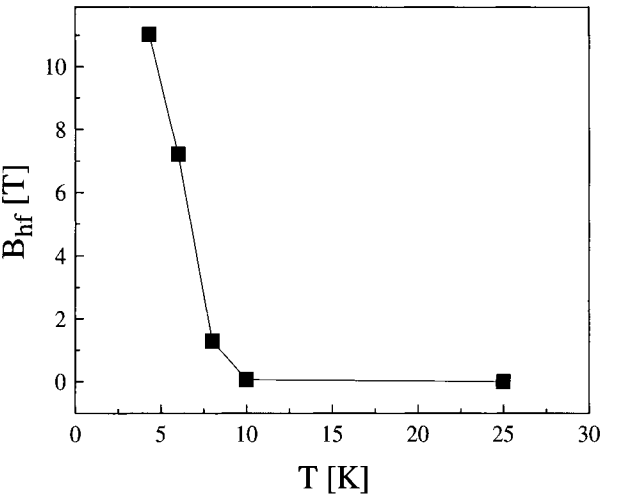

Figure 3 Mean hyperfine field versus temperature for $Fe_{0.5}In_{1.5}S_3$.

Below 10 K magnetic hyperfine splitting appears (Figure 1). The spectra could only be analysed by a superposition of several subspectra (the chosen number is arbitrary), representing a hyperfine field distribution and strongly supporting the presence of a spin glass order as observed in the magnetic measurements. The appearance of hyperfine splitting (Figure 3) above the magnetically determined freezing temperature can be attributed to the different time windows of the two experiments and is typical for spin glasses [12]. The spin glass ground state is caused by the high degree of disorder present in this spinel structure, which does not allow that all nearest neighbour antiferromagnetic exchange interactions (indicated by the high Curie–Weiss temperature of −50 K [11]) are satisfied.

To sum up, in complete accord with the recent X-ray, neutron, and magnetic investigations [11] the present Mössbauer experiments confirm the classification of the prepared $Fe_{0.5}In_{1.5}S_3$ compound as inverse cubic spinel of the form $(Fe_{0.04}In_{0.89}\square_{0.07})^A(Fe_{0.72}In_{1.28})^BS_4$ and the appearance of spin glass order below 10 K.

References

1. Risbud, A.S., Seshadri, R., Ensling, J., Felser, C.: J. Phys., Condens. Matter **17**, 1003–1010 (2005)
2. Diehl, R., Nitsche, R.: J. Cryst. Growth **28**, 306–310, (1975)
3. Diehl, R., Nitsche, R., Carpentier, C.-D.: J. Appl. Crystallogr. **6**, 497–498 (1973)
4. Steigmann, G.A., Sutherland, H.H., Goodyear, J.: Acta Crystallogr. **19**, 967–971 (1965)
5. Likforman, A., Guittard, M., Tomas, A., Flahaut, J.: J. Solid State Chem. **34**, 353–359 (1980)
6. Eibschütz, M., Hermon, E., Shtrikman, S.: Solid State Commun. **5**, 529–531 (1967)
7. Riedl, E., Karl, R.: J. Solid State Chem. **38**, 40–47, (1981)
8. Womes, M., Py, F., Moubtassim, E., Jumas, J.-C., Olivier-Fourcade, J., Aubertin, F., Gonser, U.: J. Phys. Chem. Solids **55**, 1323–1329 (1994)
9. Yagnik, C.M., Mathur, H.B.: Solid State Commun. **5**, 841–844 (1967)
10. Sawatzky, G.A., van der Woude, F., Morrish, A.H.: Phys. Rev. **183**, 383–386 (1969)
11. Krimmel, A., Seidov, Z., Guseinov, G.G., Najafov, A.I., Krug von Nidda, H.-A., Loidl, A., Többens, D.M.: J. Phys., Condens. Matter **17**, 3611–3618 (2005)
12. Bogner, J., Schachner, H., Reissner, M., Steiner, W.: Australian J. of Phys. **51**, 349–362 (1998)

Hyperfine Interact (2006) 169:1309–1313
DOI 10.1007/s10751-006-9459-2

Mössbauer study of $Fe_{0.05}Ni_{0.95}Cl_2$

T. Tamaki · M. Tamaki

Published online: 22 December 2006

Abstract Mössbauer spectra of $Fe_{0.05}Ni_{0.95}Cl_2$ were recorded at temperatures between 4.5 and 50 K and fitted by a sum of two sub-spectra as was done previously for $Fe_xNi_{1-x}Cl_2$ with x=0.034, 0.068 or 0.079. We have found that temperature variations of the hyperfine magnetic field H_{hf} and the quadrupole splitting $(1/2)e^2qQ$ of one of the sub-spectra are similar for the different compositions while some changes are observed for the other sub-spectrum. A particularly interesting result is found for $Fe_{0.05}Ni_{0.95}Cl_2$ which clearly shows the effect of a spin growth when temperature decreases.

Key words Mössbauer study · $Fe_xNi_{1-x}Cl_2$ · H_{hf} · $(1/2)e^2qQ$ · Θ_{hf}

1 Introduction

A theoretical study of a mixed magnetic system of two kinds of magnet with orthogonal spin easy axis was initiated in the mid-1970s. A new magnetic order phase was predicted on a concentration temperature (*c-t*) magnetic phase diagram by Aharony and Fishman as a 'mixed ordering phase' [1] or as an 'oblique antiferromagnetic (OAF) phase' by Matsubara and Inawashiro [2].

Many experimental studies on the mixed systems were intensely performed by several groups [3–8]. Mössbauer studies were reported for the $Fe_{1-x}Co_xCl_2{\cdot}2H_2O$ [5], $Fe_xCo_{1-x}TiO_3$ [7] and $Fe_{1-x}Co_xCl_2$ [8] systems, i.e. magnetic ions with strong anisotropies. On the contrary, we took the $Fe_xNi_{1-x}Cl_2$ system, which has both weak and strong anisotropies.

$FeCl_2$ as well as $NiCl_2$ have a $CdCl_2$-type crystal structure. In $FeCl_2$, the Fe^{2+} spins are arranged ferromagnetically intra the *c*-plane and antiferromagnetically inter the *c*-plane. The

T. Tamaki (✉)
Faculty of Engineering, Department of General Studies II, Gunma University, 4-2, Aramaki, Maebashi, Gunma 371-8150, Japan
e-mail: KHB12730@nifty.ne.jp

T. Tamaki · M. Tamaki
Mathematical Assist Design Laboratory, 54-2, Kamisadori, Maebashi, Gunma 371-0816, Japan

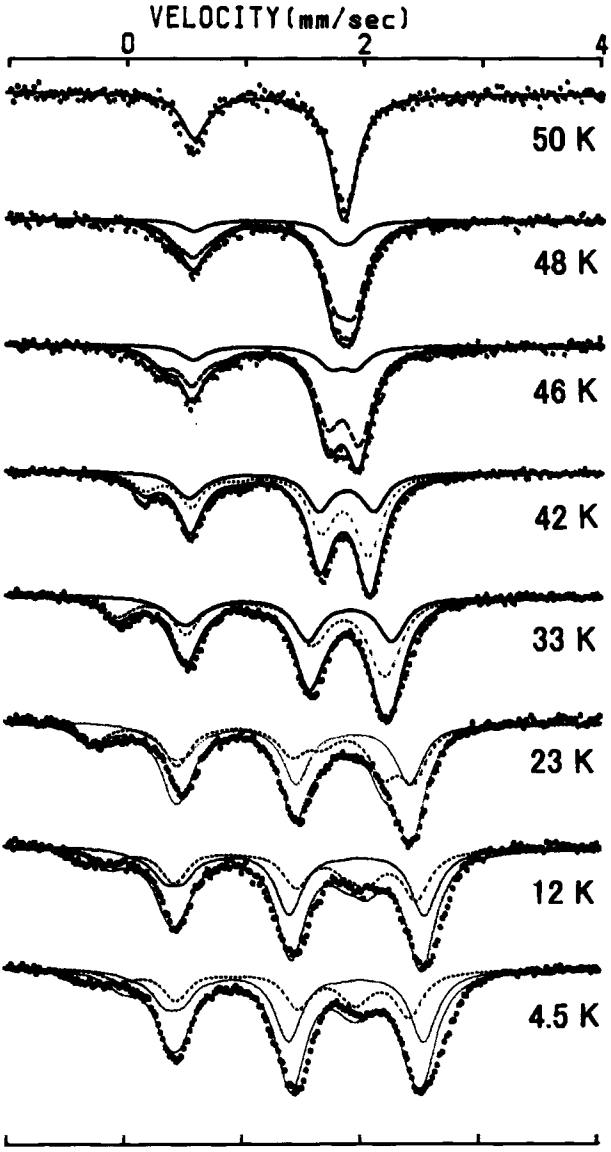

Fig. 1 Temperature variations of the Mössbauer spectra obtained for $Fe_{0.05}Ni_{0.95}Cl_2$. The subspectra I and II are shown by a *smooth* and *dotted line*, respectively

Fe^{2+} spin has a strong Ising-type anisotropy towards the hexagonal c-axis and the Ni^{2+} spin has a weak XY-type anisotropy in the c-plane.

The new phase of $Fe_xNi_{1-x}Cl_2$ appeared in the $0.02<x<0.15$ concentration region [9]. From the Mössbauer study of many concentrations, we have found that when $x \geq 0.068$ most of the Fe^{2+} spins approach the c-axis at 4.5 K [10]. Temperature variations of the Mössbauer spectra showed that the above-mentioned Fe^{2+} spins increased as temperature decreased for the $x=0.034$, 0.068 and 0.079 samples [11]. In the systematic Mössbauer study of the new phase, we found a sharp phenomenon for the $x=0.05$ sample. Therefore we hereby report the result of the Mössbauer study of the $x=0.05$ sample and compare it with those of the $x=0.034$, 0.068 and 0.079 samples.

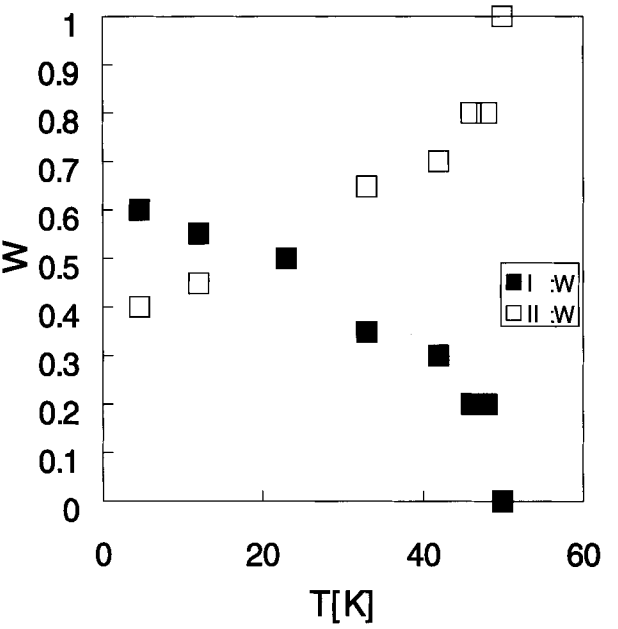

Fig. 2 Temperature variations of the relative absorption areas of the sub-spectra I: W_I (*filled squares*) and II: W_{II} (*open squares*) obtained for $Fe_{0.05}Ni_{0.95}Cl_2$

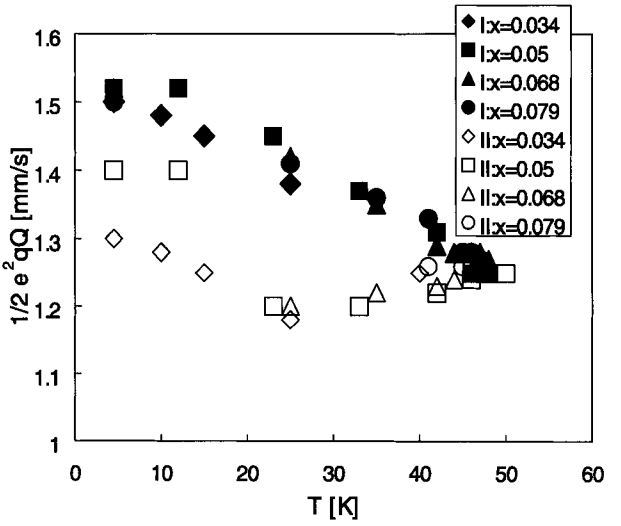

Fig. 3 Temperature variations of $(1/2)e^2qQ$ obtained for the two sub-spectra I (*filled symbols*) and II (*open symbols*) of $Fe_xNi_{1-x}Cl_2$ with x=0.034, 0.05, 0.068 and 0.079

2 Experimental

A single crystal sample of $Fe_{0.05}Ni_{0.95}Cl_2$ was made by the Bridgeman method. The enriched isotope ^{57}Fe was introduced at a concentration of 2 at.% of the total amount of magnetic ions. The Fe concentration is in line with that calculated for the sample preparation.

The absorber was mounted in a cryostat so that the incident γ-rays were perpendicular to the sample plane, i.e., parallel to the c-axis. A constant-acceleration Mössbauer spectrometer was used in a transmission arrangement. The temperature of the sample was

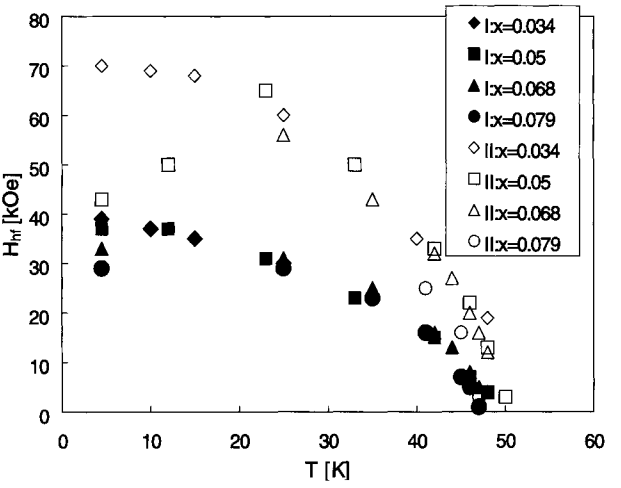

Fig. 4 Temperature variations of H_{hf} obtained for the two subspectra I (*filled symbols*) and II (*open symbols*) of $Fe_xNi_{1-x}Cl_2$ with x=0.034, 0.05, 0.068 and 0.079

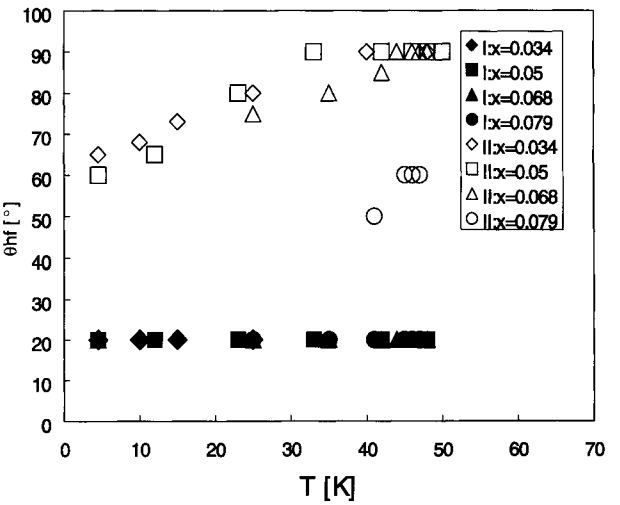

Fig. 5 Temperature variations of Θ_{hf} obtained for the two subspectra I (*filled symbols*) and II (*open symbols*) of $Fe_xNi_{1-x}Cl_2$ with x=0.034, 0.05, 0.068 and 0.079

measured with a thermocouple of Au(2%Co)–Cu and was controlled by an electrical controller – with accuracy higher than ±0.05 K.

3 Results and discussions

In Fig. 1 we show the Mössbauer spectra of $Fe_{0.05}Ni_{0.95}Cl_2$ recorded at different temperatures between 4.5 and 50 K. The same computer program was used for both the fitting of the spectra and that of the x=0.034, 0.068 and 0.079 samples. In the program, the Mössbauer parameters are H_{hf}, $(1/2)e^2qQ$, (Θ_{hf}, Φ_{hf}) and η, i.e., the hyperfine magnetic field, the quadrupole splitting, the polar and azimuthal angles of H_{hf} to the x, y, z principal axes of the electric field gradient (EFG) tensor and the asymmetry parameter, respectively. We made the following assumptions. (1) The z-axis of the EFG tensor coincides with the c-axis. (2) The

value of Φ_{hf} equals 0°; this is based on the results of the computer calculations. The Φ_{hf} dependence of the Mössbauer spectra is very small in our case.

As shown in Fig. 1, the Mössbauer spectra were fitted by the sum of two kinds of sub-spectra labelled I and II, respectively. The Fe^{2+} spin giving spectrum I has a tilting angle of Θ_{hfI} (Θ_I)=20° from the *c*-axis. On the other hand, the Fe^{2+} spin giving spectrum II has a tilting angle of $\Theta_{hf\ II}$ (Θ_{II}) larger than that of type I. The relative absorption areas of the sub-spectra I and II are referred to as W_I and W_{II}, respectively.

Temperature variations of W_I and W_{II} are shown in Fig. 2. The ratio of W_I:W_{II} equals 0.6:0.4 at 4.5 K and becomes 0:1 at 50 K. W_I (W_{II}) decreases (increases) smoothly as the temperature increases.

In Figs. 3, 4 and 5, we show the temperature variations of $(1/2)e^2qQ$, H_{hf} and Θ_{hf}, respectively, for the sub-spectra I and II obtained from the different samples.

The values of $(1/2)e^2qQ$, H_{hf} and Θ_{hf} are related to each other. For example, at 4.5 K, if a spin directs near the *c*-axis (Θ_{hf}=20°), $(1/2)e^2qQ$ is 1.52 mm/s and H_{hf} is 28 kOe. On the other hand, if a spin exists in the *c*-plane (Θ_{hf}=90°), these values are 1.17 mm/s and 92 kOe, respectively [10]. The values of $(1/2)e^2qQ$ and H_{hf} for the sub-spectra I show similar trends in the temperature variations of the different compositions: x=0.034, 0.05, 0.068 and 0.079. This is a reasonable result if we consider that the value of Θ_{hf}=20° was fixed for the different values of the concentration and of the temperature. On the other hand, the values of Θ_{hf} for the sub-spectra II are different from each other regarding the concentration or the temperature as shown in Fig. 5. In the case of the x=0.05 sample, W_I: W_{II} equals 0.5:0.5 at 23 K. Below this temperature, W_I becomes larger than W_{II}, where $(1/2)e^2qQ$ increased significantly and H_{hf} decreased rapidly. At the same time, Θ_{hf} decreased from 80 to 60°.

The number of type I spins increases as the Fe concentration x increases. It was simulated that an increase in the number of Fe–Fe bonds leads to an increase in W_I, namely the number of type I spins [12]. As for the temperature variations, we consider that the spin growths with the increase in the number of type I spins as clearly shown for the x=0.05 sample.

Acknowledgement The author T. Tamaki gratefully thanks Ochanomizu University for giving her the opportunity to perform Mössbauer experiments over the years.

References

1. Aharony, A., Fishman, S.: Phys. Rev. Lett. **37**, 1587 (1976)
2. Matsubara, F., Inawashiro, S.: J. Phys. Soc. Jpn. **42**, 1529 (1977)
3. Bevaart, L., Lebesque, J.V., Frikkee, E., de Jongh L.J.: Physica **86–88B**, 729 (1977)
4. Katsumata, K., Kobayashi, M., Sato, T., Miyako, Y.: Phys. Rev. **B19**, 2700 (1979)
5. Ito, A., Someya, Y., Katsumata, K.: Solid State Commun. **36**, 681 (1980)
6. Wong, P., Horn, P.H., Birgeneau, R.J., Safinya, C.R., Shirane, G.: Phys. Rev. Lett. **45**, 1974 (1980)
7. Ito, A., Morimoto, S., Someya, Y., Ikeda, H., Shono, Y., Takei, H.: Solid State Commun. **41**, 507 (1982)
8. Wiltshire, M.C.K., Howes, B.D., Burton, C.H.: J. Magn. Magn. Mater. **31–34**, 1465 (1983)
9. Ito, A., Tamaki, T., Someya, Y., Ikeda, H.: Physica **120B**, 207 (1983)
10. Tamaki, T., Ito, A.: In: Ortalli, I. (ed.) Conference Proceedings 50 "ICAME-95," pp 223. SIF, Bologna (1996)
11. Tamaki, T., Ito, A.: J. Radioanal. Nucl. Chem. **246**, 101 (2000)
12. Tamaki, T.: Hyperfine Interact. **5**, 205 (2001)

Hyperfine Interact (2006) 169:1315–1318
DOI 10.1007/s10751-006-9444-9

Formation of Fe_i–B pairs in silicon at high temperatures

H. P. Gunnlaugsson · K. Bharuth-Ram · M. Dietrich · M. Fanciulli · H. O. U. Fynbo · G. Weyer

Published online: 5 December 2006

Abstract We report on the detection of Fe_i–B pairs in heavily B doped silicon using ^{57}Fe emission Mössbauer spectroscopy following implantation of radioactive $^{57}Mn^+$ parent ions ($T_{1/2}$=1.5 min) at elevated temperatures >850 K. The Fe_i–B pairs are formed upon the dissociation of Fe_i–V pairs during the lifetime of the Mössbauer state ($T_{1/2}$=100 ns). The resulting free interstitial Fe_i diffuses over sufficiently large distances during the lifetime of the Mössbauer state to encounter a substitutional B impurity atom, forming Fe_i–B pairs, which are stable up to ~1,050 K on that time scale.

Key words Fe_i–B · p^{++} B doped silicon · Mössbauer spectroscopy

1 Introduction

The physics of interstitial iron, Fe_i, in silicon has been investigated extensively [1]. In p-type material Fe_i is known to form stable and meta-stable pairs with substitutional acceptor impurities, e.g. Fe_i–B pairs. In irradiated material also pair formation with vacancies, Fe_i–V, has been observed by electron paramagnetic resonance [2] and Mössbauer spectroscopy [3]. In the latter experiments ion implantation of radioactive $^{57}Mn^+$ has been employed. The Mn^+ ions are predominantly located on substitutional sites for implantations at temperatures ≥450 K. However, an average recoil energy of 40 eV in the decay to the Mössbauer state of

H. P. Gunnlaugsson · H. O. U. Fynbo · G. Weyer (✉)
Institute of Physics and Astronomy, Aarhus University, Ny Munkegade, 8000 Åarhus C, Denmark
e-mail: gw@phys.au.dk

K. Bharuth-Ram
School of Physics, University of KwaZulu-Natal, Durban 4041, South Africa

M. Dietrich
EP Division, CERN, CH-1211, Geneva 23, Switzerland

M. Fanciulli
Laboratorio Nazionale MDM-INFM, Via C. Olivetti 2, 20041 Agrate Brianza, Italy

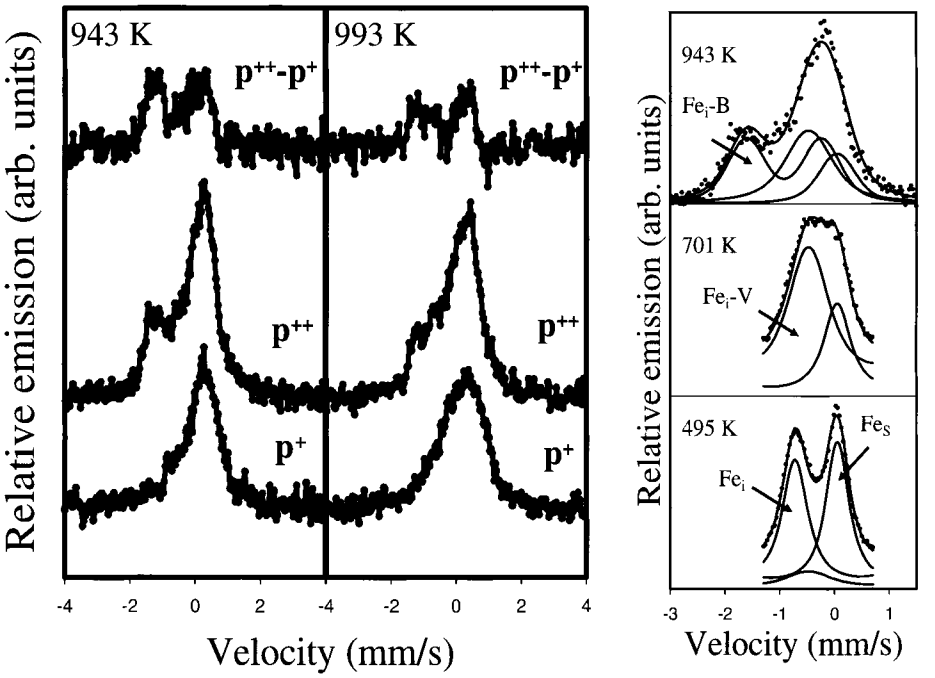

Figure 1 *Left*: Mössbauer spectra obtained after implantation at the temperatures indicated into the type of Si single crystal material indicated together with difference spectra (*top*). *Right*: Temperature series of spectra indicating the positions of spectral lines. The velocity has been adjusted to the second order Doppler shift to show velocity at room temperature. The spectra at 495 K and 701 K were measured using an α-Fe resonance detector due to its superb energy resolution and the six line pattern has been convoluted into a single emission feature.

^{57}Fe expels the majority of the daughter atoms into tetrahedral interstitial sites and creates a vacancy in the lattice. At temperatures >600 K a few diffusional jumps of the interstitial Fe_i lead to the formation of Fe_i–V pairs [4].

2 Experimental

Radioactive, 60 keV $^{57}Mn^+$ ($T_{1/2}$=1.5 min) ions were implanted at the ISOLDE facility at CERN at temperatures of 600–1,100 K to fluences $<10^{12}$ ions/cm^2 to assure single ion implantations. Si single crystals with B doping concentrations of 10^{18}–10^{20}/cm^3 (p^+–p^{++} type) were employed. Mössbauer spectra were measured with resonance detectors, equipped with either ^{57}Fe-enriched stainless steel or α-Fe, mounted on a conventional drive system outside the implantation chamber. Velocities and isomer shifts are given relative to α-Fe at room temperature.

3 Results and analysis

The spectra could be analysed simultaneously with two single lines, which are well-known to be due to interstitial and substitutional Fe, respectively [3], and two quadrupole-split

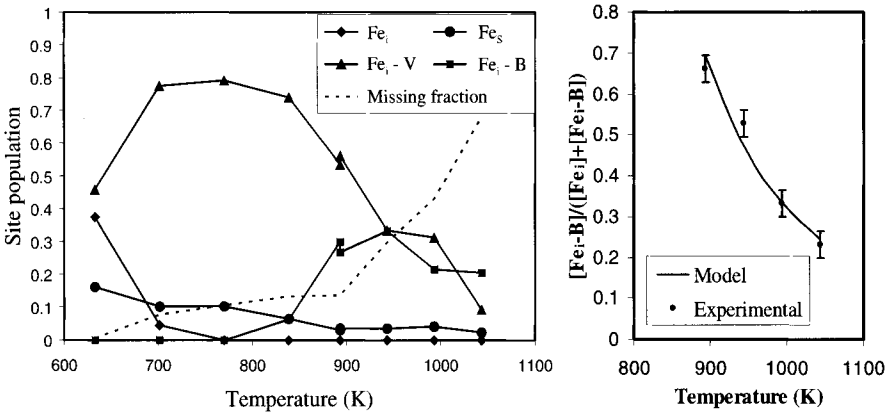

Figure 2 *Left*: Site populations of the different components in B doped p^{++} type Si. The results depend significantly on the Debye temperatures used. Here is applied 246 K for Fe_i, 460 K for Fe_S, 244 K for Fe_i–V and 260 K for Fe_i–B. *Right*: The relative fraction of Fe_i–B pairs to the sum of free interstitial Fe_i and Fe_i–B pairs as a function of temperature; the fit with the dissociation model of [7] is indicated and yields a binding energy of 0.6(1) eV.

doublets. One doublet has been identified previously as due to Fe_i–V pairs [4]. When these are formed at ~630 K and reach a fraction >70% of the probe atoms at 700–850 K, simultaneously the line from interstitial Fe_i disappears in the spectra. The occurrence of the second doublet at higher temperatures is attributed to the gradual dissociation of the Fe_i–V pairs and to the formation of Fe_i–B pairs. Figure 1 illustrates the spectral differences at two temperatures between p^{++} material, where Fe_i–B pairs are observed, and p^{+} material, where the formation of Fe_i–B pairs does not take place in measurable amounts.

The isomer shift for the Fe_i–B pair extrapolated to room temperature is found to be 0.93 (3) mm/s and the quadrupole splitting is 1.6(1) mm/s at 893 K. The isomer shift is in accordance with an interstitial Fe location and a quadrupole splitting is to be expected due to the axial symmetry of the pair. The values are, however, not in good agreement with previously published values for ^{57}Co doped p-type material [5].

To obtain site populations $p(T,c)$ as a function of temperature for a spectral component labelled c, in the analysis we take the relative spectral areas, $A(T,c)$, for component c at temperatures T and solve

$$A(T,c) = A_0 \times f(T,\theta_D(c)) \times p(T,c). \quad (1)$$

A_0 is a constant depending on the experimental setup, $f(T,\theta_D(c))$ are the Debye-Waller factors depending on the Debye temperatures, θ_D, of the site. At temperatures below 650 K, applying this relationship with the constraint $\sum_c p(T,c)=1$, leads to the determination of site fractions and Debye temperatures [3, 4]. For substitutional Fe, the Debye temperature has been found to be 460(30) K [3], in good agreement with the value expected from the mass defect approximation; for interstitial Fe_i defects roughly half this value has been found. In the temperature range of this study, however, the interstitial Fe diffuses so fast that the corresponding line broadening exceeds the velocity scale and the line disappears practically from the spectra. Therefore, to solve Eq. 1 a "missing" fraction is introduced to account for the presence of the invisible interstitial Fe_i. Assuming the Debye temperature of the Fe_i–B component to be in the typical range for interstitial impurities, it is possible to determine approximately its fraction as is shown in Figure 2.

4 Discussion and conclusions

At T>650 K, the diffusion of interstitial Fe_i leads to the formation of Fe_i–V pairs and a moderate increase of the missing fraction. At T>850 K the Fe_i–V fraction decreases suggesting the dissociation of the pairs. Using the methods from [3] we can estimate the dissociation barrier energy to 1.1 eV, corresponding to a binding energy of the Fe_i–V pair of E_b=(0.4–0.5) eV when adopting the free Fe_i migration energy of 0.67 eV from [6]. Simultaneously, the formation of the Fe_i–B pairs is observed. During the lifetime of the Mössbauer state the Fe_i^+ diffusion length at 900 K is $R = (D\tau)^{1/2} = 16$ Å. This is larger than the average distance to a B atom in the p^{++} material (~10 Å), whereas it is shorter than that in the p^+ type material (~40 Å). The diffusion length of the Fe_i^+ atoms is <30 Å at 1,050 K, which is probably the reason why Fe_i–B pairs are not observed in p^+ material. At temperatures >1,000 K an increase in the missing fraction is seen while the Fe_i–B fraction may dissociate. As done for the Fe_i–V pair, the dissociation barrier is estimated to 1.3(1) eV, yielding a binding energy of 0.6(1) eV. It is interesting to note that assuming the Fe_i–B fraction to be in thermal equilibrium and using the method described in [7], the same binding energy value is obtained for the Fe_i–B pair (cf. right side of Figure 2). Furthermore, this value is consistent with that derived under thermal-equilibrium conditions in [7] (0.65(2) eV). Thus, although on the time scale of the present experiments thermal equilibrium may just be reached, this experimental method allows to observe Fe_i–B pairs at 1,000 K, where they are stable for just ≈200 ns. It is noteworthy that the physics of pair formation/dissociation apparently does not change on a temperature scale of 300–1,000 K, corresponding to changes in the association constant by nine orders of magnitude.

Acknowledgements This work has been supported by the Danish Natural Science Research Council within the ICE center and by the EU under contract no. HPRICT-1999-00018. K. Bharuth-Ram acknowledges support from the South African National Research Foundation, grant GUN2064730. U. Wahl is acknowledged for providing the p^{++} sample.

References

1. Istratov, A.A., Hieslmair, H., Weber, E.R.: Appl. Phys., A **69**, 13 (1999)
2. Mchedlidze, T., Suezawa, M.: Jpn. J. Appl. Phys. **41**, 7288 (2002)
3. Gunnlaugsson, H.P., Dietrich, M., Fanciulli, M., Bharuth-Ram, K., Sielemann, R., Weyer, G., the ISOLDE Collaboration: Phys. Scr., T **101**, 82 (2002)
4. Gunnlaugsson, H.P., Weyer, G., Christensen, N.E., Dietrich, M., Fanciulli, M., Bharuth-Ram, K., Sielemann, R., Svane, A., the ISOLDE Collaboration: Physica B **340–342**, 532 (2003)
5. Bergholz, W.: Physica **116 B**, 312 (1983)
6. Gunnlaugsson, H.P., Fanciulli, M., Dietrich, M., Bharuth-Ram, K., Sielemann, R., Weyer, G., the ISOLDE Collaboration: Appl. Phys. Lett. **89**, 2657 (2002)
7. Kimerling, L.C., Benton, J.L.: Physica B **116**, 297 (1983)

Hyperfine Interact (2006) 169:1319–1323
DOI 10.1007/s10751-006-9445-8

Identification of substitutional and interstitial Fe in 6H-SiC

H. P. Gunnlaugsson · K. Bharuth-Ram · M. Dietrich · M. Fanciulli · H. O. U. Fynbo · G. Weyer

Published online: 14 December 2006

Abstract Iron impurities on interstitial (Fe_i) and substitutional sites (Fe_S) in SiC have been detected by ^{57}Fe emission Mössbauer spectroscopy following implantation of radioactive $^{57}Mn^+$ parent ions. At temperatures <900 K two Fe_i species are found, assigned to quasi-tetrahedral interstitial sites surrounded by, respectively, four C ($Fe_{i,C}$) or Si atoms ($Fe_{i,Si}$). Above 900 K, the $Fe_{i,Si}$ site is proposed to "transform" into the $Fe_{i,C}$ site by a single Fe_i jump during the lifetime of the Mössbauer state ($T_{1/2}$=100 ns). $Fe_{i,C}$ and substitutional Fe_S sites are stable up to >1,070 K.

Key words SiC · Fe defects · ^{57}Mn · Mössbauer spectroscopy

1 Introduction

Defects in semiconductors are an issue of increasing importance both for the well-established, technologically dominating Si material as well as for promising new (compound-) semiconductor materials [1]. Among the latter, SiC, a wide band gap material, may become useful for high temperature and high power applications, owing to its thermal and electrical properties. Lattice defects and impurities in this material are presently by far not as well understood and controlled as for Si. The 3d transition metals play particular roles in all group IV semiconductors, ranging from generally harmful, deep-level centres (Si, Ge) to beneficial catalysts in the growth of diamond crystals. The physics of

H. P. Gunnlaugsson · H. O. U. Fynbo · G. Weyer (✉)
Institute of Physics and Astronomy, Aarhus University, Ny Munkegade, 8000 Aarhus C, Denmark
e-mail: gw@phys.au.dk

K. Bharuth-Ram
School of Physics, University of KwaZulu-Natal, Durban 4041, South Africa

M. Dietrich
EP Division, CERN, CH-1211 Geneva 23, Switzerland

M. Fanciulli
Laboratorio Nazionale MDM-INFM, Via C. Olivetti 2, 20041 Agrate Brianza, Italy

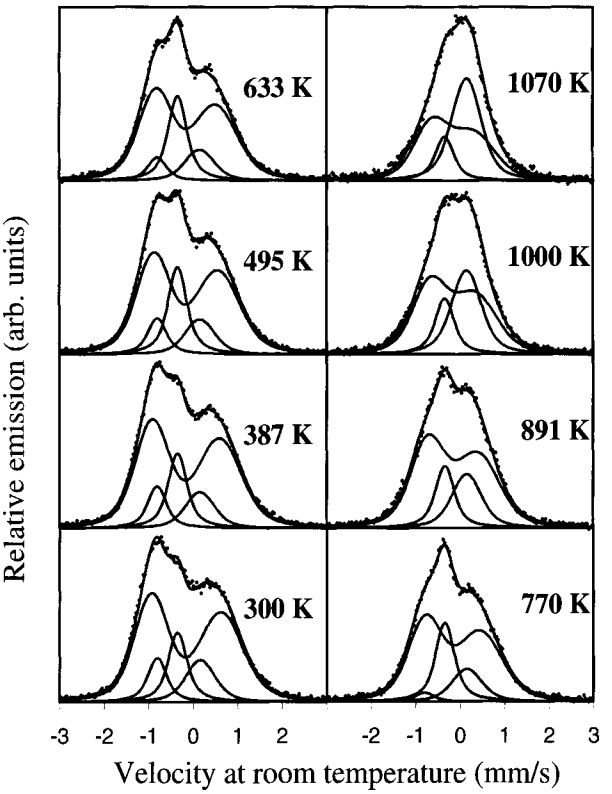

Figure 1 Spectra obtained after implantation into SiC at the temperatures indicated. The *solid lines* indicate the fitting components and their sum. The velocity scale has been adjusted by the second order Doppler shift to show the velocity at room temperature.

interstitial Fe_i has been investigated in detail in Si [2]. Recently, both interstitial Fe_i and substitutional Fe_S have been identified by Mössbauer spectroscopy in diamond [3], Si [4] and Ge [5]. Here we report on the identification interstitial Fe_i on two different sites and of substitutional Fe_S in SiC.

2 Experimental

Radioactive, 60 keV $^{57}Mn^+$ ions ($T_{1/2}$=1.5 min) were implanted at the ISOLDE facility at CERN at temperatures of 300–1,100 K into 6H SiC crystals to fluences $<10^{12}/cm^2$ to assure single ion implantations. In the β-decay to the 14 keV Mössbauer state of ^{57}Fe ($T_{1/2}$= 100 ns) an average recoil energy of 40 eV is imparted on the daughter atoms, which may lead to a relocation of a fraction of the atoms. Mössbauer emission spectra were measured with a ^{57}Fe-enriched stainless steel resonance detector mounted on a conventional drive system outside the implantation chamber. Velocities and isomer shifts are given relative to α-Fe at room temperature.

3 Results and discussion

The spectra obtained are shown in Figure 1. The spectra have been analysed with three single lines and a quadrupole split component. The single lines are assigned to two interstitial sites, $Fe_{i,1,2}$, and a substitutional site, Fe_S, and the asymmetrically broadened

Table I Hyperfine parameters from the simultaneous analysis of the spectra in Figure 1: isomer shifts (δ), quadrupole splitting at room temperature (ΔE_Q), Gaussian broadening of lines (σ) (having subtracted the detectors line width), and Debye temperatures (θ_D)

	Fe_D	Fe_S	$Fe_{I,1}$	$Fe_{I,2}$
δ (mm/s)	0.15(1)	−0.16(2)	0.35(1)	0.81(4)
ΔE_Q (mm/s)[a]	1.57(3)			
σ (mm/s)	0.31(2)/0.41(2)	0.16(2)	0.03(2)	
θ_D (K)	720(150)		270(50)	

The numbers in the parentheses give 1σ errors in the last digit and confidence limit on Debye temperatures

[a] T_k=1,860(50) K and $\Delta E_{Q,0}$=1.68(2) mm/s

doublet (Fe_D) is assigned to a damage site. Simultaneous analysis was performed under the constraint that the position of spectral components follow the second order Doppler shift. As the line widths did not vary, temperature independent Gaussian broadenings were applied; these were fixed to the same constant for the two interstitial lines. The observed temperature dependence of the Fe_D quadrupole splitting, ΔE_Q, was interpreted as a $T^{3/2}$ dependence and the splitting was constrained to follow $\Delta E_Q = \Delta E_{Q,0}\,(1-(T/T_k)^{3/2})$ in the analysis, where $\Delta E_{Q,0}$ and T_k are fitting variables. Having obtained an adequate analysis, the area fractions were assumed to follow a Debye behaviour to determine Debye temperatures (θ_D) and to extract site populations. Only rough θ_D values resulted, not distinguishable for Fe_D and Fe_S or the two interstitial components independently. They were assumed to be equal pair wise, akin to the case in Si and Ge. The obtained parameters are gathered in Table I. The isomer shifts and the quadrupole splitting are displayed in Figure 2a; the extracted site populations in Figure 2b.

The Fe_D component has strikingly similar properties as those in other group IV elements (cf. Figure 2A), where both the isomer shifts and the average quadrupole splittings are seen to increase or decrease, respectively, in a systematic way with the bond length. This component is attributed to Fe atoms located in small amorphous pockets, resulting from the implantation damage. Despite the line broadening, which is attributed to the variation of local surroundings in amorphous material, the basic atomic configurations must be relatively well defined and similar in all group IV elements. Fe in the Fe_D components has been proposed to be four-fold coordinated, however, in a locally non-cubic structure, akin to a bond defect, which gives rise to the large quadrupole splitting and the same Debye temperature as for substitutional Fe [6]. Upon the gradual annealing of the damage, increasing Fe fractions are found in sites of higher symmetry, leading to only slightly broadened single lines. The resulting approximate Debye temperatures for the Fe_D and Fe_S components are roughly twice as large as for the $Fe_{i,1}$ and $Fe_{i,2}$ components. This suggests, in analogy to the results for Si, that the Fe_S component is due to substitutional Fe and the Fe_i components due to interstitial Fe, having much weaker bonding to the lattice. Analogous also as for other group IV elements, the isomer shift for the Fe_S component is lower than that for interstitial $Fe_{i,1,2}$, however, none of these values fall exactly on the lines drawn for these components for the group IV elements in Figure 2a. The value for Fe_S in SiC is in fact close to that for substitutional Fe_S in Si, suggesting a very similar local surrounding, i.e. bonds to four Si nearest neighbour atoms as is expected for substitutional Fe on C sites in SiC. The $Fe_{i,1,2}$ isomer shift values are close to those for Fe_i in diamond or Si, respectively. Thus, neglecting minor structural and symmetry differences among various possible interstitial sites in hexagonal SiC, this indicated a location on quasi-tretrahedral

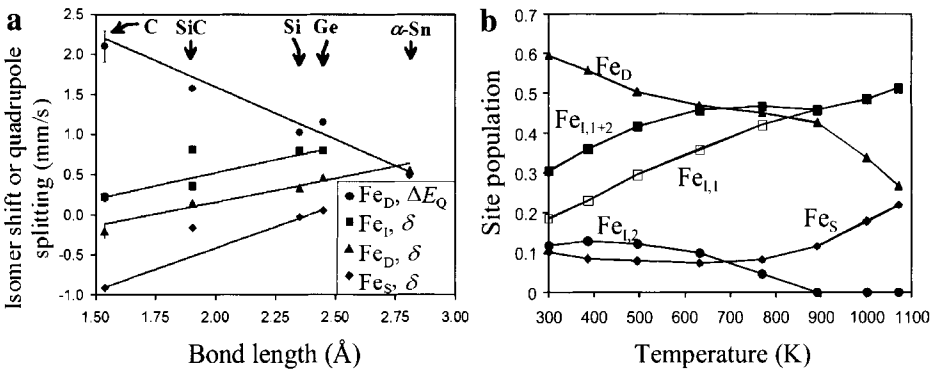

Figure 2 **a** Quadrupole splitting of Fe_D at room temperature and isomer shifts of Fe_D, Fe_i and Fe_S as a function of bond length in group IV semiconductors. SiC data are from this work (others adapted from [3]). **b** Site populations obtained using the Debye temperature given in Table I.

interstitial sites surrounded by four C or Si atoms, respectively. Accordingly these are denoted as $Fe_{i,C}$ ($Fe_{i,1}$) and $Fe_{i,Si}$ ($Fe_{i,2}$).

Figure 2b shows the site populations versus temperature. Two pronounced annealing stages of the Fe_D component at 300–500 and >900 K can be seen. These give rise to, respectively, an increase in the $Fe_{i,C}$ fraction only and both the $Fe_{i,C}$ and the Fe_S fractions. In the temperature range 600–900 K, where the Fe_D fraction does not change appreciably, the $Fe_{i,Si}$ fraction disappears and is apparently transformed into the $Fe_{i,C}$ fraction. In a recent attempt to establish a hierarchy of annealing reactions in irradiated or implanted SiC poly-types [7], annealing effects at temperatures <~500 K were generally attributed to the recombination of close Frenkel pairs on both sublattices and reactions mediated by mobile C or Si interstitials. The carbon vacancy, V_C, anneals [8], whereas the V_{Si} vacancy persists up to >900 K, where it presumably transforms into a V_C–Si_C antisite defect and anneals finally at ≈1,500 K. In more detail, annealing reactions depend on the Fermi-level of the material. These annealing models are based on low temperature irradiations/implantations and subsequent annealing, however, strong dynamic annealing effects are seen in implantations already at moderate temperatures [9]. A detailed understanding of the annealing effects in the present study appears therefore rather difficult and will remain speculative, although the results for the Fe site populations are quite clear. However, these sites are partially inherited from annealed Mn related parent defects during the ^{57}Mn lifetime and partially from the recoil in the nuclear decay, which may relocate the Fe daughter atoms. E.g., in Si and diamond, respectively, 70 or 20% of substitutionally implanted probe atoms are displaced into interstitial sites upon the decay [3, 4]. On the other hand, interstitially implanted probe atoms should be relocated predominantly again into interstitial sites. Then the constancy of the Fe_S fraction in SiC (≈0.1) up to ≈800 K suggests that a likewise constant fraction of the same order of magnitude of interstitial Fe on either quasi-tetrahedral site should be created by the recoil effect. The $Fe_{i,Si}$ fraction remains about constant up to 650 K, whereas the Fe_{iC} fraction increases strongly in that range in proportion to the annealing of the Fe_D fraction. Thus most of the Fe_{iC} fraction appears to result from the annealing of the Fe_D fraction, which then is (partially) relocated into $Fe_{i,C}$ sites again. A site preference in an athermal recoil effect is difficult to reconcile, however. The Fe_D annealing behaviour at ≈1,000 K, i.e., a simultaneous increase of the Fe_S and the $Fe_{i,C}$ fractions, is rather similar to that observed in Si at lower temperature. It is in

accordance with the creation of interstitial Fe by the recoil from substitutional Mn parent sites. Furthermore, interpreting the transformation of the $Fe_{i,Si}$ into a $Fe_{i,C}$ fraction at ≈800 K as a single jump from a quasi-tetrahedral $Fe_{i,Si}$ site to a $Fe_{i,C}$ site during the lifetime of the Mössbauer state, an activation energy of 0.8 eV is estimated. This value is lower than the known activation energy for macroscopic interstitial Fe diffusion, 1.15 eV [10]. The latter value would then be due to the reverse jump of an Fe atom and is in accordance with the stability of the $Fe_{i,C}$ fraction up to ≈1,100 K. This model is thus consistent with the assumption that the Fe_D annealing stage at >900 K results in substitutional Mn, while a fraction of the daughter atoms is displaced into either interstitial sites, however, only the $Fe_{i,C}$ site is stable within the lifetime of the Mössbauer state. That substitutional Fe is only found to be located on C sites may be attributed to the interactions of Mn with mobile V_C in the damage cascades at high temperatures. Finally, although no comprehensive annealing model seems achievable yet, the present results might contribute to future more satisfactory model developments. It is also noteworthy that the deduced diffusional barrier energy for interstitial Fe in SiC is intermediate between those determined or limited by similar experiments for interstitial Fe in Si and diamond [3, 4].

Acknowledgements This work has been supported by the Danish Natural Science Research Council within the ICE center and by the EU under contract no. HPRICT-1999-00018. K. Bharuth-Ram acknowledges support from the South African National Research Foundation, grant GUN2064730. U. Vetter is acknowledged for providing the sample.

References

1. Bonde Nielsen, K., Nylandsted Larsen, A., Weyer, G. (eds.): Proceedings of the 22nd International Conference on Defects in Semiconductors. Physica. B **340–342** (2003)
2. Istratov, A.A., Hieslmair, H., Weber, E.R.: Appl. Phys. A **69**, 13 (1999)
3. Weyer, G., Gunnlaugsson, H.P., Dietrich, M., Fynbo, H., Bharuth-Ram, K. and the ISOLDE Collaboration: Eur. Phys. J., Appl. Phys. **27**, 317 (2004)
4. Gunnlaugsson, H.P., Weyer, G., Christensen, N.E., Dietrich, M., Fanciulli, M., Bharuth-Ram, K., Sielemann, R., Svane, A., the ISOLDE Collaboration: Physica B **340–342**, 532 (2003)
5. Gunnlaugsson, H.P., Weyer, G., Dietrich, M., Fanciulli, M., Bharuth-Ram, K., Sielemann, R., the ISOLDE Collaboration: Physica B **340–342**, 537 (2003)
6. Gunnlaugsson, H.P., Dietrich, M., Fanciulli, M., Baruth-Ram, K., Sielemann, R., Weyer, G., the ISOLDE collaboration: Phys. Scr., T **101**, 82 (2002)
7. Bockstedte, M., Mattauch, A., Pankratov, O.: Phys. Rev. B **69**, 235202 (2004)
8. Dannefaer, S., Kerr, D.: Diamond and Related Materials **13**, 157 (2004)
9. Kuznetsov, A.Y., Wong-Leong, J., Hallen, A., Jagadish, C., Svensson, B.G.: J. Appl. Phys. **94**, 7112 (2003)
10. Takano, K., Nitta, H., Seto, H., Lee, C.G., Yamada, K., Yamazaki, Y., Sato, H., Takeda, S., Toya, E., Iijima, Y.: Sci. Technol. Adv. Mater. **2**, 381 (2001)

Hyperfine Interact (2006) 169:1325–1329
DOI 10.1007/s10751-006-9446-7

Mössbauer and magnetic study of Mn^{2+}- and Cr^{3+}-substituted spinel magnesioferrites of the composition $Mg_{1-x}Mn_xFe_{2-2x}Cr_{2x}O_4$

H. M. Widatallah · I. A. Al-Omari · A. M. Gismelseed · O. A. Yassin · A. D. Al-Rawas · M. E. Elzain · A. A. Yousif · O. A. Osman

Published online: 14 November 2006

Abstract Chromium and manganese co-substituted spinel magnesioferrites of the composition $Mg_{1-x}Mn_xFe_{2-2x}Cr_{2x}O_4$ (x=0.0, 0.1, 0.2, 0.3, and 0.5) were investigated with X-ray diffraction (XRD), Mössbauer spectroscopy and magnetic measurements. The cation distribution inferred suggests that Mn^{2+} and Cr^{3+} ions dominantly occupy the A- and B-sites respectively. The gradual decrease of the hyperfine fields and Curie temperatures with increasing x reflects a gradual weakening in the AB exchange interaction. Mössbauer data of the sample with x=0.5 is suggestive of cation clustering and/or superparamagnetism. The magnetization data is suggestive of Yafet-Kittel-type canted magnetism.

Key words Mössbauer spectroscopy · spinel ferrites · magnetization

1 Introduction

The magnetic properties of Mn-substituted spinel magnesioferrites of the composition $Mg_{1-x}Mn_xFe_2O_4$ are technologically attractive and explicable in terms of Néel's model of ferrimagnetism [1–3]. The basic idea is that the magnetic spins in the tetrahedral (A) and octahedral (B) sites of the spinel structure are coupled antiferromagnetically [3]. Co-substitution of these materials with a magnetic cation, such as Cr^{3+}, can thus lead to different spin configurations and magnetic interactions. Here we present a structural and magnetic study of Cr^{3+}-substituted $Mg_{1-x}Mn_xFe_2O_4$ samples of the form $Mg_{1-x}Mn_xCr_{2x}Fe_{2-2x}O_4$.

H. M. Widatallah (✉) · I. A. Al-Omari · A. M. Gismelseed · A. D. Al-Rawas · M. E. Elzain · A. A. Yousif
Depertment of Physics, Sultan Qaboos University, P. O. Box 36, Muscat 123, Oman
e-mail: hishammw@squ.edu.om

O. A. Yassin
School of Physics, Al-Neelain University, P. O. Box 12702, Khartoum, Sudan

O. A. Osman
Physics Department (Fac. of Ed.), University of Khartoum, P. O. Box 123, Khartoum, Sudan

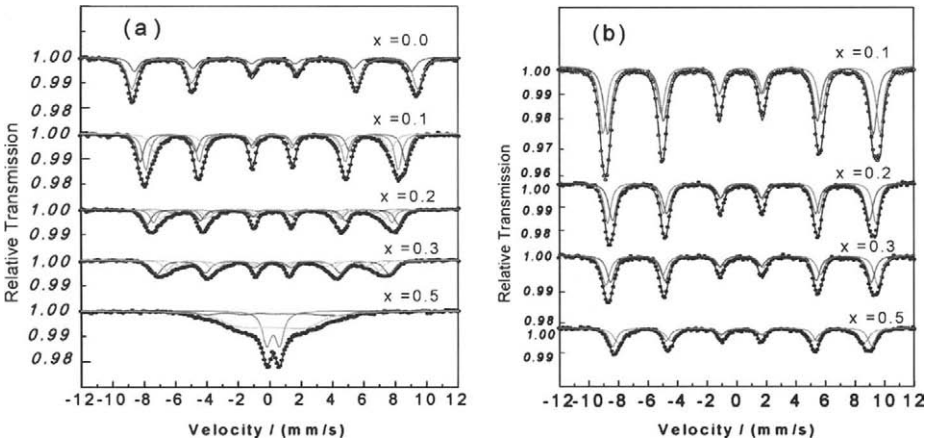

Figure 1 The Mössbauer spectra recorded form the $Mg_{1-x}Mn_xFe_{2-2x}Cr_{2x}O_4$ samples at 300 K (a) and 78 K (b). The 300 K Mössbauer spectrum of $MgFe_2O_4$ is shown for comparison.

2 Experimental

Polycrystalline samples of the composition $Mg_{1-x}Mn_xFe_{2-2x}Cr_{2x}O_4$ (x=0.0, 0.1, 0.2, 0.3, and 0.5) were synthesized using the standard ceramic method from appropriate quantities of high purity α-Fe_2O_3, MnO, MgO, and Cr_2O_3 as described elsewhere [1]. XRD data were recorded with a Philips PE1820 diffractometer using Cu$K\alpha$ radiation. ^{57}Fe Mössbauer spectra were recorded at 300 K and 78 K using a 25 mCi ^{57}Co/Rh source. Isomer shifts are quoted relative to metal Fe. The thermal variation of the saturation magnetization was recorded using a DMS-1660 vibrating sample magnetometer (VSM) in a magnetic field of 13.5 kOe.

3 Results and discussion

The XRD patterns of the various $Mg_{1-x}Mn_xFe_{2-2x}Cr_{2x}O_4$ samples revealed them to be monophasic cubic spinels (space group $Fd\bar{3}m$). The lattice parameters were found to increase linearly with x. This sheds light on how the substitute cations are distributed. It is known that Cr^{3+} has a larger octahedral ionic radius (76 pm) relative to the substituted Fe^{3+} (69 pm) and preferentially occupies the B-sites [4]. Mn^{2+}, on the other hand, has a larger tetrahedral ionic radius (80 pm) relative to both Mg^{2+} (71 pm) and Fe^{3+} (63 pm) and is likely to occupy the A-sites. This scenario is generally consistent with the cationic distributions of both $MgFe_2O_4$ and $MnFe_2O_4$ which are $\left(Fe^{3+}_{0.9}Mg^{2+}_{0.1}\right)\left[Mg^{2+}_{0.9}Fe^{3+}_{1.1}\right]O_4$ and $\left(Fe^{3+}_{0.2}Mn^{2+}_{0.8}\right)\left[Mn^{2+}_{0.2}Fe^{3+}_{1.8}\right]O_4$ respectively, where () and [] refer to the A- and B-sites respectively [3]. Assuming similar cation distributions and that all Cr^{3+} reside in the B-sites, we propose for our $Mg_{1-x}Mn_xFe_{2-2x}Cr_{2x}O_4$ samples a structural formula of the type:

$$\left(Mg^{2+}_{(0.1-0.1x)}Mn^{2+}_{0.8x}Fe^{3+}_{(0.9-0.7x)}\right)\left[Mg^{2+}_{0.9(1-x)}Cr^{3+}_{2x}Mn^{2+}_{0.2x}Fe^{3+}_{(1.1-1.3x)}\right]O_4. \quad (1)$$

The Mössbauer spectra of the $Mg_{1-x}Mn_xFe_{2-2x}Cr_{2x}O_4$ samples at 300 and 78 K are shown in Figures 1a and 1b respectively. The spectra show broadened six-line magnetic patterns except at 300 K for the sample with x=0.5 that exhibits a central doublet

Table I The Mössbauer parameters of the $Mg_{1-x}Mn_xFe_{2-2x}Cr_{2x}O_4$ samples at 300 and 78 K (between parentheses)

x	Sub-spectrum	I.S. (mm/s)	Q.S. (mm/s)	Γ (mm/s)	H_{eff} (mm/s)	A (%) (exp.)	A (%) (theo.)
0.0	A	0.26	0.02	0.47	47.1		
	B	0.35	0.00	0.56	49.7		
0.1	A	0.28(0.33)	0.02(0.00)	0.47(0.63)	44.9(50.2)	(47)	46
	B_1	0.31(0.39)	0.00(0.02)	0.48(0.61)	47.1(52.2)	(53)	53
	B_2	0.30	0.00	0.61	42.3		
0.2	A	0.29(0.34)	0.00(0.01)	0.53(0.65)	41.7(49.2)	(50)	48
	B_1	0.31(0.40)	0.01(0.01)	0.58(0.62)	44.3(50.8)	(50)	52
	B_2	0.31	0.00	0.70	38.3		
0.3	A	0.30(0.38)	0.02(0.02)	0.66(0.63)	41.0(48.9)	(52)	49
	B_1	0.34(0.38)	0.02(0.01)	0.71(0.54)	37.9(50.5)	(48)	51
	B_2	0.31	0.00	0.80	33.0		
0.5	Doublet	0.27	0.81	0.64			
	A	0.30(0.38)	0.02(0.04)	2.27(0.81)	15.1(46.9)	(53)	55
	B	0.33(0.39)	0.10(0.04)	1.86 (0.62)	26.2(49.0)	(47)	45

A and B refer to sextets due to Fe^{3+} at tetrahedral and octahedral sites respectively.

I.S. isomer shift, *Q.S.* quadrupole splitting, *Γ* line broadening; H_{eff} hyperfine field, A (%)(exp.)=fitted experimental spectral area; A (%)(theo.)=calculated spectral area from Eq. 1.

superimposed on a relaxing magnetic sextet. However, the well resolved six-line magnetic pattern recorded from the same sample at 78 K is indicative of a short range magnetic cation ordering (clustering), and/or superparamagnetic relaxation due to small particle size with blocking temperature <300 K [5]. The magnetic components of the spectra were fitted assuming the superposition of two or more magnetic sextets due to Fe^{3+} ions in A- and B-sites. The criterion used to assign the sextets to either site is that the higher values of isomer shift and hyperfine field are due to Fe^{3+} in B-sites, whereas the lower values of the same parameters refer to Fe^{3+} in A-sites [6]. This resulted in the A-site Fe^{3+} always having one sextet. However, two sextets, B_1 and B_2, were required to fit the 300 K spectral component due to the B-site Fe^{3+} for x=0.1, 0.2 and 0.3. These sextets can, respectively, be attributed to B-site Fe^{3+} ions having low and high concentrations of nearest-neighbor cation substitutes. The Mössbauer parameters obtained from the different fits are presented in Table I.

The values of the isomer shifts at both sites show, within experimental errors, no appreciable change with increasing x. This implies that the s-electron density at the nucleus of the Fe^{3+} remains largely unaffected by the increasing numbers of the Mn^{2+} and Cr^{3+} nearest neighbors [2, 7]. Also, we note that the isomer shifts at both sites are of comparable values. This indicates similar covalence effects of Fe^{3+} ions at both sites [2]. The electric quadrupole splitting values of all sextets are nearly zero. This suggests that both sites retain their cubic symmetry, as inferred from the XRD patterns regardless of the value of x [7].

At 78 K a better resolution for the Mössbauer sub-spectra at both sites is attainable relative to 300 K. Thus, we opt for the 78 K spectra to infer reliable information about the cation distribution in the various compounds. The lines of the A-site sextets (Table I) broaden faster relative to those of the B-site as x increases. In accordance with the Néel's model, such broadening reflects the strength of the magnetic linkages of the Fe^{3+} ions [3]. In spinels, each A-site ion is surrounded by 12 B-site ions whereas each B-site ion is surrounded by 6 A-site ions. The AB super-exchange interaction is known to be stronger

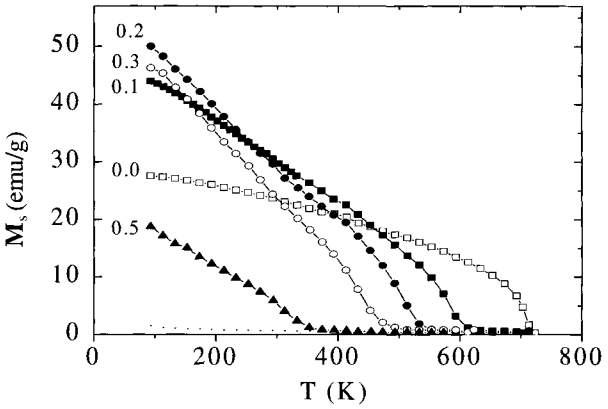

Figure 2 Saturation magnetization (M_s) vs temperature (T) for the various $Mg_{1-x}Mn_xFe_{2-2x}Cr_{2x}O_4$ compounds.

than both AA and BB ones [7, 8]. Thus, the larger line broadening of the A-site sextets relative to that of the B-site ones is suggestive of the presence of more non-Fe^{3+} cations at the B-site than at the A-one. This is consistent with our proposed cation distribution of Eq. 1 where all Cr^{3+} (i.e., two thirds of the substituent cations), most of Mg^{2+} and 20% of Mn^{2+} ions occupy B-sites. The different magnetic moments of $Fe^{3+}(5\mu_B)$, $Cr^{3+}(3\mu_B)$, $Mn^{2+}(5\mu_B)$ and $Mg^{2+}(0\mu_B)$ lead to different exchange interactions among which the $Fe_A^{3+} - O - Fe_B^{3+}$ is the strongest relative to $Fe_A^{3+} - O - Mn_B^{2+}$, $Fe_A^{3+} - O - Cr_B^{2+}$, and $Mn_A^{2+} - O - Mn_B^{2+}$ [2]. Consequently the magnetizations experienced by Fe^{3+} nuclei at both sites weaken with increasing x, resulting in the gradual decrease in the magnetic hyperfine fields.

Assuming the recoilless fractions, f_A and f_B, of the A- and B-sites are equal at 78 K [9], the relative Mössbauer spectral areas for both sites will be proportional to their respective Fe^{3+} ions numbers. It can be easily shown that if the Cr^{3+} ions were only to replace Fe^{3+} ions at the B-site, then the ratio of A-site spectral area to that of the B-site would sharply change from 1:1 to 1:9 as x changes form 0.1 to 0.5. This is, however, not the case as seen in Table I. It is thus evident that while the B-site Fe^{3+} ions are being replaced by Cr^{3+}ions, an appreciable and concomitant decrease in the number of the A-site Fe^{3+} ions takes place, keeping the ratio of spectral areas in the region of 1:1. This again agrees with Eq. 1, which shows Fe^{3+} ions to decrease at both sites subsequent to substitution with Mn^{2+} and Cr^{3+}. Indeed the last two columns of Table I, show that the ratios of numbers (spectral areas) of Fe^{3+} ions at both sites derived from the 78 K Mössbauer spectra remarkably agree with those calculated using Eq. 1.

Figure 2 shows the temperature variation of the saturation magnetization $|M_s|$ of the samples (including x=0.0). According to Néel's model of ferrimagnetism, $|M_s|$ per chemical formula unit at 0 K is given by the difference of the magnetic moments at the B- and A-sublattices $|M_B|$ and $|M_A|$ respectively. Using our cation distribution of Eq. 1, which is consistent with XRD and Mössbauer data, it is easy to show that Néel's model yields a constant value of the magnetization ($1\mu_B$) at 0 K for all the values of x. However, it is apparent from Figure 2 that, the different samples do not have the same extrapolated $|M_s|$ value at 0 K. Rather, the value increases with x reaching a maximum at x=0.2 and then start to decrease at higher values of x. The discrepancy can be explained assuming canted spins within both A- and B- sub-lattices as proposed by Yafet-Kittel in their extended Néel's model [3]. With increasing x value, the AA and BB interactions fail to hold all the magnetic spins parallel in their respective sub-lattices, thus leading to spin canting. The resultant magnetic moments are again antiferromagnetically aligned leading to ferrimagnetism. So

the variation of $|M_s|$ value with increasing x reflects different effective magnetic moments at both sub-lattices. Finally, we see from the M_s vs T curves (Figure 2) that the Curie temperature, T_c, decreases as x increases. Again, as we argued for the hyperfine fields, this is attributable to weakening of magnetic bonds with increasing x.

References

1. Lakshman, A., Rao, K.H., Mendiratta, R.G.: J. Magn. Magn. Mater. **250**, 92 (2002)
2. Lakshman, A., Subba Rao, P.S.V., Rao, K.H.: J. Magn. Magn. Mater. **284**, 352 (2004)
3. McCurrie, R.A.: Ferromagnetic Materials: Structure and Properties, pp. 121–188. Academic, London (1994)
4. Winter, M.J.: http://www.webelements.com, © 1993– 2005, University of Sheffield, UK
5. Coey, J.M.D., Khalafalla, D.: Phys. Status Solidi. A **11**, 229 (1972)
6. Greenwood, N.N., Gibb, T.C.: Mössbauer Spectroscopy, pp. 259. Chapman and Hall, London (1971)
7. Puri, R.K., Singh, M., Sud, S.P.: J. Mater. Sci. **29**, 2182 (1994)
8. Dogra, A., Kumar, R., Kumar, N., Sen, P., Singh, M.: Mater. Sci. Eng. B. **110**, 243 (2004)
9. O'Neill, H.St.C., Annersten, H., Virgo, D.: Amer. Mineral. **77**, 725 (1992)

Hyperfine Interact (2006) 169:1331–1336
DOI 10.1007/s10751-006-9447-6

Critical behavior of $La_{0.67-y}(Sr, Ba, Ca)_{0.33+y}Mn_{1-x}Sn_xO_3$ (x=0.01, 0.02, y=0, 0.07) perovskites

H. Assaridis · I. Panagiotopoulos · A. Moukarika · V. Papaefthymiou · T. Bakas

Published online: 16 November 2006

Abstract The magnetic critical behavior of the manganese perovskite series $La_{0.67-y}(Sr, Ba, Ca)_{0.33+y}Mn_{1-x}Sn_xO_3$ (x=0.01, 0.02, y=0, 0.07) is studied by means of dc magnetic measurements and ^{119}Sn Mössbauer spectroscopy. The structure can be described by a rhombohedral unit cell (space group R–3C) for the samples where the A-site is occupied by La and Sr or La and Ba ions and orthorhombic unit cell (space group Pnma) for the samples where the A-site is occupied by La and Ca ions. Arrott and scaling plots show that the samples, where the A-site is occupied by La and Sr or La and Ba ions, follow the behavior of a conventional second-order ferromagnetic transition. In contrast, the samples that contain La and Ca ions in the A-site show anomalous behavior around Curie point. Mössbauer measurements show two magnetic phases below T_c. One of them exhibits stronger exchange interactions with more rapid electron transfer between Mn^{3+}/Mn^{4+}, compared to the other.

Key words Mössbauer spectroscopy · critical exponents · manganese oxides · magnetic measurements

1 Introduction

Research on perovskite manganites of the form $La^{3+}_{1-x}A^{2+}_xMn^{3+}_{1-x}Mn^{4+}_xO^{2-}_3$ (where A can be Ca, Sr or Ba) has revived during the last decade, after the discovery of the colossal magnetoresistance (CMR) phenomenon, associated with simultaneous ferromagnetic to paramagnetic and metal insulator transitions [1]. Several studies have focused on the critical behavior in the temperature range near these interdependent magnetic and electronic phase transitions in order to investigate their nature (first or second order) and to derive critical

H. Assaridis · A. Moukarika · V. Papaefthymiou · T. Bakas (✉)
Physics Department, University of Ioannina, P.O. Box 1186, 451 10 Ioannina, Greece
e-mail: tbakas@cc.uoi.gr

I. Panagiotopoulos
Department of Materials Science and Technology,
University of Ioannina, P.O. Box 1186, 451 10 Ioannina, Greece

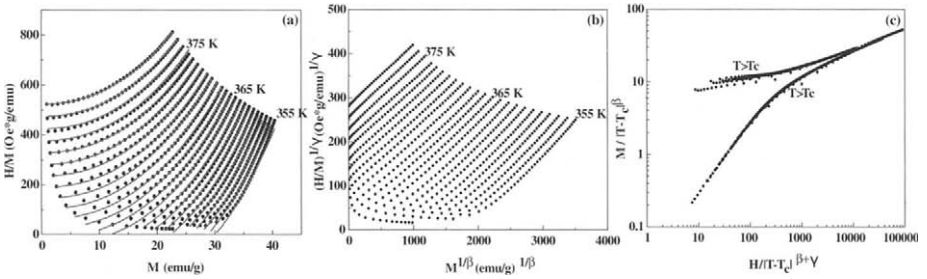

Figure 1 (a) Arrott plots (H/M vs. M). *Solid lines* stand for best fits. (b) Modified Arrott plots, (c) Scaling plot $M/|T-T_c|^{\beta}$ vs. $H/|T-T_c|^{\beta+\gamma}$ for the sample $La_{0.67}Sr_{0.33}Mn_{0.99}Sn_{0.01}O_3$ with β=0.453, γ=1.10 and T_c=365.4 K. The *numbers inside the frames* indicate the temperature of the isotherms.

exponents in the latter case. Scaling plots based on the measurement of magnetic isotherms near the critical temperature have been used in order to derive the critical exponents and verify the second order type of the transition [2, 3]. Using ^{57}Fe Mössbauer spectroscopy, it was found recently that the ferromagnetic (FM) metallic phase in $La_{1-x}Ca_xMnO_3$ (x~0.3) has a rather complex character, since at least two spatially separated FM regions exist, which possess temperature-dependent volumes and different internal hyperfine fields [4]. The long-range ferromagnetic ordering breaks down into small magnetic clusters exhibiting superparamagnetic-like behavior below T_c. It was reported that in the series $La_{1-x}Sr_xMnO_3$ (x~0.3), using NMR spectroscopy, two different ferromagnetic phases with mobile holes coexist below Tc [5]. In this work we present a study of the structural and critical magnetic properties of the manganese perovskite series $La_{0.67-y}(Sr, Ba, Ca)_{0.33+y}Mn_{1-x}Sn_xO_3$ (x=0.01, 0.02, y=0, 0.07). We report a Mössbauer study of the samples doped with 1% Sn. The aim is to observe microscopically the evolution of the phases that appear as the temperature varies. The Sn ions substitute for Mn^{4+} and serve as a probe for the magnetic state of the host lattice as the transferred hyperfine interactions rise from their neighbour Mn magnetic ions.

2 Experimental

$La_{0.67-y}(Sr, Ba, Ca)_{0.33+y}Mn_{1-x}Sn_xO_3$ (x=0.01, 0.02, y=0, 0.07) samples were prepared by standard solid state reaction from stoichiometric amounts of high purity La_2O_3, $SrCO_3$, $BaCO_3$, $CaCO_3$, Mn_2O_3 and SnO_2 (enriched in ^{119}Sn) powders, sintered at 1,350°C for 6 days with several intermediate grindings. X-ray powder diffraction (XRD) diagrams were collected with a Bruker D8 Advance Diffractometer using CuK_a (λ=1.5418 Å). Magnetic measurements were performed on a Lakeshore 3700 VSM magnetometer. Magnetization isotherms at various temperatures around the critical region have been measured in applied fields of 1.85 T at temperature steps 1 K apart. Mössbauer spectra were recorded with a conventional constant acceleration spectrometer. The source was moving at room temperature (RT), while the absorbers were kept fixed at a variable temperature (80–250 K).

3 Results and discussion

The refinement of the XRD patterns was carried out by the Fullprof Rietveld program [6]. All samples were found to be single phase and the structure can be described by a

Table I Unit cell volume, critical exponents (β, γ) and T_c in the series of samples $La_{0.67-y}(Sr, Ba, Ca)_{0.33+y}Mn_{1-x}Sn_xO_3$ (x=0.01, 0.02, y=0, 0.07)

	Volume (Å^3)	β	γ	T_c (K)
$La_{0.67}Ba_{0.33}Mn_{0.99}Sn_{0.01}O_3$	358.861(2)	0.483(3)	1.17(2)	329
$La_{0.67}Ba_{0.33}Mn_{0.98}Sn_{0.02}O_3$	359.747(2)	0.531(2)	1.07(2)	314
$La_{0.60}Ba_{0.40}Mn_{0.99}Sn_{0.01}O_3$	358.685(2)	0.492(2)	1.28(3)	332
$La_{0.60}Ba_{0.40}Mn_{0.98}Sn_{0.02}O_3$	359.586(2)	0.511(3)	1.10(2)	308
$La_{0.67}Sr_{0.33}Mn_{0.99}Sn_{0.01}O_3$	350.574(1)	0.453(1)	1.10(1)	366
$La_{0.67}Sr_{0.33}Mn_{0.98}Sn_{0.02}O_3$	351.271(2)	0.479(3)	1.26(2)	352
$La_{0.60}Sr_{0.40}Mn_{0.99}Sn_{0.01}O_3$	347.560(2)	0.523(2)	1.19(1)	360
$La_{0.60}Sr_{0.40}Mn_{0.98}Sn_{0.02}O_3$	349.155(2)	0.607(3)	1.38(2)	354
$La_{0.67}Ca_{0.33}Mn_{0.99}Sn_{0.01}O_3$	230.714(1)	–	–	238
$La_{0.67}Ca_{0.33}Mn_{0.98}Sn_{0.02}O_3$	231.252(2)	–	–	228
$La_{0.60}Ca_{0.40}Mn_{0.99}Sn_{0.01}O_3$	229.142(2)	–	–	253
$La_{0.60}Ca_{0.40}Mn_{0.98}Sn_{0.02}O_3$	230.910(1)	–	–	244

Numbers in parenthesis are errors of the last significant digit.

rhombohedral unit cell (space group R–3C) for the samples where the A-site is occupied by La and Sr or La and Ba ions and orthorhombic unit cell (space group Pnma) for the samples where the A-site is occupied by La and Ca ions. An increase in the lattice constants and the cell volume is observed in the series $La_{0.67-y}(Sr, Ba, Ca)_{0.33+y}Mn_{1-x}Sn_xO_3$ (x=0.01, 0.02, y=0, 0.07) as the six-coordinated smaller Mn ions (r^{Mn4+}=0.53 Å) are substituted by the larger Sn ions (r^{Sn4+}=0.69 Å), in all samples. Magnetization curves were measured as a function of temperature (M vs. T) in an applied field of H=100 Oe. The transition temperature was determined from the inflection point of the M vs. T curves and it was found to decrease with increasing the amount of tin doping.

The ferromagnetic behavior at temperatures around T_c can be studied with the use of M^2 vs. H/M plots (Arrott plots). In the mean-field approximation, M^2 and H/M are related by $H/M = 2\alpha + 4bM^2$ [7]. From this linear relation the M^2 vs. H/M curves should be straight lines, the intercept of which on the H/M axis, determines the magnetic state, which should be negative below T_c, originating from a ferromagnetic state, and positive above T_c, originating from a paramagnetic state. This mean-field approximation can be generalized to the so-called modified Arrott-plots expression

$$(H/M)^{1/\gamma} = C_1(T - T_c) + C_2M^{1/\beta} \quad (1)$$

which combines the relations for the spontaneous magnetization below T_c, $M \sim (T - T_c)^{\beta}$ and the inverse susceptibility above T_c, $\chi^{-1} \sim (T - T_c)^{\gamma}$.

According to Eq. 1 and with an appropriate choice of β and γ, the $(H/M)^{1/\gamma}$ vs. $M^{1/\beta}$ plots should give parallel straight lines. The critical exponents of the transition can be equivalently determined by scaling plots of the form $M/|t|\beta = f_{\pm}\left(H/|t|^{\beta-\gamma}\right)$ where $t = |T - T_c|$, $f_{\pm}$ is a scaling function and the plus or minus sign correspond to the ferromagnetic and paramagnetic regions, respectively. By appropriate selection of the parameters T_c, β, and γ the data should collapse on two different branches for $T > T_c$ and $T < T_c$ (Figure 1c; Table I).

It can be seen that for samples with higher T_c, like the series $La_{0.67-y}Sr_{0.33+y}Mn_{1-x}Sn_xO_3$ and $La_{0.67-y}Ba_{0.33+y}Mn_{1-x}Sn_xO_3$, most of the data fall on straight lines. In contrast the samples that contain La and Ca ions in the A-site show anomalous behavior around Curie point. By fitting the H/M vs. M curves using Eq. 1 we determined the T_c and critical

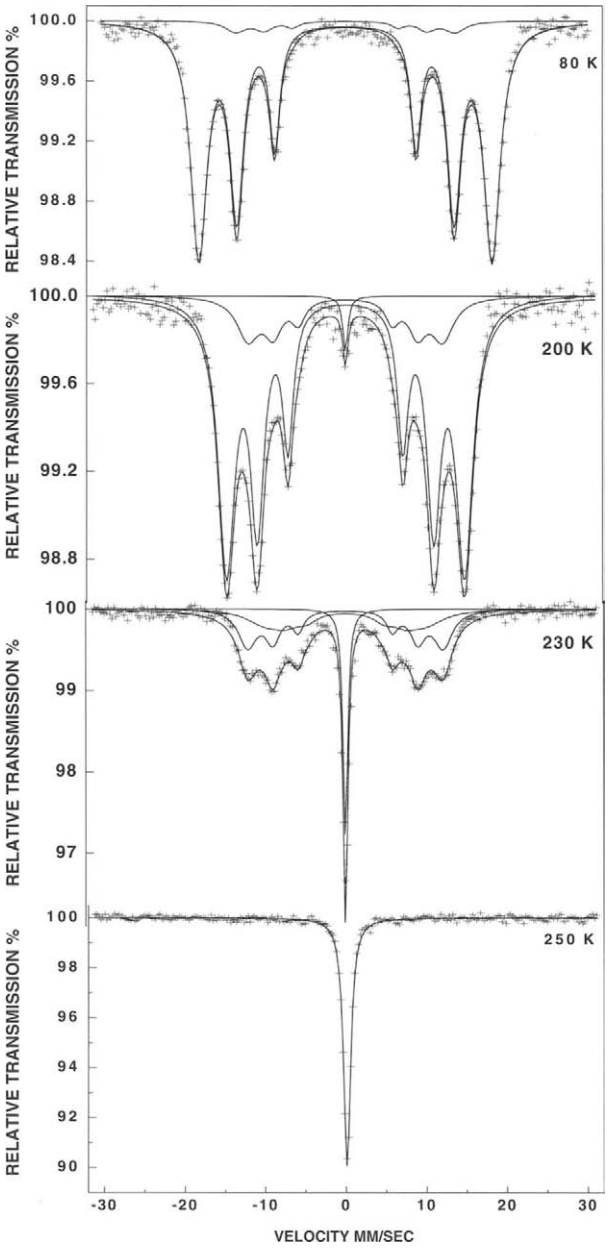

Figure 2 Typical Mössbauer spectra for the $La_{0.60}Ca_{0.40}Mn_{0.99}Sn_{0.01}O_3$ sample at various temperatures.

exponents (β, γ). Based on these parameters the modified Arrott and scaling plots can be constructed, proving therefore the validity of the resulting β, γ, and T_c values (Figure 1b, c).

At 80 K the Mössbauer spectrum is fitted with two magnetic components (Figure 2). Their hyperfine magnetic fields is the result of the overlap between the 5s orbitals of the Sn and the 3d orbitals of the Mn ions. The component with the higher spectral area (main component) has the larger hyperfine field ($H_{hf} \approx 28$ T) originating from a ferromagnetic environment where all the Mn moments are parallel and add up to a large transferred

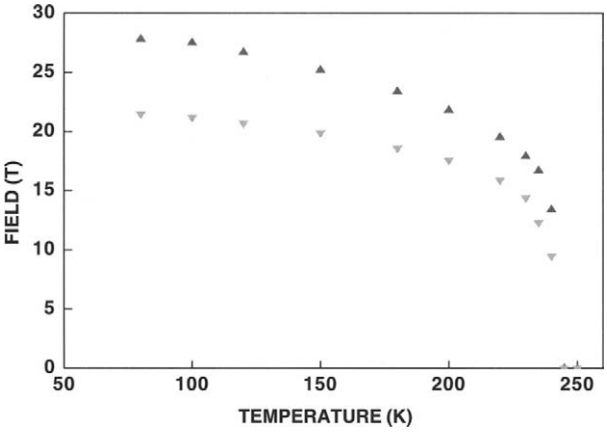

Figure 3 The temperature variation of hyperfine fields of the components which apperars in the Mössbauer spectra for the sample $La_{0.60}Sr_{0.40}Mn_{0.99}Sn_{0.01}O_3$.

hyperfine field at the Sn nucleus, in agreement with previous results [8, 9]. The value of the hyperfine field of the second component is $H_{hf} \approx 20.8$ T. The area of this magnetic component increases with temperature up to the vicinity of T_c and then vanishes at Curie point whereas the area of the main ferromagnetic component decreases as the temperature increases and disappears at the same T_c point. The analysis of the Mössbauer spectra shows that the material consists of magnetic clusters with different average exchange interactions within each cluster. At low temperature, the strong coupling constant dominates, but as the temperature increases clusters with smaller coupling constants develop, due to the evolution of regions with different electronic densities. The size of these clusters is estimated to be $\sim 25\alpha$, where $\alpha \sim 0.4$ nm is the Mn–Mn distance [10]. It is expected that by applying an external magnetic field at temperatures below T_c, these magnetic clusters will reduce drastically, as it has been observed by Fäth et al. [11] using scanning tunnelling spectroscopy, giving a satisfactory explanation to the CMR effect. The above mentioned breakdown of the long-range ferromagnetic order is an intrinsic property of magnetoresistive manganites as it is also reported for similar samples [4, 5].

Figure 3 shows the temperature variation of hyperfine fields of the two magnetic components of the Mössbauer spectra. It is observed that the magnitude of the hyperfine fields of each component decreases as the temperature increases and finally, disappears in the Curie point. The hyperfine magnetic fields do not follow the relation $H(T) \sim M(T) \sim (1 - T/T_c)\beta$ where T_c is the Curie point and β is a constant with values between 0.3 (Heisenberg's model) and 0.5 (mean field theory) [12].

4 Conclusions

In short, we have studied the critical behavior of the series $La_{0.67-y}(Sr, Ba, Ca)_{0.33+y}Mn_{1-x}Sn_xO_3$ (x=0.01, 0.02, y=0, 0.07). Though the introduction of non-magnetic Sn^{4+} impurities leads to a decrease of the transition temperature in all samples, the ferromagnetic transition retains its second-order character in Sr or Ba containing samples. In contrast the samples that contain Ca show anomalous behavior around Curie point. From Mössbauer study we find that all samples exhibit two distinct (spectral components) electronic phases below Tc, in the whole temperature interval studied, one of them exhibits stronger exchange interactions with more rapid electron transfer between Mn^{3+}/Mn^{4+}, compared to the other.

Acknowledgments This research was funded by the program "Heraklitos" of the Operational Program for Education and Initial Vocational Training of the Hellenic Ministry of Education under the 3rd Community Support Framework and the European Social Fund. The authors would like to acknowledge the use of XRD and VSM units of the Laboratory Network, UOI.

References

1. Salamon, M.B.: Rev. Mod. Phys. **73**, 583 (2001) (and references therein)
2. Novák, P., et al.: Phys. Rev., B **60**, 6655 (1999)
3. Uehara, M., et al.: Nature **399**, 560 (1999)
4. Chechersky, V., et al.: Phys. Rev., B **62**, 5316 (2000)
5. Savosta, M.M., et al.: J. Magn. Magn. Mater. **242–245**, 672 (2002)
6. Wiles, D.B., Young, R.A.: J. Appl. Crystallogr. **14**, 149 (1981)
7. Moutis, N., et al.: Phys. Rev., B **59**, 1129 (1999)
8. Papavassiliou, G., et al.: Phys. Rev. Lett. **84**, 761 (2000)
9. Simopoulos, A., et al.: Phys. Rev., B **63**, 054403 (2000)
10. Moreo, A., et al.: Phys. Rev. Lett. **84**, 5568 (2000)
11. Fäth, M., et al.: Science **285**, 1540 (1999)
12. Stanley, H.E.: Introduction to Phase Transitions and Critical Phenomena. Clarendon, Oxford (1971)

Hyperfine Interact (2006) 169:1337–1342
DOI 10.1007/s10751-006-9448-5

Magnetization and magnetostriction studies of TbFeCo/YFeCo multilayers

D. T. Huong Giang · N. H. Duc · J. Juraszek · J. Teillet

Published online: 20 December 2006

Abstract Exchange-spring TbFeCo/YFeCo multilayers exhibit interesting magnetic and magnetostrictive properties that are rather promising for application in microsystems. In this paper, we present a study of the effect of the exchange coupling on the magnetic properties of these magnetostrictive multilayers. An exchange bias phenomenon, revealed by a shift of the minor hysteresis loop along the applied field axis, is found as the result of the creation of interfacial domain walls. This effect strongly depends on the magnetic properties of the soft YFeCo layer, and becomes more pronounced at low temperatures due to the enhancement of the magnitude of the exchange coupling between the layers.

Key words RE–MT multilayers · magnetostriction · magnetization process · microstructure · Mössbauer

1 Introduction

When two grains are directly in contact with each other, the magnetic moments at the grain interface cause exchange-coupling interaction between the two grains. The fundamental understanding of the exchange-coupling mechanism has been successfully applied to the so-called low-field giant magnetostrictive exchange-spring TbFeCo/YFeCo multilayers, in which giant magnetostrictive (e.g., TbFeCo) and soft magnetic (e.g., FeCo) layers alternate [1, 2]. The structural, magnetic and magnetostrictive properties of TbFeCo/YFeCo

D. T. Huong Giang (✉) · J. Juraszek · J. Teillet
Groupe de Physique des Matériaux, Université de Rouen, UMR CNRS 6634,
76801 St Etienne du Rouvray, France
e-mail: dth.giang@univ-rouen.fr

D. T. Huong Giang
Faculty of Physics, Vietnam National University,
Hanoi, 334 Nguyen Trai, Thanh Xuan, Hanoi, Vietnam

N. H. Duc
College of Technology, Vietnam National University,
Hanoi, 144 Xuan Thuy Road, Hanoi, Vietnam

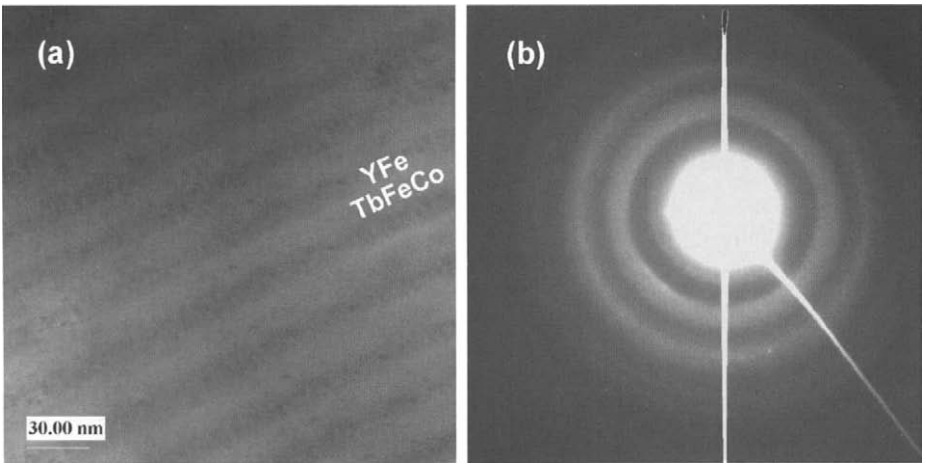

Fig. 1 Bright field TEM (a) and electron diffraction pattern (b) of $TbFeCo/Y_{0.2}Fe_{0.8}$ multilayers

multilayers have been previously studied in relation with concentration as well as the annealing treatments [2]. Most of recent results for such magnetostrictive materials have attracted much attention mainly in magnetic and magnetostrictive softness improvement. However, the exchange bias phenomenon caused by the formation of the interfacial domain wall has not been taken into account.

In this article, we have focused on the interfacial exchange-coupling interaction and exchange bias phenomenon and their correlation with magnetization and magnetostriction process in the sputtered $Tb(Fe_{0.55}Co_{0.45})_{1.5}/Y_{0.2}Fe_{0.8}$ and multilayers.

2 Experimental procedures

$\{Tb(Fe_{0.55}Co_{0.45})_{1.5}/Y_{0.2}Fe_{0.8}\}_{50}$ and $\{Tb(Fe_{0.55}Co_{0.45})_{1.5}/Y_{0.2}(Fe_{0.7}Co_{0.3})_{0.8}\}_{50}$ multilayers with the individual layer thicknesses $t_{TbFeCo}=12$ nm and $t_{YFeCo}=10$ nm were alternately deposited by RF-magnetron sputtering method on glass microscope cover slips with a nominal thickness of 200 μm. The typical power during sputtering was 200 W, the high-purity argon gas was used and deposition pressure was 10^{-2} mbar.

Structure analyses were done using transmission electron microscopy (TEM) and magnetization curves were measured with a superconductor quantum interference device (SQUID) in applied fields up to 5 T. Magnetic behavior of layers was also observed by the conversion electron Mössbauer spectroscopy (CEMS) and magnetic force microscopy (MFM). Magnetostriction was measured by using an optical deflectometer (resolution of 5×10^{-6} rad).

3 Results and discussion

The bright-field cross-sectional TEM image of the as-sputtered $TbFeCo/Y_{0.2}Fe_{0.8}$ sample in Fig. 1a shows clearly the layered structure with well-defined boundaries between TbFeCo (bright) and YFe (dark) layers. A high degree of smooth stripe periodicity, smooth interfaces and no evidence of the existence of any crystalline phase are visible in the

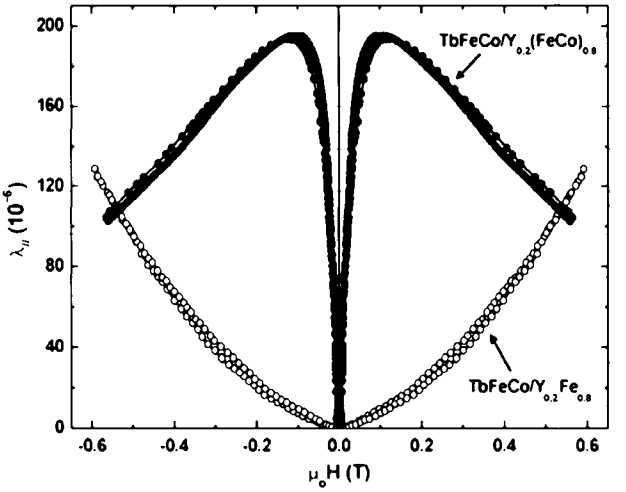

Fig. 2 Parallel magnetostriction of $TbFeCo/Y_{0.2}Fe_{0.8}$ and $TbFeCo/Y_{0.2}(Fe_{0.7}Co_{0.3})_{0.8}$ multilayers

micrograph. This indicates that the amorphous state exists in the whole sample, i.e., in both the magnetostrictive TbFeCo and the soft magnetic YFe layers. The amorphous structure of sample is further revealed in Fig. 1b by bright spread rings from the inside diffraction spot, the first one characteristics of the amorphous TbFeCo layers and the others of the amorphous YFe layers. The same behavior was also observed in the $TbFeCo/Y_{0.2}(FeCo)_{0.8}$ film.

Although the microstructure is the same, these two samples exhibit a significantly different magnetostrictive behavior (Fig. 2). For the TbFeCo/YFe multilayer, the magnetostriction curve has a parabolic shape and does not reach saturation in the field range of magnetostriction measurement. This behavior is characteristic of films with perpendicular magnetic anisotropy [3]. In the case of the TbFeCo/YFeCo multilayer, a first enhancement of low-field magnetostriction, which is characteristic of in-plane anisotropic materials, is followed by a highly negative slope at high magnetic fields. Such behavior is ascribed to the formation of interfacial extended domain walls (EDW). The difference between the two systems is due to the different magnetic behavior between YFe and YFeCo layers. Amorphous $Y_{0.2}Fe_{0.8}$ alloy is paramagnetic at room temperature [4]. Thus, the coupling between successive TbFeCo/YFe layers is weak and the magnetostrictive layers preserve their intrinsic perpendicular magnetic anisotropy, as already found in TbFeCo single layer films [5]. On the other hand, partial substitution of Fe by Co makes the $Y_{0.2}(FeCo)_{0.8}$ layers becoming magnetic at room temperature and the exchange coupling between the layers is strengthened. In this case, the effective spring-magnet configuration results in an enhancement of the low-field magnetostriction.

The difference in the magnetic anisotropy between $TbFeCo/Y_{0.2}Fe_{0.8}$ and $TbFeCo/Y_{0.2}(FeCo)_{0.8}$ samples is also evidenced in MFM images (Fig. 3). For the $TbFeCo/Y_{0.2}Fe_{0.8}$ sample, a stripe domain structure indicates the presence of magnetic domains with different directions of magnetization oriented perpendicular to the film plane (Fig. 3a). In contrast, for the $TbFeCo/Y_{0.2}(FeCo)_{0.8}$ specimen, the existence of perpendicular stripe domains is no longer clearly revealed (Fig. 3b) reflecting the in-plane magnetic anisotropy in this sample.

Further evidence for above statement is given by the Mössbauer analysis of the $TbFeCo/Y_{0.2}Fe_{0.8}$ sample (Fig. 4). The spectrum was fitted with three components: (1) a doublet (δ= 0.2 mm s^{-1}, $<B_{hf}>$=1.5 T and 40% of the total spectrum area) attributed to a non-magnetic

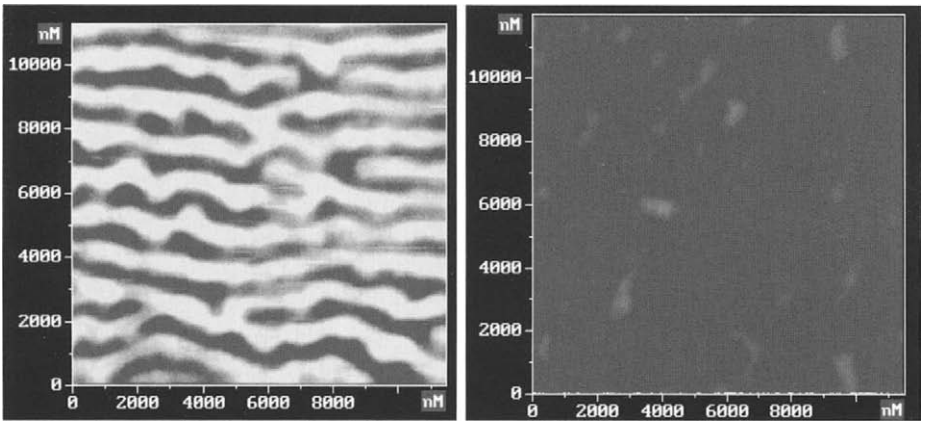

Fig. 3 MFM images of TbFeCo/$Y_{0.2}Fe_{0.8}$ (a) and TbFeCo/$Y_{0.2}(FeCo)_{0.8}$ (b) multilayers in zero field

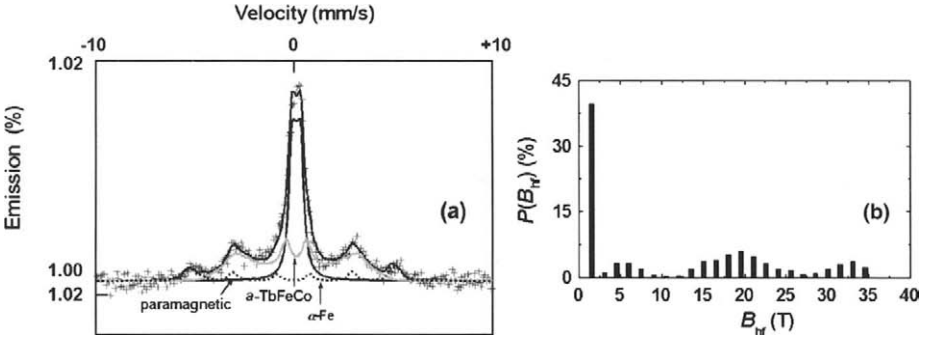

Fig. 4 Mössbauer spectrum (a) and hyperfine-field distribution (b) of the TbFeCo/$Y_{0.2}Fe_{0.8}$ multilayer at 300 K

part of YFe phase (Fe-poor), (2) a broad sextet (δ=0.094 mm s^{-1}, $<B_{hf}>$=32 T and 13% of the total spectrum area) attributed to a magnetic part of YFe phase (Fe-rich) and (3) a broad distribution of sextet with same isomer shift ($<\delta>$=0.094 mm s^{-1}, $<B_{hf}>$=16 T, and 47% of the total spectrum area) attributed to the different Fe environments in amorphous TbFeCo layers. The value of the average "cone-angle" between the direction of γ-ray and Fe spins is 35°, evidencing for out of plane magnetic anisotropy.

For a better understanding of the exchange-coupling in the TbFeCo/YFeCo multilayer, the magnetization data measured at 5 K are presented in Fig. 5. When sweeping the field from high positive to negative field, the hysteresis loop exhibits the field-induced magnetization transitions. The corresponding magnetization configurations in the magnetization process are illustrated in the inserted figures. The magnetization process in this system is governed by the competition between three energies: exchange coupling, magnetic anisotropy and Zeeman energy [6]. For a very high applied field, the Zeeman energy dominates and the sample is saturated. In this state, the FeCo moments of TbFeCo

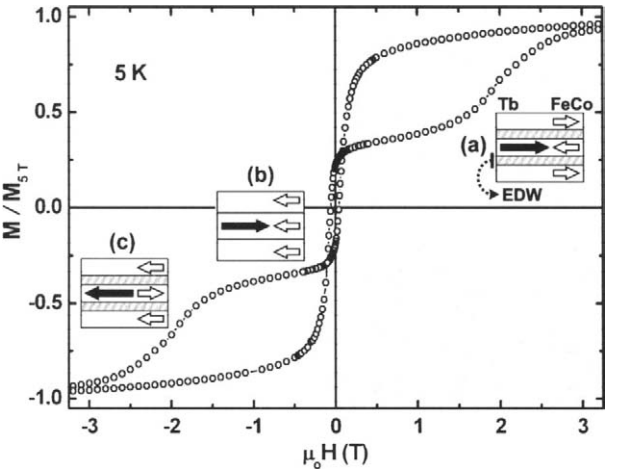

Fig. 5 Hysteresis loops and magnetization process at 5 K for TbFeCo/YFeCo multilayers

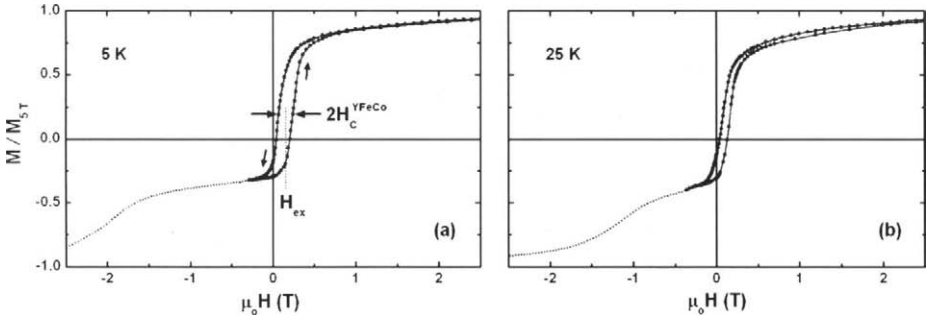

Fig. 6 Magnetization (*dotted line*) and minor loop (*closed circles*) at 5 K (a) and 25 K (b) for TbFeCo/YFeCo film

(dominated by Tb) and YFeCo layers are directed in opposite directions and EDW is formed at the interfaces (state a). When the field is decreased, the EDW vanishes by the reversal of the YFeCo layer (state b). In this case, because K_{TbFeCo} is very large compared to K_{YFeCo}, meanwhile M_{TbFeCo} is comparable to M_{YFeCo}, the TbFeCo-layers would be still more strongly pinked along the field direction than FeCo-layers when the applied field decreases. Only the YFeCo magnetization rotates easily by antiferromagnetic interaction between these two layers. As the field is further decreased, a EDW in which TbFeCo moments rotate out of the external field direction is formed (state c). This results in a negative contribution to the parallel magnetostriction and a decrease of magnetostriction at high fields [7].

The minor hysteresis loops have been recorded at 5, 25 and 50 K for TbFeCo/YFeCo multilayer (Fig. 6). The measurement was obtained by sweeping the field from 5 T to a small negative value ($\mu_0 H$=−0.3 and −0.4 T for 5 and 25 K, respectively) in the hysteresis loops that corresponds only to the reversal of the soft layers (state b; see in Fig. 5). The width of the loops can be roughly considered as the coercive field of the soft magnetic YFeCo-layer. The shift of the minor hysteresis loop is defined as the exchange bias field H_E that is usually found in antiferromagnetic (AF)/ferromagnetic (F) bilayer systems [8]. H_E is found to decrease from 165 to 115 and 36 mT when the temperature increases from 5 to 25

and 50 K, respectively. This observation is in good accordance with the decreasing tendency of magnetization and magnetic anisotropy of constituted layers [6].

4 Conclusion

In this work, we have studied the magnetization and magnetostriction in the spring-magnet TbFeCo/YFe and TbFeCo/YFeCo multilayers. Among them, the later system with the soft YFeCo layer exhibits an exchange-bias phenomenon and interfacial domain wall as a result of antiferromagnetic exchange-coupling interaction between layers.

Acknowledgement This work was partially supported by CNRS (France) through a PICS program. The authors would like to thank Dr. S. Schulze from Institute of Physics, Chemnitz University of Technology (Germany) for his help in TEM investigations.

References

1. Quandt, E., Ludwig, A., Betz, J., Mackay, K., Givord, D.: J. Appl. Phys. **81**, 5420 (1997)
2. Huong Giang, D.T., Duc, N.H., Thuc, V.N., Vu, L.V. Chau, N.: Appl. Phys. Lett. **85**, 1565 (2004)
3. Chatz, F., Hircher, M., Schnell, M., Flik, G., Kronmüller, H.: J. Appl. Phys. **76**, 5380 (1994)
4. Hansen, P.: Handbook of Magnetic Materials, vol. 6. In: Buschow, K.H.J. (ed.), p. 289. Elsevier Science, North Holland, Amsterdam (1991)
5. Duc, N.H., Huong Giang, D.T., Thuc, V.N., Minh Hong, N.T., Chau, N.: Physica B **327**, 328 (2003)
6. Montaigne, F., Mangin, S., Henry, Y.: Phys. Rev., B **67**, 144412 (2003)
7. Givord, D., Betz, J., Mackay, K., Toussaint, J.C., Voiron, J., Wüchner, S.D.: J. Magn. Magn. Mater. **159**, 71 (2004)
8. Fullerton, E.E., Jiang, J.S., Bader, S.D.: J. Magn. Magn. Mater. **200**, 392 (1999)

Hyperfine Interact (2006) 169:1343–1347
DOI 10.1007/s10751-006-9451-x

Thickness dependence of the magnetic anisotropy of Fe layers separated by Al

J. Balogh · D. Kaptás · L. F. Kiss · T. Kemény · L. Bujdosó · I. Vincze

Published online: 8 November 2006

Abstract Magnetic multilayers of ^{57}Fe with nominal thickness, T_{nom}, between 0.4 and 1.0 nm separated by 3.0 nm Al spacer layers were prepared by alternate deposition of the constituents in high vacuum. The samples were investigated at 4.2 K in external magnetic field. A fraction of Fe atoms corresponding to about 0.3 nm equivalent Fe-thickness was found to mix into the Al spacer. The extremely strong magnetic anisotropy observed for $T_{nom}<0.8$ nm is attributed to Fe layers of approximately two atomic planes thick. The anisotropy decreases considerably after the building up of the third Fe atomic layer starts at $T_{nom}=0.8$ nm, but full saturation was not achieved even for $T_{nom}=1$ nm and 3 T magnetic field applied perpendicularly to the sample plane.

Key words multilayers · magnetic properties

The Fe–Al system is well suited for the study of thin Fe layers by Mössbauer spectroscopy since both the magnetic moment and the hyperfine field of Fe depend strongly on the Fe nearest neighbour environment. Fe is nonmagnetic when five or more of the eight bcc nearest neighbour sites are occupied by Al ($n_{Al}\geq 5$). It has a magnetic moment of about 1.8 μ_B for $n_{Al}=4$, and 2.2 μ_B for $n_{Al}\leq 3$ [1, 2]. The dependence of the Fe hyperfine field on n_{Al} is somewhat more complicated because of the conduction electron polarization and/or transfer contribution of the nearest and farther magnetic neighbours beyond the core polarization contribution of the hyperfine field. The latter contribution is proportional (about 6.8 T/μ_B) to the own magnetic moment of the Fe atom; the former will depend on the magnetic moments of the surrounding Fe atoms. As a result, nonmagnetic Fe atoms may also have hyperfine fields in the 0–12 T range when they are in the neighborhood of magnetic Fe atoms. The hyperfine field is in the approximate range [3–8] of 15–26 T for $n_{Al}=4$ and above 25 T for $n_{Al}\leq 3$.

The samples were evaporated onto Si(111) wafers in a vacuum of 10^{-7} Pa with evaporation rates around 0.1 nm/s. The substrate was first covered by 10 nm Ag and the

J. Balogh (✉) · D. Kaptás · L. F. Kiss · T. Kemény · L. Bujdosó · I. Vincze
Research Institute for Solid State Physics and Optics, 1525 Budapest, P.O. Box 49, Hungary
e-mail: baloghj@szfki.hu

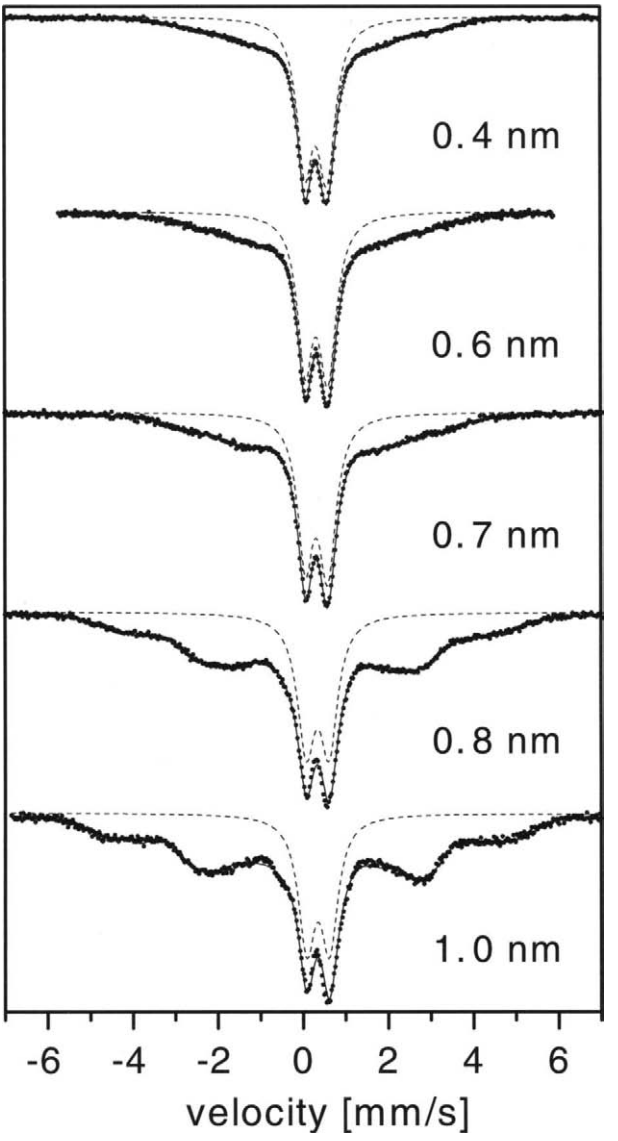

Figure 1 Mössbauer spectra of $^{57}Fe(T_{nom})/A1(3\ nm)$ multilayers measured at 4.2 K. The nominal ^{57}Fe layer thickness values (T_{nom}) of the samples are indicated in the figure. The paramagnetic quadrupole doublet corresponding to Fe atoms diffused into the Al layers is shown by *dotted line*. Its relative area in the spectra is marked by f_p.

topmost layer was 200 nm Al to ensure that the samples could be removed from the substrate. The Ag and Al were evaporated by two electron guns, the ^{57}Fe was evaporated from a heated W crucible. The layer thickness was controlled by a quartz oscillator and the nominal layer thickness is given using bulk density data. The thickness of the Al layers (3.0 nm) was kept constant in this multilayer series, while the thickness of the Fe layers was varied from T_{nom}=0.4 to 1.0 nm. The number of ^{57}Fe layers varied from 15 to 6 as the layer thickness increased. ^{57}Fe Mössbauer spectra at 4.2 K in various external magnetic fields were recorded by a standard constant acceleration spectrometer using a 50 mCi $^{57}CoRh$ source at room temperature. The magnetic field was applied parallel with the γ-beam (perpendicular to the sample plane) using a 7 T Janis superconducting magnet. Standard

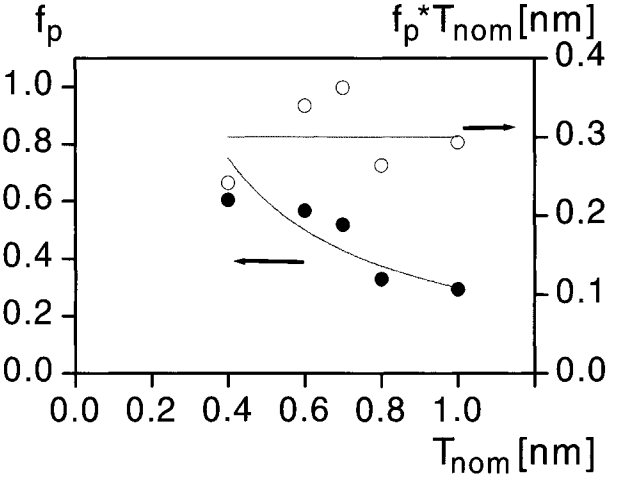

Figure 2 Relative area of the paramagnetic doublet corresponding to Fe atoms diffused into the Al layers, f_p (*dots*), and the equivalent iron-deposited thickness, f_pT_{nom} (*empty circles*) are shown as a function the nominal thickness, T_{nom} of the Fe-layers. The *lines* are guides to the eye.

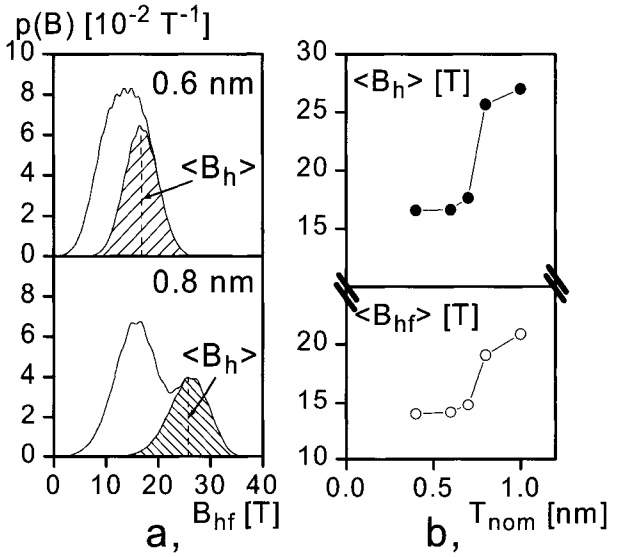

Figure 3 Hyperfine field distribution of the magnetically split component of the Mössbauer spectra at 4.2 K for T_{nom}=0.6 and 0.8 nm, respectively (**a**). The *lightly shaded* area marks the high field component of the fitted binomial distribution. The average hyperfine field of the high field part of the distribution, $<B_h>$ (*dots*), and the average hyperfine field of the full distribution is $<B_{hf}>$ (*empty circles*) are shown as a function of T_{nom} (**b**).

procedures were used for the evaluation of the spectra, the hyperfine field distributions were obtained by the binomial distribution method [9].

The large paramagnetic fraction observed at 4.2 K for all the samples, see Figure 1, indicate that many Fe atoms mix into the Al spacer layers. The Fe atoms surrounded by $n_{Al}\geq 5$ Al in the spacer layer are nonmagnetic, and show an average quadrupole splitting of 0.54(2) mm/s. The relative area of this component, i.e. the relative number of these Fe atoms, f_p is shown in Figure 2 as a function of the nominal Fe thickness, T_{nom}. The thickness decrease of the Fe layer due to atoms mixed into the Al spacer, $T_0=f_pT_{nom}$ is roughly constant for the whole investigated T_{nom} range and $T_0\approx 0.3$ nm. Thus the effective Fe layer thickness should be $T_{nom}-T_0$. The formation of magnetic Fe layer was not observed for $T_{nom}<0.4$ nm, which supports this assumption.

Intermixing at the Fe/Al interfaces has already been found by room temperature conversion electron Mössbauer spectroscopy e.g., in [10, 11]. Its magnitude obviously

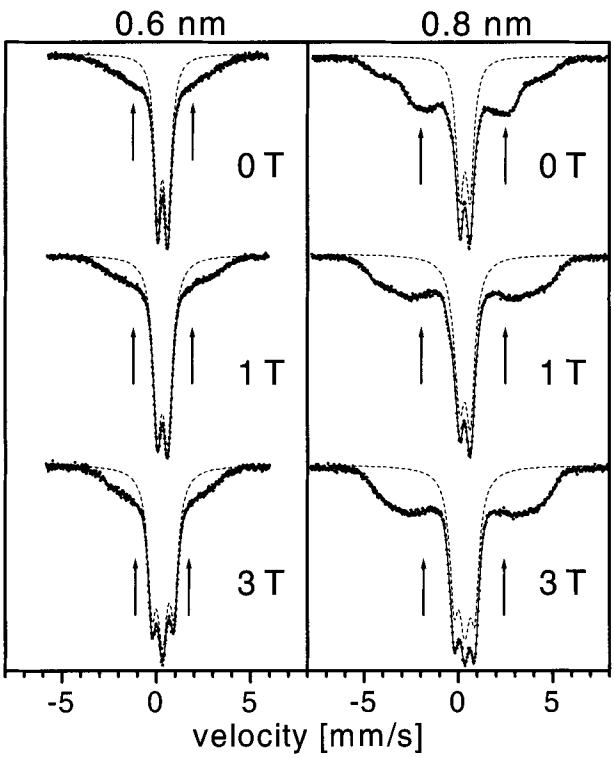

Figure 4 Mössbauer spectra of the T_{nom}=0.6 and 0.8 nm samples at 4.2 K in external magnetic fields, B_{ext} applied perpendicularly to the sample plane. *Arrows* mark the positions of the 2–5 lines of the spectra. The *dotted lines* show the paramagnetic quadrupole dublet component of the spectra broadened by the applied field. Note the significant decrease in the intensity of the 2–5 lines of the T_{nom}=0.8 nm sample, but also that they do not disappear even in B_{ext}=3 T.

depends on the deposition method: much larger for laser deposited than thermally evaporated samples. However, the recent result [12] of X-ray absorption spectroscopy investigation, that the equivalent of an iron-deposited thickness of 0.9 nm is mixed at the interface of a thermally deposited sample, should be explained by experimental differences.

Up to T_{nom}=0.7 nm the hyperfine fields indicate the formation of Fe layers containing no more than two atomic planes. In two atom thick planes the Fe neighborhood consists of four Al, and four Fe first neighbors and correspondingly the Fe hyperfine fields terminate below ≈25 T, as seen in Figure 3a. Similar hyperfine field distribution was found [13] in ball-milled stochiometric bcc FeAl alloys where ferromagnetic antiphase grain boundaries consisting of two atomic layers of Fe were formed. The large magnetic anisotropy was characteristic to these two Fe atom thick grain boundaries. Magnetization measurements [14, 15] on cold-worked Fe–Al alloys also report large magnetic anisotropies.

The high field tail at T_{nom}=0.8 nm in Figure 3 corresponds to the appearance of a third atomic plane of Fe. In a perfect three Fe atom thick layer, atoms in the middle Fe–layer have eight Fe first neighbors and thus a significantly higher hyperfine field. Figure 3b shows the average hyperfine field of the high field component of the distribution, $\langle B_h \rangle$, together with the average hyperfine field of the full hyperfine field distribution, $\langle B_{hf} \rangle$, respectively. Note the jump in both values between T_{nom}=0.7 and 0.8 nm which signifies the formation of Fe layers consisting of at least three atomic planes. If the Fe layer consists of exactly three atomic planes, the ratio of the areas under the high vs low field part of the distribution should be 1:2, which is quite close to the observed ratio for the T_{nom}=0.8 nm sample. (We note that nonmagnetic Fe atoms of the interface with magnetic neighbors may as well contribute to the low field part through the conduction electron polarization.) This is

in line with the effective thickness $(T_{nom}-T_0)$=0.5 nm of this sample. The agreement between the number of Fe atomic layers deduced from the shape of the hyperfine field distribution and the effective Fe layer thickness is reassuringly good.

The magnetic anisotropy of the Fe layers decreases with increasing thickness as it shows in the spectra of Figure 4 measured in applied magnetic field. The relative intensity of the 2–5 lines with respect to the 3–4 lines of the six-line patterns is given as $I_{2-5} = 4\sin^2\theta/(1+\cos^2\theta)$, where θ is the angle between the magnetic field applied parallel with direction of the γ-rays and the magnetization of the sample. The Fe layers consisting of two atomic planes are practically not affected by the 3 T external magnetic field. It is in line with the observation [13] of a large magnetic anisotropy for similar grain boundary thickness values. The addition of the third Fe atomic plane results in a considerable decrease of I_{2-5}, but the magnetic moments are still not fully parallel with the external field. Complete saturation (i.e., disappearance of the 2–5 lines) was not observed even at T_{nom}=1.0 nm and well above the demagnetization field of a bulk Fe layer.

There is a strong correlation between the shape of the evaluated hyperfine field distribution and the I_{2-5} line intensity due to the overlap of the six-line patterns. The hyperfine field distributions of the samples with $T_{nom}\leq$0.7 nm are less influenced by this correlation than those above this thickness. In all cases I_{2-5}=2 was found to provide the best fit for B_{ext}=0 T, indicating a random distribution of the direction of the Fe magnetic moments. In external magnetic field of 3 T the decrease of I_{2-5} was negligible for the T_{nom}=0.6 nm sample, and was about 20% for the T_{nom}=0.8 nm sample.

The present results show that a large magnetic anisotropy is present in Fe layers of two atomic plane thickness when they are separated by Al spacer. The Fe layer thickness where the anisotropy begins to decrease remarkably coincides with the one where the appearance of an appreciable high field component of the hyperfine field distribution, i.e. complete Fe first neighbor coordination (n_{Al}=0) was observed.

Acknowledgements This work was supported by the Hungarian Research Founds OTKA T031854 and T048965.

References

1. Srinivasan, T.M., et al.: Phase Stability in Metals and Alloys. In: Rudman, Stringer, Jaffe (ed.), p.151. McGraw-Hill, New York (1967)
2. Vincze, I.: Phys. Status Solidi A **7**, K43 (1971)
3. Stearns, M.B.: Phys. Rev. **147**, 439 (1966)
4. Stearns, M.B.: Phys. Rev. **168**, 588 (1968)
5. Huffman, G.P.: J. Appl. Phys. **42**, 1606 (1971)
6. Vincze, I., Campbell, I.A.: J. Phys. F Met. Phys. **3**, 647 (1973)
7. Makhlouf, S.A., et al.: J. Phys. Soc. Jpn. **60**, 3537 (1991)
8. Fultz, B., Gao, Z.Q.: Nucl. Instrum. Methods **B76**, 115 (1993)
9. Vincze, I.: Nucl. Instrum. Methods Phys. Res. **199**, 247 (1982)
10. Carbucicchio, M., Palombarini, G., Rateo, M., Ruggiero, G.: Philos. Mag. **B76**, 425 (1997)
11. Geilman, T., Chevallier, J., Fanciulli, M., Weyer, G., Nevolin, V., Zenkevitch, A.: Appl. Surf. Sci **109/110**, 570 (1997)
12. Fonda, E., Traverse, A.: J. Magn. Magn. Mater. **268**, 292 (2004)
13. Kiss, L.F., Kaptás, D., Balogh, J., Bujdosó, L., Kemény, T., Vincze, I., Gubicza, J.: Phys. Rev. **B70**, 12408 (2004)
14. Takahashi, S., et al.: J. Phys. Condens. Matter **8**, 11243 (1996)
15. Takahashi, S., et al.: J. Phys. Condens. Matter **9**, 9235 (1997)

Hyperfine Interact (2006) 169:1349–1353
DOI 10.1007/s10751-006-9449-4

CEMS characterisation of Fe/high-κ oxide interfaces

R. Mantovan · C. Wiemer · A. Zenkevich · M. Fanciulli

Published online: 16 November 2006

Abstract The interfaces between Fe and different high-κ oxides are investigated by means of conversion electron Mössbauer spectroscopy (CEMS). Information on the magnetic ordering at the interface is obtained from the magnetic hyperfine splitting of the Mössbauer spectra. The reactivity of the Fe atoms at the interface (intermixing) is also estimated by CEMS. X-ray diffraction (XRD) and X-ray reflectivity (XRR) provide additional information on the intermixing and different phases present at the interface. CEM-spectra show the presence of both ferromagnetic and paramagnetic phases. CEMS and XRD results show that the Fe/HfO_2 and Fe/Al_2O_3 interfaces are the least reactive. The degree of intermixing between Fe and the high-κ oxide is determined by the oxide surface roughness.

Key words interfaces · conversion electron Mössbauer spectroscopy · intermixing

1 Introduction

The interfaces between ferromagnetic layers and oxides play a crucial role in the performances of novel spin-based electronic devices such as ferromagnetic tunnel junctions, which have attracted considerable interest due to their potential applications in Magnetic-RAM [1]. The achievement of an ideal "flat-interface" is of paramount importance in order to enhance the performances of such devices. In the present work, we investigate the structural and magnetic properties of the Fe/Al_2O_3, Fe/ZrO_2, Fe/HfO_2, and Fe/Lu_2O_3 interfaces, by performing conversion electron Mössbauer spectroscopy (CEMS). We estimate with CEMS the reactivity of Fe atoms at the different interfaces (intermixing). Complementary information are obtained by X-ray diffraction (XRD) and X-ray reflectivity (XRR).

R. Mantovan (✉) · C. Wiemer · M. Fanciulli
Laboratorio Nazionale MDM-CNR-INFM, via C. Olivetti 2, Agrate Brianza I-20041, Italy
e-mail: roberto.mantovan@mdm.infm.it

A. Zenkevich
Moscow Engineering Physics Institute, 115409 Moscow, Russia

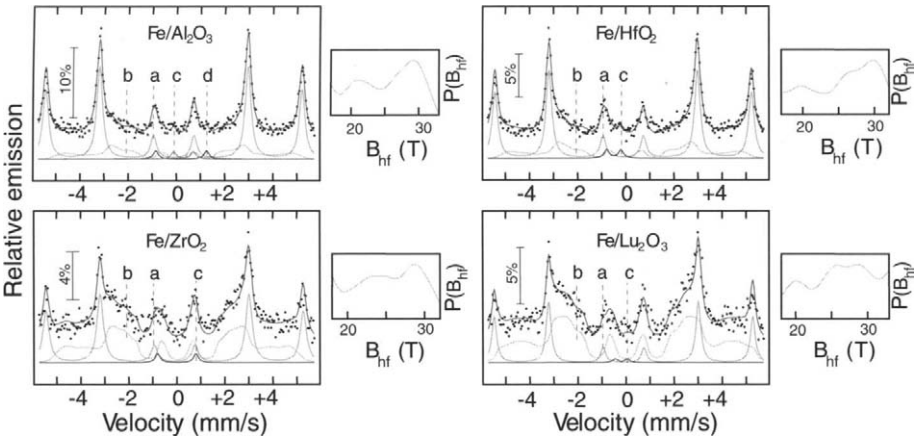

Figure 1 CEMS results at RT for the Fe/oxide interfaces. The spectra can be analysed in terms of a fraction that yields to a magnetically split sextet (component *a*), a fraction represented by a broad magnetic component (component *b*), and contributions from paramagnetic doublets (*c* and *d*). The hyperfine field distributions related to the components *b* are reported as well.

2 Experimental

The Al_2O_3, ZrO_2, HfO_2, and Lu_2O_3 oxides (in the 7 to 20 nm thickness range) are deposited by atomic layer deposition (ALD) on a Si(100) substrate. Their surface roughnesses, as measured by atomic force microscopy (AFM), are 0.1, 1.1, 0.6, and 2.4 nm, respectively. In order to perform an interface investigation by CEMS, a thin layer (<2 nm) of ^{57}Fe is deposited on the top of the oxides by pulsed laser deposition (PLD) at room temperature (RT), followed by the deposition of 10–20 nm of ^{54}Fe. We measure the total Fe thickness (between 15 and 23 nm) by RBS and by using the total CEMS resonant effect for ^{57}Fe. CEMS measurements have been performed at RT using a 50 mCi ^{57}Co source in a Rh-matrix, which is moved by a standard constant acceleration drive. The samples are incorporated as electrodes in a parallel-plate avalanche counter. The detector is filled with acetone at 20 mbar, and the operating voltage is 700–800 V. Isomer shifts are given relative to α-Fe. Grazing angle XRD and XRR measurements have been performed on Fe/ZrO_2, Fe/HfO_2, and Fe/Lu_2O_3, and the data are analyzed using the software package MAUD [2].

3 Results and discussion

Figure 1 shows the CEMS results for the analysed samples. The CEM-spectra are fitted with the least-squares fitting program NORMOS 90 [3].

All the CEM-spectra show the presence of a fraction denoted α-Fe that yields a magnetically split sextet characterized by a magnetic field of 33.0(3) T (component *a* in Figure 1); a fraction represented by a distribution of sextets (component *b*); and a low contribution (<5%) from paramagnetic doublets (components *c* and *d*). α-Fe is not sensitive to the reactions at the interface, while the *b* and *c*+*d* components account for the atomic-mixing at the interfaces. For all the samples, the broad magnetic component *b* is fitted with a Gaussian distribution of hyperfine fields (B_{hf}). The corresponding B_{hf} distributions are

Table 1 Hyperfine parameters for the phases *b*, *c*, and *d*

Sample	Phases	δ (mm/s)	Δ (mm/s)	Γ (mm/s)	$\langle B_{hf} \rangle$ (T)	d_{mix} (nm)
Fe/Al_2O_3	*b*	0.12(3)	–	–	25.4(6)	
	c	0.41	0.80	0.25	–	0.703
	d	0.31	2.10	0.25	–	
Fe/ZrO_2	*b*	0.14(2)	–	–	25.04(3)	0.900
	c	0.11	1.60	0.25	–	
Fe/HfO_2	*b*	0.09(2)	–	–	25.6(4)	0.495
	c	−0.39	0.60	0.25	–	
Fe/Lu_2O_3	*b*	0.09(1)	–	–	26.2(2)	1.484
	c	−0.09	0.50	0.25	–	

δ is the isomer shift, Δ is the quadrupole splitting, Γ is the linewidth, and $\langle B_{hf} \rangle$ is the average hyperfine field of the distribution.

The total intermixed fraction (d_{mix}), as deduced from the CEMS relative resonant effects, is also given.

reported at the right side of the spectra in Figure 1. Table 1 summarizes the hyperfine parameters as obtained from the fit of the CEM-spectra, i.e. the isomer shift (δ), the quadrupole splitting (Δ), the line width Γ, and the average hyperfine field $\langle B_{hf} \rangle$ of the distribution. The intermixed fractions (d_{mix}) at the interfaces, as calculated by normalizing the CEMS resonant effects of the $b+c+d$ phases to the total amount of ^{57}Fe deposited by PLD, are reported as well.

Fe/Al_2O_3 interface The equilibrium phase diagram of the Fe–Al intermetallic system includes the DO_3-structure-type Fe_3Al alloy, which is ferromagnetic at RT [4]. In Fe_3Al, the Fe atoms are distributed between two different sites: one with 8 Fe nearest neighbours (n.n.), and the other with 4 Fe and 4 Al as n.n. They give hyperfine fields close to 30 and 21 T, respectively [5], which approximately correspond to the main peaks in the measured B_{hf} distribution. The presence of a broad distribution is possibly due to a varying Al-atoms concentration around the ^{57}Fe nucleus. The *c* and *d* doublets show hyperfine parameters that are consistent with those observed for Fe^{3+} substituting Al^{3+} in Al_2O_3 [6], and for Fe^{2+} in an organometallic biferrocene compound [7], respectively. The identification of the *c* and *d* components is not trivial, also due to their low contribution to the total spectral area. However, the organic contamination of the Al_2O_3 surface is likely to occur due to the air exposure of the sample before the PLD of Fe performed at RT. The $Al(CH_3)_3$ precursor used for the Al_2O_3 growth contains C, being another possible source of organics on its surface.

Fe/ZrO_2 interface Among the intermetallic Fe–Zr alloys, the crystalline Fe_2Zr compound is ferromagnetic at RT, and it shows a well resolved six-line pattern with B_{hf} close to 18 T [8]. In amorphous alloys, the Fe–Zr system exhibits magnetic ordering below RT for Fe contents ≤90 at.% and the corresponding Mössbauer spectra are characterized by a broad sextet with a peak in the 80 K B_{hf} distribution, located at 22 T [9]. Hydrogenation of these amorphous systems increases both the Curie temperature T_C (up to 400 K) and the magnetic moment at the Fe site [9]. For instance, $Fe_{89}Zr_{11}H_{20}$ shows a distribution with an average B_{hf} of 29 T. The H-absorption from the Fe–Zr (and Fe–Hf) intermetallic compounds is likely to occur due to their large negative enthalpy of formation [10], and a relatively stable ternary hydride can be expected. The H incorporation possibly originates from the two-steps process to grow the samples and in particular to air exposure of the oxides prior to the

Fe deposition. We conclude that the component *b* is due to the amorphous Fe_xZr_{1-x} alloy ($x \leq 90$), and its hydrogenated phase as well. The presence of the crystalline Fe_2Zr phase cannot be excluded from CEMS results. However, XRD measurement does not show evidence for a Fe-rich Fe–Zr phase, supporting the idea of an amorphous compound present at the interface. The Δ value for the paramagnetic doublet is higher than those reported for such intermetallics as $FeZr_2$ and $FeZr_3$ [8]. Saturation of the $FeZr_3$ lattice with O_2 may lead to an increased Δ value [11]. Both CEMS and XRD results confirm the presence of a Zr-rich Fe–Zr phase, although its chemical composition cannot be simply determined.

Fe/HfO$_2$ interface The magnetic properties of amorphous Fe_xHf_{1-x} alloys are very similar to those of the corresponding Fe–Zr ones [12]. Compounds with 80–90 at.% Fe are magnetically ordered at RT, and B_{hf} values from 20 to 25 T are reported at 4.2 K [12]. Hydrogenation of the amorphous Fe–Hf alloys causes the increase of T_C above RT, and B_{hf} rises to 30 T [13]. We conclude that the B_{hf} distribution is due to the presence of an amorphous Fe-rich Fe_xHf_{1-x} alloy, together with its hydrogenated phase. This conclusion is supported by the absence, in the XRD spectra, of any signal related to Fe-rich Fe–Hf alloys. On the other hand, XRD detects a small fraction of $FeHf_2$. Since the values of δ and Δ for this compound are similar to those of the *c* component in our spectra [14], we conclude that a low paramagnetic contribution arising from the cubic $FeHf_2$ phase is present at the interface.

Fe/Lu$_2$O$_3$ interface The crystalline $LuFe_2$ alloy displays T_C=610 K and B_{hf} ~18–19 T at RT [15], while the corresponding amorphous alloy has T_C<100 K [16]. The lower peak in the distribution reported in Figure 1 is at ~20 T. From CEMS results, the majority of the Fe atoms are located at sites characterized by higher fields (25–30 T), and this contribution possibly accounts for a hydrogenated $LuFe_2$ compound, having a higher B_{hf} than $LuFe_2$ [10]. XRD confirms the presence of crystalline $LuFe_2$, and shows a possible contribution from the hydrogenated $LuFe_2H_x$ phase. XRD does not detect any signal from Lu-rich Fe–Lu compound. The component *c* in the Fe/Lu_2O_3 CEM-spectrum could be related to an amorphous Lu-rich Lu–Fe alloy, but the low statistics prevents any definitive conclusions.

The intermixed fraction for the Fe/HfO_2 and Fe/Al_2O_3 interfaces is about half that occurring at the Fe/ZrO_2 and Fe/Lu_2O_3 ones (Table 1). XRR is used to estimate the interfacial layer thickness at the Fe/HfO_2, Fe/ZrO_2, and Fe/Lu_2O_3 interfaces, and the values measured are 1, 2, and 3–4 nm, respectively. Due to the fact that XRR measures the total thickness of the interfacial layer (including the physical interface roughness), these values are higher than d_{mix}. We observe that d_{mix}, as determined by CEMS, matches the interface layer thickness, as determined by XRR, and the oxide surface roughness as determined by AFM. For oxides showing similar roughness (HfO_2 and Al_2O_3), the different observed intermixed zones could be related to different enthalpies of formation for the corresponding Fe–Al and Fe–Hf alloys.

4 Conclusions

CEMS was used to investigate with sub-monolayer resolution the interfaces between Fe and different high-κ oxides. For all samples, CEM-spectra evidence the presence of both ferromagnetic and paramagnetic phases. A considerable contribution to the spectral total intensity is given by broad B_{hf} distributions, which are due to Fe-rich Fe–X binary alloys

(X=Al, Zr, Hf, and Lu). Hydrogenation of the Fe–X phases takes place for X=Zr, Hf, and Lu, while at the Fe/Al_2O_3 there is a possible contamination from organics. Contaminations of the oxides surface can originate from their exposure to the atmospheric air prior to the Fe deposition. A low paramagnetic contribution (<5%) is found at all interfaces. CEMS and XRD results show that the Fe/HfO_2 and Fe/Al_2O_3 interfaces are the least reactive. A higher intermixing, observed by CEMS, correlates with a higher interfacial layer thickness, determined by XRR, and a larger oxide surface roughness, measured by AFM.

Acknowledgments AFM measurements were performed by Dr. G. Tallarida, and the high-κ oxides were grown by Dr. G. Scarel at the MDM National Laboratory.

References

1. Prinz, G.A.: Science **282**, 1660 (1998)
2. http://www.ing.unitn.it
3. Brandt, R.A.: Wissenschaftliche Elektronik GmBH, Starubey, Germany (1994)
4. Checchetto, R., Tosello, C., Mioltello, A., Principi, G.:J. Phys., Condens. Matter **13**, 811 (2001)
5. Lin, M.C., Barnes, R.G., Torgeson D.R.: Phys. Rev. B **24**, 3712 (1981)
6. Ogale, S.B., Phase, D.M., Chaudhari, S.M., Ghaisa, S.V., Kanetkar, S.M., Patil, P.P., Bhide, V.G., Date, S.K.: Phys. Rev. B **35**, 1593 (1987)
7. Dickson, D.P.E., Berry, F.J.: Mössbauer spectroscopy. Cambridge Universtity Press (1986)
8. Vincze, I., van der Woude, F., Scott, M.G.: Solid State Comm. **37**, 567 (1981)
9. Ryan, D.H., Coey, J.M.: Phys. Rev. B **35**, 8630 (1987)
10. Buschow, K.H.J., Bouten, P.C.P., Miadema, A.R.: Rep. Prog. Phys. **45**, 937 (1982)
11. Filippov, V.P.: Met. Sci. Heat Treat. **45**, 452 (2003)
12. Liou, S.H., Xiao, G., Taylor, J.N., Chien, C.L.: J. Appl. Phys. **57**, 3536 (1985)
13. Ryan, D.H., Coey, J.M.D., Ström-Olsen, J.O.: J. Magn. Magn. Mat. **67**, 148 (1987)
14. Maurer, M., Friedt, J.M., Sanchez, J.P.: J. Phys. F: Met. Phys. **15**, 1449 (1985)
15. Atzmony, U., Dariel, M.P.: Phys. Rev. B **10**, 2060 (1974)
16. Heiman, N., Kazama, N.: Phys. Rev. B **19**, 1623 (1979)

Hyperfine Interact (2006) 169:1355–1362
DOI 10.1007/s10751-006-9450-y

Hematite thin films: growth and characterization

J. D. Uribe · J. Osorio · C. A. Barrero · D. Giratá · A. L. Morales · A. Devia · M. E. Gómez · J. G. Ramirez · J. R. Gancedo

Published online: 27 October 2006

Abstract We have grown hematite ($\alpha - Fe_2O_3$) thin films on stainless steel and (001)-silicon single-crystal substrates by RF magnetron sputtering process in argon atmosphere at substrate temperatures from 400 to 800°C. Conversion Electron Mössbauer (CEM) spectra of the sample grown on stainless steel at 400°C exhibit values for hyperfine parameter characteristic of bulk hematite phase in the weak ferromagnetic state. Also, the relative line intensity ratio suggests that the magnetization vector of the polycrystalline film is aligned preferentially parallel to the surface. The X-ray diffraction (XRD) pattern of the polycrystalline thin film grown on steel substrates also corresponds to $\alpha - Fe_2O_3$. The samples were also analyzed by Atomic Force Microscopy (AFM), those grown on stainless steel reveal a morphology consisting of columnar grains with random orientation, given the inhomogeneity of the substrate surface.

Key words iron oxides · hematite · thin films · CEMS

1 Introduction

Transition metal oxides have been extensively researched for their interesting physical phenomenology [1] and technological importance. There is growing interest in

J. D. Uribe · J. Osorio · C. A. Barrero (✉) · D. Giratá · A. L. Morales
Instituto de Física, Universidad de Antioquia, Medellín, A.A. 1226, Colombia
e-mail: cbarrero@pegasus.udea.edu.co

A. Devia
Laboratorio de Física del Plasma, Universidad Nacional, Seccional Manizales, Colombia

M. E. Gómez · J. G. Ramirez
Departamento de Física, Universidad del Valle, Cali, A.A. 25360, Colombia

J. R. Gancedo
Instituto de Química Física Rocasolano, CSIC, C/Serrano 119, E-28006 Madrid, España

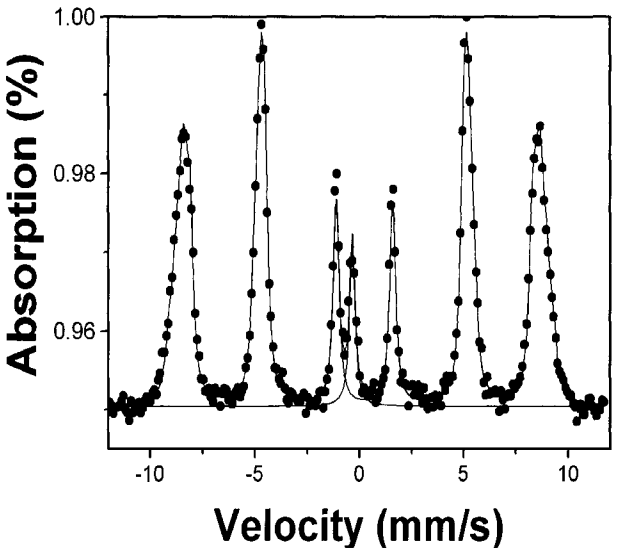

Figure 1 Room-temperature CEM spectrum of the $\alpha - Fe_2O_3$ thin film grown on stainless steel substrate at 400°C.

the growth of metal oxide thin films on various oxide and metal substrates to obtain high-quality surfaces [2].

Studies into magnetic properties of surfaces and interfaces have stirred much attention ever since the existence of magnetically dead layers was reported [3]. However, studies have revealed both increases and decreases of magnetization at the surface of metallic iron, metals, or insulators in very thin foils or small grains [4–6] and at interfaces of multilayered iron metal films sandwiched between thin silver films [7]. Investigations of magnetic interactions at solid-vacuum interfaces, at surface atoms with adsorbed impurities, or at solid–solid interfaces are essential for the fundamental understanding of exchange interactions in magnetically ordered materials [8].

Film production methods and procedures significantly affect the character of the end product. In sputter depositions, the nature of the substrate, deposition temperature, deposition pressure and vacuum quality are some parameters influencing film properties [9]. These properties are key in predicting the reliability of thin film systems and their applications.

In this case, the ferromagnetic hematite has been considered an important potential material for technological uses, primarily as thin film sensors and photoelectrodes [10–14].

This work will focus on the determination of some physical properties of hematite ($\alpha - Fe_2O_3$) thin films, such as a structural, morphological and magnetic characteristics, to develop these systems for corrosion protective coatings in steels and metals. A Conversion Electron Mössbauer Spectroscopy (CEMS) detector was built to study sub-surface film properties.

2 Experimental details

Hematite thin films were deposited by RF magnetron sputtering process in an argon atmosphere, on stainless steel and (001)-silicon single-crystal substrates. The steel

Table I The most probable hyperfine interaction parameters corresponding to the CEM spectrum of the $\alpha - Fe_2O_3$ thin film grown on stainless steel substrate

Hyperfine parameters	Singlet	Sextet
Isomer shift (mm/s)	–0.45 ± 0.01	0.27 ± 0.01
Quadrupole shift (mm/s)	0.07 ± 0.01	–0.14 ± 0.01
Hyperfine magnetic field (T)	–	50.6 ± 0.5

substrates were subjected to a mirror-like polishing process with sandpaper and abrasive products. Total pressure and RF power were held constant at 10 mTorr and 30 W, respectively. Substrate temperatures varied from 400 to 800°C. All films were sputter-deposited from a high-purity hematite target (99.95%) for 2 h.

Structural and magnetic properties were studied by means of CEMS at room temperature, using a home-made CEMS chamber with parallel plate avalanche counter (PPAC) [15, 16]. Another stage of the structural characterization was made with X-ray diffraction (XRD), using a Bruker D-8 Advanced Diffractometer with secondary graphite monochromator and Cu-Kα monochromatic radiation of parallel beams with scintillation counter. Low-angle incidence was used, scanning angles from 20 to 80 (2Θ), 2 s per step, and step as 0.02 (2Θ). Surface features and morphology of the films were examined using a Park Scientific Instruments scanning probe microscope, in Atomic Force Microscope (AFM) in contact mode, using a v-shaped ultra lever with a square pyramidal tip of Si_3N_4.

3 Results and discussion

3.1 Conversion electron Mössbauer spectroscopy (CEMS)

CEM spectra were measured at room temperature for the stainless steel substrate, and the $\alpha - Fe_2O_3$ films grown at 400 and 800°C. These experimental spectra were fitted with program DIST3E [17].

Figure 1 shows the CEM spectrum of the $\alpha - Fe_2O_3$ thin film grown at 400°C substrate temperature. The spectrum was fitted using discrete distributions of hyperfine fields associated to the $\alpha - Fe_2O_3$ thin film and one singlet associated to the substrate signal corresponding to the paramagnetic fcc iron phase ($\gamma - Fe$) of the stainless steel. We take the CEM spectrum of the substrate without film and we also observed a sextet generated by the ($\alpha - Fe$) iron nuclei that still show magnetic effects. The presence of the magnetic phase on the stainless steel substrate is a product of the thermal and/or mechanical deformation in the elaboration process [18]. The most probable hyperfine parameters are illustrated on Table I.

Within the error bars, these parameters closely match those reported for bulk $\alpha - Fe_2O_3$ phase [19]. According to the quadrupole shift, the $\alpha - Fe_2O_3$ thin film appears in its weakly ferromagnetic state. Furthermore, the relative line intensity ratio of the six lines suggests a preferential orientation of the magnetization vector parallel to the film surface.

The line-widths of Mössbauer components are broader than expected for bulk crystalline oxides, indicating a dimensional change [20]. The broadening of the lines

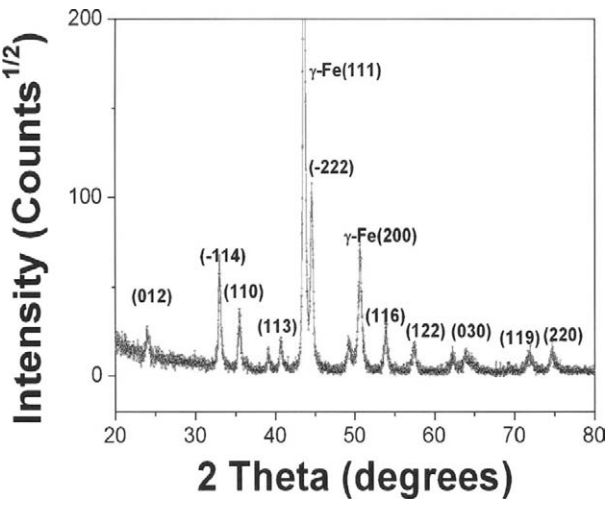

Figure 2 X-ray diffraction pattern of the $\alpha - Fe_2O_3$ thin film grown on stainless steel substrate at 400°C.

can also be related to a distribution of hyperfine fields associated to different atomic environments of the Fe^{3+} irons from the substrate surface to the film top. In fact, the mismatch of the unit cell parameters between substrate and film, and the polycrystalline character of substrate could be associated to the polycrystalline growth of the hematite film and, then, to the formation of hematite grain size distributions. These features are also reflected in the lower magnitude of the quadrupole shift value.

The CEM spectrum of the sample grown at 800°C shows similar features suggesting that substrate temperature does not noticeably affect the growth phase. In the spectra we still observe the substrate signal and, given the re-solution of our CEMS technique, with a maximum depth of 300 nm, film thickness is less than 300 nm [16].

At this stage it was difficult to obtain a CEM spectrum of the samples grown on silicon, mainly due to the *n*-type character of the substrate.

3.2 X-ray diffraction (XRD)

Figure 2 shows the diffraction pattern of the hematite polycrystalline film grown on the stainless steel substrate at 400°C with an incidence angle of 7°. This pattern exhibits structural and compositional characteristics consistent with pure hematite ($\alpha - Fe_2O_3$). We were able to identify diffraction peaks detected in the sample attributable to hexagonal hematite [21] labeled in the figure as the (hkl) plane family. Peaks associated with other phases (e.g., magnetite, maghemite, etc.) are not observed. Steel substrate peaks are also seen, which are the most intense. The substrate signal corresponds to the (111) and (200) planes of the $\gamma - Fe$ phase [21], characteristics of stainless steel and found at 44.5 and 50.8° in a 2-theta scale. The diffraction pattern exhibits pronounced peaks with preferential growth in the (-222), (-114) and (116) crystallographic planes. There is no evidence of epitaxial growth. This result is in line with AFM data. The lack of epitaxy could be attributed to the irregular morphology of the steel substrate.

The XRD were analyzed by Rietveld refinement method with MAUD program [22]. We found lattice parameter values of the hematite hexagonal unit cell of $a =$

Table II Diffraction peaks associated to the $\alpha - Fe_2O_3$ thin film grown on steel substrate at 400°C, the standard values and the corresponding crystallographic planes [21]

2-Theta (degrees)	2-Theta standard (degrees)	hkl index
24.0	24.298	012
33.0	33.389	-114
35.5	35.833	110
40.8	41.117	113
43.0	43.768	-222
54.0	54.457	116
57.1	57.801	122
62.3	62.845	214
64.0	64.395	030
72.0	72.868	119
74.8	75.943	220

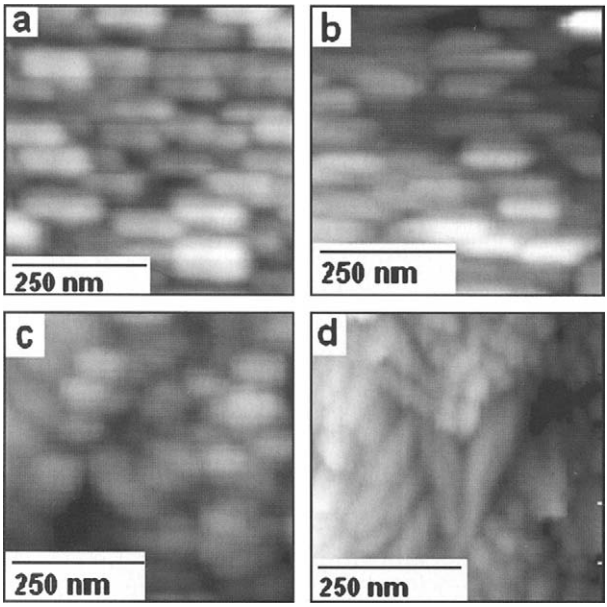

Figure 3 Atomic Force Microscopy (AFM) images of the growth stages of $\alpha - Fe_2O_3$ thin films on stainless steel at 400°C: **a** 30 min, **b** 60 min, **c** 90 min, and **d** 120 min.

0.50(4) nm and $c = 1.38(2)$ nm. Table II shows all diffraction peaks related to the sample, the standard values and their corresponding Miller indices.

Thin films grown on silicon substrates at 400°C do not show Bragg peaks, suggesting that at this temperature hematite grains do not nucleate. Upon increasing subs-trate temperature to 800°C, crystal effects appears.

3.3 Atomic force microscopy (AFM)

Figure 3 shows AFM images performed in an area of 0.25 μm^2 of $\alpha - Fe_2O_3$ thin films grown on stainless steel at different growth times as stated herein. Images

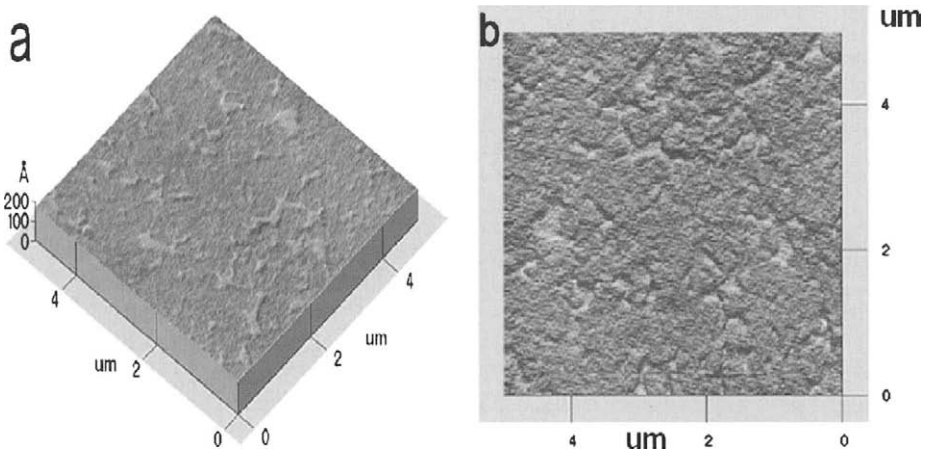

Figure 4 AFM images of the $\alpha - Fe_2O_3$ thin film grown on silicon substrate at 800°C. **a** 3-D view and **b** frontal view.

were taken for each sample after growth. Note the morphological evolution of the surface. The images show that the film is still discontinuous after 30 min and finally becoming continuous around 90 min. Different grain sizes could be seen aligned on the substrate surface, as a result of growth time. The latest growth stage shows fibrous grain shape. Within this scheme, four stages are identified, depending on growth time. The first stage (Figure 3a and b) show uniform distribution of hematite grains on inhomogeneous substrate surface, generating stable layers, and new hematite particles grow on them. As growth time increases (from 30 to 60 min), cluster formation notably increases and grain shape is more granular – from 60 to 90 min – (Figure 3c), that is, the first hematite layers are the most appropriated surfaces for the nucleation phenomenon. In the latest stage (Figure 3d), the structural evolution shows a fibrous or columnar morphology, films grown at 800°C show the same morphology. In this scale of observation, we were able to see an increase in film roughness with growth time increase. Columnar grains are oriented randomly on the surface. Alteration of the column inclination depends on the substrate morphology and substrate temperature. Indeed, careful analysis of Fe and Co films deposited under controlled conditions revealed similar effects [23]. In fact, this structural evolution of the hematite grains in the perpendicular direction of the film is consistent with our results on the broadening of peaks as taken from CEM spectra of these samples. The broadening can be related to a non-homogeneous distribution of hyperfine fields associated to different atomic environments of the Fe^{3+} irons in the substrate surface and the film top.

In Figure 4 we can see AFM images of $\alpha - Fe_2O_3$ films grown on silicon substrate in an area of 5 μm^2. We observed non-columnar grain formation. Films grown on Si substrates at low temperatures (400°C) do not exhibit crystalline structures, according to XRD patterns, polycrystalline effects only appear at substrate temperatures of 800°C.

This is associated to the structural mismatch between the cubic silicon and the hexagonal hematite.

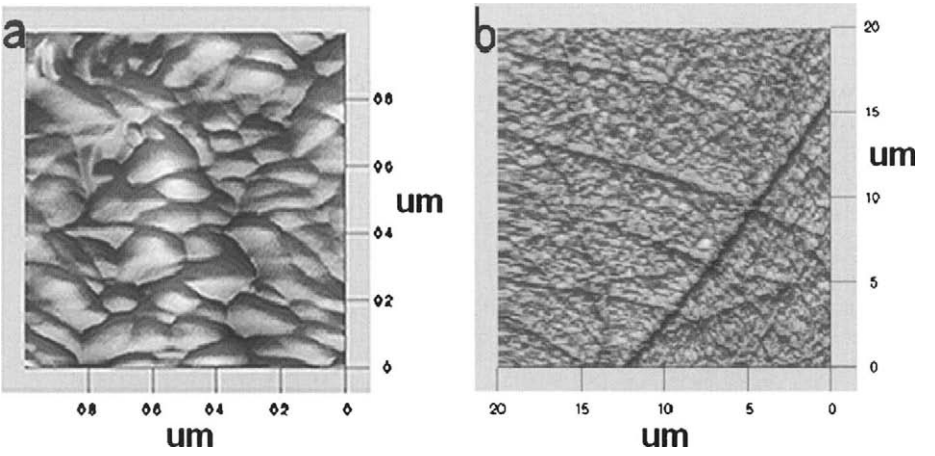

Figure 5 AFM images of the $\alpha - Fe_2O_3$ thin film grown on stainless steel at different scan areas: **a** $1\mu m^2$, and **b** $400\mu m^2$.

Figure 5 shows AFM images of a $\alpha - Fe_2O_3$ thin film grown on steel substrate during 2 h at 800°C, scan areas are 1 μm^2 and 400 μm^2, permitting us to see a continuous film with grain morphology and crevices (Figure 5b), which appear as a result of the polishing process with abrasive grains used. At the 1 μm^2 scale, films were found to have an average grain size of 211 nm and surface roughness of 45.0 nm.

4 Conclusions

Hematite ($\alpha - Fe_2O_3$) polycrystalline thin films were grown on stainless steel substrates by RF magnetron sputtering deposition. The most probable hyperfine interaction parameters extracted from the CEM spectra reveal single hematite phase. The relative line intensity ratio suggests a preferred orientation of magnetic moments on the film plane. XRD analysis shows that $\alpha - Fe_2O_3$ films grown on silicon substrates have amorphous structures and only become polycrystalline at high substrate temperatures (800°C), as revealed from XRD patterns. AFM images allowed us to see the granular morphology of the film surface and we found columnar grain formations with random orientation, due to the inhomogeneity of steel substrate surface. We also saw shape and size variations of the grains during the growth stages as functions of growth time and substrate surface morphology. Hence, grain formation is shown for increased substrate temperature. Thin film samples grown on silicon substrates show non-columnar grain growth, covering the substrate surface. These formations may be due to the structural mismatch between the silicon and the hematite.

Acknowledgements This work was supported by COLCIENCIAS contract N° 115-05-12409, CODI project N° 24-1-009, and the Excellence Center for Novel Materials under Colciencias contract 043-2005.

References

1. Sivakov, V., Petersen, C., Daniel, C., Shen, H., Mücklin, F., Mathur, S.: Appl. Surf. Sci. **247**, 513 (2005)
2. Lie, M., Fjellvåg, H., Kjekshus, A.: Thin Solid Films **488**, 74 (2005)
3. Margulies, D.T., Parker, F.T., Goldman, R.S., Li, J., Sinclair, R., Berkowite, A.E.: Phys. Rev. B **53**, 9175 (1996)
4. Taniyama, T., Kitamoto, Y., Yamazaki, Y.: J. Appl. Phys. **89**, 7693 (2001)
5. Topsøe, H., Dumesic, J.A., Mørup, S.: In: Cohen, R.L. (ed.) Applications of Mössbauer Spectroscopy, vol. 2. Academic, New York (1980)
6. Akl, A.A.: Appl. Surf. Sci. **221**, 319 (2004)
7. Wang, D.S., Freeman, A.J., Krakauer, H.: Phys. Rev. B **24**, 1126 (1981)
8. Bae, S., Judy, J.H., Chen, P.J., Egelhoff, F., Zurn, S.: Appl. Phys. Lett. **78**, 4163 (2001)
9. Pan, L., Zhang, G., Fan, L., Qiu, H., Wu, P., Wang, F., Zhang, Y.: Thin Solid Films **473**, 63 (2005)
10. Miller, E.L., Paluselli, D., Marsen, B., Rocheleau, R.E.: Thin Solid Films **466**, 307 (2004)
11. Nilsen, O., Lie, M., Foss, S., Fjellvåg, H., Kjekshus, A.: Appl. Surf. Sci. **227**, 40 (2004)
12. Selim, M., Sawaby, A., El Mandouch, Z.: Mater. Res. Bull. **35**(13), 2123 (2002)
13. Mulenko, S.A., Izvekov, A.V., Petrov, Y.N., Mygashko, V.P., Ovechko, V.S.: Appl. Surf. Sci. **248**, 475 (2005)
14. Moshfegh, A.Z., Azimirad, R., Akhava, O.: Thin Solid Films **484**, 124 (2005)
15. Gancedo, J.R., Gracia, M.: Hyp. Interact. **29**, 1097 (1986)
16. Gancedo, J.R., Gracia, M., Marco, J.F.: Hyp. Interact. **66**, 83 (1991)
17. Vandenberghe, R., de Grave, E., de Bakker, P.M.A.: Hyp. Interact. **83**, 29 (1994)
18. Mészáros, I., Prohászka, J.: J. Mater. Process. Technol. **161**, 162 (2005)
19. Vandenberghe, R.E.: In: Mössbauer Spectroscopy and Applications in Geology. International Training Centre for Post-graduate Soil Scientists State University Gent, Belgium (1990)
20. Joshi, S., Bilurkar, P.G., Chaudhari, S.M., Kanetkar, S.M., Ogale, S.B.: Phys. Rev. B **40**, 10635 (1989)
21. JCPDS, X-ray diffraction data cards of the joint committee on powder diffraction standards (2001)
22. Lutterotti, L.: In: Matthies, S., Wenk, H.R. (eds.) Proceedings of the Twelfth International Conference on Textures of Materials, ICOTOM-12 2001, **1**, 15599 (2001)
23. Ohring, M.: In: Material Science of Thin Films: Deposition and Structure. Academic, New York (2002)

Hyperfine Interact (2006) 169:1363–1369
DOI 10.1007/s10751-006-9452-9

Mössbauer and optical investigation of $Co_{3-x}Fe_xO_4$ thin films grown by sol–gel process

Kwang Joo Kim · Hee Kyung Kim · Young Ran Park · Geun Young Ahn · Chul Sung Kim · Jae Yun Park

Published online: 14 November 2006

Abstract Structural transformation and the related variation in magnetic and optical properties of $Co_{3-x}Fe_xO_4$ thin films grown by a sol–gel method have been investigated as the Fe composition varies up to $x=2$. The normal spinel phase is dominant below $x=0.55$ and the inverse spinel phase grows as x increases further. Conversion electron Mössbauer spectroscopy (CEMS) measurements indicate that the normal spinel phase have octahedral Fe^{3+} ions mostly while the inverse spinel phase contain octahedral Fe^{2+} and tetrahedral Fe^{3+} ions. For higher Fe composition ($x>1.22$), Co^{2+} ions are found to substitute the octahedral Fe^{2+} sites. The measured optical absorption spectra for the $Co_{3-x}Fe_xO_4$ films by spectroscopic ellipsometry support the CEMS interpretation.

Key words spinel · structural transformation · Mössbauer spectroscopy · optical absorption

1 Introduction

Over decades oxide compounds with the spinel structure have been under extensive study due to their wide range of applications as various magnetic, electronic, and optical materials. Such spinel oxides, described by the general formula AB_2O_4 with A and B representing tetrahedral and octahedral sites, respectively, have been found to exhibit interesting physical and chemical properties, depending on how the cations distribute among the A and B sites, sometimes in more than one ionic valence.

K. J. Kim (✉) · H. K. Kim · Y. R. Park
Department of Physics, Konkuk University, Seoul 143-701, South Korea
e-mail: kjkim@konkuk.ac.kr

G. Y. Ahn · C. S. Kim
Department of Physics, Kookmin University, Seoul 136-702, South Korea

J. Y. Park
Department of Materials Science and Engineering, University of Incheon, Incheon 402-749, South Korea

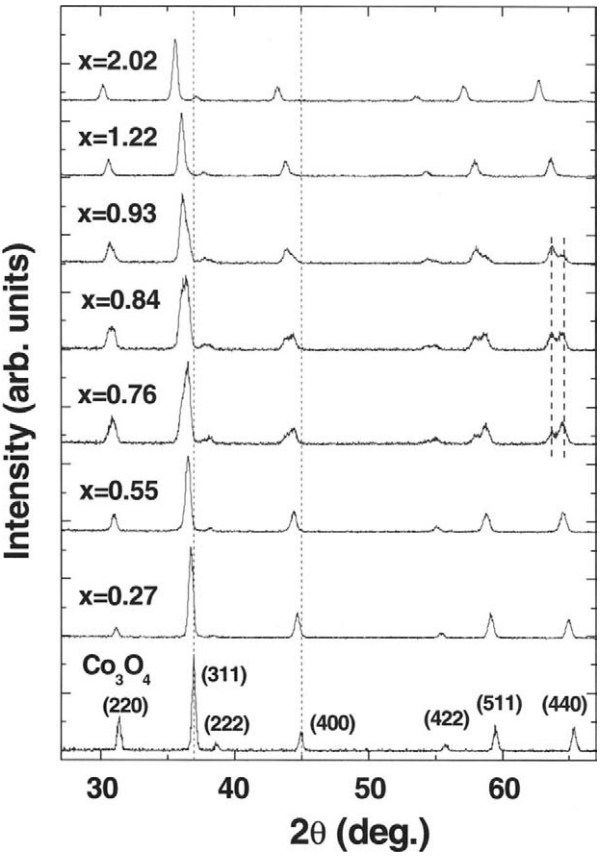

Figure 1 Evolution of XRD pattern of $Co_{3-x}Fe_xO_4$ films.

In this work, disordered spinel compounds $Co_{3-x}Fe_xO_4$ were prepared as thin films by a sol–gel method and their structural, magnetic, and optical properties were investigated as the Fe composition (x) varies up to two. As a base compound, Co_3O_4 is known as a normal spinel in which the octahedral Co^{3+} ions have a d^6 configuration of low-spin state with zero magnetic moment, while the tetrahedral Co^{2+} ions have a d^7 configuration of high-spin state. When Fe is added to Co_3O_4, both Fe^{2+} and Fe^{3+} ions are expected to exist in $Co_{3-x}Fe_xO_4$ and whether these ions occupy either octahedral or tetrahedral sites may result in different physical properties.

2 Experimental

The precursor solution for the present sol–gel film deposition was prepared by dissolving $Co(CH_3CO_2)_24H_2O$ and $Fe(NO_3)_39H_2O$ powders together in 2-methoxyethanol at 70°C.

The substrate, Si(100), was spin-coated by the precursor solution at 3,000 rpm for 20 s and then heated at 260°C for 5 min after each deposition in order to remove the organic substance. This process was repeated for increasing the film thickness. Annealing of the precursor films at 800°C for 4 h in vacuum is found to improve the crystalline quality and surface flatness of the resultant $Co_{3-x}Fe_xO_4$ films.

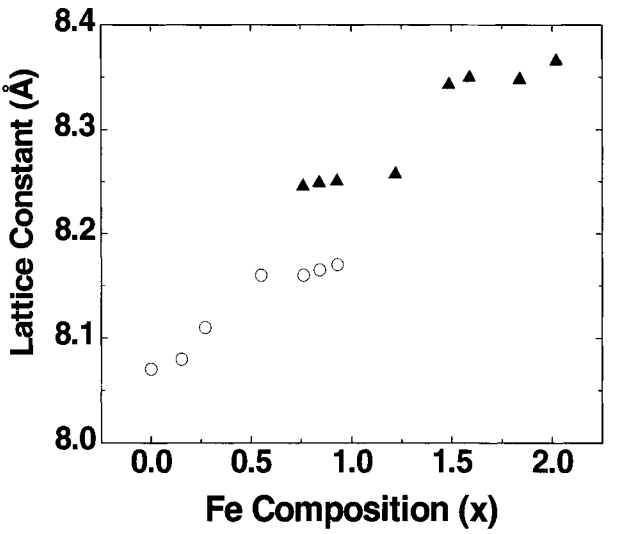

Figure 2 Variation of lattice constant of $Co_{3-x}Fe_xO_4$ films calculated using XRD (311) peak position.

The Fe composition of the film was determined by energy-dispersive X-ray spectroscopy. The thickness of the films estimated by scanning electron microscopy was close to 1 μm. The crystalline structure of the samples was monitored by X-ray diffraction (XRD) measurements in θ–2θ geometry using Cu K_α radiation. The site preference of the Fe^{2+} and Fe^{3+} ions in the compound was explored by conversion electron Mössbauer spectroscopy (CEMS) at room temperature with a single-line 50 mCi ^{57}Co source in a rhodium matrix. The optical properties of the films were investigated by spectroscopic ellipsometry (SE) in the visible-ultraviolet range.

3 Results and discussion

As shown in Figure 1, XRD data indicate that the $Co_{3-x}Fe_xO_4$ films maintain normal spinel structure as in Co_3O_4 for low x (≤ 0.55) but a new structure appears for higher x, attributed to a formation of inverse spinel phase. The inverse spinel phase is seen to become dominant above $x=0.93$. Figure 2 exhibits the variation of the lattice constant of the $Co_{3-x}Fe_xO_4$ films calculated using the strongest (311) peak position in the XRD spectra. The observed linear increase of the lattice constant with x (denoted by open circle) for $x \leq 0.55$ is interpreted as due to the substitution of the octahedral sites by Fe^{3+} ions, thus maintaining the normal spinel structure as in Co_3O_4.

The ionic radius of octahedral Co^{3+} ion in its low-spin state is known to be 0.665 Å, while that of octahedral Fe^{3+} ion 0.785 Å in its high-spin state [1]. On the other hand, the ionic radius of high-spin Fe^{2+} ion at the octahedral site is 0.92 Å, larger than that of the octahedral Fe^{3+} ion. Thus, the phase with the larger lattice constant (denoted by filled triangle in Figure 2) for $x \geq 0.76$ is attributed to the Fe^{2+} occupation of the octahedral sites, leading to a formation of inverse-spinel phase. In such inverse-spinel phase, same density of the tetrahedral sites needs to be occupied by Fe^{3+} ions in order to maintain the charge neutrality of the compound.

As seen in Figure 2, the lattice constants of both the normal and the inverse spinel phase vary little with x where the two phases coexist. However, the inverse spinel phase becomes

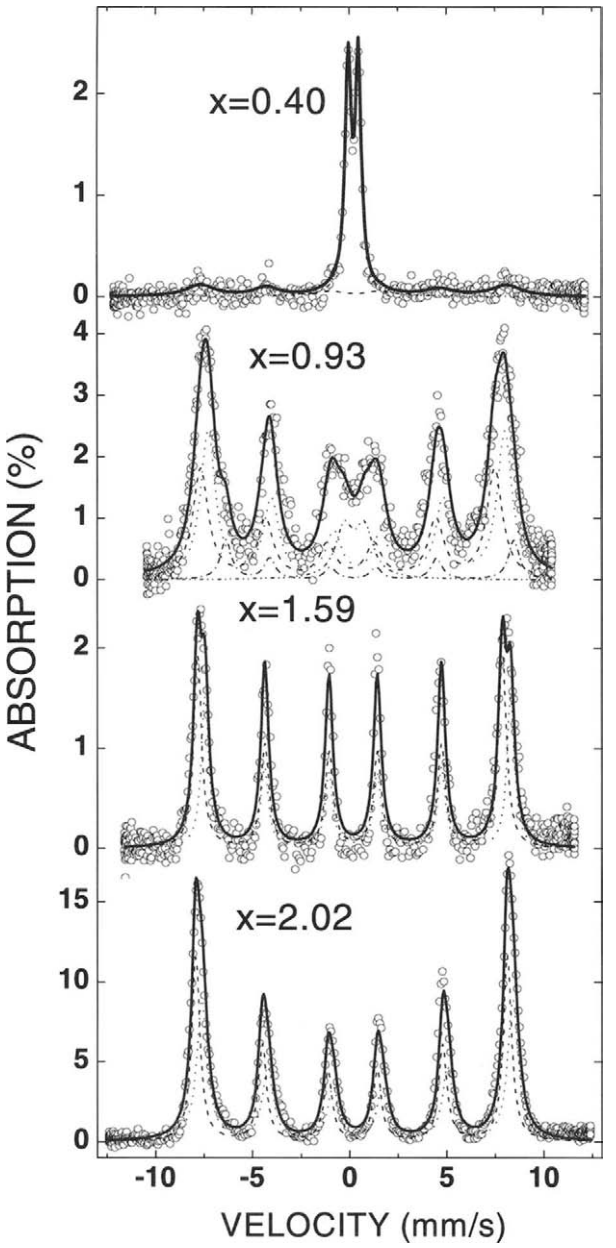

Figure 3 CEMS spectra of $Co_{3-x}Fe_xO_4$ films measured at room temperature.

stronger with increasing x while the normal spinel phase weaker as seen in Figure 1. For $x \geq 1.22$, the inverse spinel phase is seen to be dominant in the films. It is also noted that a large increase of lattice constant is observed when the Fe composition increases beyond $x=1.22$. The estimated lattice constant of the $x=2.02$ sample from its XRD pattern is 8.365 Å, close to the reported value of 8.380 Å for inverse spinel $CoFe_2O_4$ in which Co^{2+} ions occupy the octahedral sites [2]. The ionic radius of high-spin Co^{2+} is known to be

Table I Relevant parameters fitted to the CEMS spectra of $Co_{3-x}Fe_xO_4$ measured at room temperature

	A (tetrahedral) sites Fe^{3+}			B (octahedral) sites Fe^{3+}			B (octahedral) sites Fe^{2+}			
x	$H_{hf,A}$ (kOe)	$\Delta E_{Q,A}$ (mm/s)	δ_A (mm/s)	$H_{hf,B}$ (kOe)	$\Delta E_{Q,B}$ (mm/s)	δ_B (mm/s)	$H_{hf,B}$ (kOe)	$\Delta E_{Q,B}$ (mm/s)	δ_B (mm/s)	I_T/I_O
0.40				490	0.013	0.22				
0.93	459	−0.035	0.20	487	−0.042	0.26	459	0.45	0.63	1.28
1.59	476	−0.003	0.20	501	0.006	0.21				0.89
2.02	489	−0.044	0.27	507	0.011	0.20				1.04

0.885 and 0.72 Å in the octahedral and the tetrahedral sites, respectively [1]. Thus, the large increase of the lattice constant for $x > 1.22$ is interpreted as due to the migration of the Co^{2+} ions from the tetrahedral to the octahedral sites.

Only the films having the inverse spinel phase exhibited net magnetization at room temperature observed by vibrating sample magnetometry (VSM) [3]. Figure 3 shows the result of CEMS measurement on the films at room temperature. The curve-fitting analyses on the observed spectra indicate that Fe^{3+} ions tend to occupy the octahedral sites in the normal spinel phase (x=0.40) where paramagnetic signal is dominant. This is consistent with the results of XRD and VSM measurements. On the other hand, Fe^{3+} ions are found to occupy both the tetrahedral and the octahedral sites when the inverse spinel phase appears (x=0.93). The fact that the site preference ratio (I_T/I_O) between the tetrahedral and the octahedral Fe^{3+} ions is found to be 1.04 while Fe^{2+} ions occupy the octahedral sites suggests the appearance of an inverse spinel phase. For the x=0.93 sample, the Fe^{2+} sextet with a quadrupole shift ΔE_Q=0.63 mm/s coexists with the central doublet with an isomer shift δ=0.27 mm/s and ΔE_Q=1.04 mm/s, indicating the existence of paramagnetic Fe^{3+} component at the octahedral sites. When the Fe composition increases further (x=1.59), only the octahedral and the tetrahedral Fe^{3+} ions are observed, indicating that Co^{2+} ions replace the octahedral Fe^{2+} ions at such large x in the inverse spinel phase. The I_T/I_O of Fe^{3+} ions for x=1.59 is found to be 0.89, suggesting a Co^{2+} migration to the octahedral sites. Such Co^{2+} migration obtained from the CEMS measurements agrees with the interpretation of the rapid increase of the lattice constant for $x > 1.22$. The parameters obtained from curve-fitting of the CEMS data are listed in Table I. The used ratio of the recoil-free fractions of A- and B-site Fe ions (f_A/f_B) at 298 K is 1.0 [4]. By referring to the values of magnetic hyperfine field H_{hf} and ΔE_Q, we assigned A- and B-subspectra in CEMS analyses [5, 6].

Figure 4 exhibits the imaginary parts of the dielectric functions of the $Co_{3-x}Fe_xO_4$ samples measured by SE at room temperature. The observed strong absorption structures of Co_3O_4 have been interpreted in terms of charge-transfer (CT) transitions between different ionic sites at about 1.65, 2.4, and 2.8 eV as marked by arrows in Figure 4. As the Fe composition increases, the strengths of the 1.65- and 2.8-eV transitions are reduced more than that of the 2.4-eV transition.

The 1.65-eV absorption structure has been assigned to a d–d CT transition from the $d(t_{2g})$ states of the octahedral Co^{3+} ion to the $d(t_2)$ states of the tetrahedral Co^{2+} ion, $t_{2g}(Co^{3+}) \rightarrow t_2(Co^{2+})$, constituting the Mott-Hubbard gap of Co_3O_4 [7]. The absorption structures at the higher energies are interpreted as involving the $p(O^{2-})$ states located below the $t_{2g}(Co^{3+})$ states of Co_3O_4. Thus, the 2.4- and 2.8-eV absorptions are assigned to p–d CT transitions, $p(O^{2-}) \rightarrow t_2(Co^{2+})$ and $p(O^{2-}) \rightarrow e_g(Co^{3+})$, respectively [8]. Both the 1.65- and 2.8-eV transitions involve the d states of the octahedral Co^{3+} ion. Therefore, the reduction of the 1.65- and 2.8-eV transition strength at low x is attributed to the reduction of the Co^{3+}

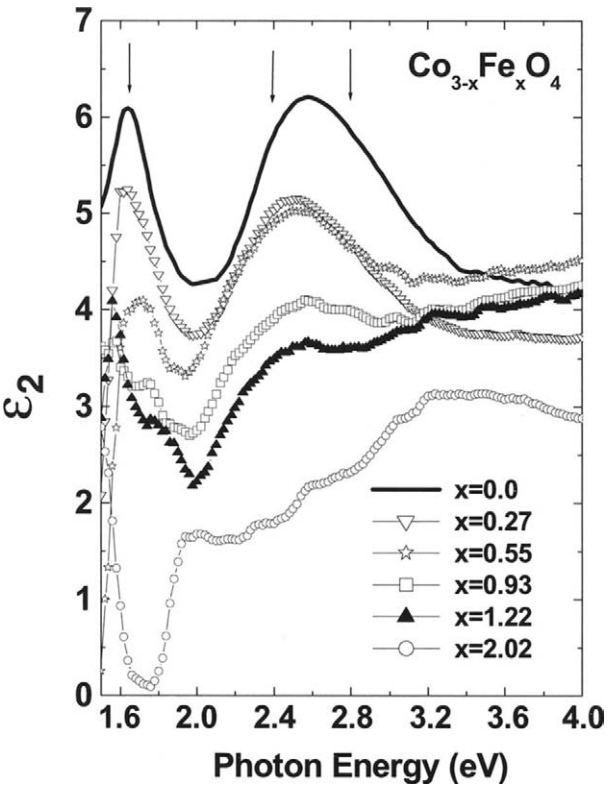

Figure 4 Imaginary part of measured dielectric functions of $Co_{3-x}Fe_xO_4$ films by SE.

density through the occupation of the octahedral sites by Fe^{3+} ions. Thus, the $Co_{3-x}Fe_xO_4$ compound maintains the normal spinel structure for low x, consistent with the XRD and CEMS results.

For x=0.93 and above, the 2.4-eV transition also suffers from a noticeable reduction of its strength, interpreted as due to a reduction of the tetrahedral Co^{2+} density through the substitution by Fe ions. In the inverse spinel phase, the tetrahedral sites are expected to be occupied by Fe^{3+} ions and the same amount of Fe^{2+} ions are expected to occupy the octahedral sites in order to maintain the charge neutrality.

The existence of the tetrahedral Fe^{3+} ions is also confirmed by the detection of a sharp crystal-field (CF) transition structure at 1.6 eV for x=0.93 and 1.22. It is attributed to a d–d CF transition from the ${}^6A_1\left(e^2, t_2^3\right)$ ground state to the ${}^4T_1\left(e^3, t_2^2\right)$ excited state of the crystal-field-split $3d^5$ multiplets of the tetrahedral Fe^{3+} ion [9, 10]. The increase of its absorption strength with increasing x justifies the assignment on the peak. The increase of the absorption strength above 3 eV compared to those of the lower-energy structures is attributable to the CT transitions involving the octahedral Fe^{3+} ions.

4 Conclusion

As the Fe composition increases in $Co_{3-x}Fe_xO_4$, the crystal structure goes through a phase transition from normal to inverse spinel. The two phases are found to coexist in a certain

range of x. The normal spinel phase is dominant below x=0.55 while the inverse spinel phase above x=0.93. In the normal spinel phase, most Fe ions occupy the octahedral sites as Fe^{3+}. For the inverse spinel phase, octahedral Fe^{2+} and tetrahedral Fe^{3+} ions are observed. Migration of Co^{2+} ions from tetrahedral to octahedral sites, replacing the Fe^{2+} ions, is detected for large x (>1.22). Analysis on the optical absorption spectra of the $Co_{3-x}Fe_xO_4$ films supports the results from the XRD and CEMS investigations.

Acknowledgement This work was supported by the financial support of Konkuk University made in the program year of 2005.

References

1. Muller, O., Roy, R.: The Major Ternary Structural Families, p. 5. Springer, Berlin Heidelberg New York (1974)
2. Guillot, M. In: Cahn, R.W., Haasen, P., Kramer, E.J. (eds.) Materials Science and Technology, vol. 3B, pp. 73. VCH, Weinheim (1994)
3. Kim, K.J., Kim, H.K., Park, Y.R., Ahn, G.Y., Kim, C.S., Park, J.Y.: IEEE Trans. Magn. **41**, 3478 (2005)
4. Robbins, M., Wertheim, G.K., Sherwood, R.C., Buchanan, D.N.E.: J. Phys. Chem. Solids **32**, 717 (1971)
5. Evans, B.J.: In: Gruverman, I.J. (ed.) Mossbauer Effect Methodology, vol. 4, pp. 140. Plenum, New York (1966)
6. Persoons, R.M., De Grave, E., de Bakker, P.M.A., Vandenberghe, R.E.: Phys. Rev., B **47**, 5894 (1993)
7. van Elp, J., Wieland, J.L., Eskes, H. Kuiper, P. Sawatzky, G.A., de Groot, F.M.F., Turner, T.S.: Phys. Rev., B **44**, 6090 (1991)
8. Kim K.J., Park, Y.R.: Solid State Commun. **127**, 25 (2003)
9. Fazzio, A., Caldas, M.J., Zunger, A.: Phys. Rev., B **30**, 3430 (1984)
10. Kim, K.J., Park, Y.R.: J. Appl. Phys. **96**, 4150 (2004)

Hyperfine Interact (2006) 169:1371–1377
DOI 10.1007/s10751-006-9453-8

Mössbauer spectroscopical investigation of the exchange biased Fe/MnF_2 interface

B. Sahoo · W. A. A. Macedo · W. Keune · V. Kuncser · J. Eisenmenger · J. Nogués · I. K. Schuller · I. Felner · Kai Liu · R. Röhlsberger

Published online: 27 October 2006

Abstract Two different Fe/MnF_2 samples have been prepared by e-beam evaporation on MgO(001) substrates. The Fe layer in the samples includes a 10 Å thick ^{57}Fe probe layer either at the Fe/MnF_2 interface (interface sample) or 35 Å away from the interface (center sample). The samples are characterized by X-ray diffraction,

B. Sahoo (✉) · W. Keune · V. Kuncser
Fachbereich Physik, Universität Duisburg-Essen, 47048 Duisburg, Germany
e-mail: balaram_sahoo@uni-duisburg.de

W. A. A. Macedo · J. Eisenmenger · I. K. Schuller
Physics Department, University of California – San Diego, La Jolla, CA 92093, USA

W. A. A. Macedo
Laboratório de Física Aplicada, Centro de Desenvolvimento da Tecnologia Nuclear, Belo Horizonte MG, 30123-970, Brazil

V. Kuncser
National Institute of Physics of Materials, Bucharest-Magurele 76900, Romania

J. Eisenmenger
Abteilung Festkörperphysik, Universität Ulm, 89069 Ulm, Germany

J. Nogués
Institució Catalana de Recerca i Estudis Avançats (ICREA) and Departament de Física, Universitat Autónoma de Barcelona, 08193 Bellaterra, Spain

I. Felner
Racah Institute of Physics, The Hebrew University, Jerusalem 91904, Israel

K. Liu
Physics Department, University of California, Davis, CA 95616, USA

R. Röhlsberger
HASYLAB@DESY, Hamburg, Germany

conversion electron Mössbauer spectroscopy (CEMS) and SQUID magnetometry. ^{57}Fe CEMS has been employed to study the depth dependent hyperfine interactions in Fe/MnF_2 as a function of temperature between 18 K to 300 K. The hyperfine field B_{hf} has been obtained for the interfacial and off-interfacial ^{57}Fe layers. At the interface, besides B_{hf} of bcc-Fe, the presence of a component with a distribution $P(B_{hf})$ is observed. The latter is assigned to interfacial ^{57}Fe atoms, indicating some (~15%, equivalent to ~1 Fe atomic layer) intermixing at the Fe/MnF_2 interface and a decrease of the average $<B_{hf}>$ by 21%. The influence of the interface disappears as the ^{57}Fe probe layer is placed away from the interface. The temperature dependence of the average $<B_{hf}>$ of the interface has been measured. The Fe spins, at remanence, are found to lie in the film plane.

Key words conversion electron Mössbauer spectroscopy · exchange bias · Fe/MnF_2 · interfacial properties · spin structure

1 Introduction

Bilayers of Fe/MnF_2 are an archetype system showing exchange bias effect [1–15] evidenced by the shift of the magnetic hysteresis loop. This effect originates from the exchange coupling at the interface of the ferromagnet (Fe) and antiferromagnet (MnF_2). The roughness and the intermixing at the interface are among the important parameters which can control the interfacial coupling and hence the exchange bias [4–6]. Therefore, for the understanding of the exchange bias effect, information on interface parameters such as magnetic moment or hyperfine field, interdiffusion, etc. are highly desirable along with the interfacial spin structure. ^{57}Fe conversion electron Mössbauer spectroscopy (CEMS) in combination with the ^{57}Fe probe layer method is a unique isotope selective technique in order to explore depth-dependent physical properties such as spin structure [7], metallurgical and magnetic phases present in the sample, temperature dependent magnetic ordering and local magnetic moment at the interface. The change in the remanent spin structure in this exchange biased systems below and above the Néel temperature (T_N = 67 K) has been reported earlier [7]. In this work the CEMS investigation of the interfacial parameters of Fe/MnF_2 bilayers will be discussed.

2 Sample preparation and characterisation

Two kinds of exchange biased Al/Fe/MnF_2/ZnF_2/MgO(001) heterostructures were prepared by sequential electron beam evaporation [8]. In both kinds of samples a 160 Å ZnF_2 buffer layer was deposited in order to relax the large (8%) lattice mismatch between the MgO substrate and MnF_2. The typical thicknesses of the Al, Fe and MnF_2 layers are 30, 80 and 520 Å, respectively. The samples differ only by their ferromagnetic Fe layer. Out of the 80 Å Fe layer, a 10 Å ^{57}Fe probe layer was deposited just at the interface between the AFM (MnF_2) and the FM (Fe) layer in the first kind of sample called 'interface sample' (labeled MFEMF01). Hence, the FM layer for the interface sample contains 70 Å^{nat}Fe/10 Å^{57}Fe. The other kind of sample is called 'center sample' (labeled MFEMF03). In this sample the ^{57}Fe probe

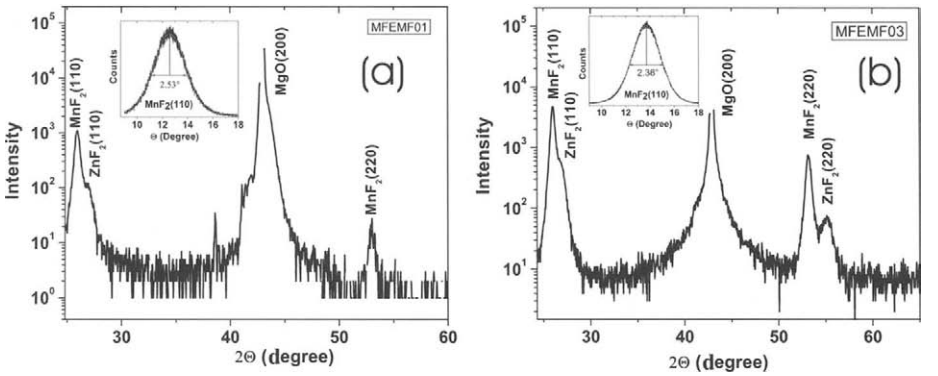

Figure 1 XRD pattern of Fe/MnF_2 interface sample (**a**) and center sample (**b**). *Inserts* show the corresponding *rocking curves* taken at the MnF_2(110) peak. (Cu–K_α radiation).

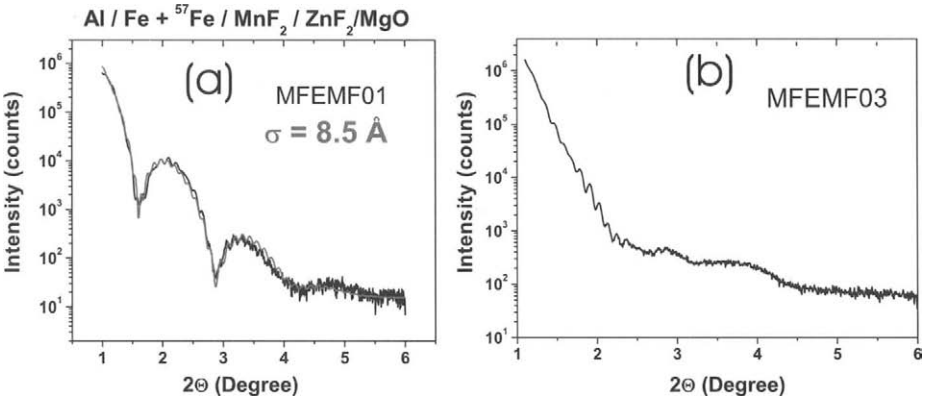

Figure 2 Small-angle XRD scans of Fe/MnF_2 interface sample (**a**) and center sample (**b**). The *light-gray curve* (*red, in color*) is the fitting to the measured curve in (**a**). (Cu–K_α radiation).

layer was placed at the center of the Fe layer (35 Å^{nat}Fe/ 10 Å^{57}Fe/35 Å^{nat}Fe), i.e. 35 Å away from the interface. Prior to deposition the MgO(001) substrate was heated to 450°C for 15 min and then cooled to 200°C for ZnF_2 deposition. The base pressure of the system was 3×10^{-8} Torr and the pressure during MnF_2 deposition was around 6×10^{-7} Torr. The deposition temperatures, and deposition rates for Al, Fe, MnF_2 and ZnF_2 layers were 150, 150, 325 and 200°C, and 0.5, 1, 2 and 2 Å/s, respectively. The thickness of the fluoride layers was monitored by calibrated quartz crystal oscillators and the Fe layer thickness was monitored by optical sensors.

After deposition the structural and magnetic characterizations of the samples were performed by high and small angle XRD (Cu–K_α radiation, λ = 1.5418 Å), CEMS and SQUID magnetometry. The high-angle and small-angle XRD patterns for the interface sample are shown in Figures 1a and 2a, respectively. The high-angle XRD pattern confirms the epitaxial nature of the film with MnF_2(110) in the sample plane.

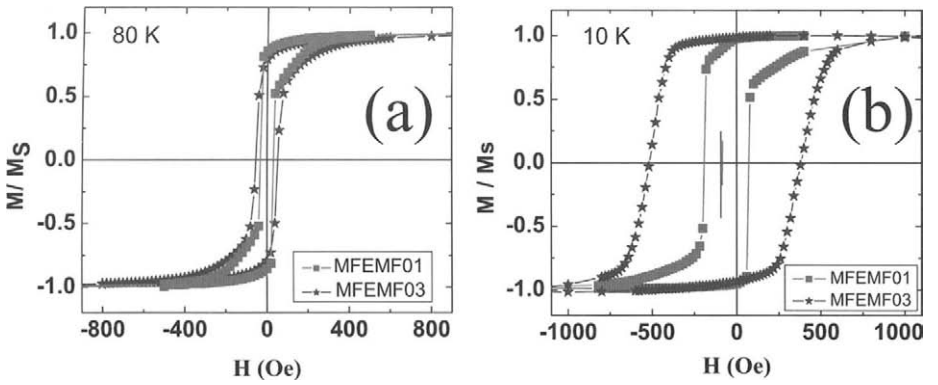

Figure 3 The normalized SQUID hysteresis loops for the interface sample (*squares*) and center sample (*asterisks*) taken at 80 K (**a**) and 10 K (**b**).

The relatively sharp rocking curve (insert in Figure 1a) of the $MnF_2(110)$ reflection has a full width at half maximum (FWHM) of about 2.5°. The small-angle XRD suggests good homogeneity of the MnF_2 and Fe layer. The high frequency (low frequency) oscillations are due to the fluoride layer (Fe layer). The light-gray curve is the least-squares fitting to the measured black curve. The fitting gives the interface roughness σ of about 8.5 Å. The epitaxial nature of the center sample has also been verified by the high-angle XRD pattern shown in Figure 1b. The relatively sharp rocking curve (insert, Figure 1b) has a FWHM of about 2.4°. In comparison to the interface sample, the small angle scattering (Figure 2b) indicates a higher roughness for the center sample. It is worth mentioning that the MnF_2 layers (for interface and center sample) are growing as twinned epitaxial layers [10–13].

3 SQUID magnetometry results

SQUID magnetometry has been used to measure the exchange bias field, H_E, and the coercivity, H_c for the two samples. The results are shown in Figure 3a and b. Prior to the measurement the sample was cooled from 150 K to either 80 or 10 K in an in-plane applied field of 2 kOe. Clearly the samples show no exchange bias above T_N (at 80 K). However, below T_N (at 10 K), H_E of about 55 Oe has been observed for both samples. It should be noticed that H_c of the two samples is different, which is associated with the different microstructure (roughness and intermixing) of the two samples.

4 CEMS results and discussion

The samples were also characterized by ^{57}Fe CEMS with the γ-ray either normal to the sample plane ($\Phi = 90°$) or at an angle $\Phi = 45°$. Typical Mössbauer spectra for the interface sample (MFEMF01) taken at different temperatures are given in Figure 4. Each spectrum clearly shows a dominant six-line pattern superimposed to

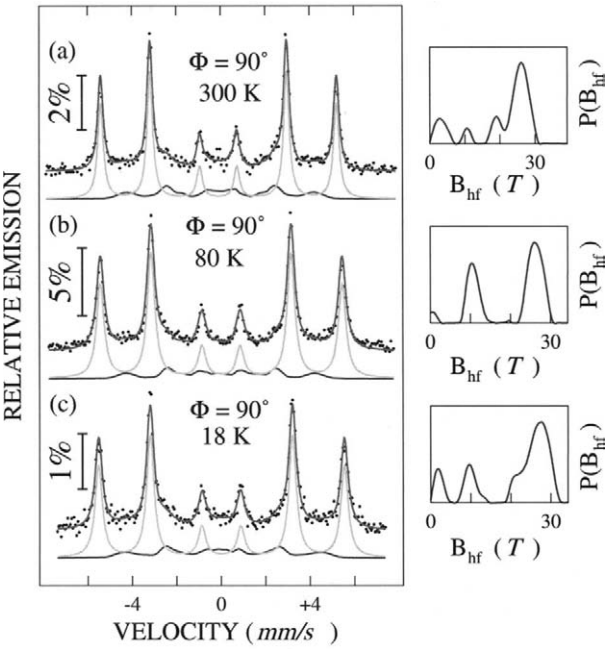

Figure 4 CEM spectra of the Fe/MnF_2 interface sample taken at 300 K (**a**), 80 K (**b**) and 18 K (**c**). The spectra have been fitted by a dominant sextet assigned to bcc-Fe, and a component with a distribution of hyperfine fields, $P(B_{hf})$ (*right-hand side*) which accounts for the chemical intermixing at the interface.(Angle between γ-ray direction and film plane $\Phi = 90°$).

a weak distribution of magnetic hyperfine fields. Each spectrum has been fitted by a dominant sextet ($B_{hf} = 32.8$ T) and a subspectrum with distribution of hyperfine fields $P(B_{hf})$. The dominant sextet is unambiguously assigned to the bcc-Fe layer, and the distribution of hyperfine fields, which has a dominant peak at about 26 T, is attributed to the chemical intermixing at the Fe/MnF_2 interface. The typical relative spectral area of the hyperfine field distribution is about 15% of the total area. Considering the ^{57}Fe layer thickness (10 Å), 15% intermixing corresponds about 1.5 Å of the ^{57}Fe layer, i.e., about one monolayer (ML) of Fe is chemically intermixed at the interface. It should be noticed that the roughness of 8.5 Å obtained from the simulation of the small-angle XRD results (Figure 2) is larger than the 1.5 Å intermixing at the interface. The CEM spectra (not shown) measured with the γ-ray incident angle of $\Phi = 45°$ with respect to the film plane resulted in similar hyperfine parameters (isomer shift, magnetic hyperfine field, and spectral area) as those obtained at $\Phi = 90°$. The isomer shifts, magnetic hyperfine fields and the spectral area contribution for both, the dominant sextet and the distribution $P(B_{hf})$, are shown in Figure 5. It is worth mentioning that in all cases the average isomer shifts of the $P(B_{hf})$ distribution are very small and similar to that of the dominant sextet.

For the center sample, the CEM spectra (Figure 6) are measured in the same way as that for the interface sample. The spectra have been least-squares fitted by using a single sextet typical of bcc Fe. No interfacial intermixing has been observed because the ^{57}Fe-probe layer is about 35 Å away from the AFM/FM interface. It is interesting to note that the intensity ratio between the second and third line (R_{23}) of the dominant Mössbauer sextet (for $\Phi = 90°$) is 4.0 for both samples. This indicates that the Fe spins are in the plane of the sample at all temperatures between 300 K and 18 K.

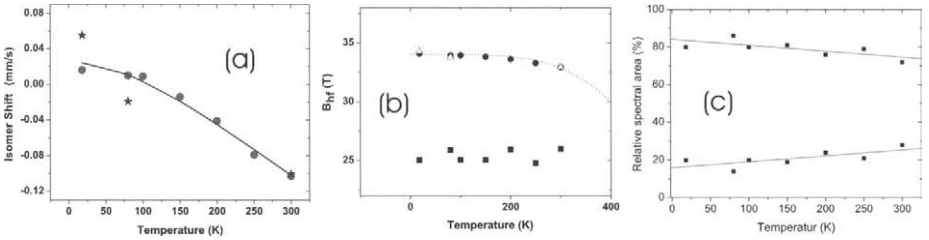

Figure 5 Temperature dependence of: (**a**) isomer shift of the bcc-Fe phase relative to the ^{57}Co(Rh) source (*full dots*: $\Phi = 45°$, *asterisks*: $\Phi = 90°$). The *solid line* is a Debye model fit to the data yielding a Debye temperature $\Theta_D = 466$ K.; (**b**) magnetic hyperfine field of the bcc-Fe phase (*circles*: $\Phi = 45°$ and *triangles*: $\Phi = 90°$) and of the component with the $P(B_{hf})$ distribution (*average hyperfine field, squares*). The *dotted curve* is a Brillouin function (J = 1/2) fit to the data points yielding $T_C = 627$ K for the Fe layer; (**c**) relative spectral area of the bcc-Fe sextet (*top*) and of the component with the $P(B_{hf})$ distribution (*bottom*). The *straight lines* are linear fits to the data points.

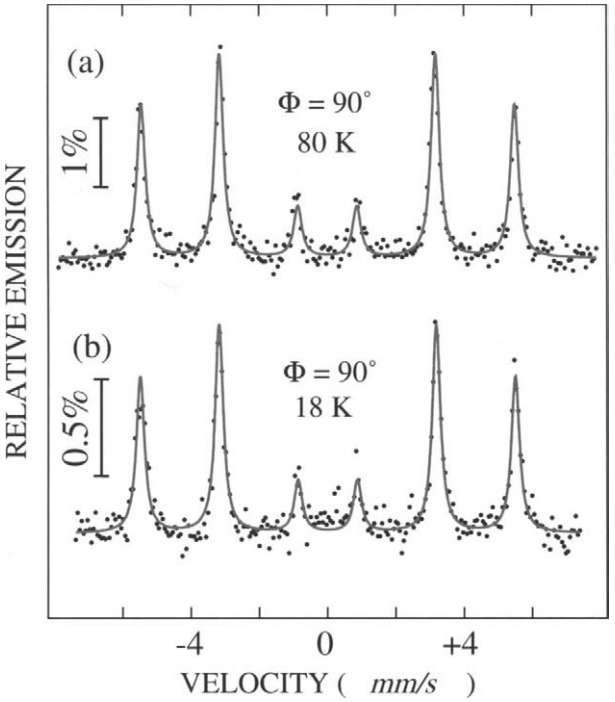

Figure 6 CEM spectra of the Fe/MnF_2 center sample taken at 80 K (**a**) and 18 K (**b**). The spectra have been fitted by a sextet assigned to bcc-Fe. (Angle between γ-ray direction and film plane $\Phi = 90°$).

5 Summary

In summary, we have prepared two different Fe/MnF_2 samples with an ^{57}Fe-probe layer at and away from the AFM/FM interface, respectively. The structure, magnetic properties and hyperfine parameters have been obtained by using XRD, SQUID magnetometry and CEMS. Our CEMS results indicate very small interfacial intermixing, equivalent to ~1 ML of Fe, a reduced interfacial hyperfine field, and fully in-plane magnetization of the Fe films.

Acknowledgements Work supported by the DFG (SFB 491), the US-DOE, the US–Israel BSF, the CNPq (Brazil), the AvH Foundation, the Spanish CICYT (MAT2001-2555), the Alfred P. Sloan Foundation, and the Catalan DGR (2001SGR00189). W.A.A.M. gratefully acknowledges the hospitality during his stay at the UCSD, and thanks J. Santamaria and R. Paniago for assistance with GIXR simulations.

References

1. Nogués, J., Schuller, I.K.: J. Magn. Magn. Mater. **192**, 203 (1999)
2. Berkowitz, A.E., Tanako, K.: J. Magn. Magn. Mater. **200**, 552 (1999)
3. Kiwi, M.: J. Magn. Magn. Mater. **234**, 584 (2001)
4. Lund, M.S., Macedo, W.A.A., Liu, K., Nogués, J., Schuller, I.K., Leighton, C.: Phys. Rev., B **66**, 054422 (2002)
5. Leighton, C., Nogués, J., Jönsson-Åkerman, B.J., Schuller, I.K.: Phys. Rev. Lett. **84**, 3466 (2000)
6. Fitzsimmons, M.R., Leighton, C., Hoffmann, A., Yashar, P.C., Nogués, J., Liu, K., Majkrzak, C.F., Dura, J.A., Fritzsche, H., Schuller, I.K.: Phys. Rev., B **64**, 104415 (2001)
7. Macedo, W.A.A., Sahoo, B., Kuncser, V., Eisenmenger, J., Felner, I., Nogués, J., Lui, K., Keune, W., Schuller, I.K.: Phys. Rev., B **70**, 224414 (2004)
8. Leighton, C., Nogués, J., Suhl, H., Schuller, I.K.: Phys. Rev., B **60**, 12837 (1999)
9. Leighton, C., Fitzsimmons, M.R., Hoffmann, A., Dura, J., Majkrzak, C.F., Lund, M.S., Schuller, I.K.: Phys. Rev., B **65**, 064403 (2002)
10. Krivorotov, I.N., Leighton, C., Nogués, J., Schuller, I.K., Dahlberg, E.D.: Phys. Rev., B **65**, 100402 (2002)
11. Krivorotov, I.N., Leighton, C., Nogués, J., Schuller, I.K., Dahlberg, E.D.: Phys. Rev., B **68**, 054430 (2002)
12. Fitzsimmons, M.R., Yashar, P., Leighton, C., Schuller, I.K., Nogués, J., Majkrzak, C.F., Dura, J.A.: Phys. Rev. Lett. **84**, 3986 (2000)
13. Pechan, M.J., Bennett, D., Teng, N., Leighton, C., Nogués, J., Schuller, I.K.: Phys. Rev., B **65**, 064410 (2002)
14. Leighton, C., Fitzsimmons, M.R., Yashar, P., Hoffmann, A., Nogués, J., Dura, J., Majkrzak, C.F., Schuller, I.K.: Phys. Rev. Lett. **86**, 4394 (2001)
15. Kiwi, M., Mejía-López, J., Portugal, R.D., Ramírez, R.: Appl. Phys. Lett. **75**, 3995 (1999)

Hyperfine Interact (2006) 169:1379–1382
DOI 10.1007/s10751-006-9454-7

Intermixing during epitaxial growth and Mössbauer spectroscopy with probe layers

V. G. Semenov · V. M. Uzdin

Published online: 5 January 2007

Abstract Mössbauer spectroscopy with ^{57}Fe (^{119}Sn) probe layers is a useful method to study the local magnetic structures at buried interfaces. However interface alloying, which always exists in the real samples, have to be taken into account for accurate interpretation of experimental data. We developed an algorithm, which describes the interface intermixing in the multilayers. Substituting deposited atoms by atoms of substrate and floating of deposited atoms in the upper layers during epitaxial growth leads to the formation of asymmetric chemical and magnetic interfaces. This asymmetry in the M_1/M_2 superlattices can explain the difference between magnetic responses from M_1 on M_2 and M_2 on M_1 interfaces which were observed in experiments. Applying this intermixing model to the systems with probe layers located at different distances from the interfaces gives the natural explanation of hyperfine fields distributions on probe atoms and helps us clarify some discrepancies reported in the literature.

Key words interface asymmetry · interdiffusion · hyperfine fields in multilayers

Interface alloying is a common phenomenon, which always takes place to some degree during epitaxial growth of metallic multilayers. Atomic scale intermixing is one of the main types of interface roughness, and, therefore, it has to be taken into account for accurate interpretation of experiments. Mössbauer spectroscopy can be used to study the local magnetic interface structure in the superlattices with probe ^{57}Fe (or ^{119}Sn) layers. Insertion of such layers at set distances from the interface makes it possible to obtain the distribution of magnetic hyperfine fields (hff) in these particular layers [1]. The existence of probe atoms with various magnetic moments and with different local environments near the interface leads to the appearance of satellite lines in the Mössbauer spectra. However, interpretating these data happens to be a complicated and ambiguous task. If interdiffusion was present during the sample preparation process, the probe atoms are distributed in

V. G. Semenov (✉) · V. M. Uzdin
Saint-Petersburg State University, Saint-Petersburg, Russia
e-mail: semenov@moss.pu

different layers. In order to infer the interface magnetic structure, it is necessary to know their concentration profile.

In recent years various metallic multilayer systems M_1/M_2 (Fe/Cr [1, 2], Fe/Ag [3], Fe/V [4], Cr/Sn/V [5]) have been studied by means of Mössbauer spectroscopy and differences in hff distributions at the interfaces M_1/M_2 (M_1 on M_2) and M_2/M_1 (M_2 on M_1) were reported. To explain these general phenomena, the intermixing process at the interface has to be thoroughly understood.

We present an atomistic model of interface alloying which presupposes that, during the growth of each monolayer, a determinate fraction (ζ) of deposited atoms exchanges with atoms of the upper surface layer. Consequently, substrate atoms can float up a considerable distance determined by the parameter ζ. Any other internal diffusion is prohibited and deposited atoms cannot move deep inside the substrate. This leads to an asymmetric interface in the direction of sample growth [6]. The magnitude of ζ is the only parameter which determines the intensity of intermixing. For infinite superlattice which consists of periodically repeated n layers of element M_1 and m layers of element M_2 the fraction of M_1-atoms in the k layer, $x_{M_1}(k)$ for can be expressed as

$$x_{M_1}(k) = 1 - \varsigma^k(1-\varsigma)\frac{1-\varsigma^m}{1-\varsigma^{n+m}} - \varsigma\delta_{k,n}, \quad 1 \le k \le n$$

$$x_{M_1}(k) = \varsigma^{k-n}(1-\varsigma)\frac{1-\varsigma^n}{1-\varsigma^{n+m}} + \varsigma\delta_{k,n+m}, \qquad n \le k \le n+m$$

Here, δ is the Kronecker symbol. These formulas are taking into account the possibility for the atom to float trough several periods of superlattice. Layer by layer concentration of M_1-atoms in the superlattice $M_1(7ML)/M_2(5ML)$ with interdiffusion is shown in Fig. 1. The profile of component concentrations in the superlattice depends on the ratio between the nominal thickness of each layer and the characteristic length of diffusion in growth direction. In principle, the intermixing parameter ζ can be different for different interfaces. Such a model for intermixing with subsequent self-consistent calculations of magnetic moments on each site was applied to describe the magnetic properties of the Fe/V superlattices under hydrogenation [7], for interpretation of Mössbauer spectra in Fe/V [8] and Fe/Cr [6] multilayers and for explanation of the π-phase shift of the interlayer exchange coupling oscillations in the Fe/Cr/Fe trilayers on Fe whisker [9].

The floating model of the intermixing explains the difference in the hff distributions from M_1/M_2 and M_2/M_1 interfaces in various multilayers. It can also be used for the description of experiments with probe layers. The ^{119}Sn probe layers were used to study the Cr magnetic structure in Cr/V multilayers. It was found that the hff on ^{119}Sn atoms drops faster near the V-on-Cr interface than at the Cr-on-V interface [5]. Floating algorithm explains this phenomenon: when Sn atoms flow from the V-on-Cr interface they enter inner magnetic Cr layers, whereas from the V-on-Cr interface they come to the non-magnetic V-slabs. Quite significant differences in the hff distributions for the sample with ^{119}Sn probe layers nominally placed at a distance of 10 Å from interfaces shows that the typical scale of intermixing achieved in these multilayers is six to seven atomic layers.

In the Fe/Ag superlattice ^{57}Fe monolayer was utilized as a probe layer in molecular-beam-epitaxy-grown Ag/Fe(001)/Ag(001) structures [3]. The isomer shift (IS) and quadrupole splitting (QS) depend on the local environment of particular ^{57}Fe atoms and, therefore, Mössbauer spectra can be used to find the interface structure. Six subspectra with different IS, hff and QS were found for the structure Ag/^{57}Fe(1.4ML)/^{nat}Fe(5.4ML)/Ag(10ML)/Au.

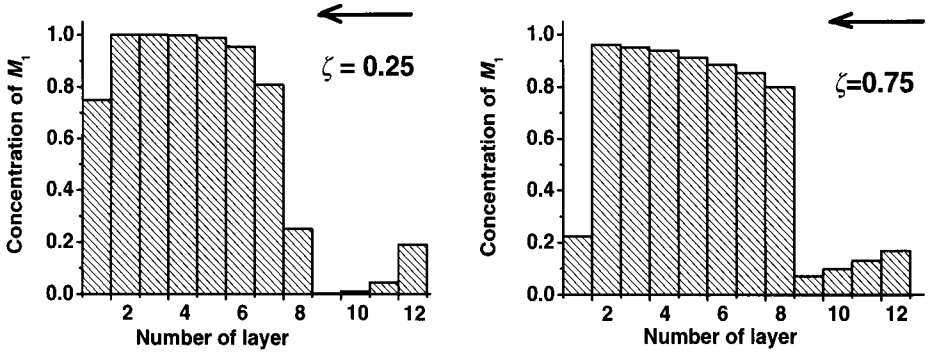

Fig. 1 Profile of M_1 concentration for superlattice $M_1(7ML)/M_2(5ML)$ with interdiffusion modeled by floating algorithm with different intermixing parameters ζ. *Arrows* show growth direction

They were identified [3] as atoms at different sites on the stepped interface. This interpretation is based on the assumption that roughness is associated only with steps and, moreover, atoms with larger IS values (smaller hff) have more Ag (first, second?) nearest neighbors (nn). It was concluded that after the deposition of 1.4 monolayer (ML) of Fe on the Ag substrate only 54% of the substrate was covered by Fe atoms. In contrast, in the multilayer $Ag/[Fe(5.4ML)/{}^{57}Fe(1ML)/Ag(10ML)]_3/Au$, the top Fe/Ag interface is very sharp with 90% of the deposited 1-ML ^{57}Fe atoms actually making the contact with Ag. The hff value for the step-edge atoms at Fe/Ag and Ag/Fe interfaces were found to be significantly different: for the lower (Fe-on-Ag) interface it is about 10 kOe larger than that of the upper interface. The authors [3] proposed that the difference in hff for top and bottom Fe/Ag interfaces is connected with spin-polarized quantum well states responsible for the interlayer exchange coupling in the multilayers. However, this statement, looks quite artificial, whereas supposition of the floating mechanism of epitaxial growth removes most of discrepancies and gives a straight-forward explanation of experimental data. Indeed, subspectra with enhanced IS and reduced hff originate from ^{57}Fe atoms inside the Ag layers. Obviously the number of such atoms has to be larger at the upper (Ag-on-Fe) interface, because ^{57}Fe atoms float into the Ag slab. These ^{57}Fe atoms have a larger number of nn Ag atoms, and this is the reason why their hff is not as large as that of ^{57}Fe atoms at lower (Fe-on-Ag) interfaces. ^{57}Fe atoms from the lower interface float into the slab of natural Fe, and about half of them has no Ag among nn atoms.

Such a physical picture agrees with an earlier study of Fe/Ag multilayers, where 2-ML thick ^{57}Fe probe layers were placed in different samples at the upper or lower interfaces, or in the middle of the Fe slab [10]. These authors obtained a broad distribution of hff, but for the upper interfaces the average hff measured at 6 K was found to be smaller than for lower interfaces.

In summary, our floating algorithm of epitaxial growth, combined with self-consistent calculations of atomic magnetic moments, allows us to give a new interpretation of Mössbauer experiments with ^{57}Fe and ^{119}Sn probe layers in Fe/Cr, Fe/Cr/Sn, V/Cr/Sn, and Fe/Ag superlattices, as reported in the literature. This leads to a revision of the reasons for the suppression of Cr magnetic moments in Fe/Cr/Sn and V/Cr/Sn and of the interface structure in Fe/Ag heterostructures.

The possibility of interpretation of various experimental data on different samples demonstrates that our intermixing model is quite general and can be used as an initial approach for the deduction of chemical and magnetic interface structures. However, steps at the interface, islands and other large-scale defects can essentially change the effective

parameters of our algorithm; this can be important for a quantitative comparison with experimental results.

Acknowledgements This work was partially supported by Russian Foundation of Basic Research (grant 04-02-16024) and INTAS NETWORK project 03-51-4778.

References

1. Shinjo, T., Keune, W.: J. Magn. Magn. Mater. **200**, 598 (1999)
2. Heinrich, B., Cochran, J.F., Monchesky, T., Urban, R.: Phys. Rev., B **59**, 14520 (1999)
3. Schurer, P.J., Celinski, Z., Heinrich, B.: Phys. Rev., B **51**, 2506 (1995)
4. Kalska, B., Blomquist, P., Häggström, L., Wäppling, R.: Europhys. Lett. **53**, 395 (2001)
5. Almokhtar, M., Mibu, K., Nakanishi, A., Kobayashi, T., Shinjo, T.: J. Phys.: Condens. Matter **12**, 9247 (2000)
6. Uzdin, V., Keune, W., Walterfang, M.: J. Magn. Magn. Mater. **240**, 504 (2002)
7. Uzdin, V., Westerholt, K., Zabel, H., Hjörvarsson, B.: Phys. Rev., B **68**, 214407 (2003)
8. Uzdin, V.M., Häggström, L.: Phys. Rev., B **72**, 24407 (2005)
9. Uzdin, V.M., Demangeat, C.: Phys. Rev., B **66**, 92408 (2002)
10. Keavney, D.J., Wieczorek, M.D., Storm, D.F., Walker, J.C.: J. Magn. Magn. Mater. **121**, 49 (1993)

Hyperfine Interact (2006) 169:1383–1388
DOI 10.1007/s10751-006-9455-6

Mössbauer and SEM study of Fe–Al film

Varkey Sebastian · Ram Kripal Sharma · N. Lakshmi · K. Venugopalan

Published online: 14 November 2006

Abstract Fe–Al alloy with Fe/Al ratio of 3:1 was first prepared by argon arc melting. It was subsequently coated on glass slide and cellophane tape using an electron beam gun system to have a thickness of 2,000 Å. X-ray diffraction spectrum of the coated sample indicates a definite texture for the film with a preferential growth along the Fe(110) plane. SEM micrographs of the film showed the presence of nano islands of nearly $3\times10^{12}/m^2$ surface density. Composition of different parts of the film was determined using EDAX. Room temperature Fe-57 Mössbauer spectrum of coated sample showed the presence a quadrupole doublet with a splitting of 0.46 mm/s, which is typical of Al-rich iron compounds. MOKE study shows an in-plane magnetic moment.

Key words Fe–Al film · ^{57}Fe Mössbauer · hyperfine fields

1 Introduction

Magnetic behavior of bulk and nano Fe–Al systems has been the subject of numerous theoretical and experimental studies because of the subtle relation between their structural and magnetic properties. On the Fe rich side, the system has two ordered phases based on the bcc α-Fe lattice, around the stoichiometric structure of Fe_3Al and FeAl with the DO_3 and B_2 type structures respectively. FeAl in the ordered state is non-magnetic while Fe_3Al is ferromagnetic [1]. Evolution towards a ferromagnetic state at room temperature is seen in disordered systems prepared by non-equilibrium techniques like ball milling [2, 3] and rapid solidification [4] for up to 50 at.% Fe. On the Al rich side of the phase diagram, the stable orthorhombic Fe_2Al_5 phase is non-magnetic. However, in ball-milled Al-34 at %Fe and Al-25 at %Fe, formation of metastable bcc solid solutions, which are ferromagnetic at room temperature, have been reported [5]. Fe/Al multilayers and single layer thin films are also of great interest because phase formation in thin nanometer-scale systems often differs

V. Sebastian (✉) · R. K. Sharma · N. Lakshmi · K. Venugopalan
Department of Physics, M.L. Sukhadia University, Udaipur, Rajasthan 313 001, India
e-mail: vseba@yahoo.com

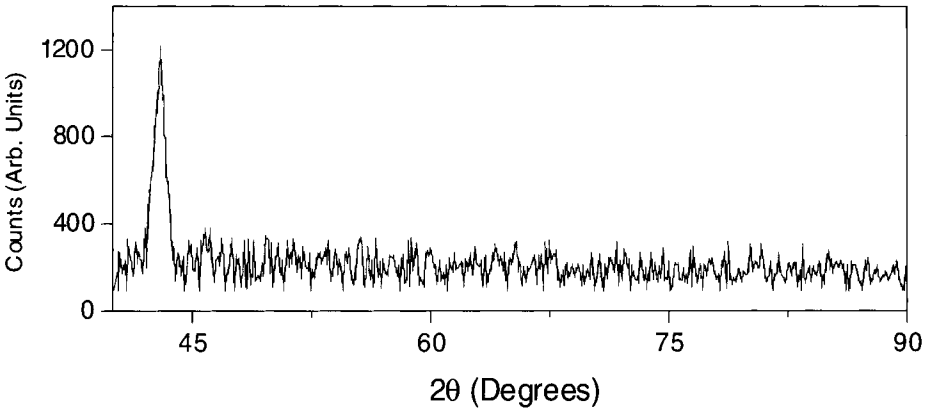

Figure 1 X-ray diffractogram of 2,000 Å Fe–Al alloy coated on glass.

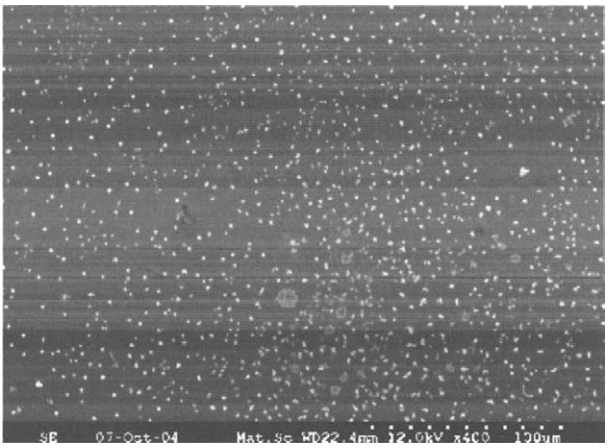

Figure 2 SEM micrograph of film showing Fe–Al nano islands in film.

from the bulk material. While there have been many studies on Fe/Al multilayers [6–8], only a few studies have been made on Fe–Al thin films [9, 10].

In the present study, we report the preparation of Fe–Al thin films by electron beam evaporation and their characterization by X-ray diffraction, Scanning electron microscopy (SEM) and EDAX, magneto-optical Kerr effect (MOKE) and Mössbauer spectroscopy.

2 Experimental methods

Pure Al and Fe metals (of 99.99% purity) in the ratio 1:3 were arc melted in argon atmosphere to form an alloy. The ingot formed was melted two more times to ensure homogeneity. Weight loss after melting was observed to be less than 1%. The as prepared alloy was then used to deposit films of thickness 2,000 Å onto glass and cellophane substrates using electron beam evaporation at 20 mA current, under a vacuum of 4×10^{-5} Torr.

The thin films thus obtained were characterized using X-ray diffraction, SEM and EDAX, Fe-57 Mössbauer spectroscopy and magneto-optical Kerr effect (MOKE). XRD spectrum of the film coated on glass substrate was recorded at room temperature with a

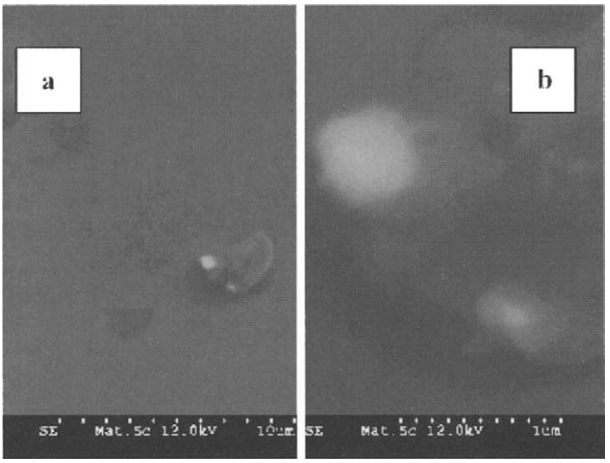

Figure 3 SEM micrograph showing enlarged view of one of the bright islands.

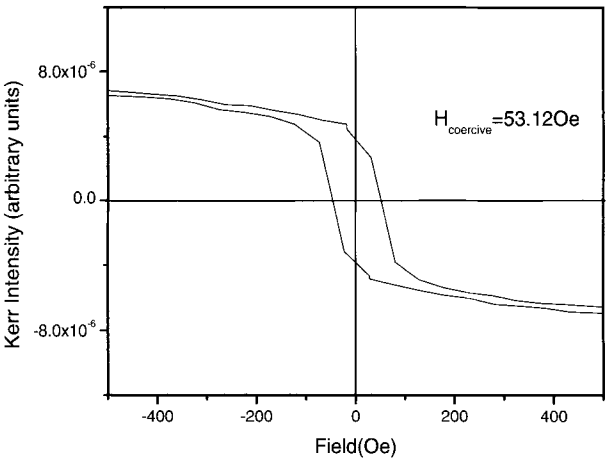

Figure 4 MOKE of Fe–Al film.

Rigaku miniflex diffractometer using Cu Kα radiation. SEM was done using a Hitachi S-3000N machine and EDAX was taken using JEOL-JSM-5600 with a Si(Li) Oxford detector.

Mössbauer spectrum of the film coated on cellophane substrate was recorded at room temperature in the transmission mode. A 25 mCi ^{57}Co in rhodium matrix was used as source along with a standard Austin drive and controller assembly in the constant acceleration mode. Velocity calibration was done using metallic iron. The data was analyzed using a standard program that fits for Lorentzians [11]. EFG distribution fitting was made using the WMOSS program (version 2.5).

3 Results and discussion

The structure of the arc-melted Fe_3Al sample used for depositing the film has been confirmed by X-ray diffraction. XRD of the thin film coated on glass substrate is shown in Figure 1, which shows the presence of a broad peak at $2\theta=43^0$ and no other clear peaks.

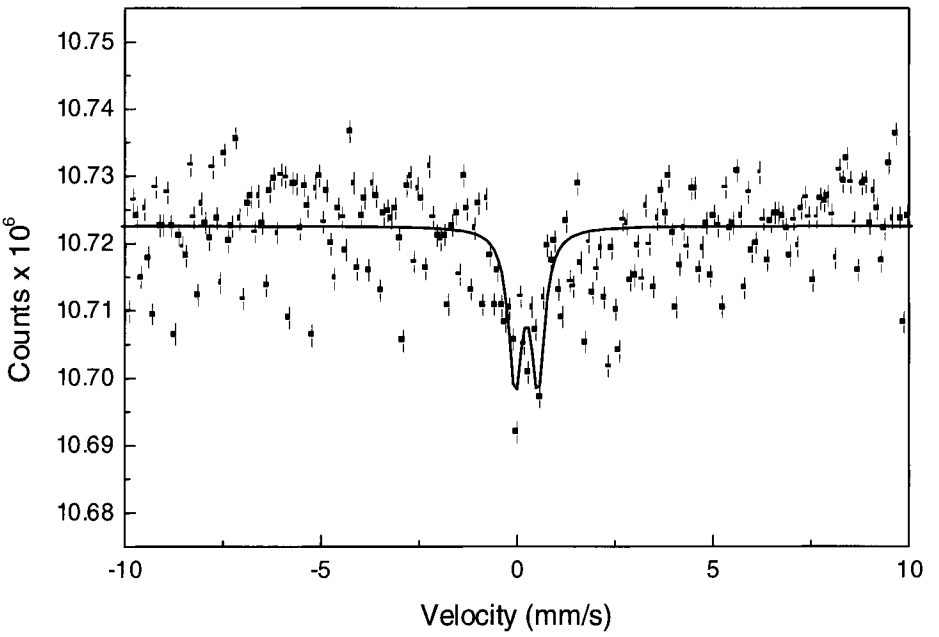

Figure 5 Mössbauer spectrum of 2000 Å Fe–Al film.

Figure 6 Quadrupole splitting distribution.

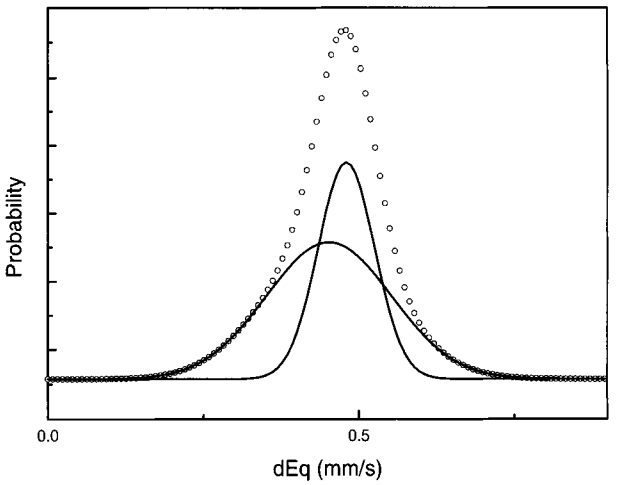

The absence of other peaks in the XRD spectrum indicates that the film has a definite texture. Both EDAX and Mössbauer studies of the film show the formation of an Al rich Fe–Al phase, which does not correspond to the original Fe_3Al composition. This indicates that during the evaporation process, differential evaporation of the constituents has occurred. Hence, the single peak in the XRD spectrum can be attributed to the preferential growth of the film the Fe (110) direction. Such preferential growth of Fe layers along the (110) direction has also been observed in Fe/Al multilayers [12]. The shift in the peak towards lower 2θ values is because of the expansion of the lattice due to the high amount of incorporated Al.

The SEM micrograph (Figure 2) of the film shows that it is made up of a number of nano islands that are distributed almost uniformly. On an average, the density of these islands is $3 \times 10^{12}/m^2$. Figure 3 shows an enlarged view of a typical island, the size of which is about 3 μm. Sizes of the larger and smaller clusters are about 588 and 382 nm. Composition of different parts of the film was determined using EDAX. The even background corresponds, on an average, to a composition of 36.6 at.% Fe and 63.5 at.% Al. The bright clusters correspond to a composition of 27.6 at.% of Fe and 72.4 at.% of Al.

MOKE study (Figure 4), shows a nearly square hysteresis loop with a coercive field= 53.12 Oe. The shape of the hysteresis loop suggests that the net magnetic moment is in the plane of the film. The observed magnetic moment can be attributed to the oxidation of the surface layer.

The room temperature Mössbauer spectrum of the sample is given in Figure 5. Although the spectrum appears to have a sextet along with a doublet, meaningful fitting of the sextet is not possible due to the very low percentage transmission effect, even with the high statistics that has been obtained (>10 million). Hence no attempt was made to fit the spectrum with a sextet. It was first fitted for a single quadrupole doublet, with a quadrupole splitting of 0.4604(±0.0155) mm/s and isomer shift 0.138(±0.01) mm/s (with respect to metallic iron). The peak width of the doublet (0.45 mm/s) is large, compared to metallic iron width of 0.24 mm/s. Hence, the central quadrupole doublet can be considered to be consisting of a number of close-lying Lorentzians corresponding to a distribution in the EFG. On fitting this doublet with a distribution corresponding to two distinct Fe sites, quadrupole splittings of 0.4478 and 0.476 mm/s are obtained. These distributions are close lying and the FWHM of the Gaussians in the probability distribution (Figure 6) are 0.2364 and 0.1065 mm/s respectively. The average quadrupole splitting derived from the theoretical fit is that obtained on fitting a single broad doublet. When the number of nearest Al neighbors to ^{57}Fe is ≥5, no magnetic splitting is observed and so a singlet is obtained if the nucleus is in a cubic environment or a doublet if the cubic symmetry is distorted. The observed average quadrupole splitting of 0.4604 mm/s is typical of Al rich Fe–Al systems [7] and compares well with the 0.46 mm/s reported for the non-cubic Fe_2Al_5 phase [13]. The analysis suggests that the formation of Al-rich Fe_2Al_5 non-cubic phase is thermodynamically favored during the condensation process. This conclusion is supported by EDAX results which show that the average Fe/Al concentration does not exceed 1:2.6. The formation of Fe_2Al_5 phase has been observed in Al-rich Fe–Al systems prepared by other non-equilibrium process also [7, 14].

Acknowledgement This work has been supported by the UGC-DRS and COSIST schemes of the Department of Physics, M.L. Sukhadia University, Udaipur. Varkey Sebastian and Ram Kripal acknowledge financial support under the UGC-FIP scheme and from CSIR. The authors also thank the Materials Science department, Sardar Patel University, India and IUC–Indore, India for SEM /EDAX, MOKE.

References

1. Arrot, A., Sato, H.: Phys. Rev. **114**, 1420 (1959)
2. Amils, X., Nogués, J., Suriñach, S., Baró, M.D., Muñoz, J.S.: IEEE Trans. Magn. **34**, 1129 (1998)
3. Principi, G.: Hyperfine Interact. **134**, 53(2001)
4. Dunlap, R.A., Lloyd, D.J., Christie, I. A., Stroink, G., Stadnik, Z.M.: J. Phys. F. Met. Phys. **18**, 1329 (1988)
5. Enzo, S., Frattini, R., Mulas, G., Principi, G.: J. Mater. Sci. **39**, 6333 (2004)
6. Noetzel, J., Brand, K., Geisler, H., Gorbunov, A., Tselev, A., Wieser, E., Möller, W.: Appl. Phys., A **68**, 497 (1999)

7. Noetzel, J., Meyer, D.C., Tselev, A., Mücklich, A., Paufler, P., Prokert, F., Wieser, E., Möller, W.: Appl. Phys. A **71**, 47 (2000)
8. Carbucicchio, M., Rateo, M., Ruggiero, G., Solzi, M., Turilli, G.: J. Magn. Magn. Mater. **196–197**, 33 (2000)
9. Hodges, J.A.: Nature **198**, 471 (1963)
10. Tutovan,V., Luca, D.: Appl Surf Sci **65–66**, 145 (1993)
11. von Meerwall, E.: Comp. Phys. Comm. **9**, 117 (1975)
12. Mengucci, P., Majni, G., Di Cristoforo, A., Checchetto, R., Miotello, A., Tosello, C., Principi, G.: Thin Solid Films **433**, 205 (2003)
13. Nasu, S., Gonser, U., Preston, R.: J. Phys. C **41**, 385 (1980)
14. Cardellini, F., Contini, V., Gupta,R., Mazzone, G., Montone, A., Perin, A. and Principi,G.: J. Mater. Sci. **33**, 2519 (1998)

Hyperfine Interact (2006) 169:1389–1392
DOI 10.1007/s10751-006-9456-5

Light-induced spin crossover observed for a Fe(II) complex embedded in a Nafion membrane

H. Winkler · V. Rusanov · J. J. McGarvey · H. Toftlund · A. X. Trautwein · J. A. Wolny

Published online: 17 November 2006

Abstract Light-induced spin crossover has been observed for the first time by means of Mössbauer spectroscopy for a Fe(II) complex embedded in a Nafion membrane. The results obtained confirm other independent observations we have made, which point to the possibility of generating a long-lived HS state by means of laser irradiation of the same system (C. Brady, PhD thesis Queens University, Belfast 2002; J.A. Wolny, H. Toftlund, J.J. McGarvey, C. Brady, manuscript in preparation).

Key words light induced spin crossover · Nafion membrane

1 Introduction

The spin–crossover complex [Fe(II)(btpa)]$(PF_6)_2$ (btpa=*N*,*N*,*N*′,*N*′-tetrakis(2-pyridymethyl)-6,6′-bis(aminomethyl)-2,2′-bipyridine, see Figure 1), that had previously been shown to undergo a complicated stereochemical rearrangement [2, 3] involving two distinct high-spin states, was investigated under various conditions by means of Mössbauer spectroscopy. We have addressed the question whether this complex is a suitable candidate for a photonic molecular switch. For this purpose, in particular to allow the homogenous

H. Winkler (✉) · V. Rusanov · A. X. Trautwein · J. A. Wolny
Institute of Physics, University of Lübeck, Lübeck, Germany
e-mail: winkler@physik.uni-luebeck.de

V. Rusanov
Department of Atomic Physics, University of Sofia, Sofia, Bulgaria

J. J. McGarvey
School of Chemistry, Queens University, Belfast, Northern Ireland, UK

H. Toftlund
Department of Chemistry, University of Southern Denmark, Odense, Denmark

J. A. Wolny
Faculty of Chemistry, University of Wroclaw, Wroclaw, Poland

Figure 1 The cation $[Fe(btpa)]^{2+}$.

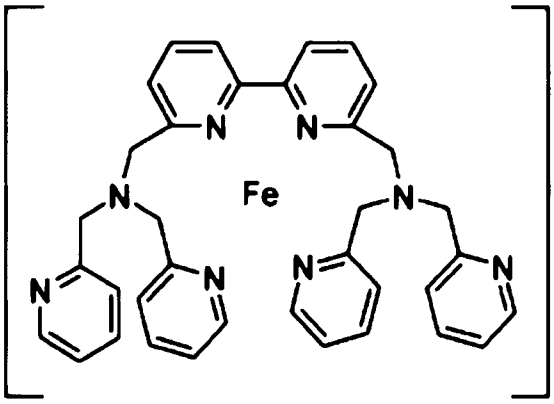

Table I Isomer shifts (IS) and quadrupole splittings (QS) for various preparations of $[Fe(btpa)]^{2+}$ at T=80 K and T=290 K

	80 K						290 K					
	IS (mm/s)			QS (mm/s)			IS (mm/s)			QS (mm/s)		
	LS	HS1	HS2	LS	HS1	HS2	LS	HS1	HS2	LS	HS1	HS2
$[Fe(bpta)](PF_6)_2$ solid powder	0.40	1.08	1.38	0.44	3.01	3.21	0.32	0.99	1.08	0.45	2.44	3.07
$[ZnFe(bpta)](PF_6)_2$	0.44	1.09	–	0.50	2.92	–	0.35	0.99	–	0.46	2.78	–
$[Fe(bpta)](PF_6)_2$ in Nafion without light	0.38	1.05	1.41	0.41	2.77	3.02	0.34	0.97	1.20	0.47	2.35	3.29
$[Fe(bpta)](PF_6)_2$ in Nafion with light	0.38	1.02	1.33	0.45	2.86	3.11	0.39	0.94	1.17	0.47	2.22	3.14

The error margins of the parameters are estimated to be about ±2%.

illumination of the sample with light, the molecules have been embedded in a membrane of Nafion®, which is a poly(tetrafluoroethylene) based ionomer developed by DuPont in the 1980s. The sample was illuminated by means of an array of 12 blue LEDS ($\lambda \approx 450$ nm).

2 Results

Comparison of the Mössbauer parameters of solid $[Fe(btpa)](PF_6)_2$ powder with those of the embedded species reveal no significant differences (see Table I). Two distinct high-spin states (HS1 and HS2) can be distinguished by differences in their hyperfine parameters. In the spectra taken from $[Zn_{0.9}Fe_{0.1}(btpa)](PF_6)_2$, however, only the high-spin doublet with the lower isomer shift and the lower quadrupole splitting is visible. This observation leads to the conclusion that these parameters are attributable to sixcoordinate Fe(II) corresponding to the C_2 symmetry of the zinc complex [3], while the larger values of both parameters correspond to quasi sevencoordinate Fe(II) (for a more detailed description of the two molecular conformations see ref. [4]).

Prior to illumination the sample displays a spin–crossover equilibrium, similar to that already reported for the complex in solution [2]. In Figure 2 the temperature dependence of the Mössbauer spectra taken with and without light irradiation are presented and the relative

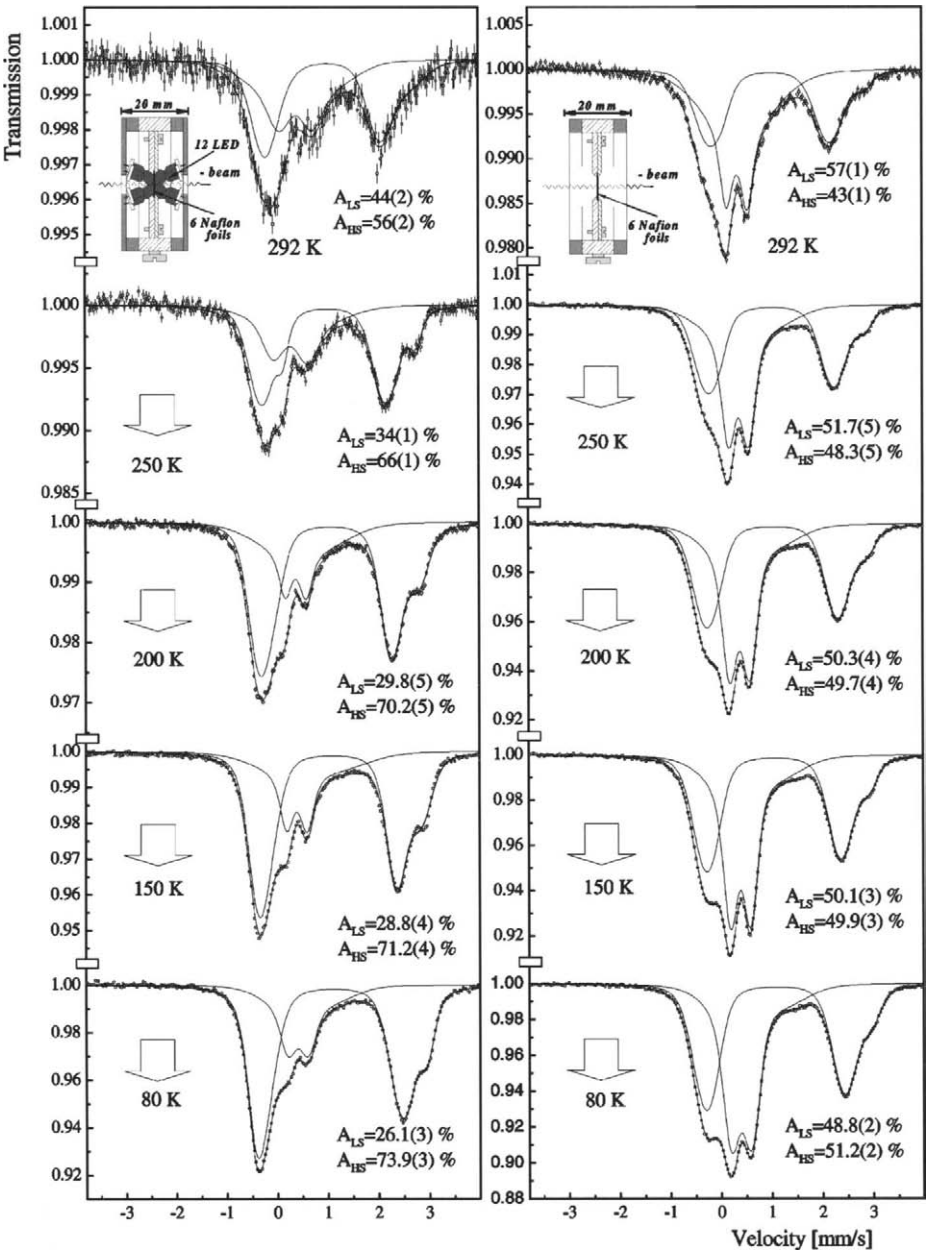

Figure 2 Temperature dependence of the Mössbauer spectra of $[Fe(II)(btpa)(PF_6)_2]$ embedded in Nafion with light irradiation (*left*) and for a dark sample (*right*). The *solid lines* represent the two subspectra corresponding to low-spin (LS) and high-spin (HS) Fe(II).

fractions of low- and high-spin iron are given. These fractions are determined by evaluating the spectra, taking into account a proper distribution of the electric field gradients for the two spin isomers. The distribution for the high-spin Fe(II) is chosen such that it encompasses both distinct high-spin states and the two solid curves in Figure 2 represent the contributions of either isomer. Continuous illumination of the sample during the whole temperature series with blue light obviously promotes the dynamics of the interconversion processes between the low- and high-spin isomers, as seen from the line broadening at temperatures above 250 K. Simultaneously, the spin equilibrium is shifted by the light in the direction of the high-spin (HS) isomer so that a depletion of the low-spin subspectrum (LS) is seen with decreasing temperature. There seem to exist two tentative explanations for this situation: either the continuous irradiation results in an enhanced population of the two HS states, of which one is trapped as the long-lived state while the other is in fast exchange with the LS one, or we deal with an example of the so-called paradoxical effect of light as described in [5]. In that work, the seemingly contradictory character of the photo-effect is suggested to become manifest by inducing the LS–HS conversion on the molecular scale while, under some conditions, speeding up the HS–LS cooperative relaxation in the solid due to the destruction of correlations.

3 Conclusion

The results obtained confirm other independent observations we have made by means of laser irradiation of the same system, i.e. that it is possible to switch the system partially into a long-lived high-spin state by means of visible light [1] (J.A. Wolny, H. Toftlund, J.J. McGarvey, C. Brady, manuscript in preparation).

References

1. Brady, C.: PhD thesis Queens University, Belfast (2002)
2. Schenker, S., Stein, P.C., Wolny, J.A., Brady, C., McGarvey, J.J., Toftlund, H., Hauser, A.: Inorg. Chem. **40**, 134 (2001)
3. Brady, C., Callaghan, P.L., Ciunik, Z., Coates, C.G., Døssing, A., Hazell, A., McGarvey, J.J., Schenker, S., Toftlund, H., Trautwein, A.X., Winkler, H., Wolny, J.A.: Inorg. Chem. **43**, 4289 (2004)
4. Wolny, J.A., Paulsen, H., Winkler, H., Trautwein, A.X., Tuchagues, J.-P.: in press
5. Varret, F., Boukheddaden, K., Codjovi, E., Enachescu, C., Linares, J. In: Gütlich, P., Goodwin, H.A. (eds.) Spin Crossover in Transition Metal Compounds. Top. Curr. Chem. **234**, 199 (2004) and refs. therein

Author Index to Volumes 167/1–3, 168/1–3 and 169/1–3 (2006)